

Anales de Mecánica de la Fractura

Conferência Ibérica de Fractura e Integridade Estrutural 2010

17, 18 e 19 de Março de 2010

Faculdade de Engenharia da Universidade do Porto, Portugal

XXVII Encuentro del Grupo Español de Fractura / 12^{as}. Jornadas de Fractura da SPM

Conferencia Ibérica de Fractura e Integridad Estructural 2010

17, 18 y 19 de Marzo de 2010

Facultad de Ingeniería de la Universidad de Oporto, Portugal

XXVII Encuentro del Grupo Español de Fractura / 12^{as}. Jornadas de Fractura da SPM

© ANALES DE MECÁNICA DE LA FRACTURA

Editado por la Secretaría del Grupo Español de Fractura

Reservados todos los derechos para todos los países.

Ninguna parte de esta publicación, incluido el diseño de la cubierta puede ser reproducida, almacenada o transmitida de ninguna forma, ni por ningún medio, sea electrónico o cualquier otro, sin previa autorización escrita por parte de la Editorial

I.S.S.N.: 0213-3725

Depósito Legal:

Impressão: RioGráfica

E-book: www.engebook.com

CIFIE 2010
March 17-19, 2010

organized by
Sociedade Portuguesa de Materiais – SPM and Grupo Español de Fractura GEF
Faculdade de Engenharia da Universidade do Porto - FEUP, Portugal,

Sponsors



walter+bai ag



Zwick / Roell

FUNDAÇÃO
LUSO-AMERICANA

FCT
Fundação para a Ciência e a Tecnologia
MINISTÉRIO DA CIÊNCIA, TECNOLOGIA E ENSINO SUPERIOR

U. PORTO

INDEX

KEY NOTE LECTURES

QUANTIFYING THE EFFECTS OF PLASTICITY ON CRACK STRESS FIELDS <u>E. A. Patterson</u>	3
ON A UNIFIED FATIGUE MODEL FOR STRUCTURAL ANALYSIS BASED ON SHAKEDOWN CONCEPT <u>Ky Dang Van</u>	9
FRACTURE MECHANICS APPLICATIONS FOR SPACE STRUCTURE WITHIN ESA PROGRAMS <u>Michael Windisch</u>	19
ELASTIN ANISOTROPY IN VASCULAR STRAIN ENERGY FUNCTIONS R. Rezakhaniha, E. Fonck, C. Genoud, <u>N. Stergiopoulos</u>	25

BIOMATERIALS AND BIOLOGICAL MATERIALS

6	INFLUENCIA DE LA EDAD Y LOS ANEURISMAS EN LA ROTURA DE LA PARED DE LA AORTA ASCEDENTE J.M. Atienza, F.J. Rojo, E. Claes, C. M. García-Herrera, C. García-Montero, R.L. Burgos, G.V. Guinea	31
42	MODE II FRACTURE OF CORTICAL BONE TISSUE N. Dourado, M.F.S.F. de Moura, J.J.L. Morais	37
91	EFFECTO DE LA LONGITUD DE ONDA DE LA RADIACIÓN UV SOBRE LA SEDA DE ARAÑA G. B. Perea , J. Pérez-Rigueiro, G. R. Plaza, G. V. Guinea, M. Elices	41
92	MODE I FRACTURE OF CORTICAL BONE TISSUE F.A.M. Pereira, N. Dourado, J.J.L. Morais, M.F.S.F. de Moura, J.M.C. Xavier, M.I.R. Dias, J.M.T. Azevedo	47
119	CONTACT DAMAGE IN ARTIFICIALLY AGED 3Y-TZP Z de Armas Sancho, A Mestra, E Jiménez-Piqué, M Anglada	51
121	DEVELOPMENT OF STRENGTHENING SOLUTIONS FOR DOWEL-TYPE WOOD CONNECTIONS C.L. Santos, A.M.P. de Jesus, J.J.L. Morais, E.R.M.A. Queirós, A.M.V. Lima	57
133	INFLUENCE OF SINTERING CONDITIONS ON THE MICROSTRUCTURAL AND MECHANICAL PROPERTIES OF POROUS Ti c.p. FOR BIOMEDICAL APPLICATIONS Y. Torres, J. Pavón, I. Nieto, J. A. Rodriguez	63

CASES

14 - P	RISK OF FAILURE INDICES APPLIED TO SELECTION OF MATERIAL FOR PIPELINES	
	M. V. Biezma, J. R. San Cristóbal, R. Martínez	71
16	ESTUDO DE ANÁLISE DE FALHA DE UM CABO DE AÇO PRÉ-ESFORÇADO DE UMA PONTE SUSPENSA	
	C. M. Branco, A. Sousa e Brito, T. L. M. Morgado	75
22	FRACTURA DEL VIDRIO TEMPLADO EN MUROS CORTINA	
	Francisco Capel, J Pablo Calvo	81
32 - P	ANÁLISIS DE FALLO DEL TUBO DE DRENAJE DE UN SOBRECALENTADOR	
	S. Cicero, R. Lacalle, R. Cicero, J. García	85
47	ANÁLISIS DEL FALLO POR FRACTURA FRÁGIL DE UNA TURBINA PELTON	
	D. Ferreño, J.A. Álvarez, E. Ruiz, D. Méndez	91
66 - P	ANÁLISIS DE FISURACIÓN EN COMPENSADORES DE DILATACIÓN DE LA RED DE AGUA SANITARIA DE UN HOSPITAL	
	R. Lacalle, S. Cicero, R. Cicero, J. García	97
83 - P	ANÁLISE DO COMPORTAMENTO ESTRUTURAL E À FADIGA DE ANTEPARAS DE LANCHAS RÁPIDAS EM ALUMÍNIO	
	Pedro Catarino, Rui F. Martins, Paulo Silva	103
88 - P	PREVISÃO DE VIDA À FADIGA DE UM COMPONENTE FERROVIÁRIO BASEADA NAS FUNÇÕES DA DISTRIBUIÇÃO CUMULATIVA NORMAL ESTANDARDIZADA DA TENSÃO EQUIVALENTE	
	T. L. Morgado, C. M. Branco, V. Infante	109
104 - P	UTILIZATION OF DURABILITY CRITERION TO DEVELOP AUTOMOTIVE COMPONENTS	
	L. C. H. Ricardo	115
109	FAILURE ANALYSIS OF HIGH-PERFORMANCE SURFACES USED FOR TRANSVERSAL STABILITY OF SHIPS (BILGE KEELS)	
	Hugo Rodrigues, Rui F. Martins, L. Leal das Neves, Paulo Silva	121

126	FATIGUE LIFE TIME PREDICTION OF POAF EPSILON TB-30 AIRCRAFT - PART I: IMPLEMENTATION OF DIFERENT CYCLE COUNTING METHODS TO PREDICT THE ACCUMULATED DAMAGE	
	B. A. S. Serrano, V. I. M. N. Infante, B. S. D. Marado	127
146 - P	PRE-VALIDATION OF WELDED JOINTS IN A BIKE FRAME	
	P. Machado, R.A. Cláudio, A. Valido, R. Duarte, O. Martins	133
155 - P	STRESS INTENSITY FACTOR CALIBRATION FOR A LONGITUDINAL CRACK IN A FUSELAGE BARREL	
	S.M.O. Tavares, P.M.S.T. de Castro	139

COMPOSITES, COATINGS

9	THIN OPTICAL FILMS FRACTURE: BEHAVIOR WITH INCREASING TEMPERATURE C. Baptista, A. Dantas, C. Matos, V. Belchior, R. Martins, E. Fortunato	147
18	RESISTANCE CURVES IN THE TENSILE AND COMPRESSIVE LONGITUDINAL FAILURE OF COMPOSITES Pedro P. Camanho, Giuseppe Catalanotti, Carlos G. Dávila, Claudio S. Lopes, Miguel A. Bessa, José C. Xavier	149
20	TAPER ANGLE OPTIMIZATION OF SCARF REPAIRS IN CARBON-EPOXY LAMINATES R.D.S.G. Campilho, A.M.G. Pinto, M.F.S.F. de Moura, I.R. Mendes, M.D. Banea, L.F.M. da Silva	155
21	MECANISMOS DE DEFORMACIÓN EN LAMINADOS DE MATRIZ POLIMÉRICA: CORRELACIÓN DIGITAL DE IMÁGENES Y MICROMECAÁNICA COMPUTACIONAL L. P. Canal, J. M. Molina-Aldareguía, C. González, J. Segurado, J. Llorca	161
23 - P	MECHANICAL BEHAVIOUR OF SANDWICH COMPOSITES WITH DIFFERENT CHARGED FOAM LAYERS C. Capela, J.A.M. Ferreira, F.V. Antunes, J.D. Costa	167
68 - P	STUDY OF CRACK ONSET AT HOLES IN PMMA. DIFFICULTIES IN CHARACTERIZING THE MATERIAL A. Leite, V. Mantič, F. París	173
70	COMPORTAMIENTO TERMOMECAÁNICO DE MATERIALES BASADOS EN TITANATO DE CIRCONIO Y CIRCONA CÚBICA E. López-López, R. Moreno, C. Baudín	179
76	CHARACTERIZATION OF DELAMINATION FRACTURE SURFACES UNDER MIXED MODE LOADING R.M.M. Marat-Mendes, M.M. de Freitas	185
77	MEASUREMENT OF THE ADHESION ENERGY IN A Cu-C INTERFACE D. Marcos-Gómez, J. Tamayo-Ariztondo, J. Garagorri, D. González, J.M. Molina-Aldareguia, M.R. Elizalde	191

100	ASSESSMENT OF THE MECHANICAL PROPERTIES ON NANOCLAYED POLYMER BASED COMPOSITES	
	P.N.B. Reis, J.A.M. Ferreira, J.D.M. Costa, S.S. Saucedo, M.O.W. Richardson	197
105	COMPORTAMIENTO EN FRACTURA DE UN FIELTRO DE FIBRA DE VIDRIO	
	Á. Ridruejo, C. González, J. LLorca	203
111	AN EXPERIMENTAL AND NUMERICAL STUDY OF THE INFLUENCE OF LOCAL EFFECTS ON THE APPLICATION OF THE FIBRE PUSH-IN TESTS.	
	Jon M. Molina-Aldareguía, M. Rodríguez, C. González, J.LLorca	209
134	ACCURATE SIMULATION OF DELAMINATION GROWTH UNDER MIXED-MODE LOADING USING COHESIVE ELEMENTS WITH MODE-DEPENDENT PENALTY STIFFNESS	
	A.Turon, E.V. González, P. Maimí, P. Camanho, J. Costa	215
138	COMPLIANCE REAL TIME MONITORING IN MODE II DELAMINATION FATIGUE TESTS	
	J. Vicens, J. Costa, J. Renart	221

CONCRETE, CEMENT

1	EFFECTO DE LAS CONDICIONES DE CURADO DEL HORMIGÓN EN SU COMPORTAMIENTO FRENTE A LOS CICLOS HIELO-DESHIELO Ghaida Al-Assadi, María Jesús Casati, Jaime Fernández, Jaime C. Gálvez	229
24	ESTUDIO EXPERIMENTAL SOBRE LAS TRANSICIONES ENTRE LOS MODOS DE FALLO EN VIGAS DE HORMIGÓN ARMADO SIN CERCOS A. Carpinteri, J. R. Carmona, G. Ventura	235
41	ENERGÍA DE FRACTURA DE PANELES DE MORTERO DE CEMENTO REFORZADOS CON FIBRAS DE VIDRIO (GRC) SOMETIDOS A IMPACTOS DE BAJA VELOCIDAD A. Enfedaque, V. Sánchez-Gálvez	241
69	ANÁLISIS DEL HORMIGÓN EN MODO MIXTO DE FRACTURA UTILIZANDO UN MODELO MESOESTRUCTURAL CON ELEMENTOS JUNTA C.M. López, M. Rodríguez, I. Carol	247
79	COMPORTAMIENTO MECÁNICO A ALTAS TEMPERATURAS DE CEMENTOS DE CENIZA VOLANTE ACTIVADOS ALCALINAMENTE Antonia Martín, Ana Fernández-Jiménez, José Ygnacio Pastor, Ángel Palomo	253
98	ESTUDIO SOBRE PANELES ESBELTOS DE HORMIGÓN DE BILMENTE ARMADOS R. Porras-Soriano, G. Ruiz, J. R. Carmona, R.C. Yu	259
122	COMPARISON OF THE CRACK PATTERN IN ACCELERATED CORROSION TESTS AND IN FINITE ELEMENTS SIMULATIONS B. Sanz, J. Planas, J.M. Sancho	265
124 - P	MODELING THE STATIC-DYNAMIC FRACTURE IN REINFORCED CONCRETE Luis Saucedo, Rena C. Yu, Gonzalo Ruiz	271
143 - P	DEVELOPMENT AND GROWTH OF THE FRACTURE PROCESS ZONE IN HSC UNDER A WIDE RANGE OF LOADING RATES Rena C. Yu, XiaoXin Zhang, Gonzalo Ruiz, Manuel Tarifa, Miguel Camara	277
149 - P	ANÁLISIS MESO-MECÁNICO DEL HORMIGÓN BAJO LA ACCIÓN DE PROCESOS EXPANSIVOS INTERNOS A. Campos, C.M. López, A. Aguado	283

EXPERIMENTAL METHODS

12 - P	CONTROLLED FRACTURE TESTS OF BRITTLE CERAMICS	
	C. Baudín, A. García, J. Hernández, M. López	291
17 - P	APLICACIÓN DE LA TOMOGRAFÍA AXIAL COMPUTERIZADA AL ESTUDIO DE MATERIALES Y PIEZAS FABRICADAS	
	P. M. Bravo, J. M. Alegre, I. I. Cuesta, M. Preciado	297
27	INFLUENCIA DE DIFERENTES VARIABLES DEL ENSAYO DE TRACCIÓN EN LA DEFORMACIÓN DE ROTURA	
	D. A. Cendón, J. M. Atienza, M. Elices	303
36 - P	ESTUDIO DE LAS TÉCNICAS PARA LA OBTENCIÓN DE PROBETAS SPT PREFISURADAS	
	I.I. Cuesta, C. Rodriguez, F.J. Belzunce, J.M. Alegre	309
39	NUEVO PROCEDIMIENTO EXPERIMENTAL PARA EL CÁLCULO DE FACTORES DE INTENSIFICACIÓN DE TENSIONES A PARTIR DEL ANÁLISIS DE IMÁGENES FOTOELÁSTICAS	
	F.A. Díaz, A. García-Collado, P. Siegmann, E.A. Patterson	315
51	METODOLOGÍA PARA LA OBTENCIÓN DE LA TENACIDAD DE FRACTURA DINÁMICA. APLICACIÓN A UN ACERO ESTRUCTURAL	
	N. García, D. Cendón, F. Gálvez, V. Sánchez-Gálvez	321
65	DETERMINACIÓN DE LA TENACIDAD A FRACTURA MEDIANTE EL ENSAYO SMALL PUNCH Y CURVAS ISO-A	
	R. Lacalle, D. Ferreño, J. García, J.A. Álvarez, F. Gutiérrez-Solana	327
73	ICE NECK FRACTURE EXPERIMENTS	
	A. Luque, J. Aldazabal, A. Martín–Meizoso, J.M. Martínez–Esnaola, J. Gil Sevillano, R.S. Farr, A. Hoodle	333
84 - P	ELASTOPLASTIC CONTACT IN AN INDENTATION IMPACT TEST BY FRACTIONAL CALCULUS	
	M. Mateos, F. Cortés, L. Aretxabaleta	339

96 - P		
TENSILE BEHAVIOUR OF SINGLE AND DOUBLE-STRAP REPAIRS ON ALUMINIUM STRUCTURES		
A.M.G. Pinto, R.D.S.G. Campilho, I.R. Mendes, R.F. Silva, A.G. Magalhães, A.P.M. Baptista		345
142		
IMPROVED EXPERIMENTAL TECHNIQUES FOR LIFE PREDICTION UNDER THERMOMECHANICAL FATIGUE (TMF) CONDITIONS		
Aitor García de la Yedra, Antonio Martín-Meizoso, Jose Luis Pedrejón		351
148		
USE OF OPTICAL TECHNIQUES IN THE ASSESSEMENT OF THE DISPLACEMENT FIELD NEAR THE CRACK TIP		
J. Ribeiro, M. Vaz, H. Lopes, F. Q. de Melo, J. Monteiro		357
152		
METHODOLOGY FOR IN-SITU STRESS INTENSITY FACTOR DETERMINATION ON CRACKED STRUCTURES BY DIGITAL IMAGE CORRELATION		
V. Richter-Trummer, P.M.G.P Moreira, S.D. Pastrama, M.A.P. Vaz, P.M.S.T. de Castro		361

FATIGUE

2	COMPARATIVE STUDY OF DIFFERENT FATIGUE CRACK GROWTH METHODS FOR THE DESIGN OF WIRE-WOUND VESSELS J.M. Alegre, I.I. Cuesta, P.M. Bravo	369
13	EFFECT OF CLAMPING FORCE ON FRETTING FATIGUE BEHAVIOUR OF BOLTED ASSEMBLIES: NUMERICAL AND EXPERIMENTAL ANALYSIS A. Benhamena, A. Amrouche, R.R. Ambriz, N. Benseddiq, G. Mesmacque, M. Benguediab	375
30 - P	ANÁLISIS DE LAS METODOLOGÍAS DE EVALUCIÓN DEL FACTOR AMBIENTAL EN TRANSITORIOS REALES DE CENTRALES NUCLEARES. R. Cicero, S. Cicero, R. Lacalle, I. Gorrochategui, J.A. Laso	381
37	ANALYSIS OF LOW-CYCLE FATIGUE DATA OF MATERIALS FROM SEVERAL PORTUGUESE RIVETED METALLIC BRIDGES A.M.P. de Jesus, A.L.L. da Silva, J.A.F.O. Correia, M.V. Figueiredo, J.M.C. Maeiro, A.S. Ribeiro, A.A. Fernandes	387
45	UN MODELO DE CRECIMIENTO DE GRIETA COMPATIBLE CON EL CAMPO DE WÖHLER A. Fernández Canteli, E. Castillo, D. Siegele	393
54	COMPORTAMIENTO EN FATIGA DE UNIONES ROSCADAS B. González, J.C. Matos, F.J. Ayaso, J. Toribio	399
62	FATIGUE BEHAVIOUR OF RESIN-INJECTED BOLTS: AN EXPERIMENTAL APPROACH A.M.P. de Jesus, J.F.N. da Silva, M.V. Figueiredo, A.S. Ribeiro, A.A. Fernandes, J.A.F.O. Correia, A.L.L. da Silva, J.M.C. Maeiro	405
64	COMPORTAMIENTO MECÁNICO DE MATERIALES MASIVOS SUPERCONDUCTORES DE SEGUNDA GENERACIÓN EN FUNCIÓN DE LA TEMPERATURA K. Konstantopoulou, J. Y. Pastor	411
85 - P	FATIGUE AND FRACTURE PATHS IN STRAIN-HARDENED EUTECTOID STEEL WIRES J.C. Matos, B. González, J. Toribio	417

87	SIMULACIÓN DEL CRECIMIENTO DE GRIETAS POR FATIGA BAJO CARGAS ALEATORIAS CON NASGRO	
	B. Moreno, J. Zapatero, P. Lopez-Crespo, J. Domínguez	423
101	EFFECTS OF MULTIAXIAL LOADING ON CYCLIC PLASTICITY AND FATIGUE BEHAVIOUR OF AUSTENITIC STAINLESS STEEL (AISI 303)	
	L. Reis, A. Cabrita, B. Li, M. de Freitas	429
102	MULTIAXIAL LOADINGS WITH DIFFERENT FREQUENCIES BETWEEN AXIAL AND TORSIONAL COMPONENTS IN 42CrMo4 STEEL	
	L. Reis, G. Perpétuo, B. Li, M. de Freitas	435
103	CRACK PROPAGATION IN PLANE STRAIN UNDER VARIABLE AMPLITUDE LOADING	
	L. C. H. Ricardo	441
131	RESISTENCIA A FATIGA DE LA ALEACIÓN DE ALUMINIO 7075-T6 EN FUNCIÓN DEL TIPO DE ENSAYO Y ESPESOR DEL RECUBRIMIENTO	
	M. Toledano, M. A. Arenas, J.J. Galán, L. Ramirez, S.M. Borja, A. Conde, A. Monsalve	447
154 - P	LIGHTWEIGHT STIFFENED PANELS FABRICATED USING EMERGING FABRICATION TECHNOLOGIES: FATIGUE BEHAVIOUR	
	P.M.G.P. Moreira, V. Richter-Trummer, M. A. V. Figueiredo, P. M. S. T. de Castro	453

FRACTURE

5	ANÁLISIS DEL COMPORTAMIENTO DINÁMICO DE VIGAS DE VIDRIO LAMINADO D. Rodríguez Argüelles, P. Fernández Fernández, M. López Aenlle, A. Fernández Canteli, M. J. Lamela Rey	461
7 -P	FRACTURA ANISÓTROPA DE ALAMBRES DE PRETENSADO COMERCIAL SOMETIDOS A ENSAYOS DE CORROSIÓN BAJO TENSIÓN F. J. Ayaso, A. Fernández-Viña, J. Toribio	467
31	UNA REVISIÓN CRÍTICA DE LOS DIFERENTES ENFOQUES INGENIERILES PARA LA EVALUACIÓN DE CONDICIONES DE BAJO CONFINAMIENTO TENSIONAL. S. Cicero, F. Gutiérrez-Solana, J.M. Varon	473
35	DETERMINACIÓN DE LA CARGA DE COLAPSO PLÁSTICO A TRAVÉS DE SUPERFICIES DE RESPUESTA EN PROBETAS SPT PREFISURADAS I.I. Cuesta, J.M. Alegre, P.M. Bravo	479
53	A UNIFIED APPROACH FOR IN-PLANE AND OUT-OF-PLANE CONSTRAINT ANALYSIS IN LINEAR ELASTIC CRACKED PLATES E. Giner, D. Fernández Zúñiga, J. Fernández Sáez, A. Fernández Canteli	485
72 - P	SIZE EFFECT IN THE SHEAR-COUPLED MIGRATION OF TILT BOUNDARIES WITH INTERGRANULAR NANOCRACKS A. Irastorza, A. Luque, J. Aldazabal, J.M. Martínez-Esnaola, J. Gil Sevillano	491
82	ESTUDIO DEL COMPORTAMIENTO EN FRACTURA DE VAINAS DE COMBUSTIBLE NUCLEAR FRAGILIZADAS POR HIDRUIROS. M.A. Martin-Rengel, F.J. Gomez, J. Ruiz-Hervias, L. Caballero, A. Valiente	497
90	INFLUENCIA DE LA GEOMETRÍA Y DE LA PROFUNDIDAD DE LA ENTALLA EN LA TRIAxIALIDAD Y COMPORTAMIENTO A FRACTURA DE PROBETAS SPT ENTALLADAS I. Peñuelas, R. Montero, C. Rodríguez, C. Betegón, F.J. Belzunce	503
97	MECHANICS OF INTERFACIAL CRACKS BETWEEN DISSIMILAR QUASICRYSTALS J. Planas, E. Radi, M.M. Stickle, P.M. Mariano	509

117	STRESS CORROSION CRACKING. A NEW MECHANISM APLIED TO HIGH STRENGTH STEELS	
	Javier Sánchez, José Fullea, Carmen Andrade	515
118	MOLECULAR DYNAMICS SIMULATIONS OF HYDROGEN EMBRITTLEMENT: PRELIMINARY RESULTS.	
	Javier Sanchez, Pedro de Andres, Carmen Andrade, José Fullea	521
125	DEFECTOS DISCRETOS EN GRAFENO	
	R. Serrano, M.P. Ariza, M. Ortiz	527
156 - P	NEW PARAMETER FOR DETERMINING PLASTIC FRACTURE DEFORMATION OF METALLIC MATERIALS	
	Rafael Bueno, José Sánchez , Teresa Rodríguez	533

NUMERICAL AND PROBABILISTIC METHODS

19	ESTUDIO NUMÉRICO DE LA INFLUENCIA DE LA CURVATURA DEL PERFIL DE FRENTE DE GRIETA EN LA EVOLUCIÓN DEL ESTADO TENSIONAL A LO LARGO DEL ESPESOR EN PROBETAS CT	
	D. Camas-Peña, J. García-Manrique, P. López-Crespo, A. González-Herrera	541
38	NUMERICAL MODELLING OF CORNER POINT SINGULARITIES AND THEIR EFFECT ON THE CLOSURE BEHAVIOUR OF 3D FATIGUE CRACKS	
	P. F. P. de Matos, D. Nowell	547
46 - P	USING A STANDARD SPECIMEN GEOMETRY FOR CRACK PROPAGATION UNDER PLAIN STRAIN CONDITIONS	
	J.M. Silva, V. Infante, F. Antunes, F. Ferreira	553
55	NANOINDENTATION INDUCED SILICON FRACTURE AND 3D MODELLING	
	E. Gorostegui-Colinas, J. Garagorri, M.R. Elizalde, D. Allen, P. McNally	559
58	NUMERICAL MODELING OF THE DYNAMIC COMPRESSION OF A CLOSED-CELL ALUMINUM FOAM	
	I. Irausquín, F. Teixeira-Dias, V. Miranda, J.L. Pérez-Castellanos	565
61	FEM ANALYSIS OF RIVETED CONNECTIONS AIMING FATIGUE AND FRACTURE ASSESSMENTS	
	A.M.P de Jesus, R. M. G. Pereira	571
67	A METHODOLOGY FOR RETICULAR STRUCTURES MODELING APPLIED TO THE FATIGUE ANALYSES OF RIVETED BRIDGES	
	R. C. Guedes Leite, R. Natal Jorge, A. M. P. de Jesus	577
75	A MODIFIED GTN MODEL FOR THE PREDICTION OF DUCTILE FRACTURE AT LOW STRESS TRIAXIALITIES	
	F. Reis, L. Malcher, F. M. Andrade Pires, J. M. A. César de Sá	583
89	FRETTING FATIGUE LIFE PREDICTION USING THE EXTENDED FINITE ELEMENT METHOD	
	C. Navarro, E. Giner, M. Sabsabi, M. Tur, J. Domínguez, F.J. Fuenmayor	589

141	COMPORTAMIENTO DEL MODELO DE FISURA COHESIVA EN PROCESOS DE CARGA-DESCARGA	
	J. Zahr Viñuela, J. L. Pérez Castellanos	595
147 - P	APLICAÇÃO DE TÉCNICAS DE SUB-MODELAÇÃO NO CONTEXTO DA ANÁLISE DE PROPAGAÇÃO DE FENDAS DE FADIGA EM ESTRUTURAS DE GRANDES DIMENSÕES	
	C.M.C. Albuquerque, P.M.S.T. de Castro, R.A.B. Calçada	601
150 - P	DUCTILE-TO-BRITTLE IMPACT TRANSITION TEMPERATURE FOR LOW-CARBON MICROALLOYED STEELS WITH HIGH NIOBIUM CONTENTS. A STATISTICAL APPROACH	
	M. Pérez-Bahillo, A. Martín-Meizoso	607
151	MODELING OF FATIGUE CRACK GROWTH IN MONOLITHIC INTEGRAL STIFFENED PANELS TAKING INTO ACCOUNT RESIDUAL STRESS	
	S. M. O. Tavares, V. Richter-Trummer, P. M. G. P. Moreira, P. M. S. T. de Castro	613
153 - P	NON-LINEAR ANALYSIS OF THE WHEEL / RAIL CONTACT	
	D.F.C. Peixoto, L.A.A. Ferreira, P.M.S.T. de Castro	619

POLYMERS

8	MODE I FRACTURE TOUGHNESS OF ADHESIVELY BONDED JOINTS IN A HIGH TEMPERATURE ENVIRONMENT	
	M. D. Banea, L. F. M. da Silva, R. D. S. G. Campilho	625
25 - P	EFFECTO DEL ENVEJECIMIENTO DE PLACAS DE ASIENTO DE CARRIL INYECTADAS CON TPE EN LA ELASTICIDAD DE LA VÍA PARA ALTA VELOCIDAD	
	I. A. Carrascal, J. A. Casado, S. Diego, J. A. Polanco, F. Gutiérrez-Solana	631
26	ESTIMACIÓN DE LAS CONDICIONES CRÍTICAS EN FATIGA DE UN COMPUESTO DE POLIAMIDA Y FIBRA DE VIDRIO POR MEDIO DE UN ENSAYO DE FATIGA ACELERADA (LOCATI) A PARTIR DE LA MEDIDA DEL DAÑO NETO.	
	I. Carrascal, J. A. Casado, S. Diego, J. A. Polanco, F. Gutiérrez-Solana, P. Miengo	637
29	DETERMINATION OF THE ENVELOPES FOR MODE-MIXITY EVALUATION OF ADHESIVELY BONDED STEEL	
	Filipe J.P.Chaves, L.F.M. da Silva, M.F.S.F. de Moura, D. Dillard	643
50	COMPORTAMIENTO A FRACTURA DE DOS GRADOS COMERCIALES DE PLA: INFLUENCIA DE LA ESTRUCTURA CRISTALINA	
	J. Gamez-Perez, J. Velázquez, E. Franco-Urquiza, J.I. Velasco, M.Ll. MasPOCH	647
80	FRACTURE BEHAVIOR OF AN EPBC FILM. STUDY OF THE RELATIONSHIP BETWEEN J_0 AND EWF	
	A.B. Martinez, A. Delgado, A. Segovia, M.A. Sanchez-Soto, A. Salazar	653
81 - P	DETERMINATION OF THE CRACK INITIATION ENERGY OF FILMS IN PLANE STRESS	
	A.B. Martínez, A. Segovia, D. Arencón, S. Illescas, J. Rodríguez	657
106	TEMPERATURE AND STRAIN RATE EFFECT ON MECHANICAL PROPERTIES OF ETHYLENE-PROPYLENE BLOCK COPOLYMERS	
	T. Gómez-del Río, A. Salazar, A. Cea, R. Hernández, J. Rodríguez	661
112	DETERMINACIÓN DE LA TENACIDAD A LA FRACTURA POR DIFERENTES METODOLOGÍAS DE UN PLA CON COMPORTAMIENTO DÚCTIL	
	J. Oropeza, C. Rodríguez, J. Belzunce, O. O. Santana, M. Ll. MasPOCH	667

116	DETERMINATION OF THE J-R CURVES OF ETHYLENE-PROPYLENE BLOCK COPOLYMERS BY MEANS OF DIFFERENT J-INTEGRAL METHODOLOGIES	
	A. Salazar, M. A. Garrido, J. Rodríguez, A. B. Martínez	673
128	COHESIVE LAWS IN ADHESIVES JOINTS: THE TEARING/DEBONDING TEST FOR CHARACTERIZATION OF THIN ADHESIVE FILMS	
	J.C. Suárez, S. Miguel, F. López, M.A. Herreros	679
129 - P	MIXED MODE DOUBLE CANTILEVER BEAMS TEST SPECIMEN FOR CHARACTERIZATION OF STRUCTURAL ADHESIVE JOINTS	
	J.C. Suárez, P. Pinilla, F. López, M.A. Herreros, M.V. Biezma	685

RESIDUAL STRESS, PEENING, SHAPE

11	DEVELOPMENT PROCESS OF A NUMERICAL SIMULATION FOR THE HAMMER PEENING FATIGUE LIFE IMPROVEMENT TECHNIQUE	
	R. Baptista, V. Infante, C. M. Branco	693
52 - P	OPTIMIZACIÓN DEL PROCESO DE ENDEREZADO POR LLAMA E IMPACTO SOBRE LAS PROPIEDADES DEL MATERIAL	
	J. García, R. Lacalle, D. Ferreño, J. A. Álvarez, F. Gutiérrez-Solana	699
71	INFLUENCIA DE LAS TENSIONES Y DEFORMACIONES RESIDUALES SUPERFICIALES EN LA DURABILIDAD DE ALAMBRES DE PRETENSADO EN AMBIENTE DE HIDRÓGENO	
	M. Lorenzo, V. Kharin, J. Toribio	705
108	CONSTRAINT EFFECT ON THE FRACTURE BEHAVIOUR OF THE SIMULATED HEAT AFFECTED ZONE OF AN X-70 STEEL	
	S. Rivera, R. Lezcano, C. Rodríguez, F.J. Belzunce, C. Betegón	711
110 - P	EVOLUCIÓN DE LAS INCLUSIONES DURANTE EL PROCESO DE TREFILADO EN ACEROS PERLITICOS	
	R. Rodríguez, F. J. Ayaso, M. Lorenzo, J. Toribio	717
120	EFFECTO DEL SHOT PEENING EN EL COMPORTAMIENTO A FATIGA DE ACEROS INOXIDABLES DÚPLEX	
	P. Sanjurjo, C. Rodríguez, I. F. Pariente, F. J. Belzunce	723
135 - P	EXPERIMENTAL RESULTS IN FRETTING FATIGUE WITH SHOT AND LASER PEENED SPECIMENS	
	J. Vázquez, C. Navarro, J. Domínguez	729
136	PREDICCIÓN DE VIDA A FATIGA POR FRETTING INCLUYENDO TENSIONES RESIDUALES	
	J. Vázquez, C. Navarro, J. Domínguez	735
137	FRAGILIZACIÓN POR HIDRÓGENO DE ACEROS PERLÍTICOS TREFILADOS SOMETIDOS A ESTADOS TRIAXIALES DE TENSION	
	D. Vergara, J. Toribio	741

WELDING

3	FATIGUE CRACK GROWTH BEHAVIOR IN 6061-T6 ALUMINUM ALLOY WELDS OBTAINED BY MIEA	
	R.R. Ambriz, G. Mesmacque, A. Benhamena, A. Ruiz, A. Amrouche, V. H. López	749
10 - P	EXPERIMENTAL AND NUMERICAL ANALYSIS OF FATIGUE LIFE IMPROVEMENT TECHNIQUES IN WELDED JOINTS OF STAINLESS STEELS	
	R. Baptista, V. Infante, C. M. Branco	755
34	FATIGUE BEHAVIOUR OF AA6082-T6 ALUMINIUM ALLOY FRICTION STIR WELDS UNDER VARIABLE AMPLITUDE LOADING	
	J.D. Costa, J.A.M. Ferreira, L.P. Borrego	761
56	THERMAL INFLUENCE OF WELDING PROCESS ON STRENGTH OVERMATCHING OF THIN DISSIMILAR SHEETS JOINTS	
	M. Iordachescu, J. Ruiz-Hervias, D. Iordachescu, A. Valiente, L. Caballero	767
60 - P	FATIGA DE BAJO NÚMERO DE CICLOS (LCF) A ALTAS TEMPERATURAS DE TUBOS SOLDADOS DE INCONEL® 625	
	L. Iturrioz, M. Isasa, R. Rodríguez-Martín, I. Ocaña, M.R. Elizalde, A. Martín-Meizoso	773
74	HYBRID FORMULATION SOLUTION FOR STRESS ANALYSIS OF CURVED PIPES WITH WELDED JOINTS UNDER BENDING	
	Luísa Madureira, Francisco Q. Melo	779
86	FATIGUE CRACK GROWTH BEHAVIOUR OF FRICTION STIR WELDED ALUMINIUM-LITHIUM ALLOY 2195 T8X	
	P.M.G.P Moreira, A.M.P. de Jesus, M.V.A. de Figueiredo, M. Windisch, G. Sinnema, P.M.S.T. de Castro	783
93	TENSILE-SHEARING STRENGTH IN ALUMINIUM RESISTANCE SPOT WELD AND WELDBONDED JOINTS	
	A.M. Pereira, J.A.M. Ferreira, F.V. Antunes, P.J. Bártolo	789
114 - P	EFFECT OF FATIGUE DAMAGE ON THE DYNAMIC TENSILE BEHAVIOR OF CARBON STEEL WELDED JOINTS	
	C. Rubio-Gonzalez, E. Miranda-Paniagua, G. Mesmacque	795

123 - P	
MICROESTRUCTURA Y RESPUESTA MECÁNICA A ALTAS TEMPERATURAS DE UNIONES SOLDADAS DE HAYNES 230®	
B. Sarasola, J. L. Pedrejón, R. Rodríguez-Martín, I. Ocaña, M.R. Elizalde	801
139	
APPLICATION OF TAGUCHI METHOD IN THE OPTIMIZATION OF FRICTION STIR WELDING PARAMETERS OF AN AERONAUTIC ALUMINIUM ALLOY	
C. Vidal, V. Infante, P. Peças, P. Vilaça	807

Fatigue

COMPARATIVE STUDY OF DIFFERENT FATIGUE CRACK GROWTH METHODS FOR THE DESIGN OF WIRE-WOUND VESSELS

J.M. Alegre¹, I.I. Cuesta¹, P.M. Bravo¹

¹Structural Integrity Group. Escuela Politécnica Superior.
University of Burgos. C/Villadiego s/n, 09001. Burgos. Spain.
E-mail: jalegre@ubu.es

ABSTRACT

This work presents a comparative study of different fatigue crack growth methods for the assessment of wire-wound pressure vessels. The winding consist of a wire helically wound edge-by-edge in pretension in a number of turns and layers around the outside of an internal cylinder. The final result is a cylinder with compressive stress and the wire layers under tension. Under working pressure conditions, the vessel will be subjected to pressurization-depressurization cycles. According to the ASME code requirements, for the assessment of the vessel under cyclic loading an analysis of the fatigue crack growth must be performed. In general, three different approaches can be used: (a) Postulate a 1/3 semi-elliptical shape unchanged during crack growth, (b) Postulate a semi-elliptical shape that is updated at the deepest point and at the surface points, and (c) calculate by numerical analysis the crack front evolution during crack growth. The last approach will be obviously the most accurate, but the increase on the final number of cycles must be evaluated in order to justify the computational effort. This is one of the aims of this work. In addition, the procedure for the 3D crack growth simulation on the wire-wound vessels is widely explained in this paper. The effect of the mesh size in the computation of the stress intensity factor along the crack front has been analysed, and important recommendations for 3D crack simulations are provided. The strategy to update the crack front geometry during the crack growth process, useful for ANSYS users, is also provided.

KEY WORDS: fatigue design, wire-wound vessels, crack growth simulation.

1. INTRODUCTION

The wire-winding of high pressure vessels is a technique usually applied to introduce initial compressive stresses in the inner core of the vessel, with the aim to improve the fatigue life under cyclic pressure conditions [1-3].

Basically, the winding method consists of a wire helically wound edge-to-edge in pretension in a number of turns and layers around the outside of the inner cylinder. With each wound-wire layer becomes greater and greater compressive stresses in the cylinder, while the internal wire layers are slightly relieved as a consequence of the radial compressive stress generated by the last wound layer. The final winding process is a vessel with internal compressive stress in the inner cylinder and a wire winding block under tensile stress. Under working pressure conditions the initial compressive stress in the cylinder decreases and the winding tensile stress increases, but the internal core of the vessel can remain under compression if the initial compressive stresses are low enough. The compressive stress level that can be introduced in the vessel is obviously limited by the yield stress of the material under compression.

In order to calculate the number of design cycles based on crack propagation approaches it is necessary to define an initial crack size and an allowable final crack.

The initial crack size to be used for the calculation of the crack propagation design cycles shall be based on the nondestructive examination method to be used. In general, a semielliptical surface crack with a ratio of depth to surface length of 1/3 can be assumed. The allowable final crack depth must be calculated using the Failure Assessment Diagram (FAD) present on the Fitness For Service procedures (FFS).

In this work, three different levels of fatigue analysis are evaluated and discussed. First, a semi-elliptical crack shape unchanged during crack growth is postulated. This allows the tabulated solutions provided by the main design codes to be used. However, the natural tendency of the crack growth is not considered. Second, a semi-elliptical crack shape that is continuously updated, using the deepest and surface points, during the crack propagation is assumed. And finally, a finite element analysis to calculate step-by-step the crack front evolution during crack growth is analysed. This last approach will be obviously the most accurate, but the increase on the final number of cycles must be evaluated in order to justify the computational effort. This is one of the aims of this work.

In addition to this study, the numerical procedure for the 3D crack growth simulation on the wire-wound vessels is widely explained. The effect of the mesh size in the computation of the stress intensity factor along the crack front is discussed. The strategy for updating

the crack front geometry during the crack growth process, as well as important recommendations for 3D crack simulations, is provided.

2. GEOMETRY AND STRESS DISTRIBUTIONS FOR WIRE-WOUND VESSELS

In order to compare the approaches mentioned above and hypothetical vessel is considered in this study. The main dimensions of the cylinder and winding block are presented on Figure 1. An internal diameter of $D_i = 100\text{ mm}$, an external diameter of the cylinder of $D_{if} = 200\text{ mm}$, and an external diameter of the winding block of $D_o = 300\text{ mm}$ are assumed. The vessel material is a high strength stainless steel with a yield limit of $\sigma_y = 1000\text{ MPa}$. The pretension in wire is $S_w/\sigma_y = 0.8$ and the design pressure of the wire-wound vessel is $P_w = 5000\text{ bar}$.

Analytical solutions can be found in literature to obtain the stress distributions generated by the winding process [1]. The radial and circumferential stress components, $\sigma_r(x_1)$ and $\sigma_t(x_1)$, for a cylinder coordinate x_1 , are defined by the following expressions:

$$\sigma_r(x_1) = - \left[1 - \left(\frac{D_i}{x_1} \right)^2 \right] \int_{D_{if}}^{D_w} \left(\frac{x}{x^2 - D_i^2} S_w(x) \right) dx \quad (1)$$

$$\sigma_t(x_1) = - \left[1 + \left(\frac{D_i}{x_1} \right)^2 \right] \int_{D_{if}}^{D_w} \left(\frac{x}{x^2 - D_i^2} S_w(x) \right) dx \quad (2)$$

where D_i is the inside diameter, D_{if} is the interface diameter between the winding and cylinder, D_w is the outside diameter of the actual winding layer.

Moreover, the corresponding stress in the winding diameter coordinate x_2 can be derived by:

$$\sigma_t(x_2) = S_w(x_2) - \left[1 + \left(\frac{D_i}{x_2} \right)^2 \right] \int_{x_2}^{D_w} \left(\frac{x}{x^2 - D_i^2} S_w(x) \right) dx \quad (3)$$

$$\sigma_r(x_2) = - \left[1 - \left(\frac{D_i}{x_2} \right)^2 \right] \int_{x_2}^{D_w} \left(\frac{x}{x^2 - D_i^2} S_w(x) \right) dx \quad (4)$$

Subsequently, the above equations can be easily integrated for a constant tensile stress value in wire during the winding process, $S_w(x)$, and they provide the stress distribution through the winding operation. Once the winding process has been concluded, the radial and circumferential stress components, both in the cylinder and the winding, can be obtained replacing D_w for D_o in the above expressions, where D_o

represents the outside diameter when the winding process is finished.

Figure 2 shows the circumferential stress distributions for the hypothetical vessel considered in this study, after the winding operation and under pressure conditions.

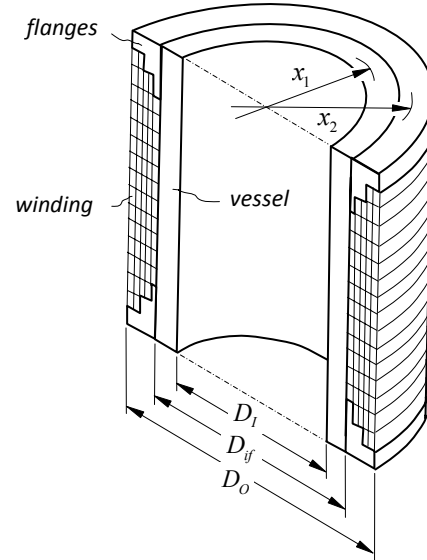


Figure 1. Nomenclature used for wire-wound vessels

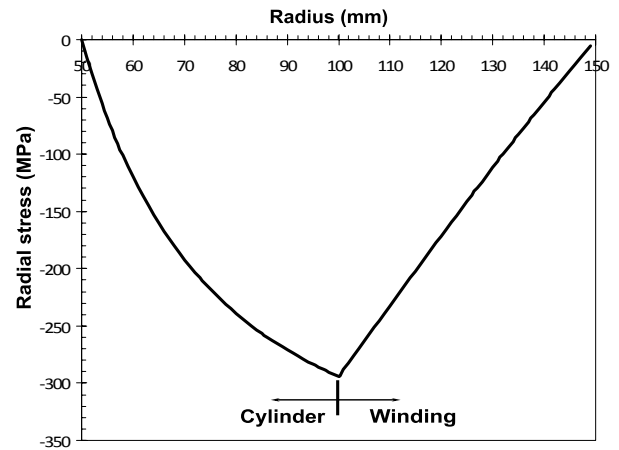
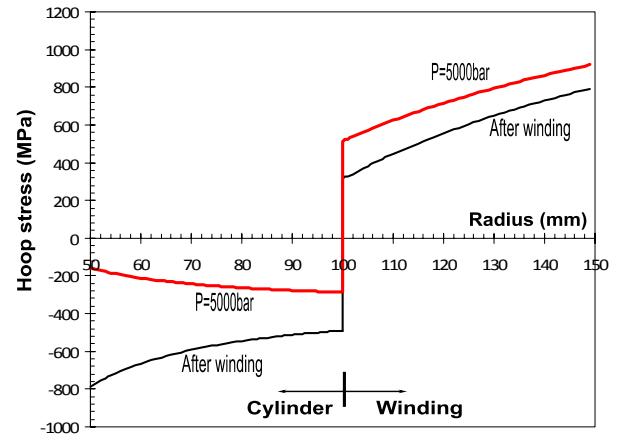


Figure 2. Radial and circumferential stress.

3. FATIGUE LIFE PROCEDURE

The first step for a fatigue life calculation is to consider an initial crack. In this paper, an internal crack in the longitudinal direction of the internal cylinder has been assumed, as is shown in Figure 3. A typical initial aspect ratio a_0/ℓ_0 of $1/3$ and an initial crack depth of $a_0 = 0.2 \text{ mm}$ are postulated.

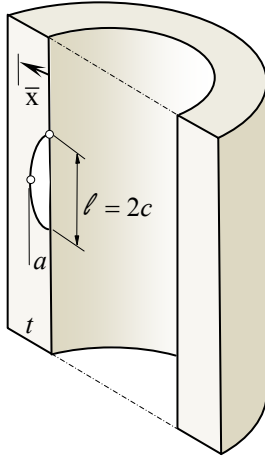


Figure 3. Semi-elliptical initial crack considered in the wire-wound pressure vessel

The next step consists on calculating the stress intensity factor range ΔK_I during crack propagation. Only the deepest point is considered for the first approach, both the deepest and surface points for the second approach, and all points along the crack front for the third approach.

According with the ASME code [1], the residual stresses introduced by the wire winding process have been considered separately by calculating an equivalent negative stress intensity factor $K_{I, res}$. The SIF by the internal pressure changes from a minimum stress intensity factor value of $K_{I(min)} = 0$ when $P=0$, to a maximum value of $K_{I(max)}$ for the working pressure $P = P_w$.

As a consequence, a crack in the vessel without internal pressure has a stress intensity factor of $K_{I(min)} + K_{I, res}$, and a crack in the vessel under internal pressure is subjected to an stress intensity factor of $K_{I(max)} + K_{I, res}$. Then, the SIF range is:

$$\begin{aligned} \Delta K_I &= (K_{I(max)} + K_{I, res}) - (K_{I(min)} + K_{I, res}) = \\ &= K_{I(max)} - K_{I(min)} = K_{I(max)} \end{aligned} \quad (5)$$

And the stress intensity ratio factor,

$$R = \frac{K_{I(min)} + K_{I, res}}{K_{I(max)} + K_{I, res}} \quad (6)$$

Note that the effect of the wire winding leads to a translation of the R -ratio towards negative values, without influence on the stress intensity range value.

Once the SIF range at the interest points is calculated, an incremental crack advance Δa for the deepest point is imposed (e.g. $\Delta a = 0.01 \text{ mm}$). The number of cycles ΔN_i needed to produce this crack advance is estimated using the propagation law as,

$$\Delta N_i = \frac{\Delta a}{C \cdot [f(R) \cdot \Delta K_I(a_0)]^m} \quad (7)$$

Where a propagation law that includes the effect of the R -ratio effect must be used, as

$$\frac{da}{dN} = C \cdot [f(R) \cdot \Delta K_I]^m \quad (8)$$

In this work the ASME code expression for R -ratio effect was considered [1], assuming material constants of $C(\text{mm}/\text{cycle}) = 5.29 \cdot 10^{-9}$ and $m = 3$ respectively.

The next step is to calculate the new crack size and shape for the next step. In general, the stress intensity range at any point of the crack front will be different. As a consequence, a different crack advance for each point is obtained after a block of cycles ΔN_i . At the deepest point the crack advance is the imposed value Δa , and the crack advance at other crack front point, Δc , is:

$$\Delta N_i = \frac{\Delta a}{C \cdot [f(R) \cdot \Delta K_I(a_0)]^m} = \frac{\Delta c}{C \cdot [f(R) \cdot \Delta K_I(c_0)]^m} \quad (9)$$

Where it can be easily derived that the crack advance at the surface is related with the imposed value at the deepest point, the stress intensity factor range for both positions, and the Paris law exponent m ,

$$\Delta c = \Delta a \cdot \left[\frac{\Delta K_I(c_0)}{\Delta K_I(a_0)} \right]^m \quad (10)$$

The procedure defined by the before steps is continuously repeated until the allowable final crack depth is reached. The number of cycles accumulated, from the initial crack to the allowable final crack, defines the fatigue life of the vessel. For the three approaches, the allowable final crack depth has been considered when the maximum SIF of the fatigue cycle reach a value of $K_{mat} = 150 \text{ MPa} \cdot \text{m}^{1/2}$. The maximum value of the SIF can be found at the deepest point or at the surface points of the crack, depending on the stress level of the vessel and the actual aspect ratio of the crack.

4. FATIGUE LIFE USING ANALYTICAL SOLUTIONS

An internal crack in the longitudinal direction of the vessel has been assumed in this study, as is presented in Figure 3. A typical initial aspect ratio of $a_0/\ell_0 = 1/3$, with an initial depth of $a_0 = 0.2\text{ mm}$, has been postulated. Other initial crack shape or sizes can be analyzed during the design stage of the vessel.

The first approach to obtain the fatigue life has been widely used over the past decades. It considers a semielliptical initial crack shape, and the stress intensity factor (SIF) is then calculated at the deepest point and used to define the next crack advance maintaining constant the aspect ratio of the crack. Its application is quiet direct, because nearly every one of the SIF solutions provided in the literature for semielliptical cracks is presented in tabulated form, as a function of the aspect flaw ratio.

The second approach can provide a more accurate fatigue life design, however the numerical procedure is more time-consuming because of the crack aspect ratio a/ℓ shall be updated as the crack size increases. The stress intensity factor, both at the deepest crack point and at the corner point, must be calculated in order to update the aspect ratio of the crack, assuming a semielliptical shape thought its fatigue propagation. This continuous crack shape updating requires tedious double interpolations if the conventional tabular solutions provided on the main design codes for SIF calculation are used [2]. Other closed-form equations can be used for this purpose [3].

For both approaches, the commonly method used to calculate the stress-intensity factor for internal semi-elliptical cracks in cylinders subjected to internal pressure (Figure 3) is based on the calculation of the stress distribution along the thickness, and then to fit it using a third-order polynomial equation as follows,

$$\sigma = A_0 + A_1 \cdot (\bar{x}/a) + A_2 \cdot (\bar{x}/a)^2 + A_3 \cdot (\bar{x}/a)^3 \quad (11)$$

Where A_0, A_1, A_2 y A_3 are the coefficients of the polynomial equation, a is the crack depth, and \bar{x} is the distance thought the wall measured from the flawed surface, as is shown in Figure 3.

If the distribution of stresses normal to the crack surface can be accurately represented by a single equation on the form of eq. (11) over the entire range of crack depths of interest, an alternate method can be used to compute K_I over this crack depth. The stress distribution can be obtained as:

$$\sigma = A'_0 + A'_1 \cdot (\bar{x}/t) + A'_2 \cdot (\bar{x}/t)^2 + A'_3 \cdot (\bar{x}/t)^3 \quad (12)$$

For each value of a/t the values of A'_i are converted to A_i values as,

$$\begin{aligned} A_0 &= A'_0 & ; & & A_1 &= A'_1 \cdot (a/t) \\ A_2 &= A'_2 \cdot (a/t)^2 & ; & & A_3 &= A'_3 \cdot (a/t)^3 \end{aligned} \quad (13)$$

The stress-intensity factor can be then calculated using the cubic polynomial stress relation given by eq. (11):

$$K_I = \sqrt{\frac{\pi a}{Q}} \cdot [G_0(A_0 + A_p) + G_1 A_1 a + G_2 A_2 a^2 + G_3 A_3 a^3] \quad (14)$$

where A_0, A_1, A_2, A_3 are the coefficients from eq. (11), A_p is the internal pressure of the vessel p that must be considered if the pressure can acts on the crack surfaces, G_0, G_1, G_2, G_3 are the free surface correction factors, and Q is the shape factor for an elliptical shape defined as,

$$Q = 1 + 1.493 \left(\frac{a}{c}\right)^{1.65} \quad \text{for } 0 \leq a/c \leq 1 \quad (15)$$

Each G_j has been obtained from the appropriate finite-element analysis by several authors, as Newman and Raju [2], and they are usually provided in tabulated form as a function of the crack shape, $a/2c$, and the crack size, a/t . These tabulated G_i -coefficients, or other similar, can be found in the pressure vessels design codes, as the ASME or API-ASME [3], or in usual literature [4]. In recent investigations analytical closed equations are provided, allowing the numerical integration of the propagation law to be more easily accomplished [3].

5. FATIGUE LIFE USING NUMERICAL SIMULATIONS

The last approach considered here uses the same postulated initial crack as the others approaches, but the crack shape is continuously updated along the fatigue crack growth process. In this sense, the SIF for all the points along the crack front must be determined. A consistent numerical procedure must be developed in order to carry out this approach.

The FE code ANSYS 10 [5] has been used for this numerical simulation. The mesh of the crack tip front has been constructed with 10 nodes singular elements, which have a quarter-node from the crack tip on the sides. A rate mesh transition of 1.5 has been considered from the crack tip to far from crack tip.

The displacement correlation technique (DCT) has been used for computing stress intensity factors in association with quarter-point elements [6-7].

The optimum value of the number of elements along the crack front was calibrated by comparison with analytical solutions. A reference geometry with a semi-elliptical crack was used. Figure 4 is shown two typical meshes for the crack line, and on Figure 5 is shown the effect of the number of elements on the crack front in the value for the calculated SIF. A mesh with 40 elements along the crack front, concentrated at the corner points has been selected as the most adequate.

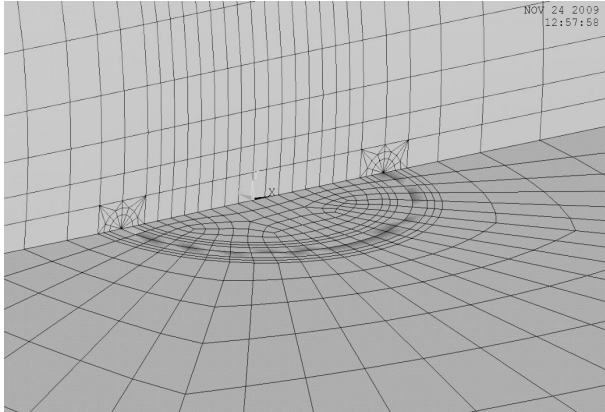


Figure 4. FE meshing used for crack growth simulation.

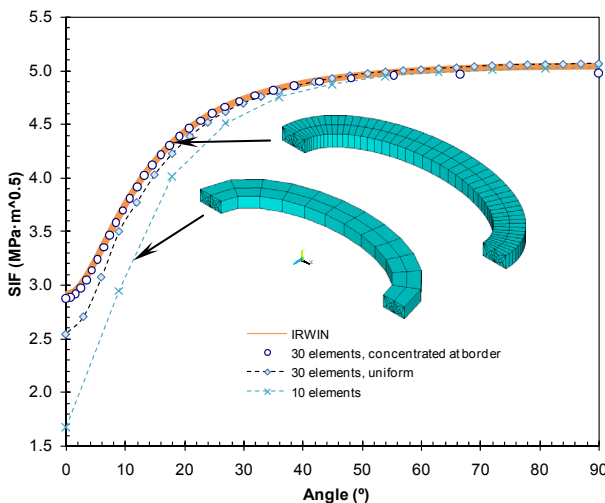


Figure 5. Effect of mesh on the SIF along the crack.

At each step, the fatigue crack growth has been estimated using the stress intensity range ΔK_I calculated for all points of the actual crack front and the propagation law of the material, according to the procedure explained on Paragraph 3. After a set of cycles, ΔN , the crack advance for each point of the crack front was obtained, and then a new crack front was defined to be used as the initial shape for the next step. This methodology allows the simulation, step by step, of the crack evolution from an initial crack to a final crack without assuming any standard shape during fatigue process. Figure 6 shows a simulation from an initial crack of $a_0 = 0.2mm$ and an initial crack shape of $a_0 / 2c_0 = 1/3$.

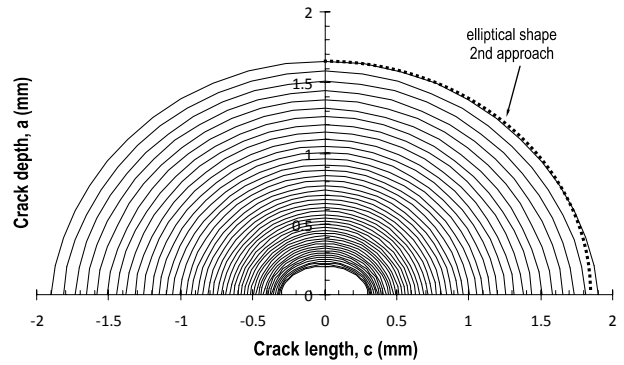


Figure 6. FE simulation of the fatigue crack growth.

In order to control the process the number of cycles for each step ΔN , is defined using the crack advance Δa_i , corresponding to the maximal ΔK_I in the crack front.

Also, in order to achieve numerical convergence a great number of steps must be done due to the small coefficients of the propagation law, that it must be integrated using small steps in order to well obtain the number of cycles. For both reasons, as an example, if the initial crack size considered was 0.2 mm, a maximum crack advance of 0.01 mm has been used. After that, the crack advance was increased proportionally to the actual crack size $\Delta a_{i+1} = \Delta a_i + \Delta a_i / 20$. The maximum increase used was 0.1 mm in order to obtain a correct crack evolution for the longer cracks.

6. COMPARATIVE RESULTS

In the next figures are provided the comparative results for the three approaches considered in the present paper. For all the cases analysed, an initial crack depth of $a_0 = 0.2mm$ was considered, and the final crack depth is considered when the maximum stress intensity factor on the crack front reaches a value of $K_{mat} = 150 MPa\sqrt{m}$.

Figure 7 presents the stress intensity factor evolution $K_{I(max)}$, at the deepest point, for the three approaches. It can be observed that for the 1st approach the value of the critical SIF is reached when the crack extends up to 9.70mm, and the number of cycles to failure is estimated to be $N_f(1) = 91200$, as shows the Figure 8.

Figure 9 presents the crack shape evolution during the fatigue calculation using the 2nd approach and the FE simulation. It can be clearly observed that the crack shape grows up to a value of $a/2c = 0.45$. The number of cycles to failure using the 2nd approach was $N_f(2) = 128047$, and using FE simulation up to $N_f(3) = 124200$.

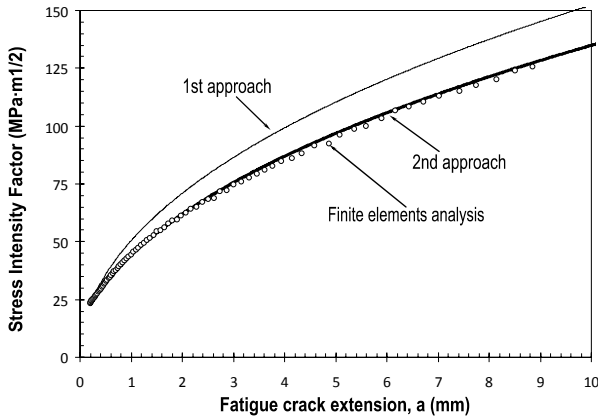


Figure 7. $K_{I(max)}$ at the deepest point

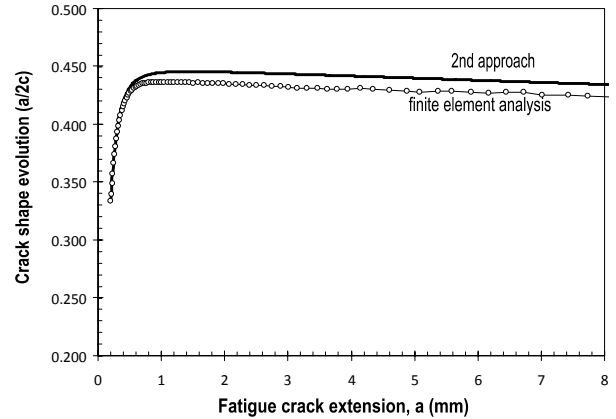


Figure 9. Crack shape evolution from $a_0 / 2c_0 = 1/3$.

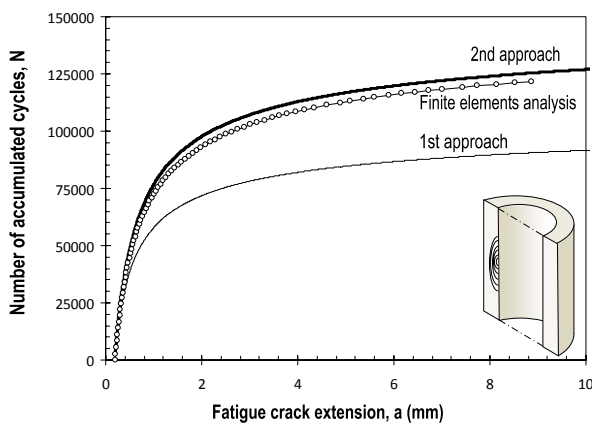


Figure 8. Number of accumulated cycles along the crack propagation, for the three approaches.

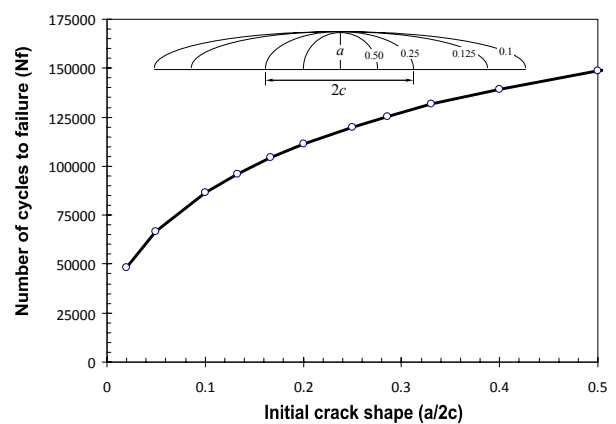


Figure 10. Effect of initial crack shape on the number of cycles to failure (2nd approach).

The initial crack shape considered has a relatively important effect on the fatigue life estimation. As an example, considering an initial crack shape of $a/2c = 0.45$ the number of estimated fatigue cycles using the 2nd approach reach a value of $N_f(2') = 139520$. The effect of the initial crack shape on the final fatigue life, using the 2nd approach is presented on Figure 10.

7. CONCLUSIONS

Three different approaches have been analysed to simulate the fatigue life of the wire-wound vessels. The results show that the first approach is not adequate to estimate the fatigue life, and a difference near the 50% can be obtained compared to the other approaches. The initial crack shape is also quite important in the number of cycles predicted. A tendency to $a/2c = 0.45$ is observed along the crack propagation, that results in a difference about 7% for the fatigue life respect to the initial assumption of $a_0 / 2c_0 = 1/3$. Finally, the difference between the numerical simulation and the 2nd approach is only 3%. In this case, the second approach provides a very good estimation of the fatigue life compared to a numerical simulation.

ACKNOWLEDGEMENTS

The authors acknowledge to JCyL research program (Project No.BU012A08) and NC-HYPERBARIC for sponsoring this research work.

REFERENCES

- [1] ASME (2007), *Alternative Rules for Construction of High Pressure Vessels in Boiler and Pressure Vessel Code, Section VIII, Division 3*. American Society of Mechanical Engineers.
- [2] ASME, *API 579-1/ASME FFS-1, in Fitness-For-Service*. (2007). American Society of Mechanical Engineers
- [3] Alegre JM, Bravo P.M., Cuesta I.I. (2009) Fatigue design of wire-wound pressure vessels using ASME-API 579 procedure. *Eng Fail Anal*, doi:10.1016/j.engfailanal.2009.08.008.
- [4] Newman J.C. and I.S. Raju, (1982) *Stress intensity factor for internal and external surface cracks in cylindrical vessels*. *J Press Vess Technol*. **104**: p. 293-298.
- [5] ANSYS 11 (2009). Finite elements code. User Manual.
- [6] Barsoum R.S. (1976) On the use of isoparametric finite elements in linear fracture mechanics, *Int. J. for Numerical Methods in Engineering* **10**, 25–37.
- [7] Bouchard P.O., Bay F., Chastel Y. (2003) Numerical modeling of crack propagation: automatic remeshing and comparison of different criteria. *Comput. Methods Appl. Mech. Engrg.* **192**, 3887-3908.

EFFECT OF CLAMPING FORCE ON FRETTING FATIGUE BEHAVIOUR OF BOLTED ASSEMBLIES: NUMERICAL AND EXPERIMENTAL ANALYSIS

A. Benhamena^{1,2,3,4}, A. Amrouche^{1,2,3,5}, R.R. Ambriz^{1,2,3}, N. Benseddiq^{1,2,3},
G. Mesmacque^{1,2,3} and M. Benguediab⁶

¹ Université Lille Nord de France, F-59000 Lille, France.

² USTL, LML, F-59650 Villeneuve d'Ascq, France.

³ CNRS, UMR 8107, F-59650 Villeneuve d'Ascq.

⁴ Laboratoire LPQ3M BP 763, University of Mascara, Algeria

⁵ UA, (Université d'Artois), France

e-mails: ali_benhamena@yahoo.fr,

abdelwaheb.amrouche@univ-lille1.fr, ricraf74@gmail.com

nouredine.benseddiq@univ-lille1.fr, gerard.mesmacque@univ-lille1.fr,

⁶ Department of Mechanical engineering, University of Sidi Bel Abbes,
BP 89, Cité Ben M'hidi, Sidi Bel Abbes, 22000, Algeria
e-mail: benguediab_m@yahoo.fr

ABSTRACT

One of the principal failures of bolting assemblies is the fretting. The combination of vibration and service load can introduce the damage of fretting fatigue on the contact surfaces of the assembly which trend to evoke a nucleation of crack and then the structure fracture. Contact pressure or clamping force and displacement at the interface or relative slip are two important factors which control the fretting wear and the fretting fatigue. This paper describes the effect of clamping force (tightening torque) on the fretting fatigue behavior of bolted assemblies. Both fretting fatigue experiments and simulation with FEM were carried out. With the increase of contact force, the sites of cracks initiation changed from the edge of the central hole to the free edge of the contact zone and the fretting fatigue life increase dramatically. A good correlation was found between the FEM simulations and the experimental results.

KEY WORDS: Clamping force, torque, fretting fatigue, crack initiation site, adhesive wear and abrasive wear.

1. INTRODUCTION

Bolted joints in mechanical structures transmit a more important effort in various applications. According to Valtinat et al [1] bolted joints have higher tensile and fatigue strengths than welded joints. The prediction of fracture and the reliability of such assembly in various practical applications are primordial given their impact on the economic plan and security. Fretting is caused by the oscillating movement with small amplitude that may occur between contacting surfaces subjected to vibration. The oscillations cause sliding to occur in a small region at the edge of contact, while the center of contact remains stuck together. Fretting causes wear and very high local stresses to occur at or near the edge of contact, which in turn, can result in the nucleation of cracks and the reduction of the fatigue life endurance. In high speed train vehicles, the fretting fatigue can be a serious problem and is one of the costliest sources of in-service damage According to Guo et al [2]. This damage is related to cyclic loading and relative displacement at

interface in such assembly. Because of its dramatic impact on structural integrity, the phenomenon of fretting has been extensively studied by various methods [3-4], analytical, numerical and experimental works have been carried out in order to achieve a better understanding the effect of some local mechanical parameters. Such as: The material behaviour, The contact pressure, the friction coefficient, the amplitude of relative displacement and tangential stress at the interface in order to predict the lifetime of assembly under fretting. The effect of contact force on the fretting fatigue life has received considerable attention from many investigations [5-8]. In the same context, an extensive examination of this subject can be found in references [9-11] in order to investigate the effect of relative displacement on the fretting fatigue life. The references cited above show that considerable work has been done to study the problems of fretting fatigue in various industrial applications. However, relatively few studies have focus only the effect of clamping force on

the fatigue behaviour of bolted plates by Aragon et al [12]. In service and under cyclic loading, the relative displacement at the interface is inevitable for bolted assemblies, in addition the effect of clamping force on the stress concentration close to the hole, the frictional stresses and the friction coefficient are not fully understood and represent a very active research field. The contact force and the amplitude of relative displacement are two key variables with which to control the fretting fatigue life in bolted assemblies. This fact has led the authors to the focus of the current study, which involves in first part, an experimental analysis to investigate the effect of contact force on the fretting fatigue life of bolted assembly, the sites of crack initiation, the fretting marks were examined by SEM/EDS. Numerical studies were carried out in order to identify the fields of compressive strain due to the clamping force and to validate the FEM model.

2. EXPERIMENTAL AND NUMERICAL MODEL

2.1. Experimental procedure

The experimental part of this work is subdivided in three steps: Tension test, fatigue test and microscopic examination (SEM and EDS).

2.1.1 Materials and specimens

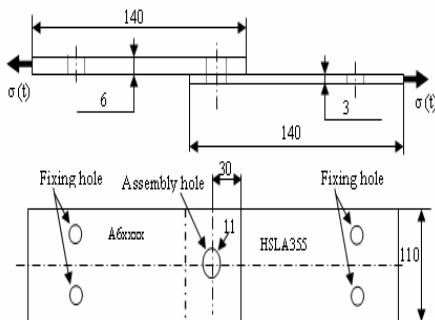


Figure 1. Specimen geometry (all dimensions in mm).

Aluminium alloy A6xxx from 6.0 mm thickness and high strength low alloy steel (HSLA355) of 3.0 mm thickness were used to produce (6.0 mm A6xxx + 3.0 mm HSLA355) joints for this investigation. Tensile specimens were machined with the dimensions and geometry as specified by the ASTM B57-06 designation. The quasi-static tension test was performed with a head speed displacement of 0.02 mm s⁻¹. Tensile strain of specimens was measured with an Instron® extensometer model 2620-601. Nominal mechanical properties of the A6xxx are 196 MPa in yield strength, 315 MPa in tensile strength, and 12% in elongation and

of the HSLA355 are 525 MPa in yield strength, 585 MPa in tensile strength, and 15% in elongation, [13].

2.1.2 Fretting fatigue test

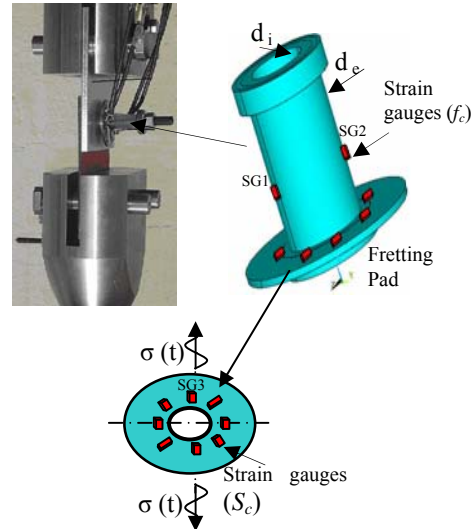


Figure 2. Schematic drawing of central part of the specimen used in fretting fatigue tests and the strain gauges

Fretting fatigue test method is shown in Fig. 1. Fretting fatigue occurs when a component subjected to cyclic loading is in contact with other component under a normal loading. Surface damage is induced by the microscopic motion at the contact surface between these two components which in turn reduces the fatigue life as compared to plain fatigue without fretting. In present work, the fretting pad was used to calibrate the fastening torque (clamping force) in the bolt during the fretting fatigue tests. The fixture, specially designed, includes steel bolts with a nominal diameter of 10 mm (M10x1.5), stainless steel nut, stainless steel washer and a pad, which is used for fixing strain gauges more easily, in order to control the clamping force. The pad was manufactured from steel with circular contact surface at the bottom (Fig.3) were stuck ten strain gauges pasted in different positions; CEA-06-062UW-120 strain gauges (SG) are used to measure the strains. At the pad, two strain gauges (SG1, SG2) have been glued on axial directions every 180° in order to measure the compressive axial strain due to the clamping force (f_c) and eight strain gauges (SG3 to SG10) have been glued on perpendicular plan to axial directions every 45° in order to establish a mean value for the strain due to the cyclic loading (S_c) during the fretting fatigue test, The gauge locations (SG) are shown in Fig. 2. The pad was placed between the washer and the aluminum plate in order to control the crack initiation at contact surface (position 1, see Fig. 3). Software was developed in the environment (LabVIEW) to detect

indirectly the crack initiation in a hidden area (contact zone) by the treatment of gauge signals.

Fretting-fatigue tests were conducted using constant amplitude loading using a sinusoidal waveform in tension-tension mode. The ratio of the minimum load and the maximum load or R ratio was 0.1 and the test frequency was 20 Hz in all the tests. The level of maximum load is 42.KN, which are approximately 35 percent of the average peak load observed in static tension tests of aluminum plate.

Contact pressure or clamping force and displacement at the interface or relative slip are important factors that control fretting wear and fretting fatigue. Four values of clamping force (tightening torque, $T = 2, 4, 6,$ and 8 daNm) was taken in order to determine the effect of this parameter (tightening torque) and to localize the zone where the fretting mechanism occur in bolted assemblies during the fretting fatigue test. It is known that the strain is proportional to the clamping force. After fretting fatigue test, the strain was measured using a digital data acquisition system (LabVIEW) and the Wheatstone bridge theory. Finally, examination of the wear scars on the joining surfaces between the two plates (aluminum-steel, position 2) and the interfaces between aluminum plate and pad (position 1) were investigated by scanning electron microscopy/energy dispersive X-ray (SEM/EDX) analysis in order to characterize the type of fracture damage in contact surface and to obtain insight into the failure mechanisms.

2.2 Finite element model

Fretting tests may be carried out in the partial slip regime. As highlighted by Hills et al. [14], it is very difficult to achieve a well controlled experiment using an external actuator due to the low displacement amplitudes. Finite element analysis (FEA) is an important tool to design practical mechanical joints, such as the bolted assemblies. According to the dimensions of the structure, a three dimensional model was generated using the commercial software ANSYS® (ANSYS 11, [15]). The bolted assembly shown in Fig. 2 is symmetric in the longitudinal direction (y direction). So, a half model with symmetry conditions was used in the finite element model FEM in order to reduce the calculation time (Fig. 4a). A three-dimensional brick elements (SOLID45) is used for modelling of bolted assembly. In addition, a surface-to-surface contact element, which consists of contact elements (CONTAC173) and target surface elements (TARGE169), is used on the interfaces between all connected parts of bolted assembly in order to simulate numerically the contact problems. Friction between the contact surfaces at the connection is modeled using the classical Coulomb model, where the friction coefficient was set at 0.2. A two-step nonlinear analysis was performed.

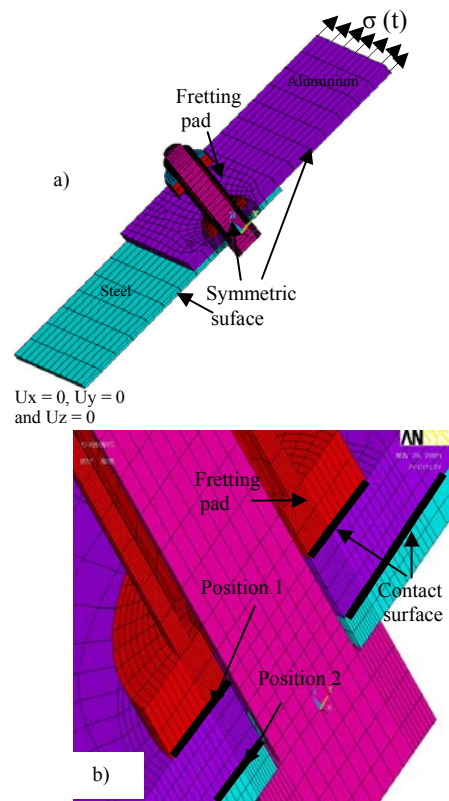


Figure 4. (a) Geometrical and finite-element mesh of assembly and (b) mesh near the contact (damaged surface: Position 1 and Position 2).

In order to simulate the clamping force numerically, in the first step, the preload (clamping force) was modelled as a uniform negative pressure applied on the screw and a positive pressure applied over a ring of 10.mm inner radius and 16.mm outer radius, this ring represents the action of the nut. This phase represent the joining of bolted assembly. After this operation, there is a relaxation of the tensile strain due to the deformability of the pad and the plates under the clamping force action, on attaining equilibrium and in the second step, this assembly was subjected to cyclic loading that generated a multi-axial stress fields at contact zone. The theory of incremental plasticity is introduced to modelling the material nonlinearity. The iterative method of Newton-Raphson is used as an approach to solve nonlinear equations by finite elements.

3. RESULTS AND DISCUSSIONS

3.1. Validation of the finite element model

The amount of tightening torque T required to achieve a set amount of preload f_c (clamping force) in a bolt

depends upon thread pitch, the friction coefficient in threading, bolt diameter, the friction coefficient between the nut and bolt and the mean collar diameter. For the threaded fasteners according to the ISO normalisation, there is a relationship between the tightening torque and the clamping force expressed by the following:

$$T = (0.161p + 0.583\mu_t d + \mu_h r_m) f_c \quad (1)$$

where, p : is the pitch, d : is the major diameter, f_c : is the clamping force, μ_t : is the friction coefficient between the nut and bolt, μ_h : is the coefficient of collar friction, r_m : is the mean collar diameter ($r_m = 1.25d$ and $r_m = 2$).

Although the torque-preload relationship can be calculated theoretically (eq. 1). But in practice it is not possible to accurately measure the bolt tension in a joint in service. So, it is better to measure both parameters (T , f_c) and hence calibrate the bolt tension experimentally. To ensure that a desired preload (clamping force) has been achieved with a bolt, it is more practical to use a torque wrench to apply the load to the bolt through the nut (see Fig. 1). The axial strain measured by the strain gauges (SG1, SG2) were recorded for each applied torque level. The theoretical expression for the relation between the clamping force and the axial strain is

$$f_c = \pi E_p \varepsilon_m \frac{d_e^2 - d_i^2}{4} \quad (2)$$

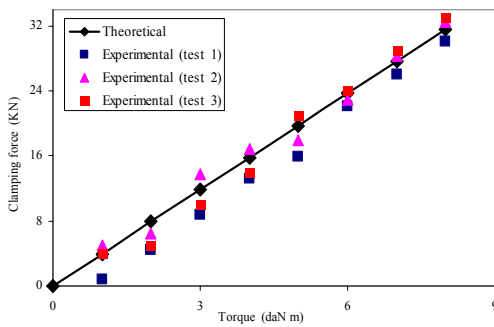


Figure 5. Clamping force versus tightening torque

where, d_i and d_e : are the internal and external diameters of the pad, respectively. E_p : is the young's modulus of the pad. ε_a : is the compressive axial strain measured by SG1 and SG2. The theoretical (Eq. 1) and experimental results are illustrated in Fig. 5; this presents the clamping force variation according to the tightening torque. We note a fairly good agreement between the theoretical and experimental results.

These results were confirmed by the numerical analysis presented in Fig. 6. This latter shows the compressive strain axial during the simulation of a fretting fatigue test

under maximal cyclic loading equal to 70MPa and a tightening torque value of 8daN.m.

We also notice in this case that the compressive strain is strongly concentrated at the interface between the pad and the aluminium plate. This phenomenon can be explained by the fact of strain incompatibility at the interface and the frictional coefficient effect.

Indeed, under this condition and in position at the pad, the compressive strain measured by the strain gauges (SG1, SG2) is 0.001195. At the same position, the compressive strain is calculated numerically and its value equal to 0.001273.

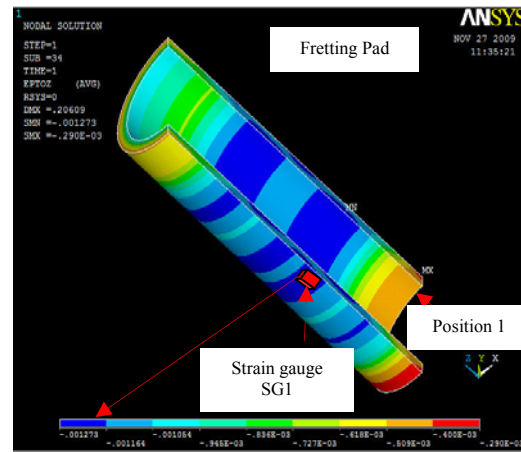


Figure 6. Compressive strain at the pad under maximal cyclic loading 70.MPa and torque 8. daN.m

According to the experimental, theoretical and numerical analysis, it can be seen that the result gave excellent correlation between various methods, thus establishing confidence in the results of the finite element modelling for bolted assemblies.

3.2. Inspection of damage

Many contact problems can be solved with the help of the Hertz theory [16] in order to obtain the surface stress distribution and subsequent bulk stress and strain states. However when a contact does not fulfil the Hertz assumptions, the analytical solution may differ significantly from the real one. This problem has been solved by [17] for the case of the spherical contact submitted to stick-slip behaviour. This situation happens when the tangential load is lower than the product between the normal load and the friction coefficient. Globally the contact is sticking (adhesion), but to respect the Coulomb friction law over the entire contact interface, a slipping annulus appears at the periphery of the contact zone. According to these authors, the contact

zone is subdivided in two zones (adhesion and slip zones).

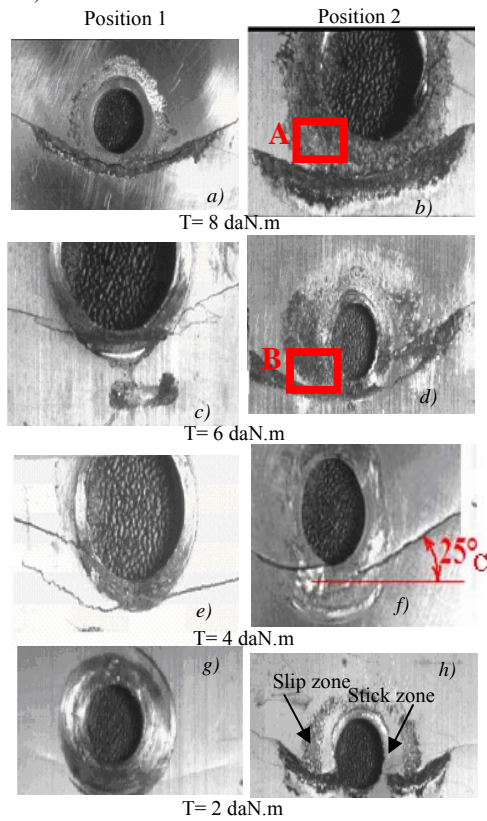


Figure 7. Crack propagation at various tightening torque under maximal cyclic loading 70 MPa.

In this study, we can see the appearance of adhesion and slip zones only at lower values of torque (Fig. 7h) while for higher value; the slip zone is disappeared completely and appears only the adhesion zone. This behaviour can be explained by the fact that the decrease of torque value (clamping force) leads a decreasing of the adhesion zone and therefore an increasing of the slip zone, which favoured the partial sliding at the interface of bolted assemblies. We note that the initiation and cracks propagation taken a position at the interface between the adhesion and slip zones (Fig. 7c-h). One can thus conclude that the position of crack initiation is related directly on the change of adhesion zone size. This latter is varied as function of clamping force level. In other words, for higher torque value, a large zone of adhesion leading to a slip zone very narrow, the initiation and crack propagation occurs at the border contact in the interface or outer edge of the contact region. However, it can be observed that for the range of means value of torque, which lead to reduce the size of adhesion zone and to raise the size of slip zone, consequently, the

initiation and crack growth is located within the contact zone at the interface between the adhesion and slip zones. This phenomenon can be explained by the fact of change of net pressure acting on each zone (adhesion and slip zones) in the contact zone. We note also that, whatever the torque value, the frictional marks take an elliptical shape parallel to the cyclic loading direction and its size is more pronounced for higher torque value. This behaviour is in good agreement with experimental observations of Wagle et al. [18].

3.3. Wear mechanisms

To better understand the torque effect on the wear mechanism of such bolted assembly (steel-aluminium) under cyclic loading, a thorough examination of damage surface at the interface between the plates (position 2) using SEM-EDS. Because the degradation and crack initiation was more pronounced in this position for each torque level according to experimental result (Fig. 7) and the experimental observations of Wagle et al. [18]. Fig. 8a showed the overall topography of aluminium alloy, before the fretting fatigue test (in state virgin). The analysis by EDS (Fig. 8b) indicates a strong presence of Al, is a typical in this kind of aluminium alloy. The SEM micrograph of Fig. 8c (from area 'B' of Fig. 7d) shows the presence of wear debris of the damaged surface of aluminium for a torque value equal to 6 daN.m. The damaged areas is covered by with narrow grooves (typically in the range of 5–50 μm wide), wear debris and a number of micro cracks, were produced at a position and orientation different relative to sliding direction (cyclic loading direction). According to this figure, we can be noted that the wear mechanism occurred in this case by adhesion. Comparison of EDS analyses of worn surface (Fig. 8d) and that of unworn surface (without fretting, Fig. 8b), shows the loss of aluminium (Al) from damaged surface with increasing of the torque. So, the intensity of Al peak decreased and that of Fe and Si peaks increased with increased in torque value (6 daN.m). It is likely that this loss of Al occurs under the action of harder particles components of Fe and Si of steel specimen under fretting condition. From the above observations, we showed that the torque value is a very important effect on the size of adhesion zone (Fig. 7). At very high torque (8 daN.m), we can be note that the morphology of damaged area (Fig. 8e) is very different compared to a torque value of 6 daN.m (Fig. 8c). This means that the wear mechanism is related to the torque value. In other words, the increasing of torque leads to an increasing of the frictional stresses and to reduce the relative slip at the interface of bolted assembly

4. CONCLUSIONS

The aim of this study is to analyze the effect of tightening torque on bolted assemblies under fretting fatigue condition, from these experimental and numerical results, we can deduce the following conclusions:

- The developed finite element modelling approach to simulate clamping force (tightening torque) in the bolt of such bolted assembly was validated against the experimental results.
- The wear mechanism and contact surfaces degradation depends on the magnitude of tightening torque.
- The adhesive wear dominates at tightening torque and fretting fatigue cyclic number lower while the abrasive wear dominates for tightening torque and fretting fatigue cyclic number higher.
- The size of the adhesion and slip zones on contact zone is related at the magnitude of tightening torque

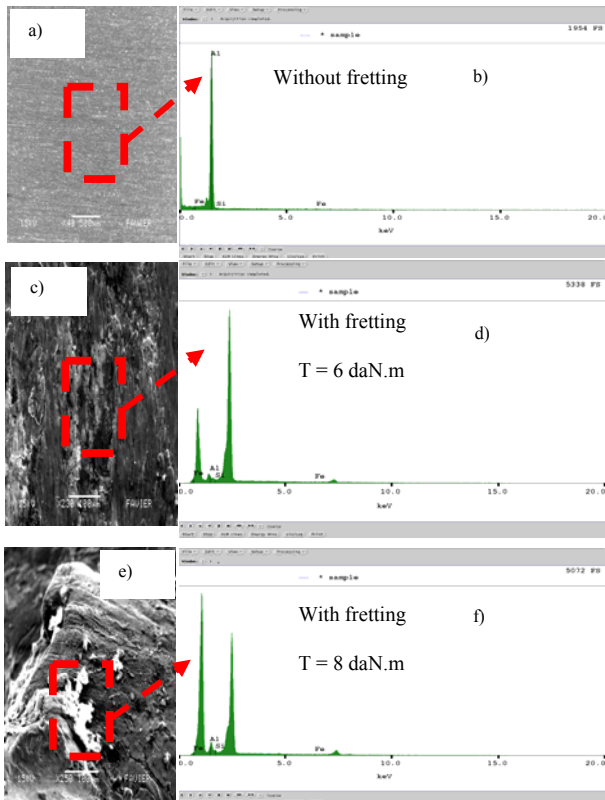


Figure 8. (a-f) SEM micrographs and EDS analysis of aluminium plate under fretting and without fretting at different tightening torques.

5. RERERENCES

[1] Valtinat, G., Hadrych, I., Huhn, H., “Strengthening of riveted and bolted steel constructions under fatigue loading by preloaded fasteners experimental and theoretical investigations”. AISC, Roanoke/ USA 2000.

[2] Guo, R., Duan, R.C., Mesmacque, G., Zhang, L., Amrouche A. and Guo, R., Fretting fatigue behavior of riveted Al 6XXX components”, *Materials Science and Engineering A*, pag. 398-401, 2008 (483-484).

[3] Zhou, Z.R., Nakazawa, K., Zhu, M.H., Maruyama, N., Kapsac, P.h. and Vincent, L., “Progress in fretting maps”, *Tribol Int*, pag. 1068-1073, 2006 (39).

[4] Shinde, S., Hoepfner, D.W., “Quantitative analysis of fretting wear crack nucleation in 7075-T6 aluminum alloy using fretting maps”, *Wear*, pag. 271-276, 2005.

[5] Nakazawa, K., Maruyama, N. and Hanawa, T., “Effect of contact pressure on fretting fatigue of austenitic stainless steel”, *Tribol Int*, pag. 79-85, 2003.

[6] Anton, D.L., Lutain, M.J., Favrow, L.H., Logan, D. and Annigeri, B., “The effects of contact stress and slip distance on fretting fatigue damage in Ti-6Al-4V/17-4PH contacts”, *ASTM STP 1367*; pag. 119-140.

[7] Waterhouse, R.B., “Plastic Deformation in Fretting Processes - A Review -”, *ASTM STP 1367*; pag. 3-18.

[8] Fernando, U.S., Farrahi, G.H., Brown, M.W., “Fretting fatigue crack growth behaviour of BS L45 4 percent copper aluminium alloy under constant normal load”. *ESIS. Mech Eng*; pag. 183-195, 1994.

[9] Lee, H., Mall, S., “Investigation into effects and interaction of various fretting fatigue variables under slip-controlled mode”, *Tribol Int*, pag. 1213-1219, 2006.

[10] Nakazawa, K., Sumita, M., and Maruyama, N., “Effect of relative slip amplitude on fretting fatigue of high strength steel”, *Fatigue Fract Engng Mater Struct*, pag. 751-759, 1994 (17).

[11] Vingsbo, O., Soderber, S., “On fretting maps”, *Wear*, pag. 131-147, 1988 (126).

[12] Aragon, A., Alegre, J.M., Gutiérrez, S.F., “Effect of clamping force on the fatigue behaviour of punched plates subjected to axial loading”, *Engineering Failure Analysis*, pag. 271-281, 2006.

[13] Catimel, A., Savanne, F., “Durabilité en fatigue de structures assemblées par rivetage”, *Rapport interne*, Mechanic laboratory of Lille (LML), 2008.

[14] Hills. D.A., Nowell. D., “Mechanics of fretting fatigue”. Dordrecht: Kluwer Academic publishers; 1994.

[15] ANSYS v11.0, Ansys Inc. Documentation.

[16] Hertz, H., “On the contact of elastic solids”, *Journal für die reine und angewandte Mathematik*, pag. 156-171, 1882.

[17] Mindlin, R.D., “Compliance of elastic bodies in contact”, *ASME Journal of Applied Mechanics*, pag. 259-268, 1949.

[18] Wagle S, Kato H. “Ultrasonic detection of fretting fatigue damage at bolt joints of aluminium alloy plates”, *International Journal of Fatigue*, pag. 1378-1385, 2009.

ANÁLISIS DE LAS METODOLOGÍAS DE EVALUACIÓN DEL FACTOR AMBIENTAL EN TRANSITORIOS REALES DE CENTRALES NUCLEARES.

R. Cicero^{1,2}, S. Cicero¹, R. Lacalle^{1,2}, I. Gorrochategui³, J.A. Laso¹

¹ Departamento de Ciencia e Ingeniería de Materiales, E.T.S. de Ingenieros de Caminos, Canales y Puertos, Universidad de Cantabria
E-mail: cicror@unican.es

² Inesco Ingenieros, S.L

³ Centro Tecnológico de Componentes

ABSTRACT

El medio en el que se encuentran inmersos los componentes de las centrales nucleares disminuye, generalmente, la vida a fatiga de estos. A este respecto, se han obtenido diferentes expresiones para el cálculo del efecto ambiental ante unas condiciones dadas, si bien todavía no se ha conseguido desarrollar una metodología de aplicación para la evaluación de transitorios, y especialmente los transitorios reales que suceden en planta y que son analizados mediante sistemas de monitorización. En este trabajo se analizan y discuten las metodologías empleadas actualmente para el cálculo del factor ambiental y, además, se propone un nuevo procedimiento implementable fácilmente en los actuales sistemas de monitorización.

Palabras clave: factor ambiental, fatiga, sistemas de monitorización, pares de carga, picos, valles.

1. INTRODUCCIÓN

En la actualidad se hace necesario centrar esfuerzos en la búsqueda de métodos precisos para la evaluación de la influencia del medio ambiente en el daño a fatiga de los componentes de centrales nucleares. Estos métodos han de tener en cuenta las variaciones que suceden en las condiciones del medio a lo largo de los transitorios (temperatura, concentración de oxígeno...), la composición de los materiales, el proceso de carga,...

La implantación de un sistema de monitorización (SM) que registre e implemente las condiciones reales del medio y el tipo de sollicitación en todo momento, y que aplique estos datos en tiempo real para el cálculo del daño por fatiga, puede ser la solución idónea para la evaluación del daño por fatiga, dado que de este modo se podría (por ejemplo) establecer un criterio fiable para la toma de decisiones sobre extensiones de vida de las centrales nucleares (ej., 60 años), en lo que a este mecanismo de degradación se refiere.

Por este motivo, en este artículo se analizan y discuten las principales metodologías empleadas actualmente para el cálculo del factor ambiental y, además, se propone un nuevo procedimiento implementable de forma sencilla en los actuales sistemas de monitorización.

2. CONCEPTO DE FACTOR AMBIENTAL

El factor F_{en} , que puede ser entendido como un factor de corrección ambiental en los ciclos térmicos, tiene la forma siguiente [1]:

$$F_{en} = \frac{N_{25A}}{N_{25W}} (\dot{\epsilon}_T)^{-P} \quad (1)$$

siendo:

- N_{25} : número de ciclos que producen un descenso del 25% en la tensión respecto al valor máximo de la curva cíclica de un ensayo de tracción.
- N_{25A} : vida a fatiga (en ciclos) en aire a temperatura ambiente
- N_{25W} : vida a fatiga (en ciclos) en agua a la temperatura de interés
- P : constante dependiente de la temperatura y de la cantidad de oxígeno disuelto
- $\dot{\epsilon}_T$: velocidad de deformación en la fase de crecimiento ($\% \cdot s^{-1}$)

El factor F_{en} , tiene su efecto en el daño acumulado (CUF, Cumulative Usage Factor) de la siguiente forma:

$$CUF = F_{en,1} \frac{n_1}{N_1} + F_{en,2} \frac{n_2}{N_2} + \dots + F_{en,m} \frac{n_m}{N_m} \quad (2)$$

siendo (n_i) el número de ciclos aplicado de un cierto transitorio, (N_i) el número de ciclos admisible a la amplitud producida por el suceso y (m) los tipos de transitorios considerados.

3. EXPRESIONES PARA EL CALCULO DEL FACTOR AMBIENTAL

Se han realizado numerosos estudios con el fin de determinar el valor del factor ambiental, obteniéndose una serie de expresiones a partir de modelos estadísticos [2]. A continuación se expone la expresión aprobada [3]

para el acero al carbono, al tratarse del material del componente que se va a evaluar en este trabajo.

$$F_{en} = \exp(0.632 - 0.101 \cdot S^* \cdot T^* \cdot O^* \cdot \epsilon'^*) \quad (3)$$

siendo:

· T^* , O^* , S^* y ϵ'^* : valores según la temperatura, el oxígeno disuelto (OD), contenido de azufre del acero y la velocidad de deformación, definidos de la siguiente forma:

$$\begin{aligned} - T^* &= T - 150 & (T \geq 150 \text{ }^\circ\text{C}) \\ - T^* &= 0 & (T < 150 \text{ }^\circ\text{C}) \end{aligned} \quad (4)$$

$$\begin{aligned} - O^* &= 0 & (OD < 0.05 \text{ ppm}) \\ - O^* &= \ln(12.5) & (OD \geq 0.5 \text{ ppm}) \\ - O^* &= \ln(25 \cdot OD) & (0.05 \leq OD \leq 0.5) \end{aligned} \quad (5)$$

$$\begin{aligned} - S^* &= S & (DO \leq 1.0 \text{ ppm y } S \leq 0.015 \text{ \% peso}) \\ - S^* &= 0.015 & (DO > 1 \text{ ppm}) \\ - S^* &= 0.015 & (DO \leq 1.0 \text{ ppm y } S > 0.015 \text{ \% peso}) \end{aligned} \quad (6)$$

$$\begin{aligned} - \epsilon'^* &= 0 & (\epsilon'^* > 1 \text{ \% s}^{-1}) \\ - \epsilon'^* &= \ln(\epsilon'^*) & (0.001 \leq \epsilon'^* \leq 1 \text{ \% s}^{-1}) \\ - \epsilon'^* &= \ln(0.001) & (\epsilon'^* < 0.001 \text{ \% s}^{-1}) \end{aligned} \quad (7)$$

En el análisis del efecto del medio se determinaron [4, 5] unos umbrales de actuación para los diferentes parámetros, que justifican las condiciones en las cuales el efecto del medio ambiente es aplicable, los cuales, para el caso del acero al carbono, se muestran en la Tabla 1.

Tabla 1. Umbrales de los parámetros ambientales[4, 5]

Velocidad de deformación	$\geq 1\% \text{ s}^{-1}$
OD	$< 0.04 \text{ ppm}$
Temperatura	$\leq 150 \text{ }^\circ\text{C}$
Contenido de azufre	$< 0.002 \text{ \%}$
Amplitud de deformación	$< 0.07\%$

4. EVALUACIÓN DEL FACTOR AMBIENTAL

Actualmente no se ha definido un procedimiento claro y concluyente para evaluar el factor ambiental, si bien existen guías al respecto, siendo la más extendida la referenciada en [6]. En la misma se establecen una serie de pautas para llevar a cabo la evaluación del factor ambiental en transitorios. Sin embargo, y tal como se muestra más adelante, la evaluación del factor ambiental en los transitorios reales que tienen lugar en planta es muy difícil de realizar con las indicaciones descritas en [6], las cuales sí pueden tener una aplicación menos compleja en transitorios de diseño.

4.1. Principal metodología de evaluación (MRP-47)

El documento MRP-47 [6] se ha convertido en los últimos tiempos en la guía principal para la evaluación del factor ambiental en los transitorios que tienen lugar en planta. A lo largo de la vida de una central se suceden una serie de transitorios que introducen cargas variables en los componentes, generando en ellos

tensiones variables. El análisis a fatiga se realiza empleando los puntos más representativos del historial de tensiones, los cuales se denominan picos y valles. Los picos y valles de tensión se ordenan y se unen formando “pares de carga”, cuyas amplitudes de tensión son introducidas en la curva S-N para obtener el daño a fatiga del material debido a cada par de carga. Como se puede intuir, los pares de carga se forman por un valle y un pico separados en el tiempo (pertenecientes a diferentes transitorios) y entre los que existen otros picos y valles, los cuales también serán parte de pares de carga diferentes. En este documento [6] una serie de indicaciones para unir estos picos y valles, que (generalmente) pertenecen a diferentes transitorios y que forman un par de carga, y que tal como se indica en la Figura 1 presentan una doble discontinuidad, tanto en el tiempo como en el nivel de tensión. El modo de unión de estos dos transitorios (de sus respectivos valle y pico) mostrados en la Figura 1 puede tener una influencia importante en el resultado del cálculo de la velocidad de deformación. La discontinuidad de los transitorios se elimina siguiendo las siguientes indicaciones [6]:

► *Discontinuidad en el tiempo.* Se ha establecido que el punto final (b) del primer transitorio se produce cuando se alcanza el 90% del valor del estado de tensión final (90% del *steady state*).

► *Discontinuidad en el valor de tensión.* Se ha determinado que la unión se realiza mediante una línea vertical, sin que transcurra ningún instante de tiempo.

El factor ambiental se evalúa empleando las expresiones características [5] de cada material (acero al carbono, Ec.(3)), y solamente en los periodos de tiempo en el que la velocidad de deformación es positiva, esto es, la deformación (tensión) es creciente.

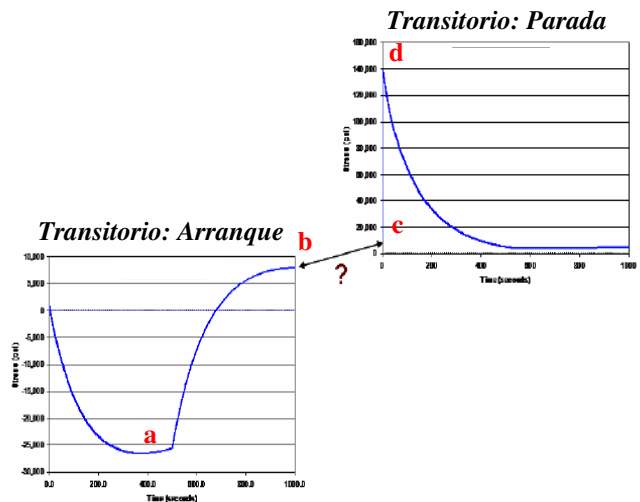


Figura.1 Discontinuidad al crear un par de carga con un valle y un pico [4]

Existen tres propuestas de evaluación planteadas para el cómputo del factor ambiental, según las cuales el cálculo de la velocidad de deformación en el periodo de análisis, y por consiguiente, del factor ambiental, será

más o menos exacto, y por ende, más o menos conservador. Las tres propuestas de evaluación del factor ambiental [4] en función de la exactitud requerida en el análisis son las siguientes:

- Propuesta #1 (VDM): Velocidad de Deformación Media (*Average Strain Rate*)
- Propuesta #2 (VDD): Velocidad de Deformación Detallada (*Detailed Strain Rate*)
- Propuesta #3 (VDI): Velocidad de Deformación Integrada (*Integrated Strain Rate*)

La propuesta VDI proporciona resultados más exactos [6], y por tanto, será la elegida para los análisis de este trabajo y la que se explica a continuación.

4.2. Propuesta de evaluación VDI

La propuesta de la velocidad de deformación integrada evalúa el factor ambiental F_{en} en cada uno de los intervalos de tiempo en que se divide el periodo entre el valle y el pico de análisis, pero con deformación creciente. El valor global del factor ambiental en este tramo creciente se calcula según la siguiente expresión:

$$F_{en} = \frac{\sum Fen_i \cdot \Delta \epsilon_i}{\sum \Delta \epsilon_i} \quad (3)$$

siendo:

- Fen_i =factor ambiental evaluado en el instante i , considerando:
 - Velocidad de deformación: $\epsilon' = 100 \cdot (\Delta \epsilon_i / \Delta T)$
 - Temperatura: $T = \text{máximo}(T_i - T_{i-1})$
 - Concentración de oxígeno:
 - O = máximo($O_i - O_{i-1}$) para aceros al carbono y de baja aleación
 - O = mínimo($O_i - O_{i-1}$) para aceros inoxidables
 - Contenido de azufre: $S = \text{constante}$ según las especificaciones del material
- ϵ' = velocidad de deformación detallada (%/seg)
- $\Delta \epsilon_i$ = variación de deformación en el punto i , $[(S_i - S_{i-1})/E]$
- S_i = valor de tensión en el instante i (psi)
- S_{i-1} = valor de tensión en el instante $i-1$ (psi)
- Δt = intervalo de tiempo en el instante i (seg), $[t_i - t_{i-1}]$
- E = módulo de elasticidad (psi)

4.3. Análisis de la metodología MRP-47

Esta metodología evalúa el factor ambiental en los pares de carga una vez se ha procedido a la unión de los transitorios (Figura 1), esto es, de los valles y picos. Por lo tanto, la metodología MRP-47 se fundamenta en unas bases teóricas correctas, y en las que las evaluaciones del daño a fatiga y del factor ambiental se ajustan o acoplan entre sí. En la Figura 2 se mostró el procedimiento de unión de dos transitorios cuyos puntos significativos (pico y valle) formaban un par de carga. Este ejemplo, así como los pasos a realizar para la evaluación del efecto ambiental, parecen claros y no

excesivamente complicados de ejecutar. Sin embargo, las tensiones de los transitorios reales que suceden en planta y que son evaluadas mediante los sistemas de monitorización, difieren notablemente en la forma y aspecto de la que se han presentado en la Figura 2.

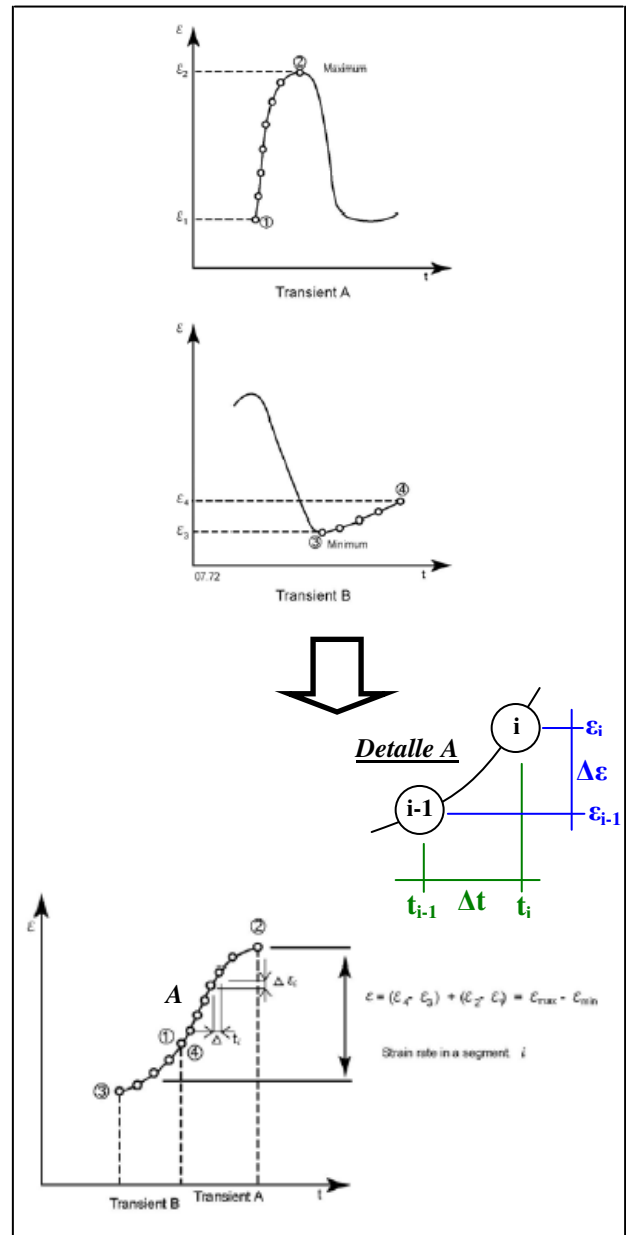


Figura 2. División del transitorio para el cálculo preciso de la velocidad de deformación [4]

En la Figura 3 se muestra un ejemplo de las tensiones reales obtenidas en un el blend radius de la tobera de agua de alimentación del lazo A de una central nuclear. Como se puede observar, las tensiones no evolucionan generalmente de una forma suave y continua, sino que existen variaciones bruscas asociadas a las condiciones variables del reactor. Esta situación dificulta notablemente las indicaciones detalladas en [4] para la unión de los transitorios, y especialmente para la localización del valor de tensión del 90% de su estado tensional estable (*steady state*). En consecuencia, la

aplicación de la metodología de referencia MRP-47 es posible en la evaluación de transitorios de diseño, y muy difícil de aplicar con datos reales de transitorios que han tenido lugar en planta.

Existe otra característica del método que dificulta aún más la aplicación de esta metodología, y es la constante variación que se produce en la unión de picos y valles para la formación de pares de carga. A medida que se suceden los transitorios y aparecen nuevos puntos significativos, esto es, nuevos picos y valles, éstos se reordenan continuamente, de tal modo que los pares de carga están constantemente variando. La metodología MRP-47 analiza el factor ambiental en pares de carga una vez realizado la unión del valle y el pico (Figura 1). Por lo tanto, la aplicación de esta metodología implica una modificación de los cálculos según ocurren nuevos transitorios, tanto en la unión de los nuevos pares de carga como en el cálculo del factor ambiental asociado a ellos. Esta situación hace inviable el empleo de esta metodología, y prácticamente imposible su implantación en los sistemas de monitorización actuales.

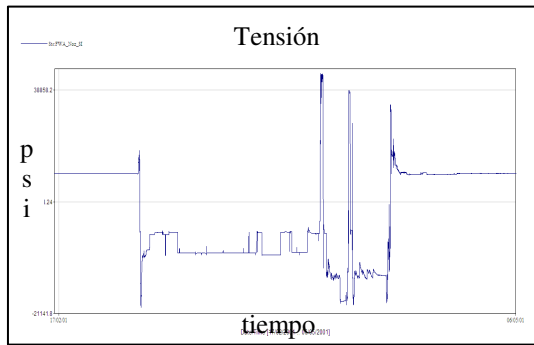


Figura 3. Tensiones reales en un componente

Por lo tanto, la metodología MRP-47 se enfrenta de forma directa al procedimiento de evaluación del daño a fatiga basado en la ordenación continua de los picos y valles para formar pares de carga.

5. METODOLOGÍA PROPUESTA: P&V

Las metodologías hasta ahora desarrolladas presentan incompatibilidades con los actuales sistemas de monitorización, dificultades de aplicación en transitorios reales o inexactitudes inaceptables en la ingeniería nuclear.

Esta situación ha propiciado el estudio y desarrollo de una nueva metodología de evaluación que aquí se propone y se define como “Metodología pico y valle (P&V)”. El fundamento de esta metodología se basa en el principio de que el medio en el que se encuentran inmersos los componentes de las centrales produce un aumento del daño a fatiga de estos. Además el medio actúa o tiene efecto cuando la velocidad de deformación es positiva. El ambiente, por tanto, reduce la vida a fatiga de los componentes, y su efecto puede ser comparado con una situación de mayor tensión sobre estos componentes pero ante un ambiente no agresivo,

esto es, al aire. Por lo tanto, el objetivo de esta metodología es establecer una equivalencia entre una variación tensional en un medio agresivo y una variación tensional mayor en un medio no agresivo (aire). Además, el procedimiento ha de tener en cuenta la morfología que presentan los transitorios reales (Figura 3), e igualmente ha de posibilitar de forma sencilla su implementación en los actuales sistemas de monitorización. Bajo estas condiciones se plantea la “Metodología P&V” como nuevo procedimiento de evaluación del daño a fatiga considerando el efecto del medio.

En primer lugar, se propone realizar la evaluación del factor ambiental ($F_{en_{P\&V}}$) entre valles y picos consecutivos, esto es, periodos con velocidad de deformación positiva, al contrario que la metodología MRP-47, que plantea su evaluación entre los valles y picos que forman los pares de carga. En segundo lugar, el factor ambiental ($F_{en_{P\&V}}$) calculado entre un valle y pico consecutivo se aplicará sobre el rango de tensión existente entre dicho valle y pico consecutivo, de tal modo que esta variación de tensión se verá aumentada proporcionalmente a dicho factor ambiental ($F_{en_{P\&V}}$). El aumento de la diferencia de tensión entre el valle y el pico se realizará aumentando únicamente el valor de tensión del pico, de tal modo, que el valor de tensión de los valles nunca se verá modificado.

En la Figura 4 se muestra el modo de proceder para calcular la variación de tensión equivalente, que se ha de ser mayor que el rango de tensión inicial entre el valle y pico original. Se supone un valor de rango de tensión (ΔS_{PV}) entre el valle (V) y pico (P) iniciales. Con la amplitud de tensión $S_a = 0.5 \cdot \Delta S_{PV}$, y empleando la curva S-N del material, se puede calcular el número de ciclos (N) admisibles para ese nivel de tensión, y por consiguiente el daño a fatiga (U_{PV}) originado. Por otro lado, y aplicando la propuesta VDI (apartado 4.1), se evalúa el factor ambiental ($F_{en_{PV}}$) en el periodo entre el valle y pico, con el cual se puede obtener el daño a fatiga causado por la variación tensional entre el valle y el pico considerando los efectos del ambiente ($U_{PV_{env}}$). Procediendo de modo inverso, con este valor de daño a fatiga ambiental, se puede obtener fácilmente el número de ciclos admisibles teniendo en cuenta el efecto del medio (N_{env}), y empleando la curva de fatiga S-N, se calcula la nueva amplitud de tensión (S_a').

La amplitud de tensión (S_a') produce un daño a fatiga en el aire equivalente a la amplitud de tensión inicial (S_a) considerando los efectos del medio. De igual forma, la amplitud de tensión (S_a') nos permite calcular el rango o diferencia tensional ($\Delta S_{P\&V}$) que ha de existir entre el valle y el nuevo pico, y ya que el valor de tensión del valle es fijo, el valor de tensión del nuevo pico se obtiene de forma directa. Por lo tanto, la aplicación de esta metodología, supone una modificación del valor de los picos. Una vez se hayan calculado éstos, se procederá a aplicar un análisis a fatiga convencional, esto es, reordenación de los nuevos picos y los valles, posterior formación de pares de carga

y aplicación de la curva de fatiga para evaluar el daño que produce cada par de carga.

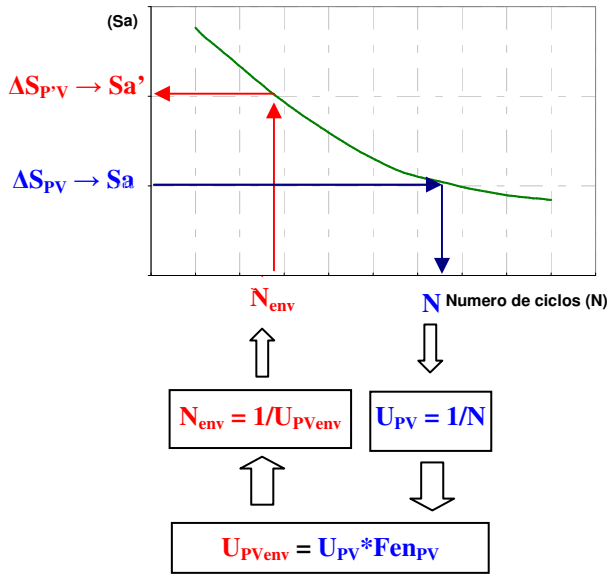


Figura 4. Procedimiento para la obtención del valor de los nuevos picos

En la Figura 5 se muestra un ejemplo práctico que permite entender mejor la metodología en su conjunto. Se han supuesto cuatro transitorios, en cada uno de los cuales se han producido dos puntos significativos de tensión, esto es, un pico y un valle. En la Tabla 2 se puede seguir el procedimiento aplicado paso a paso, y explicado anteriormente. En ella, además, se puede observar como el valor de tensión de los valles no varía, y solo se aumenta la tensión de los picos. El tercer pico (P3) permanece invariable, ya que el factor ambiental en el periodo asociado a este punto significativo es la unidad, es decir, el ambiente no tiene efecto alguno en el daño a fatiga durante ese periodo de tiempo.

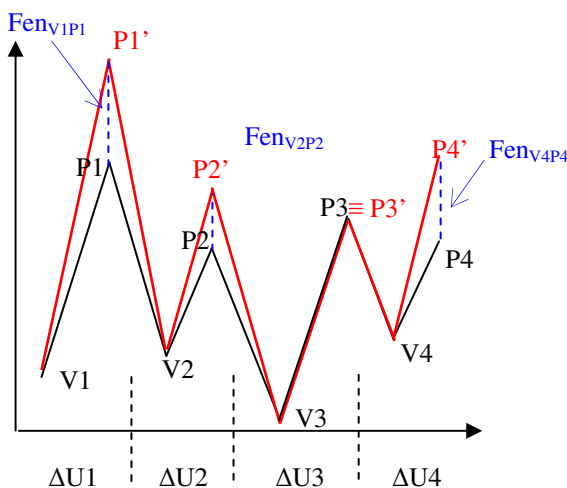


Figura 5. Metodología P&V en secuencia transitorios

En la Figura 5 se puede apreciar como se modifica el perfil de tensiones una vez aplicado el efecto del medio. Con los valles y los nuevos picos se procede a realizar un análisis a fatiga convencional, esto es, ordenación de

estos nuevos puntos significativos, formación de nuevos pares de carga y evaluación del daño empleando la curva de fatiga S-N que corresponda. La metodología P&V aquí propuesta elimina los inconvenientes y dificultades presentadas por la metodología MRP-47 anteriormente explicada. El cálculo del factor ambiental entre valles y picos consecutivos aplicando la propuesta VDI no presenta ninguna dificultad, ya que son periodos de tiempo totalmente definidos y delimitados. Además no se precisa de ninguna unión previa de transitorios, ni tampoco una definición de cómo y dónde éstos se conectan, con lo que se elimina la dificultad planteada por la forma y aspecto que presentaban las tensiones en los transitorios reales.

Tabla 1. Ejemplo de proceder de la metodología P&V

P&V consecutivos	Pico (P) (psi)	Valle (V) (psi)	Upv	Fenpv	Upvenv = Fenpv*Upv
V1P1	42819	8143	1.099E-5	3.54	3.889E-5
V2P2	26994	8203	1.994E-7	18.16	3.621E-6
V3P3	31843	5269	4.684E-6	1.00	4.684E-6
V4P4	28582	11156	8.617E-8	16.20	1.396E-6

P&V consecutivos	Nenv (ciclos)	Sa' (psi)	ΔSpv (psi)	Pico modificado (P') (psi)	Valle (V) (psi)
V1P1	25711	29070	51452	59595	8143
V2P2	276169	13855	24522	32725	8203
V3P3	213487	15014	26574	31843	5269
V4P4	716323	12647	22384	33540	11156

Otras de las ventajas que presenta esta metodología es que la aparición de nuevos transitorios, y por tanto nuevos picos y valles, no supone ningún problema, ya que el factor ambiental es calculado entre valles y picos consecutivos, y la posición de estos en el tiempo es invariable. Por lo tanto, en este sentido, su implementación en los sistemas de monitorización es sencilla. Por último, y tal como se ha observado, esta metodología se basa en la aplicación “instantánea” del efecto ambiental sobre el daño a fatiga de los componentes a medida que estos se ven sometidos a estados de deformación creciente.

6. CASO PRÁCTICO.

Se analizan seis transitorios reales ocurridos en una central nuclear en el periodo 2003-2005. Los transitorios, en orden de ocurrencia son: 1. Prueba hidrostática; 2. Arranque; 3. Scram; 4. Reducción de potencia; 5. Scram; 6. Parada.

La localización de análisis es de acero al carbono, y por tanto la expresión utilizada se muestra en la expresión (3). En la Figura 6 se muestra la tensión (línea verde) y los puntos significativos (puntos rojos), esto es, picos y valles, durante los transitorios mencionados.

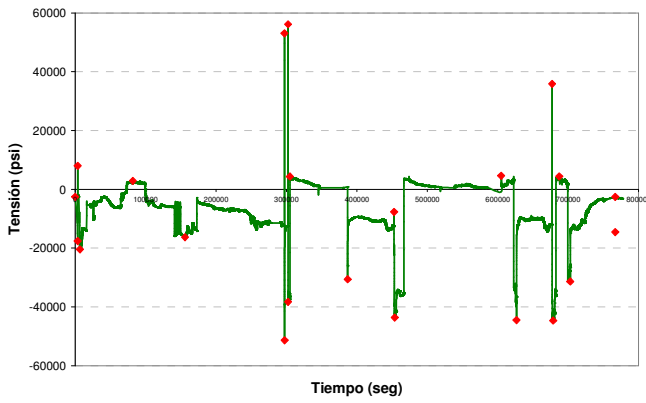


Figura 6. Tensión y P&V

Se calcula el factor ambiental (Fen) según la propuesta VDI, y se aplica en función de las particularidades de las metodologías de evaluación empleadas: metodología MRP-47 y metodología P&V propuesta. En la Tabla 3 y Tabla 4 se muestran los resultados del factor ambiental obtenidos al aplicar las dos metodologías de evaluación. Como puede observarse, en el caso estudiado, la metodología P&V proporciona mayores valores tanto para el factor ambiental como para el daño acumulado en fatiga

Tabla 3. Metodología MRP-47

P&V (Par de carga)	Valle	Pico	Fen	U _{ENV} TOTAL
	Fen(v-ss)	Fen(ss-p)		
V4-P5	6.77	6.77	6.77	0.00475
V9-P4	1.00	5.29	5.29	
V8-P9	3.44	3.66	3.56	
V7-P2	1.25	1.00	1.15	
V5-P8	1.00	2.69	1.13	
V10-P10	2.47	1.00	1.54	
V6-P6	3.68	1.00	1.88	
V2-P3	1.00	1.00	1.00	
V1-P1	1.00	1.00	1.00	
V3-P11	1.00	2.47	2.11	
V11-P7	--	3.39	3.39	
			Fen	4.51

Tabla 4. Metodología P&V

P&V	Pico	Valle	U _{TOTAL}	Fen	Pico'	Valle	U _{ENV} TOTAL
V2P3	7995	-17567	0.00105	1.00	7995	-17567	0.00588
V3P4	2896	-20444		1.00	2896	-20444	
V4P5	53079	-16262		4.38	93695	-16262	
V5P6	56182	-51384		6.76	175420	-51384	
V6P7	4362	-38256		1.00	4362	-38256	
V7P8	-7678	-30577		3.51	3310	-30577	
V8P9	4636	-43603		1.63	12583	-43603	
V9P10	35899	-44474		3.57	75097	-44474	
V7P8	4447	-44644		1.00	4447	-44644	
V8P9	-2521	-31383		2.47	6891	-31383	
				Fen			

7. DISCUSIÓN Y CONCLUSIONES.

La metodología MRP-47 se considera que proporciona resultados muy ajustados a la realidad en el cálculo del efecto ambiental en el daño a fatiga. Uno de los inconvenientes de esta metodología, y que posiblemente impide su aprobación definitiva, es la dificultad enorme

de adaptación al calculo de transitorios reales, y las continuas re-evaluaciones que implica la aparición de nuevos transitorios.

La metodología P&V propuesta, en el caso estudiado, ofrece un valor del factor ambiental ligeramente superior al obtenido con la metodología de referencia MRP-47, y por tanto, un valor del daño a fatiga ambiental levemente superior al real.

La metodología P&V, basada en el efecto del ambiente en los periodos en los que la velocidad de deformación es positiva muestra resultados muy buenos y ajustados al procediendo MRP-47, o expresado de otro modo, a la realidad.

La facilidad de implementar la metodología P&V, unido a su perfecta flexibilidad de calculo ante la aparición de nuevos transitorios (reales o de diseño) y, como se ha podido comprobar, la exactitud y ligero conservadurismo de los resultados, sugiere la utilización de dicha metodología en la evaluación del daño a fatiga considerando los efectos ambientales en componentes de centrales nucleares.

La aprobación de esta nueva metodología implica sin duda, la realización de más evaluaciones de componentes y transitorios, así como ensayos de fatiga que puedan confirmar los resultados obtenidos teóricamente.

8. RERERENCIAS

- [1] H.S. Mehta, and S.R. Gosselin "Environmental Factor Approach to Account for Water Effects in Pressure Vessel and Piping Fatigue Evaluations".
- [2] Omesh K. Chopra and William J. Shack. "The Effect of LWR Coolant Environments on the Fatigue Life of Reactor Materials", 2006 ASME Pressure Vessel and Piping Division Conference, July 2006.
- [3] "Guidelines For Evaluating Fatigue Analyses Incorporating the Life Reduction of Metal Components due to the Effects of The Light-Water Reactor Environment for New Reactors" REGULATORY GUIDE 1.207, March 2007
- [4] NUREG/CR-5704 (ANL-97/31), "Effects of LWR Coolant Environments on Fatigue Design Curves of Austenitic Stainless Steel" ", U.S.Nuclear Regulatory Commission, April 1999.
- [5] NUREG/CR-6583 (ANL-97/18), "Effects of LWR Coolant Environments on Fatigue Design Curves of Carbon and Low-Alloy Steel" , U.S.Nuclear Regulatory Commission, March 1998.
- [6] "Guidelines for Addressing Fatigue Environmental Effects in a License Renewal Application" Code Case, MRP-47-Revision1, EPRI. September 2005.

ANALYSIS OF LOW-CYCLE FATIGUE DATA OF MATERIALS FROM SEVERAL PORTUGUESE RIVETED METALLIC BRIDGES

A.M.P. de Jesus^{1,3}, A.L.L. da Silva¹, J.A.F.O. Correia^{1,3}, M.V. Figueiredo^{2,3}, J.M.C. Maceiro¹,
A.S. Ribeiro^{1,3}, A.A. Fernandes^{2,3}

¹ Departamento de Engenharias, Escola de Ciências e Tecnologia,
Universidade de Trás-os-Montes e Alto Douro,
Quinta de Prados, 5001-801 Vila Real, Portugal.

E-mail: ajesus@utad.pt; a.luis.l.silva@gmail.com; jcorreia@utad.pt; j_maceiro@hotmail.com; aribeiro@utad.pt

² Departamento de Engenharia Mecânica,
Faculdade de Engenharia da Universidade do Porto,
Rua Dr. Roberto Frias, 4200-465 Porto, Portugal
E-mail: mfiguei@fe.up.pt; aaf@fe.up.pt

³ Instituto de Engenharia Mecânica – IDMEC,
Rua Dr. Roberto Frias, 404, 4200-465 Porto, Portugal

ABSTRACT

Fatigue failures are a concern for metallic bridges due to the likelihood of metal to deteriorate under variable stresses. Residual life calculations of existing old metallic riveted bridges in operation should take into account fatigue as a progressive damaging mechanism. A consistent residual life prediction should be based on actual fatigue data from bridge materials. This paper presents an analysis of low-cycle fatigue data from four representative ancient Portuguese riveted metallic bridges. This data can be used within the local approaches framework to assess the number of cycles to crack initiation. In particular, samples from the Luiz I, Eiffel, Fão and Trezói bridges are analysed. Strain-life relations are derived based on the classical deterministic Morrow proposition, as well as using a probabilistic strain-life regression model. Furthermore, the cyclic elastoplastic behaviour of the materials are characterized, namely the cyclic hardening/softening behaviours and the cyclic stress-strain curves of the materials.

KEY WORDS: Riveted bridges, puddled iron, construction steel, low-cycle fatigue, cyclic elastoplastic behaviour.

1. INTRODUCTION

The maintenance and safety of existing bridges is a major concern of governmental agencies. In particular, the safety of old riveted road and railway bridges fabricated and placed into service at the end of the 19th century/ beginning of 20th century deserve a particular attention, since they were designed taking into account traffic conditions, both in terms of vehicle gross weight and frequency, completely different from those observed nowadays. Also, the current design procedures were not yet fully developed or even did not exist in the 19th century and design engineers were not aware of some important phenomena, such as fatigue. Fatigue was only intensively studied in the 20th century. In order to assure high safety levels in old riveted metallic bridges, road and railway authorities have to invest heavily in their maintenance and retrofitting.

The approach widely used to assess the fatigue damage of riveted connections is the S-N approach, which is included in design codes of practice (ex: EC3 [1], AASTHO [2]). This approach is based on detail category S-N curves, which relates the total number of

cycles to failure with the applied stress range. Alternatively, Fracture Mechanics has been applied to assess the residual fatigue life of damaged riveted connections [3]. This approach requires the knowledge of the initial defect, which may be assessed by inspection. In order to make Fracture Mechanics a truly design alternative to the S-N approach, it must be complemented by another approach for assessing crack initiation [3]. Local approaches, based on local or notch stresses or strains, are frequently used to assess the fatigue crack initiation [4].

This paper presents strain-life fatigue data obtained for original materials from four ancient Portuguese riveted metallic bridges, namely the Eiffel (Viana), Luiz I, Fão and Trezói bridges, using smooth specimens. Figure 1 gives a global overview of the four bridges. The Eiffel bridge, a piece of iron architecture, was designed by Eiffel and inaugurated on 30th of June, 1878. This bridge, crossing the Lima river between Darque and Viana, serves both road and railway traffic. The bridge has total length of 573 meters and a width of 6 meters, made of a continuous deck composed by nine spans. The Luiz I bridge links the cities of Porto and Gaia. It was

designed by Eiffel and commissioned in 31st October 1886. The construction was initiated in the 1st December 1881. The bridge shows a double deck, supported by an arch with a radius of 45 meters. The lengths of upper and lower decks are respectively 391.25 and 174 meters. At present, the lower deck serves road traffic; the upper deck serves the metro. The Fão bridge is a road bridge that was designed by Abel Maria Mota, under the supervision of the engineer Reynau, at the end of 19th century. It was inaugurated at 7th of August 1892. This bridge is representative of the architecture of the iron. The bridge shows eight spans of 33.5 meters each. Finally, the Trezói bridge is a railway bridge that makes part of the Beira Alta railway line. It was inaugurated on 20th of August 1956. The deck is composed by three continuous spans, of 39, 48 and 39 meters, totalizing a bridge length of 126 meters. While the first three bridges were probably built using puddle or wrought iron, materials predecessors of modern steels, the Trezói bridge was built using modern construction steel.

Besides the basic characterization of the materials, the low-cycle fatigue and cyclic elastoplastic behaviour of the materials is presented. The low-cycle fatigue data of the materials is correlated using the deterministic relation proposed by Morrow [5]:

$$\frac{\Delta\varepsilon}{2} = \frac{\Delta\varepsilon^E}{2} + \frac{\Delta\varepsilon^P}{2} = \frac{\sigma'_f}{E} (2N_f)^b + \varepsilon'_f (2N_f)^c \quad (1)$$

where: $\Delta\varepsilon$, $\Delta\varepsilon^E$ and $\Delta\varepsilon^P$ are, respectively, the total, elastic and plastic strain ranges; σ'_f and b are the fatigue strength coefficient and exponent; ε'_f and c are de fatigue ductility coefficient and exponent; $2N_f$ is the number of reversals and E is the Young modulus. Furthermore, a Weibull-based probabilistic relation, as proposed by Castillo and Fernández-Canteli [6] is adopted to describe the strain-life data:

$$N_f = \exp \left[B + \frac{\lambda + \delta(-\log(1-p))^{1/\beta}}{\log(\varepsilon_a) - C} \right] \quad (2)$$

The previous equation defines strain-life curves associated to a certain probability of failure, p (percentile curves). Specifying the probability of failure, p , and the strain amplitude, ε_a , the number of cycles to failure, N_f , may be assessed. Therefore, Equation (2) defines the complete P- ε -N field. In Equation (2) B , C , λ , δ and β are constants to be evaluated for each material. Reference [6] gives the details concerning the identification of the constants of this model.

The stabilized cyclic elastoplastic behaviour of the materials is correlated using the well known Ramberg-Osgood relation [7]:

$$\frac{\Delta\varepsilon}{2} = \frac{\Delta\sigma}{2E} + \left(\frac{\Delta\sigma}{2K'} \right)^{1/n'} \quad (3)$$

where: $\Delta\varepsilon$ and $\Delta\sigma$ are the strain and stress ranges; K' and n' are the cyclic strain hardening coefficient and exponent and E is the Young modulus.



Figure 1: Investigated bridges: a) Eiffel bridge; b) Luiz I bridge; c) Fão bridge and d) Trezói bridge.

2. EXPERIMENTAL DETAILS

This paper reports low-cycle fatigue data from four materials, derived from strain-controlled fatigue tests of smooth specimens, machined from original members

that were removed and replaced in the four referred bridges. Flat specimens, with rectangular cross section, were manufactured in accordance with the ASTM E606 standard [8]. Specimens were manufactured from the Fão and Trezói bridges with a nominal cross section of 7.5x8 mm²; specimens from the Eiffel and Luiz I bridges were prepared with a nominal cross section of 5x6 mm². The surfaces of the specimens in the gauge length were polished. All experiments were carried out in a close-loop servo hydraulic machine, rated to 100 KN. The fatigue tests were conducted under fully reversible constant strain amplitudes, at room-temperature in air and with a frequency adjusted to result an average strain rate of 0.008/s. The longitudinal strain was measured using a longitudinal extensometer with a base length equal to 25 mm and limit displacements of ±2.5 mm.

Additionally to the fatigue tests, monotonic tensile tests were carried out according the NP 10002-1 standard [9], using round specimens. Also, chemical analyses of the materials were carried out.

3. BASIC CHARACTERIZATION OF THE MATERIALS

Table 1 shows the average tensile properties of the materials, namely the yield strength, tensile strength, elongation at fracture and the reduction in the cross section. The analysis of the results shows that the material from the Trezói bridge – similar to modern steels - shows simultaneously the highest strength and ductility values. The other materials, which are very likely puddle/wrought iron, exhibit lower strength and ductility properties. The material from the Fão shows the lowest yield strength; the material from the Eiffel bridge shows very low ductility.

Table 1. Tensile properties of the steels.

Material	Yield strength (MPa)	Tensile strength (MPa)	Elongation at fracture (%)	Reduction in cross section (%)
Eiffel	292	342	8	12
Luiz I	297	397	21	27
Fão	220	359	23	13
Trezói	401	464	23	66

Table 2. Chemical composition (weight, %).

Material	C	Si	P	Mn
Eiffel	0.03	0.15	0.49	0.02
Luiz I	0.42	2.09	>0.15	0.34
Fão	0.09	0.06	0.14	0.13
Trezói	0.06	0.03	0.02	0.34

Table 2 summarizes the average values of the chemical composition, which were assessed using the spark emission spectrometry technique. The material from the Trezói bridge exhibits the lowest contents of silicon and

phosphorus, which is consistent with the age of the material. The Trezói material is a ferritic steel (structural steel), since it has a very small amount of carbon. The materials from the centenary bridges show variable chemical composition, due to the typical heterogeneous microstructures of these materials. The material from the Luiz I bridge shows a very high carbon and silicon content. The material from the Eiffel bridge exhibits a very high phosphorus content.

4. STRAIN-LIFE DATA

4.1. Deterministic assessment

This section shows the main results from the strain-controlled fatigue tests. In particular, the experimental strain-life data was correlated using Equation (1) – the Morrow’s relation. Table 1 summarizes the constants of the Morrow’s relation as well as the number of reversals of transition between the plastic strain governed behaviour to the elastic strain governed behaviour. Figure 2 compares the strain-life relations obtained for the materials from the four bridges. The analysis of the results shows that the material from the Eiffel, Luiz I and Fão bridges (the centenary brides) have a strain-life behaviour governed essentially by the elastic strain amplitude. The number of reversals of transition are very low when compared with the value obtained for the Trezói bridge – the youngest material. The elastic strain – life curves are very similar for the four materials. The major differences were found in the plastic strain-life curves. The material from the Trezói bridge exhibits the higher fatigue resistance in the low cycle fatigue regimes (significantly higher fatigue ductility coefficient). The older materials – materials from Eiffel and Luiz I bridges - show the lower fatigue resistances.

Table 3. Strain-life data: Morrow’s constants.

Material	σ'_f MPa	b	ϵ'_f -	c	$2N_t$
Eiffel	531.6	-0.0610	0.0362	-0.5380	222
Luiz I	469.6	-0.0540	0.0461	-0.6437	154
Fão	592.4	-0.0781	0.0809	-0.5747	771
Trezói	609.7	-0.0920	1.4733	-0.8137	5193

4.2. Probabilistic assessment

Since the fatigue data is usually characterized by significant scatter, the probabilistic models are preferable to correlate the experimental data. The probabilistic strain-life model defined by Equation (2) is used in this section to correlate the strain-life data obtained for the investigated materials. Figure 3 shows the P-ε-N field obtained for each material. Five percentil curves are represented, corresponding to the following probabilities of failure: p=1, 10, 50, 90 and 99%. Each graph includes the derived constants of the model. It is

worth noting that this model does not requires the split of the total strain into elastic and plastic components. Figure 4 compares the P-ε-N fields between each material. Only the percentil curves corresponding to probabilities of failure p=1%, p=50% and p=99% are shown. The material from the Eiffel bridge shows the lowest P-ε-N field.

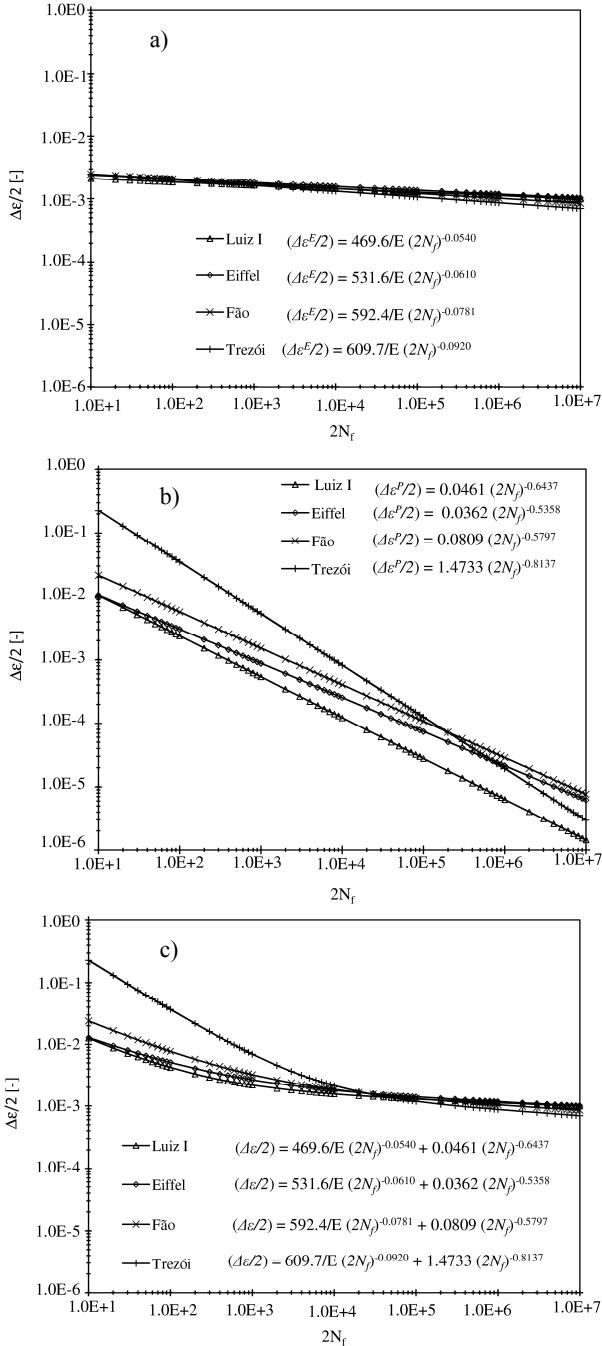


Figure 2: Comparison of strain-life relations: a) elastic behaviour; b) plastic behaviour; c) elastic plus plastic behaviour.

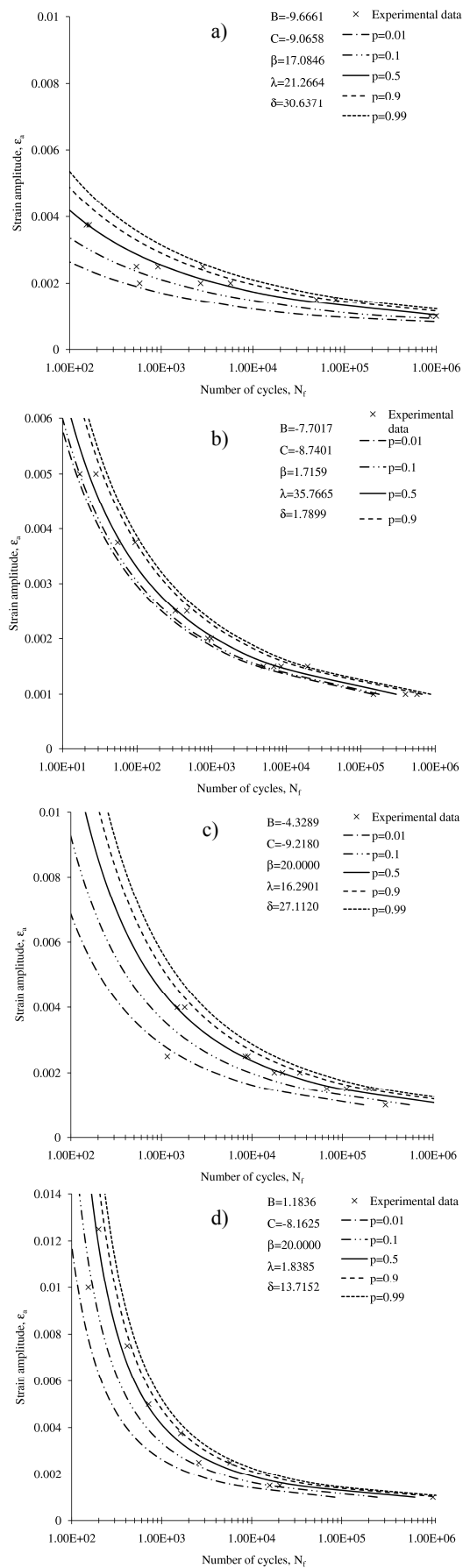


Figure 3: P-ε-N fields: a) Eiffel bridge; b) Luiz I bridge; c) Fão bridge and d) Trezói bridge.

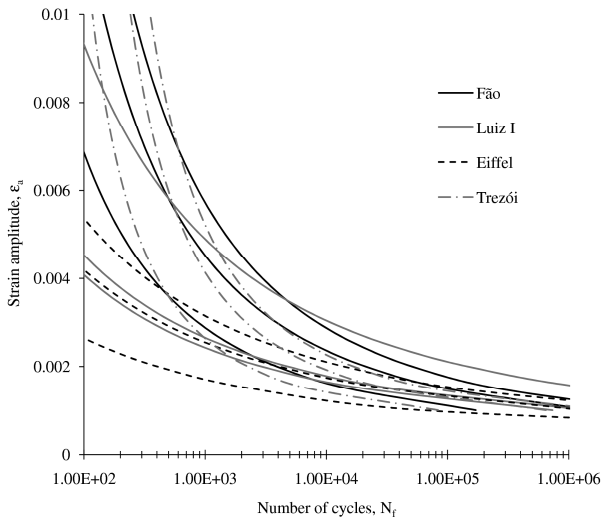


Figure 4: Comparison of the P - ε - N fields.

5. CICLIC ELASTOPLASTIC BEHAVIOUR

The strain-controlled fatigue tests, additionally to the strain-life data, they allow the evaluation of the cyclic plastic behaviour of the materials. Figure 5 shows the evolution of the stress amplitude with the number of cycles. The analysis of the results shows that materials from the centenary bridges show some hardening for higher strain ranges. The material from the Trezói bridge shows softening. For some tested series, this latter material exhibits stabilized behaviour. Therefore, a distinctive behaviour clearly exists between the centenary materials and the construction steel from the Trezói bridge.

Using the stabilized or pseudo-stabilized (half-life) behaviour of the materials, the respective cyclic curves were identified, resulting the constants presented in Table 4. The Young moduli were assessed using strain gauges for the materials from Luiz I and Fão bridges. For the other two materials, indirect estimates were obtained from the analysis of the hysteresis loops. Figure 6 shows the stabilized hysteresis loops as well as the cyclic curve and the cyclic curve scaled by a factor of two. Due to scatter in the cyclic behaviours, none of the materials shows a pure Masing behaviour. However, materials from Eiffel and Luiz I bridges shows a reasonable Masing behaviour. Due to scatter, the material from the Fão bridge shows two hysteresis loops that deviates significantly from the twice cyclic curve, making the material essentially a non-Masing material. Material from the Trezói bridge, which typically exhibits low scatter in its cyclic behaviour, have a consistent non-Masing behaviour.

6. CONCLUSIONS

Low-cycle fatigue data was derived for samples of materials from four riveted metallic bridges, namely the Eiffel, Luiz I, Fão and Trezói bridges. The following

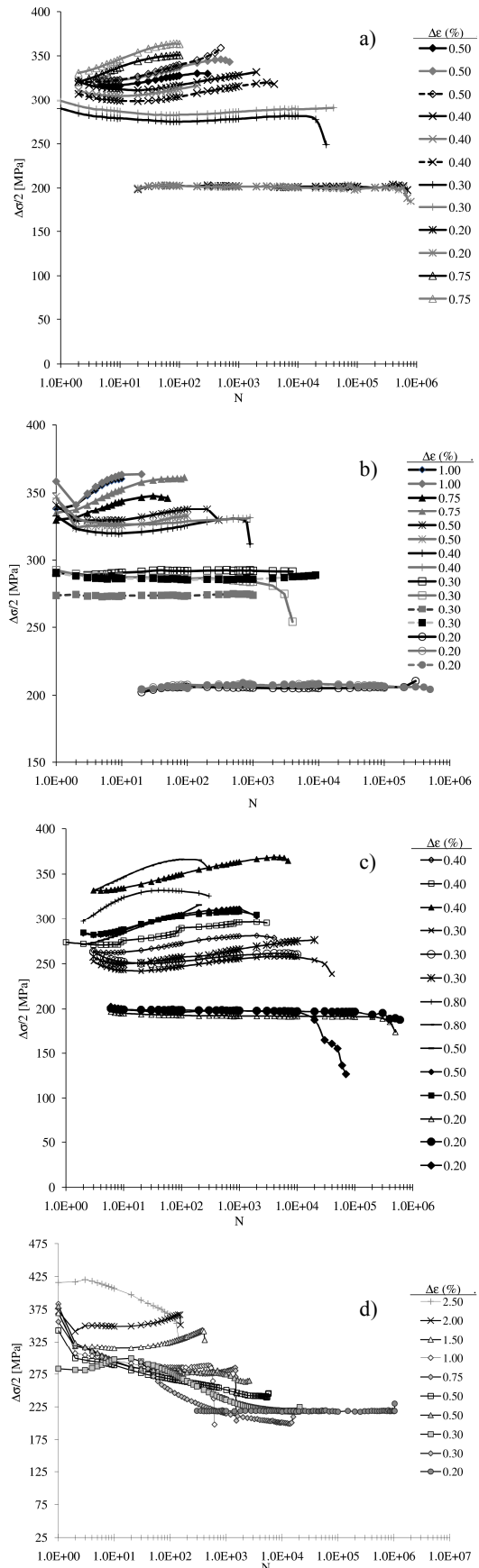


Figure 5: Cyclic behaviour of the materials: a) Eiffel bridge; b) Luiz I bridge; c) Fão bridge and d) Trezói bridge.

conclusions are formulated:

- The fatigue and cyclic elastoplastic behaviour observed for the centenary bridges are clearly distinct from the behaviour of the Trezói bridge. While the material from the Trezói bridge is a structural steel, materials from the centenary bridges are very likely puddle or wrought irons. These latter materials are characterized by higher scatter in properties due to characteristic microstructural heterogeneities.
- Materials from the centenary bridges show low-cycle fatigue behaviours with a very limited plastic behaviour, i.e., a very small number of transition reversals, $2N_f$.
- While the materials from the centenary bridges show trends of cyclic strain hardening, the material from the Trezói bridge exhibits cyclic strain softening. The older materials agree better with Masing behaviour than the material from the Trezói bridge.

Table 4. Cyclic elasto-plastic constants.

Material	E GPa	K' MPa	n'
Eiffel	193.1	458.1	0.115
Luiz I	192.7	604.2	0.083
Fão	198.7	852.1	0.139
Trezói	198.6	821.3	0.177

ACKNOWLEDGEMENTS

The authors acknowledge the Portuguese Science and Technology Foundation (FCT) for his support through the project PTDC/EME-PME/78833/2006.

REFERENCES

[1] Technical Committee CEN/TC 250, EN 1993 (Eurocode 3): *Design of steel structures*, 2006.

[2] AASHTO, *AASHTO LRFD: Bridge Design Specification*, 1995.

[3] De Jesus, A.M.P., Correia, J.A.F.O., “Fatigue Assessment of Riveted Railway Bridge Connections. Part II: Numerical Investigations”, *7th International Conference on Steel Bridges Steel Brigdes*, Guimarães, pag. II:339-II:348, 2008.

[4] De Jesus, A.M.P., Pinto, H., Fernández-Canteli, A., Castillo, E., Correia, J.A.F.O., “Fatigue assessment of a riveted shear splice based on a probabilistic model”, *International Journal of Fatigue*, Vol. 32, pag. 453-462, 2010.

[5] Morrow, J.D., “Cyclic Plastic Strain Energy and Fatigue of Metals”, *In: Internal Friction, Damping and Cyclic Plasticity*, ASTM STP 378, American Society for Testing and Materials, Philadelphia, PA, pag. 45-87, 1965.

[6] Castillo, E., Fernández-Canteli, A., *A Unified Statistical Methodology for Modeling Fatigue Damage*, Springer, 2009.

[7] Ramberg, W., Osgood, W.R., “Description of stress-strain curves by three parameters”, *Naca TN 402*, National Advisory Committee for Aeronautics, 1943.

[8] American Society for Testing and Materials. “ASTM E606-92: Standard Practice for Strain-Controlled Fatigue Testing”, *In: Annual Book of ASTM Standards*, Part 10, pag. 557-57, 1998.

[9] NP EN 10002-1, “Materiais metálicos. Ensaio de tracção. Parte 1: Método de ensaio à temperatura ambiente”, Instituto Português da Qualidade, 2006.

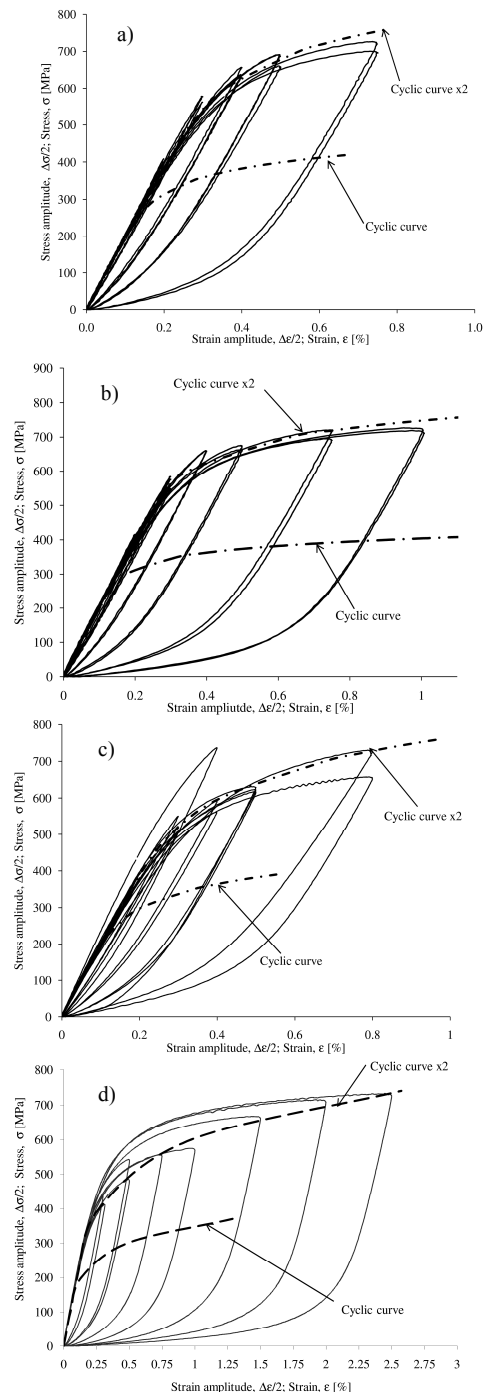


Figure 6: Stabilized hysteresis loops: a) Eiffel bridge; b) Luiz I bridge; c) Fão bridge and d) Trezói bridge.

UN MODELO DE CRECIMIENTO DE GRIETA COMPATIBLE CON EL CAMPO DE WÖHLER

A. Fernández Canteli¹, E. Castillo², D. Siegele³

¹Dpto. de Construcción e Ingeniería de Fabricación, E.P.S.I.G.
 Universidad de Oviedo, Campus de Viesques, 33203 Gijón, España.
 E-mail: afc@uniovi.es

²Dpto. de Matemática Aplicada y Ciencias de la Computación, E.T.S.I.C.C.P.
 Universidad de Cantabria, Avda. de los Castros s/n 38008 Santander, España.
 E-mail: castie@unicani.es

³Fraunhofer Institut für Werkstoffmechanik
 Wöhlerstrasse 11, 70108 Freiburg i. B., Alemania
 E-mail: sj@iwf.fhg.de

RESUMEN

En este trabajo se desarrolla un modelo dimensionalmente congruente que reproduce la curva completa de velocidad de crecimiento de grieta. El modelo considera un rango del factor de intensidad de tensiones normalizado ΔK^{**} , definido en el dominio $[0, 1]$, que puede interpretarse como una función de distribución, aprovechando la experiencia estadística sobre este tipo de funciones, particularmente en lo relativo a los métodos de estimación de parámetros. Por otro lado, se aplica un trascendental teorema que posibilita relacionar entre sí las curvas de crecimiento de grieta $a-N$ obtenidas para diferentes rangos de tensión $\Delta\sigma$ y longitudes iniciales de grieta a_0 , permitiendo derivar las curvas $S-N$ en función del tamaño inicial de grieta a partir de curvas de velocidad de crecimiento de grieta y probando la relación existente entre el modelo basado en tensiones y el basado en la mecánica de fractura. El modelo se aplica a un conjunto de datos experimentales de un cierto acero aleado obteniéndose las curvas de velocidad de crecimiento de grieta y de curvas $S-N$ para su posterior aplicación en la evaluación práctica de vida de fatiga en estructuras y elementos mecánicos.

PALABRAS CLAVE: Curvas de velocidad de crecimiento de grietas, Campo S-N, modelo de Gumbel

ABSTRACT

In this work, a dimensionally congruent model is developed to reproduce the complete crack growth rate curve. The model considers a normalized stress intensity factor range ΔK^{**} defined in the domain $[0, 1]$ that can be interpreted as a cumulative distribution function, thus taking advantage of the statistical experience inherent to this type of functions, in particular, in what concerns the parameter estimation methods. Beside this, a relevant theorem is then used showing the possibility of deriving crack growth curves $a-N$ for different stress ranges $\Delta\sigma$ and initial crack lengths a_0 from a unique reference curve. Thus, the $S-N$ curves can be derived from the crack growth rate curves as a function of the initial crack size proving the close relation between the stress based model and that based on the fracture mechanics. The model is applied to a set of experimental data from a certain steel alloy allowing us the derivation of crack growth rate curves and $S-N$ curves for subsequent application in the practical assessment of the fatigue life of structures and mechanical elements.

KEY WORDS: Crack growth rate curves, S.N field, Gumbel model

1. INTRODUCCIÓN

La relación entre velocidad de crecimiento de grieta y el rango del factor de intensidad de tensiones $da/dN = C\Delta K^m$ propuesta por Paris-Erdogan [1], ha supuesto una meritoria contribución en la evaluación de vida a fatiga de componentes agrietados. De ella han surgido innumerables publicaciones que han introducido mejoras en lo relativo al rango de aplicabilidad da/dN , relación de tensiones $R = \sigma_{min} / \sigma_{max}$, referencia del límite elástico y consideración de efectos plásticos de cierre de grieta

[2,3]. Todas ellas proponen algún tipo de función analítica para representar la curva de crecimiento de grieta mediante adecuado algoritmo. Otros modelos propugnan, desde su inicio, el empleo consecuente de variables y parámetros adimensionales [4]. La consideración de una posible relación entre las curvas de crecimiento de grieta y el campo $S-N$ o $\varepsilon-N$ se plantea sólo excepcionalmente y, en todo caso, desde modelos inspirados en la ley de Paris [5].

En este trabajo se propone un nuevo modelo basado en el análisis dimensional y en propiedades específicas de la curva $da/dN - \Delta K$. La propuesta de un rango del

factor de intensidad de tensiones normalizado ΔK^{*+} definido en el dominio [0, 1] permite la consideración de la curva como función de distribución f.d.d., aprovechando la experiencia estadística con este tipo de funciones, particularmente en lo relativo a los métodos de estimación de parámetros a partir de los resultados experimentales. Tras la integración de la ecuación diferencial se prueba, mediante un importante teorema, que si la dependencia del factor de intensidad de tensiones respecto a geometría y carga puede ser descrita mediante unas determinadas familias de funciones, cualquier curva de crecimiento de grieta, correspondiente a una grieta inicial a_0 y un rango de tensión $\Delta\sigma$, queda definida a partir de una única solución particular, o curva de referencia, lo que constituye una alternativa a modelos basados en auto-similaridad. De este modo es posible establecer una relación entre las curvas de crecimiento de grieta y el campo de Wöhler, permitiendo una propuesta unificada para el análisis de fatiga en elementos y estructuras.

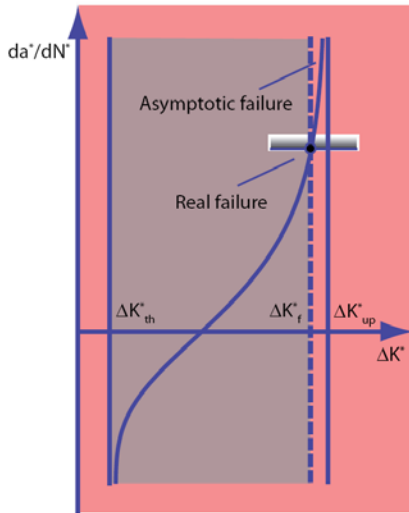


Figura 1. Curva de velocidad de crecimiento de grieta

2. EL MODELO PROPUESTO

De acuerdo con investigaciones previas [6-8] la dependencia del tamaño de grieta puede definirse, simplificada mediante la relación

$$a^*(N^*) = q_1(a_0^*, \Delta K^*(a^*(N^*)), \Delta K_{th}^*, \Delta K_{up}^*), \tag{1}$$

en la que

$$a^* = a/W, a_0^* = a_0/W, N^* = N/N_0, \Delta K_{th}^* = \Delta K_{th}/K_c$$

$$\Delta K_{up}^* = \Delta K_{up}/K_c \text{ con los significados siguientes: } a, \text{ tamaño de grieta, } a_0, \text{ tamaño inicial de grieta, } W, \text{ anchura de probeta, } N, \text{ número de ciclos, } N_0, \text{ número de ciclos de referencia, } \Delta K_{th}, \text{ rango umbral del factor de intensidad de tensiones, } \Delta K_{up}, \text{ rango límite del factor de intensidad de tensiones y } K_c, \text{ tenacidad a fractura característica del material.}$$

Derivando (1) se obtiene

$$\frac{da^*(N^*)}{dN} = q_2(\Delta K^*(a^*(N^*)), \Delta K_{th}^*, \Delta K_{up}^*); \quad a^*(0) = a_0^* \tag{2}$$

de la que la ley de Paris es una simplificación. Las curvas de crecimiento de grieta se pueden obtener por integración de la ecuación (2), que representa una solución determinista para una geometría de probeta y tamaño dados de un determinado material bajo condiciones fijas de ensayo (relación de tensiones $R^* = \sigma_{min}/\sigma_{max}$ y rango de tensiones adimensional $\Delta\sigma^*$).

2.1 Establecimiento del modelo

En el modelo se consideran dos posibles mecanismos de rotura competitivos, el debido a un crecimiento estable de grieta y el asociado con la propagación inestable de grieta (fig.1), que es el determinante en la práctica. Esto conduce a la consideración de un valor asintótico superior, ΔK_{up}^* , que con el valor asintótico inferior, o umbral, ΔK_{th}^* marcan el rango de existencia teórica de ΔK^* . De acuerdo con ello se define la variable

$$\Delta K^{*+} = \frac{\log \Delta K^* - \log \Delta K_{th}^*}{\log \Delta K_{up}^* - \log \Delta K_{th}^*}, \tag{3}$$

que toma valores en el intervalo [0,1] y es monótonicamente creciente en la función (2), lo que permite interpretarla como la inversa de una función de distribución F , en particular:

$$\begin{aligned} \log \frac{da^*(N^*)}{dN} &= F^{-1}(\Delta K^{*+}(a^*(N^*))) = H(\Delta K^*(a^*(N^*))) \\ &= H(\Delta\sigma^* Y^*(a^*(N^*)) \sqrt{\pi a^*(N^*)}) = H(\Delta\sigma^* Z(a^*(N^*))), \end{aligned} \tag{4}$$

en la que

$$H(\Delta K^*) = F^{-1} \left[\frac{\log \Delta K^* - \log \Delta K_{th}^*}{\log \Delta K_{up}^* - \log \Delta K_{th}^*} \right] \tag{5}$$

y

$$Z(a^*(N^*)) = Y^*(a^*(N^*)) \sqrt{\pi a^*(N^*)}, \tag{6}$$

con lo que

$$\frac{da^*(N^*)}{dN} = \exp[H(\Delta\sigma^* Z(a^*(N^*)))] = V(\Delta\sigma^* Z(a^*(N^*))). \tag{7}$$

La forma de la curva de velocidad de crecimiento de grieta identificada como una función de distribución, es atribuible a los cambios microestructurales continuos que se suceden en el material durante todo el proceso de fatiga. En este caso se aprovecha la experiencia acumulada en el estudio de las f.d.d. y en los métodos de estimación de parámetros en el análisis del crecimiento de grieta para reproducir no sólo la zona lineal de Paris, sino el conjunto de curva de velocidad de crecimiento de grieta.

2.2 Solución de la ecuación diferencial

La ecuación diferencial (7) permite obtener la curva de crecimiento de grieta $a^*(N^*)$ en función de N^* para la condición inicial $a^*(0) = a_0^*$ cuando el rango de tensión $\Delta\sigma^* = \Delta\sigma_0^*$ permanece constante. Entre las deducciones teóricas desarrolladas en [9], se demuestra un teorema, según el cual si $a_0^*(N^*)$ representa la solución de la ecuación diferencial (7) para $\Delta\sigma^* = \Delta\sigma_0^*$ y $a^*(0) = a_0^*$ y la función $Z(a^*(N^*))$ presenta una de las formas siguientes:

$$Z(a^*) = \begin{cases} T \exp(U a^*) \\ (Q a^* + T)^V \end{cases}, \quad (8)$$

en la que T, U, Q y V son constantes arbitrarias, el tamaño de grieta $a^*(N^*)$ tras N^* ciclos para cualquier combinación $\Delta\sigma^* = \Delta\sigma_1^*$ y $a^*(0) = a_1^*$, viene dado por la expresión

$$a^*(N^*) = Z^{-1} \left\{ \frac{1}{\rho} Z \left[a_0^* \left(\rho^k N^* + a_0^{*-1} \left(Z^{-1}(\rho Z(a_1^*)) \right) \right) \right] \right\} \quad (9)$$

donde $\rho = \frac{\Delta\sigma_1^*}{\Delta\sigma_0^*}$.

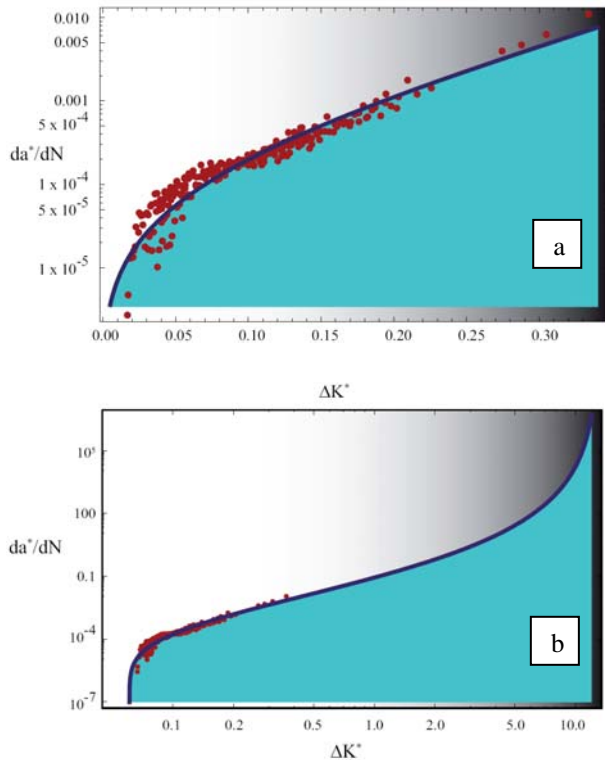


Figura 2. Resultados experimentales y ajuste del modelo de velocidad de crecimiento de grieta.

2.3 El modelo de Gumbel

Dentro de las posibles funciones de distribución a elegir para el modelo, se considera conveniente la de Gumbel para máximos:

$$F(x) = \exp \left[-\exp \left(\frac{\alpha - x}{\gamma} \right) \right]; \quad \gamma > 0 \quad (10)$$

lo que conduce al modelo

$$\begin{aligned} \left[\frac{\log \Delta K^* - \log \Delta K_{th}^*}{\log \Delta K_{up}^* - \log \Delta K_{th}^*} \right] &= F \left(\log \frac{da^*}{dN^*} \right) \\ &= \exp \left[-\exp \left(\frac{\alpha - \log \frac{da^*}{dN^*}}{\gamma} \right) \right] \end{aligned} \quad (11)$$

dependiente de cuatro parámetros: $\alpha, \gamma, \Delta K_{th}^*$ y ΔK_{up}^* .

2.4 Estimación de los parámetros del modelo

En este caso, dado que las magnitudes observadas son deterministas, no está justificado el método de máxima verosimilitud, por lo que se aplica la técnica de mínimos cuadrados, en particular

$$\text{Minimize}_{\alpha, \gamma, \Delta K_{th}^*, \Delta K_{up}^*} Q(\alpha, \gamma, \Delta K_{th}^*, \Delta K_{up}^*), \quad (12)$$

donde $Q(\alpha, \gamma, \Delta K_{th}^*, \Delta K_{up}^*)$ viene dado por

$$\sum_{i=1}^n \left\{ \log \Delta K_i^* - \log \Delta K_{th}^* - (\log \Delta K_{up}^* - \log \Delta K_{th}^*) \exp \left[-\exp \left(\frac{\alpha - \alpha_i^*}{\gamma} \right) \right] \right\}^2 \quad (13)$$

siendo $\alpha_i^* = \frac{da^*}{dN^*}$ y $\Delta K_i^*, i = 1, 2, \dots, n$ los puntos de los datos.

2.5 Ejemplo de aplicación

Como ilustración se presenta la aplicación del modelo a un caso práctico, en el que se tratan los resultados experimentales obtenidos en el Fraunhofer IWM para un determinado acero estructural. Para la determinación de los resultados relativos a la curva de velocidad de crecimiento de grieta se utilizaron probetas del tipo CCT [9].

Se consideraron como variables de normalización:

$$\begin{aligned} N_0 &= 1000 \text{ ciclos}, D = W = 24 \text{ mm}, B = 10 \text{ mm}, \\ K_c &= 200 \text{ MPa m}^{1/2}, \end{aligned}$$

obteniéndose, tras la minimización de la función (11), siguientes valores estimados de los parámetros

$$\begin{aligned} \alpha &= -4.5155, \gamma = 4.8092, \log \Delta K_{th}^* = -2.7981, \\ \log \Delta K_{up}^* &= 2.5709, \end{aligned} \quad (14)$$

es decir, $\Delta K_{th} = 12 \text{ MPa m}^{1/2}, \Delta K_{up} = 2615 \text{ MPa m}^{1/2}$.

En la fig. 2 se representan los datos experimentales para el material ensayado y la curva de velocidad de crecimiento de grieta $da^*/dN^* - \Delta K^*$ ajustada, que muestran una buena concordancia. Como consecuencia de la concentración de datos en la parte inferior de la curva y la práctica carencia en su parte superior, el valor de ΔK_{up}^* no resulta creíble. Una solución conservadora se puede alcanzar imponiendo inicialmente $\Delta K_{up}^* = \Delta K_f^*$, donde ΔK_f^* corresponde al crecimiento inestable de grieta, determinado al alcanzarse $K_{max}^* = K_c^*$.

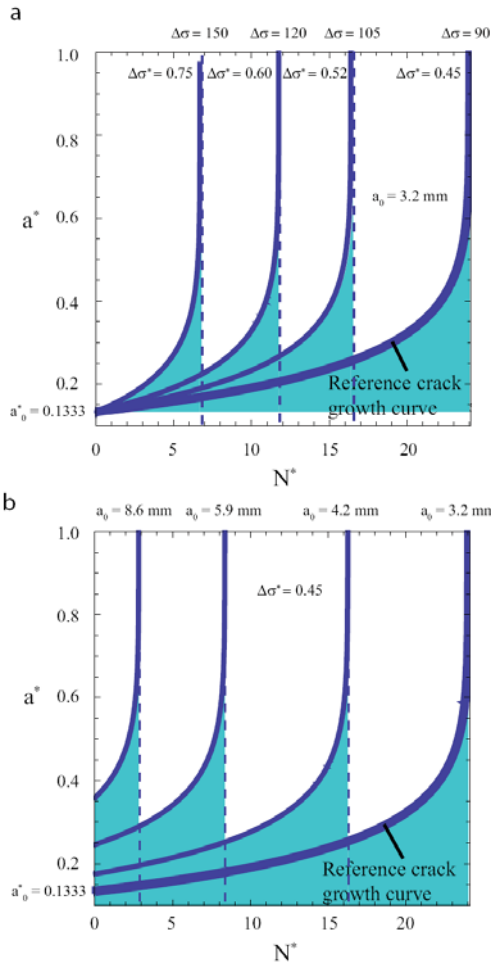


Figura 3. Curvas de crecimiento de grieta resultantes de la aplicación de (8).

En la fig. 3, se muestra la curva de crecimiento de grieta de referencia, obtenida para $\Delta\sigma = 90 \text{ MPa}$ y $a = 3.2 \text{ mm}$ tras la integración de la ecuación (7) mediante el procedimiento *Dsolve* de Mathematica, basado en el método Runge-Kutta. A partir de esta solución se puede determinar la curva de crecimiento de grieta para cualquier condición de carga y tamaño inicial de grieta, tal como se desprende de la figura 3a, en la que se representan, junto a la curva de referencia, las curvas resultantes de aplicar la ecuación (9) a los casos $\Delta\sigma = 105, 120$ y 150 MPa para un mismo tamaño

inicial de grieta. De manera similar, la figura 3b recoge las curvas de crecimiento de grieta para el mismo rango de tensión $\Delta\sigma = 90 \text{ MPa}$ y diferentes tamaños iniciales de grieta $a = 3.2, 4.2, 5.9$ y 8.6 mm .

3. CRECIMIENTO DE GRIETA Y CURVAS S-N

La trascendencia del teorema mencionado en el apartado 2.2, queda patente al permitir la obtención de curvas S-N, en el sentido de vida remanente a fatiga, a partir de las curvas de crecimiento de grieta. Si se considera un tamaño inicial de grieta aleatorio, representado por A_0^* , la relación entre el tamaño final de la grieta a_f^* y el número de ciclos hasta la rotura viene dada por:

$$a_f^*(N_f^*) = Z^{-1} \left\{ \frac{1}{\rho} Z \left[a_0^* \left(\rho^k N_f^* + a_0^{*-1} \left[Z^{-1}(\rho Z(A_0^*)) \right] \right) \right] \right\}, \quad (15)$$

que permite, a su vez, calcular el tamaño inicial de la grieta en función de la vida a fatiga mediante

$$A_0^* = Z^{-1} \left\{ \frac{1}{\rho} Z \left[a_0^* \left(a_0^{*-1} \left[Z^{-1}(\rho Z(a_f^*)) \right] - \rho^k N_f^* \right) \right] \right\}, \quad (16)$$

en la que a_f^* se determina a través de la condición de fractura bajo propagación inestable estática

$$a_f^* = \frac{I}{(Y^*(a_f^* \sigma_{max}^*))^2 \pi}. \quad (17)$$

En este caso, optando por la segunda variante de (8), se obtiene

$$Z(a^*) = (Qa^* + T)^V = (0.126115617 a^* + 0.9701834)^{30}, \quad (18)$$

cuyos coeficientes se estimaron mediante el método de los mínimos cuadrados, permitiendo un ajuste prácticamente perfecto de la expresión clásica

$$Z(a^*) = Y^*(a^*) \sqrt{a^*} = \sec(\pi a^*) (1 - 0.025(2a^*)^2 + 0.06(2a^*)^4) \sqrt{\pi a^*}$$

propuesta en los textos clásicos [10]. Con ello queda justificada la forma requerida en (8) y, en consecuencia, garantizada la condición de aplicabilidad del teorema, al menos en el presente caso.

Si se define a_p^* como el tamaño de grieta asociado al percentil p , el campo S-N probabilístico vendrá dado por

$$a_p^* = Z^{-1} \left\{ \frac{1}{\rho} Z \left[a_0^* \left(a_0^{*-1} \left[Z^{-1}(\rho Z(a_f^*)) \right] - \rho^k N_f^* \right) \right] \right\} = F_{A_0^*}^{-1}(1-p) \quad (19)$$

o, respectivamente,

$$N_f^* = \frac{a_0^{*-1} \left[Z^{-1}(\rho Z(a_f^*)) \right] - a_0^{*-1} \left[Z^{-1}(\rho Z(a_p^*)) \right]}{\rho^k}, \quad (20)$$

que representa la ecuación de la curva percentil p en el campo S-N para una grieta inicial a_p^* .

4. RELACIÓN ENTRE LAS FUNCIONES DE DISTRIBUCIÓN CORRESPONDIENTES A LA LONGITUD DE GRIETA Y VIDA EN FATIGA

En esta sección se muestra cómo derivar la f.d.d. del tamaño de la grieta inicial o la f.d.d. de la vida en fatiga para un $\Delta\sigma^*$ dado. De acuerdo con (21), es posible obtener la f.d.d. de a_0^* a partir de la f.d.d. de N_f^* como sigue:

$$\begin{aligned}
 F_{A_0^*}(a_0^*) &= Pr(A_0^* \leq a_0^*) \\
 &= Pr\left(Z^{-1}\left\{ \frac{1}{\rho} Z\left[a_0^* \left(a_0^{*-1} \left[Z^{-1}(\rho Z(a_f^*)) - \rho^k N_f^* \right] \right) \right] \right\} \leq a_0^* \right) \\
 &= Pr\left(N_f^* \geq \frac{a_0^{*-1} \left[Z^{-1}(\rho Z(a_f^*)) \right] - a_0^{*-1} \left[Z^{-1}(\rho Z(a_0^*)) \right]}{\rho^k} \right) \\
 &= 1 - F_{N_f^*}\left(\frac{a_0^{*-1} \left[Z^{-1}(\rho Z(a_f^*)) \right] - a_0^{*-1} \left[Z^{-1}(\rho Z(a_0^*)) \right]}{\rho^k} \right).
 \end{aligned}
 \tag{21}$$

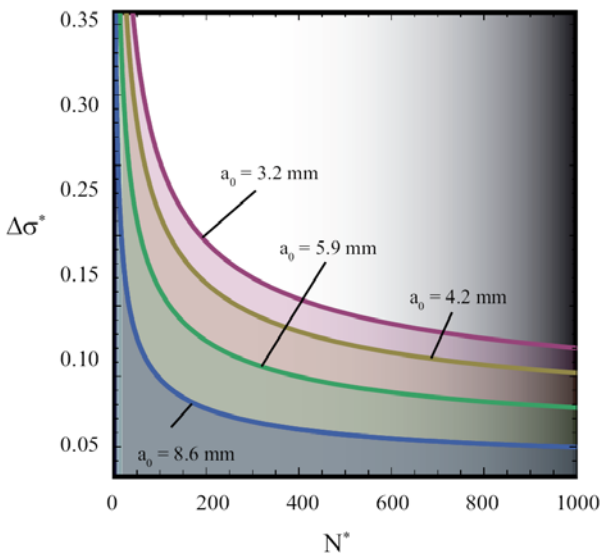


Figura 4. Curvas S-N obtenidas de la ecuación (19).

Como se puede observar, para conocer la forma de las curvas percentiles del campo S-N no se requiere conocer la f.d.d. $F_{A_0^*}(a_0^*)$, mientras que para identificar el percentil asociado a un determinado valor de p sí es preciso conocerla previamente, aunque puede ser deducida a partir de la f.d.d. $F_{N_f^*}(N_f^*)$, como se verá en la próxima sección.

Retomando el ejemplo de la sección 3, en la figura 4 se muestran los percentiles de las curvas S-N correspondientes a los tamaños iniciales de grietas $a_0 = 3.2, 4.2, 5.9$ y 8.6 mm para un tamaño crítico de grieta $a_f = 12$ mm ($a_f^* = 0.5$). Obsérvese que, contraria-

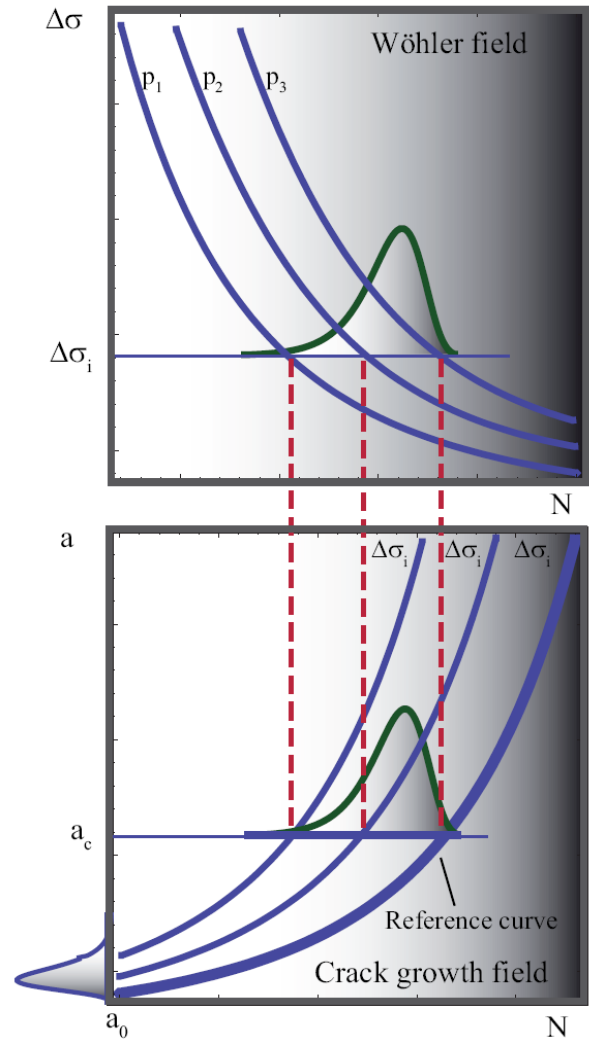


Figura 5. Correspondencia entre las curvas de crecimiento de grieta y las curvas S-N.

mente al campo S-N convencional, el límite de fatiga depende del percentil.

A su vez, la correspondencia existente entre las curvas de crecimiento de grieta y el campo S-N queda ilustrada esquemáticamente en la figura 5, en la que se puede observar la relación entre la función de densidad del tamaño inicial de grieta y la función de densidad de la vida de fatiga para un rango determinado de tensión $\Delta\sigma_i$. Esta última, deducida de las curvas de crecimiento de grieta, tiene que coincidir con la función de densidad resultante en el campo S-N.

Esto demuestra que la información estadística proporcionada por $F_{N_f^*}(N_f^*)$ relativa a un particular rango de tensión del campo S-N, juntamente con la curva de crecimiento de grieta de referencia $a_0^*(\cdot)$ permite la determinación de la f.d.d. de la longitud

inicial de grieta $F_{A_0^*}(A_0^*)$. De este modo, combinando ensayos de fatiga para $\Delta\sigma$ y R fijos con ensayos de crecimiento de grieta, es posible determinar $F_{A_0^*}(A_0^*)$.

Siguiendo un proceso similar, se deduce

$$F_{N_f^*}(n_f^*) = 1 - F_{A_0^*} \left(Z^{-1} \left\{ \frac{1}{\rho} Z \left[a_0^* \left(a_0^{*+1} \left[Z^{-1}(\rho Z(a_f^*)) \right] - \rho^k N_f^* \right) \right] \right\} \right), \quad (22)$$

que implica que la f.d.d. de la longitud inicial de grieta a_0^* , juntamente con la curva de crecimiento de grieta de referencia $a_0^*(\cdot)$ permite determinar la f.d.d. $F_{N_f^*}(N_f^*)$ relativa a la vida en fatiga.

5. CONCLUSIONES

Las principales conclusiones que se derivan del presente trabajo son:

- La identificación de la variable normalizada ΔK^{*+} , que toma valores en el intervalo [0,1], como una f.d.d. permite definir analíticamente la relación entre da/dN y ΔK^{*+} aprovechando la experiencia acumulada en el campo estadístico sobre estas funciones y los métodos de estimación de los parámetros.

- Si la función $Z(a^*(N^*))$ responde a las formas descritas, tal como queda confirmado en los resultados considerados en este trabajo, resulta posible obtener las curvas de crecimiento de grieta para cualquier combinación de $\Delta\sigma^*$ y tamaño inicial de grieta, a partir de una única curva de referencia.

- El modelo propuesto proporciona una expresión analítica de la curva de velocidad de crecimiento de grieta a emplear en el cálculo a fatiga de elementos mecánicos y estructurales mediante ajuste de los resultados experimentales por el método de mínimos cuadrados.

- La información estadística contenida en $F_{N_f^*}(N_f^*)$ suministrada para un rango particular del campo S-N, junto con la curva de crecimiento de grieta de referencia $a_0^*(\cdot)$ permite la determinación de la f.d.d. $F_{A_0^*}(A_0^*)$ de la longitud inicial de la grieta. Análogamente la f.d.d. $F_{A_0^*}(A_0^*)$, juntamente con $a_0^*(\cdot)$ permite la determinación de la f.d.d. de la vida en fatiga $F_{N_f^*}(N_f^*)$ para cualquier rango de tensión $\Delta\sigma^*$.

- Se demuestra que es posible obtener el campo S-N a partir de $F_{N_f^*}(N_f^*)$ o de $F_{A_0^*}(A_0^*)$ y de la curva de referencia $a_0^*(\cdot)$, lo que tiene importantes consecuencias en la práctica.

6. AGRADECIMIENTOS

Los autores agradecen el apoyo económico recibido a través de la subvención de los proyectos MEC (Ref.: DPI 2007-66903-C02-01) y FICYT (Ref.: IB08-171), así como la beca del Ministerio de Ciencia e Innovación que permitió la estancia del primer autor en el Fraunhofer IWM de Freiburg (Alemania).

7. REFERENCIAS

- [1] Paris P., Erdogan F., *A critical analysis of crack propagation laws*, J. of Basic Engineering, 85, 528-534, 1960.
- [2] NASGRO, *Fatigue crack growth computer program NASGRO, version 3- Reference Manual 2000*.
- [3] Pugno A., Ciavarella M., Cornetti A., Carpinteri A., *Paris' law for fatigue crack growth*, J. of Mech. Physics of Solids, 54, 1333-1349, 2006.
- [4] Agha H.Y., Béranger A.S., Billardon R., Hild F., *A probabilistic approach to predict the very high cycle fatigue behaviour of spheroidal graphite cast iron*. Fatigue and Fracture of Engineering Materials and Structures, 23, 173-180, 2000.
- [5] Vormwald M., *Anrisslebensdauervorhersage auf der Basis der Schwingbruchmechanik für kurze Risse*, Ph.D. Thesis, Techn. Hochschule Darmstadt, 1989.
- [6] Spagnoli A., *Self-similarity and fractals in the Paris range of fatigue crack growth*. Mechanics and Materials, 37, 519-529, 2005, 2009.
- [7] Ritchie R.O., *Incomplete self-similarity and fatigue-crack growth*, Int. J. Of Fracture, 132, 197-203, 2005.. Submitted to Theoretical and Applied Fracture Mechanics, 2009.
- [8] Carpinteri A., Paggi M., *Selfsimilarity and crack growth instability in the correlation between the Paris' constants*, Eng. Fracture Mechanics, 74, 1041-1053, 2007.
- [9] Castillo E., Fernández Canteli A., Siegele D., *Obtaining S-N curves from crack growth curves. An alternative to self-similarity*. Submitted to Theoretical and Applied Fracture Mechanics, 2009.
- [10] Anderson, T.L., *Fracture mechanics. Fundamentals and applications*, Taylor and Francis, Boca Raton, 3rd edition 2006.

COMPORTAMIENTO EN FATIGA DE UNIONES ROSCADAS

B. González¹, J.C. Matos², F.J. Ayaso¹, J. Toribio¹

¹ Ingeniería de Materiales (Universidad de Salamanca),
E.P.S., Campus Viriato, Avda. Requejo, 33,
49022 Zamora. España.
Correo-e: bgonzalez@usal.es

² Departamento de Informática y Automática (Universidad de Salamanca),
E.P.S., Campus Viriato, Avda. Requejo, 33,
49022 Zamora. España.
Correo-e: jcmatos@usal.es

RESUMEN

En este trabajo se han ensayado uniones atornilladas sometidas a sollicitaciones monótonas crecientes y a fatiga en control de carga, empleando intervalos de oscilación de tensiones constantes con distintos valores del factor R . Algunas de estas probetas se han sometido a una precarga de tracción de forma previa a la aplicación de la carga cíclica. Los resultados muestran que en sollicitación monótona creciente la unión roscada no es la zona de fallo del tornillo, mientras que sí lo es para carga cíclica. La vida en fatiga disminuye con el aumento del intervalo de oscilación de tensiones y con la tensión máxima, y la precarga aumenta la vida en fatiga para intervalos de oscilación de tensiones pequeños. La superficie de fractura por fatiga muestra una geometría de *luna creciente* para fisuras cortas que evoluciona hacia frentes de fisura casi rectos para fisuras largas. La fractura por fatiga normalmente ocurre en el fondo del primer filete del tornillo que está dentro de la unión roscada, aunque puede existir iniciación en varios filetes consecutivos, aumentando el ángulo de iniciación de la fisura en fatiga con la disminución de la tensión aplicada.

ABSTRACT

In this work, bolted joints were tested under both monotonic tensile loading and fatigue, in the latter case using constant stress amplitude with different values of the R ratio. Some of the specimens were subjected to a tensile (monotonic) pre-loading before the fatigue (cyclic) loading. Results show that under increasing monotonic tensile loading the bolted joint is not the failure zone of the bolt, whereas such a bolted joint is the failure region under cyclic loading. The fatigue life decreases with the increase of the stress range and with the maximum stress, and pre-loading enlarges the fatigue life for small stress ranges. Fatigue fracture surface shows a geometry of *increasing moon* in the case of short (shallow) cracks and such a shape evolves towards a quasi-straight crack front in the case of long (deeper) cracks. Fatigue fracture usually happens at the root of the first notch inside the bolted joint, although fracture initiation may happen in several consecutive notch roots, increasing the initiation angle of the fatigue crack as the applied stress diminishes.

PALABRAS CLAVE: Uniones roscadas, Vida en fatiga, Fisuración por fatiga.

1. INTRODUCCIÓN

En muchas ocasiones las uniones roscadas resultan ser las zonas más débiles en estructuras o en mecanismos, por lo que conocer su comportamiento resulta clave cuando se someten a una carga monótona creciente hasta rotura (por ejemplo en un mal diseño) o cuando aparecen cargas fluctuantes (fatiga). Aunque en muchos casos los tornillos pueden estar sometidos a múltiples tipos de fuerzas (torsión, flexión) siempre presentan una fuerte componente a tracción, condición de carga que ha sido estudiada en este trabajo.

La fatiga en tornillos suele caracterizarse a partir de las curvas de Wöhler, donde el aumento del factor R disminuye la vida en fatiga [1]. El cálculo del límite de fatiga es a menudo un factor condicionado por el

tiempo, pudiéndose medir en tiempos menores mediante un método acelerado usando la tensión umbral para la iniciación de fisuras por fatiga en el fondo del filete [2]. El fallo de tornillos ocurre hasta un determinado número de ciclos, a partir del cual no hay fractura [3].

Los tornillos de paso normal tienen una vida en fatiga mayor que los de paso fino, mostrando además el tornillo un efecto tamaño respecto a su vida en fatiga [4] (ésta disminuye con el aumento del diámetro nominal) debido al efecto entalla del fondo de los filetes [5]. El coeficiente de fricción en los hilos disminuye con el aumento de la velocidad del apriete y por tanto la carga en la unión roscada aumenta [6]. El nivel de precarga influye en la vida en fatiga de la unión: una precarga inicial insuficiente, o su pérdida, puede producir una reducción en la vida en fatiga del tornillo [1].

Los tornillos laminados mejoran el comportamiento en fatiga respecto a los mecanizados por arranque de material, debido a las tensiones residuales compresivas originadas en el fondo de los filetes [1,7]. Los factores que más influyen sobre el límite de fatiga de elementos roscados mecanizados son el desgaste de la herramienta y la velocidad de corte, mientras que el método de corte y el avance radial son menos significativos [8]. En los tornillos laminados las altas velocidades de penetración de la herramienta aumentan el límite de fatiga, debido a la aparición de mayores tensiones residuales axiales de compresión y al endurecimiento por deformación [9].

El laminado de los tornillos de acero después del recocido (comparándolo con el procedimiento contrario, que es lo usual) aumenta notablemente la vida en fatiga para tensiones mínimas bajas [10,11]. Por el contrario, para tensiones mínimas altas apenas hay cambios si los tornillos son de paso normal [10] y el aumento es mucho menor si los tornillos son de paso fino [11].

2. PROCEDIMIENTO EXPERIMENTAL

2.1. Probeta de ensayo

Las probetas de estudio se realizaron mediante el roscado de un tornillo comercial M10x200 calidad 8.8 (DIN 931), de acero, pavonado y sin cabeza, en una pieza cilíndrica (con rosca interior mecanizada) de 16mm de diámetro, 150mm de longitud y del mismo material que el tornillo (figura 1).

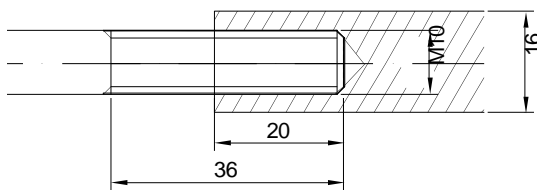


Figura 1. Unión roscada.

2.2. Procedimiento experimental

El comportamiento mecánico del acero de los tornillos se ha determinado a través de ensayos de tracción simple, con probetas obtenidas de la caña de los tornillos, usando una velocidad de desplazamiento de la mordaza de 2mm/min. También se han efectuado ensayos de microdureza Vickers.

Sobre las probetas con la unión roscada se han realizado ensayos con sollicitación monótona axial en control de desplazamiento (velocidad de movimiento de mordaza de 2mm/min), hasta rotura.

Para la caracterización en fatiga se realizaron ensayos en control de carga ($\Delta\sigma$ constante), con una forma de onda sinusoidal, frecuencia de 10Hz y diferentes valores del factor R (0, 0.25 y 0.50). Los ensayos se mantuvieron hasta rotura o hasta que se consiguieron 10^6 ciclos. Algunas de las probetas fueron sometidas a una precarga en tracción del 80% del límite elástico teórico

del material de los tornillos, para estudiar el efecto de la misma sobre la vida en fatiga.

3. RESULTADOS

3.1. Caracterización del material

El acero de estudio, después de su preparación metalográfica y ser atacado con nital al 4%, presentó una microestructura ferrítico-perlítica, como se puede observar en la figura 2.

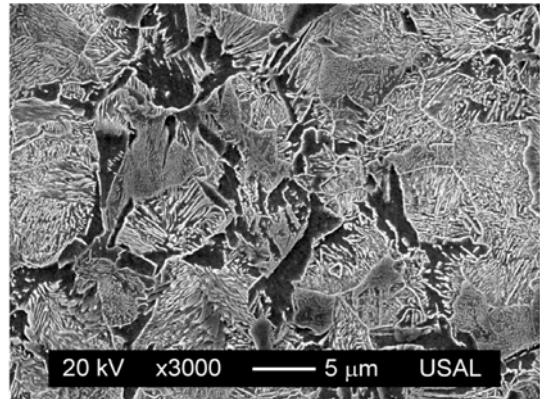


Figura 2. Microestructura del acero.

Se realizaron tres ensayos de tracción simple, cuyas curvas tensión-deformación se muestran en la figura 3. Las características mecánicas obtenidas fueron: módulo de Young $E=199\text{GPa}$, límite elástico convencional al 0.2% $\sigma_{0.2}=546\text{MPa}$, resistencia a tracción $\sigma_{\text{max}}=715\text{MPa}$ y deformación para carga máxima $\epsilon_{\text{max}}=0.04$. Los resultados alcanzados presentaron valores inferiores a los correspondientes a la calidad 8.8 de los tornillos.

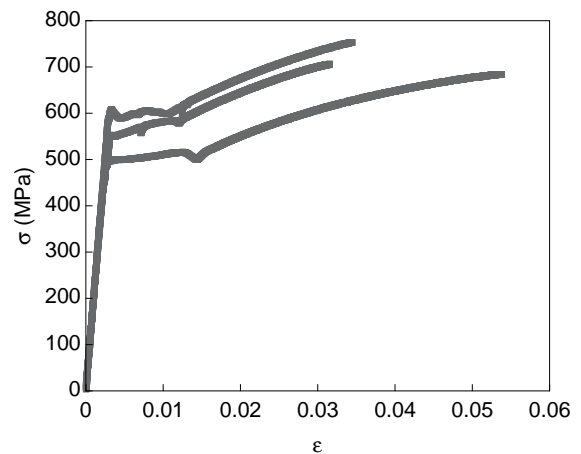


Figura 3. Curvas tensión-deformación (tracción simple).

La superficie de fractura resultante del ensayo de tracción simple (figura 4) es la típica fractura copa-cono presente en muchas aleaciones metálicas (dúctiles). Ésta presenta una zona central plana y fibrosa formada por microhuecos irregulares y una corona exterior con paredes a 45° de microhuecos alargados.

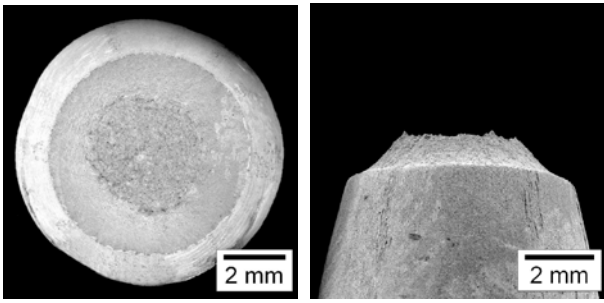


Figura 4. Superficie de fractura en tracción simple.

La microdureza Vickers se ha medido de forma radial sobre la sección longitudinal del tornillo (figura 5). Se obtuvieron valores mayores en la zona superficial que en la central, probablemente debido a una velocidad de enfriamiento diferente entre ambas regiones durante el tratamiento térmico posterior al proceso de conformado. Además, la microdureza obtenida presenta una gran dispersión en sus resultados, lo que sugiere la existencia de diferentes microestructuras.

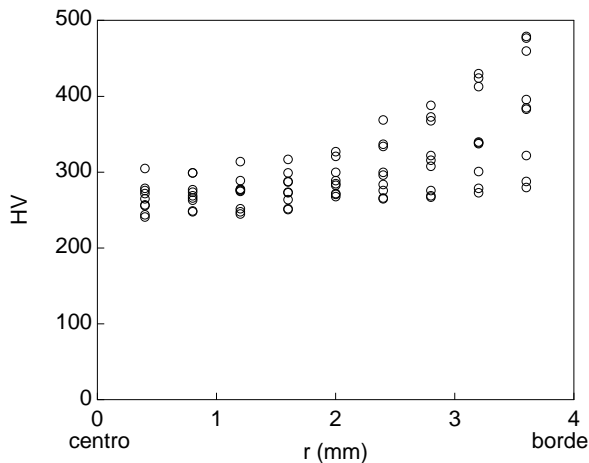


Figura 5. Microdureza Vickers.

3.2. Ensayos bajo sollicitación monótona creciente

Al aplicar sollicitación monótona creciente sobre las probetas con la unión roscada la fractura sucedió fuera de ésta. En las probetas donde no se introdujeron varios filetes del tornillo en la unión, la fractura tuvo lugar en el fondo de alguno de estos filetes exteriores y la tensión de rotura coincidió con el límite elástico del material. En cambio, si todos los filetes estaban dentro de la unión (todos habían sido roscados), la rotura sucedía fuera de ésta (en la caña del tornillo o en el enlace con la rosca) a una tensión superior al límite elástico del material.

La superficie de fractura resultado de los ensayos es de tipo copa-cono, con la particularidad de la presencia de los filetes que originan una superficie de fractura más asimétrica, donde además hay que salvar la altura de un filete (figura 6). En dicha superficie apareció la zona fibrosa, de menor tamaño que en tracción simple (respecto a la superficie total de fractura), y la corona exterior con forma más irregular.

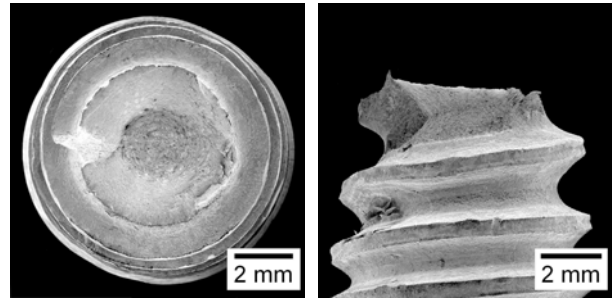


Figura 6. Superficie de fractura en carga monótona.

3.3. Ensayos de fatiga

Factor R

Se han obtenido las curvas de Wöhler ($\sigma_{max}-N_f$ y $\Delta\sigma-N_f$) para probetas con unión roscada sometidas a carga cíclica, para $\Delta\sigma$ constante y varios valores del factor R (0, 0.25 y 0.50). Éstas se muestran en las figuras 7 y 8.

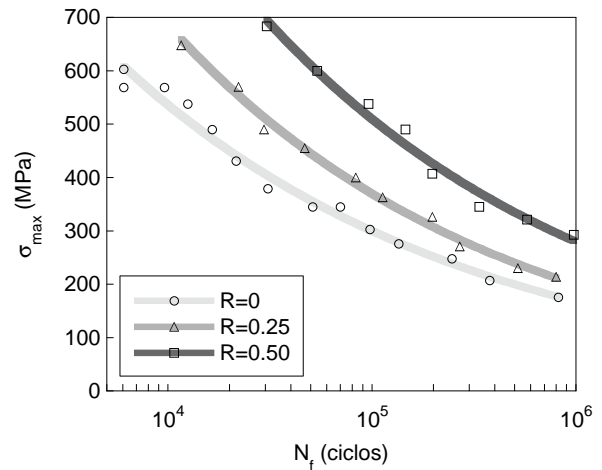


Figura 7. Curvas de Wöhler ($\sigma_{max}-N_f$).

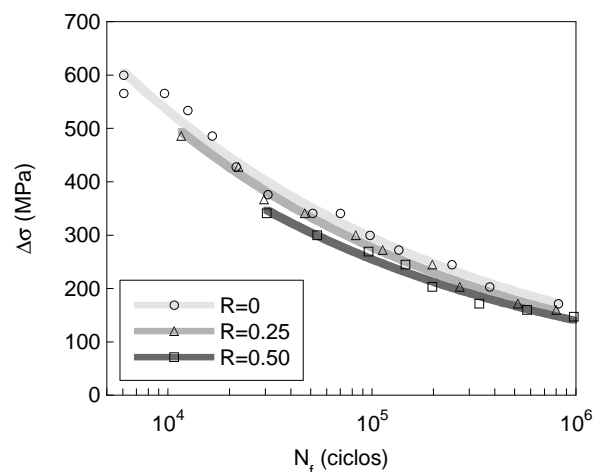


Figura 8. Curvas de Wöhler ($\Delta\sigma-N_f$).

Puede observarse que las curvas $\sigma_{max}-N_f$ se desplazan hacia la derecha con el aumento del factor R, mientras que las curvas $\Delta\sigma-N_f$ lo hacen hacia la izquierda. Por tanto la fatiga es un fenómeno biparamétrico, donde el

aumento de σ_{max} o de $\Delta\sigma$ disminuye la vida en fatiga. Además se ha obtenido un ajuste de tipo potencial para la vida en fatiga, único para todas las curvas, que tiene en cuenta ambos parámetros,

$$N_f = 2.82 \cdot 10^{14} \sigma_{max}^{-1} \Delta\sigma^{-2.82} \quad (1)$$

Efecto de la precarga

En algunos ensayos los tornillos fueron sometidos a una precarga con el objeto de estudiar su efecto sobre la fatiga (figuras 9 y 10, donde el valor de la precarga se representa con una línea horizontal discontinua). Las curvas de Wöhler muestran que la vida en fatiga de los tornillos para $R=0$ y $R=0.50$ aumenta con la aplicación de la precarga para intervalos de oscilación de tensiones por debajo de ~ 220 MPa.

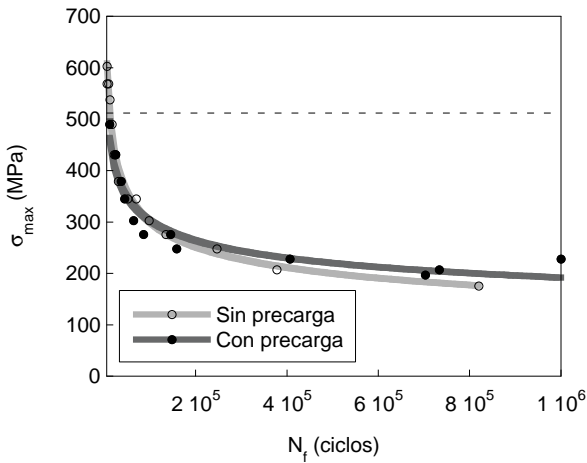


Figura 9. Curvas de Wöhler para $R=0$, con y sin precarga.

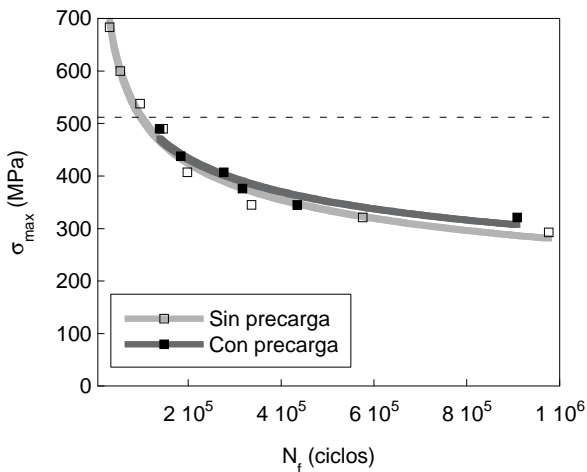


Figura 10. Curvas de Wöhler para $R=0.50$, con y sin precarga.

En tornillos libres de tensiones residuales, cómo los conformados por arranque de material, la precarga de tracción resulta siempre beneficiosa por las tensiones compresivas originadas en el fondo de los filetes. En cambio, en los tornillos conformados por deformación

plástica (después de realizar el tratamiento térmico) ya existen tensiones residuales producto del conformado que serán redistribuidas afectando a la vida en fatiga [1].

Superficies de fractura

La fractura por fatiga (figura 11) ocurre en el fondo del primer filete dentro de la unión roscada [3,4,10-12], donde existe la mayor tensión superficial. La superficie de fractura muestra una primera región fatigada, a continuación una zona con fractura plana y finalmente una fractura inclinada o labio cortante [10].

Las fisuras cortas (figura 11 superior), de poca profundidad, presentan un frente de fisura de fatiga en forma de “luna creciente” rodeando casi todo el borde del tornillo. Las fisuras intermedias (figura 11 media), de profundidades cercanas al centro del tornillo, tienen un frente de fisura aún de “luna creciente” pero con menos circunferencia cubierta. Por último, las fisuras largas (figura 11 inferior), de grandes profundidades, presentan un frente casi plano.

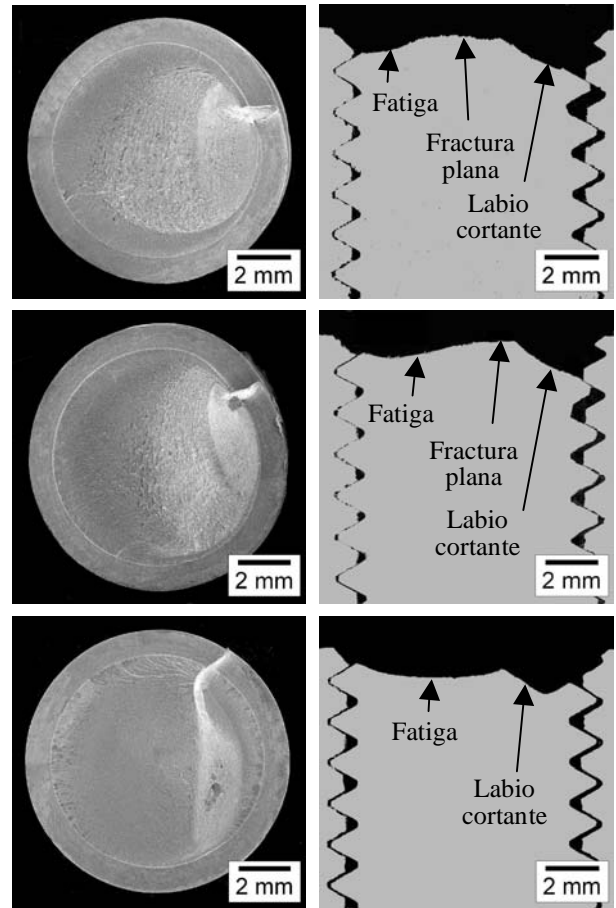


Figura 11. Superficie de fractura en fatiga. (Superior) $\Delta\sigma=600$ MPa, $R=0$ y $N_f=6056$ ciclos. (Media) $\Delta\sigma=486$ MPa, $R=0$ y $N_f=17850$ ciclos. (Inferior) $\Delta\sigma=203$ MPa, $R=0$ y $N_f=377911$ ciclos.

La tensión aplicada influye en el camino seguido por la fatiga, pero especialmente en su iniciación. Se realizó un ensayo de fatiga sin llegar a fracturar la probeta

(con $\Delta\sigma=486\text{MPa}$, $R=0$ y durante $0.75N_f$ ciclos) y a continuación se sometió ésta a una carga elevada para hacer más visible la fisura, ya que así se produce redondeo y aumento de la apertura de fisura (COD). En su corte longitudinal (figura 12) se observa cómo se inician fisuras en el fondo de filetes sucesivos, siendo la de mayor longitud la fisura del primer filete dentro de la unión, que es el más cargado, y así sucesivamente. Además, inicialmente las fisuras de fatiga se propagan desde el fondo del filete con cierta inclinación respecto la sección transversal del tornillo, de forma que el ángulo formado aumenta con la disminución de la carga aplicada (figura 11 derecha y figura 12), debido a la localización y a la direccionalidad de las tensiones principales máximas [13].

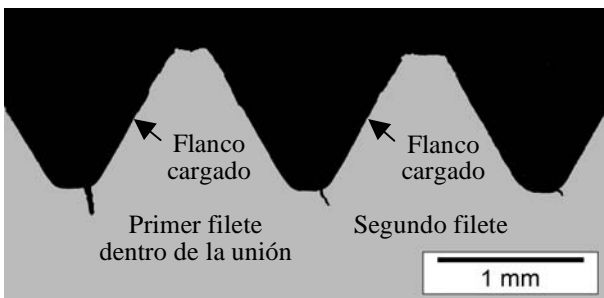


Figura 12. Iniciación de fisuras por fatiga.

Después de la superficie de fatiga aparece la fractura, cuando la fisura pasa a ser crítica. Ésta presenta una región casi plana cuyo tamaño disminuye con el aumento de la profundidad de fisura en fatiga, casi desapareciendo para $\Delta\sigma$ pequeñas (figura 11 inferior), y un labio dúctil que se corresponde con la fractura final donde se rompe longitudinalmente el filete. Ésta última región tiene en su perfil una inclinación de 45° hacia el flanco cargado del primer hilo.

En los cortes longitudinales de las probetas (figura 11 derecha) se muestra como apenas hay deformación plástica en la zona fatigada, donde existe un perfecto ajuste entre la rosca interior y la exterior. Mientras, en la parte fracturada inclinada (labio cortante) se observa, principalmente en la zona del primer filete dentro de la unión, un aumento de la deformación plástica conforme la tensión aplicada durante el ensayo es mayor.

La superficie de fractura por fatiga de los tornillos de acero está formada por microdesgarros dúctiles (figura 13), donde es posible observar estrías de fatiga que corresponden al crecimiento de la fisura en un ciclo de carga en el régimen de Paris [12,14]. En los aceros sometidos a tensiones máximas bajas, con gran parte de su superficie fatigada, se observan marcas de fatiga en el inicio de ésta sobre el borde de los tornillos, que muestran la dirección del avance de la fatiga (figura 14). El corte longitudinal de la probeta fatigada (sin llegar a la fractura total), después de revelar su microestructura (fractometalografía), muestra que el camino de fisura presenta frecuentes deflexiones y ramificaciones, lo que supone la existencia de un fuerte modo mixto local.

A continuación de la superficie de fatiga el mecanismo de fractura son los microhuecos (figura 15), apareciendo una zona intermedia entre ambas superficies donde se mezclan las dos fractografías.

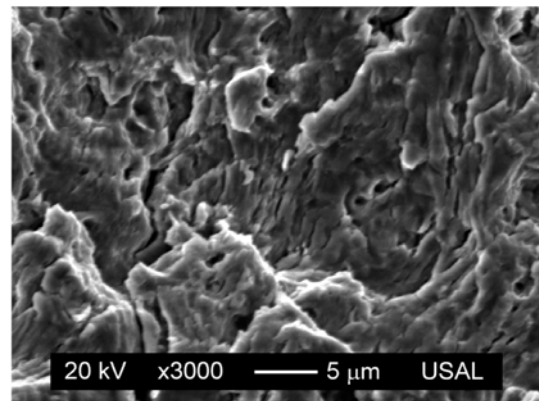


Figura 13. Microdesgarros dúctiles.

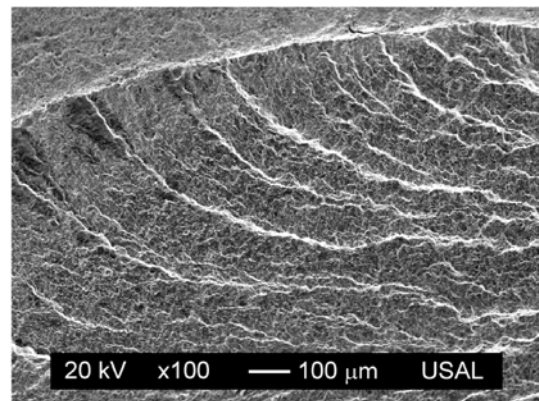


Figura 14. Marcas de fatiga en el borde del tornillo.

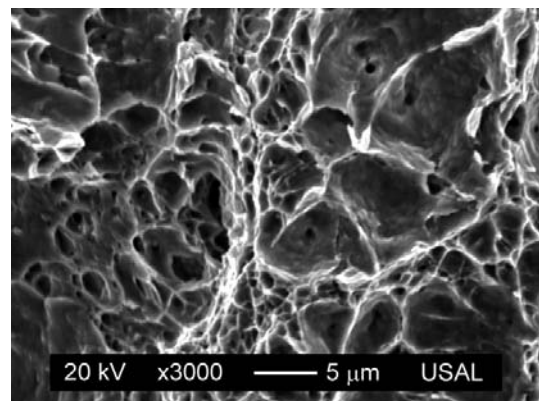


Figura 15. Microhuecos.

4. CONCLUSIONES

Con sollicitación monótona creciente la rotura de probetas con una unión roscada no sucede en dicha unión. Si el tornillo no ha sido completamente roscado la rotura se produce en el fondo de alguno de los filetes exteriores a la unión, con la tensión correspondiente al límite elástico del material.

En fatiga, la curva $\sigma_{\max}-N_f$ para probetas de acero con uniones roscadas se desplaza hacia la derecha con el aumento del factor R , mientras que la curva $\Delta\sigma-N_f$ lo hace hacia la izquierda. La fatiga es por tanto un fenómeno biparamétrico, donde el aumento de σ_{\max} o de $\Delta\sigma$ disminuye la vida en fatiga, pudiéndose efectuar un ajuste potencial único función de ambos parámetros.

La realización de una precarga de tracción (512MPa) previa a la carga cíclica, con factores $R=0$ y $R=0.50$, alarga la vida en fatiga de los tornillos para intervalos de oscilación de tensiones pequeños (~220MPa).

La superficie de fractura por fatiga es prácticamente plana y casi perpendicular al eje longitudinal del alambre. Para fisuras de poca profundidad el frente de fisura presenta forma de luna creciente que se prolonga por casi todo el borde del tornillo, para fisuras de profundidad intermedia la forma se mantiene pero con menor superficie exterior cubierta y para fisuras de gran profundidad el frente llega a ser casi recto.

La fractura por fatiga sucede en el fondo del flanco cargado correspondiente al primer filete dentro de la unión roscada, donde existe la mayor tensión superficial. La propagación inicial de la fisura de fatiga presenta cierta inclinación, con un ángulo que aumenta con la disminución de la tensión aplicada. Además, si la tensión aplicada es suficientemente alta pueden iniciarse fisuras en el fondo de varios filetes consecutivos.

AGRADECIMIENTOS

Los autores desean expresar su agradecimiento a la Universidad de Salamanca (USAL) por la financiación concedida para el desarrollo del presente trabajo a través de la convocatoria para nuevas líneas de investigación a desarrollar por equipos propios de la Universidad (Proyecto USAL2008A09).

REFERENCIAS

- [1] Olsen, K.W., Rimnac, C.M., Ferrell, D.W., Garrett, C.E. Fatigue crack growth analyses of aerospace threaded fasteners, Part II: Material/stress state and bolt strength. En: Structural Integrity of Fasteners Vol. 3 (ASTM STP 1487), 2007, pp. 141-158. American Society for Testing and Materials, USA.
- [2] Raymond, L. Accelerated small specimen test method for measuring the fatigue strength in the failure analysis of fasteners. En: Structural Integrity of Fasteners Vol. 2 (ASTM STP 1391), 2000, pp. 192-203. American Society for Testing and Materials, USA.
- [3] Berger, C., Pyttel, B., Trossmann, T. (2006). Very high cycle fatigue tests with smooth and notched specimens and screws made of light metal alloys. Int. J. Fatigue 28, 1640-1646.
- [4] Majzoobi, G.H., Farrahi, G.H., Habibi, N. (2005). Experimental evaluation of the effect of thread pitch on fatigue life of bolts. Int. J. Fatigue 27, 189-196.
- [5] Kephart, A.R. Fatigue acceptance test limit criterion for larger-diameter rolled thread fasteners. En: Structural Integrity of Fasteners Vol. 2 (ASTM STP 1391), 2000, pp. 143-161. American Society for Testing and Materials, USA.
- [6] Oliver, M.P., Jain, V.K. Effect of tightening speed on thread and under-head coefficient of friction. En: Structural Integrity of Fasteners Vol. 3 (ASTM STP 1487), 2007, pp. 45-52. American Society for Testing and Materials, USA.
- [7] Ifergane, S., Eliaz, N., Stern, N., Kogan, E., Shemesh, G., Sheinkopf, H., Eliezer, D. (2001). The effect of manufacturing processes on the fatigue lifetime of aeronautical bolts. Eng. Fail. Anal. 8, 227-235.
- [8] Akyildiz, H.K., Livatyali, H. (2010). Effects of machining parameters on fatigue behavior of machined threaded test specimens. Mater. Des. 31, 1015-1022.
- [9] Kim, W., Kawai, K., Koyama, H., Miyazaki, D. (2007). Fatigue strength and residual stress of groove-rolled products. J. Mater. Process. Technol. 194, 46-51.
- [10] Stephens, R.I., Bradley, N.J., Horn, N.J., Arkema, J.M., Gradman, J.J. Influence of cold rolling threads before or after heat treatment on the fatigue resistance of high strength coarse thread bolts for multiple preload conditions. En: Structural Integrity of Fasteners Vol. 3 (ASTM STP 1487), 2007, pp. 29-41. American Society for Testing and Materials, USA.
- [11] Bradley, N.J., Stephens, R.I., Horn, N.J., Gradman, J.J., Arkema, J.M., Borgwardt, C.S. Influence of cold rolling threads before or after heat treatment on the fatigue resistance of high strength fine thread bolts for multiple preload conditions. En: Structural Integrity of Fasteners Vol. 3 (ASTM STP 1487), 2007, pp. 98-112. American Society for Testing and Materials, USA.
- [12] Olsen, K.W., Rimnac, C.M. Fatigue crack growth analyses of aerospace threaded fasteners, Part III: Experimental crack growth behavior. En: Structural Integrity of Fasteners Vol. 3 (ASTM STP 1487), 2007, pp. 17-28. American Society for Testing and Materials, USA.
- [13] Renauld, M.L., Lien, H., Wilkening, W.W. Probing the elastic-plastic, time dependent stress response of test fasteners using finite element analysis. En: Structural Integrity of Fasteners Vol. 3 (ASTM STP 1487), 2007, pp. 61-70. American Society for Testing and Materials, USA.
- [14] Gaudett, M., Tregoning, R., Focht, E., Zhang, X.J., Aylor, D. Laboratory techniques for service history estimations of high strength fastener failures. En: Structural Integrity of Fasteners Vol. 2 (ASTM STP 1391), 2000, pp. 16-35. American Society for Testing and Materials, USA.

FATIGUE BEHAVIOUR OF RESIN-INJECTED BOLTS: AN EXPERIMENTAL APPROACH

**A.M.P. de Jesus^{1,3}, J.F.N. da Silva¹, M.V. Figueiredo^{2,3}, A.S. Ribeiro^{1,3}, A.A. Fernandes^{2,3}, J.A.F.O. Correia^{1,3},
A.L.L. da Silva¹, J.M.C. Maeiro¹**

¹ Departamento de Engenharias, Escola de Ciências e Tecnologia,
Universidade de Trás-os-Montes e Alto Douro,
Quinta de Prados, 5001-801 Vila Real, Portugal.

E-mail: ajesus@utad.pt; joaofnsilva@hotmail.com; aribeiro@utad.pt; jcorreia@utad.pt; a.luis.l.silva@gmail.com;
j_maeiro@hotmail.com

² Departamento de Engenharia Mecânica,
Faculdade de Engenharia da Universidade do Porto,
Rua Dr. Roberto Frias, 4200-465 Porto, Portugal

E-mail: mfiguei@fe.up.pt; aaf@fe.up.pt

³ Instituto de Engenharia Mecânica – IDMEC,
Rua Dr. Roberto Frias, 404, 4200-465 Porto, Portugal

ABSTRACT

Resin-injected bolts have been used in reparation of existing bridges. This technology is used in shear connections as an alternative to rivets, fitted bolts or preloaded high strength friction grip bolts. The use of resin-injected bolts allows similar behaviour as fitted bolts, but with lower costs, since it only requires a standard preparation of the holes. The use of resin injected bolts improves the slip resistance of the joint. In rehabilitation of old riveted bridges, resin-injected bolts may be used to replace faulty rivets, preserving null sleep, as the original rivet. However, creep may occur if bearing stresses on resin are excessive. The performance of resin-injected bolts has been essentially demonstrated by quasi-static or creep tests. Very few studies concerning the assessment of the fatigue behaviour of resin-injected bolts can be found in literature. This paper presents the results of an experimental program aiming the evaluation of the fatigue behaviour of two types of joints (single and double shear) with preloaded resin-injected bolts. Results are compared with test data obtained with standard preloaded bolts, revealing a systematic fatigue strength reduction.

KEY WORDS: bolted connections, resin-injected bolts, fatigue behaviour, experimental analysis

1. INTRODUCTION

Repairing and strengthening operations of old riveted steel bridges may use alternative fastening techniques, such as rivets, welding, high strength friction grip bolts, fitted bolts and resin-injected bolts, also known as injection bolts. Riveting is usually preferred in order to preserve the original architecture of the bridge. However, riveting is not attractive either, because of the difficulties to find good equipment and skilled riveters. The use of welding may be impossible due to the poor weldability properties of the old steel. The used of high strength friction grip bolts is not a good option, because of the very uneven surfaces of corroded plates as well the presence of paint layers, leading to low friction coefficients. Fitted bolts are attractive, but expensive solutions. Therefore, resin injected bolts appears as a good solution that have been applied in reparation of old bridges, both in Portugal (e.g. reparation of the bridge in Figueira da Foz [1], over Mondego river) and abroad (e.g. reparation of the bridge in Oranienburg, linking Netherlands to Germany [2]). Injection bolts are

bolts in which the cavity produced by the clearance between the bolt and the wall of the hole is completely filled up with a resin. Filling of the clearance of an injection bolt is carried out through a small hole in the head of the bolt. After injection and full curing of the resin, the connection is slip resistant. Shear load is transferred through bearing and shear of the bolt. Injection bolts can be manufactured from normal standard structural bolts, representing an inexpensive solution. The bolts and washers are adapted to enable the injection of the resin. Figure 1 represents schematically a resin-injected bolt.

The mechanical performance of resin-injected bolts has been demonstrated essentially based on quasi-static tests, cyclic tests representing seismic loading and creep tests [1-3]. The resin-injected bolts provide a low slip factor and good bearing resistance. Also, it allows a good corrosion resistance. The epoxy resins have been proved to be a best solution for resin-injected bolts [1].

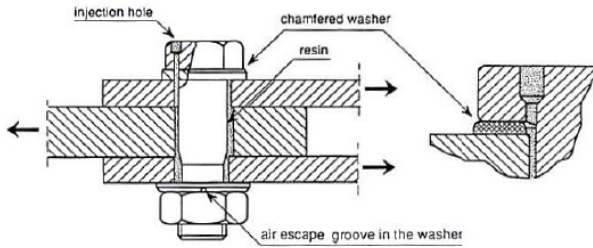


Figure 1. Injection bolt in a double lap joint [3].

High-cycle fatigue tests of resin-injected bolts are very rare. Eurocode 3 [4] suggests the same fatigue detail category for preloaded high strength bolts and preloaded injection bolts (class 110 for double covered symmetrical joints and class 90 for one sided connections). The same detail category is also proposed for fitted bolts and non-preloaded injection bolts (class 90 for double covered joints and class 80 for one sided connection).

This paper presents the results of an experimental program, consisted of fatigue tests on both bolted and resin-injected bolted connections. Two types of connections were investigated, using materials from two distinct bridges, namely the Fão (double shear connection) and Trezói (single shear connection) bridges. A total of four series of specimens were tested. The results showed that, for the same initial preload applied to the standard and resin-injected bolts, a systematic fatigue strength reduction is observed in resin-injected bolts, thus contradicting the Eurocode 3 recommendations, which suggests the same fatigue strength for both types of fastening techniques.

2. EXPERIMENTAL DETAILS

The experimental program consisted of fatigue tests of both standard bolted connections and resin-injected bolted connections. In addition, two distinct geometries and materials were tested, namely:

- a double shear connection made of puddle iron, extracted from the Fão riveted road bridge (see Figure 1a);
- single shear connection made of construction steel from the Trezoi riveted railway bridge (see Figure 1b).

The Fão bridge was inaugurated in 1892 and was built in Puddle iron, which is a material with many heterogeneities, responsible for significant scatter in material properties. The Trezói bridge was inaugurated in 1956 and was built using construction steel similar to the current steels.

In all connections (standard and injection bolts), bolts were preloaded using a torque of 80 N.m. Bolts with diameter equal to 22 mm were inserted into holes drilled

with a diameter equal to 24 mm, resulting a radial clearance of 1 mm. The same type of bolts was used in both standard joints and resin-injected bolts. A hole was drilled in the standard nuts and a channel was machined in the washer to allow resin injection. Figure 2a) illustrates the procedure to inject the resin that can be summarized as follows:

- Preparation of the nuts and washers;
- Surfaces cleaning;
- Preloading of bolts;
- Application of the resin using a syringe;
- Cure of the resin.

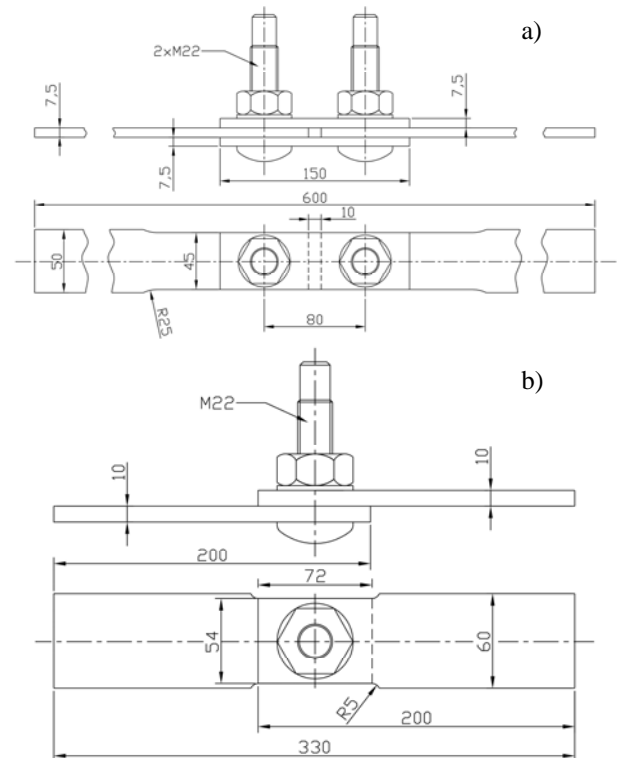


Figure 1. Geometry of the bolted joints considered in this study: a) double shear connection; b) single shear connection (dimensions in mm)

Figure 2b) shows injection bolts with the respective nuts removed. The figure shows that the clearance was filled by the resin as expected. Besides Figure 2b) was obtained after fatigue failure, it shows an apparently undamaged adhesive. It was not easy to remove the bolts from the connection. Only using a hammer or other loading device was possible to extract the bolts.

The resin used in the preparation of the injection bolts was a commercial epoxy, available as SIKADUR 30®. Table 1 summarizes the evolution of the mechanical strength properties of the adhesive, with the cure time, from the manufacturer. The Young modulus of the adhesive is equal to 12800 N/mm². All resin-injected bolts were subjected to a cure time of at least 8 days, which resulted near maximum strength properties.

The double shear connections were tested on a INSTRON 8801 servohydraulic machine rated to 100 kN. The single shear connections were tested on a MTS 321.21 servohydraulic machine rated to 250 kN. All fatigue tests were carried out under stress control with a stress R-Ratio equal to 0, for the double shear connection, and a stress R-Ratio equal to 0.1, for the single shear connection. The fatigue failures were considered to be the break of the resisting sections of the specimens.

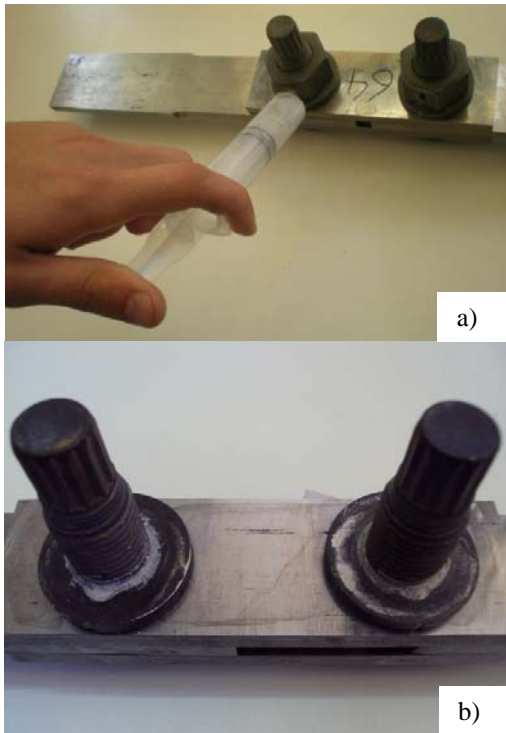


Figure 2. Resin-injection bolts: a) injection of resin; b) injection bolts with nuts removed, showing the filled clearance.

Table 1. Cure properties of the SIKADUR 30 adhesive.

Cure time	Compressive strength (+10°C)	Shear strength (+15°C)	Tensile strength (+15°C)
1 day	50-60 N/mm ²	3-5 N/mm ²	18-21 N/mm ²
3 days	65-75 N/mm ²	13-16 N/mm ²	21-24 N/mm ²
7 days	70-80 N/mm ²	14-17 N/mm ²	24-27 N/mm ²
14 days	-	15-18 N/mm ²	25-28 N/mm ²

3. RESULTS AND DISCUSSION

Tables 2 and 3 summarize the fatigue test results obtained for the four test series. Regarding the double shear connection, from the Fão bridge, 7 specimens were tested with resin-injected bolts and 7 were tested

with standard bolts. The test frequencies ranged from 2.5 to 10 Hz. The specimens with resin-injected bolts were tested always with the same net stress range (355.5 MPa). A huge scatter was observed in the fatigue lives for this series. The specimens with the standard bolts were tested with net stress ranges from 355.5 MPa to 398.6 MPa, with two specimens being tested for the stress range of 355.5 MPa. One of these specimens was a run-out. Taking into account the run-out life, results an average life of 2 394 976 cycles for the joints with standard bolts, under a stress range of 355.5 MPa. It is interesting to note that the average life obtained for the joints with resin-injected bolts was 333 548 cycles, which is significantly lower than observed for the connections with standard bolts. Also, none of the specimens with resin-injected bolts failed for a life higher than the lowest life obtained for the specimens with standard bolts.

Two series of single shear connections composed, respectively, of 4 connections with resin-injected bolts and 3 connections with standard bolts, made of steel from the Trezói bridge, were fatigue tested. Two stress levels were defined, namely: net stress ranges about 271 MPa (lower stress range) and about 362 MPa (higher stress range). Tests for the higher stress range were conducted at a frequency of 4 Hz; tests for the lower stress range were conducted according to a frequency of 6 Hz. Despite the reduced number of tests, a relative small scatter is observed in the fatigue results, for these connections made with the steel from the Trezói bridge.

Table 2. Fatigue data from the double shear connection made of material from the Fão bridge.

	$\Delta\sigma$ [MPa]	R	f [Hz]	N_f [cycles]
Resin-Injected Bolts	355.5	0.0	5.0	376856
	355.5	0.0	5.0	102854
	355.5	0.0	5.0	166294
	355.5	0.0	5.0	52949
	355.5	0.0	8.0	1321738
	355.5	0.0	8.0	183212
	355.5	0.0	8.0	130935
Standard Bolts	355.5	0.0	8.0	3245417→
	377.0	0.0	10.0	428551
	377.0	0.0	5.0	556452
	398.6	0.0	5.0	72355
	398.5	0.0	2.5	666412
	398.5	0.0	2.5	417582
	355.5	0.0	2.5	1544535

Table 3. Fatigue data from the single shear connection made of material from the Trezói bridge.

	$\Delta\sigma$ [MPa]	R	f [Hz]	N_f [cycles]
Resin-injected bolts	361.8	0.1	4	91993
	362.6	0.1	4	120808
	271.5	0.1	6	325865
	271.9	0.1	6	235780
Standard bolts	362.2	0.1	4	297700
	271.3	0.1	6	827824
	271.4	0.1	6	765606

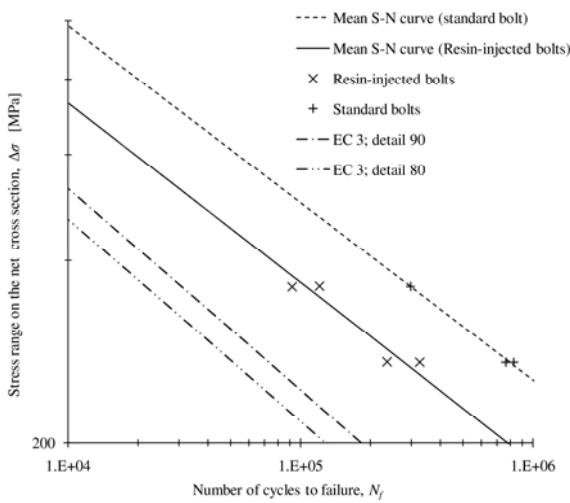


Figure 3. Comparison of S-N fatigue data from the single shear connections made of the material from the Trezói bridge.

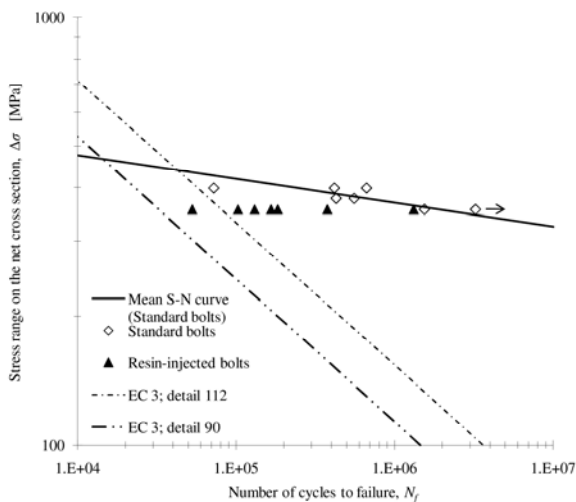


Figure 4. Comparison of S-N fatigue data from the double shear connections made of the material from the Fão bridge.

Test fatigue results from the single shear connections were also consistent with a fatigue life reduction with the use of resin-injected bolts.

Figures 3 and 4 plot the fatigue data obtained respectively for the single and double shear connections. The figures include mean S-N curves obtained using the experimental data, except for the double shear connection made of resin-injected bolts, since just one stress range level was tested for this latter series. Also, curves proposed in Eurocode 3 for double and single shear bolted connections, are included in the graphs. Two detail categories are plotted, the higher one being proposed for preloaded bolts, with or without injected resin; the lower detail category is proposed for fitted bolts and non preloaded injection bolts. The Eurocode S-N curves are conservative as expected. Only one data point exception is found for the single shear connection build with resin-injected bolts. Comparing the experimental mean S-N curves with the code-based S-N curves, it is interesting to note that S-N curves obtained for the single shear joints are approximately parallel to the code S-N curves. Also, the mean S-N curves for the resin-injected bolts and standard bolts are parallel. For the double shear connection, the experimental S-N curve is no longer parallel to the code-based S-N curve. This observation may be justified by the significant differences in the materials, being the material from Trezói bridge a construction steel similar to current ones. Its crack propagation properties should be very similar to the materials served as the basis for the definition of the S-N curves slopes ($m=3$).

The use of resin-injected bolts produced a consistent fatigue strength reduction in all test series. This is a surprising result, since Eurocode 3 does not distinguish the detail category between preload bolted connections and preload resin-injected bolted connections. This conclusion raises some concerns since resin-injected bolts are often used in rehabilitation of old structures.

A plausible explanation may be advanced, based on effects of preload (clamping stresses) applied to the bolts. The preload reduces the stress concentration around the holes, therefore increasing the fatigue strength. For high stress levels, responsible for some localized plastic strain, the initial preload on bolts may increase. On effect, the compressive contact stresses between the bolt and the hole increase the thickness of the plates, due to the Poisson effect, being responsible for a clamping stress increasing. Higher compressive stresses are obtained in standard bolts; the injected resin produces a redistribution of stress around the holes, reducing the magnitude of the compressive stresses, and the clamping stresses by consequence. This hypothesis must be verified by numerical simulation in future works.

4. CONCLUSIONS

This paper reported experimental research on fatigue behaviour of standard and resin-injected bolted connections. Two types of connections were tested, namely single and double shear connections. Each one of these connections were made of distinct materials, from the Fão and Trezói bridges. The main conclusion derived from the experimental data, was the fatigue strength reduction verified with the use of the resin-injected bolts. This conclusion was verified with two independent test configurations, which makes it stronger. This conclusion is somewhat surprising since the Eurocode 3 does not propose a lower detail category for resin-injected bolts. Also, it is common sense that the resin-injected bolts are a better fastening technique, than standard bolts.

This experimental investigation highlights the need for more research on fatigue behaviour of resin-injected bolts, including more testing and numerical modelling.

ACKNOWLEDGEMENTS

The authors acknowledge the Portuguese Science and Technology Foundation (FCT) for his support through the project PTDC/EME-PME/78833/2006.

REFERENCES

- [1] Mattes, J.F., *Substituição de Rebites por Parafusos Injectados com Resina*, M.Sc. Thesis, 180 pag., IST/UTL, Lisboa, 2007.
- [2] A.M. Gresnigt, G. Sedlacek, M. Paschen, *Injection Bolts to Repair Old Bridges*, pag. 349-360, website: <http://www.pcisltd.com>, Consulted on 11th November, 2009.
- [3] European Convention for Constructional Steelwork (ECCS), *European Recommendations for bolted connections with injection bolts*, ECCS Publication No. 79, First Edition, 44 pag., 1994.
- [4] European Committee for Standardisation, *Eurocode 3: Design of steel structures. EN 2003-1-9: fatigue*, Brussels, Belgium, 2003.

COMPORTAMIENTO MECÁNICO DE MATERIALES MASIVOS SUPERCONDUCTORES DE SEGUNDA GENERACIÓN EN FUNCIÓN DE LA TEMPERATURA

K. Konstantopoulou, J. Y. Pastor

¹ Departamento de Ciencia de Materiales, E.T.S. de Ingenieros de Caminos, Canales y Puertos, Universidad Politécnica de Madrid, C/ Profesor Aranguren s/n, 28040 Madrid, España.

E-mail: konstantina@mater.upm.es

J. J. Roa, M. Segarra

² Departamento de Ciencia de Materiales e Ing. Metalúrgica, Universidad de Barcelona, Facultad de Química, C/ Martí y Franqués 1, 08028, Barcelona, España

E-mail: joanjosep_roa@ub.edu

RESUMEN

En este trabajo se han analizado dos materiales masivos superconductores de base YBaCuO, con el objetivo de analizar la influencia del método de procesado (método de Bridgman y método Top-Seeding melt growth) y de la temperatura de ensayo en su comportamiento mecánico. Ambos materiales se ensayaron a temperatura ambiente (300 K) y a baja temperatura (77 K), realizándose ensayos rotura y de tenacidad de fractura en flexión en tres puntos. Además, en uno de los materiales, que presentaba anisotropía microestructural, se realizaron ensayos en las dos direcciones microestructuralmente más relevantes. Los resultados obtenidos muestran que el comportamiento mecánico del material está controlado por los defectos y grietas introducidas durante el procesado y, por lo tanto, si se quiere mejorar las propiedades, debería reducirse la cantidad y el tamaño de estas imperfecciones.

PALABRAS CLAVES: YBaCuO, comportamiento mecánico, fractura, baja temperatura.

ABSTRACT

In the present study, have been researched two superconductor bulk materials of YBaCuO, with the aim of analyzing the influence of the processing method (Bridgman method and Top-Seeding Melt Growth method) and the test temperature in their mechanical behavior. Both of them have been tested at room temperature (300 K) and at low temperature (77 K) and have been carried out three point bending tests and fracture toughness from three point bending tests. Moreover, one of the two materials, which present microstructural anisotropy, has been tested for the both more relevant directions. The obtained results present that the mechanical behaviour of the material is controlled by the defects and the cracks, that have been introduced during the processing and therefore, if we want to improve the mechanical properties, we have to reduce the amount and the size of the defects.

KEY WORDS: YBaCuO, mechanical behavior, fracture, low temperature

1. INTRODUCCIÓN

Los materiales masivos superconductores presentan una densidad de alta corriente crítica y alto campo magnético en su estado superconductor, además de una resistencia nula al paso de corriente a su través. El descubrimiento de materiales que pueden tener este comportamiento superconductor a temperaturas superiores a los 77 K (superconductores de alta temperatura crítica, T_c) ha abierto una vía de gran interés tanto científico como tecnológico. Sin embargo, su aplicación industrial está bastante limitada por sus pobres propiedades mecánicas, que aunque secundarias

para su aplicación funcional son cruciales para asegurar su durabilidad a medio y largo plazo.

Los materiales superconductores tienen la fragilidad intrínseca por su estructura tipo perovskita, y por eso la resistencia y la tenacidad de fractura son bajas y, en general, anisótropas. Por esta razón, es muy importante estudiar y mejorar las propiedades mecánicas para conseguir fiabilidad estructural para sus aplicaciones. De otro lado, se ha prestado muy poca atención a la caracterización mecánica de estos materiales, en especial en sus condiciones de trabajo, es decir a 77 K. En este trabajo se pretende profundizar en el conocimiento del comportamiento mecánico de

materiales superconductores de alta T_c de segunda generación, cuya base son compuestos de $\text{YBa}_2\text{Cu}_3\text{O}_{7-\delta}$.

2. PRODUCCIÓN DE LOS MATERIALES Y TÉCNICAS EXPERIMENTALES DE CARACTERIZACIÓN

Se ha estudiado el comportamiento mecánico en función de la temperatura de dos tipos de material masivo de base YBaCuO , fabricados mediante dos métodos distintos. El primer material fue fabricado por el método *Top-Seeding Melt Growth (TSMG)* y el segundo, por el método *Bridgman*. El proceso de fabricación y caracterización se describe de forma más detallada a continuación.

2.1. Proceso de síntesis

El material de estudio para la fabricación del YBaCuO ha sido obtenido mediante la técnica de atrapamiento catiónico con alcohol polivinílico [1], con una composición de: 69% w/w $\text{YBa}_2\text{Cu}_3\text{O}_{7-\delta}$ (Y-123), 30% w/w Y_2BaCuO_5 (Y-211) y un 1% w/w CeO_2 . Posteriormente, el material es sometido a un proceso de desnitrificación y de calcinación. Posteriormente, se moltura en un mortero de ágata. Las piezas superconductoras de YBaCuO en verde fueron obtenidas mediante prensado uniaxial en frío.

2.2. Proceso de texturación

Técnica de crecimiento inducido por semilla (TSMG)

Este método consiste en colocar una semilla de $\text{NdBa}_2\text{Cu}_3\text{O}_{7-\delta}$ en la parte superior de la pastilla que actuará como plantilla cuando la temperatura en el proceso de texturación se encuentra por debajo de la temperatura peritética (T_p). La reacción que se lleva a cabo se conoce como reacción peritética, donde el YBaCuO progresa a partir de un frente de crecimiento rico en Ba y Cu ($\text{BaCuO}_2 + \text{CuO}$) y una fase sólida existente, Y-211 [2], para obtener un monocristal. De ahora en adelante a este material se le denominará material YBaCuO-1 .

Técnica Bridgman

Este método consiste en desplazar una muestra con forma cilíndrica a lo largo de un gradiente térmico desde una temperatura superior a la T_p hasta una inferior. De esta manera se establece una interfase sólido-líquido produciendo un crecimiento direccional a lo largo del cilindro. El crecimiento monocristalino es debido a un proceso de competición entre granos nucleados en el extremo inicialmente más caliente del cilindro (zona de polidominio) [3]. De ahora en adelante a este material se le denominará material YBaCuO-2 .

2.3. Proceso de oxigenación

Finalmente, las muestras han sido sometidas en un proceso de oxigenación en un horno horizontal con un flujo de oxígeno de 99,999 % de pureza, a 0,4 l/min y 450 °C durante 240 h [1]. El proceso de oxigenación es la etapa limitante durante la obtención de los materiales superconductores. En esta etapa el oxígeno debe difundirse desde la superficie del material hasta su interior para transformar el material de fase tetragonal (no superconductora) a ortorrómbica (superconductora). Durante este proceso se genera la mayor cantidad de microgrietas en el material debido a la diferencia del parámetro de red entre ambas estructuras, por lo que se ha de ser especialmente cuidadoso en este proceso.

2.4. Preparación de muestras para su ensayo mecánico

Las muestras producidas por TSMG se obtuvieron en forma de paralelepípedos de dimensiones nominales unos 6x5 mm de sección y entre 10 y 20 mm de longitud. Estas muestras fueron embutidas en resina para proceder a su corte en proceder a su corte longitudinal de forma que de cada sección se obtuvieron cuatro probetas prismáticas con secciones nominales de 2,0x1,6 mm. Para desembutir las probetas, se realizó un calentamiento hasta 400 °C.

Las probetas que estaban fabricadas por el método Bridgman se obtuvieron en forma de cilindros de unos 6 mm de diámetro nominal y entre 15 y 30 mm de longitud. Dada la limitación de material cada cilindro fue embutido en resina y cortado longitudinalmente (Fig. 1, pasos 1 y 2) para obtener una superficie plana. A continuación se desembutió la probeta por calentamiento a 400 °C (Fig. 1, paso 3), y el proceso se repitió varias veces hasta conseguir las cuatro caras del prisma. Seguidamente, a partir de este prisma se extrajeron dos probetas en un proceso similar al descrito para el material producido por TSMG.

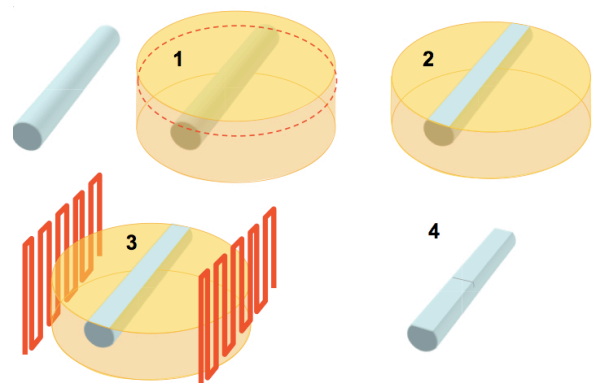


Figura 1. Método empleado para cortar las probetas obtenidas por el método Bridgman.

Las entallas fueron introducidas mediante un hilo diamantado de 130 μm de diámetro de forma que se consiguió un radio de fondo de entalla de unas 75 μm en todas las probetas. La longitud nominal de entalla fue de un 15% del canto de la probeta en todos los casos.

2.5. Caracterización mecánica

Para la caracterización mecánica de los materiales se realizaron ensayos de rotura y de tenacidad a fractura en flexión en tres puntos con una longitud entre apoyos de entre 8,5 y 10 mm, dependiendo de las dimensiones de la probeta tras su mecanizado. Ambos ensayos se realizaron en dos direcciones para el primer material (YBaCuO-1), a fin de analizar el efecto de la anisotropía microestructural en las propiedades mecánicas, y en una única dirección para el YBaCuO-2, dada la isotropía microestructural del material. Todos los ensayos se realizaron en una maquina servo-hidráulica, Instron 8501, equipada con una célula de carga de 100 N de capacidad y un LVDT de ± 1 mm de recorrido para medir la flecha del centro de la viga en los ensayos de rotura y fractura.

El dispositivo de ensayo fue similar en los ensayos a temperatura ambiente y a 77 K. En la línea de carga de la máquina de ensayos se acopló una cámara criogénica. El fondo de la vasija y el punto de la aplicación de la carga de la misma estaban conectados, respectivamente, al actuador y a la célula de carga de la máquina a través de sendas varillas huecas de acero inoxidable, lo cual impidió el enfriamiento excesivo de los dispositivos de medida.

Para los ensayos a baja temperatura se usó nitrógeno líquido como refrigerante, y también poliuretano como recubrimiento de la cámara, para mantener el sistema perfectamente aislado y la temperatura estable. Antes de empezar los ensayos se aplicaba una pequeña carga constante de flexión de 5 N con el fin de mantener el sistema en equilibrio y evitar el movimiento de la probeta durante el enfriamiento.

Tanto los ensayos de flexión en rotura en tres puntos como los ensayos de tenacidad de fractura en flexión en tres puntos, se realizaron en control de posición a una velocidad de actuador de 100 $\mu\text{m}/\text{min}$.

La resistencia mecánica se calculo a partir de la carga máxima utilizando las ecuaciones clásicas de resistencia de materiales, mientras que determinación de la tenacidad de fractura se hizo a partir de la carga máxima y la longitud *post-mortem* de entalla mediante la ecuación desarrollada por Guinea *et al.* [4].

Por último, después de ensayar las probetas sus superficies de fractura fueron analizadas mediante microscopia electrónica de barrido (JEOL 6130), a fin de encontrar los micromecanismos responsables del comportamiento macroscópico del material.

3. RESULTADOS Y DISCUSIÓN

3.1. Resistencia de flexión

Se realizaron no menos de tres ensayos para cada material, dirección microestructural, y temperatura de ensayo. En todos los casos la rotura fue frágil y los resultados se muestran en la Fig. 2 (valor medio y error cuadrático medio). En esta gráfica se puede ver que las muestras de YBaCuO-1, y ensayadas con los planos cristalográficos *ab* perpendicular a la fuerza aplicada (*dirección T1*), la resistencia mecánica a flexión, σ_f , tiene un valor un 40% más alto que el mismo material ensayado con los planos cristalográficos *ab* paralelos a la fuerza aplicada (*dirección T2*). Por otro lado, cuando la temperatura de ensayo descienda a 77 K, la resistencia mecánica de tal forma que iguala los resultados obtenidos para las dos direcciones. Este efecto está bien documentado en la bibliografía [5] es debido a la formación de cristales de hielo durante el enfriamiento a partir de la humedad ambiente. Estos cristales son capaces de cerrar poros y grietas presentes en el material, disminuyendo de esta forma el tamaño de defecto crítico.

Por otra parte, las muestras de YBaCuO-2 ensayadas a 300 K, muestran la misma resistencia mecánica que el YBaCuO-1 en la dirección T2, mientras que a 77 K el valor medio de la resistencia mecánica parece descender. No obstante, esto puede ser un mero artefacto dada la elevada dispersión que aparece en los resultados.

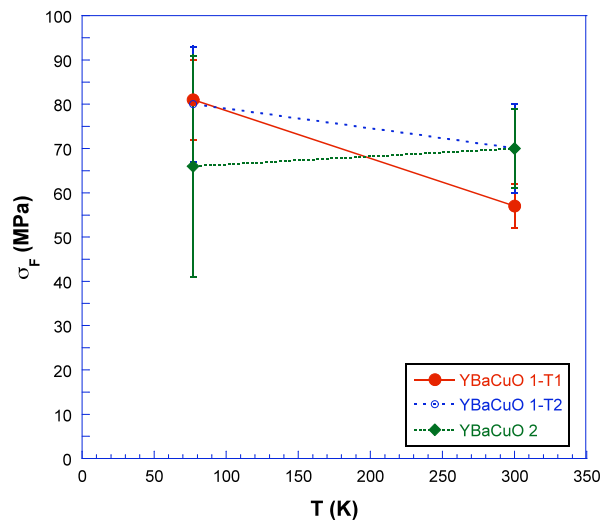


Figura 2. Evolución de la resistencia mecánica en función de la temperatura, dirección de ensayo y método de procesado. Cada punto corresponde al valor medio de al menos tres ensayos y las barras indican el error cuadrático medio.

3.2. Tenacidad de fractura

De nuevo se realizaron no menos tres ensayos para material, dirección microestructural, y temperatura de ensayo. En todos los casos la rotura fue frágil y los resultados de tenacidad a fractura, K_{IC} ; se muestran en la Fig. 3 (valor medio y error cuadrático medio). Tal y como puede verse en esta gráfica las muestras de YBaCuO-02, ensayadas tanto en dirección T1 como en

dirección T2, tienen un valor similar de tenacidad a fractura a 300 K. La pequeña diferencia que aparece entre ellos queda dentro de la dispersión de datos experimental, por lo que o se puede decir que haya diferencias apreciables entre ambas direcciones del mismo material. La falta de material para poder realizar más ensayos impidió la medida de la tenacidad a 77 K, pero dado lo sucedido con la resistencia mecánica es previsible que esta aumente al descender la temperatura de ensayo.

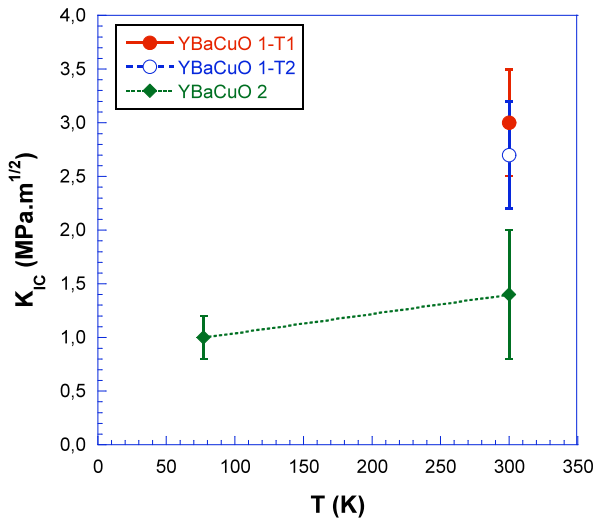


Figura 3. Evolución de la tenacidad de fractura en función de la temperatura, dirección de ensayo y método de procesado. Cada punto corresponde al valor medio de al menos tres ensayos y las barras indican el error cuadrático medio.

De otra parte, el YBaCuO-02 a 300 K presenta menor tenacidad (del orden del 50%) que el YBaCuO-01. Este es un resultado sorprendente que será analizado en detalle más adelante cuando se realice la caracterización fractográfica del material. Por último, en la Fig. 3 puede verse como para el YBaCuO-02 el valor medio de la tenacidad disminuye apreciablemente a 77 K, lo cual justificaría la reducción de la resistencia mecánica observada en el apartado anterior.

3.3. Fractografía

Para ambos materiales, tras los ensayos, se estudió su superficie mediante microscopía electrónica de barrido. Según se muestra en las Figs. 4 y 5, tanto el YBaCuO-1 como el YBaCuO-2 presentan porosidad apreciable, tanto en cantidad como en tamaño de poro. La diferencia entre ambos es que en el primero el tamaño de los poros es mayor, mientras que en el segundo tenemos más porosidad, pero con tamaño de poros más pequeño.

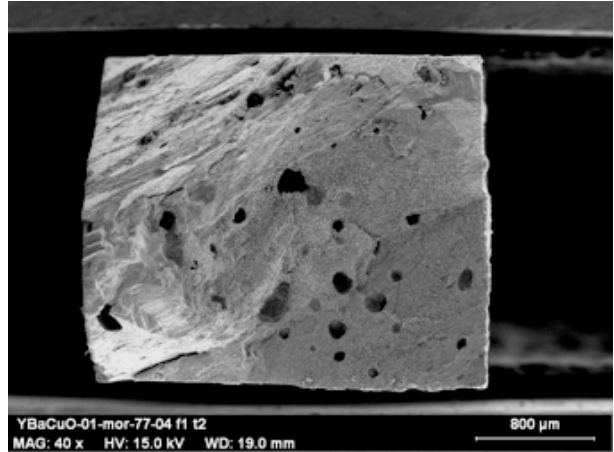


Figura 4. Superficie de fractura de YBaCuO-1, dirección T2 a 77 K. Se muestra la cantidad y el tamaño grande de los poros.

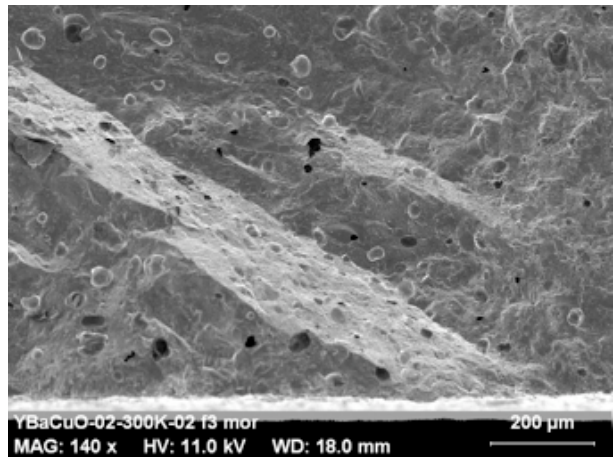


Figura 5. Superficie de fractura de YBaCuO-2 a 300 K. Se muestra porosidad y el tamaño más pequeño de los poros.

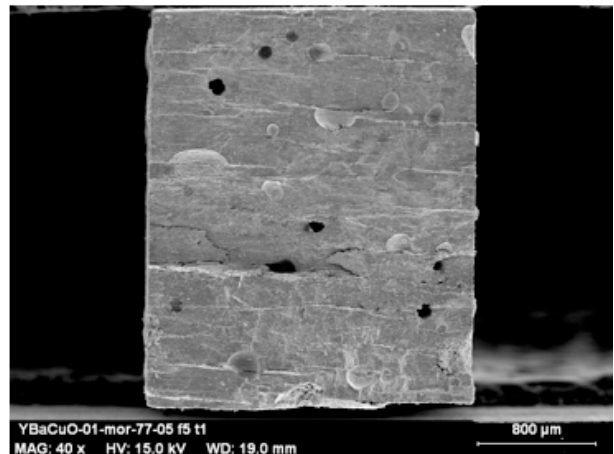


Figura 6. Superficie de fractura de YBaCuO-1 en dirección T1. Fractura frágil y macroscópicamente plana.

Las superficies de fractura de los dos materiales son características de una frágil por clivaje (Figs. 4-12) en todos los casos, independientemente del material, temperatura o dirección de ensayo. Lo que sí puede

observarse es que en el YBaCuO-01 la superficie de fractura en la dirección T1 es microscópicamente más plana que para la dirección T2, Figs. 7 y 8, en la que además aparecen continuos cambios de plano en la superficie de fractura.

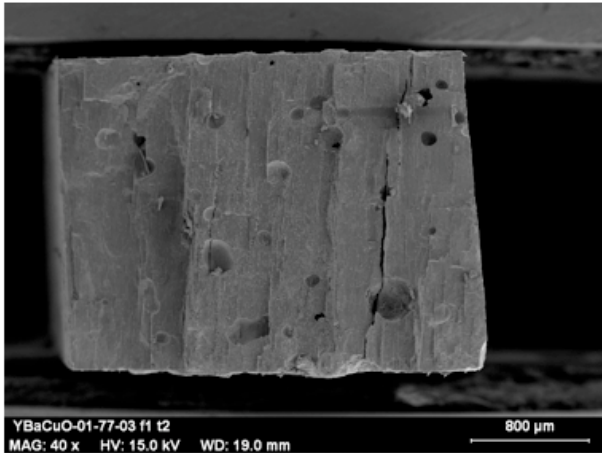


Figura 7. Superficie de fractura de YBaCuO-1 en dirección T2 y a 77 K.

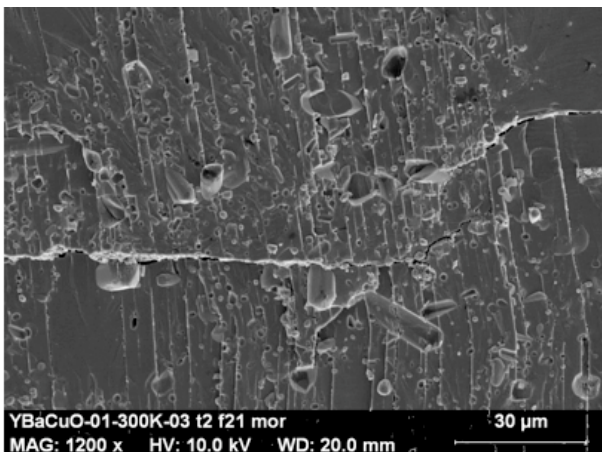


Figura 8. Superficie de fractura de YBaCuO-1 en dirección T2. Superficie de fractura en la que hay cambio del plano de fractura.

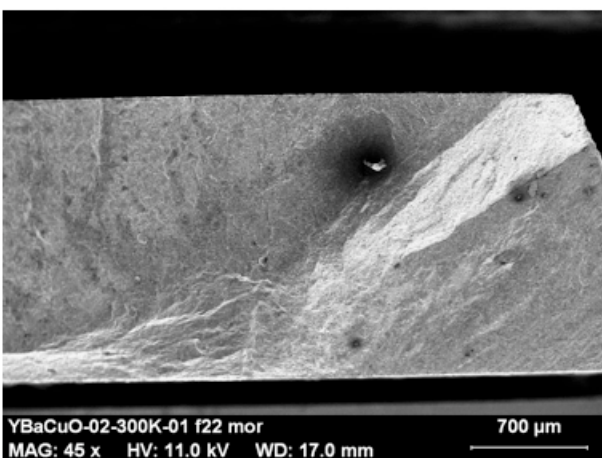


Figura 9. Superficie de fractura de YBaCuO-2 a 300 K. Es una superficie frágil y curvada.

Por otro lado, la superficie de fractura de YBaCuO-2 (Fig. 10) es abrupta y curvada, siendo más similar a la de YBaCuO-1 en dirección T2 que a la de la dirección T1. Además, se observa que tanto para el material YBaCuO-2 como para el YBaCuO-1 en la dirección T2 durante los ensayo de resistencia mecánica aparecen fisuras en dirección perpendicular al plano de propagación de la grieta principal (Figs. 7-10); esto que supone una ramificación a nivel local del proceso de fractura, con el consecuente aumento del consumo de energía y por tanto de la resistencia mecánica del material. Este proceso explica la mayor resistencia obtenida para estos caros respecto de la dirección T1 del material YBaCuO-1.

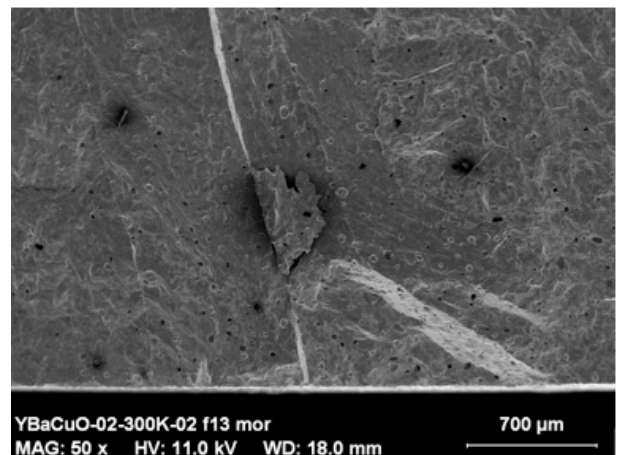


Figura 10. En la superficie de fractura de YBaCuO-2 se muestra una grieta perpendicular a la superficie de fractura generada durante el proceso de rotura.

En las Figs. 9 y 11 podemos ver claramente que tanto con el método de Bridgman como con el TSMG, se han obtenido materiales con zonas donde el sinterizado es imperfecto, lo cual ha sido, posiblemente, responsable de buena parte de la porosidad observada.

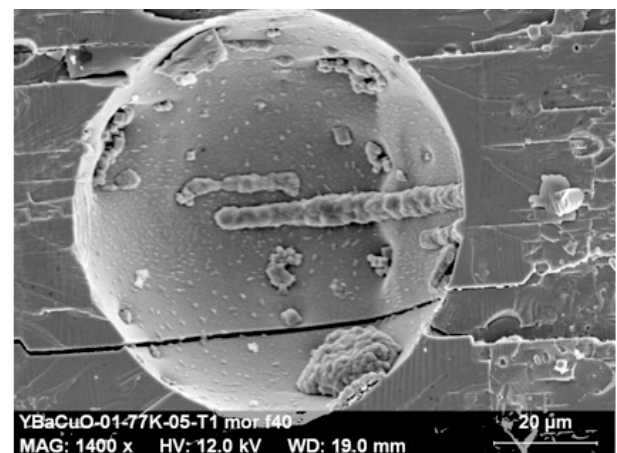


Figura 11. Zonas en la superficie de fractura de YBaCuO-1 en dirección T1 a 77 K. En el interior de la cavidad se pueden ver restos del mal sinterizado que ha provocado la oquedad.

En el caso del YBaCuO-2, estas zonas del material mal sinterizado son más extensas (Fig. 9), lo que provoca descohesión entre los granos (Fig. 12), siendo este efecto responsable de la menor tenacidad a fractura que en el material procesado por método Bridgman, y de la mayor dispersión en los resultados debido a la aleatoriedad del proceso. Este efecto parece agravarse durante el enfriamiento para el ensayo a 77 K del material. No obstante dada la elevada dispersión de resultados a temperatura ambiente no es claro que la tenacidad se reduzca al disminuir la temperatura de ensayo

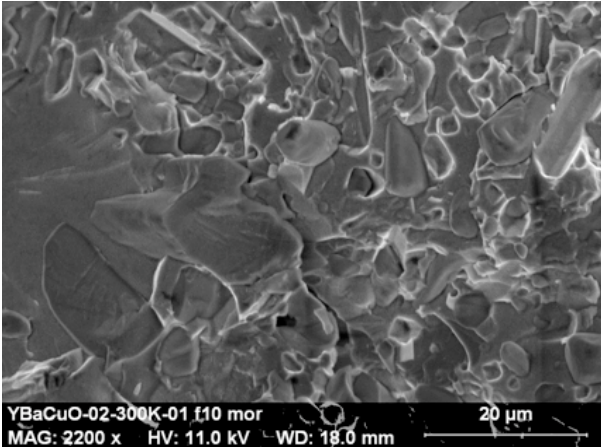


Figura 12. Superficie de fractura de YBaCuO-2 a 300 K en la que se aprecia la descohesión entre granos.

Respecto a la resistencia mecánica, vemos que para el material 1 hay una tendencia clara al aumento de la misma al disminuir la temperatura. Este efecto es bien conocido en otros materiales porosos [5, 6] como el hormigón; durante el enfriamiento el vapor de agua presente en la atmósfera se condensa y da lugar a la formación de cristales de hiel que tienden a cerrar los poros o reducir su tamaño. Esto tiene como consecuencia un menor tamaño de defecto microestructural y por tanto una mayor resistencia mecánica del material. Esto explica que para el material YBaCuO-1 las dos direcciones de ensayo converjan en un mismo resultado resistencia mecánica en los ensayos a baja temperatura. Por otro lado, para el material YBaCuO-2 este efecto es menos notable (de hecho queda enmascarado por la dispersión en los resultados experimentales) debido al considerable menor tamaño de los poros.

4. CONCLUSIONES

En este trabajo se ha fabricado material masivo superconductor de segunda generación (YBaCuO) mediante el método TSMG y el método Bridgman. Se ha observado que para el primer caso la microestructura es transversalmente isotropa, mientras que para el segundo tenemos una anisotropía microestructural que condiciona las propiedades mecánicas medidas macroscópicamente. El otro aspecto importante a resaltar es la presencia de una abundante porosidad que al presentar poros considerablemente mayores en el

material obtenido por el método Bridgman condiciona los resultados de la resistencia mecánica. Los principales hallazgos realizados en este trabajo respecto a las propiedades mecánicas son:

- Se observa una tendencia al aumento de la resistencia mecánica al disminuir la temperatura de ensayo, que se ha relacionado con una disminución del tamaño de defecto por efecto sellado del vapor de agua que pasa a forma sólida. Este efecto es tanto más evidente cuanto mayor es el tamaño de poro.
- La tenacidad de fractura es menor en el material isotropo debido a que en este caso el proceso de sinterizado ha sido peor y ha dado lugar a la descohesión de los granos. Esto también provoca un aumento de la dispersión de los resultados.
- EL material producido por método Bridgman presenta mejores propiedades (especialmente en la dirección T2) a pesar de tener poros más grandes que el YBaCuO-02, por lo que consideramos que el YBaCuO-02 probablemente presentaría mejor comportamiento mecánico, si se consiguiese optimizar el proceso de sinterización.

AGRADECIMIENTOS

Los autores quieren agradecer la financiación recibida del Ministerio de Ciencia e Innovación (MAT2009-13979-C03-02 y CSD00C-06-1410), de la Comunidad de Madrid (ESTRUMAT S-0505/MAT/0077) y del Comissionat per la Universitat i la Investigació del Departament d'innovació Universitari i d'Empresa de la Generalitat de Catalunya i el Fons Social Europeu.

REFERENCIAS

- [1] I. G. Serradilla, A. Calleja, X. G. Capdevila, M. Segarra, E. Mendoza, J. Teva, X. Granados, X. Obradors, F. Espiell. *Superconductors Science and Technology*, 15 (2002) 566-571
- [2] M. P. Delamare, H. Walter, B. Birngmann, A. Leenders, H. C. Freyhardt. *Physica C: Superconductivity and its applications*, 329 (2000) 160-167.
- [3] X. Granados, S. Piñol, B. Martín, J. Fontcuberta, F. Sandiumenge, *Spanish Patent Specification 2111435*.
- [4] Guinea, G., Pastor, J.Y., Planas, J., Elices, M., *International Journal Fracture*, 89 (1998) 103-116.
- [5] Salazar, A.; Propiedades mecánicas de cerámicos superconductores de BiSrCaCuO y sus compuestos. *Tesis doctoral*, Madrid 2003.
- [6] Planas, J. Maturana, P., Guinea, G.V., y Elices, M. *Advances in Frature Research ICF7*, Pergamon Press, Oxford 1989.

**FATIGUE AND FRACTURE PATHS IN
STRAIN-HARDENED EUTECTOID STEEL WIRES**

J.C. Matos¹, B. González², J. Toribio²

¹ Department of Computing Engineering (University of Salamanca),
E.P.S., Campus Viriato, Avda. Requejo, 33,
49022 Zamora. España.
E-mail: jcmatos@usal.es

² Materials Engineering (University of Salamanca),
E.P.S., Campus Viriato, Avda. Requejo, 33,
49022 Zamora. España.
E-mail: bgonzalez@usal.es

ABSTRACT

This paper analyses the influence of microstructural anisotropy of a progressively drawn pearlitic steel (orientation of pearlitic lamellae in the drawing direction) on the microscopic and macroscopic evolution of cracking paths produced by fatigue and fracture. The fatigue crack path is always contained in the transverse section of the wires, i.e., the subcritical propagation develops under a global mode I, so that the main crack path is associated with mode I and some very local deflections take place to produce a roughness in the fatigue crack path depending on the drawing level. The fracture crack path evolves from a global mode I propagation following the transverse plane in slightly drawn steels (including the hot rolled bar that is not cold drawn at all) to a global mixed-mode propagation associated with crack deflection in intermediate and heavily drawn steels (the latter with a strong mode II component), the deviation angle being an increasing function of the drawing degree.

RESUMEN

Este artículo analiza la influencia de la anisotropía microestructural de un acero perlítico progresivamente trefilado (orientación de las láminas de perlita en la dirección del trefilado) sobre la evolución microscópica y macroscópica de los caminos de fisura producidos por fatiga y fractura. El camino de fisura en fatiga está siempre contenido en la sección transversal del alambre, i.e., la propagación subcrítica se desarrolla bajo un modo I global, de modo que el camino de fisura principal está asociado con modo I, con deflexiones muy locales que producen rugosidad en el camino de la fisura por fatiga en función del nivel de trefilado. El camino de fisura en fractura cambia de una propagación en modo I global siguiendo el plano transversal en los aceros débilmente trefilados (incluyendo alambros, que no ha sido trefilado), a una propagación en modo mixto global asociada con deflexiones de fisura en los aceros intermedios y fuertemente trefilados (el último con una fuerte componente en modo II), siendo el ángulo de desviación una función creciente del trefilado.

KEYWORDS: Crack paths, Pearlitic steel, Fatigue and fracture.

1. INTRODUCTION

Cold drawing in eutectoid steels produces microstructural changes that can affect their mechanical behaviour. In particular, cold drawing is the responsible for the decrease of interlamellar spacing and the progressive orientation of pearlitic lamellae in the drawing direction [1-5]. In addition, heavy drawing generates curling of pearlitic lamellae [6].

In pearlitic steels, fatigue crack growth paths tend to cross the pearlite colonies and break the ferrite/cementite lamellae, exhibiting frequent local deflections, branchings and bifurcations [7]. When pearlite is uniformly distributed in ferrite, the fatigue crack path is more tortuous than in purely ferritic microstructures, and many deflections appear in the

crack path. In addition, pearlite inhibits the development of plastic deformation in the vicinity of the crack tip, thereby contributing to the improvement of fatigue resistance due to the increase of plastic constraint in that area [8]. In ferritic-pearlitic steels, banded pearlite (oriented in preferential directions) lowers the fatigue crack growth rate and raises the fatigue propagation threshold K_{th} in relation to the same steel with non oriented pearlite, and the reason is the higher roughness of the cracking path in oriented pearlite, where crack branching lowers the crack driving force and produces interlocking and a sort of retardation effect in the fatigue crack growth rate [9,10]. In fully pearlitic steels after cold drawing, markedly oriented pearlite contributes to the interlocking effect and, consequently, the fatigue crack growth rate decreases with such an orientation [11,12].

Fracture tests under bending loading on steels before and after cold drawing allowed the calculation on the directional toughness in the steel (on the basis of an energy release rate concept). Such a directional toughness is constant with the angle in the case of the hot rolled steel (isotropic material) which is not cold drawn at all, but it increases from an angle of 0° to an angle of 90° (measured in relation to the wire axis) in prestressing steel wire (commercial product which has undergone several drawing steps) [13]. As a matter of fact, heavily drawn steels exhibit strength anisotropy associated with a fracture crack path with crack deflection and mixed-mode propagation approaching the wire axis or drawing direction [14]. In these steels the longitudinal fracture toughness (associated with longitudinal fracture by delamination) is quite lower than the corresponding toughness value in transverse direction (associated with transverse fracture by breaking the strongest links) [15,16]. At a microscopical level, while in the hot rolled bar the fracture takes place by cleavage, in slightly drawn steels micro-void coalescence (MVC) fracture appears, followed by cleavage. Heavily drawn steels exhibit a fracture crack path with crack deflection at an angle of about 90° followed by a mixed propagation by micro-voids and cleavage [14].

The aim of the present paper is to analyse the evolution of the crack path in progressively drawn pearlitic steels under fatigue and fracture. To this end, fatigue and fracture tests were performed in cylindrical bars, examining the fracture surface at the microscopic and the macroscopic levels to determine the micromechanics of failure, the fracture modes and the crack paths.

2. EXPERIMENTAL PROCEDURE

2.1. Materials

The materials used were cold drawn steels with the same eutectoid composition, 0.789% C, 0.681% Mn, 0.210% Si, 0.218% Cr and 0.061% V.

Eight degrees of cold drawing were analysed, from the hot rolled steel (E0 that is not cold drawn at all) to a commercial prestressing steel wire (E7, heavily drawn steel that has undergone seven steps of cold drawing), apart from the six intermediate degrees of drawing. The steels were named with a letter E (indicating the common chemical composition) and a digit (indicating the number of cold drawing steps undergone). The drawing degree was characterised by the cumulative plastic strain in each steel.

2.2. Microstructural Analysis

Longitudinal and transverse samples were cut in the steels, polished and mounted to undergo several grinding stages, and different polishing passes followed by etching in Nital 4% to reveal the pearlitic microstructure of the steels. Later, samples were examined by means of a scanning electron microscope.

2.3. Fatigue and Fracture Tests

The specimens for the fatigue and fracture tests were samples in the form of circular rods taken directly from the wires (from 11.0 mm to 5.1 mm diameter) and a length of 30 cm, in which a mechanical notch was produced to initiate fatigue cracking.

Fatigue tests were performed at room temperature, step by step under load control, the load being constant in a step and decreasing from one to another step. Samples were subjected to tensile cyclic loading with an R factor equal to zero, and 10 Hz. The maximum load in the first loading stage corresponded to a value of about half the yield strength and was reduced between 20-30% from one to another step. Fracture tests were performed in the specimens previously precracked by fatigue, using a displacement rate of 3 mm/min.

Fatigue and fracture test were interrupted and a fracto-metallographic analysis was performed on the cracked samples by cutting along a plane perpendicular to the crack front in order to examine in detail the fatigue crack path immersed in the steel microstructure. To this end, after grinding and polishing, samples were etched with 4% Nital during several seconds and later observed by scanning electron microscopy.

3. RESULTS AND DISCUSSION

3.1. Microstructural Analysis

Pearlite is composed by alternate lamellae of ferrite and cementite forming colonies or sets of ferrite and cementite sharing a common orientation (different from that of the lamellae in the neighborhood colonies). Figs. 1 and 2 show the changing appearance of both microstructural units (the pearlite colonies and lamellae) in both longitudinal and transverse sections.

The pearlitic colonies become more slender with the cold drawing process, in agreement with previous research [17]. With regard to the lamellae, the general trend is a decrease of interlamellar spacing and a progressive orientation in the drawing direction (wire axis), also consistent with previous research [4,5]. In addition, the lamellae become curved in the transverse section as the drawing degree increases (*curling effect*).

3.2. Fatigue Crack Path

The macroscopic fatigue crack path was always contained in the transverse section of the wire, i.e., fatigue crack growth develops in mode I in spite of the markedly oriented microstructure in the progressively drawn steels.

Fatigue cracking can be modeled using semielliptical shapes to reproduce the evolving crack front, cf. Fig. 3, so that preferential cracking paths can be detected [18], and thus the crack aspect ratio is a function of the relative crack depth and of the considered steel (Fig. 4).

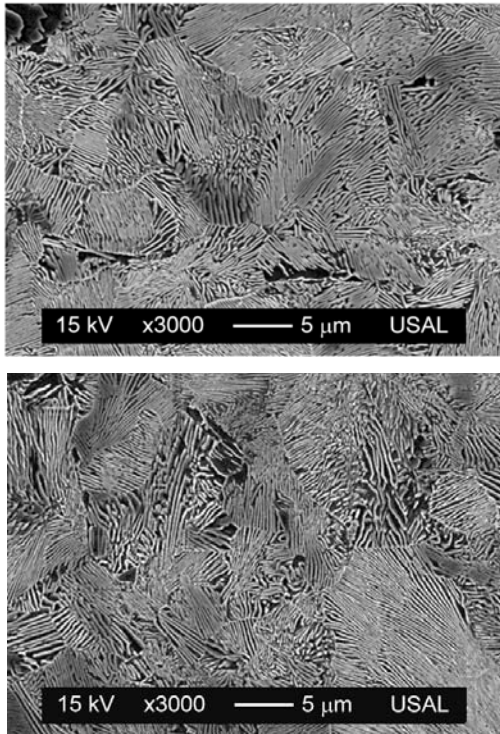


Figure 1. Microstructure of steel 0: transverse section (up), longitudinal section (down).

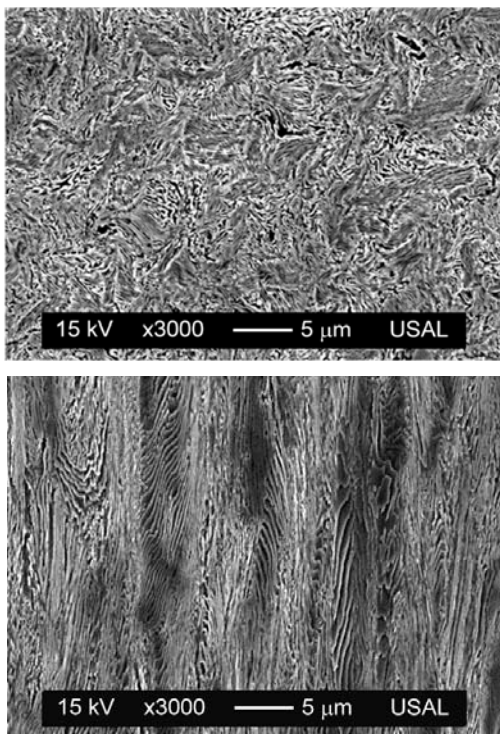


Figure 2. Microstructure of steel 7: transverse section (up), longitudinal section (down).

Steels with intermediate degree of drawing exhibit a retardation of fatigue crack growth in the central area of the wire section (Fig. 5) due to the presence of compressive residual stresses in that area and tensile ones in the vicinity of the wire surface. As a matter of fact, the cold drawing process generates an

axisymmetric residual stress profile, so that such internal stresses affect the crack growth under cyclic loading. Such a residual stress distribution does not appear neither in steel E0 (hot rolled bar which is not cold drawn at all) nor in steel E7 (prestressing steel wire that has undergone seven drawing steps and a posterior stress-relieving treatment to eliminate residual stresses).

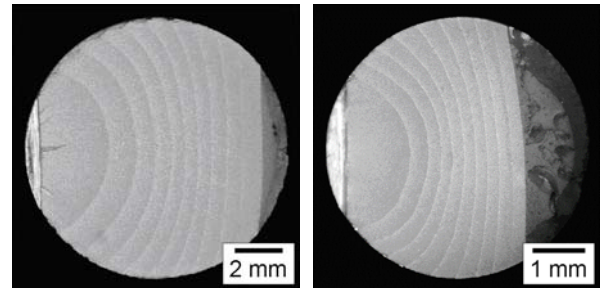


Figure 3. Fatigue crack front shapes for the hot rolled bar E0 (left) and the prestressing steel wire E7 (right).

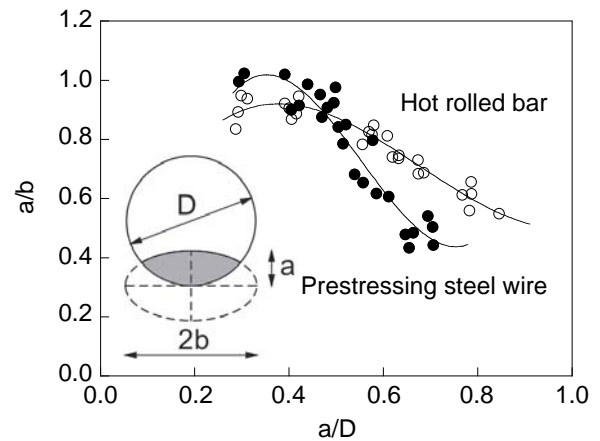


Figure 4. Fatigue crack paths for the hot rolled bar E0 and the prestressing steel wire E7.

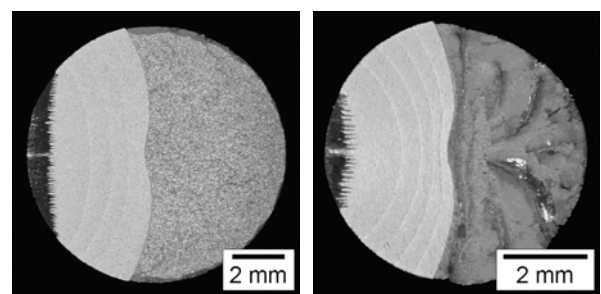


Figure 5. Fatigue crack front shapes in steels with an intermediate degree of cold drawing: E1 (left), E6 (right).

At a microscopic level, the fractographic appearance of the fatigue surface in pearlitic steels shows evidence of microplastic tearing events and subcritical crack advance by very localised plastic strain accumulation (Fig. 6). The fatigue process could be associated to a successive movement of dislocations ending at the ferrite-cementite interfaces and promoting fracture by shear cracking, similarly to the mechanism proposed by Miller and Smith [19].

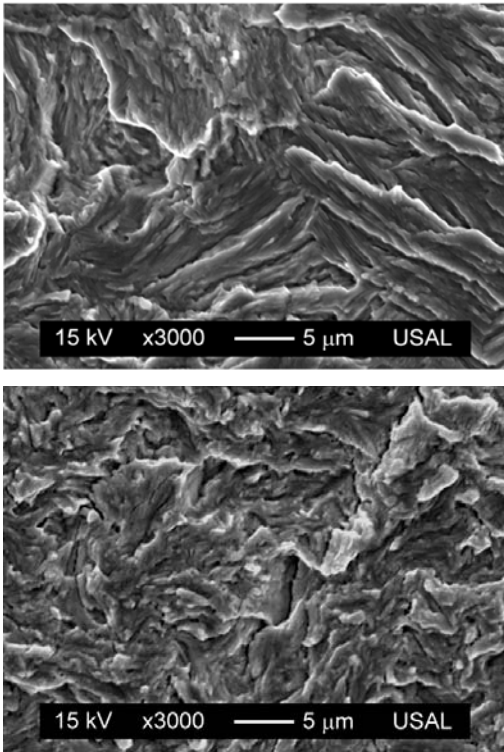


Figure 6. Fractographic analysis of the fatigue surface: E0 (up), E7 (down).

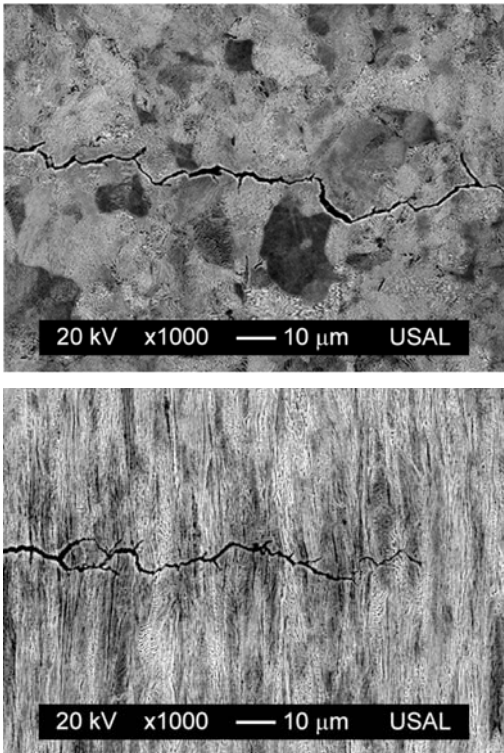


Figure 7. Fracto-metallographic analysis of the fatigue crack paths: E0 (up), E7 (down).

Fatigue cracks paths are trans-colonial and tend to fracture pearlitic lamellae. Fatigue crack propagation is tortuous, with micro-discontinuities, branchings, bifurcations and local deflections, thereby creating microstructural roughness, and even exhibiting non-

uniform crack opening displacement values (Fig. 7). These phenomena confirm the existence of a cracking path evolution under a local mixed mode in the vicinity of the crack tip.

The differences between the fractographic appearance of the hot rolled bar and the prestressing steel wire are due to the microstructural changes and the plastic strain suffered by the steel during cold drawing. In the prestressing steel wire the micro-tearing events are smaller and more curved than in the hot rolled (Fig. 6), consistent with what happens with the microstructure in the transverse section (cf. Figs. 1 and 2). The cracking path in prestressing steel shows a higher microstructural roughness (and therefore a greater net fractured area) than the respective zone in the hot rolled bar (Fig. 7).

3.3. Fracture Crack Path

The photographs of the fracture surface obtained after the fracture tests on cylindrical samples precracked by fatigue are shown in Fig. 8. In this figure, fracture propagates from left to right: mechanical notch, fatigue surface and fracture surface.

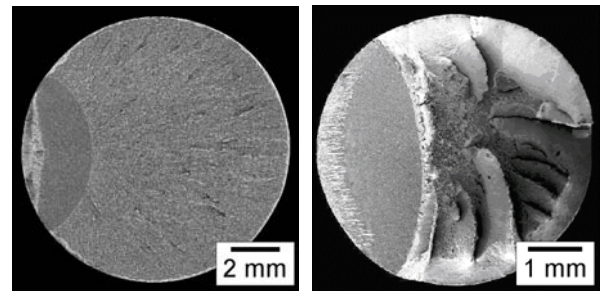


Figure 8. Fracture surface: E0 (left), E7 (right).

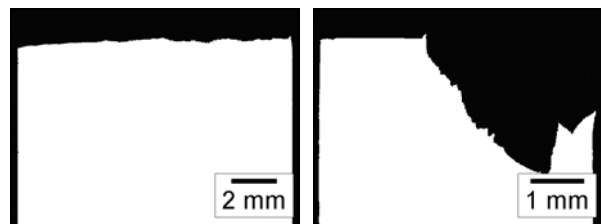


Figure 9. Fracture crack paths: E0 (left), E7 (right).

The fracture micromechanism changes with the level of plastic deformation in the different steels. At the macroscopic level, fracture is isotropic (contained in the transverse plane) in the hot rolled bar and slightly drawn steels, whereas it is clearly anisotropic (associated with a main deflection in the crack path and frequent micro-deflections) in the case of heavily drawn steels.

To characterise the main deflection angle in the fracture crack path, a fractographic analysis of the crack path profile was performed by cutting and polishing the sample in a plane perpendicular to the crack front (Fig. 9). The anisotropic behaviour becomes more intense as the drawing level increases. In heavily drawn steels, the fracture profile exhibits (after the fatigue precracking) a small step with a small vertical wall. After this step, the

fracture crack path develops in such a way that the slope increase with the level of drawing (up to 45° approximately). The angles are given in Fig. 10.

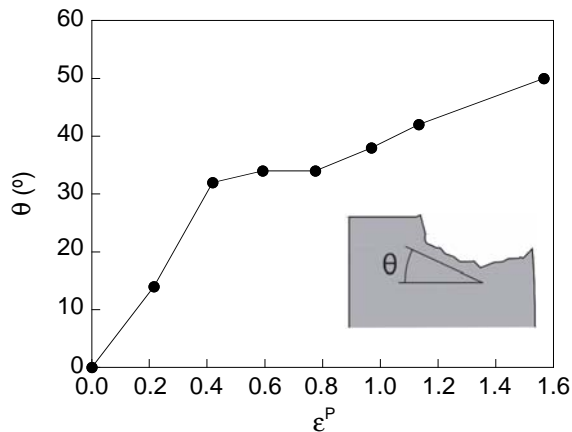


Figure 10. Crack deflection angle in the drawn steels.

The microstructural changes in the steels are associated with changes in the fracture micromechanisms. The steel E0 fails in brittle manner by cleavage (Fig. 11), with almost no plastic strain and typical river patterns indicating the crack advance. Fracture initiates at a small area of micro-void coalescence (MVC) next to the fatigue pre-crack (fracture process zone or FPZ) and it ends with shear lips at an angle of 45° with a fracture mode by MVC (external ring). Then the predominant fracture process in the hot rolled bar is by cleavage (brittle) which initiates and ends in a ductile manner.

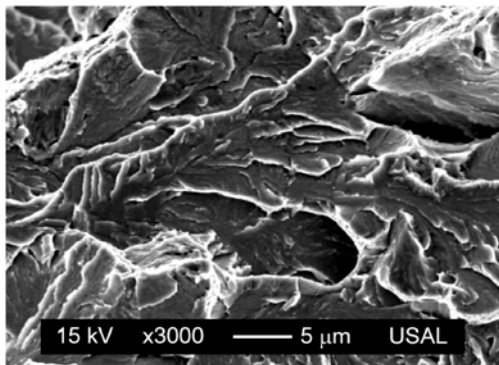


Figure 11. Main fracture surface by cleavage in E0.

In slightly drawn steels the same fracture micromechanisms take place, but the FPZ and the external ring (both formed by MVC) increase with the level of drawing. In addition, some local MVC areas appear in the main fracture area by cleavage in the internal section of the cross sectional area of the wires.

In steels with an intermediate degree of drawing (E3), and in heavily drawn steels (E7, Fig. 12) fracture initiates just at the FPZ by MVC (just after the fatigue precrack), followed by a vertical cracking path formed by oriented and enlarged cleavage facets (at certain distance from the fatigue precrack) and later by an inclined cracking path formed by a mixture of MVC and

cleavage topographies with radial cracking emanating from the centre of the cross sectional area of the wire. This main region contains vertical walls formed by enlarged cleavage and inclined zones by MVC. The final fracture area (external circular ring) is formed by shear lips inclined 45° and a micromechanism by MVC.

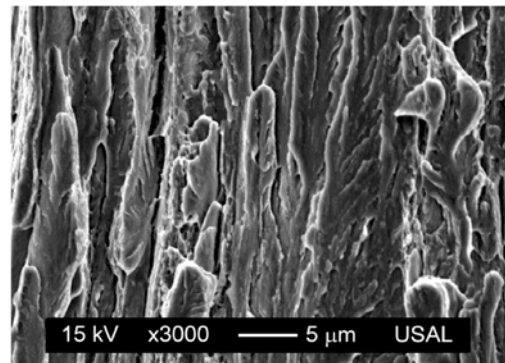
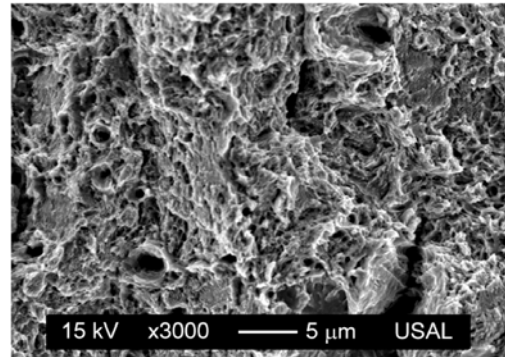


Figure 12. Horizontal (up) and vertical (down) fracture surface in the most heavily drawn steel (E7).

The horizontal (or transverse) projection of the internal fracture area is constituted by MVC and cleavage, the size of the cleavage area diminishing with the degree of cold drawing (or cumulative plastic strain level) in the progressively drawn steels in such a manner that it practically disappears in the most heavily drawn steels. In this latter case only isolated cleavage units are detected, so that the predominant fracture area develops by MVC and therefore the initial FPZ and the following inner fracture area are difficult to distinguish.

The vertical (or longitudinal) projection consists of the afore-described enlarged and oriented cleavage in the form of vertical walls, the degree of enlargement (slenderising) being an increasing function of the level of drawing (or cumulative plastic strain) in the steels (as in the case pearlitic colonies). The percentage of area of vertical walls (in relation to the whole fracture surface area) also increases with the drawing level.

Therefore, both the ductility (evaluated as a percentage of MVC fracture over the pure cleavage) and the anisotropy (probability of crack deflection in the fracture path) increase with the level of cold drawing, a consequence of the oriented microstructure in the drawn steels. However, in the matter of a property such as the ductility, and precisely as a consequence of the anisotropy of the drawn steel, one must distinguish

between the transverse ductility (horizontal direction) and the longitudinal brittleness (vertical direction). The idea about increasing ductility with the level of drawing refers to that measured in the transverse direction (the key one in evaluating the fracture resistance of the wires), whereas in the longitudinal direction the behaviour remains brittle, although the area of oriented and enlarged cleavage increases in the most heavily drawn steels, so that the oriented microstructure of these steels produces more crack deflection (because of longitudinal weakness), and such a deflection (with the associated enlarged and oriented cleavage topography) is a sign of anisotropy in the cold drawn steels.

4. CONCLUSIONS

The cold drawing process produces microstructural anisotropy in the form of orientation of the pearlitic lamellae in the drawing direction and decrease of interlamellar spacing. This phenomenon has direct consequences on the fatigue and fracture behaviour of the steels, as well as on the crack paths.

The fatigue crack path is always contained in the transverse section of the wires, so that the main crack path is associated with mode I and some very local deflections take place to produce a roughness in the fatigue crack path depending on the drawing level. The fatigue micromechanism consists of ductile micro-tearing events with very localised plastic strain, the microtearing patterns becoming more curved as the drawing level increases. With regard to the shape of the crack front, it can be assumed to be semielliptical, with a sort of retardation effect in the central area in the case of steels with an intermediate degree of drawing (gull effect), a consequence of the presence of compressive residual stresses in that area.

The fracture crack path evolves from a global mode I propagation following the transverse plane in slightly drawn steels to a global mixed-mode propagation associated with crack deflection in intermediate and heavily drawn steels (the latter with a strong mode II component), the deviation angle being an increasing function of the drawing degree in the steel. Such an evolution from mode I (slightly drawn steels) to mixed-mode propagation (heavily drawn steels) is associated with a change in the fracture micromechanisms from purely brittle cleavage in slightly drawn steels to the more ductile micro-void coalescence (MVC) fracture micromechanism appearing in the main fracture area in heavily drawn steels that exhibit also oriented and enlarged cleavage mode in the deflection crack path in vertical (drawing) direction. As a summary, both the ductility and the anisotropy (probability of crack deflection in the fracture path) increase with the level of cold drawing in the different steels, a consequence of the oriented microstructure in the drawn steels.

Therefore the microstructural anisotropy of the steels (consequence of the drawing process) creates a change in the fracture crack path with crack deflection in the

most heavily drawn steels. Nevertheless, the fatigue crack path remains globally in mode I, even in the most heavily drawn steels. In this latter case the microstructural orientation produces only an increase of micro-roughness in the fatigue crack path.

ACKNOWLEDGEMENTS

The authors wish to acknowledge the financial support provided by the following Spanish Institutions: MCYT; Grant MAT2002-01831, MEC; Grant BIA2005-08965, MCINN; Grant BIA2008-06810, JCyL; Grants SA067A05, SA111A07 and SA039A08.

REFERENCES

- [1] Embury, J.D., Fisher, R.M. (1966) *Acta Metall.* 14, 147-159.
- [2] Langford, G. (1977) *Metall. Trans.* 8A, 861-875.
- [3] Dollar, M., Bernstein, I.M., Thompson, A.W. (1988) *Acta Metall.* 36, 311-320.
- [4] Toribio, J., Ovejero, E. (1998) *Scripta Mater.* 39, 323-328.
- [5] Toribio, J., Ovejero, E. (1998) *Mech. Time-Dependent Mater.* 1, 307-319.
- [6] Gil Sevillano, J., Aernoudt, E. (1987) *Mater. Sci. Eng.* 86, 35-51.
- [7] Toribio, J., Matos, J.C., González, B. (2009) *Int. J. Fatigue* 31, 2014-2021.
- [8] Korda, A., Mutoh, Y., Miyashita, Y., Sadasue, T. (2006) *Mater. Sci. Eng. A* 428, 262-269.
- [9] Korda, A., Mutoh, Y., Miyashita, Y., Sadasue, T., Mannan, S. (2006) *Scripta Mater.* 54, 1835-1840.
- [10] Mutoh, Y., Korda, A., Miyashita, Y., Sadasue, T. (2007) *Mater. Sci. Eng. A* 468-470, 114-119.
- [11] Toribio, J., Toledano, M. (1999). In: *Proceedings of the Seventh International Fatigue Congress (Fatigue '99)*, pp. 2455-2460, Wu, X.R., Wang, Z.G. (Eds.), Higher Education Press, China.
- [12] Wetscher, F., Stock, R., Pippan, R. (2007) *Mater. Sci. Eng. A* 445-446, 237-243.
- [13] Astiz, M.A., Valiente, A., Elices, M., Bui, H.D. (1984). In: *Life Assessment of Dynamically Loaded Materials and Structures (ECF5)*, pp. 385-396, Faria, L. (Ed.), EMAS, West Midlands.
- [14] Toribio, J. (2004) *Eng. Fract. Mech.* 71, 769-777.
- [15] Toribio, J., Valiente, A. (2004) *Mater. Lett.* 58, 3514-3517.
- [16] Toribio, J., Valiente, A. (2006) *Eng. Fail. Anal.* 13, 301-311.
- [17] Toribio, J., Ovejero, E. (1997) *Mater. Sci. Eng. A* 234-236, 579-582.
- [18] Toribio, J., González, B., Matos, J.C. (2007) *Mater. Sci. Eng. A* 468-470, 267-272.
- [19] Miller, L.E., Smith, G.C. (1970) *J. Iron Steel Inst.* 208, 998-1005.

SIMULACIÓN DEL CRECIMIENTO DE GRIETAS POR FATIGA BAJO CARGAS ALEATORIAS CON NASGRO

B. Moreno¹, J. Zapatero¹, P. Lopez-Crespo¹ and J. Domínguez²

¹ Area de Ciencia de Materiales e Ingeniería Metalúrgica
E.T.S. de Ingenieros Industriales, C/ Pedro Ortiz Ramos s/n
Universidad de Málaga, 29071. España
E-mail: bmoreno@uma.es, jzapatero@uma.es, plopezcrespo@uma.es

² Departamento de Ingeniería Mecánica
ESI, Camino de los Descubrimientos s/n
Universidad de Sevilla, 41092. España
E-mail: jaime@us.es

RESUMEN

En este trabajo se hace uso del strip-yield model implementado en el software NASGRO para estimar el crecimiento de grietas bajo cargas aleatorias. Los resultados de simulación son comparados con resultados experimentales previamente obtenidos por los autores. Se dispone de los resultados de un total de 140 ensayos de crecimiento de grietas con registros de carga de amplitud variable correspondientes a cuatro procesos aleatorios gaussianos realizados sobre probetas tipo CT de la aleación de aluminio 2024-T351. Además de estos ensayos, para caracterizar el comportamiento a fatiga del material y ajustar los parámetros del modelo, se han realizado tandas de tres ensayos con carga de amplitud constante para distintas relaciones de carga ($R=0.1, 0.3, 0.5$ y 0.7). En este trabajo se analiza el procedimiento de ajuste de los parámetros del modelo, estudiando la influencia de dichos parámetros en los resultados de simulación con cargas aleatorias así como la capacidad del modelo de representar el proceso de crecimiento.

ABSTRACT

This work uses the strip-yield model implemented in NASGRO computer to estimate fatigue crack growth under variable amplitude loading. The simulated results were compared with experimental data previously obtained by the authors. A substantial number of fatigue crack growth analysis were carried out using variable amplitude load histories, corresponding to four stationary Gaussian random processes, on CT specimens of aluminium alloy 2024-T351. Crack growth tests under constant amplitude loading at four different stress ratios ($R=0.1, 0.3, 0.5$ and 0.7) were carried out to characterize the fatigue crack growth behaviour of the studied material and adjust the model parameters. The effect of the fitted parameters on the simulation results as well as the capability to represent the crack growth process are analysed.

KEY WORDS: fatigue crack growth, fatigue under random loading, strip yield model

1. INTRODUCTION

Para el diseño a fatiga de numerosos componentes mecánicos, especialmente aquellos con diseño basado en tolerancia al daño, es fundamental predecir el comportamiento de las grietas durante el crecimiento por fatiga. Los modelos empleados para ello deben ser capaces de predecir el crecimiento ante cualquier ley de variación de carga que sufra el sistema en la realidad. Desde hace muchos años se han propuesto diversos modelos para predecir el comportamiento de grietas sometidas a cargas de variación irregular o aleatoria [1-5]. Dichos modelos deben ser capaces de predecir el

efecto de las sobrecargas y, en general, el efecto de secuencia.

Entre los modelos de predicción, probablemente el grupo más extendido actualmente, especialmente en la industria aeronáutica, es el de los basados en el cierre de grieta. De los distintos procedimientos propuestos para calcular el cierre de grieta, el más difundido es el basado el Strip Yield Model (SYM) propuesto por Newman [5]. Dicho modelo se emplea para determinar la evolución de las tensiones de cierre, al mismo tiempo que definen una ley de crecimiento de grieta en función del factor de intensidad de tensiones efectivo, ΔK_{eff} . Los parámetros del modelo y de la ley de crecimiento es

necesario ajustarlos a partir de velocidades de crecimiento obtenidas experimentalmente con cargas de amplitud constante y variable a diferentes niveles de carga y relación de tensiones.

En este trabajo se presenta un análisis del modelo implementado en el código comercial NASGRO [6]. Se analiza la influencia de los parámetros de ajuste del modelo sobre los resultados de simulación, así como la capacidad del modelo para predecir el crecimiento de grieta bajo cargas aleatorias comparando los resultados de simulación con los resultados experimentales obtenidos previamente por los autores.

La organización del artículo es como sigue. En primer lugar se presentan los resultados experimentales de los ensayos realizados, que servirán para ajustar el modelo. A continuación se comentan brevemente las características del modelo y se presentan los ajustes de parámetros realizados y la influencia de estos en los resultados obtenidos. Finalmente se obtienen algunas conclusiones.

2. MATERIAL Y ENSAYOS

Para la caracterización del comportamiento del material a fatiga se han llevado a cabo ensayos de crecimiento de grietas bajo cargas de amplitud constante (CA) para cuatro relaciones de carga ($R=P_{max}/P_{min}$): $R= 0.1, 0.3, 0.5$ y 0.7 . Se han realizado tres ensayos diferentes para cada valor de R . El material de ensayo es la aleación de aluminio Al-2024-T351 ensayado con probetas tipo CT de 50 mm de ancho y 12 mm de espesor. La longitud de grieta se ha medido haciendo uso del método de caída de potencial con corriente alterna (ACPD). La velocidad de crecimiento se ha calculado de acuerdo al procedimiento descrito en ASTM E647, los resultados de dichos ensayos se muestran en la figura 1.

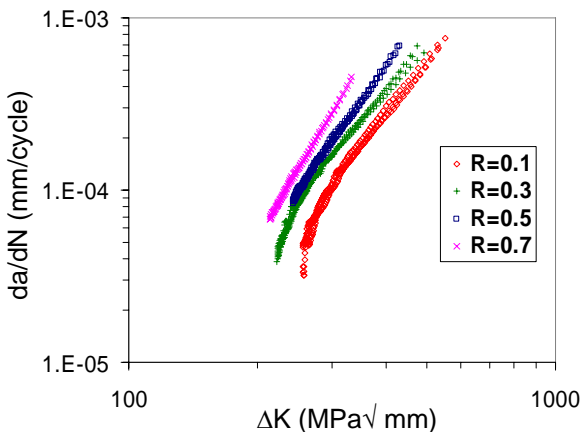


Figura 1. Resultados de los ensayos con carga de amplitud constante.

Para la validación del modelo se emplearán los resultados experimentales obtenidos en 140 ensayos de crecimiento de grieta con carga aleatoria realizados por

los autores [7,8]. Para el mismo material y tipo de probetas se realizaron ensayos empleando en cada caso un registro de carga aleatoria distinto. Cada registro se obtuvo sumando una carga constante a un registro aleatorio representante de un proceso gaussiano de media cero definido por su función de densidad espectral. Se definieron 4 procesos de carga distintos denominados A, B, C y D. Para poder considerar distintos niveles de carga se tomaron dos valores distintos de media cuadrática, denominándose nivel H y L a los niveles de carga alto y bajo respectivamente. Para cada uno de los procesos y niveles de carga, denominados AH, BH, CH, DH, AL, BL y DL, se obtuvieron 20 registros de carga diferentes cada uno con 25000 ciclos. En la tabla 1 se presentan los valores de vida media a fatiga y desviación estándar para todos los procesos.

Tabla 1. Vida media (μ_T) y desviación standard (σ_T) en miles de ciclos para todos los procesos de carga

PROCES O	AH	BH	CH	DH
μ_T	277	197	168	147
σ_T	13,4	7,7	5,1	5,4
PROCES O	AL	-	CL	DL
μ_T	1164	-	691	590
σ_T	35,4	-	17,7	24,5

3. CARACTERISTICAS DEL MODELO

El SYM implementado en Nasgro utiliza la siguiente ecuación de crecimiento:

$$\frac{da}{dN} = C \left[\left(\frac{1-f}{1-R} \Delta K \right) \right]^n \frac{\left(1 - \frac{\Delta K_{th}}{\Delta K} \right)^p}{\left(1 - \frac{K_{max}}{K_c} \right)^q} \tag{1}$$

Donde C, n, p y q , son parámetros del material a ajustar, $R= S_{min}/S_{max}$ es la relación de tensiones, $f = S_{op}/S_{max}$ y K_c, K_{th} son el factor de intensidad de tensiones crítico y umbral respectivamente.

Para tener en cuenta el estado de tensiones se hace uso del concepto de factor de constricción. Nasgro permite dos opciones distintas de cálculo. En la opción denominada VCL (variable constraint-loss option), el modelo usa un factor de constricción a tracción variable a lo largo de los elementos de la zona plástica, que además es calculado por el programa en base a la relación entre el tamaño de zona plástica y el espesor de la probeta. No obstante, el usuario debe definir el parámetro α_{new} , relación entre el factor de constricción a tracción en el borde de grieta y el factor de constricción a compresión. Una segunda opción, denominada CCL (constant constraint-loss option), usa un factor de

constricción a tracción constante a lo largo de los elementos de la zona plástica, que es definido por el usuario. El estudio presentado en este trabajo se ha realizado usando la opción VCL.

NASGRO realiza la simulación con el siguiente esquema: recibe como entrada los datos y geometría del material, los parámetros ajustados de la ecuación de crecimiento y los registros de carga aplicados, usando el Strip Yield Model determina las tensiones de cierre a partir de las cargas aplicadas y simula el crecimiento de la grieta para cada ciclo o conjunto de ciclos.

4. AJUSTE DE LOS PARÁMETROS DE LA ECUACIÓN DE CRECIMIENTO.

El software dispone de un módulo de cálculo (matgui) que permite ajustar la ecuación (1) a un conjunto de datos da/dN-ΔK. El ajuste obtiene los valores de C y n, para un conjunto de parámetros (p, q, ΔK_{th} y K_C) fijados de antemano. Nasgro provee para una amplia variedad de materiales una base de datos con información sobre factores de intensidad de tensiones umbrales y críticos que junto a ecuaciones empíricas permiten obtener ΔK_{th} y K_C. Para evaluar la función f en este módulo de ajuste se usa la función propuesta por Newman [9]:

$$\frac{S_0}{S_{max}} = A_0 + A_1R + A_2R^2 + A_3R^3$$

$$A_0 = (0.825 - 0.34\alpha + 0.05\alpha^2) [\cos(\pi S_{max}/2\sigma_0)]^{1/\alpha}$$

$$A_1 = (0.415 - 0.071\alpha) S_{max}/\sigma_0$$

$$A_2 = 1 - A_0 - A_1 - A_3$$

$$A_3 = 2A_0 + A_1 - 1$$

Donde α representa el factor de constricción que es tratado como una constante con el único propósito de ajustar las curvas de crecimiento.

Además de los parámetros de la ecuación de crecimiento, el modelo necesita de otros para su simulación: el parámetro α_{new} comentado previamente y otros parámetros ΔS_{max} y N_{max} que controlan la actualización de la tensión de cierre. Bajo cargas de amplitud constante, el valor de la tensión de cierre se mantiene en un valor estabilizado por lo que no es necesario actualizar su valor en cada ciclo, sin embargo, bajo cargas aleatorias, la frecuencia con la que la tensión de cierre es actualizada tendrá mucha influencia en el efecto de las sobrecargas.

5. INFLUENCIA DE LOS PARÁMETROS DE AJUSTE DEL MODELO

Haciendo uso del módulo matgui, para el ajuste de la ecuación de crecimiento a los datos experimentales obtenidos con carga de amplitud constante, se ha observado que ningún valor de α permite obtener un ajuste satisfactorio para todos los valores de R. Se obtiene una pobre correlación entre los resultados

obtenidos por simulación y los valores reales de vida obtenidos experimentalmente con cargas de amplitud constante. Estos resultados concuerdan por los obtenidos por otros autores [10] también en aleaciones de aluminio. Un inconveniente de este módulo de cálculo es que tan sólo proporciona una representación gráfica conjunta de da/dN frente a ΔK para los datos experimentales y los obtenidos con el ajuste a la ecuación 1, como se muestra en la figura 2, pero no proporciona ninguna herramienta que permita definir el mejor ajuste. Por otra parte, se ha comprobado que un aparente buen ajuste a datos para un determinado valor de R puede obtenerse con distintos valores del parámetro α y no obstante, esto no garantiza una buena estimación de vida en la simulación.

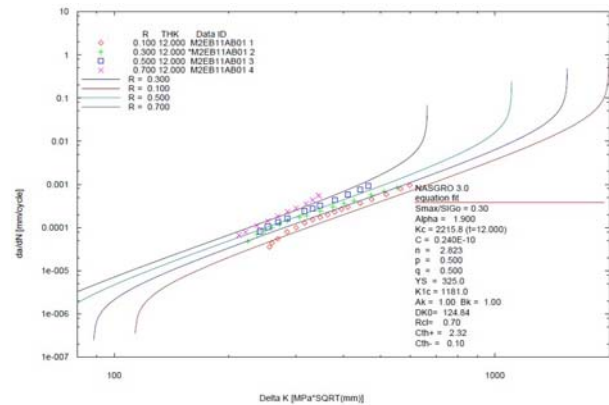


Figura 2. Salida gráfica del módulo de ajuste matgui. (5.15)

Pese a estos resultados, uno de los objetivos de este trabajo es analizar la influencia de los parámetros de ajuste del modelo sobre las estimaciones de vida bajo cargas aleatorias. La eficiencia del ajuste se va a determinar comparando la estimaciones con datos experimentales de crecimiento de grietas con cargas aleatorias. De los veinte ensayos realizados para cada proceso, a efectos de comparación, se han tomado el de mayor y menor vida para el proceso CH, que corresponden a los registros de carga que presentan los mayores y menores efectos de retardo. De esta manera, una correcta estimación del crecimiento en ambos casos garantizará unas buenas estimaciones en todos los demás. Se han realizado ajustes de la ecuación de crecimiento variando: los exponentes p y q, la relación de tensiones R sobre la que se realiza el ajuste, y el factor de constricción α, para estudiar la influencia de estos parámetros en la simulación bajo cargas aleatorias.

Ajustes realizados con valores de p y q muy distintos, apenas producen diferencias en las estimaciones del crecimiento. Variando q desde q=1 hasta q=4, las diferencias en número de ciclos de vida es menor del 10%.

Por el contrario, ajustar la ecuación de crecimiento a distintos conjuntos de relación de tensiones (R) produce grandes variaciones en la predicción del crecimiento, en la figura 3, se muestra el efecto sobre las estimaciones de la simulación, de la relación de tensiones utilizada en

el ajuste. Se observa que el valor de $R=0.3$ nos proporciona los mejores resultados. Las relaciones de vida (N_{NASGRO}/N_{EXP}) para el proceso CH varían entre 0.82 y 1.23 en función del R ajustado.

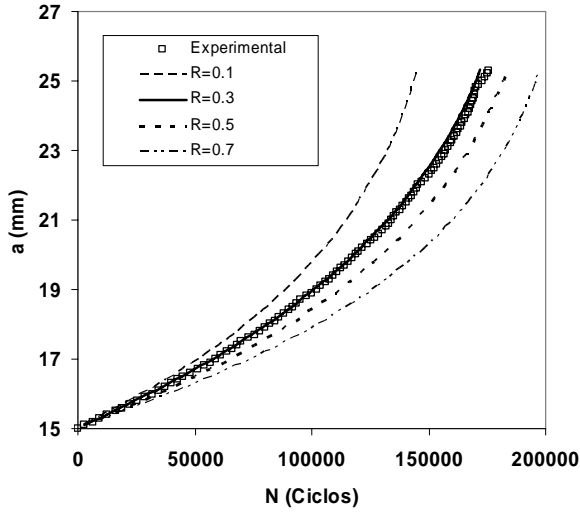


Figura 3. Curva $a-N$ experimental y estimadas usando los parámetros de la ecuación de crecimiento ajustados a distintos conjuntos de relación de tensiones R .

El factor de constricción elegido para el ajuste, influye fuertemente en las estimaciones de la simulación del crecimiento. Este resultado coincide con el obtenido por los autores en trabajos previos realizados haciendo uso del strip yield model implementado en el código FASTRAN propuesto por Newman [11]. Ajustes con factores de constricción desde 1.5 a 3 producen grandes variaciones en las estimaciones de vida, figura 4. En general los mejores resultados se obtienen para altos valores del factor de constricción, encontrándose que entre $\alpha=2.6$ y $\alpha=2.8$ son los que mejores aproximaciones obtienen para los casos estudiados.

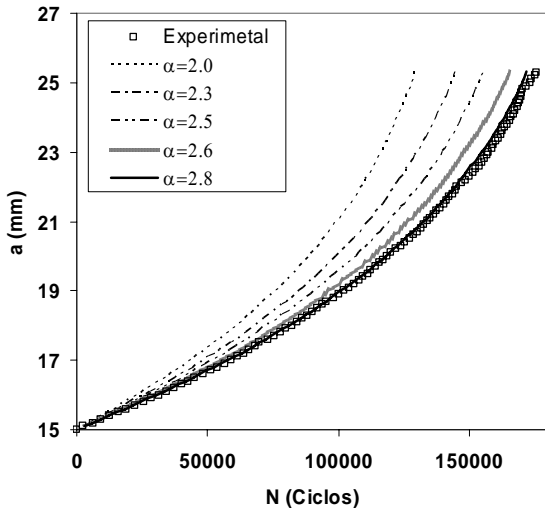


Figura 4. Curva $a-N$ experimental y estimadas usando los parámetros de la ecuación de crecimiento ajustados con distintos valores de α .

Para analizar la influencia de α_{new} se realizan simulaciones con valores entre 1.5 y 2.3. Las

simulaciones comparadas con los datos experimentales muestran un efecto muy pequeño de esta variable, las diferencias en número de ciclos de vida es inferior al 5%.

Como se ha comentado, el uso del modelo para cargas de amplitud variable, está muy influenciado por la frecuencia con la que se estima el valor de la tensión de cierre. En estos casos, el manual indica que un análisis ciclo a ciclo podría ser una elección segura pero con un consumo de tiempo de computación más alto. El software contiene dos parámetros adicionales, ΔS_{max} y N_{max} , que gobiernan el algoritmo de actualización de la tensión de cierre. El primer parámetro, ΔS_{max} , es la diferencia de tensión aplicada desde un pico máximo de carga significativo al siguiente que requiere un nuevo cálculo de la tensión de cierre. Esto asegura que el efecto de las sobrecargas sea tenido en cuenta. El segundo parámetro, N_{max} , es el número máximo de ciclos consumidos entre dos actualizaciones de la tensión de cierre. Esto asegura la actualización en posibles espectros con largos bloques de ciclos de amplitud constante. Para determinar el efecto que estos parámetros ejercen sobre la simulación del crecimiento en procesos aleatorios, se realizan simulaciones permitiendo que ΔS_{max} o N_{max} controlen la actualización de la tensión de cierre.

Para estudiar el efecto de N_{max} , se ha utilizado un valor muy alto de ΔS_{max} para que sea el número de ciclos quien controla la actualización de la tensión de cierre. Se han realizado simulaciones con $N_{max}=1$, $N_{max}=5$, $N_{max}=10$ y $N_{max}=100$, la figura 5 muestra las grandes diferencias de crecimiento estimadas al variar N_{max} . La vida estimada al considerar $N_{max}=10$ es más del doble que al realizar actualizaciones ciclo a ciclo ($N_{max}=1$).

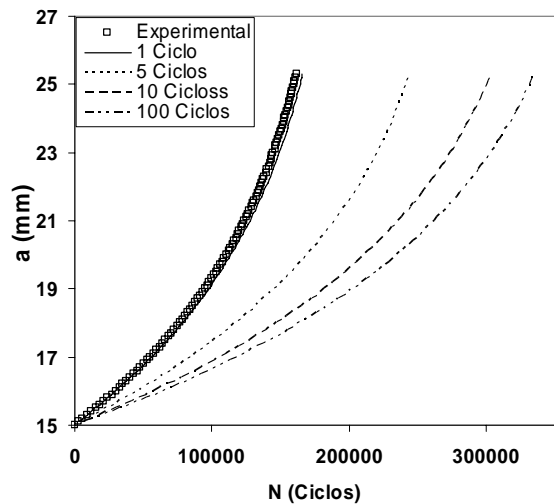


Figura 5. Curva $a-N$ experimental y estimadas usando distintos valores del parámetro N_{max} .

Contrariamente al caso anterior, para estudiar el efecto de ΔS_{max} , se fija un valor muy alto de N_{max} . ΔS_{max} se han tomado como porcentajes de la diferencia entre 1.5 veces la media de picos y la media de los picos del registro de cargas. Los valores de ΔS_{max} utilizados en el

estudio han sido 5%, 10%, 25%, 50% y 100% del incremento definido anteriormente, la figura 6 muestra dichos resultados.

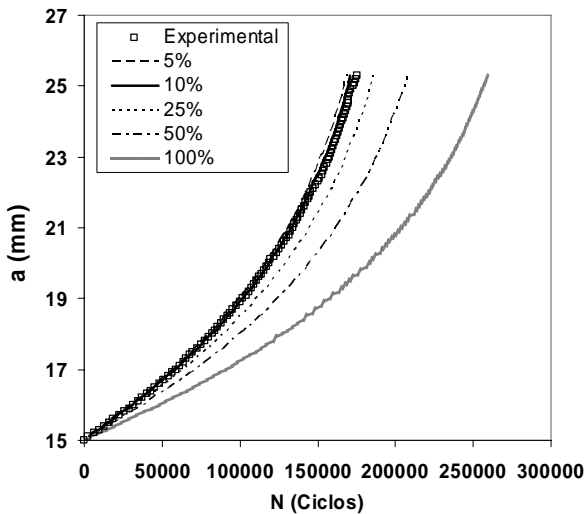


Figura 6. Curva a-N experimental y estimadas usando distintos valores del parámetro ΔS_{max} .

6. RESULTADOS Y DISCUSIÓN

En base a los resultados obtenidos se puede concluir que el ajuste de los parámetros tiene una gran influencia en los resultados obtenidos en simulación para las cargas aleatorias. El efecto de dichos parámetros sobre los resultados puede explicarse como sigue.

La pequeña influencia del parámetro q se debe a que en ningún caso el crecimiento de grieta se llevó a cabo hasta fractura. Este parámetro influye mucho en la curva de crecimiento en la zona de altos valores de ΔK , pero dichos valores no se alcanzan durante el ensayo. Para valores bajos de ΔK , en la región próxima al umbral, la forma de la curva de crecimiento está controlada por el parámetro p. La poca influencia de este parámetro se debe a que, si bien es cierto que para el proceso de cargas aleatorias hay muchos rangos de carga pequeños, y por tanto bajos valores de ΔK , su contribución al proceso es muy pequeña debido a las bajas velocidades de crecimiento.

La gran influencia del parámetro α y del conjunto de datos de distinto R elegido en el ajuste en el módulo Matgui, se debe a que dichos parámetros modifican la ecuación de crecimiento en la zona intermedia de ΔK , justo en el rango que realmente contribuye al crecimiento de la grieta con las cargas aleatorias del proceso estudiado. Ajustar con un valor bajo de α desplaza las curvas de crecimiento (da/dN vs. ΔK_{eff}) hacia la izquierda, lo contrario ocurriría con un valor alto de α . Por tanto, a un mismo valor de ΔK le corresponden velocidades de crecimiento más altas (dando vidas menores a las experimentales) si el ajuste se realiza con un valor bajo de α que el que le

correspondería si el ajuste se realiza con un valor alto de α (dando entonces vidas mayores), ver figura 4.

La influencia de los parámetros ΔS_{max} y N_{max} queda clara comparando las simulaciones realizadas ciclo a ciclo con las obtenidas para distintos valores de dichos parámetros. El que ejerce mayor efecto en la simulación es N_{max} . Cuánto más vida se consume sin actualizar la tensión de cierre, el efecto de las grandes sobrecargas predomina, aumentando los efectos de retardo y la vida estimada en la simulación. Para los procesos de carga aquí considerados, la irregularidad de las mismas y la influencia de estos parámetros, muestra claramente que no es posible un cálculo simplificado sino que es necesaria la simulación ciclo a ciclo, es decir, el cálculo o actualización de la tensión de cierre en cada ciclo.

Elegidos los parámetros del modelo que producen para el proceso CH el mejor ajuste a los dos registros de carga, el de máxima y mínima vida, las curvas a-N obtenidas son las que se muestran en la figura 7. Con dichos parámetros se realizan las simulaciones para los 20 registros de carga del proceso CH, la figura 8 representa la relación vida simulada/experimental, con valores entre 0.97 y 1.11 siendo el valor medio de 1.011.

La figura 9, muestra la relación de vidas obtenidas por simulación a vidas experimentales para los 20 registros de cada uno de los siete procesos de carga. A la vista de estos resultados, puede concluirse que ajustados los parámetros del modelo a los resultados de registros bajo cargas aleatorias, las simulaciones para todos los procesos y en los dos niveles de carga arrojan excelentes resultados con relaciones N_{NASGRO}/N_{EXP} entre 0.8 y 1.25.

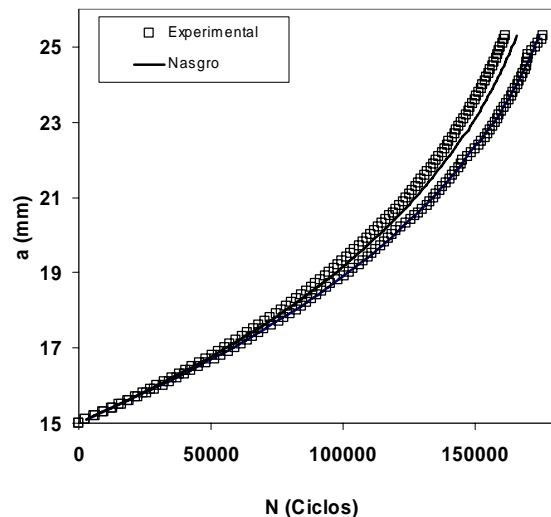


Figura 7. Curvas a-N experimental y estimadas para los registros de máxima y mínima vida del proceso CH.

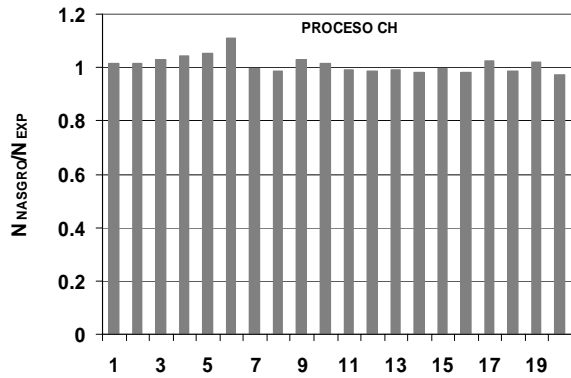


Figura 8. Relación vida estimada (N_{NASGRO}) a vida experimental (N_{EXP}) para los 20 registros del proceso CH.

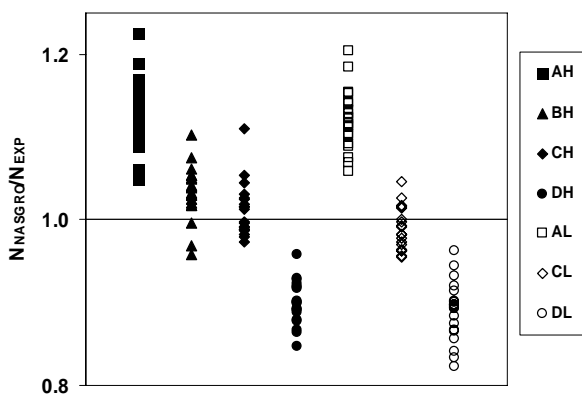


Figura 9. Relación vida estimada (N_{NASGRO}) a vida experimental (N_{EXP}) para los 20 registros de todos los procesos de carga considerados.

7. CONCLUSIONES

Finalmente, como conclusiones pueden destacarse las siguientes:

- El módulo de cálculo para el ajuste de la ecuación de crecimiento no permite obtener un ajuste satisfactorio para los resultados con cargas de amplitud constante para todos los valores de R.
- El factor de constricción usado en el ajuste, tiene una enorme influencia en los resultados obtenidos por el modelo.
- El valor de α_{new} tiene poco efecto en la simulación.
- Las variables que controlan la actualización de la tensión de cierre, ΔS_{max} y N_{max} , tienen mucha influencia en los resultados de simulación obtenidos para cargas aleatorias, justificando el uso necesario de una simulación ciclo a ciclo.
- Si los parámetros del modelo se ajustan para reproducir el crecimiento observado con un registro de cargas aleatorias de un proceso y nivel de carga

concreto, las estimaciones de crecimiento para el resto de procesos en los dos niveles de carga estudiados, son muy buenas.

REFERENCIAS

- [1] Chang JB, Hudson CM. (Eds), *Methods and Models for Predicting Fatigue Crack Growth under Random Loading*, ASTM STP 748, 1981.
- [2] Willemborg JD, Engle RM, Wood HA, *A Crack Growth Retardation Model Using an Effective Stress Concept*. AFFDL-TM-FBR-71-1, 1971.
- [3] Wheeler, O.E., *Spectrum Loading and Crack Growth*, Journal of Basic Engineering, Transactions of the ASME, Vol. 94, pp. 181-186, 1972.
- [4] Johnson, W.S., *Multi-Parameter Yield Zone Model for Predicting Spectrum Crack Growth*, *Methods and Models for Predicting Fatigue Crack Growth Under Random Loading*, J.B. Chang and C.M. Hudson, Eds., ASTM STP 748, pp. 85-102, 1981.
- [5] Newman JC Jr. *A Crack Closure Model for Predicting Fatigue Crack Growth under Aircraft Spectrum Loading*, *Methods and Models for Predicting Fatigue Crack Growth under Random Loading*, Chang JB, Hudson CM. (Eds), ASTM STP 748, pp53-84, 1981.
- [6] *Fatigue Crack Growth Computer program "NASGRO" Version 3.0*. Reference Manual, JSC-22267B, Lyndon B. Johnson Space Center. NASA, Texas, 2001.
- [7] Moreno B, Zapatero J, Dominguez J. *An experimental analysis of fatigue crack growth under random loading*. *International Journal of Fatigue*, 25, pp. 597-608, 2003.
- [8] Zapatero J, Moreno B, González-Herrera A, Dominguez, J. *Numerical and experimental analysis of the fatigue crack growth under random loading*. *International Journal of Fatigue*, 27, pp. 878-890, 2005.
- [9] Newman, Jr., J. C. *A crack opening stress equation for fatigue crack growth*, *International Journal of Fracture*, Vol. 24 No. 3, 1984.
- [10] M. Skorupa et al. *Application of the strip-yield model from the NASGRO software to predict fatigue crack growth in aluminium alloys under constant and variable amplitude loading*. *Eng. Fract. Mech.* vol. 74, pp. 291-313, 2007.
- [11] Zapatero J, Moreno B, Dominguez J. *On the use of the strip-yield model to predict fatigue crack growth under irregular loading*. *Fatigue Fract. Engng Mater Struct.*, 20, pp. 759-770, 1997.

EFFECTS OF MULTIAXIAL LOADING ON CYCLIC PLASTICITY AND FATIGUE BEHAVIOUR OF AUSTENITIC STAINLESS STEEL (AISI 303)

L. Reis, A. Cabrita, B. Li and M. de Freitas

Dept. of Mech. Engineering
 Instituto Superior Técnico
 Av. Rovisco Pais, 1,
 1049-001, Lisboa, Portugal
 E-mail:
luís.g.reis@ist.utl.pt
bli@ist.utl.pt
mfreitas@dem.ist.utl.pt

ABSTRACT

Components and structures are usually under multiaxial loading conditions. Among several structural steels the austenitic stainless steels are widely used in various engineering applications, one of their main features is the strong corrosion resistance. Materials are usually submitted to complex loadings, which could cause micro-structural changes, affecting their physical and mechanical properties and consequently causing multiaxial fatigue damage. The purposes of this work are to study the influence of the different multiaxial fatigue loading paths on fatigue life and crack orientation, comparing the test results with theoretical results from multiaxial fatigue models. Tests were carried out in load control for several multiaxial loading paths and then fractographic analyses of specimen fracture surface were carried out. Results show that the different multiaxial loading paths have a relevant preponderance on fatigue life and are determinant on the fatigue crack initial orientation, which is predicted by critical plane models.

KEY WORDS: Austenitic stainless steel, Multiaxial fatigue, Loading paths, Proportional and non-proportional loadings, Fatigue life prediction, Fractographic analysis.

1. INTRODUCTION

Mechanical components are generally submitted to complex fatigue loadings that generate multiaxial stress states in correspondent critical points. During the last forty years researchers have extensively investigated the problem of multiaxial fatigue assessment in order to provide engineers safe methods for the fatigue life prediction in the presence of complex stress states [1]. One recent inquiry had demonstrated that 70% of the companies have encountered with fatigue problems [2]. Stainless steels are present in many industries applications and therefore are submitted to multiaxial stress states. Austenitic stainless steels are ductile, tough and, most importantly, easy to form and weld. They have f.c.c. microstructure. There are numerous applications for this type of stainless steel, ranging from domestic kitchen thinks and building façades to commercial food processing equipment and chemical plant piping [3, 4].

In this study, several non-proportional multiaxial fatigue tests were carried out on *AISI 303* steel. The objective of these fatigue tests is to study the behavior of the material when subject to the multiaxial fatigue loading paths. To evaluate the shear stress amplitude two approaches were used, the *von Mises* equivalent stress, [5], and the MEC approach [6, 7]. Fatigue

critical plane models, such as the Findley, the Fatemi-Socie, the SWT and the Liu criterions are used to analyse the potential crack plane orientation. The predictions given by these models are compared with experimental results.

2. MATERIAL DATA, SPECIMEN FORM AND TEST PROCEDURE

In this work, the material studied is the austenitic stainless steel *AISI 303*. The chemical composition is shown in Table 1. In order to characterize the cyclic stress-strain behavior of the material studied tension-compression low cycle fatigue tests were carried out, [8]. Monotonic and cyclic mechanical properties are shown in Table 2.

Table 1- Chemical composition of the material studied – AISI 303 steel (in wt%) [5].

AISI 303 Stainless steel	Chemical composition								
	C	Si	Mn	P	S	Cr	Ni	Mo	Cu
	0.12	1.00	2.00	0.060	0.25	18.00	9.00	----	---

In order to study the effects of the multiaxial loading paths and in particular both the axial and the torsional

component on the fatigue life, a series of loading paths were applied in the experiments as shown in Table 3. In Table 4 are shown the reference multiaxial fatigue loading paths. A biaxial servo hydraulic machine performed the tests of biaxial cyclic tension-compression with cyclic torsion. Test conditions were as follows: frequency 3-5 Hz at room temperature and laboratory air. Tests ended up when the specimens were completely broken or after a million cycles.

Table 2 - Monotonic and cyclic mechanical properties of AISI 303 [5].

Tensile strength	R_m (MPa)	625
Yield strength	$R_{p0.2,monotonic}$ (MPa)	330
Elongation	A (%)	58
Young's modulus	E (GPa)	178
Yield strength	$R_{p0.2,cyclic}$ (MPa)	310
Strength coefficient	K' (MPa)	2450
Strain hardening exponent	n'	0.35
Fatigue strength coefficient	σ'_f (MPa)	534
Fatigue strength exponent	b	-0.07
Fatigue ductility coefficient	ϵ'_f	0.05
Fatigue ductility exponent	c	-0.29

The geometry and dimensions of the specimen are shown in Figure 1:

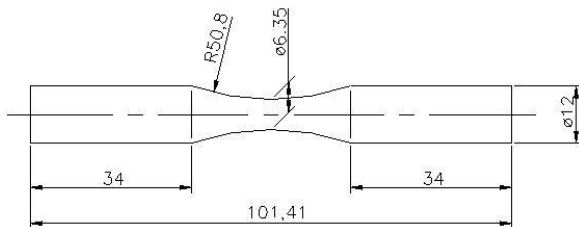


Figure 1 - Specimen geometry for biaxial cyclic tension-compression with cyclic torsion tests [8].

Table 3 - Multiaxial fatigue loading paths.

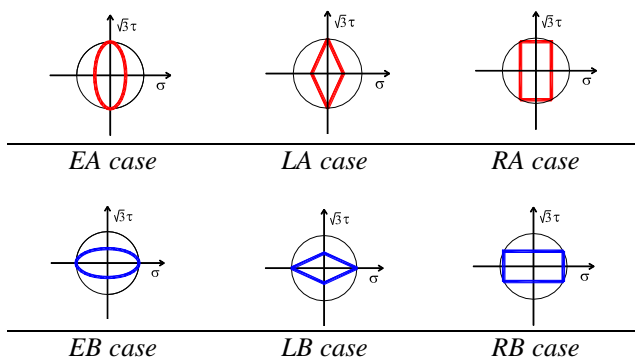
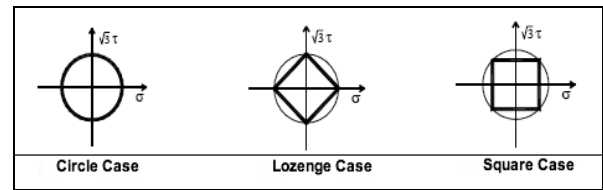


Table 4 – Reference Multiaxial fatigue loading paths.



3. THEORETICAL ANALYSIS OF THE FATIGUE LIFE PREDICTION

Many multiaxial fatigue models have been proposed in the last decades [9] and some of them are applied in this work; the shear stress amplitude is one of the important parameters in the formulations of the multiaxial fatigue damage models.

3.1. von Mises approach

According to von Mises criterion [10], the shear stress occurs in a plane equally inclined to all the main directions. For x-y-z Cartesian system the *von Mises* equivalent stress can be written as equation (1):

$$\sigma_{eq} = \frac{1}{\sqrt{2}} \sqrt{(\sigma_x - \sigma_y)^2 + (\sigma_y - \sigma_z)^2 + (\sigma_x - \sigma_z)^2 + 6(\tau_{xy}^2 + \tau_{yz}^2 + \tau_{xz}^2)} \quad (1)$$

For biaxial loading of tension-compression with cyclic torsion the expression can be simplified, equation (2):

$$\sigma_{eq} = \sqrt{\sigma_x^2 + 3(\tau_{xy})^2} \quad (2)$$

3.2. MCE Approach for evaluating shear stress amplitude

From the stress invariant (Sine's criterion), which is express by the amplitude and the mean value of equivalent shear stress and by the hydrostatic stress, in which the equivalent shear stress amplitude is represented by the square root of the second invariant of the stress deviator, $\sqrt{J_{2,a}}$ [6], avoiding the search of critical plane, equation (3):

$$\sqrt{J_{2,a}} + \alpha(\sigma_{H,med}) \leq \beta \quad (3)$$

where α and β are material constants. The innovation of this model is the $\sqrt{J_{2,a}}$ calculation. Whereas minimum circumscribed circle (MCC) approach [11] defines the shear stress amplitude as the radius of the minimum circle circumscribing to the loading path, minimum circumscribed ellipse (MCE) approach compute the effective shear stress amplitude taking into account the non-proportional loading effect. The load traces are represented and analyzed in the transformed deviatoric stress space, where each point represents a

value of $\sqrt{J_2}$ and the variations of $\sqrt{J_2}$ are shown during a loading cycle. The schematic representation of the MCE approach and the relation with MCC approach are illustrated in Figure 2:

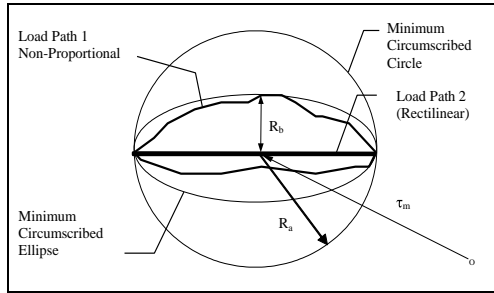


Figure 2 - The MCC and MCE circumscribing to shear stress traces, R_a and R_b are the major and minor radius of MCE, respectively [6].

The idea of the MCE approach is to construct a minimum circumscribed ellipse that can enclose the whole loading path throughout a loading block in the transformed deviatoric stress space. Rather than defining $\sqrt{J_{2,a}} = R_a$, by the MCC approach, in MCE approach R_a and R_b are the lengths of the major semi-axis and the minor semi-axis of the minimum circumscribed ellipse respectively. The ratio of R_b/R_a represents the non-proportionality of the shear stress path. The important advantage of this new MCE approach is that it can take into account the non-proportional loading effects in an easy way. As shown in Figure 2, for the non-proportional loading path 1, the shear stress amplitude is defined as, equation (4):

$$\sqrt{J_{2,a}} = \sqrt{R_a^2 + R_b^2} \quad (4)$$

For the proportional loading path 2, it is defined as $\sqrt{J_{2,a}} = R_a$ since R_b is equal to zero (rectilinear loading trace).

3.3. Critical Plane models

The ingredients of the critical plane criteria are the normal and shear stresses acting on a material plane Δ . The various proposed formulae are different, but the process to follow is merely the same. One must firstly, found the critical plane and secondly, check if the criterion is satisfied on this plane. If the criterion is not satisfied, then a fatigue crack may appear on the critical plane. Therefore, the orientation of the initiated crack coincides with the orientation of the critical plane [11].

Findley criterion

Findley [12] proposed a critical plane model, which predicts that the fatigue crack plane is the plane

orientation θ with maximum Findley damage parameter, equation (5):

$$\max_{\theta} (\sigma_a + k\sigma_{a,\max}) \quad (5)$$

where τ_a is the shear stress amplitude on a plane θ , $\sigma_{n,\max}$ is the maximum normal stress on that plane θ and k is a material parameter ($k_{AISI303} = 0.2$).

Brown-Miller criterion

Brown and Miller [13] proposed that the shear and normal strain on the plane of maximum shear must be considered. The simplified formulation of the theory for case A cracks is (equation (6):

$$\max_{\theta} \left(\frac{\Delta\gamma_{\max}}{2} + S\Delta\varepsilon_n \right) \quad (6)$$

Critical plane is the plane of maximum shear strain range $\Delta\gamma_{\max}$ with major value of normal strain range $\Delta\varepsilon_n$; S is the normal strain effects coefficient and is determined experimentally ($S_{AISI303} = 0.2$).

Fatemi-Socie criterion

Fatemi-Socie [14] proposed a model that predicts the critical plane is the plane orientation θ with the maximum F-S damage parameter, equation (7):

$$\max_{\theta} \left[\frac{\Delta\gamma_{\max}}{2} \left(1 + k \frac{\sigma_{n,\max}}{\sigma_y} \right) \right] \quad (7)$$

where $\frac{\Delta\gamma_{\max}}{2}$ is the maximum shear strain amplitude on a plane θ , $\sigma_{n,\max}$ is the maximum normal stress on that plane, σ_y is the material monotonic yield strength and k is a material constant ($k_{AISI303} = 0.2$).

S-W-T criterion

Smith, Watson and Topper [15] proposed a model that predicts that the fatigue crack plane is the plane orientation θ with maximum normal stress (the maximum principal stress), equation (8):

$$\max_{\theta} \left(\sigma_n \frac{\Delta\varepsilon_1}{2} \right) \quad (8)$$

where σ_n is the normal stress on a plane θ , $\Delta\varepsilon_1$ is the principal strain range on that plane.

Liu criterion

Liu [16] proposed an energy method to estimate the fatigue life, based on virtual strain energy (VSE). This

4.2 Fractographic analysis of fracture surface and estimation of critical plane orientation

From Figure 5 to Figure 10 it is presented the fractographic analysis of the macroscopic plane of crack initiation.

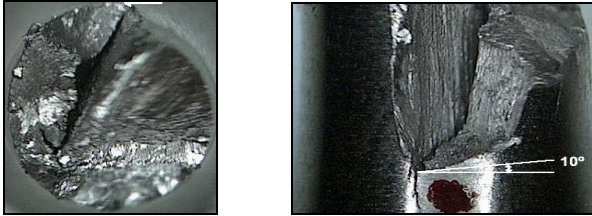


Figure 5 - Fractographic analysis of the fatigue failure plane orientation under EA loading path shown in Table 3.

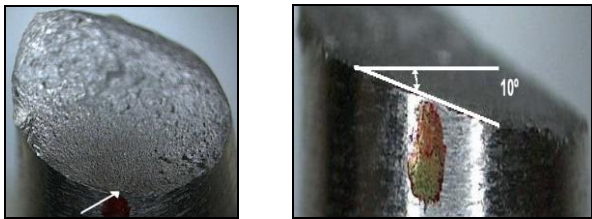


Figure 6 - Fractographic analysis of the fatigue failure plane orientation under EB loading path shown in Table 3.

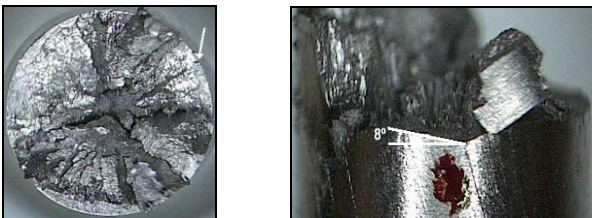


Figure 7 - Fractographic analysis of the fatigue failure plane orientation under RA loading path shown in Table 3.

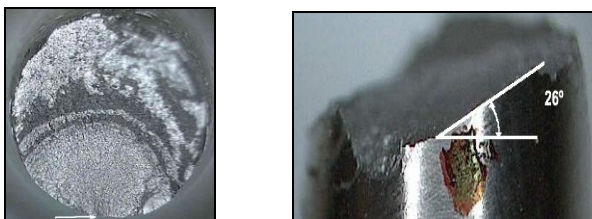


Figure 8 - Fractographic analysis of the fatigue failure plane orientation under RB loading path shown in Table 3.

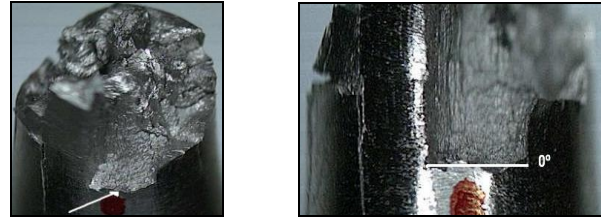


Figure 9 - Fractographic analysis of the fatigue failure plane orientation under LA loading path shown in Table 3.

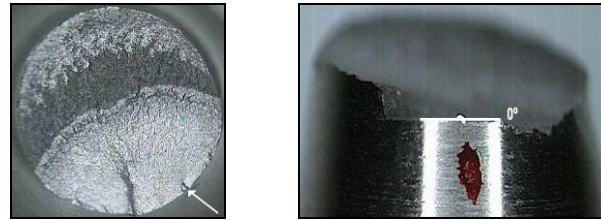


Figure 10 - Fractographic analysis of the fatigue failure plane orientation under LB loading path shown in Table 3.

It can be observed that specimens fracture surfaces that were submitted to the down trajectories showed well-defined fatigue typical characteristics. On the other hand, specimens that were submitted to the up trajectories showed fractures surfaces with large cracking and multiple morphologies in the same type of trajectory

4.3 Theoretical analysis of the fatigue crack planes

Critical plane models such as, Findley, Brown-Miller, Fatemi-Socie, S-W-T and Liu criterion, were used to analysed the potential crack plane orientation. Table 5 presents the comparison of the measured crack plane with predictions given by the critical plane models.

Table 5 - Comparison of the measured crack plane with predictions.

	Multiaxial Loading Paths								
	Case Circle	Case EA	Case EB	Case Square	Case RA	Case RB	Case Losangle	Case LA	Case LB
Measured	24°	6,5°	6,83°	32°	7,3°	19°	-	7,4°	2°
Findley	0°	0°	±39°	±22°	±9°	±28°	0°	0°	±39°
B-M	0°	0°	±40°	±21°	±7°	±28°	0°	0°	±41°
F-S	0°	0°	±42°	±21°	±7°	±29°	0°	0°	±43°
S-W-T	0°	±38°	0°	±25°	±41°	±15°	0°	±45°	0°
Liu I	0°	±38°	0°	±25°	±41°	±15°	0°	±45°	0°
Liu II	0°/±90°	0°/±90°	±45°	±21°/±69°	±4°/±86°	±30°/±60°	0°/±90°	0°/±90°	±45°

From the results in Table 5, it is easy to observe that the predictions made by the critical plane models depend of the multiaxial fatigue loading paths. The multiaxial fatigue models can be classified as shear-based models (Findley, Brown-Miller, Fatemi-Socie and Liu II) and tensile-based models (SWT and Liu I). Shear-based models give good predictions of the orientation of the crack initiation plane in up loading

cases, Case EA, Case RA and Case LA. Tensile-based models give good predictions of the orientation of the crack initiation plane in down loading cases, Case EB, Case RB and Case LB. The RA and RB cases show the larger difference between measured angles, nearly 12°.

The difference between crack orientation plane in EA and EB cases and Circle case is about 17°. The difference between crack orientation plane in RA and RB cases and Square case is about 25° and 13° respectively. For up loading cases the models that give a better approach for experimental results were *Brown-Miller* and *Fatemi Socie* models; while for down loading cases the models that give a better approach for experimental results were *S-W-T* and *Liu II* models.

5. CONCLUSIONS

A wide range of fatigue loading paths was applied to the austenitic stainless steel *AISI 303*. It was found that the loading paths have significant influences on fatigue life and on the crack plane orientations. Experimental results show that the ratio between normal stress component and shear stress component has a strong influence to fatigue damage and consequently in fatigue life. Down trajectories, with normal component bigger than shear component, have proven to be worse for fatigue life than up trajectories.

The MCE approach gives better correlations than von Mises approach for the studied loading cases and material. The MCE approach also shows that is more independent of the loading case.

The fracture surfaces of the specimens that were submitted to the down trajectories showed well-defined fatigue typical characteristics. Otherwise, specimens that were submitted to the up trajectories showed fractures surfaces with large cracking and multiple morphologies in the same type of trajectory.

Shear-based models give good predictions of the orientation of the crack initiation plane in up loading cases, Case EA, Case RA and Case LA. Tensile-based models give good predictions of the orientation of the crack initiation plane in down loading cases, Case EB, Case RB and Case LB.

ACKNOWLEDGEMENTS

The authors gratefully acknowledge financial support from FCT - Fundação para Ciência e Tecnologia (Portuguese Foundation for Science and Technology), through the project POCTI/EME/59577/2004.

RERERENCES

[1] Susmel, L., Petrone, N. (2003). "Multiaxial Fatigue Life Estimations for 6082-T6 Cylindrical Specimens under In-Phase and

Out-of-Phase Biaxial Loadings", *Biaxial/Multiaxial Fatigue and Fracture*, Editors: A. Carpinteri; M. Freitas; A. Spagnoli, 83-104.

[2] Papadopoulos, I. V. (2001). "Long Life Fatigue under Multiaxial Loading", *International Journal of Fatigue* 23: 839-849.

[3] Tuthill, A. H. (2002). "Stainless Steels and Specialty Alloys for Modern Pulp and Paper Mills", Reference Book, Series No. 11 025, Nickel Development Institute.

[4] Nickel Institute Web Page (11-10-2008). http://www.nickel institute.org/index.cfm/ci_id/11021.htm.

[5] Reis, L., (2004). "Comportamento Mecânico de Aços em Fadiga Multiaxial a Amplitude de Carga Constante e Síncrona", Universidade Técnica de Lisboa, IST, Tese de Doutoramento

[6] Freitas, M., Li, B. e Santos, J. L. T. (2000). "A numerical approach for high-cycle fatigue life prediction with multiaxial loading." *Multiaxial Fatigue and Deformation: Testing and Prediction*, ASTM STP 1387.

[7] Cruz, A. (2007). "Análise da não Proporcionalidade entre Tensões em Carregamentos Multiaxiais", Universidade Técnica de Lisboa, IST, Tese de Mestrado.

[8] ASTM E606 (2003). "Standard Practice for Strain-Controlled Fatigue Testing - E 606 - 92 (Reapproved 1998)." ASTM 03.01: 1-15.

[9] Socie, D.F. and Marquis, G.B., (2000) *Multiaxial Fatigue*, SAE, Warrendale, PA.

[10] Shigley, J. E., Mischke, C. R., Budynas, R. G. (2004). "Mechanical Engineering Design", Seventh Edition, Int. Edition, McGraw Hill.

[11] Papadopoulos, I. V., Bernasconi, A., Davoli, P., Filippini, M., Gorla, C. (1997). "A Comparative Study of Multiaxial High Cycle Fatigue Criteria for Metals", *International Journal of Fatigue*, vol. 19, No. 3, 219-235.

[12] Findley, W. N. (1956). "Theory For Combined Bending And Torsion Fatigue With Data For SAE 4340 Steel", *International Conference on Fatigue Metals*: 150-157.

[13] Brown, M., Miller, K. J. (1973). "A Theory for Fatigue Failure Under Multiaxial Stress-strain Conditions." *Proceedings of the Institute of Mechanical Engineers* 187: 745-755.

[14] Fatemi, A., Socie, D. (1988). "A Critical Plane Approaches to Multiaxial Fatigue Damage including Out-of-Phase Loading", *FFEMS* 11(3): 149-165.

[15] Smith, K. N., Watson, P., Topper, T. H. (1970). "A Stress-Strain Function for the Fatigue of Metals", *Journal of Materials*, *JMLSA* 5(4): 767-778.

[16] Liu, K. (1993). "A Method Based on Virtual Strain-Energy Parameters for Multiaxial Fatigue Life Prediction", *Advances in Multiaxial Fatigue*, ASTM STP 1191: 67-84.

MULTIAXIAL LOADINGS WITH DIFFERENT FREQUENCIES BETWEEN AXIAL AND TORSIONAL COMPONENTS IN 42CrMo4 STEEL

L. Reis, G. Perpétuo, B. Li and M. de Freitas

Dept. of Mech. Engineering
 Instituto Superior Técnico
 Av. Rovisco Pais, 1,
 1049-001, Lisboa, Portugal
 E-mail:
luís.g.reis@ist.utl.pt
bli@ist.utl.pt
mfreitas@dem.ist.utl.pt

ABSTRACT

Multiaxial loading conditions are a key issue in several mechanical components, specially when considering the effects of different frequency between the axial and the torsional stress components. This paper presents a study about the behavior of 42CrMo4 steel when subjected to multiaxial loads where the frequency of the axial solicitation is different from the torsional one. The theoretical predictions by five Critical Plane models are compared with experimental results. In addition a fractographic analysis of the fracture surfaces is carried out, as well as an analysis to the number of cycles and their intensity in each loading path.

KEY WORDS: Multiaxial fatigue, Non-proportional loading, Fractographic Analysis, Fatigue life prediction, Asynchronous loadings, loading paths.

1. INTRODUCTION

In mechanical design, studying the life of components subject to cyclic stresses, and consequently, subject to fatigue, is of utmost importance to avoid the unexpected failure of equipment, vehicles or structures. In the literature, a limited number of multiaxial fatigue experiments have been reported for tests where the applied stresses vary with different frequencies. Tests considering this factor have been performed by Mielke and Kaniut; the results are reported in Liu and Zenner [1]. Mielke and Kaniut used stress systems of two normal stresses or of one shear and one normal stress.

Similar tests have been conducted by Heidenreich [2]. Tests with two normal stresses with different frequencies have been performed by McDiarmid [3, 4], whereas Froustey [5] performed a limited number of bending and torsion tests. Both the effect of the stress waveform and the effect of different frequencies have been addressed by the tests with two normal stresses by Dietmann [6]. More recently, Bernasconi made tension-torsion tests in 39NiCrMo3 steel, [7]. However, these tests only focused on the cyclic yield strength with the variation of the frequencies between the normal and shear stress. Additionally, the author concludes that integral based models, Liu and Zenner-Papadopoulos

provided better correlation than the critical plane models, Dang Van and Findley.

Thus, the main objective of this study is to deepen knowledge on the fatigue life of the 42CrMo4 steel, especially when subjected to cyclic loading with different frequencies between axial and shear loading conditions. This material is particularly suitable for medium section components that subjected to strong solicitations due to alternate bending and torsion. The main industrial applications are in the automobile industry where it is used in gears, shafts, spindles, uprights, connecting rods and other mechanical components of high resistance. It is also used in the manufacture of moulds for plastics, [8, 9]. Given the characteristics mentioned and its application in general industry, this steel was chosen because it is representative of a material regularly used in applications where the risk of failure is highly prevalent and where it will be most valuable to obtain a deeper understanding of its fatigue behaviour.

2. EXPERIMENTS

The material used for the fatigue experiments is a steel of grade 42CrMo4, supplied in quenched and tempered bars of 25 mm diameter.

In Table 1 it is presented the monotonic and cyclic mechanical properties. These properties were determined by Reis [10] on previous studies.

Table 1 - Monotonic and cyclic properties of the 42CrMo4 steel used in the experiments.

Tensile Strength	Rm (MPa)	1100
Yield Strength	Rp (MPa)	980
Young's Modulus	E (GPa)	206
Elongation at failure	A (%)	16
Hardness	HV	362
Cyclic Yield Strength	Rp' (MPa)	540
Cyclic strength coefficient	K' (MPa)	1420
Cyclic strength exponent	n'	0.12
Fatigue strength coefficient	σ_f' (MPa)	1154
Fatigue strength exponent	b	-0.061
Fatigue ductility coefficient	ϵ_f'	0.18
Fatigue ductility exponent	c	-0.53

Specimens used in the tests were made from 25mm rod acquired through a certified company which guarantees the chemical composition of the steel and that the level of metallurgical imperfections is minimized.

Throughout the process of machining, grinding and finishing, care was taken by choosing appropriate speeds and advances in cutting tool so as not to introduce a significant increase in residual stresses and changes in surface microstructure.

After machining all specimens were polished manually with sandpaper of decreasing grain size of No. 200 to No. 1200 with the help of a small lathe. To remove marks made by the radial polishing a final sanding with 1200 grit sandpaper was then carried out in the longitudinal direction of the sample, as indicated by ASTM E 466 (2007) [11].

Figure 1 shows the dimensions and geometry of the specimens, used in the multiaxial fatigue tests, by the ASTM E606 (2004) standard.

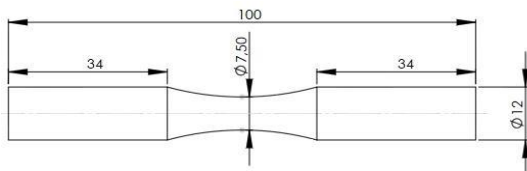


Figure 1 - Specimen shape and dimensions in mm.

All the tests were performed in load control mode by an Instron multiaxial tension/torsion servo-hydraulic testing system, model 8874, with a capacity of 25kN axial force and of 250N.m torque. Tests were interrupted at specimen failure or after 1.5×10^6 cycles. In Figure 2 it is shown the experimental setup.



Figure 2 – Experimental setup.

In order to perform the experimental study of the influence of different frequencies between the normal and shear stress in 42CrMo4 steel, for comparison with theoretical predictions different loading paths have been defined, which are illustrated in Figure 3.

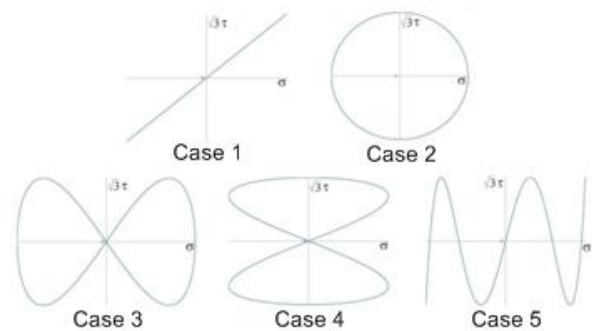


Figure 3 - Loading paths carried out.

Case 1 is a combination of sinusoidal loadings at the same frequency and in phase. Case 2 differs from the previous because there is a lag of 90° between axial and shear loading. Cases 3 and 4 result from the combination of loadings with a dual-frequency from each other and in phase start. Finally, case 5 is obtained with a torsional frequency five times higher than tension frequency and in phase start. The stress system employed is defined by $\sigma(t) = \sigma_a \sin(\omega t) + \sigma_{mean}$ and $\tau(t) = \tau_a \sin(\lambda \omega t) + \tau_{mean}$. The multiaxial fatigue tests were performed with a constant stress amplitude ratio of $\sigma = \sqrt{3}\tau$.

3. THEORETICAL ANALYSIS

3.1. von Mises approach

For x-y-z Cartesian system the von Mises equivalent stress can be written as equation (1):

$$\sigma_{eq} = \frac{1}{\sqrt{2}} \sqrt{(\sigma_x - \sigma_y)^2 + (\sigma_y - \sigma_z)^2 + (\sigma_x - \sigma_z)^2 + 6(\tau_{xy}^2 + \tau_{yz}^2 + \tau_{xz}^2)} \quad (1)$$

For biaxial loading of tension-compression with cyclic torsion the expression can be simplified, equation (2):

$$\sigma_{eq} = \sqrt{\sigma_x^2 + 3(\tau_{xy})^2} \quad (2)$$

3.2. Critical Plane models

Several critical plane models were considered in this study, as follows:

Findley criterion

Findley [12] proposed a critical plane model, which predicts that the fatigue crack plane is the plane orientation θ with maximum Findley damage parameter, equation (3):

$$\max_{\theta} (\sigma_a + k\sigma_{a,max}) \quad (3)$$

where τ_a is the shear stress amplitude on a plane θ , $\sigma_{n,max}$ is the maximum normal stress on that plane θ and k is a material parameter ($k_{AISI303} = 0.2$).

Brown-Miller criterion

Brown and Miller [13] proposed that the shear and normal strain on the plane of maximum shear must be considered. The simplified formulation of the theory for case A cracks is (equation (4)):

$$\max_{\theta} \left(\frac{\Delta\gamma_{max}}{2} + S\Delta\varepsilon_n \right) \quad (4)$$

Critical plane is the plane of maximum shear strain range $\Delta\gamma_{max}$ with major value of normal strain range $\Delta\varepsilon_n$; S is the normal strain effects coefficient and is determined experimentally ($S_{AISI303} = 0.2$).

Fatemi-Socie criterion

Fatemi-Socie [14] proposed a model that predicts the critical plane is the plane orientation θ with the maximum F-S damage parameter, equation (5):

$$\max_{\theta} \left[\frac{\Delta\gamma_{max}}{2} \left(1 + k \frac{\sigma_{n,max}}{\sigma_y} \right) \right] \quad (5)$$

where $\frac{\Delta\gamma_{max}}{2}$ is the maximum shear strain amplitude on a plane θ , $\sigma_{n,max}$ is the maximum normal stress on that plane, σ_y is the material monotonic yield strength and k is a material constant ($k_{AISI303} = 0.2$).

S-W-T criterion

Smith, Watson and Topper [15] proposed a model that predicts that the fatigue crack plane is the plane orientation θ with maximum normal stress (the maximum principal stress), equation (6):

$$\max_{\theta} \left(\sigma_n \frac{\Delta\varepsilon_1}{2} \right) \quad (6)$$

where σ_n is the normal stress on a plane θ , $\Delta\varepsilon_1$ is the principal strain range on that plane.

Liu criterion

Liu [16] proposed an energy method to estimate the fatigue life, based on virtual strain energy (VSE). This model considers two parameters associated with two different Modes of fatigue cracks, a tensile failure mode (Mode I), ΔW_I , and a shear failure mode (Mode II), ΔW_{II} . Failure is expected to occur on the plane θ in the material, having the maximum VSE quantity. According to Mode I fracture, the parameter, ΔW_I is, equations (7) and (8):

$$\Delta W_I = \max_{\theta} (\Delta\sigma_n \Delta\varepsilon_n) + (\Delta\tau \Delta\gamma) \quad (7)$$

For Mode II fracture, the parameter, ΔW_{II} is:

$$\Delta W_{II} = (\Delta\sigma_n \Delta\varepsilon_n) + \max_{\theta} (\Delta\tau \Delta\gamma) \quad (8)$$

where $\Delta\tau$ and $\Delta\gamma$ are the shear stress range and shear strain range, respectively, $\Delta\sigma_n$ and $\Delta\varepsilon_n$ are the normal stress range and normal strain range, respectively.

4. RESULTS AND DISCUSSION

4.1. Fatigue Life Results

Figure 4 presents the results of the fatigue life by the von Mises criteria for the various loading paths considered.

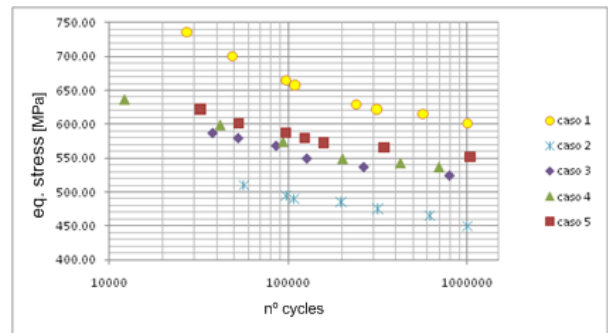
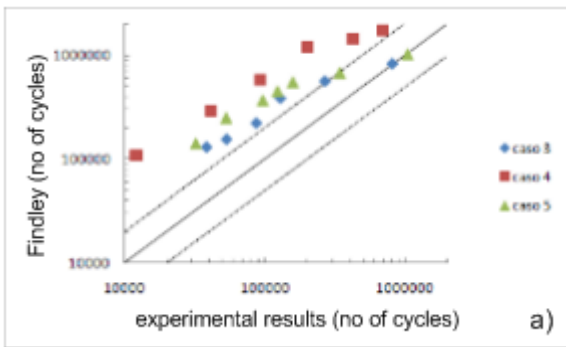


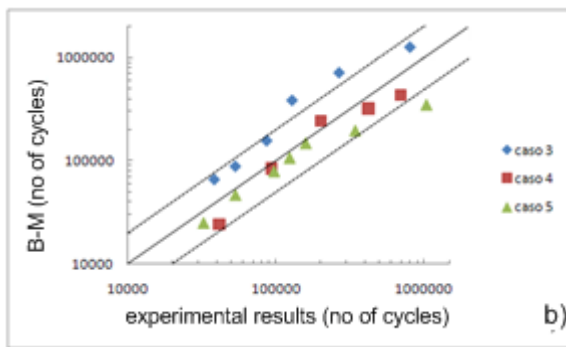
Figure 4 - Results of the fatigue life according to the von Mises criterion for steel 42CrMo4.

Since all used models, with the exception of Findley, use strain terms, it became necessary to use a cyclic plasticity model in order to predict the actual extensions after the introduction of a load control path.

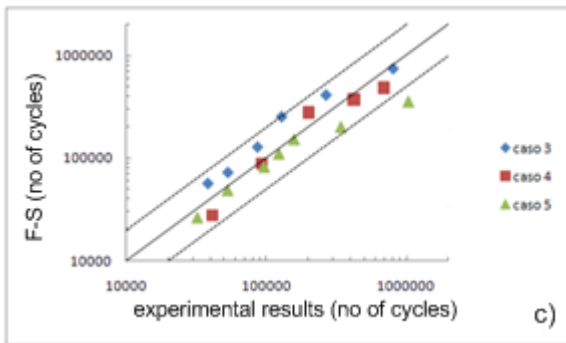
In Figure - 5 it is presented comparisons between the predictions of the models and the experimental values of fatigue life.



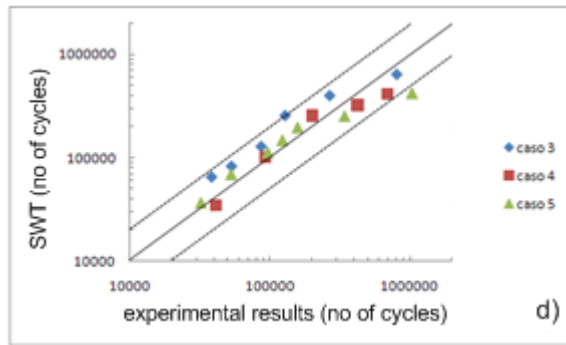
a)



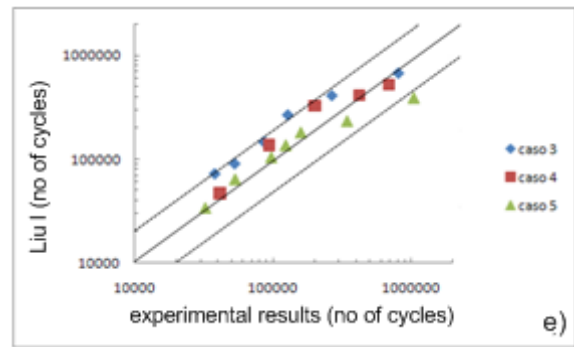
b)



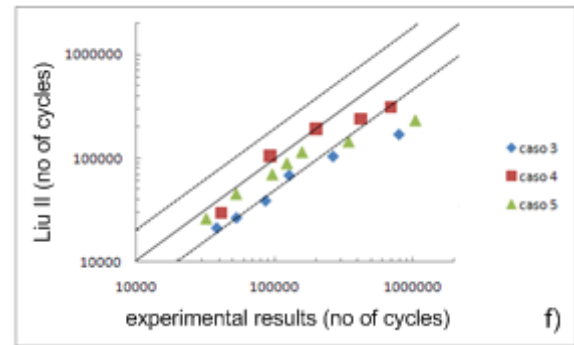
c)



d)



e)



f)

Figure - 5 a) to f): Comparisons between experimental and theoretical results for the various models.

From the used models, the two which provided the worst results were the *Findley* and *Brown-Miller*, both with a greater dispersion of results and with the first presenting a too optimistic fatigue life prediction. *Fatemi-Socie*, *SWT* and *Liu I* models had the best results although being a bit optimistic predicting fatigue life for case 3. *Liu II* and *Findley* recognize that case 3 is more damaging than case 5. All remaining models reveal the same error as the models used by Bernasconi, considering that case 5 is more damaging than case 3 and 4.

Although experimental results between case 3 and 4 differ in just 2%, the used theoretical models give a larger difference in fatigue life prediction. As an example in Figure 6 it is shown the shear strain evolution over time in planes from -90° to $+90^\circ$, for case 3.

By observing what happens in material planes, for case 3, between the two highest equivalent stresses in tension, the material is constantly being subjected to fatigue damage but in different planes. As a result, there is only one cycle of damage in each material plane. In case 4 was observed the same behaviour but in different planes, while in case 5 it was visible small sub cycles. Taking the shear strain values from the critical plane in function of time, it results the evolution depicted in Figure 7.

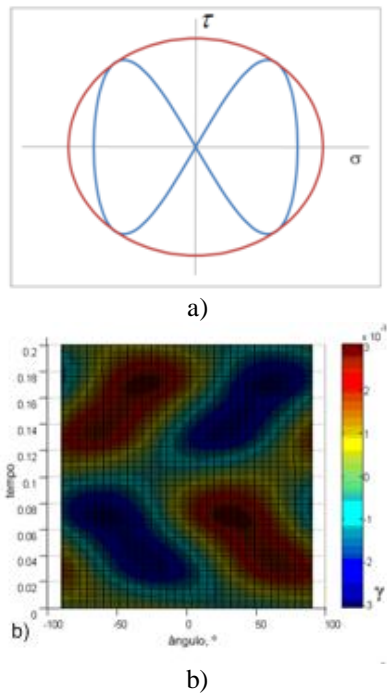


Figure 6 - a) Case 3 loading path; b) Shear strain evolution for case 3.

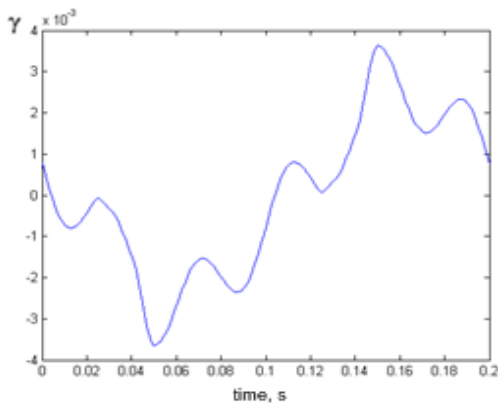


Figure 7 - Shear strain evolution in case 5.

Observing Figure 7 it is easy to identify the various existing cycles, ie, 4 sub cycles with an intensity one order of magnitude below the main cycle. As such, the expected life for the 4 sub cycles is much higher than the infinite life level being above 10^{12} cycles for all methods of predicting the fatigue life, thereby, causing irrelevant material damage. It can be concluded that a good approximation to consider only a single cycle for each loading path of the cases studied in this paper.

4.2. Fractographic Analysis

All fracture surfaces show a similar morphology presenting considerable crush zones in the initiation and progression of stable crack region, due to friction

caused by cyclic torsion in compression. Figure 8 shows a fracture surface of the case 5.

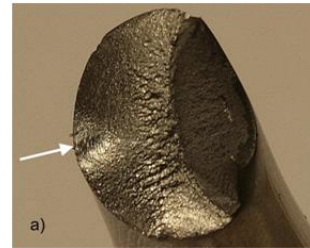


Figure 8 – Fractography of the L5.5 specimen subjected to case 5 loading path

The results obtained on the initial orientation of fatigue crack are compared with theoretical models based on the critical plane theory: *Findley*, *Brown-Miller*, *Fatemi-Socie*, *SWT (Smith, Watson and Topper)* and *Liu*. All the above models, scan each material plane θ , from -90° to $+90^\circ$ in order to seek for the critical plane, ie, the plane for which the specific parameter of damage is maximized. Figure 9 shows an example for the SWT model. Table 2 presents a comparison between measured and predicted crack angles.

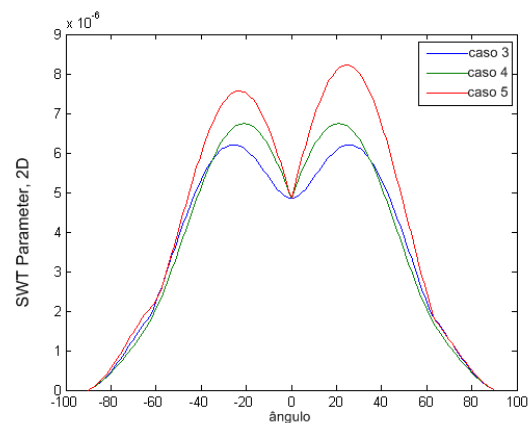


Figure 9 - Evolution of the SWT parameter on different planes for different loading paths.

Table 2 - Measured and predicted initial crack angles.

Loading Path	Case 3		Case 4		Case 5	
	L2.5	L2.6	L05.5	L05.6	L5.5	L5.6
Measured angle	+26	-18	-23	-20	-20	-22
Findley	±18		±21		-21/+23	
Brown Miller	±17/±73		±23/±67		-20/+70	
FS	±17/±73		±23/±67		-20/+70	
SWT	±25		±21		-23/+25	
Liu I	±26		-±21		-21/+25	
Liu I	±17/±73		±21/±67		-20/+70	

After analyzing the data presented in Table 2, it can be concluded that, in general, there was a good match between the theoretical models and experimental measurements from the specimens. With the exception of the specimen L2.5, all others have a maximum error of only 3° compared to theoretical models.

5. CONCLUSIONS

The cases taken as reference, cases 1 and 2, respectively, are the cases that minor and major damage cause to the material. Among the remaining cases, case 5 does less damage to the material and case 3 is the one that causes greater damage.

Excluding the proportional loading path, greater frequency relation between stress components causes less damage.

All critical plane criteria produced reasonable estimates of crack initiation angles by comparison with the experimental results.

Critical plane criteria based only in stress terms (*Findley*) or in strain terms (*Brown-Miller*) are less effective in predicting the fatigue life. Criteria with both stress and strain terms (*Fatemi-Socie*, *SWT* and *Liu*) are more likely to consider the features of each type of loading.

Criteria developed for materials with predominant failure mode I (*SWT* and *Liu I*) had good results for predicting the fatigue life of the 42CrMo4 steel in mentioned conditions.

For a correct fatigue life prediction, the use of a plasticity model to predict the actual strain values is essential.

For the axial-shear relation studied, sub cycles present in the various loading path do not show relevant magnitude to cause relevant damage.

ACKNOWLEDGEMENTS

The authors gratefully acknowledge financial support from FCT - Fundação para Ciência e Tecnologia (Portuguese Foundation for Science and Technology), through the project POCTI/EME/59577/2004.

REFERENCES

- [1] Liu J, Zenner H. Fatigue limit of ductile metals under multiaxial loading. In: Carpinteri A, de Freitas M, Spagnoli A, editors. Biaxial/ multiaxial fatigue and fracture, ESIS 31. Amsterdam: Elsevier; 2003. p. 147–63.
- [2] Heidenreich R, Richter I, Zenner H. Schubspannungsintensitätshypothese – weitere experimentelle und theoretische Untersuchungen. Konstruktion 1984;36:99–104.
- [3] McDiarmid DL. Fatigue under out-of-phase biaxial stresses of different frequencies. In: Miller KJ, Brown MW, editors. Multiaxial fatigue, ASTM STP 853. Philadelphia: ASTM; 1985. p. 606–21.
- [4] McDiarmid DL. Mean stress effects in biaxial fatigue where the stresses are out-of-phase and at different frequencies. In: Kussmaul K, McDiarmid DL, Socie D, editors. Fatigue under biaxial and multiaxial loadings, ESIS 10. London: Mechanical Engineering Publications; 1991. p. 321–35.
- [5] Froustey C. Fatigue multiaxiale en endurance de l'acier 30 NCD 16. Thèse de l'Ecole Nationale Supérieure d'Arts et Métiers, Bordeaux; 1987.
- [6] Dietmann H, Bhongbhithat T, Schmid A. Multiaxial fatigue behaviour of steels under in-phase and out-of-phase loading, including different wave forms and frequencies. In: Kussmaul K, McDiarmid DL, Socie D, editors. Fatigue under biaxial and multiaxial loadings, ESIS 10. London: Mechanical Eng. Publications; 1991. p.449–64.
- [7] A. Bernasconi, S. Foletti, I.V. Papadopoulos, (2008) "A study on combined torsion and axial load fatigue limit tests with stresses of different frequencies". Int. Journal of Fatigue 30 (2008) 1430–1440.
- [8] Shang, D-G., Sun, G-Q., Deng, J., Yan, C-L., "Multiaxial fatigue parameter and life for a medium-carbon steel based on critical plane approach". Int. Journal of Fatigue (2007)
- [9] Reis, L., Li, B., Freitas, M., (2007). "Evaluation of a Multiaxial Fatigue Models for a Structural Steel (42CrMo4), "8° International Conference on Multiaxial Fatigue & Fracture"
- [10] Reis, L., (2004). "Comportamento Mecânico de Aços em Fadiga Multiaxial a Amplitude de Carga Constante e Síncrona", Universidade Técnica de Lisboa, IST, PhD Thesis in Portuguese.
- [11] ASTM E 466 (2007). Standard Practice for Conducting Force Controlled Constant Amplitude Axial Fatigue Tests of Metallic Materials1.
- [12] Findley, W. N. (1956). "Theory For Combined Bending And Torsion Fatigue With Data For SAE 4340 Steel", Int. Conf. Fatigue Metals: 150-157.
- [13] Brown, M., Miller, K. J. (1973). "A Theory for Fatigue Failure Under Multiaxial Stress-strain Conditions." Proceedings of the Institute of Mechanical Engineers 187: 745-755.
- [14] Fatemi, A., Socie, D. (1988). "A Critical Plane Approaches to Multiaxial Fatigue Damage including Out-of-Phase Loading", FFEMS 11(3): 149-165.
- [15] Smith, K. N., Watson, P., Topper, T. H. (1970). "A Stress-Strain Function for the Fatigue of Metals", J. of Materials, JMLSA 5(4): 767-778.
- [16] Liu, K. (1993). "A Method Based on Virtual Strain-Energy Parameters for Multiaxial Fatigue Life Prediction", Advances in Multiaxial Fatigue, ASTM STP 1191: 67-84.

CRACK PROPAGATION IN PLANE STRAIN UNDER VARIABLE AMPLITUDE LOADING

L. C. H. Ricardo

Assistant Professor in Structural Mechanics Division of Structural Mechanics
 Department of Civil Engineering Aalborg University Sohngårdsholmsvej 57,
 Aalborg, Denmark, 9000
 E-mail: lchr@civil.aau.dk

ABSTRACT

Crack propagation simulation began with developing of finite element method; the analyses were conducted to obtain a basic understanding of the crack growth and closure processes. Today structural and materials engineers develop structures and materials properties using this technique. In this paper procedures to determine the crack opening and closure by finite elements analyses in plane strain will be presented. The objective of this paper is also provide a review of retardation models under variable spectrum loading considering plane strain constraint as well as their correlation with experimental data.

KEY WORDS: Crack Propagation Simulation, Finite Element Method, Variable Amplitude Loading, Plane strain.

1. INTRODUCTION

The major links between fatigue and fracture mechanics were done by Christensen [1] and Elber [2]. The crack closure concept put crack propagation theories on a firm foundation and allowed the development of practical life prediction for variable and constant amplitude loading, as experienced by modern day commercial aircrafts, wind turbine components and automotive applications. Analytical models were developed to predict crack growth and crack closure processes like the Dugdale model [3].

2. REVIEW OF CRACK PROPAGATION MODELS

In Newman [4] a review is presented of a chronological development of fracture mechanics and crack propagation simulation. The list of some of the finite-element and finite-difference analyses [5-14] is given in Table 1; the vast majority of these analyses were conducted using two-dimensional analyses under either plane-stress or plane-strain conditions. Since the mid-1980s, only a few three-dimensional finite element analyses have been conducted basically Neman [10] and Chermahini [11]. Today have others authors that work with tridimensional models in special in plane strain like Roychowdhury & Dodds [15] and Josefson et al. [16].

Table 1. Finite element models of fatigue crack growth and closure

Two-dimensional cracks	Three-dimensional cracks
Newman and Armen [5]	Newman et al. [10]
Ohji, Ogura and Ohkubo [6]	Chermahini [11]
Blom and Holm [7]	Chermahini et al. [12,13]
Fleck and Newman [8-9]	Dawicke et al. [14]

Newman and Armen [5] and Ohji *et al.* [6] were the first to conduct two-dimensional, finite-element analyses of the crack-closure process. Their results under plane-stress conditions were in quantitative agreement with the experimental results of Elber [17] and showed that crack-opening stresses were a function of R ratio (S_{min}/S_{max}) and stress level (S_{max}/σ_0). Blom and Holm [7] and Fleck and Newman [8-9] studied crack-growth and closure under plane-strain conditions and found that cracks did close but the crack-opening levels were much lower than those under plane-stress conditions.

Matos & Norwell [18] present a literature review of the phenomenon of plasticity-induced fatigue crack closure under plane stress and plane strain conditions and mention that there are controversial topics concerning the mechanics of crack propagation. In general there is no consensus in the scientific community. Table 1 shows the Chronological crack advance scheme.

Table 1: Chronological crack advance scheme

Year	Author	Node Release Scheme	Constraint	Target	Element Type
1985	Blom and Holm [7]	Maximum load	PStress; PStrain	COP and CCL	Triangle linear
1986	Fleck and Newman [8]	Maximum load	PStress; PStrain	COP	Triangle linear
2000	Wei and James [19]	Maximum load	PStress; PStrain	COP and CCL	Triangle linear
2002	Pommier [20]	Minimum Load	PStrain	COP and CCL	Quadrilateral linear
2003	Solanski [21]	Maximum load	PStress; PStrain	COP and CCL by COEL	Quadrilateral linear
2004	Solanski et al. [22]	Maximum load	PStress; PStrain	COP and CCL by COEL	Quadrilateral linear
2004	Zhao et al. [23]	Maximum load	PStrain	COP and CCL by CME	Quadrilateral linear
2005	Gonzalez-Herrera and Zapatero [24]	Maximum load	PStress; PStrain	COP and CCL by DME	Quadrilateral linear

PStress- plane stress; *PStrain*- plane strain; *COP*- crack opening; *CCL*- crack closing; *COEL*- crack opening and closing by contact element; *CME*- crack opening and closing by compliance method; *DME*- crack opening and closure by displacement method

Numerical methods, such as the finite element method are often used to simulate plasticity-induced fatigue crack closure in 2D geometries under plane strain [2–6]. The phenomenon of plasticity-induced fatigue crack closure under plane strain conditions is one of the most controversial topics concerning the mechanics of crack propagation. No general consensus exists among in the scientific community concerning the physical mechanism for crack closure under plane strain conditions. One of the problems is in the way to prepare the mesh and the procedure used in crack propagation. With the three-dimensional models it becomes necessary to use normal contact approach to node release; in plane stress spring is normally used to help the crack propagation, using contact issues for crack propagation and considering nonlinear analysis it will result in a big result file and will spend a considerable time processing to end the simulation.

Fleck [2] According to his work the source of discontinuous closure appears to be a residual wedge of material on the crack flanks, located just ahead of the initial position of the crack tip. He suggested that closure involves only a few elements relatively distant from the current crack tip and the closure levels decay steadily as the crack grows beyond its initial length.

More recently Wei and James [19] reported that after growing a plane strain fatigue crack for a few cycles, there is no contact in the region immediately behind the crack tip and the contact pressure along the crack faces is discontinuous. Zao et al. [17] modelled a CT specimen under plane stress and plane strain.

They did not observe plasticity-induced crack closure under plane strain during steady state crack growth under cyclic tension, although they found significant levels of closure under plane stress. Chermahini et al. [11] present the crack propagation in 3D and in plane strain to determine the crack opening level, the crack-opening stress was found to vary through the thickness for a middle-crack tension specimen.

On the specimen surface and in the mid-plane the crack-opening stress levels tend to be two-dimensional solutions for plane stress and plane strain conditions, respectively. Figure 1 shows the model used by Chermahini et al. [12]. In Figure 2 it is possible to see the finite element model used for crack propagation. The model was prepared in layer of elements, considering the lower element in the reverse plastic zone computed by Irwin equation and then will increasing the size of hexahedron element until arriving in region that the results will not affect the stress level in the crack propagation area. Spring was used spring for node release cycle after cycle like Newman [10].

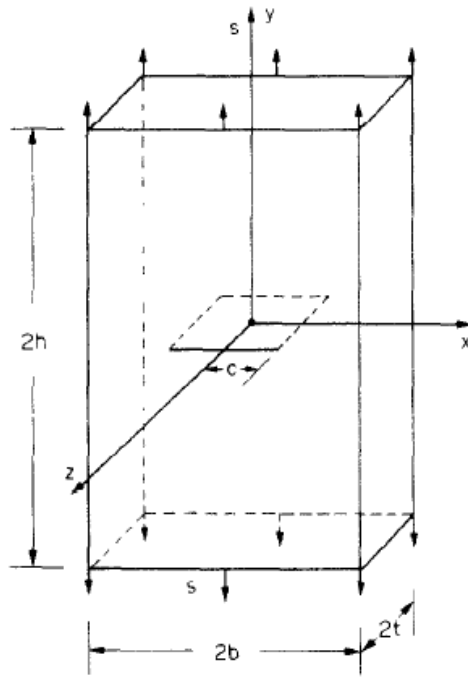


Figure 1 Middle-Crack Tension Specimen Subjected to uniform stress [11]

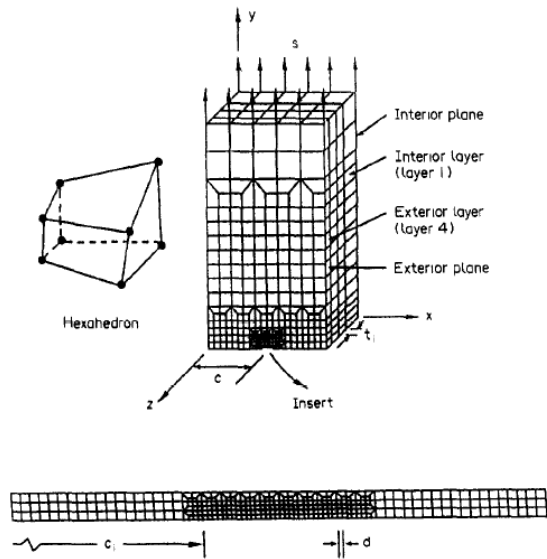


Figure 2 Crack Propagation Model Quarter of Middle Tension [11]

Solanki et al. [22] present a review of crack propagation in plane stress and plane. Figure 3 shows a M(T) specimen modeled with an externally induced T -stress to observe the subsequent change in closure levels under plane-strain. A T -stress was induced by applying tractions parallel to the crack in addition to the conventional tractions perpendicular to the crack. They found a significant drop in the closure level as the T -stress was varied from compressive to tensile as shown in Figure 3. Figure 4 also shows the difference of result in node release at minimum and maximum load compared by Solanski et al. [22].

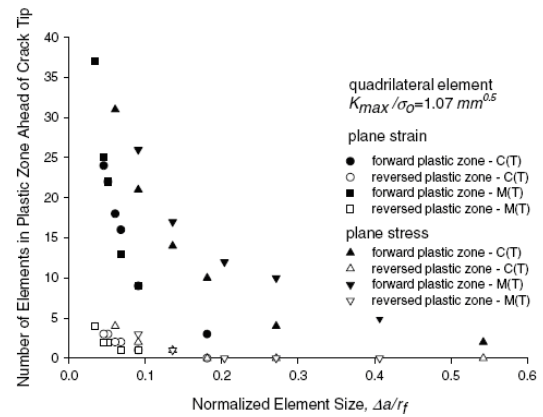


Figure 3 Variations in Crack Tip Plastic Zone Size with Mesh [22]

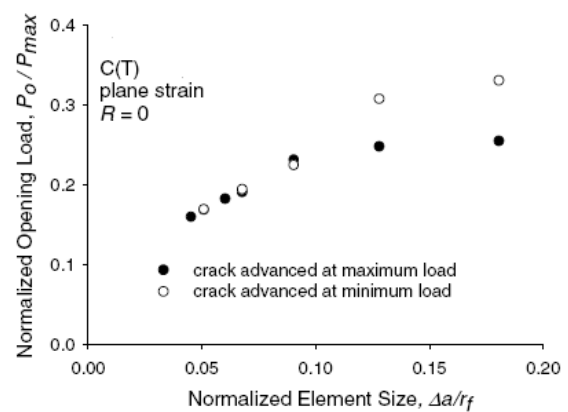


Figure 4 Comparison of Crack opening values based on crack advance scheme [22].

Wu and Ellyin [25] have used a truss element together with pairs of contact elements and the element death option for crack propagation simulation. This technique used in plane stress and plane strain models is usual in commercial finite element codes. The element death option was incorporated to remove truss elements. With their approach, a node can be released any time during a load cycle irrespective of the magnitude of the deformation caused by the release of the node. Consequently, fewer problems with convergence were encountered and also several nodes could be released simultaneously if desired.

3. FATIGUE CRACK GROWTH UNDER VARIABLE AMPLITUDE LOADING

Schijve [26] was one of the first to study the process of fatigue crack growth (macrocracks) under variable-amplitude loading was extensively investigated in numerous experimental programs. The promising application of the ΔK -concept to predictions of fatigue crack growth under constant-amplitude loading was drastically upset by the first experiments with overloads in constant-amplitude tests carried out around 1960 [26, 27].

Three overloads depicted in Figure 5 induced highly retarded crack growth.

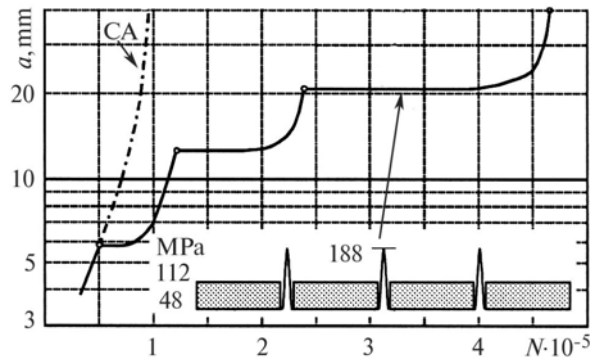


Figure 5 Effects of Overloads in Sheets Specimens

Originally, this was attributed to compressive residual stresses in the crack-tip plastic zone of an overload. Later, it was related to crack closure in the plastic zone leading to smaller effective stress ranges. Actually, there is no contradiction between these two explanations because both are associated with plastic deformation in the crack-tip zone. The pronounced effect of high loads on fatigue crack growth stimulated a lot of research, both experimental investigations and analytic studies.

The significance of crack-tip plasticity was easily recognized and an obvious assumption was made that the size of the plastic zone must be important for crack-growth retardations.

Since the size of the plastic zone depends on the stressed state (plane strain or plane stress, or intermediate situations), the retardation of the growth of a through crack after an overload must depend on the thickness of the material and its yield stress. This observation was amply confirmed by experimental results, starting in the mid-70s (see, e.g., [28, 29]). More detailed observations also indicate that the maximum retardation of the crack-growth rate after an overload does not occur immediately but after a certain period of time required for the penetration of the crack tip into the plastic zone of the overload (the so-called delayed crack-growth retardation).

The first analytic models of crack growth under variable-amplitude loading were based on the sizes of plastic zones.

The Willenborg [30] and Wheeler [31] models are two notable examples published in the early 70s. They are now considered to be rather primitive. The second generation of crack-growth reduction models for variable amplitude loading was based on the effect of plasticity-induced crack closure. The crack extension Δa_i in a cycle i is a function of ΔK_{eff} in this cycle. Thus, we can write

$$a = a_0 + \sum \Delta a_i, \quad \text{where} \quad \Delta a_i = \left(\frac{da}{dN} \right)_i = f(\Delta K_{eff,i}). \quad (1)$$

The quantity ΔK_{eff} depends on the applied $\sigma_{max, i}$ and predicted $\sigma_{op, i}$ stresses. The crack-opening level of stresses σ_{op} must be predicted by a crack-growth model taking into account the effect of plastic deformation left in the wake of the crack as a residue of the previous loading cycles. As an illustration, in Figure 6, we present a sample of a variable-amplitude loading history with variable values of σ_{op} . The quantity $\Delta \sigma_{eff}$ is determined by using a relation similar to relation (1).

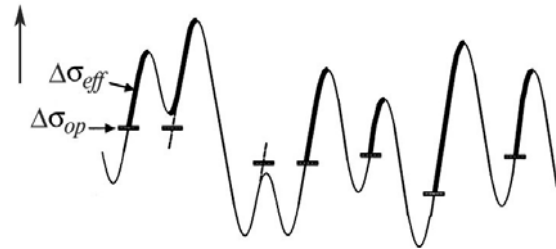


Figure 6 Variation of the Crack-Opening Stress

Corbly & Packman [32] describe some aspects of the retardation phenomenon. Despite the recent increase in research into retardation effects in crack propagation, there are many aspects of load interaction phenomena that lack adequate explanations. Three aspects of the retardation phenomena that are generally agreed upon are presented below.

1. Retardation increases with higher values of peak loading σ_{peak} for constant values of lower stress levels [33,34].
2. The number of cycles at the lower stress level required to return to the non-retarded crack growth rate is a function of ΔK_{peak} , ΔK_{lower} , R_{peak} , R_{lower} , and number of peak cycles [35].
3. Increased percentage delay effects of peak loading, given a percent overload, are greater at higher baseline stress intensity factors [36].

Ljustell, P. & Nilsson, F. [37] perform an investigation of crack growth in notched specimens with part through cracks, subjected to variable amplitude block loading.

A related goal investigated is if closure corrected LEFM methods could predict crack growth at relatively high loads. In order to compare the closure levels estimation as outlined above with numerical predictions finite element simulations of plasticity induced crack closure was performed with the commercial code, ABAQUS v.6.3 [38]. A two-dimensional finite element model, plane strain, with four-node quadrilateral elements of the NT specimen was used for the analyses. Figure 7 shows the good correlation with numerical and experimental results.

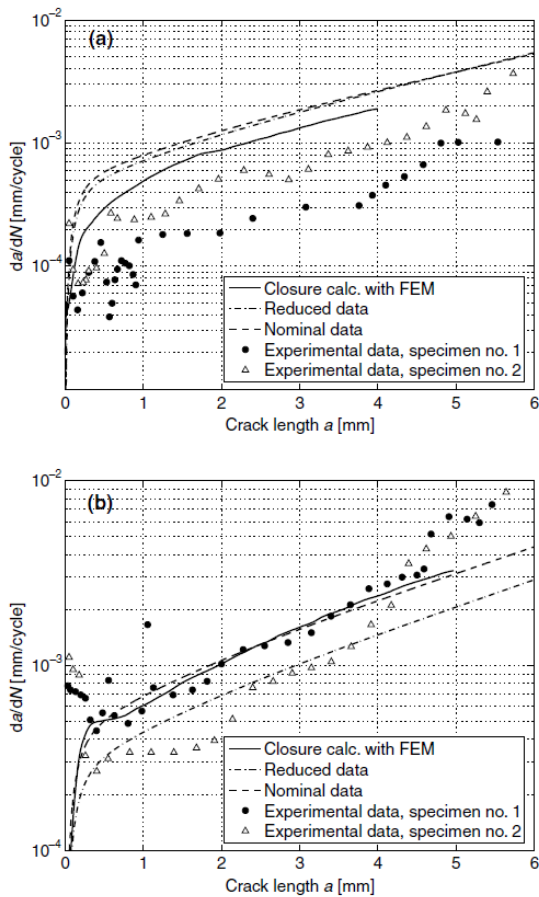


Figure 7 Results from the NT-experiments marked with dots and predictions as lines: (a) and (b) are cycle type 1 and 2 respectively [37]

4. CONCLUSION

The paper presented a review of some procedures used to simulate crack propagation under variable amplitude loading. In the literature there are many different techniques used and of course much discussion also in terms of applicability of these techniques in a general case. Normally the authors work with particular cases and few load blocks history to avoid complexities in the edition of signal for example. There is much work to do in plane strain due the models in order to run requests on non usual informatics facilities.

The good agreement is that the time processing must be lower than a real crack propagation test.

This is one of the challenges the researchers have to solve as well as simulating with good quality of results the threshold area.

5. RERERENCES

[1] Christensen, R. H. "Fatigue Crack Growth Affected by Metal Fragments Wedged Between Opening Closing Crack Surface", **Appl. Mater. Res.**, n° 2, October, pp. 207-210, USA, 1963

[2] W. Elber *Fatigue crack propagation*. PhD Thesis, University of New South Wales, 1968.

[3] Dugdale, D.S. " Yielding of Steel Sheets Containing Slits ", *J. Mech. Phys. Solids*, pp. 100-104, n.0 8,USA, 1960

[4] Newman, J.C. Jr., *Fracture Mechanics Concepts a Historical Perspective*", *Progress in Aerospace Sciences*, n° 34, pp. 347-390, USA, 1998

[5] Newman JC Jr, Armen H Jr. " Elastic plastic analysis of a propagating crack under cyclic loading", *AIAA Journal* 1975;13: pp.1017-1023.

[6] Ohji K, Ogura K, Ohkubo Y. *Cyclic analysis of a propagating crack and its correlation with fatigue crack growth*. *Eng. Fract. Mech. Journal* 1975;7: pp. 457-464.

[7] Blom AF, Holm DK. *An experimental and numerical study of crack closure*. *Eng. Fract. Mech. Journal* 1985;22: pp. 997-1011.

[8] Fleck NA. *Finite-element analysis of plasticity induced crack closure under plane strain conditions*. *Eng. Fract. Mech. Journal* 1986;25: pp. 441-449

[9] Fleck NA, Newman JC Jr. *Analysis of crack closure under plane strain conditions*. *ASTM STP 982*, 1988: pp.319-341.

[10] Newman JC Jr, Bigelow CA, Shivakumar KN. *Three-dimensional elastic-plastic finite-element analysis of constraint Variations in cracked bodies*. *Eng. Fract. Mech. Journal*, 1993;46,1,pp.1-13.

[11] Chermahini RG. *Three-dimensional elastic- plastic -finite-element analysis of fatigue crack growth and closure*. PhD Thesis, Old Dominion University, Norfolk, VA, 1986.

[12] Chermahini RG, Shivakumar KN, Newman JC Jr. *Three-dimensional finite-element simulation of fatigue crack growth and closure*. *ASTM STP 982*, 1988, pp.398-413.

[13] Chermahini RG, Blom AF. *Variation of crack-opening stresses in three-dimensions: finite thickness plate*. *Theoret Appl Fract Mech*, 1991;15:pp.267-276.

[14] Dawicke D, Shivakumar K, Newman J, Grandt A. *An inverse; method for the calculation of through-thickness fatigue crack closure behavior*. *ASTM STP 1131*, vol. II, 1992,pp.46-57.

- [15] Roychowdhury S, Dodds Jr RH. A numerical investigation of 3-D small-scale yielding fatigue crack growth. *Eng. Fract. Mech. Journal*, Mech. Journal, 70, 2003, pp. 2363–2383
- [16] Josefson, B.L. Svensson, T. Ringsberg, J.W. Gustafsson, T., de Mare, J.” Fatigue life and crack closure in specimens subjected to variable amplitude loads under plane strain conditions”, *Eng. Fract. Mech. Journal* 66,2000, pp. 587-600
- [17] W., Elber “The significance of fatigue crack closure”, *ASTM STP 486*, 1971: pp. 230-242.
- [18] Matos, P.F.P. & Nowell, D. “ Numerical Simulation of Plasticity Induced Fatigue Crack Closure with Emphasis on the Crack Growth Scheme: 2D and 3D Analyses”, *Eng. Fract. Mech. Journal*, 75, 2008, pp. 2087-2114
- [19] Wei LW, James MN. A study of fatigue crack closure in polycarbonate ct specimens. *Eng. Fract. Mech. Journal* 2000,66,pp. 223–42.
- [20] Pommier S. Plane strain crack closure cyclic hardening. *Eng. Fract. Mech. Journal*, 2002, 69, pp. 25–44.
- [21] Solanki K, Daniewicz SR, Newman Jr JC. Finite element modelling of plasticity-induced crack closure with emphasis on geometry and mesh refinement effects. *Eng. Fract. Mech. Journal*, 2003,70, pp.1475–89.
- [22] Solanki K, Daniewicz SR, Newman Jr JC. A new methodology for computing crack opening values from finite element analyses. *Eng. Fract. Mech. Journal* 2004,71, pp.1165–75
- [23] Zhao LG, Tong J, Byrne J. The evolution of the stress–strain fields near a fatigue crack tip and plasticity-induced crack closure revisited. *Fatig Fract Eng Mater Struct* 2004,27, 1, pp.19–29.
- [24] Gozalez-Herrera A, Zapatero J. Influence of minimum element size to determine crack closure stress by finite element method. *Eng. Fract. Mech. Journal* 2005,72, pp.337–355.
- [25] Wu J, Ellyin F. A study of fatigue crack closure by elastic–plastic finite element analysis for constant-amplitude loading. *Int J Fract*, 1996,82, pp.43–65.
- [26] Schijve, J. Fatigue of Structures and Materials in the 20th Century and The State of the Art, *Materials Science*, Vol. 39, No. 3, 2003, pp. 307-333
- [27] Schijve, J. “Fatigue crack propagation in light alloy sheet material and structures,” in: *Advances in Aeronautical Sciences*, Vol. 3, Pergamon Press,1961, pp. 387–408.
- [28] Hudson , C. M. and Hardrath, H. F. *Effects of Changing Stress Amplitude on the Rate of Fatigue Crack Propagation in Two Aluminum Alloys*, NASA TN D-960,1961.
- [29] Mills, W. J. and Hertzberg, R. W. “The effect of sheet thickness on fatigue crack retardation in 2024-T3 aluminum alloy,” *Eng. Fract. Mech. Journal*, 7, 1975, pp. 705–711.
- [30] Willenborg, J.D.; Engle, R.M. & Wood, H.A “A Crack Growth Retardation Model using na Effective Stress Concept”; **AFFDL, TM-71-FBR**, Air Force Flight Dynamics Laboratory, Wright Patterson Air force Base, OH, 1971.
- [31] Wheeler, O E. “*Spectrum Loading and Crack Growth*” Transactions of the ASME Series D’,**Journal of Basic Engineering**, vol. 94, 1972, pp 181-186,.
- [32] Corbly, D.M. & Packerman, P.F. “ On The Influence of Single and Multiple Peak Overloads on Fatigue Crack Propagation in 7075-T6511 Aluminum” , *Eng. Fracture Mech. Journal* 5, 1973, pp. 479-497,
- [33] Schijve, J. ; Brock, D. & de Rigne, P., *Report M2094*, Amsterdam, 1962
- [34] Hardrath, H.F. & McEvily, A . T., *Proc. Crack Propagation Symposium*, Vol. 1 Cranfield, 1961
- [35] Jonds, D. & Wei, R.P. , An Exploratory Study of Dealy in Fatigue Crack Growth, *Eng. Fracture Mech. Journal*, 7,1971
- [36] von Ewu, E. ; Hertzberg, R. & Roberts, R., Delay Defects in Fatigue Crack Propagation, *Nat. Symposium F.M.*; 7; 1971
- [37] *Abaqus* version 6.3.3, USA, 2004.
- [38] Ljustell, P.& Nilsson, F. Variable amplitude crack growth in notched specimens, *Eng. Fract. Mech. Journal* 1,72, 2005,pp. 2703–2720

RESISTENCIA A FATIGA DE LA ALEACIÓN DE ALUMINIO 7075-T6 EN FUNCIÓN DEL TIPO DE ENSAYO Y ESPESOR DEL RECUBRIMIENTO

M. Toledano¹, M. A. Arenas², J.J. Galán¹, L. Ramirez¹, S.M. Borja², A. Conde², A. Monsalve³

¹Área de Ciencia e Ingeniería de Materiales, E.T.S.I. Caminos, Canales y Puertos.
Campus de Elviña s/n, 15071 Coruña. E-mail: mtoledano@udc.es

²Departamento de Corrosión y Protección
Centro Nacional de Investigaciones Metalúrgicas (CENIM/CESIC)
E-mail: geles@cenim.csic.es

³Departamento de Ingeniería Metalúrgica, Facultad de Ingeniería, USACH, Santiago, Chile.
E-mail: amonsalv@usach.cl

RESUMEN

En el presente trabajo se analizan los principales tipos de ensayos de fatiga existentes en la bibliografía científica para determinar las curvas S-N, y se comparan los distintos resultados que se obtienen en función de la metodología elegida. Los autores han desarrollado su trabajo con la aleación de aluminio 7075-T6 y se ha valorado las diferencias entre los métodos de ensayo de fatiga en flexión rotativa, flexión reversible sobre probetas planas y flexión en cuatro puntos. Utilizando como metodología de ensayo la fatiga en flexión en cuatro puntos (four point bending), se ha evaluado la influencia del espesor del recubrimiento de anodizado en probetas planas sobre la resistencia y el límite de fatiga. Los resultados obtenidos con distintos espesores han puesto de manifiesto que el aumento de espesor de la capa de recubrimiento anódica no afecta negativamente a la respuesta a fatiga de la aleación. Finalmente, en el artículo se presentan y analizan las diferencias fractográficas obtenidas para los recubrimientos más representativos y como influye en ellos los distintos niveles de carga.

ABSTRACT

This paper analyses and compares the influence of the experimental methods of testing cracking parameters in the fatigue behaviour studies. For this purpose, the authors have taken into account several bibliographical data for 7075-T6 aluminium alloy obtained from rotating bending fatigue and reverse plane rotating bending tests. Four point bending tests were carried out to evaluate the importance of anodize coating thicknesses in fatigue strength. These results seem to indicate that the increase of the coating thickness improve the fatigue life. Finally, we compare the fractographic differences between several specimens of the more representative coating thicknesses and the influence of the level of external load on them.

PALABRAS CLAVE: fatiga, flexión en cuatro puntos, anodizado, aleación de aluminio

1. INTRODUCCIÓN

Las aleaciones de aluminio 7075 son un material de referencia en la industria aeronáutica por sus excelentes propiedades de resistencia mecánica y química frente a la corrosión. Desde hace varios años el campo de estudio de estos materiales se ha enfocado en mejorar estas propiedades utilizando recursos que no sean agresivos al ser humano y al medio ambiente [1]. Una de las alternativas con las que más se trabaja en industria es el anodizado porque supone un proceso económicamente rentable y los resultados obtenidos desde el punto de vista de la corrosión y la tenacidad son notables. Aunque existen bastantes datos en la literatura sobre el proceso del anodizado en distintas

aleaciones de aluminio (material base) y utilizando distintos tipos de electrolitos en el baño electrolítico, todavía son muy escasos los estudios enfocados a dilucidar la influencia del espesor del recubrimiento anódico en la respuesta a fatiga de los aluminios [2]. Con este trabajo de investigación, los autores pretende aportar información en este campo estudiando las variaciones que se obtienen en las curvas S-N cuando se con 3 espesores bien diferenciados y uniformes sobre la superficie del material. Teniendo en cuenta que la variable principal de estudio es la variación de las condiciones superficiales, se descartó como metodología de ensayo la fatiga axial. Otros aspectos muy importantes que también se analizaron para elegir la metodología de ensayo fue la geometría de las

probetas disponibles y la simplicidad del mecanizado. Por ambos motivos se descartaron los ensayos de fatiga en flexión rotativa, por la dificultad para mecanizar probetas de sección circular adaptadas a ese ensayo, y el de flexión reversible sobre probetas planas. Finalmente los autores se decidieron por utilizar el ensayo de fatiga en flexión en cuatro puntos, considerando las ventajas ya mencionadas por los autores en otro artículo publicado en esta revista [3]. Por otra parte, cuando se analiza el comportamiento de un nuevo tipo de material o recubrimiento con una metodología de ensayo diferente a las convencionales es importante considerar si los cambios en la metodología pueden influir en las magnitudes numéricas de las propiedades que se analizan. En el caso de los ensayos de fatiga son varios los tipos de ensayos que pueden utilizarse para definir las curvas de Wholer o curvas S-N, y existe una amplia bibliografía relativa al comportamiento de los materiales en distintas condiciones relativas al acabado superficial, tratamiento térmico o de fatiga a altas temperaturas. Los principales ensayos para los que es posible encontrar datos de referencia son los ensayos de fatiga en flexión rotativa (rotating bending fatigue – RBF), flexión reversible de probetas planas (reversed plane bending fatigue – RPB) y flexión axial, pero los autores no han encontrado en los manuales de referencia datos de fatiga relativos a los ensayos de fatiga en flexión en cuatro puntos (four point bending – 4PB). En este sentido, la primera parte del estudio se centra en analizar la influencia que el método de ensayo tiene sobre la respuesta del material, comparando distintos tipos de ensayos, para continuar el trabajo con los datos aportados por los autores y que servirán como referencia para trabajos futuros.

2. MATERIALES

La aleación de estudio es una aleación AA7075 en estado T6. En las Tablas 1 y 2 se describe la composición nominal, y las propiedades mecánicas, respectivamente. El material disponible para los ensayos procede de chapas laminadas de 2 mm de espesor, con orientación T-L. Las probetas fueron mecanizadas con un ancho de 1,95 mm.

Tabla 1. Composición de la aleación de aluminio

	Al	Zn	Cu	Mg	Mn
7075-T6	bal	5.1-6.1	1.2-2.0	2.1-2.9	0.30

Tabla 2. Propiedades mecánicas en tracción

Aleación	σ_{uts} (MPa)	σ_{ys} (MPa)	Alargamiento 50mm (%)	E (GPa)	K_{Ic} (MPam ^{1/2})
7075-T6	570	505	11	71	25

En la Tabla 3 se indican las nomenclaturas utilizadas para cada tipo de material.

Tabla 3. Nomenclatura de los tratamientos utilizados.

Nomenclatura	Recubrimiento
A7R	Ninguno - Material de referencia
A7SA2	Anodizado sulfúrico con espesor de 2 μ m
A7SA5	Anodizado sulfúrico con espesor de 5 μ m
A7SA10	Anodizado sulfúrico con espesor de 10 μ m

Las capas anódicas se crecieron sobre probetas planas de sección rectangular en una disolución de H₂SO₄ 0,4 M a una temperatura de 35°C, aplicando un voltaje constante de 20V durante 5 minutos para las capas de 2 μ m de espesor. Las capas más gruesas, de 5 μ m y 10 μ m se obtuvieron aplicando un potencial en rampa de 4V/min, hasta alcanzar un valor de 20V, y después se mantuvo constante durante distintos periodos de tiempo hasta alcanzar el espesor deseado. La medida de los espesores se hizo con un equipo Fischerscope.

3. PROCEDIMIENTO EXPERIMENTAL

Para conocer como influye la metodología de ensayo en los resultados de la medida se consultaron los datos disponibles de la Royal Aeronautical Society [4] para los ensayos RBF (rotating bending fatigue) y RPB (reversed plane rotating bending) de la aleación de aluminio 7075-T6.

El esquema seguido por los autores para los ensayos de fatiga en flexión en cuatro puntos (4PB), consistió en dos puntos de apoyo separados una distancia L, de 45 mm, con una separación entre los puntos de carga (2/3)L. La Figura 1 que representa la distribución de tensiones de una viga sometida a flexión pura, es equivalente al estado en que se encuentran las probetas en el ensayo de flexión en cuatro puntos. Según se observa en el esquema, el estado tensional más desfavorable se localiza en la superficie de la probeta, porque es donde las tensiones alcanzan la máxima intensidad, siendo de tracción en la cara inferior y de compresión en la superior.

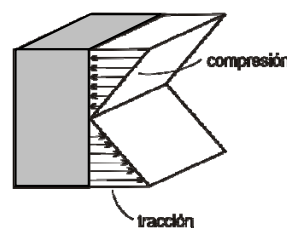


Figura 1. Distribución de tensiones en el material

Utilizando la formulacion propia de resistencia de materiales se puede deducir que la tensión nominal de tracción máxima, que se alcanza en la superficie inferior está dada por la expresión:

$$\sigma = \frac{3a}{wh^2} F \quad (1)$$

donde F es la fuerza aplicada, a la distancia entre los puntos de carga y apoyo, w es el ancho y h el espesor.

Una vez definido y fijada la configuración del ensayo el único parámetro que es necesario medir en la probeta es el ancho. El ancho nominal que se definió para el ensayo fue de 19,5 mm. Es importante destacar en este punto que, el poder utilizar esta fórmula para la expresión de la tensión representa una ventaja con respecto al ensayo de fatiga en flexión rotativa, porque el único parámetro que es necesario medir sobre la probeta es el ancho, y la tensión es inversamente proporcional a este valor. En cambio en el ensayo de fatiga RBF la tensión es inversamente proporcional al cubo del diámetro que se mide. Por tanto, la incertidumbre del resultado debido a la medida de la dimensión de la probeta se reduce sensiblemente en el ensayo de fatiga 4PB.

Los ensayos de fatiga 4PB se realizaron a temperatura ambiente en una máquina de ensayos universales servo-hidráulica Instron con un controlador de la serie 8500 y con una célula de carga de 5kN de clase 0,5, calibrada por un laboratorio acreditado. El control del ensayo se realizó en carga aplicando una onda senoidal de amplitud constante y con razón de carga R=0,1. Debido a las limitaciones mecánicas de la máquina de ensayo, los ensayos de fatiga no superaron los 15 Hz de frecuencia y se consideró el límite de ciclos tecnológico en 2×10^6 ciclos.

5. RESULTADOS

5.1. Curvas S-N

En la Figura 2 se representan los datos de la amplitud de tensión frente al número de ciclos (curvas S-N), obtenidos de la bibliografía consultada [3] para una aleación de aluminio 7075-T6. En esta gráfica se presentan los datos del comportamiento a fatiga para el material de referencia, utilizando el ensayo de flexión rotativa (RBF). También se incluyen los datos de fatiga obtenidos para esta aleación con un tratamiento superficial de anodizado sulfúrico. Se observa que en función del tipo de ensayo utilizado (RBF ó RPB) los datos serán diferentes, tanto la resistencia como la vida a fatiga, y la valoración global del proceso de anodizado no será la adecuada si se compararan datos obtenidos con metodologías diferentes.

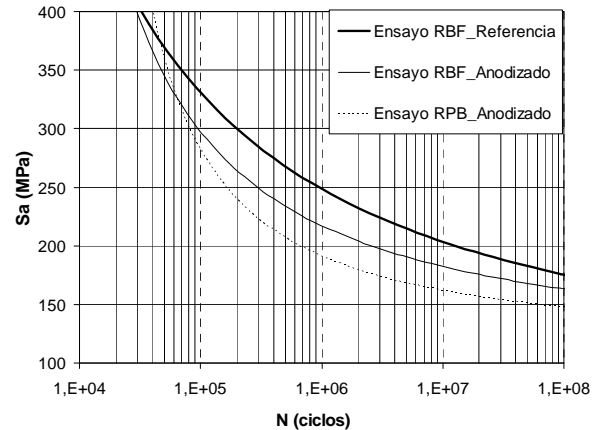


Figura 2. Datos bibliográficos del comportamiento a fatiga de la aleación 7075 en función de la metodología de ensayo y del recubrimiento.

A partir de este resultado se puede deducir que para acometer el estudio de la influencia del espesor del recubrimiento en la respuesta a fatiga de la aleación de aluminio 7075-T6, se hace necesario disponer de una base bibliográfica homogénea, en relación al tipo de ensayo, para poder comparar los resultados y valorar los efectos del tratamiento superficial.

Para analizar la influencia del recubrimiento en la respuesta a fatiga de la aleación de aluminio se utilizó como tratamiento superficial el anodizado sulfúrico, y se trabajó con tres espesores de recubrimientos, de 2, 5 y 10 μm . Los niveles de tensión aplicados para los ensayos de fatiga se establecieron en función de un porcentaje del valor del límite proporcional obtenido en el ensayo estático de flexión. Utilizando como valor promedio del límite proporcional, σ_p , 548 MPa, los niveles de carga con los que se trabajó fueron del 35%, 40%, 45%, 50%, 60% y 70%. Se comprobó que en todos los casos por debajo del $0,30 \sigma_p$ el número de ciclos hasta rotura superaba los 5×10^6 ciclos, y para niveles de carga de $0,70 \sigma_p$, las roturas se producían para $(1-2) \times 10^3$ ciclos.

Los datos experimentales fueron tratados estadísticamente utilizando la metodología de W. Maening [5] y aplicada según queda definido en otras publicaciones de los autores [6] para obtener las gráficas S-N-P (curvas S-N de probabilidad). Finalmente los datos de probabilidad del 1%, 50% y 99% fueron ajustadas con la ecuación hiperbólica (2).

$$(\log N+B) (\log S+D) = A \quad (4)$$

donde A, B y D son las constantes del ajuste.

En la Figura 3 se han incluido las curvas obtenidas después de aplicar a los datos la metodología estadística y el ajuste antes explicados. Los datos se representan en un gráfico S-N, que representan la máxima tensión cíclica de tracción frente a la vida a

fatiga. Destacar también que las gráficas que se presentan son las que corresponden a una probabilidad de fractura del 50%.

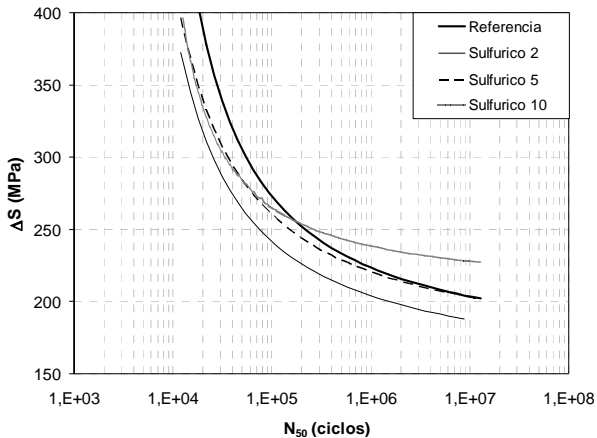


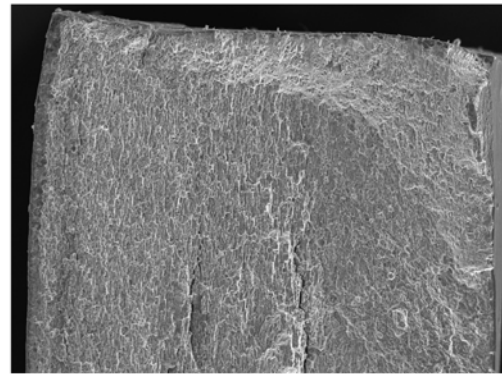
Figura 3. Curvas experimentales S-N₅₀ (50% de probabilidad de fractura) obtenidas en el ensayo de fatiga 4PB para la aleación de aluminio AA7075 sin tratamiento superficial, y con tres espesores de anodizado sulfúrico.

El análisis de los datos incluidos en la Figura 3 son bastante relevantes. Por un lado se observa que la respuesta a fatiga de la aleación con un anodizado convencional de 2 μm , realmente disminuye la respuesta a fatiga del material, dato que está suficiente corroborado en la literatura científica. Sin embargo, cuando se aumenta el espesor de anodizado, sobre las probetas planas con las que se trabaja, la respuesta a fatiga mejora con respecto a lo obtenido para el recubrimiento de 2 μm , y la misma tendencia se observa cuando el espesor del recubrimiento alcanza las 10 μm . En los niveles de carga más altos, que se corresponden con tensiones del 0,70 σ_p , el número de ciclos para los que se produce la rotura en los tres casos del material anodizado son muy similares y las diferencias no son muy significativas, teniendo en cuenta la dispersión propia de los ensayos de fatiga. Sin embargo, a medida que disminuye la carga la diferencia en la respuesta a fatiga se hace más clara. En particular, cabe destacar la tendencia observada a aumentar el límite de fatiga según aumenta el espesor del recubrimiento. Cuando se aumenta el espesor del recubrimiento desde 5 a 10 μm , no se observa una mejora significativa en la respuesta a fatiga del material hasta los 10^5 ciclos, pero a partir de estos valores es evidente que mejora la respuesta del material, y que incluso se supera el límite de fatiga que se obtiene para el material de referencia.

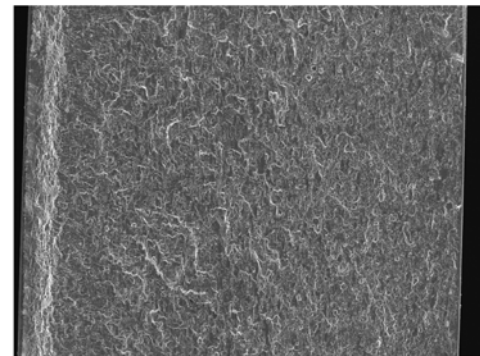
5.2. Análisis fractográfico de las superficies de rotura

En las figuras 4a, 4b y 4c presentan las imágenes de la fractura de tres secciones contiguas de una probeta A7SA10 cuya fractura se ha producido para un bajo nivel de carga (alto número de ciclos). Este es el

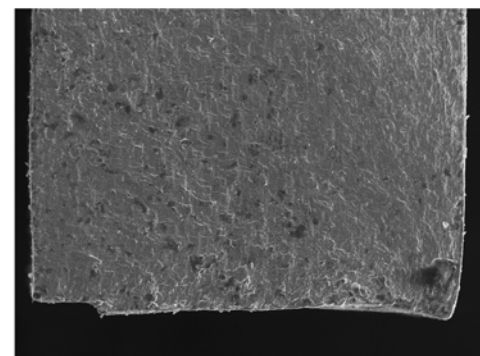
aspecto general que presentan las fracturas cuando se aplican niveles de carga bajos. El lugar donde se origina la fractura corresponde en la figura 4c a la esquina inferior derecha. A partir de este punto la grieta de fatiga se propaga hacia arriba y hacia la izquierda. A medida que avanza la grieta la superficie de fractura se va haciendo más dúctil, como se observa en las figuras 4a y 4b. En la figura 4b se observa que en el lado opuesto a la cara donde por donde avanza la grieta se produce un pequeño escalón con un ancho de 150 μm .



(a)



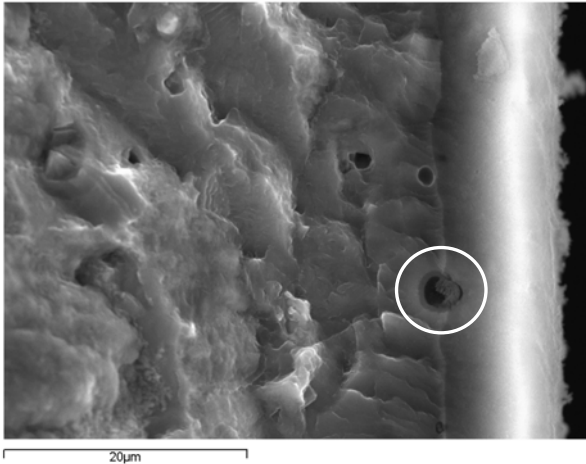
(b)



(c)

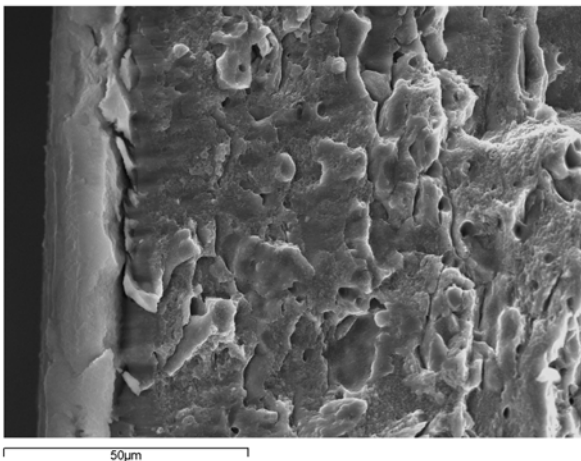
Figuras 4 a, b y c. Imágenes de la superficie de fractura de la aleación A7SA10 a 60x. La rotura se produce para $\Delta S = 45\% \sigma_p$ a 1.430.500 ciclos.

La Figura 5 corresponde a la superficie de la probeta por donde se produce el avance de la grieta de fatiga. En esta imagen se aprecia claramente la capa de óxido de alúmina con un espesor de 10 μm . La rotura de esta capa es frágil y existe una perfecta adherencia con el material de base. También destaca la presencia de partículas de segunda fase con un tamaño aproximado de 2,5 μm en la interfase metal-óxido.



Figuras 5. Superficie de la probeta que se corresponde con el lado por donde avanza la grieta de fatiga. Imagen a 2500x.

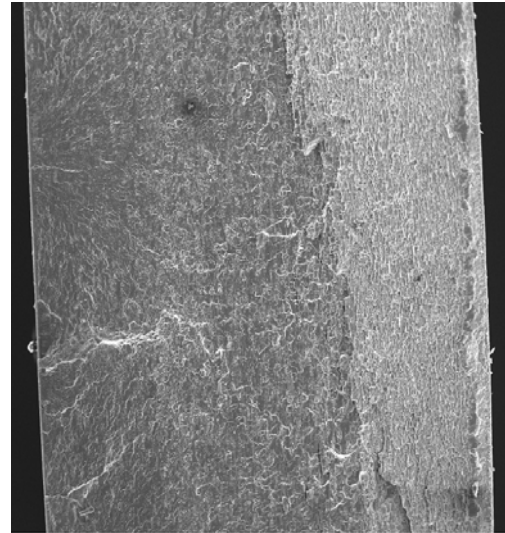
En la superficie opuesta al avance de la grieta de fatiga, en donde la fractura es más brusca porque se produce la rotura final de la probeta, la imagen de la capa de óxido ofrece un aspecto deslaminado según se observa en la Figura 6. Además, aparece una grieta entre la capa de óxido y el metal, que supone la pérdida de adherencia del recubrimiento con la aleación de aluminio.



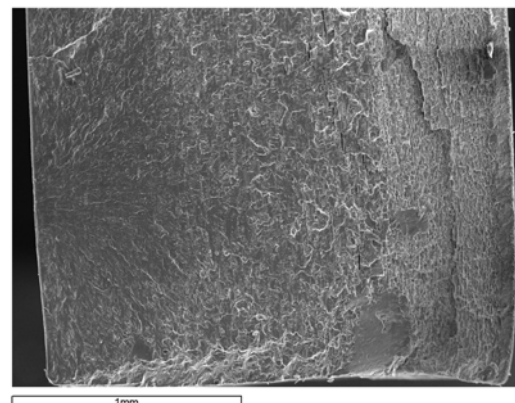
Figuras 6. Superficie de la probeta que se corresponde con la cara superior (opuesta al lado de avance de la grieta de fatiga). Imagen tomada a 1000x.

Las fractografías de las Figuras 7 a y b corresponde a la fractura de la aleación de aluminio A7SA10 con bajo número de ciclos. A diferencia del caso anterior la

fractura se inicia en varios puntos. El origen de estas fracturas múltiples podría encontrarse en los poros de la interfase metal-óxido que actuarían como desencadenantes de la descohesión entre el metal y el óxido, dando lugar a grietas que favorecerían la rápida propagación de la fractura frágil.



(a)



(b)

Figuras 7 a, y b. Imágenes de la superficie de fractura de la aleación A7SA10. La rotura se produce para $\Delta S=70\% \sigma_p$ a 13.500 ciclos.

CONCLUSIONES

- La metodología de ensayo de fatiga influye sobre el resultado numérico de la resistencia y límite de fatiga.
- El aumento del espesor del recubrimiento de anodizado no supone un deterioro en las propiedades de fatiga.
- El aumento del espesor del recubrimiento de anodizado mejora sensiblemente el límite de fatiga del material.

AGRADECIMIENTOS

Los autores desean agradecer a la Xunta de Galicia el apoyo y la confianza otorgadas para la ejecución de este proyecto de investigación, mediante la adjudicación de la subvención con código PGIDIT 09TMT011CT.

REFERENCIAS

- [1] S. Wernick, R. Pinner, P.G. Sheasby, The surface treatment and finishing of aluminium and its alloys, Vol.1 5th ed., ASM International, Metals Park, OH 1995.
- [2] E. Cirik, K. Genel. Effect of anodic oxidation on fatigue performance of 7075-T6 alloy. Surface & Coatings Technology 202 (2008) 5190–5201.
- [3] M. Toledano, M.A. Arenas, A. Monsalve, A. Conde et al. “Caracterización del rango de vida finita en fatiga de la aleación AA7075 con distintos tratamientos superficiales utilizando el ensayo de fatiga en flexión en cuatro puntos”. Anales de Mecánica de la Fractura, vol. 31, 2009.
- [4] Royal Aeronautical Society. EDU 87026. “Fatigue strength of anodised aluminium alloy”.
- [5] Maenning WW. “Planning and evaluation of fatigue tests”. ASM Handbook fatigue and fracture, 1997, pp, 303-313.
- [6] A. Monsalve, M. Páez, M. Toledano et al. “S-N-P curves in 7075 T7351 and 2024 T3 aluminium alloys subjected to surface treatments”. Fatigue Fract. Engng. Mater. Struct. 30, 2007, 748-758.

LIGHTWEIGHT STIFFENED PANELS FABRICATED USING EMERGING FABRICATION TECHNOLOGIES: FATIGUE BEHAVIOUR

P.M.G.P. Moreira¹, V. Richter-Trummer², M. A. V. Figueiredo², P. M. S. T. de Castro²

¹ Instituto de Engenharia Mecânica e Gestão Industrial, INEGI-FEUP
Faculdade de Engenharia da Universidade do Porto,
Rua Dr. Roberto Frias, 4200-465 Porto, Portugal
E-mail: pmgpm@fe.up.pt

² Faculdade de Engenharia da Universidade do Porto and IDMEC-Porto
Rua Dr. Roberto Frias, 4200-465 Porto, Portugal
E-mail: ptcastro@fe.up.pt

ABSTRACT

The need for lower costs and the emergence of adequate welding technologies has brought interest in large integral metallic structures for aircraft applications; however, in integral structures, a crack approaching a stiffener propagates simultaneously in the skin and into the stiffener and breaks it. The use manufacturing techniques as high speed machining (HSM), laser beam welding (LBW) and friction stir welding (FSW) requires further experimental and numerical work concerning the fatigue behaviour of panels manufactured using those processes. A testing programme including fatigue crack growth rate characterization in panels fabricated using HSM, LBW and FSW was performed. Data obtained at IDMEC-Porto testing panels under R (min. load / max. load) of 0.1 and 0.5 is presented, and the performance of panels manufactured using the different processes is discussed and compared. The work was developed in the frame of the European Union DATON project.

KEY WORDS: Fatigue crack growth; Forman law; residual stress; stiffened panels.

1. Introduction.

Minimum weight is a major concern in aircraft design, [1]. Because of interest in integral structures, it has become increasingly important to develop methodologies to predict failure in fatigue damaged fuselage structures, [2], since the fuselage is supposed to sustain cracks safely until it is repaired or its economic service life has expired. Strength assessment of the structures is necessary for their in-service inspection, repair and health monitoring, [3]. Therefore, damage tolerance analysis should provide information about the effect of cracks on the strength of the structure. Recently, studies are being conducted to validate monolithic designs aiming at equal or better performance than conventional designs with regard to weight and structural integrity, while achieving a significant reduction in manufacturing cost, [4].

An aircraft fuselage structure includes, among other parts, the external skin and longitudinal stiffeners (stringers and longerons) [5]. Stiffened panels are light and highly resistant metal sheets reinforced by stringer structures designed to cope with a variety of loading conditions. Stiffeners improve the strength and stability of the structure and provide a means of slowing down or arresting the growth of cracks in the panel. Most common stiffener cross-sections are bulb, flat bar or T- and L-sections, that can be bonded, extruded, connected

by means of fasteners, machined or welded to form a panel. When experimentally testing stiffened panels attention should be given to the loading and boundary conditions to ensure that the behaviour of the panel in the complete structure is reproduced, [6]].

The skin structure of a pressurized fuselage for transport aircraft is fatigue sensitive. The residual strength concept permits the determination of the maximum crack length that can be safely sustained. With this information and the characterization of the crack growth behaviour of the material, the number of loading cycles that will be necessary for the crack to grow up to its critical length can be estimated in order to ensure safe operation, [7]. The development of numerical methodologies with the help of small laboratory coupon test results should be used to predict the residual strength of complex built-up aircraft fuselage structures, [8].

Riveted and bolted stiffeners tend to remain intact as the crack propagates under them providing an alternative path for the panel load to pass. Also, riveted stiffeners continue to limit crack growth after the crack propagates past the stiffener since a crack cannot propagate directly into the stiffener. The permanent need for low cost and the emergence of new technologies has brought interest in large integral metallic structures for aircraft applications. Evaluative programs for replacement of

traditional fastening with these new emerging technologies have been carried out all over the aircraft sector, *e.g.* [9]. In an integral stiffener (machined, extruded or welded) a crack propagates simultaneously in the stiffener and in the skin beyond the stiffener. In this case the crack may propagate into and break the stiffener, [10], although in [11] it was observed that the rate of crack growth is significantly reduced in the skin in the presence of stiffeners.

There is an urgent pressure from the manufacturing side in the aerospace industry to apply advanced structural concepts, since they promise considerable cost and production time benefits, producing, in addition, a smaller number of fatigue and corrosion critical locations. The main drawback of integrally stiffened structures is the damage tolerance behaviour. Such design behaves totally different from the differential designs created by using riveted stiffeners. The prime problem is the crack arresting capability of the stiffeners both in fatigue crack growth as well as in residual strength

The first task in this study was the finite element method analysis of the stiffened panel geometry that was defined by the project guide lines.

2. Finite element analysis of the selected panel geometry.

The geometry of the specimen studied in the experimental component of the European Union DATON project [12] is presented in Figure 1. A three-dimensional (3D) stress analysis of the specimen was done using the finite element method (FEM) and ABAQUS [13].

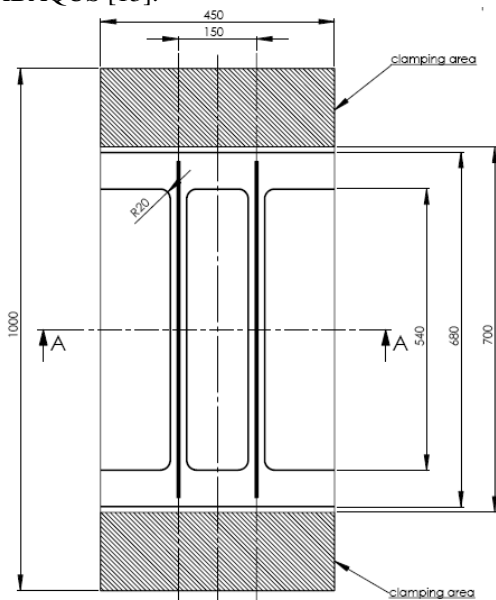


Figure 1 - Geometry of specimens to be used in the experimental component of the DATON project, [12].

The centre of gravity is located 2.76mm above the specimen front face. In all the analyses carried out the load was applied aligned with the centre of gravity. The remote load chosen for all analyses corresponds to a 100MPa uniformly distributed nominal stress. Three

different situations were analysed: stiffened panel without and with a central crack, and stiffened panel with a central crack and an anti-bending device.

In the following analyses x (and 1) is the coordinate axis in the thickness direction, y (and 2) is the coordinate axis in the loading (longitudinal) direction, and z (and 3) is the coordinate axis in the transversal direction. The specimen side containing the stiffeners will be named back side, whereas the opposite side will be named front side.

8-nodes brick elements (C3D8) and 6-nodes brick elements (C3D6) were used to model the specimen. These elements use linear interpolation in each direction and are often called linear elements or first-order elements. A total of 60083 elements were used to model half of the stiffened panel.

The deformed 3D FEM model, that presents the stress in the load direction, σ_y throughout the un-cracked stiffened panel, is shown in Figure 2. In this figure, displacements were enlarged (deformation scale factor of 20) in post-processing of the FEM analysis.

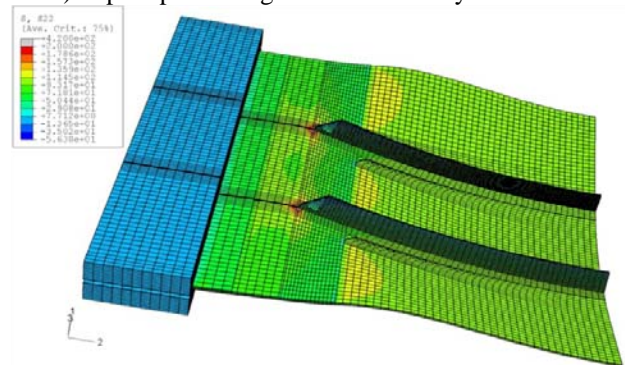


Figure 2 - Deformed model and stress distribution on the un-cracked stiffened plate, stress in the load direction.

A crack with length $2a=55.39mm$ was also modelled in the centre of the specimen. The detail of σ_y stress distribution in the cracked specimen middle cross section is presented in Figure 3. The σ_y stress distribution and displacements in the x direction were analysed along the nodes on the side of the plate containing the stiffeners and on the opposite side, in the direction of the arrow b) plotted in this figure.

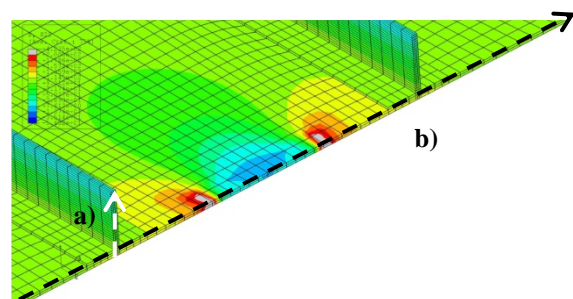


Figure 3 - Detail of specimen middle cross section, stiffened panel with a crack.

The evolution of σ_y stress along the nodes that lay on the arrow a), for the case of the un-cracked and cracked panels, is presented in Figure 4. For the un-cracked

panel, the stress values are higher in the plate and decrease through the stiffener moving away from the plate, as indicated by the arrow. The higher and lower σ_y stress values along this line are 112.2MPa and 17.5MPa respectively.

The introduction of a crack in the stiffened panel leads to an increase of the stress values in the plate and a decrease at the top of the stiffener.

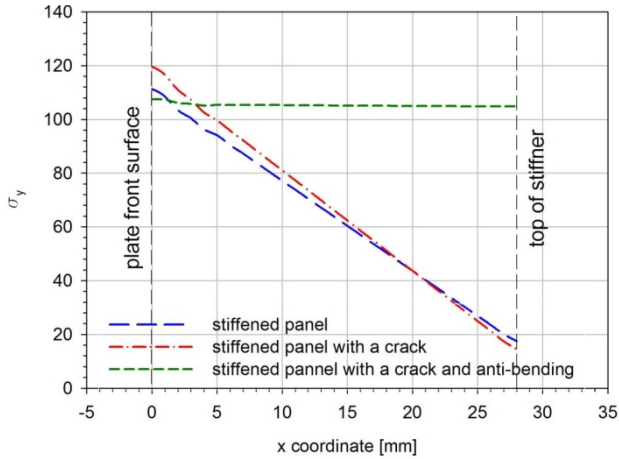


Figure 4 - Stress distribution along the nodes that lay on the arrow a) presented in Figure 3.

The σ_y stress distribution along the specimen longitudinal direction is presented in Figure 5. In this figure three lines - a), b) and c) - are marked. The σ_y stress and displacements in the x direction were determined along these lines. Results presented for lines b) and c) were obtained in the plate side opposite to the stiffeners (front side).

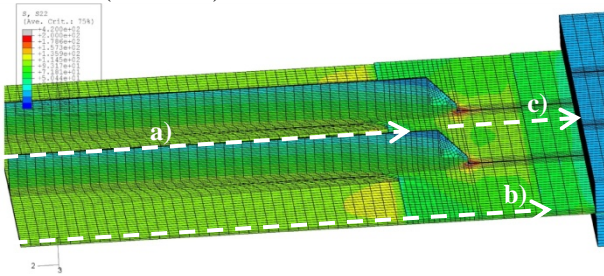


Figure 5 - σ_y distribution along the specimen longitudinal direction.

The σ_y stress distribution throughout the specimen longitudinal direction in the stiffener top surface a), panel lateral surface b) and panel longitudinal central line c) (as presented in Figure 5) is presented in Figure 6.

For the un-cracked panel, the higher stress values are found in the centre of the plate, but they are of the same magnitude as those found in the side layer. Stress values on the stiffener top surface are near 18MPa, except in the stiffener end where some low compressive values are found. When a crack is present there is a decrease of the σ_y stress value in the stiffener near the crack, but in the remaining stiffener σ_y stress has similar values as in the un-cracked panel. In the case of the cracked panel, σ_y stress is similar to the un-cracked panel, except in the

middle plane near the crack face where σ_y has zero or very low values as expected.

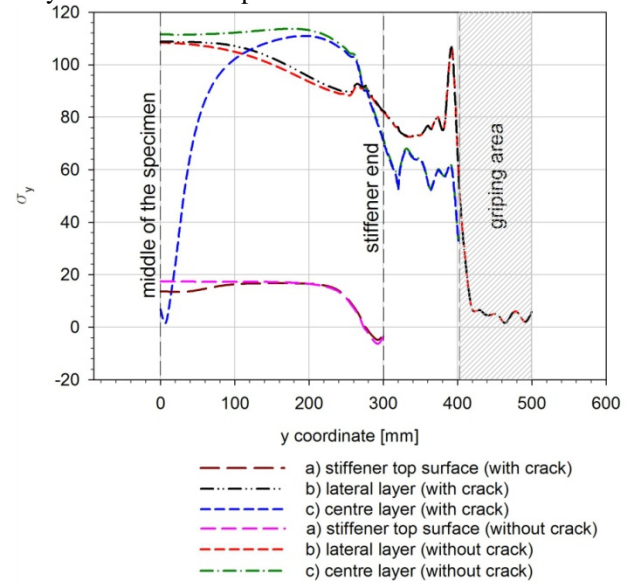


Figure 6 - σ_y distribution through the specimen longitudinal direction in stiffener top surface a), lateral surface b) and centre layer c), as presented in Figure 5. Stiffened panel with and without a crack.

3. DATON stiffened panels fatigue life; experimental measurements.

Fatigue tests of two stiffener specimens (Figure 1) manufactured by three different processes were carried out, HSM (High Speed Machining), LBW (Laser Beam Welding) and FSW (Friction Stir Welding). The stiffened panels were manufactured using the AA6056, a modified variant of the AA6013, which is considered a promising airframe candidate for processing by fusion laser beam welding and solid-state friction stir welding. The AA6056 is an Al-Mg-Si-Cu alloy that can be heat treated to different strength levels by precipitation hardening and has a good corrosion resistance. A total of ten specimens were tested.

Measurements of crack length in all specimens were performed according to the scheme presented in Figure 7. The specimen front and back sides are the sides of the plate side without and with stiffeners, respectively.

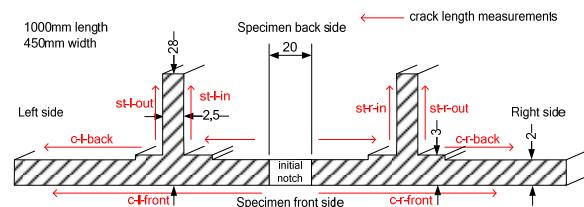


Figure 7 - Fatigue crack measurement scheme.

3.1 Base material tensile and crack growth tests.

Base material characterization was presented in [14]. It was verified that for both material conditions the specimens with $R=0.5$ presented a higher crack growth rate for the same ΔK value, as expected. Also, when tested at the same R value the specimens extracted from

the LBW panels have higher crack growth rate than those extracted from HSM panels.

3.2 High Speed Machining AA6056 panels.

Two stiffened HSM panels of aluminium 6056-T651 were fatigue tested at a maximum stress of 80MPa with R=0.1 (specimen HSM01) and at a maximum stress of 110MPa with R=0.5 (specimen HSM02). The stress distributing for static and fatigue loading was recorded and the crack growth rate was also measured. An initial central full depth notch (crack) with 20mm length and 0.2mm width was created by electro-discharge machining. In this paper, more complete details of the test procedure are given in the case of these HSM specimens. Testing of the remaining specimens, although also covering all aspects dealt with for HSM, is recorded here giving only the *a vs N* data, which was indeed the main testing objective.

Two panels with a central notch of 20mm length were instrumented and loaded at five incremental loads to acquire the stress distribution in specific sites of the specimen. The strain gages were distributed in the specimen according to the scheme presented in Figure 8: two couples (C1, C5, C6 and C7), on both faces of the panel, bonded on the skin at the centre of each bay (spaced 225mm in horizontal direction), on the horizontal symmetry plane; another couple (C3 and C8), placed on the longitudinal axis of the panel, 200mm above the horizontal symmetry plane; two couples (C2, C4, C7 and C9), placed in correspondence of a stringer, with a strain gauge bonded on top of the stringer and the other one on the skin.

An accurate symmetry of load distribution along the specimen width was identified. At the specimen horizontal middle line, the stiffener top surface has the lower values of stresses.

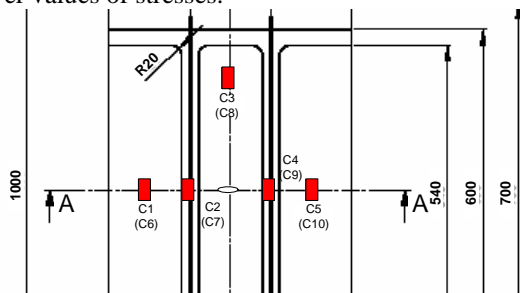


Figure 8 - DATON panel strain gages location (front gages in brackets, see Figure 7).

A value of 70GPa was used for the Young modulus in order to convert strain to stress.

Fatigue crack propagation tests were carried out and strain was measured in order to understand the different load transfer stages.

The strain gages values were measured in periodic stops of the fatigue test at the average fatigue load (44MPa, 47.98kN). The stress distribution on the stiffened panel along the fatigue test is presented in Figure 9. When the crack is near and reaches the stiffener most of the load is transmitted to the plate front side.

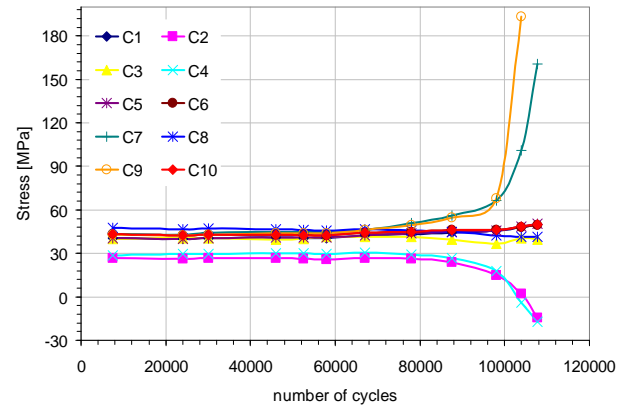


Figure 9 - Stress distribution during the fatigue crack growth test, HSM01 ($\sigma_{max}=80MPa$, $R=0.1$).

For specimen HSM02 ($\sigma_{max}=110MPa$, $R=0.5$) the strain gages values were measured in periodic stops of the fatigue test at the maximum fatigue load (119.95kN). Again, when the crack grows through the stiffener most of the load is carried out by the plate front side.

Fatigue crack propagation tests were carried out and crack length was measured at periodic stops of the fatigue test. Specimen HSM01, tested at a maximum stress of 80MPa and R=0.1, had a fatigue life of 113784 cycles. The fatigue crack growth in the stiffened panel during the fatigue test is presented in Figure 10. The first fatigue crack was only detected at 15000 cycles. The crack started to grow through the stiffener at 109800 cycles, 96.5% of the total fatigue life. The crack in the left stiffener bifurcated at nearly 113000 cycles.

Specimen HSM02, tested at a maximum stress of 110MPa and R=0.5, had a fatigue life of 117744 cycles. The first fatigue crack was first detected at 7500 cycles. The crack started to grow through the stiffener at 113000 cycles, 96.0% of the total fatigue life. After 115000 cycles the fatigue crack in both stiffeners bifurcated and started to propagate parallel to the panel along the stiffener.

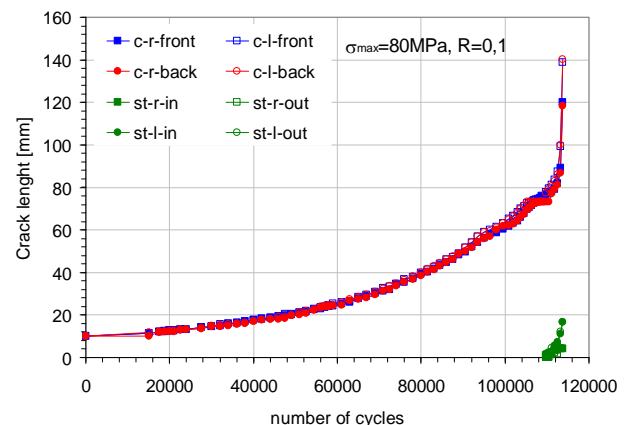


Figure 10 - Fatigue crack growth test, specimen HSM01.

3.3 Laser Beam Welded AA6056 2-stiffener panels.

Six laser beam welded panels of aluminium 6056 were fatigue tested. Half of the panels were tested at a maximum stress of 80MPa with R=0.1 and the

remaining at 110MPa and $R=0.5$. Panels with two different heat treatment conditions were tested:

- i- after the welding procedure panels were submitted to an aging treatment T6 (PWHT) which corresponds to $4h$ at 190°C . The machining of the panels has performed on T4 tempered 5mm thickness sheet;
- ii- another set of panels were previously heat treated to the condition T6 and than tested (as-welded).

Two different welding configurations were analyzed (LBW1 and LBW2), as presented in Figure 11. The main difference between LBW1 and LBW2 is the position of the weld bead. In the LBW1 configuration the weldment is at the junction of the skin with the blade (T-joint); in the LBW2 configuration the weldment is at the lower part of the stringer web (butt-joint), 1mm above the skin.

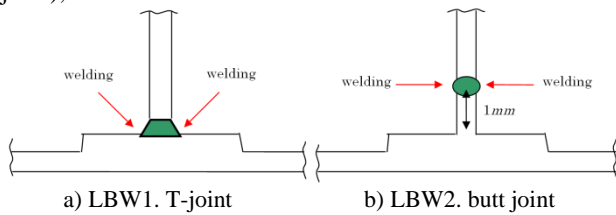


Figure 11 - Welding configurations for the LBW specimens.

In subsequent sections of this paper, overall comparative plots of the data obtained for the remaining specimens will be given, and for the sake of concision no reference to specific features will be made.

3.4 Friction Stir Welding AA6056 2-stiffener panels.

Two stiffened friction stir welded panels of aluminium 6056 PWHT-T6 were fatigue tested: i) at a maximum stress of 80MPa with $R=0.1$; ii) and at a maximum stress of 110MPa with $R=0.5$. Panels were welded in the T4 condition, and after welding were tempered to achieve the T6 condition.

3.5 Results discussion

A comparison of the specimens tested with $R=0.1$ and $R=0.5$ (HSM, LBW1 PWHT-T6, LBW2 (as-welded and PWHT-T6) and FSW PWHT-T6) are presented in Figure 12 and Figure 13, respectively. For both values of R , the HSM specimen presented the lower fatigue lives. At the opposite, the PWHT-T6 specimens tested in the LBW2 configuration (butt joint) presented the higher fatigue lives for both R ratios.

The FSW specimen tested at $R=0.1$ presented a fatigue life similar to the LBW2 as-welded specimen. For $R=0.5$ the FSW specimen performed higher than the LBW1 PWHT-T6 specimen and lower than the LBW2 as-welded specimen.

In all specimens tested it was found that the crack arrest feature (decrease of crack growth rate) introduced by the stiffener was not significant, probably due to the low width of these specimens. Nevertheless when the stiffeners are fractured the remaining life of the specimen is marginal.

In a test of a multi-stiffener panel performed for AIRBUS [15] it was verified that there was a marked slow-down of crack growth rate as the crack reaches the

stiffeners. However this phenomenon was not identified in the present tests of panels with two stiffeners. This difference can be attributed to the relatively light stiffeners used in the DATON panels when compared with the AIRBUS panel. These observations emphasise the need for further research studying the behaviour of stiffened panels with other ratios of stiffener to skin cross sections. Also, the number of stiffeners per panel, and the location of the initial crack (between stiffeners, or broken stiffeners) should be considered.

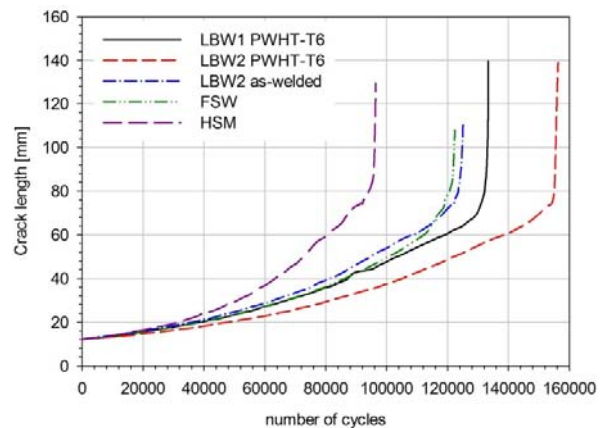


Figure 12 - Comparison of $a-N$ for all specimens tested at $R=0.1$.

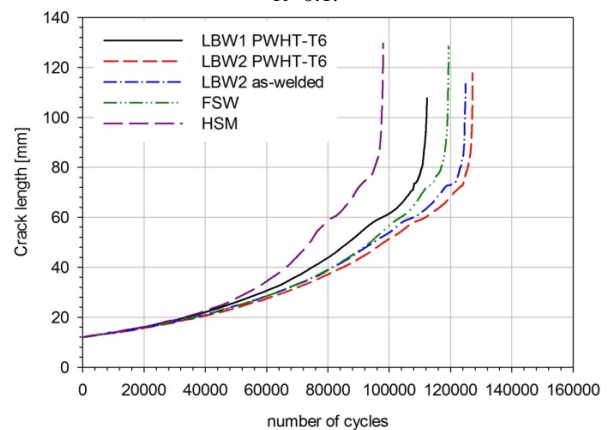


Figure 13 - Comparison of $a-N$ for all specimens tested at $R=0.5$.

3.6 Crack growth prediction

Modeling of crack growth of HSM panels was carried out using the virtual crack closure technique (VCCT) for SIF calculation, ABAQUS finite element software and the Paris law with the constants mentioned earlier in the paper, [14]. Using an algorithm in MAPLE that integrates the Paris law equation and takes into account the SIF curve fit presented in [14], the number of cycles as a function of crack length was calculated and good agreement between experiments and model. The results of this modelling exercise were compared with the experimental measurements of the two HSM panels. The panels were tested at $\sigma_{\max}=80\text{MPa}$ $R=0.1$ and $\sigma_{\max}=110\text{MPa}$ $R=0.5$.

For both HSM specimens a good agreement between the predicted fatigue life and the experimental measurements was found. Once compared with panels

fabricated by welding, HSM panels are expected to present very low residual stress values. In the following discussion any machining residual stress were not taken into consideration. For the case of $R=0.5$ the predicted fatigue life was found to be slightly higher than the experimental measurements at a crack length $a=60\text{mm}$, and approximately 30% higher when critical crack length was reached. This difference can be due to the complex test setup used for experimental tests and to the simplified numerical model. It is to be noted that a difference of 20% in fatigue life is of the order of the scatter found when testing similar DATON panels under similar loading conditions, [16].

4. Conclusions

- The SIF calibration of the DATON panel was obtained using the VCCT technique in conjunction with a finite element model. The resulting SIF solutions for both skin and stiffener, used with the Paris law, gave adequate predictions of experimental crack propagation behaviour in HSM panels.
- When fatigue testing the DATON stiffened panels it was found that, although SIF decreases when cracks approach the stiffeners, there is no clear slowing down of the crack propagation.
- Welded panels presented longer lives up to rupture, implying that during most of their fatigue testing the crack growth rates were smaller than with HSM panels. This somewhat unexpected result is certainly associated to the residual stress fields existing in the welded panels, and also to the location of the initial artificial defect, placed in the skin precisely in the middle distance between the two stiffeners.
- In the LBW panels, at the centre of the weld, pores with a maximum diameter of approximately 0.24mm were identified. These pores seem to be coincident with the laser maximum penetration depth from each side of the T-joint. In the transition area between the melted and un-melted material cracks out of the weld bead were identified.
- In the FSW panels it is verified that outside the weld affected area the fracture shows a more regular structure than in the weld affected area. This difference was reflected in the striation identification process; it was harder to perform the analysis under the shoulder limits. In the thermomechanically affected zone, inside the stiffener, a change in the fracture surface occurs.

References

1. J. Paik, S. van der Veen, A. Duran, and M. Collette, *Ultimate compressive strength design methods of aluminum welded stiffened panel structures for aerospace, marine and land-based applications: A benchmark study*. Thin-Walled Structures, 2005. **43**(10): p. 1550-1566.
2. P. Wen, M. Aliabadi, and A. Young, *Fracture mechanics analysis of curved stiffened panels using BEM*. International Journal of Solids and Structures, 2003. **40**(1): p. 219-236.
3. A. Murthy, G. Palani, and N. Iyer, *Remaining life prediction of cracked stiffened panels under constant and variable amplitude loading*. International Journal of Fatigue, 2007. **29**(6): p. 1125-1139.
4. R. Pettit, J. Wang, and C. Toh, *Validated feasibility study of integrally stiffened metallic fuselage panels for reducing manufacturing costs*, in NASA / CR-2000-209342. 2000.
5. A. Murphy, M. Price, C. Lynch, and A. Gibson, *The computational post-buckling analysis of fuselage stiffened panels loaded in shear*. Thin-Walled Structures, 2005. **43**(9): p. 1455-1474.
6. A. Aalberg, M. Langseth, and P. Larsen, *Stiffened aluminium panels subjected to axial compression*. Thin-Walled Structures, 2001. **39**(10): p. 861-885.
7. N. Salgado and M. Aliabadi, *The application of the dual boundary element method to the analysis of cracked stiffened panels*. Engineering Fracture Mechanics, 1996. **54**(1): p. 91-105.
8. B. Seshadri, J. Newman, and D. Dawicke, *Residual strength analyses of stiffened and unstiffened panels - Part II: wide panels*. Engineering Fracture Mechanics, 2003. **70**(3-4): p. 509-524.
9. E. Hoffman, R. Harley, J. Wagner, D. Jegley, R. Pecquet, C. Blum, and W. Arbogast, *Compression buckling behavior of large-scale friction stir welded and riveted 2090-T83 Al-Li alloy skin-stiffener panels*, in NASA/TM-2002-211770. 2002.
10. H. Mahmoud and R. Dexter, *Propagation rate of large cracks in stiffened panels under tension loading*. Marine Structures, 2005. **18**(3): p. 265-288.
11. S. Mellings, J. Baynham, R. Adey, and T. Curtin, *Durability prediction using automatic crack growth simulation in stiffened panel structures*, in <http://www.beasy.com/>. 2002.
12. DaToN, *Innovative Fatigue and Damage Tolerance Methods for the Application of New Structural Concepts*. Strengthening the competitiveness, Specific Targeted Research Project. 2004: A Proposal for the 6th European Framework Program.
13. Hibbitt, Karlsson, and Sorenson, *ABAQUS Users Manual*. 2006.
14. P. M. G. P. Moreira, V. Richter-Trummer, S. M. O. Tavares, and P. M. S. T. de Castro, *Characterization of fatigue crack growth rate of AA6056 T651 and T6: Application to predict fatigue behaviour of stiffened panels*. Materials Science Forum, 2010. **636-637**: p. 1511-1517.
15. R. Franke, B. Brenner, V. Ulbricht, and W. Zink. *Moderne werkstoffe und testmethoden in flugzeugbau*. in *Tagungsband zum 6. Chemnitzer Symposium Fugetechnik/Schweisstechnik*. 2004. Technische Universitat Chemnitz.
16. University of Pisa, *WP3: Manufacturing and testing, Status at month 30*. DaToN project, meeting at Brno, slides presentation, 15-16 October 2007.

Fracture

ANÁLISIS DEL COMPORTAMIENTO DINÁMICO DE VIGAS DE VIDRIO LAMINADO

D. Rodríguez Argüelles, P. Fernández Fernández, M. López Aenlle, A. Fernández Canteli, M. J. Lamela Rey.

Dpto. de Construcción e Ingeniería de Fabricación, EPS de Ingeniería de Gijón
 Universidad de Oviedo, Campus de Viesques, 33203 Gijón
 E-mail: aenlle@uniovi.es
 Tfno: 985152057. Fax: 985182055

RESUMEN

El vidrio laminado es un elemento tipo sándwich formado por dos o más placas de vidrio, entre las que se colocan una o más láminas de butiral polivinilo (PVB). Para el análisis de vigas tipo sándwich, como son las vigas de vidrio laminado se han propuesto distintos modelos, en los que el vidrio se suele modelizar como material elástico-lineal, mientras que el PVB presenta un comportamiento viscoelástico, cuyas propiedades dependen de la temperatura y de la frecuencia. En este trabajo se utiliza el modelo propuesto por Ross, Kerwing y Urgar (RKU) para predecir el comportamiento dinámico de vigas de vidrio laminado. Los resultados obtenidos se validan con los obtenidos experimentalmente mediante análisis modal operacional.

ABSTRACT

Laminated glass is a sandwich element consisting of two or more glass sheets, with one or more interlayers of polyvinyl butyral (PVB). Several analytical methods have been proposed to estimate the dynamic response of sandwich elements, such as laminated glass beams. In these models, glass is usually modeled as a linear-elastic material, whereas PVB present a linear viscoelastic-behavior, whose mechanical properties present frequency-temperature dependence. In this work the Ross-Kerwin-Urgar model is used to predict the dynamic behavior of laminated glass beams. The analytical results are compared with those obtained by operational modal analysis.

KEY WORDS: vidrio laminado, análisis modal, vigas sándwich, viscoelasticidad.

1. INTRODUCTION

El vidrio laminado más común se compone de dos o más placas de vidrio monolítico que se unen entre sí mediante una lámina de PVB (butiral polivinilo). La lámina de PVB tiene un espesor de 0.38 mm o un múltiplo de este valor. Al someter el conjunto a una presión y temperatura elevadas en un autoclave, se produce la adherencia entre la lámina de PVB y las placas de vidrio.

En los últimos años, la aplicación del vidrio laminado en la edificación ha experimentado un gran crecimiento, especialmente en acristalamiento de fachadas, cubiertas, escaleras o escaparates. La principal ventaja del vidrio laminado sobre el monolítico es la mayor seguridad que aporta en caso de rotura, ya que los fragmentos quedan adheridos a la lámina de PVB, reduciendo así el riesgo de accidente. Además, la capa intermedia aumenta notablemente el amortiguamiento del conjunto, reduciendo de esta forma las vibraciones debidas a cargas de viento o de carácter sísmico.

La simulación del comportamiento dinámico de elementos estructurales de vidrio laminado mediante métodos analíticos o numéricos, requiere la caracterización de los elementos que lo componen. El vidrio se suele caracterizar mediante ensayos estáticos a flexión y el PVB mediante ensayos de relajación o fluencia, estáticos o dinámicos.

El PVB es un termoplástico amorfo que presenta un comportamiento viscoelástico lineal. Una característica fundamental de los materiales viscoelásticos es que sus propiedades mecánicas dependen de la frecuencia (o del tiempo) y de la temperatura. Estas variaciones en las propiedades dificultan el cálculo resistente de elementos con comportamiento viscoelástico.

Por su parte, el vidrio se puede considerar un material elástico-lineal. La presencia de microdefectos superficiales que tienen su origen en la fabricación o la posterior manipulación del vidrio hacen que presente una gran dispersión en los valores de su resistencia mecánica a tracción.

En este trabajo se realiza un estudio analítico del comportamiento dinámico de vigas de vidrio laminado, a partir de las propiedades mecánicas de los materiales que lo componen (vidrio y PVB), por medio del modelo de RKU para vigas sándwich. Posteriormente, las predicciones analíticas se comparan con los resultados obtenidos experimentalmente, mediante la aplicación de análisis modal operacional.

2. CARACTERIZACIÓN DINÁMICA DE LOS MATERIALES VISCOELÁSTICOS

Los materiales viscoelásticos se caracterizan dinámicamente mediante sus módulos complejos. En el caso de carga axial, el módulo complejo de un material viscoelástico $E^*(\omega)$ se define como:

$$E^*(\omega) = E'(\omega) + iE''(\omega) = E'(\omega)(1 + i\eta_E(\omega)) \quad (1)$$

donde $E'(\omega)$ y $E''(\omega)$ se conocen como módulo de almacenamiento y pérdidas, respectivamente. A la relación entre ambos módulos, η_E , se le denomina factor de pérdidas.

Análogamente, el comportamiento del material a cizalladura, se define mediante el módulo de cortante complejo $G^*(\omega)$:

$$G^*(\omega) = G'(\omega) + iG''(\omega) = G(\omega)(1 + i\eta_G(\omega)) \quad (2)$$

En el caso de materiales viscoelásticos lineales, la aplicación del principio de correspondencia permite relacionar los módulos en el dominio de la frecuencia, usando la misma expresión que en la teoría de la elasticidad [1], es decir:

$$G^*(\omega) = \frac{3E^*(\omega)K(\omega)}{9K(\omega) - E^*(\omega)} \quad (3)$$

siendo $K(\omega)$ el módulo volumétrico.

Los módulos complejos de un material viscoelástico lineal, también se pueden obtener de forma indirecta por medio de sus módulos definidos en el dominio del tiempo. A pesar de existir relaciones matemáticas entre ambos módulos, no resulta sencillo calcular su solución exacta y, por tanto, se han desarrollado métodos alternativos de interconversión [2]. Utilizando el modelo de Maxwell generalizado [3], el módulo de relajación $E(t)$ se puede expresar como:

$$E(t) = E_\infty + \sum_{i=1}^n e_i \cdot \exp\left(-\frac{t}{\tau_i}\right) \quad (4)$$

donde e_i y τ_i son los coeficientes de las series de Prony.

A partir de estos coeficientes, el módulo en el dominio de la frecuencia se puede obtener mediante:

$$E'(\omega) = E_\infty + \sum_{i=1}^n \frac{\tau_i^2 \omega^2 e_i}{\tau_i^2 \omega^2 + 1} \quad (5)$$

$$E''(\omega) = E_\infty + \sum_{i=1}^n \frac{\tau_i \omega e_i}{\tau_i^2 \omega^2 + 1} \quad (6)$$

3. CARACTERIZACIÓN DEL PVB: PARTE EXPERIMENTAL

3.1. Equipo y descripción de ensayos

Los ensayos para caracterizar el PVB fueron realizados en un analizador dinamo-mecánico. El equipo dispone de una cámara de temperatura controlada, que permite realizar ensayos en un rango de temperaturas de -60 °C a 150 °C.

Para obtener el módulo de relajación a tracción del PVB, se realizaron ensayos cuasi-estáticos de relajación (se somete a la probeta a una deformación constante) de 10 minutos de tiempo a diferentes temperaturas.

A partir de las curvas a diferentes temperaturas, se obtuvo la curva maestra del material a la temperatura de referencia de 20°C, aplicando el principio de superposición temperatura-tiempo (TTS) [3]. Los factores de ajuste horizontal para la aplicación del principio TTS, se obtuvieron a través de la ecuación de William, Landel y Ferry (WLF) [4].

3.2. Resultados experimentales y conversiones.

Los parámetros de WLF empleados para obtener la curva maestra de relajación son: $C_1=49.806$ y $C_2=328.46$.

Aplicando las ecuaciones (5) y (6), se obtuvo las componentes del módulo complejo $E'(\omega)$ y $E''(\omega)$, a partir de la curva de relajación en el dominio del tiempo. Posteriormente, aplicando la ecuación (3) y tomando un valor constante en frecuencia del módulo volumétrico de 2 GPa [5], se obtuvo el módulo complejo a cortadura, Figura 1.

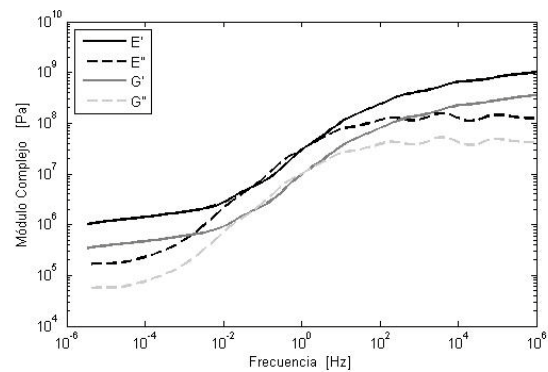


Figura 1. Componentes del módulo complejo axial y a cortadura del PVB a 20°C.

4. ANÁLISIS MODAL OPERACIONAL (OMA)

El análisis modal operacional (OMA) es una técnica adecuada para la estimación de parámetros modales en un amplio abanico de aplicaciones [6]. La diferencia principal con el análisis modal clásico radica en que no es necesario conocer las cargas que se aplican sobre la estructura para estimar los parámetros modales.

Los ensayos se llevan a cabo midiendo las respuestas de la estructura (aceleraciones) bajo las condiciones de servicio de la misma, como por ejemplo, cargas de viento, oleaje, cargas de tráfico, etc. En el caso de ensayos en laboratorio, se utilizan cargas artificiales de naturaleza aleatoria que simulen las condiciones reales de trabajo de la estructura.

5. PREDICCIÓN ANALÍTICA DEL COMPORTAMIENTO DINÁMICO DE VIGAS SANDWICH

Las vigas de vidrio laminado pueden considerarse vigas sándwich simétricas (Figura 2). Para el cálculo el vidrio de las capas externas se suele considerar un material elástico-lineal, mientras que la capa intermedia de PVB se considera un material viscoelástico-lineal, siendo sus módulos dependientes de la frecuencia y de la temperatura.

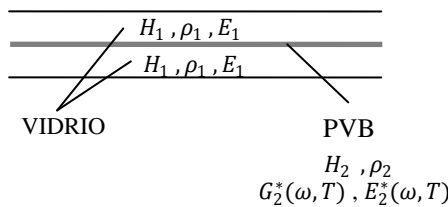


Figura 2. Vista transversal de una viga de vidrio laminado

Desde finales de los años 50 se han desarrollado diversos modelos analíticos para predecir la respuesta dinámica de vigas sándwich con comportamiento viscoelástico. Entre los más conocidos se encuentran los desarrollados por Ross, Kerwin, y Ungar [7] o Mead y Markus [8]. El desarrollo de programas de elementos finitos ha aumentado considerablemente la precisión en las predicciones de la respuesta dinámica de estructuras amortiguadas. Sin embargo, en el caso de vigas, estos métodos analíticos proporcionan unos resultados lo suficientemente precisos.

4.1. Modelo de RKU

Ross, Kerwin y Ungar (RKU) desarrollaron uno de los primeros modelos para vigas sándwich, formada por dos capas elásticas externas y una capa viscoelástica intermedia. Cuando las dos capas externas experimentan flexión cíclica, deforman por cortante la capa

viscoelástica. La deformación por cortante es un mecanismo por el cual se disipa más energía que si la capa estuviera sometida sólo a deformaciones axiales, lo cual permite que las oscilaciones estructurales se atenúen más rápido [9].

El modelo propuesto por RKU supone que el comportamiento dinámico a flexión de una viga sándwich está gobernado por la teoría de flexión de Euler-Bernoulli. Las frecuencias naturales de flexión de una viga simple que cumple la teoría de Euler-Bernoulli, vienen dadas por:

$$\omega_n^2 = k_n^4 \frac{EI}{\bar{m}} \tag{7}$$

donde E es el módulo de elasticidad, I la inercia de la viga, \bar{m} la masa por unidad de longitud y k_n el número de onda, cuyos valores para vigas biapoyadas y libre-libre se indican en la Tabla 1.

Tabla 1. Valores de $C_n=(k_n L)^2$, según la condición de contorno.

Nº Modo	$C_n = (k_n L)^2$	
	Libre-Libre	Biapoyada
1	22.3733	π^2
2	61.6728	$4\pi^2$
3	120.9034	$9\pi^2$
4	199.8594	$16\pi^2$

En el caso de vigas biapoyadas los modos de vibración vienen dados por una senoide:

$$\phi(x) = \text{sen} \frac{n\pi x}{L} \tag{8}$$

siendo n es el número del modo.

Para vigas sándwich simplemente apoyadas, el modelo de RKU supone que los modos de vibración también son sinusoides, por lo que proponen utilizar la ecuación (7) para determinar las frecuencias naturales, pero considerando una rigidez equivalente $(EI)^*$, es decir:

$$\omega_n^{2*} = k_n^4 \frac{(EI)^*}{\bar{m}} \tag{9}$$

Esta suposición se considera aceptable sólo en los modos altos, por lo que se recomienda no considerar el primer modo [10]. Para otras condiciones de apoyo distintas de apoyada, se introduce un factor corrector en el número de onda. En el caso de vigas libre-libre, este factor es igual a la unidad para todos los modos.

Considerando una viga sándwich de longitud L y ancho b compuesta por dos capas externas elásticas de espesores H_1 y H_3 y módulo elásticos E_1 y E_3 respectivamente, una capa viscoelástica intermedia de

espesor H_2 y módulo cortante complejo G_2^* , la rigidez a flexión equivalente $(EI)^*$ en el modelo RKU, viene dada por:

$$(EI)^* = b \left[\frac{H_1^3}{6} + E_1 H_1 (H_1 + H_2)^2 \frac{g^*}{1+2g^*} \right] \quad (10)$$

$$g^* = G_2^* L^2 / E_3 H_2 H_3 k_n^2 \quad (11)$$

siendo g^* el denominado “parámetro de cortadura”. El símbolo “*” representa un valor complejo.

La expresión (10) corresponde al modelo de RKU en el que se considera despreciable la contribución del módulo axial viscoelástico en la rigidez a flexión de la viga, es decir: $E_2^* \cong 0$.

La expresión (9) proporciona un valor complejo para la frecuencia. La parte real corresponde a la frecuencia natural de la viga, mientras que la parte imaginaria contiene información sobre el amortiguamiento de la misma, es decir:

$$\omega_n^{2*} = \omega_n^2 (1 + i\eta_n) \quad (12)$$

siendo η_n es el amortiguamiento de la viga.

4.2 Aplicación del modelo RKU a vigas de vidrio laminado.

Los valores de las frecuencias naturales y amortiguamientos de las distintas vigas de vidrio laminado estudiadas, se obtuvieron mediante un proceso iterativo, ver Figura 3.

Partiendo de los valores del número de onda de una viga de Euler-Bernoulli (Tabla 1), se obtiene una estimación de la frecuencia natural para una viga de vidrio monolítico, ω_{n0} . A partir de este valor de frecuencia se obtiene el módulo dinámico del PVB $G_2^*(\omega, T)$, el parámetro de cortadura g^* (ecuación 11) y la rigidez compleja de la viga $(EI)^*$ (ecuación 10). El proceso iterativo concluye cuando converge la ecuación (9).

Mediante este proceso se estiman las frecuencias naturales e índices de amortiguamiento en vigas de vidrio laminado de diversos espesores y longitudes con dos condiciones de contorno: libre-libre y biapoyadas. Las características mecánicas y geométricas de las vigas consideradas pueden verse en la Tabla 2, mientras que las frecuencias naturales y los índices de amortiguamiento obtenidos con este modelo, se indican en las Tablas 3 y 4.

Un proceso iterativo semejante al anterior se ha empleado también mediante el modelo propuesto por Mead. Ambos métodos, RKU y Mead proporcionan aproximadamente los mismos resultados de ω_n y η_n para las vigas de vidrio laminado.

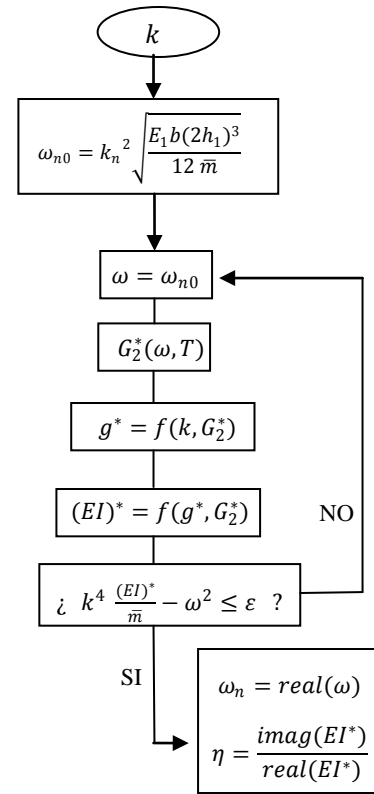


Figura 3. Esquema del proceso iterativo empleado para obtener los parámetros modales analíticamente, donde ϵ es la tolerancia de convergencia.

6. ENSAYOS DINÁMICOS EN VIGAS DE VIDRIO LAMINADO

Las predicciones realizadas con el modelo RKU se validaron con ensayos modales operacionales, a partir de los cuales se obtienen los parámetros modales de las vigas (frecuencias naturales, ω_n , modos de vibración, Φ_n , e índices de amortiguamiento, ζ_n .)

5.1. Descripción de ensayos

Los ensayos modales se realizaron aplicando una carga aleatoria mediante impactos sucesivos. Las respuestas en aceleración se registraron utilizando 8 acelerómetros Brüel & Kjær 4508B, dispuestos equiespaciadamente, Figura 4. Las aceleraciones se registraron con una tarjeta DSA 4472 PCI y la aplicación LabView, ambas de la firma Nacional Instruments.

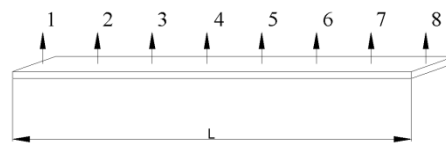


Figura 4. Distribución de los acelerómetros en las vigas de vidrio laminado

Los parámetros modales se estimaron aplicando los métodos de identificación de subespacios estocásticos (SSI) [11], concretamente CVA-SSI, implementado en la aplicación ARTEMIS Extractor. En cada ensayo se registraron las aceleraciones durante un tiempo de 2 minutos a una frecuencia de muestreo de 4000 Hz. Para cada viga se identificaron los cuatro primeros modos de flexión y se controló la temperatura de la viga con un termopar. Los resultados obtenidos experimentalmente se muestran en las Tablas 3 y 4.

Tabla 2. Características de las vigas de vidrio laminado

	Viga 1	Viga 2	Viga 3
ρ_1 [kg/m ³]	2500		
ρ_2 [kg/m ³]	1070		
b [m]	0.1		
L [m]	1	1	1.4
H ₁ [mm]	3	4	4
H ₂ [mm]	0.38	0.38	0.38

7. ANÁLISIS DE LOS RESULTADOS

En las Tablas 3 y 4 se observa que las frecuencias naturales obtenidas analíticamente son ligeramente superiores a los resultados experimentales. El promedio de los errores relativos cometidos es del 3%, por lo que el modelo de RKU estima con una precisión razonable las frecuencias naturales. Por otro lado, en el cálculo analítico sólo se ha tenido en cuenta la masa de la viga, despreciando la influencia de la masa de los acelerómetros, cableado, etc. Por tanto, si se hubiera tenido en cuenta estas masas los errores hubiesen sido menores.

Tabla 3. Frecuencias naturales experimentales y analíticas para vigas libre-libre

Viga	Modo	T [°C]	fn [Hz]		ε [%]
			EXPERIMENTAL	ANALÍTICO	
1	1	25.7	31.9	34.4	7.2
	2	25.7	86.9	94.0	7.6
	3	25.7	172.1	182.7	5.8
	4	25.7	280.5	298.9	6.2
2	1	25.5	44.1	45.3	2.6
	2	25.5	120.3	123.6	2.7
	3	25.5	232.9	239.6	2.8
	4	25.5	378.3	390.6	3.1
3	1	24.4	22.5	23.2	3.1
	2	24.4	62.0	63.6	2.6
	3	24.4	121.0	123.9	2.3
	4	24.4	198.0	203.3	2.6

En lo que se refiere al amortiguamiento, los resultados presentan bastante dispersión, efecto que, por otra parte es habitual en análisis modal. Las predicciones analíticas y los resultados experimentales se muestran en las Figuras 5 y 6, en las que se observa que los

valores obtenidos experimentalmente son mayores que las estimaciones analíticas. El promedio de los errores relativos cometidos, sin considerar el primer modo donde los errores son superiores, es del 28%. En las representaciones de las Figuras 5 y 6 se ha supuesto que el amortiguamiento viscoelástico η , es el doble del amortiguamiento modal ζ , es decir: $\eta=2\zeta$.

Tabla 4. Frecuencias naturales experimentales y analíticas para vigas biapoyadas.

Viga	Modo	T [°C]	fn [Hz]		ε [%]
			EXPERIMENTAL	ANALÍTICO	
1	1	25.1	14.8	15.2	2.9
	2	25.1	57.9	60.5	4.3
	3	25.1	129	135.1	4.5
	4	25.1	226.7	237.9	4.7
2	1	24.4	19.9	20.1	0.8
	2	24.4	78.4	79.7	1.6
	3	24.4	173.7	177.6	2.2
	4	24.4	304.2	311.7	2.4
3	1	24.9	10.6	10.3	3.4
	2	24.9	40.9	40.8	0.3
	3	24.9	91.0	91.2	0.3
	4	24.9	160.2	161.2	0.6

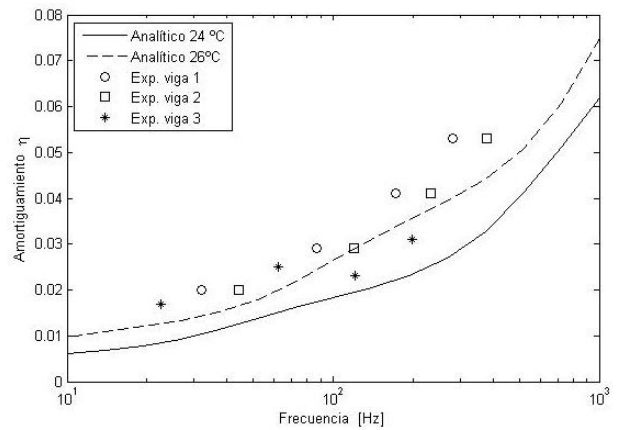


Figura 5. Índices de amortiguamiento de las vigas libre-libre, en función de la frecuencia.

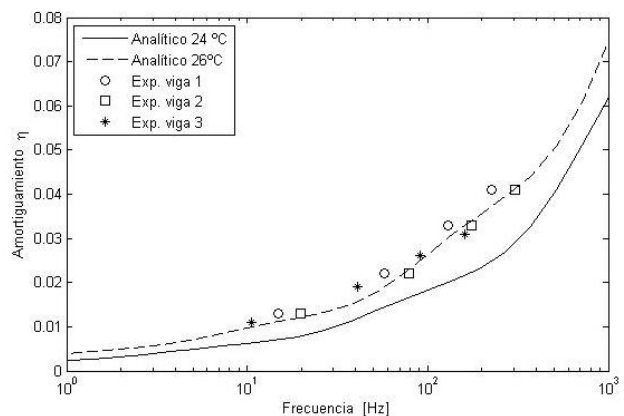


Figura 6. Índices de amortiguamiento de las vigas biapoyadas, en función de la frecuencia.

8. EFECTO DE LA TEMPERATURA

Resulta importante destacar la gran influencia que tiene la temperatura de la lámina de PVB en los resultados modales, especialmente en el amortiguamiento. Este efecto se ha comprobado tanto experimental como analíticamente, Figura 7. Por tanto, resulta imprescindible el control preciso de la temperatura en los ensayos.

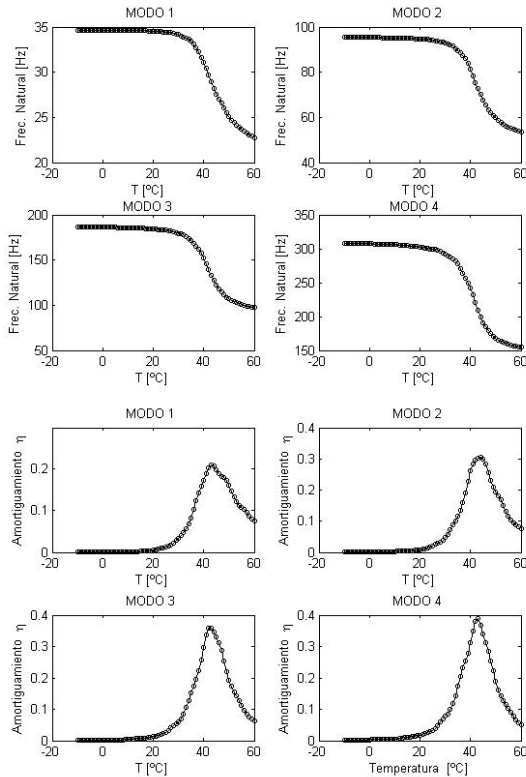


Figura 7. Influencia de la temperatura en los valores modales. Estimaciones del modelo RKU para la viga I.

9. CONCLUSIONES

- Se han estimado los parámetros modales de vigas de vidrio laminado mediante el modelo de RKU y el modelo de Mead. Los ensayos modales realizados confirman que estos modelos predicen con una precisión razonable las frecuencias naturales de estos elementos, mientras que existe una gran dispersión en los índices de amortiguamiento.
- La temperatura es una variable fundamental, que tiene una gran influencia en el comportamiento dinámico de las vigas de vidrio laminado, especialmente en el amortiguamiento.

AGRADECIMIENTOS

Los autores agradecen la financiación económica recibida de la CICYT a través del proyecto de investigación BIA2008-06816-C02-01.

REFERENCIAS

- [1] Tschoegl N.W.; Knauss W.G.; Emri I. *Poisson's Ratio in Linear Viscoelasticity – A critical review.* Mechanics of Time-Dependent Materials, Volume 6, Number 1, 2002 , pp. 3-51(49).
- [2] P. Fernández Fernández, D. Rodríguez Argüelles, M.J. Lamela Rey, A. Fernández Canteli. *Estudio de la interconversión entre las funciones de comportamiento de un material viscoelástico.* Anales de Mecánica de la Fractura 26, Vol. 1 (2009)
- [3] Ferry, J. D. *Viscoelastic Properties of Polymers.* John Wiley & Sons. 3ª Edición, New York. (1980).
- [4] Williams, M.L., Robert F. Landel and John Ferry. *The Temperature Dependence of Relaxation Mechanisms in Amorphous Polymers and Other Glass-forming Liquids.* Department of chemistry, niversity of Wisconsin. 1955.
- [5] Alex Van Duser, Anand Jagota, Stephen J. Bennison. *Analysis of glass/polyvinylbutyral laminates subjected to uniform pressure.* Journal of Engineering Mechanics, 125(4):435–442, April 1999.
- [6] R. Brincker, C. Ventura and P. Andersen: *Why Output-Only Modal Testing is a Desirable Tool for a Wide Range of Practical Applications.* In Proc. Of the International Modal Analysis Conference (IMAC) XXI, paper 265, February, 2003.
- [7] Ross, D., Ungar, E.E., Kerwin, E.M. Jr. 1959. *Damping of plate flexural vibrations by means of viscoelastic laminate.* In ASME (Ed.). *Structural Damping* (pp. 49-88). New York: ASME.
- [8] Mead, D.J., and Markus, S. 1969. *The forced vibration of a three-layer, damped sandwich beam with arbitrary boundary conditions.* Journal of Sound and Vibration. 10(2), 163-175.
- [9] Jones D.I.G., *Reflections on damping technology at the end of the twentieth century.* Journal of Sound and Vibration,190(3).449462. 1996
- [10] Jones, D.I.G., *Handbook of viscoelastic vibration damping.* John Wiley&Sons, Ltd, 2001.
- [11] Van Overschee, P., De Moor, B. *Subspace identification for linear systems – Theory, Implementation, Applications,* Kluwer Academic Publishers, Dordrecht, The Netherlands,1996.

FRACTURA ANISÓTROPA DE ALAMBRES DE PRETENSADO COMERCIAL SOMETIDOS A ENSAYOS DE CORROSIÓN BAJO TENSIÓN

F. J. Ayaso, A. Fernández-Viña y J. Toribio

Ingeniería de Materiales, Universidad de Salamanca
E.P.S., Campus Viriato, Avda. Requejo 33, 49022 Zamora
Telf: (980) 54 50 00; Fax: (980) 54 50 02, Correo-e: fja@usal.es

RESUMEN

En este artículo se estudia el comportamiento anisótropo en fractura que exhiben probetas, inicialmente lisas, de alambres de acero de pretensado comercial sometidos a ensayos de tracción en presencia de un ambiente agresivo generado por una célula de corrosión. Se han empleado dos velocidades de ensayo, una velocidad moderadamente rápida (0,1 mm/min) y una velocidad moderadamente lenta (0,01 mm/min). En cuanto al potencial se refiere se ha trabajado con un amplio espectro del mismo (desde -400 hasta -1400 mV ECS), abarcando desde condiciones anódicas hasta condiciones catódicas. Como resultado de la investigación se ha observado que las probetas que han fallado como consecuencia del ambiente agresivo (dentro de la célula de corrosión) muestran una superficie de fractura con un marcado comportamiento anisótropo, esto es, manifiestan desviaciones muy acusadas del camino de fractura desde su zona de inicio hasta su zona de llegada, siendo dichas desviaciones mayores que las observadas en las probetas que han fallado en ambiente inerte (fuera de la célula de corrosión).

ABSTRACT

This paper analyses the anisotropic fracture behaviour exhibited by initially-smooth samples of commercial prestressing steel wires subjected to tensile tests in aggressive environment promoted by a corrosion cell. Two testing rates were used: one moderately fast (0,1 mm/min) and another moderately slow (0,01 mm/min). The electro-chemical potential used covers a wide range (from -400 to -1400 mV SCE), thus including from anodic to cathodic conditions. As a result from the study, a clear anisotropic fracture behaviour was exhibited by those samples failing as a consequence of the aggressive environment (fracture of specimen inside the corrosion cell). The anisotropic fracture behaviour shows marked deviations of the fracture path from the initial fracture zone till the fracture end zone, such deviations being higher than those observed in the specimens failing in inert environment (outside the corrosion cell).

PALABRAS CLAVE: Acero perlítico, Trefilado, Fragilización por Hidrógeno.

1. INTRODUCCIÓN

En el presente artículo se estudia la corrosión bajo tensión (CBT) de alambres de acero perlítico trefilado comercial destinado a formar parte de estructuras de hormigón pretensado. El estudio se lleva a cabo mediante ensayos de tracción hasta fractura realizados sobre probetas representativas del acero perlítico trefilado (producto comercial, listo para su puesta en servicio). Los ensayos se realizan con la presencia de una célula de corrosión para simular las condiciones electro-químicas que existen en la punta de una fisura presente en el acero perlítico en su puesta en servicio como armadura activa del hormigón. Los ensayos se han llevado a cabo a dos velocidades de sollicitación (0.1 y 0.01 mm/min respectivamente), bajo la presencia de una disolución corrosiva (pH = 12.5) y empleando diversos potenciales ECS (*electrodo de calomelanos saturado*), desde -400 hasta -1400 mV, abarcando de esta forma tanto el estudio de la disolución anódica

localizada (DAL) como de la fisuración asistida por hidrógeno (FAH). En cuanto a las propiedades mecánicas, se ha observado una disminución de la carga de rotura, así como de la ductilidad, de los distintos alambres estudiados. En cuanto a su comportamiento en fractura, se ha centrado el estudio tanto en el inicio como en la propagación de la misma, atendiendo a los diferentes micro-mecanismos que la gobiernan.

2. PROCEDIMIENTO EXPERIMENTAL

Para la realización de los ensayos se han empleado probetas lisas de acero perlítico correspondiente a la última etapa del proceso de trefilado, i.e., alambre de pretensado comercial; las probetas tienen una longitud y diámetro de 300 y 5 mm respectivamente. Para la realización de los ensayos de tracción hasta rotura se han empleado dos velocidades de sollicitación (ensayos en control de velocidad), una velocidad moderadamente rápida (0.1 mm/min) y otra moderadamente lenta (0.01

mm/min). Para estudiar la influencia del fenómeno de CBT se han tenido en cuenta dos categorías básicas: los mecanismos catódicos y los anódicos, definiéndose ambos en función de su ubicación respecto a la línea de descarga de hidrógeno (H) mostrada mediante trazo discontinuo en el diagrama de Pourbaix (Fig. 1).

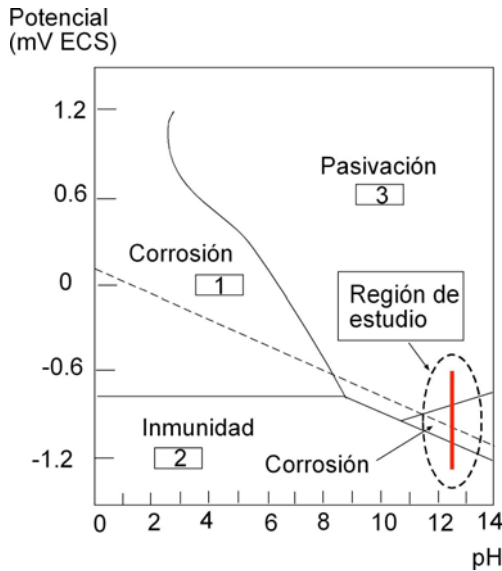


Fig. 1. Diagrama de Pourbaix Fe-H₂O: se indica la región de estudio del presente trabajo.

Los mecanismos catódicos se establecen con una combinación de potencial electroquímico-pH de la disolución corrosiva por debajo de la línea de descarga de H, caracterizándose tales mecanismos mediante la absorción, difusión y fragilización por H (i.e., fisuración asistida por hidrógeno, FAH). El paso de una corriente eléctrica a través de la disolución provoca la disociación del agua en iones H⁺ los cuales se adherirán a la superficie de la probeta, penetrando en su interior y reduciendo su resistencia y ductilidad, efectos que se producen hasta alcanzar una concentración crítica que provoca la rotura final [1]. Cuando la combinación potencial electroquímico-pH se sitúa por encima de la línea de descarga de hidrógeno (H) el mecanismo es anódico, i.e., la disolución corrosiva arranca átomos de la aleación en contacto, formándose sales y precipitados de hierro (disolución anódica localizada, DAL).

Para el presente estudio el pH de la disolución ha sido de 12.5, empleando valores del potencial desde -400 hasta -1400 mV ECS, con un incremento de -200 mV en cada tramo. La elección de los potenciales se ha realizado a partir de estudios previos [2-5]. El acero empleado es del tipo eutectoide con la composición indicada en la Tabla 1, en cuanto a sus propiedades mecánicas el acero posee los siguientes valores: E= 208 GPa, σ_Y = 1.49 GPa y σ_R = 1.83 GPa. En cuanto a la disolución corrosiva se refiere ésta se ha mantenido a un pH de 12.5 para todos los ensayos realizados, siendo una disolución en agua destilada de 0.2 gramos de Ca(OH)₂ y de 0.02 gramos de NaCl. En la Fig. 2 se

representa el montaje de la probeta con su célula de corrosión de la máquina de ensayo. Cabe señalar en este punto que se han ensayado tres probetas para cada tipo de ensayo, función del potencial electro-químico y de la velocidad empleada

Tabla 1. Composición química del acero (%).

C	Mn	Si	P	S	Al	Cr	V
0.79	0.68	0.21	0.01	0.01	0.003	0.22	0.06

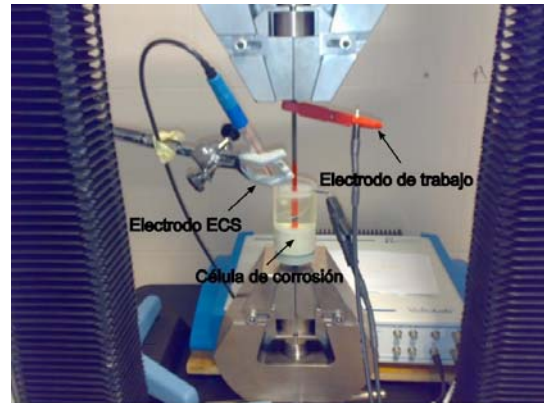


Fig. 2. Disposición de la probeta y de la célula de corrosión en la máquina de ensayo.

3. RESULTADOS

Un primer resultado que se observa a partir de los distintos ensayos realizados es que todas las probetas ensayadas entre -200 y -1000 mV ECS alcanzan la fractura final sin verse afectadas por el medio corrosivo instalado mediante la célula de corrosión y, para ambas velocidades de ensayo empleadas, la fractura (del tipo copa y cono) se produce en zonas muy distantes a dicha célula de corrosión, pudiéndose establecer como una *fractura en aire* o *fractura en ambiente inerte* (FAI) puesto que las probetas no se ven afectadas por el medio agresivo. Por el contrario, las probetas ensayadas en el rango entre -1200 y -1400 mV ECS muestran un claro comportamiento de *fractura en ambiente agresivo* (FAA) para ambas velocidades de ensayo estudiadas, obteniéndose que la fractura se produce dentro de la célula de corrosión y con claros signos del fenómeno de corrosión bajo tensión (CBT).

En vista de lo indicado en el párrafo anterior se realizaron ensayos a -1100 mV ECS para ambas velocidades de ensayo, encontrándose que para la velocidad de 0.01 mm/min todas las probetas rompieron por efectos del medio agresivo, mientras que para la velocidad más alta (0.1 mm/min) sólo una probeta se ha visto afectada por el medio agresivo; las otras dos alcanzaron la fractura final en secciones muy distantes con relación a la célula de corrosión instalada (fractura en ambiente inerte).

En la tabla nº 2 se indican las variaciones observadas en cuanto a la carga de rotura, alargamiento hasta rotura y ductilidad con relación al comportamiento en fractura de dichas probetas en ambiente inerte [6]. En la mencionada tabla se observa que la disminución de la carga de rotura F_R en ambiente inerte es insignificante para los ensayos realizados a 0.1 mm/min y más acusada para los ensayos efectuados a 0.01 mm/min, notándose también en este último caso que la disminución de F_R es más acusada cuanto menor es el potencial aplicado, aunque dicha disminución no es muy significativa (valores inferiores a un 5%).

Tabla 2. Disminución de la carga de rotura (F_R), del alargamiento hasta rotura (u_R) y de la ductilidad (Z) con relación a los ensayos en ambiente inerte.

		Potencial (mV ECS)		
		-1100	-1200	-1400
	Velocidad (mm/min)			
ΔF_R (%)	0.1	-1.239	-0.310	-0.208
	0.01	-0.684	-3.997	-4.276
Δu_R (%)	0.1	-0.952	-19.290	-15.849
	0.01	-20.104	-38.311	-39.354
ΔZ (%)	0.1	-19.821	-20.833	-17.313
	0.01	-15.398	-16.999	-14.962

En cuanto a la variación del alargamiento de las probetas en el instante de producirse la fractura final (u_R), así como de su ductilidad medida a través del porcentaje de reducción de área (Z), ésta se produce de forma más acusada que en el caso de la F_R . De forma general se observa que la disminución del alargamiento que soportan las probetas previo a la fractura final Δu_R es más acusada en los ensayos realizados a baja velocidad, así como una tendencia a ser mayor dicha disminución cuanto menor es el potencial empleado. Para el caso de la ductilidad, la cual al ser una medida del grado de deformación plástica que soporta un material también puede considerarse como una medida del grado de *fragilización* del material durante los ensayos realizados, se ha obtenido que la mayor disminución ΔZ la han soportado las probetas ensayadas a baja velocidad (0.01 mm/min), obteniéndose –para ambas velocidades de ensayo– que los valores máximos de ΔZ a -1200 mV y los mínimos a -1400 mV.

El comportamiento en fractura que muestran las probetas que sí han fallado bajo la influencia del medio corrosivo (rango de potenciales -1100 hasta -1400 mV ECS para ambas velocidades de sollicitación) es bastante similar entre sí. En las Figs. 3 y 4 se muestra la fractografía en planta y en perfil de las superficies de fractura de dos probetas ensayadas bajo distintas condiciones, no apreciándose diferencias significativas, si bien se puede observar un claro comportamiento anisótropo en fractura en las vistas de perfil.

Con independencia de las condiciones de ensayo, las probetas que se han fracturado por el fenómeno de CBT

exhiben un comportamiento anisótropo en fractura, esto es, su superficie de fractura presenta una marcada deflexión con relación al plano diametral del alambre, mostrando un superficie de fractura en diversos planos y de forma muy diversa, véanse las Figs. 3a y 4b a modo de ilustración de dicho comportamiento en fractura.

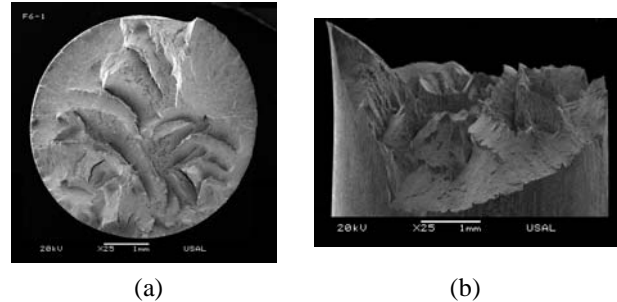


Fig. 3. Fractografía en planta (a) y en perfil (b) de una probeta ensayada a 0,1 mm/min y -1400 mV ECS.

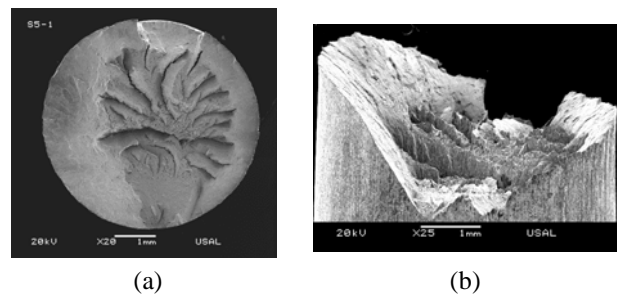


Fig. 4. Fractografía en planta (a) y en perfil (b) de una probeta ensayada a 0,01 mm/min y -1200 mV ECS.

Esquemáticamente el comportamiento en fractura de las probetas ensayadas se puede describir en cuatro zonas según se representa en la Fig. 5: una primera zona (1) en la cual se observa una fractura con topografía de desgarramiento TTS (*tearing topography surface*, cf [4,5]) con un ángulo de orientación α_1 (con relación al diámetro del alambre) muy elevado (Fig. 6); una segunda zona (2) asociada con el inicio de la zona intermedia ZI y en la cual microscópicamente se observa una suerte de marcas curvas y paralelas muy similares a las estrías de fatiga con un espaciado o separación entre dos marcas consecutivas mucho mayor que en aquéllas (Fig. 7), pero que observada a menor escala muestra que es una fractografía conjunta formada por TTS y micro-huecos con aspecto irregular y rugoso denominada CMH* [7], formando pequeñas elevaciones y depresiones (a modo de micro-valles y micro-crestas) con un ángulo de inclinación moderado α_2 . La parte final de la zona intermedia (3) tiene un ángulo de inclinación α_3 más suave que los anteriores y presenta una fractografía a base de coalescencia de microhuecos (Fig. 8) y con presencia ocasional de facetas muy aisladas de clivaje CMH (+C); finalmente se observa la existencia de una cuarta zona (4), que se corresponde con la corona exterior (CE) final típica con un ángulo α_4 aproximado de 45°, formada por microhuecos de tamaño pequeño, uniformemente distribuidos y de aspecto liso, tal como se representa en la Fig. 9.

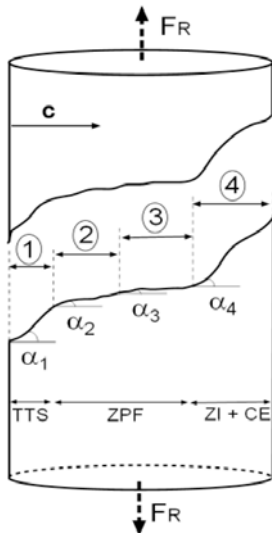


Fig. 5. Esquema del comportamiento anisótropo en fractura: vista longitudinal del alambre.

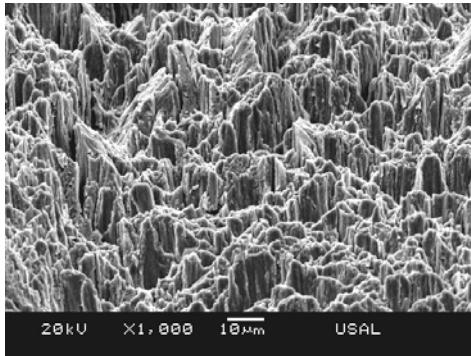


Fig. 6. Escalones abruptos en la zona TTS.

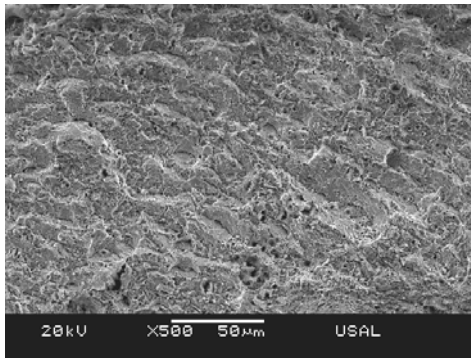


Fig. 7. Zona intermedia: marcas como estrías de fatiga.

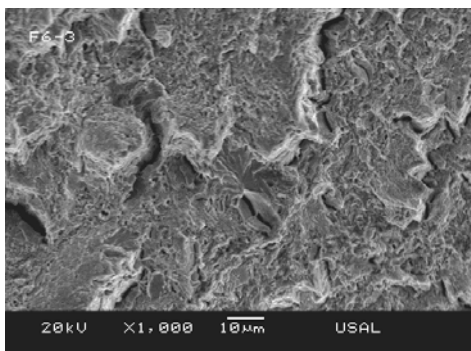


Fig. 8. CMH y presencia aislada de clivaje: CMH (+C).

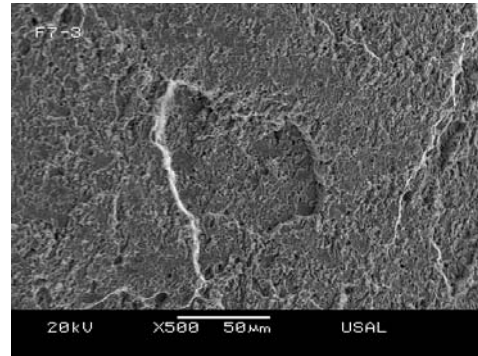


Fig. 9. Corona exterior: coalescencia de microhuecos.

4. DISCUSIÓN

El análisis de la superficie externa del alambre, una vez fracturado, ha permitido comprobar al menos dos formas de introducción de H en el alambre de acero para provocar en un principio la fisuración asistida por el mismo, manifestando dicho daño en la forma de una fractografía tipo TTS –para todas las condiciones de contorno del ensayo realizado (velocidad y potencial electroquímico)–. La primera de ellas es la presencia de defectos en la superficie externa del alambre de acero de pretensado; dichos defectos son concentradores de tensiones que facilitan de esta forma, a modo de puertas de entrada, que el H se difunda hacia el interior del alambre por difusión atómica. En la Fig. 10 se muestra el rastro de un defecto superficial generado debido a la más que posible incrustación de una partícula externa dura en el alambre durante el proceso de trefilado.

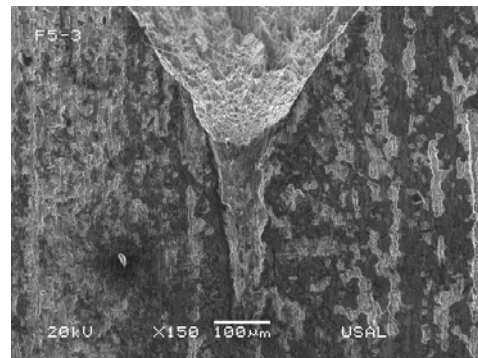


Fig. 10. Defecto en la superficie externa del alambre.

La segunda forma de introducción del hidrógeno (H) dentro del material se ha podido observar que se produce a través de pequeñas bandas de deslizamiento que aparecen en la superficie externa del alambre como consecuencia de la deformación plástica que soporta el mismo durante el ensayo de tracción, o incluso durante el proceso de trefilado, toda vez que se supera el límite elástico del material (Fig. 11). En estas bandas de deslizamiento se concentra una alta densidad de dislocaciones que pueden transportar el H hacia el interior del material. A medida que transcurre el ensayo la tensión hidrostática generada durante el mismo aumenta, así como también aumenta la presencia de

estas bandas de deslizamiento al igual que lo hace la densidad de dislocaciones, permitiendo de esta manera la penetración de un mayor flujo de H hacia el interior del alambre. Externamente esto se traduce en una suerte de microfisuraciones orientadas 45° con relación al eje longitudinal del alambre (al igual que las bandas de deslizamiento, Fig. 12), microfisuras que a veces alcanzan un tamaño subcrítico, i.e., no producen la fractura final del material (Fig. 13) aunque en el interior de ellas existe una fractografía tipo TTS, mientras que otras si llegan a provocar la fractura total del alambre, tal y como se representa en la Fig. 13, donde se aprecia que la fractura final tiene el mismo perfil de inicio que las microfisuras existentes en la pared exterior.

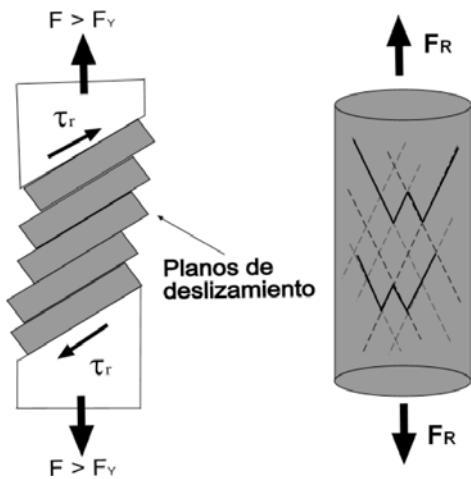


Fig. 11. Deformación plástica por deslizamiento.

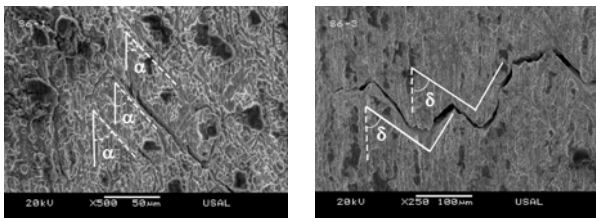


Fig. 12. Fisuración subcrítica del alambre por H.

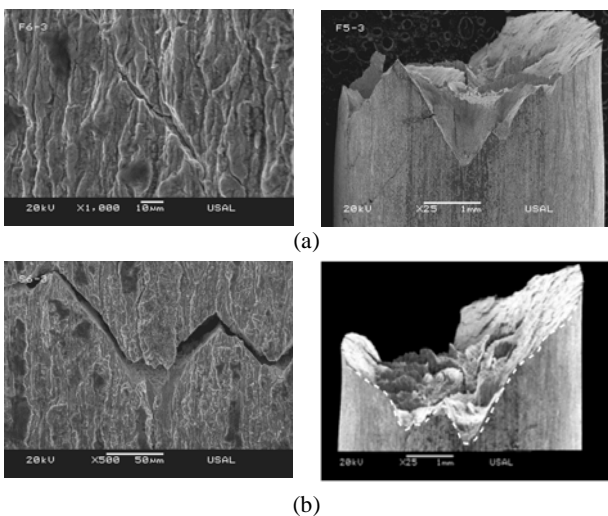


Fig. 13. Correspondencia de la fisuración superficial de los alambres con la morfología de la fractura final.

La observación al microscopio de las *marcas como estrías de fatiga* (Figs. 7 y 8) en la zona de proceso de fractura, inmediatamente posterior a la primera zona de fractura inicial por TTS, ha permitido constatar que está formada tanto por una topografía irregular de microhuecos (CMH*) como por topografía de fractura por desgarramiento (TTS) gracias a la acción del hidrógeno. Observando con más detalle dicha zona se puede distinguir diversas colonias de perlita (en la forma de grupos de pequeñas láminas paralelas) en determinados lugares de la superficie de fractura examinada, dando la apariencia de una fractura transcolonial (Fig. 14).

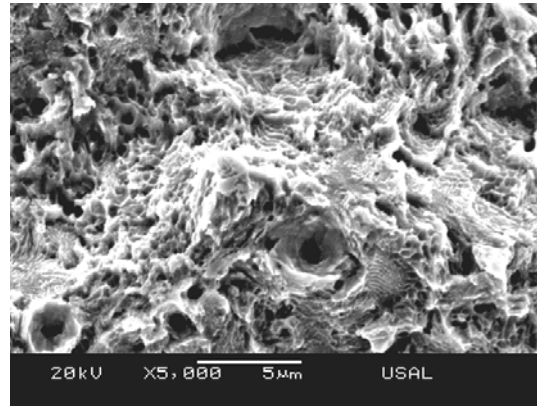


Fig. 14. Detalle de la zona de proceso de fractura

Ahora bien, visto lo indicado en párrafos anteriores cabe tener en cuenta lo siguiente con relación a la zona de inicio de fractura por TTS, así como a la zona de proceso de fractura (ZPF) adyacente:

- ✓ clara presencia de colonias perlíticas;
- ✓ el espaciado medio entre las distintas *marcas como estrías* (entre dos crestas o dos valles consecutivos) es de un valor claramente superior ($\approx 18 \mu\text{m}$) al del espesor medio de las colonias perlíticas ($\approx 4 \mu\text{m}$) en el material fuertemente endurecido por deformación;
- ✓ que en esta ZPF (así como en la zona de inicio de fractura por TTS) el avance del camino de fractura se realiza de forma escalonada, tendiendo a desviarse claramente hacia la dirección del eje longitudinal del alambre (dirección del trefilado),

por lo que puede establecerse la hipótesis de que el camino de fractura se propaga a través del límite del grano austenítico previo muy deformado en la dirección de trefilado al igual que la microestructura perlítica [8], dando lugar a una fractura del tipo transgranular. Conocido es que el grano austenítico se transforma en diversas colonias perlíticas por debajo de la temperatura eutectoide, desapareciendo dicho grano como tal; por otra parte durante la fabricación del acero, atendiendo a su obtención a partir del estado líquido (colada) existe un intervalo de tiempo –así como de temperaturas– en el cual todo el acero se encuentra en estado austenítico, tiempo durante el cual diversas sustancias se difunden preferente hacia los límites de grano de la austenita para disminuir la energía superficial asociada al propio límite de grano (existencia de un gran número de átomos sin

enlazar), sustancias las cuales permanecen en dichas posiciones durante la transformación perlítica, así como también el propio límite de grano de la austenita. Muchas de las sustancias que emigran hacia los límites de grano son de carácter frágil o se vuelven frágiles bajo la presencia de un ambiente corrosivo, y es aquí donde entra en juego la presencia del hidrógeno (H) durante los ensayos de tracción en ambiente agresivo realizados, tal y como se esquematiza en la Fig. 15:

1. El H penetra en el material mediante difusión atómica creando una fisuración inicial mediante micro-desgarros (fractografía tipo TTS).
2. Una vez dentro del material el H se puede mover con relativa facilidad a través del rastro que ha dejado el límite del grano austenítico previo (GAP).
3. Al difundirse el H por el límite del GAP debilita enlaces atómicos que encuentra en su camino (ayudado por la más que posible presencia de partículas fragilizantes en dicha zona) dando lugar a una futura fractura a través de la huella dejada por el propio límite del GAP, creando de esta forma la zona de proceso de fractura ZPF, dejando a la vista las colonias perlíticas en contacto con dicho borde.
4. Finalmente el material restante no es capaz de soportar la tensión remota, dando lugar a la rotura catastrófica del mismo: zona intermedia (ZI) y corona exterior (CE).

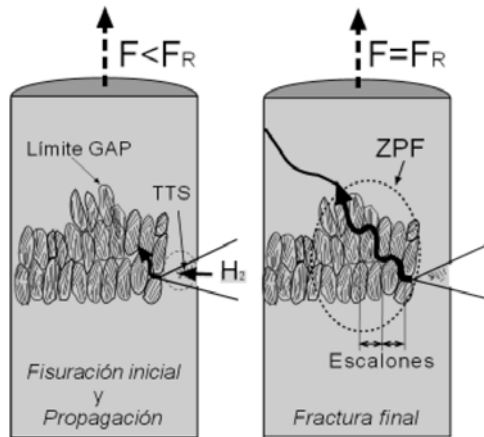


Fig. 15. Esquema de la propagación del camino de fractura a través del límite del grano austenítico previo.

5. CONCLUSIONES

Se ha realizado un estudio de CBT sobre probetas representativas de acero perlítico trefilado comercial bajo distintas condiciones de ensayo, en cuanto a velocidad y potencial electroquímico se refiere, llegando a las siguientes conclusiones:

- ✓ Bajo las condiciones de ensayo empleadas las probetas sólo muestran signos de Corrosión Bajo Tensión a potenciales por debajo de -1100 mV.
- ✓ Desde el punto de vista de la respuesta mecánica de las probetas durante los ensayos se observa una notoria merma de su capacidad para deformarse

plásticamente a medida que el ensayo es más lento (0.01 mm/min) con independencia del potencial empleado. En cuanto a la disminución de la carga de rotura, ésta se puede considerar despreciable para todos los casos estudiados.

- ✓ Se observa un claro comportamiento anisótropo en fractura (muy distinto a la fractura en copa y cono en ambiente inerte) entre -1100 y -1400 mV ECS.
- ✓ Se propone un mecanismo de difusión de hidrógeno a través del *límite del grano austenítico previo* como canal inductor del marcado comportamiento anisótropo en fractura del material, provocando una fisuración progresiva y subcrítica (previa a la fractura final de las probetas) que genera una superficie de fractura *escalonada*. Macroscópicamente, dicha fisuración subcrítica se muestra como unas “*marcas como estrías de fatiga*” las cuales, examinadas a escala microscópica, muestran unos escalones con una fractografía tipo CMH* + TTS, dejando a la vista diversas colonias perlíticas.

AGRADECIMIENTOS

Los autores desean hacer constar su agradecimiento a las siguientes instituciones financiadoras: MCYT (Proyecto MAT2002-01831), MEC (Proyecto BIA2005-08965), MCINN (Proyecto BIA2008-06810), JCyL (Proyectos SA067A05, SA111A07 y SA039A08), y a Trefilerías Quijano por el suministro del material.

BIBLIOGRAFÍA

- [1] Kharin, V. *et. al.* “Influencia del campo residual tenso-deformacional en la fragilización por hidrógeno de aceros de pretensado”. *Anales de Mecánica de la Fractura* 23, vol. 1, 207-212 (2006).
- [2] Parkins, R.N., Elices, M., Sánchez-Gálvez, V., Caballero, L. “Environment sensitive cracking of prestressing steels”. *Corrosion Science* 22, 379-405 (1982).
- [3] Sánchez-Gálvez, V., Caballero, L., Elices, M. “The effect of strain rate on the stress corrosion cracking of steels for prestressing concrete”. *ASTM STP* 866, 428-436 (1985).
- [4] Lancha, A.M. “Influencia del trefilado en la corrosión bajo tensión de aceros eutectoides”. Tesis Doctoral, Universidad Complutense de Madrid (1987).
- [5] Ovejero, E. “Fractura en ambiente agresivo de aceros perlíticos con distinto grado de trefilado”. Tesis Doctoral, Universidad de La Coruña (1998).
- [6] Ayaso, F. J. *et. al.* “Análisis fractográfico cuantitativo del comportamiento en fractura de aceros perlíticos progresivamente trefilados”. *Anales de Mecánica de la Fractura* 22, 128-133 (2005).
- [7] Ayaso, J., Toribio, J. “Micromecanismos de fractura en aceros perlíticos progresivamente trefilados”, *Anales de Mecánica de la Fractura* 19, 141-146 (2002).
- [8] Toribio, J., Ovejero, E. “Microstructure evolution in a perlitic steel subjected to progressive plastic deformation”. *Materials Science and Engineering A* 234-236, 579-582 (1997).

UNA REVISIÓN CRÍTICA DE LOS DIFERENTES ENFOQUES INGENIERILES PARA LA EVALUACIÓN DE CONDICIONES DE BAJO CONFINAMIENTO TENSIONAL.

S. Cicero, F. Gutiérrez-Solana. J.M. Varona

Universidad de Cantabria, ETS Ingenieros de Caminos, Canales y Puertos
 Departamento de Ciencia e Ingeniería del Terreno y de los Materiales
 Av/Los Castros s/n, 39005, Santander, Cantabria, Spain
ciceros@unican.es

RESUMEN

En las dos últimas décadas el confinamiento ha sido una de las mayores áreas de investigación en mecánica de la fractura e integridad estructural. La posibilidad de realizar evaluaciones más ajustadas y menos conservadoras (permaneciendo del lado de la seguridad) requiere, en muchos casos, la consideración de las condiciones de confinamiento tensional en el frente del defecto, con el objetivo de realizar mejores predicciones de la capacidad resistente de un componente o del tamaño crítico de defecto correspondiente. A este respecto, se han propuesto diversas metodologías, desde aquellas basadas en modelos micromecánicos (enfoques locales) o métodos energéticos, hasta los basados en enfoques ingenieriles. De entre estos últimos destacan las propuestas de la mecánica de la fractura biparamétrica y, en especial, dos de sus metodologías: la corrección biparamétrica de K_{IC} y la corrección biparamétrica del CTOD.

Desde un punto de vista práctico, los anteriormente llamados enfoques ingenieriles tienen un interés máximo. En este trabajo se presenta una completa revisión de este tipo de metodologías, con especial atención a la propuesta de corrección de confinamiento del FITNET FFS Procedure y a la metodología IST. De igual forma, se valoran las ventajas y desventajas de cada uno de ellos, así como las posibles interacciones entre ambos.

ABSTRACT

In the last two decades, constraint has constituted one of the major issues in fracture mechanics and structural integrity research. The possibility of performing more adjusted less conservative (and still safe) assessments requires, in many cases, the consideration of the constraint conditions in the crack tip in order to make better predictions of the load bearing capacity or the critical crack dimensions. Several methodologies have been proposed, from those based on micromechanical models (local approaches) or energy methods to those based on engineering approaches. Among the latest, two methodologies stand out: the biparametric correction to K_{IC} and the biparametric CTOD constraint correction.

From a practical point of view, the so called engineering approaches are of maximum interest. Here, a complete overview of such methodologies is presented, with special emphasis on the FITNET FFS Procedure proposal for the assessment of loss of constraint and also on the IST methodology. Advantages and disadvantages of both approaches are also discussed, as well as the possible interactions between them.

PALABRAS CLAVE: Confinamiento, tensiones, defecto, FITNET, CTOD.

1. INTRODUCCIÓN

Una fuente de conservadurismo implícita en muchas evaluaciones de integridad estructural es el hecho de que el valor de la tenacidad a fractura utilizado en el cálculo es obtenido a partir de probetas con fisuras profundas sometidas a cargas predominantemente flectoras, de acuerdo con las distintas normas existentes. Sin embargo la resistencia a fractura del material es mayor cuando los ensayos se realizan sobre probetas con fisuras superficiales y/o sometidas a cargas de tracción [1-3], dado que bajo esas condiciones surgen tensiones hidrostáticas y tensiones principales máximas

menores en el frente de fisura, lo que genera un menor grado de confinamiento y un aumento de la resistencia a fractura (tanto frágil como dúctil) del material.

En los últimos años se han desarrollado diversas metodologías para cuantificar la dependencia geométrica de la resistencia a fractura del material mediante el uso de los denominados parámetros de confinamiento. Son varias las teorías o metodologías existentes para el análisis del confinamiento en estructuras fisuradas. Las más comúnmente aceptadas son las aproximaciones locales, los métodos energéticos y la mecánica de la

fractura biparamétrica. Esta última, la más utilizada en la práctica y la analizada en este trabajo, postula que basta con la definición de un segundo parámetro de fractura para la consideración del efecto del confinamiento. Una vez definido dicho parámetro, la evaluación del componente resulta relativamente sencilla. Por esta razón, y porque desde el punto de vista práctico proporciona resultados que pueden llegar a ser tan próximos a la realidad como los proporcionados por otras metodologías con (quizá) mayor base física, en este trabajo se van a denominar “enfoques ingenieriles” a las metodologías de evaluación de la pérdida de confinamiento basadas en la mecánica de la fractura biparamétrica.

2. LA MECÁNICA DE LA FRACTURA BIPARAMÉTRICA

Tomando la integral J como la fuerza motriz, la mecánica de la fractura biparamétrica asume que el crecimiento de fisura a lo largo del frente, s, está gobernado por la expresión:

$$J(s; P, a) = J_R(\Delta a(s), \kappa(s), \text{Temperature}) \quad (1)$$

en donde P es la carga aplicada, a es la longitud de fisura, κ es el parámetro de confinamiento y J_R es una función del material que depende del crecimiento de fisura, Δa .

Se han propuesto diferentes parámetros de confinamiento. Tradicionalmente los más utilizados son la tensión T, el parámetro Q y el parámetro h, aunque en el apartado 4 dedicado a la metodología IST se presentará el parámetro β .

La tensión T se define como el segundo término de la serie de Williams para el campo elástico de tensiones en el frente de una fisura:

$$\sigma_{ij} = \frac{K_I}{\sqrt{2\pi r}} f_{ij}(\theta) + T \delta_{ij} \delta_{ij} \quad (2)$$

en donde K_I es el factor de intensidad de tensiones, δ_{ij} es la delta de Kronecker y $f_{ij}(\theta)$ son funciones de posición en el entorno del frente de fisura.

Los campos de tensiones y deformaciones en el interior de la zona plástica (asumiendo la teoría de pequeñas deformaciones) pueden expresarse de forma aproximada como la solución HRR más un término adicional que representa términos de mayor orden. O’Dowd y Shih [2] proponen la siguiente formulación:

$$\sigma_{ij} = (\sigma_{ij})_{HRR} + Q\sigma_0\delta_{ij} \quad (3)$$

en donde σ_0 es el límite elástico. Estos autores definen el parámetro Q en base a la tensión normal al plano de la fisura:

$$Q = \frac{\sigma_{yy} - (\sigma_{yy})_{T=0}}{\sigma_0} \quad (4)$$

En condiciones de plastificación a pequeña escala, T y Q están relacionados entre sí, siendo la relación dependiente del comportamiento plástico del material.

No hay un acuerdo general acerca de cuál de estos parámetros de confinamiento es el más adecuado.

3. ANÁLISIS DEL CONFINAMIENTO SEGÚN EL PROCEDIMIENTO FITNET FFS

La metodología utilizada por el FITNET FFS [3], antes de la metodología de análisis del confinamiento (apartado 6.4.3 del procedimiento) recoge, en el punto 6.2.3.10, orientaciones sobre la aplicación de este tipo de análisis:

- El beneficio es mayor en componentes sometidos predominantemente a cargas de tracción (frente a las cargas de flexión).
- Los efectos del confinamiento son más significativos en componentes estructurales con defectos superficiales.
- El beneficio proporcionado por el análisis es pequeño en materiales dúctiles analizados con valores de tenacidad asociados al inicio de la propagación, dado que este fenómeno es poco sensible al confinamiento. Implícitamente, indica que este tipo de análisis ha de realizarse con enfoque de desgarro dúctil, más sensible al confinamiento que la iniciación.
- El beneficio es pequeño para valores bajos del parámetro L_r (relación entre la carga aplicada y la de colapso plástico). La razón es que para que la pérdida de confinamiento se va produciendo a medida que aumenta la carga, y valores de L_r reducidos implican cargas bajas.
- El beneficio es reducido en situaciones dominadas por el colapso plástico.

Una vez en el punto 6.4.3, el FITNET FFS propone el enfoque biparamétrico para las evaluaciones de confinamiento en forma de dos alternativas diferenciadas, aplicable tanto al análisis de iniciación como al de desgarro dúctil: el Procedimiento I, mostrado en la Figura 1, consiste en modificar el Diagrama de Fallo (FAD) manteniendo invariable la tenacidad a fractura utilizada para definir K_{rc} ; el Procedimiento II, por su parte, modifica la tenacidad y mantiene invariable el FAD utilizado en cálculos ordinarios. Como puede observarse en la Figura 1, un punto inicialmente situado fuera del Diagrama de Fallo (y,

por lo tanto, evaluado como situación de fallo) puede finalmente quedar dentro del FAD corregido por confinamiento (y, por lo tanto, quedando demostrada su situación segura frente al fallo).

En el Procedimiento I el FAD modificado resulta:

$$K_r = f(L_r)(1 + \alpha(-\beta L_r)^k) \quad ; \quad L_r \leq L_{rmax} \quad (5)$$

en donde α y k son constantes del material que definen la influencia del confinamiento en la tenacidad a fractura y β es una medida normalizada del confinamiento estructural que no hay que confundir con la β de la metodología IST presentada más adelante.

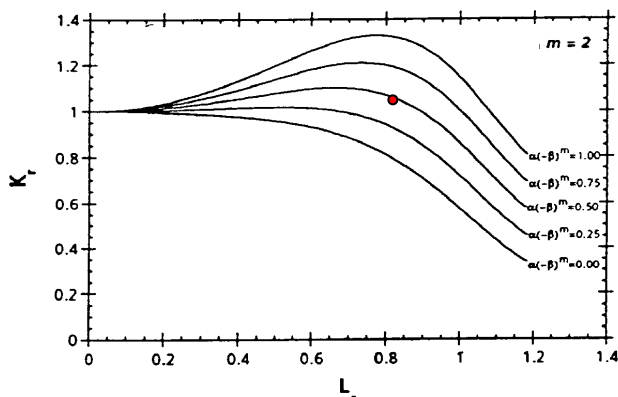


Figura 1. Modificaciones del FAD para distintos valores de los parámetros del material α y k y niveles de confinamiento β (<0).

β puede definirse en función de la tensión T (expresión (6)) o en función del parámetro Q (expresión (7)):

$$\beta_T = \frac{T^p}{L_r \sigma_y} + \frac{T^s}{L_r \sigma_y} \quad (6)$$

$$\beta_Q = \frac{Q}{L_r} \quad (7)$$

en donde T^p y T^s son los valores de la tensión T correspondientes a las tensiones primarias y secundarias.

El método también incorpora una metodología desarrollada en el proyecto VOCALIST [4] que permite obtener los valores de los parámetros α y k a partir del límite elástico y del coeficiente de endurecimiento por deformación del material, así como de su parámetro de forma de la tensión de Weibull, m . Por lo tanto el FITNET, en su propuesta biparamétrica del análisis del confinamiento, hace uso de resultados obtenidos a partir de un modelo de aproximación local (Beremin).

Más allá de la propia metodología de análisis del confinamiento, el procedimiento FITNET FFS pone en relación dicho análisis con dos cuestiones de gran trascendencia en el análisis a fractura: la Curva Maestra [5] y el efecto entalla:

El procedimiento FITNET incluye la formulación propuesta por Wallin para la evaluación del desplazamiento ocasionado por la pérdida de confinamiento en la Curva Maestra. La expresión de la Curva Maestra para situaciones de bajo confinamiento resulta ($T < 0$):

$$K_{mat}^c = 20 \text{ MPa} \sqrt{m} + (K_{mat} - 20) \exp(0.019[-T_{stress}/10 \text{ MPa}]) \quad (8)$$

De igual forma, la relajación tensional ocasionada por las entallas (con el consiguiente aumento de resistencia frente al caso fisurado) no ha sido incluida previamente en ningún procedimiento de fractura. El FITNET FFS, en su apartado 12.5, lo considera otra forma más de pérdida de confinamiento en el plano de aplicación de la carga (independiente de la anterior) y, haciendo uso de la metodología desarrollada en [6], propone la utilización de los modelos de la tensión media crítica [7] o de la mecánica de la fractura finita (MFF) [8] para la evaluación del incremento de tenacidad ocasionado por este tipo de defectos. En el caso del modelo de tensión media crítica, la resistencia a fractura modificada por efecto entalla sería:

$$K_{IN} = K_{IC} \sqrt{1 + \frac{\rho}{2X_{ef}}} \quad (9)$$

Siendo ρ el radio de entalla y X_{ef} la distancia efectiva, definida en [7]. Una vez obtenido el valor de la tenacidad aparente los cálculos continúan de igual forma que en evaluaciones ordinarias.

En el caso de combinarse ambas fuentes de pérdida de confinamiento, el FAD modificado en el Procedimiento I resulta:

$$K_r = f(L_r) \cdot (1 + \alpha(-\beta L_r)^m) \sqrt{1 + \frac{\rho}{2X_{ef}}} \quad L_r \leq L_{rmax} \quad (10)$$

4. ANÁLISIS DEL CONFINAMIENTO SEGÚN LA METODOLOGÍA IST

El proyecto japonés IST (*International Standardization of Fracture Toughness Evaluation Procedure for Fracture Assessment of Steel Structure*) se desarrolló entre los años 2002 y 2005 (simultáneamente al FITNET) con el objetivo de desarrollar un procedimiento de evaluación a fractura de componentes de acero a partir de los valores de tenacidad a fractura obtenidos de

probetas de laboratorio. Se basa en estudios preliminares (ej., [9]) en los cuales se correlaciona el CTOD (*Crack Tip Opening Displacement*) de las probetas normalizadas y de los componentes analizados a un mismo nivel de tensión de Weibull, σ_w .

El enfoque vuelve a ser, al igual que en el FITNET, de tipo biparamétrico, ya que usa un parámetro de fractura tradicional, el CTOD, y un segundo parámetro denominado “ratio equivalente del CTOD”, denominado β en dicho procedimiento y que, para evitar confundirle con el β del FITNET, aquí se va a denominar β_{IST} . De esta manera, el valor crítico del CTOD, δ_{cr} , obtenido en probetas normalizadas se transforma en un valor crítico de CTOD para el componente estructural (a la misma tensión de Weibull), $\delta_{WP,cr}$:

$$\delta_{WP,cr} = \delta_{cr} / \beta_{IST} \quad (11)$$

De esta manera, β_{IST} depende de la relación entre el límite elástico y la tensión de rotura, del parámetro de forma de Weibull (m), de la geometría de la fisura y , en menor medida más allá de los límites de la plasticidad a pequeña escala (*SSY, Small Scale Yielding*), del nivel de deformación alcanzado en el componente estructural.

El análisis a fractura según esta metodología consiste, en definitiva, en dividir por β_{IST} el valor de la tenacidad a fractura obtenida de ensayos normalizados sobre probetas con alto confinamiento. El valor de β_{IST} a utilizar se puede obtener según tres niveles de análisis diferentes, tanto menos conservadores cuanto mayor sea la información disponible:

- *Nivel I* (evaluación simplificada): se aplica a casos en los cuales no se dispone de la información necesaria para estimar β_{IST} . En tales casos se considera un valor por defecto de 0.5, lo cual es un valor tomado por defecto que asegura resultados conservadores.
- *Nivel II* (evaluación normal): se aplica en aquellos casos en los que se conocen las propiedades mecánicas del material y la geometría de la fisura, pero no se conoce el parámetro de forma de la tensión de Weibull, m . En este nivel de análisis, la metodología IST propone utilizar valores por defecto de m : 10 cuando δ_{cr} es inferior a 0.05 mm y 20 cuando es superior a 0.05 mm. Una vez determinado m , proporciona gráficas y formulación para determinar β_{IST} en una serie de geometrías (cuatro tipos diferentes de fisuras en chapas).
- *Nivel III* (evaluación específica): en este caso se determina el valor exacto de m de forma estadística a partir de una serie de resultados experimentales y se aplican las gráficas y la formulación

mencionadas para el Nivel II. Generalmente, este Nivel III de análisis proporciona menores valores de β_{IST} que el Nivel II.

Una vez determinado β_{IST} se obtiene directamente la resistencia a fractura del componente (ecuación (11)) y se pasa a realizar el análisis a fractura según la metodología elegida (ej. FAD).

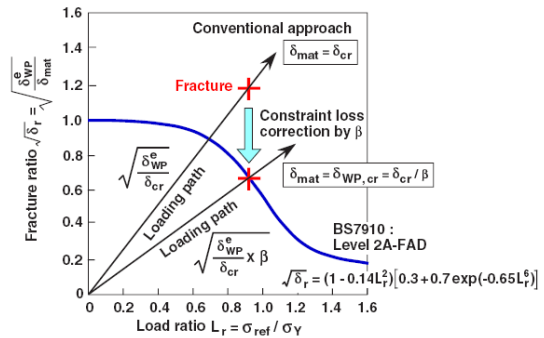


Figura 3. Análisis FAD aplicando la metodología IST [10].

5. VALORACIÓN CRÍTICA DEL FITNET FFS Y DE LA METODOLOGÍA IST

5.1. Valoración y aportaciones del FITNET FFS

En cuanto al FITNET FFS, cabe destacar las siguientes aportaciones:

- Proporciona una orientación acerca de la conveniencia o no de considerar el grado de confinamiento en el análisis, lo cual puede evitar importantes esfuerzos en el análisis que no proporcionan beneficio alguno en el resultado final.
- El análisis mediante la tensión T resulta muy sencillo. Una vez determinado β_T basta con conocer α y k para completar el análisis.
- Propone el uso de la mecánica de la fractura biparamétrica, igual que otros procedimientos, pero lo hace proporcionando una gran cantidad de datos en relación a los parámetros utilizados en el análisis (constantes del material, soluciones para la tensión T ...).
- Se puede aplicar a un gran número de geometrías.
- Puede aplicarse tanto a situaciones frágiles como a situaciones dúctiles.
- Es un método de evaluación del confinamiento muy versátil, ya que aunque describe el análisis en términos de Diagramas de Fallo, permite realizarlo también mediante Diagramas de Fuerza Motriz. De igual modo, pueden realizarse análisis de iniciación o de desgarro dúctil.
- El FITNET FFS incluye a la Curva Maestra como herramienta de análisis del confinamiento.
- Recoge la posibilidad de analizar entallas y fisuras que nacen en el fondo de una entalla. Se trata del primer procedimiento de evaluación de la

integridad estructural que contempla esta posibilidad.

- Finalmente, propone una metodología que permite analizar situaciones en las que se dan de forma simultánea las diferentes fuentes de pérdida de confinamiento en el plano de aplicación de la carga (defecto superficial tipo entalla sometido a cargas de tracción) [6]. De nuevo, el FITNET FFS es el primer procedimiento en recoger esta posibilidad.

Sin embargo, se pueden señalar una serie de cuestiones conceptuales que es necesario considerar al aplicar este procedimiento:

- Las soluciones numéricas de α y k se basan en un análisis de elementos finitos en 2D con condiciones de deformación plana y según un modelo MBL (*Modified Boundary Layer*).
- No considera el efecto del volumen en la tensión de Weibull, σ_w .
- En el caso de realizar el análisis según el parámetro Q , el valor del parámetro de confinamiento estructural, β_Q , varía con el nivel de carga aplicada, por lo que es necesario conocer su valor en rotura. Esto requiere un análisis adicional para determinar dicho valor.

5.2. Valoración y aportaciones de la metodología IST

Las principales aportaciones del procedimiento IST son las siguientes:

- Es un procedimiento de evaluación del confinamiento realmente sencillo, ya que consiste en afectar a la tenacidad a fractura obtenida en probetas normalizadas por un parámetro, β_{IST} , de muy sencilla obtención incluso en situaciones con muy pocos datos sobre el material.
- Presenta un procedimiento jerárquico en función de la información disponible, de manera que incluso cuando esta es muy limitada permite que el análisis a fractura se beneficie de la consideración de la pérdida de confinamiento tensional (Nivel I).
- En situaciones en las que se conocen las propiedades mecánicas del material propone un nivel intermedio de análisis (Nivel II) en el cual se ajusta más el resultado a la física del problema (con respecto al Nivel I) haciendo uso de dos valores de referencia para el parámetro m de Weibull en aceros (10 y 20).
- El parámetro β_{IST} se obtiene por comparación entre dos situaciones, la de la probeta normalizada y la del componente estructural, con idéntica tensión de Weibull. En este caso no se da el problema del efecto volumen que se ha indicado en el FITNET.
- Al igual que el FITNET FFS, permite análisis a fractura haciendo uso de Diagramas de Fallo.

Tal y como ocurría con el FITNET FFS, tiene una serie de limitaciones que es preciso comentar:

- Es un procedimiento desarrollado para análisis de fractura por clivaje, por lo que no considera la posibilidad de análisis de situaciones con propagación estable por desgarro dúctil [10].
- Siendo cierto que es un procedimiento de sencilla aplicación, lo es para un conjunto de geometrías muy limitado: CTCP, *Center Through-thickness Crack Panel*, CSCP, *Center Surface Crack Panel*, ESCP, *Edge Surface Crack Panel* y ETCP, *Edge Through-thickness Crack Panel*.
- Con respecto al FITNET FFS, no contempla el análisis de otro tipo de pérdidas de confinamiento en el plano de aplicación de la carga (efecto entalla), ni la interacción entre todas ellas. Tampoco pone en relación el análisis de confinamiento con la ZTDF del material (Curva Maestra).

5.3. Interrelaciones entre FITNET FFS e IST.

En este punto es posible determinar la relación existente entre la corrección por confinamiento del FITNET y la IST. Teniendo en cuenta la relación entre factor de intensidad de tensiones y CTOD (δ):

$$\delta = \frac{K_I^2}{1.5 \cdot \sigma_y \cdot E'} \quad (12)$$

El análisis FAD cuando se utiliza δ como parámetro de fractura resulta:

$$K_r = \sqrt{\delta_r} = \sqrt{\frac{\delta}{\delta_{cr}}} = f(L_r) \quad (13)$$

Al incluir el confinamiento en este último análisis resultaría:

$$K_r = \sqrt{\delta_r \text{ conf.}} = \sqrt{\frac{\delta}{\delta_{cr} / \beta_{IST}}} \quad (14)$$

Por lo que, finalmente:

$$K_r = \sqrt{\delta_r \text{ conf.}} = f(L_r) \cdot \sqrt{\beta_{IST}} \quad (15)$$

Y, en definitiva, la equivalencia entre las dos correcciones por confinamiento es:

$$(1 + \alpha(-\beta L_r)^m) \Leftrightarrow \sqrt{\beta_{IST}} \quad (16)$$

Es decir, para poder comparar en cada caso las correcciones propuestas por ambas metodologías habría que comparar los términos recogidos en la ecuación (16). A este respecto, cabe señalar que en el caso del FITNET la corrección por confinamiento depende del nivel de carga aplicado (a medida que aumenta la carga lo hace el efecto de

la pérdida de confinamiento), mientras que la corrección del IST es la misma para cualquier valor de carga aplicada (o lo que es lo mismo, para cualquier valor del parámetro L_r del FAD).

Por otra parte, el FITNET FFS podría tomar, en principio, los valores por defecto que propone la metodología IST para el parámetro m de Weibull en aceros, eliminando así una de sus mayores dificultades de aplicación. Esto convertiría, de hecho, al análisis FITNET de confinamiento en una metodología de análisis jerárquica con dos niveles de análisis: el primero, equivalente al Nivel II de la IST, en el cual se asumen los valores de m por defecto; el segundo, equivalente al Nivel III de análisis de la IST que requeriría una evaluación específica de m . El primer nivel de análisis del FITNET ya ha sido aplicado en [6].

6. CONCLUSIONES

Los procedimientos FITNET e IST de análisis del confinamiento constituyen una herramienta de análisis muy avanzada y permiten analizar la pérdida de confinamiento tensional en el fondo de una fisura.

Mientras el FITNET contempla la conveniencia o no de realizar análisis de este tipo, así como el análisis de un mayor número de geometrías de fisura (e incluso el análisis de otro tipo de defectos), la IST se centra en un número reducido de geometrías. Igualmente, el FITNET es aplicable a la fractura por clivaje y al desgarro dúctil, mientras que la IST solo está indicada para el análisis de fractura por clivaje. Más aún, el FITNET relaciona el análisis de confinamiento con la Curva Maestra del material en la ZTDF, con lo cual pone en relación dos problemas de primer orden en la mecánica de la fractura. De forma general, se puede decir que el FITNET recoge una trayectoria de investigación realizada en las últimas dos décadas que permite analizar mayor número de situaciones y encontrar a través de referencias (proporcionadas por el propio procedimiento) multitud de información sobre los *inputs* necesarios en el análisis.

Por otro lado, la IST presenta un procedimiento jerárquico capaz de aplicarse (en su primer nivel) sin apenas información de las propiedades mecánicas del material. Igualmente, la IST proporciona dos valores por defecto del parámetro m de Weibull (se elige uno u otro en función de la tenacidad del material) que resultan de gran utilidad y permiten realizar un análisis más avanzado que el del primer nivel.

Finalmente, se han establecido las interrelaciones entre ambas metodologías. Comenzando por el

hecho de que son dos metodologías biparamétricas, se ha determinado la equivalencia entre sus respectivas correcciones y se ha mostrado como los valores por defecto para el parámetro m de Weibull que propone la IST pueden tomarse como referencia en el FITNET, eliminando el principal problema de este procedimiento, que no es otro que la determinación del parámetro m de Weibull.

REFERENCIAS

- [1] Landes, J.D., McCabe, D.E., y Ernst, H.A., 1989, "Geometry effects on the R-curve, in non linear fracture mechanics: Volume 2 - Elastic Plastic Fracture" (eds J D Landes, A Saxena y J G Merkle) ASTM STP 905, pp. 123-143.
- [2] O'Dowd, N.P. y Shih, C.F., "Family of Crack-Tip Field Characterized by a Triaxiality Parameter-I. Structure of Fields". *Journal of the Mechanics and Physics of Solids*, Vol. 39, pp. 898-1015, 1991.
- [3] FITNET Fitness-for-Service (FFS) Procure - Volume 1, Editors: M. Kocak, S. Webster, J.J. Janosch, R.A. Ainsworth, R. Koers, ISBN 978-3-940923-00-4, Printed by GKSS, Germany, 2008.
- [4] Sherry, A.H., et al., "Material Constraint Parameters for the Assessment of Shallow Defects in Structural Components- Part I: Parameter Solutions", *Eng. Fract. Mech.*, Vol. 72 (15), pp. 2373-2395, 2005.
- [5] Wallin, K., "The scatter in KIC results", *Eng. Fracture Mechanics*, 19, pp. 1085-1093, 1984.
- [6] Cicero S, Gutiérrez-Solana F, Álvarez JA. "Structural integrity assessment of components subjected to low constraint conditions", *Eng Fract Mech.*, Vol. 75, pp. 3038-3059, 2008.
- [7] Kim, J.H., Kim, D.H., y Moon, S.I., "Evaluation of static and dynamic fracture toughness using apparent fracture toughness of notched specimens", *Materials Science and Engineering A*, Vol. 387-389, pp. 381-384, 2004.
- [8] Taylor, D., Cornetti, P. y Pugno, N., "The fracture mechanics of finite crack extension", *Eng Fracture Mechanics*, 72, pp. 1021-1038, 2005.
- [9] Minami F., et al., "Equivalent CTOD concept for fracture toughness requirement of materials for steel structures", *Proceedings of OMAE 18*, St. John's, OMAE99/MAT-2130, 1999.
- [10] Minami F et al., "Method of constraint loss correction of CTOD fracture toughness for fracture assessment of steel components", *Eng. Fract Mech.*, Vol. 73(14), pp. 1996-2020, 2006.

DETERMINACIÓN DE LA CARGA DE COLAPSO PLÁSTICO A TRAVÉS DE SUPERFICIES DE RESPUESTA EN PROBETAS SPT PREFISURADAS

I.I. Cuesta¹, J.M. Alegre¹, P.M. Bravo¹

¹Grupo de Integridad Estructural, Universidad de Burgos, Escuela Politécnica Superior
C/Villadiego s/n, 09001, Burgos
E-mail: iicuesta@ubu.es

RESUMEN

El ensayo miniatura de punzonado (SPT) sobre probetas prefisuradas tiene por objetivo la obtención de las propiedades a fractura del material (K_{mat}) cuando no se dispone de suficiente material para la realización de ensayos convencionales. La aplicación de los procedimientos de integridad estructural, a través del uso del diagrama de fallo (FAD), permiten evaluar cuando un componente fisurado alcanza la rotura. La combinación de los ensayos de probetas SPT prefisuradas con el diagrama FAD permite estimar la tenacidad a fractura del material. Para poder aplicar esta metodología uno de los parámetros que es necesario determinar es la carga de colapso plástico (P_U) de las probetas SPT prefisuradas, para conocer la coordenada L_r en el diagrama FAD. Una forma habitual de obtener dicha carga es mediante la simulación numérica de la probeta fisurada. El presente trabajo aporta una expresión para obtener P_U en probetas SPT prefisuradas, que pueda ser utilizada sin necesidad de realizar la simulación numérica. Dicha expresión ha sido calculada aplicando técnicas de superficie de respuesta basada en el diseño de experimentos, para materiales cuya ley de comportamiento se ajusta a una ecuación tipo Ramberg-Osgood. La expresión permite obtener la carga de colapso plástico en función de las dimensiones de la probeta y de los parámetros elastoplásticos del material, cubriendo el rango habitual de comportamiento de los aceros.

ABSTRACT

The main objective of the Small Punch Test (SPT) using pre-cracked specimens is to determine the fracture properties of the material (K_{mat}) when there is not enough material for conducting conventional tests. The accomplishment of the structural integrity procedures, through the Failure Assessment Diagram (FAD), allows predicting the failure of cracked components. In this sense, the combination of pre-cracked SPT specimens and the FAD allows the fracture toughness of the material to be estimated. In order to apply this methodology it is necessary to calculate the plastic collapse load (P_U) of the pre-cracked SPT specimens, so the load ratio L_r of the FAD is determined. The common method to calculate this load is performing a numerical simulation of the cracked geometry. This paper provides a closed expression for P_U in pre-cracked SPT specimens, which can be used avoiding the necessity to perform a finite element numerical simulation. This expression has been calculated using response surface models based on the experiment design for materials whose behavior follows a Ramberg-Osgood equation. The expression provides the plastic collapse load as a function of the specimen dimensions and the elastoplastic material parameters, covering the common behavior range of the steels.

KEY WORDS: Ensayo Small Punch, Diagrama FAD, Superficie de Respuesta.

1. INTRODUCCIÓN

El ensayo de probetas miniatura (SPT) consiste básicamente en un punzonado sobre una probeta cuadrada o circular de reducidas dimensiones, mediante un punzón de gran rigidez, estando la periferia de la probeta empotrada por dos matrices.

En las últimas décadas han sido muchos los investigadores que han utilizado el SPT con el fin de obtener las propiedades de fractura de un material, en

los casos que no se dispone de material suficiente para poder realizar ensayos normalizados, como por ejemplo en el caso de soldaduras o material irradiado. La gran mayoría de los trabajos [1-5] sobre este tema hasta el momento han sido realizados con probetas convencionales de SPT, siendo muy pocos los autores que han utilizado probetas prefisuradas [6-8].

Por otro lado, dentro del campo de la integridad estructural, se está imponiendo el uso de diagramas de fallo (FAD), los cuáles permiten establecer cuando un

componente fisurado alcanza las condiciones de rotura. Es un gráfico de doble entrada, donde en el eje horizontal esta representando el grado de plastificación alcanzado por la probeta en el instante de fallo, a través de un parámetro denominado ratio de carga (L_r). El eje vertical representa el ratio del factor de intensidad de tensiones alcanzado en el instante de fallo, normalizado con respecto a la tenacidad a fractura del material (K_{mat}), quedando descrito a través del ratio de tenacidad (K_r).

El presente trabajo nace de la necesidad de mejorar la aplicabilidad de la metodología desarrollada en un trabajo previo [8], la cuál combina los resultados obtenidos en el SPT sobre probetas prefisuradas con el diagrama FAD para la evaluación de la tenacidad a fractura del material analizado, apoyándose el estudio en la simulación numérica. El esquema de dicha metodología se puede consultar en la Figura 1.

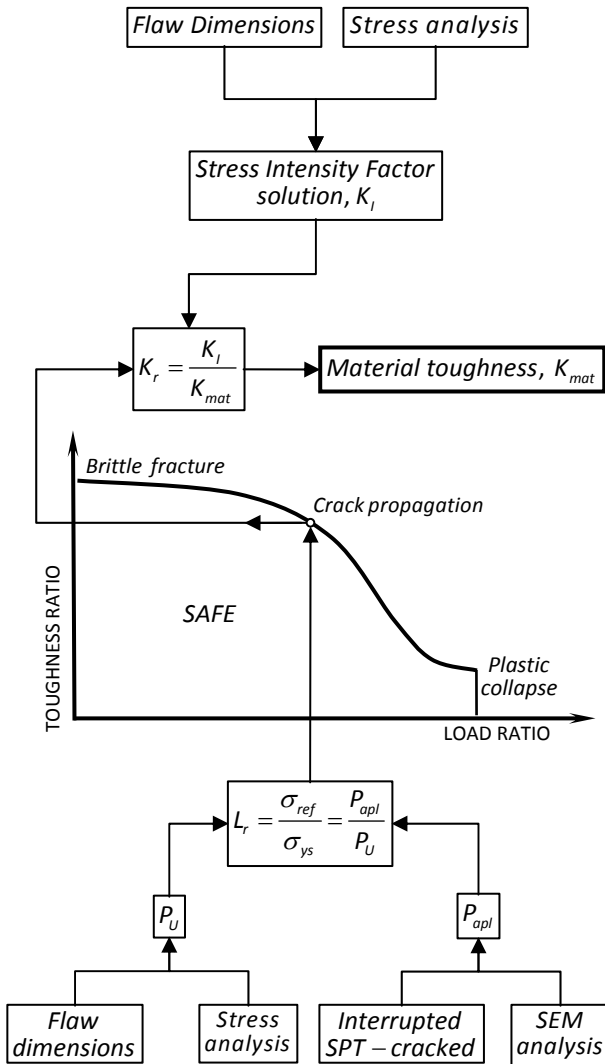


Figura 1. Esquema de la metodología para la evaluación de K_{mat} [8].

Como se puede comprobar, dicha metodología gira entorno al uso del diagrama de fallo, donde la entrada vertical K_r es desconocida, al serlo K_{mat} , por lo que se comienza entrando en el diagrama FAD por el eje horizontal. Para ello, el primer paso a realizar es la determinación mediante simulación numérica, de la carga de colapso plástico de la probeta fisurada (P_U), y de la carga aplicada sobre la probeta en el punto de inicio de la propagación de la fisura (P_{apl}) que puede obtenerse a partir de la realización de ensayos interrumpidos de SPT prefisurados y su posterior análisis fractográfico.

El objetivo de este trabajo es aportar una expresión para obtener P_U en probetas SPT prefisuradas, que pueda ser utilizada sin necesidad de realizar la simulación numérica, permitiendo de esta manera el uso de la metodología de la Figura 1 en aquellos casos que no se disponga de los medios necesarios para llevar a cabo una simulación numérica con la que determinar el valor de la carga de colapso plástico P_U .

2. PROBETAS SPT PREFISURADAS

En el desarrollo de la presente investigación, al igual que en el trabajo previo [8], se han utilizado probetas SPT prefisuradas, de dimensiones 20x20x1mm y con una fisura inicial de tipo longitudinal no pasante, como se puede ver en la Figura 2.

La generación de la fisura inicial en las probetas SPT, previa al ensayo, se ha realizado a través de microfisuración por láser. Tras una calibración inicial, el láser, en forma de haz de pulsos de diámetro 30µm, es aplicado longitudinalmente a partir de la cara inferior, desde el centro de un lado de la probeta hacia el centro del lado opuesto.

Para la realización de los ensayos SPT interrumpidos se pueden utilizar probetas SPT prefisuradas con diferentes profundidades de fisura (a). Dicha profundidad se puede adimensionalizar con respecto al espesor de probeta (t), obteniendo de esta manera diferentes valores de la relación a/t , siendo los más habituales valores teóricos de a/t entre 0.2 y 0.5.

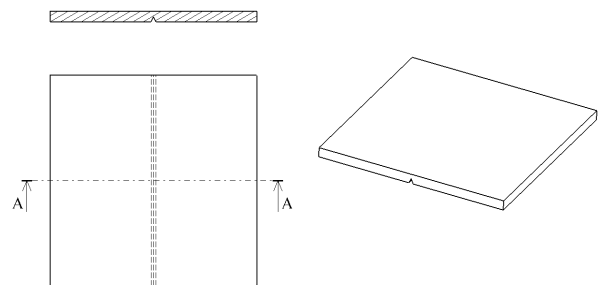


Figura 2. Probeta SPT prefisurada.

3. SIMULACION NUMERICA DE P_U

Para determinar la carga de colapso plástico de la probeta SPT prefisurada P_U , es habitual efectuar un análisis por elementos finitos de la geometría fisurada. Existen dos definiciones posibles de la carga de colapso plástico, el colapso global y el colapso de la sección neta. En el presente trabajo se ha utilizado el segundo de los procedimientos, por considerarse más preciso el resultado obtenido [9]. Este procedimiento requiere la realización de un cálculo elastoplástico con contactos.

El software elegido para la realización de esta tarea ha sido el programa MSC.Marc [10]. Debido a la simetría que presenta el SPT con probeta prefisurada se ha modelizado un cuarto de la geometría en 3D con elementos hexaédricos de 8 nodos (HEX 8), utilizando los planos YZ y ZX como planos de simetría, como se puede ver en la Figura 3. El punzón y las matrices inferior y superior se han modelado como superficies rígidas. El cálculo se ha controlado a través del desplazamiento del punzón, imponiendo un valor de este, similar al de los ensayos SPT experimentales. El material de la probeta se ha considerado como elastoplástico. Se utilizarían los datos experimentales de la curva tensión-deformación para obtener las propiedades elásticas, como son el módulo de Young (E) y el coeficiente de Poisson (ν), el límite elástico del material (σ_0) y las propiedades plásticas del material.

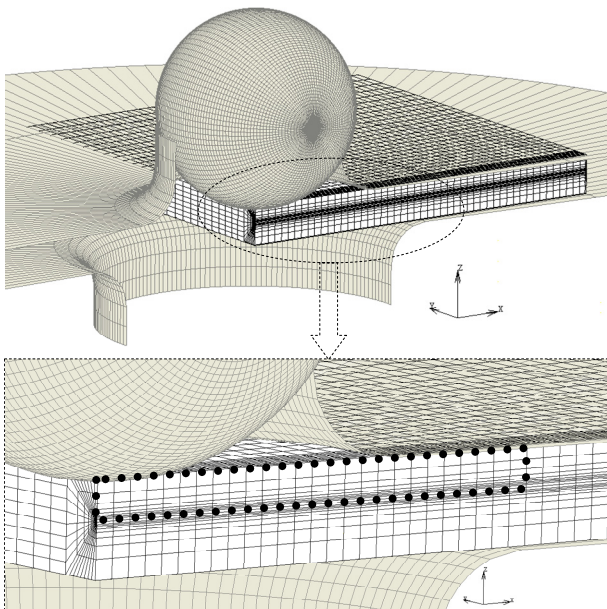


Figura 3. Modelado de la probeta SPT prefisurada y detalle de la sección neta central del plano de fisura.

Una vez realizado el cálculo, se procede a evaluar la carga para la que se alcanza la deformación plástica generalizada en la sección neta central del plano de fisura de la probeta. La cuál corresponde a la parte que no está empotrada por las matrices superior e inferior,

como se puede ver en la Figura 3 para una de las simulaciones efectuadas, coincidiendo con el área del rectángulo punteado de la figura. El valor de esta carga se considerará como P_U cuando la deformación plástica equivalente alcance el valor de 0.002 en todos los puntos de la sección neta central.

4. SUPERFICIE DE RESPUESTA DE P_U

Desde un punto de vista práctico, y para la posible aplicación ingenieril de la metodología propuesta, sería conveniente evitar la realización del cálculo elastoplástico comentado cada vez que se desee aplicar dicha metodología, lo cuál supondría una considerable reducción de los recursos de software necesarios y del tiempo de aplicación. Para tal fin, en este trabajo se han utilizado las técnicas de superficie de respuesta basadas en el diseño de experimentos, las cuáles permiten obtener una función con la que estimar el valor de P_U de una forma directa, para cualquier tipo de acero cuya ley de comportamiento se ajuste a una ecuación tipo Ramberg Osgood [11] definida por la expresión (1), siempre y cuando sus parámetros característicos estén dentro del rango de valores aquí considerados.

$$\varepsilon = \varepsilon_e + \varepsilon_p = \frac{\sigma}{E} + K_1 \cdot \left(\frac{\sigma}{E}\right)^n \quad (1)$$

Donde K_1 y n son parámetros que describen el comportamiento plástico del material. Introduciendo el límite elástico σ_0 y un nuevo parámetro $\alpha = K_1 \cdot (\sigma_0 / E)^{n-1}$, la parte plástica de la ecuación (1) se puede sustituir por la expresión (2), quedando redefinida la ecuación de Ramberg Osgood según la expresión (3).

$$K_1 \cdot \left(\frac{\sigma}{E}\right)^n = \frac{\alpha \cdot \sigma_0}{E} \cdot \left(\frac{\sigma}{\sigma_0}\right)^n \quad (2)$$

$$\varepsilon = \frac{\sigma}{E} + \frac{\alpha \cdot \sigma_0}{E} \cdot \left(\frac{\sigma}{\sigma_0}\right)^n \quad (3)$$

La utilización del modelo de Ramberg Osgood implica que la deformación plástica está presente incluso para pequeños niveles de tensión, aunque es prácticamente despreciable comparada con la deformación elástica.

Por otro lado, para niveles de tensión superiores a σ_0 , la deformación plástica comienza progresivamente a ser mayor que la deformación elástica. Cuando $\sigma = \sigma_0$ según la expresión (3) se obtiene que $\varepsilon = (1 + \alpha) \cdot \sigma_0 / E$, obteniendo las componentes elástica y plástica de la deformación tal y como se puede observar en la Figura 4.

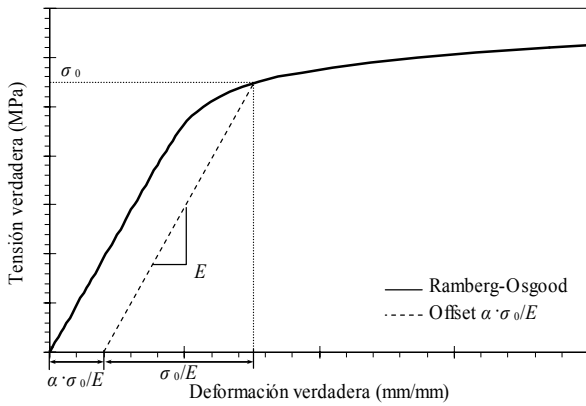


Figura 4. Curva tensión-deformación típica del modelo de Ramberg Osgood.

Comúnmente en los aceros se acepta que la deformación plástica comienza a tenerse en cuenta cuando esta alcanza un valor del 0.2%, es decir, cuando el término $\alpha \cdot \sigma_0 / E = 0.002$, con lo que el modelo de Ramberg Osgood definido en (3) puede ser simplificado según la expresión (4), en la que $\sigma_0 = \sigma_{0.2}$.

$$\varepsilon = \frac{\sigma}{E} + 0.002 \cdot \left(\frac{\sigma}{\sigma_{0.2}} \right)^n \quad (4)$$

Donde $\sigma_{0.2}$ es el límite elástico para una deformación plástica del 0.2%, y n es un parámetro que suele variar entre 4 y 50 para la mayoría de los aceros [11]. De esta manera queda definido el comportamiento del material a través de los parámetros E , $\sigma_{0.2}$ y n . Los parámetros $\sigma_{0.2}$ y n son fundamentales a la hora de establecer el valor de la carga de colapso plástico.

Antes de proceder a la determinación de la superficie de respuesta es necesario apuntar una primera reflexión sobre los parámetros que influyen en el valor de P_U . Dichos parámetros se pueden englobar en dos grandes grupos, que denominaremos parámetros elastoplásticos del material y parámetros geométricos. Todos ellos aparecen recogidos en la Tabla 1.

Resulta evidente que es extremadamente complicado obtener una superficie de respuesta que englobe la variación de todos estos parámetros, por lo que es necesario fijar algunos de ellos. Siguiendo un criterio de economía de costes, resulta justificado fijar los parámetros geométricos, dependientes del utillaje, así como el espesor de probeta asignado a cada utillaje. La profundidad de la fisura inicial a , es una dimensión claramente variable no solo por las propias variaciones asociadas al mecanizado de la misma, sino también porque su tamaño constituye uno de los parámetros fundamentales del proceso de fractura, se ha tenido en cuenta a través de la relación a/t .

Tabla 1. Parámetros influyentes en el valor de P_U .

Parámetros elastoplásticos	Parámetros geométricos
E	Profundidad fisura (a)
ν	Dimensiones probeta ($b \times b \times t$)
$\sigma_{0.2}$	Diámetro del punzón (d)
n	Diámetro matriz inferior ($d_{m_{inf}}$)
	Radio de acuerdo matriz inf. (r)

De los parámetros elastoplásticos del material, los únicos que se han fijado han sido el coeficiente de Poisson y el módulo de Young, cuyo efecto en el valor de P_U se ha comprobado irrelevante, mientras que a los demás se los ha hecho variar entre los valores típicos para los aceros. La Tabla 2 recoge tanto los intervalos de valores considerados como los valores fijos de los parámetros con los que se ha trabajado para la obtención de la superficie de respuesta de P_U , para la probeta de $20 \times 20 \times 1 \text{ mm}$.

Tabla 2. Valores de los parámetros influyentes en el valor de P_U .

Parámetros fijos		Parámetros variables	
ν	0.29	a/t	[0.1,0.7]
E (MPa)	200000	$\sigma_{0.2}$ (MPa)	[200,1400]
$b \times b \times t$ (mm)	20x20x1	n	[4,50]
d (mm)	5		
$d_{m_{inf}}$ (mm)	8		
r (mm)	1		

Los parámetros a/t , $\sigma_{0.2}$ y n son los que van a gobernar la superficie de respuesta de P_U ya que los demás permanecen fijos. La relación existente entre estos tres parámetros y el valor de P_U se puede expresar como $P_U = f(a/t^*, \sigma_{0.2}^*, n^*)$, donde f se postula como modelo cuadrático de la forma expresada en la ecuación (5), en la que a/t^* , $\sigma_{0.2}^*$ y n^* son las variables codificadas de a/t , $\sigma_{0.2}$ y n respectivamente. La codificación de los valores reales de los parámetros es necesaria para que todos ellos varíen en el mismo intervalo, favoreciendo de esta manera la estimación precisa de los coeficientes que definen la función $f(a/t^*, \sigma_{0.2}^*, n^*)$. Para cualquier valor real X_i de los parámetros variables, dicha codificación se puede realizar a través de la expresión (6), obteniendo el valor codificado x_i correspondiente. Donde X_{iNInf} es el valor real del nivel más bajo del factor i , X_{iNSup} es el valor

real del nivel más alto del factor i , y \tilde{X}_i es la media entre los valores reales del nivel más alto y más bajo del factor i .

$$f\left(\frac{a^*}{t}, \sigma_{0.2}^*, n^*\right) = b_0 + b_1 \frac{a^*}{t} + b_2 \sigma_{0.2}^* + b_3 n^* + b_{11} \frac{a^{*2}}{t} + b_{22} \sigma_{0.2}^{*2} + b_{33} n^{*2} + b_{12} \frac{a^*}{t} \sigma_{0.2}^* + b_{13} \frac{a^*}{t} n^* + b_{23} \sigma_{0.2}^* n^* \quad (5)$$

$$x_i = \frac{2 \cdot 1.682 \cdot (X_i - \tilde{X}_i)}{X_{iNSup} - X_{iNInf}} \quad i = \frac{a^*}{t}, \sigma_{0.2}^*, n^* \quad (6)$$

La determinación de los coeficientes de la función $f(a/t^*, \sigma_{0.2}^*, n^*)$ se va a realizar a través de un diseño de experimentos central compuesto [12-14], utilizando el software NEMRODW [15] para la estimación de dichos coeficientes. Las principales características de este diseño son:

- Utilización de tres factores, los cuáles son los parámetros a/t^* , $\sigma_{0.2}^*$ y n^* .
- Dominio esférico de radio clásico, el valor del radio para tres factores es 1.682.
- Codificación de los intervalos de valores de los tres factores recogidos en la Tabla 2 para que varíen en [-1.682, 1.682], según la expresión (6).
- Matriz de experimentos composite, la cuál tiene cinco niveles para cada factor.
- Sin repeticiones en el punto central del dominio (Nº de experimento 15), ya que no tiene sentido al utilizar la simulación numérica para obtener el valor de P_U .
- Utilización de la expresión (5) para el ajuste de la superficie de respuesta.

La Tabla 3 recoge, tanto la matriz de experimentos con las variables codificadas, como la matriz del plan de experimentación con los valores de los factores del diseño de experimentos propuesto para la determinación de los coeficientes de la función $f(a/t^*, \sigma_{0.2}^*, n^*)$. Cada uno de los experimentos del plan de experimentación se realiza a través de una simulación numérica tal y como se recoge en el apartado 3 del presente estudio, con la única salvedad que los valores de a/t , $\sigma_{0.2}$ y n son los recogidos en la Tabla 3, obteniendo como resultado final de cada experimento el valor de P_U , incluido en esa misma tabla.

Una vez obtenidos estos valores de P_U , con la ayuda de NEMRODW, es posible determinar los coeficientes de la función $f(a/t^*, \sigma_{0.2}^*, n^*)$, los cuáles se muestran en la Tabla 4.

Tabla 3. Diseño de experimentos realizado.

Nº exp.	Matriz de experimentos			Plan de experimentación			
	a/t^*	$\sigma_{0.2}^*$	n^*	a/t	$\sigma_{0.2}$ (MPa)	n	P_U (kN)
1	-1	-1	-1	0.222	443	13.33	2.50
2	1	-1	-1	0.578	443	13.33	1.46
3	-1	1	-1	0.222	1157	13.33	8.50
4	1	1	-1	0.578	1157	13.33	4.12
5	-1	-1	1	0.222	443	40.67	2.28
6	1	-1	1	0.578	443	40.67	1.35
7	-1	1	1	0.222	1157	40.67	7.82
8	1	1	1	0.578	1157	40.67	3.86
9	-1.682	0	0	0.1	800	27	5.62
10	1.682	0	0	0.7	800	27	2.56
11	0	-1.682	0	0.4	200	27	0.78
12	0	1.682	0	0.4	1400	27	7.03
13	0	0	-1.682	0.4	800	4	4.80
14	0	0	1.682	0.4	800	50	3.59
15	0	0	0	0.4	800	27	3.64

Tabla 4. Coeficientes de la función $f(a/t^*, \sigma_{0.2}^*, n^*)$.

Coefficiente	Valor	Significación (%)
b_0	3.664	0.0273***
b_1	-1.132	0.0149***
b_2	1.993	<0.01***
b_3	-0.243	7.8
b_{11}	0.130	46.6
b_{22}	0.065	71.0
b_{33}	0.168	35.6
b_{12}	-0.797	0.262**
b_{13}	0.068	65.5
b_{23}	-0.077	61.4

Al 99% de confianza los coeficientes significativos para la función $f(a/t^*, \sigma_{0.2}^*, n^*)$ son los que se han marcado con asteriscos en función del grado de significación, siendo los más significativos los coeficientes b_0 , b_1 y b_2 . Los coeficientes que no son significativos contribuyen a curvar correctamente la superficie de respuesta, por lo que no es conveniente eliminarlos de la función $f(a/t^*, \sigma_{0.2}^*, n^*)$. La regresión es muy significativa estadísticamente (p-valor < 10^{-4}) y explica el 99.7% de la varianza de P_U .

Analizando la Tabla 4 podemos concluir que el parámetro más influyente en el valor de P_U es $\sigma_{0.2}$, donde un aumento de este supondría un aumento de P_U , ya que el coeficiente b_2 es positivo. El segundo parámetro influyente es la relación a/t , donde un aumento de esta equivaldría a una disminución en el valor de P_U , ya que el coeficiente b_1 es negativo. El parámetro n no es relevante en el valor de P_U ya que su coeficiente b_3 no es significativo, lo que supone una ventaja a la hora de calcular su valor, ya que se puede establecer cierto margen de error porque su posible variación no va a influir significativamente en el valor estimado de P_U . Por último, se podría comentar que ni las interacciones entre los parámetros ni su efecto al cuadrado son significativos en el valor de P_U , a excepción del coeficiente b_{12} , correspondiente a la interacción entre a/t y $\sigma_{0.2}$. Dado que su valor es negativo, un aumento del producto entre a/t y $\sigma_{0.2}$ supondría una disminución del valor de P_U , sin tener en cuenta el efecto de cada uno de estos parámetros por separado.

A partir de la función $f(a/t^*, \sigma_{0.2}^*, n^*)$ que ajusta adecuadamente los valores de P_U obtenidos en el diseño, es posible determinar el valor de P_U para cualquier combinación de valores de los parámetros a/t , $\sigma_{0.2}$ y n , previa codificación, siempre y cuando nos encontremos dentro del dominio esférico definido anteriormente para este diseño. La expresión (7) representa la superficie de respuesta de P_U obtenida a partir de los coeficientes de la Tabla 4 para la probeta SPT prefisurada de dimensiones 20x20x1mm.

$$f\left(\frac{a}{t}^*, \sigma_{0.2}^*, n^*\right) = 3.664 - 1.132 \frac{a}{t}^* + 1.993 \sigma_{0.2}^* - 0.243 n^* + 0.13 \left(\frac{a}{t}^*\right)^2 + 0.065 \sigma_{0.2}^{*2} + 0.168 n^{*2} - 0.797 \frac{a}{t}^* \sigma_{0.2}^* + 0.068 \frac{a}{t}^* n^* - 0.077 \sigma_{0.2}^* n^* \quad (7)$$

5. CONCLUSIONES

Para la probeta analizada se ha obtenido una superficie de respuesta, que contempla el efecto de las propiedades elastoplásticas del material y de la geometría de la fisura en el valor de la carga de colapso plástico P_U . De este modo la metodología desarrollada previamente [8], definida en el esquema de la Figura 1, puede aplicarse sin necesidad de tener que realizar el complejo cálculo numérico de P_U . Uno de los trabajos futuros a desarrollar, que permita facilitar aun más la aplicación de dicha metodología, es la determinación de una

expresión para obtener el valor del factor de intensidad de tensiones K_I , sin necesidad de recurrir a la simulación numérica por parte del usuario final.

En el caso de tener que determinar P_U para otras configuraciones de probeta, del utillaje de ensayo o material, se podría proceder de manera análoga a la aquí recogida. Simplemente estableciendo de nuevo los valores de los parámetros fijos y el rango de variación de los variables, y siguiendo el procedimiento utilizado en el presente trabajo.

AGRADECIMIENTOS

Los autores desean agradecer la financiación recibida del proyecto MCI Ref: MAT2008-06879-C03-03/MAT.

REFERENCIAS

- [1] X. Mao and H. Takahashi, *Development of a further-miniaturized specimen of 3 mm diameter for tem disk small punch tests*, Journal of Nuclear Materials 150 (1987), 42-52.
- [2] X. Mao, H. Takahashi and T. Kodaira, *Supersmall punch test to estimate fracture toughness Jic and its application to radiation embrittlement of 2.25Cr-1Mo steel*, Materials Science and Engineering, A150 (1992), 231-236.
- [3] Maribel L. Saucedo-Muñoz, Shi Cheng Liu, Toshiyuki Hashida, Hideaki Takahashi, Hideo Nakajima, *Correlation between JIC and equivalent fracture strain determined by small-punch tests in JN1, JJ1 and JK2 austenitic stainless steels*, Cryogenics 41 (2001), 713-719.
- [4] A. Shekhter, S. Kim, D.G. Carr, A.B.L. Croker, S.P. Ringer, *Assessment of temper embrittlement in an ex-service 1Cr-1Mo-0.25V power generating rotor by Charpy V-Notch testing, Klc fracture toughness and small punch test*, International Journal of Pressure Vessels and Piping 79 (2002), 611-615.
- [5] Jai-Man Baik, J. Kameda, and O. Back, *Small Punch Test evaluation of intergranular embrittlement of an alloy steel*, Scripta Metallurgica et Materialia, Vol. 17 (1983), 1443-1447.
- [6] Jang-Bog Ju, Jae-il Jang, Dongil Kwon, *Evaluation of fracture toughness by small-punch testing techniques using sharp notched specimens*, International Journal of Pressure Vessels and Piping 80 (2003), 221-228.
- [7] I. I. Cuesta, J. M. Alegre, R. Lacalle, J. A. Álvarez, F. Gutiérrez-Solana, *Cálculo de la integral J en probetas SPT para la estimación de la tenacidad a fractura*, Anales de Mecánica de la Fractura Vol. II (2008), 486-491.
- [8] I. I. Cuesta, J. M. Alegre, P.M. Bravo, *Evaluación de la tenacidad a fractura mediante la combinación del diagrama FAD y de ensayos SPT sobre probetas fisuradas*, Anales de Mecánica de la Fractura Vol. II (2009), 382-387.
- [9] ASME, *API 579-1/ASME FFS-1, in Fitness-For-Service*, American Society of Mechanical Engineers, 2007.
- [10] MSC.Marc Volume A, *Theory and User Information*, Chapter 5, Fracture Mechanics.
- [11] Ramberg W. y Osgood W. R., *Description of stress-strain curves by three parameters*, Technical Note No. 902, National Advisory Committee for Aeronautics (1943), Washington DC.
- [12] Khuri A. I. y Cornell J. A., *Response surfaces. Design and analyses*, Statistics: Textbooks and monographs. 81, Marcel Dekker (1987). New York.
- [13] Kuehl R. O., *Diseño de experimentos*, International Thomson (2001).
- [14] Montgomery D. C., *Diseño y análisis de experimentos*, Grupo Editorial Iberoamérica (1991).
- [15] Mathieu D. et al., NEMRODW, LPRAI, Marsella. <http://www.nemrodw.com>.

**A UNIFIED APPROACH FOR IN-PLANE AND OUT-OF-PLANE CONSTRAINT
ANALYSIS IN LINEAR ELASTIC CRACKED PLATES**

E. Giner¹, D. Fernández Zúñiga², J. Fernández Sáez³, A. Fernández Canteli²

¹Dpto. de Ingeniería Mecánica y de Materiales-CITV, E.T.S. de Ingenieros Industriales
Universidad Politécnica de Valencia, Camino de Vera s/n, 46022 Valencia
E-mail: eginerm@mcm.upv.es

²Dpto. de Construcción e Ingeniería de Fabricación, E.P.S. de Ingeniería de Gijón,
Universidad de Oviedo, Campus de Viesques, 33203 Gijón.
E-mail: afc@uniovi.es

³Dto. de Mecánica del Medio Continuo y Análisis Estructural, Escuela Politécnica Superior,
Universidad Carlos III, Avda. Universidad 30, 28911 Leganés, Madrid.
E-mail: ppfer@ing.uc3m.es

ABSTRACT

The influence of the loss of constraint on the apparent fracture toughness, although early recognised, has not been adequately addressed up to present, especially in what concerns the out-of-plane case. In this paper, a tensor concept of the stress intensity and, in particular, of the first two terms of the Williams expansion is used with the aim of extending the concept of the conventional biparametric approaches to the analysis of the loss of constraint under general conditions encompassing both the in-plane and out-of-plane constraints. Based on analytical relations developed elsewhere, the components t_{11} and t_{33} of the t_{ij} tensor in the midplane of crack plates are numerically found by means of FE calculations, as well as their through-thickness variation along the crack front. The analyses are performed under different in- and out-of-plane constraint situations arising from different specimen thicknesses B , crack depth ratios a/W and Poisson coefficients ν , proving the numerical validity of the theoretical derivations.

KEY WORDS: T -stress, out-of-plane constraint, stress intensity tensor, constraint functions, Williams expansion.

1. INTRODUCTION

The increase of the apparent fracture toughness due to the loss of constraint has been recognized in the past in a number of theoretical and experimental works. In the case of the in-plane constraint, this effect has been traditionally explained as a result of the elastic T -stress giving rise, both in the LEFM [1] and EPFM [2], to the so-called two-parameter approaches, by considering the elastic T -stress as a reference magnitude. Nevertheless, this approach does not provide a definitive answer to the problem. Those studies are, in general, performed using specimen thicknesses greater than B_{\min} , what, according to the ASTM and ESIS standards, ensures plane strain conditions. As a consequence, the out-of-plane dimension of the constraint has been neglected. This is characterized by the presence of an often unconsidered out-of-plane t_{33} stress, as well as by the variation of the t_{11} stress, i.e. the conventional T -stress, as a result of the specimen thickness. Further, other parameters, as the crack depth a/W , typically identified with in-plane constraint effects, may also cause a significant variation of the out-of-plane stress t_{33} .

In previous works [3], a tensor approach based on Williams expansion is suggested to define the stress and strain state near the crack front. Sustained by analytical derivations and numerical calculations it is proved the independence of the structure of the stress intensity tensor k_{ij} with respect to the specimen thickness. The tensor k_{ij} allows to ascertain that the increase of the apparent fracture toughness due to the loss of constraint has to be assigned to the influence of higher order terms of the stresses.

In particular, this influence is assigned to the constraint tensor t_{ij} , identified as the Williams constant term tensor since it is independent of the radial distance r . The consideration of the stress intensity tensor k_{ij} and the so-called constraint curves ψ_{ij} [3] (see Section 3.3) enable us to demonstrate the correlation between the loss of constraint and the specimen thickness, and hence the necessity of considering the whole t_{ij} tensor, particularly its t_{33} component. This allows to tackle the general constraint problem under a unified approach, comprising both the in-plane and out-of-plane constraints. Current treatments of the constraint

problem contribute to a misleading identification of triaxiality with constraint that does not help to correctly establish the fracture criterion and the effect of thickness on the apparent fracture toughness.

In this work, numerical calculations are performed aiming at illustrating the influence of the specimen thickness on the t_{11} stress, i.e. the T -stress, and on the t_{33} stress and their relation to the out-of-plane strain ε_{33} . Analytical relations regarding the stress and strain tensor field at the crack front are used to numerically calculate the out-of plane stress component t_{33} and the T -stress t_{11} . This is accomplished through finite element analyses for different configurations and the results demonstrate the limitations of current approaches. This should contribute to the basic knowledge of the in- and out-of-plane constraints as a whole, paving the way to more general new fracture criteria.

2. THE TENSOR t_{ij} AS A MEASURE OF CONSTRAINT

The analytical derivations developed in [3], based on strain relations prevailing at the crack front of mode-I specimens, prove that the out-of-plane component k_{33} of the stress intensity tensor k_{ij} (defined as $k_{ij}(z;B) = K_1(z;B) f_{ij}(\theta)|_{\theta_r}$) at the midplane of the specimen normal to the crack plane is given by

$$k_{33}(z;B) = \nu(k_{11}(z;B) + k_{22}(z;B)), \quad (1)$$

irrespective of the specimen thickness including the two limiting cases $B \rightarrow 0$ and $B \rightarrow \infty$. This necessarily implies the singular behaviour of σ_{33} along the crack front. In addition, the component $k_{33}(z;B)$ equals $2\nu K_1(z;B)$, leading to the following stress intensity tensor:

$$k_{ij}(z;B) = \begin{pmatrix} K_1(z;B) & 0 & 0 \\ 0 & K_1(z;B) & 0 \\ 0 & 0 & 2\nu K_1(z;B) \end{pmatrix}, \quad (2)$$

what demonstrates the independence of the k_{ij} structure with respect to the constraint level. Contrary to what is often found in the literature, Eq. (1) does not imply plane strain conditions at the crack front since $\varepsilon_{33} \neq 0$ and ε_{33} varies along the crack front. Furthermore, the following relation between out-of-plane strain ε_{33} at the crack tip and the components of t_{ij} has been found

$$\begin{aligned} \varepsilon_{33}(z,r;B)|_{r=0} &= \lim_{r \rightarrow 0} \frac{\sigma_{33}(z,r;B) - \nu(\sigma_{11} - \sigma_{22}(z,r;B))}{E} \\ &= \frac{t_{33}(z;B) - \nu t_{11}(z;B)}{E} \end{aligned} \quad (3)$$

because the singular terms of σ_{ij} must cancel out to avoid a singular behaviour of ε_{33} at midplane. The corresponding tensor t_{ij} is given by

$$\begin{aligned} t_{ij}(z;B) &= \begin{pmatrix} t_{11}(z;B) & 0 & 0 \\ 0 & 0 & 0 \\ 0 & 0 & t_{33}(z;B) \end{pmatrix} \\ &= \begin{pmatrix} t_{11}(z;B) & 0 & 0 \\ 0 & 0 & 0 \\ 0 & 0 & E\varepsilon_{33}(z;B) + \nu t_{11}(z;B) \end{pmatrix} \end{aligned} \quad (4)$$

For $B \rightarrow \infty$, $\varepsilon_{33} \rightarrow 0$ and $t_{33} \approx \nu t_{11}$ so that (4) transforms to

$$t_{ij}(z;B \rightarrow \infty) = \begin{pmatrix} t_{11}(z;B \rightarrow \infty) & 0 & 0 \\ 0 & 0 & 0 \\ 0 & 0 & \nu t_{11}(z;B \rightarrow \infty) \end{pmatrix}. \quad (5)$$

Therefore, in the case $B \rightarrow \infty$, the tensor depends uniquely on t_{11} , and can be adequately considered as the reference parameter of constraint, as stated in the bi-parametric approaches. However, for a real B (notably for $B < B_{\min}$), the suitable expression for the t_{ij} tensor is (4). As a result, the t_{33} value is, in general, influenced by t_{11} and ε_{33} both depending on the specimen thickness B .

3. NUMERICAL CALCULATION OF THE COMPONENTS t_{11} AND t_{33} OF THE t_{ij} TENSOR

Different techniques can be applied for the calculation of the t_{ij} tensor components [5]. A direct derivation from the stress distribution, although feasible, is prone to inaccuracies in the extrapolation to the crack front. Instead, t_{11} can be determined using the interaction integral proposed by Nakamura-Parks [6]. Once t_{11} and ε_{33} are known, t_{33} can then readily be obtained from (3).

3.1 Model description

Cracked plates of different thickness B , crack depth ratios a/W and Poisson's ratios have been analysed using the FEM to check the validity of the theoretical derivations. The interest was focussed on the influence of the above parameters on the t_{11} and t_{33} components of the t_{ij} tensor. In this work, the analysis is restricted to plates with a straight crack front and mode-I loading. A linear elastic material with Young's modulus $E = 207$ GPa and Poisson's ratio $\nu = 0.3$, unless otherwise stated, is considered for the numerical model as shown in Fig. 1. Fourteen different thicknesses $B = 0.1, 0.2, 0.5, 1, 2, 5, 10, 20, 35, 50, 75, 100, 200, 400$ mm and four different crack depth ratios $a/W = 0.1, 0.3, 0.5$ and 0.7 were considered for the calculations aiming at studying the effect of thickness and crack length. A constant width $W = 50$ mm and height $H = W$ is assumed throughout the calculations and a uniform stress $\sigma = 1$ MPa is applied on the top side of the plate in all cases. 20-node isoparametric elements with $3 \times 3 \times 3$ integration points are considered. The discretization in the transverse direction comprises 50 elements.

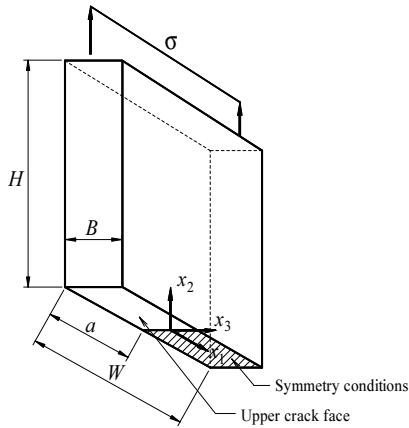


Figure 1. Geometric model of the cracked plates.

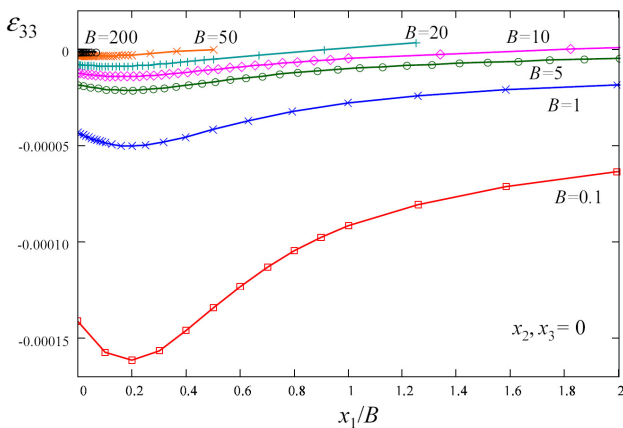


Figure 2. Normalized midplane variation of ϵ_{33} along the x_1 -axis.

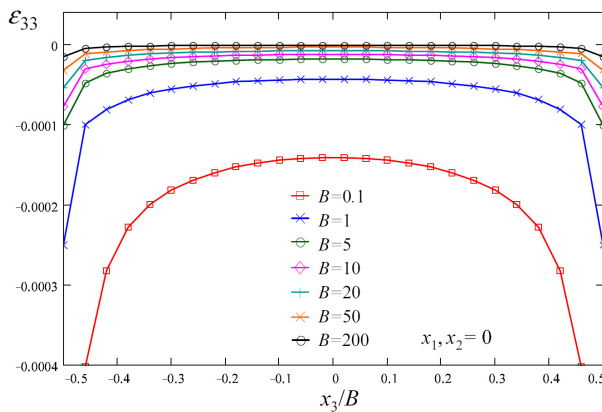


Figure 3. Normalized through-thickness variation of ϵ_{33} along the crack front.

3.2 Out-of-plane strain ϵ_{33}

Firstly, the out-of-plane strain ϵ_{33} for the different thicknesses was calculated at the midplane of the plate as a function of the normalized distance to the crack front in the x_1 direction (see Fig. 2). The same magnitude is depicted in Fig. 3 this time as a function of the normalized location x_3/B at the crack front. As

shown, the results confirm the non-nullity of ϵ_{33} along the crack front in the case of plates of finite thickness. The greatest contraction is reached at a distance of about $x_1/B \approx 0.2$ ahead of the crack front.

3.3 Constraint functions

The constraint functions $\psi_{ij}(r; B)$ represent the stress intensity fields in the direction of the prospective crack propagation ($\theta = 0$ for mode-I):

$$\psi_{ij}(r; B) = \sqrt{2\pi r} \sigma_{ij}(r, \theta; B) \Big|_{\theta=0} \quad (6)$$

At the crack front, i.e. for $r \rightarrow 0$, the constraint functions ψ_{ij} converge to the respective stress intensity tensor components k_{ij} . This is shown in Fig. 4 with plots for ψ_{11} and ψ_{22} normalized by $k_{11} = k_{22} = K_I$ at the mid-plane $x_3 = 0$ for the plate $B = 1$ mm. As expected, the constraint functions converge to 1 when $r \rightarrow 0$. For the out-of-plane constraint function ψ_{33} it is verified that converges to $k_{33} = 2\nu K_I$ when $r \rightarrow 0$. Thus, the constraint functions supply relevant information on the three-dimensional near stress field distribution.

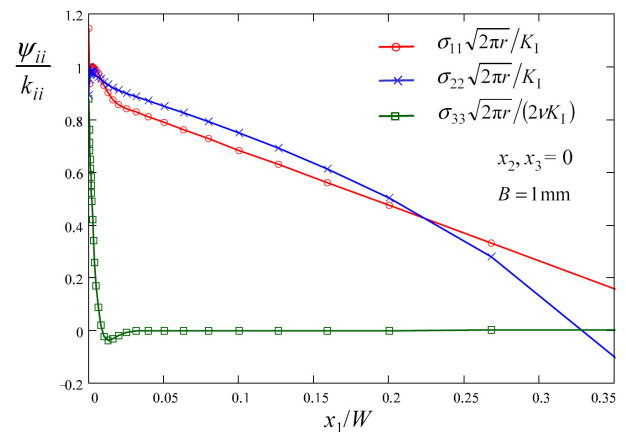


Figure 4. Mid-plane variation of ψ_{ii} (normalized by k_{ii}) along the x_1 axis.

For increasing r , the constraint function ψ_{33} shows a particularly noticeable decay rate, pointing out its close connection with the loss of constraint. This decay rate is strongly dependent on the specimen thickness. The constraint function ψ_{33} gets normalized with respect to B , when a dimensionless distance x_1/B to the crack front is used as abscissa (see Fig. 5), showing the same behaviour of the decay regardless the specimen thickness. A characterization of the loss of constraint is thus possible through the simultaneous consideration of the higher tensor terms of the Williams expansion as a whole, i.e. not only through the sole consideration of the T -stress as suggested by current approaches but also considering the out-of-plane component t_{33} .

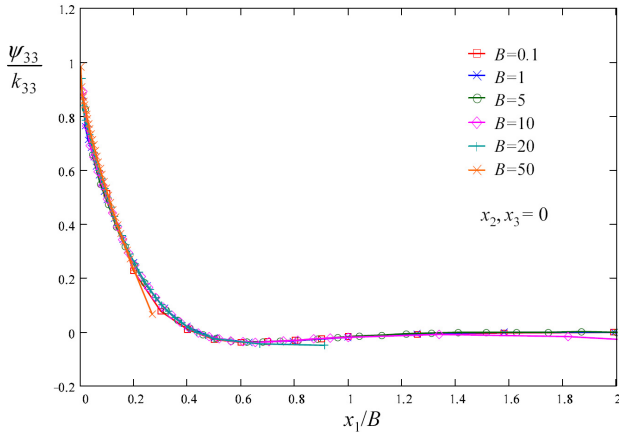


Figure 5. Constraint curves ψ_{33} (normalized by k_{33}) for different B vs. the dimensionless distance x_1/B .

3.4 Calculation of t_{11} and t_{33}

Fig. 6 and 7 show the results of t_{11} and t_{33} calculated at the mid-plane $x_3 = 0$ for the fourteen thicknesses B , four a/W ratios and four Poisson's coefficients. The results are normalized by an equivalent stress calculated from $K_{\text{local}}/(\pi a)^{0.5}$, where K_{local} is the mode-I SIF evaluated at that particular location of the crack front ($x_3 = 0$) using an equivalent domain integral for J . According to [4], a unique constant relationship between J and K_{local} exists, i.e. $K_{\text{local}} = (J_{\text{local}} E / (1 - \nu^2))^{0.5}$, which is independent of the specimen thickness. Two features merit comment: Firstly, t_{33} is always negative (it is a compressive stress) whereas t_{11} can change its sign for small values of a/W (t_{11} tends to be negative for small a/W ratios and large B). This means that the t_{11} and t_{33} values run in opposite trend for decreasing specimen thicknesses. Secondly, the absolute magnitude of t_{33} tends to be approximately one order of magnitude greater than the magnitude of t_{11} pointing out that, in general, the effect of t_{33} cannot be neglected. Moreover, the magnitudes of t_{11} and t_{33} increase for small B , for large a/W and for large ν . As expected, the sensitivity of t_{11} to the ratio a/W is greater than to the thickness B , since t_{11} is an in-plane stress. Note that, in general, t_{11} changes with B (contrary to what it is often stated in the literature) although this dependency is small for the case $a/W = 0.1$. The magnitude of t_{33} is much more sensitive to both B and a/W . Only for very large thicknesses we can observe that t_{33} is small and almost independent of a/W .

Since all the constraint effects present in 3D crack problems are ultimately due to existence of Poisson's ratio effects, its influence is very significant [6], see Fig. 7. Of course, for the case $\nu = 0$, there is no thickness effect and the plate behaves self-similarly throughout the thickness. Note that $t_{33} = 0$ because there is no Poisson contraction in the thickness direction. In this case, t_{11} is not zero and coincides with the value calculated for a 2D plate (the T -stress, like the SIF, is independent of ν and of the limiting 2-D case, plane stress or plane strain, assumed).

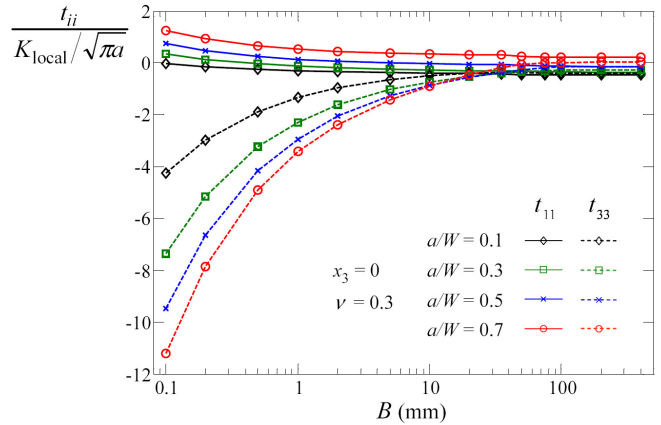


Figure 6. Variation of t_{11} and t_{33} with B and a/W at the mid-plane $x_3 = 0$.

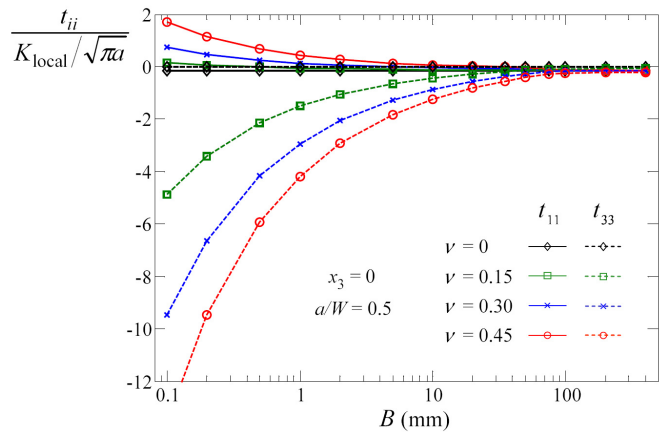


Figure 7. Variation of t_{11} and t_{33} with B and the Poisson's coefficient ν at the mid-plane $x_3 = 0$.

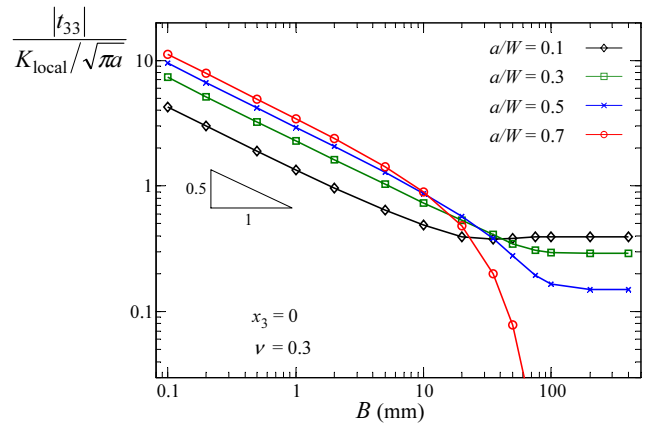


Figure 8. Log-log plot of normalized $|t_{33}|$ vs. B .

Fig. 8 shows a log-log plot of the absolute value of t_{33} (normalized by $K_{\text{local}}/(\pi a)^{0.5}$) versus thickness B . It can be observed that the values fit very well to a straight line of slope -0.5 for small thicknesses (up to approximately $B = 5$ mm). Therefore, a normalization of t_{33} at the mid-plane for small thicknesses and a given a/W ratio, can be achieved using:

$$\frac{t_{33}}{K_{\text{local}}/\sqrt{\pi a}}\sqrt{B} = \text{constant} \quad (7)$$

This relationship enables the approximate calculation of t_{33} for other B provided a computation for a certain B is known and the thicknesses are small. For thicknesses larger than $B = 5$ mm, the effect of the boundaries at $x_1 = \pm W/2$ increases due to the greater relative proximity of these borders and the agreement with a straight line is lost.

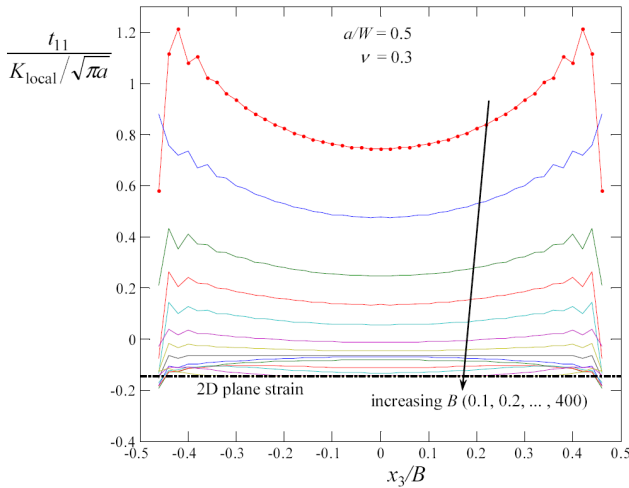


Figure 9. Through-thickness variation of t_{11} along the crack front for different thicknesses B .

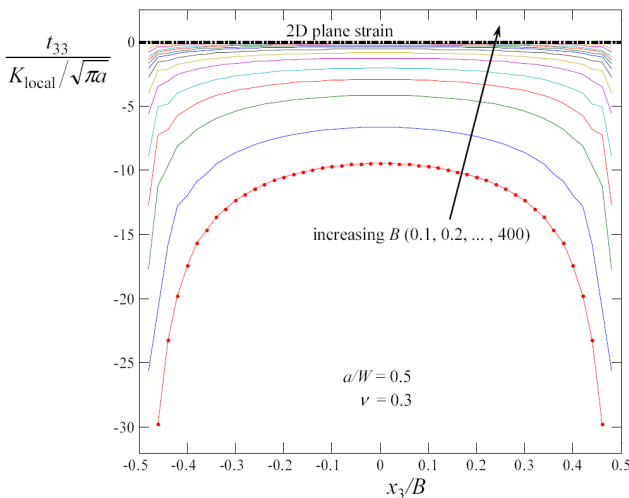


Figure 10. Through-thickness variation of t_{33} along the crack front for different thicknesses B .

In Figs. 9 and 10, the through-thickness variation of t_{11} and t_{33} for the set of fourteen thicknesses is plotted versus the normalized location x_3/B along the crack front. As for the mid-plane location analyzed in previous sections, we can observe that t_{11} and t_{33} clearly increase as $B \rightarrow 0$ for all points on the crack front. In general, the magnitude at the rest of the crack front is even greater than at mid-plane. As expected t_{11} and t_{33} converge to the 2D plane strain values as $B \rightarrow \infty$. This implies a flattening of the curves, decreasing the range of influence of the corner singularities at $x_3/B = \pm 0.5$ for large B .

Note that the value of t_{33} in the 2D plane strain problem, although small, is not zero but $t_{33} = \nu t_{11}$ as commented in Section 2. The computations of t_{11} and t_{33} in the vicinity of the free surfaces must be interpreted with caution, since ϵ_{33} is singular at the corner intersections and is not well calculated using finite elements. The singular behaviour of ϵ_{33} in these zones affects in several ways: first, the computation of the interaction integral used to compute t_{11} tends to diverge [6]; second, the calculations of t_{11} and t_{33} through the interaction integral and Eq. (3), respectively, involve an explicit summation of ϵ_{33} which tends to be singular. Moreover, the validity of the extraction field used in the interaction integral (see [6]) is questioned, as the auxiliary fields corresponding to a line-load of unit magnitude assume a plane strain behaviour. In our opinion, the computation of t_{11} and t_{33} near the free surfaces still requires further research.

5. TRIAXIALITY AND CONSTRAINT

Due to the lack of a satisfactory model to analyse the constraint problem in its whole complexity, some confusion has been observed in the literature referring to triaxiality and constraint. According to the analysis performed in this work, we can state that although having some similitude both definitions represents different concepts. The consideration of the constraint curves helps to understand this question. The study of the influence of the specimen thickness proves that triaxiality is ubiquitous: it is always present in any crack stress distribution irrespective of the specimen thickness B , both in thick specimens (when $B \gg B_{min}$) as well as in thin specimens (when $B \ll B_{min}$) when analyzed sufficiently close to the crack front. Nevertheless, these dissimilar situations clearly represent two opposite constraint states, as shown by the distinct values of the apparent fracture toughness experimentally obtained in both cases. Loss of constraint means limited triaxiality extension but by no means an “absence of triaxiality”.

Applying the constraint function concept to the analysis of the phenomenon allows us to give an adequate interpretation of the constraint role and to understand the differences and affinities of the two limiting cases $B \rightarrow 0$ (not to be mistaken for plane stress) and $B \rightarrow \infty$. Outside from the out-of-constraint zone we can properly speak of 2-D conditions. Though the corresponding constraint curves are qualitatively similar (or even identical after being normalized) their quantitative differences are important depending on the geometric relations. The constraint curves define the extension of the constraint zone.

Since the structure of the k_{ij} has been demonstrated to be independent of the specimen thickness, an explanation of the differences arising in the apparent fracture toughness for specimens showing different thicknesses must be found in the local fracture criterion, based on a stress fracture criterion at a certain distance

of the crack front rather than in a stress intensity factor criterion, the former being influenced by the existing constraint, i.e. the t_{ij} tensor and the extension of the plastic zone.

6. CONCLUSIONS

The main conclusions arising from this work are the following:

- Current biparametric approaches ignore the tridimensional nature of the constant term in Williams expansion so that they cannot describe the influence of the different triaxiality degrees that exist in real specimens of finite thickness. The T -stress alone, i.e. t_{11} , does not give information about the loss of constraint as a whole comprising both in- and out-of-plane effects.
- The present approach proposes the use of the tensor t_{ij} with components t_{11} and t_{33} , and enables the proper definition of complex constraint states arising in real specimens. With this proposal, the effects of both crack length and specimen thickness on the apparent fracture toughness can be addressed.
- The validity of the biparametric approach for specimen thicknesses greater than B_{\min} can be explained as an special case in which t_{33} becomes νt_{11} due to the condition $\varepsilon_{33} \approx 0$, so that t_{ij} can be expressed solely in terms of t_{11} . On the contrary, t_{ij} depends on both t_{11} and t_{33} for thinner specimens.
- It is also shown that t_{11} depends on other factors, such as the specimen thickness B .
- The interdependence among t_{11} , t_{33} and ε_{33} has been analytically derived.
- The constraint curves ψ_{ij} facilitate the conceptual comprehension of the loss of constraint and can be used for a quantitative assessment.
- The numerical calculations prove that specimen thickness B and crack depth ratio a/W exert an influence on the results of both components of the t_{ij} tensor, i.e. on t_{11} and t_{33} , the latter being more sensitive to those factors. As a result, the influence on the apparent fracture toughness cannot be merely attributed to the in-plane component.
- It is possible to normalize t_{33} for small specimen thicknesses, enabling an easy evaluation of the thickness influence on the t_{33} stress.

ACKNOWLEDGEMENTS

The authors gratefully acknowledge the financial support given by the DGICYT of the Spanish Ministry of Science and Innovation (Projects DPI2007-66995-

C03-02 and DPI2007-66903-C02-01) and by FICYT (Project IB08-171).

REFERENCES

- [1] Seitzl S., Knésl Z., *Two parameter fracture mechanics: fatigue crack behaviour under mixed mode conditions*, Eng. Fracture Mech. 72, 857-865, 2008.
- [2] Betegón C., Hancock J., *Two-parameter characterization of elastic-plastic crack-tip fields*. J. Appl. Mech. Transactions of the ASME, 113, 104-110, 1991.
- [3] Fernández Canteli A., Castillo E., Fernández Zúñiga D., *Linear-elastic fracture mechanics based criteria for fracture including out-of-plane constraint effect*, Submitted to Theoretical and Applied Fracture Mechanics, 2009.
- [4] Giner E., Fernández Zúñiga D., J. Fernández Sáez, Fernández Canteli A., *On the J_{x1} -integral and the out-of-plane constraint in a 3D elastic cracked plate loaded in tension*, Submitted to Int. J. Solids Structures, 2009.
- [5] Fernández Zúñiga D., Kalthoff J.F., Fernández Canteli A., Grasa J., Doblaré M., *Three-dimensional finite element calculations of crack tip plastic zones and K_{Ic} specimen size requirements*, ECF 15, Stockholm, 11-13 August 2004
- [6] Nakamura T., Parks D.M., *Determination of elastic T -stress along three-dimensional crack fronts using an interaction integral*, Int. J. Solids Structures, 29, 1597-1611, 1992.
- [7] Kwon S., Sun C., *Characteristics of three-dimensional stress fields in plates with a through-the-thickness crack*, Int. J. Fracture, 104, 291-315, 2000.
- [8] Williams M.L., *On the stress distribution at the base of a stationary crack*. J. Appl. Mech., 24, 109-114, 1957.

SIZE EFFECT IN THE SHEAR-COUPLED MIGRATION OF TILT BOUNDARIES WITH INTERGRANULAR NANOCRACKS

A. Irastorza, A. Luque, J. Aldazabal, J.M. Martínez-Esnaola, J. Gil Sevillano

CEIT and TECNUN (University of Navarra).

Paseo Manuel de Lardizábal 15, 20018 San Sebastián. Spain.

E-mail: aluque@ceit.es. Phone: +34 943212800. Fax: +34 943213076.

ABSTRACT

In this work, we present molecular dynamics simulations of the shear-coupled migration behaviour of symmetrical tilt boundaries $\Sigma 17(530)$ perturbed by the presence of nanocracks lying on the grain boundary. The simulations were performed for copper bicrystals at 300 K. The focus has been on the study of crack size effects. The simulations were carried out using the embedded atom method with temperature control. Systems of constant width, X , and different crack sizes, $2a$, were generated at 0 K. The ratio $2a/X$ characterizes the system. Periodic boundary conditions were set along the direction of application of the load and the tilt axis. After relaxation, the virtual shear of the bicrystals was carried out at a constant rate of 10^8 s^{-1} . The response of the cracked specimens can be divided into: (i) shear-coupled migration of the grain boundary with increasing applied shear stress, (ii) intergranular propagation of the crack and (iii) emission of dislocations and closing of the grain boundary dislocation loop.

KEY WORDS: Copper, molecular dynamics, shear-coupled migration, nanocracks, mode II loading.

1. INTRODUCTION

Shear-coupled migration (SCM) [1–10] has been recognized as a particular plastic strain mechanism that can complement or compete with other plastic mechanisms available to polycrystals: dislocation-mediated slips, grain boundary (GB) sliding, twinning... Conservative SCM of pure tilt boundaries is diffusionless and occurs by collective atomic motion without recourse to long-range diffusion. The process is thermally activated but can take place at low temperatures. In fact, at these temperatures, it can be the dominant shear-driven GB migration mechanism. The SCM phenomenon implies that, as a consequence of the applied shear stress, τ , the GB shows two types of motions, which are depicted in Figure 1. The first one is the sliding of the GB, a movement parallel to the plane containing the boundary and characterized by the GB sliding velocity, $v_{//}$. The second one is the migration of the GB, a movement perpendicular to the plane that contains the boundary and characterized by the GB migration velocity, v_n .

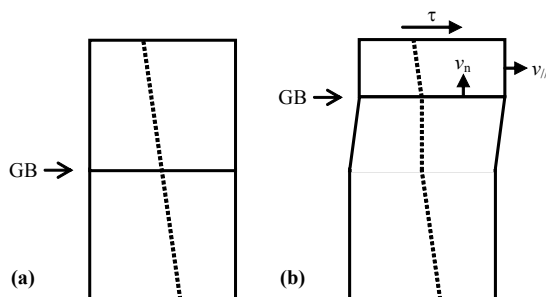


Figure 1. SCM phenomenon in a planar boundary of a free bicrystal: (a) initial configuration and (b) after the application of a shear stress. The dotted fiducial lines permit following the response of the bicrystal [6].

The effectiveness of the applied shear stress in the SCM phenomenon can be characterized in terms of the shear

coupling factor, β , defined as

$$\beta = \frac{v_{//}}{v_n} \tag{1}$$

Some authors [6] have proposed a geometrical model based on the dislocation content of the symmetrical tilt boundary which permits obtaining β in terms of the GB misorientation, φ , as

$$\beta = 2 \tan\left(\frac{\varphi}{2}\right) \tag{2.a}$$

$$\beta = -2 \tan\left(\frac{\pi}{4} - \frac{\varphi}{2}\right) \tag{2.b}$$

Equation 2.a applies to low misorientations ($\varphi < 35^\circ$ – 40°) and produces a “positive” coupling between the applied shear stress and the GB migration (GB moving upwards when τ is applied to the right). Equation 2.b applies to high misorientations and produces a “negative” coupling, this is, the GB migration occurs in the opposite sense compared to “positive” coupling.

The current burst of interest on SCM is due to its active role in the mechanical behaviour of nanograined materials and in the structural changes taking place in such materials when subjected to stress at low temperatures. Some examples of this are load around crack tips, grain growth during nanoindentation and fatigue [11]. SCM requires high resolved shear stresses that cannot be reached in polycrystals with conventional grain size. Therefore, a good understanding and mastering of SCM in nanostructured materials is essential to warrant their structural stability.

In this work, we present molecular dynamics (MD) simulations of the SCM behaviour of the symmetrical

tilt boundary $\Sigma 17(530)$ perturbed by the presence of nanocracks lying on the GB. The simulations have been performed for copper bicrystals at 300 K. We have compared the behaviour of a perfect boundary with the behaviour of a GB presenting nanocracks and the crack size effect on this kind of systems.

2. SIMULATION CHARACTERISTICS

2.1. Molecular dynamics technique

The MD technique used for these atomistic simulations was the embedded atom method (EAM) [12,13]. The potentials that we have used in this EAM approach correspond to copper [14]. Further details of both this MD technique and these potentials can be found elsewhere [15,16]. It is particularly important to mention that the cut-off radius, r_{cut} , of the atomic interactions is 0.55 nm. For the numerical integration of the motion equations, the time increment, Δt , equals 2.5×10^{-15} s. The Nosé–Hoover thermostat [17,18] was implemented to control the system temperature, T , which, in this case, equals 300 K.

2.2. The $\Sigma 17(530)$ tilt boundary

In this work, the generated bicrystals present a symmetrical tilt boundary $\Sigma 17(530)/[001]$. Σ is the relationship between the number of lattice points in a unit cell of the generating lattice and the number of lattice points in a unit cell of the coincidence site lattice (CSL). The first Miller indices after $\Sigma 17$, namely (530), indicate the plane where the GB lies and correspond to the y axis. The following Miller indices, namely [001], are the tilt axis and correspond to the $-z$ direction. In these simulations, the crack is contained in the plane (530) and the crack tip lies on the [001] direction. The symmetrical tilt boundary $\Sigma 17(530)$ corresponds to a high-angle misorientation of $\varphi = 61.9^\circ$. According to Equation 2.b, this misorientation yields a shear coupling factor of $\beta = -0.5$ for the case of a planar free GB.

2.3. Specimen generation and test features

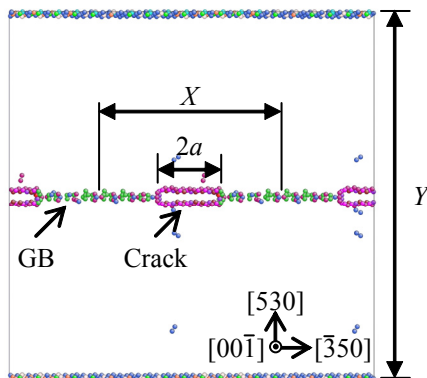


Figure 2. Initial configuration of the cracked copper bicrystals presenting a symmetrical tilt boundary $\Sigma 17(530)$. The case of $2a/X = 1/3$ is shown.

The uncracked and cracked bicrystals were constructed at 0 K. For both types of samples, the number of specimens is three. For the uncracked samples, the X dimension is 4.2 nm, 10.6 nm or 14.9 nm. The Y dimension is 8.4 nm, 21.1 nm or 29.2 nm. In all cases, the Z dimension is 2.2 nm. In the case of the cracked specimens, sample dimensions are $10.6 \text{ nm} \times 2.2 \text{ nm} \times 21.1 \text{ nm}$. Nanocracks were formed by removing the atoms located in a band of 0.55 nm of thickness, centred in the GB, along $1/2$, $1/3$ and $1/4$ of the specimen size along the x axis. Thus, $2a/X$ equals $1/2$, $1/3$ and $1/4$ (see Figure 2).

After generation of the bicrystals, the samples were relaxed to let the GB acquire a metastable configuration. The relaxation process proceeded at 0 K during 5 ps. Then, the temperature was increased linearly up to 300 K during 7.5 ps. Finally, the samples were kept at 300 K for 12.5 ps. Surface tension lead to some global and local geometrical distortion of the initial shape (particularly, at the crack tip).

After relaxation, two rigid zones of 0.55 nm of thickness were set in the upper and lower layers of the sample. During the simulations, carried out under displacement control, the lower layer remained fixed, whereas the upper rigid zone was displaced along the x axis at constant speed of $v_{//} \approx 2.1 \text{ m s}^{-1}$. This corresponds to a shear strain rate, $\dot{\gamma}$, of 10^8 s^{-1} . The rest of the atoms of the system can freely move. Periodic boundary conditions were set along the x and z axes. Thus, the specimens are in fact periodically cracked samples, as shown in Figure 2.

The imposed shear displacement and the resulting required force were stored during the simulations, in order to compute the shear stress vs. shear strain τ - γ curves. Atomic positions were also periodically stored to analyze any structural changes (GB migration and slip, dislocation nucleation and emission, crack propagation) [19].

3. RESULTS AND DISCUSSION

Before presenting the results of these simulations, we will briefly explain the method used for the calculation of the applied stress. The applied (global) stress tensor, σ_∞ , can be computed through the virial expression [20]:

$$\sigma_\infty = \frac{1}{V} \sum_{i=1}^N \left(m \mathbf{v}_i \otimes \mathbf{v}_i - \frac{1}{2} \sum_{j \neq i} \mathbf{r}_{ij} \otimes \mathbf{f}_{ij} \right) \quad (3)$$

where V is the system volume, m is the atomic mass, \mathbf{v}_i is the velocity of atom i , \mathbf{r}_{ij} is the distance vector between atoms i and j and \mathbf{f}_{ij} is the force between these two atoms. The result of the tensor product $\mathbf{a} \otimes \mathbf{b}$ is a matrix \mathbf{C} such that $C_{\alpha\beta} = a_\alpha \cdot b_\beta$ ($\alpha, \beta = x, y, z$). Thus, the applied shear stress τ corresponds to the term τ_{xy} of the

stress tensor σ_∞ . The virial theorem is generally applied to each atom to get a local stress tensor. However, some authors have developed a more accurate way of representing local stresses [21,22]:

$$\sigma = \frac{1}{\Omega} \left(\Lambda_i (m \mathbf{v}_i \otimes \mathbf{v}_i) - \frac{1}{2} \sum_{j \neq i} \lambda_{ij} (\mathbf{r}_{ij} \otimes \mathbf{f}_{ij}) \right) \quad (4)$$

where Ω is the volume of some representative partition element, Λ_i equals 1 if atom i is within the volume element and 0 otherwise, and λ_{ij} is the fraction of the length of the bond between atoms i and j lying within the volume element. In this work, we have chosen the volume element to be a sphere of radius equal to the copper lattice parameter, $a = 0.36$ nm, centred on each atom. Therefore, each σ can be associated to the local stress at the position of the central atom.

3.1. Uncracked samples

Figure 3 shows the τ - γ responses for the three uncracked bicrystals simulated at 300 K. The discussion of the main results corresponding to the uncracked configuration of the symmetrical tilt boundary $\Sigma 17(530)$ can be found elsewhere [11,23]. However, it is important to note that:

- The negative coupling is observed: the GB migrates downwards when the shear stress is applied to the right. A shear coupling factor $\beta \approx -0.5$ is computed.
- The slopes of the intermittent elastic loading stages are very similar to the elastic shear modulus, namely $G = 27.3$ GPa, for a single crystal with the same orientation as the samples and considering the elastic anisotropy of copper [24,25].
- The SCM is associated to a stick-slip phenomenon characterized by the overcoming of a critical value of applied shear stress, namely $\tau_c \approx 0.4$ GPa [26].

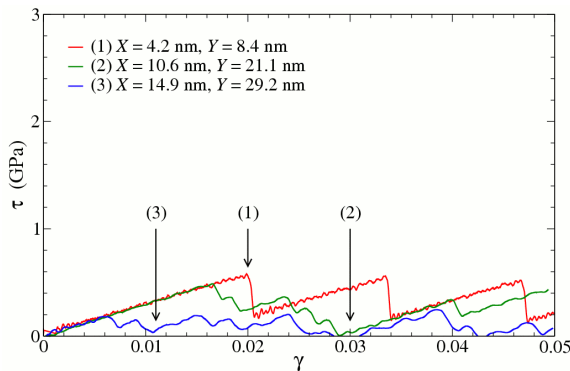


Figure 3. Shear stress, τ , vs. shear strain, γ , curves at 300 K of the uncracked copper bicrystals presenting a symmetrical tilt boundary $\Sigma 17(530)$.

3.2. Cracked samples

Figure 4 shows the τ - γ responses for the three cracked bicrystals simulated at 300 K. Besides, Table 1 summarizes some relevant mechanical properties of

these samples: shear modulus, G , shear stress and shear strain for crack propagation, τ_{prop} and γ_{prop} , respectively, maximum applied shear stress, τ_{max} , and shear strain at the maximum shear stress, γ_{max} . The first thing that we can observe in Figure 4 is that the presence of cracks significantly affects their mechanical response. Surprisingly, the cracked samples are strengthened by the intergranular cracks. In the following sections, we detail and explain this behaviour.

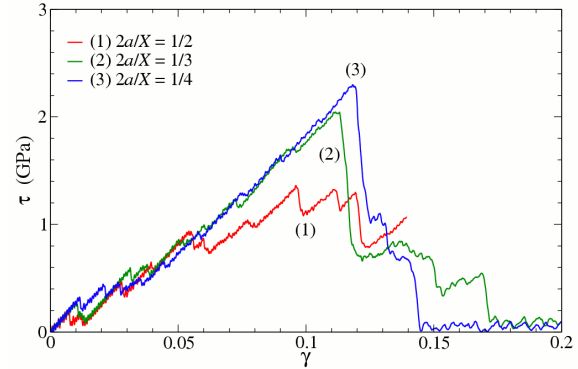


Figure 4. Shear stress, τ , vs. shear strain, γ , curves at 300 K of the cracked copper bicrystals presenting a symmetrical tilt boundary $\Sigma 17(530)$.

Table 1. Summary of the mechanical properties of the cracked copper bicrystals presenting a symmetrical tilt boundary $\Sigma 17(530)$ at 300 K.

	(1) $2a/X = 1/2$	(2) $2a/X = 1/3$	(3) $2a/X = 1/4$
G (GPa)	24.3	26.3	28.6
τ_{prop} (GPa)	0.93	1.24	–
γ_{prop} @ τ_{prop}	0.055	0.073	–
τ_{max} (GPa)	1.35	2.04	2.29
γ_{max} @ τ_{max}	0.096	0.111	0.119

3.2.1. SCM behaviour

Figure 4 shows that the cracked samples behave as uncracked specimens do [11,23]. This is, they behave elastically, with G values summarized in Table 1, and when a critical value of τ is overcome, the SCM of the GB occurs, with the same stick-slip behaviour. This is the main deformation mechanism while $\gamma < 0.05$ – 0.07 . Unlike the uncracked samples, the applied shear stress does not remain at a low level. It needs to be increased for producing further deformation of the cracked sample. This is caused by the intergranular cracks which pin the GB [27,28]. Thus, the SCM can only take place away from the crack tips and that makes the GB to bow out (downwards, as $\beta < 0$; see Figure 5.a). The misorientation between the GB and the crack tip progressively increases and, therefore, further GB migration becomes more and more complicated [11].

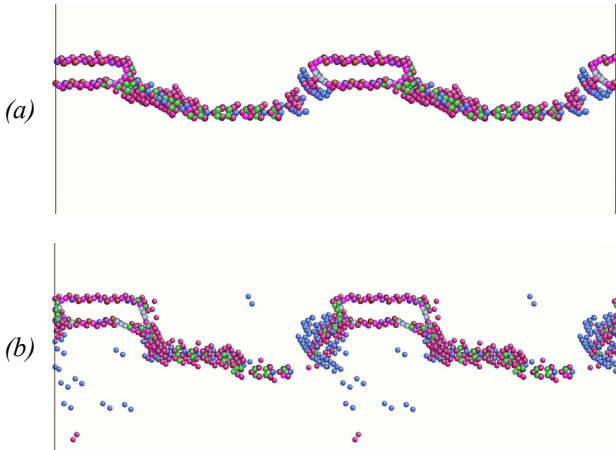


Figure 5. Detail of the cracked copper bicrystal ($2a/X = 1/3$) presenting a symmetrical tilt boundary $\Sigma 17(530)$ at 300 K with (a) $\gamma = 0.071$ (the GB bows out), and (b) $\gamma = 0.11$ (the crack propagates, the GB keeps on migrating).

3.2.2. Crack propagation

When the angle formed by the GB and the crack plane is $\sim 31^\circ$, a different deformation mechanism activates. The propagation of the crack through the GB can be observed. That occurs at $\gamma = 0.055$ and $\gamma = 0.073$ for the samples with $2a/X = 1/2$ and $2a/X = 1/3$, respectively. However, it does not take place in the sample with $2a/X = 1/4$. Therefore, there must also be a significant contribution of the crack length (the $2a/X$ ratio) and the stress concentration at the crack plane. As shown in Figure 5.b, the crack opening close to the crack tip produces different events of intergranular fracture along the GB when it lies on a (100) plane, indicating a possible ductile fracture. Further crack propagation is hindered and the SCM mechanism is enabled again.

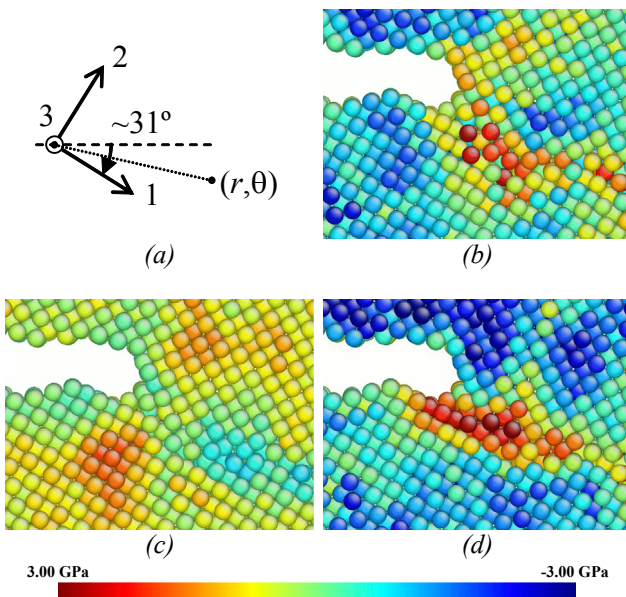


Figure 6. (a) Local coordinate system for the crack study [29]. (b) σ_1 , (c) τ_{12} and (d) σ_2 , for the cracked copper bicrystal ($2a/X = 1/3$) presenting a symmetrical tilt boundary $\Sigma 17(530)$ with $\gamma = 0.074$ at 300 K.

We are going to analyse the stress distribution ahead of the crack front ($\theta = 0$), too. For that, we first calculate the local stress associated to the atoms, according to Equation 4. However, we have already mentioned that the crack advances at a particular angle. Therefore, we have to rotate the obtained stress tensor to a coordinate system as the one depicted in Figure 6. This coordinate system is such that the crack propagation occurs along the 1 direction. Note that, in all of the cases, the components τ_{13} , τ_{23} and τ_{33} of the local stress tensor, are nearly zero or small compared with the other stress terms. Therefore, they are not presented here. The rest of stress terms are shown in Figure 6. Figure 7 shows the stress distribution ahead of the crack for the samples which showed crack propagation.

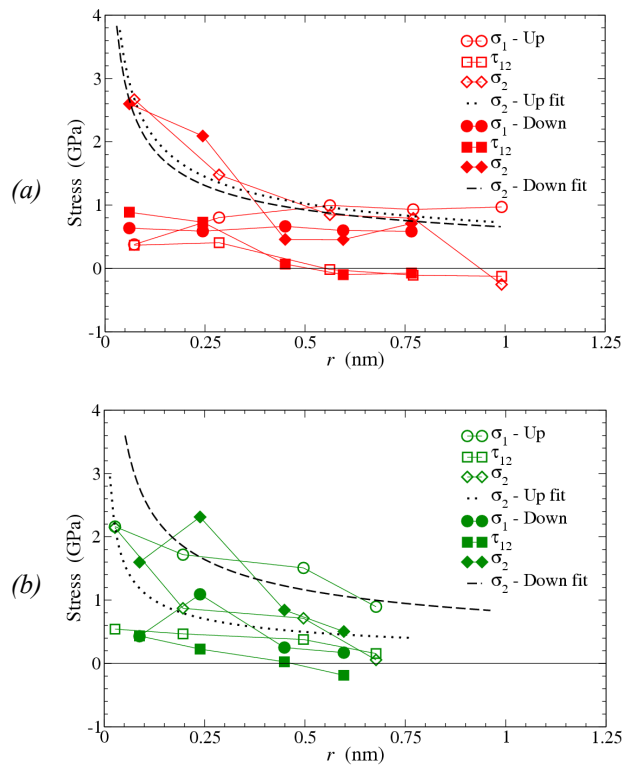


Figure 7. Stress distribution as a function of the distance to the crack tip, r : (a) $2a/X = 1/2$ and (b) $2a/X = 1/3$, at the corresponding γ_{prop} (see Table 1). The power-law fits of σ_2 , namely $\sigma_2 \propto r^{-1/2}$, are also shown.

In Figure 7, for each simulation, two different groups of data have been collected: the data series labelled “Up” refer to atoms just above the (100) plane (the crack propagation plane) and lying along the [010] direction, and the label “Down” refers to atoms just below the (001) plane and lying along [010]. Note that the curves depicted in Figure 7 represent the values of σ_1 , τ_{12} and σ_2 , averaged along the z axis, at different distances from the crack tip, r . However, it should also be reminded that, connaturally to the atomistic simulations, the position of the “crack tip” is not well defined, and that concepts such as “sharp crack” have no sense here. However, the position of crack tip can be bounded in the plane of the crack propagation. For this reason, the origin of the distances to the crack tip has been

considered as a parameter in the fits shown in Figure 7. These curves show that σ_2 can be fitted with a power-law function of r . Note that the fit of the cracked bicrystal of $2a/X = 1/2$ (Figure 7.a) is particularly good and consistent above and below the propagation plane. For both samples, $\sigma_2 \propto r^{-\lambda}$, with $\lambda = 1/2$, which corresponds to the linear elastic solution proposed in the continuum for a sharp crack [29]. This is in line with other atomistic fracture results which indicate that it is possible to express the opening displacement, Δu_2 , of the atoms of the crack faces ($\theta = \pm\pi$) in terms of $r^{1/2}$ [15,16]. These fits yield a critical stress intensity factor, K_{Ic} , ranging between 30 kPa \sqrt{m} and 65 kPa \sqrt{m} . Although small, these values are of the same order of other stress intensity factors calculated on a stress basis and reported in the literature for heterogeneous dislocation nucleation in a different crystal orientation but at the same temperature [15,16]. This may indicate that the observed crack propagation is a dislocation-mediated process, and, thus, ductile, in which the generated dislocations are accommodated in the GB as they are emitted. In turn, dislocation generation would help explain why SCM is active after crack propagation.

3.2.3. Closing of the GB

As mentioned, the SCM mechanism is enabled again as consequence of the dislocation activity in the sample. When crack propagation stops and, as shown in Figure 4, the applied shear stress is as high as 2 GPa (see Table 1), the emission of dislocations from the GB takes place (see Figure 8.a) [11]. That occurs at $\gamma = 0.111$ and $\gamma = 0.119$ for the samples with $2a/X = 1/3$ and $2a/X = 1/4$, respectively. However, it is not observed in the cracked sample of $2a/X = 1/2$ as τ is not high enough.

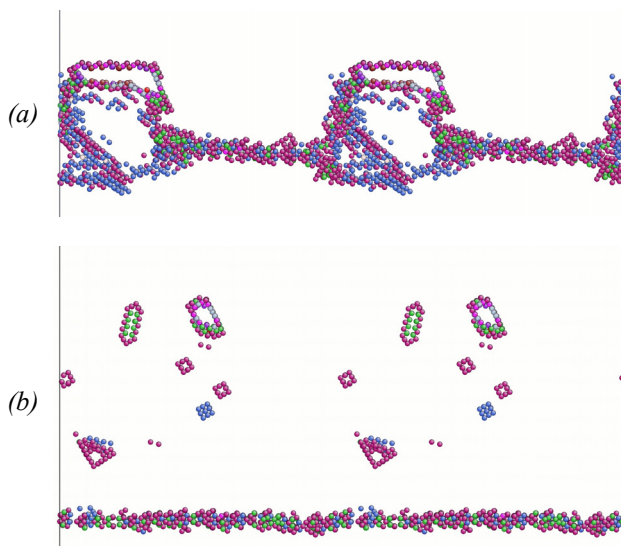


Figure 8. Detail of the cracked copper bicrystal ($2a/X = 1/3$) presenting a symmetrical tilt boundary $\Sigma 17(530)$ at 300 K with (a) $\gamma = 0.116$ (partial dislocation emission and closing of the GB), and (b) $\gamma = 0.2$ (the GB is free from the crack and other obstacles).

The dislocations emitted during this step of the simulation are partial dislocations in the $\{111\}\langle 211\rangle$ system. As it can be seen in Figure 8.a, they propagate in the lower crystal until they permit closing the GB dislocation loop. This implies the formation of a new GB below the crack and, thus, the pinning effect exerted by the crack starts to disappear. In the case of the cracked sample of $2a/X = 1/3$, this process is helped by the reduction of the crack size, as shown in Figure 8.b. Nevertheless, the sample of $2a/X = 1/4$ does not show that crack size reduction. Once the GB gets to detach from the crack (and from other softer obstacles formed during the unpinning process: note, in Figure 4, the differences in the τ - γ response after the big stress drop in these two cracked samples), the boundary configuration of the cracked specimens and the GB of the uncracked bicrystals look very much alike. Therefore, further deformation of the samples produces SCM of the GB at shear stresses of the same order of the τ_c observed in the uncracked samples.

Finally, it is worth mentioning that, in the cracked sample of $2a/X = 1/2$, as the nucleation of dislocations does not occur, the SCM of the GB cannot be enabled again. Nevertheless, a different mechanism activates in order to accommodate the introduced deformation. That mechanism is the GB slip [11], which is also possible due to the reduced dimension of the ligament. As a consequence, the crack changes of shape, as shown in Figure 9.

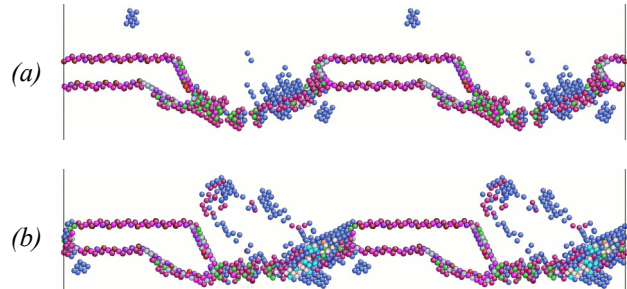


Figure 9. Detail of the cracked copper bicrystal ($2a/X = 1/2$) presenting a symmetrical tilt boundary $\Sigma 17(530)$ at 300 K with (a) $\gamma = 0.11$ (before GB slip), and (b) $\gamma = 0.138$ (after GB slip).

4. CONCLUSIONS

The shear-coupled migration of the symmetrical tilt boundary $\Sigma 17(530)/[001]$ is hindered by the presence of intergranular nanocracks. The tilt boundary is pinned by the crack tip and migration occurs with the bowing-out of the grain boundary. The applied stress needs to be increased above the critical shear stress value that makes a flat boundary migrate. Hence, nanocracks strengthen the material. However, intergranular crack propagation is observed and that permits further advance of the grain boundary. We have reasonably fitted the stress ahead of the crack with $r^{-1/2}$, as proposed within the linear elastic solution for sharp

cracks. The applied shear stress grows until new plastic-deformation mechanisms activate, such as dislocation emission of grain boundary sliding. The emission of dislocations takes place at the same time as shear-coupled migration, and, finally, the boundary can detach from the crack tip.

ACKNOWLEDGMENTS

This work was supported by the Department of Industry, Commerce and Tourism of the Basque Government (project ETORTEK inanoGUNE). A. Luque also acknowledges the Spanish Ministry of Science and Innovation and the European Social Fund (Torres Quevedo Programme).

REFERENCES

- [1] Li, C.H., Edwards, E.H. and Parker, E.R., “Stress-induced movement of crystal boundaries”, *Acta Metall.* 1, 223–229, 1953.
- [2] Bainbridge, D.W., Li, C.H. and Edwards, E.H., “Recent observations on the motion of small angle dislocation boundaries”, *Acta Metall.*, 2, 322–333, 1954.
- [3] Winning, M., Gottstein, G. and Shvindlerman, L.S., “Stress induced grain boundary motion”, *Acta Mater.*, 49, 211–219, 2001.
- [4] Winning, M., Gottstein, G. and Shvindlerman, L.S., “On the mechanisms of grain boundary migration”, *Acta Mater.*, 50, 353–363, 2002.
- [5] Winning, M., “Motion of <100>-tilt grain boundaries”, *Acta Mater.*, 51, 6465–6475, 2003.
- [6] Cahn, J.W., Mishin, Y. and Suzuki, A., “Coupling grain boundary motion to shear deformation”, *Acta Mater.*, 54, 4953–4975, 2006.
- [7] Cahn, J.W., Mishin, Y. and Suzuki, A., “Duality of dislocation content of grain boundaries”, *Philos. Mag.*, 86, 3965–3980, 2006.
- [8] Molodov, D.A., Ivanov, V.A. and Gottstein, G., “Low angle tilt boundary migration coupled to shear deformation”, *Acta Mater.*, 55, 1843–1848, 2007.
- [9] Winning, M., “In-situ observations of coupled grain boundary motion”, *Philos. Mag.*, 87, 5017–5031, 2007.
- [10] Zhang, H., Du, D. and Srolovitz, D.J., “Effects of boundary inclination and boundary type on shear-driven grain boundary migration”, *Philos. Mag.*, 88, 243–256, 2008.
- [11] Luque, A., Aldazabal, J., Martínez-Esnaola, J.M. and Gil Sevillano, J., “Plastic deformation by conservative shear-coupled migration of tilt boundaries with intergranular nano-cracks or precipitates”, *Philos. Mag.*, 2009, available online. DOI: 10.1080/14786430903097715.
- [12] Daw, M.S. and Baskes, M.I., “Semiempirical, quantum mechanical calculation of hydrogen embrittlement in metals”, *Phys. Rev. Lett.*, 50, 1258–1288, 1983.
- [13] Daw, M.S. and Baskes, M.I., “Embedded-atom method: Derivation and application to impurities, surfaces and other defects in metals”, *Phys. Rev. B*, 29, 6443–6453, 1984.
- [14] Mishin, Y., Farkas, D., Mehl, M.J. and Papaconstatopoulos, D.A., “Structural stability and lattice defects in copper: Ab-initio, tight-binding and embedded-atom calculations”, *Phys. Rev. B*, 63, 224106/1–6, 2001.
- [15] Luque, A., Aldazabal, J., Martínez-Esnaola, J.M. and Gil Sevillano, J., “Atomistic simulation of tensile strength and toughness of cracked Cu nanowires”, *Fatigue Fract. Engng. Mater. Struct.*, 29, 615–622, 2006.
- [16] Luque, A., Aldazabal, J., Martínez-Esnaola, J.M. and Gil Sevillano, J., “Molecular dynamics simulation of crack tip blunting in opposing directions along a symmetrical tilt boundary of copper bycrystal”, *Fatigue Fract. Engng. Mater. Struct.*, 30, 1008–1015, 2007.
- [17] Nosé, S., “A unified formulation of the constant temperature molecular dynamics methods”, *J. Chem. Phys.* 81, 511–519, 1984.
- [18] Hoover, W.G., “Canonical dynamics: Equilibrium phase-space distributions”, *Phys. Rev. A*, 31, 1695–1697, 1985.
- [19] Li, J., “AtomEye: An efficient atomistic configuration viewer”, *Modell. Simul. Mater. Sci. Eng.*, 11, 173–177, 2003.
- [20] Sun, Z.H., Wang, X.X., Soh, A.K. and Wu, H.A., “On stress calculations in atomistic simulations”, *Modell. Simul. Mater. Sci. Eng.*, 14, 423–431, 2006.
- [21] Van Swygenhoven, H. and Derlet, P. M., “The atomistic simulation of dislocations in FCC metallic nanocrystalline materials”, *Dislocations in Solids*, Ch 81, 1–42 (2008) Eds. J. Hirth, 2007.
- [22] Cormier, J., Rickman, J.M. and Delph, T.J., “Stress calculation in atomistic simulations of perfect and imperfect solids”, *J. Appl. Phys.*, 89, 99–104, 2001.
- [23] Luque, A., Aldazabal, J., Martínez-Esnaola, J.M. and Gil Sevillano, J., “Mode II loading behaviour of intergranular cracks lying on $\Sigma 17(530)/[001]$ symmetrical tilt boundary in copper”, *Phys. Status Solidi C*, 6, 2107–2112, 2009.
- [24] Sharif, A.A., Chu, F., Misra, A., Mitchell, T.E. and Petrovic, J.J., “
- [25] Gale, W.F. and Totemeier, W.F. (editors), *Smithells Metal Reference Book*, Elsevier, Amsterdam (The Netherlands), 2004.
- [26] Mishin, Y., Suzuki, A., Uberuaga, B.P. and Voter, A.F., “Stick-slip behaviour of grain boundaries studied by accelerated molecular dynamics”, *Phys. Rev. B*, 75, 224101/1–7, 2007.
- [27] Scattergood, R.O. and Bacon, D.J., “The strengthening effect of voids”, *Acta Metall.*, 30, 1665–1677 (1982).
- [28] Osetsky, Y.N. and Bacon D.J., “Comparison of void strengthening in fcc and bcc metals: Large-scale atomic-level modelling”, *Mater. Sci. Eng. A*, 400/401, 374–377, 2005.
- [29] Martín-Meizoso, A. and Martínez-Esnaola, J.M., *Mecánica de la Fractura*, Tecnun-Universidad de Navarra, Donostia-San Sebastián (Spain), 1999.

ESTUDIO DEL COMPORTAMIENTO EN FRACTURA DE VAINAS DE COMBUSTIBLE NUCLEAR FRAGILIZADAS POR HIDRUIROS.

M.A. Martin-Rengel^(1,2), F.J. Gomez⁽¹⁾, J. Ruiz-Hervias⁽¹⁾, L. Caballero⁽¹⁾, A. Valiente⁽¹⁾

¹Departamento de Ciencia de Materiales, UPM, E.T.S.I. Caminos, Canales y Puertos
Profesor Aranguren s/n, E-28040 Madrid, Spain
E-mail: jr@mater.upm.es

²Consejo de Seguridad Nuclear (CSN)
Justo Dorado 11, E-28040 Madrid, Spain
E-mail: mamartin@mater.upm.es

RESUMEN

En este artículo se ha estudiado, mediante el ensayo de compresión diametral (RCT), el comportamiento mecánico y en rotura de vainas de combustible nuclear de ZIRLO™ hidruradas. El hidrógeno se introdujo en las muestras mediante carga catódica y se precipitó en forma de hidruros circunferenciales mediante un tratamiento térmico. Los ensayos de compresión diametral se realizaron para concentraciones de hidrógeno de 150 a 2000 ppm. Los resultados experimentales obtenidos muestran que este ensayo es particularmente útil para el estudio del comportamiento en fractura de las vainas. Con este fin, se desarrolló un modelo de elementos finitos en el que se implementó la teoría de la fisura cohesiva. Aplicando dicho modelo se ha logrado calcular la energía de fractura de las vainas de combustible nuclear en dirección circunferencial para los distintos contenidos de hidrógeno estudiados a partir de los registros experimentales carga-desplazamiento del ensayo.

Palabras clave: Vaina de combustible nuclear, ensayo de compresión diametral, fractura, fragilización por hidrógeno.

ABSTRACT

The mechanical and fracture behaviour of unirradiated hydrogen-charged ZIRLO™ cladding was studied in this paper by using the ring compression test (RCT). Cathodic charging followed by a thermal treatment was employed to precipitate hydrides in the circumferential direction of the cladding samples. Samples with hydrogen concentrations from 150 ppm to 2000 ppm were prepared and tested using the RCT. The experimental results have shown that this test seems to be particularly useful to study cladding fracture. To this end, a finite element model incorporating the cohesive crack theory was developed. As a result, the fracture energy of nuclear fuel claddings in hoop direction was calculated as a function of the hydrogen concentration from the experimental RCT load vs. displacement curves.

Key words: Nuclear fuel cladding, ring compression test, fracture, hydrogen embrittlement.

1. INTRODUCCIÓN.

Las vainas de combustible nuclear constituyen la primera barrera estructural de contención de las pastillas cerámicas del combustible y de los productos de fisión generados. Estas vainas se fabrican con aleaciones de circonio debido a la transparencia al flujo neutrónico que presenta este material, a sus buenas propiedades mecánicas y a su resistencia a la corrosión en condiciones de operación. En servicio, la reacción de oxidación que tiene lugar en la superficie exterior de la vaina (en contacto con agua o vapor de agua a 300°C), produce hidrógeno, el cual es absorbido por la vaina y se difunde por la misma debido a los gradientes de temperatura existentes. Este hidrógeno precipita en forma de hidruros cuando se sobrepasa su límite de solubilidad. Dichos hidruros de circonio degradan las propiedades mecánicas de las vainas [1-3].

El hinchamiento de las pastillas cerámicas del combustible y los gases de fisión generados a lo largo del ciclo de vida del combustible generan una tensión circunferencial en la vaina. Dado que las vainas son anisótropas, es necesario disponer de ensayos para caracterizarlas mecánicamente en la dirección circunferencial. En la literatura se proponen distintos ensayos para la caracterización mecánica de las vainas en dirección circunferencial, aunque no hay acuerdo sobre cuál de ellos es el mejor [4].

El ensayo de compresión en anillo ha sido utilizado para simular las condiciones a las que se encuentran sometidas las vainas durante algunos transitorios de potencia [5] y para el estudio de reorientación de hidruros en dirección radial [6]. Este ensayo es particularmente atractivo a la hora de trabajar con material irradiado, ya que consume muy poca cantidad

de muestra y las probetas empleadas no requieren de una compleja mecanización.

En este trabajo se han empleado muestras no irradiadas de vainas de ZIRLO™ con distintos contenidos en hidrógeno (0, 150, 250, 500, 1200 y 2000 ppm) fueron sometidas a compresión diametral a 20 °C. El hidrógeno se introdujo en las muestras mediante un procedimiento de carga catódica en disolución básica. Se desarrolló un modelo de elementos finitos para simular los resultados experimentales. Implementando en dicho modelo la teoría de la fisura cohesiva fue posible determinar los parámetros del comportamiento en fractura del material entre ellos la energía de fractura.

2. EXPERIMENTAL

2.1. Material y ensayos.

En este trabajo se emplearon vainas sin irradiar de ZIRLO™ [7] con 9.5 mm de diámetro exterior y 0.57 mm de espesor de pared.

Las probetas utilizadas para los ensayos de compresión diametral fueron tubos de 10 mm de longitud axial cortados de vainas de combustible nuclear.

Los ensayos se realizaron en una máquina universal de ensayos usando una célula de carga de 5 kN. Para comprimir las probetas se utilizaron platos de acero plano paralelos, como se muestra en fig.1. Los ensayos se realizaron con una velocidad de desplazamiento del pistón constante de 0,3 mm/min. Este desplazamiento se midió con un LVDT de ± 5 mm de recorrido.

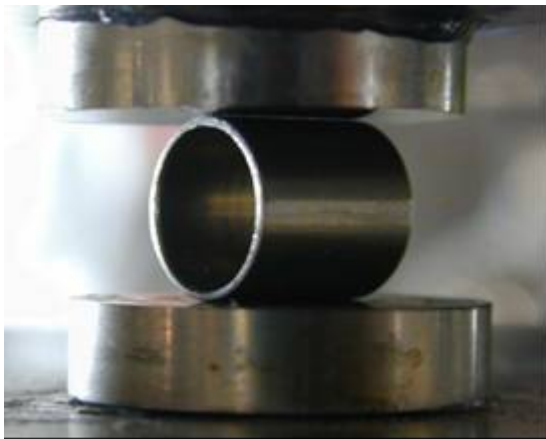


Figura 1. Probeta de compresión diametral al comienzo del ensayo.

Al final del ensayo, la sección transversal de la probeta se deforma adoptando forma de ocho, como puede verse en la figura 2.

2.2. Carga con hidrógeno.

Se desarrolló e implementó una técnica de carga catódica para introducir cantidades conocidas de hidrógeno en las muestras. Este proceso se efectuó en

medio básico, concretamente en una disolución acuosa de KOH. La temperatura de la disolución se mantuvo entre 299 K (150 ppm de hidrógeno) y 353 K (2000 ppm de hidrógeno). Durante el proceso de carga las muestras de ZIRLO™ se emplearon como cátodo de la reacción electroquímica, mientras que como ánodo se empleó un hilo de platino enrollado alrededor de la muestra. La densidad de corriente se mantuvo constante para cada concentración (con valores entre 0.25 y 2.15 A/cm²) variando el tiempo (de 3 a 25 horas) en función de la cantidad de hidrógeno a introducir en la muestra.

Después de la carga catódica, se sometió a las muestras a un tratamiento térmico en atmósfera de Ar. Primeramente se mantuvieron las muestras a 723 K durante 7 horas, para lograr que el hidrógeno se distribuyese de forma homogénea por toda la muestra, y posteriormente, las probetas fueron enfriadas muy lentamente hasta temperatura ambiente (1.2 K/min) para conseguir que el hidrógeno precipitase en forma de hidruros δ , por ser éstos los que se encuentran en condiciones de operación. El tratamiento térmico empleado no modifica el comportamiento mecánico de las muestras. El procedimiento de carga con hidrógeno y la morfología de los hidruros obtenidos se describen detalladamente en [8].



Figura 2. Probeta de compresión diametral al final del ensayo.

La concentración de hidrógeno en las muestras fue medida usando el método de extracción en caliente en corriente de gas inerte con un analizador HORIBA JOBIN-YVON EMGA-621W.

Se realizó un estudio metalográfico de las muestras para observar la morfología y distribución de los hidruros. Las muestras se montaron en resina epoxi y se pulieron usando suspensión de diamante (llegando hasta 1 μ m). En la última etapa de pulido se empleó una mezcla de dispersión de sílice coloidal (0.05 μ m), H₂O₂ (30 % vol.) y HF (40% w) en proporción (50 volúmenes, 10 vol., 1 vol). Después del pulido, las muestras fueron atacadas durante 90 segundos en una disolución de HNO₃ (69 %w), ácido láctico (95 % w) y HF (40 % w) en proporción (48.5 w: 48.5 wt: 3 wt) con el objetivo de revelar los hidruros creados.

2.3. Modelo de elementos finitos

Para simular el ensayo de compresión diametral se desarrolló un modelo de elementos finitos en 2D con el programa comercial ABAQUS v. 6.7-5. Debido a las simetrías geométricas y de carga se consideró solamente un cuarto de la probeta.

Se empleó una malla semiestructurada en la zona de daño y en la región de aplicación de carga (ver figura 3). Los elementos de la zona estructurada son cuadriláteros de 8 nodos, con un tamaño de 5 μm. En la figura 4 se muestra un detalle de la zona estructurada, correspondiente a la zona marcada con un círculo en fig.3.

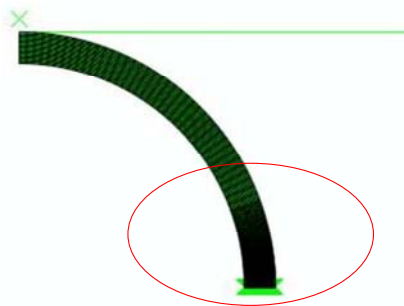


Figura 3. Esquema de la malla empleada

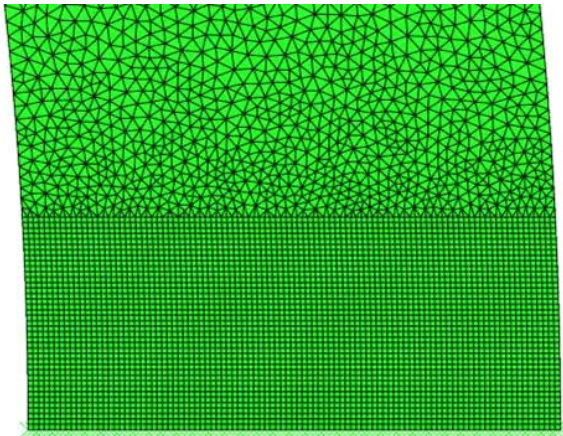


Figura 4. Detalle de la zona estructurada de la malla empleada

La muestra fue modelizada como una malla deformable mientras que el sistema de carga como una superficie rígida. Se restringieron los desplazamientos perpendiculares al plano vertical de simetría.

La ecuación constitutiva del material se obtuvo de la simulación numérica de ensayos de tracción en anillo realizados sobre vainas de ZIRLO™ con los mismos contenidos de hidrógeno [8].

El comportamiento del material se consideró elastoplástico, y para la modelización numérica se empleó un material isótropo con criterio de

plastificación de Von Mises [1]. En todos los cálculos se consideró no linealidad geométrica.

La caída de la carga que se produce debido a la fisuración de la probeta se simuló mediante el modelo de la fisura cohesiva. Para ello fue necesario programar una subrutina de elemento especial en el código ABAQUS. Se trata de una subrutina para modelizar la intercara entre los elementos. Dicha subrutina se aplica a elementos lineales de tres nodos y consiste en calcular el valor de las cargas nodales y de la derivada de las cargas nodales respecto a los desplazamientos de los nodos.

Debido a la gran deformación que se produce durante el ensayo, es necesario plantear la subrutina en grandes deformaciones para conseguir transmitir adecuadamente la tensión cohesiva. Este es el motivo que hizo necesaria dicha subrutina dado que el código ABAQUS v 6.7-5 sólo proporciona elementos cohesivos aplicables a cálculos sin no linealidad geométrica.

Para evitar problemas de bloqueo volumétrico en el resto de la malla se emplearon elementos bilineales (el elemento tiene nodos en los vértices y en el punto medio del lado) de tres y cuatro lados. Esto obliga a poner en la zona cohesiva o bien dos elementos cohesivos de dos nodos por lado o bien un elemento cohesivo de tres nodos. En las modelizaciones se ha optado por esta última posibilidad.

Para conseguir la convergencia de los cálculos, éstos se realizaron controlando el desplazamiento del nodo cohesivo crítico (donde se produce la fisura real).

En la literatura se recoge que para el caso de materiales metálicos, una curva de ablandamiento rectangular modeliza bien su comportamiento [9]. La curva de ablandamiento está caracterizada por dos parámetros: la resistencia cohesiva, f_t , y la energía de fractura, G_F . La energía de fractura está determinada por el área bajo la curva de ablandamiento, y para el caso que nos ocupa (curva de ablandamiento rectangular) viene dada por el producto entre la resistencia cohesiva y w_c , la separación crítica entre los labios de la fisura. En la figura 5 se presenta una curva de ablandamiento rectangular y los parámetros del modelo de la fisura cohesiva.

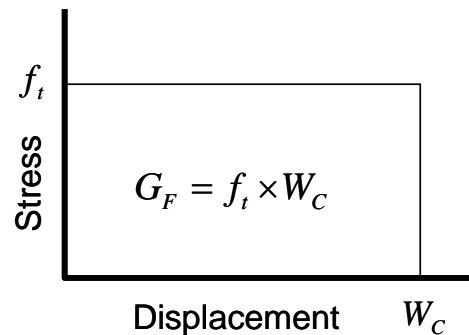


Figura 5. Curva de ablandamiento rectangular

El comportamiento real de la zona cohesiva no es una curva rectangular ideal, puesto que sería imposible de modelizar [10]. Los lados del rectángulo tienen una ligera pendiente. La pendiente en la línea vertical se ha introducido para facilitar la descarga y es del 1%. Al emplear valores inferiores a éste se han encontrado problemas de convergencia.

Los dos parámetros de la curva de ablandamiento se determinan por prueba y error a partir del punto donde se produce la descarga y de la pendiente de dicha descarga. El procedimiento seguido es el siguiente. Se propone un valor de la resistencia cohesiva f_{i0} . Este valor está acotado entre el límite elástico del material y su tensión de rotura. Se calcula la curva carga-desplazamiento con el valor propuesto de f_{i0} y una energía de fractura elevada. En el punto donde se separan las curvas carga-desplazamiento experimental y numérica se calcula el valor de w_{c0} que produciría la descarga y se repite el cálculo con los valores f_{i0} y w_{c0} . A continuación se rehace el proceso con varias parejas de valores (f_{ti} , W_{ci}) y se obtiene una familia de curvas numéricas. Finalmente, se toma como solución la curva que mejor ajusta los resultados experimentales.

Una vez conocida la energía de fractura, G_F , bajo las suposiciones realizadas, se puede calcular la tenacidad del material aplicando la ecuación de Irwin:

$$E'G_F = K_{IC}^2 \tag{1}$$

Donde K_{IC} es la tenacidad del material, G_F , la energía de fractura y E' (en condiciones de deformación plana) viene dada por la ecuación (2)

$$E' = \frac{E}{1-\nu^2} \tag{2}$$

Donde E es el módulo de Young y ν es el coeficiente de Poisson.

3. RESULTADOS Y DISCUSIÓN

El método de carga de hidrógeno empleado da lugar a población de hidruros de elevado tamaño distribuidos de forma homogénea en el espesor de la muestra, como se puede apreciar en la figura 6. Los hidruros son las líneas negras sobre la superficie clara del circonio.

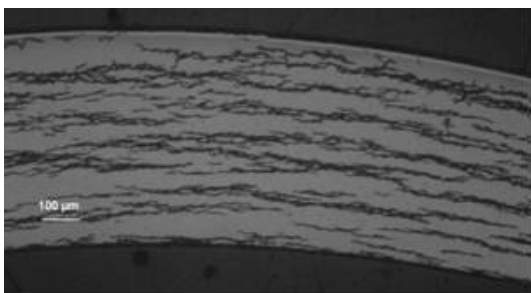


Figura 6. Distribución de hidruros en una muestra de compresión diametral con 500 ppm de hidrógeno.

Se prepararon muestras para la realización de ensayos de compresión diametral con distintas concentraciones de hidrógeno (150, 250, 500, 1200 y 2000 ppm), realizándose tres ensayos para cada una de las concentraciones. Dichos ensayos se efectuaron a 20 °C. Las curvas carga vs. desplazamiento obtenidas se presentan en la figura 7.

En las curvas experimentales de la figura 7 se puede observar un máximo de carga. Este máximo corresponde con el instante anterior a que las generatrices del tubo contenidas en el plano medio del mismo y que es perpendicular a la dirección de compresión comienzan a fisurarse. A partir de ese momento la fisura comienza a propagarse a lo largo de la dirección axial del tubo, lo que provoca una caída de la carga. Una vez que la fisura se ha propagado a lo largo de toda la probeta la carga comienza a incrementarse rápidamente debido a que las dos partes del tubo sobre las que se está ejerciendo la carga entran en contacto. Esta es la última etapa del ensayo (ver figura 2).

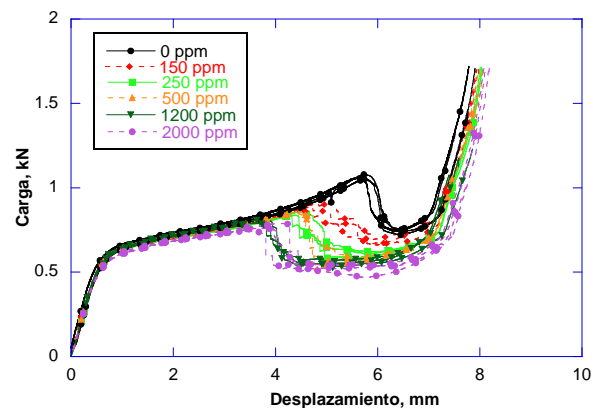


Figura 7. Curvas experimentales carga-desplazamiento para distintas concentraciones de hidrógeno.

Observando la figura 7, se puede afirmar que con sólo 150 ppm de hidrógeno se aprecian cambios importantes en los registros experimentales carga-desplazamiento, con lo que el ensayo de compresión diametral es muy sensible a la presencia de hidrógeno en las muestras. Un aumento en la concentración de hidrógeno hasta 250 ppm hace que el valor del máximo de carga, y el desplazamiento al que se alcanza disminuyan. Dicho máximo es muy similar para 250 y 500 ppm, y vuelve a decrecer para 1200 ppm. Las curvas experimentales carga-desplazamiento son prácticamente coincidentes para 1200 y 2000 ppm.

En las siguientes figuras, fig.8-fig.13, se muestra, para cada concentración, los registros experimentales y los ajustes numéricos efectuados por el método de los elementos finitos implementando la teoría de la fisura cohesiva. Puede observarse como los ajustes recogen la caída de carga, existiendo una muy buena concordancia entre los resultados experimentales y numéricos.

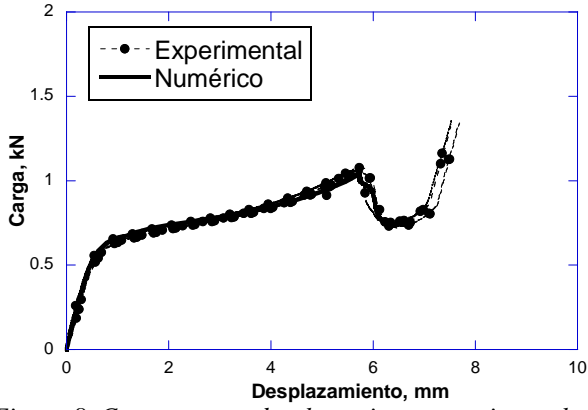


Figura 8. Curvas carga-desplazamiento experimentales y numéricas, 0 ppm

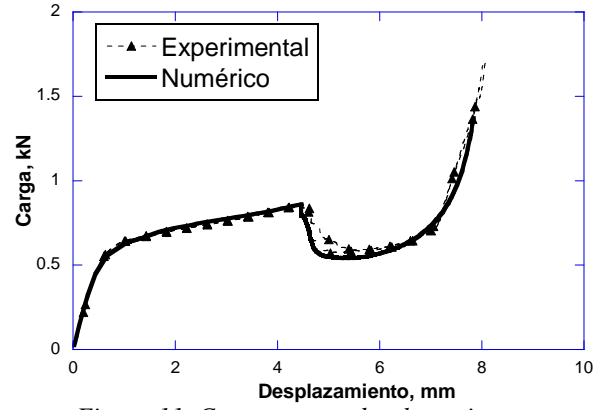


Figura 11. Curvas carga-desplazamiento experimentales y numéricas, 500 ppm

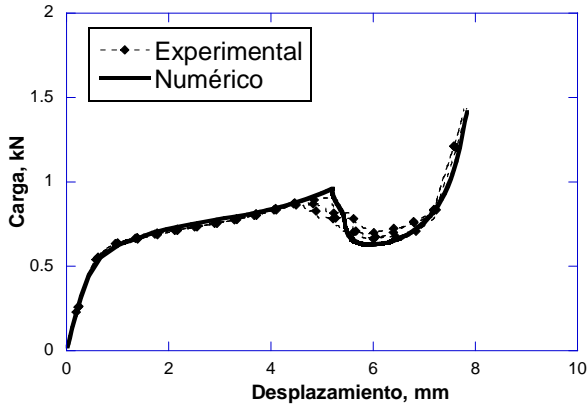


Figura 9. Curvas carga-desplazamiento experimentales y numéricas, 150 ppm

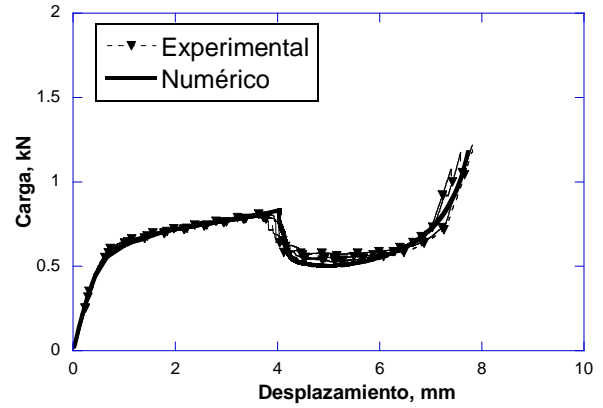


Figura 12. Curvas carga-desplazamiento experimentales y numéricas, 1200 ppm

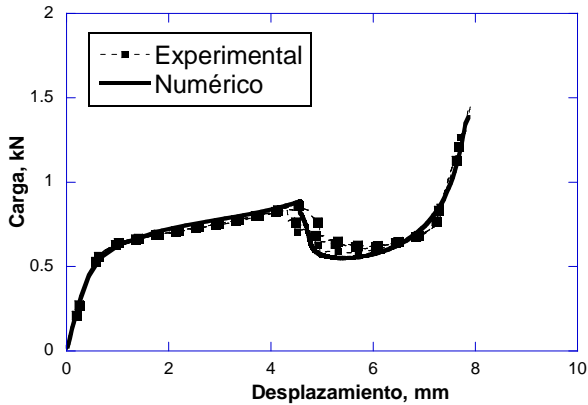


Figura 10. Curvas carga-desplazamiento experimentales y numéricas, 250 ppm

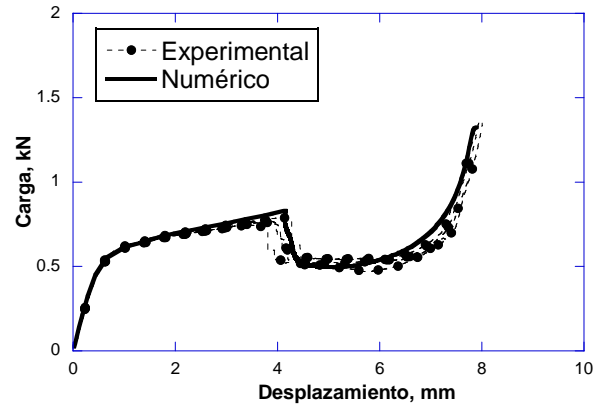


Figura 13. Curvas carga-desplazamiento experimentales y numéricas, 2000 ppm

Los parámetros del modelo cohesivo empleado en los cálculos numéricos para las distintas concentraciones de hidrógeno se recogen en la tabla 1.

Tabla 1: Parámetros del modelo cohesivo para las distintas concentraciones de hidrógeno

H, ppm	f_t (MPa)	w_c (μm)	G_F (kJ/m)
0	930	41.0	38.13
150	928	36.6	33.96
250	922	34.4	31.72
500	915	34.0	31.11
1200	912	33.0	30.10
2000	906	32.4	29.98

Los resultados de la tabla 1 muestran que la resistencia cohesiva no varía de forma determinante por la presencia de hidruros en la muestra. Su valor sólo se reduce un 3 % cuando la concentración de hidrógeno cambia de 0 a 2000 ppm. Sin embargo, el valor del desplazamiento crítico, w_c , y consecuentemente el valor de la energía de fractura, G_F , cambian considerablemente. Ambos valores sufren una reducción del 30 % cuando la concentración de hidrógeno pasa de 0 a 2000 ppm.

Puede observarse que con tan solo 150 ppm de hidrógeno, w_c y G_F se reducen en un 11 %. Esto vuelve a indicar la sensibilidad del ensayo a la presencia de hidruros en la muestra. Para concentraciones de hidrógeno superiores a 500 ppm no se producen variaciones importantes de G_F .

Como se ha explicado anteriormente, la tenacidad de fractura se puede calcular a partir de G_F , utilizando las ecuaciones (1) y (2). Los valores del módulo de Young ($E = 88$ GPa) y del coeficiente de Poisson ($\nu = 0.37$) son los mismos para todas las concentraciones de hidrógeno, dado que dichas constantes no varían con la concentración de hidrógeno en el intervalo estudiado [8].

En la figura 14 se muestra la variación de K_{IC} con la concentración de hidrógeno. Puede observarse que hasta concentraciones de 500 ppm las variaciones en la concentración de hidrógeno provocan cambios sustanciales en los valores de K_{IC} , sin embargo, para concentraciones superiores a 500 ppm, K_{IC} se mantiene prácticamente constante.

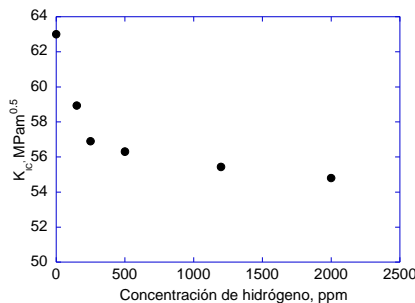


Figura 14. Tenacidad de fractura calculada K_{IC} en función del contenido de hidrógeno en la muestra

4. CONCLUSIONES

El ensayo de compresión diametral ha demostrado ser muy sensible a la presencia de hidruros en las muestras, ya que una pequeña concentración de hidrógeno, 150 ppm, modifica apreciablemente los registros experimentales carga-desplazamiento del ensayo.

Implementando la teoría de la fisura cohesiva en el modelo numérico, se ha conseguido recoger en los ajustes la caída de carga producida por la fisuración de la probeta. A partir de las constantes cohesivas empleadas en el modelo, se ha podido determinar la

energía de fractura para las distintas concentraciones de hidrógeno.

Se puede concluir que para concentraciones bajas de hidrógeno, hasta 500 ppm, K_{IC} permanece prácticamente constante.

AGRADECIMIENTOS

Los autores quieren agradecer la financiación recibida del ministerio de Educación y Ciencia (proyecto ENE2005-06478/CON) y a ENUSA, ENRESA y al CSN por su colaboración y financiación del proyecto. El presente proyecto se encuadra dentro de los proyectos DUMEINPA financiados por la comunidad de Madrid y SEDUREC del plan nacional CONSOLIDER-INGENIO 2010.

REFERENCIAS

- [1] Arsène, S. "Effet de la microstructure et de la temperature sur la transition ductile-fragile des zircaloy hydrures". Ph.D. dissertation, École Centrale Paris (1997).
- [2] Grange, M. "Fragilisation du zircaloy-4 par l'hydrogene: comportement, mecanismes d'endommagement, interaction avec la couche d'oxyde, simulation numerique". Ph.D. dissertation, École des Mines de Paris (1998)
- [3] Bertolino, G., Meyer G. y Perez-Ipiña, J. "Effects of hydrogen content and temperature on fracture toughness of Zircaloy-4". Journal of Nuclear Materials 320. 272-279 (2003).
- [4] Desquines J., Cazalis B., Possad Ch., Averty X., Yvon P. "Mechanical Properties of zircaloy-4 PWR Fuel cladding with Burnup 54-64 Mwd/KgU and Implications for RIA Behaviour" Journal of ASTM international 2 n°6 paper ID JA112465 (2005)
- [5] Kim, J.H., Lee, M.H., Choi, B.K., "Failure behaviour of zircaloy-4 cladding after oxidation and water quench" Journal of Nuclear Materials 362 36-45 (2007)
- [6] Robert S. Daum, S. Majumdar, Y. Liu, M. C. Billone "Radial-hydride embrittlement of high-burnup zircaloy-4 fuel cladding" Journal of nuclear science and technology. 43 n°9. 1054-1067 (2006)
- [7] George P. Sabol "ZIRLOTM an alloy development success". Journal of ASTM international. 2 n°2, paper ID JA112942 (2005)
- [8] M.A. Martín-Rengel, "Integridad estructural de vainas de combustible nuclear en condiciones de almacenamiento temporal en seco". Tesis doctoral. Universidad Politécnica de Madrid (2009).
- [9] F.J. Gómez, A. Valiente, M. Elices, "Cohesive modelling of the fracture of a neutron irradiated pressure Wessel steel". Nuclear engineering and Design. 219 111-125 (2002)
- [10] J. Planas, D. Cendón, J.M Sancho, "Oscilaciones de tensiones y rigidez inicial en elementos de interfaz para simulación numérica de fisuras cohesivas". Anales de mecánica de la fractura 20 119-124 (2003) (in Spanish).

INFLUENCIA DE LA GEOMETRÍA Y DE LA PROFUNDIDAD DE LA ENTALLA EN LA TRIAXIALIDAD Y COMPORTAMIENTO A FRACTURA DE PROBETAS SPT ENTALLADAS

I. Peñuelas¹, R. Montero¹, C. Rodríguez¹, C. Betegón¹ y F.J. Belzunce²

¹Dpto. Construcción e Ingeniería de Fabricación, Escuela Politécnica Superior de Ingeniería de Gijón, Universidad de Oviedo, Campus de Viesques s/n, 33203 Gijón, Asturias, Spain.
E-mail: penuelasines@uniovi.es

²Dpto. Ciencia de los Materiales e Ingeniería Metalúrgica, Escuela Politécnica Superior de Ingeniería de Gijón, Universidad de Oviedo, C/ Independencia 13, 33004 Oviedo, Asturias, Spain

RESUMEN

El presente trabajo tiene como objeto el estudio de la influencia de la geometría y de la profundidad de la entalla en la triaxialidad y comportamiento a fractura de distintas probetas SPT entalladas, tras la realización del ensayo miniatura de punzonado o Small Punch Test (SPT). Para ello se han realizado simulaciones numéricas de probetas SPT de espesor $T=0.5$ mm y $T=1$ mm, y distintas geometrías de entalla, con profundidades relativas $a/T=0.1, 0.2, 0.3, 0.4, 0.5$ y 0.6 (donde a es la profundidad de la entalla), y tres configuraciones diferentes, consistentes en una probeta con entalla central circular de diámetro 3 mm; una probeta con entalla longitudinal; y una probeta con entalla longitudinal y transversal. Las simulaciones se han realizado mediante el código comercial de elementos finitos ABAQUS, considerando grandes deformaciones y contactos. Las probetas han sido simuladas mediante una malla 3D con elementos cuadriláteros de 8 nodos e integración reducida. Dada la baja velocidad de punzonamiento (0.2 mm/min) se considera un análisis cuasiestático. El modelo micromecánico de daño utilizado es el modelo de Gurson-Tveergard-Needleman (GTN). Para cada una de las configuraciones analizadas se ha determinado la triaxialidad en el instante en el que se comienza a producir el crecimiento de grieta. Se ha estudiado asimismo la evolución de la triaxialidad con la carga en todos los casos simulados

PALABRAS CLAVE: ensayo miniatura de punzonado (SPT), triaxialidad de tensiones, probetas entalladas.

ABSTRACT

The aim of this paper is to analyze the influence of the specimen width, the geometry and the depth of notch on the stress triaxiality and the fracture behavior of notched SPT specimens. Thus, numerical simulations of SPT specimens of 0.5 mm and 1 mm width with different geometries and notches of relative depths $a/t=0.1, 0.2, 0.3, 0.4, 0.5$ and 0.6 , have been studied. The three different geometries of notches analyzed have been square plate specimens of 10×10 mm² with: 1) a central circular notch of 3 mm diameter, 2) a longitudinal notch and 3) a longitudinal and transverse notch. The numerical simulations have been carried out with the finite element commercial code ABAQUS, considering large deformations and contact. Specimens have been discretized by means of three-dimensional meshes of eight-node reduced integration elements. Die and punch were modeled as rigid bodies. Besides, large displacements and contact between surfaces have been taken into account. In addition, due to the low punching speed (0.2 mm/min) quasistatic analyses have been considered. The micromechanical damage model used is the Gurson-Tveergard-Needleman (GTN). For each configuration analyzed the triaxiality at the time when the crack begins its growth has been obtained. Furthermore, the evolution of the triaxiality with the load has also been studied.

KEY WORDS: small punch test (SPT), stress triaxiality, notched specimens.

1. INTRODUCCIÓN

El ensayo miniatura de punzonado es de gran interés en todas aquellas aplicaciones en las que se requiere caracterizar materiales de los que bien no se dispone de cantidades suficientes de material como para extraer

probetas convencionales, o bien no se quiere comprometer el funcionamiento en servicio de un componente [1]. Este ensayo se ha aplicado recientemente a la caracterización mecánica de la zona afectada térmicamente de soldaduras, y a la de

recubrimientos metálicos de base níquel [2], obteniéndose en ambos casos interesantes resultados.

2. ENSAYO MINIATURA DE PUNZONADO

El ensayo miniatura de punzonado es un ensayo que puede considerarse como no destructivo debido al reducido tamaño de las probetas que utiliza (pequeñas láminas cuadradas de 10x10 mm y espesores de 0.5 mm ó de 1 mm), a partir del cual se pueden obtener parámetros que permiten predecir directamente las propiedades mecánicas fundamentales del material, como el límite elástico, la resistencia a la tracción, la ductilidad y la energía de rotura [3,4,5].

El ensayo consiste en la aplicación de una carga a baja velocidad (0.2 mm/min) con la ayuda de un punzón de cabeza semiesférica de 2.5mm de diámetro, sobre una probeta, que está firmemente sujeta en todo su contorno. La probeta es de este modo obligada a deformarse cuasiestáticamente en el interior de un orificio de 4mm de diámetro (expansión biaxial) hasta su rotura. Mediante un extensómetro se obtiene el desplazamiento del punzón y, tras la corrección de la flexibilidad del dispositivo de ensayo, se calcula el desplazamiento del punto central de la probeta.

Los datos de carga y de desplazamiento generados, nos permiten obtener la curva característica del ensayo, que para un material dúctil muestra la forma que se expone en la Figura 1.

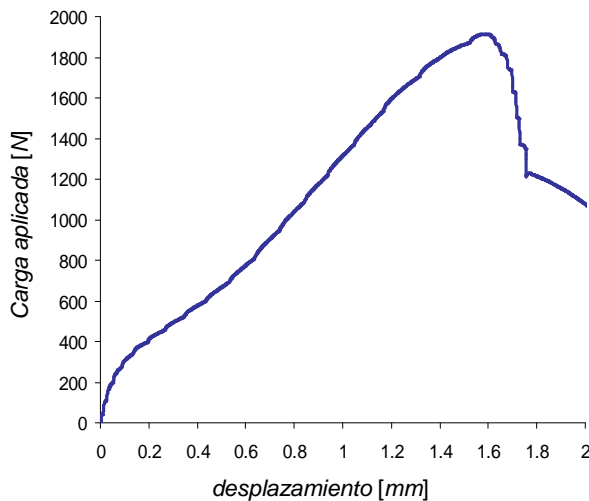


Figura 1. Curva característica obtenida en un ensayo SPT sobre un material dúctil

3. SIMULACIONES REALIZADAS

Se han desarrollado distintos modelos para reproducir el ensayo mediante cálculo numérico. Para ello se ha utilizado el código comercial de elementos finitos ABAQUS [6]. Al tratarse de probetas agrietadas ha sido necesario recurrir a mallas tridimensionales, si bien se ha utilizado simetría para disminuir el tiempo de

computación. La probeta se ha discretizado mediante una malla de elementos sólidos de ocho nodos con integración reducida. La matriz y el punzón se han modelado como sólidos rígidos y se han considerado contactos entre superficies. Los cálculos se han realizado bajo el supuesto de grandes deformaciones.

Las propiedades macroscópicas del material que se han introducido en el modelo, se han obtenido a partir de ensayos convencionales. Se ha considerado asimismo que la fractura dúctil del material se produce de acuerdo con el modelo micromecánico de daño de Gurson-Tvergaard-Needleman, en el que se considera la nucleación, el crecimiento y la coalescencia de cavidades, de modo que es posible simular el comportamiento del material hasta la rotura. Por otra parte, se ha supuesto que el coeficiente de rozamiento durante el ensayo es aproximadamente $\mu=0.1$, ya que este valor es adecuado para un contacto acero-acero inicialmente lubricado, que es el que se produce en el ensayo. La Figura 2 muestra el modelo y un detalle del mallado utilizados para algunas de las simulaciones.

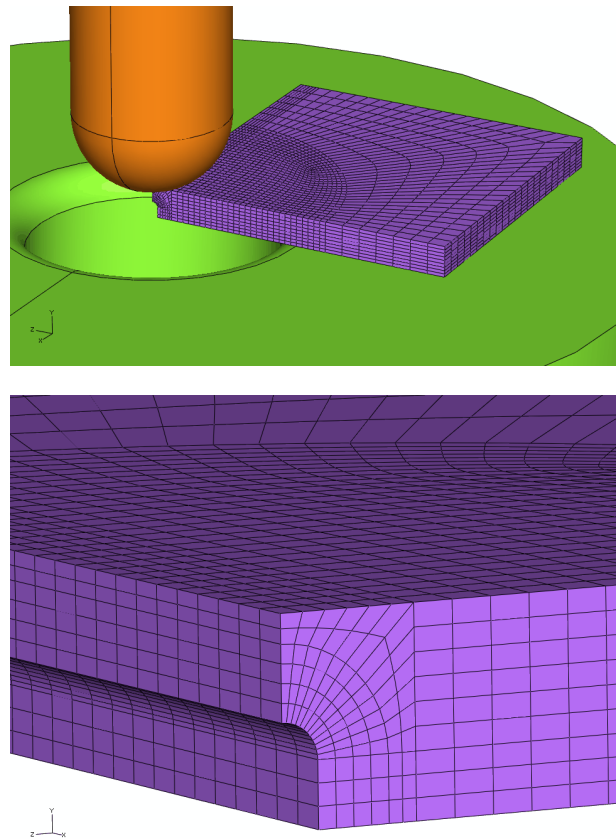


Figura 2. Modelo y detalle del mallado utilizado para algunas de las simulaciones

Se han realizado simulaciones numéricas de probetas miniatura de punzonado (SPT) de 0.5 mm y 1 mm de espesor, distintas geometrías de entalla con profundidades relativas $a/t=0.1, 0.2, 0.3, 0.4, 0.5$ y 0.6 , donde a es la profundidad de la entalla y t el espesor de la probeta (ver Figura 3) con $e=cte$, y tres configuraciones diferentes, consistentes en:

- a) probeta con entalla longitudinal (en adelante L);
- b) probeta con entalla longitudinal y transversal (en adelante L+T);
- c) probeta con entalla central circular (en adelante C) de diámetro 3 mm.

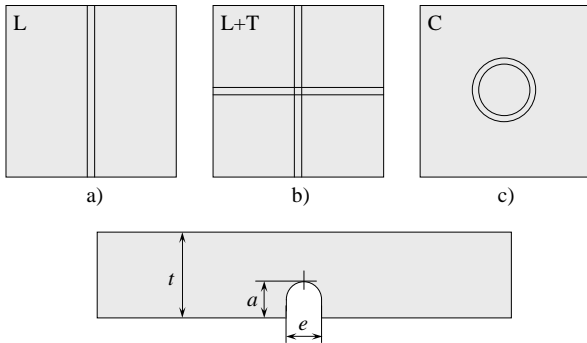


Figura 3. Configuraciones de entalla estudiadas y relación a/t

En total se han analizado 36 configuraciones distintas. En la Figura 4 se muestra una de las geometrías utilizadas para la simulación:

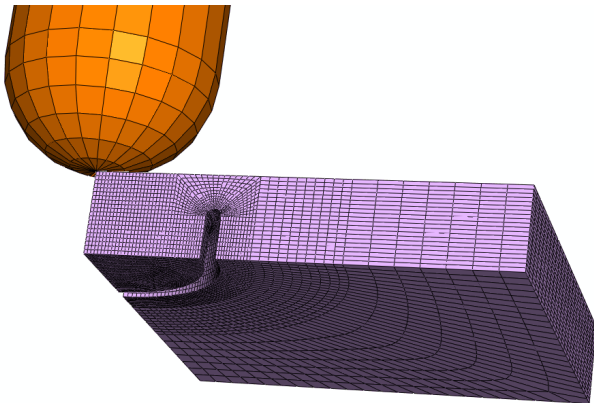


Figura 4. Punzón y probeta para el modelo de probeta C con relación $a/t=0.6$

Se ha procurado que las mallas sean en todos los casos similares, para evitar, en la medida de lo posible, la influencia de la misma en el estudio de las distintas configuraciones.

4. ANÁLISIS DE LA TRIAXIALIDAD

La determinación de la tenacidad a fractura de un material requiere, en primer lugar, elegir la geometría más adecuada para la determinación de dicha tenacidad [7]. En este trabajo se ha estudiado la influencia que el espesor de la probeta y la profundidad de la entalla tienen en la triaxialidad de la probeta, como paso previo a la elección de la configuración más adecuada para una aplicación determinada.

Son varios los criterios que se han considerado para la determinación de la triaxialidad de la probeta, ya que nos encontramos ante una propiedad que depende tanto de la carga como de la posición respecto al frente de grieta. Estos criterios son:

- 1) Valores constantes de distancia al frente de entalla adimensionalizada $r\sigma_0/J=2$ y $r\sigma_0/J=1$. Se consideran estos dos valores por encontrarse los máximos de tensiones de apertura entre ellos.
- 2) Máxima tensión de apertura
- 3) Distancia fija al frente de entalla. Se han considerado dos distancias distintas: $x = 45\mu\text{m}$ y $90\mu\text{m}$ para las probetas de $t=0.5$ mm y $90\mu\text{m}$ para las probetas de espesor $t=1$ mm)
- 4) Triaxialidad según J, en la que se ponderan los valores de triaxialidad obtenidos con el criterio de máxima tensión de apertura, con el valor de J en cada instante, de modo que se da más peso a los valores de triaxialidad próximos al instante de rotura

La Figura 4 muestra la evolución de dicha triaxialidad para una configuración cualquiera de las configuraciones estudiadas, en función de la distancia al frente de grieta y de la carga aplicada. Ha sido necesario, por tanto, calcular la integral J [6] media en cada instante, así como definir una distancia respecto al frente de grieta en la que realizar los cálculos. Esta distancia se ha relacionado con el CTOD de la entalla, habiendo utilizado además un factor de escala en el caso de las probetas de menor espesor.

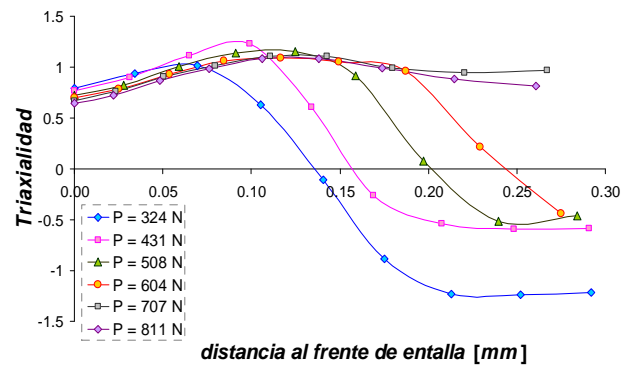


Figura 4. Evolución de la triaxialidad de una configuración determinada (L, $t=4$ mm, $a/t=0.4$) en función de la distancia al frente de grieta y la carga aplicada

5. RESULTADOS Y DISCUSIÓN

En la Figura 5 se muestra para una de las configuraciones estudiadas cómo el aumento de la

profundidad de la entalla incrementa la flexibilidad de la probeta.

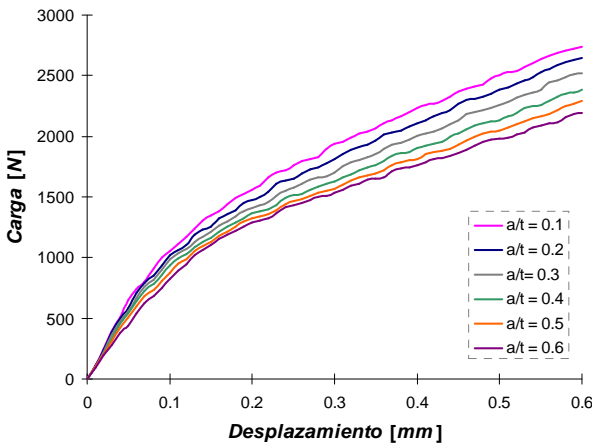


Figura 5. Relación carga-desplazamiento de punzón para una misma configuración (entalla L+T), con distintas profundidades de entalla y espesor 1 mm

Las Figuras 6 y 7 muestran los resultados obtenidos tras la realización de los ensayos miniatura de punzonado sobre las probetas de 0.5mm y de 1mm de espesor, respectivamente. En la figura 6 se comparan los valores de triaxialidad de las distintas probetas entalladas (con entalla longitudinal, longitudinal + transversal o entalla doble, y con entalla circular) en función de la relación entre la profundidad de la entalla y el espesor, para probetas de 1 mm de espesor. En dicha figura se observa que, de acuerdo con lo esperado, la triaxialidad aumenta al hacerlo la profundidad de la entalla, para todas las configuraciones. No obstante, cuando el tamaño relativo inicial de la entalla es próximo a 0.6mm, el ligamento resistente es muy pequeño y se observan fuertes fenómenos de flexión en la zona de la entalla, que se traducen en una disminución de la triaxialidad.

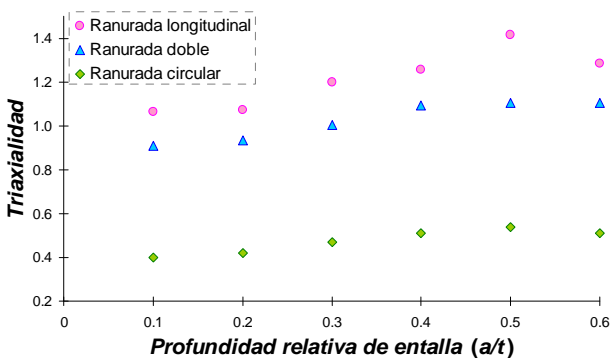


Figura 6. Triaxialidad en función de la profundidad relativa de entalla para las distintas configuraciones de 1 mm de espesor

Por otra parte, de las tres geometrías analizadas, las probetas con una única entalla longitudinal son las que permiten obtener mayores valores de triaxialidad. Hay que tener en cuenta que los valores de triaxialidad representados en estas gráficas corresponden a los

obtenidos con el criterio de distancia fija al frente de entalla, por lo que si se varía el criterio de obtención de triaxialidad, variarán los valores de triaxialidad, aunque la tendencia observada es la misma.

En el caso de probetas de 0.5 mm se ha obtenido la triaxialidad para dos distancias distintas: a) la misma que para el caso de probetas de 1 mm, y b) la mitad que para el caso de probetas de 1 mm, con el objeto de tener en cuenta un cierto factor de escala en las simulaciones, ya que el efecto de una entalla de 90 μm es mucho mayor en una probeta de 0.5 mm que una de 1 mm de espesor.

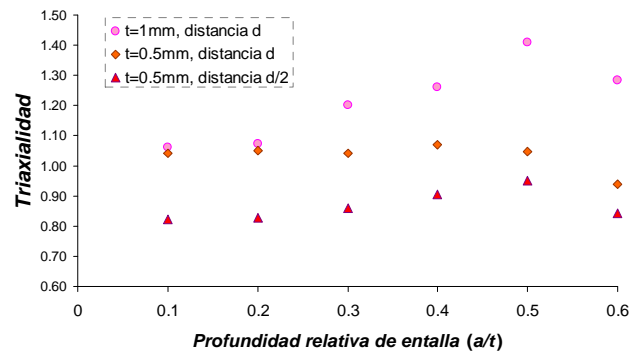


Figura 7. Triaxialidad en función de la profundidad relativa de entalla y el espesor para una misma geometría

En la Figura 7 se presentan los resultados para una misma geometría con los dos espesores de probeta estudiados y los dos criterios de triaxialidad para el espesor de 0.5 mm. Se observa que para valores muy elevados de a/t , es decir para entallas de gran longitud, empiezan a ser muy importantes los efectos de flexión y se observa una disminución de las triaxialidad.

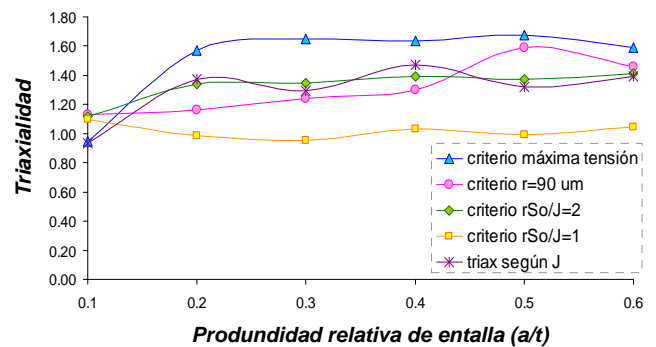


Figura 8. Triaxialidad para la configuración L de 1 mm de espesor, en función de la profundidad relativa de entalla y criterio utilizado para el cálculo de triaxialidad

Ya se ha comentado anteriormente que los valores de triaxialidad dependen del criterio utilizado para la determinación de la misma, llegando a observarse importantes diferencias en los mismos (hasta del 75% en

algunos casos) en función del criterio elegido. La figura 8 muestra los resultados de triaxialidad para la configuración con entalla longitudinal y 1mm de espesor, en función de la profundidad relativa de la entalla y del criterio de cálculo.

6. CONCLUSIONES

En el presente trabajo se ha realizado la comparación del comportamiento a fractura de distintas probetas SPT agrietadas, de cara al estudio de la influencia del espesor de la probeta, la configuración agrietada de la probeta y el tamaño relativo de la entalla de la misma.

A la vista del estudio realizado se deducen las siguientes conclusiones:

- 1) El valor de la triaxialidad es sensible a la malla utilizada en la situación.
- 2) Es necesario definir qué criterio se va a utilizar para la determinación de los valores de triaxialidad de las distintas probetas, al haber dependencia espacio-temporal de la misma.
- 3) La triaxialidad y la flexibilidad de la probeta aumentan al hacerlo la profundidad de la entalla.
- 4) La triaxialidad de las probetas entalladas de mayor espesor es, por lo general, mayor que las de las probetas entalladas de menor espesor, en las que se observan además efectos importantes de flexión para entallas de gran longitud relativa.
- 5) Las configuraciones con una única entalla longitudinal presentan mayor triaxialidad que las de entalla longitudinal y transversal, y estas a su vez, mayor triaxialidad que las de entalla circular.

AGRADECIMIENTOS

Los autores desean agradecer por su financiación, al Ministerio de Educación y Ciencia (plan Nacional I+D+I), mediante los proyectos MEC-04-MAT2004-06992-C02-01 y MAT2008-06879-C03-00, a Hibbit, Karlsson y Sorensen por el acceso a ABAQUS mediante la licencia educacional. Sin todas ellos no hubiera sido posible la realización de este trabajo.

REFERENCIAS

- [1] Lucas G.E. et al., *Recent progress in small specimen test technology*, J. Nucl. Mater., vol. 307-311, pp. 1600-1608, 2002.
- [2] I. Peñuelas, R. González, M.A. García, A. Higuera, C. Rodríguez, R. Vijande., *Caracterización mecánica*

de recubrimientos mediante ensayos miniatura de punzonamiento, Actas del IX congreso iberoamericano de Ingeniería Mecánica, 2009.

[3] Contreras MA., *Tesis doctoral*, Universidad de Oviedo, 2007.

[4] Autillo J., Contreras M.A., Betegón C., Rodríguez C., Belzunce F.J., *Utilización del ensayo miniatura de punzonamiento en la caracterización mecánica de aceros*, Anales de Mecánica de la Fractura, 23, 77-83, 2006

[5] M.A. Contreras, C. Rodríguez, F.J. Belzunce, C. Betegón, *Use of the small punch test to determine the ductile-to-brittle transition temperature of structural steels*, Fatigue Fract Engng Mater Struct, 31, 727-737, 2008.

[6] ABAQUS 6.4., Hibbit, Karlsson and Sorensen, Inc., Pawtucket, 2003

[7] I. Peñuelas, C. Rodríguez, F.J. Belzunce y C. Betegón, *Análisis de la determinación de la tenacidad a fractura mediante el ensayo SPT*, Anales de Mecánica de la Fractura 2009

[8] I. I. Cuesta et al., *Cálculo de la integral J en probetas SPT para la estimación de la tenacidad a fractura*, Anales de Mecánica de la Fractura 2008

MECHANICS OF INTERFACIAL CRACKS BETWEEN DISSIMILAR QUASICRYSTALS

J. Planas¹, E. Radi², M.M. Stickle³, P.M. Mariano⁴¹Universidad Politécnica de Madrid, Departamento de Ciencia de Materiales, E.T.S. de Ingenieros de Caminos, Canales y Puertos, C/ Profesor Aranguren s/n, 28040 Madrid, Spain.

E-mail: jaime.planas@upm.es

²Di.S.M.I., Università di Modena e Reggio Emilia
via Amendola 2, I-42100 Reggio Emilia, Italy
e-mail: eradi@uimore.it³Departamento de Medios Continuos y de Estructuras, E.T.S. de Ingenieros de Caminos, Canales y Puertos, Universidad Politécnica de Madrid, C/ Profesor Aranguren s/n, 28040 Madrid, Spain

e-mail: morfo1@caminos.upm.es

⁴DICeA, Università di Firenze
via Santa Marta 3, I-50139 Firenze, Italy
e-mail: paolo.mariano@unifi.it

ABSTRACT

We analyze the steady propagation of a straight interfacial crack between two dissimilar planar quasicrystals in pure elastic setting and infinitesimal deformation regime. A closed form solution to the balance equations is furnished. Inertia is attributed only to the macroscopic motion.

KEY WORDS: Quasicrystals, Complex bodies, Fracture**1 INTRODUCTION AND STATEMENT OF THE PROBLEM UNDER SCRUTINY**

We analyze the steady propagation of a crack located at the interface between two dissimilar planar quasicrystals. The equilibrium conditions for an analogous crack between a quasi-crystalline alloy and a standard linear elastic material is also viewed in a sense as a limiting case. The formal statement of the problem under scrutiny requires preliminary notions sketched in the ensuing section.

1.1 Nature of quasicrystals

Electron diffraction experiments on *Al - Mn*-based alloys reveal the presence of atomic aggregates having point group symmetry which is inconsistent with lattice translation. The observation has been presented first in 1984 [12]. Six fivefold, ten threefold, and fifteen twofold axes characterizing icosahedral symmetry are displayed by diffraction patterns [12]. Essentially atomic clusters with pentagonal symmetry in the plane and icosahedral symmetry in the three-dimensional ambient space appear (Figure 1 furnishes a schematic picture). These symmetries are forbidden by the standard classification of crystallographic groups. A x-ray diffraction pattern obtained from the icosahedral phase could not be indexed to any Bravais lattice [12, 11, 4]. The basic reason is that the three-dimensional ambient space cannot be covered by using icosahedra only – the plane cannot be covered only by a tessellation of pentagons – a result known in elementary geometry.

To fill the space by means of icosahedra with atoms located at the vertices (alternatively the plane by means of pentagons), in fact, the insertion of topological alterations is necessary. Such alterations are due to clusters of atoms with different point group symmetry. Their formation is favoured or obstructed by the local energy landscape which can be altered by deformation induced by the interaction with the external environment.

The resulting atomic lattice is intrinsically quasi-periodic. Quasi-periodicity is determined by local rearrangements due to jumps of atoms between neighboring

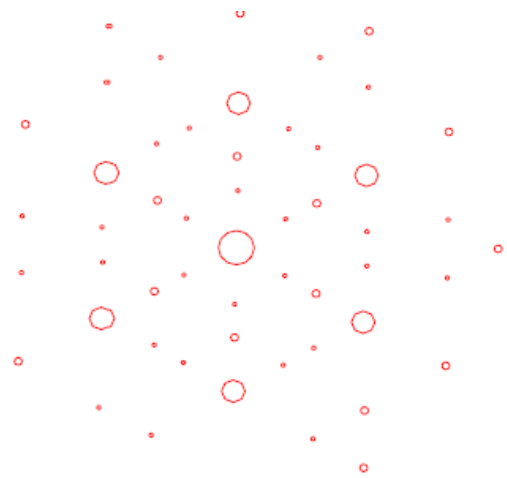


Figure 1: Cluster of atoms with icosahedral symmetry.

places and/or collective atomic modes generated for example by the flipping of crisscrossing alterations needed to maintain matching rules [2, 3, 1].

1.2 Modeling quasicrystals at continuum level

Local rearrangements of the atomic clusters do not have specific location. “Even if a quasicrystal is energetically stabilized representing a ground state, it was shown numerically that above some critical temperature the system is in a random-tiling-like phase or unlocked phase”[1].

If \mathcal{B} is the region in the ambient space \mathbb{R}^3 occupied by a quasi-crystalline body, for example in its reference place, it is possible to assume that local atomic arrangements assuring quasi-periodicity can occur at any point x in \mathcal{B} . If we assume that x is representative of a sub-cluster of atoms – a material element in the common jargon of continuum mechanics – the degrees of freedom exploited in principle to generate topological alterations generating quasi-periodicity are additional to the ones associated with x itself. The latter ones are, in fact, the translational degrees of freedom of the cluster of atoms at x . Rotation of that local sub-cluster are neglected. Only local rotation between neighboring sub-clusters are accounted for. In fact, the continuum modelling implies the decision of an internal length characterizing material elements. In standard continuum mechanics such a length is not specified because degrees of freedom inside the material element are not considered. Also, here such an internal length is not specified: we define only a vector field

$$x \mapsto \nu(x) \in \hat{\mathbb{R}}^3 \tag{1}$$

over \mathcal{B} , with $\hat{\mathbb{R}}^3$ a copy of the ambient space \mathbb{R}^3 which is distinct from it. The value $\nu(x)$ collects at each point the inner degrees of freedom exploited to assure quasi-periodicity of the atomic lattice. Commonly the field $x \mapsto \nu(x)$ is called a **phason field** and is assumed to be differentiable. The word ‘phason’ recalls that it describes the potential local phase rearrangement of the atomic clusters needed for assuring quasi-periodicity (Figure 2 indicates schematically possible rearrangements).

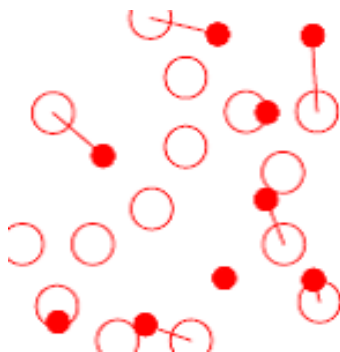


Figure 2: Sketch of rearrangements of an atomic cluster.

So, although quasi-periodicity is a global property in quasicrystals, the representation in terms of phason field [2, 3, 10, 5] constitutes an appropriate picture. In a sense, it accounts at macroscopic level for the mechanism generating quasi-periodicity rather than the periodicity itself that re-appears in the structure of the constitutive equations.

The point of view justifies the claim that the mechanics of quasicrystals in long wavelength approximation – that is the point of view of continuum mechanics – can be viewed appropriately as a special paradigmatic offspring of the general model-building of the mechanics of complex materials [7]. The adjective ‘complex’ is attributed to bodies characterized by a prominent influence of alterations in the material texture on the macroscopic mechanical behavior [6]. Such an influence is exerted through actions that can be hardly portrayed in terms of standard stresses. In fact, they require descriptions in terms of entities power-conjugated with the variations of appropriate geometrical descriptors of the material microstructure. In the case of quasicrystals, the descriptor of the microstructure (better of the microstructural effects) is the phason field. Non-standard actions are associated with the variation of the phason field and its gradient: they are, respectively, so-called self-actions and phason stresses. The former have purely dissipative nature and give rise to phason diffusion [10, 5]. The latter can be purely conservative [3, 2].

1.3 The problem tackled here

We consider a two-dimensional ambient space. A bi-material planar body fills the space. Precisely, a quasicrystal occupies half plane, the remaining half plane contains a quasi-crystalline alloy with different mechanical properties. The two materials are attached along a planar coherent interface.

A semi-infinite crack is located at the interface. It is indicated by \mathcal{C} . Figure 3 describes the situation. A frame of reference is chosen as in Figure 3. It is attached at the crack tip.

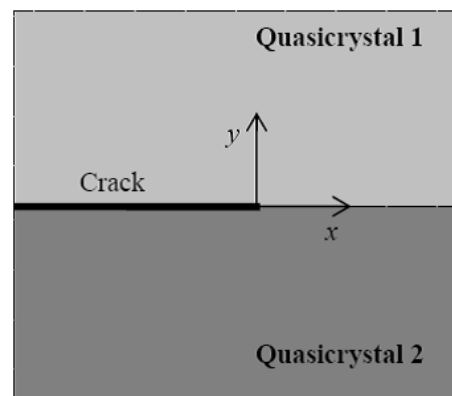


Figure 3: A bi-quasi-crystalline body with an interfacial straight crack.

In the analysis, phason diffusion in the bulk material is neglected. The attention is focused only on the purely elastic behavior in linearized setting. Dissipation can occur only at the tip of the crack when the crack opens further.

The two-dimensional setting selected here allows the use of Stroh formalism [14], a complex variable representation of balance equations in linear elasticity. We adapt it to the mechanics of quasicrystal by following the path used to describe the steady-state crack propagation of straight cracks in bodies constituted by a single type of quasicrystal [8]. When applied directly to the mechanics of quasicrystals, the procedure based on the standard Stroh formalism involves a degenerate eigenvalue problem, so appropriate modifications have to be considered [8]. The bi-material nature of the body under scrutiny here is accounted for by using an appropriate technique [13]. We furnish a closed-form solution to the balance equations for the body in Figure 3 when the margins of the cracks are not loaded and the bulk actions are neglected. Boundary conditions are prescribed at infinity and along the interface, including the crack.

2 A SUMMARY OF THE MECHANICS OF QUASICRYSTALS IN LONG WAVELENGTH APPROXIMATION

The reference place \mathcal{B} is considered as a regular set in the ambient space. Macroscopic motions are described by one-to-one, orientation preserving, differentiable maps

$$(x, t) \mapsto y := y(x, t) \in \mathbb{R}^3, \quad (2)$$

with $x \in \mathcal{B}$, $t \in [0, d]$. The displacement field u is then defined by

$$(x, t) \mapsto u(x, t) = y(x, t) - x, \quad (3)$$

with $Du(x, t)$ its spatial derivative with respect to x . The condition $|Du| \ll 1$ at any x and t , characterizes the infinitesimal deformation setting.

In time, phason degrees of freedom are described by differentiable maps

$$(x, t) \mapsto \nu(x, t) \in \hat{\mathbb{R}}^3. \quad (4)$$

Interactions associated with the rates of changes of the displacement fields are standard stresses σ (Cauchy stress tensor) and body forces b . Interactions associated with the rate of change of the microstructural phason activity are in this special case only a microstress S and a dissipative self-action ζ .

Balance equations then read as follows:

$$\operatorname{div} \sigma + b = \rho \ddot{u}, \quad (5)$$

$$\operatorname{div} S = \zeta, \quad (6)$$

$$\operatorname{skw}(\sigma + \nu \otimes \zeta + S^T N) = 0, \quad (7)$$

where ρ is mass density. The nature and the derivation of the balance equations from first principles has been discussed in previous works [5, 7]. Some authors claim the presence of phason inertia [2], other researchers exclude it suggesting the sole diffusive role of phason modes [10]. Here, we do not consider neither phason inertia nor phason diffusion which has dissipative nature. Our analysis is restricted only to pure elastic setting.

Constitutive issues are selected in the following way:

- The stress measures σ and S are purely conservative. There exists an elastic energy density $e(Du, D\nu)$ such that

$$\sigma = \frac{\partial e}{\partial Du}, \quad S = \frac{\partial e}{\partial D\nu}.$$

That e be independence of ν alone is suggested by experimental evidence [2, 3]. Independence of u is due to invariance requirements with respect to changes in observers.

- The self-action ζ is purely dissipative. So, since phason diffusion is neglected, here we assume $\zeta = 0$.
- In infinitesimal deformation setting, the elastic energy e can be considered as a quadratic form of its entries, namely

$$\begin{aligned} e(Du, D\nu) &= \frac{1}{2} (\mathbb{C}Du) \cdot Du + \\ &+ \frac{1}{2} (\mathbb{K}D\nu) \cdot D\nu + (\mathbb{K}'D\nu) \cdot Du, \end{aligned}$$

where \mathbb{C} , \mathbb{K} and \mathbb{K}' are fourth-rank constitutive tensors. \mathbb{C} is the standard elastic tensor, \mathbb{K}' describes the coupling between gross deformation and phason activity, \mathbb{K} is peculiar of the phason degrees of freedom. Appropriate explicit structures of the constitutive tensors are given by [2]

$$\begin{aligned} \mathbb{C}_{ijhk} &= \lambda \delta_{ij} \delta_{kl} + \mu (\delta_{ik} \delta_{jl} + \delta_{il} \delta_{jk}), \\ \mathbb{K}_{ijkl} &= k_1 \delta_{ik} \delta_{jl} + k_2 (\delta_{ij} \delta_{kl} - \delta_{il} \delta_{jk}), \\ \mathbb{K}'_{ijkl} &= k_3 (\delta_{i1} - \delta_{i2}) (\delta_{ij} \delta_{kl} - \delta_{ik} \delta_{jl} + \delta_{il} \delta_{jk}) \end{aligned}$$

where in the last equation no summation over repeated indices is assumed. λ and μ are the standard Lamé constants, k_1 and k_2 are associated with the pure phason activity and k_3 is the so-called *coupling coefficient*.

Once constitutive structures are substituted in the balance equations, in the two-dimensional setting treated here, the balance equations themselves can be written in matrix form by listing the components of Du and $D\nu$ in vectors. An eigenvalue problem then arises.

3 SOLUTION

In two-dimensional setting, set $\mathbf{u} := (u_1, u_2, v_1, v_2)$ and $\mathbf{t} := (\sigma_{1j}\bar{n}_j, \sigma_{2j}\bar{n}_j, \mathcal{S}_{1j}\bar{n}_j, \mathcal{S}_{2j}\bar{n}_j)$, where \bar{n} is the normal to the interface. Attribute also an index $k = 1, 2$ to both \mathbf{u} and \mathbf{t} , with the convention that $k = 1$ refers quantities to the half-plane occupied by the first type of quasicrystal and $k = 2$ to the second one.

Solution in terms of u_k and t_k to the balance equations, under the assumptions made here, are given by

$$u_{k,x} = 2 \operatorname{Re} [E_k g_k], \quad t_k = 2 \operatorname{Re} [H_k g_k], \quad (8)$$

where no summation over repeated indices is understood from now on, and g_k can be expressed in terms of a vector function h_k as

$$g_k(z_k) = h_k(z_k) - \frac{i}{2} \bar{z}_k N h'_k(z_k) \quad (9)$$

where N a nilpotent 4×4 matrix with $N_{43} = 1$ and 0 in all other entries. Define

$$f_k(z_k) = h_k(z_k) - \frac{i}{2} z_k N h'_k(z_k). \quad (10)$$

For $x \in \mathbb{R}$, we get $g_k(x) = f_k(x)$ and also

$$t_k(x) = H_k f_k(x) + \bar{H}_k \bar{f}_k(x). \quad (11)$$

Boundary conditions along the interface read as follows:

$$u_{1,x}(x) = u_{2,x}(x), \quad t_1(x) = t_2(x), \quad x \notin \mathcal{C}, \quad (12)$$

$$t_1(x) = t_2(x) = 0, \quad x \in \mathcal{C}. \quad (13)$$

Moreover, it is also imposed that $g_k(z_k) \rightarrow 0$ as $|z_k| \rightarrow \infty$. The continuity of normal standard and phason stresses along the interface, namely $t_1(x) = t_2(x)$ for any x , yields [13] the identity $H_1 f_1(z) = \bar{H}_2 \bar{f}_2(z)$ in the half-plane with positive y , z a complex variable. As a consequence, we get

$$\bar{f}_2(x) = \bar{H}_2^{-1} H_1 f_1(x), \quad (14)$$

$$\bar{f}_1(x) = \bar{H}_1^{-1} H_2 f_2(x). \quad (15)$$

The vector $\delta(x) := u_{1,x}(x) - u_{2,x}(x)$ takes the form

$$\delta(x) = E_1 f_1(x) + \bar{E}_1 \bar{f}_1(x) - E_2 f_2(x) - \bar{E}_2 \bar{f}_2(x), \quad (16)$$

that is

$$\delta(x) = (E_1 H_1^{-1} - \bar{E}_2 \bar{H}_2^{-1}) H_1 f_1(x) - (E_2 H_2^{-1} - \bar{E}_1 \bar{H}_1^{-1}) H_2 f_2(x) \quad (17)$$

Define the matrix $Y_k := i E_k H_k^{-1}$ and call Z the sum

$$Z := Y_1 + \bar{Y}_2 = i (E_1 H_1^{-1} - \bar{E}_2 \bar{H}_2^{-1}). \quad (18)$$

Then, we can write

$$i\delta(x) = Z H_1 f_1(x) + \bar{Z} H_2 f_2(x). \quad (19)$$

Consider now the solution for $Z = \bar{Z}$, that is for Z a real matrix. In this case, consider

$$h(z) = \begin{cases} H_1 f_1(z), & \text{if } y > 0 \\ H_2 f_2(z), & \text{if } y < 0 \end{cases}. \quad (20)$$

The condition of vanishing standard and phason tractions at the crack margins, namely $t_1(x) = t_2(x) = 0$ for $x \in \mathcal{C}$, implies

$$h(z_k) = \frac{1}{2\sqrt{2\pi z_k}} \mathbf{k}, \quad (21)$$

with \mathbf{k} a vector collecting stress intensity factors: $\mathbf{k} = \{K_I, K_{II}, T_I, T_{II}\}$, the first two entries are standard factors, the last two indicate phason factors. Moreover, in terms of \mathbf{k} , the energy release rate \mathcal{G} is given by

$$\mathcal{G} = \frac{1}{4} \mathbf{k} \cdot Z \mathbf{k}. \quad (22)$$

By taking into account that

$$f_k(z_k) = H_k^{-1} h(z_k), \quad (23)$$

then

$$h_k(z_k) = \frac{i}{2} z_k N h'_k(z_k) + H_k^{-1} h(z_k), \quad (24)$$

so that

$$g_k(z_k) = H_k^{-1} h(z_k) + \frac{i}{2} (z_k - \bar{z}_k) N h'(z_k), \quad (25)$$

which completes the analysis.

- The two quasicrystals occupying the plane in Figure 3 have the same Mach numbers when they have the same Lamé constants and the coupling coefficients are related by

$$\kappa_3^{(1)} = \kappa_3^{(2)} \sqrt{\frac{\kappa_1^{(1)}}{\kappa_1^{(2)}}}. \quad (26)$$

In this case, $z_1 = z_2$.

- The analysis of the same situation with one of the half spaces occupied by a simple linear elastic body can be considered in a sense as a limiting case by imagining to freeze the phason degrees of freedom. However, by letting to zero arbitrarily one of the two κ_3 's, we realize that at least one row vanishes in a matrix that must be inverted, with the consequent difficulty. Small perturbation techniques are then necessary.

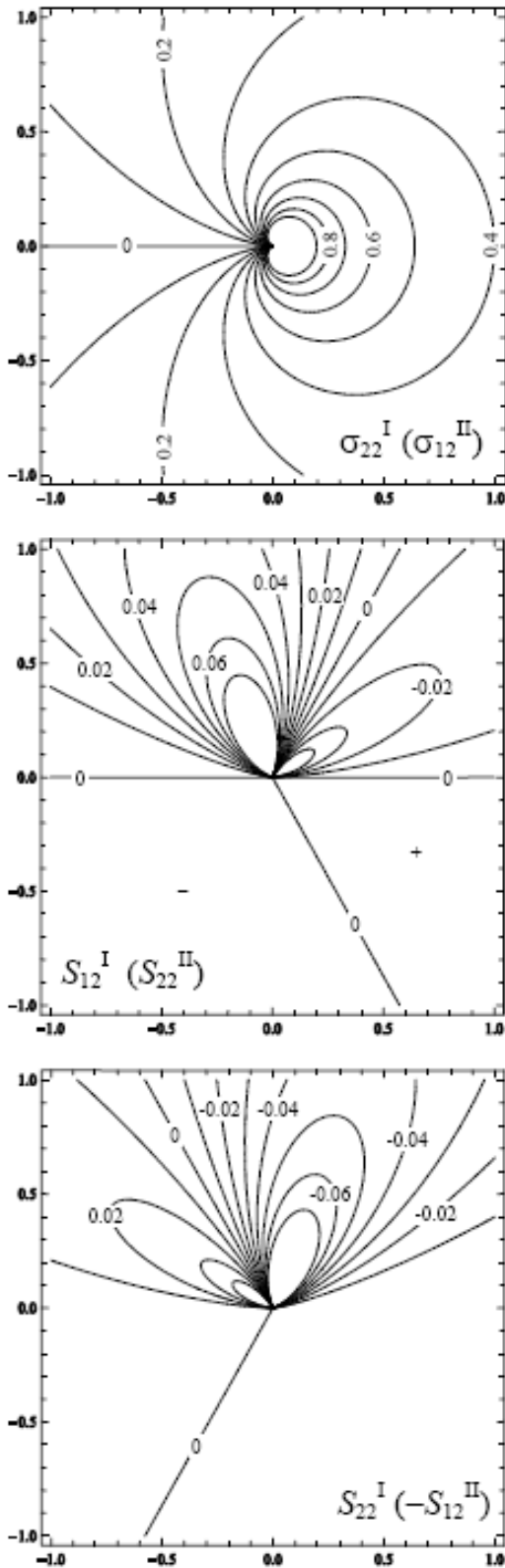


Figure 4: Contours of normalized phonon and phason stress fields for a semi-infinite rectilinear crack under remote Mode I (Mode II) loading conditions, for $\lambda^{(1)} = \lambda^{(2)} = 85GPa$, $\mu^{(1)} = \mu^{(2)} = 65GPa$, $k_1^{(1)} = k_1^{(2)} = 0.044GPa$, $k_2^{(1)} = k_2^{(2)} = 0.0396GPa$, $\chi^{(1)} = 5$ and $\chi^{(2)} = 0.1$.

Details of the analyses summarized here can be found in a forthcoming paper [9]. Figure 4 shows the portrait of the solution for the data reported in the captions, data taken from the thesis of C. Walz [15]. In the figure the crack is located in the interval $[-1, 0]$ along the horizontal axis. Figure 5 indicates sensibility of the solution interms of standard Cauchy stress with respect to the ratio

$$\chi := \frac{k_3}{k_1}, \quad (27)$$

variation due to the circumstance that the constitutive constants k_1 and k_2 can be determined with certain safety for specific classes of quasicrystals while there is a degree of uncertainty in the evaluation of the coupling coefficient k_3 . The results in Figure 4 show the behaviour of the solution when phason stresses tend to vanish in one of the two quasicrystals.

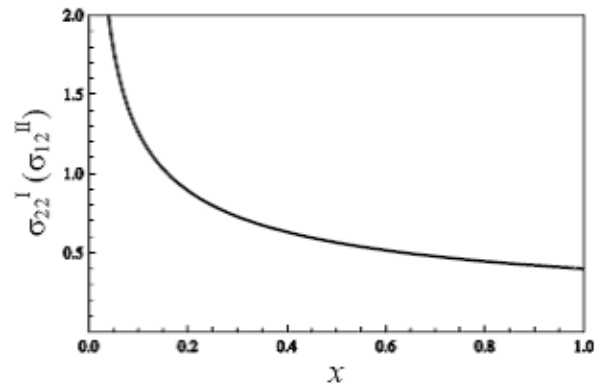


Figure 5: Variation of normalized phonon tensile (shear) stress along the interface ahead of the crack tip under remote Mode I (Mode II) loading conditions.

REFERENCES

[1] de Boissieu, M., Boudard, M., Hennion, B., Bellissent, R., Kycia, S., Goldman, A., Janot, C. and Audier, M. (1995), Diffuse scattering and phason elasticity in the AlPdMn icosahedral phase, *Phys. Rev. Letters*, **75**, 89-92.

[2] Hu C., Wang R. and Ding D.-H. (2000), Symmetry groups, physical property tensors, elasticity and dislocations in quasicrystals, *Rep. Prog. Phys.*, **63**, 1-39.

[3] Jeong H.-C. and Steinhardt P. J. (1993), Finite-temperature elasticity phase transition in decagonal quasicrystals, *Physical Review B*, **48**, 9394-9403.

[4] Lifshitz R. (2003), Quasicrystals: a matter of definition, *Found. Phys.*, **33**, 1703-1711.

[5] Lubensky T. C., Ramaswamy S. and Toner J. (1985), Hydrodynamics of icosahedral quasicrystals, *Physical Review B*, **32**, 7444-7452.

- [6] Mariano P. M. (2002), Multifield theories in mechanics of solids, *Adv. Appl. Mech.*, **38**, 1-93.
- [7] Mariano P. M. (2006), Mechanics of quasi-periodic alloys, *J. Nonlinear Sci.*, **16**, 45-77.
- [8] Radi E. and Mariano P. M. (2009), Dynamic steady-state crack propagation in quasicrystals, *preprint*.
- [9] Radi E., Planas J., Stickle M. M. and Mariano P. M. (2009), Steady-state propagation of interfacial cracks in dissimilar quasicrystals, *in preparation*.
- [10] Rochal S. B. and Lorman V. L. (2002), Minimal model of the phonon-phason dynamics in icosahedral quasicrystals and its application to the problem of internal friction in the *i*-AlPbMn alloy, *Physical Review B*, **66**, 144204 (1-9).
- [11] Rokhsar D. S., Wright D. C. and Mermin N. D. (1988), Scale equivalence of crystallographic space groups, *Phys. Rev. B*, **37**, 8145-8149.
- [12] Shechtman D., Blech I., Gratias D. and Cahn J. W. (1984), Metallic phase with long-range orientational order and no translational symmetry, *Phys. Rev. Letters*, **53**, 1951-1954.
- [13] Suo Z., Kuo C. M., Barnett D. M., Willis J. R. (1992), Fracture mechanics for piezoelectric ceramics, *J. Mech. Phys. Solids*, **40**, 739-765.
- [14] Stroh A. N. (1962), Steady state problems in anisotropic elasticity, *J. Math. Phys.*, **41**, 77-103.
- [15] Walz C. (2003), Zur Hydrodynamik in Quasikristallen, *Thesis*, University of Stuttgart.

STRESS CORROSION CRACKING. A NEW MECHANISM APLIED TO HIGH STRENGTH STEELS.**Javier Sánchez¹, José Fulla¹, Carmen Andrade¹**¹ Instituto de Ciencias de la Construcción Eduardo Torroja (CSIC). C/ Serrano Galvache, 4.
28033 Madrid, España.E-mail: javiersm@ietcc.csic.es, fulla@ietcc.csic.es, andrade@ietcc.csic.es**ABSTRACT**

The stress corrosion cracking (SCC) process is at present a not fully elucidated mechanism of deterioration. It is a surface process that implies a corrosion and stress synergy, but the most practical consequence is that stress corrosion cracking can modify the mechanical characteristics of the metal causing brittle failure.

Previously, we present some results about stress corrosion cracking, crack propagation rate or, even, crack arrest conditions in High Strength Steels. This kind of steels is usually used in prestressed and postensioned structures. These wires are of eutectoid composition and cold drawn. It is well established that failures occur when the wires are in contact with electrolytes of specific compositions while under stress. In the case of concrete, the electrolyte is its pore solution and the stress levels result from the different loads applied due to structural requirements.

In this work we suggest some improvements of the Mechanism of SCC based in the Surface Mobility of vacancies on the crack surface proposed by Galvele. Improvements consist in incorporating the electrochemical corrosion as one of the sources for the creation of vacancies and some mechanical effects, both produce synergic effect in the crack propagation rate and they are important for a more comprehensive explanation of the process.

KEY WORDS: Stress Corrosion Cracking, Mechanism, Surface Mobility, High Strength Steel.

1. INTRODUCTION

La Corrosión Bajo Tensión (CBT) es un fenómeno que afortunadamente ocurre con poca frecuencia, pero sus consecuencias son catastróficas para el ser humano. Los primeros casos documentados sobre problemas ocasionados por la CBT datan del siglo pasado y se refieren a explosiones sufridas por calderas fabricadas con aceros de bajo carbono. Desde entonces, este problema se ha estudiado desde diferentes perspectivas que han tenido lugar y han ido desarrollándose a medida que lo hacían la metalurgia, los métodos de ensayo y el conocimiento científico. En la actualidad, con el desarrollo de nuevos materiales y su aplicación en otros tantos sistemas nuevos, los casos de CBT publicados crecen de forma exponencial. No hay industria ni aplicación práctica de aleaciones metálicas que esté exenta de sufrir CBT, lo que la convierte en un ámbito de estudio que ha despertado gran interés.

Hasta hoy, el proceso de CBT no ha sido explicado satisfactoriamente por la mayoría de las teorías. Numerosos mecanismos han sido propuestos para explicar la fractura de metales por efecto del medio, pero sólo algunos de ellos se han mantenido vigentes. Entre ellos hay que destacar cinco mecanismos como los más relevantes:

1. El Mecanismo de Disolución Anódica; cuyo

desarrollo se debe principalmente a Parkins [1].

2. El Mecanismo de Fisuración Discontinua; cuyos aspectos teóricos han sido desarrollados por Newman [2].
3. El Mecanismo de la Movilidad Superficial; desarrollado por Galvele [3].
4. Plasticidad favorecida por el ambiente o Environmentally Enhanced Plasticity; desarrollada por Magnin [4,6].
5. Fragilización por Hidrógeno o Hydrogen Embrittlement; de la que existen varios mecanismos [4,5,7,8,9,10,11,12,13,14].

El Mecanismo de la Movilidad Superficial, propuesto por Galvele, aporta una innovación relevante al campo de la CBT, condicionando el crecimiento de la fisura a parámetros electroquímicos y mecánicos. Además este mecanismo permite hacer **predicciones** de velocidad de propagación de la fisura en función de las tensiones, de las condiciones electroquímicas y de las características del material.

Sin embargo, Galvele reduce el campo de estudio al proceso que tiene lugar en un entorno de 10^{-8} m alrededor de la punta de la fisura, ignorando la incidencia del gradiente de tensiones a lo largo de los labios de la fisura y la causa principal de la generación

de vacantes lejos de la punta de la fisura, es decir, la reacción anódica de corrosión.

Del mismo modo que no existe un mecanismo que permita explicar todos los casos de CBT, no existe una única metodología de ensayo para determinar la CBT o la Fragilización por Hidrógeno (HE) [15]. Para el caso de los aceros de alta resistencia empleados en las estructuras existen diversos ensayos estandarizados en los cuales se ha incrementado la agresividad del medio para reducir el tiempo de ensayo. Este tipo de ensayos permite predecir la susceptibilidad a la HE y se aplican como control de calidad [16,17]. Otros autores han sugerido métodos de ensayo más próximos a las condiciones reales de trabajo de los aceros dentro del hormigón [18-24]. En anteriores trabajos, se ha mostrado el efecto del medio sobre el comportamiento mecánico, y más concretamente el efecto del H sobre la tenacidad de fractura. Los valores de tenacidad de fractura obtenidos son inferiores a los valores medidos al aire [25-28], y este hecho se ha atribuido al efecto del medio y en concreto al efecto del hidrógeno sobre la red de Fe [14].

La CBT es el resultado de una sinergia entre el **materia**, el **medio** en el que se encuentra y las condiciones **mecánicas** a las que está sometido. De esta forma, tanto la metodología de ensayo como el mecanismo de CBT deben de aplicarse desde ese triple enfoque. En anteriores trabajos se ha presentado una metodología de ensayo que permite medir parámetros mecánicos y electroquímicos [25-28]. A su vez, esta metodología de ensayo permite combinar la Mecánica de Fractura con la Teoría de la Movilidad Superficial en base a un modelo teórico. Por lo tanto, se establece una interacción entre el modelo teórico propuesto y la metodología de ensayo.

2. MÉTODO EXPERIMENTAL

El método experimental ha sido descrito por Sánchez y col [25,28]. El objetivo de esta metodología de ensayo es conseguir unas condiciones de trabajo más próximas a la realidad y controlando la mayor cantidad de parámetros (mecánicos y electroquímicos). De esta forma se ha desarrollado un método que permite generar una fisura por CBT partiendo de una entalla mecánica y protegiendo el resto de la superficie para evitar la mayor cantidad de ruido posible durante las medidas. La parte experimental se ha dividido en 3 etapas: i) generación de la fisura bajo carga y potencial electroquímico controlados, ii) ensayo de tracción lenta al aire y, iii) análisis de la superficie de fractura.

3. MODIFICACIÓN DEL MECANISMO DE MOVILIDAD SUPERFICIAL

El mecanismo de Movilidad Superficial propuesto por Galvele está basado en los trabajos de Rhead [29,30] y Oda [31], los cuales observaron que la movilidad de los átomos de la superficie depende del material y del medio en el que se encuentren según la siguiente

ecuación:

$$D_s = 7.40 \cdot 10^{-4} \exp\left(-\frac{30T_m}{RT}\right) + 0.014 \cdot 10^{-4} \exp\left(-\frac{13T_m}{RT}\right) \quad (1)$$

donde: D_s es el coeficiente de difusión superficial y T_m es la temperatura de fusión del material o de los compuestos que se formen sobre la superficie por efecto del medio.

A raíz de esta ecuación Galvele [3] propone un **mecanismo de CBT** basado en **cuatro postulados**: i) el medio en el que se encuentra el metal cambia la movilidad superficial propia del metal; ii) la temperatura a la cual tiene lugar la CBT es inferior a la mitad de la temperatura absoluta de fusión del metal; iii) únicamente las tensiones elásticas son importantes en el proceso de CBT; iv) el avance de la grieta tiene lugar por la llegada de vacantes desde la red metálica al frente de la misma. La captura de una vacante superficial por la punta de la grieta permite su propagación en una distancia atómica. Estos cuatro postulados dan lugar a una ecuación que permite predecir la velocidad de propagación de la fisura por CBT (cpr):

$$cpr = \frac{D_s}{L} \left[\exp\left(\frac{\sigma\alpha^3 + \alpha E_b}{kT}\right) - 1 \right] \quad (2)$$

donde: L es la distancia de la difusión de las vacantes, σ es la tensión correspondiente al límite elástico, a es el tamaño del átomo, α es un parámetro adimensional, E_b es la energía de unión H-vacante, k es la constante de Boltzmann y T es la temperatura absoluta.

A raíz de los resultados experimentales obtenidos se ha observado que hay diversas hipótesis del modelo propuesto por Galvele que es necesario modificar:

- Galvele establece la velocidad de propagación de la fisura en función de la tensión de plastificación, que la establece como la máxima tensión que se alcanza en la fisura. De esta forma se establece una simplificación del **gradiente de tensiones** que se genera en la superficie de la fisura y no se establece el efecto de este gradiente sobre el **coeficiente de difusión** (D_s).
- Galvele establece que la velocidad de propagación de la fisura depende de los óxidos generados en la superficie, sin embargo estos óxidos no han sido observados en la experimentación. Por lo tanto hay que tener en cuenta las **condiciones electroquímicas** para establecer el coeficiente de difusión superficial.
- Galvele no establece de forma clara una **fuentes de vacantes** para el caso de que no se formen estos óxidos sobre la superficie de la fisura.

A continuación se va a establecer el marco teórico para el modelo de CBT. Este **marco teórico** se basa en: i) la determinación de un coeficiente de difusión de las vacantes en base a parámetros del material, del medio y

mecánicos, y ii) la definición de la fuente de vacantes.

3.1. Definición del coeficiente de difusión superficial (D_s).

En 1967 Gjostein [35] y posteriormente Rhead en 1969 [29] plantean una ecuación para expresar la movilidad superficial propia del **material y la influencia de los contaminantes** sobre la movilidad superficial. Kubo y col. [36] muestran la influencia del potencial electroquímico en el coeficiente de difusión superficial. Estos autores modifican la energía de activación de la ecuación propuesta por Gjostein e introducen el efecto del medio bajo la hipótesis de que la variación en la energía de activación es debida a la carga superficial en exceso (equation 3). La energía de activación disminuye al trabajar a potenciales mayores que el potencial de carga cero (E_{PZC}) y el coeficiente de difusión superficial alcanza un mínimo en el potencial de carga cero y aumenta de forma exponencial al trabajar a potenciales más anódicos.

$$D_s = D_{s0} \exp\left\{\frac{-Q_{s0} + (1/2)\alpha\beta Na|e|(E - E_{PZC})}{RT}\right\} \quad (3)$$

donde: α y β son constantes, Na es el número de Avogadro y e es la carga del electrón.

Jaime González Velasco [37,38] plantea el mecanismo de difusión superficial en la interfase electrodo-electrolito. En el caso de un metal inmerso en un electrolito, la movilidad de un átomo superficial se encontraría influida por la presencia de las moléculas de agua, iones, átomos y otras entidades presentes en el plano interno de Helmholtz (IHP). Como en el caso de Kubo y col. [36], J. González establece el máximo del coeficiente de difusión superficial en el potencial de carga cero.

El tercer factor que interviene en el coeficiente de difusión superficial es **el estado tensional** en la fisura, es decir, la influencia de la tensión en el coeficiente de difusión. Los resultados encontrados en la bibliografía no son todos coincidentes y atribuyen la variación en el comportamiento frente a la tensión a las diferencias en la estructura cristalina y la orientación estudiada [39]. De esta forma para metales con estructura cúbica centrada en el cuerpo, como es el caso de la fase alpha del hierro, se produce un comportamiento contrario al mostrado en el Cu(111) [40]. El mecanismo que relaciona el coeficiente de difusión con la deformación no está aún desarrollado. Shu y col. [39] presentan varios caminos de difusión en función del tipo de red cristalina, ya sea cúbica centrada en el cuerpo (bcc), centrada en las caras (fcc) o hexagonal compacta (hcp). Por lo tanto, las barreras de difusión varían en función de la estructura cristalina, el camino de difusión y la deformación. Wang y col. [41] describen dos tipos de barreras a la difusión: una debida a la variación en la distancia de "salto", y otra, debida a la energía de enlace.

La variación en el coeficiente de difusión depende de la influencia de la tensión en las mencionadas barreras a la difusión. Al generarse un gradiente de tensiones, los átomos difunden hacia las zonas de menor tensión, mientras que las vacantes difunden hacia las zonas de mayor tensión.

En resumen, la energía de activación viene definida en ausencia de tensiones por Q^{act} , considerando en este término el efecto del material y el medio. En los estudios mostrados, a pesar de la diversidad de resultados, para materiales con estructura cúbica centrada en el cuerpo (bcc), en presencia de tensiones la energía de activación disminuye, ya que mediante la tensión se aporta energía a los átomos, o lo que es lo mismo, disminuye la energía necesaria para el movimiento de las vacantes puesto que se modifica la energía de unión de los átomos.

Por lo tanto, se propone corregir la expresión del coeficiente de difusión superficial variando la **energía de activación** en función del **factor de intensidad de tensiones**, según se muestra en la Ecuación 4. En esta ecuación se incorporan los tres factores que intervienen en el proceso de CBT y que se acaban de exponer: el material, el medio y las tensiones.

$$D_s = D^o \exp\left[\frac{-Q^{act}}{RT} + \beta K_I^2\right] = D_{s,\sigma=0} \exp[\beta K_I^2] \quad (4)$$

donde: R es la constante de los gases, T es la temperatura absoluta, β es una constante, K_I es el factor de intensidad de tensiones, $D_{s,\sigma=0}$ es el valor del coeficiente de difusión superficial en ausencia de tensión.

De esta manera se trata de integrar la mecánica de fractura en la teoría de la movilidad superficial propuesta por Galvele.

3.2. Definición de la fuente de vacantes.

Para comprender mejor la situación electroquímica creada por la fisura, se ha realizado una simulación por Elementos Finitos [32,33] de las líneas de corriente entre un contra-electrodo y la superficie de un electrodo de trabajo con una entalla y una fisura. Se ha podido observar como las líneas de corriente se concentran en primer lugar en la entalla, pero a medida que se forma la capa de óxidos la corriente se desplaza hasta que alcanza el "inicio" de la fisura o fondo de la entalla (Figura 1). Sin embargo las líneas de corriente no penetran en los labios de la fisura. Por lo tanto, no hay óxidos en la fisura y para su propagación es necesario que las vacantes difundan desde la entalla hasta el frente de la fisura, y entonces el camino de difusión de las vacantes (valor de L correspondiente al modelo de Galvele) no tiene por qué permanecer ni constante ni en valores de una pocas distancias atómicas. Cuando la fisura se propague, este valor de L irá creciendo si las vacantes se generan en la entalla.

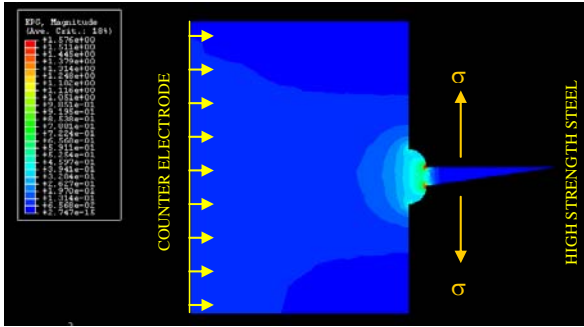


Figura 1. Líneas de corriente en el entorno de la entalla y la fisura.

Una consecuencia derivada es que no es posible proponer un modelo basado en la 1ª ley de Fick, sino que es necesario realizar los cálculos de transporte de vacantes en **estado no estacionario** desde la entalla, lugar donde se generan por disolución anódica, hasta el frente de la fisura donde producen el crecimiento de la fisura.

4. APLICACIÓN DEL MODELO PROPUESTO A LOS ACEROS DE ALTA RESISTENCIA.

Según el potencial que adopte el metal, en el caso del acero se puede estimar un coeficiente de difusión superficial a partir de la ecuación de Gjostein (Ecuación 1) [35], con la **composición** y la **temperatura** de fusión, y modificar la ecuación de Gjostein teniendo en cuenta la interacción del medio con las vacantes. De esta forma se puede añadir a la movilidad superficial propia de las vacantes en la superficie del metal, el **efecto del medio**.

Los ensayos de CBT se han realizado en disoluciones acuosas donde se debe tener en cuenta, además del potencial electroquímico de trabajo o, lo que es lo mismo, además de tener en cuenta el sobrepotencial (respecto al potencial de carga cero), hay que considerar la interacción del hidrógeno generado en las reacciones electroquímicas con las vacantes a través de una “energía de enlace”. Sin embargo, no se han observado productos de corrosión adsorbidos sobre la fisura por lo que no es posible atribuirles ningún efecto adicional a la movilidad superficial. Esta singularidad, se encuentra en los trabajos de Li, Gangloff y Scully [42]. La energía de unión del hidrógeno-vacante en la interfase ferrita-cementita, presente en los aceros eutectoides, según estos autores es de 11.4-11.6 kJ/mol. De esta forma, se ha **incorporado un nuevo término correspondiente a la influencia del hidrógeno** (Q_H) en la energía de activación de la Ecuación 1, que para temperaturas $T < 0.77T_m$ se puede expresar como:

$$D_{s,\sigma=0} = 0.014 \cdot 10^{-4} \exp\left[\frac{-13T_m + Q_H}{RT}\right] \quad (5)$$

Teniendo en cuenta las ecuaciones 4 y 5 es posible estimar el coeficiente de difusión en función del material, el medio y la geometría de la fisura.

Los materiales empleados en este estudio, el alambón y el trefilado obtenido a partir del alambón, tienen una composición eutectoide. En la Ecuación 5 se ha considerado la temperatura eutéctica del hierro, 727 °C [43].

Para incorporar el efecto del medio se ha considerado la interacción del hidrógeno generado durante el proceso de corrosión con las vacantes, disminuyendo la energía de activación como se propone en la Ecuación 5.

Teniendo en cuenta las consideraciones anteriores se obtiene un coeficiente de difusión superficial en ausencia de tensiones, $D_{s,\sigma=0} = 10^{-14} \text{ m}^2/\text{s}$.

Según la Ecuación 4 propuesta, el coeficiente de difusión es necesario actualizarlo a medida que la fisura avanza, ya que el **campo tensional** varía. En esta ecuación aparece un parámetro de ajuste, β . Este parámetro debe de mantenerse constante para cada material ya que depende de constantes elásticas y propiedades del material.

En el modelo se ha considerado que la generación de las vacantes tiene lugar por corrosión. De esta forma se puede obtener el flujo de vacantes en el límite entre la entalla y la fisura a través de la corriente de corrosión aplicando la Ley de Faraday. Se ha tomado como intensidad de corrosión la corriente de celda, en condiciones potenciostáticas, una vez generada la capa de óxidos de la entalla, momento a partir del cual la corriente de celda se estabiliza y se genera la fisura. En la Ecuación 6 se formula el flujo de vacantes en la fisura (J) empleando la Ley de Faraday:

$$J = \frac{\left(\frac{I N_A}{n F}\right)}{\text{Area}} \quad (6)$$

donde: I es la intensidad media de celda en el ensayo, n es la valencia, F es la constante de Faraday y Area es el área en el que se generan las fisuras en la entalla.

El flujo de vacantes depende linealmente de la intensidad de corrosión (según la Ecuación 7) y experimentalmente se ha observado que la intensidad de corrosión se mantiene prácticamente constante durante la generación de la fisura [25,28].

$$J = I \cdot \text{Cte} \quad (7)$$

donde: $\text{Cte} = 5.20 \cdot 10^{+30} \text{ Atom}/\text{m}^2 \text{Culomb}$

Teniendo en cuenta los datos experimentales [25-28], se ha estimado el valor del parámetro β (ecuación 4). En la Figura 2 se muestra el valor promedio junto con la desviación típica del parámetro β para el **alambón** y el **acero trefilado**.

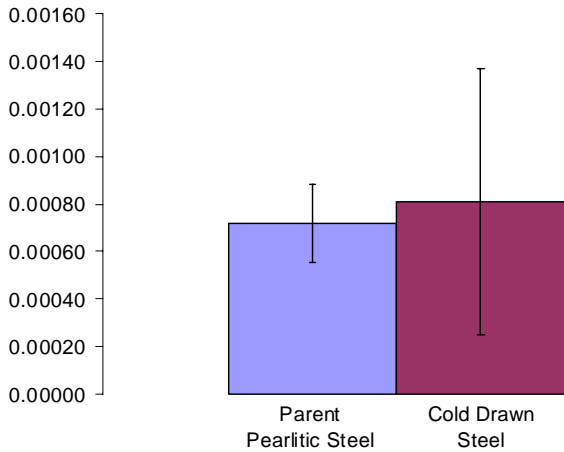


Figura 2. Valores el parámetro β para el alambón y el acero trefilado.

En las siguientes figuras se muestran algunos de los posibles resultados que es posible obtener con el mecanismo de CBT desarrollado y en base a los resultados experimentales obtenidos con la metodología de ensayo propuesta.

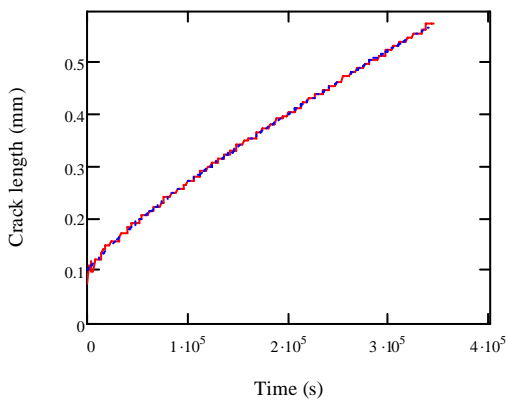


Figura 3. Crecimiento de la fisura con el tiempo según el modelo propuesto. Material: alambón.

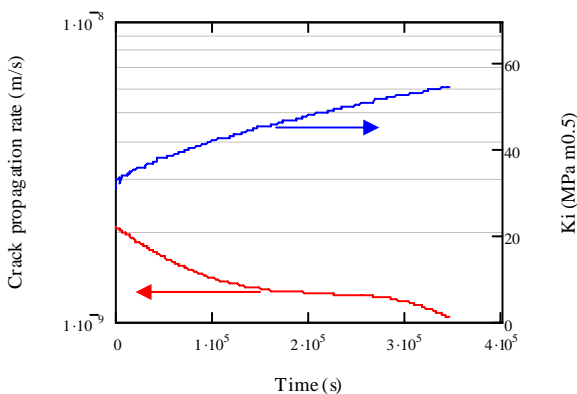


Figura 4. Velocidad de propagación de la fisura y factor de intensidad de tensiones según el modelo propuesto. Material: alambón.

5. CONCLUSIONES

Se ha propuesto un modelo de CBT basado en la hipótesis de que el mecanismo que permite explicar la CBT está basado en la movilidad superficial de vacantes en los labios de la fisura, que estas vacantes se generan por la corriente anódica en el proceso de corrosión, y que se mueven, no sólo bajo la influencia de un medio, sino también bajo la influencia de las tensiones mecánicas que tienen lugar en los labios de la fisura. De esta forma se ha unido la teoría de la Movilidad Superficial y la Mecánica de la Fractura.

El modelo incluye parámetros característicos del material, las condiciones mecánicas, la geometría y las condiciones electroquímicas. No existe una relación unívoca entre la intensidad de corrosión, el factor de intensidad de tensiones y la velocidad de propagación de la fisura. En ocasiones se produce la parada de la fisura a pesar de aumentar el valor de K_I y otras veces se produce un aumento brusco de la velocidad de propagación de la fisura hasta alcanzar la rotura, que se corresponde con el valor de K_{IC} para el acero en el medio.

ACKNOWLEDGEMENTS

Los autores quieren agradecer al Prof. J. R. Galvele las conversaciones y discusiones realizadas. También agradecer la financiación recibida a través del Proyecto CONSOLIDER-SEDUREC.

REFERENCES

- [1] Parkins R. N. "Metal Environmental Reactions" Vol. 1, Ed. Newness Butterworths, 1976.
- [2] Sieradzke K., Newman R. C. "Stress Corrosion Cracking" Journal of Phys. And Chem. of Solids, Vol. 48, nº 11, 1987.
- [3] Galvele J. R. "A Stress Corrosion Cracking Mechanism Based on Surface Mobility." Corr. Scie., Vol. 27, nº 1, 1987.
- [4] Magnin T., Chieragatti R., Oltra R. "Mechanism of brittle fracture in a ductile 316 alloy during stress corrosion" Acta. Metall. Mater. 38, 1313-1319, 1990.
- [5] Serebrinsky S., Carter E. A., Ortiz M. "A quantum-mechanically informed continuum model of hydrogen embrittlement" Journal of the Mechanics and Physics of Solids, 52 (10), 2403-2430, 2004.
- [6] Magnin T. Corrosion-Deformation Interactions CDI'92, ed. T. Magnin and J. M. Gras, Les Editions de Physique, Les Ulis, France, 27-41, 1993.
- [7] Westlake D. G. "A generalized model for hydrogen embrittlement" Trans. ASM 62 (4), 1969.
- [8] Nelson H. G. "Film-rupture model of hydrogen-induced, slow crack growth in acicular alpha-beta titanium" Metall. Trans. A - Phys. Metall. Mater. Sci. 7A (5), pp. 621-627, 1976.
- [9] Beachem C. D. "A new model for hydrogen-assisted

- cracking (hydrogen “embrittlement”)” *Metall. Trans.* 3 (2), pp. 437–451, 1972.
- [10] Birnbaum H. K., Sofronis P. “Hydrogen-enhanced localized plasticity - A mechanism for hydrogen-related fracture” *Mater. Sci. Eng. A - Struct. Mater. Prop.* 176A (1–2), pp. 191–202, 1994.
- [11] Troiano A. R. “The role of hydrogen and other interstitials in the mechanical behavior of metals” *Trans. ASM* 52, pp. 54–80, 1960.
- [12] Oriani R. A. “Mechanistic theory of hydrogen embrittlement of steels. Ber. Bunsenges” *Phys. Chem.* 76 (8), pp. 848–857, 1972.
- [13] Oriani R. A., Josephic P. H. “Equilibrium and kinetic studies of the hydrogen-assisted cracking of steels” *Acta Metall.* 25 (9), pp. 979–988, 1977.
- [14] Sanchez J., Fullea J., Andrade C., de Andres P. L. “Hydrogen in alpha-iron: Stress and diffusion” *Phys. Rev. B*, 78, 014113, 2008.
- [15] Fullea J. “Experimental Methods to Evaluate the Susceptibility of Prestressing Steels to Stress Corrosion Cracking” *Proceedings of the International Workshop on Failures of Post-tensioned Concrete Structures Messina*, pp.17, 2000.
- [16] Elices M. “Problemas de Corrosión Bajo Tensión en el Hormigón Pretensado” *I Congreso Iberoamericano de Corrosión y Protección*, 1983.
- [17] Toribio J., Elices M. “Nuevas Aportaciones al Ensayo FIP de Fragilización por Hidrógeno en Tiocianato Amónico” *Hormigón y acero*, Vol. 27 (168), pp. 121-130, 1988.
- [18] Pakins R. N., Zhou S. “The Stress Corrosion Cracking of C-Mn Steel in CO₂-HCO₃⁻ - CO₃²⁻ Solutions I: Stress Corrosion Data” *Corr. Sci.*, Vol. 39, Nº 1, pp. 159-173, 1997.
- [19] Caballero L., Elices M. “Influencia de la velocidad de deformación en la propagación de fisuras por corrosión bajo tensión.” *Revista Iberoamericana de Corrosión y Protección*, 17 (1), pp. 15-22, 1986.
- [20] Caballero L., Elices M. “Un método para la medida de la cinética de las fisuras de corrosión bajo tensión en ensayos a velocidad de deformación constante.” *Revista Iberoamericana de Corrosión y Protección*, 17 (1), pp. 43-48, 1986.
- [21] Acha-Hurtado M. “Corrosión Bajo Tensión de Alambres de Acero Pretensado en Medios Neutros con HCO₃⁻ y Alcalinos con SO₄⁼.” *Instituto de Ciencias de la Construcción “Eduardo Torroja” C.S.I.C. Madrid*, 1993. PhD Thesis.
- [22] Alonso M. C., Andrade C., Procter R. P. M., Saenz de Santa María M. “Susceptibilidad a la Corrosión Bajo Tensión del Acero Pretensado en Disoluciones de NaHCO₃” *Hormigón y Acero*, Nº 166, pp. 121-126, 1988.
- [23] Lancha A. M. “Influencia del Trefilado en la Corrosión Bajo Tensión de Aceros Eutectoides” *Universidad Complutense de Madrid. Facultad de Ciencias Químicas*. 1987.
- [24] Valiente A., Elices M. “Premature Failure of Prestressed Steel Bars” *Engineering Failure Analysis*, Vol. 5, nº 3, pp. 219-227, 1998.
- [25] Sanchez J., Fullea J., Andrade C., Alonso C. “Stress corrosion cracking mechanism of prestressing steels in bicarbonate solutions” *Corr. Sci.* 49(11), 4069-4080, 2007.
- [26] Sanchez J., Fullea J., Andrade C. “Fracture toughness variation induced by stress corrosion cracking of prestressing steels” *Materials and Corrosion*, 59(2), 2008.
- [27] Sanchez J., Fullea J., Andrade C. “Reasons for Crack Arrest in Stress Corrosion Cracking Tests. Crack Propagation Rate in High Strength Steels” *Corrosion*, 65(6), 2009.
- [28] Sanchez J., PhD, Thesis. Eduardo Torroja Institute, IETcc-CSIC, Spain, 2007.
- [29] Rhead G. *Surf. Sci.* 15, 1969.
- [30] Rhead G. y Perdureau J., *C.R. Acad. Sc. Paris*, t260, Groupe 7, 1965.
- [31] Oda O., Rhead G. E. *Scripta Metall.*, 13, 985, 1979.
- [32] ABAQUS 6.5.3 Student Edition, 2005.
- [33] COMSOL Multiphysics 3.2, 2006.
- [34] Toribio J. “Relationship between microstructure and strength in eutectoid steels” *Materials Science and Engineering A* 387-389, pp. 227-230, 2004.
- [35] Gjostein N.A. “Surfaces and Interfaces 1”, Chap. 11, p. 271.
- [36] Kubo K., Hirai N., Hara S. “Decay of nano-islands on Au(1 0 0) electrode in sulfuric acid solution with Cl₋ anions” *Applied Surface Science* 237, pp. 301–305, 2004.
- [37] González Velasco J. “A study at the molecular level of the mechanism of surface diffusion at electrode-electrolyte interfaces” *Chemical Physics Letters* 313, pp. 7-13, 1999.
- [38] González Velasco J. “A theoretical explanation of the surface diffusion mechanism in metal electrodes in contact with electrolytes” *Surface Science* 410, pp. 283-289, 1998.
- [39] Shu D. J., Liu F., Gong X. G. “Simple generic method for predicting the effect of strain on surface diffusion” *Physical Review B*, Vol. 64, 2001.
- [40] Schroeder M., Wolf D. E. “Diffusion on strained surfaces” *Surface Science* 375, pp. 129-140, 1997.
- [41] Wang Y. X., Pan Z. Y., Li Z. J., Wei Q., Zang L. K., Zhang Z. X. “Effect of tensile strain on adatom diffusion on Cu(111) surface” *Surface Science* 545, pp. 137-142, 2003.
- [42] Li D., Gangloff R. P., Scully J. R. “Hydrogen trap states in ultrahigh-strength AERMET 100 steel” *Metallurgical and Materials Transactions*, Vol. 35A, pp. 849-864, 2004.
- [43] Callister W. D. “Introducción a la Ciencia e Ingeniería de los Materiales” *Ed.Reverté SA, Barcelona* 1995.

MOLECULAR DYNAMICS SIMULATIONS OF HYDROGEN EMBRITTLEMENT: PRELIMINARY RESULTS.

Javier Sanchez¹, Pedro de Andres², Carmen Andrade¹, José Fullea¹

¹ Instituto de Ciencias de la Construcción Eduardo Torroja (CSIC). C/ Serrano Galvache, 4.
28033 Madrid, España.

E-mail: javiersm@ietcc.csic.es, andrade@ietcc.csic.es, fullea@ietcc.csic.es

² Instituto de Ciencias de Materiales de Madrid (CSIC).

E-28049 Cantoblanco, Madrid, España.

E-mail: pedrodeandres@icmm.csic.es

ABSTRACT

Hydrogen embrittlement is believed to be one of the main reasons for cracking of structures under stress. High strength steels in these structures often include a ferritic core made of alpha-iron (body centered cubic lattice).

Previous work [1] was concerned with the interaction of atomic hydrogen with iron using first principles calculations. We studied the effect of interstitial hydrogen in the iron lattice and the stress induced by the interstitial hydrogen in the host lattice.

In this paper we study the dynamical behaviour of hydrogen inside the iron lattice. Using ab-initio Molecular Dynamics we obtain hydrogen diffusion paths and by taking statistical averages we extract diffusion coefficients from Einstein's equation. Depending on temperature, the diffusion path involve going through tetrahedral or octahedral sites. Simulations where a number of hydrogens occasionally coincide in one unit cell have been performed to elucidate the effect of interactions between hydrogens. .

KEY WORDS: Hydrogen Embrittlement, Molecular Dynamics, alpha-iron.

1. INTRODUCTION

Los aceros de alta resistencia empleados en estructuras civiles o estructuras singulares se componen de una matriz ferrítica, o lo que es lo mismo de una estructura de hierro cúbica centrada en el cuerpo (BCC). Uno de los más empleados a nivel mundial es el acero trefilado de composición eutectoide. Diversos estudios muestran el crecimiento de fisuras para valores de tensión inferiores a su correspondiente tenacidad de fractura bajo la acción de un medio agresivo. Este fenómeno, conocido como Corrosión Bajo Tensión (CBT), es uno de los problemas que afectan a estos aceros.

Existe un convencimiento general de que el hidrógeno juega un papel importante en este proceso, de hecho se supone que la fragilización por hidrógeno es una de las causas más frecuentes de fallo en estructuras sometidas a esfuerzos mecánicos [1]. Teniendo en cuenta esta hipótesis se desarrolló un ensayo basado en una disolución de tiocianato amónico para determinar la susceptibilidad de los aceros de alta resistencia a la Fragilización por Hidrógeno. Este ensayo se denominó FIP-78, y fue propuesto por la Federación Internacional de Pretensado.

Existe evidencia de la variación de parámetros mecánicos [2], pero la fragilización por hidrógeno no está completamente explicada desde un punto de vista teórico. En este sentido, varios modelos tratan de explicar la propagación de la fisura por la presencia en el metal de átomos de hidrógeno. Generalmente se asume que el hidrógeno se genera electroquímicamente en la superficie del material y difunde hasta la zona en proceso de fractura. Para explicar el proceso por el cual el hidrógeno fragiliza el material existen varias teorías:

- Cambio estructural o de fase producido por el hidrógeno [3, 4, 5].
- Plastificación producida por el Hidrógeno o hydrogen-enhanced localized plasticity (HELP) [6, 7].
- Reducción de la energía cohesiva por el efecto del hidrógeno [8, 9, 10].

Para entender mejor estas teorías, hemos realizado cálculos atómicos de primeros principios [11] con el objetivo de determinar la posición preferente del hidrógeno intersticial y las tensiones que genera en la red bcc del hierro en función de la densidad de hidrógeno en la red de hierro. Dado que estos cálculos son computacionalmente muy costosos cuando incluyen muchos átomos en la celda unidad, hemos extendido estos resultados por medio de cálculos de Elementos

Finitos.

En este trabajo se presentan los resultados preliminares obtenidos a través de cálculos de Dinámica Molecular Ab-Initio. Esta técnica es complementaria a los resultados obtenidos anteriormente y permite observar los procesos dinámicos que tienen lugar dentro de la red de Fe con diferentes concentraciones de H.

2. METODOLOGÍA

Los cálculos de Dinámica Molecular Ab-Initio se han llevado a cabo con el programa CASTEP [12,13]. Se han realizado en una supercelda 2x2x2 incluyendo 16 átomos de Fe y en la cual se han introducido diferente número de átomos de H según el caso. De esta forma es posible estudiar el efecto de la concentración de H. Se ha considerado la aproximación de Born-Oppenheimer que aplica los principios de la mecánica clásica a los iones, los cuales son objetos que se mueven en potencial creado por los electrones, que se tratan como objetos cuánticos y obedecen a la ecuación de Schroedinger. Las funciones de onda de Kohn-Sham se han desarrollado en una base de ondas planas. La precisión de los cálculos viene determinada básicamente por dos parámetros: (i) la máxima energía de corte (“cut-off”) que en este caso es de 375eV y (ii) el número de puntos usados en la zona de Brillouin para muestrear las funciones de onda en espacio recíproco (“puntos k”), que en este caso se ha considerando una malla 4x4x4 tipo Monkhorst-Pack [MP]. Se han utilizado pseudopotenciales ultra-suaves [14] y la aproximación de gradientes generalizados de Perdew, Burkeand Ernzerhof [15].

En el estudio de la difusión de H dentro de la red de Fe hemos realizado simulaciones previas en el conjunto micro-canónico (la energía total es una constante del movimiento y el volumen de la celda es constante). Se han realizado simulaciones de 1-2ps con pasos de tiempo de 0.5-1.0fs, en los cuales la energía total se conserva con un error de 0.01%. De los cálculos se han excluido los resultados de los primeros 100-200fs en los cuales el sistema se está equilibrando.

Los coeficientes de difusión se han calculado asumiendo que los átomos intersticiales de H se mueven de forma aleatoria (random-walk). Se han trazado las trayectorias de los átomos de H durante el tiempo de la simulación y se han calculado los desplazamientos para obtener el coeficiente de difusión (D) de acuerdo a la ecuación de Einstein en tres dimensiones:

$$\langle |r(t) - r(0)|^2 \rangle = 6Dt. \tag{1}$$

donde: r es la posición del átomo y t es el tiempo.

Las barreras de difusión se han obtenido a través de la ecuación de Arrhenius:

$$D = D_0 \cdot \exp[-E_a/k_B \cdot T] \tag{2}$$

donde D₀ es el factor pre-exponencial, E_a es la energía de activación o barrera de difusión, k_B es la constante de

Boltzmann y T es la temperatura absoluta.

3. RESULTADOS

A continuación se presentan los resultados obtenidos de los cálculos de Dinámica Molecular para diferentes concentraciones de H. En primer lugar se muestran los resultados obtenidos para el caso de 1 átomo de H en la supercelda 2x2x2 de Fe, es decir, una relación H/Fe=1/16. En la Figura 1 se muestra la trayectoria del H dentro de la red de Fe para una temperatura de 300K. Para esta concentración y esta temperatura el camino de difusión del H es a través de los huecos tetraédricos, evitando los huecos octaédricos.

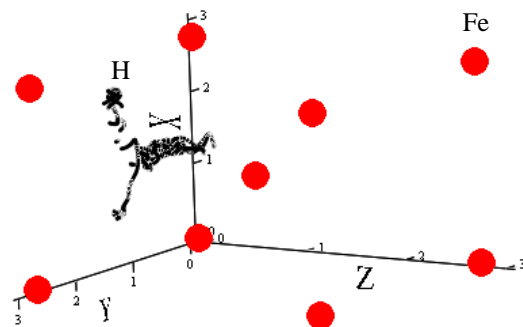


Figura 1. Trayectoria del H (puntos negros) dentro de la red de Fe (círculo rojo). T=300K.

En la Figura 2 se muestra el camino recorrido por el H a lo largo del tiempo. A través de la ecuación de Einstein (ecuación 2) es posible estimar el coeficiente de difusión para el H.

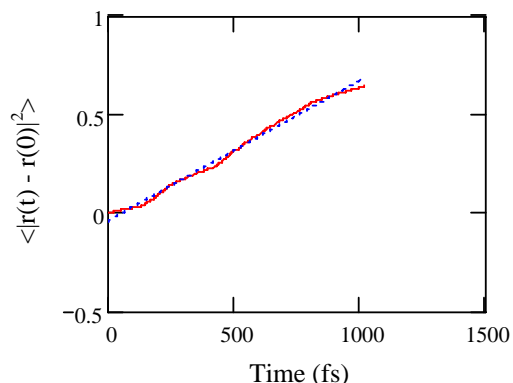


Figure 2. Random-walk para un H a 300K.

En la Figura 3 se muestra la trayectoria del H dentro de la red de Fe para una temperatura de 700K. Al aumentar la temperatura aumenta la movilidad del átomo de H de acuerdo con la ley de Boltzmann (Eq. 2). Al mismo tiempo, cambia el camino de difusión: a 300 K el átomo de H reside aproximadamente un 0.65% del tiempo cerca del hueco octaédrico, mientras que a 700 K permanece algo más del 6%. Este efecto se puede entender fácilmente calculando la función de partición de un sistema con dos niveles y al igual que el aumento de movilidad solo depende de la relación entre la

energía cinética, kT , y la diferencia de energía entre los dos sitios (o la barrera en el caso de la difusión).

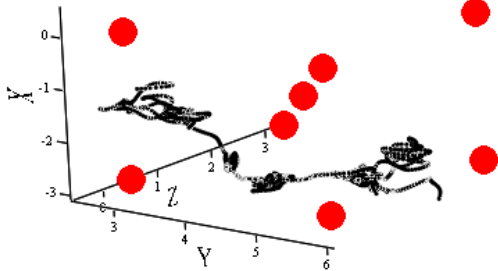


Figure 3. Trayectoria del H (puntos negros) dentro de la red de Fe (circulo rojo). $T=700K$.

En la Figura 4 se muestra el camino recorrido por el H a lo largo del tiempo a 700 K. Los cálculos indican un incremento del coeficiente de difusión desde $5.6 \cdot 10^{-9} \text{ m}^2/\text{s}$ a 300K hasta $2.3 \cdot 10^{-7} \text{ m}^2/\text{s}$ a 700K.

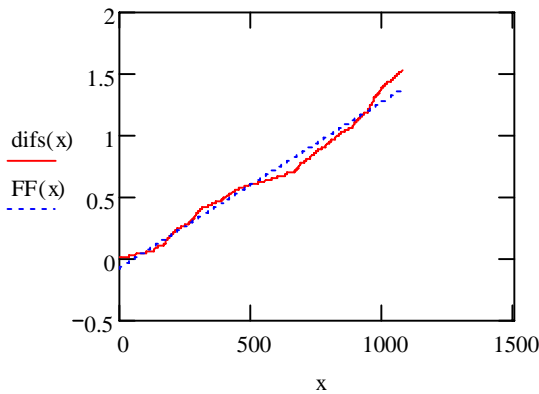


Figure 4. Random-walk para un H a 700K.

En la Figura 5 se han representado los coeficientes de difusión obtenidos de los cálculos de Dinámica Molecular para diferentes temperaturas y una concentración $H/Fe=1/16$. Teniendo en cuenta la ecuación de Arrhenius (ecuación 2) es posible obtener la Energía de Activación (E_a) correspondiente a la difusión del H dentro de la red de Fe. En este caso (baja concentración de H) se obtiene una $E_a= 145 \text{ meV}$. Esta energía de activación está próxima a la calculada por Primeros Principios en trabajos anteriores [11,16].

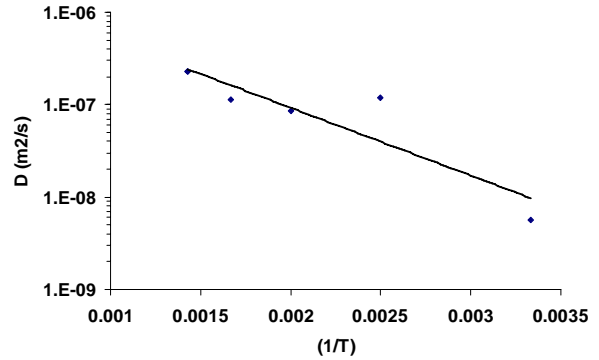


Figure 5. Arrhenius plot. $E_a= 145\text{meV}$

Hasta ahora se ha estudiado el efecto de la temperatura sobre la difusión del H en la red de Fe. La segunda variable de interés es la concentración de H dentro de la red de Fe. Se han repetido los cálculos para diferentes concentraciones: $H/Fe = 2/16, 4/16$ y $8/16$, y para diferentes temperaturas: $T = 300, 400, 500, 600$ y $700K$.

En la Figura 6 se muestran los coeficientes de difusión para el caso de una concentración de $H/Fe = 8/16$. En este caso, para cada cálculo de Dinámica Molecular se obtienen 8 valores del coeficiente de difusión, uno por cada átomo de H: los resultados presentados corresponden al promedio de todos ellos. De acuerdo con la ecuación de Arrhenius (ecuación 2) el valor de la E_a obtenido es de 47 meV , concluyendo que la barrera de difusión es afectada por el número de intersticiales difundiendo simultáneamente.

En nuestro trabajo previo hemos concluido que la estabilidad de los sitios de alta simetría puede depender de la densidad de H y las restricciones de simetría que se utilicen como condiciones de contorno [11,16]. Para baja concentración de H el sitio mas estable es el tetraédrico mientras que para una concentración de $1/2$ el hueco octaédrico se convierte en mas estable y se favorece una distorsión tetragonal de la simetría cúbica. Este aspecto se ha confirmado con los cálculos de Dinámica Molecular, donde se observan dos hechos relevantes: (i) se produce un cambio en el camino de difusión para baja concentración de H (de tetraédrico a tetraédrico), a un camino de difusión para alta concentración de H que va de octaédrico a octaédrico pasando por el tetraédrico. En segundo lugar, (ii) se produce una disminución de la barrera de difusión (E_a) o, lo que es lo mismo, se produce un aumento del coeficiente de difusión.

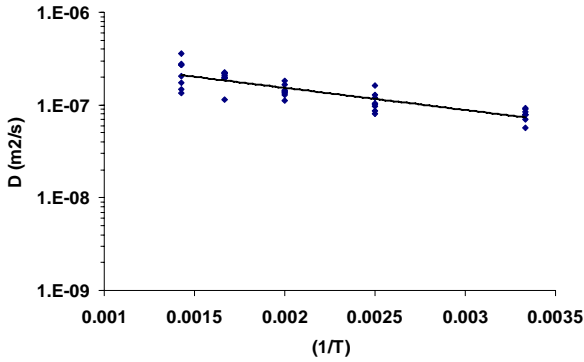


Figure 6. Arrhenius plot. $E=47\text{meV}$

En la Figura 7 se muestra cómo aumenta la ocupación de los huecos octaédricos al aumentar la concentración de H. En este caso se muestran los resultados correspondientes a una temperatura de 500K. El efecto de la concentración de H sobre la ocupación de los huecos octaédricos es superior al efecto de la temperatura porque la variación en la diferencia de energía de los dos sitios de simetría es más importante que la variación de energía térmica al pasar de 300 a 700 K.

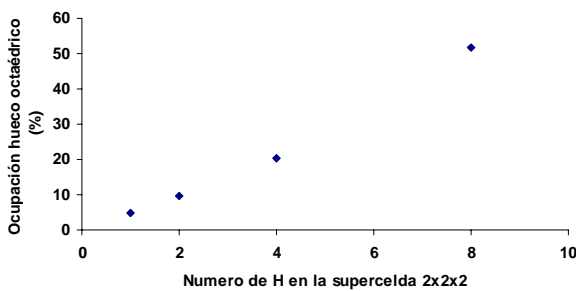


Figure 7. Ocupación de los huecos octaédricos frente a la concentración de H para $T=500\text{K}$.

3.1. Comportamiento de los átomos de Fe.

Otro aspecto a analizar es el comportamiento de los átomos de Fe en presencia de H. Los átomos de Fe se mueven alrededor de su posición de equilibrio. El desplazamiento cuadrático medio $\langle u^2 \rangle$ de los átomos de Fe se puede calcular en un modelo isotrópico de Debye en función de un único parámetro ajustable, la temperatura de Debye (Θ),

$$\langle u^2 \rangle = \frac{3\hbar^2}{4k_B M \Theta} \left(\frac{T}{\Theta} \int_0^{\frac{\Theta}{T}} \frac{x dx}{e^x - 1} + \frac{1}{4} \right) \quad (3)$$

En la Figura 8 se muestra un ejemplo del desplazamiento de un átomo de Fe alrededor de su posición de equilibrio durante un cálculo de Dinámica Molecular.

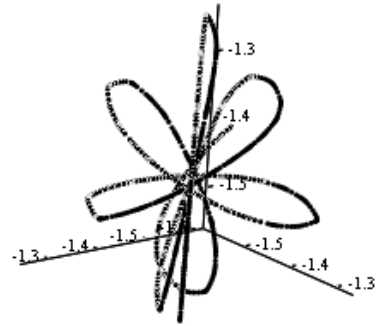


Figure 8. Vibración del átomo de Fe alrededor de su posición de equilibrio.

En la Figura 9 se muestra la distribución de desplazamientos ajustada a una distribución normal centrada en la posición de equilibrio y cuya varianza coincide con el desplazamiento cuadrático medio ($\sigma^2 \sim \langle u^2 \rangle$). Como para el caso del coeficiente de difusión, se ha estudiado la influencia de la concentración de H sobre el comportamiento del Fe, ya que el comportamiento frente a la temperatura viene definido por el modelo de Debye-Waller (ecuación 3). Como se puede observar en la Figura 10, el desplazamiento cuadrático medio de los átomos de Fe respecto a su posición de equilibrio aumenta de forma considerable al aumentar la concentración de H intersticial. En este caso se muestran los resultados obtenidos a 700K, pero este comportamiento se repite en todo el rango de temperaturas estudiado. El aumento del desplazamiento $\langle u^2 \rangle$ de los átomos de Fe indica el debilitamiento del enlace de los mismos por la presencia del H. Esto está de acuerdo con los diversos resultados experimentales existentes en la literatura sobre la Fagilización por Hidrógeno y ensayos de Corrosión Bajo Tensión [17-28], donde el efecto del H se manifiesta con la reducción del tiempo de rotura y la reducción de propiedades mecánicas, como por ejemplo la tenacidad de fractura.

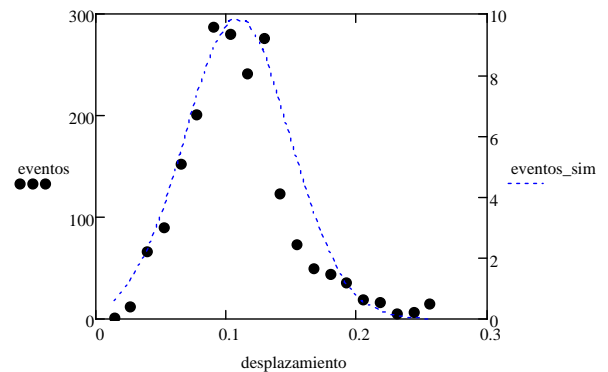


Figure 9. Desplazamiento de los átomos de Fe respecto su posición de equilibrio.

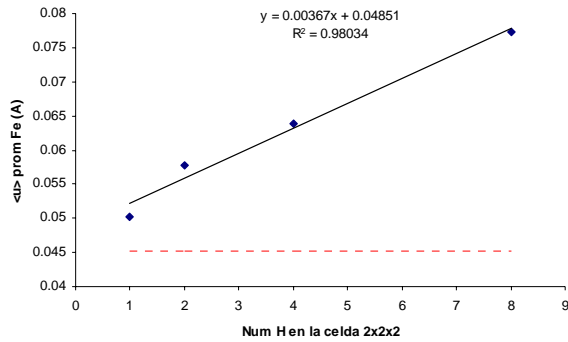


Figure 10. Desplazamiento promedio de los átomos de Fe en función de la concentración de H para $T=700\text{K}$.

4. CONCLUSIONES

i. El proceso de difusión del H depende de la temperatura de una forma estándar a través de un factor de Boltzmann, pero también de la concentración de H intersticial.

ii. El aumento de la concentración de H produce un cambio en el camino de difusión: para bajas concentraciones el H difunde a través de huecos tetraédricos contiguos, mientras que para alta concentración de H la difusión se produce a través de huecos octaédricos pasando por el tetraédrico que queda entre ellos.

iii. El aumento de la concentración de H produce la disminución de la barrera de difusión, o lo que es lo mismo, produce el aumento del coeficiente de difusión.

iv. La presencia de los átomos de H dentro de la red de Fe producen un debilitamiento del enlace, lo cual puede llegar a modificar la resistencia mecánica de los aceros de alta resistencia.

Estos resultados obtenidos con los cálculos de Dinámica Molecular permiten entender mejor los resultados experimentales disponibles.

ACKNOWLEDGEMENTS

This work has been financed by the Spanish CICYT (MAT2008-1497), and MEC (CONSOLIDERS CSD2007-41 "NANOSELECT" and "SEDUREC").

REFERENCES

[1] M. Elices "Influence of residual stresses in the performance of cold-drawn pearlitic wires" Journal of Materials Science, Volume 39, Number 12, 2004, pp. 3889 – 3899.

[2] Y. Liang, P. Sofronis and N. Aravas "On the effect of hydrogen on plastic instabilities in metals" Acta

Materialia 51 (2003), pp. 2717–2730.

[3] DG Westlake - Trans. Metall. Soc. AIME, 1969.

[4] Nelson H.G. "Film-rupture model of hydrogen-induced, slow crack growth in acicular alpha-beta titanium" Metall. Trans. A - Phys. Metall. Mater. Sci. 7A (5), pp. 621–627, 1976.

[5] Oriani R.A. "Hydrogen Effects in High-strength Steels" In: Gangloff, R.P., Ives, M.B. (Eds.), First International Conference on Environment-induced Cracking of Metals, NACE-10. NACE, Houston, TX, pp. 439–447, 1990.

[6] Beachem, C.D., 1972. "A new model for hydrogen-assisted cracking (hydrogen embrittlement)". Met. Trans. 3, 437–451.

[7] Birnbaum, H.K., Sofronis, P. "Hydrogen-enhanced localized plasticity – a mechanism for hydrogen related fracture". Mater. Sci. & Eng. A 176, 191–202., 1994.

[8] Troiano A R 1960 Trans. ASM 52 54.

[9] Oriani R.A. "Mechanistic theory of hydrogen embrittlement of steels. Ber. Bunsenges" Phys. Chem. 76 (8), pp. 848–857, 1972.

[10] Oriani, RA; Josephic, PH, "Equilibrium and kinetic studies of the hydrogen-assisted cracking of steel" Acta Metall. 1977. pp. 979-988.

[11] J. Sanchez, J. Fulla, C. Andrade, and P. de Andres, Phys. Rev. B 78, 014113 (2008).

[12] S. Clark, M. D. Segall, C. Pickard, P. Hasnip, M. J. Probert, K. Refson, and M. C. Payne, Z. fuer Kristallographie 220, 567 (2005).

[13] (CASTEP 4.4); <http://www.accelrys.com>.

[14] D. Vanderbilt, Phys. Rev. B 41, 7892, 1990.

[15] J. P. Perdew, K. Burke, and M. Ernzerhof, Phys. Rev. Lett. 77, 3865 (1996).

[16] J. Sánchez, P. de Andrés, J. Fulla, C. Andrade. "Aproximación por simulación ab-initio a la fragilización por hidrógeno en una red de hierro bcc". Anales de Mecánica de la Fractura, Vol. 24, 387-392, 2007.

[17] Toribio J., Elices M. "Nuevas Aportaciones al Ensayo FIP de Fragilización por Hidrógeno en Tiocianato Amónico" Hormigón y acero, Vol. 27 (168), pp. 121-130, 1988.

[18] Pakins R. N., Zhou S. "The Stress Corrosion Cracking of C-Mn Steel in $\text{CO}_2\text{-HCO}_3^-$ - CO_3^{2-} Solutions I: Stress Corrosion Data" Corr. Sci., Vol.

39, Nº 1, pp. 159-173, 1997.

- [19] Caballero L., Elices M. "Influencia de la velocidad de deformación en la propagación de fisuras por corrosión bajo tensión." *Revista Iberoamericana de Corrosión y Protección*, 17 (1), pp. 15-22, 1986.
- [20] Caballero L., Elices M. "Un método para la medida de la cinética de las fisuras de corrosión bajo tensión en ensayos a velocidad de deformación constante." *Revista Iberoamericana de Corrosión y Protección*, 17 (1), pp. 43-48, 1986.
- [21] Acha-Hurtado M. "Corrosión Bajo Tensión de Alambres de Acero Pretensado en Medios Neutros con HCO_3^- y Alcalinos con SO_4^{2-} ." Instituto de Ciencias de la Construcción "Eduardo Torroja" C.S.I.C. Madrid, 1993. PhD Thesis.
- [22] Alonso M. C., Andrade C., Procter R. P. M., Saenz de Santa María M. "Susceptibilidad a la Corrosión Bajo Tensión del Acero Pretensado en Disoluciones de NaHCO_3 " *Hormigón y Acero*, Nº 166, pp. 121-126, 1988.
- [23] Lancha A. M. "Influencia del Trefilado en la Corrosión Bajo Tensión de Aceros Eutectoides" Universidad Complutense de Madrid. Facultad de Ciencias Químicas. 1987.
- [24] Valiente A., Elices M. "Premature Failure of Prestressed Steel Bars" *Engineering Failure Analysis*, Vol. 5, nº 3, pp. 219-227, 1998.
- [25] Sanchez J., Fullea J., Andrade C., Alonso C. "Stress corrosion cracking mechanism of prestressing steels in bicarbonate solutions" *Corr. Sci.* 49(11), 4069-4080, 2007.
- [26] Sanchez J., Fullea J., Andrade C. "Fracture toughness variation induced by stress corrosion cracking of prestressing steels" *Materials and Corrosion*, 59(2), 2008.
- [27] Sanchez J., Fullea J., Andrade C. "Reasons for Crack Arrest in Stress Corrosion Cracking Tests. Crack Propagation Rate in High Strength Steels" *Corrosion*, 65(6), 2009.
- [28] Sanchez J., PhD, Thesis. Eduardo Torroja Institute, IETcc-CSIC, Spain, 2007.

DEFECTOS DISCRETOS EN GRAFENO

R. Serrano¹, M.P. Ariza² and M. Ortiz³¹Instituto Andaluz de Tecnología, Leonardo da Vinci, 2, 41092 Sevilla, Spain.²Escuela Superior de Ingenieros, Universidad de Sevilla, Camino de los descubrimientos S.N., 41092 Sevilla, Spain.³ Graduate Aeronautical Laboratories, California Institute of Technology, 1200 E. California Blvd. Pasadena, 91125 CA, USA.

RESUMEN

El presente artículo describe el estudio de defectos en grafeno basado en la elasticidad de cristales discretos. Se ha desarrollado una mecánica de redes discretas utilizando conceptos del cálculo discreto diferencial y el álgebra topológica. La noción de redes complejas ofrece una potente herramienta para manipular formas y campos definidos en el cristal. En la aproximación armónica, la energía es una forma cuadrática del campo de desplazamientos y de las autodeformaciones. Dentro de esta teoría las dislocaciones se tratan como estructuras que minimizan la energía y que llevan a invariantes de red locales, al tiempo que a autodeformaciones globalmente incompatibles. La naturaleza inherentemente discreta de este enfoque elimina la necesidad de regularizar el núcleo de la dislocación. Los defectos estudiados se han simulado también mediante el programa de dinámica molecular LAMMPS para validar el comportamiento predicho por la mecánica de la teoría de redes discretas.

También se discute la incorporación de potenciales empíricos en la teoría discreta y se obtienen constantes de fuerza para el caso particular del modelo dinámico propuesto por Aizawa *et al.* que más tarde hemos utilizado en nuestras simulaciones. El modelo fue validado mediante la comparación de curvas de dispersión de fonones con datos experimentales disponibles.

ABSTRACT

The present article describes the study of several defects in graphene based on discrete crystal elasticity. A mechanics of discrete lattices is built using ideas from discrete differential calculus and algebraic topology. The notion of lattice complexes provides a powerful means of manipulating forms and fields defined over the crystal. In the harmonic approximation, the energy is a quadratic form in the displacement field and the eigendeformations. Dislocations are treated within this theory as energy minimizing structures that lead to locally lattice-invariant but globally incompatible eigendeformations. The inherently discrete nature of this approach eliminates the need for regularization of the dislocation core. The studied defects have been also simulated using the LAMMPS molecular dynamics code for validation of the behaviour predicted by the mechanics of discrete lattices theory.

We also discuss the incorporation of empirical potentials in the discrete approach and obtain force-constants for the particular case of the dynamical model by Aizawa *et al.* which we use subsequently in our computations. The model is validated through phonon dispersion curves comparison with available experimental data.

PALABRAS CLAVE: nanomecánica, dinámica de dislocaciones, grafeno.

1. INTRODUCCIÓN

El grafeno es una lámina monoatómica de átomos de carbono dispuestos en una red hexagonal, la cual ha sido observada en forma estable sobre diferentes sustratos [1] o de manera aislada [2]. Recientemente, debido a su anómalo comportamiento electrónico y sus singulares características mecánicas, el grafeno está siendo considerado como un prometedor material

semiconductor con numerosas aplicaciones potenciales, que van desde su uso en sensores químicos a nanomecanismos, pasando por pantallas flexibles, o biosensores. Sin embargo, el grafeno observado en laboratorio contiene ciertos defectos, los cuales además pueden introducirse de manera artificial por irradiación de haz de electrones [3], átomos añadidos [4,5], mono y multivacantes [6,5,7], entre otras formas. La presencia de defectos modifica sus propiedades

mecánicas y químicas y juega un importante papel en las aplicaciones. Este efecto motiva la necesidad de comprender los mecanismos fundamentales de equilibrio y las propiedades cinéticas de los defectos en el grafeno.

Uno de los defectos más estudiados en el grafeno y en nanotubos de carbono monocapa consiste en dos pares de anillos pentágono-heptágonos (5-7) que se obtienen al rotar un enlace atómico sencillo 90° (defecto SW). Existe un amplio consenso al afirmar que el mecanismo SW constituye un proceso unitario subyacente a una gran variedad de transformaciones estructurales en materiales basados en carbono [e.g., 8]. En [3] se observaron pares 5-7 unidos a una cadena de vacantes de átomos en zig-zag dando lugar a un dipolo de dislocación. Por otra parte, [7] ha estudiado la estabilidad de los dipolos de dislocaciones con la estructura de núcleo 5-7 usando una teoría de funcional de densidad. Sus cálculos muestran que los dipolos 5-7 son energéticamente más estables que una estructura *haeckelítica* compuesta por tres pares 5-7. Los pares 5-7 se han observados formando estructuras de defectos más complejas. Más recientemente, [9] ha observado configuraciones con defectos y su dinámica en tiempo real y ha concluido que la dinámica de los defectos en láminas bidimensionales de grafeno es diferente de las que se encuentran en estructuras cerradas como nanotubos o fullerenos.

Adicionalmente a cálculos basados en primeros principios, se han utilizado habitualmente potenciales interatómicos para modelar estructuras de carbono [10,11,12,13,14,15,16,17,18]. Los potenciales más simples son armónicos y se definen en términos de constantes de fuerza. Así, [16] desarrolló modelos de constantes de fuerza que consideraban los seis vecinos más cercanos. Una nueva parametrización de [16] se halla en [10] gracias a la teoría de funcional de densidad haciendo uso de la aproximación de gradiente generalizado.

En este trabajo se presenta una aplicación de la teoría de dislocaciones discretas de [19] al análisis de dislocaciones en grafeno. La teoría supera las limitaciones propias de los modelos atómicos convencionales, dotando a las redes cristalinas de estructuras diferenciales discretas que generalizan los operadores diferenciales comunes y las identidades integrales del cálculo diferencial. Se formula una teoría discreta de defectos recurriendo a la teoría de autodeformaciones, que nos permite caracterizar de forma precisa y clara defectos topológicos que incluyen dislocaciones. El marco geométrico discreto que resulta, permite la formulación de los mecanismos de redes de una manera paralela a las teorías clásicas para medios continuos. Además, podemos plantear un problema de equilibrio que tiene solución exacta y aplicar herramientas analíticas, tales como análisis asintóticos y de convergencia- Γ .

En este artículo se expone cómo la teoría de dislocaciones discreta predice estructuras con núcleos de anillos 5-7 y energías de formación que son consistentes con lo observado, dentro del rango de precisión de las capacidades de la teoría.

2. COMPLEJO DE RED DEL GRAFENO

Según [19] podemos considerar la red de grafeno como una celda compleja, i.e., como un conjunto de átomos interconectados (0-celdas, e_0), enlaces atómicos (1-celdas, e_1) y áreas elementales (2-celdas, e_2). Haciendo uso del esquema de complejo simplicial (ver Figura 1) en el que se especifica la convención de orientaciones entre las celdas, escribimos las reglas que determinan los operadores frontera y co-frontera. Como puede verse, la red de grafeno tiene dos tipos de 0-celdas, tres tipos de 1-celdas y un tipo de 2-celda. Así, cada clase de equivalencia tiene la estructura de una red de Bravais simple y sus miembros pueden ser nombrados identificados en términos de un par de coordenadas enteras $l \equiv (l^1, l^2) \in \mathbb{Z}^2$. La red es generada con los vectores básicos $a_1 = (3/2, -(\sqrt{3})/2)$ y $a_2 = (3/2, (\sqrt{3})/2)$. Al referirnos a una celda específica por esta convención, designamos $e_p(l, \alpha)$ a la p -celda de tipo α y coordenadas enteras $l \in \mathbb{Z}^2$, siendo p la dimensión de la celda.

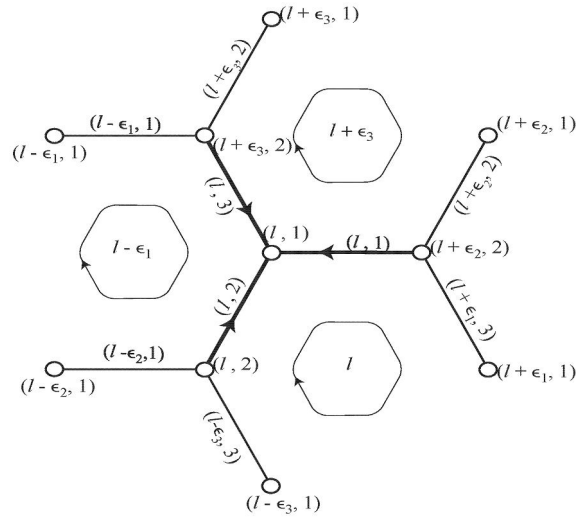


Figura 1. Complejo simplicial del grafeno, con $l \equiv (l^1, l^2) \in \mathbb{Z}^2$, donde $\epsilon_1 = (1, 0)$, $\epsilon_2 = (0, 1)$ y $\epsilon_3 = (-1, 1)$.

A modo de ejemplo, el operador de contorno ∂e_2 se calcula según (1)

$$\partial e_2(l) = -e_1(l,1) - e_1(l + \epsilon_1,3) + e_1(l + \epsilon_1,2) + e_1(l - \epsilon_3,1) - e_1(l - \epsilon_3,3) + e_1(l,2) \quad (1)$$

A partir de las reglas se deducen las representaciones de la transformada discreta de Fourier (DFT) de la estructura diferencial del complejo (ecuaciones 2 a 5),

$$Q_1 = \begin{pmatrix} 1 & 1 & 1 \\ -e^{-i\theta_2} & -1 & -e^{i(\theta_1-\theta_2)} \end{pmatrix} \quad (2)$$

$$Q_2 = \begin{pmatrix} -1 + e^{i(\theta_2-\theta_1)} \\ 1 - e^{-i\theta_1} \\ e^{-i\theta_1} - e^{i(\theta_2-\theta_1)} \end{pmatrix} \quad (3)$$

$$P_1 = \begin{pmatrix} 1 & -e^{-i\theta_2} \\ 1 & -1 \\ 1 & -e^{i(\theta_1-\theta_2)} \end{pmatrix} \quad (4)$$

$$P_2 = \begin{pmatrix} -1 + e^{i(\theta_1-\theta_2)} & 1 - e^{i\theta_1} & e^{i\theta_1} - e^{i(\theta_1-\theta_2)} \end{pmatrix} \quad (5)$$

3. TEORÍA DE AUTODEFORMACIONES DE DISLOCACIONES EN REDES DISCRETAS

Siguiendo a [19] por invariancia de traslaciones se tiene que la energía de una red armónica puede ser expresada según:

$$E(u) = \frac{1}{2} \sum_{e_1 \in E_1} \sum_{e'_1 \in E_1} B_{ij}(e_1, e'_1) du_i(e_1) du_j(e'_1) \quad (6)$$

donde $B_{ij}(e_1, e'_1)$ es la matriz de constantes de fuerza entre aristas relativa a la energía de interacción resultante de un desplazamiento diferencial unidad en la dirección j -ésima en la arista e_1 y un desplazamiento diferencial unidad en la dirección i -ésima en la arista e_1 , o de manera equivalente:

$$E(u) = \frac{1}{2} \langle Bdu, du \rangle \quad (7)$$

La principal diferencia entre la representación discreta diferencial de la energía de una red armónica y la representación convencional de constantes de fuerza es que la primera aprovecha la invariancia de la energía frente a traslaciones para poder expresarla en términos de constantes de fuerza entre aristas y el diferencial du del campo de desplazamientos. Desde el punto de vista de las autodeformaciones, la energía de una red con defectos en su seno se toma:

$$E(u, \beta) = \frac{1}{2} \langle B(du - \beta), (du - \beta) \rangle \quad (8)$$

o de manera equivalente:

$$E(\alpha) = \frac{1}{2} \langle B\delta\Delta^{-1}\alpha, \delta\Delta^{-1}\alpha \rangle \quad (9)$$

$$-\frac{1}{2} \langle A^{-1}\delta B\delta\Delta^{-1}\alpha, \delta B\delta\Delta^{-1}\alpha \rangle$$

$$\equiv \frac{1}{2} \langle \Gamma * \alpha, \alpha \rangle$$

donde $\alpha=d\beta$ es la densidad discreta de dislocaciones, Δ es el Laplaciano discreto de la red, A es la matriz de constantes de fuerza interatómicas, dada por la identidad $\langle Bdu, du \rangle = \langle Au, u \rangle$, y $\Gamma(l)$ es el doble de la energía de interacción entre una dislocación unidad en el origen $e_2(0)$ y otra dislocación unidad en $e_2(l)$, mientras que * denota la convolución discreta.

4. CONSTANTES DE FUERZA

3.1. Expresión general de las matrices de constantes de fuerza

La red de grafeno pertenece al grupo de simetría D_{6h} , que es generado por $\{C_3, \sigma_v, \sigma_z\}$, siendo C_3 las rotaciones de 120° alrededor del eje z , σ_v la reflexión en el plano xz , y σ_z la reflexión en el plano xz ([20, 21, 22]).

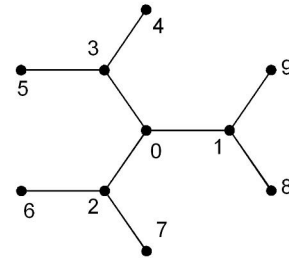


Figura 2. Numeración de primeros y segundos vecinos.

Aplicando estas propiedades se deducen las expresiones generales de las matrices de constantes de fuerzas para primeros y segundos vecinos. Por ejemplo, para el primer vecino “1” y el segundo vecino “4” según la numeración de la Figura 2, se obtiene las ecuaciones 10, 11. El resto de matrices se obtienen girando convenientemente ϕ_{01} ó ϕ_{04} , según corresponda.

$$\phi_{01} = \begin{pmatrix} a & 0 & 0 \\ 0 & b & 0 \\ 0 & 0 & c \end{pmatrix} \quad (10)$$

$$\phi_{04} = \begin{pmatrix} d & f & 0 \\ -f & e & 0 \\ 0 & 0 & g \end{pmatrix} \quad (11)$$

3.2. Constantes de fuerza a partir de potenciales empíricos

El potencial de [16] consiste en seis términos de energía:

$$E(u) = V_1 + V_2 + V_3 + V_4 + V_5 + V_6 \quad (12)$$

donde V_1 y V_2 tienen en cuenta la interacción entre primeros y segundos vecinos respectivamente, V_3 la flexión en el plano, V_4 idem fuera del plano, V_5 la torsión y V_6 la interacción con el sustrato. Operando con cada uno de estos términos es posible expresarlos en términos de diferencias de desplazamientos entre átomos, lo que permite calcular las matrices de constantes de fuerza que se han usado en los cálculos posteriores. Por ejemplo, para los átomos 1 y 4 según la numeración de la Figura 2 se obtiene:

$$\Phi^{01} = \begin{pmatrix} -\alpha_1 & 0 & 0 \\ 0 & -\frac{6\gamma_1}{d^2} & 0 \\ 0 & 0 & -\frac{3\gamma_2}{d^2} \end{pmatrix} \quad (13)$$

$$\Phi^{04} = \begin{pmatrix} \frac{3\gamma_1}{4d^2} & -\frac{\sqrt{3}\gamma_1}{4d^2} & 0 \\ \frac{\sqrt{3}\gamma_1}{4d^2} & -\frac{4d^2\alpha_2 + \gamma_1}{4d^2} & 0 \\ 0 & 0 & -\frac{\delta}{3d^2} \end{pmatrix} \quad (14)$$

El resto de matrices de constantes de fuerza se obtiene sin más que aplicar los giros y reflexiones $\{C_3, \sigma_v, \sigma_d\}$. Para los cálculos posteriores se han utilizado los valores de los parámetros proporcionados por [16] que pueden consultarse en la Tabla 1.

Tabla 1. Valores de los parámetros en el modelo de constantes de fuerza de [16] para el grafeno.

α_1 (dyn / cm)	3.64×10^5
α_2 (dyn / cm)	0.57×10^5
γ_1 (erg)	6.08×10^{-12}
γ_2 (erg)	3.28×10^{-12}
δ (erg)	3.46×10^{-12}

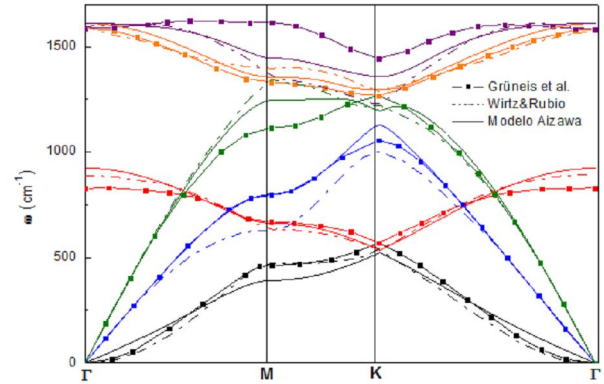


Figura 3. Comparación entre curvas de dispersión de fonones calculadas con los modelos de [10, 16] y los datos experimentales de [13].

Una manera habitual de asegurar la fidelidad y estabilidad de los modelos de constantes de fuerza es por comparación con curvas experimentales de dispersión de fonones. Así, la Figura 1 muestra una comparación entre curvas calculadas a partir de los modelos de [10, 16] y los datos experimentales de [13]. Como puede comprobarse, el modelo refleja tanto la estructura general como gran parte de los detalles de los datos experimentales.

5. RESULTADOS

Como ejemplo de validación se ha considerado una distribución periódica de dislocaciones discretas, en particular cuadrupolos de tamaño creciente integrados en celdas periódicas de grafeno, también de tamaño creciente. En este ejemplo las constantes de fuerza entre aristas B se han deducido del modelo de [16] ya mencionado. La distribución de autodeformaciones $\beta_i(e_1)$ que define un cuadrupolo consiste en dos vectores de Burgers constantes y opuestos según dos cadenas en zig-zag de aristas atómicas (Figura 4). La densidad de dislocaciones correspondiente se muestra en la Figura 5.

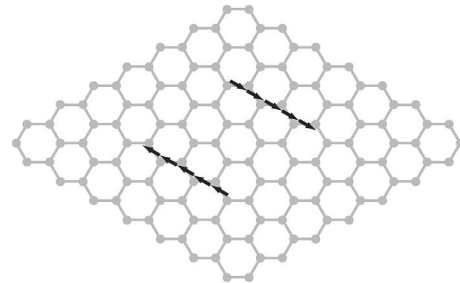


Figura 4. Distribución de autodeformaciones $\beta_i(e_1)$ que definen un cuadrupolo.

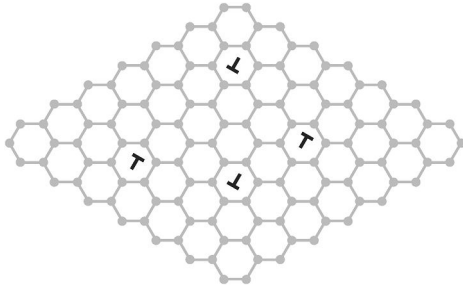


Figura 5. Densidad de dislocaciones $\alpha_i(e_2)$ que describe al cuadrupolo.

La configuración deformada para una celda periódica de 1144 átomos se muestra en la Figura 6. El núcleo de la dislocación discreta presenta una estructura con núcleo de anillo pentágono-heptágono (5-7) consistente con las observaciones de [3] de pares de pentágono-heptágonos unidos a una fila vacante de átomos en una cadena en zig-zag en un nanotubo de carbono de gran diámetro y una sola capa irradiado con un haz de electrones. La energía de la distribución periódica de cuadrupolos por célula periódica unidad, la cual puede ser vista como energía por dipolo, se muestra en la Figura 7 como función de de la separación entre dislocaciones y el tamaño de la celda unidad. Para separaciones entre dislocaciones mucho menores que el tamaño de la celda la energía por cuadrupolo es ostensiblemente independiente del tamaño de la celda y depende sólo del tamaño del cuadrupolo. Exceptuando los casos de los cuadrupolos más pequeños, la energía del cuadrupolo depende logarítmicamente del tamaño del cuadrupolo.

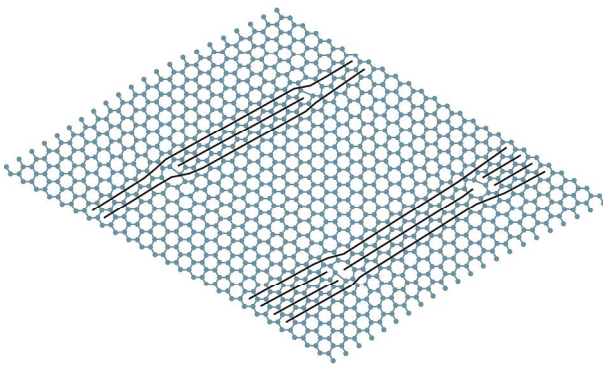


Figura 6. Configuración deformada de una distribución periódica de cuadrupolos en grafeno exhibiendo una estructura periódica con núcleo de anillo pentágono-heptágono.

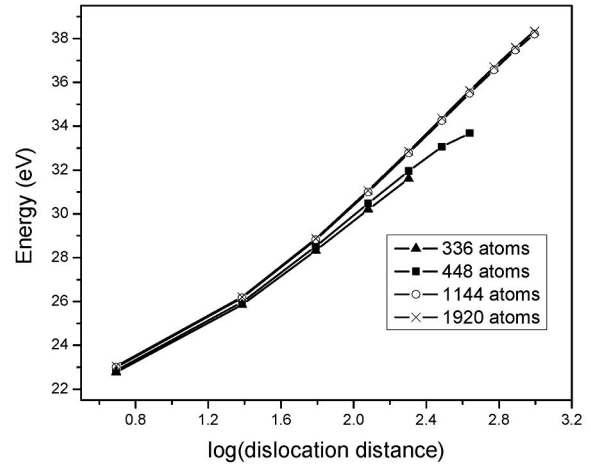


Figura 7. Energía de la dislocación periódica de cuadrupolos en grafeno como función de la separación entre dislocaciones y el tamaño de la celda unidad.

En la Figura 8 se muestra un detalle de las simulaciones efectuadas con el código de dinámica molecular LAMMPS del defecto mencionado, una vez producido y más tarde al alcanzar la estabilidad.

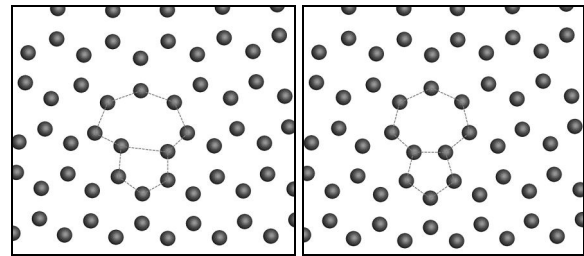


Figura 8. Detalle de la estructura atómica en las proximidades de un anillo 5-7 obtenida a partir de la teoría discreta (izq.) y posteriormente relajada en LAMMPS (der.).

6. CONCLUSIONES

En este trabajo hemos extendido la teoría discreta desarrollada por Ariza y Ortiz al estudio de defectos en grafeno. Hemos demostrado que aplicando sistemáticamente la transformada discreta de Fourier, es posible encontrar una solución exacta del problema de equilibrio resultante, lo cual supone una clara ventaja de la teoría discreta frente a los modelos atomísticos convencionales. Hemos obtenido expresiones explícitas de los campos de desplazamiento en equilibrio para el modelo de constantes de fuerza de [16] que pueden aplicarse a estructuras generales de dislocaciones. Se ha demostrado la habilidad de la teoría discreta de dislocaciones para predecir las estructuras de los núcleos de dislocaciones y sus correspondientes energías de configuraciones periódicas de cuadrupolos de dislocaciones mediante su comparación con resultados de otros autores [5,7].

AGRADECIMIENTOS

Los autores desean expresar su agradecimiento por el apoyo recibido al Ministerio de Educación y Ciencia (DPI2006-05045) y a la Consejería de Innovación, Ciencia y Empresa de la Junta de Andalucía (P06-TEP1514).

REFERENCIAS

- [1] Novoselov, K.S., Geim, A.K., Morozov, Jiang, S. V. D., Zhang, Y., Dubonos, S. V., Griegorieva, I. V. Firso, A., *Electric field effect in atomically thin carbon films*. Science, 306, 666, 2004.
- [2] Meyer, J. C., Geim, A. K., Katsnelson, M. I., Novoselov, K. S., J., B. T., S., R., *The structure of suspended graphene sheets*. Nature 446, 60, 2007.
- [3] Hashimoto, A., Suenaga, K., Gloter, A., Urita, K., Iijima, S.. *Direct evidence for atomic defects in graphene layers*. Nature 430, 870, 2004.
- [4] Ewels, C.P., Heggie, M. I., Briddon, P. R., 2002. *Adatoms and nanoengineering of carbon*. Chemical Physics Letters 351, 178-182, 2002.
- [5] Li, L., Reich, S., Robertson, J.. *Defect energies of graphite: Density-functional calculations*. Phy. Rev. B 72, 184109, 2005.
- [6] Xu, C. H., Fu, C. L., Pedraza, D.. *Simulations of point-defect properties in graphite by a tight-binding-force model*. Phy. Rev. B 48 (18), 13273-13279, 1993.
- [7] Jeong, B. W., Ihm, J., Lee, G. D.. *Stability of dislocation defect with two pentagon-heptagon pairs in graphene*. Phys. Rev. B 78 (16), 165403, 2008.
- [8] Lee, I.-H., Jun, S., Kim, H., Kim, S. Y., Lee, Y. *Adatom-assisted structural transformations of fullerenes*. Applied Physics Letters 88, 011913, 2006.
- [9] Meyer, J. C., Kisielowski, C., Erni, R., Rossell, M. D., Crommie, M. F., Zettl, A.. *Direct imaging of lattice atoms and topological defects in graphene membranes*. Nano Letters 8 (11), 3582-3586, 2008.
- [10] Wirtz, L. y Rubio, A. *The phonon dispersion of graphite revisited*. Solid State Commun. 131, 141-152, 2004.
- [11] Falkovsky, L. A. *Symmetry constraints on phonon dispersion in graphene*. Physics Letters A, 372, 5189-5192, 2008.
- [12] Mounet, N., Marzari, N.. Phys. Rev. B 71, 205214, 2005.
- [13] Grüneis, A. *et al.* *Determination of two-dimensional phonon dispersion relation of graphite by Raman spectroscopy*. Phys.Rev.B 65, 155405, 2002.
- [14] Tersoff, J. *Empirical Interatomic Potential for Carbon, with Applications to Amorphous Carbon*. Phys. Rev. Lett. 61, 2879, 1988.
- [15] Brenner, D. W. *Empirical potential for hydrocarbons for use in simulating the chemical vapor deposition of diamond films*. Phys. Rev. B 42, 9458, 1990.
- [16] Aizawa, T., Souda, R., Otani, S., Ishizawa, Y. y Oshima, C. *Bond softening in monolayer graphite formed on transition-metal carbide surfaces*. Phys. Rev. B 42, 11469, 1990.
- [17] Stuart, S. J., Tutein, A. B., Harrison, J. A.. *A reactive potential for hydrocarbons with intermolecular interactions*. J. Chem. Phys. 112 (14), 6472-6486, 2000.
- [18] Tewary, V. K., Yang, B.. *Parametric interatomic potential for graphene*. Phys. Rev. B 79 (7), 075442, 2009.
- [19] Ariza, M. P. y Ortiz, M. *Discrete Crystal Elasticity and Discrete Dislocations in Crystals*. Archive for Rational Mechanics and Analysis 178, 149-226, 2005.
- [20] Falkovsky, L. *Phonon dispersion in graphene*. Journal of Experimental and Theoretical Physics 105, 397-403, 2007.
- [21] Kundu, R. *Towards Phonon Spectrum of Graphene*. arXiv:0710.2077. 2007.
- [22] Nicholson, A.P.P. y Bacon, D.J.. *A new force-constant model for graphite*. Journal of Physics C: Solid State Physics 10, no. 13:2295, 1977

NEW PARAMETER FOR DETERMINING PLASTIC FRACTURE DEFORMATION OF METALLIC MATERIALS

Rafael Bueno, José Sánchez , Teresa Rodríguez

Department of Mechanics and Structures. University of Seville, Spain
 Avenida Reina Mercedes, 2. 41012 Seville, Spain
 E-mail address: rbueno@us.es
 December 2009

ABSTRACT

This study develops a new parameter for determining the plastic fracture deformation of metallic materials, using for this purpose the simple standardized tensile test on a cylindrical test specimen and evaluating the sectional deformation in the necking after rupture by means of the analytical expression proposed, as developed from the Theory of Plasticity.

The procedure for measuring this parameter by means of an optical profile projector is also explained, as are the practical applications of this parameter.

This formulation will eliminate the disadvantages of presents parameters (like A5d and A10d) and will enable a definite value which permit comparison with other values obtained by means of geometrically different samples, opening up the path to immediate applications in the field of Science and Engineering of Materials, Quality Control of Metals and Numerical Method.

KEY WORDS : Elongation , Ductility , Necking , Uniaxial Tension Test

1.- INTRODUCTION

The maximum fracture deformation that a metal is capable of withstanding appears amongst the basic mechanical characteristics when it comes to defining the technical properties of this material.

Nowadays a procedure is employed to determine fracture deformations in metallic materials. This procedure is accepted worldwide and standardized in the same way by the two main international standards:

- Euronorm EN-10002-1 “*Metallic materials. Tensile tests*”
- American standard ASTM E8 / E8M-08 “*Methods for tension testing of metallic materials*”

This method, referred to in Article 11 of Euronorm EN-10002-1 as “*Determination of percentage elongation after fracture (A)*” consists, in the case of round section metallic test specimens, of joining together the two broken pieces of the sample, after the simple tensile test, so that their axes are situated in a straight line and checking the longitudinal elongation that has taken place. It is necessary to establish calibration marks on the test specimen beforehand for subsequent calculation of its percentage elongation (Fig 1).

The main drawback of this procedure lies in that the phenomenon of necking or localized deformation predetermines the measurement tremendously and arouses considerable doubts as to the result.

Considering, furthermore, that local necking elongation (α) depends in turn on the diameter of the bar, we reach the conclusion, validated experimentally, that total plastic deformation at fracture (ϵ_f) for round-section test specimens is a function of the geometry of the sample.

Numerous attempts have been made to rationalize the distribution of tensile test deformations. Perhaps the most generally acceptable conclusion that may be drawn is that geometrically similar test specimens develop geometrically similar neckings. In accordance with Barba (1880), local elongation at the necking may be expressed as $\alpha = \beta \sqrt{A_0}$, where β is a coefficient of proportionality and A_0 the initial area.)

The above equation shows that, in order to compare deformations at fracture of different-sized test specimens, these have to be geometrically proportional, the geometric factor being the one that has to be maintained.

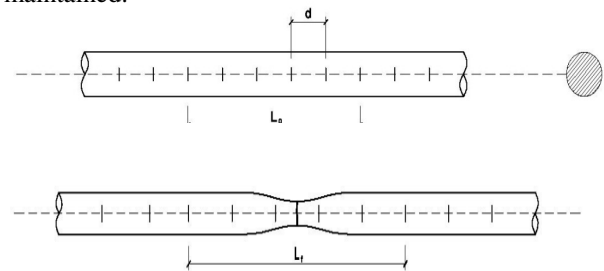


Fig 1.- A5d measuring procedure

Thus, as for the same steel the elongation of a centimetre of bar at the neck depends on the actual diameter of the bar, we are forced to define the necking elongation by taking as the measurement base not a centimetre, but a multiple of the bar diameter. The fact that a multiple is set in some standards but not in others underscores the conventionalism surrounding the procedure used at the present time. By way of example, in countries such as Spain or Germany five diameters (A_{5d}) was adopted as the measuring standard, while other countries, like Italy or Austria adopted ten diameters (A_{10d}) as the base.

The main disadvantages of the present parameter are, on the one hand, the lack of physical sense of A_{5d} or A_{10d} , as this parameter will weigh the overall longitudinal deformations in this range, but it does not indicate the maximum plastic deformations which are generated at fracture. Furthermore, depending on the diameter of the sample, different necking deformation values are obtained, so no comparison may be made between one another.

Despite research to try and establish a correlation between plastic deformations at fracture for samples of different geometry, to date no conclusive result has been reached. In fact, International Standard ISO 2566-1 "Steel. Conversion of elongation values" sets out to allay this disadvantage by means of the use of proportional samples as well as tabulating with tables and graphs the correspondences between values obtained with samples of different lengths. In practice, the infinite number of cases makes this unfeasible.

The aim of this article is the development of a new procedure that will eliminate the disadvantages described above and which will enable a definite value to be obtained for the plastic tensile deformation of round section bars.

2.- DESCRIPTION.

The main innovative aspect of the new parameter lies in the quantification not of the longitudinal plastic deformations, as at the present time, but of the sectional necking deformations. We will go on to give a brief description of the fundamentals of this proposal, as this is essential in the method proposed.

Study of the distribution of stresses and deformations in the necking of a bar subjected to traction was first undertaken by Bridgman in 1944. His work opened up a path to various contributions on this subject. Davidenkov and Spiridinova (1946) put forward expressions on the basis of experimental evidence. Kaplan (1973) extends the work of Bridgman beyond the minimum section and predicts the shape of the neck of the test specimen with its same parameters. Eisenberg/Yen (1983) generalize their expressions for

orthotropic bars, while Cabezas/Celentano (2004) and Jones/ Gillis (1983) extend it to flat sheets.

The result obtained from using cylindrical coordinates is that, in the central section of the test specimen, where the necking takes place, the state of deformation is defined by the following tensor (Bridgman):

$$\dot{\epsilon}_{ij} = \begin{pmatrix} \dot{\epsilon}_r & 0 & 0 \\ 0 & \dot{\epsilon}_\theta & 0 \\ 0 & 0 & \dot{\epsilon}_z \end{pmatrix} \quad \text{where} \quad \begin{aligned} \dot{\epsilon}_r &= \frac{\partial \dot{u}}{\partial r} \\ \dot{\epsilon}_\theta &= \frac{\partial \dot{v}}{\partial \theta} \\ \dot{\epsilon}_z &= \frac{\partial \dot{w}}{\partial z} \end{aligned} \quad (4)$$

Considering the hypothesis that radial deformations are uniform (Davidenkov/Spiridinova (1946) and Goicolea (1985)), we get:

$$\dot{\epsilon}_r = \frac{\dot{r}}{r} = \frac{\dot{D}}{D} \Rightarrow \epsilon_r = \int \frac{\dot{D}}{D} dt = Ln \frac{D}{D_0} \quad (5)$$

$$\dot{\epsilon}_\theta = \dot{\epsilon}_r$$

where r and D are the radius and the diameter at the necking at any time of the test and D_0 at the initial time

Similarly, in order to obtain the distribution of axial deformations, elastic deformations are disregarded and the condition of incompressibility is imposed:

$$lD^2 = l_0D_0^2 \Rightarrow (l_0 + u_z)D^2 = l_0D_0^2 \Rightarrow \dot{u}_z = -2l \frac{\dot{D}}{D} \Rightarrow \dot{\epsilon}_z = \frac{\partial \dot{u}_z}{\partial z} \Rightarrow \epsilon_z = -2 \cdot Ln \frac{D}{D_0} \quad (6)$$

Effective or equivalent plastic deformations at the neck are obtained by again disregarding elastic deformations and considering that tangential deformations are nil, whereby:

$$\epsilon^p = \int d\epsilon^p = \int_0^t \sqrt{\left(\frac{2}{3} \epsilon^p \cdot \epsilon^p\right)} dt = 2 \int_0^t \frac{\dot{D}}{D} dt = -2Ln \frac{D}{D_0} \quad (7)$$

On the basis of the state of deformations deduced above, it is necessary to make an immediate check that the stress tensor at the neck section is:

$$\sigma = \begin{pmatrix} \sigma_r & 0 & 0 \\ 0 & \sigma_r & 0 \\ 0 & 0 & \sigma_z \end{pmatrix} \quad (8)$$

Bridgman resolves the plastic problem by introducing the following hypotheses:

- The neck contour is approached by means of an arc of circumference
- The cross section in the necking area remains round during the test
- The deformations are constant at the neck cross-section points.

Obtaining the expression:

$$\frac{\sigma_{eq}}{\bar{\sigma}_z} = \frac{1}{\left[1 + \frac{2}{\sqrt{\epsilon_z - 0,1}}\right] \cdot \left[Ln\left(1 + \frac{\sqrt{\epsilon_z - 0,1}}{2}\right)\right]} \quad (9)$$

On the basis of these studies and on the confirmation of their hypotheses by means of numerical simulation, we reach the following conclusions regarding the state of the necking stresses and deformations:

1.- The components of the tensor deformation and the equivalent plastic deformation are equivalent at the neck section and may be expressed as:

$$\begin{aligned} \epsilon_r = \epsilon_\theta &= -Ln \frac{D_0}{D} \quad (\text{radial and circumf. deformation}) \\ \epsilon_z &= 2Ln \frac{D_0}{D} \quad (\text{axial deformation}) \\ \epsilon_{eq}^p &= 2Ln \frac{D_0}{D} \quad (\text{equivalent plastic deformation}) \end{aligned}$$

where D_0 is the initial diameter of the test specimen and D the necking diameter, for a given moment, during the progress of the tensile test.

2.- From the previous point we observe how parameter $\epsilon_{eq}^p = \epsilon_z = 2Ln D_0 / D$ defines the state of neck section deformation and determines the triaxial stress state that arises at the necking.

3.- At the time of fracture, the maximum deformation reached, which is the parameter we want to measure, may be therefore be found by means of the expression

$$\epsilon_f^p = 2 \cdot Ln \frac{D_0}{D_f}, \text{ where } D_0 \text{ is the initial diameter of}$$

the test specimen and D_f is the necking diameter at the time of fracture.

We will refer to this new parameter as DUCT, in reference to ductility. This expression, which we will use to quantify plastic deformation at fracture and

which, as may be appreciated, does not evaluate longitudinal, but sectional deformations. In this way, we successfully eliminate the present drawbacks described in the previous point.

3.- MEASURING PROCEDURE

We describe below the simple procedure that may be used for measuring the new parameter proposed. Owing to its actual formulation we only have to measure the diameter of the test specimen before and after the test.

Although D_0 may also be determined with a gauge or a Vernier calliper, for measuring the smallest necking diameter and determining D_f the profile projector provides an accuracy and promptness that has not been proposed in other methods (e.g. JP 2004325403 and JP 144588). Besides the aforementioned advantages, a further benefit of the use of this equipment is that it is standard in materials testing laboratories.

This equipment, used by materials testing laboratories for measuring the corrugation geometry of reinforcements, is an optical instrument that allows us to measure distances directly on a screen where the enlarged profile of the sample is shown. The precision of this equipment is 0.005 mm, ten times greater therefore than that of the gauge (0.05 mm).

In the photographs we show the following images of this equipment during measuring. Figure 3 shows the placement of the test specimen and the optical measuring equipment. Figure 4 shows the screen of the projector on which the measuring is carried out.



Fig.3.- Arrangement of the sample on the profile projector.



Fig.4.- Profile projector screen where the formation of necking in the sample may be observed after the tensile test. The neck diameter is measured on this screen.

4.- APPLICATION OF THE NEW PARAMETER.

4.1.- Range of validity in the creep curve.

We can express the creep curve using σ_{eq} and ϵ_{eq}^p by means of Hollomon's potential function (1945) $\sigma_{eq} = K(\epsilon_{eq}^p)^n$, which may be used to predict tensile plastic deformation performance in metallic materials, in modes of loading other than those of tensile testing.

In relation to the necking study, this equation is used recurrently in the finite element models in elastoplastic regime with considerable metal deformations: García-Garino (2006), Mansoo (2008) and Valiente (2001).

Parameters K and n have a clear physical interpretation: K is equal to the stress corresponding to a unitary deformation and it is easily shown that n corresponds to the actual deformation at maximum load $\epsilon_s = Ln(I + A_{gt})$. Parameter n is referred to as the cold deformation embrittlement or hardening coefficient, and we may observe its significance graphically by representing the pencil of curves, fixing $K = 662$ and varying n between 0.15 and 0.25.

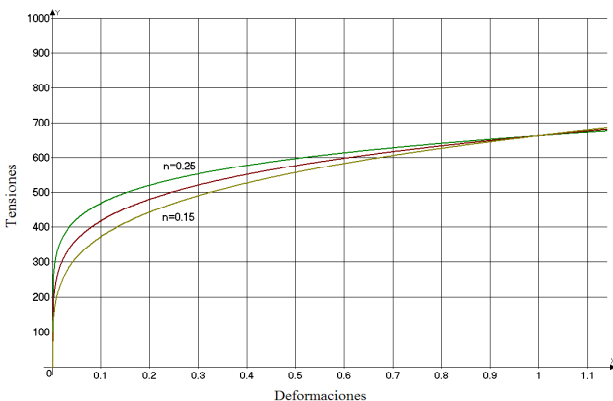


Fig. 6.-Representation of $\sigma_{eq} = 662(\epsilon_{eq}^p)^n$, for values of n of 0.15, 0.20 and 0.25

For manufacturing processes, said factor n has an immediate application. Thus, for instance, materials with a high n are of interest for cold forming purposes. In this way, when the load applied eventually brings about localized necking at a given point, the material in that area will undergo considerable consolidation and it will be the less resistant adjoining areas that will advance the deformation.

More uniform deformation of the material will therefore be achieved, instead of there being a progression in the localized necking at the early stages of the forming process, which would give rise to the fracture of the material.

The above-stated curve coefficients may be found easily after the tensile test, since, by forcing this curve to pass through the point (σ_s, ϵ_s) , at that moment, prior to the start of necking, we have:

$$K = \frac{\sigma_s}{\epsilon_s^n} \quad \text{where } \sigma_s \text{ is the real stress at}$$

maximum load: $\sigma_s = f_s(I + A_{gt})$

ϵ_s the real deformation at maximum load:

$$\epsilon_s = Ln(I + A_{gt})$$

n the exponent of hardening: $n = \epsilon_s$

And therefore the expression of the creep curve may be formulated as:

$$\sigma_{eq} = K \cdot (\epsilon_{eq}^p)^n = \frac{\sigma_s}{\epsilon_s^n} \cdot (\epsilon_{eq}^p)^{\epsilon_s} \quad (10)$$

an equation valid in the range $0 \leq \epsilon_{eq}^p \leq DUCT$ and dependent only on f_s and A_{gt} . In this range our ductility parameter specifies and defines the maximum plastic deformation possible.

4.2.- Ductility quantification in steels.

At the start of this study characterisation of the maximum plastic deformation at fracture of a metal by means of a single parameter was set as the main aim. Obviously, this purpose is the prime and immediate application of the parameter $DUCT$ proposed.

To show this experimentally, we tested bars 16 mm in diameter and 500 mm long, belonging to two different types of steel, SAE 1015 and SAE 1045. Three specimens of each type of steel were tested and similar results were obtained for each group. The figure below shows the conventional $\sigma - \epsilon$ diagrams for each type of steel considered.

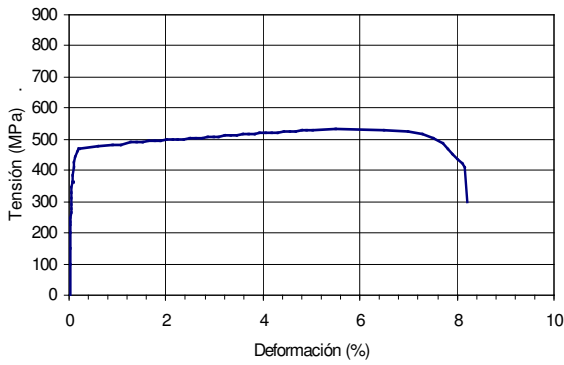


Table 2.- Sample 1. SAE 1015 steel.
Conventional $\sigma - \epsilon$ diagram

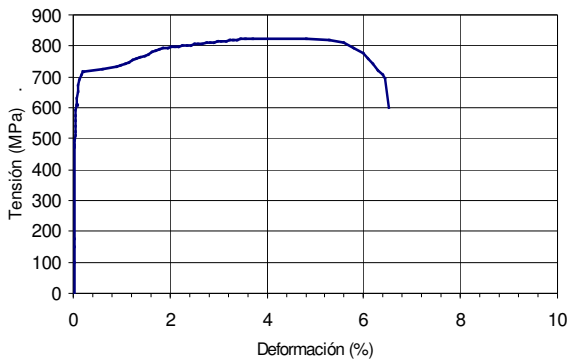


Table 3.- Sample 2. SAE 1045 steel.
Conventional $\sigma - \epsilon$ diagram

The mechanical characteristics obtained experimentally after the tensile test for each type of steel are summarized in the table below:

Test	f_y (MPa)	f_s (MPa)	f_s/f_y	A_{gt} (%)	A_{sd} (%)
1	482,9	532,6	1,103	5,28	16,38
2	728,8	823,9	1,130	3,38	11,36

Table 4.- Mechanical characteristics of the SAE 1015 and SAE 1045 tested.

In the table of mechanical values (Table 4) we see that Sample 1 presents lower values for yield strength and maximum loading stress. Following metallurgical logic, we observe that the greater the resistance is the lower the deformation, and vice versa.

For this reason, the maximum load deformation and elongation at fracture values, on the basis of five diameters, are greater in Sample 1 than in Sample 2 . The hardening factor (f_s / f_y), however, is greater for the second sample, than for the first one.

Analysis of the geometry at fracture, using the method proposed in this article, enables us to obtain information supplementary to that set out above.

The image below (Fig. 7) shows a photograph with the original geometry of the bar and the two types steel subjected to tensile testing. We may observe at first glance that the degree of deformation in the neck achieved by Sample 1 is greater in comparison to Sample 2, which breaks without hardly any necking.

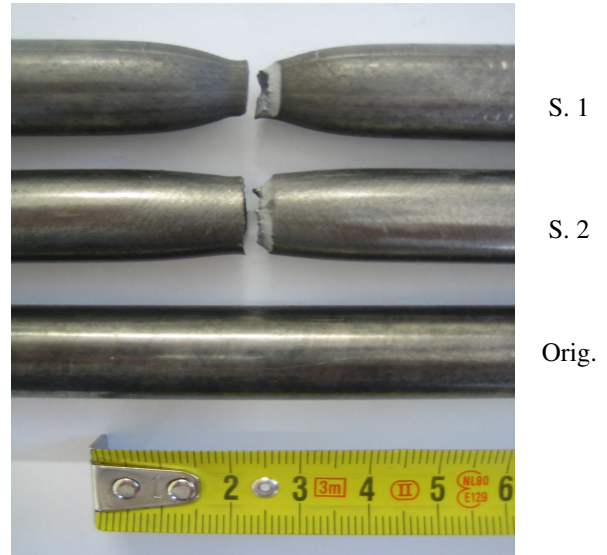


Fig. 7.- Comparative image of the fracture in the two types of steels tested and the initial geometry. We may observe the greater deformation in the neck of Sample 1.

If we examine the geometry of the fracture using the profile projector method suggested, we may quantify the shortening of the bar diameter occurring in the necking area, with a precision of ± 0.005 mm .

The following images (Figures 8 and 9) show the projection of both geometries on this equipment. With these measurements and the application of the proposed parameter ($DUCT$) we can quantify the plastic deformation at fracture capacity for each type of steel.

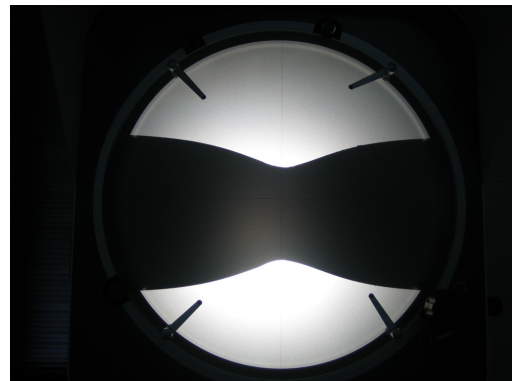


Fig. 8.- Sample 1.-Necking.

Initial diameter (D_0) = 16.02 mm

Final diameter (D_f) = 8.87 mm. --- $DUCT = 1.18$

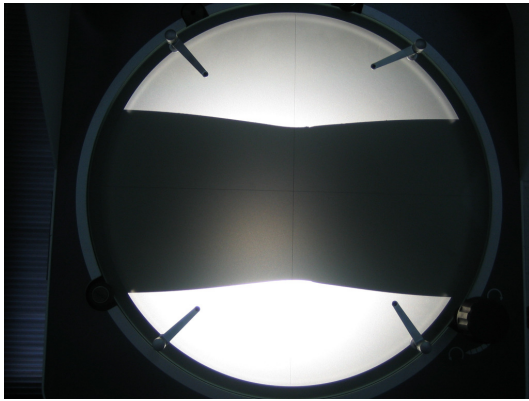


Fig. 9.- Sample 2.- Necking.

$$D_0 = 15.97 \text{ mm}$$

$$D_f = 12.79 \text{ mm} \text{ --- } DUCT = 0.44$$

Once the initial and final (diameters are known, the expression $DUCT = 2 \cdot \ln(D_0 / D_f)$ enables us to ascertain the ductility of each type of steel. In the images we may observe that Sample 1 presents what we could call “ductile fracture” as compared with the “brittle fracture” presented by the second Sample, which breaks without hardly any deformation.

In fact, for Sample 1 we obtain a ductility factor of 1,18, while for Sample 2 we obtain the value of 0,44. Sample 1 is, therefore, 2.7 times more deformable than Sample 2.

We observe, therefore, that the factor proposed allows us to quantify the ductility of metals by means of a single parameter, which is the main aim of this research.

5.- CONCLUSIONS

This article has carried out an in-depth examination of the current procedure for measuring deformations at fracture of metallic materials. Starting from Bridgman’s studies and analysing the necking stress-deformation state of a round test specimen subjected to tensile testing, we have reached the following conclusions:

1.- We set out to quantify the maximum plastic deformation at fracture of a metal by means of the factor $DUCT = 2 \cdot \ln(D_0 / D_f)$, where D_0 is the initial diameter of a round test specimen and D_f is the necking diameter after fracture.

2.- The main advantage compared with other parameters proposed, including that currently used for measuring deformations at fracture (A_{5d}), is its physical sense. This parameter represents the equivalent plastic deformation (ϵ_{eq}^p) in the neck section at the time of fracture, which, defined for

consistency and parallelism with Von Mises stress, is a measure of overall plastic deformation.

3.- The parameter proposed may be obtained simply by means of the tensile test, the internationally accepted procedure for characterizing a steel mechanically. A Vernier type gauge may be used for measuring the diameters, although use of the profile projector, standard equipment in laboratory mechanical testing, is recommended on account of its greater precision ($\pm 0.005 \text{ mm}$) = (0.005·E-3 m.).

4.- The creep curve may be adjusted by means of a potential expression of the type $\sigma_{eq} = K \cdot (\epsilon_{eq}^p)^n$, an expression valid in the range $0 \leq \epsilon_{eq}^p \leq DUCT$, the range of validity of the equation being defined therefore by the new parameter. This curve may be used in numeric models with plasticity and large deformations.

5. The new parameter allows a definite value of maximum plastic deformation to be obtained and its comparison with geometrically different test specimens.

6.-REFERENCES

BRIDGMAN, P.W., 1944. The stress distribution at the neck of a tensile specimen. Trans. Amer. Soc. Metals, Vol 32, pp. 553-574.

CABEZAS, E., CELENTANO, D., 2004. Experimental and numerical analysis of the tensile test using sheet specimen. Finite Elements in Analysis and Design, pp. 555-575.

COSENZA et al., 1993. An equivalent steel index in the assesment of the ductility performances of the reinforcement. CEB-218.

GROMADA, M., MISHURIS, G., 2004. Critical analysis of the evaluation of plastic material properties obtained from standard round tensile specimens. University of Aveiro (Portugal).

KAPLAN, M.A., 1973. The stress and deformation in mild steel during axisymmetric necking. J. Appl. Mech., Vol 40, pp. 271-276.

MANSOO, J. et al., 2008. A new method for acquiring true stress-strain curves over a large range of strains using a tensile test and finite element method. Mechanics of Materials, pp. 586-893.

VALIENTE, A., 2001. On Bridgman’s stress solution for a tensile neck applied to axisymmetrical blunt notched tension bars. ASME Journal of Applied Mechanics, pp 412-419.

Numerical and Probabilistic methods

ESTUDIO NUMÉRICO DE LA INFLUENCIA DE LA CURVATURA DEL PERFIL DE FRENTE DE GRIETA EN LA EVOLUCIÓN DEL ESTADO TENSIONAL A LO LARGO DEL ESPESOR EN PROBETAS CT

D. Camas-Peña^{1a}, J. García-Manrique^{1b}, P. López-Crespo^{1c}, A. González-Herrera^{1d}

¹Departamento de Ingeniería Civil, de Materiales y Fabricación, E.T.S. de Ingenieros Industriales, Universidad de Málaga, C/ Dr. Ortiz Ramos s/n, 29071 Málaga, España.
E-mail: ^{1a}dcp@uma.es; ^{1b}josegmo@uma.es; ^{1c}plc@uma.es; ^{1d}agh@uma.es

RESUMEN

El presente trabajo es un estudio numérico sobre la evolución del estado tensional a lo largo del espesor de la grieta y la influencia de variables como la carga aplicada, el espesor de la probeta y la curvatura del frente de grieta. El objetivo final es poder determinar la influencia de estos parámetros en el cierre de grieta en fatiga. Para ello se ha modelado por elementos finitos una probeta CT de aluminio en tres dimensiones, realizando una batería de cálculos combinando las distintas variables cuya influencia se desea estudiar. A partir de los resultados obtenidos relativos a la zona plastificada en el entorno del frente de grieta y del estado tensional a lo largo de la misma, se puede concluir que el cierre de grieta se ve afectado por la carga aplicada, desplazándose al interior al aumentar ésta; por el radio de curvatura del frente de grieta, desplazándose hacia el interior al disminuir el radio de curvatura; siendo sin embargo independiente del espesor de la probeta.

ABSTRACT

In this paper is presented a numerical study of the influence of the load level, the specimen thickness and the crack front curvature on the stress state. The aim of the work is to determine the influence of these parameters on fatigue crack closure. For this, a CT aluminium specimen has been modelled tri-dimensionally and several finite elements calculations have been made considering a large combination of the variables under consideration. From the analysis of the evolution of the plastic zone and the stress state along the thickness, it is concluded that the crack closure is under the influence of the load level, moving to the inside of the specimen when it increase; of the crack front curvature, moving to the inside of the specimen when it decrease; and that it is independent of the specimen thickness.

PALABRAS CLAVE: Elementos finitos, curvatura frente de grieta, zona plástica, estado tensional.

1. INTRODUCCIÓN

Cuando la teoría clásica de la Mecánica de la Fractura Elástica Lineal aborda el estudio del comportamiento de grietas bidimensionales, ignora cualquier tipo de efecto tridimensional que pueda afectar a la propagación del frente de la grieta.

Aspectos como la potencial influencia del espesor de la probeta o la propia curvatura del frente de grieta no son tenidos en cuenta. Simplemente se consideran dos casos extremos: tensión plana o deformación plana, de forma que se asume como bidimensional un problema que en esencia es tridimensional.

En trabajos anteriores en los que se ha analizado el efecto del cierre de grieta en fatiga con simulaciones por elementos finitos [1], se ha detectado que el efecto tridimensional de transición desde el interior al exterior de la probeta cobra gran importancia. El cierre se produce en una franja exterior de la probeta que no es proporcional al espesor, y la distribución y forma de la

zona plástica depende del valor de la carga máxima (K_{max}) y del espesor [2].

Dado el gran coste computacional de estas simulaciones, se ha abordado el problema desde la mecánica de la fractura en simulaciones en las que únicamente es aplicado el primer ciclo de carga.

De la misma forma, en un trabajo anterior [3] se estudiaba la evolución del estado tensional, en función de diversas combinaciones de niveles de K_{max} y espesores. Los modelos numéricos empleados siempre consideraban que el frente de grieta era recto.

Es conocido que el perfil del frente de una grieta que ha crecido bajo cargas cíclicas no es recto y presenta cierta curvatura. Por tanto, en este nuevo trabajo se añade una nueva variable de estudio y se analiza la dependencia de la evolución del estado tensional en las proximidades del frente de grieta en función de tres parámetros: la carga máxima aplicada, el espesor y la curvatura del perfil del frente de la grieta.

2. DESCRIPCIÓN DEL MODELO

Se ha modelado con elementos finitos una probeta CT de aluminio Al-2024-T35 ($w=50$ mm, $a=20$ mm) en tres dimensiones, con comportamiento plástico del material.

La zona más crítica corresponde al vértice de la grieta donde se produce la mayor concentración de tensiones y los mayores gradientes en tensiones y deformaciones. Por tanto, es necesario disponer de un elevado número de elementos para captar con cierta precisión estas variaciones.

Pero al mismo tiempo, para no penalizar en exceso el coste computacional, es preciso realizar una transición grande y violenta desde estas zonas hasta las más alejadas. Para ello se ha dividido la probeta en dos zonas distintas, una en el entorno del vértice de grieta, que ha sido mallada de una forma ordenada con elementos hexaédricos, y una segunda zona, mallada con elementos tetraédricos que permiten transiciones más bruscas.

Existen en la bibliografía recomendaciones sobre cómo seleccionar el número preciso de elementos [4,5]. En el presente trabajo se considera el radio plástico de Dugdale como parámetro de referencia para establecer el orden de magnitud de la zona plastificada. De esta forma, se consigue que en todos los casos estudiados, el radio plástico siempre se encuentra dividido en el mismo número de elementos, y que el tamaño de los mismos sean proporcionales a la carga aplicada.

Cuando el frente de grieta es recto, todos los nodos que constituyen el frente de grieta se colocan a una distancia igual a la longitud de la grieta. Sin embargo, cuando el frente de grieta es curvo, hay que definir un punto a lo largo del espesor que defina la longitud de la grieta, a partir de la cual se determina el valor de K . En el presente trabajo se ha considerado que el centro de gravedad de la línea que constituye el frente de grieta es el que determina la longitud de la grieta.

En cuanto al espesor, el tamaño de los elementos se ha realizado considerando que el elemento más cercano al plano medio de la probeta tiene una longitud doble que el situado en el exterior de la probeta, con el fin de poder determinar con mayor definición la zona de transición propia de la zona plastificada, la cual se manifiesta en las proximidades al exterior de la probeta, mientras que en el interior, donde predominan las condiciones de deformación plana, la zona plastificada es homogénea y requiere una menor definición. En la figura 1 se muestra tanto el mallado empleado en el entorno del vértice de grieta, como el modelo completo para una probeta de 3 mm de espesor y frente de grieta curvo.

Las propiedades que determinan el comportamiento elástico del material son el módulo de elasticidad E y el módulo de Poisson ν , suponiendo que el comportamiento del material es isótropo. Para la probeta

de estudio estos valores han sido de 73.5 GPa y de 0.35, respectivamente.

El modelo de plastificación que se emplea es del tipo elasto-plástico con endurecimiento por deformación, el cual se asemeja bastante al comportamiento de muchos metales entre los que se encuentra el aluminio.

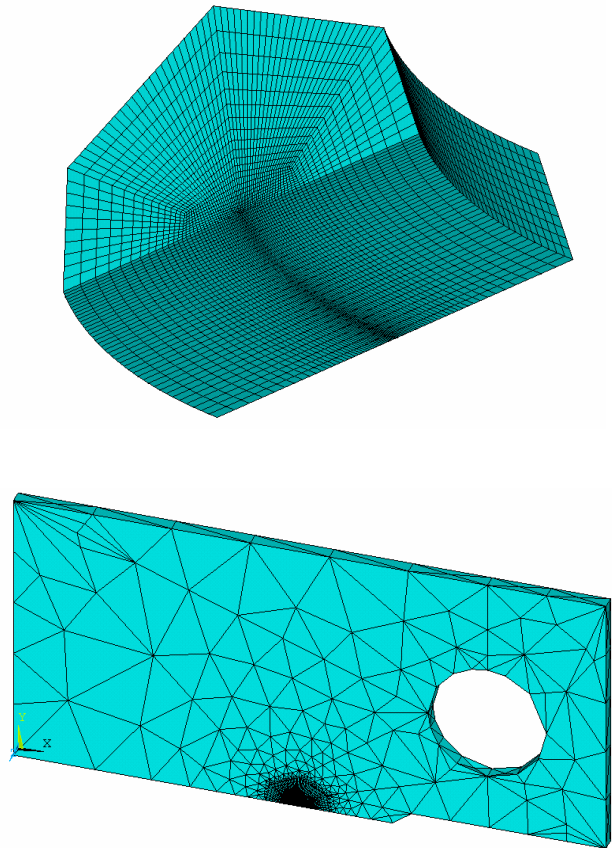


Figura 1. Mallado del entorno del frente de grieta y de una probeta de 3 mm de espesor

Se ha realizado una matriz completa de cálculos combinando tres espesores (3, 6 y 12 mm) con 7 valores de K_{max} , que abarcan desde $K=10$ hasta $K=40$ MPa·m^{1/2} y 5 valores distintos de radio de curvatura que abarcan desde el frente de grieta recto, radio de curvatura infinito, hasta un radio de curvatura de valor igual a las dos terceras partes del espesor de la probeta, lo cual permite cubrir un amplio rango de comportamiento.

3. RESULTADOS OBTENIDOS

3.1 Zona plástica

De entre los distintos mecanismos de cierre, el inducido por plasticidad es el más determinante en una gran variedad de situaciones prácticas. Según éste, el crecimiento de la grieta se encuentra muy influenciado por el efecto de una pequeña zona deformada plásticamente en el entorno del frente de grieta. Por lo tanto, es necesario conocer con profundidad la forma de esta zona plastificada y su dependencia con parámetros

hasta ahora ignorados como el espesor y la curvatura del frente de la grieta. La forma de tener una visión precisa de la zona plástica es por medio de la representación de las plastificaciones alcanzadas en los elementos.

En la figura 2 se muestra la zona plastificada en una probeta de 6 mm de espesor con un frente de grieta que presenta un radio de curvatura de 10 mm, sometida a una carga $K_{max}=25 \text{ MPa}\cdot\text{m}^{1/2}$.

Se observa que, al igual que ocurre cuando el frente de grieta es recto [3] las zonas plastificadas en la superficie y en la zona cercana a la misma no coincide con los resultados habituales para tensión plana en dos dimensiones, según los cuales, la zona plastificada en el exterior de la probeta (tensión plana) debería ser tres veces superior a la zona plastificada en el interior de la probeta (deformación plana).

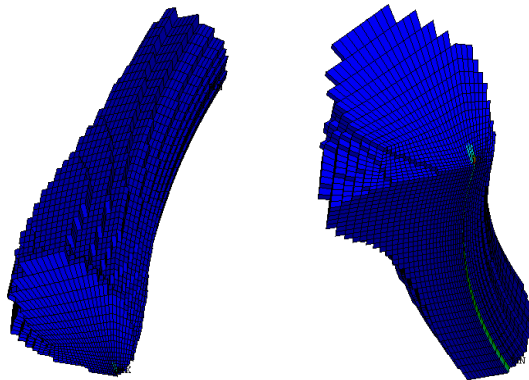


Figura 2. Zona plastificada en el entorno del frente de grieta

En la figura 3, se muestra una imagen comparativa de las zonas plastificadas en el exterior, el plano donde el radio plástico es máximo y el plano medio de la probeta. En la fila superior se muestran los resultados obtenidos cuando el frente de grieta es recto, mientras en la fila inferior se muestran los resultados con frente de grieta curvo. Se observa que el área plastificada en el plano medio de la probeta apenas se ve influenciada por el radio de curvatura, mientras que el área plastificada en el exterior de la probeta aumenta significativamente al disminuir el radio de curvatura del frente de grieta.

Debido a esto, se estudia la influencia de la curvatura del frente de grieta en las áreas plastificadas tanto en la superficie como en el plano medio de la probeta. En la figura 4 se muestra la evolución del área plastificada (A_p) en la superficie adimensionalizada por el área asociada al radio plástico de Dugdale en tensión plana ($A_{rpd tp}$), de probetas de 3mm de espesor al variar la carga aplicada y la curvatura del frente de la grieta. En primer lugar, se observa que en el caso de frente de grieta recto (fgr), los resultados muestran la existencia de una dependencia lineal del área plastificada adimensionalizada en las condiciones de tensión plana con la K_{max} aplicada. Por otro lado, para los valores inferiores de carga, se muestra una gran dependencia del

área plastificada en el exterior con el radio de curvatura, de tal forma, que radios de curvatura menores implican mayores áreas plastificadas. Al incrementarse el valor de la carga aplicada se produce una convergencia de los resultados obtenidos para los distintos radios de curvatura considerados hacia los valores obtenidos con el frente de grieta recto.

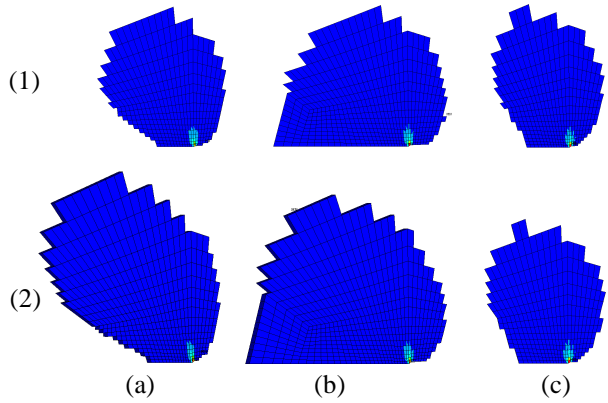


Figura 3. Zonas plastificadas en la superficie (a), plano de máximo radio plástico (b) y plano medio de la probeta (c). Frente de grieta recto (1) y frente de grieta con curvatura (2)

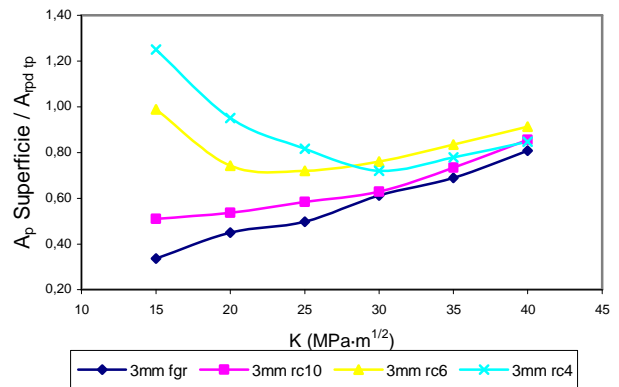


Figura 4. Evolución de las áreas plastificadas en la superficie de probetas de 3mm de espesor

En la figura 5 se muestran las áreas plastificadas (A_p) adimensionalizadas en el plano medio de la probeta, que corresponde con el caso de deformación plana. En esta ocasión, para adimensionalizar el área se ha empleado el área asociada al radio plástico de Dugdale en deformación plana ($A_{rpd dp}$). Se observa que existe una dependencia del área plastificada adimensionalizada en el plano medio de la probeta con la carga aplicada, en principio lineal hasta que se alcanza un determinado valor de la carga aplicada ($K_{max}=30 \text{ MPa}\cdot\text{m}^{1/2}$), a partir del cual se produce una saturación y pasa a tener un valor aproximadamente constante. Sin embargo, no ocurre lo mismo con el radio de curvatura que presenta el frente de grieta, obteniéndose valores prácticamente iguales para los distintos radios de curvatura sometidos a los mismos estados de carga.

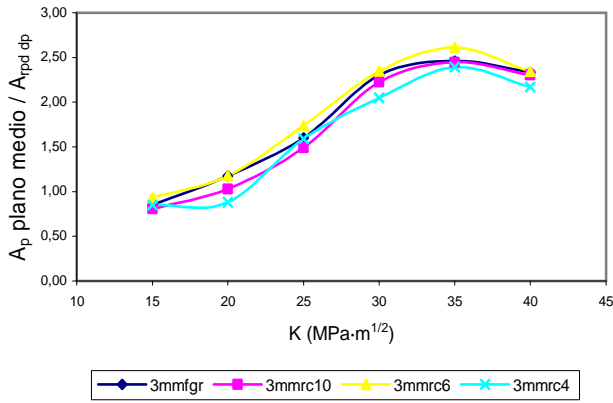


Figura 5. Evolución de las áreas plastificadas en el plano medio de probetas de 3mm de espesor

En la figura 6 se muestra la relación existente entre las áreas plastificadas en la superficie de la probeta, que corresponde con el estado de tensión plana, y en el plano medio de la probeta, que coincide con las condiciones de deformación plana. Se observa que para los casos con frente de grieta recto (fgr), el área plastificada en condiciones de deformación plana es prácticamente igual al área plastificada en las condiciones de tensión plana para todo el rango de cargas considerado. Sin embargo, se observa que la presencia de curvatura provoca que para los valores de carga inferiores el área plastificada en el exterior de la probeta sea muy superior a la que plastifica en el plano medio, tanto más cuanto menor sea el radio de curvatura del frente de grieta. Por otro lado, el incremento de la carga aplicada tiende a igualar las áreas plastificadas en el interior y en el exterior de la probeta independientemente de la geometría del frente de grieta, presentando cuantías prácticamente coincidentes para valores superiores a $K_{max}=30 \text{ MPa}\cdot\text{m}^{1/2}$.

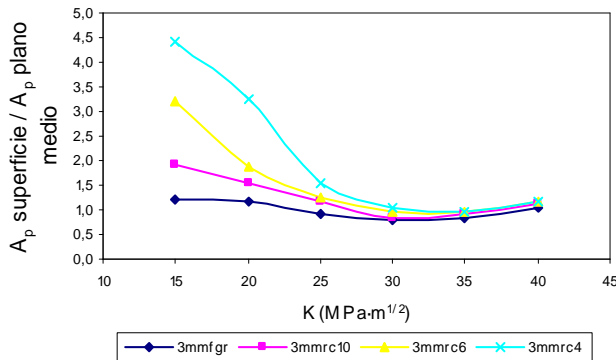


Figura 6. Evolución de la relación de las áreas plastificadas en el exterior y el plano medio de la probeta

Otra variable importante para caracterizar la zona plastificada en el entorno del frente de grieta, es el radio plástico a lo largo del frente de grieta. Se considera que el radio plástico es la zona plastificada en el plano de simetría de la probeta que contiene a la grieta. Para poder comparar los radios plásticos

obtenidos para distintos niveles de carga y las distintas geometrías, es necesario adimensionalizar estos valores. Para ello, se ha dividido los radios plásticos obtenidos por el radio plástico de Dugdale (rpd) correspondiente para cada caso.

En la figura 7 se muestra la evolución del radio plástico de una probeta de 3mm de espesor sometida a una $K_{max}=15\text{MPa}\cdot\text{m}^{1/2}$ al variar el radio de curvatura del frente de grieta. Para todos los casos se observa que en el interior de la probeta, la zona plastificada se mantiene constante, de forma que conforme nos vamos acercando al exterior de la probeta, se produce un notable incremento de las dimensiones de la zona plastificada, la cual disminuye rápidamente, formando un adelgazamiento de la zona plástica en la superficie de la probeta.

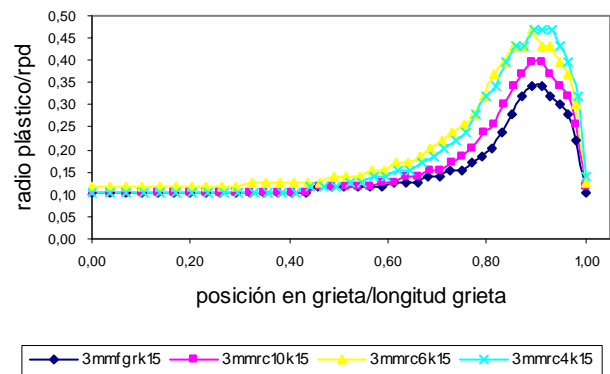


Figura 7. Evolución del radio plástico al variar el radio de curvatura del frente de grieta

Por trabajos anteriores [3] era conocido que conforme aumenta la carga aplicada, la zona de transición se va extendiendo hacia el interior, hasta que llega a ocupar todo el espesor de la misma, siendo este comportamiento más acusado en las probetas de menor espesor. Conforme aumenta el ancho de la pieza, para un mismo estado de carga, disminuye la extensión de la zona plastificada con respecto al espesor de la probeta.

En relación a la influencia del radio de curvatura en el radio plástico, la figura 7 muestra que conforme disminuye el radio de curvatura, se produce una extensión hacia el interior de la zona de transición, así como un aumento de los radios plásticos asociados a esta zona.

Con objeto de cuantificar en cierta medida la dominancia del estado de deformación plana, el estudio de la posición del centro de gravedad del radio plástico a lo largo del frente de grieta con respecto al exterior de la probeta en dirección ortogonal a la misma (d) determina la existencia de tres comportamientos diferenciados en función de la carga máxima aplicada, tal y como se puede observar en la figura 8. Se observa que la curvatura del frente de grieta únicamente afecta al primero de los comportamientos observados.

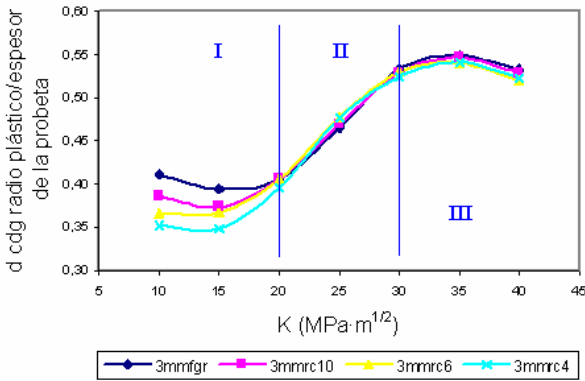


Figura 8. Posición del centro de gravedad del radio plástico respecto al exterior de una probeta de 3mm

Por último, se ha analizado el volumen de la zona plastificada en el entorno del frente de grieta. Para que estos valores sean independientes de la carga aplicada, se adimensionaliza dividiendo cada uno por el volumen que presenta un cilindro de diámetro igual al radio plástico de Dugdale correspondiente en cada caso y de altura el espesor de la probeta.

La curva de comportamiento del volumen adimensionalizado respecto a la carga aplicada presenta dos comportamientos diferenciados [3]. El primero presenta una relación lineal del volumen plastificado adimensionalizado con la carga aplicada y a partir de un determinado valor de K_{max} , el cual depende del espesor de la probeta, se produce una saturación, pasando a tener un comportamiento constante independiente del valor de la carga.

En la figura 9 se refleja la dependencia de los volúmenes plastificados en una probeta de 12 mm de espesor con el radio de curvatura del frente de grieta. Se muestra que se produce un aumento del volumen plastificado al disminuir el radio de curvatura para un mismo estado de cargas. De la misma forma, se observa el mismo comportamiento lineal del volumen plastificado con la carga aplicada para los distintos radios de curvatura considerados.

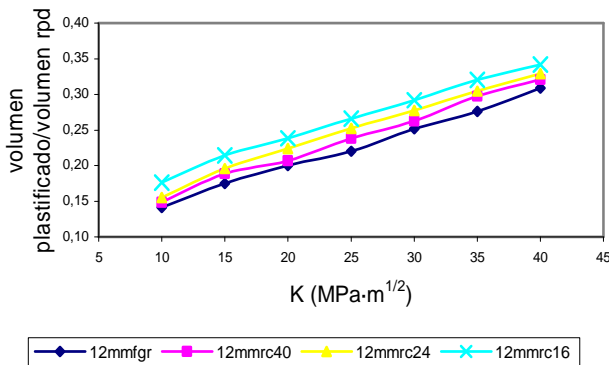


Figura 9. Volúmenes plastificados para una probeta de 12 mm de espesor

3.2 Tensiones

Para poder medir la influencia del estado de deformación plana a lo largo del frente de grieta, se han obtenido los valores de la tensión en la dirección ortogonal a la superficie de la probeta (σ_z) en todos los nodos pertenecientes al frente de grieta.

En la figura 10 se muestra la evolución de las tensiones en z a lo largo del frente de grieta al variar para una misma carga aplicada, la curvatura del frente de grieta. En concreto, se muestran los resultados obtenidos para una probeta de 6mm de espesor sometida a una carga $K_{max} = 35 \text{ MPa}\cdot\text{m}^{1/2}$. En el eje de abscisas se representa la posición en la grieta adimensionalizada por el espesor de la probeta. En el eje de ordenadas se representa la tensión en la dirección z en N/m^2 . Este valor no se adimensionaliza, ya que su valor está gobernado por el criterio de plastificación (von Mises) y es independiente de la carga aplicada.

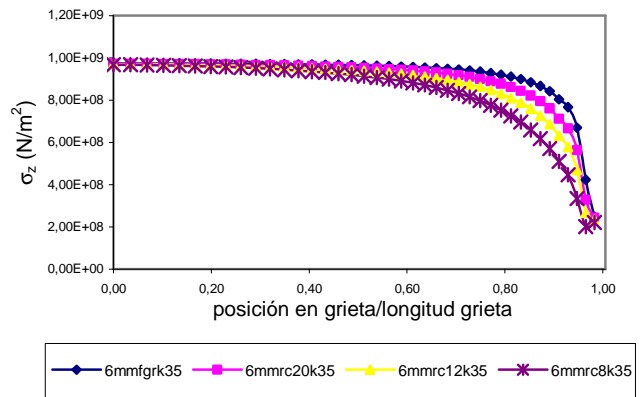


Figura 10. Evolución de las tensiones en z al variar el radio de curvatura del frente de grieta

En el exterior de la probeta no se alcanza el valor nulo debido a que los valores de las tensiones se calculan en los puntos de integración del elemento y, posteriormente, por interpolación, se determina el valor en los nodos. Además, el elevado valor del gradiente de las tensiones en esta zona, acentúa el error cometido.

Se observa que conforme disminuye el radio de curvatura del frente de grieta, la transición de los valores propios del estado de deformación plana a los correspondientes al exterior de la probeta es más suave.

Se busca determinar la dominancia del estado de deformación plana a lo largo del espesor de la probeta. Recorriendo el espesor de la probeta desde el interior hacia el exterior, mientras esté presente el estado de deformación plana las tensiones permanecerán inalterables. Por ello, se consideran como variable de estudio, la distancia con respecto al exterior de la probeta en la que se produce un descenso del valor de la tensión correspondiente al estado de deformación plana del 5% para cada uno de los casos estudiados.

En la figura 11 se muestra los valores obtenidos para una probeta de 3mm de espesor. Se observa que existe una clara dependencia lineal entre el espesor de la probeta bajo un estado de deformación plana y la carga aplicada, de tal forma que incrementos de carga implican una menor dominancia del estado de deformación plana. En cuanto a la configuración del frente de grieta, se observa que conforme disminuye el radio de curvatura, disminuye la dominancia del estado de deformación plana.

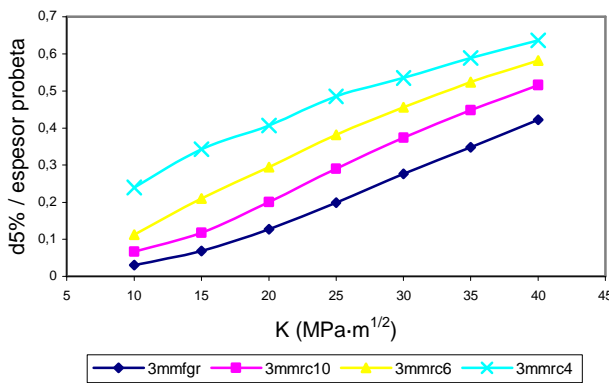


Figura 11. Distancia respecto al exterior de la probeta a la que se encuentra el estado de deformación plana

4. CONCLUSIONES

Del estudio de la zona plástica se concluye que existen diferencias importantes con el modelo teórico. Se ha demostrado la existencia de una fuerte dependencia entre la forma de la zona plastificada en el entorno del frente de grieta con variables tridimensionales no consideradas hasta el momento, tales como el espesor de la probeta y la curvatura del frente de la grieta, así como de variables que en principio no deberían presentar dependencia alguna, tales como el factor de intensidad de tensiones.

De esta forma, las áreas plastificadas en el exterior de la probeta se ven fuertemente influenciadas por el radio de curvatura, de tal forma que radios de curvaturas menores, implican áreas plastificadas mayores. Por el contrario, se ha visto que el área plastificada en el plano medio de la probeta, apenas se ve influenciada por el radio de curvatura del frente de grieta.

Con respecto a la carga aplicada, se ha observado que los valores del área plastificada tanto en el exterior como el interior adimensionalizadas por el área correspondiente al radio plástico de Dugdale muestra una fuerte dependencia, siendo más acusada en el caso de deformación plana.

La relación entre las áreas plastificadas en el exterior y en el interior muestra una dependencia con la curvatura del frente de grieta para valores de carga pequeños. A partir de un determinado valor, esta dependencia desaparece y los valores de las áreas plastificadas en el

exterior son del orden de las áreas plastificadas en el interior.

El volumen plastificado adimensionalizado por el volumen ideal constituido por el radio plástico de Dugdale, muestra un comportamiento lineal con la carga aplicada, hasta que se alcanza un determinado valor a partir del cual se alcanza un estado de saturación. El valor del factor de intensidad de tensiones a partir del cual se obtiene esta saturación depende del espesor de la probeta. Con respecto al radio de curvatura del frente de grieta, se puede observar que una disminución del radio de curvatura implica un aumento del volumen adimensionalizado.

Con respecto a la dominancia del estado de deformaciones, se puede decir que muestra una triple dependencia con el espesor, la curvatura y la carga aplicada. A partir de los resultados obtenidos en este y otros trabajos [3], se puede concluir que incrementos del factor de intensidad de tensiones implica una disminución del espesor de la probeta bajo condiciones de deformación plana; disminuciones del espesor de la probeta, implican menores influencias relativas del estado de deformación plana; y disminuciones del radio de curvatura del frente de grieta, implica una menor dominancia del estado de deformación plana.

A partir de las conclusiones directas obtenidas en el presente estudio, se puede inferir que en el comportamiento a fatiga, el cierre de grieta se ve afectado por el valor de K_{max} aplicado, desplazando el cierre de grieta hacia el interior. De la misma forma, la presencia de curvatura en el frente de grieta implica un desplazamiento del cierre de grieta hacia el interior.

REFERENCES

- [1] Gonzalez-Herrera A, Zapatero J. *Tri-dimensional numerical modelling of plasticity induced crack closure*. Engineering Fracture Mechanics. 2008;75:4513
- [2] Gonzalez-Herrera A, Garcia-Manrique J, Cordero A, Zapatero J. *Key Engineering Materials*. 2006;334-335:555.
- [3] Camas-Peña, D., García-Manrique, J., López-Crespo, P., González-Herrera, A., *Estudio numérico de la evolución del estado tensional a lo largo del espesor en probetas CT*, Anales de Mecánica de la Fractura, 26, pp. 259-264, 2009.
- [4] McClung, R.C., Sehitoglu, H., *On the finite element analysis of fatigue crack closure, part-1: basic modelling issues*, Engineering Fracture of Mechanics, 33, pp. 237-252, 1989.
- [5] González-Herrera, A., Zapatero, J., *Influence of minimum element size to determine crack closure stress by the finite element method*, Engineering Fracture Mechanics, 2005;72:337
- [6] González Herrera, A., *Determinación numérica de las tensiones de apertura y cierre de grieta en fatiga*, Tesis doctoral, Universidad de Málaga, 2004.

NUMERICAL MODELLING OF CORNER POINT SINGULARITIES AND THEIR EFFECT ON THE CLOSURE BEHAVIOUR OF 3D FATIGUE CRACKS

P. F. P. de Matos¹ and D. Nowell²

¹Instituto Superior de Entre Douro e Vouga, Rua António de Castro Corte Real, 4520-909 Santa Maria da Feira, Portugal.
E-mail: pfpmat@engenhheiros.pt

²University of Oxford, Department of Engineering Science, Parks Road, Oxford, OX1 3PJ, United Kingdom.
david.nowell@eng.ox.ac.uk

ABSTRACT

Although real cracks are inherently three-dimensional, relatively little effort has been put into the study of 3D cracks from both linear elastic and elastic-plastic points of view. Analytical solutions are difficult to obtain, and three-dimensional numerical simulations are complex and time consuming. Due to these limitations, the understanding of three-dimensional fatigue crack propagation has remained a challenging problem for the fatigue research community. The need to improve fatigue life predictions, particularly in aircraft structures, has been a motivation for research in this area. One of the outcomes of the research carried out over the last few decades is that fatigue cracks in metals are partially closed over part of the load cycle. This phenomenon of crack closure is thought by many to be the key to understanding the effect of non-uniform loading. This paper investigates the influence of surface effects on the closure behaviour of 3D fatigue cracks. Linear elastic analyses of 3D cracks show that Poisson's ratio influences the stress field close to the free surface. A 'corner point' singularity exists which differs from the usual $1/\sqrt{r}$ value for 2D cracks. In this region, both crack closure and corner point singularities are essentially "free surface" effects and it is difficult to investigate 3D crack closure without addressing the associated stress singularity problem. The aim of this paper is to investigate the influence of free surface effects on the closure behavior of 3D fatigue cracks, addressing some numerical difficulties related to FE modeling of the problem.

KEY WORDS: 3D cracks; Corner point singularity; Free surface; Crack closure.

1. INTRODUCTION

One of the difficulties in modelling 3D cracks is related to the shape of the crack front, which is often assumed to intersect the free surface at 90°. Under these conditions, the order of the stress singularity may differ from the usual square root singular K-field. In such 3D crack problems the order of the singularity at the free surface depends on Poisson's ratio and the intersection angle of the crack front with the free surface [1,2,3,4]. It seems reasonable to suggest that, real mode I fatigue cracks might choose to preserve the $1/\sqrt{r}$ singularity and therefore the crack front tends to intersect the free surface at a critical angle ($\beta_c \neq 0^\circ$) which is a function of the Poisson's ratio of the material and ensures square-root singularity.

In a recent paper, Heyder *et al.* [1] report experimental measurements of the angle at which crack fronts break the free surface for transparent specimens (PMMA) under four-point bending. They have shown that, at least for mode I crack propagation, the crack front is shaped so as to ensure square-root singularity at the intersection of the crack front with the free surface. Therefore, in real materials ($\nu \neq 0$) the assumption, frequently made in models, that the crack front intersects the free surface

at 90° will modify the order of singularity of the stress field in the region of the crack front close to the free surface. This may complicate the interpretation of crack closure in this region, and is important, since it is in the surface layer where closure effects are likely to be most significant [5,6,7]; incorrect modelling of the stress state will present difficulties when comparing modelling to experimental data. Since both phenomena, corner point singularities and crack closure, may co-exist and have a significant effect close to the free surface, we have divided our work in two parts. In the first part, we examine a 3D linear elastic crack and modify the shape of the crack front, for different values of Poisson's ratio, in order to ensure square-root singularity at the corner point (see Figure 1). In the second part of the paper, an elasto-plastic growing crack is modelled in a finite plate. The closure behaviour is studied for different values of Poisson's ratio for both, straight and modified crack fronts. Finally, based on the results obtained, some conclusions are drawn.

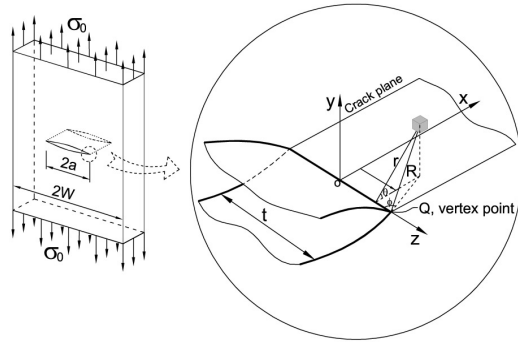


Figure 1. Rectangular plate with a central straight through crack. Coordinate system for a point in the vicinity of the crack front.

2. SINGULARITIES IN 3D CRACKED BODIES

Shivakumar and Raju [4] show that two different types of stress singularities co-exist along the crack front of 3D cracks, such as in the problem to be analysed (Fig. 1.). One is the conventional cylindrical singularity, and the second is the vertex singularity, which is assumed to exist at the corner point (point Q in Figure 1).

2.1. Cylindrical singularity

The stress and displacement fields of the cylindrical singularity can be expressed as,

$$\sigma_{ij} = C_{ij}(\theta, z) \cdot r^{\lambda_{\sigma}} \quad (1)$$

$$u_{ij} = D_{ij}(\theta, z) \cdot r^{\lambda_u} \quad (2)$$

where C_{ij} and D_{ij} are functions of z and θ . Both λ_{σ} , λ_u are independent of spatial coordinates r , θ and z and $\lambda_{\sigma} = \lambda_u - 1$.

2.2. Vertex singularity

Benthem [2, 3] used the vertex type of singularity to describe the singular stress field at the intersection of crack front and free surface (point Q in Figure 1). The stress and displacement field equation for this type of singularity can be written as follows,

$$\sigma_{ij} = E_{ij}(\theta, \phi) \cdot R^{\lambda_{\sigma}} \quad (3)$$

$$u_{ij} = F_{ij}(\theta, \phi) \cdot R^{\lambda_u} \quad (4)$$

where the functions E_{ij} and F_{ij} are functions of θ and ϕ , and R is the distance between the corner point and the point at which the stress is evaluated. In this case λ_{σ} , λ_u are functions of the Poisson's ratio and, once again, $\lambda_{\sigma} = \lambda_u - 1$.

2.3. Cylindrical and Vertex singularities

Based on a superposition argument, Shivakumar and Raju [4] suggested that the stress field of a 3D plate under remote tension can be written as the superposition of the stress field from a plane strain plate under remote tension together with corrective tractions on the free

surface of the 3D plate. Hence they concluded that the stress and displacement fields can be expressed as follows,

$$\sigma_{ij} = C_{ij}(\theta, z) \cdot r^{-1/2} + E_{ij}^i \cdot R^{\lambda_{\sigma}} \quad (5)$$

$$u_{ij} = D_{ij}(\theta, z) \cdot r^{-1/2} + F_{ij}^i \cdot R^{\lambda_u} \quad (6)$$

In these equations the first term is the conventional cylindrical singularity associated with the stress intensity factor, which is dominant along most of the crack front. The second term is either a vertex or cylindrical singularity. Shivakumar and Raju [4] obtained good agreement between their FE solution and Benthem's [2, 3] solution for a vertex singularity. The relative influence of each of these singularities depends on the value of Poisson's ratio.

3. SINGULARITIES IN 3D CRACKED BODIES

This section presents details of the finite element analysis performed to quantify the order of stress singularity along the crack front, using a log-log type of regression analysis. The case where the crack front is normal to the free surface was studied for different values of Poisson's ratio ($\nu = 0, 0.1, 0.2, 0.3, 0.4$ and 0.45). The material is assumed to be isotropic with positive Poisson's ratio. After identifying the region where the classical square-root singularity is not the dominant term, the shape of the crack front was modified for specific values of the Poisson's ratio ($\nu = 0.2, 0.3$ and 0.4), in order to ensure square-root behaviour at the corner point.

3.1. Linear elastic FE modelling

The geometry of the problem under study is presented in Figure 2. It consists of a square plate with a finite central crack. For convenience only one eighth of the plate was modelled. The dimensions of the plate are $W = 100$ mm with a central crack $a_0 = 10$ mm, and thickness t of 10 mm. For a linear elastic analysis the material behaviour is defined by Young's Modulus (E) and Poisson's ratio. In the present work $E = 100$ GPa and Poisson's ratio $\nu = 0, 0.1, 0.2, 0.3, 0.4$ and 0.45 .

Figure 3 shows the finite element mesh used. This mesh has 106160 isoparametric brick elements (C3D20), each with twenty nodes, and was designed with an increasing level of refinement towards the crack front region. The level of mesh refinement was set by reference to a convergence analysis carried out in 2D plane strain. The element size for the 3D analysis corresponded to that for the highest refinement level in 2D. Twenty layers of elements were used through the thickness of the plate with decreasing thickness from the centre of the plate towards the free surface (see Figure 3b). The thickness of the layers at the center of the plate and at the free surface is 0.469 mm and 0.031 mm, respectively.

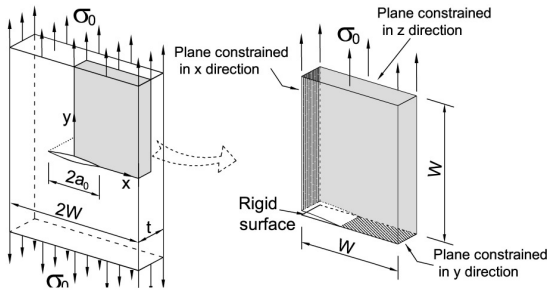


Figure 2. Rectangular plate with a central straight through crack, geometry and boundary conditions.

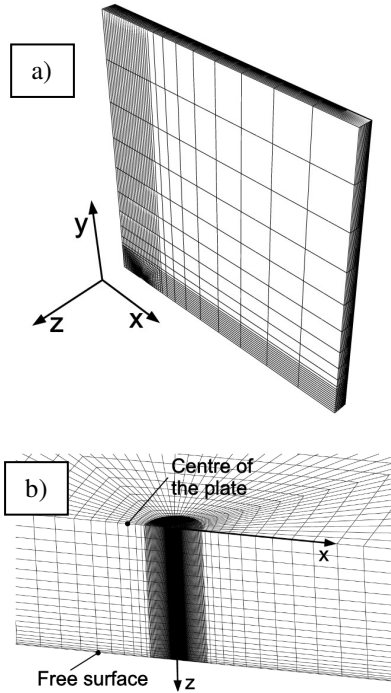


Figure 3. Mesh details, 3D model: (a) Mesh of a square plate with 100 x 100 mm with an initial crack (a_0) of 10 mm and thickness (t) of 10 mm; (b) Mesh detail of the crack front, crack front lies along z axis.

3.2. Log-log regression analysis

The log-log regression analysis is based on the nodal stresses and displacements from the finite element analysis (FEA). A Matlab routine was written to read the nodal coordinates, nodal stresses and displacements from the FEA at different inclinations h for different r values and different coordinates z . For each inclination θ , an analysis along the crack front was performed for 41 rows with different z coordinates shown schematically in the following figure.

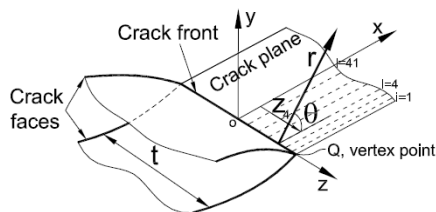


Figure 4. 3D crack front, coordinate systems.

The analysis was carried out for five different θ values ($\theta = 0^\circ, 45^\circ, 90^\circ, 135^\circ$ and 180°). It will be apparent that σ_y is zero along the crack faces ($h = 180^\circ$) and $u_y = 0$ along the plane ahead of the crack tip ($\theta = 0^\circ$). Hence, for $\theta \leq 90^\circ$ the regression analysis was performed based on the stresses on the y direction (σ_y), for $\theta = 135^\circ$ and 180° displacements on the y direction (u_y) were used. Given the difficulty of evaluating two coefficients and one exponent in equations (5) and (6), these equations were simplified to one constant and one exponent as suggested in [4]

$$\sigma_y = C \cdot r^{\lambda_\sigma} \tag{7}$$

$$u_y = D \cdot r^{\lambda_u} \tag{8}$$

Taking logarithms on both sides of equations (7) and (8) we obtain the following two equations

$$\log(\sigma_y) = \log(C) + \lambda_\sigma \cdot \log(r) \tag{7}$$

$$\log(u_y) = \log(D) + \lambda_u \cdot \log(r) \tag{8}$$

λ_σ and λ_u may now be calculated based on the best fit of a straight line to the plot of $\log(\sigma_y$ or $u_y)$ vs. $\log(r)$. As an example Figure 5 shows the stresses and displacements for different z/t coordinates for $\theta = 0^\circ$ and 180° , respectively.

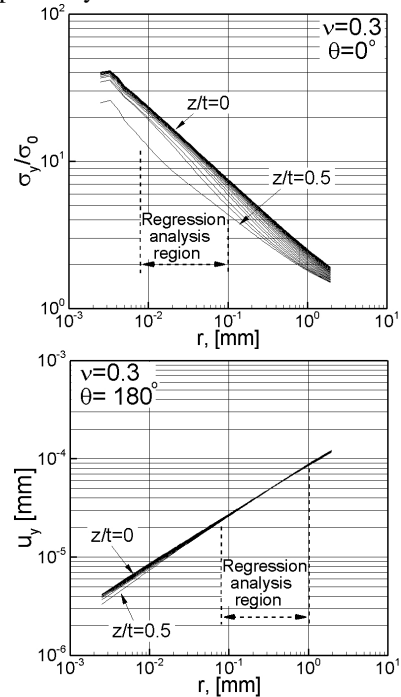


Figure 5. Log-log regression analysis region: a) Stresses for different z/t coordinates and $\theta = 0^\circ$; b) Displacements u_y for different z/t coordinates and $\theta = 180^\circ$.

The lower and upper limits for the regression analysis were chosen taking into account that values very close to the crack tip will be inaccurate due to an inability of the FE shape functions to model displacements accurately; and values further away from the crack tip will include higher order terms. The upper limit was selected taking into account the region close to the crack tip where classical the stress intensity factor governs the stress field, $r/a \approx 0.1$ is usually taken as a reference.

3.3 Power of the stress singularity and displacement and thickness of the boundary layer

Using the regression analysis described above it was possible to estimate the power of the dominant stress singularity (λ_σ) and displacement (λ_u) along the crack front. This analysis was performed for a range of Poisson's ratio values as shown in Figure 6.

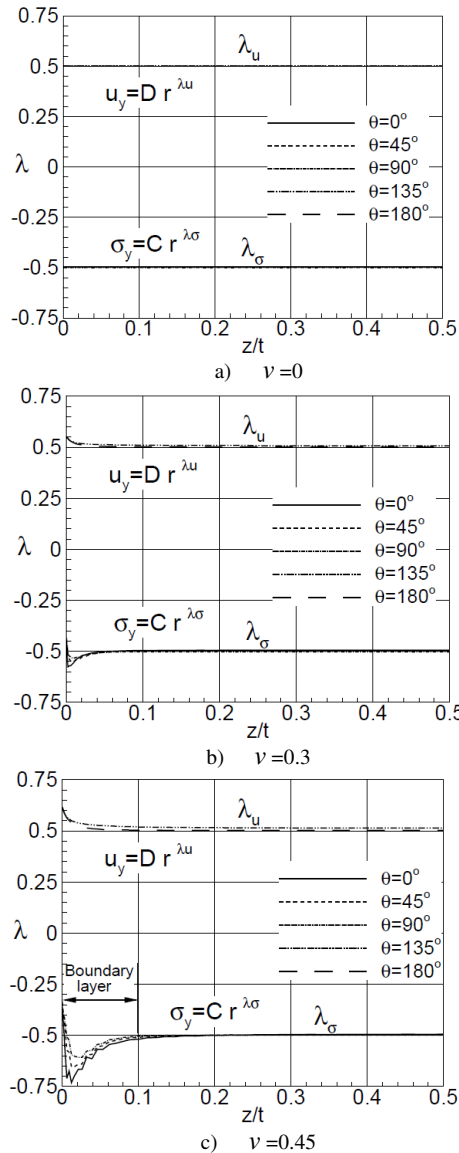


Figure 6. Log- Power of the stress singularity and displacement along the crack front for $\nu =0, 0.3$ and 0.45 .

It can be clearly seen that, independently of the value of Poisson's ratio and of the plane of analysis, θ , the power of the stress singularity at the centre of the plate ($z/t = 0$) is 0.5. In addition, the variables separable assumption is valid on this region since ($\lambda_\sigma = \lambda_u - 1$). For the case $\nu = 0$, the power of the stress singularity along the crack front is constant and square-root singular without showing any influence of the free surface, this is expected since $\beta_c = 0^\circ$ for $\nu = 0$. For larger values of Poisson's ratio the

stress singularity is weaker at the free surface ($z/t=0.5$). Some specific results are shown in Table 1, which can be compared with results available in the literature shown in Table 2.

Table 1 - Power of the stress and displacement at mid-plane and free surface for different values of the Poisson's ratio

Poisson's ratio (ν)	Present work – free surface ($z/t = 0.5$)				
	λ_σ ($\theta = 0^\circ$)	λ_σ ($\theta = 45^\circ$)	λ_σ ($\theta = 90^\circ$)	$\lambda_u - 1$ ($\theta = 135^\circ$)	$\lambda_u - 1$ ($\theta = 180^\circ$)
0.00	-0.495	-0.496	-0.501	-0.499	-0.499
0.10	-0.489	-0.485	-0.492	-0.488	-0.489
0.20	-0.477	-0.467	-0.475	-0.473	-0.474
0.30	-0.452	-0.434	-0.447	-0.449	-0.451
0.40	-0.395	-0.401	-0.408	-0.413	-0.412
0.45	-0.354	-0.334	-0.374	-0.386	-0.382
0.49	-	-	-	-0.359	-0.354
0.50	-	-	-	-0.341	-0.333
	Present work – mid-plane ($z/t = 0$)				
0.00	-0.495	-0.496	-0.501	-0.499	-0.499
0.10	-0.495	-0.496	-0.503	-0.497	-0.499
0.20	-0.494	-0.496	-0.504	-0.495	-0.499
0.30	-0.494	-0.497	-0.503	-0.507	-0.498
0.40	-0.496	-0.498	-0.501	-0.489	-0.499
0.45	-0.494	-0.496	-0.499	-0.487	-0.498
0.49	-0.491	-0.496	-0.499	-0.483	-0.498
0.50	-	-	-	-0.485	-0.496

Table 2 - Reference values for the power of the stress singularity and displacement for different values of the Poisson's ratio at the free surface

Poisson's ratio, ν	Benthen [2,3]	Shivakumar and Raju [4]	Bažant and Estenssoro [8]
	λ_σ	λ_σ ($\theta=0^\circ$)	$\lambda_u - 1$ ($\theta=180^\circ$)
0,00	-0,5	-0,497	-0,497
0,30	-0,452	-0,451	-0,452
0,40	-0,414	-0,407	-0,413
0,45	---	-0,356	-0,391
0,50	-0,332	---	---

It can be seen that the present results are in good agreement with those from references [2,3,4,8].

The region close to the free surface where the stresses are not square-root singular (e.g. Figures 6 b and c) is usually called the boundary layer region. In interpreting the results the thickness of the boundary layer was calculated using the first point along the crack front where the stress singularity exceeds 1% of the order of the stress singularity at the centre of the plate (see Figure 6 c). Using this criteria the thickness of the boundary layer is 0%, 1%, 2.5%, 4%, 12.5% and 15 % of the thickness of the plate for $\nu = 0, 0.1, 0.2, 0.3, 0.4$ and 0.45 , respectively. Results of the same order of magnitude were obtained by Shivakumar and Raju [4].

3.4. Critical intersection angle

Bažant and Estenssoro [8] argued from energy and other considerations that the front edge of a propagating crack must terminate at the free surface obliquely, at a critical

angle which is a function of the Poisson's ratio, ensuring square-root singularity at the corner point. An analytical solution for the critical intersection angle is not available, although some numerical [2,3,9] solutions and experimental [1] data are available in the literature. The critical intersection angle is calculated imposing square-root singularity at the corner point, for different Poisson's ratio values. The aim of the present work was not the calculation of the critical intersection angle, therefore results available in the literature were taken as a reference. Figure 7 presents data for β_c given in reference [16]. The solution given by the dashed curve was obtained by Heyder *et al.* [1] based on the 3D dual discontinuity method, the continuous line is an empirical equation proposed by Pook [10]. The solution proposed by Heyder *et al.* [16] was adopted in this work.

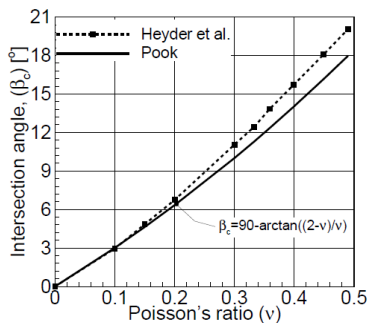


Figure 7. Intersection angle of the crack front with the free surface ensuring square-root singularity under mode I, after Heyder *et al.* [1].

3.5. Modification of the crack front geometry

As described above, the geometry of the crack front was modified (see Figure 8) in order to enforce square-root singularity at the corner point.

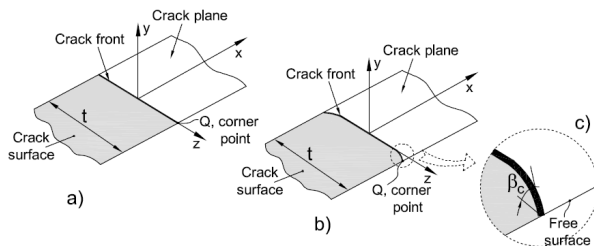


Figure 8. Different crack front geometries: a) Crack front normal to the free surface; b) and c)

- The procedure adopted consisted of the following steps:
- (1) Running a finite element simulation for a crack with a straight front, see Figure 8a;
 - (2) Calculation of the boundary layer thickness based on the log-log regression analysis previously described;
 - (3) Modifying the shape of the crack front in the boundary layer region so that for the chosen value of m the crack front intersects the free surface at the critical angle, see Figure 8b and c;
 - (4) Running a finite element analysis of the same problem with a modified crack front shape;
 - (5) Log-log regression analysis of the modified crack front problem and comparison of results.

Two different shapes were studied (see Figure 9): 1) a circular arc crack front within the boundary layer and 2) a linear crack front with a circular transition between the boundary layer and "plane strain" like region.

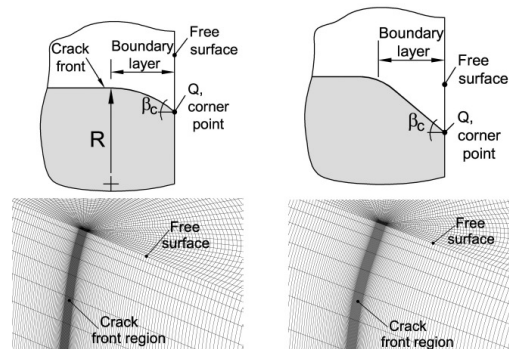


Figure 9. Geometrical and mesh details of different crack front shapes close to the free surface ($\nu=0.3$).

Figure 8 and 9 show details of the modified crack front. Figure 10 shows the improvement in the power of the displacements obtained by modifying the shape of the crack front.

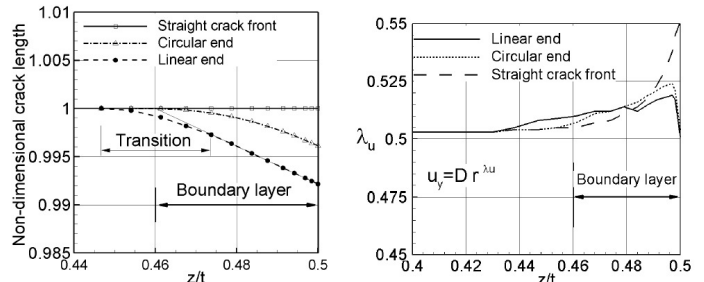


Figure 10. (a) Geometric details of the crack fronts close to the free surface; (b) power of the displacement for different crack front geometries and $\nu = 0.3$.

It can be seen that within the boundary layer region a significant improvement takes place within $0.49 < z/t < 0.5$, however little improvement is obtained for points further away from the free surface ($0.44 < z/t < 0.49$). The results obtained with both crack front geometries are quite similar, therefore for simplicity the crack front with the linear end close to the free surface was adopted for further calculations.

4. 3D FINITE ELEMENT MODELLING OF PLASTICITY-INDUCED CRACK CLOSURE

The aim of this section is to investigate the relevance of corner point singularities to the closure behaviour of 3D cracks. The first step is to characterize the closure behaviour of fatigue cracks with a crack front normal to the free surface for $\nu = 0, 0.2, 0.3$ and 0.4 . Secondly, for $\nu = 0.2, 0.3$ and 0.4 the shape of the crack front will be modified according to the procedure previously described in order to assure a square-root singularity at the corner point. Three-dimensional simulations of plasticity-induced crack closure were carried out using a standard node

release scheme [5]. The crack is allowed to grow by one element size by releasing nodes ahead of the initial crack front every two load cycles. The nodes are released sequentially by modifying the appropriate boundary conditions. The node displacement method was used to calculate the opening stresses. This method consists of monitoring the displacement of a node (the first node behind the crack tip in the present work) as the load is applied [11]. The opening stresses are found when the displacement of the node monitored became positive during the loading stage of a load cycle. It should be noted that issues such as mesh refinement, crack growth scheme, method of calculating the opening stresses and number of load cycles between node releases can affect the results. The current work does not seek to address any of these aspects explicitly, therefore all simulations were performed under the same conditions, i.e, same mesh density, crack growth scheme, opening stress calculation method and load conditions ($\sigma_{max}/\sigma_{yield}=0.5$ and $R=0$).

Figures 11 a) and b) compare the opening stresses for the case of straight crack front a) and corrected crack front b) it can be seen that the different levels of stresses singularity along crack imposed by the elasticity solution do not seem to be of great practical significance in terms of the magnitude of the opening stress levels. For lower levels of remote applied stresses this difference may increase.

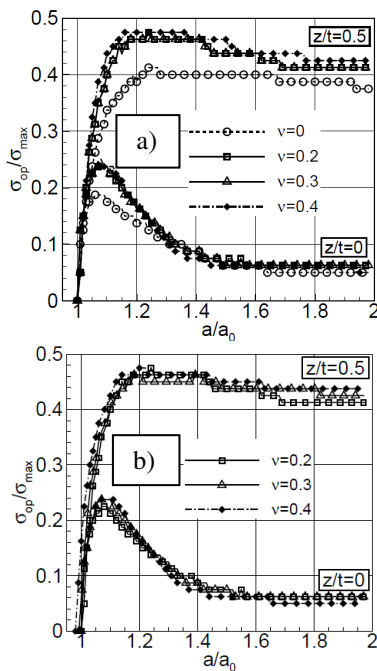


Figure 11. Comparison of the opening stresses for the case of straight crack front a) and corrected crack front b) respectively. $\sigma_{max}/\sigma_{yield}=0.5$, $R=0$ and $a_0=1.0mm$.

5. DISCUSSION OF THE RESULTS AND CONCLUSIONS

The results presented show that modelling of plasticity-induced crack closure is not significantly influenced by the nature of the elasticity solution where the crack front

meets the free surface. The effect of different types of stress singularities along the crack front for different values of the Poisson's ratio and crack front geometries was shown to have little effect on the closure behaviour in particular for $0.2 < \nu < 0.4$. It seems that, at least for the loading conditions used in the present work, the plasticity associated with the stress field along the crack front dominates the solution in such a way that the different levels of elastic stress singularity along the crack front do not have significant influence on the closure behaviour.

REFERENCES

- [1] Heyder, M., Kolk, K., Kuhn, R.J., *Numerical and experimental investigations of the influence of corner singularities on 3D fatigue crack propagation*, International Journal of Fatigue, 72:2095-2105, 2006.
- [2] Benthem, J.P., *State of Stress at Vertex of a Quarter-Infinite Crack in a Half-Space*, International Journal of Solids and Structures, 13(5):479-492, 1977.
- [3] Benthem, J.P., *Quarter-Infinite Crack in a Half-Space - Alternative and Additional Solutions*, International Journal of Solids and Structures, 16(2):119-130, 1980.
- [4] Shivakumar, K.N., Raju, I.S., *Treatment of Singularities in Cracked Bodies*, International Journal of Fracture, 45(3):159-178, 1990.
- [5] de Matos, P.F.P., Nowell, D., *Numerical simulation of plasticity-induced fatigue crack closure with emphasis on the crack growth scheme: 2D and 3D analyses*, Engineering Fracture Mechanics, 75(8): 2087-2114, 2008.
- [6] Roychowdhury, S., Dodds, R. H., *Three-dimensional effects on fatigue crack closure in small-scale yielding regime - a finite element study*, Fatigue & Fracture of Engineering Materials & Structures, 26:663-673, 2003.
- [7] Dawicke, D.S., Grandt, A.F., *Three-Dimensional Crack Closure Behavior*. Engineering Fracture Mechanics, 36(1):111-121, 1990.
- [8] Z. P. Bažant, Z.P., Estenssoro, L.F., *Surface Singularity and Crack-Propagation*, International Journal of Solids and Structures, 16(5):479-481, 1980.
- [9] Hartranft, R.J., Sih, G.S., *An approximate three-dimensional theory of plates with application to crack problems*, International Journal of Engineering Science, 8:711-729, 1970.
- [10] Pook, L.P., *Some Implications of Corner Point Singularities*, Engineering Fracture Mechanics, 48(3):367-378, 1994.
- [11] de Matos, P.F.P., Nowell, D., *On the accurate assessment of crack opening and closing stresses in plasticity-induced crack closure problems*, Engineering Fracture Mechanics, 2007;74(10):1579-601.

USING A STANDARD SPECIMEN GEOMETRY FOR CRACK PROPAGATION UNDER PLAIN STRAIN CONDITIONS

J.M. Silva¹, V. Infante², F. Antunes³, F. Ferreira¹

¹ Departamento de Ciências Aeroespaciais,
Universidade da Beira Interior; 6201-001 Covilhã – Portugal
E-mail: jmas@ubi.pt

² Departamento de Engenharia Mecânica
Instituto Superior Técnico; 1049-001 Lisboa – Portugal
E-mail: virginia@dem.ist.utl.pt

³ Departamento de Engenharia Mecânica
FCTUC; 3030-788 Coimbra – Portugal
E-mail: fernando.ventura@dem.uc.pt

ABSTRACT

This work is a preliminary approach to evaluate the possibility of using a conventional M(T) specimen with lateral notches aiming at obtaining plane strain conditions required for certain type of phenomena concerning crack propagation. This type of specimen geometry can be advantageous since it allows the use of moderate component thicknesses with triaxial stress conditions in the most part of the crack propagation region.

Several computational simulations of fatigue cracks in an aluminium alloy were carried out by using commercial FEM codes. The influence of different types of variables was considered, namely the geometry of the lateral notches (circular or V shaped) and the thickness of the specimen. Stress intensity factor K was determined for several crack front positions to evaluate the effect of these geometrical features, as well as the influence of both stress fields and crack length in the fatigue behaviour of the material. Also, two stress triaxility parameters were used in order to confirm the stress state condition in the crack propagation region.

The conclusions of this preliminary study are encouraging concerning the possibility of using a reduced thickness MT specimen with a plane strain condition, which can be a useful experimental tool when considering the investigation of particular crack propagation mechanisms, such as those related with high temperature conditions.

KEY WORDS: M(T) specimen, triaxility parameters, stress intensity factor, fatigue

1. INTRODUCTION

Stress state is a main independent parameter with a notorious effect in fatigue crack growth under certain types of loading and environmental conditions. As an example, high temperature fatigue crack propagation in some types of materials, such as nickel base superalloys, is a complex phenomenon characterized by different damage micromechanisms, namely cyclic plastic deformation, oxidation and creep [1,2]. Depending on the conditions at the crack tip one of these mechanisms may be dominant and the propagation is either transgranular (cyclic plastic deformation), intergranular (oxidation or creep) or mixed. Stress state directly affects these distinct propagation modes: a plane stress state was found to promote transgranular propagation, whilst the triaxility associated to plane strain state promote diffusion mechanisms associated with time dependent propagation [3].

Plasticity induced crack closure (PICC) [4,5] is another phenomenon which can be greatly influenced by the

stress state condition. There is a general agreement that plane stress state induces significantly larger levels of crack closure compared with those related to plane strain loading conditions. However, the intensity and even the existence of PICC under plane strain conditions are still controversial. From a theoretical point of view, the main problem is to visualise the additional volume of material necessary to explain PICC, since out-of plane flow is not allowed under plane strain conditions, by definition. So, if a constant volume during deformation is taken into account, the assumption of an additional wedge is not reasonable [6,7]. A significant number of numerical studies focusing on PICC under plane strain conditions have been developed. However, their validation through a convenient experimental work is difficult due to the inexistence of a pure plane strain specimen geometry.

In fact, for experimental fatigue testing purposes, plane stress conditions are usually obtained by simply using thin specimens based on standard geometries. BS 6835

1988 [8] and ASTM 647-95a [9] indicate the use of CT, MT and bending specimens. By the other hand, when plane strain is intended to occur as a sole condition, specimens are required to have increased thicknesses which, in turn, does not eliminate possible surface effects and leads to more complex and expensive testing procedures. The inclusion of lateral notches on the specimens is a possible solution to overcome these limitations, allowing obtaining plane strain conditions in relatively thin specimens, which will be explored here.

Fatigue crack growth in specimens with lateral notches and under different loading conditions has been widely reported by several authors [10-15], but without aiming at obtaining plain strain conditions in all the positions of the crack front.

The analysis and optimization of pure plane strain specimens requires numerical parameters to quantify stress triaxiality. Several authors [16-20] used the triaxiality parameter Θ as defined by Eq. (1):

$$\Theta = \frac{\sigma_m}{\sigma_v} = \frac{\frac{1}{3}(\sigma_{xx} + \sigma_{yy} + \sigma_{zz})}{\frac{1}{\sqrt{2}}[(\sigma_{xx} - \sigma_{yy})^2 + (\sigma_{xx} - \sigma_{zz})^2 + (\sigma_{zz} - \sigma_{yy})^2]^{1/2}} \quad (1)$$

Θ is the ratio between the average hydrostatic stress and equivalent Von Mises stresses, and σ_{xx} , σ_{yy} and σ_{zz} are the stresses along x , y and z directions, respectively. Lemaitre [20] proposed another triaxiality parameter defined by Eq. (2):

$$R_v = \frac{2}{3}(1-\nu) + 3(1-2\nu) \left(\frac{\sigma_H}{\sigma_{eq}} \right)^2 \quad (2)$$

This triaxiality parameter is based in the ratio of the hydrostatic stress and equivalent Von Mises stresses, and for practical engineering problems its value is typically between 0 (pure shear) and 5 to 6 in the vicinity of very sharp notches.

A third possible triaxiality parameter h given by Eq. (3) can be derived from the general equilibrium stress equations for a cracked body:

$$h = \frac{\sigma_{zz}}{\nu(\sigma_{zz} + \sigma_{zz})} \quad (3)$$

where ν is the Poisson's ratio. h has the values of 1 and 0 for plane strain and plane stresses, respectively.

The main objective of this paper is to propose plane strain specimen geometry adequate for studies of high temperature fatigue crack growth and plasticity crack closure, among other phenomena. The effect of lateral notches on stress triaxiality is studied for different specimen geometries. Stable crack shapes are obtained and used to come to closed-form solutions for stress intensity factor.

2. NUMERICAL PROCEDURE

Fracture mechanics parameters and fatigue crack propagation were obtained from different numerical simulations based in two FEM codes: ABAQUS® v6.5 and ZENCRACK® v7.5. The first software was used to create the physical model and to obtain the visualization of the output parameters, whilst the latter was specifically oriented to generate a proper finite element mesh in the vicinity of the crack using pre-defined crack blocks. Stress intensity factor K for different crack front positions was also determined from ZENCRACK® based on the relative displacements derived from an orthogonal set of axes at each crack front node.

The geometry of the Middle-Tension, M(T), specimen considered for the FEM analysis is presented in Figure 1. All simulations were based in the same general dimensions of this specimen: 200x50x10mm (lengthxwidthxthickness). The geometric features of the lateral notches are indicated in Table 1.

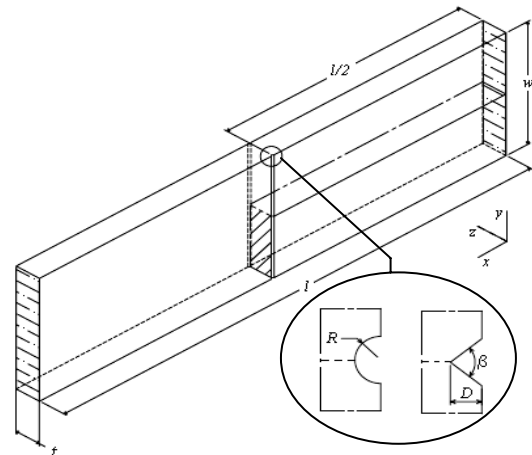


Figure 1 – Geometry of the M(T) specimen (D – Depth, R – Radius, β – Angle)

The material used in this study is a high specific strength structural aluminum alloy (6082-T6) with homogeneous and isotropic characteristics, and its main mechanical properties are indicated in Table 2.

Figure 2 shows the loading and boundary conditions applied to the specimen. A maximum distributed load of 5000 N was considered for all cases, which corresponds to a maximum nominal stress of 10 MPa. Due to symmetry conditions of both the specimen and loading, only $1/4$ of the specimen was assumed in the analysis.

Symmetry boundary conditions were also applied to the crack plane points, excluding those of the crack propagation zone which had no constraints to allow for the crack opening. Additionally, other displacement constraints were considered as follows:

1. x direction restriction in the vertical plane of symmetry (except for the crack points);
2. y direction restriction in the horizontal plane of symmetry;
3. z direction restriction in the remaining surfaces by using 2 degrees of freedom (x and y directions).

Table 1 – Notch dimensions: R , β , D

Dimensions [mm]		
R	β	D
0.5	-	-
0.75	-	-
1	-	-
0.75	-	0.5
1	-	0.5
-	30°	0.5
-	60°	0.5
-	90°	0.5
-	120°	0.5

Table 2 – Mechanical properties of aluminum alloy 6082-T6

Yield stress	307±2.7 MPa
UTS	330±2.5 MPa
Young modulus	74×10 ³ MPa
Poisson coefficient	0.33
Vickers hardness	100 kgf/mm ²

The finite element mesh was implemented using isoparametric elements with 20 nodes and full integration. Crack tip elements must incorporate a singularity in their formulation, which can be correctly represented by using a collapsed isoparametric “quarter-point” element. Finally, standard crack-blocks from ZENCRACK® were used to create the mesh of elements in the crack front. All of these blocks have a spider web shape allowing for a smooth transition between the crack front region, where a higher mesh refinement is recommended, and the remote regions of the specimen.

A special caution was driven towards the number of contours in each crack-block for K determination purposes. In fact, the number of contours must be high enough to allow for the convergence of the value of the stress intensity factor in a particular position in the crack front. In this case, it was found that the use of crack-blocks with 6 contours was enough to accomplish this requirement.

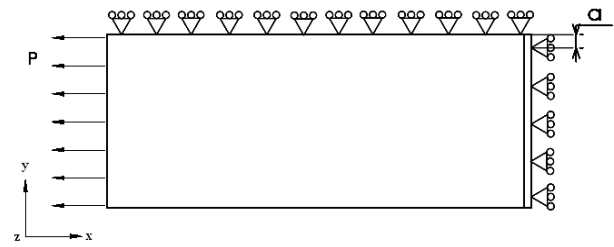


Figure 2 – Loading and boundary conditions.

3. RESULTS AND DISCUSSION

As previously mentioned, one major goal of this work is to evaluate the effect of different types of notches (dimensions and geometries) on the value of the stress intensity factor for distinct crack front positions in a M(T) specimen. Figure 3 shows the distribution of K considering four types of notches: V-notch (with $\beta=30^\circ$ or $\beta=60^\circ$), circular (with $R=0.5\text{mm}$) and elliptical ($R=0.75\text{mm}$ and $R'=0.5\text{mm}$). In all cases, a 10mm width specimen with a crack of 1mm was considered.

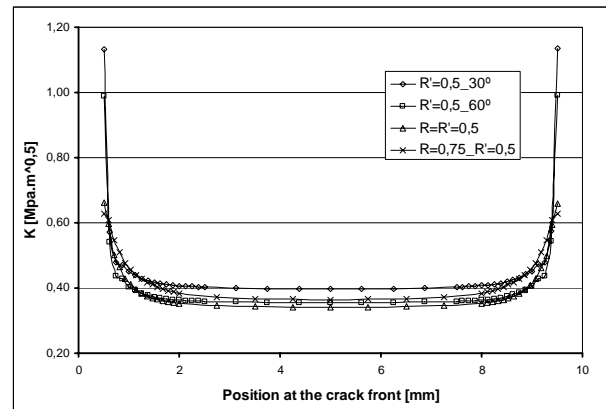


Figure 3 – Variation of the stress intensity factor K for different positions at crack fronts with 1mm.

From this figure, it is clear that the steep stress gradients induced by all notches results in a substantial increasing of the stress intensity values near the surface of the specimen, i.e., in the vicinity of the notch root. However, this effect is more evident for the case of the V-notches, particularly with $\beta=30^\circ$, since this geometry leads to the highest stress concentration factors. On the opposite side, the smallest values of K were obtained for the circular or elliptical notches, which means that these geometries are less severe in terms of stress distribution.

The triaxility effect induced by notches was evaluated for two distinct situations: with and without crack. Stress triaxility was quantified using the parameters defined by Equations (1) and (3), namely Θ and h . All situations were based in two types of geometry of notches: V-notch and circular.

Figure 4 illustrates the variation of both parameters h and Θ along half width of a non-cracked M(T) specimen with two circular lateral notches ($R=0.5\text{mm}$).

As one can see, these two parameters show a similar behaviour, which is characterized by a significant increase of its values towards the surface of the specimen and near the root of the notch. In this region, $h \rightarrow 1$ confirming the influence of the notch for the occurrence of strain plane conditions.

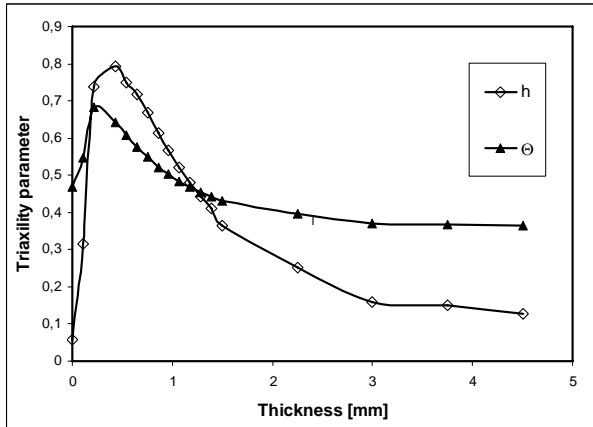


Figure 4 – Variation of parameters h and Θ along half width of a non-cracked $M(T)$ specimen with two circular lateral notches ($R=0.5\text{mm}$)

Since h and Θ evince similar qualitative behaviours regardless the type of notch geometry, all subsequent results will be based only in the analysis of the variation of h along the width of the specimen.

Figures 5 and 6 present the profile of the stress triaxiality parameter h considering the effect of a circular notch with different radius ($R=0.5\text{mm}$, $R=0.75\text{mm}$ and $R=1\text{mm}$) and a V-notch with variable angle ($\beta=15^\circ$, $\beta=30^\circ$, $\beta=45^\circ$ and $\beta=60^\circ$), respectively. From these figures, it is clear that there is a peak of the stress triaxiality parameter for both types of notch geometries near the root of the notch. At the same time, the reduction of either the notch radius (circular notch) or β angle (V-notch) results in a considerable increase of h , which assumes a value close to unity in the case of sharper V-notches (i.e. with smaller β). This means that this type of notch geometry is more effective for obtaining triaxiality stress conditions near the surface of the specimen. However, it is interesting to note that the use of circular notches leads to a larger extension of the zone of influence of the notch, which means higher values of h towards the interior of the specimen. This effect is particularly visible in the case of the circular notch with $R=1\text{mm}$.

The thickness of the specimen is another important variable with a notorious effect in the triaxiality of stresses. Figure 7 shows the variation of the triaxiality parameter h considering the effect of the alteration of the thickness for a specimen with a circular notch geometry ($R=1\text{mm}$). The results clearly show that thinner specimens have a larger region under triaxiality stress conditions, which can be concluded from the smaller variation of h from the notch root towards the

interior of the specimen. Thus, for experimental testing of components under plane strain conditions, it is important to choose the right combination between the type of notch to be used (in terms of geometry and dimensions) and the specimen's thickness.

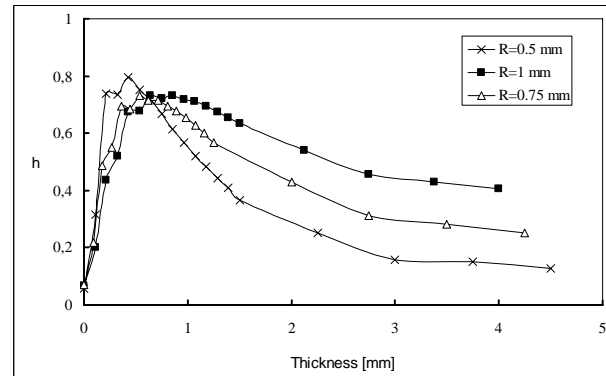


Figure 5 – Variation of triaxiality parameter h considering the effect of a circular notch with different radius ($R=0.5\text{mm}$, $R=0.75\text{mm}$ and $R=1\text{mm}$).

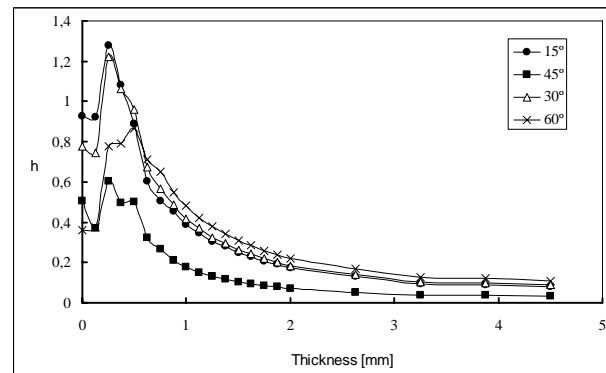


Figure 6 – Variation of triaxiality parameter h considering the effect of a V-notch with variable angle ($\beta=15^\circ$, $\beta=30^\circ$, $\beta=45^\circ$ and $\beta=60^\circ$).

As discussed in Chapter 1, the possible use of a thin specimen under plane strain conditions is determinant for the experimental investigation of certain types of phenomena, such as high temperature crack propagation. Consequently, the evaluation of triaxiality effects due to presence of notches in a cracked specimen is of utmost importance.

Figure 8 illustrates the variation of the triaxiality parameter h for two types of geometries of notches: circular ($R=0.5\text{mm}$) and V shaped ($\beta=60^\circ$, $\beta=90^\circ$ and $\beta=120^\circ$). For comparative purposes, the profile of h for a specimen without lateral notches is also indicated. All the results were obtained for a crack extension of 5mm .

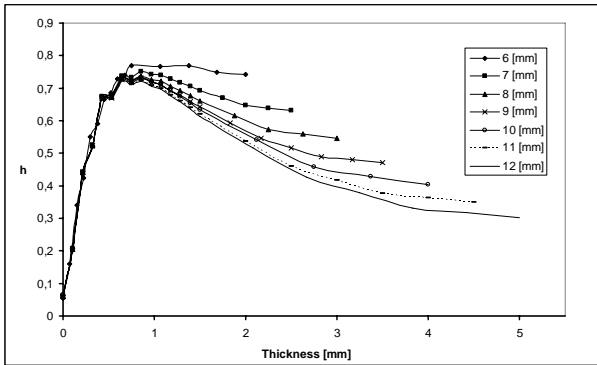


Figure 7 – Variation of the triaxility parameter h considering the effect of the alteration of the thickness for a specimen with a circular notch geometry ($R=1mm$)

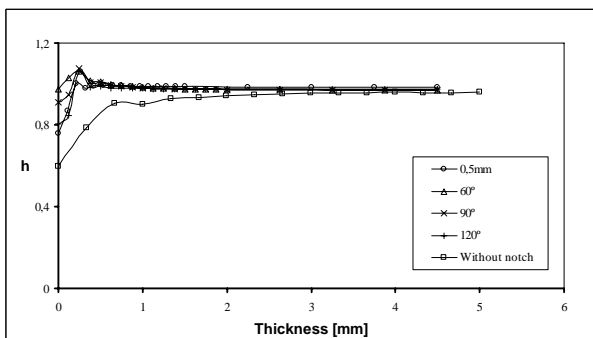


Figure 8 – Variation of the triaxility parameter h for two types of geometries of notches: circular ($R=0.5mm$) and V shaped ($\beta=60^\circ$, $\beta=90^\circ$ and $\beta=120^\circ$).

The observation of these curves allow to conclude that there is a significant effect of the notches, regardless its geometry, for obtaining a triaxility state near the surface of the specimen. Nevertheless, the presence of a crack front by itself is a promoting factor for the existence of high values of triaxility in almost all the thickness of the specimen, even without the presence of any type of lateral notches. Additionally, the triaxility effect of the V-notches is slightly higher for those crack front positions near the surface of the specimen. However, both types of geometries of notches (circular and V shaped) have very similar h values regarding the rest of the specimen's thickness. Considering the fact that a perfect sharp notch is difficult to obtain in real conditions, these results show that the use of a circular notch is a good trade-off between the easiness of fabrication of the specimen and the existence of plane strain conditions in all the positions of the crack front, which is the main goal of this work.

4. CONCLUSIONS

This preliminary work is intended to evaluate the possible use of a standard M(T) specimen geometry under plane strain conditions to investigate certain types of phenomena, such as high temperature crack propagation. From the computational results, some main conclusions can be highlighted:

- There is a clear effect of the stress concentration region induced by the presence of lateral notches, regardless its geometry. This effect results in a substantial increase of the stress intensity factor near the notch root;
- V-shaped notches have a stronger triaxility effect when compared with circular notches, which is reflected in higher values of the triaxility parameters (Θ and h) in positions near the surface of the specimen. However, the use of circular notches leads to higher values of the triaxility parameters in the interior of the specimen;
- The thickness of the specimen has a strong influence in the variation of the triaxility parameters. Thinner specimens with lateral notches are characterized by having a nearly constant value of the triaxility parameters from the surface positions towards the interior of the specimen;
- The use of either circular or V-shaped lateral notches in a standard M(T) specimen with a fatigue crack allows for its propagation under plain strain conditions in all positions of the crack front.

5. RERERENCES

[1] G.A. Webster and R.A. Ainsworth; “High Temperature Component Life Assessment”; Ed. Chapman & Hall, UK; 1994.

[2] H. Ghonem, T. Nicholas and A. Pineau; “Elevated Temperature Fatigue Crack Growth in Alloy 718- Part II: Effects of Environmental and Material Variables”; Fat. and Fract. of Eng. Materials and Structures, 16, 6; Elsevier; 1993; 577-590.

[3] F.V. Antunes, J.A.M. Ferreira, C.M. Branco e J. Byrne; “Influence of stress state on high temperature fatigue crack growth in Inconel 718”; Fatigue and Fracture of Eng. Materials and Structures 24; Elsevier; 2001; 127-135.

[4] Elber W.; “Fatigue crack closure under cyclic tension”; Eng. Fracture Mechanics, 2; 1970; 37-45.

[5] Antunes FV, Rodrigues DM.; “Numerical simulation of plasticity induced crack closure: Identification and discussion of parameters”; Engng Fracture Mech, 75; 2008; 3101–3120.

[6] R.C. McClung, B.H. Thacker, S. Roy; “Finite element visualization of fatigue crack closure in plane stress and plane strain”, Int. J. Fracture, 50; 1991; 27-49.

[7] Riemelmoser, F.O. and Pippan, R.; “Plasticity-Induced Crack Closure Under Plane Strain Conditions in Terms of Dislocation Arrangement”; Proc. of 6th International Fatigue Congress, Berlin, Germany; Ed. by G. Lütjering and H. Nowack; 6-10 May; 1996.

[8] BS 6835-1 : 1998 – “Method for the determination of the rate of fatigue crack growth in metallic materials”; BSI; London, UK; 1998.

[9] ASTM 647 - 95 a – “Standard test method for measurement of fatigue crack growth rates”; ASTM International; West Conshohocken, USA; 1995.

[10] E .N. Brown, R. S. White and N. R. Sottos; “Fatigue crack propagation in microcapsule toughened

- epoxi*"; Journal of Materials Science, 41, 19; 2006; 6266-6273;
- [11] G. Lin, A. Cornec and K.-H. Schawalbe; "*Three-dimensional finite element simulation of crack extension in aluminium alloy 2024FC*"; Fatigue and Fracture of Engineering Materials and Structures, 21; 1998; 1159-1173.
- [12] A. Carpinteri, R. Brighenti and S. Vantadori; "*Surface cracks in notched round bars under cyclic tension and bending*"; International Journal of Fatigue, 28; 2006; 251-260;
- [13] Lin XB, Smith RA.; "*Shape evolution of surface cracks in fatigued round bars with a semicircular circumferential notch*"; International Journal of Fatigue, 21; 1999; 965-973.
- [14] Lin XB, Smith RA.; "*Fatigue growth simulation for cracks in notched and unnotched round bars*"; International Journal of Mechanical Sciences, 40; 1998; 405-419.
- [15] A. Carpinteri, R. Brighenti and S. Vantadori; "*Circumferentially notched pipe with an external surface crack under complex loading*"; International Journal of Mechanical Sciences, 45; 2005; 1929-1947
- [16] G. Mirone; "*Role of stress triaxiality in elastoplastic characterization and ductile failure prediction*"; Engineering Fracture Mechanics, 74; 2007; 1203-1221
- [17] W. Shen, L.H. Peng, C.Y. Tang.; "*An anisotropic damage-based plastic yield criterion and its application to analysis of metal forming process*"; International Journal of Mechanical Science, 47; 2005; 1897-1922;
- [18] S. Chandrakanth and P. C. Pandey; "*An Isotropic Damage Model for Ductile Material*"; Engineering Fracture Mechanics, 50, 4; 1995; 457-465;
- [19] B. S. Henry and A. R. Luxmoore; "*The Stress Triaxiality Constraint and the Q-Value as a Ductile Fracture Parameter*"; Engineering Fracture Mechanics, 57, 4; 1997; 375-390;
- [20] Lemaitre J.; "*A Course on Damage Mechanics*"; Springer; New York; 1996.

NANOINDENTATION INDUCED SILICON FRACTURE AND 3D MODELLING

J. Garagorri¹, E. Gorostegui-Colinas¹, M.R. Elizalde¹, D. Allen², P. McNally²¹CEIT and TECNUN (University of Navarra). Manuel de Lardizábal 15, 20018 San Sebastián, Spain
E-mail: jgaragorri@ceit.es, egorostegui@ceit.es²Dublin City University, Research Institute for Networks and Communications Engineering, Dublin 9, Ireland

ABSTRACT

Wafer handling during the manufacturing process introduces micro-cracks and flaws at the wafer edge. Some of these grow into larger cracks during thermal treatment, which can result into wafer breakage, disrupting manufacture. A study of the morphology of the defects and the stress regimes around these micro-cracks is necessary in order to derive quantitative and predictive information to avoid catastrophic failure.

In order to reproduce mechanical damage during wafer handling, controlled damage by nanoindentation has been carried out on initially defect free square Si samples. The samples have been cleaved from 300 mm double side polished silicon wafers and loads between 75 and 150 mN have been applied using a Berkovich diamond tip. Cross-sectional FIBbing has been done in order to characterise the crack systems present under the indents, and Raman measurements have been performed to evaluate the residual stress profile after damage generation.

At the same time, 3D FE modelling has been developed to reproduce the indentation process in a small piece of silicon. Anisotropy has been introduced through elastic constants and isotropic plasticity has been also considered. Two types of simulations have been developed. On one hand, the simplest ones describe just the indentation process, where no crack evolution has been modelled. The Raman spectrum obtained from these simulations is in accordance with the experimental results. On the other hand, cohesive planes have been introduced in the positions where cracks should be developed, according to cross-sectional observations. This implemented model can simulate the evolution of cracks in the material.

KEYWORDS: Silicon, fracture, nanoindentation, FEM, cohesive zone model, FIB, Raman.

1. INTRODUCTION

The up-scaling in the size of silicon wafers in semiconductor industry generates a compromise between the benefits of enhancing the production of devices for micro electro-mechanical (MEM) and electronic applications, and the difficulties related to gravitational effects and thermal stresses on the wafers during manufacturing [1].

Every wafer diameter transition has introduced problems in high-temperature processing. Radial temperature gradients associated with larger wafer diameters cause greater stress in the wafer during heat up and cool down cycles. If the stress exceeds the yield stress of the silicon, slip can form in the wafer [2]. These defects generated during thermal treatments can cause loss of yield performance and reliability in the device. In addition to this, if there already exists surface and sub-surface extended damage in the edge due to wafer handling and shipping, thermal stresses can even induce catastrophic breakage and, subsequently, the need to stop and clean the production line at a great

cost, which is estimated in €2.5 M per year for each silicon fabrication line in the world [3].

The aim of this paper is to describe the techniques used to reproduce and characterise the damage in silicon wafers so as to obtain a source of realistic information in order to be able to simulate stress fields and fracture in this material. In particular, FEM simulation technique has been used in order to characterize the stress fields around indentations with a Berkovich tip. Two types of simulations have been considered. The first ones account just for the stress field around the indent, while the second one goes further trying to model how fracture is initiated under the indentation and its evolution during the process.

2. EXPERIMENTAL

In order to reproduce the damage introduced during wafer handling in real processes, controlled damage by nanoindentation has been carried out on initially defect free square Si samples at CEIT. The samples have been cleaved from a (100) oriented 300 mm double-side

polished (DSP) silicon wafer. Loads between 75 and 150 mN have been applied at rates of 10 mN/s, using a Nanoindenter® II (Agilent, formerly Nano Instruments Inc.) with a Berkovich diamond tip. The indents have been oriented so that one of the imprint sides is parallel to [110] direction. The arrangement is as shown in Figure 1.

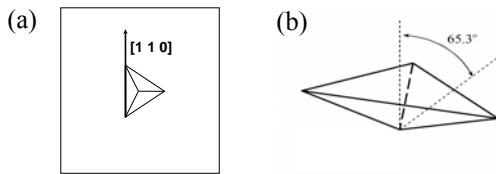


Figure 1. (a) Scheme of the orientation of an indent in a defect free square Si sample. (b) Geometry of the indenter.

A Quanta 3D Dual Beam (FEI) focused ion beam (FIB) has been used for the characterisation of the crack systems under the indents. For this, top-down and cross-section millings have been carried out on indents at different peak loads, and a 3D description of cracks has been obtained from FIB tomography using Amira® 4.0 software.

Micro Raman Spectroscopy (μ RS) has been performed at Dublin City University with a Jobin-Yvon LabRam HR800 Raman microscope to evaluate the residual stress profile generated by the indents. This experimental technique is fully explained in references [4] and [5].

3. SIMULATION

This section is dedicated to the modelling of the indentation process. It is divided in two main parts: in the first one a general description of the model is given, while the second part is left to a more detailed description of the fracture modelling fundamentals.

3.1 Description of the modeling technique

The aim of the FEM simulations that have been designed is to describe the experimental process of indentation. All the models have been run with the finite element method based commercial software ABAQUS® (6.8.3 version).

The indenter chosen has been a Berkovich tip. Its geometry is described in Figure 1. It has been implemented as a rigid part, with no material properties. This point does not affect the model since the real tip is made of diamond, whose Young modulus is much larger than the Young modulus of silicon. As for the meshing, it has been made as coarse as possible in order to have few elements. Linear triangular elements have been used in the construction.

For the piece of silicon to be indented two models have been designed depending on the aim of the simulations. The simplest model consists of a $48 \times 48 \times 96 \mu\text{m}$ piece. It has been designed using a solid deformable part in which elastic anisotropy and isotropic plasticity have been introduced [6]. The central part is meshed using a structured mesh with an element size of $0.25 \mu\text{m}$. This size for the elements is good enough for indents from 150 mN to 250 mN. For higher/lower loads the mesh should be changed to a coarser/finer one, respectively. The rest of the part is meshed much more coarsely. All this can be seen in Figure 2.

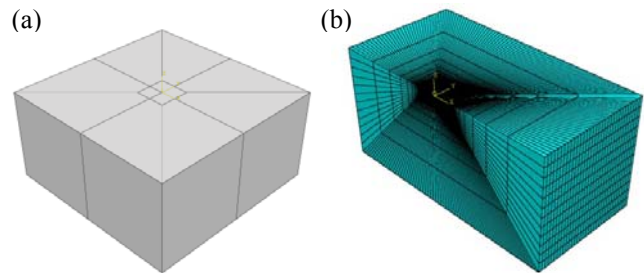


Figure 2. In (a) the geometry of the Si piece to be indented is shown. (b) shows the mesh for for half of the model in the simplest case.

The reason for this election of meshing is simple: the highest deformations appear around the indent. The mesh in this region should be fine enough to account for the correct stress fields and geometry of the indenter imprint. On the rest of the wafer a coarser mesh could be used. As for the election of the size of the Si piece, it is big enough to avoid boundary effects. This type of piece has been used to model just the stress fields during the indentation process.

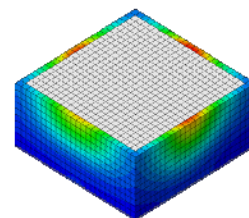


Figure 3. Central part of the big model used to get the correct boundary conditions in the borders for a piece of silicon of this size.

The second type of piece designed has the same geometry but a different technique has been used in order to be able to have a denser mesh with no higher computational exigency. In a first step the model shown in Figure 2(a) is considered with the same type of meshing, but with much bigger elements (being their size of $0.5 \mu\text{m}$). In a second step a piece with the size of the central part is used with a refined mesh and the stresses from the first simulation as boundary conditions (see Figure 3). This allows for a much denser mesh in the piece (the element size is lowered to $0.2 \mu\text{m}$), a highly important issue in order to be able to see the initiation and evolution of cracks, which is the aim of this second model.

The elements of the first models are all hexahedral structured elements. In the second model cohesive elements have been introduced in a vertical plane. This kind of elements allow for the modelling of the initiation and evolution of fracture according to the chosen cohesive law (described in the following section).

3.2 Cohesive elements and fracture

Cohesive elements are a type of special elements that can account for fracture. This kind of elements must be located in the places where fracture occurs experimentally. In the case of silicon, the correct place seems to be cleavage planes. What is more, not in all these planes fracture initiation and evolution is equally developed. This is because the cleavage tension is different in each case. The planes which present the lowest value of this magnitude are $\{1\ 1\ 1\}$ planes, then $\{1\ 1\ 0\}$ and finally $\{1\ 0\ 0\}$ [6]. In the simulations just $\{1\ 1\ 0\}$ and $\{1\ 0\ 0\}$ planes have been considered.

The simulation of fracture initiation and evolution consists of three stages [7]. First a linear elastic traction separation behavior is considered:

$$\vec{t} = K \varepsilon \quad (3.2.1)$$

where $\vec{t} = (t_n, t_s, t_t)$ represents the nominal traction stress vector, $\vec{\delta} = (\delta_n, \delta_s, \delta_t)$ the corresponding separations and finally $\varepsilon = (\varepsilon_n, \varepsilon_s, \varepsilon_t) = (\frac{\delta_n}{t_n^0}, \frac{\delta_s}{t_s^0}, \frac{\delta_t}{t_t^0})$ is the nominal strain.

The second step of the simulation begins when

$$quadsqrt(t_n, t_t, t_s) = \left(\frac{t_n}{t_n^0}\right)^2 + \left(\frac{t_t}{t_t^0}\right)^2 + \left(\frac{t_s}{t_s^0}\right)^2 \quad (3.2.2)$$

reaches the value of 1 in at least one of the elements of the cohesive layer. t_n^0, t_s^0 and t_t^0 represent the peak values of the nominal stresses and t_n^0, t_s^0 and t_t^0 the peak values. This is the moment when damage initiates.

Finally, damage evolution, the propagation of the crack, is described by:

$$t_n = \begin{cases} (1 - D)\bar{t}_n & t_n \geq 0 \\ \bar{t}_n & \text{otherwise} \end{cases} \quad (3.2.3)$$

where D is a scalar damage variable that represents the overall damage in the material. The graphical representation of the cohesive law is shown in Figure 4.

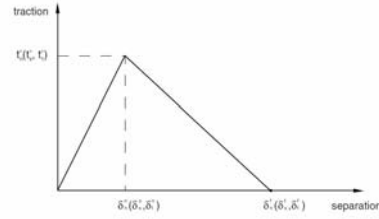


Figure 4. Graphical representation of the cohesive law.

4. RESULTS AND DISCUSSION

4.1 Damage characterization around indents

Direct observation of the crack systems beneath the indents gives an idea of the type and extension of the damage generated by nanoindentation. The micrographs obtained from top-down FIBbing, and shown in Figure 5, suggest a double crack system, i.e., radial and median cracks, coexisting under indents around 100 mN.

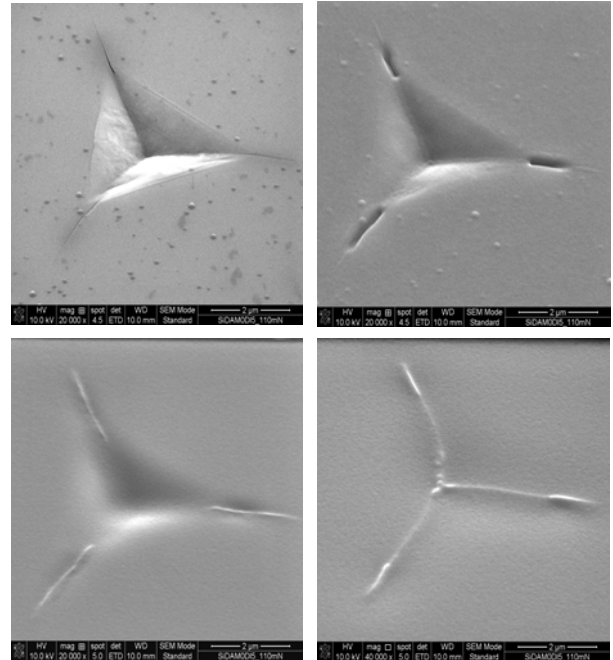


Figure 5. Sequence of FEGSEM micrographs from a top-down FIBbing on a 110 mN Berkovich indent on Si, showing the coexistence of radial (Palmqvist) and median cracks close to the surface, and further development of median cracks under the indenter imprint.

Radial or Palmqvist cracks emerge from the corners of the indenter imprint and have a maximum depth of the order of 0.5 μm . These close-surface cracks have been observed in brittle materials as a result of sharp indenters at low loads [8-11]. Recently, some studies relate the appearance of Palmqvist cracks as the first crack systems to form, reaching their maximum extent upon the unloading [12].

Besides, median cracks -also referred as half-penny cracks when related to Vickers indents- originate

beneath the remaining plastic region under the indenter imprint at higher loads and propagate along the median axis upon the unloading [8].

On the other hand, direct observation through cross-sectional FIBbing allows depicting a different landscape of the damage. In addition to the mentioned crack systems, lateral cracking has been detected under the indenter imprint at peak loads between 120 and 150 mN. According to Figure 6, lateral cracking runs across a region of well oriented dislocations and above the intersection with a median crack. Another example is shown in the 3D reconstruction in Figure 7 where, in addition to the median crack following a vertical (100) plane, a lateral crack is also initiated.

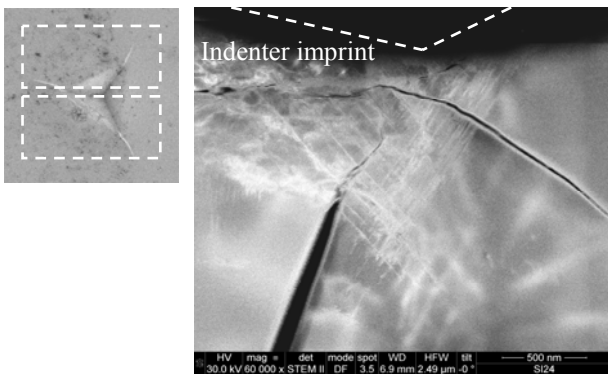


Figure 6. STEM image of a cross-section cut of median and lateral cracks under a 150 mN Berkovich indent on Si.

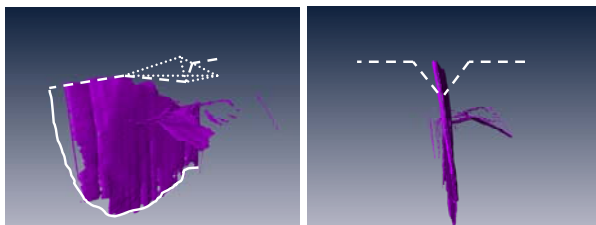


Figure 7. 3D reconstruction from FIB tomography of the median and lateral cracks under a 120 mN Berkovich indent on Si.

4.2 Simulations and comparison with experiments

4.2.1 Nanoindentation Stress Field simulations

The results shown in this section correspond to the simulations run in the first type of silicon piece model. The relative orientation of the Berkovich tip with respect to the material crystal system is shown in Figure 8. Even this simple model accounts well for the stress fields around the indentation. If experimental load-displacement curves are considered, it can be seen (Figure 9) that the predicted loading is equal to the experimental one. Differences appear, however, in the unloading. There are several reasons for these discrepancies. First of all, during the indentation process silicon suffers several phase transformations, which make the material behave differently. In the loading this

is reflected as a small pop-in while in the unloading a pop out appears in the curve. Accounting for the transformation in the loading does not seem to be crucial, since good results have been obtained for this part of the indentation process. However, the expansion that the material suffers in the phase transformation occurring at the unloading appears to change the material behaviour completely, as the simulated curve does not agree with the experimental one. Furthermore, this model does not account for cracks which usually grow up in the unloading and may also affect to the shape of the curve.

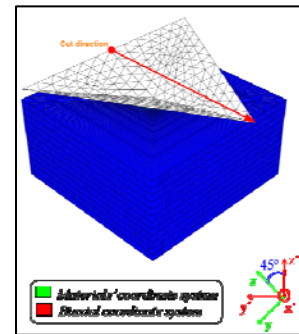


Figure 8. Relative orientation of the crystal axes of silicon and the indenter. The cut direction refers to the line where Raman measurements have been made.

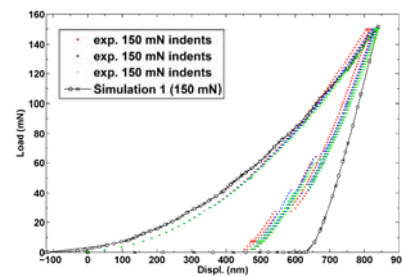


Figure 9. Experimental load displacement curves compared to those obtained with the simple model.

Another way of validating the model is considering the Raman experiments in silicon wafer and comparing the results to the corresponding frequency shifts predicted by the simulations. Details of this experimental technique can be found in references [4] and [5]. First of all, the level of approximation needed for the frequency shift computation must be determined. For this task the stress tensor components in the central uniformly meshed part of the direction line marked in Figure 8 have been plotted in Figure 10. This plot clearly shows that the components σ_{xy} , σ_{yz} and σ_{xz} are negligible, which allows for biaxial approximation. In this approximation the frequency shift observed can be written as in (4.2.1) (stress components must be introduced in MPa) when the considered coordinate system is that of the material and the measurements are made at the top of the sample [5]:

$$\Delta\omega = 1.93 \cdot 10^{-3} \cdot (\sigma_{zz} + \sigma_{xx}) \quad (4.2.1)$$

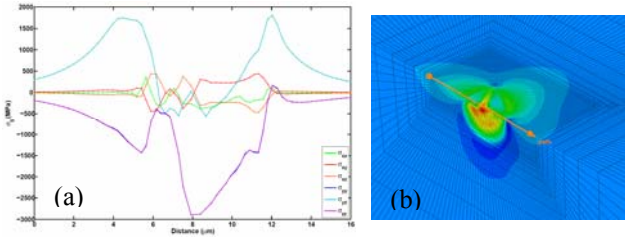


Figure 10. Stress tensor components along the direction marked in Figure 8. Just the central uniformly meshed line highlighted in b has been considered

The results obtained in the simulations agree quite well with the experiments (Figure 11). As happened with the load displacement curves, the discrepancies can be due to the lack of consideration of the phase transformations in the piece of silicon modelled. Furthermore, the resolution of the Raman measurement is limited in the central part of the indent imprint due to the inclined surface.

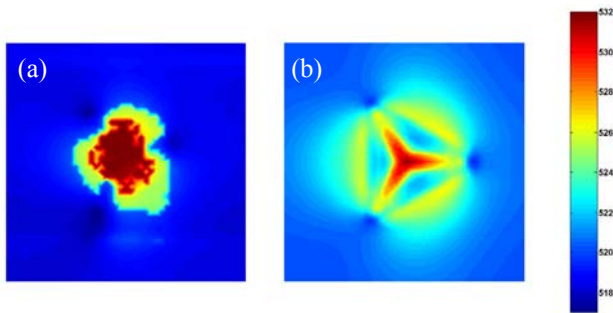


Figure 11. Comparison of the 2D Raman spectrum map (a) obtained experimentally, and (b) the simulation.

4.2.2. Modelling of fracture initiation and evolution in the indentation process

The two cohesive planes considered are a (110) plane (vertical plane) and a (001) plane (horizontal crack) (see Figure 12).

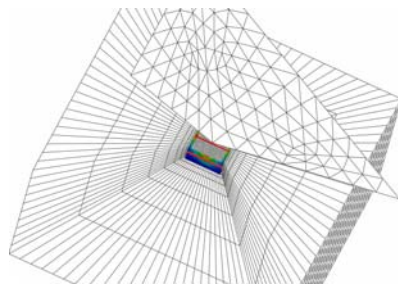


Figure 12. Relative position of the indenter and the vertical and horizontal cohesive layers (the lines are highlighted in red).

First of all, a set of test simulations were performed in the model with a vertical cohesive plane in order to determine the adequate parameters for the cohesive law. According to literature [7], the silicon fracture energy varies between 2 and 4 J/m², depending on the cleavage

plane considered. For the simulations in this paper a value of 4 J/m² has been considered. As for the value of the slope of the cohesive law, it should equal or higher than the average Young modulus of silicon in order to have the same behaviour in the layer and in the rest of the piece. Several simulations have been run with values ranging from 1.87x10⁷ MPa to 12.65x10⁸ MPa (the average Young Modulus for the type of wafer considered is about 1.80x10⁵ MPa). The results indicate that for values above 8.65x10⁸ MPa convergence issues arise. This is why finally for all the simulations the value has been set to 1.28x10⁸ MPa.

Finally, the peak stress has to be determined. Experimentally, cracks appear even for indents of 30 mN. As simulations must respect this fact, a first value of 2000 MPa was considered, noting that cleavage tension is of this order of magnitude. This value has been decreased until the initiation of damage occurred at 30 mN for a value of the nominal stress of 1200 MPa. Table 1 shows some of the attempts.

Table 1. reflect the behaviour of lowering the nominal stress in the cohesive law.

σ_c (MPa)	Load when Quadsqrt=1
1800	120
1600	75
1300	35
1200	31

Damage initiation occurs when *Quadsqrt* (ec. 3.2.2) reaches the value of 1. Figure 13(a) shows the correspondent contour plot for *Quadsqrt* at the instant of initiation of damage at a load of 30 mN. In Figure 13(b) the value of *Quadsqrt* is shown for the same instant of time but with a nominal stress of 1300 MPa. As can be seen, damage has not been generated yet in this second simulation.

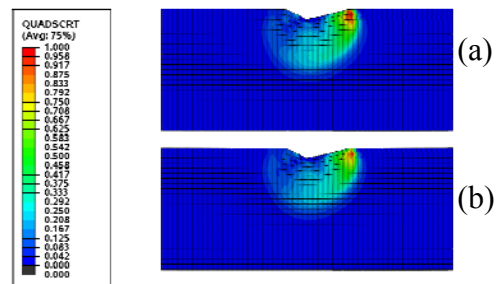


Figure 13. Contour plot of the magnitude quadsqrt for simulations with $Y=1.28 \times 10^8$, $G=4 \text{ J/m}^2$. Their difference relies in the value of the nominal stress: 1200 MPa for (a) and 1300 MPa for (b).

Once damage is initiated the damage extent is represented by SDEG, a scalar variable which varies from 0 to 0.8. Every element that reaches this value is deleted, and hence fracture propagation can be easily observed. In Figure 14 a contour plot of this magnitude is shown (a) at maximum indentation load and (b) after the indentation unload. The results indicate that during

unloading of the indentation process fracture continues propagating. The shape of the crack agrees qualitatively with experimental results. It should be noted that the maximum indentation load reached during the simulations is 75 mN. More simulations are needed to fit quantitatively the crack size measured.

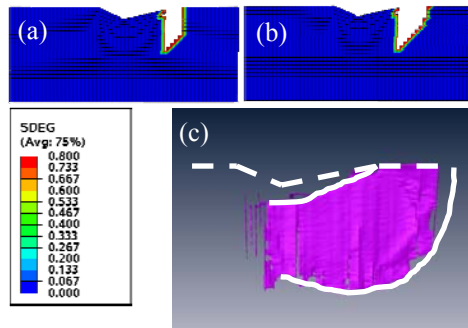


Figure 14. Vertical cohesive plane. The scalar magnitude SDEG, which is a measure of the generated damage, at (a) maximum indentation load and (b) after the indentation process. (c) is a 3D reconstruction of a vertical real crack in the same plane.

For the simulations with a horizontal cohesive plane at a distance of 1µm from the surface, a (001) plane, using the same cohesive law parameters as in the previous simulation the damage generated is almost none: *Quadsrt* is equal to 2×10^{-4} at maximum load and to 0.66 after unloading. This result indicates as well that cracks evolve during the unloading of the indentation process. It is noticeable that this result matches the experimental observations, since horizontal cracks are not observed for indents performed below 120 mN. In fact the cleavage tension of (001) planes is much higher, which is an indication of a different response of the {100} planes compared to the {110} family.

Finally, another simulation was made in order to get fracture in this plane. The nominal stress was lowered to 600 MPa. The results of this simulation are shown in Figure 15. In this case at maximum indentation load damage is again negligible but during unloading damage initiates. However, fracture is not achieved. It should be noticed that the position of the horizontal plane is fixed and could not be the most appropriate for damage to occur.

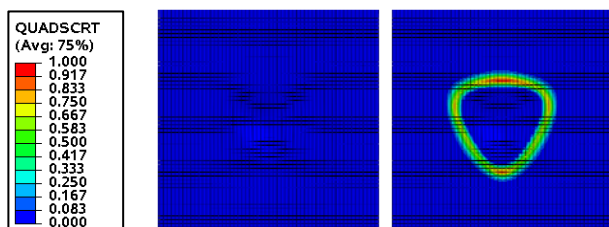


Figure 15. *Quadsrt* in the horizontal plane at maximum indentation load of 75 mN and after the unloading. The peak stress of the cohesive law was 600 MPa. No cracks appear.

5. CONCLUSIONS

First of all, the simulated stress fields agree well with Raman measurements around the indents, even though no phase transformation nor fracture are implemented in the FEM models.

Fracture simulation first attempts with cohesive elements show that the vertical model seems to be well designed since the initiation and initial evolution agrees with experiments. However, more simulations are needed in order to calibrate the cohesive law parameters to match experimental results quantitatively. In the case of the horizontal crack model the situation of the plane is another parameter to consider. In this case information from 3D FIB tomography reconstruction will be very helpful.

Finally, the fact that small values of nominal stress are required to fit the simulations with the experimental results is probably related with the brittle fracture of silicon and the cleavage stresses.

6. REFERENCES

- [1] K.C. Cho, H.T. Jeon, J.G. Park, J. of the Korean Physical Society, Vol. 46, No. 4 (2005), pp. 1001-1006.
- [2] W. Murray Bullis, Mat. Sci. and Eng. B72 (2000), pp. 93–98.
- [3] International SEMATECH Manufacturing Initiative, Industry Economic Model v8.1ss 2004.
- [4] IEEE Transactions on components and packaging technologies, Vol. 28, No. 3, 2005.
- [5] D. Allen, J. Wittge, et al. 2009, Nuclear Instruments and Methods in Physics B, DOI: <http://dx.doi.org/10.1016/j.nimb.2009.10.174>
- [6] F. J. Morin, J. P. Maita, Phys. Rev. 96, 1 (1954), pp. 28-35.
- [7] International Journal of Fracture 155 (2009), pp. 67-74.
- [8] Y. Tang, A. Yonezu, N. Ogasawara, N. Chiba, X. Chen, Proc. R. Soc. A 464 (2008), pp. 2967-2984.
- [9] F. Tancret, Scripta mater. 43 (2000), pp. 9–14.
- [10] T. Lube, Journal of the European Ceramic Society 21 (2001), pp. 211-218.
- [11] M. Manoharan, G. Muralidharan, Journal of Materials Science: Materials in Electronics 13 (2002), pp. 39-41.
- [12] K. Nihara, Journal of Materials Science Letters 2 (1983), pp. 221-223.

ACKNOWLEDGEMENTS

The authors want to acknowledge the European Commission for its financial support through SIDAM project (FP7-ICT-216382).

NUMERICAL MODELING OF THE DYNAMIC COMPRESSION OF A CLOSED-CELL ALUMINUM FOAM

I. Irausquín ^{1,2}, F. Teixeira-Dias ³, V. Miranda ³, J.L. Pérez-Castellanos ¹

¹ Departamento de Mecánica de Medios Continuos y Teoría de Estructuras,
Universidad Carlos III de Madrid, Av. De La Universidad 30,
28911 Leganés, España.
E-mail: iirausqu@ing.uc3m.es

² Departamento de Tecnología Industrial,
Universidad Simón Bolívar, AP 89000,
Caracas 1080, Venezuela.

³ Departamento de Engenharia Mecânica,
Universidade de Aveiro, Campus Universitário de Santiago,
3810-193 Aveiro, Portugal

ABSTRACT

This research has been focused in study the compression behavior of a closed-cell aluminum foam, by means of the implementation of an isotropic hardening model contained in the finite element code ABAQUS. The dynamic compression of the material was simulated according to the procedure of split Hopkinson pressure bar (SHPB) tests, for strain rates of approximately 10^3 seg^{-1} . Steel and two different low impedance materials have been considered for the striker and the incident and transmitter bars, in order to evaluate the reliability of these materials to characterize the foam. Influence of both the composition and the dimensions of the bars on the resulting strain waves has been analyzed. These results have been useful to realize the proper material of the bars to be used during the SHPB test of the selected metal foam as well as establish the suitable dimensions that must have the equipment used in this task.

KEY WORDS: High strain rate, finite element method, cellular material, Nylon and PMMA bars.

1. INTRODUCTION

Aluminum-based metal foams have recently shown interesting properties for several industrial applications, most of them related to structures with high energy absorption capacity. Despite this fact its broader use has been limited by the lack of information regarding their mechanical behavior at high strain rates and the variability that these usually exhibit, even under quasi-static loading, mostly due to their inadequate characterization [1].

Because of its morphology and properties the metal foams can not be studied by several standard dynamic experimental techniques [2]. One of the dynamic tests that can be carried out on these materials and can provide complete stress-strain data of them as a function of the strain rate is the split Hopkinson pressure bar (SHPB) test. Since its introduction by Kolsky [3] such technique has been widely used to determine the dynamic properties of numerous engineering materials; like ferrous and non-ferrous alloys, polymers, ceramics, and concrete. Nevertheless, as well as many other soft materials, metal foams have a low mechanical impedance which makes them unsuitable for the

conventional SHPB test [2,4,5], shown in Figure 1 and usually conducted by means of cylindrical steel bars. For such reason in the literature has been reported the use of some variants of the test in a search for attain reliable dynamic data of the foams [6,7]. Bars made from low impedance materials, primarily PMMA and Nylon [2,4,5,7,8,9], have also been used, owing to their ability increasing the sensitivity of the testing device.

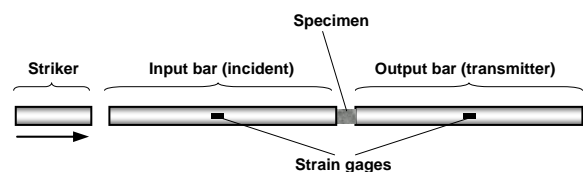


Figure 1. Scheme of the conventional SHPB test arrangement.

The absence of purely elastic materials made PMMA and Nylon a suitable viscoelastic option for the analysis of metal foams, hence, advantage should be taken of them with the intention of allow carrying out the conventional SHPB for cellular materials, either by

experimentation or by numerical modeling through the finite element method (FEM).

In the present study was performed the numerical modeling of a closed-cell aluminum foam under conventional SHPB test conditions for three different materials, so as to determine the most appropriate of them to allow the dynamic testing of the foam and provide a well defined pulse with sufficient amplitude. Likewise three different lengths of the striker and diameters of the bars have been modeled with the aim of establish the appropriate dimensions that these must have. In addition, several impact velocities were assigned to the striker to estimate the range of strain rates that can be achieved by means of this testing. All modeling has been held with the aid of FEM-based software.

2. MATERIALS

2.1. Metal foam

Alporas foam was acquired as reference material for the modeling, owing to its wide information regarding geometry and mechanical properties. This closed-cell foam is produced by Shinko Wire Co. (Japan), through a batch casting process via stabilizing gas bubbles in an aluminum melt. The nominal chemical composition of the foam is Al-1.42Ca-1.42Ti-0.28Fe-0.007Mg (wt. %). Relative density (ρ^*/ρ_s) of the foam has been measured in six specimens and the average was estimated around 0.1 (10%).

Knowledge of the quasi-static compression curve has been important to the study, because it is helpful as basis of the constitutive model to be implemented for the Alporas in the computational code.

To determine the quasi-static response of the foam, four prismatic specimens were cut having a square cross section of about 40 x 40 mm and a height of about 60 mm (Fig. 2) and then uniaxially compressed in a servohydraulic testing machine Instron 8516 at a cross head speed of 1 mm/min. This compression of the foam specimens was carried out up to approximately 70% of their nominal strain. Mean stress-strain curve obtained for the foam is shown in Figure 3. Respective strain rate was $3 \cdot 10^{-4} \text{ s}^{-1}$.



Figure 2. Alporas specimen for quasi-static compression ($\rho^*/\rho_s = 0.1$).

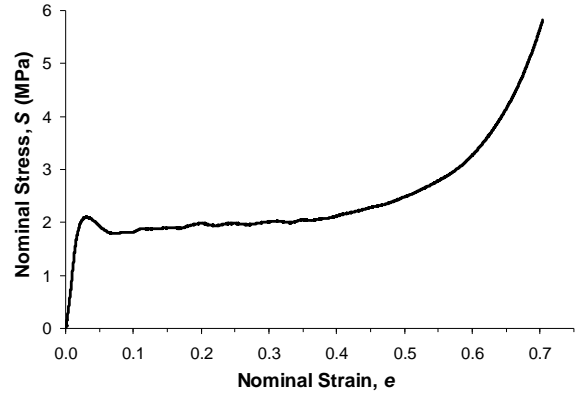


Figure 3. Stress-strain curve from quasi-static compression of the aluminium foam (Alporas 10%).

In the following table (Table 1) are summarized the most important mechanical properties of the mentioned Alporas, some of them achieved from the stress-strain data shown in Figure 2. These properties are the Young’s modulus (E), the yield stress at 0.2% of the total strain (σ_y), the compressive strength (σ_c), the plateau stress (σ_{pl}) and the densification strain (ϵ_D).

Table 1. Compressive mechanical properties of the aluminum foam (Alporas 10%).

E (GPa)	σ_y (MPa)	σ_c (MPa)	σ_{pl} (MPa)	ϵ_D (%)
1.1	1.86	2.17	1.95	60

Both relative density and mechanical properties were similar to that reported by Mukai *et al.* [10].

2.2. Bars composition

Steel and two (2) low impedance materials have been considered for the striker (projectile) and for the incident (input) and transmitter (output) bars with the aim of evaluate the sensitivity of the arrangement with each material, in terms of the incident and transmitted strain waves. Low impedance materials where PMMA and Nylon, which have been used in previous work for characterization of cellular materials at high strain rates [2,4,5,7,8,9]. Main properties of these materials used for the analysis are listed in Table 2.

Table 2. Properties of the materials considered for the striker and the input and output bars.

Material	Density, ρ (kg/m^3)	Young’s modulus, E (GPa)	Poisson’s ratio, ν	Elastic wave speed, C (m/s)
Steel	7850	205	0.30	5110
PMMA	1190	3.4	0.35	1690
Nylon	1130	3.0	0.33	1625

3. FEM MODELING

3.1. Constitutive model for the foam

The modeling of the dynamic compression of the metal foam in accordance with the split Hopkinson pressure bar (SHPB) test was accomplished by means of the computational program ABAQUS 6.7.5. [11]. Thus, the crushable foam plasticity model contained in the code has been implemented for the Alporas, considering isotropic hardening with associated flow potential, having the form:

$$G = \sqrt{q^2 + \beta^2 \cdot p^2} \quad (1)$$

where p is the pressure stress, q is the Mises stress and β represents the shape of the flow potential envelope and is related to the plastic Poisson's ratio ν_p , according to:

$$\beta = \frac{3}{\sqrt{2}} \sqrt{\frac{1 - 2 \cdot \nu_p}{1 + \nu_p}} \quad (2)$$

Based on the above relationship becomes evident the possibility of include associated plastic flow in the isotropic model providing the value of ν_p , although for many low-density foams such as the Alporas the plastic Poisson's ratio is nearly zero. Having this in mind ν_p was assumed zero. The remaining input parameters of the model, including strain hardening data, were extracted from quasi-static properties aforementioned. The use of quasi-static strain hardening data has been considered an acceptable approximation since few studies available on aluminum-based foams have not revealed significant influence of strain rate on their yield strength [1].

Appointed constitutive model was originally proposed by Deshpande & Fleck [12].

3.2. FE model

Considering the arrangement showed in Figure 1 and taking into account the dimensions of the equipment available in the Mechanical Characterization Lab of the University Carlos III of Madrid, both incident and transmitter bar were modeled with a diameter of 22 mm and a length of 1 m. Likewise, the striker had 330 mm in length and the same diameter. Meanwhile the specimen was 14 mm in diameter and 7 mm in length. The bars and the striker were modeled as elastic materials with the properties listed in Table 2.

An assembly containing all parts (bars, striker and specimen) was modeled using three-dimensional solid 8-node linear brick elements, with reduced integration and hourglass control (C3D8R in ABAQUS library). The bars and the striker had 96 elements in their cross section, whereas the specimen had 320 elements in such

area. Along their length the bars and the striker had 80 and 24 elements, respectively, whereas the specimen had 7 elements. All meshing was structured and in both bars with a little refinement where the gauges were placed and in their ends. Mesh configuration of the metal foam specimen appears in Figure 5, while in turn Figure 6 presents a detail of the model assembly in the region of contact between the specimen and both bars. In the same figure (Fig. 6) may be noted the refinement of the mesh at the ends of the input and output bars.

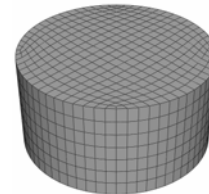


Figure 5. Mesh of the foam specimen model.

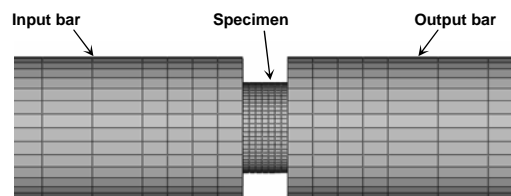


Figure 6. Detail of the model assembly at contact between the specimen and the bars.

The incident velocity of the striker was set to 9 m/s by means of a predefined velocity field. Contacting surfaces were defined as frictionless. Initial boundary conditions were applied to the striker, bars and specimen such that only movement in one direction was allowed. Reference points acting as gauges were placed on input and output bars, specifically to half the length of them, with the purpose of collect incident, transmitted and reflected waves.

Based on the consideration that both bars and the striker must have the same diameter (D), three different relative lengths of the arrangement were also modeled, trying to identify the appropriate dimensions these should possess. Being L_b the length of the bars (same for input and output) and L_p the length of the projectile, previous experimental works concerning SHPB test on metal foams involve relative lengths L_b/L_p ranging from 2 to 6 [5,7,8,9]. Since for the dimensions initially modeled $L_b/L_p = 3$, two changes in the length of striker were introduced so as to obtain additional relative length values of 2 and 5 and then elucidate the effect of this geometrical parameter by examination of resultant transmitted waves. Something similar has been done with the diameter D of the arrangement (i.e. striker and bars), which was modified in terms of a parameter L_p/D . This parameter, representative of the relative size of the striker, typically lies between 3 and 20 [5,7,8,9]. Values of 5, 15 and 20 were then assigned to this parameter with the intention of determine its influence on the longitudinal waves transmission.

Complementing the FE modeling three impact velocities V_p were implemented with the objective of estimate the range of strain rates that can be reached through the original dimensions of set-up. In this sense, such as referred laboratory equipment can reach impact velocities of the striker (V_p) in the range 6-20 m/s, values of 6, 12 and 18 m/s were chosen. Transmitted waves have been recorded in each case and strain rate has been calculated by differentiating in time of the expression developed by Kolsky [3]:

$$\varepsilon_s(t) = -\frac{2 \cdot C_0}{L_s} \int_0^t \varepsilon_r(t) dt \quad (3)$$

where $\varepsilon_s(t)$ is the strain experienced by the specimen, L_s is the length of the specimen, $\varepsilon_r(t)$ is the strain reflected in the input bar and C_0 is the wave velocity within the bars, calculated as:

$$C_0 = \sqrt{\frac{E}{\rho}} \quad (4)$$

being E and ρ the Young's modulus and density of the bars, respectively.

Then, the strain rate during the test has the form:

$$\dot{\varepsilon}_s(t) = \frac{d\varepsilon_s(t)}{dt} = -\frac{2 \cdot C_0}{L_s} \varepsilon_r(t) \quad (5)$$

Plotting the strain rate obtained for each velocity as function of the time t was possible to attain its mean value during the dynamic compression.

3.3. Validation of the SHPB test conditions

In order to verify that the numerical model reliably reproduces the real conditions of the test the following tasks have been accomplished:

- *Lagrange diagram*: A Lagrange diagram has been constructed to confirm that there was no interference in wave propagation during the test.
- *Wave dispersion*: It was corroborated that the dispersion of the wave has not been significant.
- *Uniaxial stress condition*: The uniaxial stress state was verified in the numerical simulations, so that, the hypothesis of one-dimensional elastic wave propagation can be considered.

4. RESULTS AND DISCUSSION

4.1. On the bars material

As result of the SHPB test simulation with ABAQUS of the metal foam ($\dot{\varepsilon} \approx 10^3 \text{ s}^{-1}$) were obtained the incident, reflected and transmitted strain waves shown in Figures

7 and 8, respectively. In both figures is possible appreciate the strain wave found for each material considered in the composition of the bars.

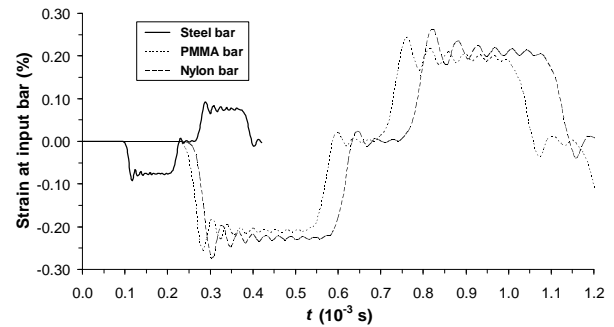


Figure 7. Incident and reflected strain waves obtained from dynamic compression of the metal foam (Alporas 10%) for different material bars.

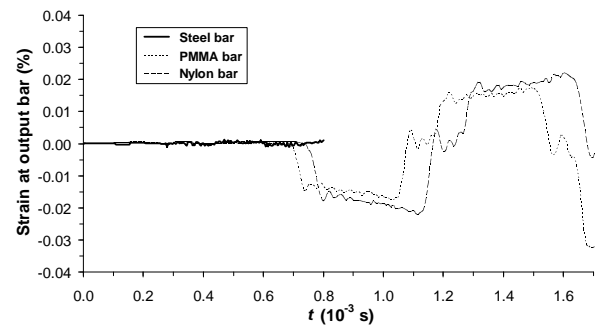


Figure 8. Transmitted strain waves obtained from dynamic compression of the metal foam (Alporas 10%) for different material bars.

Figure 7 clearly shows how the incident wave amplitude in the steel bars is less than a half that achieved in the bars of PMMA and Nylon. The same happened with the wave period. Hence, is possible to infer a difference in the strain wave of the output bars, like can be evidenced in Figure 8. In this figure can be seen that the transmitted wave in the steel bars has no significant amplitude and therefore it is not useful for dynamic characterization of the Alporas. This fact becomes more relevant taking into consideration that the transmitted wave is small compared to the incident and reflected ones, as can be appreciated in Figure 9 for the particular case of PMMA bars. Such figure shows the incident, reflected and transmitted strain waves generated by the striker with a velocity of 9 m/s as obtained from the strain gauges.

From resulting incident and transmitted waves becomes evident that SHPB test either with Nylon or PMMA bars can provide information about the dynamic response of the Alporas, unlike what would happen if conventional steel bars were used. This undoubtedly confirms (as previously reported) their ability for increase the sensitivity of the arrangement during the SHPB test.

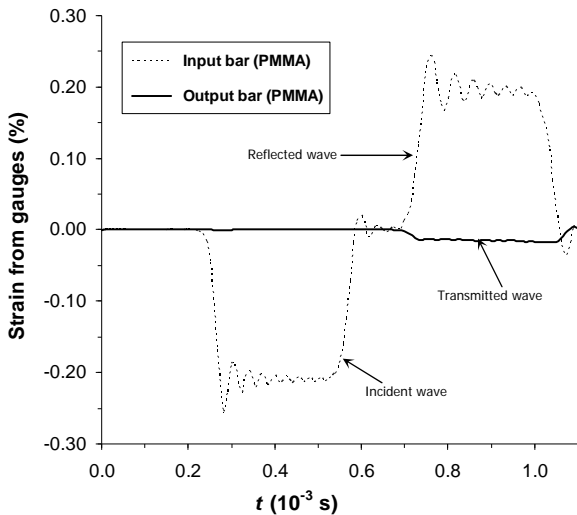


Figure 9. Incident, reflected and transmitted strain waves obtained from dynamic compression of the metal foam (Alporas 10%) for PMMA bars.

Due to its suitability for dynamic modeling of the Alporas and reliability data, the PMMA was chosen as constituent of the bars and striker to accomplish the rest of the numerical analysis.

4.2. On the striker dimensions

In figure 10 are presented the transmitted strain waves corresponding to selected values of the relative length (L_b/L_p) as measured on the strain gauge position. Can be observed that, like ratify the expressions of the one-dimensional theory of waves, if increases the length of the striker, the same happens with the pulse duration and the amount of strain. For the particular case of metal foams this implies that varying the length of striker is possible to conduct the SHPB test on foams with different relative densities (ρ^*/ρ_s) and therefore different crushability.

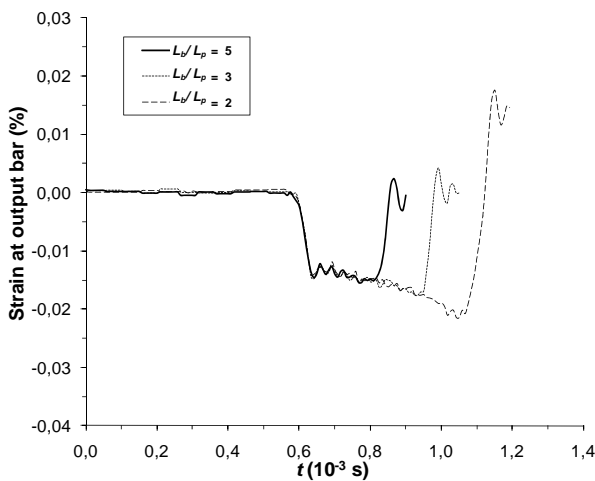


Figure 10. Transmitted strain waves obtained from dynamic compression of the Alporas ($\dot{\epsilon} \approx 10^3 \text{ s}^{-1}$) for PMMA bar at different relative lengths (L_b/L_p).

Knowledge of the relation between the length of striker (L_p) and the pulse period is very useful to choose the proper length for attain a suitable transmitted wave, even more considering that metal foams usually transmit a pulse of reduced amplitude, as was proved before.

Concerning relative size of the striker, L_p/D , figure 11 shows transmitted waves obtained on the output bar (at strain gauges) for all three values of this parameter. In the figure can be noted that by decreasing the diameter (D) of the bars increases slightly the pulse period and significantly the strain. For this reason can be argued that length of the striker, L_p , is the geometrical parameter most important for dynamical testing of metal foams.

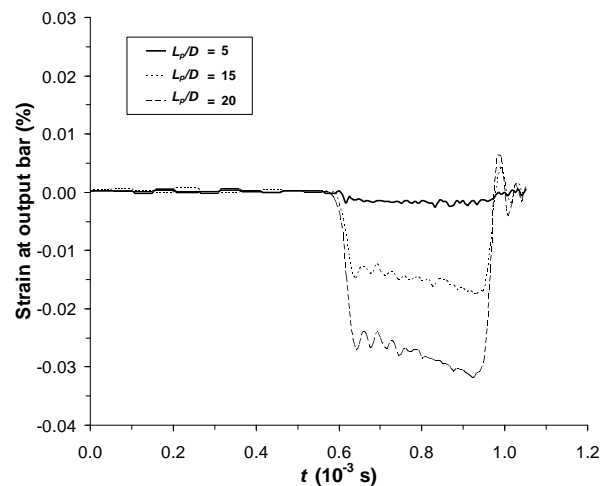


Figure 11. Transmitted strain waves obtained from dynamic compression of the Alporas ($\dot{\epsilon} \approx 10^3 \text{ s}^{-1}$) for PMMA bar at different relative sizes of the striker.

Although the modification of diameter of the bar is not operative for SHPB testing, since it leads to substantial changes in the geometry of the equipment, should be considered because diameter must be as large as to avoid cell size effects on the foam, i.e., at least seven times the cell size [1].

4.3. On the impact velocity

Figure 12 presents the strain rate ($\dot{\epsilon}$) values estimated for all three impact velocities (V_p) through the expression (5) as function of the time (t). It is evident in this figure the strong dependence that has the strain rate with the impact velocity. The curves shown allow distinguish that strain rates are in the range of 500 to 2000 s^{-1} . This data is relevant for testing because allow knowing the suitable impact velocities that can be reached and the range within the user could make his selection.

From figure 12 mean values of the strain rate have been estimated and then listed with their respective impact velocity in Table 3.

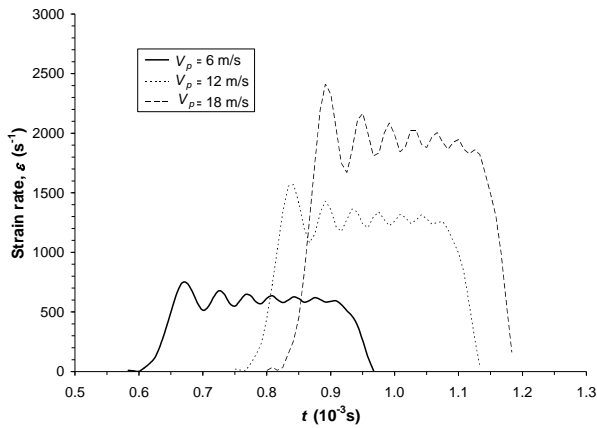


Figure 12. Strain rates reached from dynamic compression of the Alporas with PMMA bars at different impact velocities (V_p).

Table 3. Strain rates estimated for the dynamic compression of the Alporas with PMMA bars at different impact velocities.

Impact velocity, V_p (m/s)	Strain rate, $\dot{\epsilon}_s(t)$ (s^{-1})
6	600
12	1300
18	2000

5. CONCLUSIONS

A detailed FE model of the split Hopkinson pressure bar (SHPB) compression test of an aluminum foam specimen has been developed and analyzed.

Nylon and PMMA were considered in the composition of the bars and the striker and afterward have been compared with conventional steel bars, finding that both materials are very suitable for dynamical compression testing of the Alporas aluminum foam under SHPB conditions.

From the geometry and configuration of the SHPB available as reference for this study have been proposed the necessary modifications, in terms of striker length and diameter, for carry out an appropriate and reliable dynamic compression test of the aluminum foam in such device.

It was found that diameter (D) of the bars and striker is the most determinant geometrical parameter for prescribing in the metal foam specimen a wide range of strain rates ($\dot{\epsilon}$), going from 600 to 2000 s^{-1} . As the impact velocity is directly associated with the specimen size, it is indirectly limited by the cell size of the foam.

REFERENCES

[1] Ashby M., Evans A., Fleck N., Gibson L., Hutchinson J., Wadley H. *Metal Foams: A Design Guide*, Butterworth-Heinemann, 2000.

[2] Chen W., Lu F., Frew D., Forrester M. *Dynamic Compression Testing of Soft Materials*, Journal of Applied Mechanics, 69, pp. 214-223, 2002.

[3] Kolsky H., *An investigation of the mechanical properties of materials at very high rates of loading*, Proc. R. Soc. L., B62, pp. 676-700, 1949.

[4] Zhao H., Gary G., Klepaczco J., *On the use of a viscoelastic split Hopkinson pressure bar*, International Journal of Impact Engineering, 19, pp. 319-330, 1997.

[5] Kiernan S., Cui L., Gilchrist M., *Propagation of a stress wave through a virtual functionally graded foam*, International Journal of Non-Linear Mechanics, 44, pp. 456-468, 2009.

[6] Lopatnikov S., Gama B., Haque M.J., Krauthauser C., Gillespie J., Guden M., Hall I., *Dynamics of metal foam deformation during Taylor cylinder-Hopkinson bar impact experiment*, Composite Structures, 61, pp. 61-71, 2003.

[7] Zhao H., Elnasri I., Abdennadher S., *An experimental study on the behaviour under impact loading of metallic cellular materials*, International Journal of Mechanical Sciences, 47, pp. 757-774, 2005.

[8] Deshpande V., Fleck N., *High strain rate compressive behaviour of aluminium alloy foams*, International Journal of Impact Engineering, 24, pp. 277-298, 2000.

[9] Elnasri I., Pattofatto S., Zhao H., Tsitsiris H., Hild F., Girard Y., *Shock enhancement of cellular structures under impact loading: Part I Experiments*, Journal of the Mechanics and Physics of Solids, 55, pp. 2652-2671, 2007.

[10] Mukai T., Kanahashi K., Miyoshi T., Mabuchi M., Nieh T., Higashi K., *Experimental Study of Energy Absorption in a Close-Celled Aluminum Foam Under Dynamic Loading*, Scripta Materialia, 40, pp. 921-927, 1999.

[11] SIMULIA, ABAQUS *Analysis User's Manual. Volume III: Materials*, Version 6.7., 2007.

[12] Deshpande V., Fleck N., *Isotropic constitutive models for metallic foams*, Journal of the Mechanics and Physics of Solids, 48, pp. 1253-1283, 2000.

FEM ANALYSIS OF RIVETED CONNECTIONS AIMING FATIGUE AND FRACTURE ASSESSMENTS

A.M.P de Jesus^{1,2}, R. M. G. Pereira^{1,2}

¹ Departamento de Engenharias, Escola de Ciências e Tecnologia,
Universidade de Trás-os-Montes e Alto Douro, Quinta de Prados,
5001-801 Vila Real, Portugal.

E-mail: ajesus@utad.pt; rmurca@hotmail.com

² Unidade de Conceção e Validação Experimental,
Instituto de Engenharia Mecânica – IDMEC, Pólo FEUP
Rua Dr. Roberto Frias, 4200-465 Porto, Portugal

ABSTRACT

Old riveted bridges are susceptible to exhibit significant fatigue damage levels, since they were originally designed without taking into account the fatigue phenomenon and they were subjected to increasing loading, along their long operational period. Due to economic reasons, the operational period of those structures has been further increased, requiring detailed residual fatigue life studies. The usual procedures for fatigue analysis of riveted connections are based on the S-N approach. The local approaches and Fracture Mechanics appear as alternatives to the S-N approach, to derive the fatigue strength for riveted joints, with higher flexibility than S-N approaches. These alternative approaches require detailed stress analysis. This paper proposes a methodology for detailed stress analysis of multi-riveted connections using the Finite Element Method. The proposed methodology is demonstrated for a stringer-to-cross-girder intersection, using the ANSYS® commercial code. This methodology consists on 3D finite element models using both solid and shell elements as well as contact elements. The proposed model is able to account the clamping stresses of rivets on stress distributions. Also, choosing several crack propagation scenarios, the stress intensity factors are evaluated using the crack closure technique.

KEY WORDS: riveted connections, finite element analysis, stress analysis, fracture mechanics.

1. INTRODUCTION

Structural integrity assessments of old steel riveted bridges are more and more frequent. Most of these structures were built at the end of the 19th century or the beginning of the 20th century with angles and plates joined by rivets and made of puddle iron or wrought steel. Fatigue is one major concern for these structures since they show a long operational period with increasing traffic intensity, many times without the required rehabilitation procedures.

The S-N approach is widely used to assess the fatigue damage for riveted steel constructions [1-4]. This approach relates the nominal stresses applied on riveted joints with the fatigue life. It requires experimental data for the riveted joint under consideration. This approach shows some limitations such as its suitability only for simple details and loading conditions.

Fracture Mechanics appears as an alternative approach to perform residual life calculations [5,6]. However, the use of the Fracture Mechanics is very often limited to the application of simplified formulae for stress intensity factors evaluation, available in standard handbooks [7]. For example, the stress intensity factor in a cracked plate is calculated by considering an isolated plate rather than

a plate integrated in a riveted structural member. No interaction is taken into account between the cracked plate and the remaining components of the member. This may result in inconsistent residual life evaluations, motivating the search for more accurate stress intensity factors evaluation.

Very few works can be found in literature regarding the stress intensity evaluation for riveted built-up beams [8]. Riveted built-up beams are typical from the end of 19th /beginning of 20th centuries, when technology did not offer manufactured hot rolled beams nor welding techniques for making welded connections. Moreno and Valiente [8] proposed an analytical model to assess the stress intensity factors for cracked webs of riveted T beams. The proposed analytical model neglects friction effects and clamping stresses on rivets and is limited to the specific investigated geometry.

Despite numerical procedures (e.g. finite element method plus virtual crack closure technique [9]) have been intensively applied in the assessment of stress intensity factors for structural components and/or joints, they have been disregarded for riveted connections from old riveted bridges.

In a few number of cases, detailed 3D finite element

models have been used in stress analysis of uncracked riveted connections [10-15]. These models have been used to support the application of local stress- and strain-based approaches that requires the evaluation of local/peak stresses or strains for comparison with plain material fatigue strength data, obtained using smooth specimens.

This paper proposes a methodology for detailed stress analysis of multi-riveted connections using the Finite Element Method. The proposed methodology is demonstrated for a stringer-to-cross-girder intersection, using the ANSYS® commercial code [16]. This methodology consists on 3D finite element models, using both solid and shell elements as well as contact elements. The solid elements are used to represent in fine detail the region of interest for the assessment of the local stresses and the shell elements are used elsewhere, aiming a moderate computational cost. Solid-shell interfaces are used to provide required continuity between the shell and solid models. The proposed model is able to account the clamping stresses of rivets on stress distributions. Also, choosing several crack propagation scenarios, the stress intensity factors are evaluated using the crack closure technique [17].

Before the presentation of the multi-rivet joint problem, a single rivet joint is presented to discuss basic issues regarding the finite element analysis of riveted joints.

2. FINITE ELEMENT ANALYSIS OF A SINGLE RIVETED JOINT

A finite element model of a single rivet joint is presented in this section. Figure 1 illustrates the geometry of the riveted joint. This riveted joint was also investigated by Imam et al. [13]. Therefore, its inclusion in this study was the assessment of the proposed procedure. The derived results are compared with existing results available in literature. A discussion is presented regarding the main numerical issues of finite element modelling of riveted joints.

The commercial finite element code ANSYS® [16] was used to analyse the riveted connection. The ANSYS® parametric design language (APDL) was used to build the model of the connection. Both plates and rivet were modelled using 20-node hexahedra solid isoparametric elements (SOLID95).

The contact between the plates and rivet was modelled through contact elements available in ANSYS®, using the surface-to-surface and flexible-to-flexible contact options. In particular, the finite elements CONTA174 and TARGE170 were used to define the several contact pairs [16]. Materials were assumed linear elastic and isotropic ($E=210$ GPa, $\nu=0.27$). Even assuming linear elastic materials, the finite element analysis still is non-linear due to the contact, which requires an incremental analysis.

Figure 2 shows the finite element mesh of the riveted connection. Only one quarter of the joint was modelled, taking into account the two existing symmetry planes. Displacements at nodes located at planes of symmetry were restrained along the normal direction. Additionally, all degrees of freedom of nodes at face CD (see Figure 1) were restrained. Two types of alternative boundary conditions were tested for face AB: imposed displacement or pressure, applied according the longitudinal or loading direction.

The simulation was carried out using the augmented Lagrange algorithm available in the ANSYS® [16], together with the Coulomb friction model. The augmented Lagrangian method requires the definition of normal contact stiffness. The amount of penetration between the contact and target surfaces depends on the normal stiffness. Higher stiffness values decrease the amount of penetration, but can lead to ill-conditioning of the global stiffness matrix and to convergence difficulties. Lower stiffness values can lead to a certain amount of penetration and produce an inaccurate solution. Ideally, it is desirable a high enough stiffness that the penetration is acceptably small, but a low enough stiffness that the problem will be well-behaved in terms of convergence. In effect, a stiffness relationship between two bodies must be established for contact to occur. Without contact stiffness, bodies will pass through one another. The relationship is generated through an 'elastic spring' that is put between the two bodies, where the contact force is equal to the product of the contact stiffness (κ) and the penetration (δ). The amount of penetration (δ), or incompatibility, between the two bodies is therefore dependent of the stiffness (κ). Ideally, there should be no penetration, but this implies that $\kappa=\infty$, which will lead to numerical instabilities. The value of κ , that is computed by ANSYS®, depends on the relative stiffness of the contacting bodies. There is the possibility of scaling κ through the FKN factor, usually called the normal penalty stiffness factor. The usual factor range is from 0.01-1.0, with a default of 1.0. The default value is appropriate for bulk deformation. Present simulations covered FKN values equal to 0.01, 0.1 and 1.0. Another relevant contact parameter to be used in conjunction with the augmented Lagrangian method is FTOLN. FTOLN is a tolerance factor to be applied in the direction of the surface normal. The range for this factor is less than 1.0 (usually less than 0.2), with a default of 0.1, and is based on the depth of the underlying solid element. This factor is used to determine if penetration compatibility is satisfied. Contact compatibility is satisfied if penetration is within an allowable tolerance (FTOLN times the depth of underlying elements). The depth is defined by the average depth of each individual contact element in the pair. If ANSYS® detects any penetration larger than this tolerance, the global solution is still considered unconverged, even though the residual forces and displacement increments have met convergence criteria. FTOLN values equal to 0.01, 0.05

and 0.1 were simulated. For all other contact parameters not mentioned here, default values were adopted [16].

Null clearance between the rivet hole and rivet shoulder was considered, which is characteristic of riveted joints, but not typical on bolt connections. The effect of the clamping stresses on rivets was modelled. The clamping stresses were generated by a preliminary load step consisting of a temperature variation (decreasing temperature) applied exclusively to the rivet, and assuming orthotropic thermal expansion properties for the rivet: non-null expansion coefficient according the rivet axial direction ($\alpha_z=10^{-5} \text{ }^\circ\text{C}^{-1}$) and null expansion coefficients according the transverse directions ($\alpha_x=\alpha_y=0 \text{ }^\circ\text{C}^{-1}$). Despite inspired on the riveting process, the application of a temperature change to the rivet was only used as an analytical methodology to generate clamping stresses. The actual clamping stresses on rivets of existing connections are not easy to quantify. Therefore, the proposed model was used to perform sensitivity analysis, seeking the effects of several clamping stresses on the stress distributions around the rivet hole. When clamping stresses are present, the friction effects play a relevant role on stress distributions. In order to illustrate this effect three distinct friction scenarios were investigated: frictionless contact and non-null friction coefficients - $\mu=0.3$ and $\mu=0.6$. The precise value of the friction coefficients is also very difficult to estimate. The friction coefficients tested in this study seems to be plausible values for steel-to-steel contact. Furthermore, $\mu=0.3$ has already been used in literature to simulate the friction effects on riveted connections [13]; $\mu=0.6$ seems to be an upper limit for steel-to-steel contact. When compared with high strength bolts, the clamping stresses on rivets are not significant and not controllable.

A parametric study, illustrating the effects of FKN, FTOLN, μ , clamping stresses and loading conditions was conducted for the single rivet connection, based on 248 simulations. Half of these simulations were carried out for an imposed displacement, $\delta=0.1 \text{ mm}$, applied to the face AB (see Figure 1) according the longitudinal direction; the other half of the simulations were performed for a pressure $p=30 \text{ MPa}$ applied to the referred face. For each combination of FKN and FTOLN parameters, 7 distinct clamping stresses were simulated, corresponding to the following temperature variations: 0, 25, 75, 125, 175, 225 and 275 $^\circ\text{C}$. The simulations carried out for an imposed pressure showed some convergence difficulties for frictionless contact and null clamping stresses.

Figure 3 shows the variation of the average clamping stresses on rivet as a function of the temperature range applied to the rivet. From Figure 3 it is clear that FKN parameter has a significant influence on the clamping stress. The slope of the clamping stress vs. ΔT relation increases with the FKN factor. Friction and FTOLN parameter has a negligible effect on the clamping stress.

Figure 4 illustrates the evolution of the stress intensity as a function of the clamping stress on rivet. The stress intensity was computed dividing the maximum stress on the surface of the hole of the rivet at the central plate, along the loading direction, and the net stress evaluated at the resisting cross section (=remote cross section – projected area of the hole of the rivet). From Figure 4 it is possible to realize that the loading condition (displacement of pressure control) has an effect on stress concentration factor. This may be justified by the friction effect that makes the problem loading path dependent (non-linear).

The stress concentration factor, in the absence of any clamping stress, assumes a value in the range 3-3.5. It is observed that for FKN=1.0, the stress concentration at the rivet hole tends to fade; it can be even lower than unity which means that load transfer is made essentially by friction between the plates. FKN values in the range 1.0-0.1 are plausible, since they produce physically consistent stress intensity evolutions with the clamping stresses. For simulations carried out under displacement control, FTOLN variations within the range 0.1-0.01 did not influence the results. Situation changes if a remote pressure is imposed to the connection - some influence of FTOLN on results is verified.

Table 1 summarizes the stress concentration factors at three distinct locations, namely at the surface of the hole of the side plate (point F – external surface and point G – internal surface/interface) and at the surface of the hole of the middle plate (point H – external surface/interface). These points are located at the plane that contains the rivet axis and is perpendicular to the loading direction. Table 1 also presents stress concentration values obtained at references [13,18] using numerical methods. Deviations between 13% and 40% were verified. Results from reference [18] were computed assuming 2D stress analysis and accounting contact between rivet and the hole using a pressure applied at the hole. Results from reference [13] were obtained from a similar finite element model built in ABAQUS®.

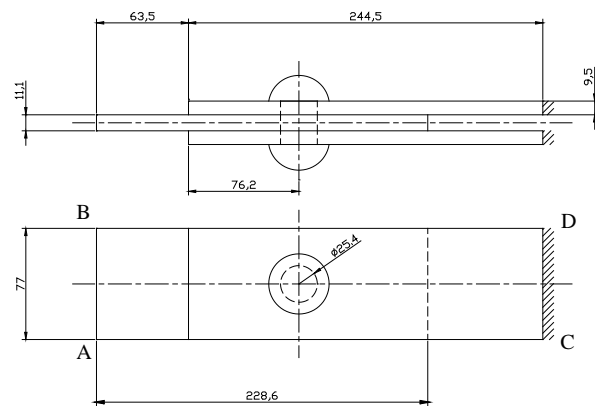


Figure 1. Single rivet joint (dimensions in mm).

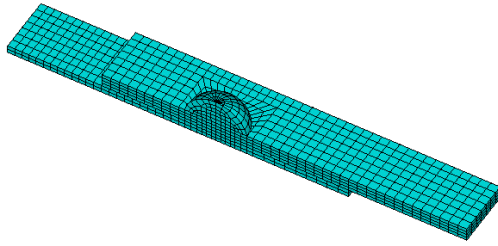


Figure 2. Finite element mesh of a single rivet joint.

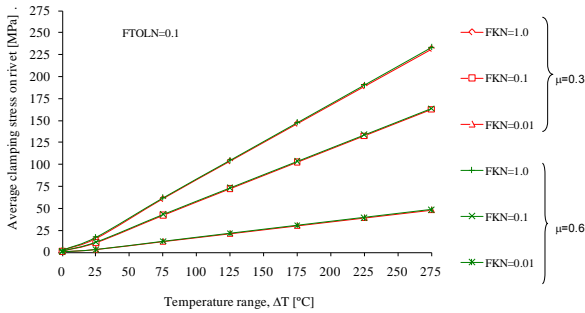


Figure 3. Average clamping stress vs temperature range - single rivet joint.

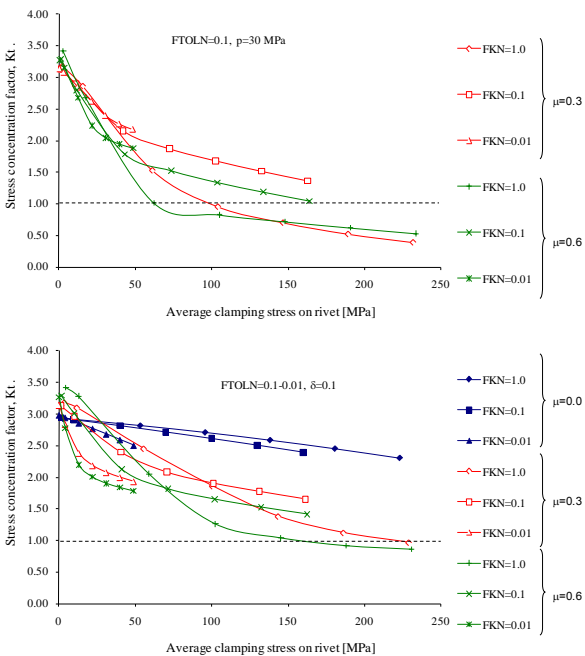


Figure 4. Stress concentration factor vs average clamping stress on rivet - single rivet joint.

Table 1. Stress concentration factor, K_t , for the single rivet joint.

Locations	F	G	H	
This study FTOLN=0.1-0.01	FKN=1.0	2.70	2.96	2.95
	FKN=0.1	2.67	2.86	3.13
	FKN=0.01	2.81	2.87	3.14
	Average	2.73	2.90	3.07
[11]	2.19	2.19	2.17	
[8]	1.97	1.75	2.68	
[11] - Deviation (%)	19.6	24.2	29.2	
[8] - Deviation (%)	27.8	39.7	12.7	

3. FINITE ELEMENT ANALYSIS OF A STRINGER-TO-CROSS-GIRDER JOINT

This section presents the results of a finite element model of a riveted structure, namely composed of one cross girder connected to two stringers, by means of rivets. Both members are I shape beams and the connection is established by means of angles and rivets, attaching the webs of the beams. Figure 5 shows the global geometry of the beam and Figure 6 the finite element mesh. Only 1/4 of the geometry was modelled taking into account existing planes of symmetry. The finite element model is composed of 3D solid elements (SOLID95) at joint location and shell elements (SHELL93) elsewhere [16]. The two types of elements are attached using contact element technology [16]. Simulations were carried with default contact parameters (FKN=1.0, FTOLN=0.1), since previous section demonstrated to yield consistent results. Furthermore, it was assumed: $\mu=0.3$, $E=210$ GPa and $\nu=0.3$. The clamping stresses on rivets were modelled through a temperature variation, as proposed in the previous section. Roughly, a linear approximation was verified between the clamping stresses and the temperature range. Figure 7 shows the vertical (P direction) displacement field. It is verified that a smooth transition is obtained at solid-shell interface, which is a good indication of the quality of the results.

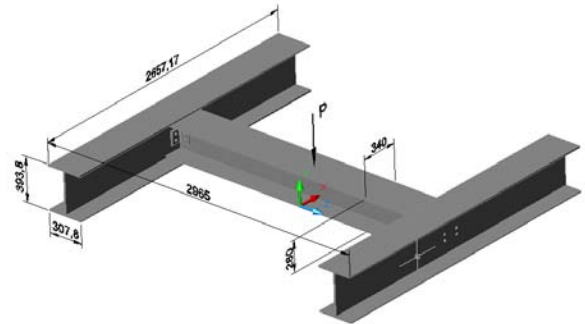


Figure 5. Riveted structure: stringer-to-cross-girder intersection (dimension in mm. $P=200$ kN).

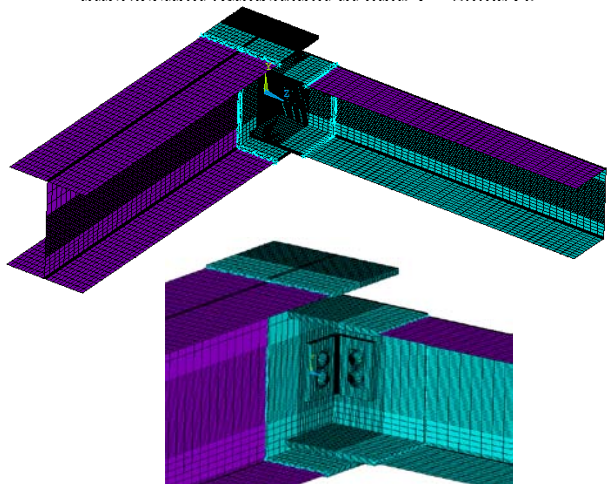


Figure 6. FE mesh of the stringer-to-cross-girder intersection.

Figure 8 shows the evolution of the maximum deflection in the cross girder, as a function of the clamping stresses (temperature range) and friction. Consistent results were derived: deflection decreases with the increasing of the clamping stresses and friction. Figure 9 illustrates the stress fields at the end of the web of the cross girder. It is verified two critical locations that may lead to crack initiation. Figure 10 shows the stress concentration evolution with clamping stresses on rivets and friction. This stress concentration was evaluated dividing the maximum stress around the rivet holes (see Figure 9) by the maximum theoretical bending stress at the end of the girder. There is a stress concentration reduction as the clamping stress and friction effects increases. Three crack propagation scenarios were investigated. Figure 11 illustrates the stress fields for representative cracks emanating from the rivet holes at the web of the girder.

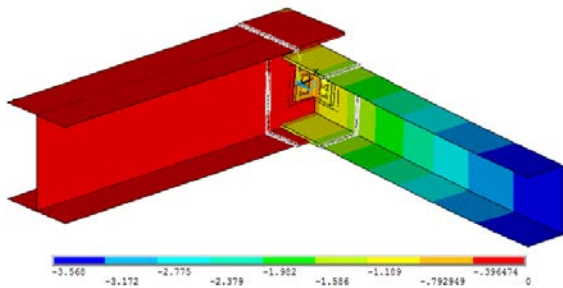


Figure 7. Stringer-to-cross-girder intersection: vertical displacement field, u_y , mm ($\Delta T=0^\circ C$).

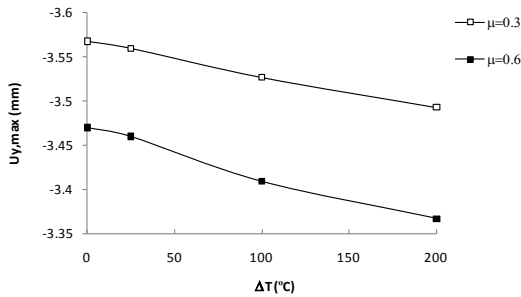


Figure 8. Stringer-to-cross-girder intersection: maximum vertical displacement at cross girder.

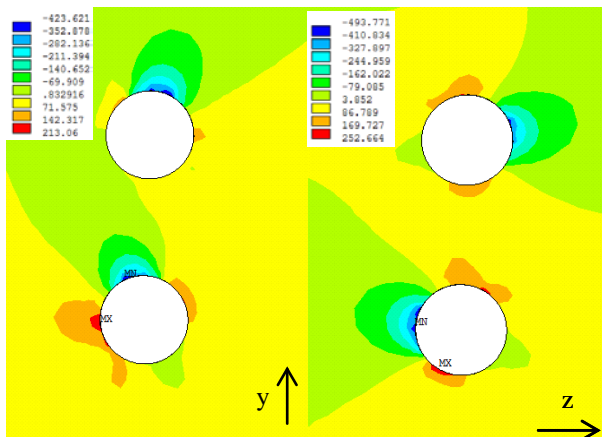


Figure 9. Stress fields along y (left) and z (right) directions at the riveted end of the cross girder.

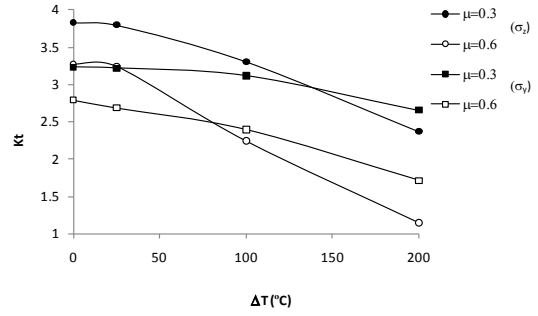


Figure 10. Stress concentration factors around rivet holes of the girder.

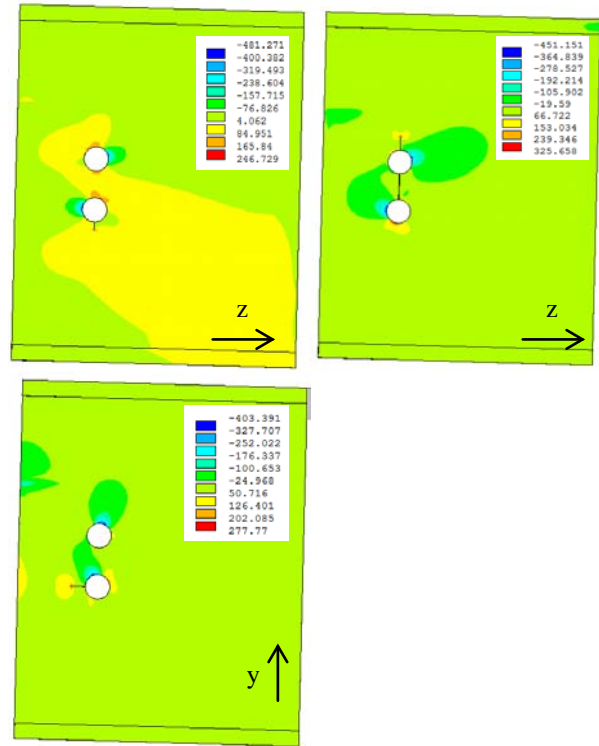


Figure 11. Stress fields along z (top) and y (bottom) directions for the cracked end of the cross girder.

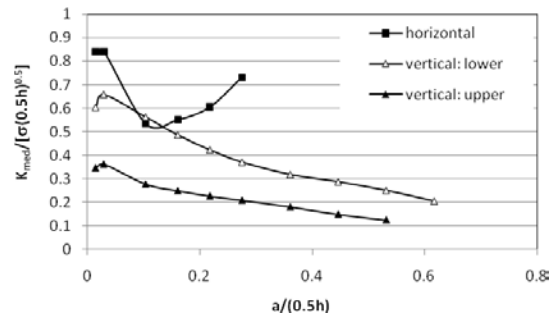


Figure 12. Stress intensity factors for the several crack propagation scenarios. (h : height of the girder; σ : maximum bending stress on girder from beam bending theory)

Figure 12 shows the stress intensity evolution for the three crack propagation scenarios. The stress intensity factors were computed using the crack closure method in two analysis steps as well the virtual crack close technique [17]. Results shown in Figure 12 are averaged

results through the web thickness, and normalized using the maximum theoretical bending stress for a fixed-fixed beam under central point load. The scenario of a horizontal propagating crack seems to be the most critical one, since the stress intensity factor is always higher than values computed for the other cracks. Stress intensity factors for the vertical cracks tends to decrease as the crack growths, therefore any vertical fatigue crack tends to slow down.

4. CONCLUDING REMARKS

A methodology for detailed stress analysis of multi-riveted connections using the Finite Element Method was proposed, using the ANSYS® commercial code. The proposed methodology is demonstrated for a stringer-to-cross-girder intersection. This methodology consists on 3D finite element models using both solid and shell elements as well as contact elements. The proposed model is able to account the clamping stresses of rivets as well as friction on stress distributions. Also, choosing several crack propagation scenarios, the stress intensity factors are evaluated using the crack closure technique. A comparison between the stress intensity factors allows the assessment of the most critical scenarios, from a fatigue perspective.

ACKNOWLEDGEMENTS

The authors acknowledge the Portuguese Science Foundation for the support through the research project PTDC/EME-PME/78833/2006.

REFERENCES

- [1] DiBattista, J.D., Adamson D.E.J. and Kulak G.L., "Evaluation of remaining fatigue life for riveted truss bridges", *Canadian Journal of Civil Engineering*, 25(4), pag. 678-691, 1998.
- [2] Geissler, K., "Assessment of old steel bridges, Germany", *Structural Engineering International*, 12(4), pag. 258-263, 2002.
- [3] Kulak, G.L., "Fatigue strength of riveted shear splices", *Progress in Structural Engineering and Materials*, 2(1), pag. 110-119, 2000.
- [4] Kim, S.-H., Lee, S.-W., Mha, H.-S. "Fatigue reliability assessment of an existing steel railroad bridge", *Engineering Structures*, 23, pag. 1203-1211, 2001.
- [5] Wang, C.S., Chen, A.R., Chen, W.Z., Xu, Y., "Application of probabilistic fracture mechanics in evaluation of existing riveted bridges", *Bridge Structures*, 2(4), pag. 223-232, 2006.
- [6] Paasch, R.K., DePiero, A.H., *Fatigue Crack Modeling in Bridge Deck Connection Details*, Final Report SPR 380, Oregon Department of Transportation, 1999.
- [7] Tada, H., Paris. P.C., Irwin, G.R., *The stress analysis of cracks handbook*, ASME Press, 2000.
- [8] Moreno, J., Valiente, A., "Stress intensity factors in riveted steel beams", *Engineering Failure Analysis*, 11, pag. 777-787, 2004.
- [9] Rijck, J.J.M., *Stress Analysis of Fatigue Cracks in Mechanically Fastened Joints. An analytical and experimental investigation*, Ph.D. Thesis, 302 pag., Delft, The Netherlands, 2005.
- [10] DePiero, A.H., Paasch, R.K., Lovejoy, S.C., "Finite-element modeling of bridge deck connections details", *Journal of Bridge Engineering*, 7(4), pag. 229-235, 2002.
- [11] Al-Emrani, M., Kliger, R., "FE analysis of stringer-to-floor beam connections in riveted railway bridges", *Journal of Constructional Steel Research* 59(7), pag.803-818, 2003.
- [12] Iman, B., *Fatigue analysis of riveted railway bridges*. Ph.D. Thesis, 258 pag., School of Engineering, University of Surrey, UK, 2006.
- [13] Imam, B.M., Righiniotis, T.D., Chryssanthopoulos, M.K., "Numerical modelling of riveted railway bridge connections for fatigue evaluation", *Engineering Structures*, 29, pag. 3071-3081, 2007.
- [14] Righiniotis, T.D., Imam, B.M., Chryssanthopoulos, M.K., "Fatigue analysis of riveted railway bridge connections using the theory of critical distances", *Engineering Structures*, 30, pag. 2707-2715, 2008.
- [15] De Jesus, A.M.P., Pinto, H., Fernández-Canteli, A., Castillo, E., Correia, J.A.F.O., "Fatigue assessment of a riveted shear splice based on a probabilistic model", *International Journal of Fatigue*, 32, pag. 453-462, 2010.
- [16] SAS - Swanson Analysis Systems Inc., ANSYS, Version 11.0, Houston, 2009.
- [17] Krueger, R., "Virtual crack closure technique: History, approach, and applications", *Applied Mechanics Reviews*, 57(2), pag. 109-143, 2004.
- [18] Shivakumar, K.N., Newman, J.C., "Stress concentrations for straight-shank and countersunk holes in plates subjected to tension, bending and pin loading", NASA Technical Paper No. 3192, 1992.

A METHODOLOGY FOR RETICULAR STRUCTURES MODELING APPLIED TO THE FATIGUE ANALYSES OF RIVETED BRIDGES

R. C. Guedes Leite¹, R. Natal Jorge², A. M. P. de Jesus³

¹ Departamento de Engenharia Civil, CEFET-MG,
Belo Horizonte, Minas Gerais, Brazil,
Av. Amazonas, 7565, 30.421-169 Belo Horizonte, Brasil
E-mail: rleite@civil.cefetmg.br

² IDMEC/ Departamento de Engenharia Mecânica,
Faculdade de Engenharia da Universidade do Porto,
Rua Dr. Roberto Frias, 4200-465 Porto, Portugal
E-mail: rnatal@fe.up.pt

³ IDMEC/Departamento de Engenharias,
Escola de Ciências e Tecnologia/UTAD,
Quinta de Prados, 5001-801 Vila Real, Portugal
E-mail: ajesus@utad.pt

ABSTRACT

Riveted bridges are ancient metallic structures that have been subjected to a long operational period, with increasing traffic loads and intensity. The fatigue damage levels experienced by these structures may be significant. S-N approaches are usually used to assess these structures. However, Fracture Mechanics and local strain approaches are gaining an increasing interest. The application of these alternative approaches requires detailed stress/strain analysis of the riveted connections, which demands considerable computation resources. This paper proposes an integrated CAD/FEA methodology for stress analysis of joints from reticular structures, based on a sub-modelling approach to mitigate the need for extensive computational resources. Detailed local three-dimensional solid finite element models of the joints are proposed, the respective boundary conditions being derived automatically from a global beam model of the structure. The procedure is demonstrated for the Trezói riveted railway bridge. The procedure to carry out a detailed stress analysis of a significant joint of the bridge for a moving train loading is illustrated.

KEY WORDS: fatigue analysis, riveted bridges, sub-modelling, finite element analysis.

1. INTRODUCTION

Today, riveted steel bridges are, mostly, centenary structures. The life time of this structures have been extended to respond to economical concerns, although, changes on traffic loads along the years, have exposed these structures to different overloads from that originally considered in design. In addition to the utilization of those bridges under new load conditions, their original designs, generally of the end of the 19th century or the beginning of the 20th century [1] did not consider fatigue as a damaging mechanism. Therefore, these bridges are an important group of metallic structures very likely to present high levels of fatigue damage. Fatigue assessment studies of existing bridges are consequently important to assess the current fatigue damage state as well as to estimate the remaining fatigue life of those structures. Adequate analysis models are then required. The usual model is based on the so-called S-N approach, which requires

the nominal stress evaluation on members under analysis, for comparison with the fatigue strength data [2].

Recently, research projects have proposed the use of Fracture Mechanics and strain-based local approaches [3, 4]. However, these approaches demand for considerable computing resources since they require detailed stress/strain analysis at the joint. To reduce these resources needs, sub-modelling techniques can be used to perform detailed stress/strain analysis using three-dimensional solid finite element models only at the joints of interest, while a global model of the structure, using beam or shell elements, is used to derive the boundary conditions of the detailed model [5, 6].

In order to facilitate the application of the local methods for fatigue analysis of reticular structures, an integrated CAD system have been developed to build a

geometric model of the structure, allowing specification and modification of geometry, boundary conditions, materials and sections. An exporting data module, that organizes the structure of the data in a compatible format with ANSYS® input [7], was developed and added to the global system. This module automates the exportation, for the finite element analysis, of the global structure data as the structure is submitted to multiple simulation scenarios (moving loads). In sequence, the system gathers the displacements results of a selected group of nodes for each one of the simulation scenarios. These results are organized in an ABAQUS® [8] input file, and are applied to the refined model of the selected structural connection. This methodology contributes to reduce the computational costs involved at the applications of the local approaches in the fatigue analysis of riveted bridges.

The developed methodology is demonstrated for a riveted bridge, namely the Portuguese Trezói railway bridge. This bridge is probably one of the last riveted bridges built in Portugal.

2. DESCRIPTION OF THE PROPOSED METHODOLOGY

In order to assist the application of the local methods to fatigue analysis of riveted bridges, an integrated CAD system has been developed to build the geometric model of reticular structures, using beam elements, and to manage and transfer data results to a local detailed solid finite element model, in the framework of sub-modelling techniques in finite element analysis.

To use the methodology, initially, a global model of the structure is built. This model represents the geometry of the structure. The system allows the definition, the application and the modification of actions, boundary conditions, materials and sections of each element of the model. A refined model with beam elements may be defined from the geometrical model, with automatic numbering of elements and nodes, and with a control that can recognize the original geometric elements and the refined elements obtained from that. With this functionality it is possible to refine only desired parts of the model.

This CAD system was developed from a framework applied to automation and integration systems applied to the reticular three-dimensional structural project process [9]. The modules of the framework responsible for the data control and the graphical view of the structure were adapted for the specific necessities of the riveted bridges. The data structure of the system had been complemented with the specific data required by the ANSYS® software and new functionalities were added to the global system, in order to better represent the model generated by that software. Those functionalities were not existent at the original systems

developed using the framework. The final methodology automates not only the construction of the three-dimension reticular model of the structure but also the data export for the finite element analysis. An exporting data module was developed and added to the global system. This module organizes the structure of the data in compatible formats with the input for the ANSYS® and ABAQUS® software. The exporting data module automates the transportation of the global structure data, submitted to multiple loading scenarios (moving loads), for the finite element analysis at the software ANSYS®, and gathers the displacement results at a select group of nodes for the simulated several loading scenarios. This set of results is then written in an input file to be automatically applied at the refined model of the selected structural joint in the ABAQUS® software.

The traffic loads may be simulated by the CAD system that automates, in an iterative way, the application of an array of loads along a set of elements chosen by the user. At each step, the loads are applied at a specific position distant for the previous step position by a value defined by the user. Each position of the loads corresponds to a load step defined at the ANSYS® software.

After applying the traffic loads along the bridge, from typical trains, the system organizes and writes out the structural data to a file as well as the code that automates the finite element analysis process and gathers the displacements values at each load step, for a set of nodes selected by the user. The process may be repeated for different train types, with different distances between loads steps and different initial and final points of application. In order to obtain the critical load step, it is possible to refine the global structure defining the desired nodes near a structural joint and refine the application of the traffic load. After the simulation of the traffic loads at the structure, the system gathers the displacements for each node around the desired structural joint, at each load step. The displacements are written in an input file for the ABAQUS® software and are automatically applied to the refined model with solid elements of the analyzed structural joint [5, 6]. The stress histories may then be evaluated for the traffic loads.

The proposed methodology consists of an object oriented integrated system [10, 11, 12] developed from an application framework, REMFrame [9]. This system integrates a modeller model, the Geometric Modeller, designed as a CAD system that uses the graphic platform AutoCAD® [13, 14] as a graphic interface, with two external analysis systems: the software ANSYS® for the global analysis and the software ABAQUS® [8] for the local analysis.

3. A CASE STUDY: THE TRÉZÓI BRIDGE

The proposed methodology was applied to model probably the latest riveted bridge built with riveted joints, the Trézói railway bridge, constructed at the Beira Alta line, in Portugal, just after the Second World War. The availability of the original drawings of the bridge and previous researches carried out on this bridge [15] allowed the construction of the Trézói Bridge geometric model, with some precision.

After constructing the geometric model of the bridge, the CAD system allows the definition and modification the actions (loads), boundary conditions, materials, sections and type of elements. The geometric model can then be transformed in a refined model, both with beam elements. A strict correspondence between the original geometric element and the refined elements generated is managed by the system, allowing successive refining. This functionality was used to define a set of nodes near the desired structural joint (see Figure 1).

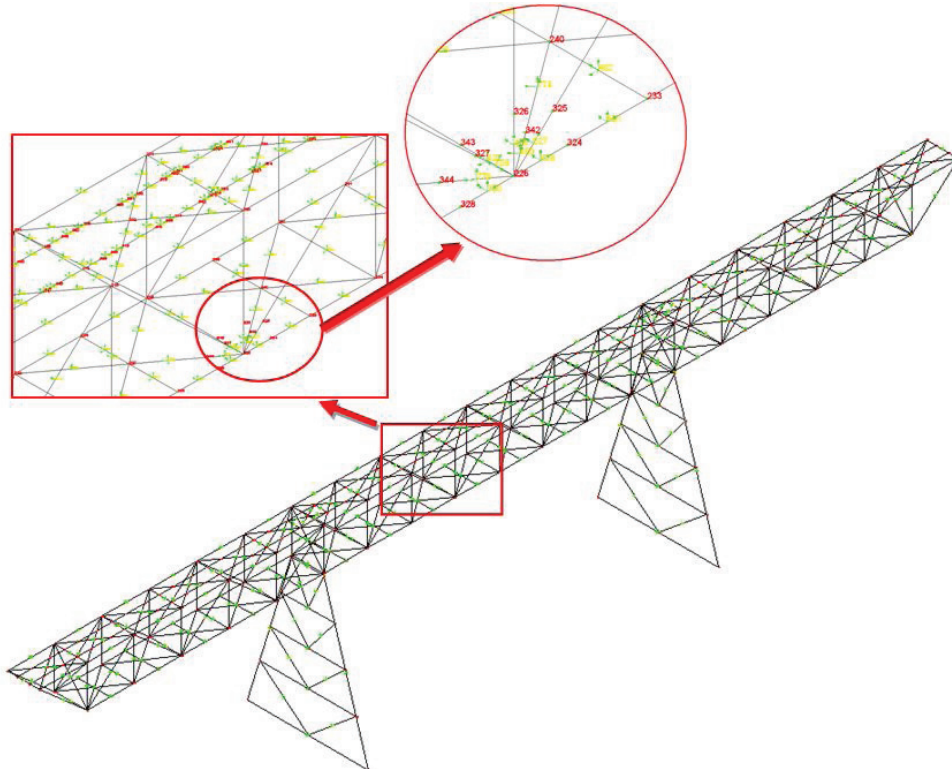


Figure 1. Geometric and refined models generated by the CAD system.

After having defined the refined model it is possible to carry out sensitivity analysis and investigate multiple simulation scenarios by the application of different load cases of different load steps. This functionality allows the simulation of a train crossing the bridge.

In the study of the Trézói bridge, three types of trains were chosen, according to the Eurocode 3, respecting the actual maximum train speeds at the bridge: 90 and 110 Km/h in different directions [15]. The chosen train types are: type 2 - a locomotive-hauled passenger train; type 7 - a locomotive-hauled freight train; type 11 - a heavy traffic with 250kN – axles [16] (see Figure 2).

The CAD system allows the application of a train type through a set of consecutive selected elements, in a regular interval of load, generating different load steps. The refined model had to be modified at each load step to insert nodes just at the application point of the loads

(see Figure 1). Those modifications are iterative and automatic, managed by the developed CAD system. For each load step the model of structure is saved in an appropriate format allowing posterior recuperation (see Figure 3).

After the application of a specific train type through all the bridge, the exporting module is automatically called to write the structural data with all the loads steps in the appropriate format required by the software ANSYS®. In sequence, the original model is recovered, allowing the application of other train types to the structure.

The exporting file written by the CAD system in the APDL Language carry out not only the structural data, but has also some line commands to automate the analysis of the structure at the software ANSYS® (see Figures 4 and 5), as well as to gather the displacements

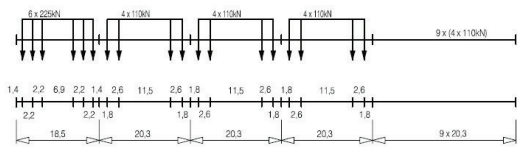
and rotations at a set of nodes chosen by the user, writing them in a specific format at a ASCII file (see Figures 1 and 6).

Using the same exporting module, the user can ask the system to read the deformations written at a specific file and to organize them in a input file, allowing the automatic application of a set of deformations to a specific node of a solid model, analyzed at the software ABAQUS® (see Figure 7).

(1) Standard and light traffic mixes

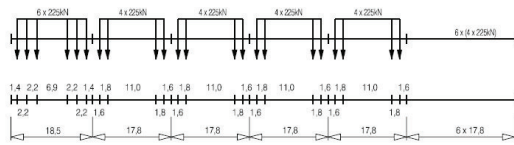
Type 1 Locomotive-hauled passenger train

$$\Sigma Q = 6630\text{kN} \quad V = 200\text{km/h} \quad L = 262,10\text{m} \quad q = 25,3\text{kN/m}'$$



Type 7 Locomotive-hauled freight train

$$\Sigma Q = 10350\text{kN} \quad V = 120\text{km/h} \quad L = 196,50\text{m} \quad q = 52,7\text{kN/m}'$$



(2) Heavy traffic with 250 kN - axles

Type 11 Locomotive-hauled freight train

$$\Sigma Q = 11350\text{kN} \quad V = 120\text{km/h} \quad L = 198,50\text{m} \quad q = 57,2\text{kN/m}'$$

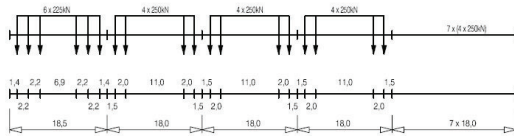


Figure 2. Train types (extract of European Committee for Standardization - EN1991-2 (2003).

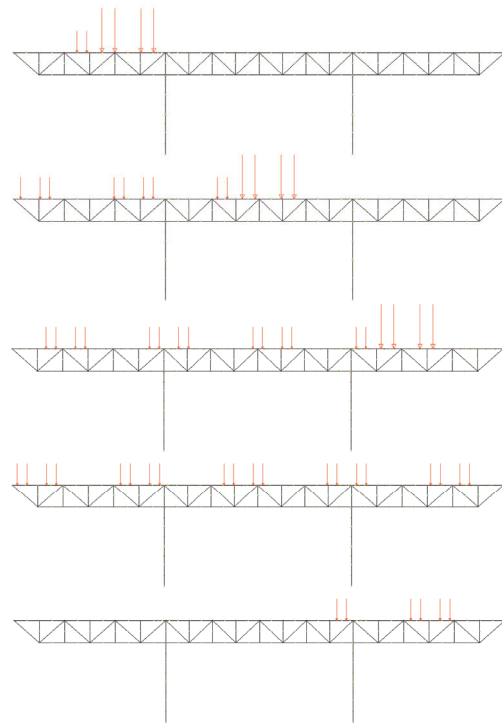


Figure 3. Load steps 2, 3, 4, 8 and 11 for train type 2, with 36m between steps.

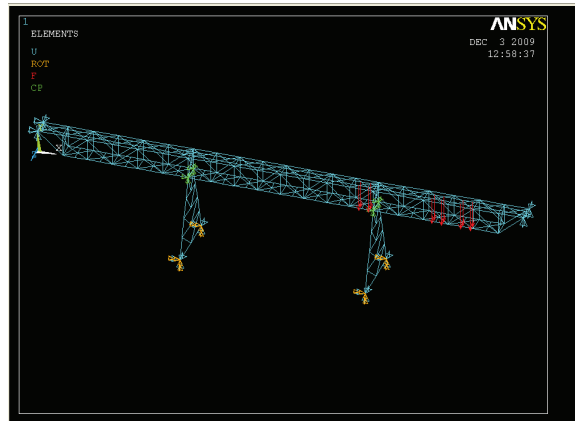


Figure 4. Analysis of the global structure: load step 11 and boundary conditions

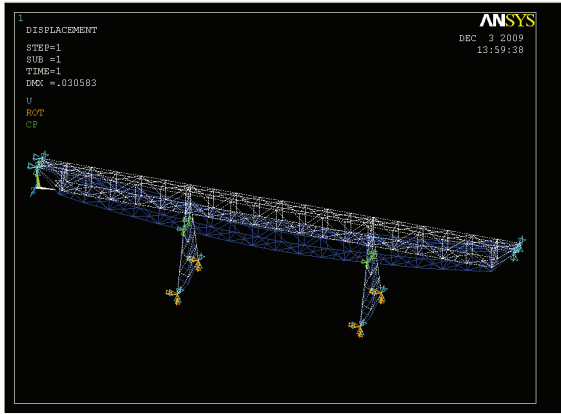


Figure 5. Analysis of the global structure: deformed shape for load step 11.

STEP	NODE	NODAL DISPLACEMENT [mm]		ROT X	ROT Y	ROT Z	
		Ux [mm]	Uy [mm]				
1.	207.0	-2268E-02	-28E-01	-2918E-04	0.62E-04	-1188E-04	-39E-03
1.	208.0	-2030E-02	-27E-01	0.7883E-04	0.47E-04	-2082E-05	-39E-03
1.	274.0	-1949E-02	-27E-01	0.2290E-04	0.41E-04	-6515E-07	-24E-03
1.	278.0	-4881E-02	-20E-01	0.6481E-05	0.40E-04	0.3174E-05	0.53E-02
1.	323.0	-2333E-02	-27E-01	-3102E-04	0.32E-04	0.1194E-04	-41E-03
1.	345.0	-2287E-02	-27E-01	-3994E-04	0.14E-03	-2864E-04	-43E-03
1.	346.0	-2313E-02	-27E-01	-1784E-04	-11E-03	-4896E-06	-38E-03
1.	347.0	-2341E-02	-27E-01	-4003E-04	0.21E-03	0.2779E-04	-38E-03
2.	207.0	-4183E-09	-54E-08	0.7324E-08	0.30E-08	0.3699E-10	-19E-10
2.	208.0	-4150E-09	-54E-08	0.9976E-08	0.38E-08	-3268E-09	-35E-10
2.	274.0	-4286E-09	-54E-08	0.1136E-07	0.36E-08	-2185E-10	0.76E-11
2.	278.0	-4903E-09	-54E-08	0.1009E-07	0.28E-08	0.7630E-09	0.50E-10
2.	323.0	-4589E-09	-52E-08	0.7300E-08	0.28E-08	-7248E-10	-20E-09
2.	345.0	-4065E-09	-33E-08	0.7276E-08	-20E-10	0.1648E-10	0.20E-08
2.	346.0	-3642E-09	-20E-08	0.7228E-08	0.27E-08	-1122E-09	0.37E-11
2.	347.0	-3725E-09	-33E-08	0.7524E-08	-17E-08	-1052E-09	-33E-08
3.	207.0	-1729E-06	-18E-05	0.7270E-07	0.34E-07	-1591E-08	0.10E-07
3.	208.0	-1769E-06	-18E-05	0.9964E-07	0.31E-07	-2387E-08	0.63E-08
3.	274.0	-1800E-06	-18E-05	0.1119E-06	0.33E-07	-1061E-08	0.10E-08
3.	278.0	-1707E-06	-18E-05	0.9938E-07	0.31E-07	0.2638E-08	-50E-08
3.	323.0	-1791E-06	-18E-05	0.7097E-07	0.29E-07	0.5625E-10	-34E-09
3.	345.0	-1731E-06	-18E-05	0.7158E-07	0.44E-07	-2623E-08	0.48E-09
3.	346.0	-1739E-06	-18E-05	0.7229E-07	0.30E-07	-2091E-08	0.72E-08
3.	347.0	-1769E-06	-18E-05	0.7063E-07	0.56E-08	0.1208E-08	-13E-07
4.	207.0	-3613E-06	-50E-05	0.9942E-07	0.48E-07	-3229E-08	0.22E-07
4.	208.0	-3681E-06	-50E-05	0.1300E-06	0.44E-07	-3263E-09	0.11E-07
4.	274.0	-3751E-06	-50E-05	0.1446E-06	0.39E-07	0.5910E-10	-39E-08
4.	278.0	-3403E-06	-50E-05	0.1383E-06	0.40E-07	0.1437E-07	-33E-07
4.	323.0	-3802E-06	-50E-05	0.9390E-07	0.41E-07	0.2293E-08	0.24E-08
4.	345.0	-3643E-06	-49E-05	0.9151E-07	0.79E-07	-6419E-08	-54E-08

Figure 6. Nodal displacements of a user selection set of nodes near a structural joint.

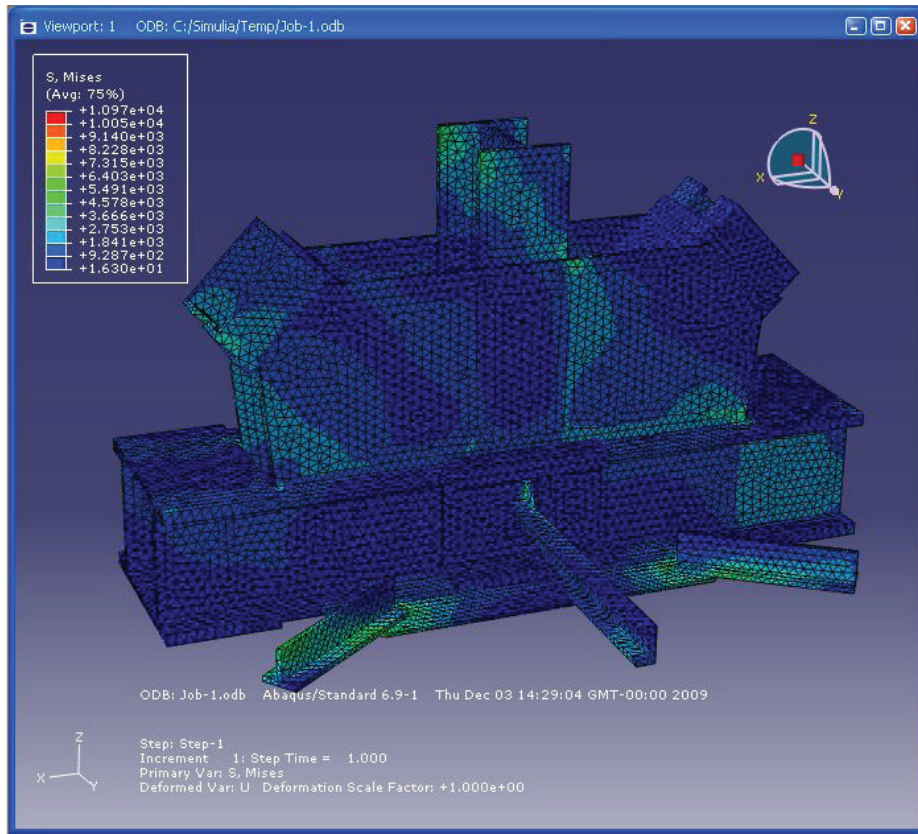


Figure 7 – Detailed FE solid model of a structural joint: Von Mises stresses.

4. FINAL REMARKS

The presented methodology allowed the application of the sub-modelling techniques to the modelling of the Trezói Railway Bridge in Portugal. The analysis of this bridge has been carried out with the construction of two basic models: a global model of the structure with beam elements and a local model of the desired joint with solid elements. The developed integrated CAD system

permits the construction and management of the structural data for the global model, as well as it automates the transportation of a huge quantity of data between different external systems: one utilized for the analysis of the global structure and other to the local analysis. The methodology contributed to reduce, significantly, the computing resources required to the application of the local approaches in the fatigue analysis of this riveted bridge, as also permitted the

simulation of different load scenarios applied through all the bridge and allowed the automatic local analyses with the corresponding deformations of a set of nodes selected by the user through the structure.

In the case study the application of the sub-modelling permitted the local approaches with a low computational cost: the global model has only about 600 nodes and 1000 beam elements, while the joint model has about 25 000 nodes and 85 000 elements. A first simulation of the traffic load utilized a distance between positions of loads applications of 36m and generates 12 load steps through all the bridge, for the train type 2, 9 load steps for the train type 7 and 10 load steps for the train type 11. For each train type and for each load step the deformations of eight nodes around a structural joint in a principal beam in the central section were obtained from the software ANSYS® and transferred to the local model at the software ABAQUS® and all stages of the analysis runs in a single computer, with no special configuration. Actually new approaches have been done with narrow space between loads steps and with a large local model. Those new approaches are possible with a little work due to the use of the developed CAD system.

The proposed integrated CAD system will be used in future works to assess the stress field histories at the main joints of the bridge. These stress histories will be used to assess the critical locations of the joint and the fatigue damage at those locations. The model presented in Figure 7 is a continuous model of the joint, however it is expected in future developments to include rivets in critical branches of the joint.

5. REFERENCES

- [1] J. Moreno, A. Valiente, 2004, "Stress intensity factors in riveted steel beams", *Engineering Failure Analysis*, 11, pp. 777-787
- [2] DiBattista, J.D., Adamson D.E.J. & Kulak G.L. 1998. Evaluation of remaining fatigue life for riveted truss bridges. *Canadian Journal of Civil Engineering* 25(4):678-691.
- [3] De Jesus, A.M.P., Correia, J.A.F.O. 2008. *Fatigue assessment of riveted railway bridge connections. Part II: numerical investigations*. In P.J.S. Cruz, L.S. Silva & F. Schröter (eds) *Steel bridges. Advances solutions & technologies*: 339-48. European Convention for Constructional Steelwork.
- [4] De Jesus, A.M.P., Pinto, H., Fernández-Canteli, A., Castillo, E., Correia, J.A.F.O. 2010. Fatigue assessment of a riveted shear splice based on a probabilistic model. *International Journal of Fatigue* 32: 453-462
- [5] B.M. Imam, T.D. Righiniotis, M.K. Chryssanthopoulos, 2007, "Application of probabilistic fracture mechanics in evaluation of existing riveted bridges", *Engineering Structures*, 29, pp. 3071-3081.
- [6] T.D. Righiniotis, B.M. Imam, M.K. Chryssanthopoulos, 2008, "Fatigue analysis of riveted railway bridge connections using the theory of critical distances", *Engineering Structures*, in press.
- [7] Swanson Analysis Systems Inc., Version 12.0, ANSYS (2009) Houston.
- [8] Dassault Systèmes Simulia Corp., Version 6.9-1, ABAQUS/CAE (2009) Providence, RI, USA.
- [9] LEITE, R. C. G. "Um Framework Para Automação/Integração do Processo de Desenvolvimento de Projetos de Estruturas Reticuladas Tridimensionais". 2007. Tese (doutorado em Engenharia de Estruturas) Escola de Engenharia, UFMG, Belo Horizonte.
- [10] ECKEL, Bruce, "Thinking in C++ - vols 1 & 2", 2nd Edition, Prentice Hall, 1999. Disponível em: <<http://www.mindview.net/Books/TICPP/ThinkingInCPP2e.html>> Acesso em mai 2002
- [11] GAMMA, E., HELM R., JOHNSON R., VLISSIDES J. "Padrões de Projeto: soluções reutilizáveis de software orientado a objetos." Porto Alegre: Bookman, 2000. 363p. Trad.: Salgado, Luiz. A. Meirelles.
- [12] BUSCHMANN, F. MEUNIER, R. ROHNERT, H. SOMMERLAD, P. STAL, M. "Pattern - Oriented Software Architecture A system of Patterns". Chichester: John Wiley & Sons, 1996. 467p
- [13] AUTODESK Inc., "ObjectARX for AutoCAD 2009". Disponível em <<http://usa.autodesk.com/adsk/servlet/index?id=773204&siteID=123112>> Acesso em Abr 2009.
- [14] AUTODESK Inc., Version C.56.0 (UNICODE), AutoCAD 2009.
- [15] MARQUES, F. M. de S. "Avaliação do Comportamento Estrutural e Análise de Fadiga em Pontes Metálicas Ferroviárias". 2006. Tese (Mestrado em Estruturas de Engenharia Civil) Faculdade de Engenharia da Universidade do Porto. Porto
- [16] European Committee for Standardization (CEN) – EN1991-2 (2003) – "Actions on Structures – Part 2: General Actions – Traffic loads on bridges", Brussels

A MODIFIED GTN MODEL FOR THE PREDICTION OF DUCTILE FRACTURE AT LOW STRESS TRIAXIALITIES

F. Reis¹, L. Malcher¹, F. M. Andrade Pires¹, J. M. A. César de Sá¹

¹IDMEC – Institute of Mechanical Engineering
 Faculty of Engineering, University of Porto
 Rua Dr. Roberto Frias, Porto 4200-465, Portugal
 e-mail: fpires@fe.up.pt

ABSTRACT

In this contribution, the so-called GTN constitutive model [1] is extended in order to include a shear mechanism on the damage evolution equation, which depends on the Lode angle. This mechanism is introduced in order to improve the damage prediction under shear dominated loads. From the numerical viewpoint, a fully implicit elastic predictor/return mapping algorithm is developed and the associated consistent elasto-plastic tangent operator is presented. The numerical model is assessed through the simulation of pure shear and combined shear/tensile stress states. Some representative results show the influence of the modifications on the constitutive model of several parameters such as porosity and accumulated plastic strain. A comparative study demonstrates that the proposed model provides better agreement with experimental evidence.

KEY WORDS: GTN model, Low stress triaxiality, Ductile materials, Shear tests, Lode angle dependence.

1. INTRODUCTION

Many classical ductile damage models have the ability to predict the correct fracture location. However, most of them is only effective within a specific range of stress triaxialities. For instance, Lemaitre’s model [2] provides good predictions under pure shear or combined shear/tensile stress states, where typically low stress triaxialities are present.

However, at high stress triaxialities, Gurson’s original model [3] is more accurate than Lemaitre’s. In this case, Gurson’s model predicts failure onset for a lower displacement value than Lemaitre’s. As reported in a previous contribution [4], this result is in agreement with experimental evidence. This stems from the fact that Gurson’s original model is particularly able to capture spherical void growth which is the most relevant mechanism present at high triaxialities. However, under shear dominated stress states, failure mechanisms are driven by shear localization of plastic strain of the inter-voids ligaments due to void rotation and distortion [5]. Since Gurson’s original model does not include such important mechanisms, it is not able to capture the behavior of the material under these conditions, yielding on poorer predictions as it will be clear in the following.

In a pure shear test, failure is predicted with reasonable accuracy with Lemaitre’s model (see Figure 1). However, this is not the case when Gurson’s original model is adopted, since the value of the porosity remains constant once we reach a prescribed displacement and never reaches its critical value. This is a direct consequence of

Gurson’s constitutive theory that only takes into account the nucleation of micro-voids. Thus, we can conclude that, in order to capture the behavior of a ductile material close to rupture under shear dominated loads, a shear mechanism must also be included.

The evolution laws for internal degradation in Lemaitre

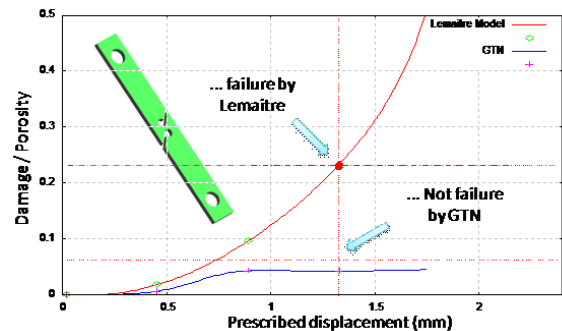


Figure 1. Evolution of the damage and porosity parameters in a pure shear test with Lemaitre’s and Gurson’s models.

and Gurson material models are dependent on the pressure through the stress triaxiality parameter. Nevertheless, many researchers advocate that damage evolution depends on more than one parameter and that its definition depending solely on the stress triaxiality is not sufficiently accurate (e.g. Brünig et al. [6], Malcher et al. [4], Xue [5], Nahshon and Hutchinson [7]). In this context, several authors (e.g. Brünig et al. [6], Bao and Wierzbicki [8], Xue [5], Nahshon and Hutchinson [7]) have proposed the introduction of the effect of the third invariant of the deviatoric stress tensor through the

so-called *Lode angle* on the set of damage evolution equations.

The goal of this work is to improve the capability of predicting the correct fracture location for a wider range of stress triaxialities. The Lode angle parameter is defined on the deviatoric plane as being the smallest angle between the line of pure shear and the projection of the stress vector on the π -plane. This parameter is responsible for the shape of the yield surface and its effect can be introduced into the constitutive model or into damage evolution law through the so-called Lode angle function.

More recently, Xue [5] has proposed an improvement on the porosity evolution law aiming to capture the behavior of the material at low stress triaxialities through a shear mechanism which is Lode angle dependent. However, although this model has shown significant improvements, its numerical implementation is extremely difficult.

Therefore, this paper has two main goals: (a) to describe the enhancements achieved by the introduction of a shear mechanism into the GTN model which was based inspired in the work of Xue [5]; (b) to suggest a suitable modification of this mechanism aiming to facilitate the numerical implementation and increase efficiency of the constitutive integration algorithm.

2. CONSTITUTIVE MODELING

Gurson's [3] approach has been proposed to describe material internal degradation in the presence of plastic strains. This model, which was developed to provide the "bridge" between material plasticity and damage accumulation, allows the prediction of the loss of resistance of porous materials due to the growth of spherical microvoids. The main feature of Gurson's model is the introduction of a yield function that is governed by first and second invariant of stress tensor and also by the damage variable f , which represents the volume fraction of microvoids embedded in the material matrix.

2.1. GTN original model

One of the most commonly employed versions of Gurson's model is the Tvergaard-Needleman modification [1], commonly referred to as GTN model. The model assumes isotropic hardening and isotropic damage (represented by the effective porosity f^*). In the GTN model, the flow potential is generalized into the form:

$$\Phi(\underline{\sigma}, k, f) = J_2(\underline{\mathbf{S}}) - \frac{1}{3} \left\{ 1 + q_3 \cdot f^{*2} - 2 \cdot q_1 \cdot f^* \cdot \cosh\left(\frac{3 \cdot q_2 \cdot p}{2 \cdot \sigma_0}\right) \right\} \cdot \sigma_0^2 \quad (1)$$

where J_2 represents the second invariant of the deviatoric stress tensor, p is the pressure, σ_0 is the isotropic

hardening rule (which can be defined as $\sigma_0 = R - \sigma_{y0}$) and R represents the isotropic hardening state variable. The parameters q_1 , q_2 and q_3 are introduced to bring the model predictions into closer agreement with full numerical analyses of a periodic array of voids.

The effective porosity reproduces the mechanisms of nucleation, growth and coalescence of voids (which may occur either simultaneously or successively):

$$f^* = \begin{cases} f & , f < f_c \\ f_c + \left(\frac{1}{q_1} - f_c\right) \frac{(f-f_c)}{(f_f-f_c)} & , f \geq f_c \end{cases} \quad (2)$$

where f_c is the value of void volume fraction that defines the beginning of coalescence phenomenon and f_f represents the porosity at fracture. The evolution of f is a sum of the nucleation and growth mechanisms:

$$\dot{f} = \dot{f}^N + \dot{f}^G \quad (3)$$

The nucleation mechanism in this case is driven by the plastic strain:

$$\dot{f}^N = \frac{f_N}{s_N \cdot \sqrt{2\pi}} \cdot \exp\left[-\frac{1}{2} \left(\frac{\bar{\varepsilon}^p - \varepsilon_N}{s_N}\right)^2\right] \cdot \dot{\bar{\varepsilon}}^p \quad (4)$$

where f_N represents the volume fraction of all second-phase particles with potential for micro-void nucleation, ε_N and s_N are the mean strain for void nucleation and its standard deviation. The variable $\bar{\varepsilon}^p$ represents the equivalent plastic strain and $\dot{\bar{\varepsilon}}^p$ is the rate of the accumulated plastic strain.

The most significant contribution is the growth of existing voids, denoted by \dot{f}^G , obtained from the condition of plastic incompressibility of the matrix material:

$$\dot{f}^G = (1 - f) \cdot \text{tr}(\dot{\varepsilon}^p) = (1 - f) \cdot \dot{\varepsilon}_v^p \quad (5)$$

where $\dot{\varepsilon}_v^p$ represents the rate of the volumetric plastic strain.

2.2. Shear mechanism

In order to improve the GTN model ability to capture the behavior of ductile materials close to rupture at low stress triaxialities, Xue [5] has proposed the inclusion of a shear mechanism which is a function of the porosity, equivalent strain and the Lode angle. Originally, the shear mechanism was developed considering geometrical considerations in a cell structure with a circular void at the center subjected to a simple shear strain (for more details, see Xue [5]). After some straightforward algebra manipulation, the rate of this mechanism is expressed as:

$$\dot{f}^{Shear} = q_4 \cdot f^{q_5} \cdot g_0 \cdot \varepsilon_{eq} \cdot \dot{\varepsilon}_{eq} \quad (6)$$

where q_4 and q_5 are parameters related to two- or three-dimensional problems, respectively set to $q_4 = 1.69$ and

$q_5 = 1/2$, $q_4 = 1.86$ and $q_5 = 1/3$. The parameter f represents the porosity, ε_{eq} is the equivalent strain and g_0 is a parameter responsible to incorporate the Lode angle dependence in the shear mechanism and that can be defined as:

$$g_0 = 1 - \frac{6 \cdot \|\theta\|}{\pi} \quad (7)$$

where θ is the Lode or azimuth angle, which can be determined as:

$$\theta = \tan^{-1} \left\{ \frac{1}{\sqrt{3}} \left[2 \cdot \left(\frac{S_2 - S_3}{S_1 - S_3} \right) - 1 \right] \right\} \quad (8)$$

in which S_1 , S_2 and S_3 are components of the deviatoric stress tensor in the principal plane.

The shear mechanism proposed by Xue can be added to the GTN model which already features the mechanisms of nucleation and growth of micro-voids. Thus, the evolution of the porosity now reads:

$$\dot{f} = \dot{f}^N + \dot{f}^G + \dot{f}^{Shear} \quad (9)$$

2.3. The proposed modification

The shear mechanism was suggested in order to introduce void elongation effect into the original GTN model. Therefore, the contribution of such mechanism is higher at low stress triaxialities and, through the definition of the parameter g_0 , for low values of the Lode angle. In this contribution, the evolution of the porosity due to shear effects will be a function of both the accumulated plastic strain and the rate of the accumulated plastic strains instead of the total strain and total strain rate. This simplification is reasonable in the majority of problems since the elastic strains can be considered negligible.

$$\dot{f}^{Shear} = q_4 \cdot f^{q_5} \cdot g_0 \cdot \bar{\varepsilon}^p \cdot \dot{\bar{\varepsilon}}^p \quad (10)$$

The Lode angle function can also be rewritten as a function of the normalized third invariant:

$$g_0 = 1 - \|\bar{\theta}\| \quad (11)$$

where $\bar{\theta}$ represents the normalized Lode angle which is a function of the normalized third invariant [8]:

$$\bar{\theta} = 1 - \frac{6 \cdot \theta}{\pi} = 1 - \frac{2}{\pi} \arccos \xi \quad (12)$$

In the equation above, ξ represents the normalized third invariant and can be calculated as:

$$\xi = \frac{27}{2} \frac{\det(\varepsilon_d^e)}{\left(\frac{3}{2} \varepsilon_d^e : \varepsilon_d^e\right)^{\frac{3}{2}}} \quad (13)$$

where ε_d^e represents the deviatoric elastic strain tensor [9]. The initial value of the normalized Lode angle for different stress conditions is represented in Figure 2 [9]. As we can see in Figure 2, in pure shear conditions, $\bar{\theta}$ is around zero which correspond a value of g_0 around 1.

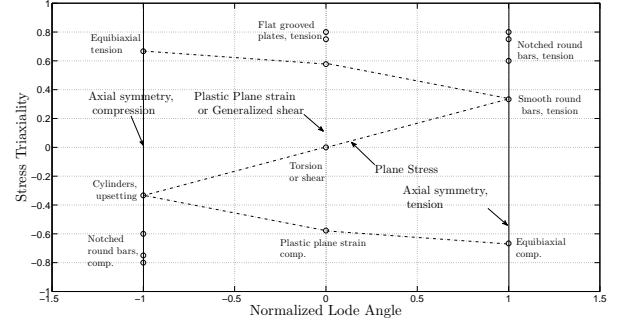


Figure 2. Triaxiality as a function of the Normalized Lode angle for initial stress states [9].

In this case, the effect of the shear mechanism is added to the damage variable of the original GTN model. On the other hand, in traction problems with round bars, the Lode angle function is approximately zero and in these cases, the shear mechanism proposed does not play any role.

2.4. Integration algorithm

As already pointed out, the proposed modification leads us to a constitutive model which is easier to implement than the model proposed by Xue. The constitutive equations of the model are integrated implicitly by using a typical elastic predictor/return mapping algorithm (a detailed discussion on return mapping algorithms can be found elsewhere, e.g., Simo and Hughes [10], de Sousa Neto et al. [11], etc.). Straightforward (pseudo-)time discretization of the constitutive equations leads to the following system of equations:

$$\begin{cases} r_{\Delta\gamma} = \frac{1}{2} \frac{s^{Trial} : s^{Trial}}{1 + 2 \cdot G \cdot \Delta\gamma^2} - \frac{1}{3} \left\{ 1 + q_3 \cdot f_{n+1}^2 - 2 \cdot q_1 \cdot f_{n+1} \cdot \cosh\left(\frac{3 \cdot q_2 \cdot p_{n+1}}{2 \cdot \sigma_0}\right) \right\} \cdot \sigma_0^2 \\ r_p = p_{n+1} - p_{n+1}^{Trial} + \Delta\gamma \cdot K \cdot q_1 \cdot q_2 \cdot f_{n+1} \cdot \sigma_0 \cdot \sinh\left(\frac{3 \cdot q_2 \cdot p_{n+1}}{2 \cdot \sigma_0}\right) \\ r_f = f_{n+1} - f_{n+1}^{Trial} - \Delta f^G - \Delta f^{Trial} \\ r_R = R_{n+1} - R_{n+1}^{Trial} - \Delta R_{n+1} \end{cases} \quad (14)$$

which needs to be solved for $\Delta\gamma$, p_{n+1} , f_{n+1} and R_{n+1} . Here, we choose to apply the standard Newton-Raphson method for the solution of the non-linear system. The residual system of equations, on the linearized form can be given by:

$$\begin{bmatrix} \frac{\partial r_{\Delta\gamma}}{\partial \Delta\gamma} & \frac{\partial r_{\Delta\gamma}}{\partial p_{n+1}} & \frac{\partial r_{\Delta\gamma}}{\partial f_{n+1}} & \frac{\partial r_{\Delta\gamma}}{\partial R_{n+1}} \\ \frac{\partial r_p}{\partial \Delta\gamma} & \frac{\partial r_p}{\partial p_{n+1}} & \frac{\partial r_p}{\partial f_{n+1}} & \frac{\partial r_p}{\partial R_{n+1}} \\ \frac{\partial r_f}{\partial \Delta\gamma} & \frac{\partial r_f}{\partial p_{n+1}} & \frac{\partial r_f}{\partial f_{n+1}} & \frac{\partial r_f}{\partial R_{n+1}} \\ \frac{\partial r_R}{\partial \Delta\gamma} & \frac{\partial r_R}{\partial p_{n+1}} & \frac{\partial r_R}{\partial f_{n+1}} & \frac{\partial r_R}{\partial R_{n+1}} \end{bmatrix}^k \cdot \begin{bmatrix} \delta \Delta\gamma \\ \delta p_{n+1} \\ \delta f_{n+1} \\ \delta R_{n+1} \end{bmatrix}^{k+1} = - \begin{bmatrix} r_{\Delta\gamma}(\Delta\gamma, p, f, R) \\ r_p(\Delta\gamma, p, f, R) \\ r_f(\Delta\gamma, p, f, R) \\ r_R(\Delta\gamma, p, f, R) \end{bmatrix}^k \quad (15)$$

where we need to determine the derivatives of $r_{\Delta\gamma}$, r_p and r_R in respect to every unknown of the problem.

The associated consistent elastoplastic tangent operator, necessary to ensure quadratic convergence rates, can be expressed in the following closed-form:

$$\begin{aligned}
 D^{ep} = & \frac{2.G}{(1+2.G.\Delta\gamma)} \left(1 - \frac{1}{3} \mathbf{I} \otimes \mathbf{I}\right) \\
 & + \left[\frac{2.G}{(1+2.G.\Delta\gamma)} \right]^2 .e_d^{trial} \\
 & \otimes \left[\left(C_{11} \frac{\partial r_{\Delta\gamma}}{\partial \epsilon_d^{trial}} + C_{13} \frac{\partial r_f}{\partial \epsilon_d^{trial}} \right) C_{12} \frac{\partial r_p}{\partial \epsilon_v^{trial}} \mathbf{I} \right] \\
 & - \mathbf{I} \otimes \left[\left(C_{21} \frac{\partial r_{\Delta\gamma}}{\partial \epsilon_d^{trial}} + C_{23} \frac{\partial r_f}{\partial \epsilon_d^{trial}} \right) + C_{22} \frac{\partial r_p}{\partial \epsilon_v^{trial}} \mathbf{I} \right]
 \end{aligned} \quad (16)$$

where C_{11} , C_{12} , C_{21} , C_{23} and C_{22} are constants associated with the non-linear system. Furthermore, \mathbf{l} and \mathbf{I} are respectively the fourth and second order identity tensors.

3. NUMERICAL RESULTS

In this section, the performance of the extended constitutive model is assessed by means of two examples. Both were simulated considering a finite strain formulation in an in-house finite element code.

3.1. Shear test

To illustrate the effectiveness of the proposed constitutive model, a shear specimen subject to a shear stress state has been analysed [6].

A three-dimensional finite element mesh with 8-node linear elements with *FBAR* technology (for more details see [11]) has been employed in all analyses (see Figure 3). The material properties adopted are listed in Table 1.

Table 1. Material properties for the aluminum alloy (Al 2024-T351).

Description	Symbol	Value
Density	ρ	$2.7 \times 10^3 \text{ kg/m}^3$
Elastic modulus	E	$7.115 \times 10^4 \text{ [MPa]}$
Poisson's ratio	ν	0.3
Initial yield stress	σ_{y0}	370 [MPa]
Hardening curve	$\sigma_y (\bar{\epsilon}^p)$	$908 (0.0058 + \bar{\epsilon}^p)^{0.1742}$ [MPa]
q_1		1.5
q_2		1
q_3		2.25
Volumetric fraction of micro-void for nucleation	f_N	0.04
Mean strain of void nucleation	ϵ_N	0.2
Standard deviation strain for nucleation	S_N	0.1

Figure 4.a shows the evolution of porosity for the two Gurson based models. In this test, where the triaxiality ratio attains a value around zero, we can observe that the modified GTN model proposed herein has the ability of predicting the degradation associated

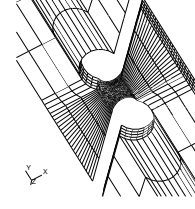


Figure 3. Finite element mesh for the shear specimen with 3432 elements and 4785 nodes.

with shear effects. The original GTN model, however, provides an inaccurate response when the shear effects are present. This can be concluded since porosity remains constant when the prescribed displacement is increased. Thus, the proposed model has the ability to predict shear effects as well as nucleation and growth of micro-voids. Even though the final values of the damage variable are considerable distinct, when we compare the distributions of damage in the shear specimen we conclude that the distribution is similar (see Figure 5).

In Figure 4.b, the evolution of accumulated plastic strain is plotted. As expected, this internal variable is larger when the new model is considered since degradation is significantly higher if compared with GTN original model that only contemplates nucleation and growth mechanisms. In contrast with the accumulated plastic strain, we can see in Figure 4.c that the reaction force associated with the new model is smaller than the similar curve associated with GTN model. Again, this difference is a consequence of an higher internal damage. One interesting aspect to note in Figure 4.c is the pronounced effect of softening in the reaction curve of the new model for the same prescribed displacement.

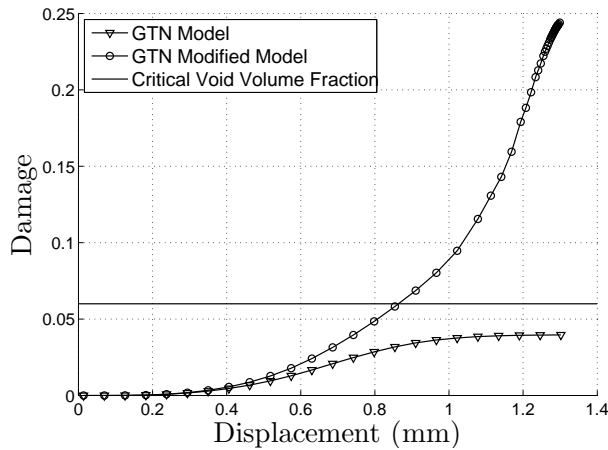
Moreover, the efficiency of the proposed algorithm is also assessed. Table 2 shows a typical residual convergence observed during the analysis of the present example. Clearly, convergence exhibits a quadratic convergence rate due to the consistent tangent operator.

Table 2. Typical global convergence of proposed model.

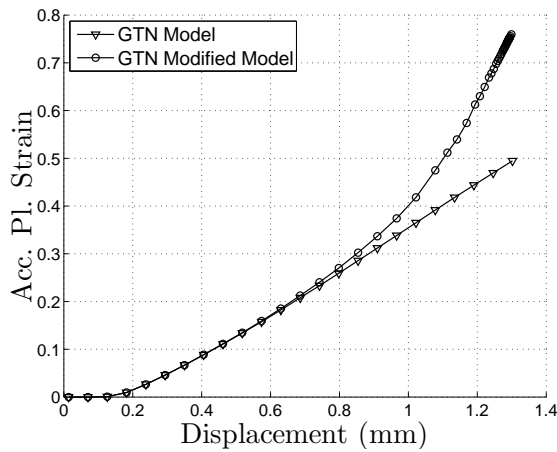
Iteration	Relative residual norm (%)
1	4.57572
2	0.559380E-01
3	0.978862E-05
4	0.495718E-09

3.2. Flat-grooved test

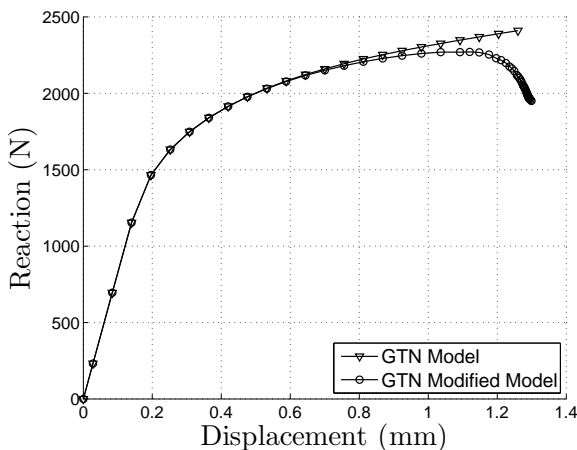
In this section, a flat-grooved plate [12] in plane strain is analysed under a tensile dominant load. The main goal of the numerical simulation is to verify the ability of the



a)



b)



c)

Figure 4. (a) Evolution of damage; (b) evolution of accumulated plastic strain; (c) reaction curve

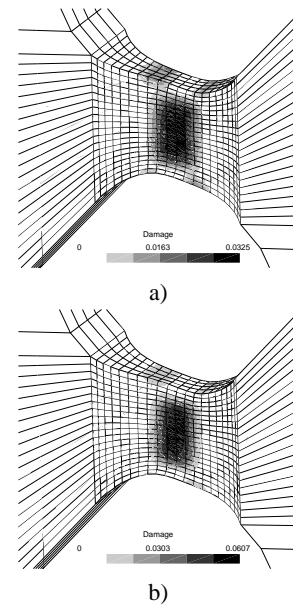


Figure 5. Distribution of damage a) GTN model; b) New model.

proposed model to predict the 45 degrees inclined shear bands observed in experimental testing [5]. The material properties are the same as the material in the preceding section (see Table 1). Spatial discretization has been done by using 8-node quadratic elements with a reduced integration scheme (see Figure 6).



Figure 6. Finite element mesh for the plane strain specimen with 1600 elements and 5033 nodes.

In Figure 6, we can clearly observe the effects of the incorporated shear mechanism. For the same applied displacement, the contours of the new damage variable have correctly predicted the shear bands inclined 45 degrees in respect to the loading direction. In the simulation with the original GTN model, however, damage has concentrated at the center of the specimen which is not in agreement with experimental results [5].

4. CONCLUSIONS

In this work, we have briefly revised the original GTN model and depicted its limitations when subject to low triaxialities. For such model, the damage variable (volume fraction of voids dependent on pressure) does not reflect the degradation associated with shear effects. The incorporation of a modified shear mechanism into the constitu-

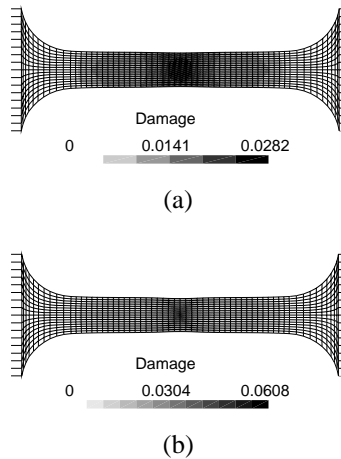


Figure 7. Damage contours at critical zone for the plane strain test: (a) original GTN model; (b) proposed model.

tive model has allowed a much more accurate prediction of failure for a wider range of triaxialities. Finally, the modified evolution of the porosity due to shear effects proposed in this paper has provided an extremely efficient numerical implementation exhibiting high asymptotic convergence rates.

ACKNOWLEDGEMENTS

Fábio Reis is supported by Portuguese Science and Technology Foundation (FCT), under scholarship number SFRH/BD/60887/2009. Lucival Malcher is supported by Portuguese Science and Technology Foundation (FCT), under scholarship number SFRH/BD/45456/2008. The authors acknowledge the support of Portuguese Science and Technology Foundation (FCT) under grant with reference PTDC/EME-TME/71325/2006.

REFERENCES

[1] V Tvergaard and A. Needleman. Analysis of cup-cone fracture in a round tensile bar. *Acta Metallurgica*, 32:157–169, 1984.

[2] J. Lemaitre. *A Course on Damage Mechanics*. Springer, 1990.

[3] A.L. Gurson. Continuum theory of ductile rupture by void nucleation and growth - part I: Yield criteria and flow rule for porous media. *Journal of Engineering Materials and Technology*, 99:2–15, 1977.

[4] L. Malcher, F. M. Andrade Pires, J. M. A. César de Sá, and F. X. C. Andrade. Comparative study between ductile damage constitutive model. In *COMPLAS*, Spain, Barcelona, 2009.

[5] L. Xue. *Ductile Fracture Modeling - Theory, Experimental Investigation and Numerical Verification*. PhD thesis, Massachusetts Institute Technology, 2007.

[6] M. Brünig, O. Chyra, D. Albrecht, L. Driemeier, and M. Alves. A ductile damage criterion at various stress triaxialities. *International Journal of Plasticity*, 24:1731–1755, 2008.

[7] L. Nahshon and J. W. Hutchinson. Modification of the gurson model for shear failure. *European Journal of Mechanics A/Solids*, 27:1–17, 2008.

[8] Y. Bao and T. Wierzbicki. On fracture locus in the equivalent strain and stress triaxiality space. *International Journal of Mechanical Sciences*, 46(81): 81–98, 2004.

[9] Y. Bai. *Effect of Loading History on Necking and Fracture*. PhD thesis, Massachusetts Institute Technology, 2008.

[10] J. C. Simo and T. J. R Hughes. *Computational Inelasticity*. Springer, 1998.

[11] E. A. de Sousa Neto, D. Perić, and D. R. Owen. *Computational Methods for Plasticity: Theory and Application*. Wiley, 2008.

[12] X. Teng. Numerical prediction of slatn fracture with continuum damage mechanics. *Engineering Fracture Mechanics*, 75:2020–2041, 2008.

FRETTING FATIGUE LIFE PREDICTION USING THE EXTENDED FINITE ELEMENT METHOD

C. Navarro¹, E. Giner^{*,2}, M. Sabsabi², M. Tur², J. Domínguez¹, F.J. Fuenmayor²

¹Departamento de Ingeniería Mecánica y de los Materiales, E.T.S. de Ingenieros,
 Universidad de Sevilla, Camino de los Descubrimientos, 41092 Sevilla, España.
 E-mail: cnp@us.es
 Tel: +34 954481365

²Departamento de Ingeniería Mecánica y de Materiales-CITV, E.T.S. de Ingenieros Industriales,
 Universidad Politécnica de Valencia, Camino de Vera s/n, 46022 Valencia, España.
 E-mail: eginerm@mcm.upv.es
 Tel: +34 963877007 Ext. 76218.

ABSTRACT

In this work, fretting fatigue tests available in the literature are modeled using the extended finite element method (X-FEM). The aim is to numerically evaluate the stress intensity factors (SIFs) for cracks of different lengths emanating at the end of the contact zone and to estimate the propagation life corresponding to each of the tests. This propagation life is combined with the initiation life calculated analytically using a multiaxial fatigue criterion (Fatemi-Socie), following an initiation-propagation approach for life estimation. The predicted lives are then compared with the reported experimental lives. It is shown that the consideration of the crack-contact interaction through the numerical models tends to improve the life estimation when compared with a fully analytical approach for the calculation of both initiation and propagation lives.

KEYWORDS: Fretting-fatigue. Extended finite element method (X-FEM). Initiation and propagation life model.

1 INTRODUCTION

In the analysis of the fretting fatigue life and other fatigue problems, two stages are usually distinguished: initiation of the crack and its subsequent propagation. In recent years, methods have been proposed to predict the total life as a combination of the life spent during the initiation phase and the life associated with the propagation phase. The point at which the initiation phase finishes and the propagation phase begins cannot be precisely defined and some authors propose a certain transition crack length on a rather heuristic basis. In this work, we use a variable initiation length model proposed in [1, 2], in which the transition length is not previously fixed, but it depends on the particular load conditions and material properties of the analyzed problem.

The initiation life can be estimated by means of multiaxial fatigue criteria, such as the McDiarmid and the Fatemi-Socie criteria, which are reported to give good results [2]. The propagation life can be analyzed using a crack growth law of the type $da/dN = f(\Delta K)$, e.g. Paris law or other variations based on linear elastic fracture mechanics assumptions (LEFM). The correct calculation of the stress intensity factors (SIFs) plays a crucial role when predicting the life associated with the crack propagation stage. This can affect the estimated total life, especially for problems in which the propagation life is a significant part of the total life, for example in certain fretting problems in which the steep gradients in the vicinity of the contact induce a rapid crack initiation.

On the other hand, the propagation stage in a fretting-fatigue problem is substantially different from that of plain fatigue only during the phase in which the crack length is less than the characteristic dimension of the contact zone. Analytical approaches have been used [1] based on the weight function method for estimating the SIF. However, these methods do not take into account the influence of the crack-contact interaction (i.e. alteration of the contact fields due to the crack presence) which can be important at the beginning of the propagation stage.

For extracting realistic values of the SIFs including the crack-contact interaction, the numerical modelling of the problem becomes necessary and the finite element method (FEM) or the more advanced extended finite element method (X-FEM) can be applied. To compute the propagation life, the SIFs must be calculated for a relatively wide range of crack lengths. This means that the mesh generation process needed in the classical FEM is very cumbersome, as it must conform to both relatively small contact zones and cracks of small size in their vicinity.

On the other hand, in recent years the X-FEM [3] has proved to be a very efficient tool for the numerical modelling of cracks in linear elastic fracture mechanics (LEFM). Compared to the standard FEM, the X-FEM presents great advantages for the numerical modelling of cracks. The main advantage is that it is not necessary to generate a mesh that conforms to the crack boundaries (faces) to account for the geometric discontinuity. Therefore only a single mesh, often generated easily, can be

used for any crack length and orientation, which enormously expedites the computation process. In addition, the method includes crack-tip enrichment functions that provide accurate estimations of the SIFs when using domain independent integrals, such as the J -integral or the interaction integral.

In this work, the use of the X-FEM is combined with the initiation-propagation model proposed in [1, 2] to assess the total life of fretting fatigue problems. The models analyzed correspond to 2D problems with cylindrical contact pressed onto flat specimens subjected to a variable bulk load. The predicted life is compared with the experimental results reported in the literature [4, 5] for fretting tests with cylindrical indenters and flat specimens. The propagation analyses have been performed by means of the X-FEM implementation carried out by the authors [6] in the framework of the commercial code ABAQUS. The results show that the use of the X-FEM to predict the propagation lives tends to improve the life estimation when compared to an analytical approach using weight functions.

2 COMBINED INITIATION-PROPAGATION MODEL

The model used to estimate life in fretting was proposed by the authors [1]. It is assumed that two different mechanisms act upon a material subjected to fretting: one during the initiation phase and another during propagation. The phenomena produced in either phase are considered different and are dealt with separately, although the consequence is the same: failure in the material.

Regarding the first phase, there is a calculation of the number of cycles needed to initiate a crack along the trajectory theoretically followed by it, N_i . This is done by evaluating the stresses along the assumed crack path and introducing them in the fatigue curve of the material. Due to the complexity of the stress field (multiaxial and non-proportional), a multiaxial fatigue criterion must be employed. In this case the well known Fatemi-Socie parameter is used.

In the second phase, the calculation is for the number of cycles needed to propagate the crack from each point until failure, using LEFM, N_p . This is done by integrating Paris crack growth law from each crack length to the final length, where the fracture of the specimen is assumed to occur. It will be assumed that the crack is initiated in the limit of the contact zone and grows perpendicular to the surface. It can be experimentally proven that these suppositions are not far from reality [1, 4].

The sum of the two curves obtained, N_i plus N_p , renders the total life associated to each point, considering each point as the crack length whose growth is governed first by initiation and then by propagation. The minimum of that curve is the most unfavourable point in it, which provides the life of the specimen. The position of the mini-

um, called initiation length, marks the end of the initiation and the beginning of propagation. This model supposes that before the initiation length the crack is initiated in each point before it has time to propagate. In contrast, once the initiation length is surpassed then propagation dominates over initiation and the evolution is predicted using fracture mechanics.

3 FUNDAMENTALS OF THE X-FEM

The essential feature of the method is the enrichment of the FE model with additional degrees of freedom (dof) for the nodes belonging to the elements geometrically intersected by the crack location (called enriched nodes and elements, respectively). Thus, the discontinuity is included in the numerical model without modifying the discretization. Fig. 1 shows a portion of the mesh used in this work, where the enriched nodes are marked. Nodes located next to the crack faces (encircled nodes in Fig. 1) are enriched with 2 additional dofs (one for each direction of the domain space) to represent the physical displacement discontinuity by means of a Heaviside function $H(\mathbf{x})$. The Heaviside function can only take the values $H(\mathbf{x}) = \pm 1$, depending on the relative position of the enriched node with respect to the crack faces.

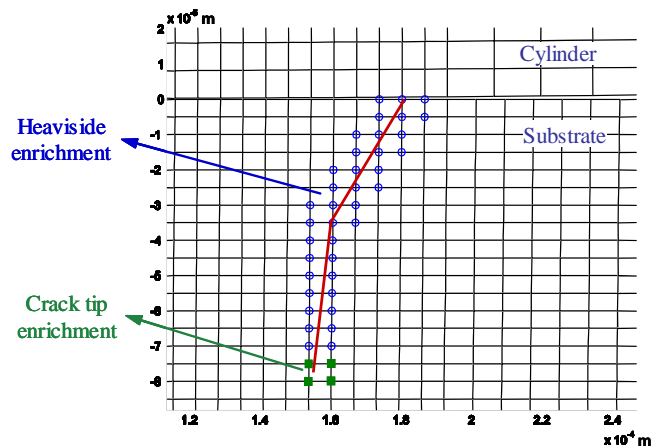


Figure 1: Enriched nodes in the X-FEM.

The X-FEM formulation allows for a further type of enrichment for those nodes that surround the crack-tip. These nodes (marked as squares in Fig. 1) are enriched with 8 additional dofs: four crack-tip functions $F_j(\mathbf{x})$ times the two directions of the domain space. The crack-tip functions constitute the basis functions that represent the first term of the LEFM displacement field, and consequently, reproduce the classical stress singular behavior of the LEFM. These functions are given by:

$$F_j(r, \theta) = \sqrt{r} \left[\sin \frac{\theta}{2}, \cos \frac{\theta}{2}, \sin \frac{\theta}{2} \sin \theta, \cos \frac{\theta}{2} \sin \theta \right] \quad (1)$$

with $j = 1 - 4$. Thus, for the 2D case, the extended finite element approximation to the displacements at a point of the domain \mathbf{x} is:

$$\mathbf{u}_{\text{x fem}}(\mathbf{x}) = \sum_{i=1}^{nn_M} N_i(\mathbf{x}) \mathbf{u}_i + \sum_{i=1}^{nn_H} N_i(\mathbf{x}) H(\mathbf{x}) \mathbf{a}_i + \sum_{i=1}^{nn_{CT}} N_i(\mathbf{x}) \left(\sum_{j=1}^4 F_j(\mathbf{x}) \mathbf{b}_{i,j} \right) \quad (2)$$

where nn_M is the number of nodes in the mesh, and nn_H , nn_{CT} are the number of Heaviside and crack-tip nodes, respectively. $N_i(\mathbf{x})$, \mathbf{u}_i are the standard shape functions and dof of each node i , respectively, and \mathbf{a}_i , $\mathbf{b}_{i,j}$ are the additional dof associated with the Heaviside function $H(\mathbf{x})$ and the crack-tip functions $F_j(\mathbf{x})$. Note that the introduction of the crack-tip functions enhance the quality of the calculated singular LEFM fields in the vicinity of the crack-tip, yielding more accurate estimations of the SIFs. This is a further advantage of the X-FEM over the standard FEM [3].

The authors have implemented the X-FEM approach in ABAQUS by defining a user element that allows 12 dof/node [6]. The combination of the powerful contact procedures available in ABAQUS with the X-FEM implementation has proved successful, as shown in the next sections. The SIFs calculation has been done by means of the path-independent interaction integral [7]. The interaction integral features the same advantages as the J -integral for the SIF computation, like good accuracy and little user intervention. In addition enables the extraction of K_I and K_{II} for mixed-mode problems by using auxiliary fields. When the interaction integral is recast as an equivalent domain integral, it has the following form:

$$I^{(1,2)} = \int_{\Omega} \left[\sigma_{ij}^{(1)} \frac{\partial u_i^{(2)}}{\partial x_j} + \sigma_{ij}^{(2)} \frac{\partial u_i^{(1)}}{\partial x_j} - W^{(1,2)} \delta_{1j} \right] \frac{\partial q}{\partial x_j} d\Omega \quad (3)$$

where $^{(1)}$ are the actual fields of the problem approximated by the X-FEM solution and $^{(2)}$ are the auxiliary fields. These fields are chosen to be the asymptotic crack-tip fields for pure mode I or pure mode II to compute K_I and K_{II} respectively. In (3), x_1, x_2 are the local directions with respect to the crack-tip, δ_{1j} is the Kronecker's delta and q is an arbitrary and continuous function which must vanish at the outer boundary of the problem domain and take the value 1 at the crack-tip. The SIFs of the problem are then calculated as follows:

$$K_I = \frac{E'}{2} I^{(1, \text{aux mode I})} \quad ; \quad K_{II} = \frac{E'}{2} I^{(1, \text{aux mode II})} \quad (4)$$

where $E' = E$ for plane stress and $E' = E/(1 - \nu^2)$ for plane strain. The q -function used in this work is an annular function defined by a radius r_q measured from the

crack-tip, in the same fashion as in [3]. Note that the application of the interaction integral to the X-FEM results must include the contribution of both standard elements and enriched elements where $\frac{\partial q}{\partial x_j} \neq 0$.

4 APPLICATION TO FRETTING-FATIGUE TESTS

4.1 Experimental tests used for comparison

Fig. 2 shows a sketch of the fretting fatigue tests modelled in this work. The test rig consists of two cylindrical fretting pads contacting onto the flat surface of a specimen made of the same material. The normal load P is held constant during the test originating a contact region of semi-width a . A variable bulk stress σ_B is applied to the specimen. Due to the coefficient of friction f , a tangential load Q is generated on the fretting pad. The values of the tangential load and the bulk stress on the left part of the specimen depend on the compliances of both the specimen and the fretting pad support (in Fig. 2 A_s denotes the cross-sectional area of the specimen). Under the loading conditions analyzed in this study, it is well known [8] that the contact area is divided into an internal stick zone of semi-width c and two slip zones. The stick zone has an eccentricity e measured from the center of the contact zone (see Fig. 2).

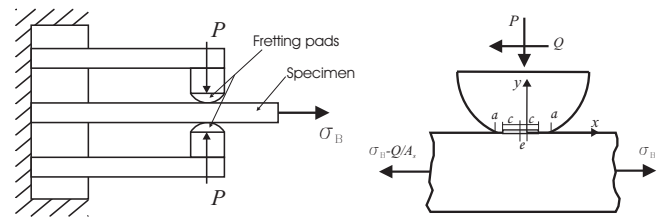


Figure 2: Sketch of the fretting fatigue tests with cylindrical pads and loads transmitted.

Two sets of fretting fatigue tests are analyzed in this paper. The first one, referred here as S&F [4], uses the material Al2024 T351. Not all the tests found in [4] are studied in this paper, only a sample including the whole range of lives. In these tests the specimens thickness was 12.7 mm and the friction coefficient 0.65. Different radii were used for the cylinders, varying between 127 and 229 mm. The test conditions are summarized in Table 1.

The second set of tests analyzed, referred here as A&N [5], was performed with the aluminium alloy Al4%Cu, which is very similar to the preceding one. As in the previous group, only a sample including the whole range of lives is studied. The specimens thickness was 12.5 mm and the friction coefficient 0.75. In these tests the radii of the contact pads were between 50 mm and 150 mm (see Table 2). The Young's modulus and Poisson's ratio is the same for both materials, 74.1 GPa and 0.33, respectively. Finally, other parameters needed for the calculations are

shown in Table 3. The crack growth properties are given for a stress ratio of $R = 0$ and cycles/meter, $\text{MPa}\sqrt{\text{m}}$.

Table 1: Tests and lives reported by S&F in [4]

Test	P (kN)	Radius R (mm)	σ_{Bulk} (MPa)	Q/P	N_{failure} (cycles)
1 (MAF1a)	5.454	229	111.7	0.43	238000
2 (MAF4x)	5.370	127	88.4	0.35	563946
3 (MAF5a)	7.226	127	101.9	0.31	545489
4 (MAF9x)	6.268	229	85.4	0.32	856524
5 (MAF14x)	5.293	229	81.0	0.31	867330
6 (MAF15x)	5.325	229	82.9	0.26	768364
7 (MAF21x)	7.153	229	97.9	0.24	463324
8 (MAF22x)	6.176	178	84.7	0.27	621442

Table 2: Tests and lives reported by A&N in [5]

Test	p_0 (MPa)	Radius R (mm)	σ_{Bulk} (MPa)	Q/P	N_{failure} (cycles)
1	157	50	92.7	0.45	1290000
2	157	75	92.7	0.45	670000
3	143	100	92.7	0.45	610000
4	143	50	77.2	0.45	1200000
5	143	100	77.2	0.45	610000
6	120	150	61.8	0.45	1230000

Table 3: Properties of alloys Al2024 T351 and Al4%Cu.

Material		Al2024 T351 [4]	Al4%Cu [5]
Tensile strength	σ_u	470 MPa	500 MPa
Yield strength	σ_y	310 MPa	465 MPa
Fatigue limit	σ_f	230 MPa	206 MPa
Fatigue strength coefficient	σ_f^j	714 MPa	1015 MPa
Fatigue strength exponent	b	-0.078	-0.11
Paris law coefficient	C	$6.529 \cdot 10^{-11}$	$1.74 \cdot 10^{-10}$
Paris law exponent	n	3.387	4

4.2 Description of the numerical models

A 2D finite element model of the fretting fatigue tests has been defined, as depicted in Fig. 3. The rectangle $2L \times h$ corresponds to the specimen and has a length of $2L = 40$ mm. The half thickness h and the pad radius R is varied according to the test, as well as the friction coefficient f considering a Coulomb's friction model. The crack modelled with X-FEM is located at the right end of the contact zone included in the specimen at $x = a$. Note that the crack length is denoted as a_c . Vertical displacements are constrained on the bottom line of the specimen. Further restrictions for displacements are applied at nodes located on the shaded sides shown in Fig. 3. Using multipoint constraints (MPCs) the displacements in the x -direction of all nodes located at $x = -L$ and $x = L$ are forced to be identical. Similarly, displacements at nodes on the pad top are enforced to be equal. The application of the force T produces a bulk stress and the amount of the tangential force Q transmitted through the frictional contact is controlled by the relative stiffness of the equivalent springs. The equivalent compliances of the left portion of the specimen and the pad support are replaced by spring elements with stiffness k_s and k_p respectively, as shown in Fig. 3. The spring stiffnesses have been varied in order to set the different ratios Q/fP for each test.

The solution is obtained in two steps. First, the normal load P is applied. Rigid body motion of the specimen is avoided by imposing a restriction in the x -direction of nodes at $x = -L$ and $x = L$. In a second step this restriction is eliminated and a monotonically increasing load T that generates the bulk stress σ_B is applied. Since the contact problem is non-linear, loads must be applied in small time increments in order to obtain the correct stress distribution.

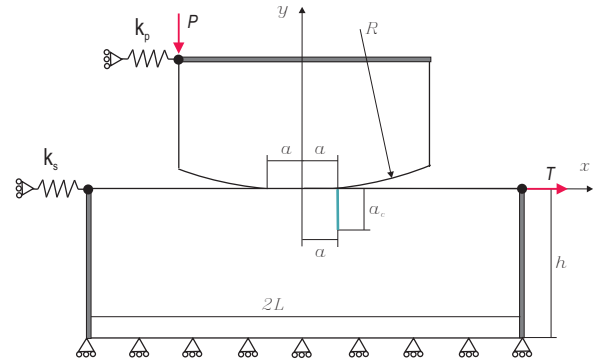


Figure 3: Geometry of the numerical model.

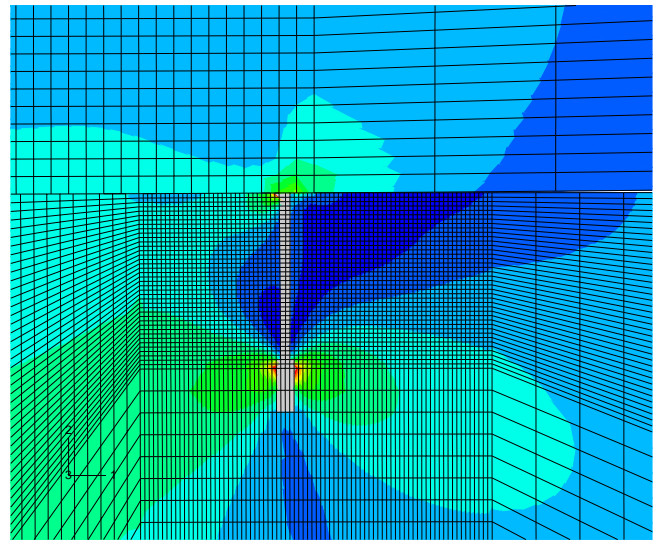


Figure 4: Von Mises contour plot for the test 1 of the A&N series for a crack length of $100 \mu\text{m}$. Elements in grey are the X-FEM enriched elements.

Fig. 4 shows an example of one of the analyses carried out for a crack length of $100 \mu\text{m}$ at the end of the contact zone with the implementation of X-FEM in ABAQUS. The location $x = a$ is estimated for each of the tests by solving the corresponding FE problem (without a crack) and verifying that the value is in good agreement with the analytical estimation for the cylindrical contact on a half-plane. In Fig. 4, it can be observed that the stress distribution is both affected by the contact and the crack

presence. A detailed analysis of the crack-contact interaction is given in [9]. In order to determine the SIF K_I as a function of crack length a , a series of lengths a has been analyzed for each test without modifying the underlying mesh thanks to the versatility of the X-FEM method. The results are discussed in the following section.

4.3 SIF calculation

Fig. 5 shows the values of the SIFs K_I obtained with X-FEM and the Eq. (4). These results are compared to the analytical estimation using the weight function method [10]. In the weight function method (WF), the stress distribution along the crack location (solved for a configuration with no-crack) is combined with a WF w derived for a given geometry to yield K :

$$K_I^{WF} = \sqrt{\frac{2}{\pi}} \int_0^{a_c} \sigma_x(x, y)w(y) dy \quad (5)$$

For the case of a straight crack normal to the surface at the end of the contact zone, the analytical stresses σ_x are evaluated at $x = a$. These stresses must include the contribution of the normal and shear contact loads plus the bulk stress. In this work we have used the WF w for a single-edge crack in tension (SENT) in a strip of finite width [10]. In Fig. 5, the WF estimations show differences with the X-FEM values, and can have an over- or underestimating trend. SIFs computed through X-FEM include the effect of crack-contact interaction and, therefore, are assumed to be more accurate. These differences have an influence on the predicted propagation life, as shown below.

As expected, for very short cracks, the agreement between the X-FEM and WF solutions is very good because the influence of the crack on the contact distribution is small. For longer cracks, the differences between both solutions are about 5%-10%. The cause of these differences is, in the first place, the consideration or not of crack-contact interactions. For much longer cracks, where this interaction is not noticeable, the cause of the difference is that the bulk stress is assumed uniform in the WF formulation. Indeed, this stress is not uniform in the vicinity of the contact, since the axial forces in the specimen are not the same on both sides of the contact (part of the axial load is diverted through the contact elements as shear load).

Another aspect that can be analyzed is the influence of the sticking zone offset e due to the bulk stress. In [9], it is verified that the eccentricity e tends to decrease as the crack length increases due to a "shadow" effect of the crack. Therefore, the shear stress distribution used in the analytical estimations of K_I should be corrected to account for this effect in a variable manner (depending on the crack length). Fig. 5 show the differences when K_I is computed through weight functions considering the full offset of the sticking zone, i.e. no crack effect ($e \neq 0$),

and zero offset as for a sufficiently long crack ($e = 0$). As expected, the calculations with a full offset effect $e \neq 0$ are in good agreement with the X-FEM values only for very small cracks, whereas calculations with zero offset $e = 0$ tend to match the X-FEM values for longer cracks. Note that for longer cracks the dominant source of discrepancy is due to the non-uniform distribution of the bulk stress, as explained above. From this analysis it is clear that the variation of the eccentricity with crack length cannot be predicted *a priori* without considering the crack-contact interaction. Therefore the application of the weight function technique introduces simplifications that are overcome by the numerical methodology proposed here.

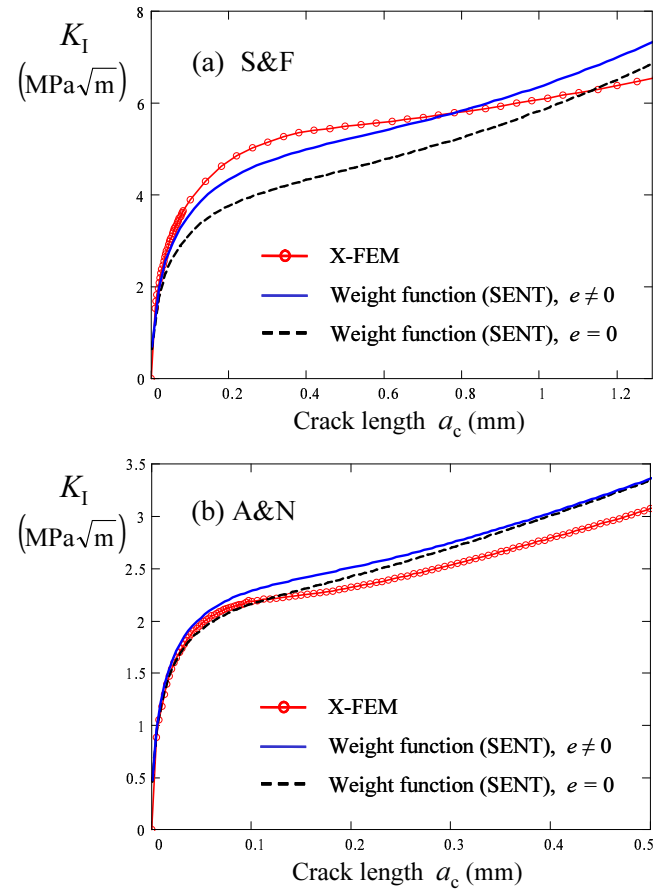


Figure 5: Values of K_I vs. crack length for (a) test 7 of the S&F series [4] and (b) test 4 of the A&N series [5].

4.4 Life prediction and correlation with experimental lives

Fig. 6 shows the predicted total life for each of the analyzed tests confronted to the experimental life reported in [4] and [5]. Two series of results are presented, in which the propagation life is calculated using the SIFs provided by X-FEM and by the WF method, respectively. The initiation life is practically the same in both cases and is calculated as given in Section 2. It can be observed

that the results given by the X-FEM tend to give slightly better results for most of the tests, which are closer to the experimental life. Although the estimated total life is similar for both approaches, the differences in the propagation life are about 20% (note the logarithmic scale of the plot). The fact that the initiation life can account for an important fraction of the total life in fretting tests with incomplete contacts does not lend itself to exhibit larger differences. Of course, there are many other factors that can affect the total real life that are not considered in the X-FEM or WF models.

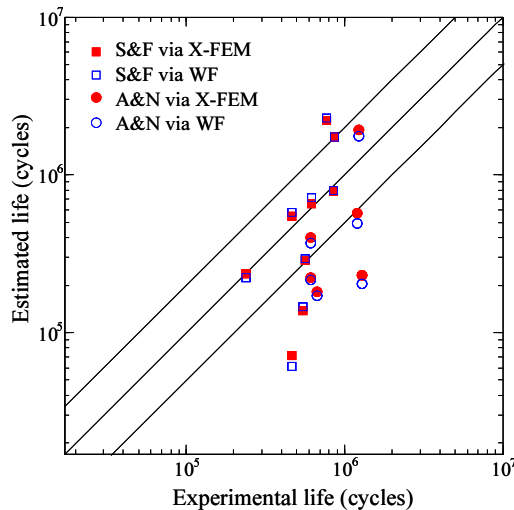


Figure 6: Correlation between the estimated and experimental lives.

It is interesting to observe that most results that are overestimated (underestimated) with the WF method are reduced (increased) with the X-FEM approach. Most of the S&F results tend to be overestimated with the WF method. However, X-FEM estimations tend to yield larger values of K_I than with WF as shown in Fig. 5(a), reducing the propagation life. For the A&N results, that tend to be underestimated, lower SIFs computations via X-FEM than with WF, Fig. 5(b), provide larger propagation lives.

5 CONCLUSIONS

In this work, propagation lives in fretting fatigue tests with cylindrical contacts are calculated numerically using an X-FEM approach. The advantage of using a numerical procedure is that the analyses incorporate the crack-contact interaction effects that cannot be included in analytical approaches, such as the weight function method. The use of the X-FEM makes this study feasible, because no remeshing is needed to study different crack lengths parametrically. This enables to compute the SIF as a function of crack length (an interaction integral is used for this purpose). The propagation lives are combined with an estimation of the initiation life following

a variable-length initiation-propagation model. For a series of experimental tests reported in the literature, results show that the use of X-FEM to predict the propagation phase tends to improve the life estimation when compared to the weight function method.

ACKNOWLEDGEMENTS

The authors gratefully acknowledge the financial support given by the DGICYT of the Spanish Ministry of Science and Innovation (Projects DPI2007-66995-C03-01 and DPI2007-66995-C03-02).

REFERENCES

- [1] Navarro C, García M, Domínguez J. A procedure for estimating the total life in fretting fatigue. *Fatigue Fract Engng Mater Struct* **26**, 459–468, 2003.
- [2] Navarro C, Muñoz S, Domínguez J. On the use of multiaxial fatigue criteria for fretting fatigue life assessment. *Int J Fatigue* **30**, 32–44, 2008.
- [3] Moës N, Dolbow J, Belytschko T. A finite element method for crack growth without remeshing. *Int J Numer Methods Engng* **46**, 131–150, 1999.
- [4] Szolwinski MP, Farris TN. Observation, analysis and prediction of fretting fatigue in 2024-T351 aluminum alloy. *Wear* **221**, 24–36, 1998.
- [5] Araújo JA, Nowell D. The effect of rapidly varying contact stress fields on fretting fatigue. *Int J Fatigue* **24**, 763–775, 2002.
- [6] Giner E, Sukumar N, Tarancón JE, Fuenmayor FJ. An Abaqus implementation of the extended finite element method. *Engng Fracture Mech* **76**, 347–368, 2009.
- [7] Chen FHK, Shield RT. Conservation laws in elasticity of the J -integral type. *J Appl Math Phys (ZAMP)* **28**:1–22, 1977.
- [8] Hills DA, Nowell D. *Mechanics of fretting fatigue*. Kluwer Academic Publishers, Dordrecht, 1994.
- [9] Giner E, Tur M, Vercher A, Fuenmayor FJ. Numerical modelling of crack-contact interaction in 2D incomplete fretting contacts using X-FEM. *Tribology Int* **42**, 1269–1275, 2009.
- [10] Bueckner HF. Field singularities and related integral representations. In: *Mechanics of Fracture 1. Methods of analysis and solutions of crack problems*, ed. GC Sih. Noordhoff International Publishing, Leyden, 1973.

COMPORTAMIENTO DEL MODELO DE FISURA COHESIVA EN PROCESOS DE CARGA-DESCARGA

J. Zahr Viñuela y J. L. Pérez Castellanos

Departamento de Mecánica de Medios Continuos y Teoría de Estructuras.
 Universidad Carlos III de Madrid. Escuela Politécnica Superior.
 Avda. de la Universidad 30, 28911 Leganés (MADRID). E-mail: percaste@ing.uc3m.es

ABSTRACT

To estimate the component of work dissipated in damage, the evolution of Young's module with the strain must be known. By unloading-loading process in a tension test, a relation between Young model and strain can be obtained. A multiparticle model which incorporates the capacity to reflect the damage by decohesion between particle and matrix, is used to simulate tensile loading-unloading processes of particulate metal matrix composite. The macroscopic stress-strain curves under load for the composite under study, as well as those corresponding to the simulated unloads-loads processes are presented. These curves show a damage increase at the beginning of unload process. An explanation for the observed phenomena is suggested, including its possible connection with the *control method* of the simulation and a possible *lack of uniqueness* in the equilibrium solution of Damage Mechanics Models when used in unloading situations.

KEYWORDS: Damage, cohesive-crack model, loading-unloading process, particulate reinforced composites.

1 INTRODUCCIÓN.

Un método de análisis que puede ser utilizado para analizar el comportamiento mecánico de los materiales compuestos de matriz metálica y refuerzo cerámico (en lo que sigue, PMMC's) es el Análisis de Celdas [1,3] en el que una celda que contiene un cierto número de partículas es discretizada y analizada frente a distintos tipos de sollicitación mecánica mediante el M.E.F. Las celdas utilizadas en este tipo de análisis suelen ser geoméricamente periódicas en la configuración *original*, a la vez que el uso de condiciones de contorno periódicas en las simulaciones garantiza la periodicidad geométrica y tenso-deformacional de la celda en la configuración *deformada*.

El daño por decohesión de las partículas respecto a la matriz circundante, puede ser analizado mediante técnicas basadas en el modelo de fisura cohesiva [2, 3], introduciendo elementos cohesivos en las interfaces matriz-partícula. El modelo de fisura cohesiva constituye una técnica eficiente que ha sido ampliamente utilizada para modelizar, entre otros procesos, el crecimiento progresivo de fisuras y la decohesión o delaminación en materiales compuestos.

La modelización cohesiva requiere definir una relación constitutiva que se considera como propiedad de la interfaz y que toma la forma de una ley de *tracción-separación*, que relaciona la tensión que transmite la *fisura cohesiva* con la deformación (separación) en la fisura. Esta ley se caracteriza por una etapa inicial en la que existe una relación lineal-elástica entre tensión y deformación y por un proceso de *ablandamiento* o degradación que culmina cuando la interfaz ha perdido totalmente su capacidad de transmitir tensión.

El punto de iniciación del proceso de daño de la interfaz se define mediante un *criterio de iniciación de daño* que puede basarse en valores cuadráticos equivalentes de tensiones o de desplazamientos. El proceso de daño o ablandamiento está controlado por un parámetro escalar de daño, cuyo crecimiento desde 0 hasta 1 durante el ablandamiento degrada simultáneamente tanto la rigidez cohesiva como la tensión máxima que la interfaz es capaz de transmitir.

Dado que la ocurrencia de fenómenos de daño resulta en una disminución del módulo de Elasticidad del material, y que el daño aumenta progresivamente al aumentar la deformación macroscópica del compuesto, se planteó obtener la evolución (degradación) del Módulo de Elasticidad del compuesto con la deformación utilizando el método de celdas en conjunto con el modelo de fisura cohesiva, a través del método clásico de las descargas elásticas intermedias.

En este trabajo, se presenta simulaciones de los procesos de carga-descarga así como observaciones sobre aspectos inesperados del comportamiento del Modelo de Daño utilizado durante la descarga.

2 SIMULACIÓN NUMÉRICA DEL PROCESO CARGA-DESCARGA

Para generar modelos numéricos multipartícula, se ha utilizado un algoritmo desarrollado por los autores [3] que produce distribuciones espaciales de partículas dentro de una celda de periodicidad geométrica. La celda contiene 40 partículas cúbicas (esbeltez constante $r = 1$) de igual tamaño y aleatoriamente orientadas (ver

fig. 3). La fracción volumétrica de partículas es del 12%.

Esta celda fue discretizada, dando origen a la correspondiente malla de elementos finitos. Para las fases sólidas (matriz y partículas) se utilizaron tetraedros cuadráticos modificados de la librería de elementos del código ABAQUS Standard [4]. Las interfaces matriz-partícula se han representado mediante los elementos cohesivos de la librería de ABAQUS, permitiendo así la modelación del daño por decohesión entre las fases sólidas, como se describió en [7].

Para la matriz se ha considerado un comportamiento elasto-plástico con endurecimiento isotrópico de tipo J_2 en una formulación incremental e independiente de la velocidad de deformación. Las constantes elásticas de la matriz fueron las siguientes: módulo de Young $E = 210$ GPa y coeficiente de Poisson $\nu = 0,3$; como ley de endurecimiento se consideró la ley Ramberg Osgood definida por una límite elástico al 0,2% de $\sigma_{0,2} = 400$ MPa y un exponente de endurecimiento $n = 10$.

Para las partículas del refuerzo se consideró un comportamiento lineal elástico de acuerdo con la ley Hooke siendo $E_p = 410$ GPa y $\nu_p = 0,16$, valores obtenidos de la literatura.

En el caso de las interfaces cohesivas, la matriz de rigidez cohesiva utilizada es de tipo desacoplado (y por lo tanto, diagonal). La rigidez cohesiva inicial es de $K_0 = 1,2 \cdot 10^9$ MPa/mm con independencia del modo de carga; con este valor la presencia de elementos cohesivos de interfaz no modifica la rigidez del compuesto [3] antes del inicio del daño. Se utilizó un criterio de iniciación de daño cuadrático en tensiones, con una resistencia cohesiva de $t^R = 600$ MPa (1,5 veces el límite elástico de la matriz) tanto para el modo de tracción pura como para los modos de cortadura. La curva de ablandamiento es de tipo lineal, con un valor de energía de fractura de $G^C = 50$ J/m².

Todas las simulaciones se realizaron utilizando condiciones de contorno periódicas a través de

$$\vec{U}_{Q_i} - \vec{U}_{P_i} = \vec{C}_i \quad (1)$$

donde P_i y Q_i son una pareja arbitraria de nodos situados en posiciones equivalentes en las dos caras opuestas de la celda que son perpendiculares al eje X ($i=1$), al Y ($i=2$) o al Z ($i=3$). La periodicidad queda impuesta cuando \vec{C}_i es un vector constante que relaciona los desplazamientos relativos para todos los pares de nodos en aquellas caras.

Los tres vectores constantes \vec{C}_i de las ecuaciones (1) se representan en la malla FEM mediante los vectores desplazamiento de 3 nodos de control, dando origen a un total de 9 componentes, algunas de las cuales son *datos de entrada* y otras son parte de la *solución* buscada, dependiendo del estado tensional en estudio.

Una simulación en *control de posición* implica prescribir un valor no nulo sobre la componente adecuada de desplazamiento, obteniendo como *resultante* del análisis el valor de su fuerza de reacción asociada. De manera análoga, una simulación en *control de fuerza* consiste en prescribir un valor no nulo para la componente adecuada, obteniendo como *resultante* el valor de la componente de desplazamiento.

Con el modelo de celda multipartícula descrito se simuló una sollicitación macroscópica de tracción uniaxial a lo largo del eje X . Para evitar dificultades de inestabilidad en el equilibrio macroscópico de fuerzas asociadas a la modelización del daño por decohesión, todas las simulaciones en *carga* se realizaron en control de posición. La deformación macroscópica total fue del 5%, obteniéndose como *resultante* el valor de la reacción. La tensión macroscópica se calcula como la fuerza de reacción dividida por el área transversal *actual*.

La presencia de fenómenos de daño degrada progresivamente la rigidez del material, de modo que justo antes de iniciar una descarga no se conoce exactamente la cuantía del retroceso elástico de la deformación macroscópica. Una prescripción excesiva para el retroceso elástico en una descarga en control de posición podría dar lugar a la entrada de la celda en compresión macroscópica.

Debido a esto, el método de control *natural* para una simulación del proceso de *descarga* es el control de fuerza. La metodología es la siguiente: se realiza una simulación previa del proceso de *carga* (en control de posición) hasta cierto valor de interés de la deformación macroscópica. Para llevar a cabo una descarga en control de fuerza se substituye en el nodo de control la fuerza de reacción (obtenida al final de la simulación en *carga*) por una fuerza puntual, de igual cuantía (para mantener el equilibrio al inicio de la descarga), fuerza que se hace disminuir progresivamente hasta cero.

Como método alternativo, para llevar a cabo una *descarga* en *control de posición* se prescribe, sobre la misma componente de desplazamiento del nodo de control que controlaba el previo proceso de carga, un valor de desplazamiento ligeramente inferior al que ese nodo tenía al iniciar la descarga; para asegurar que la descarga elástica no implica una entrada en compresión, como estimación del retroceso elástico puede usarse $\Delta c = -\rho (\sigma/E)L_0$ con ρ pequeño y, en todo caso, $0 < \rho < 1$ y donde σ es la tensión macroscópica al inicio de la descarga, E el módulo elástico macroscópico inicial y L_0 la longitud inicial de arista de la celda.

3 RESULTADOS

Se han considerado dos situaciones diferenciadas: para su uso como referencia, se consideró tanto un material indañable (con nodos compartidos en las interfaces) como un material con interfaces dañables de acuerdo a los parámetros cohesivos descritos en el apartado anterior.

Utilizando este modelo se han realizado simulaciones de un ensayo de tracción obteniéndose las gráficas σ - ϵ que se muestran en la figura 1; como se esperaba, la simulación que incorpora el efecto del daño produce una curva de endurecimiento progresivamente más baja que la curva del material indañable. Para el material dañable, se han realizado también simulaciones de ensayos de tracción con descargas (figura 1).

En primer lugar se simuló una descarga total, en control de fuerza, desde una deformación 0.213%; en la descarga se alcanzó una deformación de 0.05% verificándose elasticidad lineal durante todo el proceso. Seguidamente se simuló una descarga total, también en control de fuerza, desde una deformación 0.300%; en la descarga la deformación se redujo hasta un valor de 0.123%. A diferencia de la primera descarga, a su inicio se observó (figura 1 b) un ligero aumento de la macro deformación seguido de una pequeña incurvación, verificándose elasticidad lineal durante el resto del proceso de descarga. Finalmente se simuló una descarga total, en control de fuerza, para una deformación 0.399%; en la simulación se presentaron grandes dificultades de convergencia (llegándose a interrumpir la simulación) y aumentando la deformación con disminución de la carga.

La figura 1a muestra también valores para las pendientes de los caminos de descarga, obtenidos de rectas de regresión correspondientes a la zona elástica inicial (E_0) y a los tramos lineales de las dos descargas que sí pudieron completarse (E_1 y E_2). Como se esperaba, la pendiente de las líneas decrece cuando crece la deformación reflejando el aumento de daño macroscópicamente observable en el material compuesto.

El análisis de los resultados de las simulaciones realizadas conduce a las conclusiones iniciales siguientes. Cuando la descarga se inicia desde un relativamente bajo nivel de macro deformación, el camino de descarga es perfectamente lineal. Sin embargo, cuando la descarga se inicia desde valores más altos de la deformación, se observa una no linealidad muy marcada al comienzo del camino de descarga acompañada de aumentos locales de la variable de daño.

Como ejemplo, la figura 2 muestra el modelo multipartícula justo al inicio del proceso de descarga en control de fuerza desde la deformación de 0.3%, identificándose una partícula que había comenzado ya a decohesionar durante la etapa previa de carga. La figura 4, por su parte, muestra imágenes de la citada

partícula en tres instantes de la simulación de esta descarga.

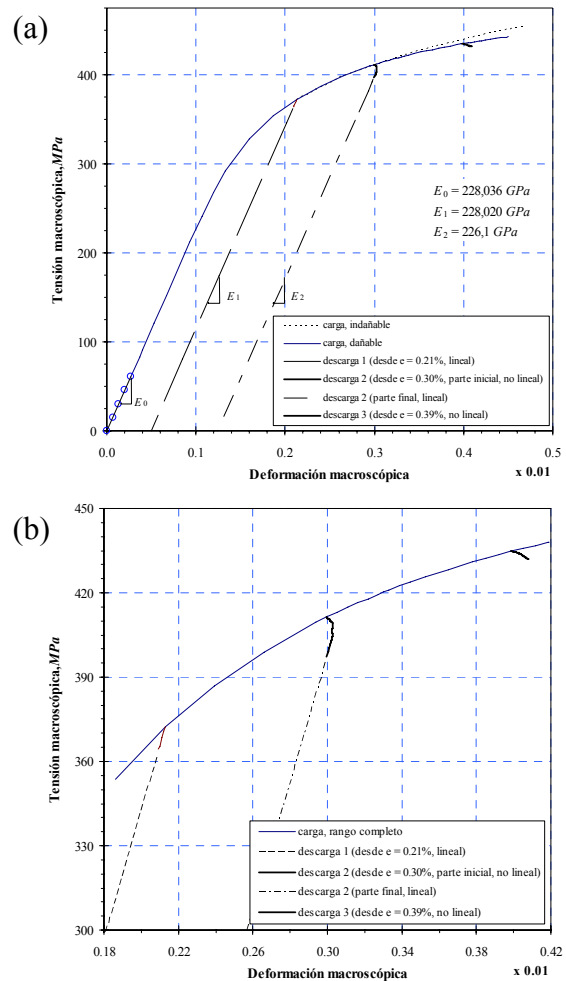


Figura 1. Curvas σ - ϵ incluyendo descargas. a) escala completa. b) zoom en la zona de inicio de las descargas.

Una inspección de los mapas de la distribución espacial del parámetro escalar de daño en esta figura reveló que incrementos locales de área dañada (interfaz decohesionada) tuvieron lugar durante la parte inicial no lineal de la descarga (desde $t = 0$ hasta $t = 0,03$); la decohesión no progresa durante el tramo final (desde $t = 0,03$ hasta $t = 1,0$). Las zonas oscuras denotan áreas totalmente decohesionadas, incapaces por tanto de transmitir tensión entre matriz y partícula.

Una vez finalizada esta no linealidad, caracterizada numéricamente por grandes dificultades de convergencia y por la necesidad de numerosas iteraciones de equilibrio, parece producirse un cierto “ordenamiento” en el campo tenso-deformacional interior del material, de tal modo que la línea de descarga pasa a ser recta hasta el final de la descarga, mejorando a la vez la convergencia de la simulación. Con el objeto de analizar las causas de la fuerte no linealidad detectada en el caso de la descarga que inicia en 0.399%, se llevaron a cabo, como **experimentos**

numéricos, otras dos simulaciones de esta descarga cuyas condiciones se describen a continuación (la figura 5 muestra un detalle de sus resultados).

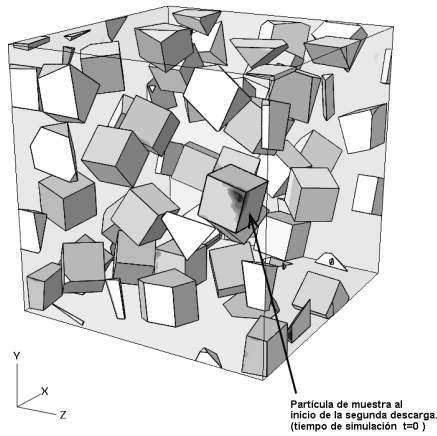


Figura 2. Celda multipartícula, al inicio de la simulación de la segunda descarga. Se representa el mapa del parámetro escalar de daño

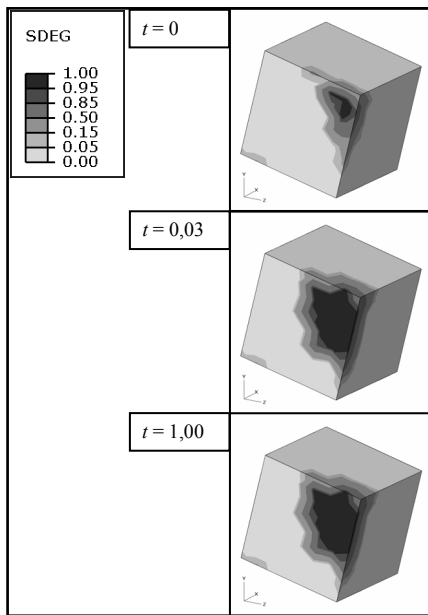


Figura 3. Evolución del parámetro de daño D , durante la segunda descarga. Las zonas más oscuras denotan interfaces totalmente dañadas.

En un **primer experimento** se analizó la posible influencia de la tolerancia utilizada en el proceso numérico de solución de las ecuaciones de equilibrio. Para ello, en la simulación se dividió el proceso de descarga en dos etapas. En la **primera etapa** se planteó un proceso de *estabilización* consistente en mantener fija la deformación macroscópica de la celda (inmovilizando el nodo de control en el valor de desplazamiento que éste tenía al final del proceso previo de *carga*), pero obligando al código de cálculo a realizar nuevas iteraciones de equilibrio, por la vía de restringir las tolerancias utilizadas por el código de cálculo en la solución del problema no lineal de

equilibrio (que el código ejecuta mediante un algoritmo full-Newton). En la **segunda etapa** se planteó el proceso de descarga en control de fuerza propiamente dicho, al modo descrito en apartados anteriores.

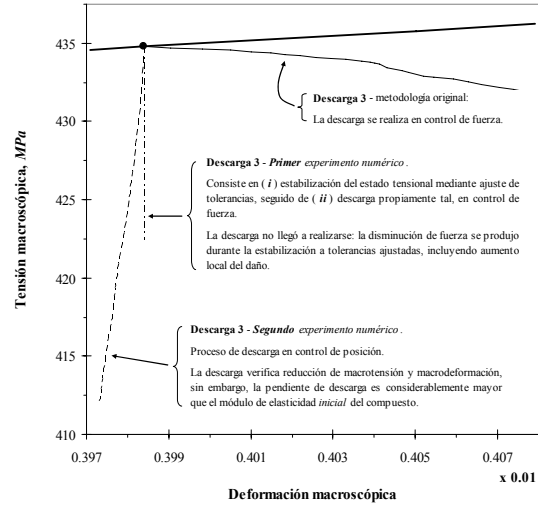


Figura 4. Detalle de la gráfica σ - ϵ incluyendo el proceso de descarga original en control de fuerza, así como los dos experimentos numéricos.

En ABAQUS, la tolerancia se define mediante comparación en cada iteración de la componente más grande del vector de residuos \vec{R} con un porcentaje de una fuerza nodal de referencia, $F_{t,av}$, es decir, $|\max(\vec{R})| \leq \alpha F_{t,av}$. Se refiere al lector a [4] para la definición de $F_{t,av}$. Para la etapa de estabilización en este experimento numérico se utilizó un valor de 0,02% (el valor usual es 0,5%). Este experimento estaba motivado en la idea intuitiva de “ordenación” del campo tenso-deformacional interior, algo que se lograría con la etapa de estabilización, previa a la descarga propiamente tal.

Durante la etapa de estabilización sin embargo, se observó que la fuerza de reacción en el nodo de control disminuyó en una cuantía no despreciable (segmento vertical en la figura 5). La segunda etapa del experimento no llegó a realizarse pues debió interrumpirse el proceso de estabilización, dados los valores muy pequeños de incrementos temporales encontrados por el algoritmo de incrementación automática de ABAQUS. Examinando los mapas de daño, se observaron incrementos locales de esta variable. Es decir, el daño aumentó durante la estabilización a macro-deformación constante, dando origen a un decremento en la macro-tensión soportada por la celda, desde 435 hasta 422 MPa.

El control de posición no es el método más natural en descargas pues se requiere conocer de antemano el retroceso máximo admisible. Sin embargo, y para analizar la influencia que el sistema de control pudiera tener en el proceso de descarga, se realizó un **segundo**

experimento numérico en el que se llevó a cabo una descarga en control de posición (utilizando las tolerancias que, por defecto, ofrece el código de cálculo). En este caso, la descarga resultó no lineal con una ligera incurvación inicial de la línea de descarga, acompañada de un aumento local del daño; la pendiente media del tramo recto de la línea de descarga resultó varias veces superior al valor del módulo de elasticidad inicial, E_0 . Lo que demuestra que la disminución registrada en la macro-tensión fue mucho mayor que la que correspondería al retroceso prescrito de la deformación macroscópica (incluso si no se estuviera en presencia de daño). Esto sólo se puede explicar por un aumento del daño *durante* esta descarga efectuada en control de posición.

4 MECÁNICA DE DAÑO EN DESCARGA.

A continuación se analiza el problema desde el punto de vista de la Mecánica del Daño estudiando la definición del Modelo Constitutivo Cohesivo usado en los elementos de interfaz.

El modelo cohesivo utilizado en todas las simulaciones previas consiste en una ley tracción-separación con una parte inicial lineal y elástica, un criterio de iniciación de daño definido en tensiones y una curva de ablandamiento lineal. Esta ley se representa en la figura 6 mediante la línea continua que une los puntos OAB . En ella, el punto A representa el criterio de iniciación de daño ($D_A = 0$), mientras que B representa una apertura totalmente dañada ($D_B = 1$). En la gráfica inferior se representa la evolución del parámetro de daño D en función de la apertura de la interfaz.

Sea P , en la figura 6, un punto al que se ha llegado a través del camino OAP , mediante aplicación de un proceso de carga monótonamente creciente en *control de posición* (esto es, con apertura *prescrita* de la interfaz cohesiva). El punto P representa un estado de equilibrio entre las tracciones externas ejercidas sobre la interfaz y las tensiones internas transmitidas por la interfaz cohesiva. Nótese que la apertura de interfaz en P ha superado la apertura de iniciación del daño, de modo que $0 < D_P < 1$. La rigidez de la interfaz se ha degradado en un factor $1-D_P$, como se indica en la figura 5.

Supóngase ahora que las tracciones externas disminuyen por alguna razón (control de fuerza), causando el decremento $\Delta t = t_Q - t_P$ en la tensión interna transmitida por la interfaz indicado en la fig.6. En una implementación práctica de este modelo cohesivo, frente a este decremento Δt el algoritmo que calcula la solución constitutiva debe ser capaz de obtener la nueva apertura de interfaz, así como la variación de las variables internas que el modelo considere, que mantienen el equilibrio de fuerzas.

Obsérvese que si en la solución constitutiva participan simultáneamente como incógnitas tanto la apertura de interfaz δ como el parámetro escalar de daño D , existen

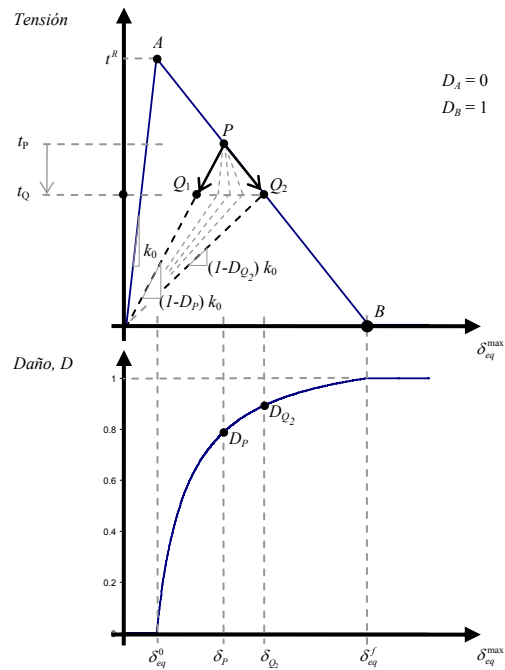


Figura 5. Ley tracción-separación (arriba) y su correspondiente ley de evolución del parámetro escalar de daño (abajo)

infinitas soluciones que garantizan el nuevo equilibrio de fuerzas. Corresponden a puntos del segmento horizontal *entre* los puntos Q_1 y Q_2 .

El camino de descarga PQ_1 ocurre con disminución de la apertura a daño constante, de modo que $D_{Q_1} = D_P$, siendo ésta la situación físicamente esperable. El camino PQ_2 en cambio, ocurre con un aumento tanto de la apertura como del parámetro de daño, de modo que $D_{Q_2} > D_P$, siendo ésta una situación que no tiene sentido físico, aunque es matemáticamente admisible si, como se dijo, ambas variables participan en las iteraciones constitutivas y el único criterio de solución es el equilibrio de fuerzas.

Si a partir del punto A se realiza un proceso de descarga macroscópica *en control de posición* (es decir, prescribiendo la apertura de la interfase) queda descartada una solución que implique aumento de la apertura de la interfaz. Por lo tanto, es claro que la solución, en este caso de descarga en control de posición, es única (punto C).

Para constatar estas observaciones, se consideró un modelo constituido por un único elemento cohesivo sobre el que actúan fuerzas iguales aplicadas sobre los cuatro vértices y normales al plano del elemento.

Con este modelo se llevó a cabo un conjunto de experimentos numéricos. Los análisis se realizaron con el código ABAQUS [4]. En la figura 6 se esquematizan los análisis realizados; el punto A representa el estado

tracción-separación del elemento cohesivo en el momento en el que se inicia la descarga. En todos los casos la carga se realizó en control de posición.

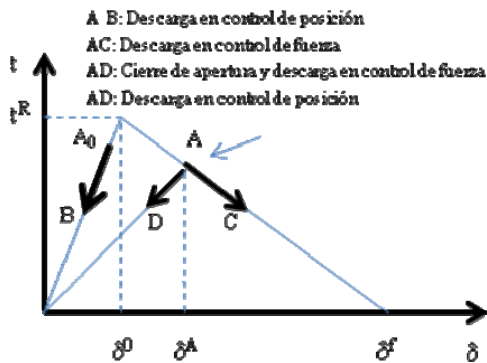


Figura 6.- Caminos de descarga

a) *Carga hasta un valor de apertura menor que el punto de iniciación de daño seguida de descarga en control de fuerza.*- La descarga se produjo, como era de esperar, por la rama elástica inicial (vector A_0B).

b) *Carga hasta un valor de apertura, δ_A , mayor que el punto de iniciación de daño, δ_0 , pero menor que el punto de interfaz totalmente dañada, δ_f , seguida de una descarga en control de fuerza.*- Se simulaban descargas desde diferentes valores de apertura en el intervalo (δ_0, δ_f) . En todos los casos la descarga dio lugar a un aumento de la apertura del elemento acompañado de un aumento en el parámetro de daño D (vector AC) correspondiente a una descarga hacia el punto B de la figura 6.

c) *Carga hasta un valor de apertura δ_A seguida de una descarga en control de posición.*- La descarga se produjo por una línea de descarga lineal-elástica cuya pendiente es la rigidez inicial reducida por el factor $1-D$, (vector AD).

d) *Carga hasta un valor de apertura δ_A seguida de una descarga en dos etapas.*- La **primera etapa** consistió en prescribir un pequeño cierre de la apertura (esto es, una pequeña descarga en control de posición). La **segunda etapa** consistió en una descarga en control de fuerza a partir del punto final de la descarga previa en control de posición. El camino de descarga en esta última etapa correspondió a un cierre de interfaz, sin aumento del daño, por una línea cuya pendiente es la rigidez inicial reducida por el factor $1-D$, (vector AD). Esto demuestra que el parámetro de daño no participó en las iteraciones de equilibrio cuando la descarga en control de fuerza se realiza desde un punto (final de la primera etapa) que no está en la curva de ablandamiento.

Observación.- Es de destacar que, en el caso de celdas multipartícula, aunque se esté llevando a cabo una descarga macroscópica en control de posición, los elementos cohesivos están embebidos en un entorno

(matriz-partícula) del que reciben únicamente una historia de tensiones, no de desplazamientos prescritos. Por lo tanto, en el caso de descarga macroscópica en control de posición, es de esperar, también, multiplicidad de soluciones.

5 CONCLUSIONES

Si se simula un proceso de descarga a partir de un valor relativamente bajo de macrodeformación, el camino de descarga en la gráfica tensión-deformación obtenida puede considerarse perfectamente lineal. Sin embargo, si el proceso de descarga se inicia para niveles más altos de deformación, el camino de descarga muestra una marcada no-linealidad inicial.

En un proceso de descarga puede haber soluciones múltiples de las ecuaciones de equilibrio cuando se modeliza $D(\epsilon)$. alguna de las soluciones puede corresponder a un camino de descarga no lineal con incremento de daño. El daño aumenta localmente durante las primeras etapas en las que el proceso de descarga muestra no-linealidad, tanto si se realiza en control de carga como en control de posición.

Para que un proceso numérico de descarga se produzca por un camino físicamente razonable (camino lineal sin incremento del daño), debería cumplirse que en las primeras iteraciones constitutivas no participara el parámetro de daño, D . Otra posibilidad es que la modelización constitutiva del elemento cohesivo incluyera, también, algún criterio de Mecánica de Fractura (integral J o K_{IC}) para controlar el eventual crecimiento de D .

6 REFERENCIAS

- [1] Segurado, J. and Llorca, J. "A numerical approximation to the elastic properties of sphere-reinforced composites". Journal of the Mechanics and Physics of Solids, Volume 50, Issue 10, Pages 2107-2121 (2002)
- [2] Segurado, J. and Llorca, J. "A computational micromechanics study of the effect of interface decohesion on the mechanical behavior of composites". Acta Materialia Volume 53, Issue 18, pages 4931-4942 (2005)
- [3] J. Zahr Viñuela and J.L. Pérez Castellanos. "Modelo multipartícula para el análisis del comportamiento mecánico de materiales compuestos reforzados con partículas". Anales de Mecánica de la Fractura, Vol.: II, Pag. 482- 488 (2007)
- [4] ABAQUS, Version 6.8-2, Dassault Systèmes Simulia Corp. 2008.

**APLICAÇÃO DE TÉCNICAS DE SUB-MODELAÇÃO
NO CONTEXTO DA ANÁLISE DE PROPAGAÇÃO DE FENDAS DE FADIGA
EM ESTRUTURAS DE GRANDES DIMENSÕES**

C.M.C. Albuquerque¹, P.M.S.T. de Castro², R.A.B. Calçada³

^{1,3} Departamento de Engenharia Civil, ² Departamento de Engenharia Mecânica,
Faculdade de Engenharia da Universidade do Porto, Rua Dr. Roberto Frias, 4200-465 Porto, Portugal
E-mail¹: cmca@fe.up.pt ; E-mail²: ptcastro@fe.up.pt ; E-mail³: ruiabc@fe.up.pt

ABSTRACT

Fracture Mechanics based fatigue analyses of structures requires the knowledge of the time dependence of the stress intensity factor K as a function of the several static and dynamic loadings. The huge scale differences between a Civil Engineering structure and its structural details may complicate those analyses, implying large computational costs. Seeking computational efficiency, a strategy was developed and tested on a simple cracked beam, consisting of the use of the concept of modal stress intensity factor and a numerical technique - shell-to-solid sub-modelling - to deal with substructures. These procedures were evaluated, and it is concluded that both contribute effectively to the reduction of the computational cost of fatigue analyses of large Civil Engineering structures.

RESUMO

A análise da resistência de estruturas à fadiga, com base na mecânica da fractura, implica a obtenção da evolução temporal do factor de intensidade de tensão, K , face aos diversos cenários de carregamento estáticos e dinâmicos a que a estrutura se encontra sujeita. Em estruturas de Engenharia Civil, esta abordagem é geralmente dificultada pela diferença de escala das dimensões da estrutura e dos detalhes, o que acarreta elevados custos computacionais. No sentido de tornar todo o processo mais eficiente computacionalmente, duas medidas foram adoptadas na análise de uma fenda numa viga simplesmente apoiada: foi introduzido o conceito do factor de intensidade de tensão modal e foi aplicada uma técnica de sub-modelação, designada *shell-to-solid submodelling*. A adequabilidade destas medidas foi analisada concluindo-se que ambas contribuem de forma efectiva para a redução do custo computacional e para tornar exequível a análise da propagação de fendas em grandes estruturas de Engenharia Civil.

KEY WORDS: fatigue, stress intensity factor, modal superposition, sub-modelling.

PALAVRAS-CHAVE: fadiga, factor de intensidade de tensão, sobreposição modal, sub-modelação.

1. INTRODUÇÃO

O fenómeno da fadiga é um dos principais responsáveis pela degradação e o eventual colapso de estruturas de Engenharia Civil. Em termos regulamentares, este problema é em geral abordado com recurso às conhecidas curvas S-N ou de Whöler. No entanto estas apresentam um elevado número de limitações.

Uma abordagem alternativa para a análise do comportamento à fadiga assenta nos conceitos da mecânica da fractura, nomeadamente no conceito de factor de intensidade de tensão, K , e na Lei de Paris e suas sucedâneas. O rigor e precisão dos resultados assim obtidos tem vindo a ser comprovado há várias décadas em áreas como a Engenharia Mecânica e Aeroespacial encontrando, contudo, menor receptividade no âmbito da Engenharia Civil. Isto deve-se, entre outros motivos, à diferença de escala de dimensões entre o detalhe da estrutura de Engenharia Civil susceptível de apresentar uma fenda e a estrutura na sua globalidade, o que leva geralmente a elevados custos computacionais [1].

Neste artigo apresentam-se os primeiros resultados de um estudo desenvolvido no sentido de tornar

computacionalmente eficiente o estudo da fadiga de estruturas de Engenharia Civil, com base na mecânica da fractura.

2. SOBREPOSIÇÃO MODAL DE FACTORES DE INTENSIDADE DE TENSÃO

Um grande número de resultados experimentais suporta a teoria de que a taxa de crescimento de uma fenda se correlaciona com a variação cíclica do factor de intensidade de tensão, K . Mais concretamente, os 3 modos de ruptura e/ou propagação de fendas conhecidos (modos I, II e III) relacionam-se com K_I , K_{II} e K_{III} , respectivamente. No presente trabalho, a designação K referir-se-á sempre a K_I .

Assim, para a determinação da lei de propagação de uma dada fenda face a um histórico de carregamento, é necessário conhecer a evolução de K ao longo do tempo (devido ao referido carregamento), bem como alguns parâmetros característicos dos materiais.

No entanto, a determinação do valor de K por via analítica é possível apenas para um número limitado de

casos simples, de interesse sobretudo académico. Assim, em estruturas de geometria complexa, sujeitas a carregamentos também eles complexos, é necessário o recurso a métodos numéricos aplicados a modelos de elementos finitos tridimensionais. Estes modelos numéricos são geralmente pesados computacionalmente, dificultando ou mesmo inviabilizando a sua utilização em análises dinâmicas.

Genericamente, K pode ser representado da seguinte forma:

$$K = \underbrace{C\sqrt{\pi a}}_{\text{Características geométricas}} \cdot \underbrace{\sigma}_{\text{Característica do carregamento}} \quad (1)$$

em que C é uma função da geometria da estrutura e das dimensões da fenda, σ é a tensão nominal a que o elemento se encontra sujeito e a é a semi-dimensão da fenda. Numa estrutura sujeita a uma carga permanente (peso próprio, tensões residuais, etc...) o estado de tensão daí decorrente dará origem a um factor de intensidade de tensão dado por:

$$K_{estático} = C\sqrt{\pi a} \cdot \sigma_{estático} \quad (2)$$

Se a mesma estrutura estiver sujeita a um carregamento dinâmico, tem-se:

$$K_{dinâmico}(t) = C\sqrt{\pi a} \cdot \sigma_{dinâmico}(t) \quad (3)$$

O factor de intensidade de tensão total será, então:

$$K_{total}(t) = K_{estático} + K_{dinâmico}(t) \quad (4)$$

Durante o processo de abertura e fecho de uma fenda ocorrem fenómenos de contacto entre as faces da mesma e como tal está-se perante um processo não linear. No entanto, se o referido fenómeno não linear local não afectar significativamente o comportamento linear global da estrutura, então, o factor de intensidade de tensão K , pode ser obtido através do método da sobreposição modal. De acordo com o método da sobreposição modal:

$$\sigma_{dinâmico}(t) = \sum_j \sigma_j \cdot Y_j(t) \quad (5)$$

referindo-se o índice j a cada um dos modos de vibração da estrutura e sendo $Y_j(t)$ a coordenada modal do j -ésimo modo de vibração. Tem-se então:

$$\begin{aligned} K_{din}(t) &= C\sqrt{\pi a} \cdot \sum_j \sigma_j \cdot Y_j(t) = \\ &= \sum_j C\sqrt{\pi a} \cdot \sigma_j \cdot Y_j(t) = \sum_j K_j \cdot Y_j(t) \end{aligned} \quad (6)$$

onde, o factor de intensidade de tensão modal, K_j , é o valor do factor de intensidade de tensão obtido na configuração deformada do j -ésimo modo de vibração. Obtém-se, então, finalmente:

$$K_{total}(t) = K_{estático} + \sum_j K_j \cdot Y_j(t) \quad (7)$$

Como é sabido, desprezando os fenómenos de fecho de fenda devido à plasticidade local na extremidade da mesma, o factor de intensidade de tensão associado ao modo I de ruptura, K_I , apenas toma valores positivos e diferentes de zero quando a fenda está aberta, assumindo o valor zero quando a mesma está fechada. No entanto, uma análise numérica com recurso a um modelo elástico levará à obtenção, em primeira instância, de valores sempre iguais ou superiores a zero, quer a fenda esteja fechada quer esteja aberta. Para distinguir as situações de fenda aberta e de fenda fechada deverá usar-se um dos seguintes parâmetros:

- o deslocamento relativo entre nós coincidentes mas de faces opostas da fenda, na direcção perpendicular ao plano da fenda;
- o sinal da força perpendicular ao plano da fenda presente ao nível da frente da mesma (positivo se for uma força de tração e negativo se for uma força de compressão).

A aplicação de qualquer um destes critérios permitirá a definição do sinal de K_I , obtido para a configuração da deformada associada quer ao carregamento estático quer aos diferentes modos de vibração. A expressão final de K ao longo do tempo será, então:

$$K_{total}(t) = \begin{cases} K_{estático} + \sum_j K_j \cdot Y_j(t) & \Leftarrow K_{estático} + \sum_j K_j \cdot Y_j(t) \geq 0 \\ 0 & \Leftarrow K_{estático} + \sum_j K_j \cdot Y_j(t) < 0 \end{cases} \quad (8)$$

Conclui-se assim, que, face à presença de uma fenda numa estrutura, o cálculo do factor de intensidade de tensão ao longo do tempo quando esta mesma estrutura é sujeita a um carregamento dinâmico, se resume aos seguintes passos:

1. Cálculo da estrutura face ao carregamento estático e extracção de $K_{estático}$ e respectivo sinal.
2. Análise modal da estrutura e obtenção, para cada j -ésimo modo, do valor de K_j e respectivo sinal.
3. Obtenção da evolução temporal das coordenadas modais $Y_j(t)$.
4. Obtenção de $K_{total}(t)$ por aplicação da expressão (8).

O presente método apresenta três vantagens principais:

1. Para uma estrutura com N modos de vibração, o factor de intensidade de tensão tem de ser calculado apenas $N+1$ vezes. A coordenada modal de cada modo pode ser determinada posteriormente, de forma eficiente, resolvendo cada um dos problemas de 1 grau de liberdade, através, por exemplo, do método de Newmark.

2. O contributo de cada modo de vibração para o valor de K em cada instante pode ser obtido directamente.
3. A aplicação de um carregamento dinâmico distinto apenas implicará recalcular $Y_j(t)$.

Pelo contrário, uma análise tradicional implicaria a análise de toda a estrutura ao longo do tempo e o cálculo de K para cada incremento de tempo (tipicamente vários milhares de vezes) [1].

3. TÉCNICAS DE SUB-MODELAÇÃO

Na secção anterior foi demonstrado como a aplicação do método da sobreposição modal à determinação da evolução temporal de K pode permitir reduzir bastante o volume de cálculos necessários.

No entanto, o problema da dimensão do modelo numérico não se encontrava ainda resolvido. Para solucionar este problema recorreu-se à técnica de *shell-to-solid submodeling* [2]. Esta técnica, especialmente adequada à análise de detalhes de dimensões reduzidas quando comparadas com a dimensão global da estrutura e sujeitas a estados complexos de tensão, compreende os seguintes passos:

1. Construção de um modelo global da estrutura, constituído por elementos de casca;
2. Construção de um modelo local do detalhe com elementos de volume (este modelo terá significativamente menos elementos do que teria toda a estrutura se fosse modelada com elementos de volume);
3. Indicação dos nós do modelo local que constituem a fronteira do mesmo;
4. Cálculo do modelo global da estrutura;
5. Imposição do campo de deslocamentos do modelo global aos nós de fronteira do modelo local, sendo a interpolação dos referidos deslocamentos feita a partir das funções de forma dos elementos de casca do modelo global e dos deslocamentos e rotações nodais do mesmo modelo;
6. Cálculo do modelo local da estrutura.

Este procedimento pode ser usado para a imposição sobre o modelo local quer de campos de deslocamentos estáticos, quer de campos de deslocamentos modais, o que permite calcular $K_{estático}$ e os vários K_j , respectivamente.

4. APLICAÇÃO AO CASO DE UMA VIGA SIMPLEMENTE APOIADA

4.1. Modelos numéricos

De forma a ilustrar e validar o método proposto, analisou-se, nesta secção, o comportamento de uma viga

simplesmente apoiada, contendo uma fenda semi-elíptica, quando sujeita a um carregamento dinâmico, provocado por um conjunto de cargas móveis. A estrutura em causa apresenta um vão de 10 m e uma secção rectangular com 0,4 m de largura e 0,15 m de altura. A fenda, situada a meio vão, na superfície inferior da viga, apresenta um comprimento de 0,10 m à superfície e uma profundidade de 0,05 m.

O material considerado foi um material elástico, isotrópico e homogéneo, com módulo de elasticidade 210 GPa e coeficiente de Poisson igual a 0,3 ou seja, propriedades semelhantes às de aços estruturais correntes.

Foram analisados 3 modelos da estrutura:

- MEF1 - modelo de controlo construído com elementos de viga (Figura 1), no qual a fenda não se encontra modelada;
- MEF2 - modelo com elementos de volume (Figura 2) e no qual foi modelada a fenda da estrutura (Figura 3).
- MEF3a - modelo com elementos de casca e no qual a fenda não se encontra modelada;
- MEF3b - sub-modelo com elementos de volume, no qual a fenda se encontra modelada (Figura 4).

Todos os modelos foram desenvolvidos com recurso ao software ANSYS®.

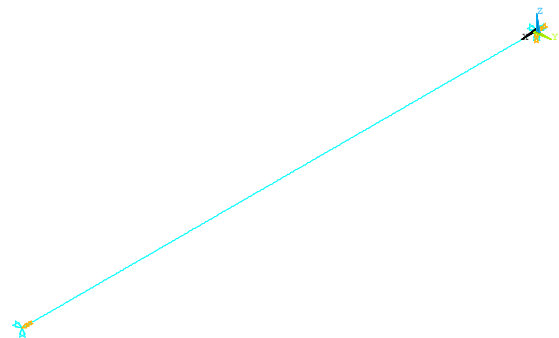


Figura 1. Modelo numérico MEF1.

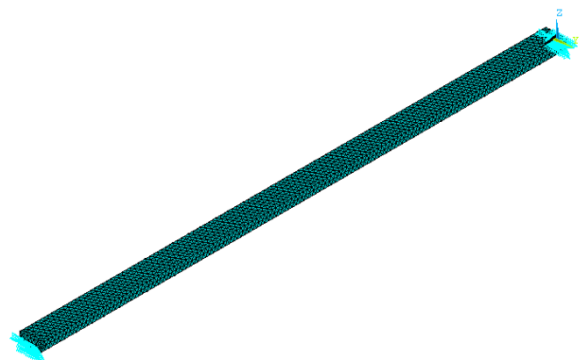


Figura 2. Modelo numérico MEF2.

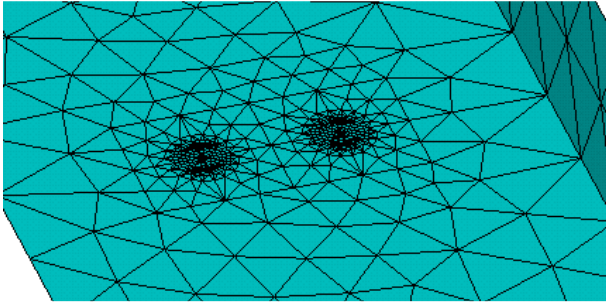


Figura 3. Malha superficial de elementos finitos nas imediações da fenda.

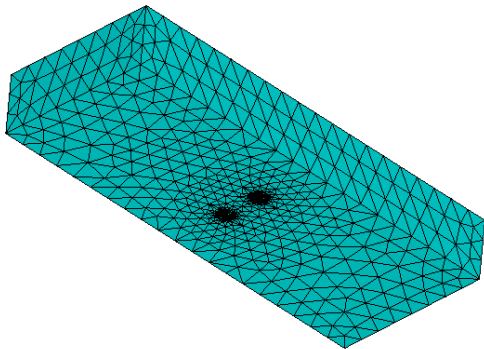


Figura 4. Sub-modelo MEF3b.

Os modelos apresentam as seguintes dimensões:

Tabela 1. Dimensões dos modelos numéricos

MODELO	Nº DE NÓS	Nº DE ELEMENTOS	GRAUS DE LIBERDADE
MEF1	501	500	3 006
MEF2	78 157	32 651	234 471
MEF3a	10 521	10 000	63 126
MEF3b	67 025	28 601	201 075

4.2. Flecha estática a meio vão

A flecha da viga face ao peso próprio foi o primeiro parâmetro da resposta de cada um dos modelos a ser comparado. Como se pode observar na Tabela 1, ambas as modelações apresentam uma boa concordância de resultados entre si, sendo os respectivos resultados idênticos ao valor teórico expectável. Este resultado indicia que a presença da fenda não afecta significativamente o comportamento global da estrutura.

Tabela 2. Flecha a meio vão

MODELO	FLECHA A 1/2 VÃO (mm)	DIFERENÇA RELATIVA
Teórico	25,47	0,00%
MEF1	25,47	0,00%
MEF2	25,55	0,34%
MEF3a	25,47	0,00%
MEF3b	25,47	0,00%

4.2. Factor de intensidade de tensão estático

Face ao efeito do peso próprio, a fenda tende a abrir (Figura 5). O valor do correspondente $K_{estático}$, ao longo da frente da fenda, foi obtido com recurso ao método do fecho virtual de fenda (VCCT - virtual crack closure technique) [3]. No caso do modelo MEF2, $K_{estático}$ foi obtido directamente do modelo sujeito ao peso próprio. No caso do modelo MEF3b, $K_{estático}$ foi obtido após a imposição, no mesmo modelo, do campo de deslocamentos obtido com o modelo MEF3a.

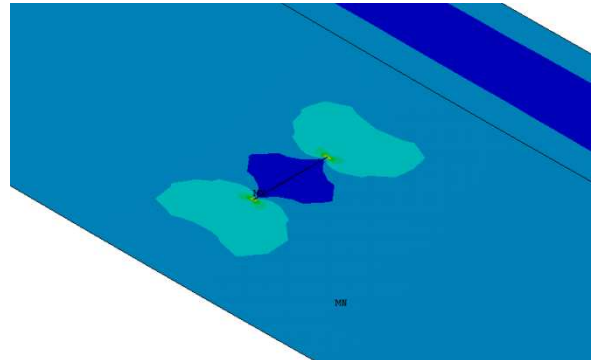


Figura 5. Amplitude máxima de tensão nas imediações da fenda.

Os resultados encontram-se apresentados na Figura 7, em função do ângulo ϕ (Figura 6). A diferença entre os resultados do modelo MEF2 e MEF3b é inferior a 4% para qualquer ponto da frente da fenda.

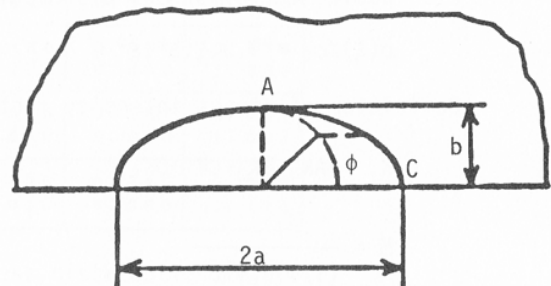


Figura 6. Convenção adoptada [4].

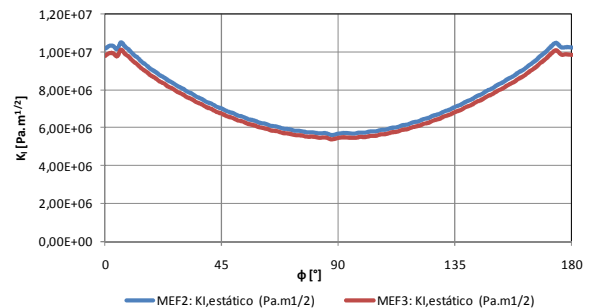


Figura 7. $K_{estático}$ ao longo da frente da fenda.

4.2. Factores de intensidade de tensão modais

Foi efectuada uma análise modal dos modelos MEF1, MEF2 e MEF3a, tendo sido determinados os modos de

vibração presentes na gama dos 0Hz aos 60Hz (Tabela 2).

Tabela 2. Frequências de vibração

#	DESCRIÇÃO	MEF1	MEF2	MEF3a
1	Flexão vertical	3,518	3,512	3,518
2	Flexão vertical	14,067	14,029	14,077
3	Flexão vertical	31,636	31,427	31,688
4	Flexão vertical	56,205	55,744	56,368

Para a configuração deformada de cada um dos modos de vibração, obteve-se, novamente através do VCCT, o factor de intensidade de tensão correspondente ao referido modo, K_j . Mais uma vez, enquanto que no caso do modelo MEF2 os valores de K_j foram obtidos directamente, no caso do MEF3b, os valores de K_j foram obtidos depois de imposto o campo de deslocamentos modais obtido com o modelo MEF3a. Novamente, a diferença entre os resultados nos modelos MEF2 e MEF3b é inferior a 4%. Nas Figuras 8 a 11 encontram-se representados os valores de K_j , bem como a forma do modo de vibração, para 2 dos modos de vibração obtidos.

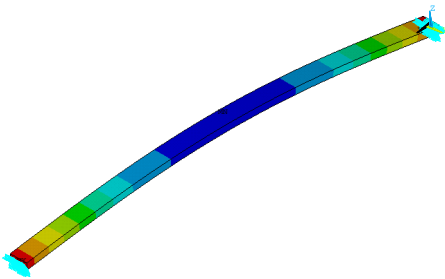


Figura 8. Configuração do 1º modo de flexão vertical.

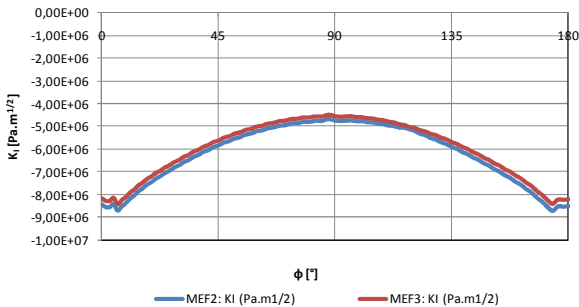


Figura 9. Modo 1: K_1 ao longo da frente da fenda.

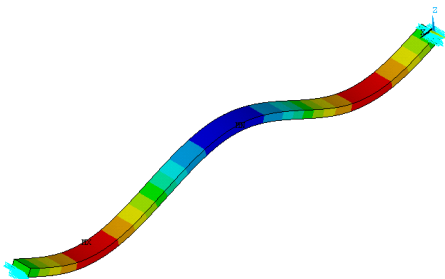


Figura 10. Configuração do 3º modo de flexão vertical.

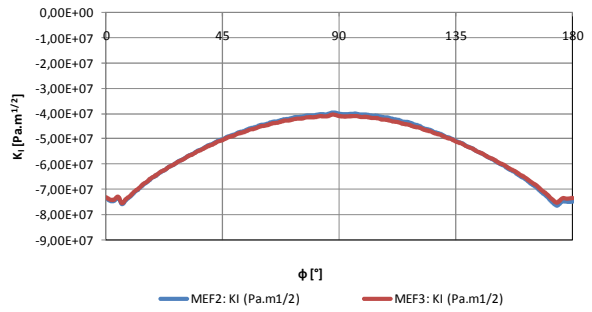


Figura 11. Modo 3: K_3 ao longo da frente da fenda.

Note-se que quer o 1º quer o 3º modos apresentam deformadas que provocam tensões de compressão na face inferior da viga e o consequente fecho da fenda. Tal traduz-se na obtenção de factores de intensidade de tensão modais, K_1 e K_3 , com sinal negativo ao longo de toda a frente da fenda.

4.2. Evolução temporal de K

A resposta dinâmica de ambos os modelos da ponte, face à passagem do conjunto de cargas móveis a 125 m/s, foi obtida, pela aplicação do método da sobreposição modal. Foi considerado o contributo dos vários modos de vibração presentes na gama de frequências analisada (0 Hz aos 60 Hz), tendo-se adoptado um coeficiente de amortecimento constante para todos os modos de vibração ($\zeta = 0,5\%$). Na resolução do problema numérico utilizou-se o método de Newmark com incrementos de tempo de $\Delta t=0,001s$.

A evolução do factor de intensidade de tensão ao longo do tempo foi, então, obtida, para o modelo MEF 2, por aplicação da expressão (8). Os resultados assim obtidos, para o ponto A, cuja localização se indica na Figura 6, encontram-se representados na Figura 12:

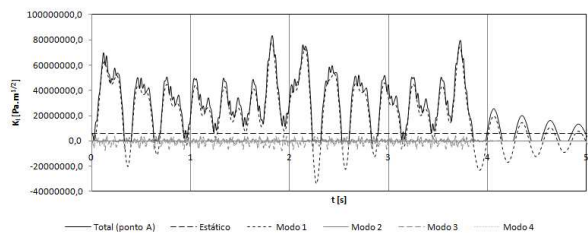


Figura 12. Evolução temporal de K para a passagem do conjunto de cargas móveis.

Comparando os resultados obtidos nos modelos MEF2 e MEF3b, observa-se uma concordância grande entre os dois modelos (Figuras 13 e 14).

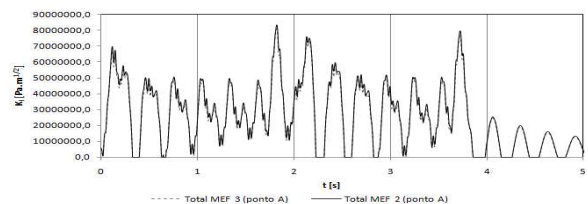


Figura 13. K_{total} para $t \in [0; 5]$ seg.: MEF2 vs. MEF3b.

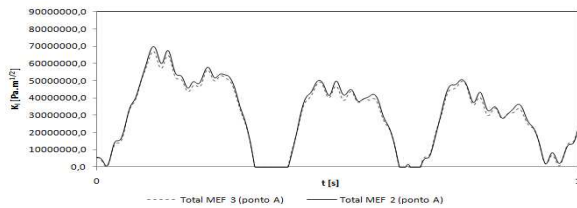


Figura 14. K_{total} para $t \in [0; 1]$ seg.: MEF2 vs. MEF3b.

De forma a validar os resultados obtidos, estes foram comparados com os resultantes da aplicação da expressão empírica proposta por Newman e Raju [5], para a situação de fenda semi-elíptica, numa estrutura sujeita a momentos flectores. A referida expressão foi aplicada usando os momentos flectores a meio vão, extraídos do modelo MEF1, aproveitando dessa forma a semelhança de comportamento demonstrada entre este modelo e os modelos MEF2 e MEF3a. Os factores de intensidade de tensão assim calculados foram idênticos aos obtidos pela metodologia aqui apresentada, tal como ilustrado na Figura 15, referente à evolução temporal de K no ponto C da fenda, ponto esse identificado na Figura 6.

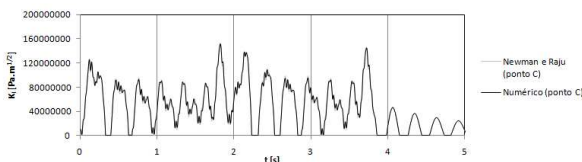


Figura 15. K_{total} : MEF2 vs. Newman e Raju.

Finalmente, comparando a evolução de K ao longo do tempo, nos pontos A e C da frente da fenda (Figura 16), verifica-se que os maiores valores de K ocorrem no ponto C. Deste modo, a propagação da fenda face ao presente carregamento não será uniforme, prevendo-se uma propagação mais rápida à superfície e uma propagação mais lenta na direcção do interior do elemento estrutural.

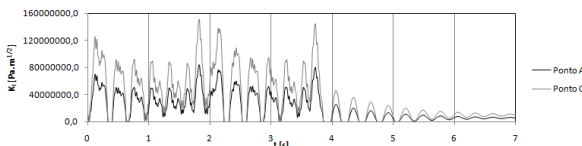


Figura 16. Evolução temporal de K em dois diferentes pontos da frente da fenda.

5. CONCLUSÕES

O problema da integridade estrutural face ao problema da fadiga, em componentes metálicos, pode ser abordado de forma rigorosa com recurso aos conceitos da mecânica da fractura. No entanto, no âmbito da Engenharia Civil, esta abordagem não é geralmente usada devido às diferentes escalas dimensionais das estruturas e dos detalhes susceptíveis de apresentar dano por fadiga. O presente artigo apresenta as primeiras conclusões relativas à aplicação da mecânica da fractura

no contexto da análise dinâmica de estruturas pelo método da sobreposição modal. Uma nova metodologia, para obtenção da evolução temporal de K , foi proposta e validada com base num caso simples. As principais conclusões obtidas foram as seguintes:

- O cálculo de K , em fendas contidas em detalhes com geometrias e carregamentos complexos, envolve a construção de modelos de elementos finitos de grandes dimensões, pelo que é importante minorar a quantidade de cálculos a efectuar sobre os referidos modelos.
- A sobreposição modal de factores de intensidade de tensão permite a drástica redução do número de cálculos envolvidos na obtenção da evolução temporal de K , pois implica resolver a estrutura apenas para o carregamento estático e para cada um dos modos de vibração a ela associados.
- Esta mesma metodologia apresenta ainda a vantagem de permitir obter de forma imediata o contributo do carregamento permanente, de cada modo de vibração ou até de grupos de modos, para o valor total de $K(t)$.
- A utilização da técnica de sub-modelação permite reduzir substancialmente a dimensão dos modelos numéricos utilizados, sendo a redução tanto maior quanto maior a diferença de escala dimensional entre a estrutura global e o detalhe que contém a fenda.

Em futuros desenvolvimentos do presente trabalho pretende-se melhorar o processo de sub-modelação através da incorporação no sub-modelo das forças de inércia associadas aos modos de vibração.

AGRADECIMENTOS

Os autores agradecem o apoio financeiro da Fundação para a Ciência e a Tecnologia (FCT) através do projecto de investigação PTDC/ECM/69697/2006.

REFERÊNCIAS

[1] Albuquerque C.M.C., de Castro P. M. S. T. and Calçada R.B., *Aplicação da mecânica da fractura no contexto da análise dinâmica de estruturas pelo método da sobreposição modal*. VII Congresso de Construção Metálica e Mista, Lisboa, 2009.

[2] Advanced Analysis Techniques Guide, in Release 12.0 Documentation for ANSYS. 2009, ANSYS, Inc.

[3] Krueger, R., *The Virtual Crack Closure Technique: History, Approach and Applications*. 2002: Hampton, Virginia, USA.

[4] Murakami, Y., *Stress intensity factors handbook*. Vol. 2. 1987, Oxford: Pergamon Press.

[5] Newman Jr., J.C. and I.S. Raju, *An empirical stress-intensity factor equation for the surface crack*. Engineering Fracture Mechanics, 1981. 15(1-2).

**DUCTILE-TO-BRITTLE IMPACT TRANSITION TEMPERATURE FOR
LOW-CARBON MICROALLOYED STEELS WITH HIGH NIOBIUM CONTENTS.
A STATISTICAL APPROACH**

M. Pérez-Bahillo, A. Martín-Meizoso

Materials Department, CEIT and Tecnun (University of Navarra).
Paseo Manuel Lardizabal, 15, 20018, San Sebastian, Spain
E-mail: mperez@ceit.es

ABSTRACT

In the present investigation, the effect of both: rolling parameters (2 reduction rates and 3 cooling rates) and chemical elements such as: C, Mn, Nb, Ti, Mo, Ni, Cr, Cu and B, has been studied in relation with toughness properties in low-carbon microalloyed steels with high niobium contents (up to 0.12 wt.% Nb). For this purpose, an experimental set-up was designed based on an intelligent design of experiments (DoE), resulting in 26 casts (laboratory casts). A combination of metallography, Electron Back-Scattered Diffraction (EBSD) and Charpy impact tests have been performed to study how processing parameters and chemical composition affect toughness, and to generate microstructure-toughness relationships. The results, where *ITT* 27J and 0.5Kvmax are the response variables, have been analysed statistically by means of multiple linear regression technique, leading to response equations. From the results, it was found that high niobium additions improve the toughness; where its effect might be related mostly to grain size refinement.

KEY WORDS: microalloyed steels, toughness properties.

1. INTRODUCTION

Strength and toughness are two of the most important mechanical properties for the design of steel structures, pressure vessels, pipelines or other similar components [1]. Thermo-mechanical rolling is used to maximise grain refinement and thus achieve both higher strength and toughness [2]. A fine grain microstructure is an optimum method for improving strength since unlike most other strengthening mechanisms, the improvement in strength is also accompanied by an improvement in toughness. The use of niobium in low-carbon bainitic steels is advantageous because when the amount of solute niobium is increased, retardation of austenite recrystallization is observed at significant higher temperatures, and also because of its ability to promote the formation of bainite [3,4].

2. INTELLIGENT DESIGN OF EXPERIMENTS

To study the effect of C, Mn, Nb, Ti, Mo, Ni, Cr, Cu and B, a statistical approach is used, by means of an intelligent design of experiments using a three-stage approach:

- In stage 1, a half fractional factorial design is used to examine five factors at two levels using sixteen casts, the factors being Mn, Ni, Cu, Mo and Cr; 16 casts in total.
- Stage 2, with combinations of low and high levels of C and Nb, was designed to check the limit

conditions of High Temperature Processing (HTP) concept. The design is full factorial.

- Stage 3 investigates the influence of B and Ti. Since only B in solid solution is effective for the phase transformation

The levels for each element are shown in Table 1.

Table 1. Intelligent Design of Experiments, Laboratory casts

Stage	Level	C	Nb	Ti	B	Mn	Ni	Mo	Cu	Cr
1	Low					1.5	0	0	0	0
	Base	0.04	0.10	0.015	0					
	High					2.1	0.5	0.3	0.5	0.5
2	Low	0.01	0.04							
	Base			0.015	0	1.8	0.25	0.15	0.25	0.25
	High	0.07	0.07							
3	Low			0.008	0.000					
	Base					1.8	0.25	0.15	0.25	0.25
	High			0.025	0.002					

In total, 26 casts: 24 casts with the aim composition from the experimental design plus 2 failed casts (with high carbon level) have been made and from each cast one 12 mm thickness plate have been rolled under six conditions. These conditions have reduction ratios below the no recrystallization temperature (T_{nr}) of 2 and 4, with a finish rolling temperature of 850°C and cooling rates between 850°C and 550°C of 0.5°C/s (Air Cooling, **AC**), 10°C/s followed by air cooling (ACcelerated Cooling + Air Cooling, **ACC + AC**), and 10°C/s followed by slow cooling (ACcelerated Cooling + Coiling simulation, **ACC + CT**). All these plates have been supplied by OCAS ArcelorMittal R&D (Belgium).

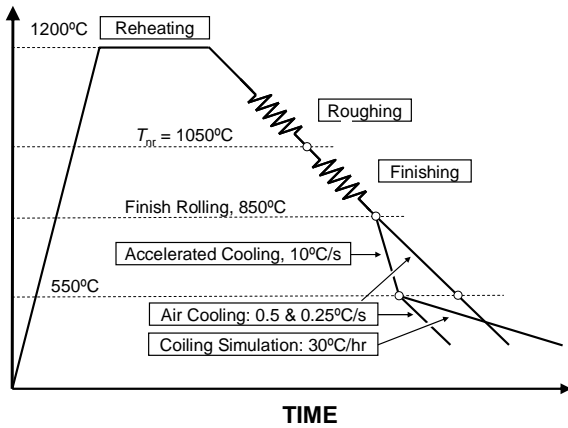


Figure 1. Schematic illustration of the thermomechanical rolling schedule of laboratory casts

Table 2 summarizes the six rolling conditions. These conditions are selected to simulate the slow cooling conditions in heavy plate mills without accelerated cooling, faster cooling in heavy mills with accelerated cooling, and in hot strip mills with coiling after rolling.

Table 2. Rolling Schedules

Rolling Schedules	Cooling Conditions		
	AC	ACC + AC	ACC + CT
RR = 2	C	E	G
RR = 4	D	F	H

Four industrially casts were used for the verification/validation of the models obtained with the laboratory casts. These industrial casts were delivered by Ruukki, Corus and Salzgitter,

Table 3. Analysis (wt. %) of the industrially cast materials

Cast	C	Mn	N	Ti	Nb	V	Ni	Mo	Cu	Cr	Ti/N
81351	0.042	1.97	0.0084	0.015	0.10	0.013	0.21	0.005	0.21	0.98	1.79
02098	0.079	1.66	0.0050	0.003	0.04	0.079	0.06	0.004	0.06	0.04	0.58
16685	0.047	1.73	0.0082	0.018	0.10	0.009	0.04	0.069	0.04	0.27	2.20
81913	0.05	1.58	0.0059	0.016	0.10	0.007	0.16	0.005	0.25	0.26	2.71

3. EXPERIMENTAL METHODS

3.1. EBSD Technique

The samples for Electron Back-Scattered Diffraction (EBSD) observations were prepared from rolling schedules samples, taking into account the rolling direction. All the scans were carried out on a Philips XL30cp Scanning Electron Microscope (SEM) at the quarter plate thickness position.

The EBSD specimens were tilted 75° from the horizontal, so that the surface was normal to the electron beam. The step size was 0.4 microns and scan

size was 160 × 100 microns. TSL OIM Analysis 4.6 software was used to analyse the data.

In order to quantify the final grain size (bainitic packets in the case of bainitic microstructures) in relation with toughness, the grain size was determined with a threshold misorientation of 15°. It is widely known that the Impact Transition temperature (ITT, °C) decreases as the grain size is refined; there is a strong effect of grain refinement on the brittle fracture stress [5]. The high angle boundaries show a resistance to brittle cleavage fracture, hindering the propagation of a cleavage crack.

3.2. Charpy Impact Tests

Charpy impact tests were performed by Aachen University (RWTH, Germany). Such tests were carried out to EN 10045 using an impact testing machine with an energy capacity of 1448 J and an impact velocity of 7.74 m/s. Impact transition curves were determined by means of the modified tanh fitting algorithm of Wallin [6]. Impact transition temperatures (ITT) were calculated following two criteria; the first one was for 27J and the second one was for half the upper shelf energy, described as 0.5Kvmax, leading to two response variables.

4. STATISTICAL ANALYSIS

4.1. Introduction

Multiple linear regression technique was used to obtain response equations from the response variables (ITT 27J and 0.5Kvmax). *Essential Regression and Experimental Design of Chemist and Engineers software*® was employed for this purpose. The sample was formed by the aforementioned 26 casts (laboratory casts). Only those parameters/variables considered in the three intelligent designs were taken into account: Chemical elements (C, Nb, Ti, Mn, B, Cr, Cu, Ni and Mo) and rolling parameters: rolling reduction (RR) and cooling rates (where CR_{800-550°C} and CR_{550-20°C} denote CR₁ and CR₂, respectively). Additional models were obtained introducing the grain size (D_{15°}) as regressor in the response equation for toughness.

A transformation of variables takes place concerning the cooling rates (CR₁, CR₂). Note that the cooling rates are basically between 0.5 - 10°C/s and 0.25 - 0.008°C/s for CR₁ and CR₂, respectively. The cooling rates variables differ by orders of magnitude, being such orders of magnitude which make the difference. Therefore the cooling rates are introduced as the decimal logarithms, log₁₀CR₁ and log₁₀CR₂, but for the sake of brevity such terms will be spelt as logCR₁ and logCR₂ from now on.

4.2. Coefficients of multiple determination

In order to figure out whether a model actually describes the data adequately or how good is the “fit” of

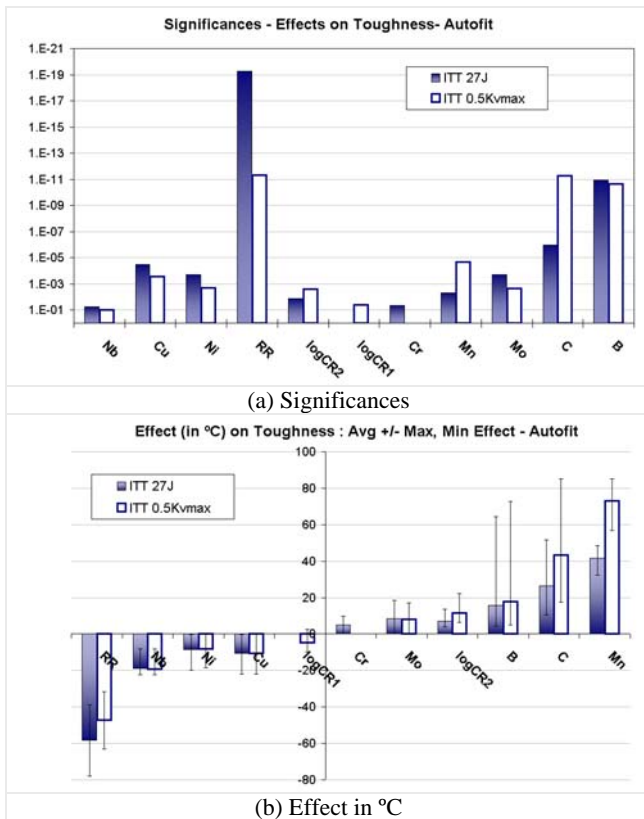


Figure 2. Plots of significances and effects of predictor variables on ductile-to-brittle impact transition temperature (ITT), without considering D_{15° .

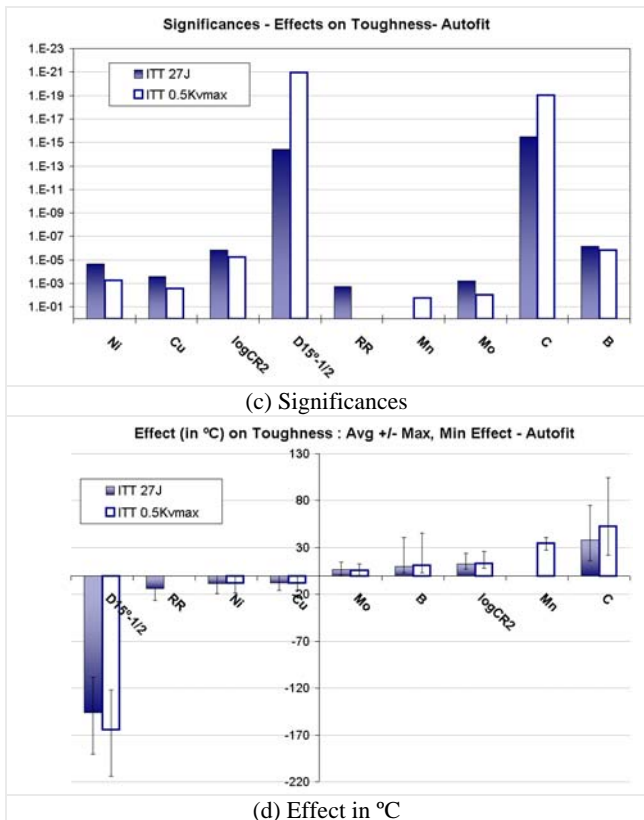


Figure 3. Plots of significances and effects of predictor variables on ITT, considering D_{15° .

From the first group (Table 4.a), it is remarkable the effect of RR , C and B , whose coefficient present the lowest significances ($\alpha \ll 0.1$), as shown in Figure 2.a. Concerning the significant effects (Autofit, $\alpha < 0.1$); C , B , Mo and Mn impair both ITT 27J and 0.5Kvmax. In opposite direction; Nb , Cu , Ni additions on the one hand, and increasing the level of RR , mainly, and CR_2 on the other, improve the toughness properties. Solely Ti shows no effect on both models, with significances well above 0.1. In the case of Cr and CR_1 , they only have significative effect on ITT 27J and 0.5Kvmax, respectively. The Figure 2.b represents the effect (in $^\circ C$) of the proved predictor variables, where the columns represent the average effects and the error bars display the maximum and minimum observed effects.

The results from the second model (Table 4.b), where the $D_{15^\circ}^{-1/2}$ has been included, are also shown in Figure 3. It is worthy noting the effect of grain size ($D_{15^\circ}^{-1/2}$). This latter presents, by far, the strongest effect improving the toughness, as shown in Figure 4.

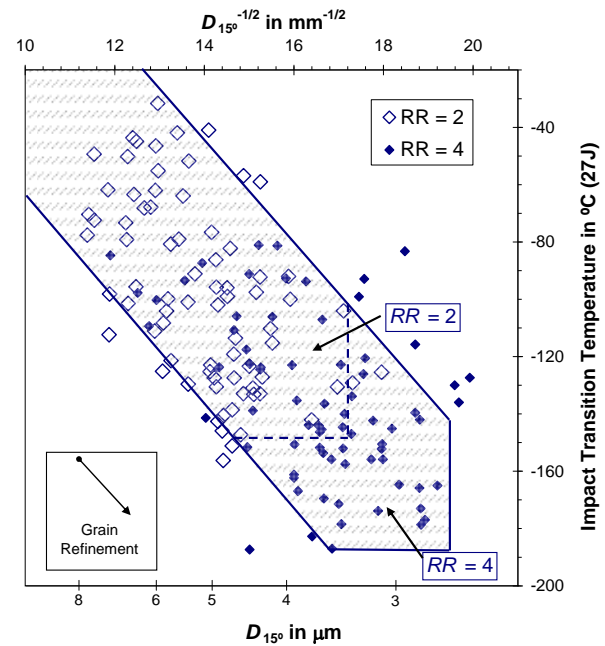


Figure 4. Effect of mean grain size of 15° (D_{15°) and Rolling Reduction (RR) on Impact Transition Temperature (ITT 27J, $^\circ C$).

Plots of experimental versus predicted parameters were generated for the 26 casts used to compute the reponse equations considering only the Autofit method ($\alpha < 0.1$), as shown in Figure 5. Additional plots show the experimental versus the predicted values for 4 additional casts (industrial cast, Table 3) to validate the proposed equations, see Figure 6.

In the light of statistical parameters obtained from both model adequacy and model validation, the models with $D_{15^\circ}^{-1/2}$ predict far more accurately. The determination coefficients (R^2) of toughness models improve

substantially from about 0.63 and 0.60 to 0.74 and 0.70 for *ITT 27J* and 0.5Kvmax, respectively. Similar behaviour is found for adjusted coefficients (R^2_{adj}) since the response equations obtain more accurate predictions with a lower number of regressors, Figure 5.

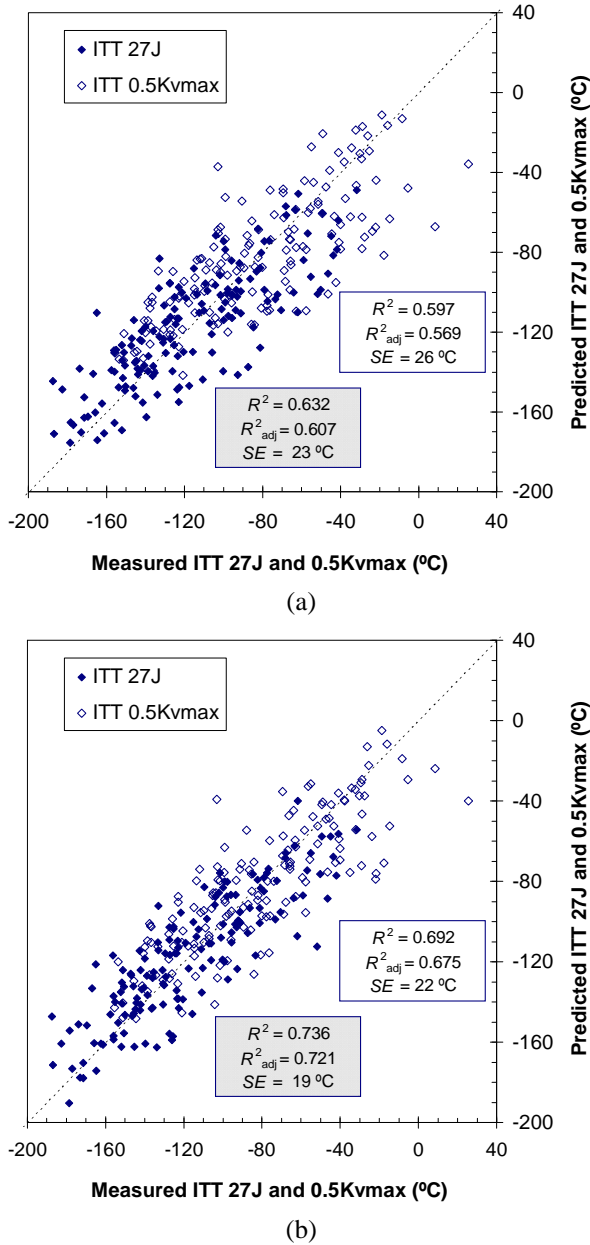


Figure 5. Experimental vs. predicted plots for toughness models (Model Adequacy), without considering D_{15° (a), and considering D_{15° (b). Autofit (26 casts).

Concerning model validation, the determination coefficients for the first models are negative, being, therefore, not included in the Figure 6.a. However, when considered the grain size (D_{15°), the models predict reasonably well, with standard errors of 17 and 21°C for *ITT 27J* and 0.5Kvmax, respectively.

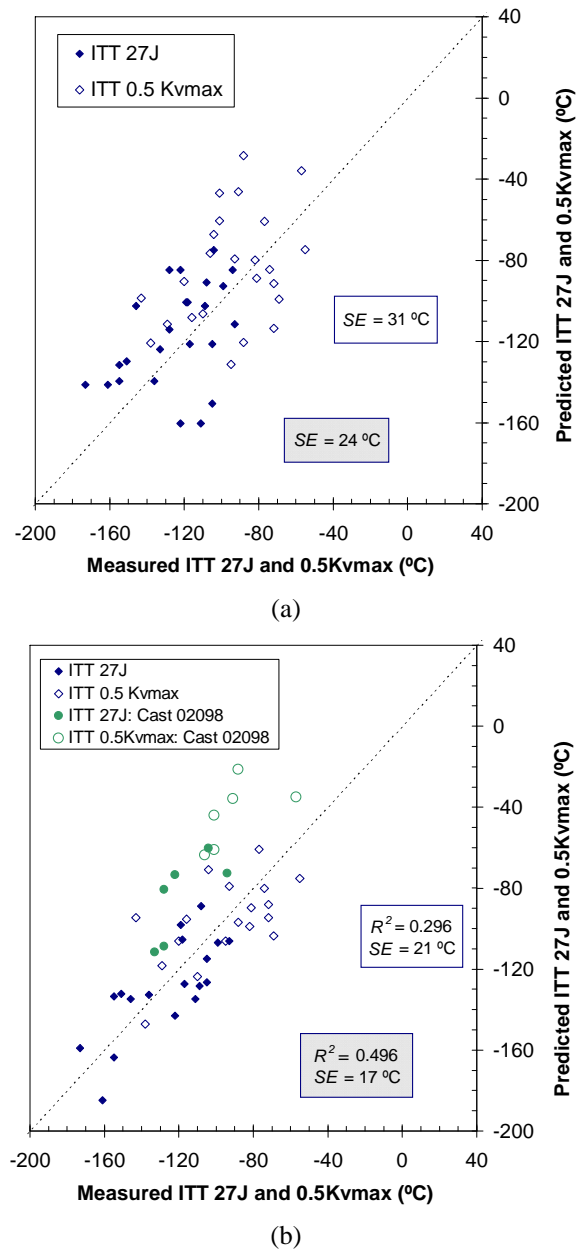


Figure 6. Experimental vs. predicted plots for toughness model (Model Validation)s, without considering D_{15° (a), and considering D_{15° (b). Autofit (26 casts).

5.1. Comparison between response equations

Taking a glance to response equations (Table 4) and/or effect of predictor variables (Figure 2, Figure 3), when the D_{15° is considered or not, it is possible to draw the following conclusions, mainly for *ITT 27J*:

- ☑ In a previous publication, the effect of both the same rolling conditions and intelligent design of experiments on grain size was studied [7], giving place to the next response equation (Autofit):

$$D_{15^\circ} = 6 + 450B - 15C - 10Nb + 1Mn + 1Cr - 0.7RR - 0.2\log CR_2 \quad (1)$$

- ☑ It is observed that the regressors coefficients which affect to D_{15° , such as B, C, Nb, Cr, CR_2 and RR , change substantially if this latter parameter is included or not, see Table 5, where such regressors are highlighted in grey. It is possible to say that the effect of these regressors can be partly included by the $D_{15^\circ}^{-1/2}$ term. Whilst on the other hand, the rest of regressors, such as Mo, Cu, and Ni which do not show proved effects on D_{15° hardly change.

Table 5. Comparison between toughness models.

ITT 27J - Autofit							
Without considering D_{15°				Considering D_{15°			
Term	Coefficient	Std Error	Significance	Coefficient	Std Error	Significance	Term
Ni	-37.2	9.7	2.0E-04	-36.8	8.2	2.2E-05	Ni
Nb	-162.6	95.8	0.059				Nb
Cu	-39.1	9.1	3.4E-05	-28.7	7.7	2.6E-04	Cu
$\log CR_2$	-6.5	2.6	0.013	-11.4	2.3	1.5E-06	$\log CR_2$
				-9.5	1.1	4.0E-15	$D_{15^\circ}^{-1/2}$
RR	-19.5	1.9	5.4E-20	-5.7	2.1	1.8E-03	RR
Constant	-126.5	17.9	6.4E-11	-3.1	14.2	0.826	Constant
$\log CR_1$							$\log CR_1$
Cr	19.1	9.5	0.045				Cr
Mn	23.1	9.0	0.005				Mn
Mo	63.1	13.9	1.9E-04	40.9	11.6	6.0E-04	Mo
Ti							Ti
C	562.0	110.2	1.1E-06	815.4	88.5	3.4E-16	C
B	21526.4	2912.5	1.1E-11	13573.8	2614.2	6.9E-07	B

- ☑ Concerning elements such as Nb, Cr and Mn on *ITT* 27J, its disappearance (null effect) when $D_{15^\circ}^{-1/2}$ is considered might indicate that their whole effects on toughness is somehow related directly by means of grain size. Nevertheless, these elements have a proved solid solution strengthening effect, because of which the toughness should have been affected. This apparent contradiction might be explained as follows: The D_{15° shows the more powerful effect on toughness, much more than other effects like precipitation strengthening or solid solution. Therefore, the effect of these elements, chiefly Nb and Mn, on solid solution may be negligible in comparison with their effect on grain size. As instance, it is well known the strong effect of manganese on strength but also on that of grain size (D_{15°) [7]. The null effect on Mn on toughness is consistent with the work developed by F. B. Pickering: In the classical equation of impact transition temperature, there was no apparent effect of manganese because its effect was incorporated in the grain size [8].
- ☑ Similar conclusions can be drawn for 0.5Kvmax.

6. SUMMARY AND CONCLUSION

- ☑ On the basis of measured grain sizes (D_{15°) and Impact Transition Temperatures (*ITT* 27J and 0.5Kvmax), multiple regression models have been developed, alloying to quantify the effect of both rolling parameters and chemical compositions on toughness properties for thermo-mechanically rolled structural and pipe steels.
- ☑ The findings show how rolling reduction (RR) plays one of the most important roles on final grain sizes distributions, refining the final grain size (D_{15°). This refinement is translated in a remarkable drop of Impact Transition Temperatures (*ITT*).

- ☑ It was observed that the alloying elements with strong effects on hardenability, promoting low transformation temperatures products (bainite), impair the toughness (B, Mn and Mo). On the other hand, it is remarkable the effect of high niobium additions (up to 0.12%) improving the toughness by means of grain size refinement.
- ☑ The results have shown that excellent toughness properties can be obtained by using low carbon contents (< 0.8 %) and high niobium additions (up to 0.12 %) without the use of more expensive alloying elements like molybdenum and vanadium.

ACKNOWLEDGEMENTS

This work has been possible thanks to the ECSC European project (HIPERC) with contract number: RFSR-CT- 2005-0007. One of the authors (M. Perez) also wants to thank to FEUN (Fundacion Empresa Universidad de Navarra) and to the Torres Quevedo Program of the Spanish Ministry of Education and Science for his fellowship.

REFERENCES

- [1] F. B. Pickering, *Towards Improved Toughness and Ductility*, Climax Molybdenum, Co. Symp., Kyoto, 1971, p. 9.
- [2] L. J. Cuddy, *Metall. Trans.*, 15^a, 1984, p. 87.
- [3] M. H. Thomas and G. M. Michal, in H. I. Aaronson *et al.* (eds.), *Solid-Solid Phase Transformation, TMS-AIME*, Warrendale, P. A, 1981, pp. 469-473.
- [4] J. Majta, R. Kuziak, M. Pretryk, *Journal of Materials Processing Technology*, Vol. 80-81 (1998), pp. 524-530.
- [5] D. Bhattacharjee, J. F. Knott and C. L. Davis, *Metallurgical and Materials Transactions A: Physical Metallurgy and Materials Science*, vol. 35 A, n° 1, 2004, p. 121.
- [6] K. Wallin, Modified Tanh fitting algorithm for Charpy impact data, ECOPRESS Research Seminar on economical and safe application of modern steels for pressure vessels, 19th and 20th of May 2003, Aachen, Germany.
- [7] M. Pérez-Bahillo, B. López and A. Martín-Meizoso, "Efecto de la rutina de laminación en el tamaño de grano en aceros con alto contenido en niobio", *X Congreso Nacional de Materiales*, Donostia - San Sebastián, Vol. 1 (2008), pp. 343-346.
- [8] F. B. Pickering: *Material Science and Technology*, Vol. 7: Constitution and Properties of Steels, Ed. by R. W. Cahn, P. Haasen and E. J. Kramer (1992), pp. 54.

MODELING OF FATIGUE CRACK GROWTH IN MONOLITHIC INTEGRAL STIFFENED PANELS TAKING INTO ACCOUNT RESIDUAL STRESS

S. M. O. Tavares¹, V. Richter-Trummer¹, P. M. G. P. Moreira², P. M. S. T. de Castro¹

¹ Faculdade de Engenharia da Universidade do Porto and IDMEC-Porto
Rua Dr. Roberto Frias, 4200-465 Porto, Portugal; E-mail: {sergio.tavares;valentin;ptcastro}@fe.up.pt

² Instituto de Engenharia Mecânica e Gestão Industrial, INEGI
Rua Dr. Roberto Frias, 4200-465 Porto, Portugal; E-mail: pmgpm@fe.up.pt

ABSTRACT

The main and primary structures in airframes are composed by stiffened panels in order to have a high specific strength. Different manufacturing processes are under study for improving this type of structures, aiming at decreasing the panel weight without compromising the global safety. In this paper stiffened panels produced by three different manufacturing processes are studied as regards their behaviour in the presence of crack, evaluating the damage tolerance of different solutions. For this purpose, numerical models using Linear Elastic Fracture Mechanics concepts are developed to simulate the fatigue behaviour of the cracked panels tested. Finite element models of the stiffened panels were made using 3D elements to determine Stress Intensity Factors (SIFs) using the modified virtual crack closure technique and taking into account the residual stress redistributions promoted by the welding processes. These SIF calibrations were applied in a fatigue crack growth law for fatigue life determination. In addition, the effect of the residual stress on the load ratio at the crack tip was estimated and incorporated into the crack growth law. The residual stress effect can significantly deteriorate or improve the fatigue life of these stiffened panels, depending upon the location of the initial crack and the intensity and type of residual stresses. Longer fatigue life is obtained when the crack starts to grow in areas with higher compression residual stresses. The results obtained were compared with experimental data for validation of the numerical models.

KEY WORDS: Fatigue crack growth; Forman law; residual stress; stiffened panels.

1. INTRODUCTION

Economical and environmental concerns force the decrease in operational costs and environmental impacts and are drivers for the development of new solutions for aeronautics [1]. In the case of airframes, the main interest is the decrease of the global weight without compromising safety. For this purpose new technologies start to be applied as in the aircrafts Boeing 787 or the Airbus A350WXB aircrafts, where the traditional material for the airframe, aluminium, was substantially replaced by carbon fibre reinforced polymer (CFRP). Nevertheless, due to the problems of the large scale application of CFRPs in airframes, as stress concentration, final cost, maintenance and aging, other alternatives using aluminium alloys are being investigated.

New manufacturing processes can replace the riveting processes creating a leaner joint and with an improvement of mechanical properties. Examples of these joining processes are the friction stir welding (FSW) and laser beam welding (LBW). In addition, new aluminium alloys with lower density and higher mechanical properties can add an additional improvement to the airframe structures. The combination of these new aluminium alloys with new

manufacturing processes can bring competitive airframes, with a reduced number of parts, higher maintenance intervals, less lead times and less global weight for the structure.

Al-Li [2] and Al-Sc [3] are examples of alloys with better material properties than the AA2024, with better weldability and suitable to be joined with welding processes as LBW, FSW and electron beam welding.

The application of new processes and materials in airframes requires an extensive study in order to take into account effects that were not considered in riveted structures, as the continuous paths for the crack growth from the skin to the stiffeners and the residual stress fields promoted by the welding processes.

The residual stresses originated by the application of welding processes in stiffened structures considerably affect their fatigue behaviour. The residual stresses arise due to the thermal gradients originated by the welding process. In the FSW process, in addition to the thermal field the mechanical work also promotes residual stresses. These residual stress fields could increase or decrease the fatigue life of the structures if they are compressive or tensile, respectively.

This paper presents a methodology, based in the Linear Elastic Fracture Mechanics (LEFM) concepts, to determine fatigue life of integral structures with residual

stresses. ABAQUS finite element models were used together with the Modified Virtual Crack Closure Technique (VCCT), [4], and the J-integral technique for stress intensity factor determination of cracked stiffened panels subjected to mode I loading.

Following the stress intensity factor calibration, crack growth laws were used to determine the fatigue life of the panel considering the effect of residual stress.

The methodology proposed was developed under the frame of an European project, Innovative Fatigue and Damage Tolerance Methods for the Application of New Structural Concepts - DaToN [5], where panels with two stiffeners was manufactured by three different processes: high speed machining (HSM), LBW and FSW, using two aluminium alloys AA2024 and

AA6056 and with different heat treatments. These panels were experimentally tested by various institutions. The acquired results were compared with the numerical models in order to validate the methodologies used.

2. EXPERIMENTAL PROCEDURE

A base geometry of the stiffened panel was selected for this benchmark. Panels were manufactured with three different processes and with two different materials. Panels are flat with 450 mm width and two simple stiffeners of rectangular cross section. Figure 1 shows the cross section of the panel with dimensions and location of the initial crack.

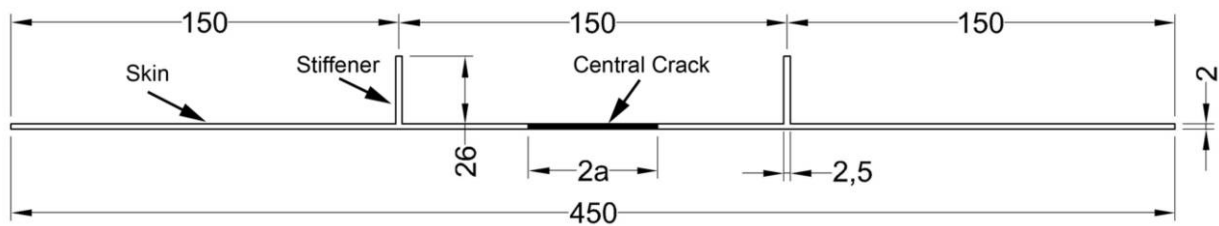


Figure 1. Cross-section of the stiffened panel and the crack location.

The HSM panels are produced from a block of aluminium with 40 mm thick that was machined until get the final shape of the panels. For LBW and FSW, the stiffeners were welded to a plate. For the LBW process two different configurations were used and are presented in Figure 2 a) and 2 b). In the stiffened panel produced by FSW, the stiffeners were welded with a tool that crosses all skin and mix the material from the stiffener with the skin, as shown in Figure 2 c).

Besides the manufacturing processes and joining configurations, different materials and heat treatment conditions were used to manufacture these panels:

- AA2024-T3;
- AA6056-T6;
- AA6056-T4 and post welding treatment (PWHT) to T6 condition.

For each configuration, the specimens were tested, in order to measure the crack growth, in the situation of an applied constant cyclic load for two different load ratios (R) with different maximum loads:

- $R=0.1 \rightarrow \sigma_{\max}=80 \text{ MPa}$;
- $R=0.5 \rightarrow \sigma_{\max}=110 \text{ MPa}$.

In the experimental program, besides the crack growth with constant load, some panels were used to test the crack growth with a flight load spectrum and other used to measure the residual stress using a destructive method, the cut method, where the residual stress are measured by strain gages that measure the residual stress release after a cut. The method was applied by Pisa University, partner of DaToN project, in 7 panels produced by the different processes and for the both materials, [6]. These panels were cut in the middle, transversally to the stiffeners, and the final strain achieved after the cut was measured with strain gages along the cutting line on both surfaces, obtaining the residual stresses acting parallel to the stiffeners. In order to not influence the residual stress state by the cutting process, the cut was done on a milling machine.

3. NUMERICAL PROCEDURE

The numerical procedure adopted to model the crack growth in these panels is based on LFM theory where SIFs were calculated from FE elastic models.

A finite element model corresponding to half of the specimen geometry was made using the symmetry of

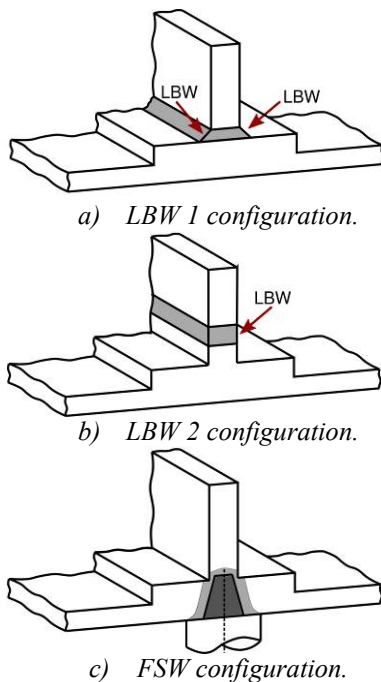


Figure 2. Welded panels, the different configurations.

the DaToN panel and including part of the gripping system for better load distribution at the top of the panel, Figure 3.

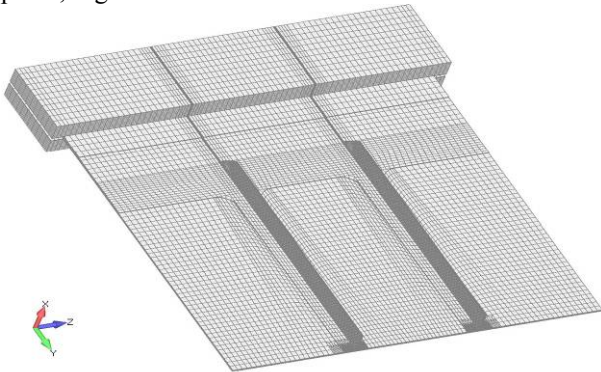


Figure 3. Mesh of the FE models of the stiffened panel.

The elements used in this model are parabolic solid elements with 20 nodes (C3D20) and 15 nodes (C3D15), from the ABAQUS element library, [7]. The global model has 47978 elements and 230287 nodes. The residual stress was applied as initial condition in the FE models.

In order to apply the residual stress data from the experiments in the three-dimensional finite element models, information along the thickness is required. This information was obtained using linear interpolations from the known points on surface. Employing an interpolation algorithm based on a Delaunay triangulation [8] the values along the thickness, were estimated

To increase the accuracy of these models, the centroid of each element was calculated and the residual stress was interpolated into these centroids. A detail of the initial stress (uncracked panel) in a contour map is presented in Figure 4 for the panel produced in AA6056-T6 with the FSW process. After this initial condition, the remote load and the boundary conditions that define the crack size were applied.

To determine the stress intensity factor calibration (SIF in function of the crack length) for each configuration the crack growth was simulated in a step, adapting the boundary conditions corresponding to each crack length.

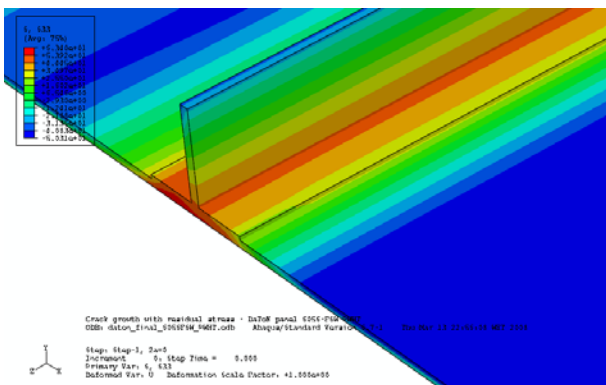


Figure 4. RS applied in the FE models of the stiffened panel (detail)

VCCT was proposed by Rybicki and Kanninen, [9], in order to calculate the energy release rate (G) based on the calculation of the strain energy release rate (U). The energy release rate when a virtual extension of crack length is imposed (Δa) can be approximated by:

$$G = \frac{\partial U}{\partial a} \approx \frac{U_{a+\Delta a} - U_a}{\Delta a} \quad (1)$$

However, this procedure requires performing two finite element simulations, one to determine the reaction loads and another to determine the displacements in order to obtain the energy release rate. This procedure could be hard working and time consuming in large finite element models.

A modification of VCCT was presented by Krueger in 2002, [4]. This modified technique presupposes that if the nodal displacements are measured, near the crack before and after grow the crack length to $a+\Delta a$, for nodes equidistant to the crack tip, the nodal displacements are identical. This assumption allows computing the energy release rate using only one finite element analysis for each crack length. For 3D parabolic finite elements, the determination of the energy release rate with the modified virtual crack closure technique can be determined using the nodal loads and nodal displacements; however it requires to consider the different weights of the nodes in the middle and in the corner of the element. As example, for a parabolic element with 20 elements, the mode I, considering the notation presented in Figure 5, the equation used to determine the energy release rate for the node at the crack surface (node 3) is:

$$G_I = -\frac{1}{2\Delta a \cdot \Delta b} \left[F_{z_3} (u_{z_1^*} - u_{z_1}) + F_{z_4} (u_{z_2^*} - u_{z_2}) + \frac{1}{2} F_{z_6} (u_{z_5^*} - u_{z_5}) \right] \quad (2)$$

where F_z is the nodal force in the z direction, u_z is the displacement in z direction and Δa and Δb are the element dimensions. For the nodes positioned in the middle of the element, in this case node 6:

$$G_I = -\frac{1}{2\Delta a \cdot \Delta b} \left[\frac{1}{2} F_{z_3} (u_{z_1^*} - u_{z_1}) + \frac{1}{2} F_{z_4} (u_{z_2^*} - u_{z_2}) + F_{z_6} (u_{z_5^*} - u_{z_5}) + \frac{1}{2} F_{z_9} (u_{z_7^*} - u_{z_7}) + \frac{1}{2} F_{z_{10}} (u_{z_8^*} - u_{z_8}) \right] \quad (3)$$

For the corner nodes inside the crack tip, as the node 9, the energy release rate will be:

$$G_I = -\frac{1}{2\Delta a \cdot \Delta b} \left[\frac{1}{2} F_{z_6} (u_{z_5^*} - u_{z_5}) + F_{z_9} (u_{z_7^*} - u_{z_7}) + F_{z_{10}} (u_{z_8^*} - u_{z_8}) + \frac{1}{2} F_{z_{12}} (u_{z_{11}^*} - u_{z_{11}}) \right] \quad (4)$$

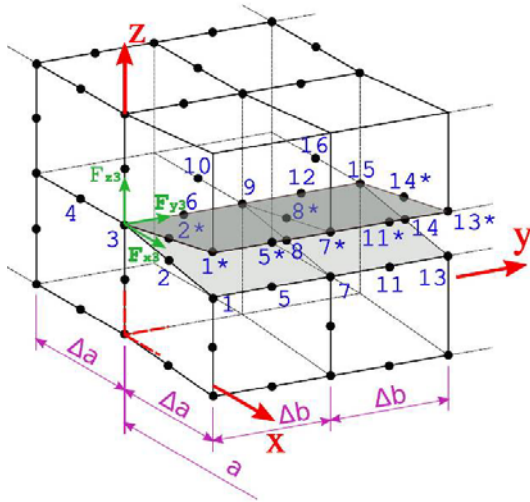


Figure 5. FE crack tip model

The results of stress intensity factors were estimated for 37 crack lengths for the different manufacturing processes, the values for each configuration are presented in Figure 5.

These three equations are able to determine the evolution of the stress intensity factor along the crack front, in mode I. Similar equations for the determination of SIFs in modes II and III can be derived from presented equations exchanging the nodal loads and nodal displacements by the ones associated to the desired mode of deformation.

The determination of the fatigue life from the stress intensity factor calibration is done using the fatigue crack growth laws that describes the number of cycles in function of the crack length using the material parameters and the stress intensity factors. The determination of the number of cycles in function of crack length is done by the integration of power laws. Several laws may be used to estimate fatigue crack growth as Paris; Walker, Forman, Terada or NASGRO. In this work the Forman law was used for the panels produced in AA6056-T6, because this law considers the load ratio (R) variation at the crack tip and it is possible to fit this law to the available material data for different load ratios with reasonable accuracy.

The Forman law, [10] is:

$$\frac{da}{dN} = \frac{C_f \Delta K^{m_f}}{(1 - R_{eff}) K_c - \Delta K} \quad (5)$$

where C_f , m_f and K_c are material constants and R_{eff} is the effective load ratio at crack tip.

As the crack law are power laws, are particularly sensitive to material characterization. Therefore, the crack growth parameters were obtained from the same material that are produced the panels. The welded panels were obtained from 4 mm thick sheets and the HSM panel was machined from a block of 40 mm. Because the materials applied in the manufacturing had different thickness, fatigue crack growth characterization was done for both material panels, [11].

An algorithm was developed to estimate the Forman law parameters, optimized for $R=0.1$ and $R=0.5$.

The Forman constants can be linearized with the logarithmic values from experimental measurements and fixing a value of K_c (that can be determined by the asymptote of the experimental data for high da/dN values) and for different load ratios, as presented in the next equation:

$$\log\left(\frac{da}{dN} \cdot [(1-R)K_c - \Delta K]\right) = n_f \log(\Delta K) + \log(C_f) \quad (6)$$

The value n_f is determined using the least mean squares technique and the C_f value using the minimisation of the error between the Forman law and the experimental points.

Figure 6 shows the fitting obtained for the Forman law parameters. The material parameters applied in the integration of the Forman law were:

- $C_f = 2.9022E-07$
- $n_f = 2.3510$
- $K_c = 3000$

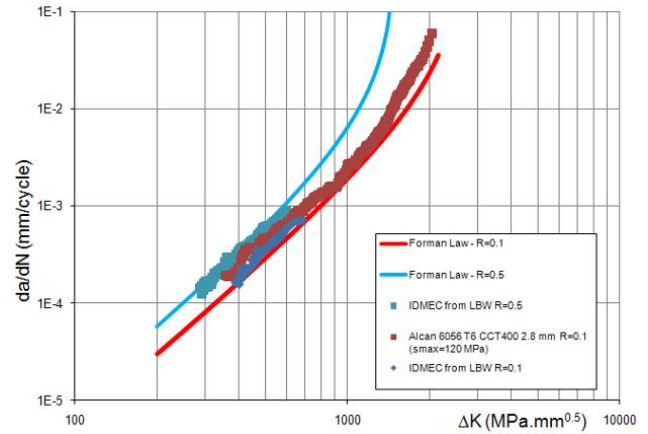


Figure 6. Forman law parameters determination.

4. RESULTS AND DISCUSSION

The results of stress intensity factors for the stiffened panel were estimated for 37 central crack lengths and for the 8 models, the values for each configuration are presented in Figure 7. In addition, the crack bifurcation, when the crack reaches the stiffener was modelled.

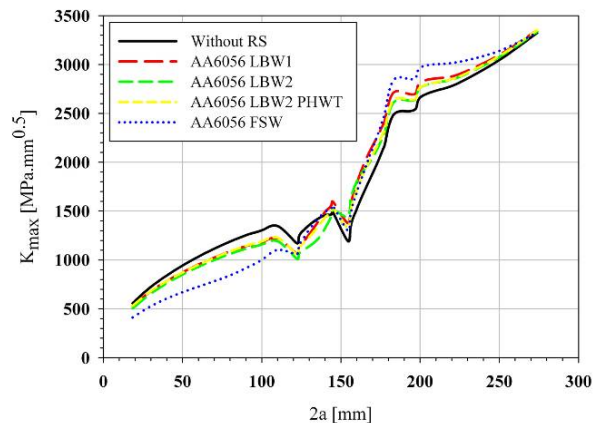


Figure 7. SIFs in function of crack length.

The stiffener influence in the retardation of the crack is noticeable, however the first decrease of the crack length is due to an increase of the skin thickness. It is perceptible from this figure that the FSW promotes a lower stress intensity factor in the middle of the specimen due the compressive residual stresses. In the case of the LBW, the effect is more concentrated in the weld zone generating higher SIFs.

Due to the residual stress field in the panels, the effective load ratio (R_{eff}) at the crack tip will is not the nominal. Thus, effective load ratios can be determined using the SIF solutions and equation 7:

$$R_{eff} = \frac{K_{min} + K_{res}}{K_{max} + K_{res}} \quad (7)$$

where the K_{min} and K_{max} are determined from the FE models and K_{res} is determined using the reference of a panel without RS (panel HSM). Figure 8 shows the evaluation of the R_{eff} at the crack tip in function of the crack length. The compressive residual stress field due the FSW process is intensive generating negative load ratios. These negative load ratios are also presented in the LBW panels although not so severe. When the crack tip reaches the stiffener, the residual stresses are in tension increasing the load ratio but now in positive values.

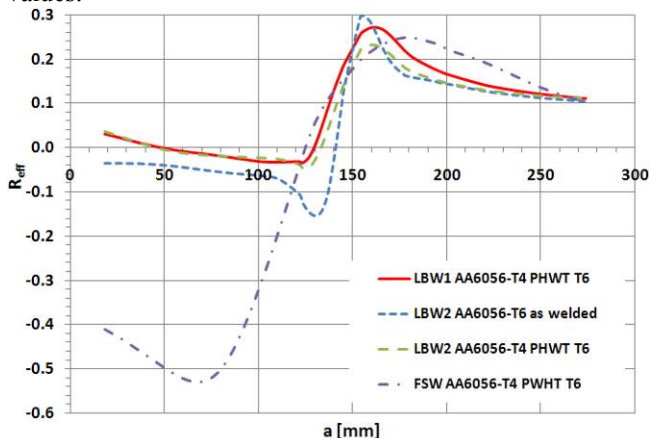


Figure 8. Effective load ratio at the crack tip.

The SIFs and R_{eff} calibrations were applied in the Forman law, equation 5, in order to determine the remaining fatigue life of the different panels by integration. For this integration of the Forman law an algorithm in MATLAB was developed where the variation of the SIF, $\Delta K(a)$, and the effective load ratio, $R_{eff}(a)$, as a function of the crack length is considered. The effective load ratio was calculated using the SIF models with and without load ratios.

The results obtained for the load ratio $R=0.1$ ($\sigma_{max}=80$ MPa) are presented in Figure 9 and for the load ratio $R=0.5$ ($\sigma_{max}=110$ MPa) are presented in Figure 10.

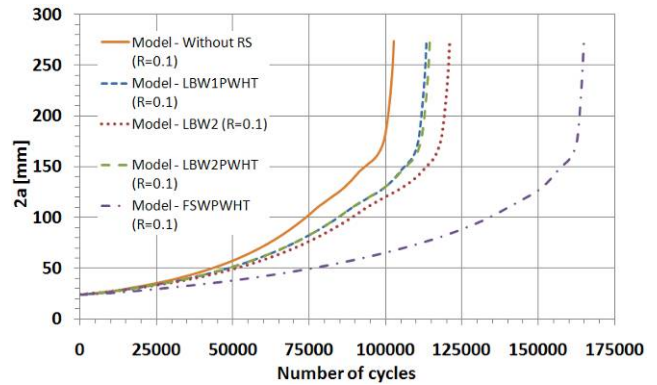


Figure 9. Fatigue life of the panels for the condition of a load ratio $R=0.1$ and $\sigma_{max}=80$ MPa.

As aspected, the higher compressive residual stresses in FSW panels promotes higher fatigue life. The HSM panel, whitout residual stresses, have the lower fatigue life, however should be taken into account that the crack starts to growth in a compressive RS field, if the cracks starts near the stiffeners, where tensile RS are present, the fatigue life will be lower for welded panels. The difference between the fatigue life for the two load ratios is not large, however the stress amplitude during the test for $R=0.5$ is lower than for $R=0.1$.

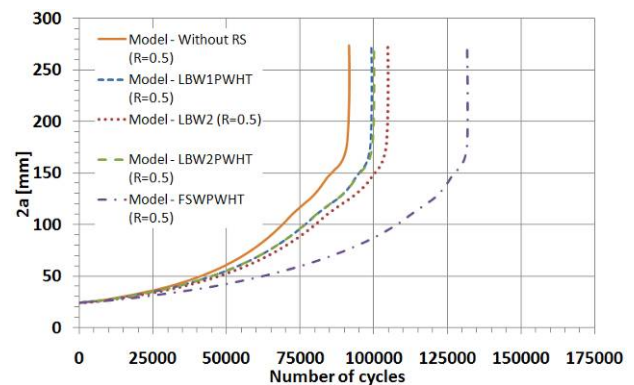


Figure 10. Fatigue life of the panels for the condition of a load ratio $R=0.5$ and $\sigma_{max}=110$ MPa.

In order to validate the numerical models, the results were compared with experimental results for the manufacturing processes, heat treatments and load conditions.

Figures 11 and 12 shows two of these comparisons. generally good agreement was found, including exceptional agreement in the case of Figure 11, and reasonable in Figure 12. The crack growth have always some variance even in the base material with controlled test conditions, therefore discrepancies about the 20%-30% is expectable due the nature of this phenomenon. In this research is also noticed the sensitivity of the calculated fatigue life to the crack growth law parameters; minor variations produce substantial differences in the fatigue life. It is suggested, when possible to measure the material parameters from similar lots of material. The residual stress quantification is also extremely important in order to obtain accurate models.

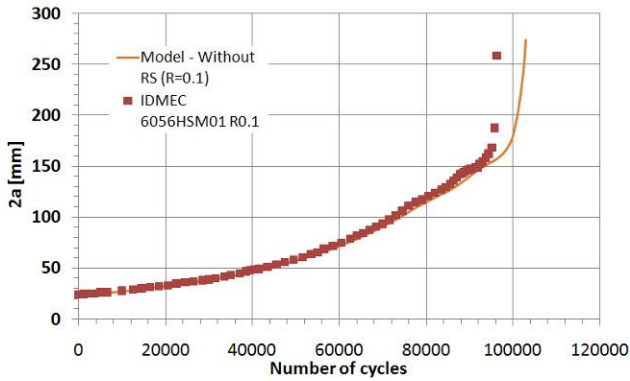


Figure 11. Comparison between numerical and experimental results, panel HSM AA6056, $R=0.1$ and $\sigma_{max}=80$ MPa.

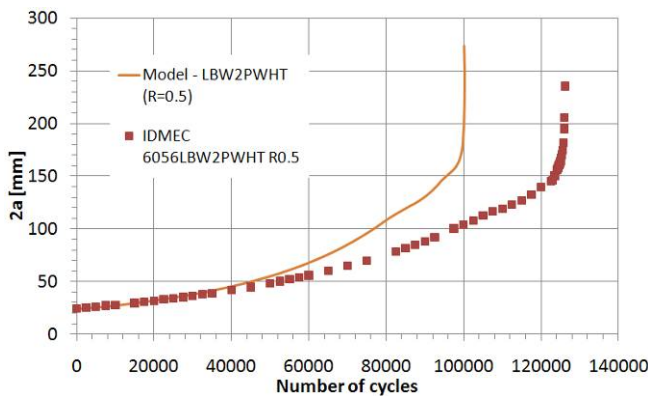


Figure 12. Comparison between numerical and experimental results, panel LBW 2, AA6056 PWHT, $R=0.5$ and $\sigma_{max}=110$ MPa.

5. CONCLUSIONS

Lightweight constructions may be optimized by reducing the number of parts, simplifying the joints, reducing weight and costs. However, the behavior of integral structures under service conditions needs to be addressed carefully.

Some of the new joining processes (welding processes) promote residual stresses that can be beneficial or detrimental for the fatigue life, depending on the location of the crack. Therefore, new approaches are required to design these structures concerning their fatigue life. In order to understand the impact of the application of these processes, a project was developed with the main purpose of studying their effect in the fatigue behavior of stiffened panels and to develop tools to model their behavior in order to predict their fatigue life when a crack arises in the structure.

With the residual stress measurements it was possible to determine and model their influence in the fatigue life of panel. With the finite element models, the redistribution of residual stresses and the stress intensity factors for different crack lengths are calculated. Afterwards, with the experimental data of the fatigue crack growth rates for the alloy AA6056-T6 in standard specimens the Forman law parameters were calculated. With these parameters and with SIF calibrations the

Forman law was integrated considering the effective load ratio at the crack tip due the residual stresses. The comparison of numerical simulation with experimental results shows good agreement and demonstrates the possibility to predict the fatigue life in this type of stiffened panels. It was confirmed that the compressive residual stress may be beneficial for the fatigue life of structures; however if the crack starts in the tensile residual stress zone it will propagates at a higher rate being detrimental for the integrity of the panel.

ACKNOWLEDGEMENTS

DaToN Project, EU FP6 contract AST3-CT-2004-516053 and FCT fellowships SFRH /BD/ 35143/2007 and SFRH/BD/41061/ 2007 are acknowledged.

REFERENCES

- [1] N.E. Antoine, I.M. Kroo, ‘Framework for aircraft conceptual design and environmental performance Studies’, AIAA Journal, Vol. 43, No. 10, pp.2100-2109, October 2005.
- [2] R.K. Gupta, N. Nayan, G. Nagasireesha, S.C. Sharma, ‘Development and characterization of Al-Li alloys’, Materials Science and Engineering: A, Vol. 420, Issues 1-2, pp. 228-234, March 2006.
- [3] J. Røyset and N. Ryum, ‘Scandium in aluminium alloys’’, International Materials Reviews, Vol.50, No.1; pp.19-44; 2005.
- [4] R. Krueger, ‘The virtual crack closure technique: History, approach and applications’, NASA Technical Report, NASA/CR-2002-211628, ICASE Report No. 2002-10, 2002.
- [5] A. Lanciotti, L. Lazzeri, C. Polese, ‘Description of the test programme’, DaToN-WD-WP3.1-1.0/DIA-UniPi, Dec 2005.
- [6] A. Lanciotti, L. Lazzeri, C. Polese; DaToN project - University of Pisa contributions to WP2 and WP3, Department of Aerospace Engineering, Pisa University, Presentation in Munich DaToN meeting, January 11, 2007.
- [7] ABAQUS Inc., ABAQUS Documentation Version 6.7, SIMULIA, Dassault Systèmes, 2007.
- [8] D.T. Sandwell, ‘Biharmonic Spline Interpolation of GEOS-3 and SEASAT Altimeter Data’, Geophysical Research Letters, 14, 2, 139–142, 1987.
- [9] E.F. Rybicki, M.F. Kanninen; ‘Finite-element calculation of stress intensity factors by a modified crack closure integral’, Engineering Fracture Mechanics, 9(4):931-938, 1977.
- [10] R.G. Forman, V.E. Kearney, R.M. Engle, ‘Numerical analysis of crack propagation in cyclic-loaded structures’, Transactions of ASME, Journal of Basic Engineering, vol. 89, pp.459–464, 1967.
- [11] P.M.G.P. Moreira, V. Richter-Trummer, S.M. O. Tavares, P.M.S.T. de Castro, ‘Characterization of fatigue crack growth rate of AA6056 T651 and T6: Application to predict fatigue behaviour of stiffened panels’, Materials Science Forum, vols. 636-637, 2010, pp.1511-1517.

NON-LINEAR ANALYSIS OF THE WHEEL / RAIL CONTACT

D.F.C. Peixoto, L.A.A. Ferreira, P.M.S.T. de Castro

Departamento de Engenharia Mecânica,
 Faculdade de Engenharia da Universidade do Porto,
 Rua Dr. Roberto Frias, 4200-465 Porto, Portugal
 E-mail: daniel.fc.peixoto@gmail.com

ABSTRACT

In the present work a three dimensional non-linear finite element analysis of the wheel/ rail contact problem was performed using the software ABAQUS. The main goal was to analyse the rail stresses field during the passage of the wheel. The finite element model was built using standard rail and wheels profiles used by the Portuguese Railways company (CP), such as the UIC60 rail and the Alfa Pendular wheel. The commercial finite element software package ABAQUS was used, and a bilinear material model was adopted as an approximation for the simulation of the contact stresses between the wheel and rail. Aiming at the subsequent use of the Dang Van fatigue criterion, τ_{Tresca} versus σ_H data is required; this report presents the τ_{Tresca} versus σ_H loading path corresponding to the first cycle only. Further work will include the simulation of the number of passages necessary for achieving a stable loading path.

Keywords: contact stresses; Dang Van criterion; fatigue initiation in rail/wheel problems; rail/wheel contact.

1. INTRODUCTION

Fatigue is progressive damage occurring in materials subjected to cyclic loads. The study of this phenomenon assumes special importance in the design of machinery and structures, since this is the most frequent cause of service rupture.

As railways axle loads and speed increase, and wear prevention methods become more effective, it is crucial to implement solutions to prevent rolling contact fatigue. For example, increasing wear resistance of rails may imply that incipient surface cracks previously eliminated by wear, are no longer eliminated.

On wheels, fatigue cracks can be initiated not only on the surface but also under it. The initiation of surface cracks seems to be highly influenced by the presence of residual stresses and thermal loads, caused by a forced brake. According to elastic analyses the maximum shear stress appears between 4 and 5 mm under the wheel surface, however some cracks can be initiated at depths between 4 and 20mm [1].

The phenomenon of fatigue in rail is more complicated because of load randomness.

Maximum shear stress appears at a depth of 3mm and cracks initiate between 3 and 15mm below rail surface [1]. Initiation of cracks under rail surface is very common in heavy haul rail.

Dang Van proposed a fatigue initiation criteria based on the instantaneous value of shear stress $\tau_a(t)$ and hydrostatic stress $\sigma_h(t)$ [2]. This criterion states that fatigue failure will occur if the condition (1) is verified:

$$\tau_a(t) + a_{DV} \times \sigma_h(t) > \tau_{-1} \tag{1}$$

where:

$\tau_a(t)$: instantaneous shear stress value on a specific point;

$\sigma_h(t)$: instantaneous hydrostatic stress value on the considered point;

τ_{-1} : material fatigue limit in reversed torsion;

a_{DV} : adimensional constant, which represents the influence of hydrostatic stress, and can be determined by:

$$a_{DV} = \frac{\tau_{-1} - \frac{\sigma_{-1}}{2}}{\frac{\sigma_{-1}}{3}} \tag{2}$$

where σ_{-1} is the material fatigue limit in pure bending. Figure 1 shows schematically the application of this criterion. For the stabilized loading path represented in the figure, fatigue is predicted when the loading path crosses the boundary represented by equation (1).

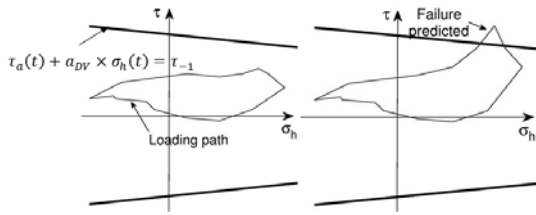


Figure 1: Dang Van criterion diagram.

The Tresca criterion can be used to calculate the maximum shear stress on the considered point [3], and the Dang Van criterion can be written as:

$$\tau_{Tresca}(t) + a_{DV} \times \sigma_h(t) > \tau_{-1} \quad (3)$$

where $\tau_{Tresca}(t)$ is the maximum shear stress.

2. FINITE ELEMENT MODEL

A 300mm long rail was used to simulate the passage of the wheel and special attention was given to the contact surfaces, where smaller elements were used to correctly define it, since contact stresses are highly dependent of contact surface geometry. Figure 2 shows the mesh used. In order to reduce computational time, only a small part of the wheel was used as showed in Figure 3 because only his surface geometry was needed. As shown in Figure 4, a refined mesh was used on the contact surfaces.

To build the finite element mesh 331 907 (256 208 to the rail and 75 699 to the wheel) 3D linear 4 nodes tetragonal elements (C3D4) were used. The wheel/rail contact surfaces were modelled using node-to-surface contact discretization and the Lagrange multiplier method was used for contact simulation.

With traditional node-to-surface discretization the contact conditions are established such that each “slave” node on one side of a contact interface effectively interacts with a point of projection on the “master” surface on the opposite side of the contact interface. The Lagrange multiplier formulation add more degrees of freedom to the model in order to guarantee non penetration between contact bodies [4].

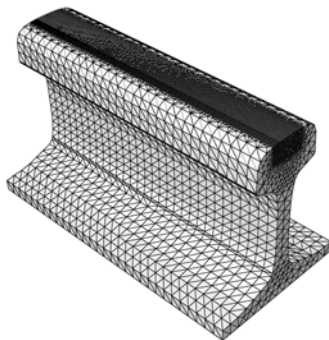


Figure 2: Rail mesh with 45 611 nodes and 256 208 C3D4 elements.

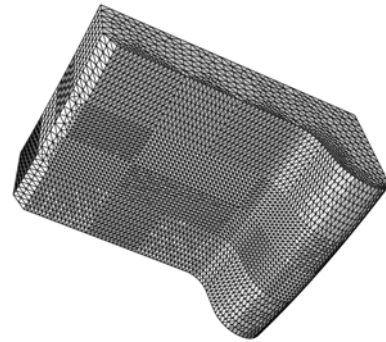


Figure 3: Wheel mesh with 15 042 nodes and 75 699 C3D4 elements.

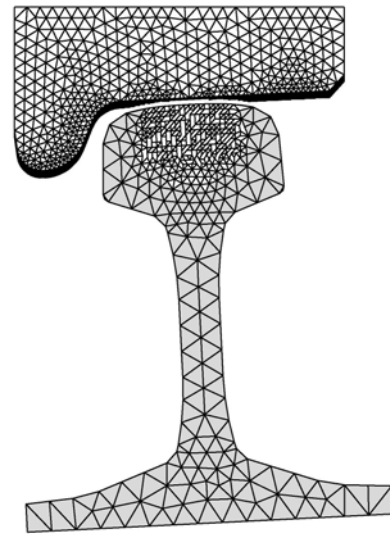


Figure 4: Model mesh.

The considered material has elastoplastic behaviour with linear-kinematic hardening and the considered properties, taken from reference [5], are shown in the Table 1. In Figure 5 the σ versus ϵ relation for the considered material is shown.

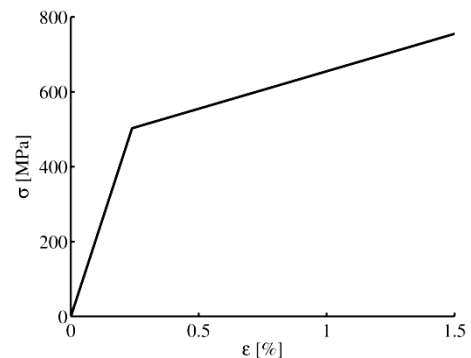


Figure 6: σ vs. ϵ relation for the considered material.

Table 1: Material properties [5].

E [GPa]	ν	k_c [MPa]	C [GPa]	σ_{-1} [MPa]	τ_{-1} [MPa]
210	0,3	237	20	460	270

The finite element model built was based on a UIC60 rail profile and a monobloc wheel with conic profile used in the train Alfa Pendular of the Portuguese Railways Company (CP). These two profiles are shown on Figure 6.

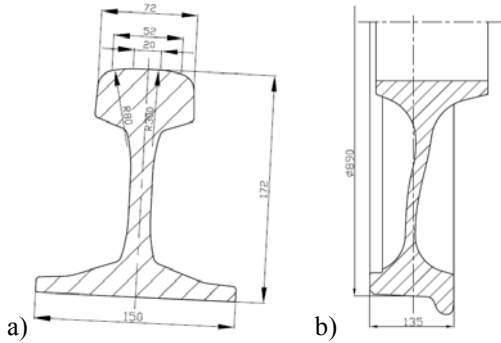


Figure 7: a) UIC60 rail profile; b) Alfa Pendular wheel profile.

In order to simulate the passage of the wheel on the rail, incremental displacements were applied to the wheel maintaining applied a normal force of 110kN, as shown in Figure 7. This load corresponds to a half of the maximum load permitted per axle.

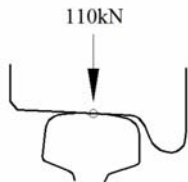


Figure 8: Load applied to FE the model.

3. RESULTS

Figure 8 presents the minimum principal strain on the rail after one passage. On Figure 9 Tresca stress distribution on the middle section of the rail after one passage can be seen. The wheel is not showed since it is not an interest of the study presented where.

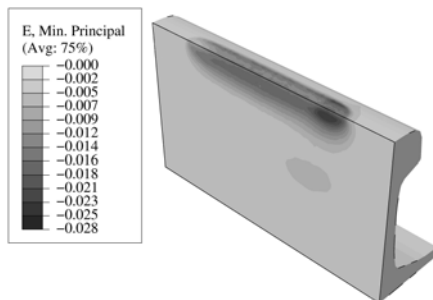


Figure 9: Minimum principal strain distribution after one passage.

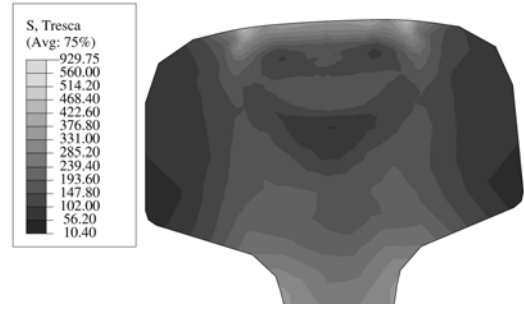


Figure 10: Tresca stress distribution on the middle section of the rail after one passage.

Aiming at the subsequent use of the Dang Van fatigue criterion, τ_{Tresca} versus σ_H data is required. Exemplifying the data to be generated by the model developed and presented in this report, Figure 10 gives the τ_{Tresca} versus σ_H loading path corresponding to the first cycle only. In this figure the path Zs corresponds to the point where the maximum shear stress occurs.

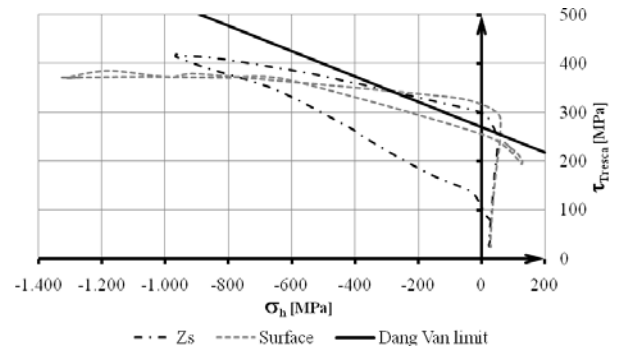


Figure 11: Application of the Dang Van's criterion to the rail after one passage

These results represent only the stress/strain evolution during the first passage.

4. CONCLUDING REMARKS

A non linear analysis of the stress/strain state resulting of the passage of one wheel on a segment of rail was performed using non-linear 3D finite elements and the commercial software ABAQUS. The work presented is a preliminary step based upon a simplified bilinear σ vs. ϵ relationship. The analysis is illustrated in the present paper through the data corresponding to the first passage; subsequent work will consist of a fatigue behaviour characterization of the rail using a more refined mesh and simulating the number of passages necessary to reach a steady state characterized by the repetition of the loading path.

ACKNOWLEDGMENTS

D. F. C. Peixoto acknowledges a Calouste Gulbenkian Foundation PhD grant (ref. number 104047).

REFERENCES

- [1] Ekberg, A., Kabo, E., “Fatigue of railway wheels and rails under rolling contact and thermal loading — an overview”, *Wear*, Vol.258 (2005), p.1288–1300.
- [2] Dang Van, K., Griveau, B. Message, O., “On a new multiaxial fatigue limit criterion: theory and applications”, *Biaxial and Multiaxial Fatigue*, EGF 3 (Edited by M. W. Brown and K. J. Miller), 1989, Mechanical Engineering Publications, London p.479-496.
- [3] Dang Van, K., “Macro-Micro Approach in High-Cycle Multiaxial Fatigue”, *Advances in Multiaxial Fatigue, ASTM STP 1191*, D.L. McDowell and R. Ellis, Eds., American Society for Testing and Materials, Philadelphia, 1993, p.120-130.
- [4] Abaqus Version 6.8-1 Documentation.
- [5] Dang Van, K., Maitournam, M. H., “On some recent trends in modelling of contact fatigue and wear in rail”, *Wear*, Vol. 253 (2002), p 219-227.

Polymers

MODE I FRACTURE TOUGHNESS OF ADHESIVELY BONDED JOINTS IN A HIGH TEMPERATURE ENVIRONMENT

M. D. Banea¹, L. F. M. da Silva², R. D. S. G. Campilho³

¹ Instituto de Engenharia Mecânica (IDMEC),
Rua Dr. Roberto Frias, 4200-465, Porto, Portugal,
E-mail: mbanea@fe.up.pt

² Departamento de Engenharia Mecânica,
Faculdade de Engenharia da Universidade do Porto,
Rua Dr. Roberto Frias, 4200-465 Porto, Portugal,
E-mail: lucas@fe.up.pt

³ Universidade Lusófona do Porto
Rua Augusto Rosa, n° 24
4000-098 Porto, Portugal,
E-mail: raulcampilho@hotmail.com

ABSTRACT

Adhesives used in structural high temperature space and aerospace applications must operate in extreme environments. They need to exhibit high-temperature capabilities in order to maintain their mechanical properties and their structural integrity at the intended service temperature.

As is known, adhesive strength and strain generally show temperature dependence. Similarly, the fracture toughness is expected to show temperature dependence. In order to determine the effect of the temperature on the adhesive fracture toughness of an adhesively bonded joint, pure mode I adhesive fracture toughness tests were performed at high temperatures (100°C, 150°C and 200°C) and at room temperature (22°C). From these experimental tests, the fracture toughness for the tested temperatures was evaluated for the selected bonded joint system. Experimental results showed a slight increase of the fracture toughness at 100°C. A drastic decrease in fracture toughness was observed at 200°C (the T_g of the adhesive was overpassed), but only a slight decrease in fracture toughness at 150°C was found compared to the room temperature.

KEY WORDS: High temperature adhesives; fracture toughness, temperature tests.

1. INTRODUCTION

There has been a growing requirement in the last years, particularly in the aerospace industry, for adhesives to withstand high temperatures. The adhesives used in structural high temperature space and aerospace applications must operate in extreme environments. Those environments include a wide operating temperature range from cryogenic to 300°C. These adhesives have to maintain their mechanical properties at the intended service temperature and to maintain their structural integrity (resist thermal breakdown at elevated temperature). Adhesive systems that meet some of these requirements include: epoxies (having high strength and temperature resistance), silicones (excellent sealant for low stress applications, high degree of flexibility and very high temperature resistance), phenolics, polyimides, bismaleimides and ceramic adhesives.

As is known, adhesive strength generally shows temperature dependence. Studies that present experimental results of adhesive joints with structural adhesives (especially epoxies) as a function of temperature generally show a decrease in strength with increasing and decreasing temperatures [1,2]. At high temperatures this is due to the low adhesive strength, while at low temperatures the high thermal stresses and the brittleness of the adhesive are the origin of such behaviour. Similarly, the fracture toughness is expected to show temperature dependence.

Several investigators addressed the determination of the fracture toughness in tension or shear of thin adhesive layers in adhesively-bonded assemblies, but these studies are often limited to room temperature testing. However, relatively only limited data are available relative to the critical strain energy release rate at low or high temperatures [3,4].

The majority of adhesively-bonded assemblies fracture characterization under pure mode I is performed using the double cantilever beam (DCB) specimen [5,6]. In a fracture mechanics analysis of this specimen, the crack is predicted to propagate when the energy release rate for mode I crack growth (G_I) becomes equal to the toughness of the adhesive or the adhesive's critical energy release rate (G_{Ic}). The main advantages of this test method include its simplicity and the possibility to obtain the fracture toughness mathematically using the beam theory for brittle materials [7].

Several techniques can be used to derive the fracture toughness of structural adhesives from fracture characterization tests. The most common methodologies for analysis are based on Linear-Elastic Fracture Mechanics (LEFM). The Compliance Calibration Method (CCM) is based on the Irwin-Kies equation [8], requiring the calculation of the compliance, C , ($C=\delta/P$, where δ is the displacement and P is the applied load) relative to the crack length during crack growth. The Direct Beam Theory (DBT), based on elementary beam theory [9], and the Corrected Beam Theory (CBT), including the effects of crack tip rotation and deflection [10], are also available within the scope of LEFM. The Compliance-Based Beam Method (CBBM) was recently developed by de Moura *et al.* [11,12] and is based on the crack equivalent concept, depending only on the specimen's compliance during the test.

In this study, the pure mode I fracture toughness of adhesive joints bonded with a high temperature adhesive was measured over a wide range of temperatures. DCB tests were performed at room temperature (RT), 100°C, 150°C and 200°C.

2. EXPERIMENTAL DETAILS

2.1. Adhesive

The adhesive investigated in this study was a one-component high temperature paste epoxy adhesive XN1244, supplied by Nagase Chemtex (Japan).

A key parameter in the testing of adhesive joints is the glass transition temperature (T_g) of the adhesive. When the adhesively bonded joints are tested below this temperature, the adhesive will behave like a low-strain rigid material while above this temperature it will have a more rubber-like behaviour. The glass transition temperature (T_g) of the XN1244 adhesive is approximately 160°C (data provided by supplier).

2.2. Specimen fabrication

Steel substrates were used for the DCB specimens. The joint surfaces were grit blasted and degreased with acetone prior to the application of the adhesive. The specimen geometry and the loading are shown in Figure 1.

The bondline thickness was nominally 0.2 mm. Spacers (calibrated steel bars of 0.20 mm) were inserted between the adherends before the application of the adhesive in order to control the bondline thickness. These spacers were removed after the adhesive was cured.

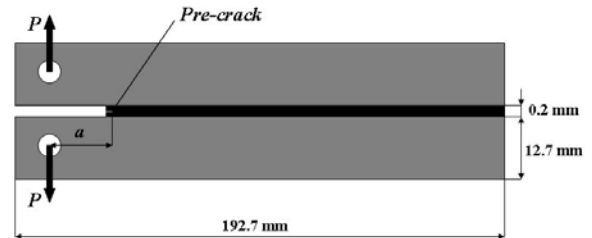


Figure 1. DCB Specimen Geometry.

A sharp pre-crack in the adhesive layer mid-thickness was assured using a razor blade. A mould with spacers for the correct alignment of the adherends was used and is shown in Figure 2. The DCB joints were cured at 140°C for 1 hour.

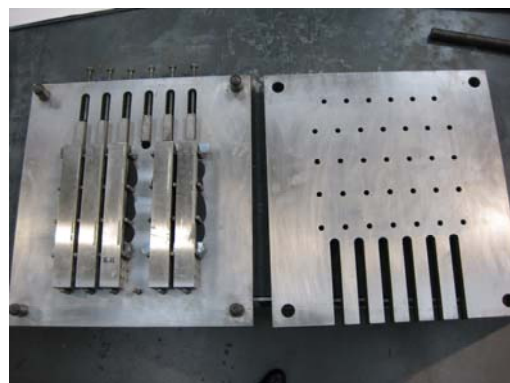
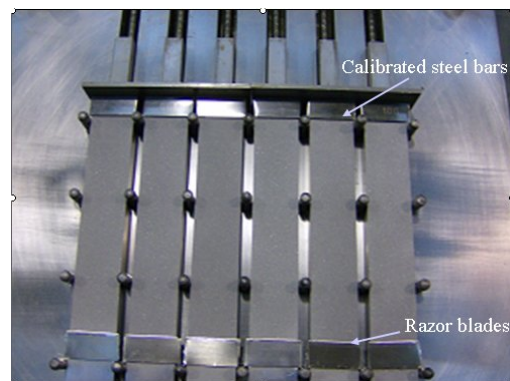


Figure 2. Mould with DCB Specimens.

2.3. Test procedure

The DCB specimens were tested at RT and high temperatures (100°C, 150°C and 200°C) using a universal testing machine Instron® model 8801 (Instron Co., USA), under a constant crosshead rate of 0.5 mm/min. For the high temperature tests, the

environmental chamber of the machine was used to reach the desired test temperatures.

Before the testing was initiated, in order to avoid a blunt crack, all specimens were slightly loaded to ensure 2-3 mm of crack propagation, after which a_0 was measured. The load–displacement ($P-\delta$) curve was registered during the test. Pictures were recorded during the specimens testing with 5 s intervals using a 10 MPixel digital camera.

This procedure allows measuring the crack length during its growth and afterwards collecting the $P-\delta-a$ parameters. This was performed correlating the time elapsed since the beginning of each test between the $P-\delta$ curve and each picture (the testing time of each $P-\delta$ curve point is obtained accurately with the absolute displacement and the established loading rate).

Figure 3 shows a picture of what was recorded during a test that shows the crack tip, allowing the crack length measurement.

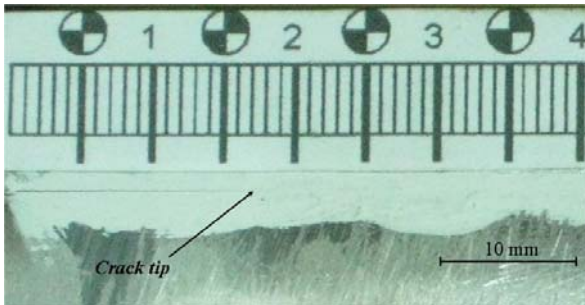


Figure 3. Crack Length Measurement During Propagation.

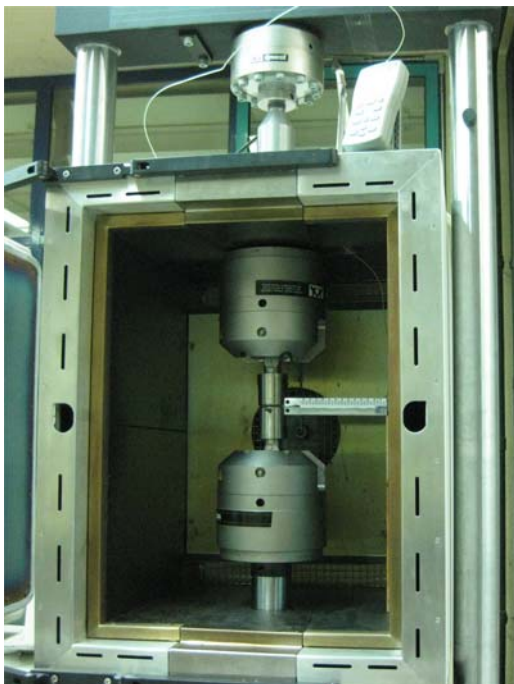


Figure 4. DCB Specimens Set-up.

Four joints were tested to failure at each temperature. The DCB specimens set-up is shown in Figure 4.

A thermocouple was applied to the specimen in order to assure that the air temperature inside the chamber was equal to the specimen's temperature. The tests were always performed after approximately 10 min of achieving the test temperature in the specimens, to ensure a steady-state temperature throughout the specimen prior to testing.

2.4. Data analysis

Different methods were employed to evaluate the critical fracture energy in pure mode I, G_{Ic} .

The Compliance Calibration Method (CCM) is based on the Irwin-Kies equation [8]:

$$G_{Ic} = \frac{P^2}{2b} \frac{dC}{da} \quad (1)$$

where P represents the load, b the specimen width and $C=\delta/P$ the compliance.

Cubic polynomials ($C=C_3a_3+C_2a_2+C_1a+C_0$) are used to fit the $C=f(a)$ curves, leading to:

$$G_{Ic} = \frac{P^2}{2b} (3C_3a_3 + 2C_2a_2 + C_1) \quad (2)$$

By the Corrected Beam Theory (CBT), G_{Ic} is obtained using [10]:

$$G_{Ic} = \frac{3P\delta}{2b(a+|\Delta|)} \quad (3)$$

where Δ is a crack length correction for crack tip rotation and deflection.

The Compliance-Based Beam Method (CBBM) was recently developed by de Moura *et al.* [11,12] and is based on the crack equivalent concept, depending only on the specimen's compliance during the test. G_{Ic} can be obtained by the following expression:

$$G_{Ic} = \frac{6P^2}{b^2t_p} \left(\frac{2a_{eq}^2}{t_p^2 E_f} + \frac{1}{5G} \right) \quad (4)$$

a_{eq} is an equivalent crack length obtained from the experimental compliance and accounting for the fracture process zone (FPZ) at the crack tip, E_f is a corrected flexural modulus to account for all phenomena affecting the $P-\delta$ curve, such as stress concentrations at the crack tip and stiffness variability between specimens, and G is the shear modulus of the adherends.

3. RESULTS AND DISCUSSION

3.1. Determination of G_{Ic} values as a function of temperature

Representative experimental $P-\delta$ curves of the DCB specimens at each temperature are presented in Figure 5.

The critical fracture energy in mode I was evaluated using the methods presented in Section 2.4.

Table 1 summarizes the test data by presenting G_{Ic} values obtained by each method as well as standard deviation, as a function of temperature. At 100°C the fracture toughness, G_{Ic} , of the adhesive slightly increased (by approximately 10%). This can be explained by the fact that, as the temperature increases, the strength decreases but the ductility increases giving an additional plastic deformation at the crack tip, hence an increase in toughness. At 150°C, G_{Ic} slightly decreased, due to the degradation of the mechanical properties of the adhesive induced by the temperature. However, a drastic drop in fracture toughness was observed at 200°C. This was expected as the testing temperature overpasses the T_g of the adhesive.

Table 1. Fracture toughness G_{Ic} [N/mm] as a function of temperature.

	CBBM	CCM	CBT
RT	0.47 ± 0.03	0.43 ± 0.07	0.46 ± 0.04
100°C	0.52 ± 0.04	0.49 ± 0.06	0.49 ± 0.03
150°C	0.43 ± 0.06	0.40 ± 0.04	0.42 ± 0.03
200°C	0.08 ± 0.01	0.06 ± 0.02	0.07 ± 0.02

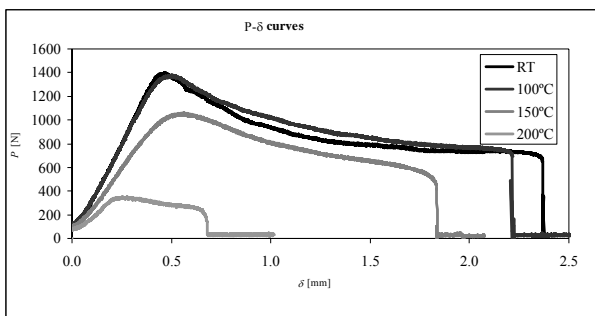


Figure 5. Representative Experimental $P-\delta$ Curves of the DCB Specimens as a Function of Temperature.

Experimental R -curves obtained by the different methods for one specimen at RT are shown in Figure 6. Similar results were obtained by CBT and CBBM. The CCM presents a slight difference, which is explained by polynomial fitting difficulties. It should be noted that the CBBM R -curve is out of phase to the right relatively to the remaining ones, since the equivalent crack used in this method is higher than the real crack length measured during the tests and used in the other two methods (Figure 6).

Experimental R -curves obtained by the different methods for one specimen at 100°C, 150°C and 200°C are presented in Figure 7a, b and c.

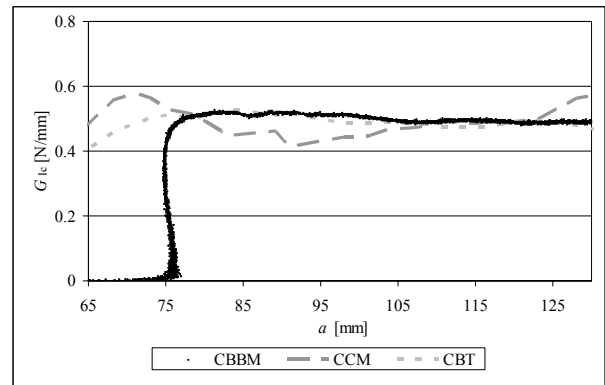
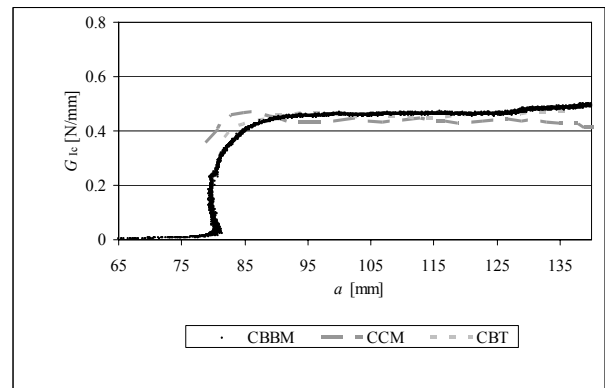
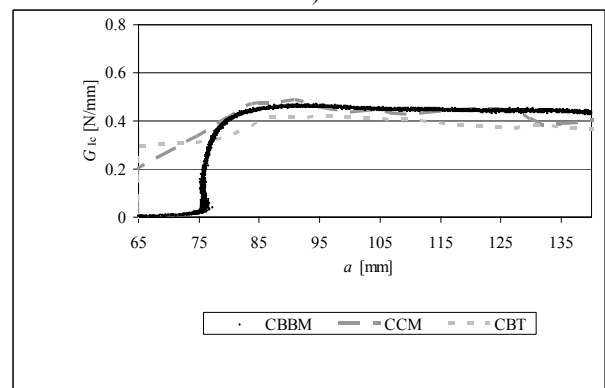


Figure 6. Typical experimental R -curves obtained by the different methods for one specimen at RT.



a)



b)

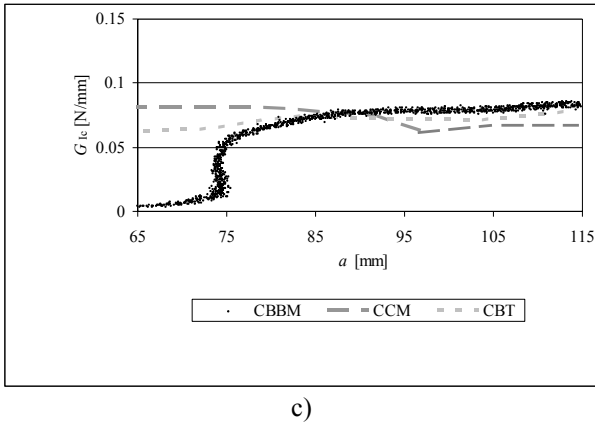


Figure 7. Experimental R-curves for one specimen at 100°C (a), 150°C (b) and 200°C (c).
3.2. Failure mode

For high strength adhesives there are four typical mechanisms of crack growth, which are represented in Figure 8 [13]. The most representative one is the cohesive failure (a1 and b1), characterized by a proper surface preparation that leads to a stronger interface with the adherends than the cohesive properties of the adhesive. Interfacial failures (c1) are frequent when bonding adherends with low surface energy or as a result of a poor preparation of the bonding surfaces. Alternative crack propagation between interfaces can also appear (d1), due to opening of micro-cracks at opposite interfaces alternatively ahead of the crack tip. The tensile stresses within the bond plane can also play an important role in this behaviour, causing the crack to oscillate within the adhesive layer or alternate from one adherend to the other. This effect is controlled by the T-stress, a non-singular stress that is parallel to the local crack path. If the tensile magnitude of the T-stress is sufficiently large, the crack path is not stable and so will continuously change direction as it propagates [14].

For ductile low strength adhesives, a number of typical failure mechanisms have been reported in the literature: (a2) near-tip void growth and coalescence, (b2) interface debonding near the crack tip, (c2) high triaxiality cavitation ahead of the crack tip and subsequent coalescence, and (d2) interfacial debonding ahead of the crack tip. Schematics of these mechanisms are also shown in Figure 8.

The adhesive studied here belongs to high strength adhesives.

As can be observed in Figure 9 the failure in the DCB specimens was a cohesive failure for all temperatures.

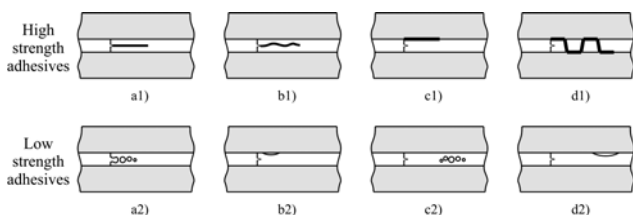


Figure 8. Typical Failure Modes at RT (a), 100°C (b), 150°C (c) and 200°C (d).

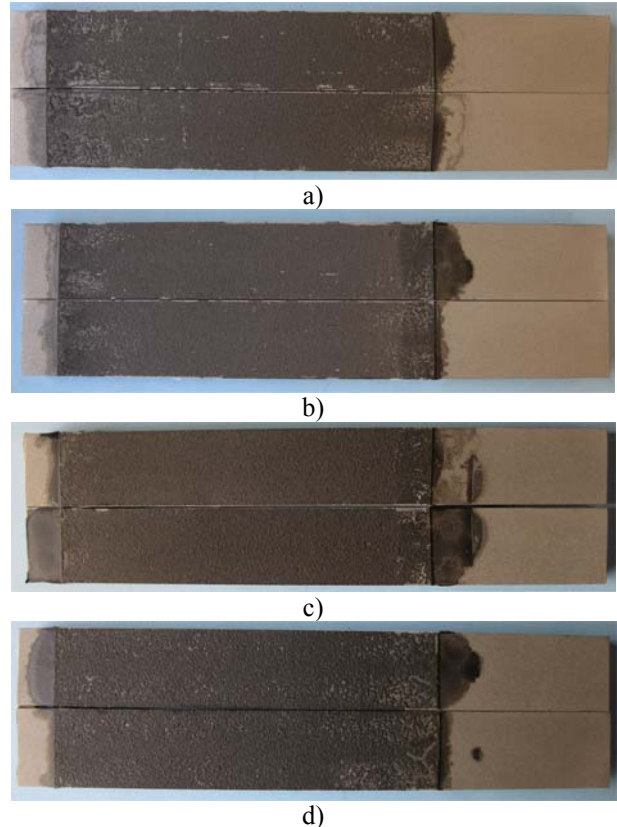


Figure 9. Typical Failure Modes at RT (a), 100°C (b), 150°C (c) and 200°C (d).

4. CONCLUSIONS

Mode I adhesive fracture toughness (G_{Ic}) tests were performed at room and high temperatures (100°C, 150°C and 200°C) and the fracture toughness G_{Ic} as a function of temperature was obtained for a high temperature epoxy adhesive/steel DCB specimens. At 100°C the fracture toughness, G_{Ic} , of the adhesive slightly increased (by approximately 10%). This can be explained by the fact that, as the temperature increases, the strength decreases but the ductility increases giving an additional plastic deformation at the crack tip, hence an increase in toughness. At 150°C, G_{Ic} slightly decreased, probably due to the degradation of the mechanical properties of the adhesive induced by the temperature. However, a drastic drop in fracture toughness was observed at 200°C, when the testing temperature overpasses the T_g of the adhesive.

ACKNOWLEDGEMENTS

The authors would like to thank the Portuguese Foundation for Science and Technology for supporting the work presented here, through the research project PTDC/EME-PME/67022/2006 and through the individual grant SFRH/BD/61880/2009, and Nagase Chemtex (Japan) for supplying the adhesive.

REFERENCES

- [1] Banea D.M., da Silva L.F.M., *Effect of temperature on the Mechanical Properties of the Adhesives for Automotive Industry*, Proc. IMechE, Part L: Journal of Materials: Design and Applications, *in press*.
- [2] da Silva, L.F.M. and R.D. Adams, *Measurement of the mechanical properties of structural adhesives in tension and shear over a wide range of temperatures*. Journal of Adhesion Science and Technology, 2005. **19**(2): p. 109-141.
- [3] Melcher, R.J. and W.S. Johnson, *Mode I fracture toughness of an adhesively bonded composite-composite joint in a cryogenic environment*. Composites Science and Technology, 2007. **67**(3-4): p. 501-506.
- [4] Banea D.M., da Silva L.F.M., Campilho RDSG, *Temperature Dependence of the Fracture Toughness of Adhesively Bonded Joints*, Journal of Adhesion Science and Technology, *in press*.
- [5] Andersson T, Stigh U. *The stress-elongation relation for an adhesive layer loaded in peel using equilibrium of energetic forces*. International Journal of Solids and Structures 2004; 41: p. 413-434.
- [6] Ducept F, Davies P, Gamby D. *Mixed mode failure criteria for a glass/epoxy composite and an adhesively bonded composite/composite joint*. International Journal of Adhesion & Adhesives 2000; 20: p. 233-244.
- [7] Yoshihara H. *Simple estimation of critical stress intensity factors of wood by tests with double cantilever beam and three-point end-notched flexure*. Holzforschung 2007; 61: p. 182-189.
- [8] Kanninen M.F. and Popelar C.H., *Advanced fracture mechanics*, University Press, Oxford (1985).
- [9] W. Ding, *Delamination Analysis of Composite Laminates*. Ph.D. Thesis. University of Toronto, Canada (1999).
- [10] Robinson, P. and S. Das, *Mode I DCB testing of composite laminates reinforced with z-direction pins: a simple model for the investigation of data reduction strategies*. Engineering Fracture Mechanics, 2004. **71**(3): p. 345-364.
- [11] de Moura, M.F.S.F., R.D.S.G. Campilho, and J.P.M. Gonçalves, *Crack equivalent concept applied to the fracture characterization of bonded joints under pure mode I loading*. Composites Science and Technology, 2008. **68**(10-11): p. 2224-2230.
- [12] de Moura, M.F.S.F., J.P.M. Gonçalves, J.A.G. Chousal, and R.D.S.G. Campilho, *Cohesive and continuum mixed-mode damage models applied to the simulation of the mechanical behaviour of bonded joints*. International Journal of Adhesion and Adhesives, 2008. **28**(8): p. 419-426.
- [13] K.M. Liechti, in: *Mechanics of Adhesion*, D. A. Dillard and A. V. Pocius (Eds.), pp. 45-75, Elsevier, Amsterdam (2002).
- [14] Chen, B. and D.A. Dillard, *The effect of the T-stress on crack path selection in adhesively bonded joints*. International Journal of Adhesion and Adhesives, 2001. **21**(5): p. 357-368.

EFECTO DEL ENVEJECIMIENTO DE PLACAS DE ASIENTO DE CARRIL INYECTADAS CON TPE EN LA ELASTICIDAD DE LA VÍA PARA ALTA VELOCIDAD

I. A. Carrascal, J. A. Casado, S. Diego, J. A. Polanco y F. Gutiérrez-Solana

Departamento de Ciencia e Ingeniería del Terreno y los Materiales.
E.T.S. de Ingenieros de Caminos, Canales y Puertos. Universidad de Cantabria
Avda. Los Castros s/n, 39005-Santander, España.
isidro.carrascal@unican.es

RESUMEN

Las placas de asiento inyectadas con termoplástico elastómero (TPE), ubicadas entre los carriles de acero y las traviesas de hormigón, desempeñan una función esencial en el buen mantenimiento general de la vía férrea. Fundamentalmente proporcionan elasticidad a la vía y amortiguan las vibraciones que el carril transmite a la traviesa, por lo que evitan la fisuración del hormigón e impiden el desgaste del balasto. Las placas de asiento, además de sufrir el desgaste propio de las acciones mecánicas cíclicas a las que se encuentran sometidas por el paso de las ruedas de los trenes por la vía, padecen un deterioro ambiental, acentuado por su naturaleza polimérica, al encontrarse expuestas a los rayos de la luz ultravioleta, a las variaciones de humedad y temperatura y a ciclos de hielo-deshielo. Adicionalmente, este material presenta un daño físico asociado a su contacto con hidrocarburos, procedentes del material móvil, que impregnan la vía. En este trabajo se ha valorado, por medio de ensayos mecánicos de elasticidad, el grado de deterioro sufrido por placas de asiento sometidas en laboratorio a diferentes tratamientos de envejecimiento artificial independientes y se ha contrastado con el daño presentado por placas procedentes de vías de ferrocarril para trenes de alta velocidad tras una vida en servicio de 3 años, que fueron sometidas de forma natural y simultánea a todos los fenómenos mecánico-ambientales citados. Se ha comprobado que el efecto acumulativo de los tratamientos de envejecimiento artificial que incrementan la rigidez del sistema equivale al daño real determinado sobre las placas de vía, estimado en un 37%.

ABSTRACT

Seat plates injected with thermoplastic elastomer (TPE), located between the steel rails and concrete sleepers, play an essential role in overall good maintaining of the track. Basically they provide elasticity to the track and dampen the vibrations that the rail transmits to the sleeper, thus avoiding cracking of the concrete and preventing the erosion of the ballast. Seat plates, besides suffering from the wear of cyclical mechanical actions which are subject to the passage of the wheels of trains along the track, experiencing environmental degradation, emphasized by their polymeric nature, to be exposed to rays of ultraviolet light, variations in humidity and temperature and freeze-thaw cycles. Additionally, this material presents a physical injury associated with contact with hydrocarbons, from the rolling material, which impregnate the track. In this work we have evaluated through mechanical elasticity tests, the degree of damage suffered by seat plates in the laboratory under independent different artificial aging treatments and it has been contrasted with the damage presented by seat plates from railroad tracks to high-speed trains after a service life of 3 years, treated naturally and simultaneously to all mechanical and environmental phenomena mentioned. There is evidence that the cumulative effect of artificial aging treatments that increase the stiffness of the system amounts to determined real damage on the plates from the track, estimated at 37%.

PALABRAS CLAVE: Placa de asiento, Termoplástico elastómero, Deterioro ambiental, Deterioro mecánico.

1. INTRODUCCIÓN Y OBJETIVO

El sistema de sujeción aporta la necesaria elasticidad al conjunto de vía para limitar dentro de tolerancias, los movimientos longitudinales y laterales del carril, así como su giro, a causa de los esfuerzos transversales y verticales transmitidos por los vehículos y, asimismo, propiciar que la rodadura sea cómoda y confortable para el usuario. La fijación aporta un contacto permanente,

sin holguras, entre carril y traviesa, manteniendo el ancho vía y proporcionando aislamiento eléctrico adecuado entre hilos [1].

La placa elástica de asiento es uno de los constituyentes del sistema de sujeción y se encuentra situada bajo el carril sobre la traviesa (Ver Figura 1). Permite dotar a la vía de la elasticidad requerida, amortiguando los esfuerzos transmitidos por los vehículos y protegiendo

las traviesas, para evitar su fisuración e impidiendo el desgaste del balasto de los impactos del tráfico ferroviario. La placa debe garantizar una alta durabilidad [2] manteniendo sus características durante la vida útil de la vía, a pesar de las condiciones atmosféricas (rayos UVA y ozono), de la temperatura ambiente y de los aceites minerales del material rodante. Los materiales utilizados deben tener una buena resistencia al rozamiento y una adecuada rigidez para soportar el apriete estático de la sujeción y, los esfuerzos verticales, longitudinales y transversales que va a tener durante su servicio de acuerdo con variaciones atmosféricas de temperatura, esfuerzos de aceleración y frenado, rampas y pendientes.



Figura 1: Esquema de la sujeción de vía

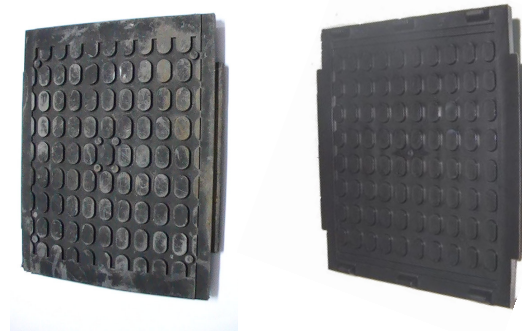
El objetivo de este trabajo es valorar, por medio de ensayos mecánicos establecidos en la E.T. 03.360.570.0. [3], el deterioro sufrido por placas sometidas en laboratorio a tratamientos de envejecimiento artificial independientes. Los resultados se han comparado con el daño de placas procedentes de vía para trenes de alta velocidad tras una vida en servicio de 1 y 3 años, que de forma natural fueron sometidas simultáneamente a todos los fenómenos mecánico-ambientales.

2. MATERIAL OBJETO DE ENSAYO

Las placas son conformadas por inyección con elastómeros termoplásticos (TPE). Estos materiales se basan en un sistema de fases separadas, en el que alternan una fase de cadenas elásticas, que le confieren las características de un caucho, con cadenas rígidas, formando fases diferentes. A temperatura ambiente presentan gran cohesión con entrecruzamientos físicos similares a los de la vulcanización [4]. El TPE es un polímero que combina las mejores características de los elastómeros con las de los termoplásticos técnicos. Destacan por presentar una tenacidad y resiliencia importantes; una elevada resistencia a la fluencia, al impacto y a fatiga; flexibilidad a bajas temperaturas y buena resistencia a disolventes y aceites [5].

Las placas empleadas en este trabajo son para carril UIC-64 (PAE-2) y tienen dos procedencias: de producción, inyectadas por la empresa Soluciones Mondragón en el año 2006, y de vía con un uso en servicio de 1 a 3 años (Ver Figura 2). Las dimensiones nominales de todas ellas son (180x148x7) mm³. Las placas de producción se inyectaron con 2 materiales diferentes: Hytrel®, marca registrada de la compañía Du

Pont y Arnitel®, marca registrada de la compañía DSM. Las placas de vía se habían inyectado con Arnitel® únicamente. Estos tipos de materiales, a parte del termoplástico elastómero como principal componente, poseen en su seno estabilizadores de calor, retardantes de llama y aditivos protectores de los UV, resistentes a la hidrólisis y al desgaste. Todos estos agentes mejoran las propiedades mecánicas, físicas y químicas del termoplástico elastómero.



Placa de vía

Placa de fábrica

Figura 2: Placas de asiento

3. FUNDAMENTO Y METODO DE ENSAYO

3.1. Procesos de deterioro artificial

La integridad del polímero que constituye la placa de puede verse afectada por el deterioro mecánico y ambiental durante su vida útil. La degradación es un proceso que modifica la estructura del polímero haciéndolo percedero. El deterioro mecánico se produce por los esfuerzos de cizalla originados en el proceso de inyección inicial y, tras su puesta en funcionamiento, por el rozamiento del carril y de la traviesa bajo cargas de fatiga originadas por el paso del tren. El deterioro ambiental se debe fundamentalmente a la acción de la luz, a las variaciones térmicas y a la humedad [7-11]. Las placas de fábrica se expusieron a los diferentes agentes durante el desarrollo del trabajo.

3.1.1.-Fatiga térmica

El envejecimiento térmico implica la rotura al azar de enlaces covalentes del polímero dando lugar a macro-radicales que, confieren un peso molecular bajo al polímero. La fatiga térmica se llevó a cabo exponiendo las placas a cambios cíclicos bruscos de temperatura (desde -10 hasta 100 °C) cada 48 horas durante 7 meses.

3.1.2.- Degradación por envejecimiento térmico

Los niveles de temperatura evaluados fueron -10 y 100 °C con periodos de exposición de 7 meses en cada caso.

3.1.3.- Fotodegradación

La energía de la luz en el intervalo UV y, en algunos casos, visible es suficiente para romper enlaces químicos en el polímero, disminuyendo el peso molecular y modificándose sus propiedades mecánicas.

La fotodegradación se realizó sometiendo a las placas de asiento a radiación UV de 313 nm de longitud de onda a 57 °C, durante un periodo de tiempo de 430 horas.

3.1.4.- *Degradación oxidativa a la intemperie*

El fenómeno de degradación oxidativa de polímeros es una reacción lenta de despolimerización iniciada por radicales.

Este ensayo se desarrolló situando las placas al aire libre registrando las condiciones atmosféricas durante los cinco meses de exposición [6].

3.1.5.- *Absorción de agua*

El agua actúa como un agente plastificante lubricando las cadenas en la región amorfa. Al aumentar la absorción se reduce la temperatura de transición vítrea, el esfuerzo a la cedencia y el módulo elástico. Además, el material cambia sus dimensiones nominales.

Para este ensayo se mantuvieron sumergidas las placas en un baño con agua a 60°C durante 5 meses.

3.1.6.- *Degradación por hidrocarburos*

Este tipo de degradación implica rotura de enlaces covalentes mediante hidrocarburos de cadena corta que penetran como solutos entre las macromoléculas del polímero.

Esta degradación se llevó a cabo introduciendo las placas en un recipiente con hidrocarburo marca ESSO, tipo NUTO 1746 ISO VG 46.

3.1.7.- *Degradación por desgaste*

Las placas de asiento durante su vida en servicio sufren, acciones erosivas debido a movimientos longitudinales y transversales del carril al paso de los trenes. Este roce provoca pérdida de material que puede traducirse en una importante variación de la rigidez.

Este deterioro se simuló rebajando el espesor de la placa de asiento, por la parte superior, en 0,5 mm mediante un mecanizado con una máquina fresadora.

3.1.8.- *Degradación mecánica*

La degradación mecánica engloba las reacciones que tienen lugar como consecuencia de la aplicación de una tensión. Éste estímulo mecánico normalmente está relacionado con las técnicas de procesado y con los esfuerzos sufridos a lo largo de su vida. Los esfuerzos aplicados sobre el material pueden desestabilizar los enlaces al alcanzar el valor de su resistencia a la rotura. La aplicación de tensiones dinámicas oscilantes o de fatiga es la agresión más habitual sufrida por las placas.

El ensayo consistió en aplicar cargas de compresión con una fuerza mínima de 20 kN y una máxima de 95 kN simulando paso de trenes, durante 200.000 ciclos a 5 Hz a temperatura ambiente. La disposición del ensayo se muestra en la Figura 3.

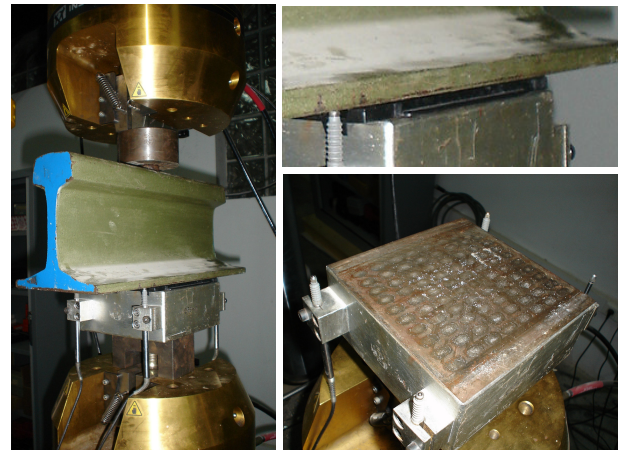


Figura 3: Ensayo de fatiga

3.2.- *Evaluación de los procesos de deterioro*

Las placas de asiento sometidas a los procesos de degradación artificial y las placas procedentes de vía se caracterizaron física y mecánicamente para evaluar el daño adquirido artificialmente y en servicio.

3.2.1.- *Verificación de la masa*

Las placas de asiento deben presentar una tolerancia admisible del 1 % sobre el valor de masa estándar según la E.T. [4]. La variación de peso, expresión (1), se determina comparando las masas antes y después del proceso de deterioro.

$$\Delta W(\%) = \frac{m_{final} - m_{inicial}}{m_{inicial}} \cdot 100 \quad (1)$$

3.2.2.- *Ensayo de rigidez estática*

El estudio de la rigidez en el intervalo de 20 a 95 kN, expresión (2), permite conocer el comportamiento de las placas en condiciones normales de explotación en vía.

$$k = \frac{95 - 20}{d_{95} - d_{20}} \text{ (kN/mm)} \quad (2)$$

El ensayo se llevó a cabo aplicando 3 ciclos de fuerza de compresión entre 0,1 y 95 kN, con la misma disposición que el ensayo de fatiga. La medida de los desplazamientos relativos de la placa de asiento (d) con respecto al soporte se efectuó con 4 comparadores, colocados en cada uno de los extremos de la placa. La secuencia de esfuerzos se muestra en la Figura 4, donde se representan las velocidades de carga y de descarga utilizadas, así como los tiempos de espera considerados entre cada ciclo de carga. La E.T. [4] establece que la rigidización de la placa tras el proceso de deterioro no debe superar el 25 %.

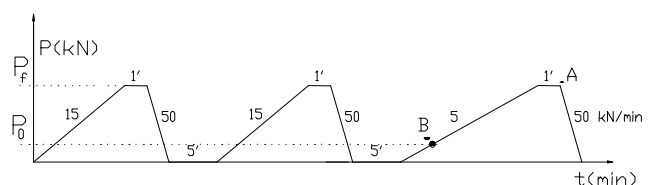


Figura 4: Velocidades de carga y descarga

4. RESULTADOS Y ANÁLISIS

4.1. Verificación de masa

En las tablas 1 y 2 se muestra la ganancia o pérdida de peso de las placas de asiento después de ser sometidas a distintos tipos de deterioro artificial.

Tabla 1: Deterioro artificial en placas Arnitel®

Tipo de deterioro	Peso placa		Variación (%)
	Antes	Después	
Intemperie	165.74	168.33	1.56
Fatiga térmica	165.58	166.24	0.39
Fatiga mecánica	166.41	165.90	-0.08
Absorción de agua	165.53	170.62	3.07
Calentamiento a 100°C	165.70	164.65	-0.64
Refrigeración a -10°C	166.01	167.72	1.02
Sin deteriorar	166.04	165.90	-0.08

Tabla 2: Deterioro artificial en placas Hytrel®

Tipo de deterioro	Peso placa		Variación (%)
	Antes	Después	
Intemperie	164.04	165.53	0.90
Fatiga térmica	164.40	165.05	0.71
Fatiga mecánica	164.58	164.70	-0.07
Absorción de agua	164.62	167.59	1.80
Calentamiento a 100°C	164.43	163.88	-0.33
Refrigeración a -10°C	164.71	165.86	0.69
Sin deteriorar	164.81	164.70	-0.07

Se comprueba que Arnitel dispone mayor capacidad de absorción, superando en un 40%, aproximadamente, a Hytrel en las dos condiciones relacionadas directamente con el agua como son exposición a la intemperie e introducción en agua a 60°C.

4.2.- Ensayo de rigidez estática a 20/95 kN

4.2.1.- Placas de producción

En la Figura 5 se representa la evolución de la carga frente al desplazamiento del carril en el último ciclo para las placas originales de referencia. En las Figuras 6 a 9 se representa el último ciclo de carga para las placas deterioradas comparándolas con la original. Las Tablas 3 y 4 recogen los valores de rigidez, energía disipada (Ed) y almacenada (Ea) medidos en el último ciclo.

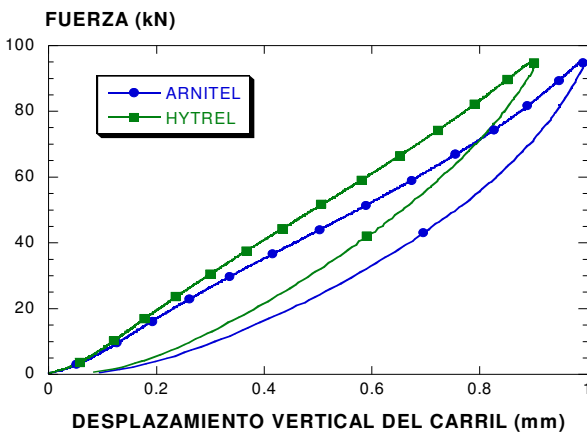


Figura 5: Evolución de las placas de referencia

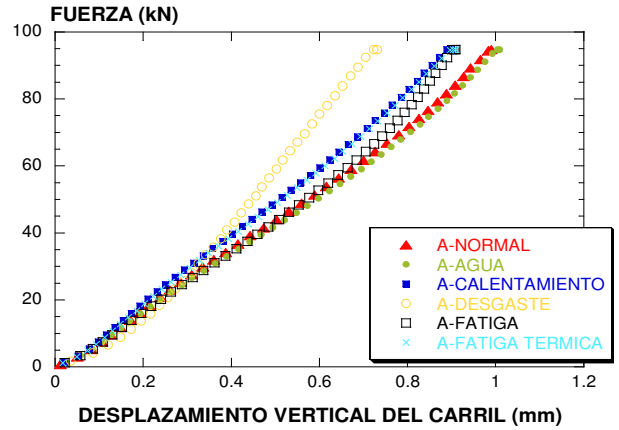


Figura 6: Evolución de las placas Arnitel® (I)

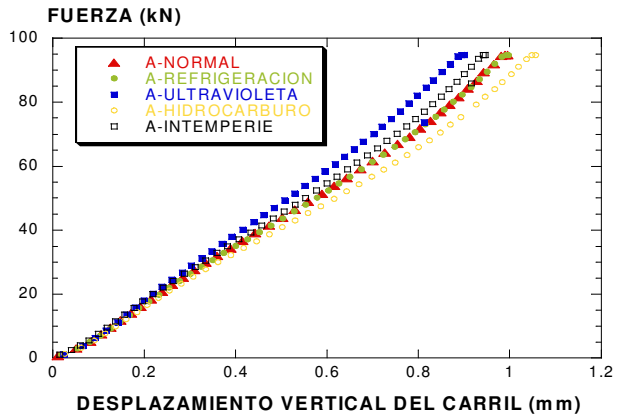


Figura 7: Evolución de las placas Arnitel® (II)

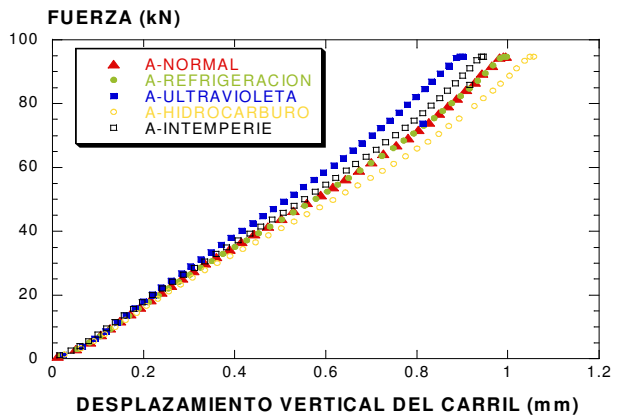


Figura 8: Evolución de las placas Hytrel® (I)

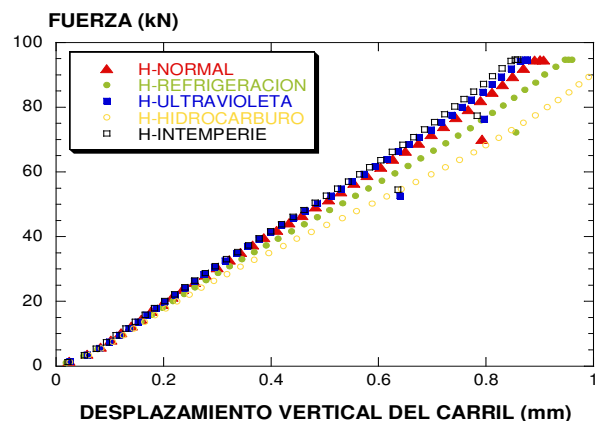


Figura 9: Evolución de las placas Hytrel® (II)

Tabla 3: Rigidez y energías de las placas Arnitel®

Tipo de deterioro	Arnitel®		
	Rigidez (kN/mm)	Energía disipada (J)	Energía almacenada (J)
Sin deteriorar	97.61	14.20	44.23
Desgaste	152.45	9.24	29.87
Fatiga	111.15	9.87	36.94
Agua	96.30	13.28	44.37
Calentamiento	107.82	11.75	40.15
Fatiga térmica	107.6	11.93	40.95
Hidrocarburo	91.56	15.80	46.66
Intemperie	102.54	11.26	41.80
Refrigeración	97.78	14.05	44.16
Rayos UV	109.52	10.97	39.95

Tabla 4: Rigidez y energías de las placas Hytrel®

Tipo de deterioro	Hytrel®		
	Rigidez (kN/mm)	Energía disipada (J)	Energía almacenada (J)
Sin deteriorar	106.65	12.62	41.92
Desgaste	164.39	7.32	27.51
Fatiga	114.40	9.28	37.33
Agua	99.17	12.56	43.89
Calentamiento	104.74	12.24	42.05
Fatiga térmica	110.42	10.22	39.94
Hidrocarburo	91.18	15.50	47.40
Intemperie	113.59	9.46	39.92
Refrigeración	100.59	13.16	43.88
Rayos UV	11.04	10.20	39.93

En las Figuras 10 - 12 se muestran las variaciones de rigidez, energías almacenada y disipada de cada placa deterioradas respecto a la original. Se comprueba que la rigidez y las energías son inversamente proporcionales. Se observa que el desgaste mecánico es el proceso de deterioro que más castiga el comportamiento de la placa, reflejado en un incremento de la rigidez superior al 50%. La fatiga mecánica es el segundo de los procesos más dañinos, pero se mantiene cerca del 10 % y por debajo de los límites establecidos en la normativa que es del 25%. El resto de procesos se mantienen por debajo del 10 % de incremento de rigidez. En los casos del hidrocarburo, la absorción de agua y refrigeración produce una flexibilización de la placa respecto a los valores iniciales. En cuanto al material se puede apreciar que Arnitel® muestra un mayor grado de deterioro en la mayoría de los casos ya que el porcentaje de rigidización es ligeramente superior.

Analizando la energía almacenada, se aprecia que son los deterioros mecánicos los que más se hacen notar, primero el desgaste (pérdida del 30 %) y a continuación la fatiga (pérdida del 15%). El resto de deterioros se sitúan por debajo del 10% de variación. Y al igual que ocurría con la rigidez, la absorción de agua, la refrigeración y el deterioro por hidrocarburos muestran una tendencia contraria al resto, provocando un aumento en las energías almacenadas. El parámetro de energía almacenada no muestra tan claramente, como la rigidez, cual de los dos materiales muestra un mayor deterioro, ya que los valores máximos de variación del deterioro se alternan entre uno y otro material indistintamente.

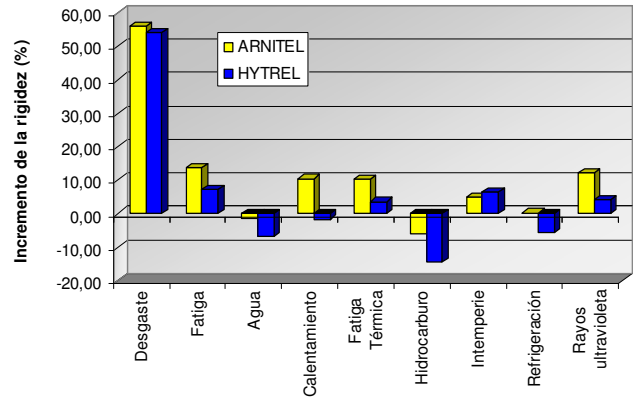


Figura 10: Variación de las rigideces

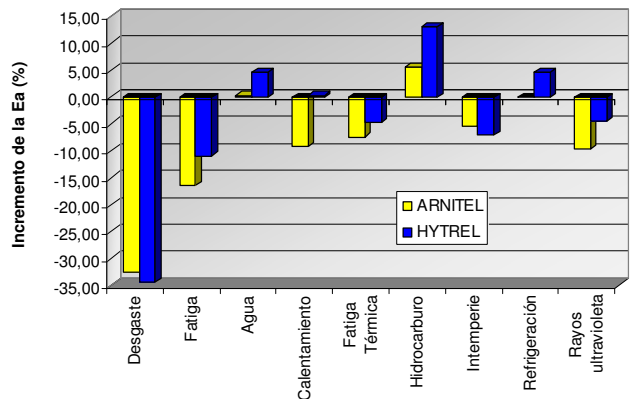


Figura 11: Variación de las energías almacenadas (Ea)

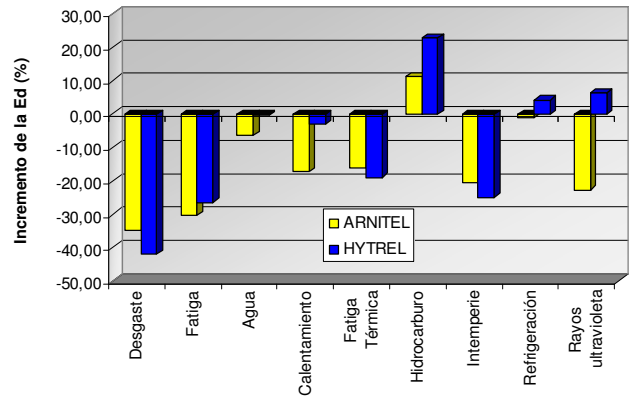


Figura 12: Variación de las energías disipadas (Ed)

La energía disipa vuelve a reflejar la mayor pérdida de propiedades sufrida por las placas en los tratamientos mecánicos, alcanzando el 40 % para el desgaste y el 30% para la fatiga. No es tan clara la diferencia con el resto de procesos, ya que el tratamiento en intemperie también se sitúa cerca del 30 %. La energía disipada, al igual que la almacenada, no muestra claramente cuál de los dos materiales se comporta mejor frente al deterioro. E_d aumenta en el caso del envejecimiento por hidrocarburos, alcanzando valores entre el 10 y 20 %, pero no aparece el fenómeno de forma tan clara con la absorción de agua.

4.2.2.- Placas de vía

Se determinó la rigidez de las placas de vía, inyectadas con Arnitel®. En la Figura 13 se representan las curvas de las placas junto con una placa referencia de fábrica.

En la Tabla 5, se recogen los valores de rigidez y energías calculados a partir de las gráficas dibujadas [12].

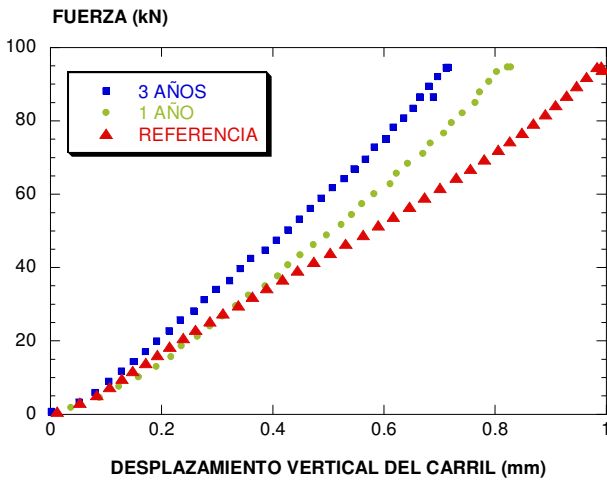


Figura 13: Evolución de la rigidez en placas de vía

Se observa un claro aumento de rigidez en función del tiempo de servicio en vía. Asimismo, si se representan todas las rigideces calculadas, Figura 14, se analiza que el proceso de degradación de desgaste es el más agresivo, seguido por las placas con un ciclo de vida en vía.

Tabla 5: Rigidez y energías de las placas de vía

Tipo de deterioro	Placas de vía (ARNITEL®)		
	Rigidez (kN/mm)	Energía disipada (J)	Energía almacenada (J)
Sin deteriorar	97.61	14.20	44.23
1 año en vía	129.67	6.66	128.63
3 años en vía	137.90	5.54	49.96

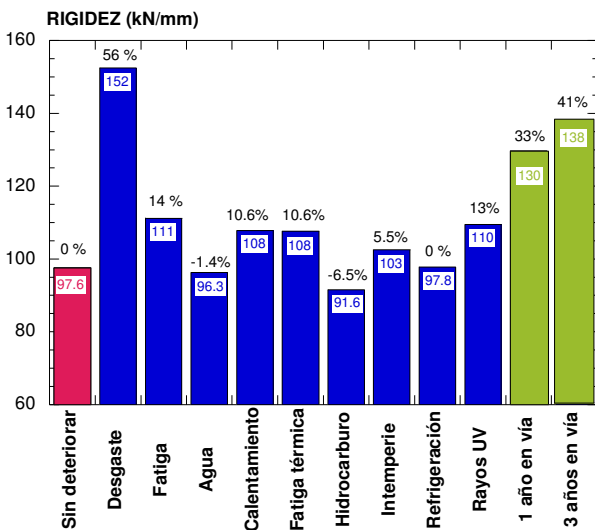


Figura 14: Comparativa de las rigideces

Si se integran todos los daños artificiales llevados a cabo, exceptuando el proceso de desgaste por haber desbastado demasiada superficie en comparación con los desgastes reales, el porcentaje total de los daños causados suma el 46%, que se aproxima al alcanzado por las placas de asiento de vía, un 41 %.

5. CONCLUSIONES

1. El desgaste mecánico artificial es el proceso más dañino, generando sobre la placa un incremento de rigidez superior al 50%.
2. Las placas elásticas con una vida en servicio en vía de 1 y 3 años experimentan una rigidización del 33 y del 41 %, respectivamente.
3. La fatiga mecánica genera el proceso de daño más acusado para la placa, pero la variación de rigidez del 10%, se sitúa dentro de los límites permitidos.
4. El resto de los procesos de deterioro mantienen el incremento de rigidez por debajo del 10%
5. Sólo en los casos de inmersión en hidrocarburos y en agua se produce una flexibilización de la placa.
6. Arnitel® muestra tras su envejecimiento, mayor rigidización, por lo que su capacidad de amortiguamiento y de absorción de energía mecánica es inferior a la Hytrel®, parámetros físico-mecánicos esenciales para el control de la elasticidad de la vía de ferrocarril para AVE.

REFERENCIAS

- [1] Gilaberte M. *El uso de los materiales en la superestructura de vía de ferrocarril para AVE*. INECO-TIFSA. Cursos de Laredo, UC. 2007.
- [2] Carrascal, Casado, Polanco y Gutiérrez-Solana, *Comportamiento dinámico de placas de asiento de sujeción*. Mecánica Fractura. Vol 22, pp 372-377.2005
- [3] E.T. 03.360.570.0, *Placas elásticas de asiento para sujeción VM*. Mantenimiento de infraestructura, líneas convencionales. ADIF. 1ª edición. Diciembre de 2005.
- [4] Holden, G., *Thermoplastic Elastomers*. A series of mini-tutorials of H. Understanding Books. Munich 2000.
- [5] Holden, G. *Thermoplastic elastomers*. Ed. Hanser.
- [6] Resumen mensual de estaciones principales. Instituto Nacional de Meteorología.
- [7] William D. Callister. *Ciencia e ingeniería de los materiales*. Vol. II. Editorial Reverté.
- [8] Enrique Otero Huerta. *Corrosión y degradación de materiales*. Editorial Síntesis.
- [9] Richard A. Flinn, Paul K. Trojan. *Materiales de ingeniería y sus aplicaciones*. Editorial Mc Graw Hill.
- [10] Javier Areizaga, M. Milagros Cortázar, José M. Elorza, Juan J. Iuin. *Polímeros*. Editorial Síntesis.
- [11] I. Carrascal. *Optimización y análisis de comportamiento de sistemas de sujeción para vías de ferrocarril de AVE*. Tesis Doctoral. UC. 2006.
- [12] Casado, Carrascal y Polanco. *Ensayos relativos a la Especificación Técnica RENFE E.T. 03.360.570.0; Placa elástica de asiento para sujeción VM*. LADICIM.

ESTIMACIÓN DE LAS CONDICIONES CRÍTICAS EN FATIGA DE UN COMPUESTO DE POLIAMIDA Y FIBRA DE VIDRIO POR MEDIO DE UN ENSAYO DE FATIGA ACELERADA (LOCATI) A PARTIR DE LA MEDIDA DEL DAÑO NETO.

I. Carrascal, J. A. Casado, S. Diego, J. A. Polanco, F. Gutiérrez-Solana y P. Miengo

Departamento de Ciencia e Ingeniería del Terreno y de los Materiales. Universidad de Cantabria
E.T.S. Ing. Caminos, Canales y Puertos. Avda. Los Castros s/n, 39005. Santander.

RESUMEN:

La técnica experimental empleada en este trabajo es el ensayo LOCATI, consistente en aplicar una fuerza máxima escalonada y creciente, a partir de un valor inferior al límite de fatiga, durante un número constante de ciclos. Al alcanzar un cierto nivel de carga, aparece un escalón crítico a partir del cual los valores del daño acumulado pierden su estabilidad y crecen con una velocidad crítica que precede a la rotura del material. La principal ventaja del método es que a partir de una única probeta se pueden estimar las condiciones críticas en fatiga. En este trabajo se propone un modelo para la cuantificación del daño acumulado en cada uno de los escalones del proceso de fatiga a través de la energía almacenada en función de la tensión aplicada. El daño se obtendrá como la variación de la energía almacenada más la disipada respecto a las condiciones iniciales, es decir como la pérdida de propiedades respecto a las condiciones de partida. El material seleccionado para el trabajo es un compuesto con matriz de Poliamida 6, reforzado con un 25 % en peso de fibra de vidrio corta inyectado en probetas de tracción normalizadas.

ABSTRACT

The experimental technique used in this work is the LOCATI test which consists of applying a maximum staggered and growing force, from a value lower than the fatigue limit for a constant number of cycles. At a certain load level, it is appeared a critical step at which accumulated damage values lose their stability and grow with a critical speed that preceded the breakage of the material. The main advantage of the method is that from a single standard tensile specimen can estimate the critical conditions in fatigue. This paper proposes a model for quantifying the accumulated damage in each of the steps of the fatigue process through the total energy per cycle (energy stored and energy dissipated) as a function of the applied stress. The damage is going to be obtained as the change in total energy in each cycle with respect to initial conditions, ie as property loss on the initial conditions. The material selected for the work is a composite of polyamide 6 reinforced with 25 wt% of short glass fiber injected into standard tensile specimens.

KEY WORDS: Daño, daño neto, fatiga, poliamida, compuesto, Locati

1. INTRODUCCIÓN

La determinación del nivel de tensión por debajo del cual no se produce la rotura del material frente a esfuerzos dinámicos, límite de fatiga o durabilidad, históricamente se ha obtenido a partir de las curvas de Wöhler o curvas S-N [1]. La realización de este ensayo presenta la problemática de tener que emplear al menos entre 16 y 20 probetas para poder obtener resultados fiables. Una alternativa a este método es el Stair-case, en el cual, a partir de 11-15 probetas, se pueden obtener resultados similares [2]. Por último, en este trabajo, se propone la metodología LOCATI [3,4], que pretende determinar el límite de fatiga a partir de una única probeta. El método LOCATI consiste en un ensayo de fatiga acelerada en el que se van aplicando tensiones crecientes hasta provocar la rotura del material.

Estudios previos han utilizado la metodología LOCATI analizando la deformación de la probeta [5] y la velocidad de la deformación máxima para la

determinación del límite de fatiga [6] ó el ángulo de desfase [7].

En este trabajo se determinará el límite de fatiga del material analizando el daño ocasionado por el proceso de fatiga acelerada por el método LOCATI.

Tradicionalmente [8, 9] la formulación relativa al daño se basa en el concepto de tensión y deformación efectiva. La tensión efectiva es la experimentada por el material debido a la reducción de sección neta por los diferentes mecanismos de daño, de forma que el daño, D , se puede definir a partir de:

$$D = 1 - \frac{\tilde{E}}{E} \quad (1)$$

Donde E es el módulo elástico del material sin daño y \tilde{E} es el módulo aparente del material dañado. El parámetro daño, D , representa el grado de deterioro del material, tomando valores desde 0 para materiales sin daño hasta D_C , daño crítico, cuando se produce el fallo.

El daño generado en fatiga en un material compuesto de matriz polimérica consiste en la creación y crecimiento de discontinuidades como micro fisuras, huecos, crazes, etc. que disminuyen la resistencia del material progresivamente hasta su rotura [10]. Se puede definir este parámetro como la variación de la energía en cada momento respecto a las condiciones iniciales.

2. MATERIAL

Las probetas usadas en este trabajo para los ensayos están fabricadas en poliamida 6 reforzada con un 25 % en peso de fibra corta de vidrio (PA6GF25). Las probetas fueron conformadas por inyección y tienen unas dimensiones formalizadas, con forma halterio tipo 1B según UNE-EN ISO 527-2 [11], cuya geometría y dimensiones se reflejan en la Figura 1.

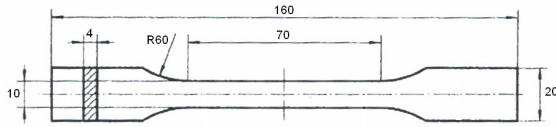


Figura 1.- Probeta tipo halterio

La PA 6 es un material altamente higroscópico y la absorción de humedad puede alterar significativamente sus propiedades mecánicas, especialmente las dinámicas. Por esta razón, previamente, se sometieron las probetas a un tratamiento para dotarlas de una humedad en torno al 2.4 %. Bajo estas condiciones la resistencia mecánica estática alcanza los 100 MPa en rotura con una deformación superior al 5% [12].

3. METODOLOGÍA EXPERIMENTAL

Para todos los ensayos de fatiga realizados en el desarrollo de este trabajo se mantuvo constante la forma de la onda sinusoidal, la relación de tensiones, $R = 0.1$, y la frecuencia, $f = 5$ Hz. Inicialmente se realizaron ensayos de fatiga monótona hasta rotura entre fuerzas máximas de 1400 y 2700 N, con incrementos de 100 N entre ensayos, con objeto de definir la curva de Wöhler y el límite de fatiga, $\Delta\sigma_c$.

Posteriormente se realizaron ensayos de fatiga monótona con interrupciones, de forma que cada 25.000 ciclos se detuvo el ensayo por espacio de una hora, hasta que la temperatura de la probeta recuperó el valor de la ambiental. Estas interrupciones permitirán comprobar el comportamiento frente a fatiga de materiales con daño previo.

Por último se ejecutaron los ensayos de fatiga acelerada LOCATI. Esta metodología consiste en aplicar una fuerza máxima escalonada y creciente a partir de un valor inferior al límite de fatiga, durante un número constante de ciclos a una frecuencia determinada. En la Figura 2 se muestra un esquema del ensayo y en la tabla 1 las variables empleadas.

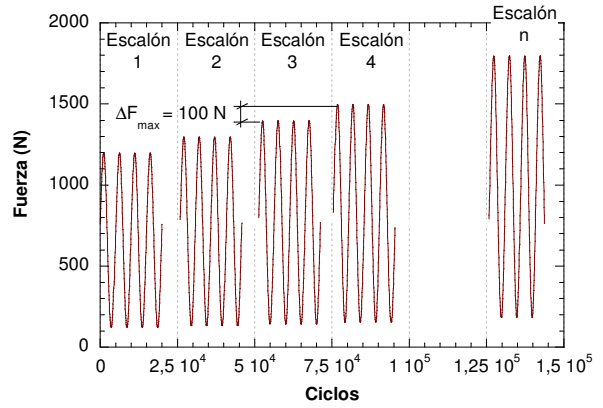


Figura 2.- Esquema de carga del ensayo Locati

Tabla 1- Niveles de carga en el ensayo locati

Esc.	F _{max} (N)	F _{min} (N)	σ _{max} (MPa)	σ _{min} (MPa)	Δσ (MPa)
1	1200	120	30	3	27
2	1300	130	32.5	3.25	29.25
3	1400	140	35	3.5	31.5
4	1500	150	37.5	3.75	33.75
5	1600	160	40	4	36
6	1700	170	42.5	4.25	38.25
7	1800	180	45	4.5	40.5
8	1900	190	47.5	4.75	42.75
9	2000	200	50	5	45
10	2100	210	52.5	5.25	47.25
11	2200	220	55	5.5	49.5
12	2300	230	57.5	5.75	51.75
13	2400	240	60	6	54
14	2500	250	62.5	6.25	56.25
15	2600	260	65	6.5	58.5
16	2700	270	67.5	6.75	60.75

Se realizaron cuatro variantes diferentes incluyendo paradas durante una hora entre cada escalón, variando la duración de los escalones y cambiando la variación de carga entre escalones, según se indica en la tabla 2.

Tabla 2- Tipos de ensayo LOCATI

Tipo	Paradas	Duración escalón	ΔF _{max}
LOCATI 1	NO	25.000 ciclos	100
LOCATI 2	SI	25.000 ciclos	100
LOCATI 3	NO	25.000 ciclos	50
LOCATI 3	NO	50.000 ciclos	100

Para la realización de los ensayos se empleó una máquina servohidráulica de ± 5 kN de capacidad a la que se acopla un extensómetro dinámico de 50 mm de base de medida y ± 12.5 mm de recorrido para la medida de las deformaciones de la probeta.

4. RESULTADOS Y ANÁLISIS

Como resumen de los resultados de fatiga monótona se muestra en la Figura 3 el diagrama de Wöhler

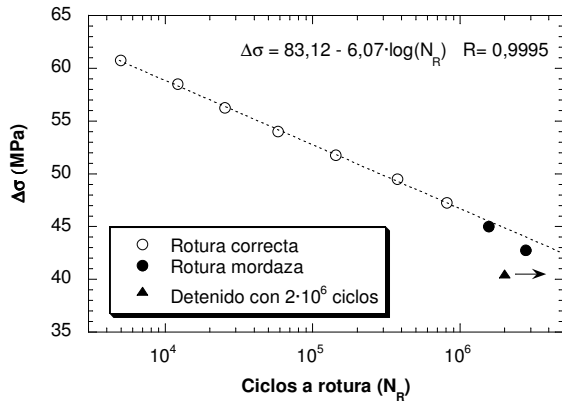


Figura 3.- Diagrama de Wöhler

El límite de fatiga se establece para $\Delta\sigma = 40.5$ MPa (180-1800 N) ya que todas las variables analizadas se habían estabilizado al cabo de $2 \cdot 10^6$ ciclos.

Durante el proceso de fatiga, la energía en el volumen de material constituido por un prisma de base la sección transversal de la probeta y de altura la separación entre puntos de referencia del extensómetro, dentro de un ciclo y entre dos instantes de tiempo t_i y t_{i+1} se obtiene a partir de [13]:

$$E_{t_i/t_{i+1}} = \int_{t_i}^{t_{i+1}} dE = \int_{t_i}^{t_{i+1}} F \cdot d\Delta \quad (2)$$

Para un ciclo completo esta energía total puede descomponerse, tal como se ve en la Figura 4, en energía disipada, E_d , representada por el bucle de histéresis y energía almacenada, E_a , recuperada por la placa tras finalizar el ciclo.

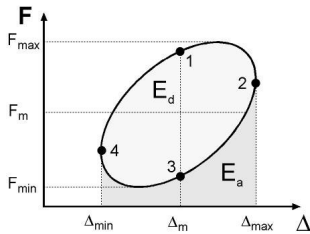


Figura 4.- Energía almacenada y disipada

Será la energía total por ciclo, E_T , la empleada para la determinación del daño generado en el proceso de fatiga.

$$E_T = E_a + E_d \quad (3)$$

Se puede apreciar en la figura 5 que en los procesos de fatiga térmica, tensiones más elevadas, la E_T tienen una clara tendencia creciente, mientras que en la fatiga mecánica los parámetros energéticos tienden a estabilizarse o incluso disminuir en alguno de los casos.

A partir de este momento se define un parámetro, que se denominará **daño total**, D_T , para cuantificar el daño sufrido por el material durante el proceso de fatiga. La definición de este parámetro se realizará a partir de la

variación de parámetros energéticos respecto a su valor inicial y se obtendrá a partir de la expresión:

$$D_T = \left(1 - \frac{E_{T0}}{E_{Ti}}\right) \cdot 100 \text{ [%]} \quad (4)$$

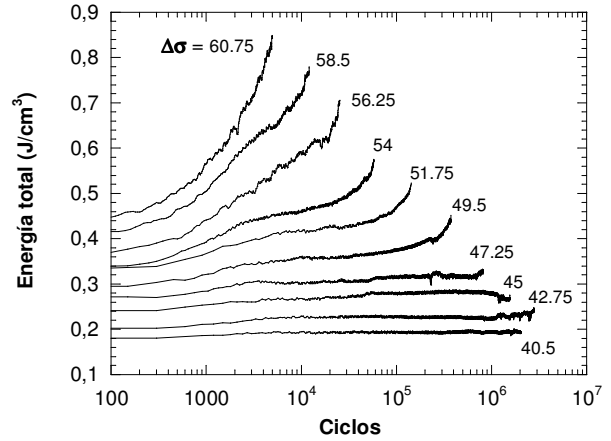


Figura 5.- Evolución de la energía total, E_T

Donde E_{T0} será la energía total medida en el primero de los ciclos de fatiga y E_{Ti} la energía total medida en el ciclo i . En el gráfico de la Figura 6 se representa la evolución del daño total para los diferentes niveles de carga.

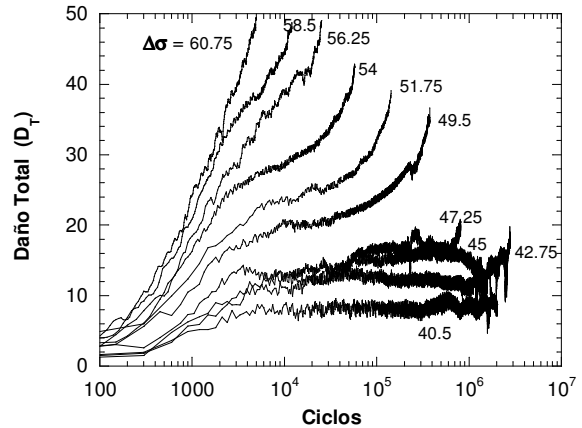


Figura 6.- Evolución del daño total para los ensayos de fatiga monótona

Se puede observar que para el límite de fatiga, $\Delta\sigma = 40.5$ MPa, tanto la E_T como el D_T se encuentra completamente estabilizada al cabo de $2 \cdot 10^6$ ciclos.

En trabajos previos [13] se comprobó que el daño en todos los casos seguía un mismo patrón, con un crecimiento rápido inicial con pendiente decreciente, zona D-I, después un crecimiento lineal del daño, zona D-II y por último un crecimiento acelerado hasta rotura, zona D-III, como se puede ver en la Figura 7. Tanto la velocidad de crecimiento, $\Delta D_T / \Delta N$, como la ordenada en el origen del ajuste del tramo D-II, D_0 , y el daño crítico, real y teórico, D_C y D_{CT} , son crecientes con el nivel tensional.

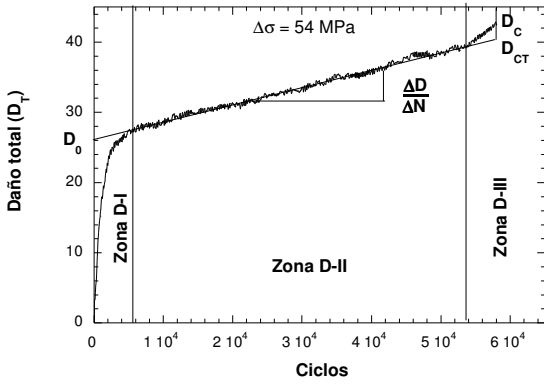


Figura 7.- Evolución del daño total ($\Delta\sigma = 54 \text{ MPa}$)

Al analizar los resultados de la fatiga monótona con interrupciones, Figura 8, se puede observar que parte del daño ocasionado durante un escalón de carga (25.000 ciclos) se recupera durante el periodo de reposo, de forma que cuando se inicia el siguiente escalón el daño inicial es inferior al daño con el que finalizó el escalón previo. Es decir que el daño estaría compuesto de un componente elástico, que se recupera al ceder el esfuerzo cíclico y otro componente plástico que es el que permanece tras el esfuerzo y el que realmente ocasiona deterioro en el material.

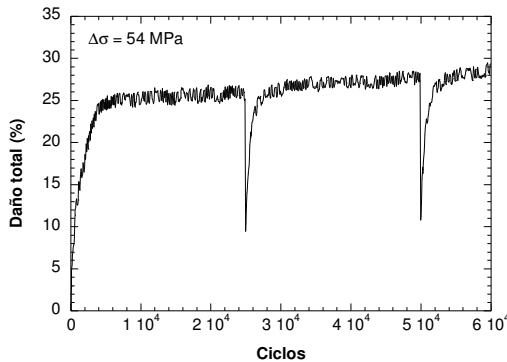


Figura 8.- Evolución del daño total con interrupciones

La componente elástica del daño se identificará con la ordenada en el origen del tramo D-II, D_0 , o daño inicial, y por tanto se podrá definir un daño plástico o neto, D_N , a partir de la expresión:

$$D_N = D_T - D_0 \quad (5)$$

La figura 9 representa la evolución del daño neto para todos los niveles de fatiga monótona sin interrupciones. A diferencia de los resultados obtenidos para el daño total, donde los valores del daño crítico dependían del nivel tensional, aumentando a medida que se incrementaba el esfuerzo, para el daño neto se puede comprobar que en el caso de fatiga térmica los valores de daño neto crítico teórico, D_{NCT} , se estabilizan en torno al 15 %, independientemente de la tensión. En el caso de la fatiga mecánica no se ha podido comprobar el valor del daño crítico porque, como se ha comentado, la rotura ha tenido lugar por la mordaza, no alcanzando por tanto el número de ciclos de rotura teórico.

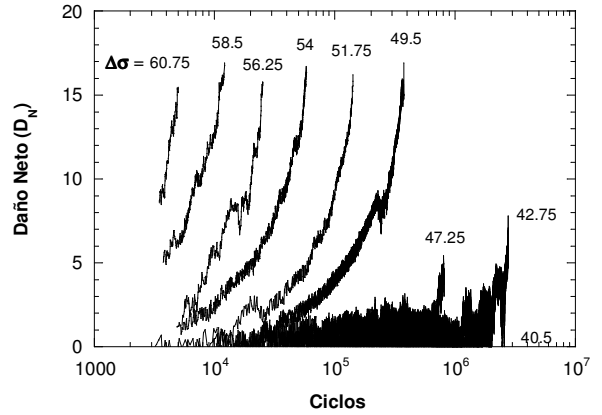


Figura 9.- Daño neto. Fatiga monótona

En la figura 10 se comprueba que en el caso de la fatiga interrumpida el número de ciclos es mayor que en la monótona del mismo nivel, pero el daño neto teórico también alcanza valores próximos al 15 %.

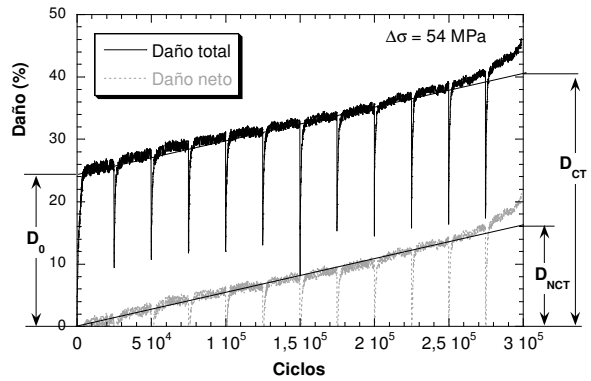


Figura 10.- Daño neto, fatiga interrumpida, (54 MPa)

Analizando la evolución del daño total, D_T , en los ensayos LOCATI, no se detecta ningún indicio que permita establecer cuál de los escalones es el que corresponde con el límite de fatiga. La figura 11 representa, en doble eje de abscisas para facilitar la comparación entre los diferentes ensayos, la evolución del daño total comprobando que los resultados de los cuatro son coincidentes alcanzando valores en rotura muy similares.

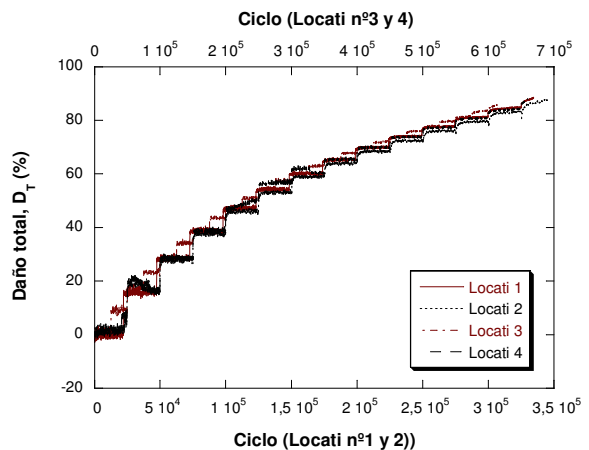


Figura 11.- Daño total ensayo LOCATI

La igualdad de comportamientos también se observa al analizar la evolución del ángulo de desfase entre la señal de carga y deformación, figura 12. También se puede comprobar en dicha figura que el valor del desfase crítico es similar en todos los casos y próximo a 0.12 radianes, por lo que este valor también podría ser una constante en rotura.

Debido a que el nivel tensional a lo largo del ensayo LOCATI es cambiante se define un nuevo parámetro que será el daño neto individual, D_I , que tendrá en cuenta la variación de energía total respecto a la inicial de cada uno de los escalones.

$$D_I = \left(1 - \frac{E_{T0j}}{E_{Tij}} \right) \cdot 100 [\%] \quad (6)$$

Donde E_{T0j} es la energía total inicial del escalón j y E_{Tij} es la energía total del instante i del escalón j .

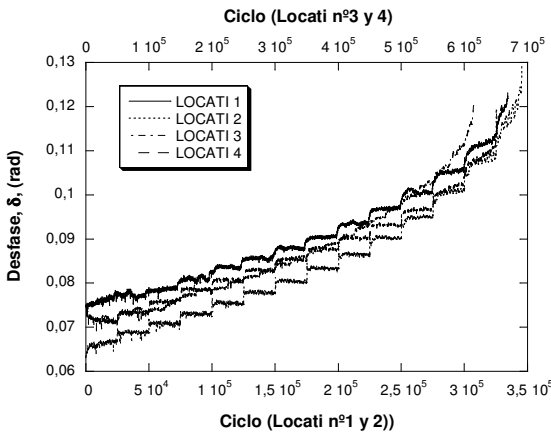


Figura 12.- Desfase, δ , ensayo LOCATI

Este daño D_I seguirá teniendo componente elástica y neta, por lo que será necesaria la determinación del daño neto individual D_{NI} .

Para el primer escalón se empleará el método comentado anteriormente, expresión (5), y para el resto de escalones se utiliza en procedimiento descrito en la expresión (7) y figura 13.

$$D_{NIj} = D_{Ij} - (D_{0j} - D_{NIj-1}) \quad (7)$$

Siendo D_{NIj-1} el último valor del daño neto individual del escalón anterior.

En las figuras 14 a 17 se representa el D_{NI} para los cuatro ensayos LOCATI realizados. Sobre los gráficos se indica el escalón que corresponde con el límite de fatiga, $\Delta\sigma_e$, medido a partir de los ensayos de fatiga monótona. Se puede observar que el D_{NI} en todos los casos se mantiene constante por debajo del $\Delta\sigma_e$ y una vez superado comienza a crecer. Por tanto se puede definir el límite de fatiga a partir del daño neto individual, D_{NI} , en un ensayo LOCATI como aquél escalón a partir del que el parámetro comienza a crecer.

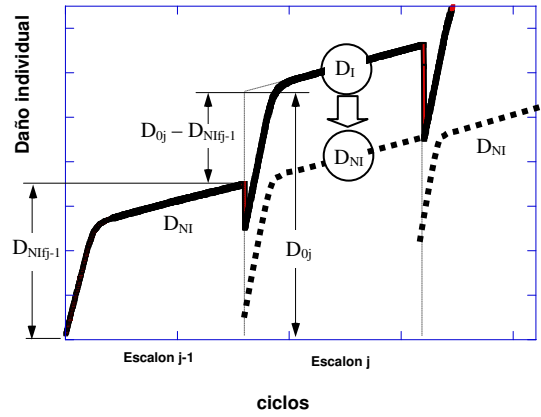


Figura 13.- Determinación del D_{NI}

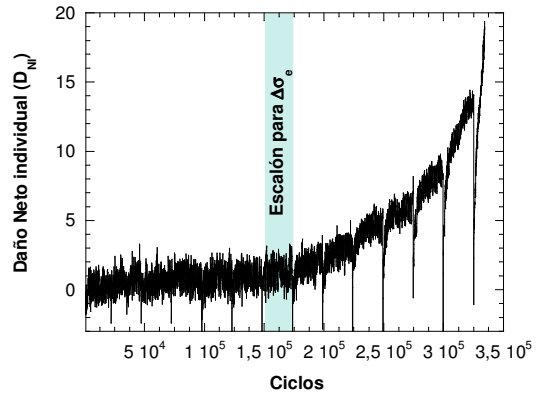


Figura 14.- D_{NI} LOCATI nº 1

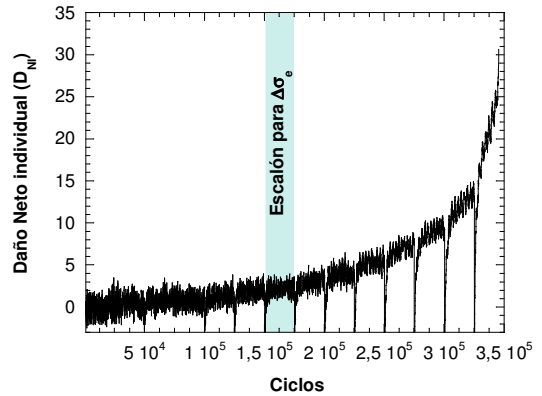


Figura 15.- D_{NI} LOCATI nº 2

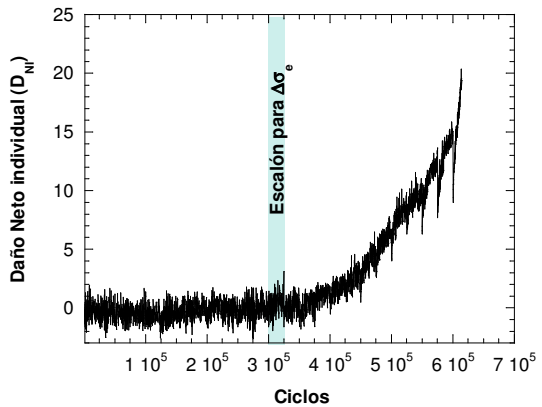


Figura 16.- D_{NI} LOCATI nº 3

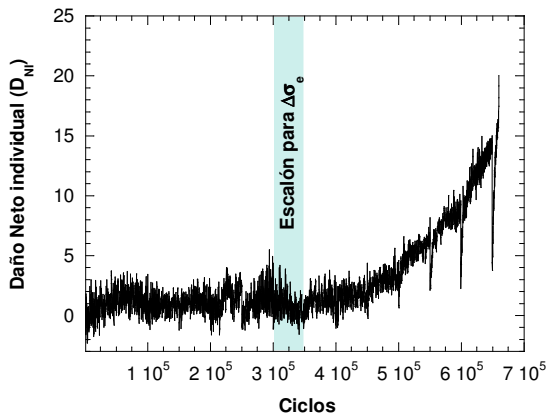


Figura 17.- D_{NI} LOCATI n° 4

Se observa, además, que el valor crítico teórico de daño neto individual se situaría en un valor ligeramente superior al 15%, como ya se vio en los ensayos de fatiga monótona e interrumpida.

5.CONCLUSIONES

En este apartado se destacan las conclusiones más relevantes derivadas del trabajo realizado:

- A partir de ensayos de fatiga monótona interrumpida se ha podido comprobar que el daño total presenta dos componentes: el daño inicial o elástico y el daño plástico o neto.
- Se propone un modelo para la identificación del daño neto sufrido en un proceso de fatiga a través de la variación de la energía total en cada momento respecto a las condiciones iniciales.
- El daño neto crítico, en procesos de fatiga térmica se mantiene constante, alcanzando valores cercanos al 15% para la PA6GF25.
- Los resultados obtenidos a partir de los cuatro ensayos LOCATI ejecutados son muy similares, de lo que se deduce la poca influencia del número de ciclos por escalón, de la existencia o no de paradas y del valor del incremento de tensiones entre los escalones. Se recomienda, por tanto, la realización del ensayo más corto: sin paradas, con 25000 ciclos por escalón y variaciones de 100 N para la F_{max} .
- Se puede definir el límite de fatiga a partir del daño neto individual, D_{NI} , en un ensayo LOCATI como aquél nivel a partir del que este parámetro comienza a crecer.

6.REFERENCIAS

[1] Wöhler, A. “Versuche über die festigkeit der Eisenbahn Wagenachsen Zeitschrift für Bauwessn”, 1860

[2] Rice, R. C. “Fatigue data Analysis” Metals Handbook, 9th edt. Vol. 8, Mechanical Testing. American Society for Metals Park, Ohio, EEUU, 1985.

[3] Locati, L. La Fatica dei Materiali Metallici. Ulrico Hoepli. Milano. 1950

[4] Locati, L. Programmed Fatigue Test, Variable Amplitude Rotat. Metallurgia Italiana. Vol 44, n° 4, págs 135-144. 1952

[5] Casado, J.A. Polanco, J.A., Carrascal, I. Gutiérrez-Solana F. Aplicación of the Locati method to material selection for reinforced polymeric parts subjected to Fatigue. International Conference on Fatigue of Composites. Pags: 454-461. Paris. 1997

[6] Casado, J. A. “Casado J.A. “Comportamiento en fatiga de poliamidas reforzadas con fibra de vidrio corta”. Tesis Doctoral. Universidad de Cantabria, 2001

[7] Casado, J. A. Carrascal, I., Polanco, J.A. Gutiérrez-Solana, F. Fatigue failure of short glass fibre reinforced PA 6.6 structural pieces for railway track fasteners. Engineering Failure Analysis 13. Pgs 182-197. 2006

[8] Sullivan, R. W. Development of a viscoelastic continuum damage model for cyclic loading. Mechanics of Time-Dependent Materials 12 (4), pp. 329-342

[9] Gamstedt, E.K, Berglund, L.A. Peijs, T. Fatigue mechanisms in unidirectional glass-fibre-reinforced polypropylene. Composites Science and Technology, 59. Pags 759-768. 1999

[10] Jessen, S.M. [1] Jessen, S.M. and Plumtree A. Continuum damage mechanics applied to cyclic behaviour of a glass fibre composites pultrusion. Composites. Vol 22. n° 3, pg 181-190. 1991,

[11] UNE-EN ISO 527-2:1997. “Plásticos. Determinación de las propiedades en tracción”. Parte 2: “Condiciones de ensayo de plásticos para moldeo y extrusión”.

[12] Carrascal, I, Casado, J. A., S. Diego, Polanco, J.A. Gutiérrez-Solana. Modelo de comportamiento en fatiga basado en el daño continuo medido a partir de parámetros energéticos de un polímero compuesto. Anales de Mecánica de la Fráctura, 26. Vol. 1. Pgs 277-282. 2009.

[13] Carrascal, I, Casado, J. A., Polanco, J.A. Gutiérrez-Solana. Aplicación del análisis dinamo-mecánico a la determinación de las condiciones críticas en fatiga de materiales poliméricos. Anales de Mecánica de la Fráctura, 25. Vol. 1. Pgs 397-402. 2008.

DETERMINATION OF THE ENVELOPES FOR MODE-MIXITY EVALUATION OF ADHESIVELY BONDED STEEL

Filipe J.P.Chaves¹, L.F.M. da Silva², M.F.S.F. de Moura², D. Dillard³

¹ IDMEC- Pólo FEUP

² DEMec

Faculdade de Engenharia da Universidade do Porto,

Rua Dr. Roberto Frias, 4200-465 Porto, Portugal

E-mail: chaves.filipe@fe.up.pt

³ Virginia Tech, 120-E Patton Hall, Mail Code 0219, Blacksburg, VA 24061

ABSTRACT

This study is about the effect of the adhesive thickness and adhesive ductility on the mixed mode loading of Double Cantilever Beam joints.

The project is divided into three main tasks. The first task is about the development of a finite element model using a cohesive zone model to design an experimental device based on the standard ASTM D6671D.

The second task is concerned with the generation of experimental results in mixed mode varying the type of adhesive and the adhesive thickness. In the third task, the experimental results will be used to develop an adhesive toughness model as a function of the mode mixity.

A dual actuator load frame from Virginia Tech's Engineering Science & Mechanics Dept. was used to obtain the envelopes for mode mixity for three different adhesives and thicknesses.

A proposal for a data reduction scheme for the determination of the strain energy release rate is presented and validated in this paper without the need of the experimental measure of the crack length.

KEY WORDS: adhesive failure, structural adhesive, double cantilever beam specimen, double actuator load frame

1. INTRODUCTION

A data reduction scheme was developed to obtain the stress energy release rate of adhesive joints loaded under mixed mode in a dual actuator load frame. This data reduction scheme does not require the observation of the crack propagation because it takes into account the fracture process zone effect with an equivalent crack length obtained by the compliance-based beam model data reduction scheme [1].

The numerical validation is presented with an envelope obtained with finite element simulations done with ABAQUS using a cohesive element subroutine.

This analysis is applied to the asymmetrical loading of Double Cantilever Beam (DCB) specimens done in a dual-actuator load frame developed by Virginia Tech.

The development of a dual-actuator load frame [2] has facilitated tests evaluating the mixed-mode fracture behavior of adhesively bonded joints. The experiments focused on evaluating the critical strain energy release rate that characterizes mode I, mode II and mixed-mode I/II fracture of different material systems. The dual-actuator load frame allows the use of standard DCB

specimens over the full range of mode mixities (Figure 1).

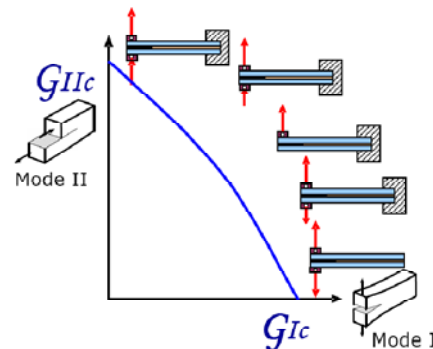


Figure 1. Mode mixity covered with asymmetric loading of symmetric DCB specimens.

The precracked ends of the specimen are connected to the grips of the two actuators and the other end of the specimen was clamped at the base. By simultaneously applying different displacement rates with the two independently controlled actuators, different levels of mode-mixity were obtained at the locus of failure, as seen in Figure 2. Presently, the determination of the strain energy release rate is done using the crack length which is often very difficult to localize and misleading

because it does not take into account the fracture process zone (FPZ).

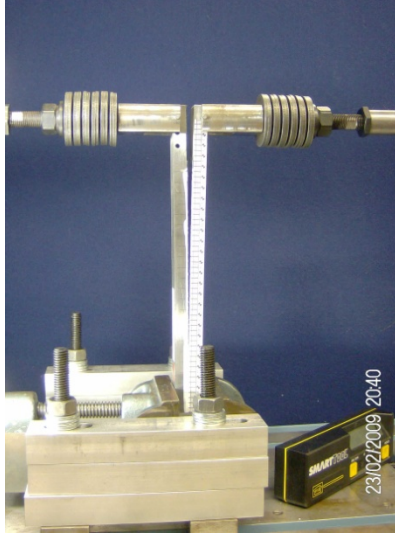


Figure 2. DCB specimen being tested.

2. Data reduction scheme description

The DCB specimens that were used in the tests were obtained with two high strength steel beams. The substrates were sandblasted before the application of the adhesive. Three adhesives of increasing ductility were used: two epoxies (Araldite AV138M and Araldite 2015 from Huntsman) and a polyurethane (Sikaflex-255 from Sika). The values for the energy release rate (G_{Ic}) for each adhesive resulting from the DCB experimental testing are shown in Table 1 [3].

Table1. Energy release rate values for the three adhesives [3].

		Average	Deviation
Araldite AV138M with HV998 hardener	G_{Ic} [N/m]	345.9	47.8
Araldite 2015	G_{Ic} [N/m]	525.7	80.8
Sikaflex-255 FX	G_{Ic} [N/m]	2901.1	121.9

Three different adhesives were studied: 0.2, 0.5 and 1 mm. The thickness layer was controlled with the insertion of spacers at the two ends of the sample.

The tests were conducted with symmetric DCB specimens and asymmetric displacement rates. Applied displacements result in a combination of pure mode I and pure mode II loading. The forces exerted on the two beams were measured by load cells attached to each actuator and the fracture components are calculated with the following:

$$F_I = (F_R + F_L)/2 \quad (1)$$

$$F_{II} = (F_R - F_L)/2 \quad (2)$$

where F_R and F_L are the forces measured by the two load cell. The two values of the strain energy release rate were calculated with the following equations.

$$J_I = \frac{F_I^2 a^2}{EIb} \quad (3)$$

$$J_{II} = \frac{3F_{II}^2 a^2}{4EIb} \quad (4)$$

where b is the width of the bond, I and E are the moment of inertia and the elastic modulus of the adherends respectively, and a is the crack length. F_I and F_{II} refer to the imposed force in mode I and II. The global mode mixity is then indicated with the angle Ψ .

$$\Psi = \text{ArcTan} \left(\sqrt{\frac{G_{II}}{G_I}} \right) \quad (5)$$

The tests were conducted imposing two displacement rates with the actuators, in order to cover different mode mixity levels. During the tests the values of the imposed displacements, the forces at the actuators and the crack length were monitored and recorded. An interesting observation is that for almost all the tests, excluding those in pure modes, the value of Ψ increases as the test progresses and the crack grows. This trend is expected from the analytical evaluation of the failure process. The value of Ψ is not uniquely set by the displacement rates imposed at the beams, but is affected by crack length and increases for a growing crack length.

The analysis described with the previous method requires the observation of the crack propagation which is not easy nor entirely accurate because it does not takes into account the FPZ. A compliance based beam method was developed trying to overcome these handicaps and improving the results obtained. Based upon the work of Oliveira et al. [1] two equations were obtained for J_I and J_{II} :

$$J_I = \frac{12P_I^2 a_{eq,I}^2}{b^2 E h^3} + \frac{6P_I^2}{5b^2 h G} = \frac{6P_I^2}{b^2 h} \left(\frac{2a_{eq,I}^2}{h^2 E} + \frac{1}{5G} \right) \quad (6)$$

$$J_{II} = \frac{9P_{II}^2 a_{eq,II}^2}{b^2 E h^3} \quad (7)$$

where:

$$P_I = \frac{P_2 - P_1}{2} \quad (8)$$

and

$$P_{II} = \frac{P_2 + P_1}{2} \quad (9)$$

During propagation equivalent cracks lengths should be considered in order to account for the FPZ effects. For beam I:

$$a_{eq,I} = a + h|\Delta_I| + \Delta a_{FPZ} \tag{10}$$

$$a_{eq,I} = \frac{1}{6\alpha} \forall - 2 \frac{\beta}{\forall} \tag{11}$$

where

$$\alpha = \frac{8}{Bh^3 E_{fl}} \quad \beta = \frac{12}{5Bh G} \quad \gamma = -C_I$$

$$\forall = \left(\left(-108\gamma + 12 \sqrt{3 \left(\frac{4\beta^3 + 27\gamma^2\alpha}{\alpha} \right)} \right) \alpha^2 \right)^{\frac{1}{3}} \tag{12}$$

And for beam II :

$$a_{eq,II} = a + h|\Delta_{II}| + \Delta a_{FPZ} \tag{13}$$

$$a_{eq,I} = \frac{1}{6\alpha} \forall - 2 \frac{\beta}{\forall} \tag{14}$$

where

$$\alpha = \frac{8}{Bh^3 E_{fl}} \quad \beta = \frac{12}{5Bh G} \quad \gamma = -C_{II}$$

$$\forall = \left(\left(-108\gamma + 12 \sqrt{3 \left(\frac{4\beta^3 + 27\gamma^2\alpha}{\alpha} \right)} \right) \alpha^2 \right)^{\frac{1}{3}} \tag{15}$$

3. RESULTS

Based on this formulation, finite element simulations were conducted with different displacements as seen in Table 2 and analyzed to obtain the fracture envelope seen in Figure 3. Crack growth was simulated by the linear fracture energetic criterion $\frac{J_I}{J_{Ic}} + \frac{J_{II}}{J_{IIc}} = 1$ with $J_{Ic} = 0.6$ [N/mm] and $J_{IIc} = 1.2$ [N/mm].

Table2. Imposed displacements for each simulation

Simul.	imposed displacem.	
	beam 1	beam 2
1	10	-9
2	10	-8
3	10	-7
4	10	-5
5	10	-3
6	10	-1
7	10	0
8	10	1
9	10	3
10	10	5
11	10	7
12	10	7.5
13	10	8
14	10	8.5
15	10	9

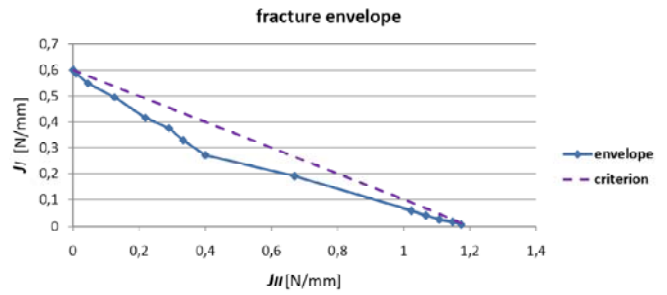


Figure 3. Fracture envelope obtained from numerical results.

Figure 4 shows the result for simulation number 3 with J_I , J_{II} and the FPZ. It shows a stable plateau from 75 mm until 200 mm, for the FPZ and the value of J_I . This emphasizes the accordance between the FPZ and the energy released with the crack growth. As observed in Figure 4, this loading case is mostly mode I. The value for J_I tends to the imposed value of J_{Ic} .

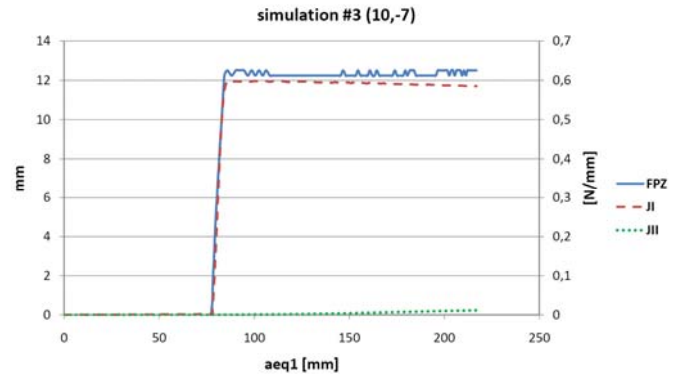


Figure 4. Number 3 simulation results plot for FPZ, J_I and J_{II} .

For simulation number 3, Figure 5 shows the deformed shape and Von Mises stress plot result from the finite element model done with a cohesive element subroutine with ABAQUS.

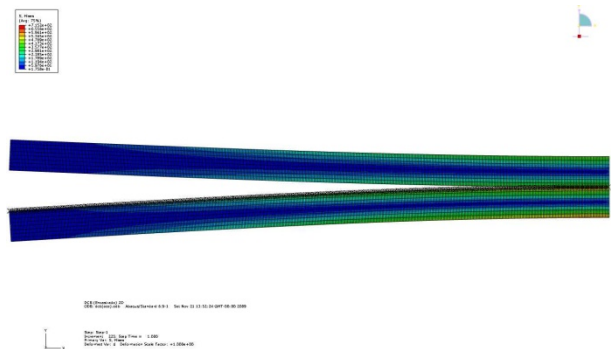


Figure 5. Von Mises stress plot for number 3 simulation.

It is also interesting to observe the results for simulation number 11 shown in Figure 6 with a small plateau near 210 mm, showing a stable crack propagation.

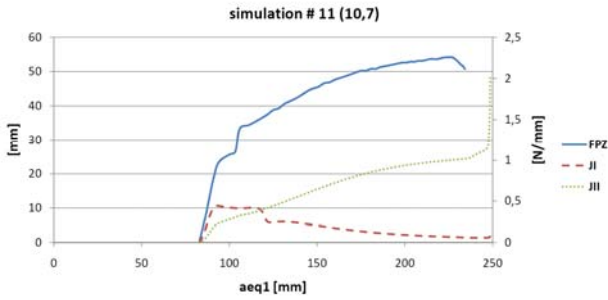


Figure 6. Number 11 simulation results plot for FPZ, J_I and J_{II} .

Figure 7 shows the Von Mises stress plot result for this same imposed displacement. The deformed shape confirms the imposed displacement in the same direction for the two beams of the DCB specimen.

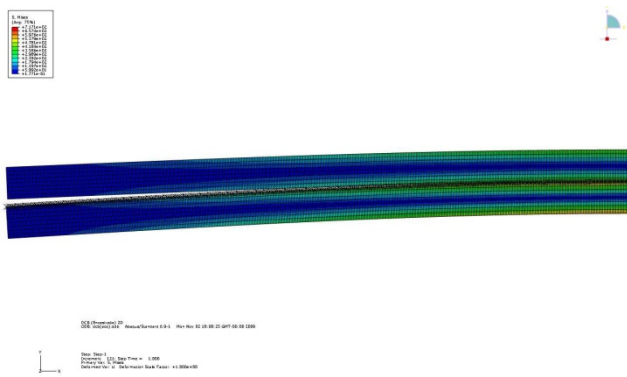


Figure 7. Von Mises stress plot for number 11 simulation.

4. Conclusions

The Asymmetric Compliance-Based Beam Method (ACBBM) data reduction scheme presented here for the determination of J for specimens tested in a dual actuator load frame were validated through a numerical model. This data reduction scheme does not require the crack length and takes into account the FPZ. This data reduction scheme will be used to determine the fracture envelope based on the experimental loading curves.

Acknowledgments

The authors would like to thank the contribution of Edoardo Nicoli, for his testing work at Virginia Tech. The authors also acknowledge the financial support of Fundação Luso Americana para o Desenvolvimento (FLAD) through project 314/06, 2007 and IDMEC.

References

- [1] Oliveira, J.M.Q., de Moura, M.F.S.F., Silva, M.A.L., Morais, J.J.L., Numerical analysis of the MMB test for mixed-mode I/II wood fracture, Composites Science and Technology Vol.67 (9), 2007, pp. 1764-1771
- [2] Hitendra K. Singh, Soojae Park, DonOhanehi and David A. Dillard, “A Design Space for a Novel Dual-Actuator Mixed-Mode Test Frame”, Proceedings of the 29th Annual Adhesion Society Meeting, Jacksonville, FL, 2006.
- [3] Lucas. F.M. da Silva, R.J.C. Carbas , G.W. Critchlow, M.A.V. Figueiredo , K. Brown, Effect of material, geometry, surface treatment and environment on the shear strength of single lap joints, International Journal of Adhesion & Adhesives 29 (2009) 621–632.

COMPORTAMIENTO A FRACTURA DE DOS GRADOS COMERCIALES DE PLA: INFLUENCIA DE LA ESTRUCTURA CRISTALINA

J. Gamez-Perez, J. Velázquez, E. Franco-Urquiza, J.I. Velasco, M.Ll. MasPOCH

Centre Català del Plàstic (CCP), Universitat Politècnica de Catalunya
C/Colom 114, 08222-Terrassa, España.
E-mail: María.lluisa.masPOCH@upc.edu

RESUMEN

En este trabajo se ha estudiado el efecto de un tratamiento de rejuvenecimiento aplicado a láminas obtenidas por extrusión-calandra a partir de dos grados comerciales de PLA, con diferentes purezas ópticas. Se han evaluado las propiedades térmicas mediante calorimetría diferencial de barrido (DSC), las propiedades mecánicas, mediante ensayos a tracción y el comportamiento a fractura con la técnica del trabajo esencial de fractura (EWF). El tratamiento de rejuvenecimiento provoca un aumento del volumen libre de las cadenas, que se manifiesta en un descenso de la temperatura de transición vítrea (T_g) y una disminución de la rigidez y tensión a cedencia con un aumento significativo de la ductilidad. Este incremento en la ductilidad permitió la aplicación de la técnica del EWF, pudiendo relacionar los parámetros obtenidos con la caracterización térmica y mecánica.

ABSTRACT

A study of the effect of a de-aging treatment applied on samples obtained by cast sheet extrusion from two commercial grades of PLA, with different optical purities, was carried out. The thermal and mechanical properties as well as the fracture behaviour have been assessed by differential scanning calorimetry (DSC), tensile tests and the essential work of fracture (EWF) approach, respectively. The de-aging treatment causes an increase in the free volume of polymer chains evidenced in a decrease of the glass transition (T_g), a decrease on the stiffness and the yield stress and a significant increase of the ductility. Such increase in ductility allowed the application of the EWF method and relates the fracture parameters with the thermal and mechanical characterization.

PALABRAS CLAVE: Poli(ácido láctico) PLA, Envejecimiento físico, Trabajo Esencial de Fractura (EWF).

1. INTRODUCCIÓN

El poli(ácido láctico) (PLA) es el polímero de origen renovable y biodegradable cuyo consumo está creciendo a mayor rapidez. El PLA comercial se sintetiza principalmente a partir del monómero ácido L-láctico, encontrando que el estereoisómero ácido D-láctico también aparece como impureza, afectando a la capacidad de cristalización y a sus propiedades [1].

El PLA se caracteriza por ser un material semicristalino con temperaturas de transición vítrea (T_g) y de fusión (T_m) en torno a 60 y 155 °C respectivamente, si bien la cristalización desde el fundido es muy lenta en comparación con las velocidades de enfriamiento que se dan en los procesos de transformación industriales [2, 3]. Como consecuencia, el PLA suele encontrarse en estado amorfo por lo que puede experimentar envejecimiento físico [4]. Este fenómeno ocurre a temperaturas cercanas a la T_g y produce una reorganización molecular que origina la presencia de dominios o zonas más ordenadas. Este reordenamiento, conocido como densificación, ocasiona una importante disminución del volumen libre, factor determinante de la movilidad molecular, y de la densidad de enredos moleculares. Esto, a su vez, limita la capacidad de

almacenamiento y disipación de energía cuando el material es sometido a una sollicitación mecánica, llegando a ocasionar el cambio de comportamiento dúctil a frágil.

Los efectos ocasionados por el envejecimiento físico en el PLA han sido objeto de diversos estudios en los últimos años [5-7]. Este proceso transcurre rápidamente a temperatura ambiente, por ejemplo, la deformación a rotura puede pasar de un 300 a un 6 % en 24 h. Las investigaciones realizadas sugieren que la fragilidad del PLA se debe a la baja densidad de enredos moleculares y a la rigidez de la cadena. Se considera, por tanto, que la variación en las propiedades del PLA está relacionada con el proceso de envejecimiento físico [6]. Sin embargo, a pesar de estos avances, aún no se conocen estudios que describan este efecto en la relación estructura-propiedades a fractura del PLA.

El envejecimiento físico, en tanto no implica cambios permanentes, es un proceso reversible. El proceso inverso, llamado en adelante rejuvenecimiento, puede lograrse por medio de un tratamiento térmico a una temperatura igual o ligeramente superior a su T_g seguido de un enfriamiento rápido. El calentamiento a esa temperatura aumenta la movilidad molecular de las

cadenas poliméricas con lo que se eliminan los dominios o zonas más organizadas generadas durante el envejecimiento y se aumenta su volumen libre. El enfriamiento brusco congela esta estructura impidiendo que las cadenas tengan tiempo de reordenarse.

Este trabajo consiste en la aplicación de un tratamiento térmico de rejuvenecimiento a dos grados comerciales de PLA con diferentes contenidos de monómero D-láctico, con el objetivo de estudiar el comportamiento a fractura mediante la aplicación de la técnica del trabajo esencial de fractura (EWF).

2. MATERIALES Y MÉTODOS

2.1. Materiales

Se han utilizado dos grados comerciales de PLA: el PLA 2002D y el PLA 4032D de Natureworks® con un contenido del isómero D de 4.25 y 2 %, una masa molecular promedio en peso de 212 y 207 kDa y un índice de polidispersidad de 3.06 y 1.72 respectivamente [8-11]. Las láminas de ambos materiales se obtuvieron por extrusión-calandra en una extrusora COLLIN Teach-Line® E16T acoplada a una calandra COLLIN Teach-Line® CR72T, previo secado en un deshumidificador PIOVAN a una temperatura de 80 °C durante 3 h para evitar degradación por hidrólisis. El perfil de temperaturas utilizado en la extrusora fue de 145 °C en la zona de alimentación y de 200 °C en la boquilla y la velocidad de giro del husillo fue de 50 r.p.m. En la calandra se estableció la temperatura de los rodillos en 50 °C. El espesor promedio de lámina obtenido fue de 0.30 mm.

A partir de las láminas extruidas se obtuvieron por troquelado las probetas para cada ensayo. Las láminas fueron sometidas a un tratamiento térmico de rejuvenecimiento a 60 °C durante 20 min. seguido de enfriamiento rápido por inmersión en un baño de hielo y agua a una temperatura de 0±2 °C durante 5 min. Las probetas se ensayaron inmediatamente después del tratamiento de rejuvenecimiento. Adicionalmente, se han caracterizado muestras de las láminas sin tratamiento (envejecidas). La nomenclatura empleada es PLA 2002D y PLA 4032D para los materiales sin tratamiento y PLA 2002D-T y PLA 4032D-T para los materiales con tratamiento térmico de rejuvenecimiento.

2.2. Caracterización Térmica

La caracterización térmica de las láminas se realizó por calorimetría diferencial de barrido (DSC), con muestras de aproximadamente 10 mg. El equipo utilizado fue un calorímetro Perkin Elmer Pyris 1 con un sistema de refrigeración Intracooler Perkin 2P, calibrado con patrones de indio y estaño. Los ensayos consistieron en un calentamiento entre 30 y 200 °C con una rampa de temperaturas de 10 °C/min, seguido de un borrado de la historia térmica y un enfriamiento controlado hasta 30°C a 10°C/min. Para cada muestra se determinó la temperatura de transición vítrea (T_g), la temperatura de

fusión (T_m), la entalpía de cristalización en frío (ΔH_{cc}) y la entalpía de fusión (ΔH_m).

2.3. Caracterización Mecánica y a fractura

La caracterización mecánica se realizó mediante ensayos de tracción. Los ensayos fueron llevados a cabo siguiendo la norma ASTM D-638 en un máquina de ensayos universal (Galdabini, Sun 2500) equipada con una célula de carga de 5kN y un videoextensómetro Mintron OS-65D. Se utilizó una geometría de probeta estándar (tipo IV) y se evaluó la tensión a cedencia (σ_y), el módulo de Young (E) y la deformación a rotura (ϵ_b). Para cada material se ensayaron al menos 5 probetas.

Para la caracterización a la fractura se aplicó la Mecánica de la Fractura Post-Cedencia (PYFM) mediante el método del trabajo esencial de fractura (EWF). La correcta aplicación de la metodología del trabajo esencial de fractura requiere que se cumplan una serie de requisitos experimentales. Uno de ellos es el establecimiento de un rango de longitudes de ligamento de las probetas DDENT (Depply Double Edge Notched Tension) que eliminen el efecto borde y que garanticen un estado de tensión plana y la completa cedencia de la zona de proceso antes de la propagación de la grieta. Por otro lado, en las curvas $F-d$ obtenidas para las probetas con diferentes longitudes de ligamento se debe observar una similitud geométrica [12].

La teoría del EWF se basa en la separación de la energía asociada durante la fractura dúctil (W_f) en dos términos: uno que tiene lugar en la superficie de fractura (denominado esencial, W_e) y el que comprende el trabajo plástico generado en el volumen de la zona que rodea a la superficie de fractura (llamado no esencial o plástico, W_p). El primer término es proporcional al área de fractura (ℓt), mientras que el segundo, al estar relacionado con el trabajo de disipación plástica, es proporcional al volumen ($\ell^2 \cdot t$). Estos tres términos se relacionan a través de la siguiente expresión:

$$W_f = W_e + W_p = w_e \ell t + w_p \beta \ell^2 t \quad (1)$$

Donde ℓ es la longitud de ligamento, t el espesor y β un factor de forma del volumen deformado plásticamente. Expresando ambos miembros en sus términos específicos obtenemos una relación lineal entre la energía específica de fractura (w_f) y la longitud de ligamento:

$$w_f = w_e + \beta w_p \ell \quad (2)$$

Obteniendo el trabajo esencial específico de fractura (w_e) y el término plástico (βw_p) como la ordenada en el origen y la pendiente, respectivamente, al representar los valores de w_f frente a ℓ .

Para aplicar el método del EWF se emplearon probetas rectangulares de geometría DDENT. Las dimensiones de las probetas fueron de 60x30x0.30 mm. Se utilizaron 5 longitudes de ligamento que oscilaron entre 5 y 25

mm con un intervalo de 5 mm Para cada longitud de ligamento se realizaron tres réplicas. La deformación se siguió mediante un videoextensómetro, según el procedimiento descrito en trabajos previos [13].

Las condiciones de ensayo para la caracterización mecánica y a fractura fueron: velocidad de desplazamiento de mordazas de 1mm/min. y temperatura ambiente controlada (22 ± 1 °C).

3. RESULTADOS Y DISCUSIÓN

3.1. Caracterización Térmica

En la figura 1 se muestran los termogramas correspondientes a los primeros calentamientos de las muestras. En el caso de las láminas de PLA sin tratamiento térmico se observa una endoterma aproximadamente a la temperatura de transición vítrea (63°C). Esta señal es típica de polímeros amorfos envejecidos físicamente. En ellos, es frecuente la absorción de calor durante la transición vítrea que corresponde a la entalpía de relajación (ΔH_{rel}), el área bajo la curva de la endoterma a T_g [14] ΔH_{rel} puede ser utilizada como un indicador del estado de envejecimiento [15, 16]. Durante el envejecimiento se produce una disminución del volumen libre y de la energía interna del material, restringiendo la movilidad de segmentos moleculares. El PLA envejecido tiene, por tanto, menor entalpía y energía potencial que el PLA no envejecido. De modo que, durante el calentamiento, el PLA envejecido necesitará más energía (ΔH_{rel}) para completar la transición vítrea. En las muestras a las que se les ha aplicado el tratamiento de rejuvenecimiento no se observa la endoterma correspondiente al ΔH_{rel} (Fig. 1-c y 1-d).

También se puede apreciar un pico exotérmico que sólo aparece en las muestras del PLA 4032D (Fig. 1-b y 1-d), correspondiente a un fenómeno de cristalización en frío. La tendencia del PLA a cristalizar en frío depende, entre otros factores, de la velocidad de calentamiento y del contenido de isómero L-láctico que tenga el material [17], siendo esta última la razón por la que el PLA 2002D requiere de un tiempo para cristalizar mayor que el utilizado en las condiciones experimentales.

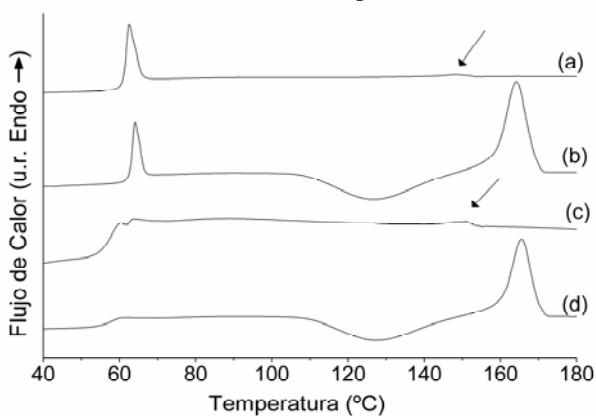


Figura 1. Termogramas de los materiales: (a) 2002 D, (b) 4032D, (c) 2002D-T y (d) 4032 D-T.

Además, se observa una endoterma en el intervalo de temperaturas situado entre 150 y 170 °C, que corresponde a la fusión de los cristales de PLA. Esta endoterma es de mayor intensidad en las muestras de PLA 4032D que en las del PLA 2002D (indicadas con una flecha en la Fig. 1). Esto se debe a que la cristalización en frío producida durante el calentamiento genera una mayor proporción de cristales en el PLA 4032D y por tanto, mayor intensidad en los picos de fusión.

El grado de cristalinidad de las diferentes muestras (X_c) se cálculo restando las entalpías de cristalización en frío (ΔH_{cc}) de las entalpías de fusión (ΔH_m), según la siguiente ecuación [2]:

$$X_c = \frac{\Delta H_m - \Delta H_{cc}}{\Delta H_o} \times 100 \quad (3)$$

Donde ΔH_o corresponde al valor teórico de la entalpía de fusión de un PLA 100% cristalino, en este caso estimado en 93 J/g [18]. Estos cálculos se realizaron sobre los datos obtenidos durante el primer barrido térmico. Los porcentajes de cristalinidad (X_c), las temperaturas de transición vítrea (T_g) y las temperaturas de fusión (T_m) de todos los materiales se muestran en la tabla 1.

Tabla 1. Resumen de las propiedades térmicas

Propiedades Térmicas	PLA 2002D	PLA 2002D-T	PLA 4032D	PLA 4032D-T
T_g (°C)	60.1±0.1	56.0±0.1	61.3±0.5	57.1±0.4
T_m (°C)	148.0±0.5	148.4±0.6	164.1±0.1	165.2±0.5
ΔH_{cc} (J/g)	-	-	29.2±1.4	30.7±0.4
ΔH_m (J/g)	0.80±0.01	1.3±0.3	31.2±0.4	33.5±0.2
X_c (%)	0.86±0.02	1.4±0.3	2.2±1.1	3.0±0.7

Se encontró que las muestras sin tratamiento en ambos PLA poseen mayores valores de T_g debido a la disminución de la movilidad molecular resultante del proceso de envejecimiento. Ésta hace que sea necesario calentar el PLA a mayores temperaturas para que se completen las transformaciones morfológicas ocurridas durante la transición vítrea.

También se observó que las muestras del PLA 4032D presentan mayores valores de T_m que las del PLA 2002D. El punto de fusión de un polímero semicristalino, de forma general, está determinado por el tamaño y la perfección de los cristales. El mayor contenido de isómero L-Láctico en PLA 4032D hace que se formen cristales de mayor espesor lamelar debido a su mayor regularidad estructural. Por otra parte, los bajos porcentajes de cristalinidad determinados indican que las láminas se encuentran en un estado esencialmente amorfo. Así mismo, no se observan evidencias de que el tratamiento de rejuvenecimiento afecte a la temperatura de fusión ni al porcentaje de cristalinidad en estos materiales.

3.2. Caracterización Mecánica

La figura 2 muestra las curvas tensión vs. deformación a tracción de los dos grados comerciales de PLA con y sin tratamiento de rejuvenecimiento. Se aprecia que los materiales no tratados son más rígidos, tienen mayor tensión a cedencia y menores deformaciones a rotura. En la Fig. 3 se muestran probetas post-mortem del PLA 4032D y PLA 4032D-T donde se puede apreciar una cedencia sin formación de cuello y con presencia de crazes en las primeras (Fig. 3-a) y un comportamiento mucho más dúctil con cedencia por cizalladura y formación de cuello en las segundas (Fig, 3-b). Estas observaciones coinciden con los resultados obtenidos por otros autores [6].

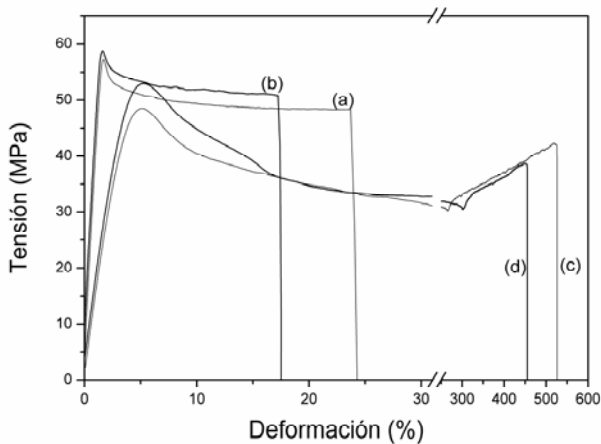


Figura 2. Curvas tensión-deformación a tracción: (a) PLA 2002D, (b) PLA 4032D, (c) PLA 2002D-T y (d) PLA 4032D-T.

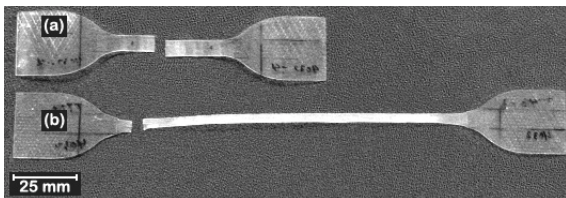


Figura 3. Probetas ensayadas a tracción: a) PLA 4032D y b) PLA 4032D-T.

En la tabla 2 se muestran los valores de las propiedades mecánicas evaluadas para los cuatro materiales. Se puede apreciar que el PLA 4032D, con y sin tratamiento de rejuvenecimiento, posee valores ligeramente superiores de módulo y de tensión a la cedencia pero menor elongación a rotura que el PLA 2002 D.

Tabla 2. Parámetros de la caracterización mecánica.

Materiales	σ_y (MPa)	E (GPa)	ϵ_b (%)
PLA 2002D	56.2±0.7	4.2±0.2	24±5
PLA 4032D	58.4±0.5	4.6±0.1	17±4
PLA 2002D-T	47.3±1.1	3.3±0.2	456±100
PLA 4032D-T	53.4±0.6	3.5±0.3	422±50

Estos resultados demuestran que las propiedades mecánicas de estos dos grados comerciales de PLA dependen significativamente de la historia térmica a la que han sido sometidos. Como se comentó anteriormente, la aplicación del tratamiento de rejuvenecimiento provoca un aumento del volumen libre de las cadenas poliméricas, con un descenso de la T_g y un aumento de la energía potencial del sistema (ΔH_{rel}). Estas variaciones facilitan la movilidad de los segmentos de cadena, lo que permite una mayor deformación local y menor aportación de energía para alcanzar la cedencia del material (menores valores de σ_y) [6].

Por último, el tratamiento de rejuvenecimiento produce una transición frágil-dúctil de los dos grados de PLA, permitiendo el estudio del comportamiento a fractura mediante la técnica del EWF. No obstante, al estar limitada esta técnica al comportamiento de fractura dúctil, sólo se puede aplicar durante pocas horas después del tratamiento de rejuvenecimiento, ya que volverá a ser frágil por el envejecimiento físico, ocurrido a temperatura ambiente.

3.3. Caracterización a la Fractura

Para comprobar la validez de la aplicación del método EWF en todos los materiales, se ensayaron probetas DDENT con tres longitudes de ligamento diferentes para los dos grados de PLA con y sin tratamiento térmico. Estos ensayos, además, se realizaron grabando imágenes de los mismos con un sistema de cámaras estereoscópicas y procesamiento de imágenes simultáneas, controlado por un paquete de software GOM-ARAMIS, el cual permite la correlación digital de imágenes en una medida del campo de deformaciones tridimensional. De esta manera se pudieron seguir las variaciones en el espesor de cada punto de la probeta durante la ejecución del ensayo.

En la Figura 4 se muestran, a modo de ejemplo, las curvas obtenidas para probetas con $l \sim 10$ mm de los materiales 4032D y 4032D-T. Se puede apreciar en esta figura una transición frágil-dúctil en el comportamiento a fractura, promovida por el tratamiento de rejuvenecimiento. El campo de deformaciones mostrado en la Fig. 4 está referenciado a una escala entre el 0 y el 5% de reducción de espesor, con el fin de apreciar la deformación elástica y plástica alrededor de las entallas en todos los materiales. Si se observa el halo de deformación alrededor del ligamento de la entalla en el momento previo al inicio de la propagación de la grieta (punto c en la Fig. 4), se aprecia que éste es mayor para el 4032D que para el 4032D-T. Este halo con reducciones de espesor inferiores al 3% se correspondería con deformaciones principalmente elásticas, por tanto reversibles. En el caso del 4032D, la energía elástica se recuperaría de forma rápida en la propagación inestable de la grieta, mientras que en el 4032D-T lo haría en forma de deformación plástica con la formación del cuello de estricción en el área de

ligamento. La variación del espesor en el centro de la probeta durante todo el ensayo muestra que en el 4032D-T alcanza el 60% y apenas el 10% en el caso del 4032D.

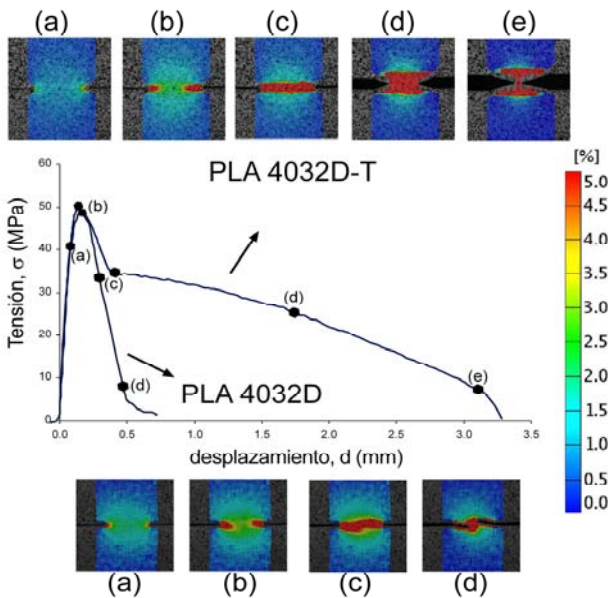


Figura 4. Curvas σ - d con micrografías mostrando el avance de la grieta y la reducción del espesor (%) para $\ell = 10\text{mm}$ (PLA 4032D y 4032D-T).

Sólo los materiales con tratamiento de rejuvenecimiento cumplen con los requisitos para la aplicación de la teoría del EWF. A modo de ejemplo, en la figura 5 se muestran las curvas fuerza-desplazamiento (F-d) obtenidas para el PLA 2002D-T en las que se puede apreciar que cumplen con el criterio de similitud geométrica [12]. En la Figura 6 se representa w_f vs. ℓ para los dos materiales con tratamiento de rejuvenecimiento, ajustando las rectas de regresión por el método de mínimos cuadrados.

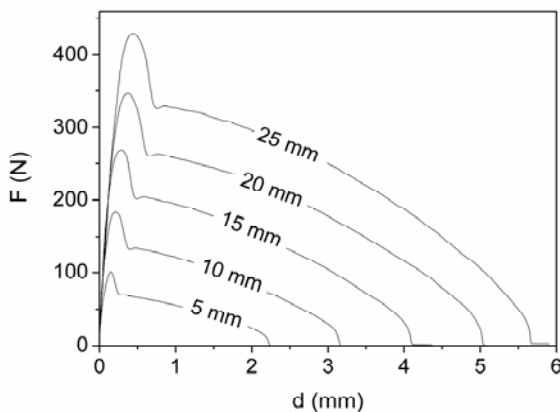


Figura 5. Curvas F-d obtenidas para el PLA 2002D-T

A pesar de no cumplir con los requisitos de EWF, los materiales sin tratamiento (2002D y 4032D) mostraron una relación lineal entre w_f y ℓ , pudiendo calcular los parámetros de fractura. Estos valores nos permiten, de forma orientativa, evaluar la variación de la tenacidad con el tratamiento de rejuvenecimiento. La Tabla 3

resume los parámetros de fractura de todos los materiales.

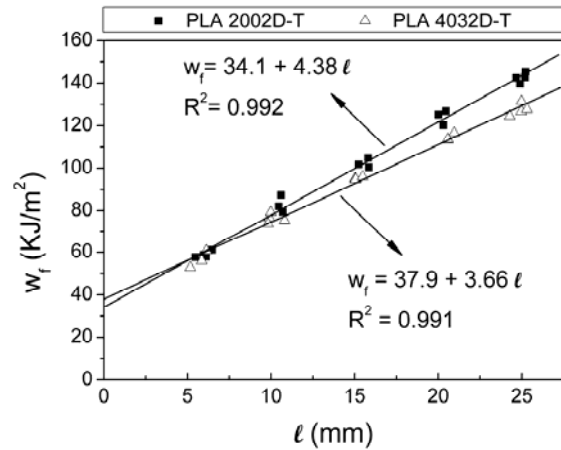


Figura 6. Gráfico de w_f vs. ℓ para el cálculo de los parámetros de fractura.

Tabla 3. Parámetros de fractura.

Materiales	w_e (kJ/m ²)	βw_p (MJ/m ³)
PLA 2002D*	12*	0.39*
PLA 4032D*	11*	0.45*
PLA 2002D-T	34.1±1.7	4.4±0.1
PLA 4032D-T	37.9±1.5	3.7±0.1

*Valores orientativos, no presentan fractura dúctil.

Se observa que los valores de w_e obtenidos para el 2002D y 4032D son similares entre sí aunque mayores que los valores estimados de G_{IC} obtenidos para el PLA 2002D mediante la LEFM en probetas inyectadas, que fue de 2.44 kJ/m² [19].

Con respecto a los casos en los que se puede aplicar la teoría del EWF, se aprecia en la Tabla 3 que el PLA 4032D-T tiene mayor valor de w_e que el 2002D-T. Teóricamente, según Mai y colaboradores [20] w_e involucra los procesos de deformación plástica para formar el cuello y el trabajo necesario para el inicio de la propagación de la grieta. Así pues, w_e será mayor cuanto mayor sea el valor de σ_y y de la deformación hasta estricción. El PLA 4032D-T presenta mayor σ_y que el 2002D-T (Tabla 2), por lo que requiere de una mayor cantidad de trabajo para la estricción de la zona de proceso de la fractura. A su vez, en la Fig. 2 se aprecia que el área bajo las curvas σ - ϵ hasta la cedencia de los materiales rejuvenecidos es mucho mayor que la de sus respectivos envejecidos, justificando los mayores valores de w_e .

Con respecto al término plástico, es el PLA 2002D-T el que posee un mayor valor de βw_p . Arkhireyeva y col. encontraron que βw_p , que representa la capacidad de disipar energía por deformación plástica, aumenta con el incremento de la ductilidad y disminuye con el aumento de σ_y [21]; el PLA 2002 D en los ensayos a tracción mostró precisamente una mayor ϵ_b y un menor σ_y (Tabla 2) por lo que estaría en concordancia con este trabajo previo.

4. CONCLUSIONES

La aplicación del tratamiento de rejuvenecimiento provoca una variación del volumen libre de las cadenas poliméricas, que se traduce en una variación de las propiedades térmicas, con un descenso de la T_g y un aumento de la energía potencial del sistema (ΔH_{rel})

Este tratamiento produjo una transición frágil-dúctil en los dos grados de PLA, permitiendo la aplicación de la técnica del EWF. El EWF no se había aplicado hasta ahora a láminas de PLA. Se encontró un incremento considerable de la tenacidad a fractura de los dos materiales producto del tratamiento de rejuvenecimiento.

Por otro lado, el empleo de uno u otro grado de PLA en estado amorfo no revierte en grandes diferencias en las propiedades mecánicas ni comportamiento a fractura.

AGRADECIMIENTOS

Los autores desean agradecer al Ministerio de Educación y Ciencia la financiación del proyecto MAT 2007-62450. J. Velázquez agradece a la Agencia Española de Cooperación Internacional para el Desarrollo (AECID) la concesión de una beca predoctoral.

REFERENCIAS

- Sarasua, J.R., A.L. Arraiza, P. Balerdi, and I. Maiza, *Pol. Eng. Sci.*, 2005. 45(5): p. 745-753.
- Auras, R., B. Harte, and S. Selke, *Macromolecular Bioscience*, 2004. 4(9): p. 835-864.
- Miyata, T. and T. Masuko, *Polymer*, 1998. 39(22): p. 5515-5521.
- Hutchinson, J.M., *Progress In Polymer Science*, 1995. 20(4): p. 703-760.
- Aou, K., S.L. Hsu, L.W. Kleiner, and F.W. Tang, *J.Phys. Che.B*, 2007. 111(42): p. 12322-12327.
- Pan, P.J., B. Zhu, and Y. Inoue, *Macromolecules*, 2007. 40(26): p. 9664-9671.
- Quan, D.P., K.R. Liao, and J.H. Zhao, *Acta Polymerica Sinica*, 2004(5): p. 726-730.
- NatureWorks® PLA Polymer 2002D - Data Sheet. 2005 [cited 27.11.2009]; Available from: <http://www.natureworkslc.com/>.
- Li, H.B. and M.A. Huneault, *Polymer*, 2007. 48(23): p. 6855-6866.
- Xiao, H.W., W. Lu, and J.T. Yeh, *J. App. Pol. Sci.* 2009. 113(1): p. 112-121.
- Carrasco, F., P. Pagès, J. Gámez-Pérez, O.O. Santana, and M.L. MasPOCH, *Pol. Deg. Sta.* doi:10.1016/j.polymdegradstab.2009.11.045.
- Clutton, E., *Essential Work of Fracture*, in *Fracture mechanics testing methods for polymers, adhesives and composites*, A.P. D.R. Moore, and J.G. Williams, Editor. 2001, Elsevier Science: Oxford. p. 177-195.
- Gamez-Perez, J., O. Santana, A.B. Martinez, and M.L. MasPOCH, *Pol. Tes.*, 2008. 27(4): p. 491-497.
- Mo, X.Q. and X.Z. Sun, *Journal Of Polymers And The Environment*, 2003. 11(1): p. 15-22.
- Arefazar, A. and J.N. Hay, *Polymer*, 1982. 23(8): p. 1129-1132.
- Cowie, J.M.G., S. Harris, and I.J. McEwen, *Macromolecules*, 1998. 31(8): p. 2611-2615.
- Kolstad, J.J., *Journal Of Applied Polymer Science*, 1996. 62(7): p. 1079-1091.
- Fischer, E.W., H.J. Sterzel, and G. Wegner, *Colloid & Polymer Science*, 1973. 251(11): p. 980-990.
- MasPOCH, M.L., L. Nascimento, J. Gamez-Perez, and O. Santana. *Anales de mecánica de la Fractura*, Santander, 2009, 26: 232-235.
- Mai, Y.W., B. Cotterell, R. Horlyck, and G. Vigna, *Pol. Eng. Sci*, 1987. 27(11): p. 804-809.
- Arkhireyeva, A. and S. Hashemi, *Polymer*, 2002. 43(2): p. 289-300.

FRACTURE BEHAVIOR OF AN EPBC FILM. STUDY OF THE RELATIONSHIP BETWEEN J₀ AND EWF

A.B. Martinez¹, A. Delgado¹, A. Segovia¹, M.A. Sanchez-Soto¹ A. Salazar²

¹ Centre Català del Plàstic. Universitat Politècnica de Catalunya
 C/ Colom 114
 08222 Terrassa, España
 E-mail: antonio.martinez@upc.edu

² Departamento de Ciencia e Ingeniería de Materiales,
 Universidad Rey Juan Carlos,
 Tulipán s/n 28933 Móstoles, España

ABSTRACT

The fracture behavior for a film of ethylene-propylene block copolymer has been studied applying the essential work of fracture method. Double-Edge Notch Tensile (DDENT) specimens were sharpened by two different techniques. The first technique has been using the conventional method of the razor blade; the second one, using a femtolaser ablation beam. The notch tip radiuses were quite similar. In the case of the razor blade method, some plastic deformation at the crack tip was found. The essential work of fracture (w_e) value for femtolaser sharpened specimens was significantly shorter than for the razor blade sharpening specimens. In this order, the slopes corresponding to the plastic work dissipation factor (βw_p) were quite similar. Results aim to say that the initiation point and the corresponding energy for which w_e is achieved may be considered as the energy of initiation (J_0) for the crack growing propagation. The propagation behavior seems to be the same for both notch sharpening methods. The J_0 value at initiation and w_e were quite similar; the βw_p terms are analyzed from J-R plots.

KEY WORDS: EWF, EPBC film, J_0 , fracture initiation.

1. INTRODUCTION

According to the European Structural Integrity Society-Technical Committee 4 (ESIS-TC4) protocol on Essential Work of Fracture (EWF), edited by Clutton [1-3], the energy associated with the fracture process may be separated in two terms; one, W_e specific to the fracture of the material and, W_p that is related to gross plastic deformation. These two terms according to the ESIS TC-4 protocol are termed essential and non-essential work of fracture respectively. In plane stress, W_e rises proportionally with the initial ligament length l_0 and the W_p is proportional to the volume of the non-reversible deformation zone. In a pre-cracked specimen with thickness “t” and ligament length “l” (fig. 1), the total work of fracture by surface unit is:

$$w_t = w_e + \beta w_p l \tag{1}$$

Where βw_p is a factor correlated with the volume of the plastic zone, w_e is the essential work of fracture and

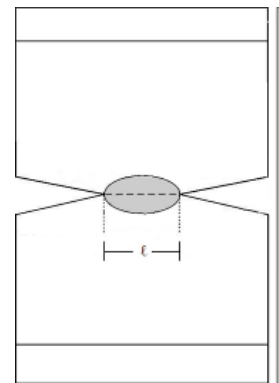


Fig. 1 Double Edge Notched Tension specimen

The here used approach of J is based on the consideration of J as an energy accumulation function, in this way J_i is the Riemann’s sum of the load-displacement multiplications from the start of the test to an instant i; divided by the initial measured section of the specimen ($l_0 t_0$), as shown in equation (2).

$$J_i = \frac{1}{l_0 t_0} \sum_{\theta=1}^i [F \cdot (Zc_{\theta} - Zc_{\theta-1})] \tag{2}$$

2. MATERIALS AND METHODS

The material, an Ethylene-Propylene Bock Copolymer (EPBC), was extruded in sheets of 0.5 mm in thickness, prepared in 90mm x 60 mm DDENT specimens at the machine direction (MD) and sharpened by femtolaser beam and by steel razor blade methods. Some physical properties are shown in table 1.

Table 1 Material characterization

Technique	Property (unit)	Value
RMN	Ethylene Content (% wt)	8.5
ASTM-D638 $v = 2$ mm/min	σ_y (MPa)	26.3 ± 0.1
	E (GPa)	1.21 ± 0.01
	Theoretical DDENT σ_m (MPa)	30.3 ± 0.1

The samples was tensile tested at 23°C in the longitudinal axis of the specimen direction, the crosshead displacement rate was stroke controlled at 2 mm/min with a ZWICK-ROELL Amsler HC 25 hydraulic test machine. The instantaneous ligament length was measured with a Digital Image Correlation System ARAMIS, distributed by GOM.

The sharpening methods was carried out as described on [4] for fresh steel razor blade and femtosecond pulsed laser ablation.

3. RESULTS AND DISCUSSIONS

3.1. EWF results

Following the ESIS-TC4 protocol for EWF, there was obtained the values of maximal net stress across a mean of 28.2 ± 0.26 MPa for razor specimens as shown in Figure 2; and a mean of 28.7 ± 0.73 MPa, Figure 3, for femtolaser specimens.

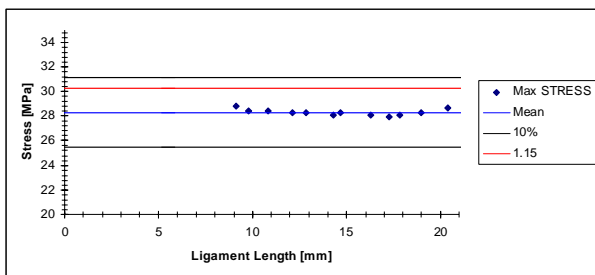


Fig. 2 Maximal stress graph with $\pm 10\%$ of the mean and 1.15 limits for Razor specimens

The regression of the total work of fracture vs. initial ligament length points is shown on Figure 4 for razor and femtolaser specimens.

For razor specimens, the w_e parameter is 164.46 ± 9.17 kJ/m²; and for femtolaser specimens, w_e is 127.05 ± 11.58 kJ/m². The βw_p factors are 22.55 ± 0.61 MJ/m³

for razor specimens and 21.34 ± 0.85 MJ/m³ for femtolaser specimens.

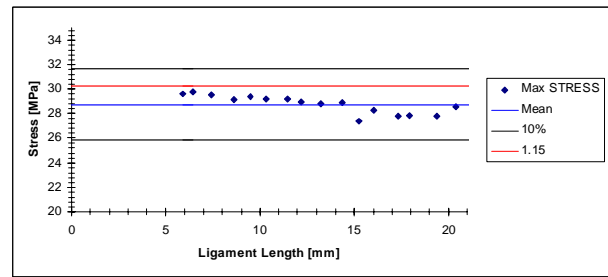


Fig. 3 Maximal stress graph with $\pm 10\%$ of the mean and 1.15 limits for Femtolaser specimens

On the w_e values for both sharpening methods is a difference of almost 40 kJ/m². This difference is probably due to the characteristics at the end of the notch tip for each sharpening method. There is an accumulation of material at the notch tip, as reported in [4].

For the βw_p factors there are no longer than 2 MJ/m³ differences on values. This is because the same region of material is considered in the displacement, as furthered in [5]. It is possible to say that these factors are quite similar, according to Figure 4.

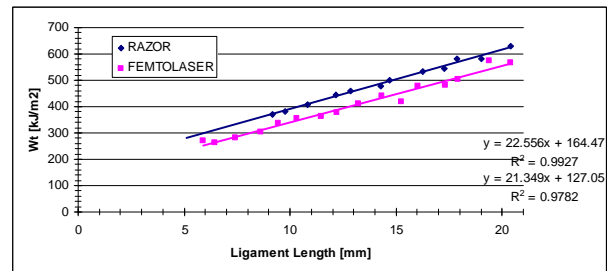


Fig. 4 Comparison between final work of fracture plots for both sharpening method specimens

Finally, for the conventional EWF considerations, it is possible to further that there exist differences on w_e value but not great differences on βw_p for different sharpening methods.

3.2. J results

When energy accumulation described in equation (2) reaches w_e , it is possible to mark a point on the fracture process plot. As well as the area under the curve is equal to w_e , for the specimens from EWF tests, these mark-points are quite similar on displacement.

For different sharpening method, the areas under the curve at w_e are different on displacement values. This aim to say that the phenomena related to this mark-point shows dependence with the sharpening method.

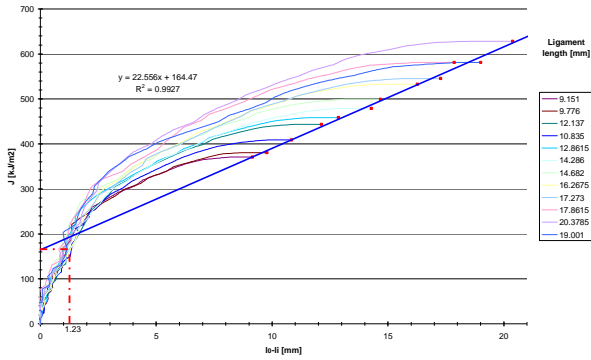


Fig. 5 Accumulated work (J) vs. Δa (l_0-l_i) with final work regression for Razor specimens

It seems that the final behavior, after w_e , for both sharpening methods is similar, there is a resistance to crack propagation. This may be shown because after w_e , the propagation of the fracture keeps the same behavior for both sharpening methods.

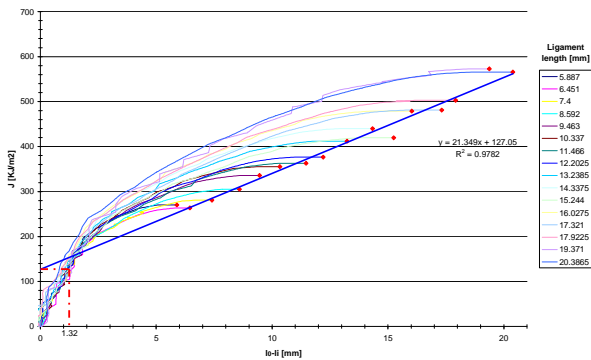


Fig. 6 Accumulated work (J) vs. Δa with final work regression for Femtolaser specimens

In Figures 5 and 6 are plotted the cumulated areas under the curve, energy J in kJ/m², for razor and femtolaser specimens respectively. These curves show the behavior or resistance in energy terms to crack propagation, J-R curves.

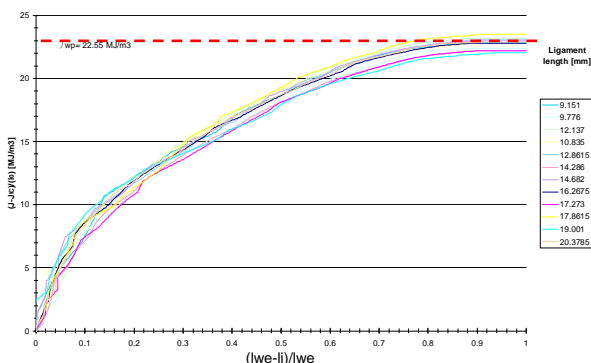


Fig. 7 Normalization of J behavior for Razor specimens

As shown in Figures 5 and 6, the regression of the final work of fracture, final J, and the maximal Δa is congruent to EWF main regression for both specimen

series. This is logic because maximal Δa in complete fracture is the initial ligament length and final J is w_t .

A normalization of the behavior is propounded on figures 7 and 8, this is done in the aim to describe the complete crack behavior. On these figures, the end values of the curves are near to βw_p .

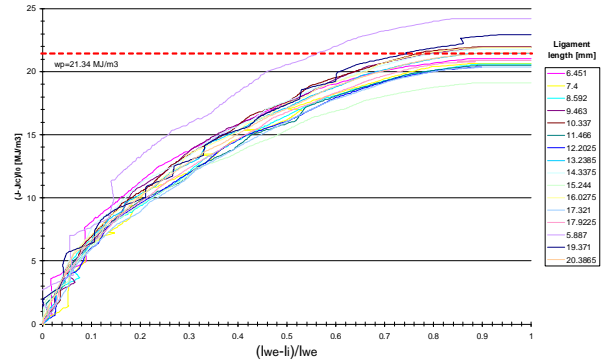


Fig. 8 Normalization of J behavior for Femtolaser specimens

On figure 8, for femtolaser specimens, it is possible to regard scatter in the end values of normalization, this may be attributed to experimental differences.

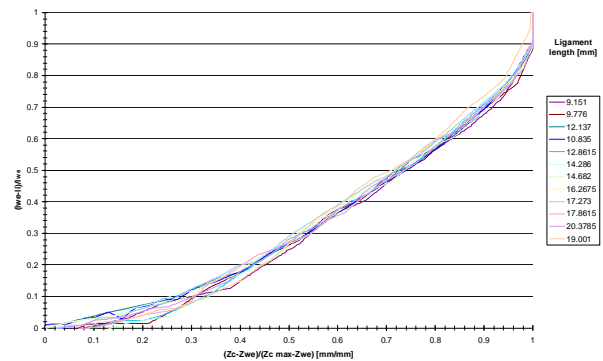


Fig. 9 Normalization of J behavior for Razor specimens

For figures 9 and 10, the crack growth was normalized as a function of the displacement, these figures shown a relative well-similarity for all specimens.

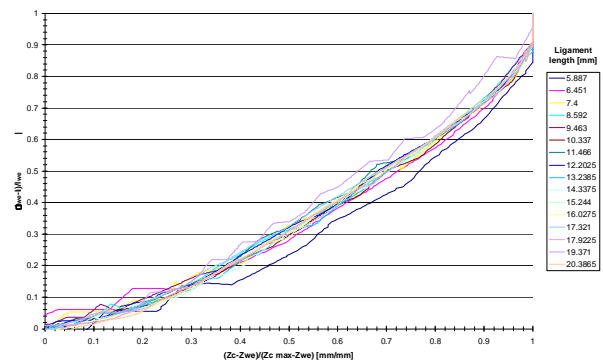


Fig. 10 Normalization of J behavior for Femtolaser specimens

On the crack behavior normalization figures it is possible to see a concordance between curves and even between notch sharpening methods, as shown in figures 11 and 12.

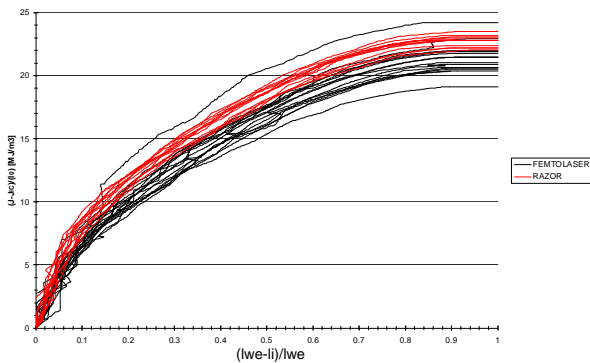


Fig. 11 Notch sharpening comparison on normalization of J behavior

No great difference are shown between notch sharpening methods on here used normalizations, it aims to say that βw_p is a material factor that does not show dependence on the notch tip conditions and that the crack growth of the material may be normalized.

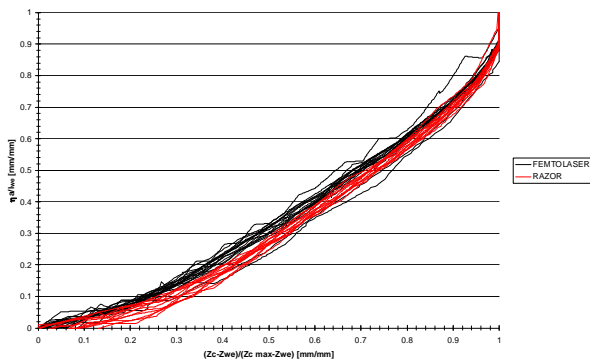


Fig. 12 Notch sharpening comparison on normalization of J behavior

Note that for all the normalizations, the crack behavior starts at w_e , and this value is determined by the EWF method. No before w_e behavior was regarded for normalizations, this behavior (blunting) is only shown on figures 5 and 6.

4. CONCLUSIONS

For the material here studied. The value of J in which the propagation of fracture process starts, J_0 , is shown similar or equal to w_e from the EWF test. This value of energy is given as a function of the conditions at the notch tip. The factor of plastic work dissipation βw_p is regarded as a factor that does not shows dependence on the notch tip characteristics. βw_p must be only correlated to the amount of material between distance measurement marks.

It is possible to normalize the fracture behavior after w_e , on energy terms as shown in figures 7 and 8; and on crack growth distance as shown in figures 9 and 10. It aims to say that J is in function of Δa and Δa is in function of displacement. The law for these relationships may be propounded.

ACKNOWLEDGEMENTS

The authors want to thank the Education and Science Ministry for the financial support of this work through the MAT2006-13354 project. A. Delgado wants to acknowledge the European Commission and the Joint European Master Programme on Advanced Materials Science and Engineering for the support through an Erasmus Mundus Scholarship.

REFERENCES

- [1] Clutton, E., *Essential Work of Fracture*, in *Fracture Mechanics testing methods for polymers, adhesives and composites*, D.R. Moore, A. Pavan, and J.G. Williams, Editors. 2001, Elsevier Science, Ltd.: Oxford. p. 177-195.
- [2] Clutton, E., *Testing Protocol for Essential Work of Fracture*, ESIS., Editor. 1997, European Structural Integrity Society (ESIS) - TC4.
- [3] Clutton, E.Q. and J.G.W.a.A. Pavan, *ESIS TC4 experience with the essential work of fracture method*, in *European Structural Integrity Society*. 2000, Elsevier. p. 187-199.
- [4] Martínez, A.B., et al., *Influence of femtolaser notch sharpening technique in the determination of essential work of fracture (EWF) parameters*. *Engineering Fracture Mechanics*, 2009. **76**(9): p. 1247-1254.
- [5] Gamez-Perez, J., et al., *Use of extensometers on essential work of fracture (EWF) tests*. *Polymer Testing*, 2008. **27**(4): p. 491-497.

DETERMINATION OF THE CRACK INITIATION ENERGY OF FILMS IN PLANE STRESS

A.B. Martínez¹, A. Segovia¹, D. Arencón¹, S. Illescas¹, J. Rodríguez²¹ Centre Català del Plàstic (CCP), Universitat Politècnica de Catalunya,
C/ Colom 114, 08222 Terrassa, Spain
E-mail: antonio.martinez@upc.edu² Departamento de Ciencia e Ingeniería de Materiales,
Universidad Rey Juan Carlos,
C/ Tulipán s/n, 28933 Móstoles, Spain

ABSTRACT

The fracture behaviour for a film of an ethylene-propylene block copolymer has been determined applying the essential work of fracture method. Double-edge notched tensile specimens were sharpened by two different techniques. The first technique has used the conventional method of the razor blade. The second one has employed a femtolaser ablation beam. It is studied the influence of the notch sharpening and it is proposed a new way to analyze the results.

KEY WORDS: essential work of fracture, sharpening method, femtolaser ablation.

1. INTRODUCTION

The technique of the essential work of fracture (EWF) is a method appropriate for the fracture toughness measurement in materials where the crack initiation occurs through a highly deformed and yielded material. However, the interpretation of the fracture parameters obtained with the essential work of fracture method is still a subject of discussion and debate [1].

One of the main problems when analyzing the fracture behaviour of a ductile thin polymer sheet is to establish the crack initiation point, which provides the evaluation of the initiation fracture energy of the crack. However, in this work, the data are presented in a novel way, that allows deducing the point of crack initiation. At the same time, the influence of the notch sharpening method is analyzed.

2. EXPERIMENTAL DETAILS

Deeply double edge notched tensile specimens (DDENT) cut out (in MD direction) from extruded films, 0.5 mm-thick, of an ethylene-propylene block copolymer with 8.5 % wt. of ethylene have been employed.

The essential work of fracture method has been applied on DDENT specimens; by one hand in some samples the notches were sharpened with the conventional method by using a razor blade, and by other hand, in some samples the notches were sharpened through an ablation with a femtolaser beam.

The tests have been carried out at room temperature in a universal testing machine, measuring the displacement of the cross-head located at 60 mm over the specimens.

3. RESULTS AND DISCUSSION

In Figure 1 are showed the micrographs obtained by scanning electron microscopy of the notches sharpened by femtolaser (Fig. 1a, 1b) and razor blade (Fig. 1c, 1d) Both notches have a similar tip radius, but the notches sharpened by razor blade display a great plastic deformation, that causes an accumulation of material in the crack tip.

Figure 2 represents in the classic way, the values of the load vs. displacement when the sharpening was made by femtolaser, whereas Figure 3 shows the validation criteria of the obtained data. In Figure 4 is displayed the EWF plot.

The stress vs. displacement plot (Figure 5) can be obtained from Fig. 2, dividing the load by the measured initial ligament section. The shadowed area corresponds with the specific essential work of fracture (w_e) value. In Fig. 5, the curves overlap among themselves up to a displacement value which corresponds with the shadowed area (w_e). From this point, they do not overlap anymore.

The frames shown in Fig. 5 indicate that prior to this point there is not crack propagation and afterwards, the crack growth has already started. Nevertheless, the exact frame where blunting becomes crack initiation is very difficult to determine. Therefore, w_e can be considered as the energy just up to crack initiation.

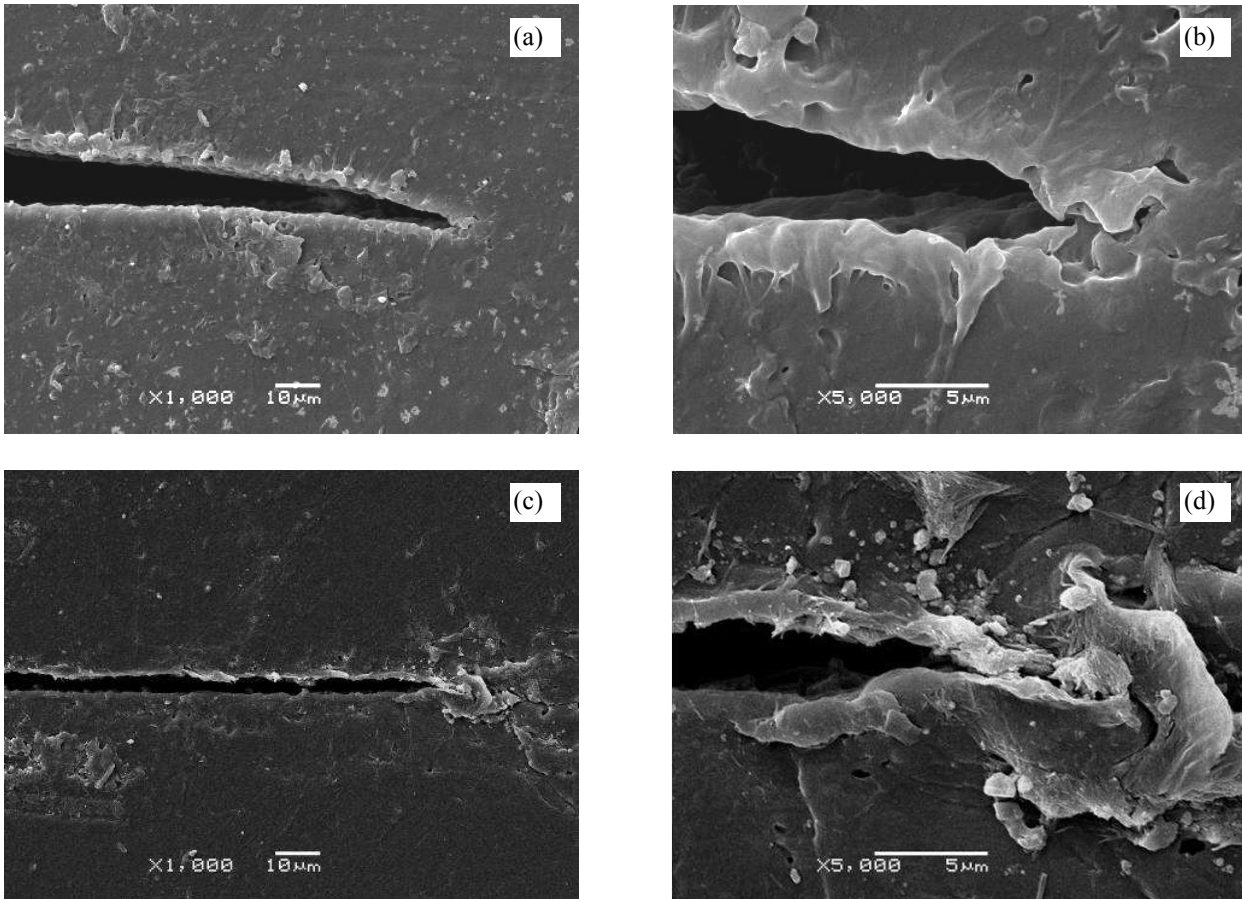


Figure 1. Scanning electron micrographs of notches sharpened by (a,b) femtolasers and (c,d) razor blade.

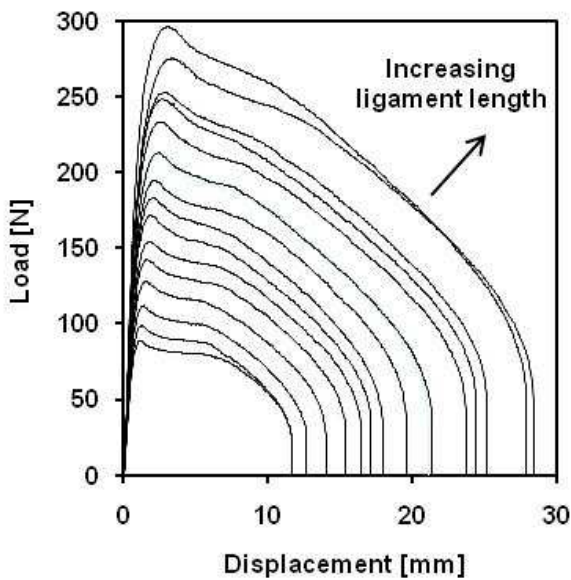


Figure 2. Load vs. displacement plots for DDENT specimens sharpened by femtolasers

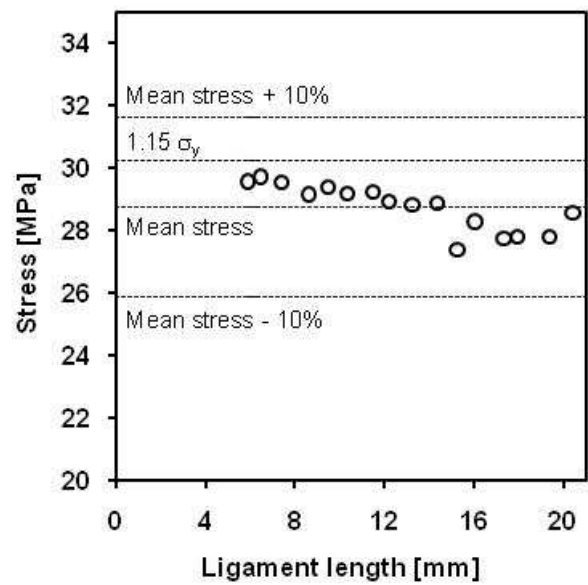


Figure 3. Validation criteria of the experimental points obtained from DDENT specimens sharpened by femtolasers.

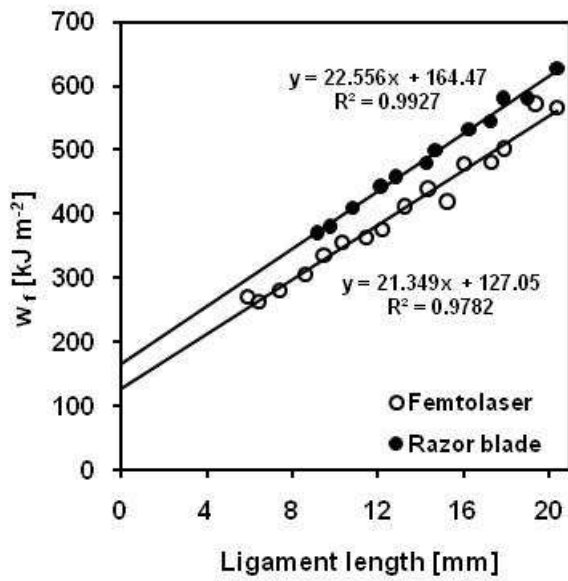


Figure 4. EWF plots obtained from specimens sharpened by femtolaser and razor blade.

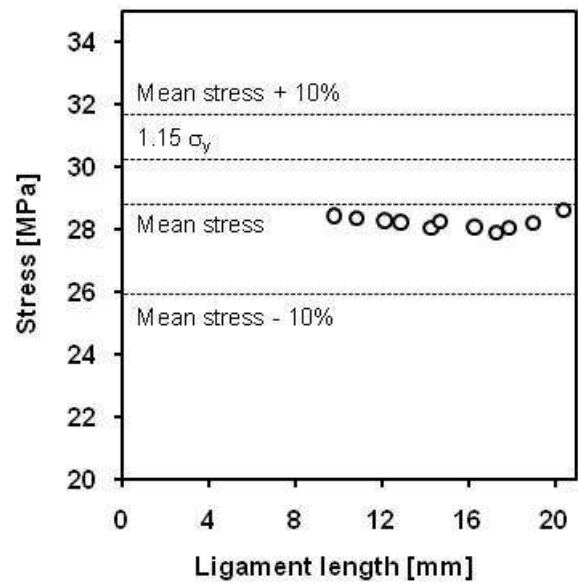


Figure 6. Validation criteria of the experimental points obtained from DDENT specimens sharpened by razor blade.

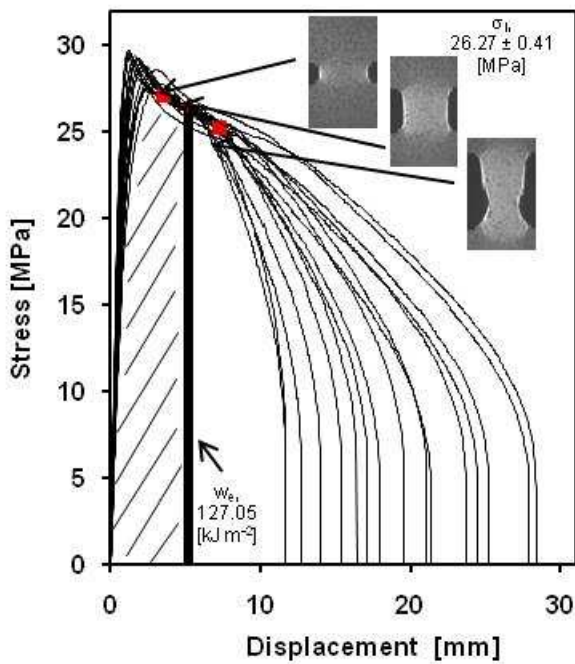


Figure 5. Stress vs. displacement plots for DDENT specimens sharpened by femtolaser.

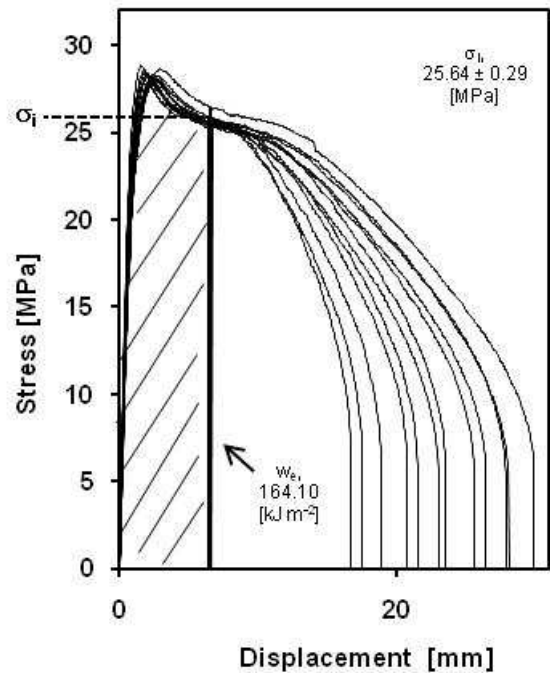


Figure 7. Stress vs. displacement plots for DDENT specimens sharpened by razor blade.

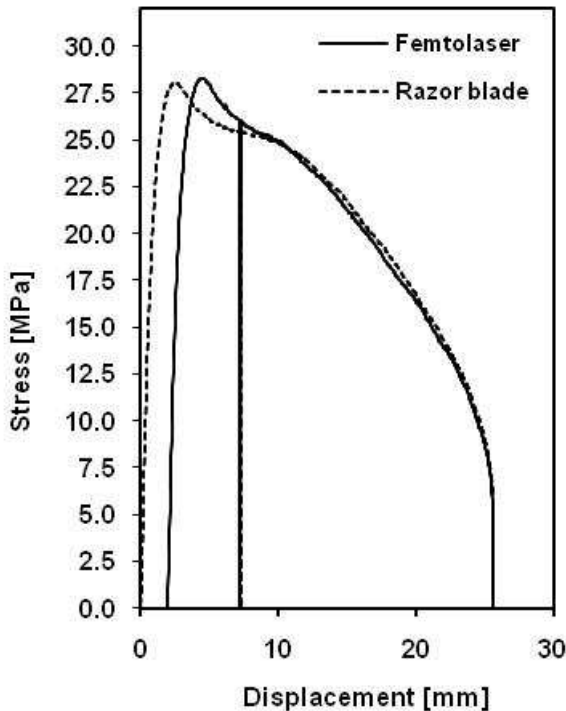


Figure 8. Stress vs. displacement plots for DDENT specimens sharpened by razor blade.

The same procedure has been employed with the specimens with notches sharpened by a razor blade. In Figure 6 is displayed the data validation, in Figure 4 the EWF plot, whereas in Figure 7 is represented the new plot stress vs. displacement.

In the specimens sharpened by a razor blade, sometimes, both notches did not initiate and propagate simultaneously. These specimens have not been taken into account in the analysis of the results, and have been eliminated.

The displacement at which the cracks start to initiate is lower for the femtolaser notched specimens than for the razor blade ones.

The higher displacement needed for razor blade sharpening specimens to start the crack growth can be attributed to the material volume accumulation at the notch tip, whereas femtolaser notch sharpening method do not produce any visible plastic damage.

The crack starts to grow at the same initiation stress, σ_i , regardless to the notch sharpening method.

In Figure 8 the results obtained with two specimens with the same ligament length (one sharpened by femtolaser and the other one by razor blade) are overlapped in the tail. The vertical lines are the values of w_c . It can be observed that from w_c both curves match, what indicates that the propagation does not depend on the sharpening method and explain why in the EWF plots the slopes are

very similar when the sharpening methods are very different [2]. By other hand, w_c is not affected by the notch sharpening and the obtained values in the specimens sharpened by femtolaser is lower than in the specimens sharpened by razor blade.

4. CONCLUSIONS

Femtolaser and razor blade sharpening methods give similar notch tip radii.

Razor blade notch sharpening method produces significant plastic deformation ahead of the crack tip, which originates accumulation of deformed material.

The crack starts to initiate at the same initiation stress, σ_i , regardless to the notch sharpening method.

Stress vs. displacement plots are a good method to evaluate self-similarity in the fracture behaviour of series of different ligament length specimens.

In femtolaser sharpened specimens, σ_i is reached at lower crosshead displacements, so the crack requires less energy to initiate than razor blade sharpened specimens.

In EWF plots, the slope is similar for both femtolaser and razor blade sharpened specimens, indicating similar propagation behaviour.

ACKNOWLEDGEMENTS

The authors would like to thank the Education and Science Ministry for the financial support of this work through the MAT2006-13354 project. A. Segovia thanks the National Council of Science and Technology (CONACYT) of Mexico, for the support of a doctoral research scholarship.

REFERENCES

- [1] Gámez-Pérez, J., Santana, O., Martínez, A.B., Maspocho, M.L., *Use of extensometers on essential work of fracture (EWF)*, Polymer Testing 27 (2008) 491-7.
- [2] Martínez, A.B., Segovia, A., Gámez-Pérez, J., Maspocho, M.L., *Influence of femtolaser notch sharpening technique in the determination of essential work of fracture (EWF) parameters*, Engineering Fracture Mechanics 76 (2009) 1247-54.

TEMPERATURE AND STRAIN RATE EFFECT ON MECHANICAL PROPERTIES OF ETHYLENE-PROPYLENE BLOCK COPOLYMERS

T. Gómez-del Río, A. Salazar, A. Cea, R. Hernández, J. Rodríguez

Departamento de Ciencia e Ingeniería de Materiales,
Escuela Superior de Ciencias Experimentales y Tecnología,
Universidad Rey Juan Carlos, C/ Tulipán s/n, Móstoles, 28933 Madrid, España.
E-mail: jesus.rodriguez.perez@urjc.es

ABSTRACT

The effect of temperature and strain rate on elastic modulus, Poisson’s ratio and yield stress of several ethylene-propylene block copolymers with different ethylene content is analyzed. To determine the elastic properties, a video-extensometer is used. The experimental results are interpreted in terms of the well known principle of temperature-time equivalence. Several models have been considered to explain the significant increase in the yield stress at lower temperatures or higher strain rates.

KEYWORDS: yield stress, strain rate, temperature, ethylene-propylene block copolymers.

1. INTRODUCTION

Polypropylene is one of the most used thermoplastics due to its balanced properties, cost and recyclability [1]. There is a severe disadvantage for the application of isotactic polypropylene as engineering plastic: its low fracture toughness, in particular at low temperatures and/or under impact conditions. The improvement of the mechanical properties under impact conditions can be achieved by the incorporation of a dispersed rubbery phase in PP matrix which induces the appearance of toughening mechanisms. The rubber modification of PP can be performed by physical blending with various types and amounts of modifiers or by copolymerization with other polyolefins with lower glass transition temperatures, T_g , than PP, such as the polyethylene. The resulting block copolymers are heterophasic materials with a two phase structure where an elastomeric phase in form of spherical domains, usually ethylene-propylene copolymer rubber (EPR), is dispersed uniformly within the PP homopolymer matrix [2, 3]. The increased application of polypropylene for load-bearing structures has led to renewed interest in the study of its mechanical behaviour at different loading rates and temperatures.

Many molecular theories have been proposed for the prediction of the yield stress of amorphous polymers. These models consider the yield behaviour as a thermally activated process affected by strain rate and temperature. The first model known is the Eyring theory [4], initially developed for shear induced in viscous fluid, but successfully used to describe the yielding process of solid polymers. Macroscopic yielding is assumed to be the result of basic processes consisting of jumps of macromolecular segments from one equilibrium position to another through a potential

energy barrier. The yield stress is given by the following expression:

$$\frac{\sigma_y}{T} = \frac{k}{V} \sinh^{-1} \left(\frac{\dot{\epsilon}}{\dot{\epsilon}_0 \exp\left(-\frac{\Delta H}{kT}\right)} \right) \quad (1)$$

where σ_y is the yield stress, T the absolute temperature, k the Boltzmann’s constant, V an activation volume, ΔH an activation energy, $\dot{\epsilon}$ the strain rate and $\dot{\epsilon}_0$ a constant.

In many systems, yielding has to be described at least by two processes simultaneously active. In those cases, two activation volumes, V_1 and V_2 , and two activation energies, ΔH_1 and ΔH_2 , have to be used. The resulting equation can be written as:

$$\frac{\sigma_y}{T} = \frac{k}{V_1} \left[\ln\left(\frac{2\dot{\epsilon}}{\dot{\epsilon}_{01}}\right) + \left(\frac{\Delta H_1}{kT}\right) \right] + \frac{k}{V_2} \sinh^{-1} \left(\frac{\dot{\epsilon}}{\dot{\epsilon}_{02} \exp\left(-\frac{\Delta H_2}{kT}\right)} \right) \quad (2)$$

where $\dot{\epsilon}_{01}$ and $\dot{\epsilon}_{02}$ are constants that can be obtained by fitting of experimental data. Bauwens-Crowet et al. [5, 6] used successfully this equation in several amorphous thermoplastics.

Fotheringham and Cherry [7] introduced the idea that yielding needs the cooperative motion of multiple chain segments. They modified the original Eyring equation raising the hyperbolic sine function to the nth power (n segments participating in the process) and introducing an internal stress as a new structural parameter. Richeton et al. [8] in a recent development extended the

cooperative model to a wide range of strain rates and temperatures, below and above the glass transition temperature. The expressions provided by the cooperative model so extended are given by:

$$\frac{\sigma_y}{T} = \frac{\sigma_i(0) - mT}{T} + \frac{2k}{V} \sinh^{-1} \left[\frac{\dot{\epsilon}}{\dot{\epsilon}_0 \exp\left(-\frac{\Delta H_\beta}{kT}\right)} \right]^{1/n} \quad \text{for } T \leq T_g \quad (3)$$

$$\frac{\sigma_y}{T} = \frac{2k}{V} \sinh^{-1} \left[\frac{\dot{\epsilon}}{\dot{\epsilon}_0 \exp\left(-\frac{\Delta H_\beta}{kT_g}\right) \exp\left(\frac{\ln 10 \times c_1^g (T - T_g)}{c_2^g + T - T_g}\right)} \right]^{1/n} \quad \text{for } T > T_g \quad (4)$$

where ΔH_β is the β activation energy; c_1^g and c_2^g are the Williams-Landel-Ferry (WLF) parameters at the glass transition temperature, T_g , $\sigma_i(0)$ is the internal stress at 0 K and m is a material parameter roughly equal to $\sigma_i(0)/T_g$ in the case of amorphous polymers [9].

Most of the previous models are not focused on semicrystalline materials. Gueguen et al. [10] considered that semicrystalline polymers, unlike amorphous ones, are less sensitive to variations of stiffness above the glass transition and below the melt temperature. As a consequence, they used the classical form of the cooperative model with the Arrhenius law, rather than the modified form according to WLF theory, for temperatures above the glass transition. They also maintain the linear dependence of the internal stress for temperatures above T_g

$$\frac{\sigma_y}{T} = \frac{\sigma_i(0) - mT}{T} + \frac{2k}{V_{eff}} \sinh^{-1} \left[\frac{\dot{\epsilon}}{\dot{\epsilon}_0 \exp\left(-\frac{\Delta H_{eff}}{kT}\right)} \right]^{1/n} \quad (5)$$

where ΔH_{eff} and V_{eff} are the effective activation energy and activation volume, respectively. These parameters were obtained from the activation parameters of the amorphous phase, ΔH_a and V_a , and of the crystalline phase, ΔH_c and V_c .

In this work, the tensile behavior of three semicrystalline ethylene-propylene block copolymers is analyzed at different strain rates in a wide range of temperatures (from -120 to 23 °C). The applicability of the previously described models will be evaluated on the base of a general acceptance of the time-temperature superposition principle.

2. MATERIALS AND EXPERIMENTAL PROCEDURE

The materials studied were three commercial grade ethylene-propylene block copolymers: EPBC1, EPBC5 and EPBC7, supplied by Repsol in form of pellets. The specimens were prepared by injection molding. The basic characteristics such as the ethylene content, the

molecular weight, M_w , and the glass transition temperatures are collected in Table 1.

Table 1. Basic properties of the copolymers under study

	Ethylene content (%)	M_w (kg/mol)	T_g PP (°C)	T_g EPR (°C)	Cryst. Index (%)
EPBC1	7.0	816	19.5	-44.4	41.6
EPBC5	8.5	353	18.1	-48.0	44.6
EPBC7	8,5	302	19.0	-45.1	45.3

Tensile tests were carried out in an electromechanical testing machine (MTS RF/100) with load cells between ± 2.5 kN and ± 30 kN, following the ISO-527 guidelines and changing the cross-head speed (from 1 mm/min to 100 mm/min) and the temperature (from -120 °C to 20 °C). Strains in the specimens were measured by a contact extensometer (MTS 634-12F-54) and also using a LIMESS video-extensometer. Raw data of longitudinal and transversal displacements were simultaneously recorded to extract Young's modulus and Poisson's ratio. From the loading history, the yield stress could be derived. The low temperature tests were conducted placing the load train (hinges, grips or bending fixture and sample) inside an environmental chamber (MTS 651.06E-03), which was connected to a Dewar flask containing liquid nitrogen. The cooling process consisted of adding liquid nitrogen continuously until the load frame ceased to move to balance the thermal contractions and maintains a constant load of 15 N on the specimen. Once the target temperature was reached and before starting the test, conditioning was held 20 minutes more to guarantee that the specimen was in thermal equilibrium.

3. RESULTS AND DISCUSSION

Figure 1 shows an example of the characteristic stress-strain curves of the copolymers tested. The effects of temperature and strain rate are presented in Figures 1a and 1b, respectively. Independently of the material and the testing conditions, the same tendency is observed: the yield stress decreases as the strain rate is reduced and the temperature is increased. It should be taken into account that at the lower temperatures of -80 °C and -120 °C no yielding but brittle fracture was detected.

The effect of temperature on the values of Young's modulus, Poisson's ratio and yield stress are summarized in Figure 2. The strain rate during the tests included in these graphs corresponds to $\sim 2.6 \cdot 10^{-4} \text{ s}^{-1}$. Young's modulus increases its value from 1.5 GPa at 20 °C to ~ 5 GPa at -120 °C. The most notable variation is observed after passing the glass transition temperature, T_g , of the polypropylene matrix. The material stiffness is mainly controlled by crystallinity. Thus, due to the very similar values of crystallinity index, no significant differences are expected between materials at room temperature. At temperatures lower than T_g , the role played by the different ethylene content or molecular weight becomes greater. The values of the

Poisson's ratio are very similar in the three materials under study, ranging from 0.4 at room temperature to 0.3 at -120 °C.

The yield stress is around 20 MPa at room temperature for the three copolymers tested. A huge increase is observed, especially at temperatures lower than the T_g of the elastomeric phase, T_g EPR, up to values close to 100 MPa. Its lower ethylene content and its higher molecular weight justify the higher values of yield stress measured in the material EPBC1.

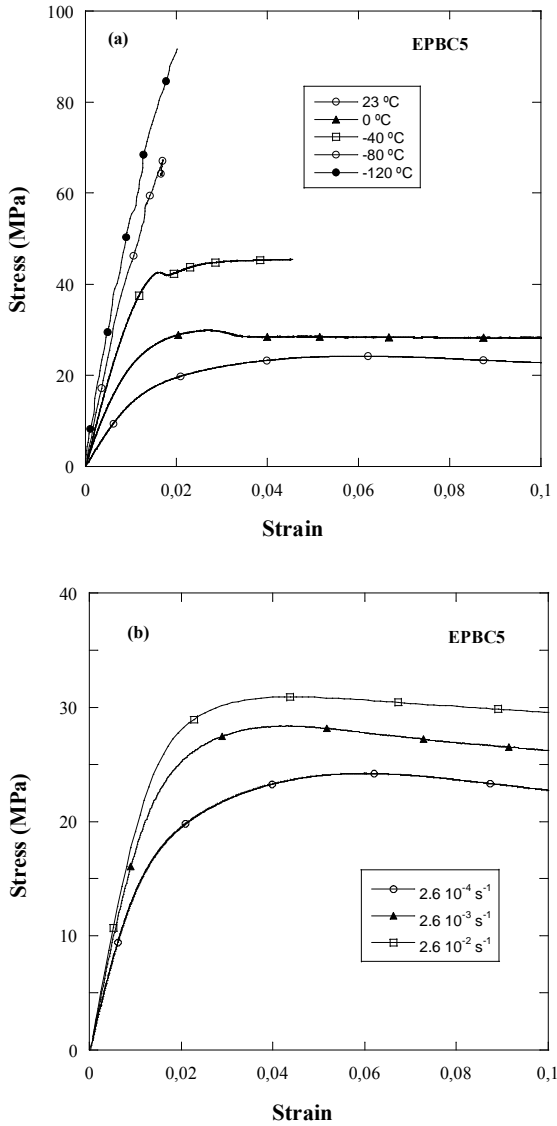


Figure 1. Stress – strain curves of EPBC5 at (a) different temperatures and 0.00026 s^{-1} and (b) different strain rates and 23 °C .

Figure 3 shows the effect of strain rate on the yield stress at several temperatures. In the limited range analyzed, from 10^{-4} to 10^{-2} s^{-1} approximately, yield stress exhibits moderate augment with the strain rate.

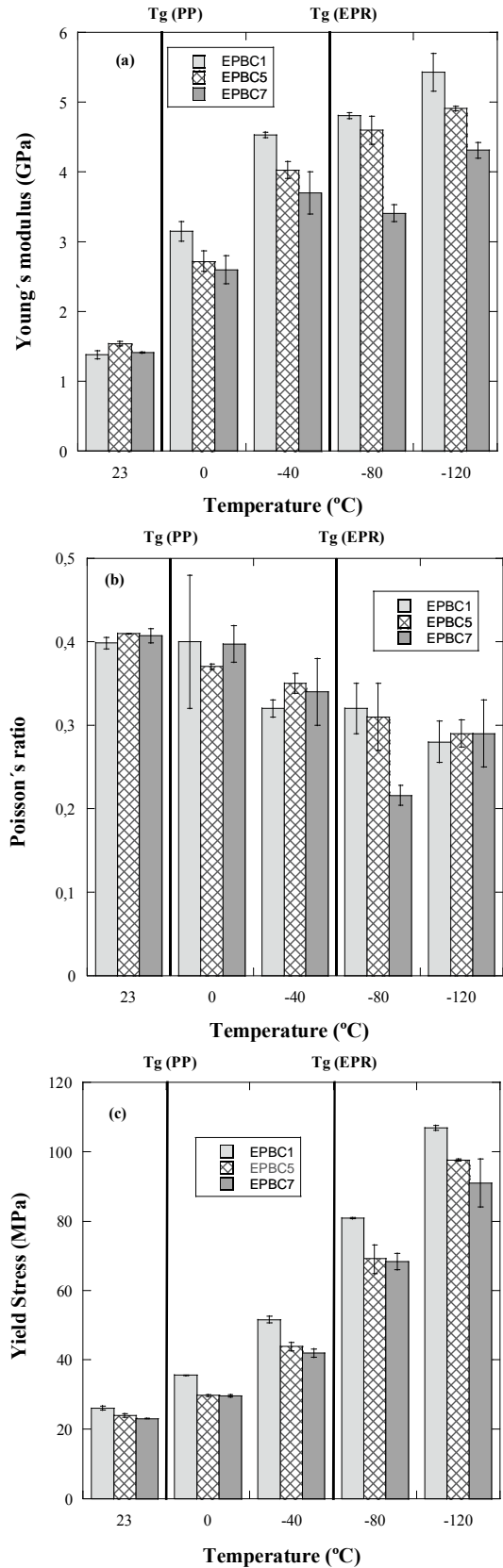


Figure 2. Influence of temperature on Young's modulus, Poisson's ratio and yield stress.

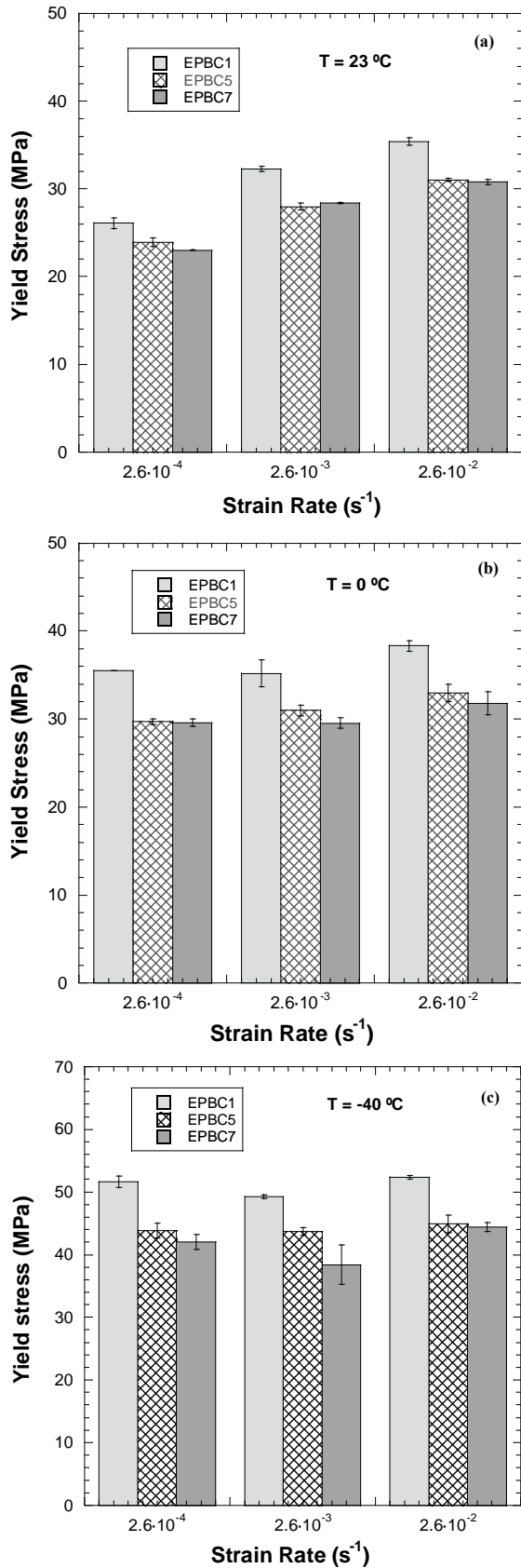


Figure 3. Influence of strain rate on the yield stress at different temperatures.

Considering the semicrystalline nature of the materials analyzed and assuming that they verify the

well known strain rate-temperature superposition principle, i. e., a decrease in temperature will have the same effect on the yield stress as an increase in strain rate, the reduced yield stresses σ_y/T versus $\log \dot{\epsilon}$ can be combined to generate a master curve at a reference temperature, T_{ref} . Original data must be shifted horizontally and vertically according to the following expressions [8]:

$$\Delta(\log \dot{\epsilon}) = \frac{\Delta H_{eff}}{k \ln 10} \left(\frac{1}{T} - \frac{1}{T_{ref}} \right) \quad (6)$$

$$\Delta \left(\frac{\sigma_y}{T} \right) = -\sigma_i(0) \left(\frac{1}{T} - \frac{1}{T_{ref}} \right) \quad (7)$$

Once the T_{ref} of 23 °C has been chosen, the parameters ΔH_{eff} and $\sigma_i(0)$ can be derived until a unique master curve is generated. The values of ΔH_{eff} and $\sigma_i(0)$ finally selected are those providing the best fit of the experiments. The remaining parameters, m , V_{eff} , n and $\dot{\epsilon}_0$, can be calculated fitting the data of the master curve to equation 5, as it is shown in Figure 4. An acceptable agreement between experiments and model is achieved, taken into account that data from tests performed at different temperatures and strain rates are considered.

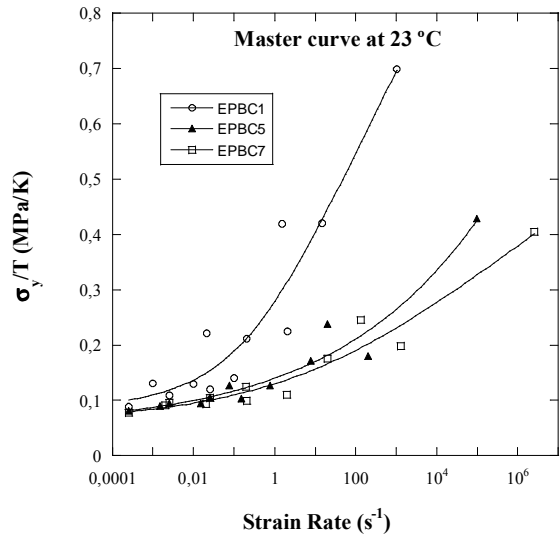


Figure 4. Master curve at 23 °C showing the reduced yield stress versus strain rate for the three different copolymers under study.

Table 2 shows the model parameters obtained for materials under study. They are in the same order of magnitude than those found in bibliography for other thermoplastics, such as PET and polyethylene [10]. Apart from this, the values of the parameters m and $\sigma_i(0)$ are consistent with the relationship predicted by Rault [9].

Table 2. Parameters of the tensile yielding model.

PARAMETERS	EPBC1	EPBC5	EPBC7
n	3,23	5,47	6,78
$V_{\text{eff}}(\text{m}^3)$	$1,38 \cdot 10^{-28}$	$2,76 \cdot 10^{-28}$	$1,70 \cdot 10^{-28}$
$\sigma_i(0)$ (MPa)	74,4	66,2	60,3
m (MPa K ⁻¹)	0,17	0,16	0,15
$\dot{\epsilon}_0$ (s ⁻¹)	$1,14 \cdot 10^7$	$6,5 \cdot 10^{11}$	$1,18 \cdot 10^{13}$
ΔH_{eff} (kJ mol ⁻¹)	40	52	60,6

4. CONCLUSIONS

Tensile tests at different temperatures (-120°C - 23 °C) and strain rates (10^{-4} - 10^{-2} s⁻¹) have been carried out in three ethylene-propylene block copolymers. From the experimental results the following conclusions can be ascertained:

- Polypropylenes under study show a significant increase of their tensile yield stress as temperature is decreased. This increase is accentuated with the strain rate, in agreement with the time – temperature superposition principle.
- Under the testing conditions, the material with the highest molecular weight exhibits more sensibility to strain rate and temperature.
- The extension of the cooperative model to semicrystalline polymers seems to provide reasonable results in ethylene-propylene block copolymers at cryogenic temperatures and moderate strain rates.

ACKNOWLEDGEMENTS

Authors are indebted to *Ministerio de Educación* of Spain for their financial support through projects MAT2006-13354 and MAT2009-14294, and to REPSOL YPF for the materials supply.

REFERENCES

[1] Moore EP Jr.: Polypropylene Handbook; Hanser Publications, Vienna, 1996.

[2] Sun Z, Yu F. SEM study on fracture behavior of ethylene/propylene block copolymers and their blends. *Macromol Chem and Phys* 1991; 192: 1439-1445.

[3] Sun Z, Yu F, Qi Y. Characterization, morphology and thermal properties of ethylene-propylene block copolymers. *Polymer* 1991; 32: 1059-1064.

[4] Eyring H. Theory of non-Newtonian flow. I. Solid plastic system. *J Chem Phys* 1936, 4:283-291.

[5] Bauwens–Crowet C, Bauwens JC, Homès G. Tensile yield-stress behavior of glassy polymers. *J Polym Sci A2* 1969; 7:735-742.

[6] Bauwens–Crowet C, Bauwens JC, Homès G. Tensile yield-stress behavior of poly(vinyl chloride) and polycarbonate in the glass transition region. *J Polym Sci A2* 1969; 7:1745-1754.

[7] Fotheringham D, Cherry BW. The role of recovery forces in the deformation of linear polyethylene. *J Mater Sci* 1978; 13:951-964

[8] Richeton J, Ahzi S, Daridon L, Rémond Y. A formulation of the cooperative model for the yield stress of amorphous polymers for a wide range of strain rates and temperatures. *Polymer* 2005; 46:6035-6043.

[9] Rault J. Yielding in amorphous and semi-crystalline polymers: the compensation law. *J of non-crystalline solids* 1998; 235-237: 737-741.

[10] Gueguen O, Richeton J, Ahzi S and Makradi A. Micromechanically based formulation of the cooperative model for the yield behaviour of semi-crystalline polymers. *Acta Materialia* 2008; 56:1650-1655.

DETERMINACIÓN DE LA TENACIDAD A LA FRACTURA POR DIFERENTES METODOLOGÍAS DE UN PLA CON COMPORTAMIENTO DÚCTIL

J. Oropeza⁽²⁾, C. Rodríguez⁽¹⁾, J. Belzunce⁽¹⁾, O. O. Santana⁽²⁾, M. Ll. Maspoch⁽²⁾

⁽¹⁾Escuela Politécnica Superior de Ingeniería de Gijón, Universidad de Oviedo.
Campus de Viesques, 33203 Gijón, España

⁽²⁾Centre Català del Plàstic – Universitat Politècnica de Catalunya. c/ Colom, 114 –08222 Terrassa. España
E-mail: María.lluisa.maspoch@upc.edu

RESUMEN

Se ha evaluado la aplicabilidad de la técnica del Trabajo Esencial de Fractura (EWF) en geometría SENB como método alternativo al concepto y metodología de Integral J. Para ello fue empleado un Poli(Ácido Láctico) amorfo sometido a un tratamiento térmico de rejuvenecimiento para favorecer su comportamiento dúctil. Los resultados demuestran que la técnica de EWF puede ser empleada como una metodología alternativa y sencilla con la que se puede determinar el valor, en condiciones de deformación plana, de J_0 según lo establecido en el protocolo ESIS 2000 y norma ASTM E813-87. Para la validación del rango de longitudes de ligamento a emplear se considera como válida la solución para geometría SENB del *Slip-line field* con una tolerancia de alrededor un 10%.

PALABRAS CLAVE: Poli(Ácido Láctico), Trabajo Esencial de Fractura, Integral J.

The applicability of the Essential Work of Fracture (EWF) in SENB geometry as an alternative to the concept and methodology of Integral J has been assessed. An amorphous Poly (lactic acid) with a deaging heat treatment in order to promote a ductile behavior has been used. The results demonstrate that the EWF technique can be used as an alternative, simple methodology to determine the value in plane strain conditions of J_0 according to ESIS 2000's protocol and ASTM E813-87 normalization. Validation of the ligament range to be used in the analysis, the SENB solution of the Slip-line field theory could be use with a 10% of tolerance.

KEY WORDS: Poly(Lactic Acid), Essential Work of Fracture, J-Integral.

1. INTRODUCCIÓN

Actualmente, el Poli(Ácido Láctico) (PLA) se presenta como alternativa para sustituir ciertos polímeros derivados de combustibles fósiles empleados en aplicaciones donde la proporción de residuos post-consumo es elevada, como por en el sector del envase y embalaje. Se sintetiza a partir del ácido L-láctico (proveniente de la fermentación del almidón) y se caracteriza por ser un material semicristalino, con una T_g de alrededor de 60°C y una temperatura de fusión (T_m) cercan a 155°C [1].

El grado de cristalinidad que puede alcanzar viene determinado por la proporción de impurezas de enantiómero D-láctico, así como la masa molecular que esté presente. Proporciones de tan sólo un 4 %

mol (típica de los grados comerciales) del enantiómero D reduce su velocidad de cristalización a niveles tales que, en condiciones de procesamiento habituales, el producto es prácticamente amorfo [1].

Debido a la proximidad de su T_g a la temperatura ambiente y las características conformacionales de su cadena, presentan un proceso de envejecimiento físico acelerado que ocasiona una disminución importante en el volumen libre (densificación) así como un aumento en la densidad de enredos moleculares. Ambos factores limitan en gran medida la movilidad molecular, disminuyendo su capacidad de almacenamiento y disipación de energía frente a una sollicitación mecánica, generando una transición de comportamiento dúctil-frágil [2].

Es bien conocido que este fenómeno es un proceso reversible, por lo que puede ser revertido aplicando un tratamiento térmico a temperaturas próximas a su T_g seguido de un enfriamiento brusco. De esta forma la alta movilidad molecular promovida por el calentamiento hace que disminuya en proporción los dominios densificados favoreciendo su comportamiento dúctil [3].

El objetivo de la presente comunicación es la de presentar los resultados obtenidos durante la evaluación del comportamiento a fractura de un PLA “rejuvenecido” en condiciones de deformación plana. Paralelamente se intenta evaluar la aplicabilidad de la técnica del Trabajo Esencial de Fractura (EWF) en geometría SENB.

2. EWF vs. INTEGRAL J

La sencillez de la metodología de trabajo ha sido la razón principal por la que el concepto del EWF ha ganado popularidad sobre todo en la evaluación del comportamiento a fractura de polímeros altamente tenaces y dúctiles, presentándose como una alternativa frente al análisis de integral J. En este caso no se requiere la determinación del inicio de propagación de grieta, con la consecuente interrupción del ensayo [4].

El EWF ha sido propuesto para evaluar el comportamiento a fractura en condiciones de colapso plástico extensivo del sistema. Sugiere que el proceso de fractura, y por tanto el trabajo consumido en el mismo (U_t), puede ser dividido en dos regiones: una interna donde tiene lugar el proceso de fractura en sí (FPZ) y a la que se asocia una componente energética esencial (W_e), dependiente de la sección de ligamento; y una externa (OPZ) donde se distribuyen las grandes deformaciones plásticas generadas por el flujo plástico y que se considera como el término no esencial (W_p), dependiente del volumen de OPZ. De esta forma [5]:

$$W_t = U_t = w_e B l + \beta w_p B l^2 \Rightarrow$$

$$w_F = \frac{U_t}{B l} = w_e + (\beta w_p) l \quad (1)$$

siendo B es el espesor, l la longitud de ligamento y β es el factor de forma de la zona deformada.

La geometría de ensayo DDENT ha sido la más empleada para la aplicación de esta técnica ya que presenta mayor probabilidad de promover la condición de colapso total antes de la propagación de la grieta y mejor reproducibilidad de los resultados [4], sobre todo en condiciones de tensión de plana. Diversos autores han buscado extender la aplicación de la técnica a otras geometrías, principalmente a la comúnmente empleada en estudios de fractura, la SENB en condiciones de deformación plana [5-7].

Williams et al. [8] establece una relación entre el análisis por EWF y el criterio Integral J. Partiendo de la definición de Integral J de acuerdo al protocolo ESIS y del ajuste potencial de la curva R se obtiene:

$$J = A(\Delta a_0 + \Delta a)^N \quad (2)$$

la cual define un crecimiento de grieta una vez iniciada su propagación, de manera que, al cumplirse $\Delta a = 0$ se obtiene el valor de iniciación de grieta J_0 . Para valores pequeños de N y cuando $\Delta a \ll \Delta a_0$, la ecuación (2) se puede aproximar a:

$$J_c = J_0 + N J_0 \cdot \frac{\Delta a}{\Delta a_0} \quad (3)$$

Integrando la ecuación (6) se obtiene

$$\frac{U_t}{B l} = J_0 + \left(\frac{N J_0}{4 \Delta a_0} \right) l \quad (4)$$

Relacionando las ecuaciones (1) y (4) se observa que $J_0 \equiv w_e$.

3. PARTE EXPERIMENTAL

Se ha empleado un Poli(Ácido Láctico) PLA 2002D de Natureworks® con un contenido de enantiómero D de 4.25 % mol y una densidad de 1.24 g/cm³, otras características de interés se presentan en la **Tabla 1**.

A partir de la granza fueron obtenidas probetas tanto halterio ASTM D-647 tipo I, como prismáticas (espesor, $B = 6.15$ mm; ancho, $W = 12.7$ mm) mediante moldeo por inyección empleando un perfil térmico entre 180 y 210°C, una presión de inyección de 100 bares y manteniendo la temperatura del molde a 25°C. En estas condiciones se obtuvieron muestras virtualmente amorfas.

Tabla 1. Características técnicas de interés del PLA 200D de Natureworks®.

Parámetro	Valor
Mw (kDa)	212.3
PDI = Mw/Mn	3.06
MFI (210°C/2.16kg)	7.0 ± 0.2
Tg ; Tm (°C)*	64 ; 154
E (GPa)*	3.3 ± 0.2 ^a
σ_y (MPa)*	45.5 ± 2 ^a

*determinaciones sobre probeta inyectada

^a tras tratamiento de rejuvenecimiento

Previo a los ensayos mecánicos realizados, se aplicó un tratamiento térmico de “rejuvenecimiento”: calentamiento a 60°C durante 90 minutos en una estufa de circulación de aire y posterior enfriamiento rápido en agua con hielo ($\approx 0^\circ\text{C}$) durante 10 min. Finalmente secado y atemperado a temperatura ambiente (22°C) durante 50 minutos, tiempo que permitía realizar los ensayos bajo equilibrio térmico sin que se iniciara el proceso de envejecimiento.

Los ensayos fueron realizados en una máquina de ensayos universales GALDABINI SUN 2500. Las determinaciones de los parámetros mecánicos a tracción se realizaron siguiendo la norma ASTM D-638 a una velocidad de movimiento de mordazas de 1 mm/min y temperatura ambiente ($22 \pm 1^\circ\text{C}$)

Para los ensayos de comportamiento a fractura se empleó la geometría SENB aplicando una agudización de la entalla mediante la indentación de una hoja de afeitar con un radio en su punta (ρ) de $0.13\mu\text{m}$. Los ensayos fueron realizados en la configuración de flexión por tres puntos, con una distancia entre apoyos (S) de 51 mm (siguiendo la relación propuesta de $S/W = 4$), a temperatura de $22^\circ\text{C} \pm 1^\circ\text{C}$ y una velocidad de desplazamiento de bastidor de 1mm/min.

En el caso del EWF se ensayaron 12 probetas hasta su completa fractura, empleando un rango de longitudes de entalla (a) comprendido $0.3 \leq a/W \leq 0.8$.

El análisis de Integral J se realizó mediante la metodología de múltiple probeta siguiendo el procedimiento sugerido por el protocolo ESIS 2000 [7] y la norma ASTM E813-87. Se ensayaron un total de 12 probetas empleando una entalla cumpliendo la

relación $a/W=0.5$. Tras 24 horas después del ensayo, las probetas ensayadas fueron finalmente “abiertas” mediante impacto. La proporción de grieta estable se determinó haciendo uso de una lupa binocular con plataforma móvil calibrada de apreciación 10^{-3} mm.

4. RESULTADOS Y DISCUSIONES

La **figura 1** muestra las curvas Carga (P) – Desplazamiento (d) para los ensayos EWF. Se observa que la similitud en la forma de las curvas se mantiene hasta una relación a/W de 0.4, por encima del cual las curvas muestran cruzamientos o comportamientos aparentemente anómalos. La similitud entre las curvas y la proporcionalidad entre ellas en función de la longitud de ligamento (l) son evidencia de que el estado de tensiones durante la propagación de grieta se mantiene uniforme en este rango de l

La **figura 2** muestra una micrografía lateral de la zona externa de proceso (OPZ) generada. Claramente se observa la forma ovalada típica de sistemas poliméricos que presentan un colapso plástico extensivo durante el proceso de fractura y cuyo campo de deformación se puede describir aplicando la teoría de “*Slip-line field*” para la geometría empleada. La aplicación de sus soluciones puede ser empleada para la validación del rango de longitud de ligamento a emplear en el análisis del EWF en geometría SENB [4].

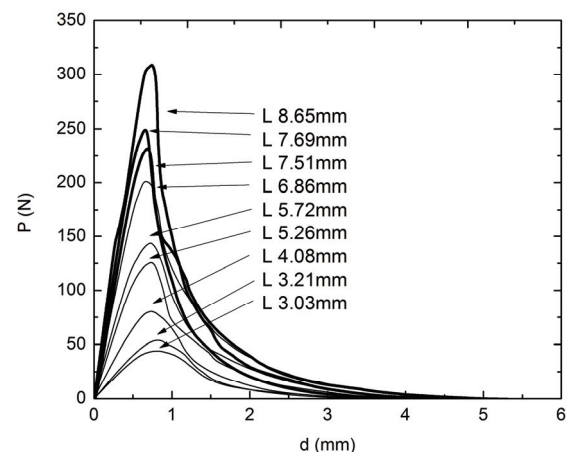


Figura 1. Curvas Carga (P)-Desplazamiento (d). Las curvas destacadas representan aquellas con comportamiento anómalo.

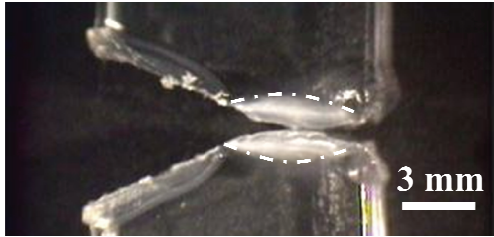


Figura 2. Vista lateral de la zona de proceso tras ensayo.

Dicha teoría propone que al momento del colapso plástico, la carga (P) alcanzada se puede expresar en función de la tensión a la cedencia (σ_y) de la siguiente forma:

$$P = \sigma_y \frac{fB}{S} (W - a)^2 \quad (5)$$

siendo un factor que representa la relación entre el momento plástico de la probeta entallada a una no entallada. Según Wu et al. [9], y para el rango de a/W empleado, f toma valores entre 1.2208 y 1.2606.

La figura 3 muestra de forma comparativa la solución teórica junto con los puntos experimentales obtenidos. Se aprecia cierta desviación, cuya proporción aumenta conforme l aumenta. No obstante para $l < 6$ mm ($a/W < 0.4$) la desviación es de un 13 % (línea discontinua), aumentando hasta un 30% para valores superiores.

De acuerdo a lo anterior la propagación de grieta se presentaría en condiciones de colapso plástico no extensivo, por lo que el análisis podría quedar invalidado.

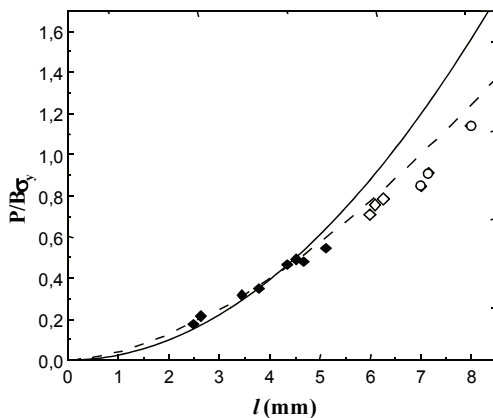


Figura 3. Solución teórica "Slip-line field" para la geometría empleada en el estudio (línea continua).

Evidencias por captura de video durante la realización de los ensayos demostró que para el rango $a/W < 0.4$ presentaban en un 90% de l colapsado previo la propagación de la grieta, siendo apreciablemente menor que para a/W superiores.

Hay que destacar que la solución a la teoría del Slip-line field ha sido planteada considerando un comportamiento elastoplástico ideal con un comportamiento similar tanto a tracción como a compresión ($\sigma_{yt} = \sigma_{yc}$), no válido para materiales poliméricos.

La variación de los datos respecto a la solución teórica solo puede ser compensada por una variación en el valor de tensión para colapso plástico tomada como σ_y en este estudio y que pudiera no ser totalmente válida si se toma en cuenta que el mecanismo de deformación en este tipo de material es de formación y propagación de "crazes" [10].

La figura 4 muestra dos micrografías de la superficie de fractura obtenida para sendas muestras (con y sin tratamiento térmico) sometidas a las mismas condiciones de ensayo.

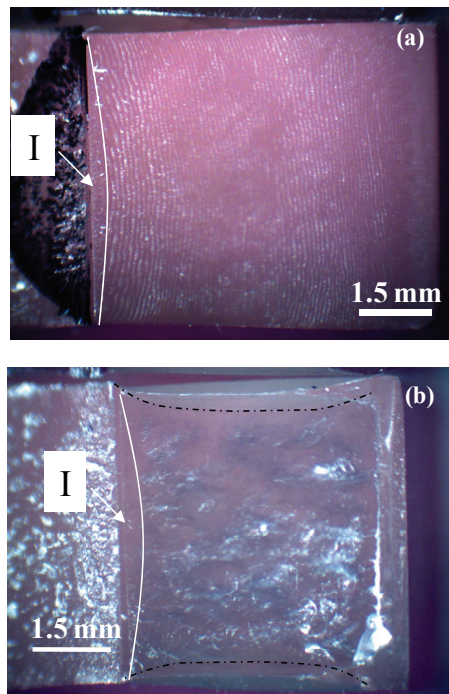


Figura 5. Micrografías de la superficie de fractura tras el ensayo para una muestra: a) sin tratamiento y b) con tratamiento térmico.

En la muestra no tratada (envejecida) (*figura 4a*) se observa una lúnula adyacente a la entalla (zona I), atribuida a una propagación lenta y estable de grieta por ruptura de central de las fibrillas de un “craze precursor”. A continuación se presenta un patrón que asemeja al de las “escamas” de un pez, atribuido a la aparición de un manojito de crazes que se propagan y rompen de forma inestable.

Por el contrario, la muestra “rejuvenecida” (*figura 4b*) además de la lúnula anteriormente descrita, muestra una superficie completa desgarrada, sin evidencias de inestabilidad, e inclusive la típica contracción lateral de sistemas con propagación de grieta lenta y estable.

El grado de estabilidad en el crecimiento de una craze (engrosamiento) viene dictado por la densidad de enredos moleculares [3]. Una disminución en este parámetro promueve mayor estabilidad. Es probable que por efecto del tratamiento de rejuvenecimiento aplicada dicha densidad se vea apreciablemente disminuida, promoviendo un crecimiento estable de craze sin ruptura de fibrilla para las condiciones de ensayo empleadas.

De acuerdo al estudio realizado por Renouf-Glauser et al. [10], la tensión de inicio de craze (σ_c) se ubica alrededor de un 85 % de σ_y (15 % inferior) para un PLA similar al empleado en este estudio, coincidiendo con el valor estimado de acuerdo a la desviación observada en los resultados aquí obtenidos aplicando un ajuste a la solución teórica del *Slip-line field*.

La *figura 6* muestra la representación gráfica del trabajo específico de fractura (w_f) vs l . Se observa un buen ajuste lineal para el rango de l validados por el análisis de plasticidad ($l < 6 \text{ mm}$) obteniéndose un valor de $w_c = 2.0 \pm 0.2 \text{ kJ/m}^2$. En el caso de $l > 6 \text{ mm}$ los valores caen fuera de dicho ajuste, situación similar a lo publicado por otros autores y que ha sido atribuido propagaciones de grieta sin colapso plástico extensivo [4,7].

La *figura 7* presenta la curva J - Δa generada a partir de los ensayos de integral J , así como el ajuste potencial obtenido de los datos considerados dentro del análisis. Es importante acotar que las líneas de exclusión fueron tomadas de acuerdo a lo estable-

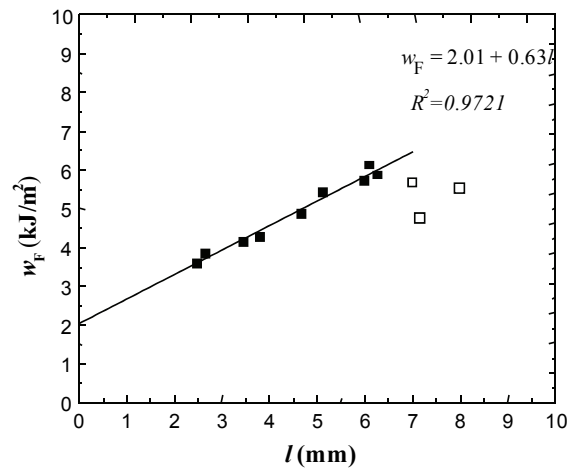


Figura 6. Trabajo específico de fractura en función de la longitud de ligamento.

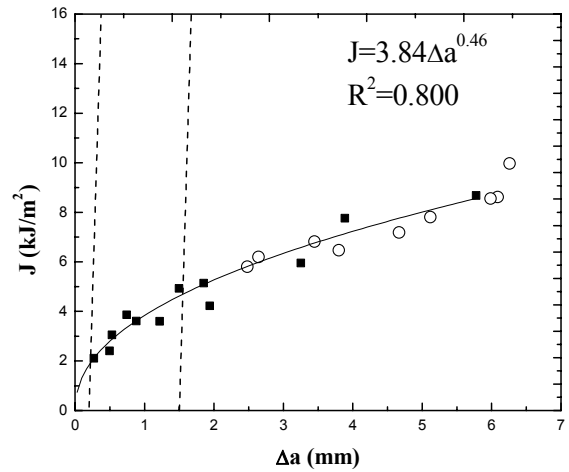


Figura 6. Curva J - Δa y ajuste potencial obtenido. Líneas segmentadas: líneas de exclusión tomadas de acuerdo a ASTM E813-87. Círculos: valores de J a partir de los ensayos de EWF.

cido en ASTM E813-87, ya que las propuestas por ESIS 2000 [8] son excesivamente restrictivas. Propagaciones inferiores a 0.2 mm fueron imposible de obtener dada la incertidumbre a la hora de discernir entre la propagación lenta de grieta o la lúnula de apertura de craze precursor durante el impacto.

Un aspecto a tener en cuenta es la incertidumbre en el uso del concepto de *línea de enroscamiento*, definida por una recta cuya pendiente es proporcional al $2\sigma_y$ considerando una zona de plástica circular en la punta de la grieta. Esta premisa se ve invalidada al

considerar que el mecanismo de deformación principal es la generación un craze precursor, por lo que la zona de deformación ya no sería circular.

Lo anterior, aunado al uso de σ_y en vez de σ_c , sobreestimaría la pendiente de esa línea, generando un valor de J_{BL} (intersección del ajuste potencial con dicha línea), bastante bajo. Es por ello que se ha optado por calcular el valor de J a una propagación de grieta de 0.2 mm (ESIS 2000) y el establecido como equivalente según ASTM E813-87 (**Tabla 2**).

Tabla 2. Valores de J_o (no de inicio) obtenidos por los diferentes métodos de Integral J.

Método	J_o (kJ/m ²)	Δa_o *(mm)	B_{min} (mm)
E813- 87	1.9 ± 0.1	0.224	1.7
ESIS 2000	1.8 ± 0.1	0.2	0.99

* determinado a partir de la relación: $B_{min} = 25J_o/\sigma_y$

Se aprecia una excelente correlación de estos valores con el w_c obtenido, pudiéndose considerar inclusive en estado de deformación plana si se considera el B_{min} y el B empleado en el estudio (6.15 mm).

Por otra parte los valores empleados en la determinación de EWF y extrapolados en el análisis de integral J se ubican de forma razonable, dentro del ajuste potencial obtenido y extrapolado a valores de propagación mayores a los empleados en el análisis de integral J. Este aspecto permitiría considerar que el término no esencial del análisis EWF (βw_p) puede dar una idea de la resistencia a la propagación de una grieta ya iniciada, similar al sentido físico dado al termino dJ/da en el análisis de integral J.

5. CONCLUSIONES

Los resultados obtenidos permiten establecer que el concepto de EWF puede ser empleado como una alternativa sencilla para la determinación del valor de integral J en condiciones de deformación plana. La validación del rango de longitudes de ligamento a emplear en el análisis puede ser establecida no sólo por la "similitud" entre las curvas Carga-Desplazamiento obtenidas de los ensayos, sino también aplicando la solución en geometría SENB para la teoría del *Slip-line field* permitiendo un 10% de desviación respecto al teórico establecido.

6. AGRADECIMIENTOS

Los autores agradecen al Ministerio de Educación y Ciencia la financiación del proyecto MAT 2007-62450.

7. REFERENCIAS

- [1] R. Auras, B. Harte, S. Selke, , *An overview of polylactides as packaging materials*. Macrom. Bioscience, 4(9), 5515-5521 (2004).
- [2] K. Aou, S.L. Hsu, L.W. Kleiner, F-W. Tang, *Roles of conformational and configurational defects on the physical aging of amorphous poly(lactic acid)*. J. Phys. Chem. B111(42), 12322-27 (2007).
- [3] RN Haward, RJ Young (Eds.) "*The physics of glassy polymers*". 2nd Ed. Chapman & Hall, UK (1997). Pp: 155-212 y 295-341.
- [4] K. Duan, X. Hu, G. Stachowiak, *Modified essential work of fracture model for polymer fracture*. Comp. Sci. and Tech. 66, 3172-78 (2006).
- [5] J. Wu, Y-W, Mai, *The essential fracture work concept for toughness measurement of ductile polymers*. Polym. Eng. Sci., 36(18) 2275-88 (1996).
- [6] OO. Santana, M.Ll. Maspoeh, AB. Martínez "*Plane strain essential work of fracture in SENB geometry at low and high rates of PC/ABS blends*." Polym. Bull., 39(4), 511-8 (1997).
- [7] P. Luna et al., *The application of the essential work of fracture methodology to the plain strain fracture of ABS 3-point bend specimens*. Polymer 44, 1145-50 (2003).
- [8] D.R. Moore, A. Pava, JG Williams (Eds). "*Fracture mechanics testing methods for polymers adhesives and composites*." ESIS Publication 28, Elsevier, Amsterdam (2001) : 119-122.
- [9] S-X Wu, B. Cotterell, Y-W. Mai. *Slip-line field solutions for three-point notch-bend specimens*." Int. J. of Fracture 37, 13-29 (1988).
- [10] A.C. Renouf-Glauser, et al. *The effect of crystallinity on the deformation mechanism and bulk mechanical properties of PLLA*. Biomaterials, 26, 5771-82 (2005).
- [11] Williams, J. (2000). "Introduction to elastic-plastic fracture mechanics." ESIS Publication 28: 119-122.

DETERMINATION OF THE J-R CURVES OF ETHYLENE-PROPYLENE BLOCK COPOLYMERS BY MEANS OF DIFFERENT J-INTEGRAL METHODOLOGIES

A. Salazar¹, M. A. Garrido¹, J. Rodríguez¹, A. B. Martínez²

¹Departamento de Ciencia e Ingeniería de Materiales,
Escuela Superior de Ciencias Experimentales y Tecnología,
Universidad Rey Juan Carlos, C/ Tulipán s/n, Móstoles, 28933 Madrid, España.
E-mail: alicia.salazar@urjc.es

² Centre Català del Plàstic, CCP, Universitat Politècnica de Catalunya,
C/ Colom, 114, 08222 Terrassa, España.
E-mail: antonio.martinez@upc.edu

ABSTRACT

A single specimen method as the normalization method has been applied to two different ethylene-propylene block copolymers with distinct structural parameters with the aim of analyzing the influence of a methodological parameter as the crack tip constraint factor, m , on the J-R curves. R-curves obtained via multiple specimen method have been taken as references. The results reveal that the crack tip constraint factor is strongly dependent on the material's properties and dimensions. The best accuracy of the J-R curves of the copolymer with a large molecular weight ~ 820 kg/mol, is attained for values of m equal to 1.5 and 1.25 for the specimens' dimensions related to 6.35 and 9 mm thick samples, respectively. Meanwhile, the PP block copolymer, with molecular weight ~ 300 kg/mol, showed the best fit between the J-R curves obtained experimentally with those determined via normalization by setting $m=1$, in accordance with the m values reported in the literature.

KEYWORDS: J-R curves, normalization method, crack tip constraint factor, multiple specimen, ethylene-propylene block copolymers.

1. INTRODUCTION

When Wells [1] attempted to measure K_{IC} values in a number of structural steels, he found that these materials were too tough to be characterized by Linear Elastic Fracture Mechanics (LEFM) and that the crack faces had moved apart prior to fracture; plastic deformation blunted an initially sharp crack. The degree of crack blunting increased in proportion to the toughness of the material [2-3]. These observations led to propose the opening at the crack tip (CTOD) as a measure of fracture toughness. Under LEFM conditions, there is a relationship between CTOD and the fracture toughness, K_I , and the energy release rate, G , given by:

$$\delta = \frac{K_I^2}{m\sigma_{YS}E} = \frac{G}{m\sigma_{YS}} \quad (1)$$

where E is the Young's modulus, σ_{YS} is the yield stress and m is a dimensionless constant that depends on stress state and materials properties, named as crack tip constraint factor.

For ductile polymers, J-integral is the method to determine the fracture toughness. The fracture toughness at crack initiation, J_{IC} , is measured by a crack resistance curve, J-R curve, where J is plotted versus the ductile crack extension, Δa . Since $J = G$ for linear elastic material behaviour, under elastic-plastic conditions equation (1) becomes in:

$$J = m\sigma_{YS}\delta \quad (2)$$

The resistance curve is divided into three stages [3]. During the initial stage, the crack is essentially stationary and the finite slope of R-curve is caused by blunting and described by [4]:

$$J = 2m\sigma_{YS}\Delta a \quad (3)$$

The crack starts to grow in stage 2. A rising R-curve occurs, being J-integral only dependent on the crack extension and thus, J-R curve is a material property at this step. Finally in stage 3, well beyond the initial blunted tip, a steady-state condition is reached, where the local stresses and strains are independent of the extent of crack growth. During the steady-state crack growth, a plastic zone of constant size sweeps through

the material, leaving a plastic wake. Therefore, the R-curve is flat; J does not increase with crack extension, provided the material properties do not vary with position.

For the J-R curves construction of polymers, ASTM [5] and ESIS [6] recommend the multiple specimen method. This methodology, though straightforward and effective, is time and material intensive, as at least a minimum of seven specimens are to be tested to generate the R-curve. For that reason, indirect methods have been developed to obtain J-R curves with fewer specimens and, thus, less time requirements. The single specimen methods are based on the load separation criterion [7], and offer an easy and effective alternative approach to obtain J-R curves. Among the single specimen methods, the normalization method and the load separation parameter method have been successfully applied to polymeric materials [8-11].

As has been previously mentioned, the first section of the J-R curve is dominated by blunting which is described by equation (2). From this equation, the crack tip constraint factor, m, attains much significance. This parameter is closely related to the stress state at the crack tip, which is described by the Q-stress [3] and usually takes a value of 1 for Ramberg-Osgood materials [4], but it is very sensitive to the material type, the loading conditions and geometry of specimens. For polymers, the m value can range between 0.5 and 2 [9]. In particular, m=1 has been reported for polypropylene (PP) based materials [9-10] and m=2 for ultra high molecular weight polyethylene (UHMWPE) materials [11].

In this work, it is analyzed the applicability of the normalization method in different ethylene-propylene block copolymers, paying special attention to the m values which provide the best J-R curves when compared with the classical multiple-specimen method, attending to the structural properties of the polymers under study.

2. THE NORMALIZATION METHOD

The objective of any single specimen method including the normalization method is to obtain accurate crack length predictions using the load (P)-displacement (δ) data alone. The instructions given by ASTM E1820-06 [4] were taken as a guide.

The first step for the determination of the J-R curve is an optical crack-length measurement of the initial, a_o , and final, a_f , crack lengths. Subsequently, each value of the load P_i up to, but not including P_{max} is normalized using the following expression:

$$P_{Ni} = \frac{P_i}{WB \left[\frac{W - a_{bi}}{W} \right]^{n_{pl}}} \quad (4)$$

where W is the specimen width, B is the specimen thickness and $\eta_{pl} = 2$ for three point bending specimens (SENB). a_{bi} is the blunting corrected crack length given by:

$$a_{bi} = a_o + \frac{J_i}{2m\sigma_{YS}} \quad (5)$$

$$J_i = \frac{K_i^2(1-\nu^2)}{E} + J_{pli} \quad (6)$$

where K_i is the stress intensity factor, E is the Young's modulus, ν is the Poisson ratio and J_{pl} is the plastic part of the J-integral [4].

Each corresponding load line displacement, δ_i , is normalized to give a normalized plastic displacement:

$$\delta'_{pli} = \frac{\delta_{pli}}{W} = \frac{\delta_i - P_i C_i}{W} \quad (7)$$

where C_i is the specimen elastic load line compliance, based on the crack length a_{bi} .

In this manner, data points up to maximum force are normalized. In order to obtain the final point, the same equations are employed, but instead of the initial crack length, the final crack length is used. The normalized plastic displacement values above 0.001 up to maximum force, excluding P_{max} value itself, and the points obtained with the use of the final crack length are used for the normalization function fit. The normalization function can be analytically expressed:

$$P_N = \frac{a + b\delta'_{pl} + c\delta'^2_{pl}}{d + \delta'_{pl}} \quad (8)$$

where a, b, c and d are searched fitting coefficients. When the fitting parameters are determined, an iterative procedure is further applied to force all P_{Ni} data to lie on the fitted curve by a_i adjustment. When the crack lengths are determined, the J-R curve can be then calculated and the critical J-integral value can be evaluated.

3. MATERIALS AND EXPERIMENTAL PROCEDURE

The materials studied were two commercial grade ethylene-propylene block copolymers, EPBC1 and EPBC5, supplied by Repsol in form of pellets. The bulk specimens for fracture characterization as well as the tensile specimens were prepared by injection molding. The basic characteristics such as the ethylene content, determined from Nuclear Magnetic Resonance (NMR), the molecular weight, M_w , obtained by Gel Permeation Chromatography (GPC) and the glass transition

temperatures corresponding to the elastomeric particles, T_g EPR, embedded in the propylene matrix, T_g PP, measured via Dynamic Mechanical Thermal Analysis (DMTA) are collected in Table 1.

The mechanical properties such as the Young's modulus, E , and the yield stress, σ_{YS} , were measured via tensile tests at cross-head speeds of 1 mm/min for the ISO-527 bulk injected tensile samples. The elastic modulus values were of 1.38 ± 0.06 and 1.54 ± 0.03 GPa while the values of yield stress were of 26.1 ± 0.6 and 23.9 ± 0.5 MPa for EPBC1 and EPBC5, respectively.

Table 1. Basic properties of the copolymers under study

	Ethylene content (%)	M_w (kg/mol)	T_g PP (°C)	T_g EPR (°C)
EPBC1	6.9	816	10.57	10.41
EPBC5	8.5	353	-45.85	-49.30

The mechanical properties such as the Young's modulus, E , and the yield stress, σ_{YS} , were measured via tensile tests at cross-head speeds of 1 mm/min for the ISO-527 bulk injected tensile samples. The elastic modulus values were of 1.38 ± 0.06 and 1.54 ± 0.03 GPa while the values of yield stress were of 26.1 ± 0.6 and 23.9 ± 0.5 MPa for EPBC1 and EPBC5, respectively.

Experimental data used to generate J-R curves using a multiple specimen approach were obtained following the guidelines described in [5, 6]. Single edge notched bend specimens (SENB) were used for fracture characterization with 6.35 mm and 9 mm in thickness, being the overall dimensions of 6.35x12.7x55 mm and 9x18x80 mm, respectively. In all the specimens, an initial straight-through slot with a length to width ratio of 0.5 and terminating in a V-notch with 0.2 mm in root radius was mechanized. The notch was sharpened by sliding a razor blade across the notch to achieve a total crack depth of ~ 7 mm and ~ 9.9 mm for the 6.35 mm and 9 mm thick specimens, respectively. A minimum of seven specimens for each material and specimen dimensions were performed at room temperature at a crosshead speed of 1 mm/min using an electromechanical testing machine (MTS RF/100) with a load cell of ± 5 kN. A three point bend fixture was used with a span to width ratio of 4. One unnotched specimen was tested to correct the indentation produced by the support on the specimen. The J integral was calculated using:

$$J = \frac{2U}{B(W - a_0)} \quad (9)$$

To measure crack extension, Δa , the tested specimens were fracture at high loading rate after soaking in liquid nitrogen. The initial and final stable crack lengths were measured physically from the broken surfaces via light

microscopy (Leica DMR). The resulting J-crack growth resistance curves were fitted to a power law $J=C \cdot \Delta a^N$, with $N \leq 1$.

J-R curves were also determined using the single specimen normalization method [4], focusing on the influence of the crack tip constraint factor on the predicted J-R curves by setting m to 1, 1.5 and 2. A computational procedure was attained to obtain J-R curves via normalization method with the help of Matlab 7.0.4 software.

For the computation of J_{IC} values, the guidelines described by Hale et al. [6] have been followed, where this critical value has been replaced by a pseudo-initiation value $J_{0.2}$, which defines crack resistance at 0.2 mm of the total crack growth. The size requirements for plane strain J_{IC} are given by:

$$B, a, W - a > 25 \frac{J_{IC}}{\sigma_{YS}} \quad (10)$$

4. RESULTS AND DISCUSSION

Figure 1 and 2 show the J-R curves predictions based on the normalization method with a value of $m=1$ together with the J-R curves obtained experimentally for EPBC1 and EPBC5, respectively. Two samples were used to generate the J-R curve from the normalization method for each material and specimen dimensions and the power law fit is also included for every case. As can be observed, independently of the EPBC5 thickness, there is a good agreement between the J-R curves of EPBC5 determined via normalization with that obtained via multiple specimen when the constraint parameter is equal to 1 (Figure 2). This contrasts with the comparison realized on EPBC1 (Figure 1). The predicted normalized curves stand further from the experimental ones, especially in the 6.35 mm thick specimens (Figure 1a), and even some of them cannot be fitted to a power law with $N \leq 1$. The well reported $m=1$ for PP block copolymers [9-10] results inaccurate for EPBC1.

The poor concordance in case of EPBC1 responds to its different structural properties with regard to EPBC5 (Table 1), especially the molecular weight. The former presents molecular weights almost three times higher than the latter. Those large values are roughly comparable to those shown by UHMWPE. For UHMWPE materials, m has been accurately determined and a value of $m=2$ can be generally used [11]. This finding suggests that it may be a strong effect of the crack tip constraint factor, m , for EPBC1. That is the reason why the normalization method was applied to EPBC1 by setting $m=1, 1.5$ and 2. The results are gathered in Figure 3 and 4 for EPBC1 with 6.35 mm and 9 mm in thickness, respectively. As can be seen, the best fit is achieved when using a value of $m=1.5$ for the 6.35 mm thick EPBC1 specimens (Figures 3a and 3b),

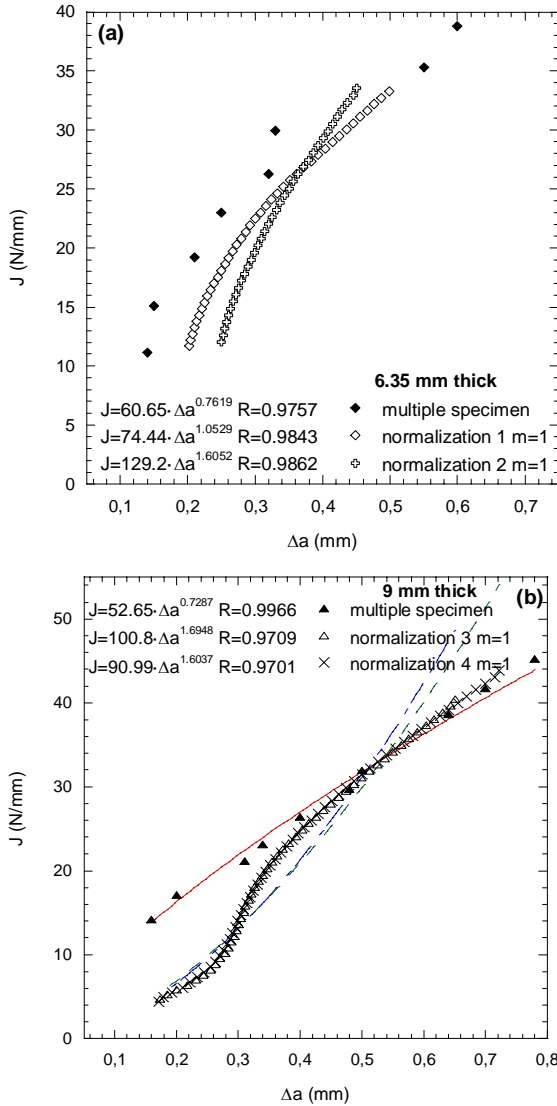


Figure 1. J-R curves of EPBC1 obtained from the multiple specimen method and from the normalization method with $m=1$ for (a) 6.35 mm and (b) 9 mm thick specimens.

Table 2. Critical values of J-integral for EPBC1 and EPBC5 determined through different methods and crack tip blunting behaviours.

Sample	Thickness (mm)	m	EPBC1		EPBC5	
			6.35	9	6.35	9
Multiple Specimen			17.8	16.3	11.1	11.2
Normalization		1	-	-	¹ 11.7 ² 10.2	³ 11.9 ⁴ 11.7
		1.25	-	³ 14.8 ⁴ 14.6	-	-
		1.5	¹ 19.0 ² 18.1	³ 18.9 ⁴ 18.7	-	-
			¹ 21.4 ² 21.3	³ 21.6 ⁴ 23.0	-	-

- J-R curve does not fit $J=C \cdot \Delta a^N$, with $N \leq 1$

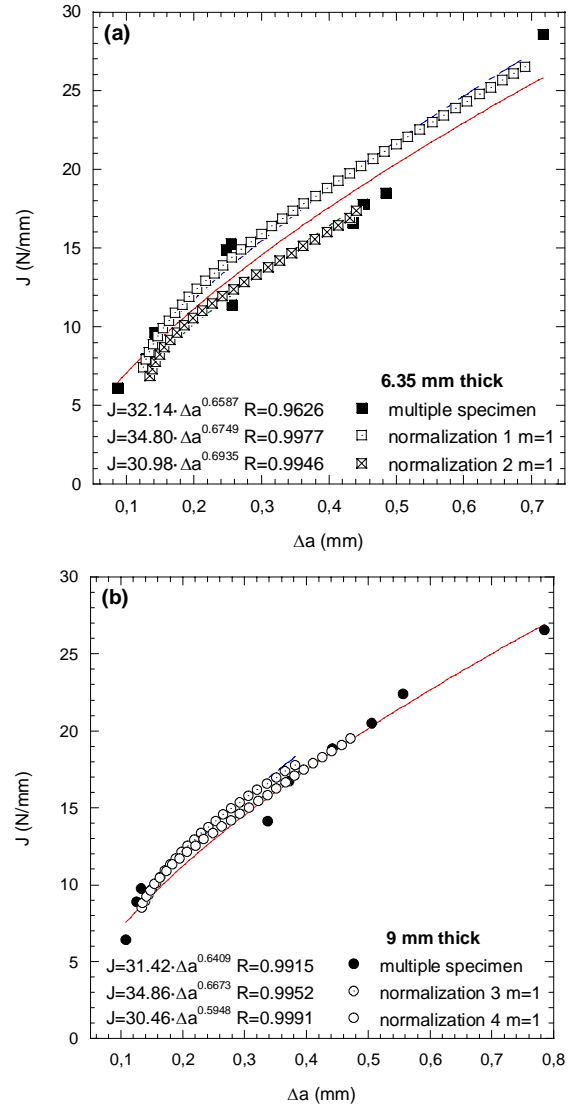


Figure 2. J-R curves of EPBC5 obtained from the multiple specimen method and from the normalization method with $m=1$ for (a) 6.35 mm and (b) 9 mm thick specimens.

while for the 9 mm thick EPBC1 specimens (Figures 4a and 4b), the best accuracy is attained with $m=1.25$.

The critical fracture toughness values, J_{IC} , obtained considering the different methods and as a function of the crack tip constraint factor, m , in case of the normalization method are collected in Table 2. None of the J_{IC} parameters verifies the size criterion specified in equation (10), so all the values are not in plane strain state. For EPBC5, the results obtained via multiple specimen method are in good agreement with those determined with the normalization method using a value of $m=1$ for the two analyzed specimens' configurations. In such PP block copolymer, it has been proved that the established value of $m=1$ [8-9] works accurately for EPBC5. On the other hand, for the other PP block copolymer, EPBC1, with a molecular weight almost three times higher than EPBC5, it has been evidenced the dependence of the crack tip constraint factor on the

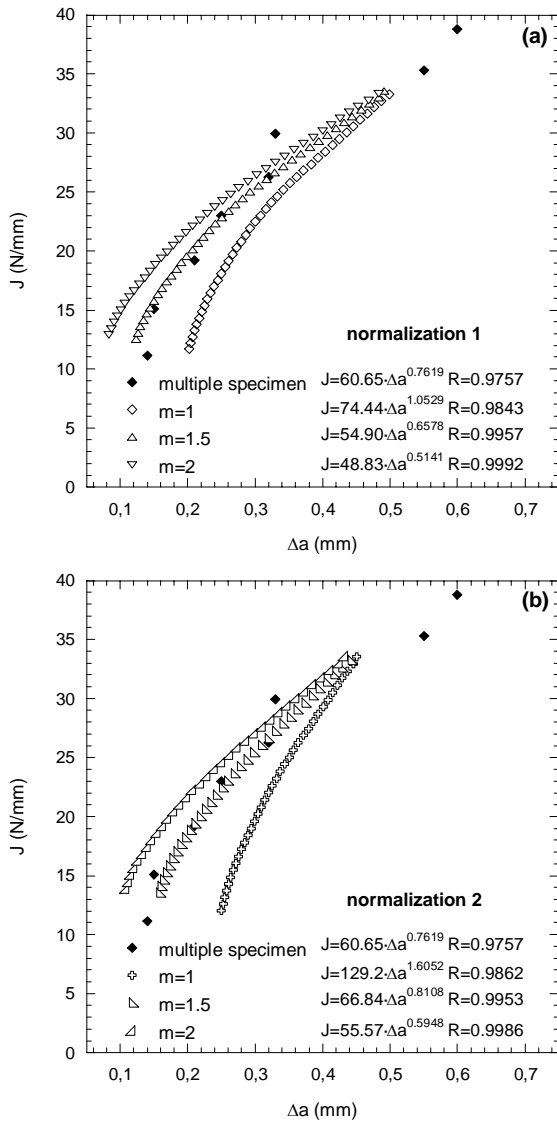


Figure 3. Influence of the crack tip constraint factor, m , on the J - R curves of EPBC1 with 6.35 mm in thickness: (a) sample normalization 1 and (b) sample normalization 2.

material properties and even geometry. Particularly, the best fit between the multiple specimen J - R curves and those determined via normalization method are achieved by setting m to 1.5 and 1.25 for 6.35 and 9 mm thick samples, respectively.

5. CONCLUSIONS

A single specimen method as the normalization method, included in ASTM E1820-06, has been applied to two different ethylene-propylene block copolymers with distinct structural parameters, especially the molecular weight, with the aim of analyzing the influence of a methodological parameter as the crack tip constraint factor, m , on the applicability of this methodology. The J - R curves obtained via multiple specimen method have been taken as references. The results reveal that the crack tip constraint factor is strongly dependent on the material's properties and dimensions. The best accuracy

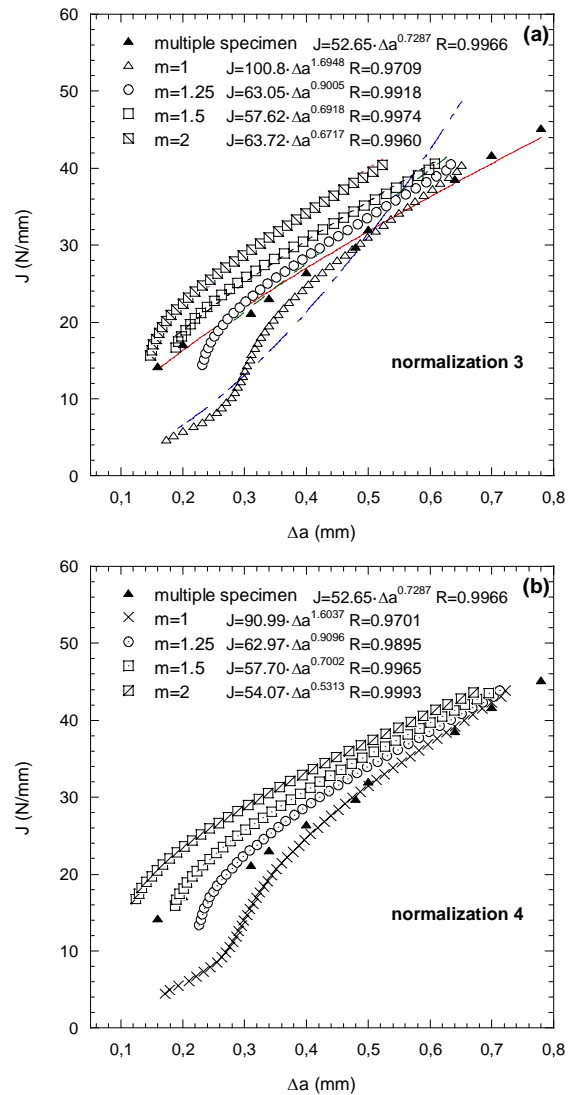


Figure 4. Influence of the crack tip constraint factor, m , on the J - R curves of EPBC1 with 9 mm in thickness: (a) sample normalization 3 and (b) sample normalization 4.

of the J - R curves of the copolymer with a huge molecular weight ~ 820 kg/mol, roughly that of UHMWPE, is attained for values of m equal to 1.5 and 1.25 for the specimens' dimensions related to 6.35 and 9 mm thick samples, respectively. Meanwhile, the PP block copolymer, with molecular weight ~ 300 kg/mol, showed the best fit between the J - R curves obtained experimentally with those determined with the normalization method by setting $m=1$, in accordance with the m values reported in the literature.

ACKNOWLEDGEMENTS

Authors are indebted to *Ministerio de Educación* of Spain for their financial support through projects MAT2006-13354 and MAT2009-14294, and to REPSOL YPF for the materials supply.

REFERENCES

- [1] Wells, A.A., "Unstable crack propagation in metals: cleavage and fast fracture", *Proceedings of the Crack Propagation Symposium*, Cranfield, UK, Vol. 1, Paper 84, 1961.
- [2] Irwin, G.R., "Plastic zone near a crack and fracture toughness", *Sagamore Research Conference Proceedings*, Vol. 4, 1961.
- [3] Anderson, T.L., *Fracture Mechanics. Fundamentals and Applications*. 2nd edition, CRC Press, 1995.
- [4] ASTM E1820-06: Standard test method for measurements of fracture toughness, ASTM standards, 2007.
- [5] ASTM D6068-96: Standard test method for determining J-R curves of plastic materials, ASTM standards, 2002.
- [6] Hale, G.E., Ramsteiner, F., *J-fracture toughness of polymers at slow speed*. In: *Fracture mechanics testing methods for polymers, adhesives and composites*, D. R. Moore, A. Pavan, J. G. Williams editors, Elsevier Science Ltd. and ESIS: The Netherlands, 2001, pp 123-157.
- [7] Ernst, H.A., Paris, P.C., Landes, J.D., *Estimations on J-integral and tearing modulus T from a single specimen test record*. *Fracture Mechanics*, ASTM STP 743 (1981) 476-502.
- [8] Salazar, A., Rodríguez, J., *The use of the load separation parameter S_{pb} method to determine the J-R curves of polypropylenes*. *Polymer Testing* 27 (2008) 977-984.
- [9] Morhain, C., Velasco, J.I., *Determination of J-R curve of polypropylene copolymers using the normalization method*. *Journal of Materials Science* 36 (2001) 1487-1499.
- [10] Rodríguez, C., Maspocho, M.Ll., Belzunce, F.J., *Fracture characterization of ductile polymers through methods based on load separation*. *Polymer Testing* 28 (2009) 204-208.
- [11] Varadarajan, R., Dapp, E.K., Rimnac, C.M., *Static fracture resistance of ultra high molecular weight polyethylene using the single specimen normalization method*. *Polymer Testing* 27 (2008) 260-268.

COHESIVE LAWS IN ADHESIVES JOINTS: THE TEARING/DEBONDING TEST FOR CHARACTERIZATION OF THIN ADHESIVE FILMS

J.C. Suárez¹, S. Miguel¹, F. López¹, M.A. Herreros¹

¹Research Group on Hybrid Materials, ETS Ingenieros Navales, Universidad Politécnica de Madrid, Avda. Arco de la Victoria, s/n, 28040 Madrid, Spain.
E-mail: juancarlos.suarez@upm.es

ABSTRACT

To be able to predict the strength of adhesive joints accurately, correct material data of adhesives are essential. Hence, it is critical to develop reliable testing methods to obtain the constitutive behaviour of adhesive layers. In use, adhesives are constrained to thin layers. Thus, an adhesive constrained into a layer is expected to behave differently compared to the adhesive as a bulk material. Under loading, the size of the Failure Process Zone (FPZ) in the adhesive layer is often much larger than the thickness of the layer. Thus, the small scale FPZ condition is not fulfilled and the traditional Linear Elastic Fracture Mechanics (LEFM) can not be applied. At the same time, experiments show that test specimens are prone to produce unstable crack propagation and combined adhesive/cohesive fracture patterns appear frequently, especially when mixed mode loading (peel and shear) is involved. Cohesive law should be taken as the basic fracture property for adhesives characterization; cohesive laws must be determined experimentally. The effects of loading rate and adhesive layer thickness on the cohesive law shape have to be investigated experimentally. The coupling of elasticity, adhesion and fracture make difficult interpretation of test results, especially if the adhesive is an elastomer, which has a failure strain of several hundred percents. A new test has been proposed, combining tearing of the adhesive layer and debonding from the substrate in a controlled way and using a simplified geometry. Results are closely related to the stiffness, work of fracture and adhesive energy of the adhesive system, all of them playing simultaneously an active role during the very same test.

KEY WORDS: adhesive, tearing, debonding, cohesive law.

1. INTRODUCTION

Some of these mechanisms of energy absorption and toughness improvement both in biological and bioinspired materials are:

1. Rupture of “sacrificial” weaker bonds in the macromolecular component.
2. Extension, pull-out and/or ligament formation of a macromolecular component bridging an interface
3. Void formation leading to bulk plastic deformation, crack blunting, pinning and branching.
4. Localized plastic deformation ahead of a crack tip.
5. Microcrack formation.
6. Phase-transformations which take place ahead of a crack tip.
7. Viscoelastic dissipation.
8. Interacting nanoasperities and mechanical interlocking leading to inelastic strain.

A recent research has paved the way to develop new strategies for energy dissipation inside hybrid materials composed mainly of a granular media [1]. The goal is to employ several of these strategies altogether to obtain light and tough materials, with a high-energy absorption capability related to their low density. It is also quiet

important to retain a certain residual strength after the impact to assess the structural integrity for the application in mind, that is, to assure also a good damage tolerance of the hybrid material.

In use, adhesives are constrained to thin layers. An adhesive constrained into a layer is expected to behave differently compared to the adhesive as a bulk material. The use of an un-cracked butt joint specimen to measure the constitutive relation can be tempting. However, experiments show that this specimen is prone to be unstable. The softening part of the constitutive relation, which contributes substantially to the fracture energy, is never captured experimentally. A few testing specimens and techniques for evaluating fracture properties have been developed. Most of these are based on LEFM and the flexibility of the adhesive layer is neglected [2].

However, there are difficulties with standard tests. The locus of failure and the issue of directional stability of cracks in adhesively bonded joints have been investigated by different authors and, over the years, several criteria have been developed [3]. According to these criteria, a crack in an adhesive bond can be steered to different locations if the local stress state at the crack tip is in mixed mode. Consequently, various failure locations can result and failure does not necessarily occur at the weakest site within the material. T-stress plays an important role in the directional stability of the

crack propagation. The crack is directionally stable if the T-stress is negative, whereas is directionally unstable if the T-stress is positive. The adherend bending effect on the T-stress induces a non negligible influence of the thickness of the adherends on the directional stability of the cracks in the adhesive joints.

Even for the most simple test specimen geometries the Strain Energy Release Rate (SERR) and /or J-integral include non clearly determined contributions of different dissipation mechanisms (fracture, debonding, viscoelastic effects). From this information, it is possible to derive the constitutive relations representing the mechanical behaviour of the entire adhesive layer. Such constitutive relations can be represented by traction-separation models, also referred to as cohesive laws, describing activities in the adhesive layer before and at fracture. It is difficult to obtain parameters that are related exclusively to only one process (interfacial debonding, fracture of the adhesive or viscoelastic behaviour of the polymer). Extrapolation to real adhesive joints is consequently limited and, specifically, there are difficulties to properly model the adhesively bonded joints in virtual testing by numerical simulation.

2. TEARING-DEBONDING TEST

A new test has been proposed, combining tearing of the adhesive layer and debonding from the substrate in a controlled way and using a simplified geometry [4]. Results are closely related to the stiffness, work of fracture and adhesive energy of the adhesive system, all of them plying simultaneously an active role during the very same test.

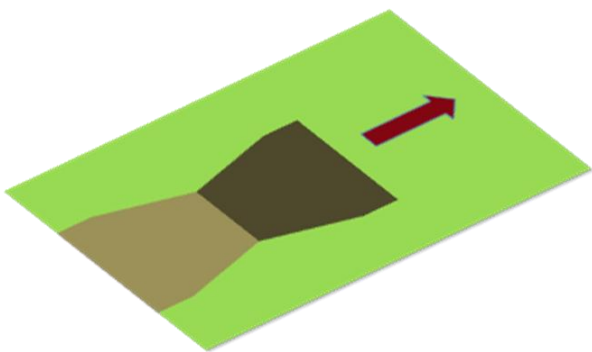


Figure 1. Simplified geometry of the tearing-debonding test.

We have all had the experience of unsuccessfully trying to remove a rectangular strip from a roll of adhesive tape by scratching the edge with a fingernail. When pulling on the partially detached piece, the strip annoyingly narrows, detaches and the final tear is often too short to be useful. Similar difficulties are experienced when trying to remove wallpaper, a sticker or a package label. The runaway tear may in fact be taking a natural physical path. Elasticity of thin sheets couples with adhesion and fracture to produce distinct

shapes characterizing the tearing process. A combined experimental and theoretical study to explore this coupling of elasticity, adhesion and fracture, in a simplified geometry shows a promising way to clarify the specific role of every energy dissipation mechanism, Figure 1. We adhere a thin elastic sheet to a solid flat surface and cut two notches on one of its edges such that a rectangular flap is created, which is then pulled at a constant speed. The two crack tips (located at the edge of the flap) are initially parallel, but as the flap starts being pulled they propagate both forwards and inwards as the material progressively de-adheres from the substrate. Eventually, the two tips converge to a point and the strip detaches completely, leaving behind a triangular tear.

The profiles of three representative tears are shown in Figure 2 in which only the width of the initial flap (distance from the initial two notches) was changed. The sides of the flap are straight and make the same angle theta with the axis of symmetry of the tear, independently of the size of the initial flap.

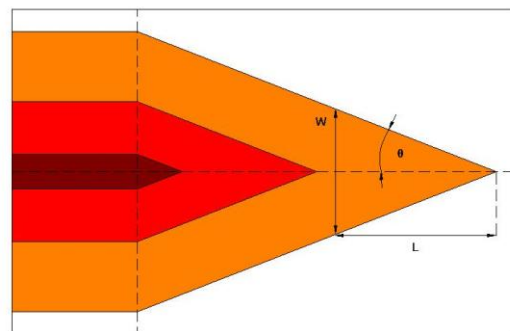


Figure 2. Profiles of three representative tears for different sizes of the initial flap.

Following Griffith's theory of fracture, a simple mechanism based on elasticity has been proposed to understand the experimentally obtained tear shapes [5]. A pulling force deforms the surface and focuses elastic energy in a fold that joins the flap with the film. This energy can be released in two ways: by decreasing its curvature (advancing the crack in the pulling direction) or by simply reducing the width of the ridge (the cracks move inwards). The actual direction is a combination of both effects, but always leads to a narrowing of the tear.

The total energy of the system that quantifies the above outlined mechanism is

$$U = U_E + 2\gamma ts + \tau A \tag{1}$$

U_E is the elastic energy, $2\gamma ts$ is the fracture energy, and τA is the adhesive energy. The factor 2 in the fracture energy term accounts for the fact that two fracture paths are propagating along the film. The work of fracture, γ , always comes in the combination γt , and this parameter has a dimension of a force, we refer to it as 'fracture

force'. Assuming that the end of the flap is always at an angle of 180° from the reference plane defined by the solid wall, we conclude that the elastic energy is only a function of the tip displacement, x , and the length of the strip along its axis of symmetry, l . The excess of length $2l - x$ is folded near the detachment line (Figure 3), so that we expect the elastic energy to be a function of the tip displacement in this combination.

$$U_E = U_E(2l - x, W) \quad (2)$$

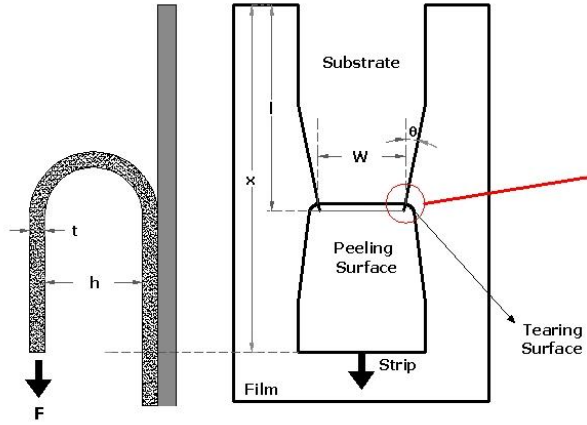


Figure 3. Folding of the adhesive film near the detachment line.

The crack tip advances to a position that minimizes the total energy. In a displacement-controlled experiment, the first variation of U with respect to the geometrical parameters is

$$\begin{aligned} \frac{\partial U}{\partial s} &= 0 \\ \delta U &= (\partial_W U_E)_{x,l} \delta W + (\partial_l U_E)_{x,W} \delta l + \dots \\ &\dots 2\gamma t \delta s + \tau W \delta l \end{aligned} \quad (3)$$

The force is given by the work theorem as

$$F = (\partial_x U_E)_{W,l} \quad (4)$$

This equation combined with the specific dependence of the elastic energy on the geometrical parameters yields for the energy minimum

$$\begin{aligned} 0 &= -2(\partial_W U_E) \sin \theta - 2F \cos \theta + 2\gamma t + \tau W \cos \theta \\ \sin \theta &= -\delta W / 2\delta s \quad \cos \theta = \delta l / \delta s \end{aligned} \quad (5)$$

To find the fracture path, we require that the tear follows the direction where a minimal force is necessary for the advancement of the crack tips. An implicit derivative of equation (3) gives the equivalent condition usually

referred to as the maximum-energy-release-rate criterion

$$\begin{aligned} \partial_\theta (\delta U / \delta s) &= 0 \\ 0 &= -2(\partial_W U_E)_{x,l} \cos \theta + 2F \sin \theta - \tau W \sin \theta \end{aligned} \quad (6)$$

Equations (5) and (6) have a clear interpretation in terms of static equilibrium of in-plane forces. These forces, acting on one half of the strip, are: the fracture force (γt) resisting crack propagation, the operator pulling force F opposed to the adhesion energy dissipation $\tau W/2$, and the lateral elastic energy gradient $\delta_W U_E$.

The forces projected along the forward and sideways directions give the equivalent equations

$$F = \tau \frac{W}{2} + \gamma t \cos \theta \quad (7)$$

$$(\partial_W U_E)_{x,l} = \gamma t \sin \theta \quad (8)$$

The pulling force is balanced by two forces: that of adhesion of the film to the substrate and that of fracture. It predicts that the force decreases proportionally to the flap width and has a finite value ($\gamma t \cos \theta$) when the width tends to zero. This implies that near the tip, adhesion forces are negligible and the fracture force is the only remaining obstacle to detachment.

3. EXPERIMENTAL

To experimentally check equations (7) and (8), we have tested an adhesive film used as a window polarizer, of several thicknesses. These materials are brittle: they are easy to tear and on fracture leave behind two planar crack lips. Although the fracture force is different for each film, the adhesion energy is the parameter that can be more easily varied systematically. This can be done in two ways: by pulling the flap at different speeds or by using different substrates.



Figure 4. Experimental set-up.

The commercial adhesive film we used in the experiment was 3M Prestige 70 film, thickness 23-38 μm . The film was adhered to glass, steel and stainless steel plates, and parallel flaps 2-6 cm wide and of variable length was then cut and detached starting from the edge of the film. To include anisotropic effects, we cut and pulled flaps in the film in two perpendicular directions. The strip was then pulled with the help of a testing machine that leads to uniform pulling in all runs of the experiment, at speeds ranging from 80 down to 2 mm/min. A typical load-displacement record is shown in Figure 5.

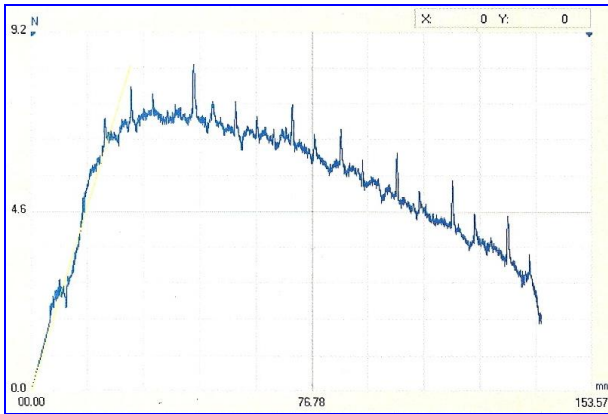


Figure 5. Load vs displacement recorded in a tearing-debonding test.

4. RESULTS AND DISCUSSION

The relation between adhesion energy and speed, $\tau = \tau(v)$, is not fully understood even though this dependence has been extensively studied in recent years [6-8]. As shown in Figure 6, by increasing the speed the adhesion energy increases and the tears become shorter.

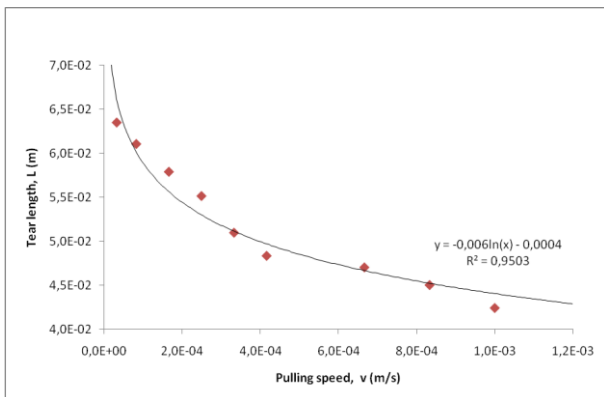


Figure 6. Tear length vs pulling speed for tearing-debonding tests.

In Figure 7, the pulling force, F , is plotted as a function of the flap width, W , for a number of experiments at a variety of pulling speeds, v . A linear decay of the force with the width of the tear is observed, as predicted by equation (7). The straight lines that fit each set of data have approximately the same intercept with the y axis. This is in accordance with equation (7), and thus the

intercept gives an estimation of the fracture force. The value of the fracture force obtained in this way is consistent with the direct measurement of the force needed to start a tear by pulling a rectangular flap when the film is not adhered to a substrate, but held on its Boundaries (ASTM D1938-06) [9].

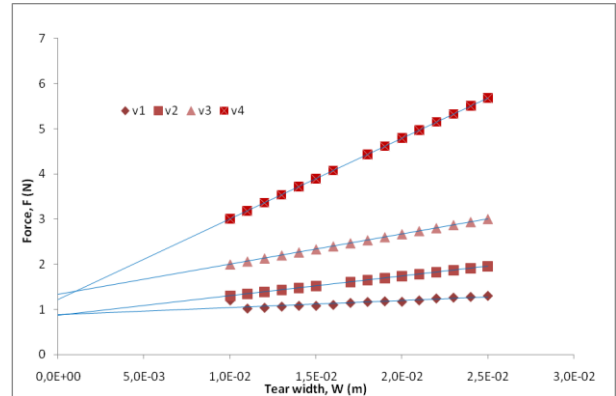


Figure 7. The pulling force versus flap width for runs made at different speeds.

The intercepts in Figure 7 are only an estimation of the fracture force since the straight lines intersect the y axis at $F = \gamma t \cos \theta$. Thus, the intercepts of those lines also depends on the tear angle θ . To obtain a better estimation of the fracture force, we extract the adhesion from the slopes in previous Figure 7 and plot the data using the modified equation:

$$\frac{F}{\cos \theta} = \frac{\tau W}{2 \cos \theta} + \gamma t \tag{9}$$

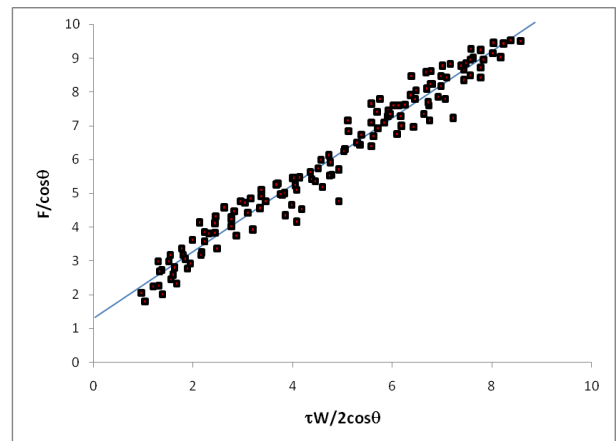


Figure 8. Estimation of the fracture force from the tearing-debonding test.

As we can expect, the slope for the best fit is ≈ 1 . Let's now turn to equation (8). We need to obtain the exact expression for the elastic energy and, in general, it can be a difficult task to compute precisely how the elastic energy is distributed in the strip because the typical displacements observed are of the order of the system size. We take advantage of the film being strongly adhered to a substrate. This configuration helps to keep the lines across the flap width with zero curvature,

allowing the surface to deform only along its longitudinal direction. The deflection can therefore be analyzed in terms of the classical elastica of Euler that accounts for arbitrary planar deformations of a sheet, and the elastic energy available for fracture can be easily obtained

$$U_E = \frac{4BW}{h} \tag{10}$$

$$\sin \theta = \frac{4B}{\gamma th} \tag{11}$$

Figure 9 shows the experimental verification of equation (11). The variation of the angle and average distance h is produced by changing the substrate and varying the pulling speed. The solid line shows the theoretical prediction. The error bars show the uncertainty obtained from the estimated error of each parameter. We find the tear angle to be constant in our experiments (triangular tear shapes), this relation implies that h is a constant, throughout the tearing process.

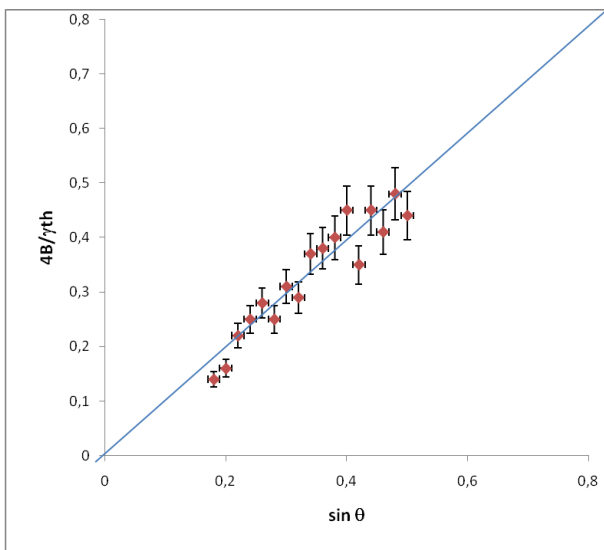


Figure 9. Experimental verification of equation (11).

So far, we have shown that relations (3) and (4) are satisfied by our experiments. It remains to be explained why these equations imply that the fracture trajectories are straight lines. This relation is consistent with the force measurements in Figure 10, but with a lower value of η than the value $\eta=1$ expected for a perfectly elastic strip. The straight solid line with a slope $\eta=0.55$ is the best fit for all of the experimental points and the dashed lines show the error bounds of our estimate. Equation (7) becomes now Equation (12)

$$4\eta^2 \frac{BW}{h^2} = \tau \frac{W}{2} + \gamma t \cos \theta \tag{12}$$

For large values of W , the last term in equation (12) is negligible, and the distance h must have the constant value

$$h = 2\eta \sqrt{\frac{2B}{\tau}} \tag{13}$$

Equation (12) shows that a larger pulling speed increases the adhesion energy, makes the fold joining the crack tips smaller (h decreases) and, the tears shorter.

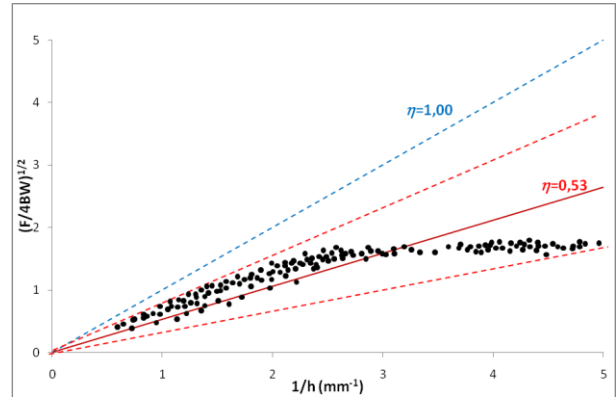


Figure 10. Value of the parameter η extracted from the experiments.

The trajectories are straight lines with a tear angle determined by three material constants: the elastic stiffness of the film, its fracture force and the adhesion energy with the substrate. When a flap is pulled to produce a tear, energy is localized in a narrow region connecting the flap with the film and becomes available for fracture. The specific geometry of the resulting fold gives a different elastic energy driving the fracture and lead to new tear shapes with no straight sides. Thus, under new conditions, different tear shapes can emerge that hide in their geometry the mechanism transforming elastic energy into surface energy of fracture and/or adhesion, and can potentially be used for mechanical characterization.

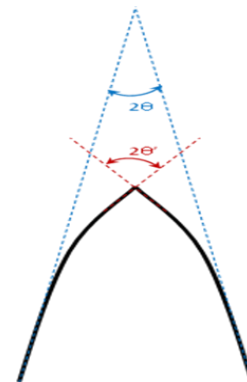


Figure 11. Deviation from straightness in the vertex of the flap.

5. CONCLUSIONS

1. A new method has been presented to investigate the mechanical properties of thin adhesive films. As thickness is reduced owing to new technologies,

traditional methods used to measure mechanical properties of a material in bulk form are not applicable, and leads to unexpected mechanical behaviour such as stress localization and wrinkling.

2. The coupling between elasticity, adhesion and fracture, imprinted in a tear shape, can be used to evaluate mechanical properties of thin films. The angle observed is a combination of three parameters: the elastic stiffness of the film, its fracture force and the adhesion energy with the substrate.

3. For a cylindrical deformation of the fold, $\eta=1$. A lower value of η observed in the experiments implies that the fold shows more rigidity than predicted by elasticity. Long interaction effects due to adhesive filaments also modify the shape of the fold.

4. The effective value of η is related to the cohesive law of the adhesive. Tear shapes hide in their geometry the mechanism transforming elastic energy into surface energy of fracture and/or adhesion, and can be used for mechanical characterization

[7] D.C. Hong, S. Yue, Deterministic chaos in failure dynamics: Dynamics of peeling of adhesive tape, *Phys. Rev. Lett.* 74 (1995) 254–257

[8] R. De, A. Maybhate, G. Ananthakrishna, Dynamics of stick-slip in peeling of an adhesive tape, *Phys. Rev. E* 70. (2004) 046223

[9] ASTM D1938-08, Standard test method for tear propagation resistance (trouser tear) of plastic film and thin sheeting by a single tear method, *ASTM International* (2008)

ACKNOWLEDGEMENTS

The authors acknowledge the support from Universidad Politécnica de Madrid through grant AM0402. Our gratitude to the laboratory technical staff: Mr. José Illescas, Ms. Ana Soria, and Ms. Ana García for their assistance in the completion of these experiments.

REFERENCES

[1] J. Hong, Universal power-law decay of the impulse energy in granular protectors, *Physical Review Letters* 94 (2005) 108001

[2] J.L. Högberg, B.F. Sørensen, U. Stigh, Constitutive behaviour of mixed mode loaded adhesive layer, *International Journal of Solid and Structures*, 44 (2007) 8335 - 8354

[3] B. Chen, D.A. Dillard, The effect of the T-stress on crack path selection in adhesively bonded joints , *International Journal of Adhesion & Adhesives*, 1 (2001) 357 - 368

[4] E. Hamm, P. Reis, M. Leblanc, B. Roman, E. Cerda, Tearing as a test for mechanical characterization of thin adhesive films, *Nature Materials*, 7 (2008) 386 - 390

[5] B. Lawn, *Fracture of brittle solids* (2nd Ed) Cambridge University Press, Cambridge (2004)

[6] P.P. Cortet, M. Ciccotti, L. Vanel, Imaging the stick-slip peeling of an adhesive tape under constant load, *J. Stat. Mech.* P03005 (2007)

MIXED MODE DOUBLE CANTILEVER BEAMS TEST SPECIMEN FOR CHARACTERIZATION OF STRUCTURAL ADHESIVE JOINTS

J.C. Suárez¹, P. Pinilla¹, F. López¹, M.A. Herreros¹, M.V. Biezma²

¹Research Group on Hybrid Materials, ETS Ingenieros Navales, Universidad Politécnica de Madrid, Avda. Arco de la Victoria, s/n, 28040 Madrid, Spain.
E-mail: juancarlos.suarez@upm.es

²Departamento de Ciencia e Ingeniería del Terreno y los Materiales, Universidad de Cantabria, Dique de Gamazo s/n, 39004 Santander, Spain.
E-mail: maria.biezma@unican.es

ABSTRACT

Numerical simulations or virtual testing are gradually replacing many expensive and time consuming experiments in the product design process. To be able to predict the performance of the adhesive joints accurately, correct material data of adhesives are essential. Hence, it is critical to develop reliable testing methods to obtain the constitutive behaviour of adhesive layers. For adhesive joints, it is convenient to let the constitutive relation represent the mechanical behaviour of the entire adhesive layer. Such a constitutive relation describes activities in the adhesive layer before and at fracture. The objective of this work is to experimentally obtain the constitutive behaviour of an adhesive layer under mixed mode loading. The Mixed Mode Double Cantilever Beams (MCB) specimen used in the experiments is designed to allow the adhesive layer to be loaded by a force varying smoothly from pure peel to pure shear. An explicit J-integral expression is derived for the MCB-specimen and used to evaluate the energy dissipation in the FPZ. The measured deformations of the adhesive layer in the FPZ show a nonlinear deformation path in all tested mode mixities and the critical deformation of the adhesive in the peel direction is virtually independent of the mode mixity. The constitutive behaviour of the adhesive layer is obtained by the inverse method. The obtained constitutive behaviour of the mixed mode loaded adhesive layer is coupled and mode dependent.

KEY WORDS: adhesive, mixed mode, J-integral, virtual testing.

1. INTRODUCTION

Adhesive joints are designed in such a way that a thin layer of adhesive is placed between two substrates, which are usually stiffer than the polymeric adhesive system, thus constraining its displacements under load. There is experimental evidence that a thin layer of adhesive behaves differently compared to the bulk material [1].

Table 1. Decomposition methods by various researchers

	Descomposition method by
Reeder and Crews [3]	Load
Ducept et al. [4]	Load
Hutchinson and Suo [5]	SIF
Shapery and Davidson [6]	SIF
Thouless et al. [7]	ERR
Fernlund and Spelt [2]	ERR
Pang [8]	SIF

SIF: Stress Intensity Factor; ERR: Energy Release Rate

Adhesive joints are much stronger when loaded in shear than in peel. Much more difficult is to assess the properties in mixed mode loading I+II [2]. The approaches for analyzing mode mixities on adhesive

joints can be classified in two categories: the global approaches and the local approaches, as summarized in Table 1. The decomposition methods that are based on the input parameters are referred to as global approaches. The methods that are based on the output parameters in terms of the SIF and the ERR are referred to as local approaches

Among the *global approaches*, the Tapered Double Cantilever Beam (TDCB) specimen has been used by the authors and results presented elsewhere for pure mode I loading [9]. The mixed mode bending (MMB) specimen is very useful for achieving a range of mode mixities on an adhesive joint, as reported by the authors for elastic adhesives [10].

The *local approaches* focus on the local condition at the crack tip region of an adhesive joint, i.e., the ends of the overlap area, in terms of the SIF and the ERR. Under this category, three types of joint models are considered:

- Bi-material models, in which unbalances of the adherends are considered and the adhesive layer is ignored;
- Adhesive-layer models, in which the adhesive layer is modeled by, e.g., the embedded process zone (EPZ) model;

- Calibrated joint models, in which an adhesive joint is modeled and compared to a specimen without the adhesive layer by the use of a calibration factor.

The mode mixity can be achieved by introducing geometrical or material unbalances into a load-balanced joint, such as the Double Cantilever Beam (DCB) and Crack Lap Shear (CLS) specimen. However, neither the DCB nor the CLS can achieve mode mixity in the complete spectrum, i.e., from pure mode I to pure mode II. In general, to make valuable conclusions for experiments, a number of specimens are required for achieving the repeatability and the reliability. It is then more suitable to use one and the same geometry of the specimen and vary the loading system in order to achieve a range of mode mixities. In such a way, only one type of specimen has to be designed and manufactured. This sets design requirements on the loading system:

- *Flexibility*: the loading system should be simply adjustable for testing different mode mixities;
- *Variety*: the ability for attaining the entire spectrum of mode mixities, i.e., from pure mode I to pure mode II;
- *Stability*: the mode mixity should vary steadily and smoothly by a pre-defined adjusting parameter in the loading system.

Based on the geometry of a semi-infinite symmetric DCB-specimen, by combining the basic loading cases of DCB, ELS and CLS, a testing specimen, referred to as the mixed mode double cantilever beam (MCB) specimen, is suggested [11, 12].

2. MIXED MODE DOUBLE CANTILEVER BEAM (MCB) SPECIMEN

To experimentally obtain the constitutive behaviour of an adhesive layer, it is advantageous to restrict the number of process zones to one in the tested adhesive layer. This can be achieved by loading the specimen at one end and using a long specimen. Due to the elastic properties of the adhesive layer, the far end of the specimen will be virtually unloaded. Thus, a reasonably long specimen can be considered semi-infinite in the analysis. Figure 1 illustrates the mixed mode double cantilever beam (MCB) specimen as superposition of the basic loading systems. Each adherend at the free end of the MCB-specimen is loaded with an external force, F , with the same magnitude but opposite direction. This pair of forces are self-balancing and their direction of action is defined by the angle α .

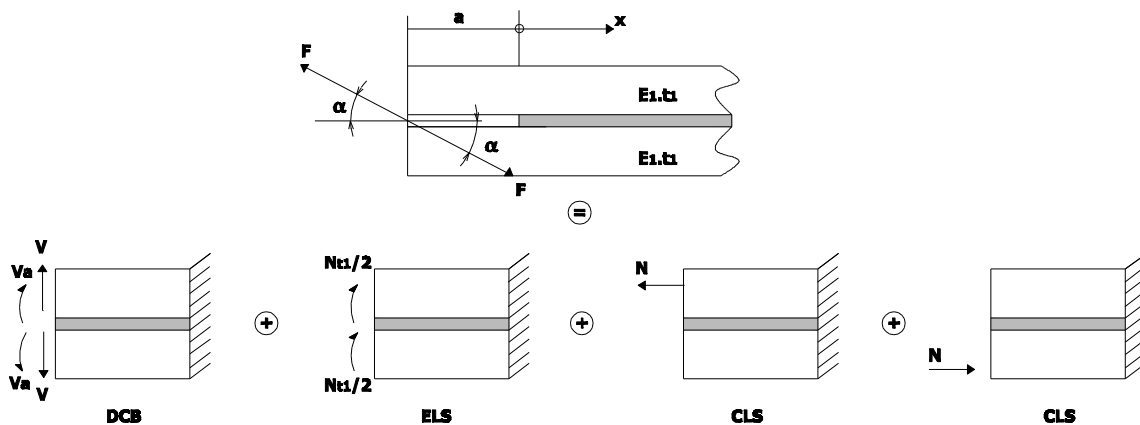


Figure 1. Mixed mode double cantilever beam (MCB) specimen as superposition of the basic loading systems.

The sectional forces at the crack tip, $x = 0$, in Figure 1 are

$$N = F \cos \alpha \quad (1)$$

$$V = F \sin \alpha \quad (2)$$

Superposition of the deformations for the basic loading systems gives the normal and tangential deformation at the crack tip

$$\hat{w} = \Delta \sin \beta = \frac{2\kappa_{pl}}{bE} (1 + \kappa_p a) F \sin \alpha \quad (3)$$

$$\hat{v} = \Delta \cos \beta = \frac{\kappa_s t}{bE} F \cos \alpha \quad (4)$$

where Δ is the total deformation of the adhesive layer at the crack tip and $\beta = \tan^{-1} \hat{w}/\hat{v}$ is the angle between the deformation modes. For a linear elastic MCB-specimen, the ERR is decomposed in mode I and mode II as

$$J_I = \frac{1}{2} \frac{\bar{E}}{t} \Delta^2 \sin^2 \beta = \frac{12}{E_1 t_1} \left(\frac{F}{b} \right)^2 \left(\frac{1}{\kappa_p t_1} + \frac{a}{t_1} \right)^2 \sin^2 \alpha \quad (5)$$

$$J_{II} = \frac{1}{2} \frac{G}{t} \Delta^2 \cos^2 \beta = \frac{4}{E_1 t_1} \left(\frac{F}{b} \right)^2 \cos^2 \alpha \quad (6)$$

With the mode mixity defined by

$$\Lambda = \frac{J_{II}}{J_I + J_{II}} \quad (7)$$

A combination of Eqs. 5, 6 and 7, gives the mode mixity of the MBC-specimen in terms of the force angle α

$$\Lambda \alpha = \frac{\cos^2 \alpha}{3 \left(\frac{1}{\kappa_p t_1} + \frac{a}{t_1} \right)^2 \sin^2 \alpha + \cos^2 \alpha} \quad (8)$$

In terms of the deformation angle β

$$\Lambda \beta = \frac{\cos^2 \beta}{\frac{\bar{E}}{G} \sin^2 \beta + \cos^2 \beta} \quad (9)$$

3. EXPERIMENTAL PROCEDURE

The specimens are fabricated by first bonding two steel plates with 1 mm thick adhesive, then cut into desired width after curing. The plates are made of naval steel grade A, 10 mm in thickness, with material data given in Table 2. The adhesive is a two-components polyurethane system. To enhance the bonding surfaces, the plates are cleaned with acetone and sand grinded. Teflon film stripes of 0.5 mm are inserted between the plates to ensure an even thickness of the adhesive layer, as well as the crack tip position. After curing at 25 °C for 24 h, the joined plates are then cut into 4 mm wide specimens.

Table 2. Material and geometrical data for the MCB-specimen used in experiments

Overall joint	Bonded length, L=100 mm
	Joint width, b=4 mm
	Crack length, a=0 mm
Adherends	Naval steel plates, grade A
	Thickness, t ₁ =10 mm
	Young modulus, E=207 GPa
	Yield strength, σ _y =275 MPa
Adhesive	Two-components polyurethane
	Thickness, t=0.5 mm

Two fixture parts, Figure 2, are designed to allow the specimen to be loaded in an uniaxial tensile test machine. Seven different mode mixities can be achieved, with loading angles $\alpha = 0^\circ, 15^\circ, 30^\circ, 45^\circ, 60^\circ, 75^\circ$ and 90° . Two forks are also manufactured to allow

the tensile machine to grip the fixtures at different angles. A electromechanic testing system, with loading capacity of ± 5 kN is used. The experiments are made at a constant displacement rate of 15 $\mu\text{m/s}$. The loading force is recorded on a computer during the experiments.



Figure 2. Fixtures with the MCB-specimen.

Another set of test specimens has been aged in sea water, and the joints have been tested after different times of immersion in order to assess the degradation of the strength along the time. The results will be presented elsewhere.

4. RESULTS AND DISCUSSION

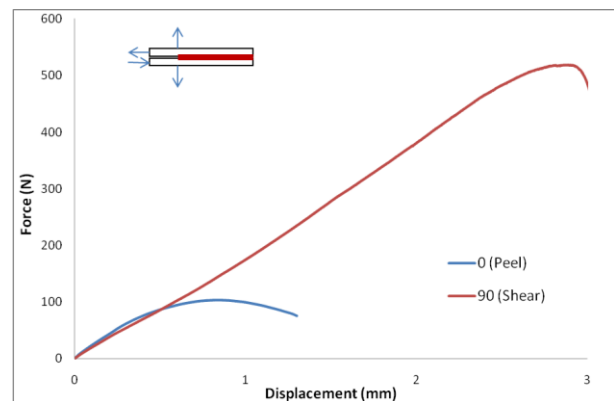


Figure 3. Loading histories for different mode mixities.

Evaluation of the energy dissipation and the constitutive relation of the adhesive layer is based on the J-integral. The parameters measured during the experiment are: the external force F, the rotation of the adherends w'_1 and w'_2 at the crack tip ($x = 0$), and the deformation of the adhesive layer w and v at the crack tip ($x = 0$). A total of 21 specimens are tested, with three specimens tested at each of the seven loading angles.

The loading histories for every mode mixities are shown in Figure 3 where the external force, F, is plotted against the total deformation of the adhesive layer at the crack tip, $\Delta = \sqrt{w^2 + v^2}$. No instability is observed; F increases to a maximum and then declines somewhat. One typical specimen is chosen from each loading angle, with increasing in shear loading from the bottom to the top.

The adherends remain elastic under the loading. For small deformation of the adherends, the rotations of the adherends at the crack tip are evaluated by

$$w'_1 = \frac{u_{x,1} - u_{x,2}}{y_1 - y_2} \quad w'_2 = \frac{u_{x,3} - u_{x,4}}{y_3 - y_4} \quad (10)$$

where $u_{x,i}$ is the displacement in x-direction and y_i is the coordinate in y-direction of point i , where $i = 1, 2, 3, 4$ (see Figure 4)

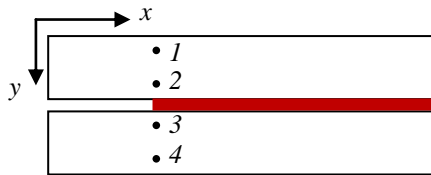


Figure 4. Displacement data of the four points and rotations of the adherends.

The rigid body rotation is given by

$$\gamma = \frac{w'_1 + w'_2}{2} \quad (11)$$

Thus, the true loading angle, α , is the design loading angle, α_{design} , modified by the rigid body rotation: $\alpha = \alpha_{\text{design}} + \gamma$.

The shear and peel deformation of the adhesive layer are defined as the differences of the longitudinal and vertical displacements of the adhesive/adherend interfaces relative to the orientation of the adhesive layer. To define these, the deformations relative to the fixed coordinate system are first given

$$v_o = u_{x,3} - u_{x,2} \quad w_o = u_{y,3} - u_{y,2} \quad (12)$$

With consideration to the rigid body rotation γ , the deformations become

$$v = v_o + w_o + t \gamma \quad w = w_o - v_o \gamma \quad (13)$$

where t is the thickness of the adhesive layer.

The chosen MCB-specimen geometry has a crack length $a = 0$ and the expression for the J-integral is [12]

$$J = \frac{F \sin \alpha}{b} (w'_1 - w'_2) + \frac{4}{E_1 t_1} \left(\frac{F \cos \alpha}{b} \right)^2 \quad \dots\dots (14)$$

The variables F, w'_1 and w'_2 in Eq. (14) are measurable in an experiment, which enables the evaluation of the constitutive behaviour of the adhesive layer in terms of stress-deformation relationships, as obtained f by partial differentiation

$$\sigma_{w,v} = \frac{\partial J_{adh}}{\partial w} \quad \tau_{w,v} = \frac{\partial J_{adh}}{\partial v} \quad (15)$$

This approach implicitly assumes that the cohesive stresses are derived from a potential function, i.e. that J_{adh} does not depend on the deformation path, just on w and v . This method is referred to as the inverse method to determine the constitutive behaviour of a material through the overall response of the structure.

The MCB-specimen with $a=0$ satisfies all the requirements set on the loading system. That is the entire spectrum of mode mixity can be achieved smoothly by one pre-defined adjusting parameter: the loading angle α . However, the theory for obtaining the constitutive behaviour of the adhesive layer sets more requirements on the MCB-geometry:

1. In order to be able to treat the adhesive layer as a continuous distribution of bi-directional springs, the adhesive layer should be thin and flexible in comparison with the adherends. This requirement sets a condition on the relative stiffness of the adherends as compared to the adhesive as

$$\frac{E_1 t}{E t_1} > 0.1 \quad (16)$$
2. The model is based on small deformations. Thus, a requirement is that the deformation of the adhesive layer at the crack tip is small in comparison with the overall dimensions of the joint.
3. The overlap length should be long since the specimen is considered as semi-infinite in the derivation of equations.
4. The adherends should deform linear elastically. Thus, the maximum stress in the adherends at $x=0$ should be smaller than the yield strength of the adherends.
5. It should be possible to exceed the fracture energy in all mode mixities. The fracture energy in mode II, J_{IIc} , is much larger than the fracture energy in mode I, J_{Ic} . It is then assumed that the maximum fracture energy is attained in pure mode II.

The adherends are modeled as Euler-Bernoulli beams and the adhesive layer is modeled by interphase elements. The cohesive behaviour of the adhesive layer is modeled by the normalised cohesive law, which is governed by the cohesive behaviour of the adhesive layer in pure mode I and mode II. The experiments are simulated with the commercial FE-program ABAQUS (v6.4), see Figure 5. The inverse method is then used to

extract the constitutive behaviour of the adhesive layer under mixed mode loading.

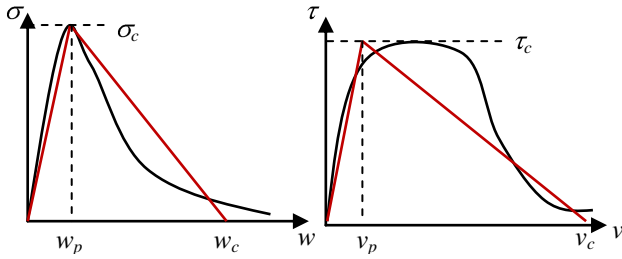


Figure 5. The saw-tooth model simplifies the cohesive behaviour of the adhesive layer.

The cohesive behaviour of the adhesive layer, or stress–deformation relations, are conveniently simplified by a saw-tooth shaped curve. Although differing from the real constitutive behaviour, the saw-tooth model capture the characteristic cohesive parameters of the adhesive layer.

A dimensionless deformation measure λ is defined by

$$\lambda^2 = \bar{v}^2 + \bar{w}^2 = \left(\frac{v}{v_c}\right)^2 + \left(\frac{w}{w_c}\right)^2 \quad (17)$$

where \bar{w} and \bar{v} are the normalised normal and tangential deformation, respectively. Softening behaviour of the adhesive layer begins when $\lambda = \lambda_p$, which is given by

$$\lambda_p^2 = \frac{\bar{v}_p^2 \bar{w}_p^2}{\bar{v}_p^2 \sin^2 \theta + \bar{w}_p^2 \cos^2 \theta} \quad (18)$$

where $\theta = \tan^{-1} \bar{w}/\bar{v}$. For each value of θ , the normalised stress, S , is defined by

$$S_{\lambda, \theta} = \begin{cases} \frac{\lambda}{\lambda_p \theta} & \text{when } 0 < \lambda < \lambda_p \\ \frac{1-\lambda}{1-\lambda_p} & \text{when } \lambda_p < \lambda < 1 \\ 0 & \text{when } \lambda > 1 \end{cases} \quad (19)$$

According to Eq. (19), Figure 6 shows the graphical presentation of the mixed mode cohesive law in the dimensionless form

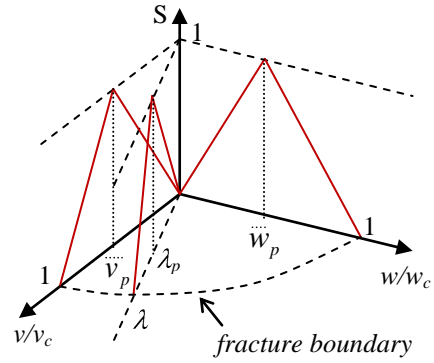


Figure 6. Graphical presentation of the mixed mode cohesive law.

5. CONCLUSIONS

1. Different mixed mode loaded specimen configurations are investigated. The decomposition methods of mode mixity in a joint can be classified into the global approaches and the local approaches. The mode mixity of an adhesive layer is due to unbalances in the loading system and/or unbalanced in the material and/or geometrical properties of the adherends.
2. A specimen for testing adhesive layers under mixed mode loading, the mixed mode double cantilever beam (MCB) specimen, is proposed based on the basic loading systems. The dimensioned MCB-specimen satisfies all requirements set on the loading system as well as the evaluation criteria.
3. A mixed mode constitutive law of the adhesive layer can be determined by the use of the J-integral.
4. The FE-simulations can catch the overall shape of the mixed mode constitutive law. The inverse method is then used to extract the constitutive behaviour of the adhesive layer under mixed mode loading.

ACKNOWLEDGEMENTS

The authors acknowledge the support from Universidad Politécnica de Madrid through grant AM0402. Our gratitude to the laboratory technical staff: Mr. José Illescas, Ms. Ana Soria, and Ms. Ana García for their assistance in the completion of these experiments.

REFERENCES

- [1] Jeandrau, JP, Int J Adhesion and Adhesives, pag. 11-71, 1991.

- [2] Fernlund G, Spelt JK. Mixed mode energy release rate for adhesively bonded beam specimen. *J Compos Technol Res* 16(3), pag. 234–243, 1994.
- [3] Reeder JR, Crews JH. Mixed-mode bending method for delamination testing. *AIAA J* 28(7), pag. 1270–1276, 1990.
- [4] Ducept F, Gamby D, Davies R. A mixed-mode failure criterion derived from tests on symmetric and asymmetric specimens. *Compos Sci Technol*, 59, pag. 609–619, 1999.
- [5] Hutchinson JW, Suo Z. Mixed mode cracking in layered materials. *Adv Appl Mech*, 29, pag. 63–191, 1992.
- [6] Shapery RA, Davidson BD. Prediction of energy release rate for mixed-mode delamination using classical plate theory. *Appl Mech Rev*, 43(5), pag. 281–287, 1990.
- [7] Li S, Thouless MD, Waas AM, Schroeder JA, Zavattieri PD. Mixed-mode cohesive-zone models for fracture of an adhesively bonded polymer–matrix composite. *Engng Fract Mech*, 73, pag. 64–78, 2006.
- [8] Pang HLJ, Seetoh CW. A compact mixed mode (CMM) fracture specimen for adhesive bonded joints. *Engng Fract Mech*, 57(1), pag. 57–65, 1997.
- [9] Suarez JC, Herreros MA, Pinilla P, Miguel S, López F. Energía de fractura en uniones adhesivas de materiales híbridos fibra-metal: ensayos TDCB modificados. *Anales de la Mecánica de la Fractura*, vol. 1, pag. 229-234, 2007.
- [10] Suárez JC, López F, Miguel S, Pinilla P, Herreros MA. Determination of the mixed-mode fracture energy of elastomeric structural adhesives: evaluation of debonding buckling in fibre–metal hybrid laminates. *Fatigue & Fracture Eng. Mat & Struct*, 32 (2), pag. 127-140, 2009.
- [11] Högberg JL, Stigh U. Specimen proposals for mixed mode testing of adhesive layer. *Engng Fract Mech*, 73, pag. 2541–2556, 2006.
- [12] Högberg JL, Sørensen BF, Stigh U. Constitutive behaviour of mixed mode loaded adhesive layer. *International Journal of Solids and Structures* 44 8335–8354, 2007.

Residual stress, peening, shape

Development Process of a Numerical Simulation for the Hammer Peening Fatigue Life Improvement Technique

BAPTISTA, R.* , INFANTE, V.** , BRANCO, C.M.**

*Department of Mechanical Engineering, Escola Superior de Tecnologia de Setúbal (IPS)
Campus do IPS, Estefanilha, 2910-761 Setúbal, Portugal*Corresponding author email: rbaptista@est.ips.pt**ICEMS/IST, Lisbon University of Technology, Av. Rovisco Pais, 1049-001
Lisbon, Portugal**Abstract**

Most rehabilitation and fatigue life improvement techniques of welded structures were developed in the 60's and 70's, when the problems introduced by the welding processes were brought up to light, by the first major accidents involving this type of structures. Nowadays, when the budgets for the experimental analysis are tighter, it is fundamental to use new simulation tools, with the principal objective of developing the fatigue life improvement techniques of welded structures.

The work presented in this paper, intends to demonstrate the viability of the finite element analysis simulation of one of the most important fatigue life improvement techniques of welded structures, the *Hammer Peening*.

It was already experimentally demonstrated that this technique allows for the treated structure to have a fatigue life equal or superior to the original one, due to the introduction of a local compressive residual stress field. Considering the difficulties encountered in the experimental determination of residual stresses introduced by this technique, the computational simulation stands out as a strong alternative to experimental analysis and development.

The residual stress fields were obtained numerically on the welded structure, using elasto-plastic material models and considering an elastic-deformable hammering tool. Several parameters of this technique were considered variable, and its influence was analysed in the simulation process, allowing for a good agreement with the experimental results.

The major advantage of the computational simulation of the hammering technique is the possibility of adding to the obtained results, a nominal load on the welded joint. Thereby it is possible to predict the fatigue life improvement, introduced by hammering, as a function of the parameters used in the process.

Key-words: Hammer Peening; Fatigue Life; Improvement; Finite Element Analysis

1 Introduction: Background

In order to reduce the cost of developing a new fatigue life improvement technique, and therefore reduce the cost of operating a more secure welded structure, the correct modeling using a FEA program is essential. These programs can nowadays easily simulate almost every detail and effect present on the experimental test runs, and a fatigue life improvement technique [1] and [2], like the hammer peening can be modeled.

Several developments have already be made by *Baptista and Infante*, on [3] and [4], in order to produce accurate simulation of this technique, and its experimental application on [5] and [6]. But most recently on [7] an extensive study on the application of several fatigue life improvement techniques on stainless steels welded joints, have been presented.

Fatigue life improvement techniques rely on extending the initiation phase, by reducing the severity of the weld toe details or introducing a compressive residual stress field [8]. Improvement techniques also reduce the crack propagation speed; which increases the total fatigue life of the structure. In a review recently presented by Maddox [9], conclusions and recommendations were defined for hammer peening which is now part of an official IIW document of Commission XIII [10].

In the present work the full development process of a simulation analysis of the hammer peening technique is described, like in [11], taking into account the latest developments on the fatigue life prediction methods [12]. This technique will be model using a deformable hammering tool and several experimental results, in order to make it closer to the real process. Finally the numerical results are compared with the ones obtained experimentally, in order to validate the numerical model.

2 Experimental and Numerical Data**2.1 Material and Specimens**

The first step for an accurate modeling of the hammer peening fatigue life improvement technique, using FEA, is to obtain a numerical model for the material behavior. There is one material in study within this work, a Stainless Steel, referred as Duplex Type S31803 (DIN 1.4462). In Table 1 the chemical composition of this material can be found. Table 2 gives us the normal tensile properties of this duplex steel, becoming clear that this material has a high ultimate stress, 789 MPa, and shows a 34% elongation at break point.

The material was received in as welded condition, with a plate thickness of 10 mm and the simplified specimen geometry can be found in Figure 1

Table 1 Chemical Composition of Duplex S31803 Stainless Steel

C	Si	Mn	P	S	Cr
0.024	0.220	1.550	0.023	0.002	22.400
Mo	Ni	N	Al	Cb	Cu
2.980	5.700	0.157	-	0.130	0.090

Table 2 Tensile Properties

Steel	$\sigma_{0.2\%}$ [MPa]	σ_R [MPa]	ϵ_R [%]
S31803	478	789	34

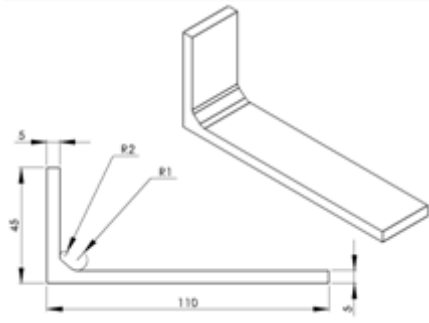


Figure 1 Simplification of the cruciform welded joint specimen

2.2 Numerical Material Models

These properties must be translated in to a numerical model using a FEA program, therefore a complete elasto-plastic material model is necessary. From all the models included on the ABAQUS material library, the “Linear kinematic hardening model” and the “Nonlinear isotropic/kinematic hardening model”, are the ones that offer the most complete behavior for a FEA of cyclic fatigue test. When a Nonlinear and Kinematic hardening model are combine, the *Lemaitre and Chaboche* [13] is obtained and therefore the most complete cyclic behavior can be simulated. Effects like the Bauschinger effect, Cyclic hardening with plastic shakedown, Ratchetting and the Relaxation of the mean stress, can be easily simulated by this model, considering one has the full sets of parameters that define the Chaboche model. Table 3 shows the parameters for a Chaboche model, were the parameters were calibrated from experimental results.

Table 3 Duplex Steel Chaboche material model [14]

E [MPa]	ν	$\sigma_{0.2\%}$ [MPa]	C	Q_{∞}	b
179000	0.3	187.6	134771	16.5	0.0073

Finally in order to apply the local approach method, [15], a Cyclic stress-strain curve is also necessary, equations (1) and (2) express the Ramberg-Osgood, model for the Duplex Steel, and a Morrow’s modified strain-life equation, [16], (3) and(4), is also required for fatigue life initiation prediction. All these equations are based on experimental data obtained in order to calibrate the material models by *Magnabosco* [17].

$$\frac{\Delta \epsilon}{2} = \frac{\Delta \sigma}{2E} - \left(\frac{\Delta \sigma}{2H} \right)^{1/n} \quad (1)$$

$$\frac{\Delta \epsilon}{2} = \frac{\Delta \sigma}{2 \cdot 179000} - \left(\frac{\Delta \sigma}{2 \cdot 733} \right)^{1/0.35} \quad (2)$$

$$\frac{\Delta \epsilon}{2} = \left(\frac{\sigma_f - \sigma_m}{(2N)^b} \right) - \epsilon_f (2N)^c \quad (3)$$

$$\frac{\Delta \epsilon}{2} = \frac{(912 - \sigma_m)}{179000} (2N)^{-0.35} - 0.254 (2N)^{-0.47} \quad (4)$$

2.3 Geometry and Boundary Conditions

The referred specimen geometry was then model using the ABAQUS design tools, using a 1/8 symmetry simplification in order to reduce the problem computational load, and the data on table Table 4. The values for the weld toe radii (R1), the weld toe angle, and the secondary radii (R2) were obtained from a experimental geometry analysis, using a digital coordinate table and were then statistically analyzed. A average value of 2.420 mm was obtained for the weld toe radii, after the weld toe hammer peening vs. the as welded value of 1.645 mm. The standard deviation (0.683 mm) value was then used to generate four other numerical specimens, by increasing and decreasing the value of R1, in order to quantify its effect on the fatigue life prediction.

Table 4 Stress Concentration Factors, obtained for a 250 MPa nominal Stress

Specimen	R1 [mm]	Angle [°]	R2 [mm]	K_t
ProvAvg02Std	1.053			1.952
ProvAvg01Std	1.737			1.770
ProvAvg	2.420	38.238	1.645	1.678
ProvAvg1Std	3.104			1.565
ProvAvg2Std	3.787			1.502

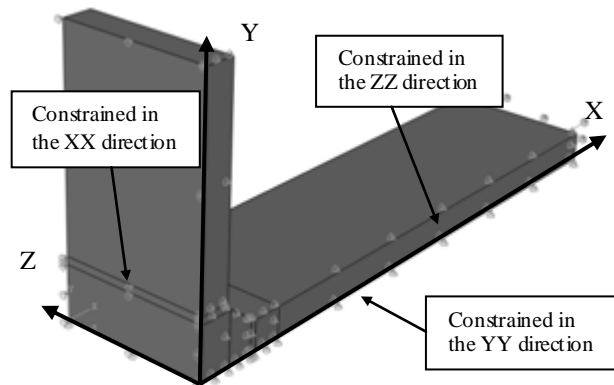


Figure 2 FEA Model and coordinate system and Boundary conditions

The model was constrained using the boundary conditions on Figure 2, that fix the model in space accordingly to the specimen symmetry conditions. Taking into account the non linear nature of the hammer peening technique, which includes a non linear material model, a contact condition and finally a dynamically applied load, like *J. Liu* in [18] recommended, the specimen wide had to be reduced from 25 mm to 1.125 mm, in order to get the best ratio between the quality of the results and the computational effort. Therefore both lateral surfaces were restrained in the ZZ (or transverse)

direction, to simulate the specimen plane strain state. Using a nominal 250 MPa stress it was also possible to calculate the stress concentration factor for the longitudinal direction (Table 4) as a way to quantify the influence of the weld toe radii.

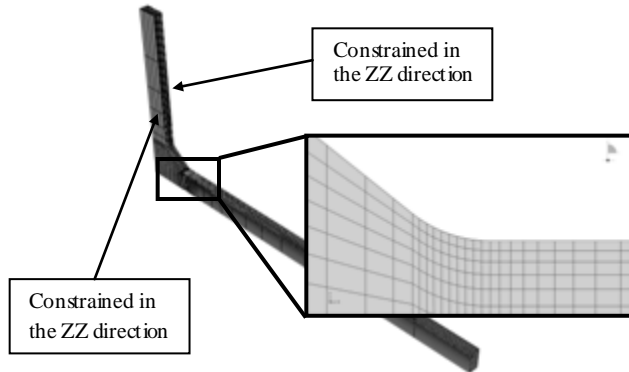


Figure 3 1.125 mm wide model

2.4 Specimen Mesh

In order to evaluate the influence of the specimens mesh on the quality of the final results, three meshes were developed, the first one had only 2'016 C3D8R elements, which are linear elements and therefore this coarse mesh had 8'127 DOF. A medium and fine mesh were then developed, using 15'855 and 26'103 DOF. The results showed that the coarse mesh does not allow obtaining consistent results, but the medium and fine meshes both resulted on very similar stress and strain distributions. Once again in order to reduce the computational effort, the medium mesh was then used from this point forward.

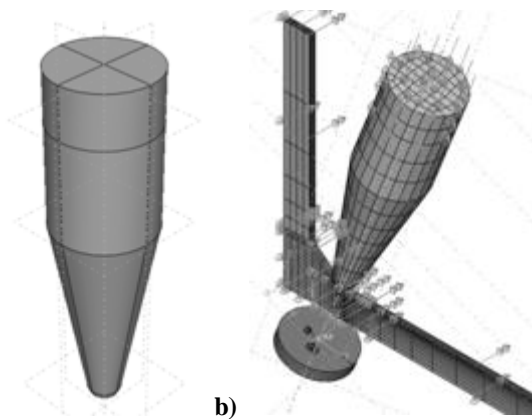


Figure 4 FEA hammer peening tool; a) model only; b) full assembly

Finally a 12 mm in diameter hammer peening tool was defined using a linear elastic material model, but the full body is deformable. Figure 4 shows the tool geometry, next to the weld toe, and the applied boundary conditions. The tool mesh uses the same element and adds 3'798 DOF to the simulation. A contact pair was also defined between the tool (master surface) and the specimen (slave surface), using a hard contact model, that allows separation after contact, for the normal to

surface direction, and a penalty model, with a 0.5 friction coefficient, for the tangential direction.

2.5 Hammer Peening Loads

The next required step was to determine the hammer peening force, needed to be applied to the numerical tool. This was done experimentally using a hammer peening tool instrumented with two strain gages; these were calibrated using a servo-hydraulic test machine, in order to translate one hammer peening run, in a load spectrum, Figure 5.

This spectrum was analyzed using the Rain-flow method and four characteristic loading cycles were defined. Table 5 shows not only these 4 loading sets, with loads ranging from 1.9 to 9.5 MPa, but also the corresponding residual stresses on the weld toe, when 4 hammering runs, each one with 5 strokes, are applied to the 1.125 mm wide specimen. The strokes were applied using the referred loads, dynamically applied on the top of the hammer peening tool, with a 0.02 Hz frequency.

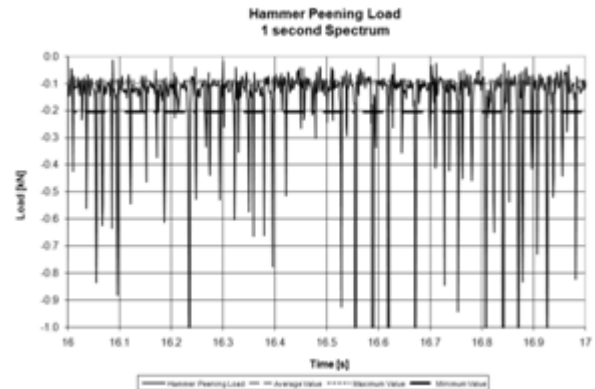


Figure 5 Hammer Peening Load 1 second spectrum

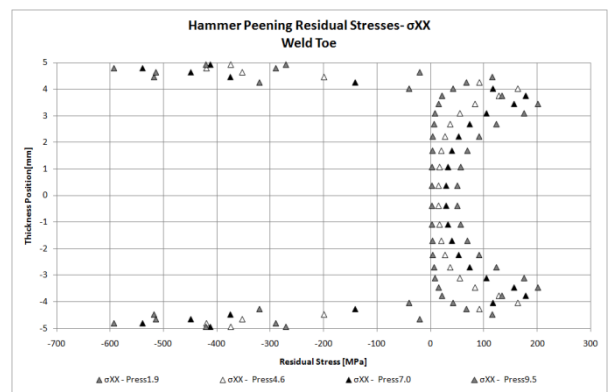


Figure 6 Residual Stress distribution, after the hammer peening process

Figure 6 shows the stress distribution in the longitudinal direction on the weld toe vs. the hammering load. A minimum value of - 592.8 MPa is obtained with a 9.5 MPa load, and a maximum residual stress of - 290.0 MPa for the 1.9 MPa load.

An experimental value of -485 MPa was obtained for the residual stresses on the duplex steel using X-Ray Diffraction technique in the longitudinal direction, and -524 MPa in the transverse direction. One can then conclude that the best solution for a numerical simulation of the hammer peening technique is the 7.0 MPa loading set. Finally it is possible to check that the compressive stress influence is about 0.5 mm to 1 mm throughout the specimen thickness.

Table 5 Weld toe Residual Stress vs. Hammer peening load

Specimen	σ_{XX} [MPa]	σ_{YY} [MPa]	σ_{ZZ} [MPa]
Press1.9	-290.0	-103.5	-243.4
Press4.6	-418.9	-101.3	-430.2
Press7.0	-538.9	-116.8	-506.9
Press9.5	-592.8	-162.0	-580.6

On the other hand, one can see in Table 6 that after a nominal load with a stress range of 225 MPa and a stress ratio of 0.1, the local stress and strain ranges are not significantly influenced by the hammering load. Only the mean stress is considerably lower (about 71 %) when a 1.9 MPa load is applied, but only 5.5 % higher when a 9.0 MPa load is applied vs. the 7.0 MPa load, used from this point on.

Table 6 Weld toe local stress range, mean stress and strain range vs. Hammer peening load

Specimen	$\Delta\sigma_{XX}$ [MPa]	σ_{mXX} [MPa]	$\Delta\epsilon_{XX}$ [μ]
Press1.9	348.9	-54.5	1933
Press4.6	368.4	-142.8	2007
Press7.0	365.1	-185.7	1969
Press9.5	366.9	-195.9	1958

3 Results and Discussion

3.1 Residual Stress in the Welded Joints

Using the above referred specimen wide, hammer peening tool tip radii, positioning and load, the 4 runs of 5 hammering strokes were applied to the five specimens with different weld toe radii from Table 4.

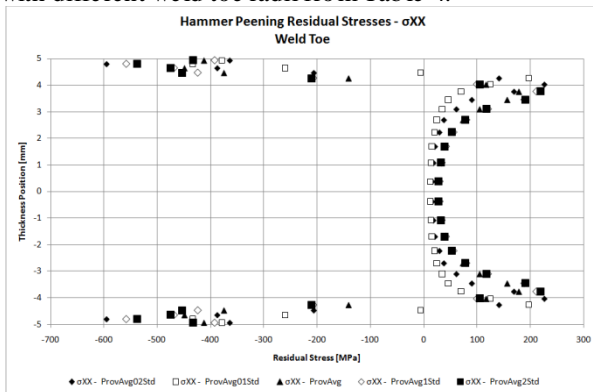


Figure 7 Residual Stress distribution, after the hammer peening process, vs. weld toe radii

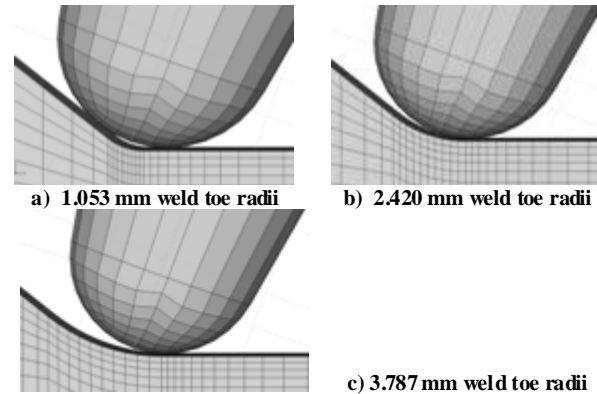


Figure 8 Weld toe radii vs. Hammer peening tool radii

Figure 7 shows the influence of the weld toe radii on the residual stress distribution on the longitudinal direction, at the weld toe. On the two smaller weld toe radii specimens the stress distribution is clearly different from the other three ones. The smaller radii means the tool tip cannot hammerpeen directly above the weld toe, as one can see on Figure 8 a) and b). when the weld toe radii is increased, Figure 8 c), d) and e), the hammer peening tool tip can now be directly place on the weld toe, so the residual stress distribution is very similar.

When one looks at the residual stress values on the weld toe in every direction, Table 7, it is possible to confirm the above referred behavior, with the highest differential occurring in the direction of the thickness.

Table 7 Residual Stress vs. Specimen weld toe radii

Specimen (Weld Toe)	σ_{XX} [MPa]	σ_{YY} [MPa]	σ_{ZZ} [MPa]
ProvAvg02Std	-594.9	-202.9	-595.0
ProvAvg01Std	-433.7	-123.2	-399.2
ProvAvg	-538.9	-116.8	-506.9
ProvAvg1Std	-558.4	-136.4	-563.1
ProvAvg2Std	-537.1	-142.4	-550.0

Table 8 Experimental and numerical Residual Stress on the weld toe [MPa]

	Weld Toe Long.	Weld Toe Transv.	1 mm Long.	1 mm Transv.
Experimental	-485 ± 31	-524 ± 26	-269 ± 9	-162 ± 18
Numeric	-539 ± 60	-507 ± 76	-300 ± 73	-93 ± 22
Diferential	11%	-3%	12%	-43%

When compared with the residual stresses obtained experimentally by the X-Ray diffraction technique, Table 8, one can see that the values show a good agreement. On the weld toe, the residual stresses obtained experimentally and the numerical value obtained with the specimen created using the average weld toe radii only differ 11% in the longitudinal direction and 3% on the transverse direction. When the values are obtained 1 mm away from the weld toe, the relative difference in the transverse direction is higher, but it must be taken into account that the residual stresses in this direction have a lower absolute value. Therefore it is possible to validate the numerical model.

3.2 Fatigue Data in the Welded Joints

Having analyzed the residual stresses after the hammer peening technique, one can apply several fatigue cycles to the specimen, in order to simulate the fatigue life tests applied to real specimens. These cycles have constant frequencies, and stress ranges, with a stress ratio of 0.1.

Table 9 therefore shows that the local stress and strain range is not significantly influenced by the weld to radii. The biggest difference is 6.8% between the strain range obtained with the average weld toe radii and the minimum one. When the mean stress is analyzed the differentials are higher, and the influence of the weld toe radii more clear. For the minimum radii, the mean stress is 32.5% lower in modulus than the solution obtained with the average radii, so one can expect a shorter fatigue life. When the radii is increased the mean stress decreases about 11.9%, which can lead to a higher fatigue life. The nominal loading also has the expected behavior, changing not only the stress and strain range values, but more significantly the mean stress value.

Table 9 Weld toe local stress range, mean stress and strain range vs Specimen weld toe radii

Specimen	$\Delta\sigma_{XX}$ [MPa]	σ_{mXX} [MPa]	$\Delta\epsilon_{XX}$ [μ]
ProvAvg02Std	377.8	-125.2	2103
ProvAvg01Std	374.7	-145.4	2060
113 MPa	177.9	-303.0	958
ProvAvg 225 MPa	365.1	-185.7	1969
400 MPa	510.9	-81.4	2756
ProvAvg1Std	375.6	-155.1	2016
ProvAvg2Std	357.5	-207.7	1920

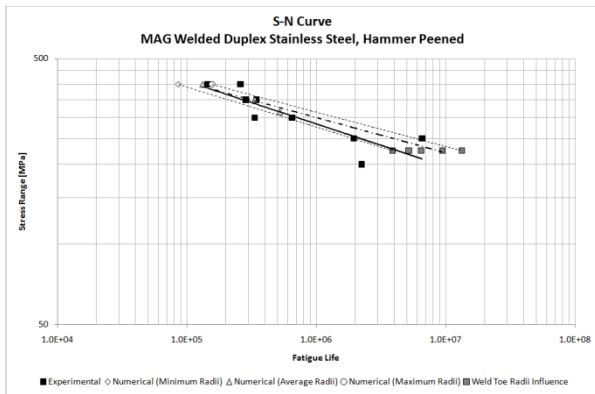


Figure 9 S-N curves experimentally and numerically obtained for the Duplex Steel

Using the above results and the local approach method it was then possible to calculate the fatigue life initiation, as *Pinho-da-Cruz et al* in [19], *Silva et al* in [20], have testified, and therefore create the S-N curves from Figure 9. Three numerical S-N curves were calculated, using the minimum, average, and the maximum weld toe radii values. It is very interesting to see that the experimentally obtained S-N curve fits between the minimum and maximum radii S-N curves, which mean that the numerical model is working well, and is able to correctly predict the fatigue life initiation.

Comparing only the experimental S-N curve with the average radii one, one can see the numerical solution is not conservative, and therefore always predicts a higher fatigue life. But when one uses the minimum radii values, the S-N curve will now predict a lower fatigue life, and therefore the numerical results are now conservative.

Table 10 shows the numerical results obtained using the FEA model, need for the fatigue life initiation prediction. The influence of the weld toe radii can also be quantified, like in [21] by *Chin-Hyung Lee et al*, using a 225 MPa stress range fatigue cycle, and several different radii. With the minimum weld toe radii the predicted fatigue life is 3'888'753 cycles, increasing to 9'445'579 cycles, when the radii changes from 1.053 mm to 2.420 mm. Increasing the radii 56.5% again, the fatigue life increases to 13'302'658 cycles, which represents a 41% change. On average the weld toe radii changes the fatigue life prediction by 30%.

Table 10 Fatigue Life Prediction for the Duplex Steel after weld toe hammer peening, $\Delta S=225$ MPa

Specimen	σ_m [MPa]	$\Delta\epsilon$ [μ]	Ni [Cycles]
ProvAvg02Std	-125.2	2100	3888753
ProvAvg01Std	-145.4	2060	5175726
ProvAvg	-185.7	1970	9445579
ProvAvg1Std	-155.1	2020	6452840
ProvAvg2Std	-207.7	1920	13302658

4 Conclusions

- In order to model the hammer peening technique it was necessary to determine the hammering force, this value was then applied to the FEA model. an instrumented hammer peening tool was used and a – 720 N average force, or an equivalent – 7 MPa hammering pressure was determined;
- The hammer peening technique is based not only on the modification of the weld toe radii, but also in the introduction of a residual compression stress distribution on the weld toe;
- Several factors were analyzed in the FEA model, like the number of strokes per specimen, the orientation of the hammer peening tool, the hammer peening tool geometry or the hammer peening applied force;
- As expected the residual stress distribution through the specimens thickness has two inflection points, the first one, near the material surface, where the higher residual stress value is obtained, and the second one, at a depth of 1 mm to 2 mm, where the residual stresses are now on the positive side;
- By adding the residual stress distributions to the nominal load stress profiles, it is possible to conclude that the resulting stress range decreases, while the strain range is slightly increased, the mean stress value

is also considerably decreased when compared with the as welded condition;

- Based on these values it is possible to predict the fatigue life, for the as welded and hammer peened conditions, attesting therefore the efficiency of the hammer peening technique as an fatigue life improvement technique;
- There is a very good agreement between the experimental and the numerically obtained S-N curves, while altering the hammer peening tool radii proves to be an effective way improve this agreement;

ACKNOWLEDGEMENTS

The authors acknowledge: TWI for the financing of the “Improving the fatigue performance of welded steels”, ECSC Contract 7210 – PR – 303.F3 project; The FCT for the PhD scholarship SFRH/BD/25984/2005 financing support.

REFERENCES

- [1] Infante, V., Branco, C.M., “A comparative Study of the Fatigue Behaviour of Repaired Joints by Hammer Peening”, Paper XIII-1836-2000
- [2] Dexter, R.J., Kelly, B.A., “Research on Repair and Improvement Methods”, Proc. 50th Annual Assembly, San Francisco, EUA, WRC, 1997, pp. 74-97
- [3] Baptista, R.M., “Estudo dos parâmetros de martelagem no comportamento à fadiga de juntas soldadas de aço estrutural”, Tese de Mestrado em Engenharia Mecânica, IST, Julho 2002
- [4] Infante, V., “Análise da melhoria do comportamento à fadiga de juntas soldadas”, Tese de Doutoramento em Engenharia Mecânica, IST, Abril 2002
- [5] Infante, V., Branco, C.M., Baptista, R., Gomes, E.C., “Residual stresses and fracture mechanics analysis of welded joints repaired by hammer peening”, Proc. 8th Portuguese Conference on Fracture, Vila Real, UTAD, Ed. SPM, Lisboa, pp. 339-354, Março 2002
- [6] Infante, V., Branco, C.M., Baptista, R. “Failure analysis of welded joints rehabilitated by hammer peening”, Paper XIII 1892/01, IIW Meeting, July 2001, Ljubljana, Slovenia, Ed. International Institute of Welding
- [7] TWI, “Improvement the Fatigue Performance of Welded Stainless Steels”, Final Report for contract No. 7210-PR-303, 2005
- [8] Huther, I, Lieurade, H.P., Sonissi, R., Nussbaumer, A., Chabrolin, B., Janosh, J.J., “Analysis of Results on Improved Welded Joints”, Welding in the World, 37, 5, pp. 242-266, 1996.
- [9] Maddox, S.J., “The Application of Fatigue Life Improvement Techniques to Steel Welds”, IIW Commission XIII Workshop on Improvement Methods, International Institute of Welding, Proc. 51st Annual Assembly, Hamburg, Germany, September 1998.
- [10] Haagensen, P.J., Maddox, S.J., “Specifications for Weld Toe Improvement by Burr Grinding, TIG Dressing and Hammer Peening for Transverse Welds”, IIW Document, Commission XIII, Working Group 2, WG2, International Institute of Welding, 2001.
- [11] B. Atzori, G. Meneghetti, “Fatigue strength of fillet welded structural steels: finite elements, strain gauges and reality”, International Journal of Fatigue 23 (2001) 713–721
- [12] Wolfgang Fricke, “Fatigue analysis of welded joints: state of development”, Marine Structures 16 (2003) 185–200
- [13] Lemaitre, J., and J.-L. Chaboche, *Mechanics of Solid Materials*, Cambridge University Press, 1990.
- [14] Jean-Christophe Le Roux, “Étude Du Comportement Et De L'endommagement En Fatigue D'un Acier Inoxydable Austéno-Ferritique Moulé Vieilli”, These.
- [15] Dowling, N.E., “Fatigue at Notches and Local Strain and Fracture Mechanics Approaches”, ASTM, STP 677, pp. 247-273, 1979
- [16] J. D. Morrow, “Cyclic Plastic Strain Energy and Fatigue of Metals, Internal Friction, Damping and Cyclic Plasticity”, *ASTM-STP* 378, 45-87 (1965)
- [17] Rodrigo Magnabosco, Gustavo Henrique Bolognesi Donato, “Comportamento Mecânico Monotônico E Cíclico De Dois Aços Inoxidáveis Dúplex”, 59^o Congresso Internacional Anual da ABM – São Paulo, 19 a 22 de Julho de 2004
- [18] J. Liu, W.X. Gou, W. Liu, Z.F. Yue, “Effect of hammer peening on fatigue life of aluminum alloy 2A12-T4”, *Materials and Design* xxx (2008) xxx–xxx
- [19] J. Pinho-Da-Cruz, F. Teixeira-Dias, P. S. Ferreira, “Aplicação Dos Métodos De Aproximação Local E Elementos Finitos À Previsão De Tensões-Deformações Em Provetes Entalhados De Alcu4,5mn”, *Revista Iberoamericana De Ingeniería Mecánica*. Vol. 10, N.º 1, pp. 93-110, 2006
- [20] V.R. Silva, J.D. Costa, J.M. Ferreira, “Fatigue Crack Initiation in Central Notch Specimens of 6082-T6 Aluminium Alloy”, 8^a Jornadas da Fractura – 2002, pp. 255-263
- [21] Chin-Hyung Lee, Kyong-Ho Chang, Gab-Chul Jang, Chan-Young Lee, “Effect of weld geometry on the fatigue life of non-load-carrying fillet welded cruciform joints”, *Engineering Failure Analysis* 16 (2009) 849–855

OPTIMIZACIÓN DEL PROCESO DE ENDEREZADO POR LLAMA E IMPACTO SOBRE LAS PROPIEDADES DEL MATERIAL

J. García¹, R. Lacalle¹, D. Ferreño¹, J. A. Álvarez¹, F. Gutiérrez-Solana¹

¹ Departamento de Ciencia e Ingeniería del Terreno y de los Materiales, E.T.S. de Ingenieros de Caminos, Canales y Puertos, Universidad de Cantabria, Avda/ Los Castros s/n, 39005 Santander, España.
E-mail: garciaidj@unican.es

RESUMEN

El enderezado por llama es un proceso de calentamiento efectuado sobre componentes metálicos que permite distorsionar o rectificar la geometría de un elemento con el fin de conseguir adecuarla a los requerimientos de construcción o ejecución. Se basa en la aplicación de calor para lograr que el material experimente tensiones térmicas que deformen el elemento de forma permanente. El propósito del estudio recogido en este artículo es el de ilustrar el procedimiento y examinar las consecuencias del sobre las propiedades del material. El estudio se realizó sobre placas de cinco aceros diferentes sometidas previamente a un proceso de deformación mediante calentamiento por llama.

PALABRAS CLAVE: enderezado por llama, S235JR, S355J2, SA460ML, S690QL, S890QL, tensiones térmicas.

ABSTRACT

Flame straightening is a heating process performed on metallic components which allows to distort or to straighten the geometry of an element with the purpose of adapt it to construction or execution requirements. The process settles its basis on a heating applying to achieve thermal stresses on the material which, in result, deform the element. The purpose of this study is to illustrate the procedure and to examine the consequences of flame straightening on the material properties. The study was performed on plates of five different steel grades, which had been flame straightened previously.

KEYWORDS: flame straightening, S235JR, S355J2, SA460ML, S690QL, S890QL, thermal stresses.

1. INTRODUCCIÓN

El enderezado por medio de llama resulta una práctica común en el procesado de aceros estructurales. El objetivo que se persigue con dicha técnica consiste en introducir o revertir modificaciones en la forma del componente metálico con el fin de ajustarse a una geometría dada. Las deformaciones introducidas, de origen térmico, se consiguen mediante la aplicación de un flujo de calor sobre el componente, dando lugar a expansiones térmicas durante el proceso y a contracciones permanentes tras el enfriado.

El espectro de posibilidades de deformación de los componentes estructurales se obtiene mediante las distintas configuraciones posibles de los patrones de aplicación de llama [1, 2]. Hasta ahora, al ejecutar la técnica del enderezado por llama no se conoce con certeza la respuesta del componente tras el proceso, dado que es un proceso basado en el conocimiento adquirido con la experiencia del operario. El hecho de que el proceso esté influido por un gran número de parámetros ha dificultado desde sus orígenes el estudio teórico que permitiese delimitar su alcance y diseñar con

antelación el proceso en función de los objetivos de deformación deseados.

Este artículo es el resultado de un proyecto que trata de dotar al proceso del enderezado por llama de una base teórica que respalde la visión del proceso desde una base científica. En particular, en él se presentan los estudios realizados sobre las consecuencias del proceso de enderezado en las propiedades mecánicas y microestructurales de cinco aceros estructurales de amplia difusión en el mundo de la construcción y de la industria.

2. FUNDAMENTOS DEL PROCESO DE ENDEREZADO POR LLAMA

Los mecanismos desencadenados por la aplicación de la llama sobre el material son dos, como se recoge en [3] y [4]. Durante la etapa de calentamiento se genera un flujo plástico de material debido a la expansión térmica del mismo. El material no calentado situado en el entorno de la zona calentada sirve de restricción a dicha elongación. Por otra parte, durante el enfriamiento, aparece una contracción longitudinal permanente. Esta

deformación final es la deformación objetivo del proceso de enderezado.

La llama se aplica directamente sobre el material mediante un equipo de oxi-fuel. El aporte de calor se realiza siguiendo patrones específicos de calentamiento (bandas, uves, líneas) correspondientes al tipo de deformación deseada y a la forma del componente a enderezar.

Para el caso de elementos estructurales de grandes dimensiones, tales como perfiles metálicos, la deformación se consigue mediante combinación y repetición de dichos patrones de calentamiento. Por lo general, la responsabilidad del diseño de las pautas y de la secuencia de aplicación de la llama recae en el juicio del operario. En la Figura 1 se observa la combinación y repetición de patrones de calor en alma y ala de un perfil HEA para conseguir una flexión sobre el eje mayor de inercia.



Figura 1. Enderezado por llama sobre perfil metálico

El flujo de calor se controla para que en la superficie del metal no se superen temperaturas que pudieran resultar en un cambio de fase en la composición del acero, usualmente no superando el límite postulado general de 750 °C. Este límite de temperatura, en realidad, depende de la calidad del acero. En el taller, el control de la temperatura es un control visual basado en la escala cromática del acero al aumentar de temperatura. Dicho control, naturalmente, presenta grandes desventajas en cuanto a variabilidad y subjetividad [5].

3. PROCEDIMIENTO DE ENSAYO Y MATERIALES EMPLEADOS

3.1. Procedimiento experimental

Para llevar a cabo el estudio se calentaron mediante llama placas rectangulares de dimensiones 500mm x 600mm x20mm de cinco aceros diferentes. El esquema de la Figura 2 ilustra el procedimiento de aplicación de la llama. El patrón de calentamiento se aplicó en sentido longitudinal, con una velocidad lineal que permitiese asegurar que en la superficie del metal se alcanzaban temperaturas por encima de las temperaturas recomendadas para cada metal por los expertos en enderezado por llama, por ejemplo en [3] y [6], tratando

de exponer al material a la condición pésima de calentamiento desde el punto de vista metalúrgico. El marco de sujeción de la placa permite la libre expansión en todas las direcciones.

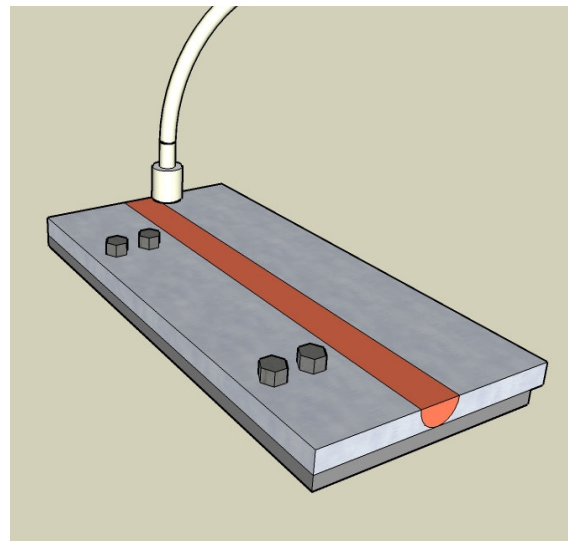


Figura 2. Esquema de la aplicación de la llama

3.2. Materiales empleados

Los aceros ensayados fueron cinco aceros estructurales, S235JR, S355J2, SA460ML, S690QL y S890QL [7]. La muestra de materiales escogidos para el ensayo cubre un amplio espectro de aceros en cuanto a diversidad de propiedades resistentes y características. La composición química de los cinco tipos de acero se recoge en la Tabla 1

Tabla 1. Composición química de los aceros

Acero	C	Si	Mn	P	S	Ni	Cr
S235JR	0,16	0,22	1,04	0,017	0,017	<0,08	<0,03
S355J2	0,106	0,493	1,57	0,013	0,0008	0,058	0,045
SA460ML	0,108	0,436	1,60	0,016	0,0006	0,050	0,052
S690QL	0,170	0,298	1,30	0,011	0,0008	0,030	0,034
S890QL	0,161	0,273	0,87	0,009	0,0010	0,51	0,471

El estudio del enderezado por llama sobre los aceros S235JR y S355J2 permite conocer las consecuencias del enderezado por llama en aceros dúctiles de bajo límite elástico de baja aleación. El acero SA460ML representa la oportunidad de conocer como afecta el enderezado a un acero laminado termomecánicamente. Las posibles desventajas o limitaciones de la técnica en templados y revenidos de alta resistencia se analizan a través del ensayo de los aceros S690QL y S890QL. Los aceros S235JR, S355J2 y SA460ML fueron calentados hasta una temperatura máxima de 850°C, mientras que los aceros de alta resistencia S690QL y S890QL hasta una temperatura máxima de 750°C.

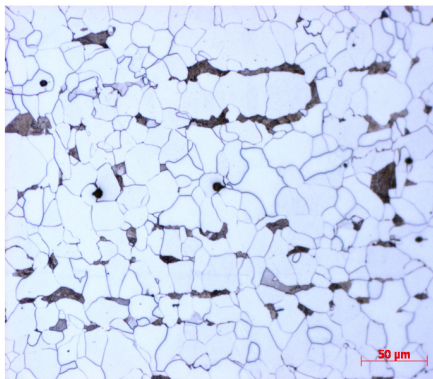
4. ESTUDIO DE LOS EFECTOS DEL CALENTAMIENTO EN EL MATERIAL

El estudio realizado sobre las propiedades del material post-calentamiento trata de valorar el efecto del aporte de calor sobre las mismas. Con este fin, se comparó la microestructura, la dureza, el comportamiento a tracción y la resistencia al impacto mediante ensayos Charpy, del material calentado y el material base.

4.1. Impacto en la microestructura

En relación al posible cambio microestructural del material como consecuencia de una reordenación o transformación de fases debida al calentamiento, se realizaron análisis mediante microscopía óptica en secciones de orientación T-S de la zona directamente calentada y de sus proximidades. Las Figuras 3 a 7 presentan la comparación entre la microestructura del material base y la microestructura existente en la zona correspondiente a la superficie directamente calentada, para todos los aceros.

Se puede observar en las mismas Figuras 3 a 7 que el material ensayado exhibe un cambio en la microestructura para los cinco casos. En el caso de los aceros que presentan microestructura ferrítico-perlítica (S235JR, S355J2, SA460ML) se evidencia un refinamiento del grano así como la pérdida de la disposición bandeada de la perlita en favor de una disposición más caótica de la misma. Para el caso de los aceros de alta resistencia (S690QL, S890QL) se pierde la microestructura de bainita revenida en la zona calentada, dando lugar a la formación de ferrita y perlita con grano fino.

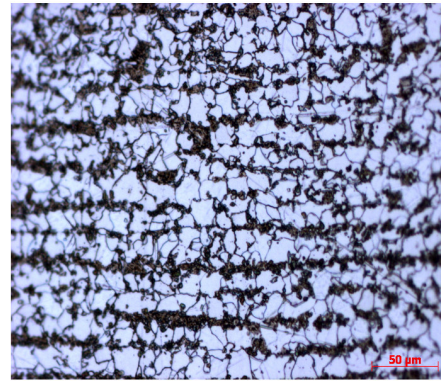


S235JR

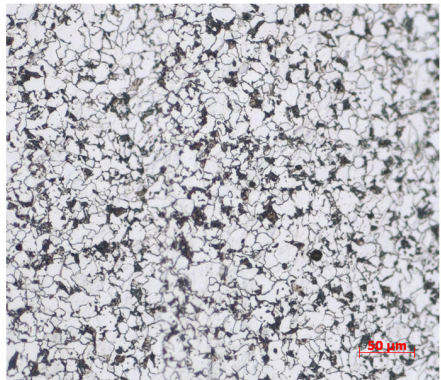


S235JR ENDEREZADO

Figura 3. Microestructuras acero S235JR

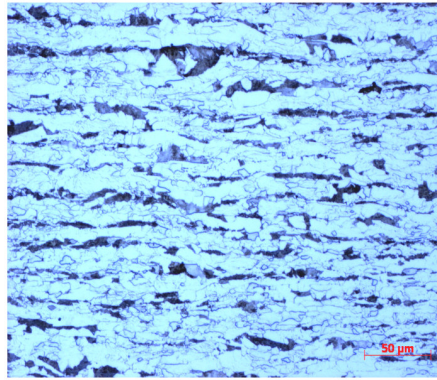


S355J2

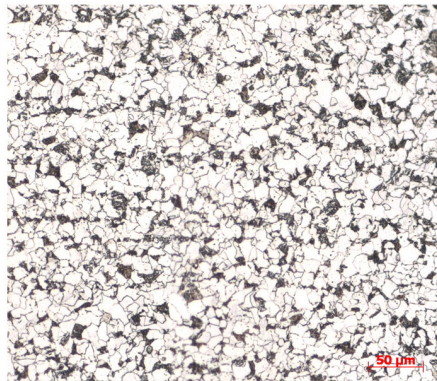


S355J2 ENDEREZADO

Figura 4. Microestructuras acero S355J2

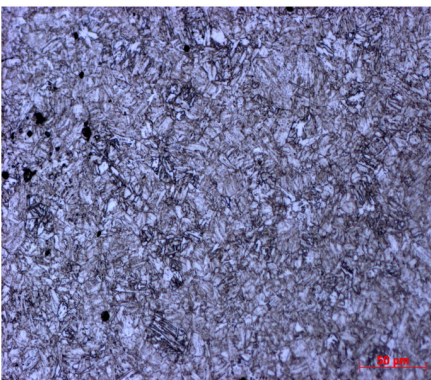


SA460ML

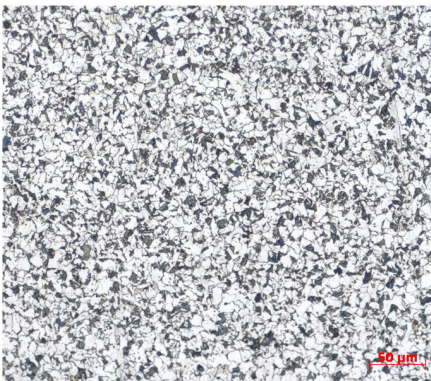


SA460ML ENDEREZADO

Figura 5. Microestructuras acero SA460ML

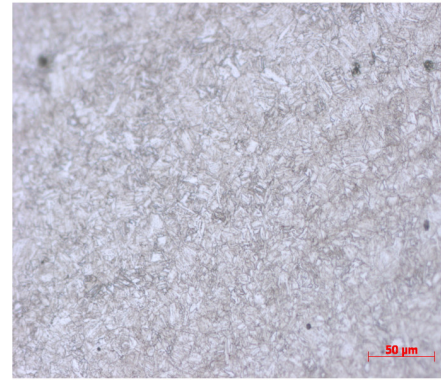


S690QL



S690QL ENDEREZADO

Figura 6. Microestructuras acero S690QL



S890QL



S890QL ENDEREZADO

Figura 7. Microestructuras acero S890QL

4.2. Impacto en la dureza

Se realizaron ensayos de microdureza Vickers 1 kg [8] sobre el material calentado para determinar los efectos del enderezado por llama sobre la dureza del material. La Tabla 2 recoge la comparación de los valores medios de la dureza a lo largo de perfiles de dureza de los 20 mm de espesor de los cinco aceros, entre el caso del material calentado y el material base.

Tabla 2. Comparación de los valores de dureza

	S235	S355	SA460	S690	S890
Mat. base	185.8	191.9	228.0	290.9	354.1
Mat. Calentado	126.4	172.9	172.4	214.9	294.5

Se comprueba en general un descenso de la dureza en los cinco aceros, cuya explicación puede realizarse a través de los hallazgos del análisis microestructural. En los aceros de microestructura original ferrítico-perlítica (S235JR, S355J2, SA460ML) tiene lugar una difusión del carbono mientras que en los aceros de alto contenido en carbono (S690QL, S890QL), la bainita de la superficie se reconvierte en una microestructura con agrupaciones de ferrita, más blanda en general.

4.3. Impacto en las propiedades de tracción

En relación a las propiedades de tracción [9], se extrajeron probetas de tracción pertenecientes a la zona directamente calentada por la llama para su ensayo. Los resultados del límite elástico al 0,2 %, $Re_{0.2\%}$, y de la tensión de rotura, σ_u , se recogen en la Tabla 2. La comparación visual de la repercusión del enderezado sobre el límite elástico y la tensión de rotura se representa en las Figuras 8 y 9.

Tabla 2. Propiedades a tracción del acero base (B) y calentado (C)

	S235 B	S235 C	S355 B	S355 C	S460 B	S460 C
Re 0.2% (Mpa)	284	247	379	349	469	470
σ_u (Mpa)	402	410	512	505	597	596
	S690 B	S690 C	S890 B	S890 C		
Re 0.2% (Mpa)	732	688	910	891		
σ_u (Mpa)	809	767	972	961		

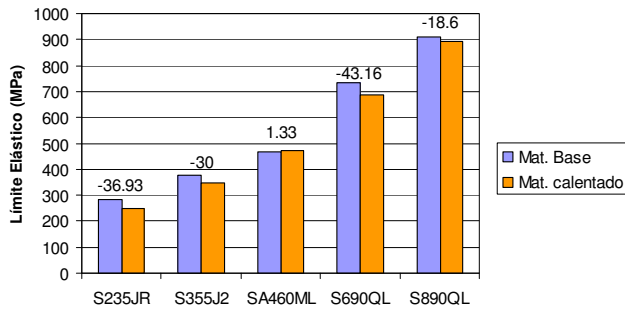


Figura 8. Comparación del límite elástico tras enderezado.

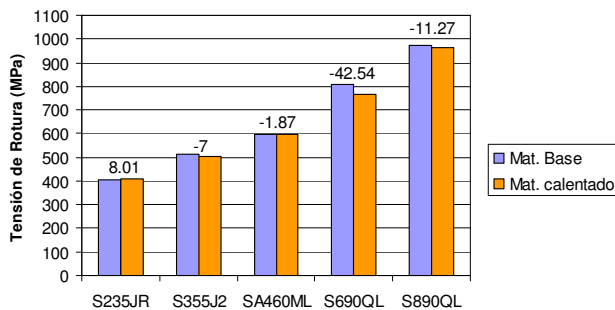


Figura 9. Comparación de la tensión de rotura tras enderezado

El estudio de los efectos que el enderezado por llama provoca sobre el material se completó con el cotejo de las propiedades ante el impacto antes y después del calentamiento. Se extrajeron probetas Charpy de la zona calentada de las chapas en dirección LT para ser ensayadas. La curva Charpy resultante se comparó con la curva Charpy obtenida con el material base. Las figuras 10 a 14 recogen la superposición de ambas curvas para cada acero.

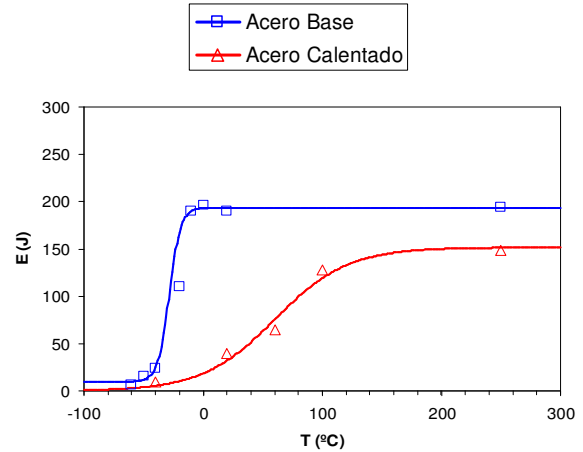


Figura 10. Comparación de resultados de impacto Charpy, acero S235JR

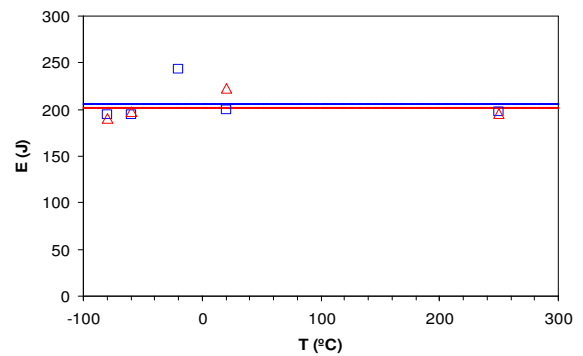


Figura 11. Comparación de resultados de impacto Charpy, acero S355J2

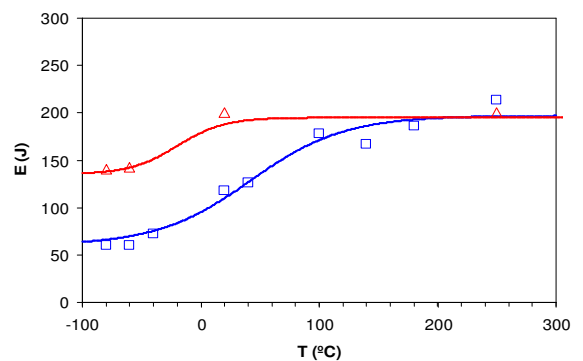


Figura 12. Comparación de resultados de impacto Charpy, acero SA460ML

4.2. Impacto en la resistencia al impacto

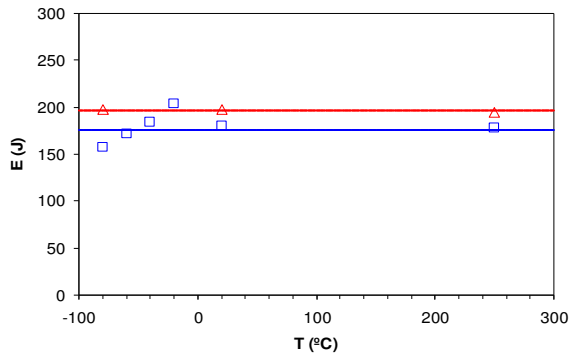


Figura 13. Comparación de resultados de impacto Charpy, acero S690QL

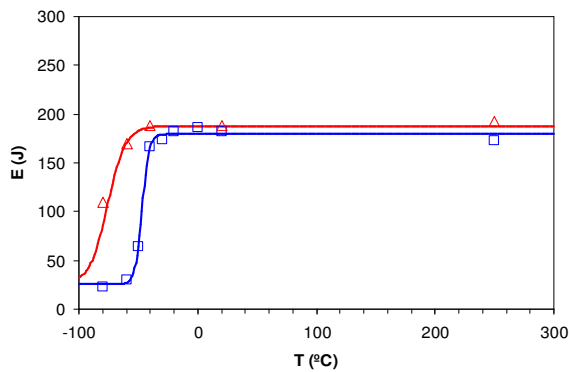


Figura 14. Comparación de resultados de impacto Charpy, acero S890QL

5. CONCLUSIONES

Es evidente, tras el estudio, que existe un cambio microestructural, más o menos acusado en función de la naturaleza del acero, tras la aplicación de la llama. Sus consecuencias más directas son la pérdida de homogeneidad en la dirección del bandeado de la perlita en los aceros ferrítico-perlíticos. Los aceros de alto contenido en carbono presentan una transformación de la microestructura en ferrita en la zona calentada.

Dichos cambios microestructurales se traducen en un descenso de la dureza del material en la zona calentada para todos y cada uno de los casos.

En cuanto a las propiedades de tracción, el calentamiento provoca un leve descenso en el límite elástico y en la tensión de rotura.

El comportamiento de los aceros calentado frente al ensayo de impacto no presenta características comunes.

Por una parte el acero S235JR presenta un desplazamiento de la temperatura de transición hacia la derecha así como un descenso en el Upper Shelf, señalando un rasgo de fragilización.

Los aceros S355J2 y S690QL no muestran evidencias de cambio en sus curvas Charpy.

En el caso de los aceros SA460ML y S890QL, sus propiedades ante el impacto mejoran levemente.

REFERENCIAS

- [1] Avent, R. R., Mukai, D. J., Robinson, P. F. “ Heat-Straightening Repairs of Damaged Steel Bridges, A Technical Guide and Manual of Practice”, *Report No FHWA-IF-99-004, Federal Highway Administration*, 1998.
- [2] Avent, R. R., Mukai, D. J. ,“ Heat-Straightening Rolled Shapes, A Technical Guide and Manual of Practice”, *Journal of Structural Engineering*, Vol. 126, pag. 755-763, 2000.
- [3] *Guidance for forming structural steels in processing*, D.D. CEN/TR 10347:2006
- [4] Avent, R. R., “ Engineered heat straightening comes of age”, *Modern steel construction*, pag. 32-39, Feb 1995.
- [5] Avent, R. R., “ Designing Heat Straightening Repairs”, *Proc., Nat. Steel Constr. Conf., American Institute for Steel Construction*, 1992.
- [6] Dennin, G.,“ Einfluss des Flammrichtens auf das Verformungsverhalten und die Korrosionsbeständigkeit von Grobblechen aus unlegierten und legierten Stählen”, *Schw. Schn* 28, pag. 421-425 1976.
- [7] UNE-EN 10025 “Productos laminados en caliente de acero para estructuras”
- [7] UNE-EN ISO 6507 “Materiales metálicos: Ensayo de dureza Vickers”
- [8] UNE-EN ISO 10002 “Materiales metálicos: Ensayo de tracción”

INFLUENCIA DE LAS TENSIONES Y DEFORMACIONES RESIDUALES SUPERFICIALES EN LA DURABILIDAD DE ALAMBRES DE PRETENSADO EN AMBIENTE DE HIDRÓGENO

M. Lorenzo¹, V. Kharin², J. Toribio²

¹ Departamento de Ingeniería Mecánica, Universidad de Salamanca
E. T. S. de Ingeniería Industrial. Avda. Fernando Ballesteros, 2 37700 Béjar (Salamanca).
E-mail: mlorenzo@usal.es

² Departamento de Ingeniería de Materiales, Universidad de Salamanca
E.P.S., Campus Viriato, Avda. Requejo 33, 49022 Zamora

RESUMEN

Como es bien sabido los aceros de pretensado son altamente susceptibles a la *fragilización por hidrógeno* (FH). En este proceso el estado tensodeformacional residual producido por el trefilado juega un papel esencial, puesto que condiciona la difusión de hidrógeno hacia determinadas zonas del material. De esta forma, las variaciones producidas en este estado tensodeformacional debidas a cambios en las condiciones del proceso de trefilado pueden modificar la vida en servicio de estos componentes estructurales. En este estudio se ha analizado el efecto en la FH de diferentes perfiles de tensiones hidrostáticas idealizados considerando en la superficie del alambre diferentes estados de tracción y compresión. Los resultados de este estudio permiten determinar la importancia de los estados tensodeformacionales en la superficie del alambre en los procesos de FH.

ABSTRACT

It is well known that prestressing steels are highly susceptible to *hydrogen embrittlement* (HE). Stress and strain states, produced by wire drawing, play an essential role in this process because stress and strains fields affect hydrogen diffusion towards specific places in the material. Therefore a variation on stress and strain fields, due to changes in wire drawing process conditions, could modify the life in service of these structural components. In this work the effect on HE of different idealized hydrostatic stresses profiles is analyzed taking into account distributions at wire surface with both tensile and compressive stress states. Results of present work demonstrate the key role of residual stress and strains states on HE process.

PALABRAS CLAVE: Estado tensodeformacional residual, fragilización por hidrógeno.

1. INTRODUCCIÓN

Los aceros trefilados de alta resistencia se utilizan ampliamente en la ingeniería civil como elementos de refuerzo en estructuras de hormigón pretensado. Se obtienen mediante un proceso de conformación plástica en frío denominado trefilado en el que se reduce de forma progresiva la sección del alambre. Las principales consecuencias mecánicas del procedimiento de fabricación son un aumento notable de la resistencia mecánica del acero [1,2]. Además, durante el conformado, el alambre sufre deformaciones plásticas no uniformes que originan la aparición de un estado tensional residual [3,4].

De acuerdo con los resultados del análisis pionero [5] estos estados residuales pueden condicionar la vida en servicio de estos alambres en ambientes agresivos. Los

estados de compresión en la superficie del alambre retardan la fisuración mientras que, por el contrario, los estados de tracción favorecen la aparición de fisuras que pueden producir la rotura del alambre mediante un proceso de crecimiento subcrítico por fatiga o por corrosión bajo tensión [6]. Por este motivo se suelen aplicar diversos procesos que generan estados de compresión en la superficie de los alambres tales como el granallado [7].

Pero es en ambientes agresivos donde aparece un tipo de fractura a la que estos alambres de acero son especialmente susceptibles, la denominada *fragilización por hidrógeno* (FH) [8]. En este tipo de fractura tanto las tensiones residuales como las deformaciones plásticas juegan un papel determinante en el proceso de daño que conduce a la fractura final [3,5].

El proceso de FH se desarrolla en diferentes etapas: transporte de hidrógeno molecular a la superficie del alambre, adsorción, disociación de la molécula en hidrógeno atómico, absorción de dichos átomos hacia el interior del alambre y finalmente transporte hacia determinados puntos del material donde se acumula hasta alcanzar una determinada concentración crítica que corresponde a la fractura a nivel microestructural [5,8]. Los estados tensodeformacionales en la superficie del alambre son decisivos en dos de las etapas en las que se desarrolla la FH: la acumulación de hidrógeno en la superficie del alambre y su posterior difusión hacia el interior de éste.

De esta forma se plantea el principal objetivo de este estudio: determinar los efectos en los procesos de FH del estado tensodeformacional que presenta un alambre en la superficie.

2. CASOS DE ESTUDIO

Para alcanzar el objetivo planteado se ha idealizado el estado tensodeformacional residual que presenta un alambre trefilado. La forma del perfil se ha elegido a partir de los perfiles empleados en el estudio [5] mostrado en la Fig. 1. Dicho perfil se puede dividir en dos zonas: en la primera, situada entre la superficie y una determinada profundidad x_0 , la tensión hidrostática varía de forma lineal desde la superficie y en la segunda zona, que se extiende entre la profundidad x_0 y el centro del alambre, el valor de la tensión hidrostática es uniforme.

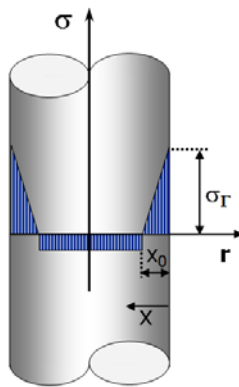


Figura 1. Esquema de los perfiles idealizados de tensiones hidrostáticas.

Por tanto para definir completamente el perfil idealizado sólo son necesarios dos parámetros: la tensión hidrostática en la superficie σ_r y la profundidad x_0 . Para determinar el efecto de la magnitud tensional en la superficie y de su signo se han considerado seis perfiles de tensiones hidrostáticas diferentes en los que se ha variado la magnitud en la superficie para cada uno de

los estados tensionales posibles: tracción (Tabla 1) y compresión (Tabla 2).

Tabla 1. Tensiones superficiales $\sigma_r > 0$ y profundidad x_0 en los perfiles teóricos con tracciones en la piel del alambre.

Perfil	I	II	III	IV	V	VI
σ_r (MPa)	100	200	500	800	1000	1200
x_0 (mm)	0.5	0.5	0.5	0.5	0.5	0.5

Tabla 2. Tensiones superficiales $\sigma_r < 0$ y profundidad x_0 en los perfiles teóricos con compresiones en la piel del alambre.

Perfil	VII	VIII	IX	X	XI	XII
σ_r (MPa)	-100	-200	-500	-800	-1000	-1200
x_0 (mm)	0.5	0.5	0.5	0.5	0.5	0.5

Finalmente, para completar la definición del estado tensodeformacional de los alambres analizados, resulta necesario definir la distribución de la deformación plástica. En este caso se ha adoptado una distribución uniforme a lo largo de la sección del alambre. El valor de dicha deformación se ha calculado a partir de los resultados del estudio [3] en el que las deformaciones plásticas obtenidas en la simulación del proceso de trefilado eran similares a las obtenidas con la ecuación (1) derivada de la hipótesis de conservación de volumen

$$\epsilon_p^{(i)} = \ln \left[\frac{d_0}{d_i} \right]^2 \tag{1}$$

donde ϵ_p representa la deformación plástica acumulada, d_0 es el diámetro inicial del alambre antes del trefilado y d_i es el diámetro del alambre después del paso de trefilado (i). Los alambres de acero analizados en este estudio corresponden al último paso de un proceso de trefilado en el que se ha reducido la sección del alambre desde un diámetro inicial de 12 mm hasta un diámetro final de 7 mm y por tanto los alambres estudiados, de acuerdo con la ecuación (1), tendrán una deformación plástica equivalente de 1.08.

3. MODELIZACIÓN NUMÉRICA

La forma más adecuada para obtener el objetivo planteado es mediante la modelización numérica del proceso de difusión de hidrógeno asistida por el estado tensodeformacional. En este modelo se considera que el flujo de hidrógeno en el interior del material viene gobernado por la ecuación de difusión de Fick modificada (ecuación (2)) en la que se incluyen dos términos que añaden el efecto del campo tensional, representado por el gradiente de tensiones hidrostáticas

$(\nabla\sigma)$, y el efecto de las deformaciones plásticas, incluido de forma indirecta a través de la solubilidad de hidrógeno en el metal que, tal como se muestra en la ecuación (3) basada en estudios previos [5], depende de la deformación plástica (ϵ_p).

$$\mathbf{J} = -D(\epsilon_p) \left\{ \nabla C - C \left[\Omega \nabla \sigma + \frac{\nabla K_{s\epsilon}(\epsilon_p)}{K_{s\epsilon}(\epsilon_p)} \right] \right\} \quad (2)$$

$$K_{s\epsilon}^{(i)}(r) = 1 + 4\epsilon_p^{(i)}(r) \quad (3)$$

donde $K_{s\epsilon}$ representa la componente de la solubilidad dependiente de la deformación plástica.

La concentración en la superficie del alambre se puede considerar que viene dada por la solución de la ecuación diferencial (1) en el estado estacionario cuya solución analítica se determina por la expresión

$$C_{eq} = K_{s\epsilon}(\epsilon_p) e^{\Omega\sigma} \quad (4)$$

La simulación del proceso de difusión establece la necesidad de definir otros parámetros que intervienen, como por ejemplo la temperatura ($T = 323 \text{ K}$) y el volumen parcial molar de hidrógeno en el acero $v_H = 2 \text{ cm}^3/\text{mol}$ [9]. Otro factor que influye en la difusión de hidrógeno es la difusividad. Este parámetro es altamente sensible a los cambios producidos a nivel microestructural, así como a los producidos por las deformaciones plásticas del material [9,10,11]. Existen estudios en los que se estima que la difusividad de hidrógeno en aleaciones BCC a temperaturas inferiores a 500 K está comprendida entre 10^{-13} a $10^{-8} \text{ m}^2/\text{s}$ [10]. El valor del coeficiente de difusión de hidrógeno en el alambre se puede tomar a partir de los resultados del estudio [5] para el acero final fuertemente trefilado analizado en este estudio: $\langle D \rangle^{(6)} = 4.99 \cdot 10^{-12} \text{ m}^2 / \text{s}$.

Las distribución de tensiones hidrostáticas y las deformaciones plásticas equivalentes son similares en todas las secciones del alambre [3], i.e., se repiten para cualquier coordenada z , cf. Figura 1. Por este motivo se ha considerado que la aproximación unidimensional (1D) del modelo de difusión asistida por el estado tensodeformacional es la más adecuada para el estudio planteado en este trabajo, puesto que en estas condiciones el flujo se producirá exclusivamente en la dirección radial (r) del alambre, no interviniendo la coordenada z [12].

4. DISTRIBUCIONES DE HIDRÓGENO

Los resultados de la simulación del proceso de difusión asistida por el estado tensodeformacional permiten conocer las distribuciones de hidrógeno a lo largo de la sección del alambre en los diferentes instantes de

tiempo en los que se desarrolla el proceso de difusión. En todos los perfiles de tensiones analizados el proceso de difusión presenta un patrón común que, a modo de ejemplo, se muestra en la Figura 2 para dos de los casos estudiados (perfiles IV y IX, con estados tensionales superficiales de tracción y compresión respectivamente). En dicha Figura se representa la evolución de las concentraciones relativas de hidrógeno en diferentes instantes de tiempo del proceso de difusión.

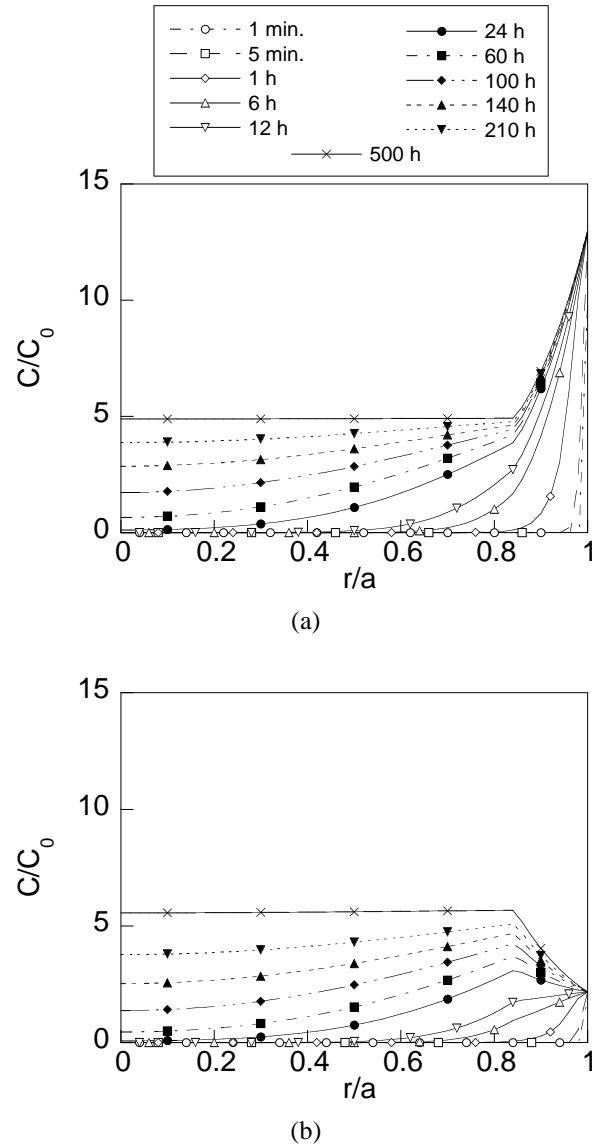


Figura 2. Evolución de la distribución de la concentración relativa de hidrógeno a lo largo del proceso de difusión en el alambre con el perfil de tensiones de compresión IV (a) y de tracción IX (b).

Tanto en los alambres con perfiles de tensiones residuales de tracción o compresión en la superficie (Figuras 2a y 2b respectivamente) se puede observar cómo se produce el proceso de acumulación de hidrógeno de forma progresiva desde la superficie hacia el interior del alambre hasta alcanzar una distribución estacionaria en la que los distintos puntos de la sección

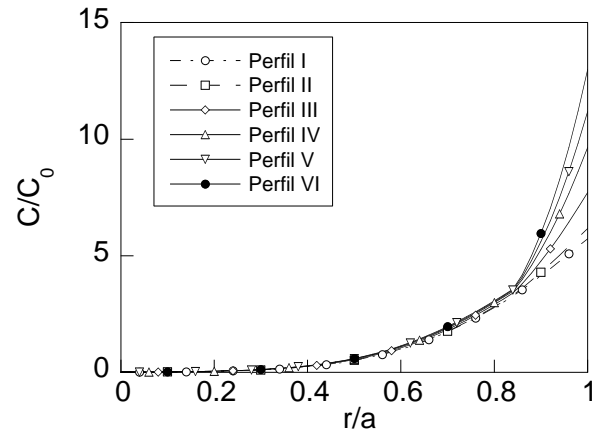
alcanzan la concentración máxima admisible que viene dada por la ecuación (4). En ambos casos el perfil de concentración de hidrógeno en el estado estacionario (tiempos de difusión largos) presenta una forma similar a la distribución idealizada del perfil de tensiones hidrostáticas.

No obstante, las distribuciones de hidrógeno obtenidas en los alambres con estados en la superficie de tracción y compresión presentan diferencias que pueden condicionar su integridad estructural durante su vida en servicio. En los perfiles con estados de tracción los valores de la concentración de hidrógeno más altos se localizan en una zona próxima a la superficie del alambre ($0.8 < r/a < 1$) donde la concentración estacionaria se alcanza a tiempos de difusión cortos ($t < 24$ h).

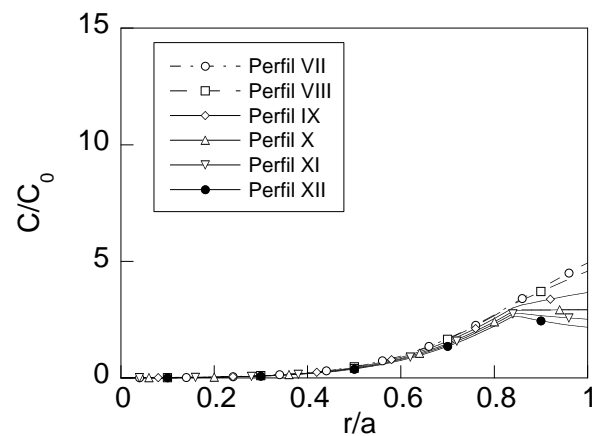
Por el contrario, en los perfiles con estados de compresión en la superficie el tiempo necesario para alcanzar el estado estacionario en la misma zona es sensiblemente mayor ($t > 100$ h). Esto, unido a que en dicha zona las concentraciones de hidrógeno son inferiores a las obtenidas en los perfiles de tracción, hace pensar que los alambres que presentan estados de compresión en la superficie tendrán una susceptibilidad menor a la acción de daño producida por el hidrógeno. Esto se debe a dos factores: por un lado la concentración en la zona donde potencialmente puede aparecer el daño por hidrógeno ($0.9 < r/a < 1$) es menor (y por tanto es menos probable que alcance la concentración crítica dada por el criterio de fractura) y por otro lado el tiempo necesario para alcanzar la concentración máxima admisible es mayor.

Para completar este análisis resulta interesante estudiar la influencia del valor de la tensión hidrostática en la superficie (σ_r) en las distribuciones de hidrógeno a lo largo de la sección del alambre. Para ello se han representado en la Figura 3 dichas distribuciones obtenidas para tiempos de difusión medios ($t = 35$ h, antes de alcanzar el estado de estacionario en todos los puntos del alambre) para cada uno de los seis perfiles de tracción (Figura 3a) así como para los seis perfiles de compresión analizados (Figura 3b).

En dichas Figuras se puede apreciar cómo aparecen en las distribuciones de la concentración de hidrógeno dos zonas claramente diferenciadas tanto en los alambres con estados tensionales de tracción en la superficie (Figura 3a) como en los alambres con estados tensionales de compresión (Figura 3b). Por un lado, la primera es la zona próxima a la superficie del alambre ($0.8 < r/a < 1$) donde existen claras diferencias entre los casos analizados y por otro la segunda corresponde a la zona interior del alambre ($r/a < 0.8$) donde las diferencias son apenas apreciables en las distribuciones de hidrógeno obtenidas en los alambres con estados tensionales de tracción y ligeramente más acusadas en las proximidades de la coordenada $r/a=0.8$ en los alambres con estados tensionales de compresión.



(a)



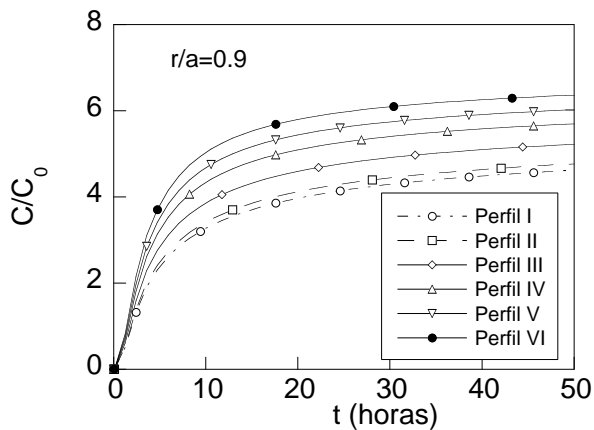
(b)

Figura 3. Distribución de la concentración relativa de hidrógeno en el alambre con los perfiles de tensiones de tracción: I, II, III, IV, V y VI (a) y compresión: VII, VIII, IX, X, XI y XII (b) (tiempo de difusión medio $t=35$ h).

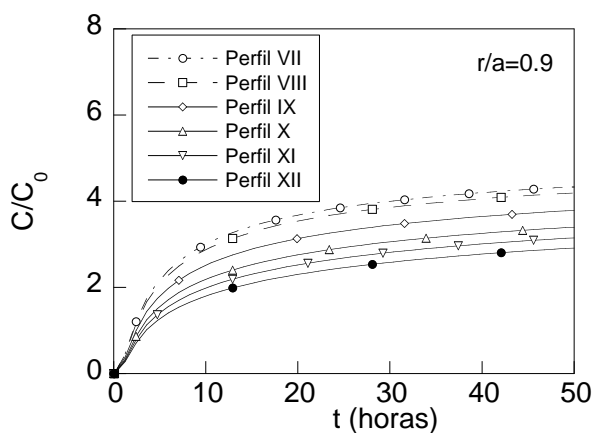
El análisis de las diferencias observadas en la primera zona ($0.8 < r/a < 1$) revela la importancia del tipo de estado tensional en la superficie del alambre (tracción o compresión), puesto que los efectos que se generan en los procesos de acumulación de hidrógeno son contrarios dependiendo de si el estado tensional en la superficie es de tracción o compresión. En el primero de los casos (estados de tracción en la superficie) se puede ver claramente en la Figura 3 cómo aumenta la concentración de hidrógeno en la zona potencialmente peligrosa [5] ($0.8 < r/a < 1$) a medida que aumenta el valor de la tensión en la superficie alcanzando el valor máximo en el alambre con la tensión más alta (perfil VI). Por el contrario en las distribuciones de hidrógeno obtenidas en los alambres con estados de compresión en la superficie la tendencia con el valor de la tensión en la superficie (en valor absoluto) es inversa, *i.e.*, la concentración de hidrógeno en la zona de análisis ($0.8 < r/a < 1$) decrece a medida que aumenta el valor de

la tensión en la superficie en valor absoluto tomando el valor mínimo en el alambre XII en el que la tensión en la superficie es la máxima de los perfiles de compresión considerados. Por estos motivos parece adecuado pensar que el efecto observado anteriormente en la Figura 2 se ve intensificado de forma gradual por el valor de la tensión que presenta el alambre en la superficie. De esta forma el efecto es muy acusado en los casos en los que se han considerado los estados tensionales más altos (perfiles VI y XII) y es muy reducido en los alambres con estados tensionales más bajos (perfiles I y VII) en los que las variaciones producidas son sensiblemente menores.

Para completar el estudio resulta interesante analizar (Figura 4) la evolución a lo largo del tiempo de difusión de la concentración de hidrógeno en un punto central ($r/a=0.9$) de la zona donde, de acuerdo con los estudios de otros autores [5], previsiblemente aparecerá el efecto del daño por hidrógeno a nivel microestructural.



(a)



(b)

Figura 4. Evolución temporal de la distribución de la concentración relativa de hidrógeno para puntos próximos a la superficie del alambre ($r/a=0.9$) con los perfiles de tensiones de tracción: I, II, III, IV, V y VI (a) y compresión: VII, VIII, IX, X, XI y XII (b).

En la Figura 4 se puede ver cómo se produce el proceso de acumulación de hidrógeno a lo largo del tiempo de exposición de forma similar en los dos tipos de alambre analizados en los que se considera estados de tracción y compresión en la superficie del alambre: la concentración de hidrógeno crece de forma progresiva (cuasi-lineal para tiempos cortos de difusión) hasta alcanzar el valor máximo admisible correspondiente al estado estacionario para tiempos largos de exposición al ambiente agresivo (cf. ecuación (4)). No obstante a pesar de dicha similitud las diferencias observadas previamente en las Figuras 2 y 3 también se pueden apreciar en la Figura 4. De esta forma los puntos situados a la profundidad $r/a=0.9$ en los alambres con estados de tracción en la superficie alcanzan una concentración de hidrógeno mayor a medida que aumenta el valor de la tensión en la superficie mientras que, por el contrario, en los alambres con estados de compresión en la superficie la concentración de hidrógeno es menor a medida que aumenta, en valor absoluto, el valor de la tensión en la superficie del alambre.

Pero la información que proporciona la Figura 4 va más allá, puesto que permite conocer de forma cualitativa la velocidad de acumulación de hidrógeno en la posición $r/a = 0.9$ de los alambres estudiados a través de la pendiente de las curvas mostradas en la Figura 4. De esta forma se puede observar que la velocidad de acumulación de hidrógeno en esa posición aumenta con el valor de la tensión en la superficie en los casos en los que el alambre presenta estados de tracción en la superficie mientras que, por el contrario, disminuye al aumentar dicho valor cuando los alambres presentan estados de compresión en la superficie.

Por tanto se puede considerar que en los alambres con estados de tracción en la superficie el proceso de acumulación de hidrógeno es más rápido. Por el contrario en los alambres con estados de compresión en la superficie el proceso de acumulación de hidrógeno se ralentiza. Esto reafirma los efectos observados previamente en las Figuras 2 y 3: los estados de tracción en la superficie hacen que los alambres sean más propensos a los fenómenos de FH no solo por alcanzar concentraciones de hidrógeno más elevadas (y por tanto probablemente más próximas a la concentración crítica dada por el criterio de fractura) sino que además los niveles altos de concentración de hidrógeno se alcanzan antes. Mientras que, por el contrario, los alambres con estados de compresión en la superficie el efecto es opuesto al de los alambres con estados de tracción: la susceptibilidad a los procesos FH es menor tanto por tener valores de concentraciones sensiblemente inferiores a los de tracción (y por tanto más alejados del valor de la concentración crítica) como por alcanzar los valores de la concentración de hidrógeno más lentamente. En ambos casos el valor de la tensión hidrostática en la superficie actúa como un intensificador de dicho efecto.

5. CONCLUSIONES

Los resultados demuestran la importancia de los estados tensodeformacionales superficiales en la fragilización por hidrógeno (FH) de los alambres. Las tensiones residuales de tracción superficial son potencialmente peligrosos para la integridad estructural en ambientes agresivos del alambre, puesto que favorecen la acumulación de hidrógeno en las proximidades de su superficie donde cabe esperar que los procesos de daño por hidrógeno a nivel microestructural tengan lugar. Esta acumulación es mayor a medida que aumenta el valor de la tensión en la superficie. Por el contrario los estados de tensión de compresión en la superficie producen el efecto contrario: la acumulación de hidrógeno es menor a medida que aumenta el valor de esta tensión en valor absoluto. Por lo que se puede pensar que los estados de compresión son adecuados para impedir la entrada de hidrógeno y reducir la acumulación de este elemento en las cercanías de la superficie. Esto supone una mejora de la vida en servicio de estos alambres en ambientes agresivos puesto que la susceptibilidad al fallo por FH de estos alambres se ve reducida.

Los resultados también permiten establecer una relación entre la magnitud de la tensión hidrostática en la superficie y la velocidad de acumulación de hidrógeno en los puntos donde potencialmente aparece el daño, dependiendo del tipo de tensión (tracción o compresión) presente en la superficie del alambre. En el caso de los alambres con estados de tracción la acumulación de hidrógeno es más rápida en aquellos perfiles de tensiones con estados superficiales más altos, mientras que en los perfiles de compresión la tendencia es inversa: la acumulación es más lenta a medida que aumenta el valor absoluto de la tensión en la superficie.

Por tanto finalmente se puede considerar que los estados tensionales de compresión reducen la concentración de hidrógeno en la zona próxima a la superficie del alambre y ralentizan el proceso de acumulación de hidrógeno en dicha zona, siendo este efecto mayor a medida que aumenta el valor de la tensión. Así pues, la susceptibilidad a los procesos de daño por hidrógeno de los alambres con estados de compresión en la superficie es menor y por tanto cabe esperar un aumento de su vida en servicio en presencia de ambientes agresivos.

AGRADECIMIENTOS

Los autores agradecen la financiación aportada por las siguientes instituciones: Ministerio de Ciencia y Tecnología (MCYT; MAT2002-01831), Ministerio de Educación y Ciencia (MEC; BIA2005-08965), Ministerio de Ciencia e Innovación (MCINN; BIA2008-06810), *Junta de Castilla y León* (JCyL; SA067A05, SA111A07 y SA039A08).

REFERENCIAS

- [1] J. Toribio, Relationship between microstructure and strength in eutectoid steels. *Mater. Sci. Engng. A* **387-389**, 227-230, 2004.
- [2] J. Toribio and E. Ovejero, Effect of cumulative cold drawing on the pearlitic interlaminar spacing in eutectoid steel. *Scripta Mater.* **39**, 323-328, 1998.
- [3] M. Lorenzo, D. Vergara, V. Kharin y J. Toribio, Influencia del estado tensodeformacional residual en la fragilización por hidrógeno de alambres trefilados. *Anal. Mec. Fract.* **24**, 123-129, 2007.
- [4] J. M. Atienza, *Tensiones residuales en alambres de acero trefilados*. Tesis Doctoral. Universidad Politécnica de Madrid, 2001.
- [5] J. Toribio and M. Elices, Influence of residual stresses on hydrogen embrittlement susceptibility of prestressing steels. *Int. J. Solids Struct.* **28**, 791-803, 1999.
- [6] S. Suresh, "Fatigue of materials". Cambridge University Press, Cambridge, 1998.
- [7] ASM Handbook Volume 5, "Surface engineering", ASM International, Materials Park, OH, 2007.
- [8] F. Bergsma, J.W. Boon, and C.F Etienne, Détermination de la sensibilité des aciers précontraints à la fragilisation par l'hydrogène. *Rev. Métall.* **75**, 153-164. 1978.
- [9] J. P. Hirth, Effects of hydrogen on the properties of iron and steel. *Metall. Trans.* **11A**, 861-890, 1980.
- [10] B. A. Kolachev, *Hydrogen Brittleness of Metals*. Metallurgia, Moscow, 1985.
- [11] R.S. Lillard, D.G. Enos and J.R. Scully, Calcium hydroxide as a promoter of hydrogen absorption in 99.5% Fe and a fully pearlitic 0.8% C steel during electrochemical reduction of water. *Corrosion* **56**, 1119-1132, 2000.
- [12] D. Vergara, M. Lorenzo, V. Kharin y J. Toribio, Análisis de la direccionalidad de la difusión de hidrógeno en las proximidades de entallas. *Anal. Mec. Fract.* **24**, 453-458, 2007.

CONSTRAINT EFFECT ON THE FRACTURE BEHAVIOUR OF THE SIMULATED HEAT AFFECTED ZONE OF AN X-70 STEEL

S. Rivera¹, R. Lezcano¹, C. Rodríguez², F.J. Belzunce² y C. Betegón²

¹Fundación ITMA, Centro Tecnológico del Acero y Materiales Metálicos, 33400 Avilés
E-mail: s.rivera@itma.es

²Escuela Politécnica de Ingeniería, Universidad de Oviedo, campus universitario, 33203 Gijón.
E-mail: cristina@uniovi.es

ABSTRACT

The typical heat affected zone developed in an X-70 steel usually used to pipeline manufacture has been simulated via thermal treatment. A non-equilibrium microstructure consisting on ferrite, bainite and some martensite has been produced and characterized to have a much larger hardness and strength than the corresponding base metal but a lower ductility. Different single end notched bend specimens (SENB) with different crack lengths (a/W between 0.1 and 0.5) have been experimentally tested in order to assess the fracture behaviour of this product under different degrees of constraint. The J - Δa resistance curves at room temperature have been determined and the obtained results have been explained due to the effect of constraint on the ductile crack growth.

KEY WORDS: X-70 steel, constraint effect, elastoplastic fracture.

1. INTRODUCTION

Fracture assessment procedures play a key role in design, fabrication and fitness-for-service methodologies in the case of many engineering products as pipelines, pressure vessels, etc. Fracture mechanics approaches are based on the use of a single parameter, most commonly the J -integral or the crack tip opening displacement (CTOD), in the case of elastoplastic behaviour, which defines the crack driving force, to characterize the fracture resistance of the material. Current engineering flaw assessment methods make extensive use of these toughness parameters to define design curves which provide simplified and conservative criteria for fracture evaluation of structural components containing defects [1,2].

Conventional testing standards used to characterize the fracture resistance of metallic materials make always use of deeply cracked specimens in order to guarantee high crack tip constraint conditions and small scale yielding (SSY) levels. However, structural defects in pipelines and pressure vessels are very often surface cracks that generate in the course of fabrication, especially in the course of welding, or during in-service operation (slag and non metallic inclusions, corrosion damage, weld cracks, dents at weld seams, corrosion damage, etc). It is well known that these crack configurations generally develop low levels of crack-tip triaxiality which sharply contrast to conditions present

in the standard deeply cracked specimens [3,4]. Consequently, predictions of fracture resistance based on standard deep cracked specimens may be in these cases unduly conservative and pessimistic and also can greatly increase the operational and maintenance costs.

There are different ways to define the crack-tip constraint. One of the most popular is the constraint ratio defined as the ratio between the hydrostatic stress to the Von Mises effective stress (σ_H/σ_e). Other constraint parameters are the T-stress [5,6] or the Q-parameter [7,8]. Whereas the T-stress is an elastic parameter which characterizes the geometrical constraint effect, the Q-parameter is a direct measure of the elastic-plastic stress fields that describes the deviation of the stress field, at a specified position ahead of the crack tip, from the reference stress distribution for which $T=0$ (SSY), which is fully accepted to be the general solution for a deep crack in an infinite specimen.

$$T = \frac{\beta K}{\sqrt{\pi a}} \quad (1)$$

$$Q = \frac{\sigma_{\theta\theta} - (\sigma_{\theta\theta})_{SSY, T=0}}{\sigma_{ys}} \quad \text{at } \theta=0, r = 2J/\sigma_{ys} \quad (2)$$

where β is the biaxility parameter, dependent on the considered geometry, K the corresponding stress intensity factor, σ_{ys} the yield strength and r and θ the polar coordinates taken from the crack tip. O'Dowd and Shih [7] demonstrated that, at least under small scale yielding, Q and T are univocally related.

It is so necessary to develop more accurate procedures for defect assessment when dealing with specific structures subjected to low levels of constraint. These approaches are based on the experimental testing of modified test specimens (shallow notch bend and tensile specimens) subjected to a constraint level that matches the one in the real structure.

2. EXPERIMENTAL PROCEDURE

A hot rolled plate of API X-70 Nb-V microalloyed steel with a final thickness of 15 mm has been employed. The plate was controlled rolled below the non-recrystallization temperature of the austenite and finally coiled at 547°C. The chemical composition of the steel is shown in Table 1.

Table 1. Chemical composition of the API X-70 plate

%C	%Mn	%Si	%S	%P	%Nb	%V
0.12	1.55	0.23	0.003	0.017	0.049	0.060

As it is well known, the longitudinal welded joints produced during the manufacture of the pipeline represent the most critical region because small cracks and defects can appear and also the heat affected zones, especially the coarse grain region which attains a very high temperature, can be harder and have a much lower toughness.

The grain growth region of the heat affected zone produced when the plate is longitudinally welded to make the pipeline was simulated by means of a heat treatment. Several pieces of 200x120x15 mm³ were quenched in water after austenitizing at 1100°C during 40 minutes. The cooling rate at 700°C at the centre of the thickness is about 80°C/s, which matches well with the cooling rate produced when this steel is welded using a low heat input (1.8-2 kJ/mm²) [9]. This point was assessed using the Rosenthal's equation to determine the cooling rate in the weld heat affected zone for a three-dimensional heat flow [10]:

$$v = \frac{2\pi\lambda(T - T_0)}{H} \quad (3)$$

being v the cooling rate at the temperature of interest T_0 (700°C), λ the workpiece thermal conductivity and H the heat input.

The microstructure of the materials were analyzed using optical and scanning electron metallographies.

Tensile test specimens with a calibrated diameter of 10 mm were machined in the transversal direction of the plate and were tested at room temperature at a displacement rate of 3 mm/min.

Fracture toughness tests were performed using single edge notched bending (SENB) specimens, with a TS orientation and different crack length to width ratios ($a/W = 0.1, 0.22$ and 0.5), in order to get different levels of constraint. It is well known that as long as the deeply cracked SENB specimen ($a/W=0.5$) corresponds to a high crack-tip triaxiality, there is a progressive constraint loss as the a/W ratio of the SENB specimen decreases. The length of the specimens always corresponded with the transversal direction of the plate and their width and thickness were 14 mm.

Specimens were fatigue pre-cracked at ambient temperature to the required nominal a/W at an R-ratio of 0.1. Fracture tests were carried out at room temperature in accordance with the ASTM E1820 standard [11] using a load-line displacement rate between 0.2 and 0.4 mm/min.

The single-specimen method, based on the use of the elastic unloading compliance was employed to determine de J- Δa resistance curves and the obtained results were corrected using the physical measure of the crack determined at the end of each test by means of a suitable low magnification microscope [12].

The J integral was determined from the procedure developed by Sumpter for non-standard bending specimens [13] and improved by Joyce [14], which consists on splitting up its elastic and plastic components. The elastic component was obtained from the stress intensity factor, K , as:

$$J_e = \frac{K_i^2 (a_i)(1 - \nu^2)}{E} \quad (4)$$

and the plastic component is given by:

$$J_{pli} = \left[J_{pl(i-1)} + \left(\frac{\eta_{i-1}}{b_{i-1}} \right) \frac{(P_i + P_{i-1})(v_{pli} - v_{pli-1})}{2B_N} \right] \cdot \left[1 - \gamma_{i-1} \frac{a_i - a_{i-1}}{b_{i-1}} \right] \quad (5)$$

being :

$$\eta_i = 0.32 + 12(a_i / W) - 49.5(a_i / W)^2 + 99.8(a_i / W)^3 \quad (6)$$

when $a_i/W < 0.282$, and

$$\gamma_i = -12.769 + 79.976(a_i / W) - 115.722(a_i / W)^2 \quad (7)$$

when $a/W < 0.325$

Otherwise, η_i and γ_i adopt the values given in the ASTM 1820 standard [11]. P_i and v_i are the applied load and the load-line displacement, E and ν the elastic modulus and the Poisson ratio, B_N , W , a , the net thickness, width and crack length and $b_i=W-a_i$ [14].

Finally, the β parameter corresponding to the different SENB tested specimens was calculated using the following expression [16, 17]:

$$\beta = - 0.462 + 0.461 (a/W) + 2.47 (a/W)^2 \quad (8)$$

Valid for $0.05 < a/W < 0.7$

3. RESULTS

Figures 1 and 2 show, respectively, the optical microstructure of the API X-70 plate and its simulated heat affected zone (HAZ). X-70 steel has a ferritic microstructure with only a small volume fraction of pearlite (about 3.3%). The ferritic grain size was between 11 to 12 ASTM (5-8 μm). The microstructure of the simulated heat affected zone consist manly in acicular bainite with some intergranular ferrite and small islands of martensite.

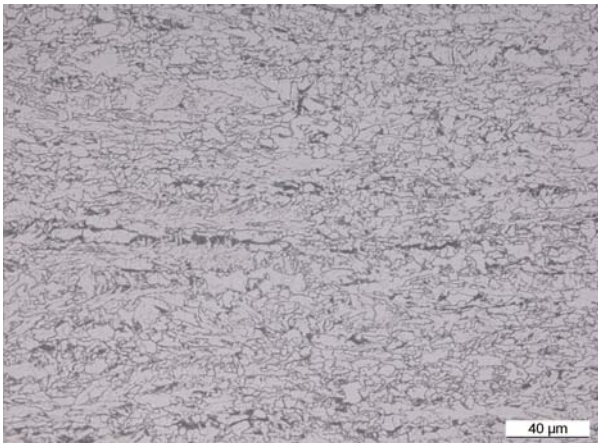


Figure 1. API X-70 steel microstructure

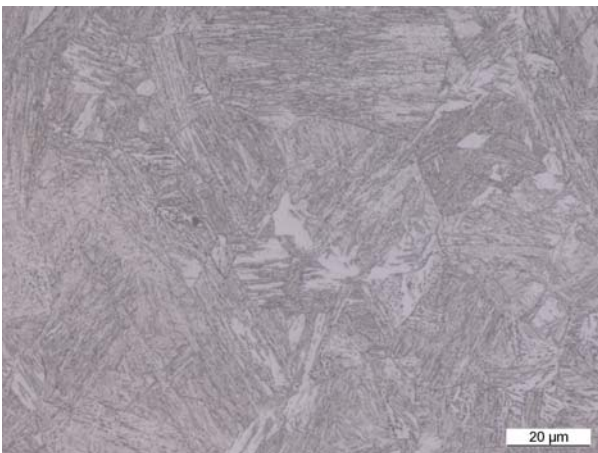


Figure 2. Simulated heat affected zone microstructure

The tensile mechanical properties and hardness of both materials, X-70 plate and its simulated heat affected zone, are presented in Table 2.

The simulated coarse grain heat affected zone has a much larger yield strength, ultimate tensile strength and hardness but a significant lower ductility than the original plate, as it could be expected.

Table 2. Tensile mechanical properties and Vickers hardness

	σ_{ys} (MPa)	σ_u (MPa)	A (%)	HV
X-70	545	660	24	205
Sim. HAZ	905	1206	12.4	318

Figure 3 shows the load versus load line displacement plots experimentally obtained with SENB specimens with different a/W ratios (0.5, 0.22 and 0.1). All the specimens have exhibited an elastic-plastic behavior, and the tests were considered ended after a significant crack growth (determined by compliance measurement during unloading) was attained. Afterwards, the specimens were heat tinted and finally fully broken in order to measure the real values of the original crack length, a , and crack growth, Δa . These measurements were used to correct the Δa values obtained by means of the already mentioned compliance technique.

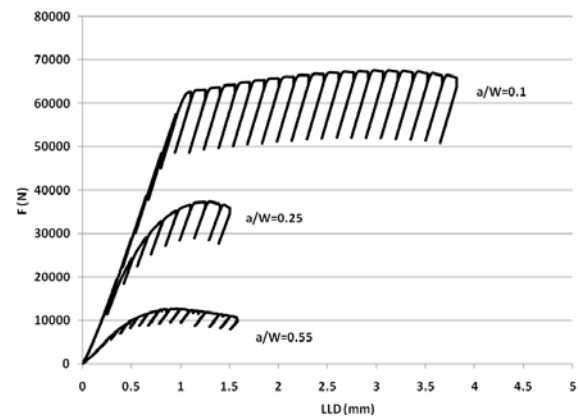


Figure 3. SENB load versus load-line displacement plots corresponding to specimens with different a/W ratios

Figure 4 shows the J-R curves experimentally obtained on the X-70 simulated coarse grain heat affected zone using the bend specimens with different a/W ratios.

The result obtained with the different geometries are clearly different and the expected constraint effect on crack growth is evident. The J initiation value, defined at a crack growth of 0.4 mm is about 200 kJ/m^2 for the deep cracked specimen but a twofold and threefold increase was observed respectively in the case of the specimens with shallow cracks ($a/W=0.1, 0.22$). The slope of the J- Δa curves also depends on the specimen geometry, hence the shorter cracks produce steeper J

crack growth resistance curves, and consequently, the differences of the measured J values among the tested geometries increase with the crack growth. For example the J values at crack extension of 0.6mm are approximately 260 kJ/m², 640 kJ/m² and 1000 kJ/m² respectively for a/W values of 0.5, 0.22 and 0.1. The same effect of constraint on the slope of the J resistance curves has been observed by different investigators in experiments made with a wide range of cracked geometries on several steels which failed in a ductile manner [14, 17].

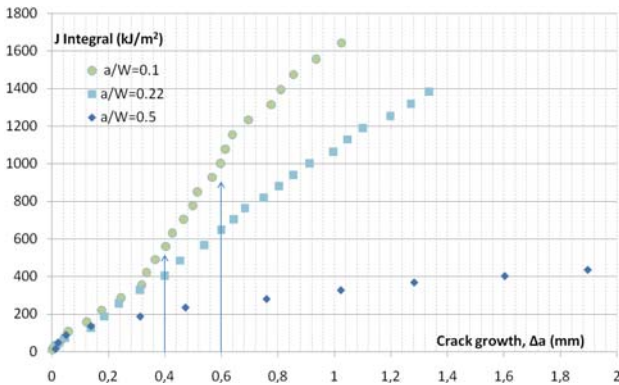


Figure 4. J-R curves of simulated coarse grain HAZ for different a/W ratios

4. DISCUSSION

Figure 5 shows the failure locus expressed as the J_{0.4mm} and J_{0.6mm} versus the normalized T-stress, τ (τ = T/σ_{ys}) for the X-70 simulated coarse grain heat affected zone. The τ factor was obtained using expressions (1) and (8) with the K value corresponding to each case.

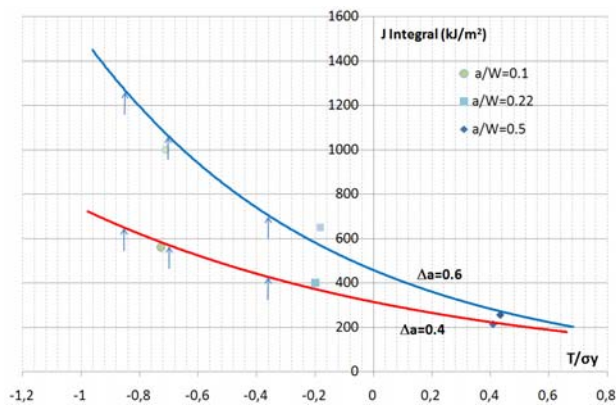


Figure 5. J - τ failure locus of API X-70 simulated HAZ

Figure 5 relates the evolution of the J resistance of this particular steel (coarse grain HAZ X-70 API steel) with the constraint factor, expressed by the elastic τ parameter. J values at crack growth initiation or after some particular crack growth are highly dependent on

the geometry constraint, with larger J-values as τ is more negative (lower constraint).

In order to apply these results to the evaluation of pressurized pipelines, we have used the results published by Cravero and Ruggieri [3], which have made finite element analysis on axially cracked pipes. The analyzed geometries typify current trends in high pressure, high strength pipelines of high outside diameters (508 mm) and low thickness (t=12.7 mm). Typical external and internal surface flaws with a/t ratios 0.1, 0.25 and 0.5 were employed (crack depth, a = 1.27mm, 3.175mm, and 6.35 mm, respectively).

Cravero and Ruggieri [3] also provide descriptions of crack-tip constraint in terms of J-Q trajectories for different axially cracked pressurized pipeline geometries and we have converted them in J-τ, making use of the polynomial relationship existing between these two parameters, which is represented in Figure 6 [18]. As it can be seen that this relationship is dependent on the materials constitutive law, we have used the curve which better matches our own steel, E/σ_y=200.

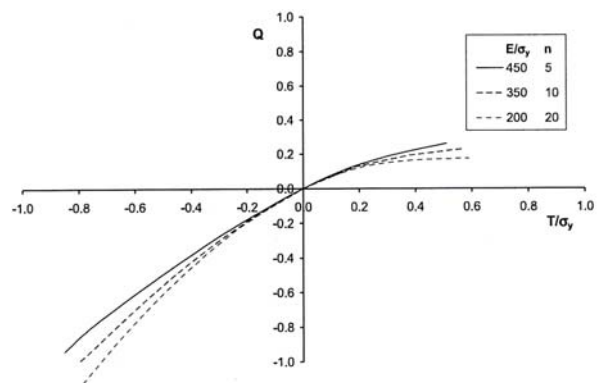


Figure 6. Relationship between Q and τ for different constitutive equations

The J-τ trajectories of the axially cracked pressurized pipelines with different crack sizes were also represented on Figure 5. The deep crack pipeline reveal a higher constraint loss than the deep notch SENB specimens, but the shallow crack pipelines exhibit much significant loss of constraint, which is even higher as the crack is shallower, but the crack location (internal or external) was demonstrate not to have influence on this point. Furthermore, the initial strong reduction in τ takes place when the global response of the specimen is still elastic, while the region with smaller change in τ with increasing J-levels confirms a fully plastic behaviour in the specimen.

It can be seen that in terms of constraint the deeply cracked pipeline (a/t = 0.5) will attain at the failure load a triaxiality τ factor of -0.4, which can be well characterized by means of a SENB specimen with an a/W ratio of 0.2 and the pressurized pipeline with a/t=0.2, will attain at fracture a triaxiality τ factor of

-0.7, which approximately corresponds to a SENB specimen with an a/W ratio of 0.1. Finally, when the pressurized pipeline has a very shallow crack ($a/t = 0.1$), the triaxiality factor at failure will be about -0.85 and this constraint value approximately corresponds to a SENB specimen with an a/W ratio lower than 0.1.

It can also be highlighted that the use of the critical J values obtained with the standard specimens (deeply cracked SENB specimens) give very low results, which give rise to unduly conservative and pessimistic expectations when they are used to predict the in-service failure of pressurized pipelines with real defects.

Nevertheless, the present study using an homogeneous microstructure corresponding to the simulated coarse grain heat affected region of an API X-70 steel is still conservative, as a real crack present in the coarse grain HAZ of an API X-70 pipeline will be embedded by the lower strength base steel, giving rise to an overmatched product (the yield strength of the region where the crack is located, the HAZ region, is larger than the yield strength of the base steel), which corresponds to a lower constraint configuration. This overmatching component behaves in the same way as an homogeneous material with a characteristic constraint parameter, so that mismatching and geometric effects can be simultaneously taken into account by the superposition of the normalized T-stresses, τ_m , originated by the constraint due to material mismatching and τ_g , originated by the geometrical constraint [19,20].

5. CONCLUSIONS

The typical coarse grain heat affected zone developed in an X-70 steel usually used to pipeline manufacture has been simulated via thermal treatment. A non-equilibrium microstructure consisting on ferrite, bainite and some martensite has been produced and characterized to have a much larger hardness and strength than the corresponding base metal but a lower ductility.

The effect of constraint on the J crack growth curves of the aforementioned simulated microstructure was studied by means of using SENB fracture specimens with different a/W ratios and the failure J - τ ($\tau = T/\sigma_y$) locus was also experimentally determined. SENB specimens with shallow cracks give always much higher initiation J values and resistant R-curves with a larger slope than the standard deep cracked specimens.

Representing the J - τ trajectories of axially cracked pressurized pipelines with different crack sizes on the studied steel biparametric failure locus, the necessity to find a SENB specimen with a crack depth with a constraint similar to that of the cracked pipe was demonstrated in order to assess the real fracture behavior of these structural components.

6. REFERENCES

- [1] British Standard Institution, BS7910, *Guide on methods for assessing the acceptability of flaws in metallic structures*, 1999.
- [2] American Petroleum Institute, API RP-579, *Recommended practice for fitness-for-service*, 2000.
- [3] Cravero S and Ruggeri C., *Correlation of fracture behaviour in high pressure pipelines with axial flaws using constraint designed test specimens-Part I: Plane-strain analysis*, Engineering Fracture Mechanics, 72, 1344-1360, 2005
- [4] Chiesa M. et al., *Efficient fracture assessment of pipelines. A constraint corrected SENT specimen approach*, Engineering Fracture Mechanics, 68, 527-547, 2001.
- [5] A.M. Al-Ani. and J.W. Hancock J.W., *J-dominance of short cracks in tension and bending*, J. Mech. Phys. Solids, 39, 23-43, 1991
- [6] C. Betegón and J.W. Hancock, *Two-parameter characterization of elastic-plastic crack-tip fields*, J. Appl. Mech., 58, 104-110, 1991.
- [7] N.P. O'Dowd and C.F. Shih, *Family of crack-tip fields characterized by a triaxiality parameter-I. Structures of fields*, J. Mech. Phys. Solids, 39, 989-1015, 1992
- [8] N.P. O'Dowd and C.F. Shih, *Family of crack-tip fields characterized by a triaxiality parameter-II. Fracture applications*, J. Mech. Phys. Solids, 40, 939-963, 1992
- [9] G. Heigt, H. Lengauer and P. Hodnik, *Heavy wall thermo-mechanically rolled plates for offshore construction use*, Steel Research Int., 79, 12, 931-937, 2008.
- [10] S. Kou, *Welding Metallurgy*, Wiley Interscience, John Wiley & Sons Pub., 2003
- [11] Tosal L, Rodríguez C, Belzunce F.J, Betegón C., *The influence of specimen size on the fracture behavior of a structural steel at different temperatures*, Journal of Testing and Evaluation, 28, N4, 276-281, 2000
- [12] ASTM E1820 Standard, American Society for Testing and Materials, 1999.
- [13] J.D.G. Sumpter, *Jc determination for shallow notch welded bend specimens*, Fatigue and Frac. Eng. Mat. & Struct., 10, 478, 1987

- [14] X.K. Zhu and J.A. Joyce, *J-R resistance curve testing of HY80 steel using SE(B) specimens and normalization method*, Eng. Fract. Mech., 74, 2007, 2263.
- [15] T.L. Sham, Rep. of the Dept. of Mech. Eng., Rensselaer Polytechnic Troy, 1989.
- [16] M.T. Kirk, K.C. Koppenhoefer and C.F. Shih, *Effect of constraint on specimen dimensions needed to obtain structurally relevant toughness measures*, ASTM STP 1171, 1993, 79
- [17] J.W Hancock, W.G Reuter and D.M Parkes, *Constraint and toughness parametrised by T*, ASTM Symposium, Indianapolis, 1991.
- [18] A.H. Sherry, M.A. Wilkes, D.W. Beardsmore and D.P.G. Lidberg, *Material constraint parameters for the assessment of shallow defects in structural components. Part.I. Parameter solutions*, Eng. Fract. Mech., 72, 2005, 2373.
- [19] C. Betegón and I. Peñuelas, *A constraint based parameter for quantifying the crack tip stress fields in welded joints*, Eng. Fract. Mech., 73, 2006, 1865
- [20] M.C. Burstow, I.C. Howard and R.A. Ainsworth, *The influence of constraint on crack tip stress fields in strength mismatched welded joints*, J. Mech. Phys. Solids, 46, 1998, 845

ACKNOWLEDGEMENTS

The authors acknowledge the support provided by FICYT (Principado de Asturias, Spain), Project FC-08-IB08-112C2.

EVOLUCIÓN DE LAS INCLUSIONES DURANTE EL PROCESO DE TREFILADO EN ACEROS PERLITICOS

R. Rodríguez¹, F. J. Ayaso¹, M. Lorenzo² y J. Toribio¹

¹Ingeniería de Materiales, Universidad de Salamanca
E.P.S., Campus Viriato, Avda. Requejo, 33, 49022 Zamora. España.
Tel: 980 54 50 00; Fax: 980 54 50 02, Correo-e: rociorg@usal.es

²Ingeniería Mecánica, Universidad de Salamanca.
E.T.S., Ingeniería Industrial, Avda. Fernando Ballesteros 2, 37700 Béjar (Salamanca).
Tel: 923 40 80 80; Fax: 923 40 81 27, Correo-e: mlorenzo@usal.es

RESUMEN

En el presente artículo se estudia la evolución de una inclusión durante el trefilado. Dicho estudio se divide en dos partes: primero, se caracteriza la evolución de las inclusiones mediante análisis visual de las micrografías (obtenidas con el microscopio electrónico de barrido) de los diferentes alambres que componen los distintos pasos de la cadena real de trefilado. La información obtenida mediante inspección visual se completa con una estimación cuantitativa de las dimensiones de la inclusión, utilizando un programa de análisis de imagen (AnaliSYS 3.1[®]). La segunda parte de este estudio se basa en la simulación, mediante el método de los elementos finitos (MEF), del proceso de trefilado de aceros con dichas microestructuras.

ABSTRACT

In the present paper the evolution of an inclusion during wire drawing is studied. The study is divided into two parts: firstly, the evolution of an inclusion is characterized by visual analysis of micrographs (obtained with scanning electron microscope) of different wires that compose the different steps of a real wire drawing chain. The information obtained by visual inspection was completed with a quantitative estimation of inclusion dimensions by using an image analysis software (AnaliSYS 3.1[®]). The second part of present study is based in simulation, by means of the finite element method (FEM), of the wire drawing process of steels with these microstructures.

PALABRAS CLAVE: Acero perlítico, Inclusiones, Trefilado.

1. INTRODUCCIÓN

El trefilado produce cambios micro-estructurales en el acero, cambios tales como una re-orientación de las colonias de perlita y de las láminas que las conforman en la dirección del eje longitudinal del alambre, una disminución progresiva del espaciado interlaminar, y un aumento en la esbeltez de las colonias [1,2]. Cabe destacar la existencia de colonias cuyas láminas no se han orientado en la dirección del proceso de trefilado (*pseudocolonias perlíticas*), las cuales presentan un espaciado interlaminar anómalo [3,4]. En la microestructura del acero se pueden encontrar inclusiones que se pueden clasificar por su origen, tamaño y composición [5]. En el acero objeto de estudio se han observado multitud de inclusiones, entre las cuales destacan por su composición algunos óxidos, silicatos, sulfuros de manganeso, carburos y en menor proporción nitruros [6]. Estas inclusiones presentes en el acero van a sufrir cambios a lo largo del proceso de trefilado, cambios que pueden tener su influencia en el posterior comportamiento en fractura del acero [7]. Algunos investigadores han estudiado la influencia de estas inclusiones en la iniciación de la fisura generada por fatiga [8] pero, en su mayoría, los estudios concernientes a éstas se centran en la distribución y la

morfología de las mismas [9]. La tendencia actual de las investigaciones acerca de dichas microestructuras se centra en la respuesta, a nivel tensional, de las mismas en los distintos procesos de fabricación del acero [10].

En el presente artículo se estudian los cambios micro-estructurales sufridos por las inclusiones a lo largo del proceso de trefilado que puedan tener una posterior influencia en la fractura de los aceros pertenecientes a los distintos pasos del proceso de trefilado. Para poder realizar un estudio de la evolución de dichas inclusiones ha sido necesario partir de la caracterización de éstas. En estudios anteriores las inclusiones presentes en este tipo de acero se dividen en tres grupos, a partir de su composición química, el primer grupo son los sulfuros, el segundo está compuesto por los óxidos y el último por silicatos. Las inclusiones formadas por sulfuros, inclusiones blandas, soportan mucha deformación, presentándose normalmente sulfuro de manganeso como principal componente. Los óxidos que se presentan como inclusiones, al contrario que los sulfuros, no admiten deformación, siendo éstos frágiles y de gran dureza. El tercer grupo, formado por silicatos, presenta comportamientos intermedios a los dos anteriores [6].

2. PROCEDIMIENTO EXPERIMENTAL

En el siguiente estudio se ha empleado acero perlítico eutectoide perteneciente a una cadena real de trefilado formada por siete hileras de trefilar, analizando desde el alambroón inicial, alambre que no ha sido sometido a ningún paso del proceso de trefilado, hasta el alambre de pretensado comercial. La nomenclatura utilizada para identificar los alambres analizados consta de una letra (en este caso acero tipo B o E, dependiendo de la familia a la cual pertenezca), que identifica la composición del acero (Tabla 1), y de un número representativo del paso de trefilado al que pertenece el alambre en cuestión: el número 0 para el alambroón inicial, 7 para el producto final, y los números del 1 al 6 para identificar los alambres correspondientes a los pasos intermedios.

Tabla 1. Composición química de los aceros B y E (%).

	C	Mn	Si	P	S	Al	Cr	V
B	0.79	0.07	0.23	0.01	0.01	0.003	0.27	0.08
E	0.79	0.68	0.21	0.01	0.01	0.003	0.22	0.06

Para el estudio de las inclusiones, en las dos familias de acero, se han realizado micrografías de las mismas en el alambroón inicial, así como en los alambres del segundo, cuarto, sexto y último paso del proceso de trefilado. En el estudio de los aceros analizados se ha determinado la gran cantidad de inclusiones que presentan las muestras pertenecientes a los alambres de la familia E, al contrario de lo que sucede en los alambres examinados de la familia B. Una vez observado este hecho en varias pruebas se ha decidido analizar el factor de forma de las inclusiones que se encuentran en los alambres pertenecientes a la familia E, pues aportan un mayor tamaño de muestra.

Las inclusiones elegidas para dicho análisis se han dividido en tres grupos, según su resistencia en comparación con la matriz perlítica circundante. Las inclusiones se dividen en duras (normalmente grupo formado por óxidos y por carburos), con mayor resistencia que la matriz perlítica, blandas (sulfuros) e inclusiones mezcla (inclusiones con óxidos y sulfuros bien definidos). Estas últimas se han analizado debido a que se presentan en mayor número que los silicatos u otro tipo de inclusiones, además de por la curiosidad de presentar los dos tipos de clasificaciones anteriores en la misma. Dichas inclusiones están formadas por óxidos, principalmente de hierro, rodeados por sulfuro de manganeso (distinguiéndose ambas inclusiones de forma clara dentro de la misma).

En la segunda parte de este estudio se simula mediante la utilización del método de los elementos finitos (MEF) el proceso de trefilado basado en estudios previos. Debido a la simetría de revolución tanto del alambre como de la hilera de trefilado el problema se puede simplificar a un caso axisimétrico tomando como eje de simetría el eje del alambre [11].

3. RESULTADOS

3.1. Análisis visual y cálculo del factor de forma.

Una vez obtenidas las micrografías y seleccionadas según el tipo de inclusión se procede a la medición de las mismas, mediante el programa AnaliSYS. 3.1®.

Para el estudio del factor de forma de las inclusiones a lo largo del proceso se ha aproximado la morfología de la inclusión a una elipse. De este modo, en las inclusiones se ha medido el eje mayor (2a), paralelo a la dirección de trefilado, representado en la Figura 1.

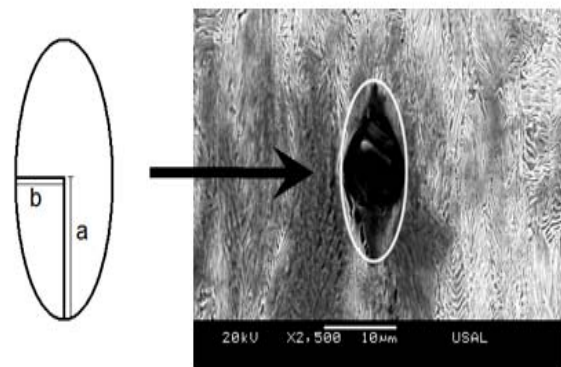


Figura 1. Aproximación de la inclusión a una elipse.

Una vez medido dicho eje de la elipse en las distintas micrografías se ha tomado la medida de la superficie de la inclusión. Con dicha superficie y la medida del eje mayor de la elipse, 2a, se obtiene el eje menor utilizando la siguiente ecuación:

$$S = \pi \times a \times b \tag{1}$$

siendo *a* y *b* los semiejes de la elipse y *S* la superficie del micro-defecto: la superficie de la inclusión o, en el caso de no coincidir, del hueco generado por la misma. El estudio se centra en la superficie del defecto por ser ésta la suma de la inclusión y la micro-fisura generada. Una vez obtenidos estos datos se procede a calcular el factor de forma de las inclusiones (*a/b*), realizando la media y la desviación típica de los distintos factores de forma obtenidos en los diferentes pasos del proceso.

En las inclusiones, en las cuales se presentaba una descohesión de la matriz perlítica debido al proceso de trefilado, se ha medido la superficie de micro-defecto generado, la cual engloba la inclusión (*S*). En aquellas en la que la interfase perlita-inclusión permanece unida se ha medido únicamente la superficie de la inclusión. Las mediciones obtenidas, es decir las medias del factor de forma de las distintas inclusiones, se encuentran recogidas en la Tabla 2. Para poder comparar dichas medidas se ha realizado un tratamiento estadístico de los datos obtenidos, no siendo en ningún caso la desviación típica superior a 2.

Tabla 2. Medias aritméticas del factor de forma

	E0	E2	E4	E6	E7
Duras	1.371	1.820	1.956	2.852	3.058
Blandas	3.280	5.966	7.034	9.117	11.763
Mezcla	2.317	6.953	7.013	7.224	7.870

En las microfotografías pertenecientes al alambroón inicial se han observado inclusiones con deformaciones previas al trefilado que pueden atribuirse al proceso previo de laminación en caliente [10].

Para poder dilucidar los cambios en la morfología de las inclusiones se han representado los datos en las Figuras 2-4 correspondientes a cada tipo de inclusión, en las cuales se muestran no sólo la media aritmética sino también la desviación típica.

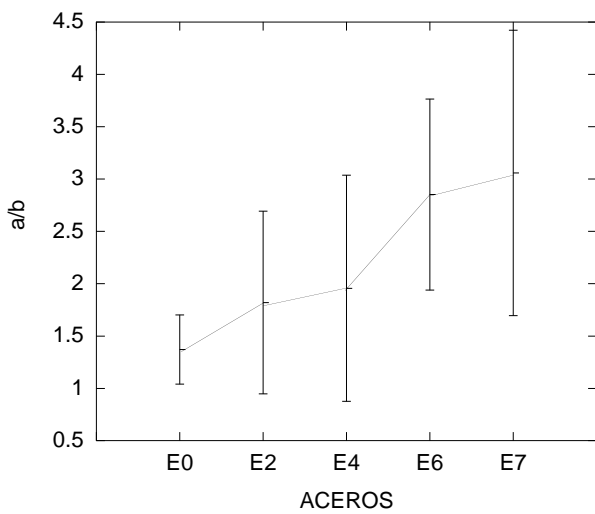


Figura 2. Evolución del factor de forma en inclusiones duras.

En la Figura 2 se muestra una evolución del factor de forma de las inclusiones de tipo duro y los micro-defectos que generan. Aún siendo más resistentes que la matriz perlítica que las rodea, aumentan su esbeltez durante el trefilado debido a la generación de microfisuras orientadas en la dirección de dicho proceso.

Las inclusiones de tipo blando y los micro-defectos generados por las mismas se comportan de igual forma que las duras, aumentando su esbeltez a lo largo del proceso, sin embargo dicho aumento es más acentuado en las blandas. En la Figura 3 se pueden observar aumentos mucho mayores del factor de forma que en las inclusiones duras.

En las inclusiones tipo mezcla, Figura 4, se observa un comportamiento análogo a los dos tipos de inclusiones anteriores, aumentando su esbeltez a lo largo del proceso de trefilado. Dicho aumento es muy similar al de las inclusiones tipo blando, resultado el cual cabía esperar puesto que la inclusión en contacto con la matriz perlítica es una inclusión de tipo blando.

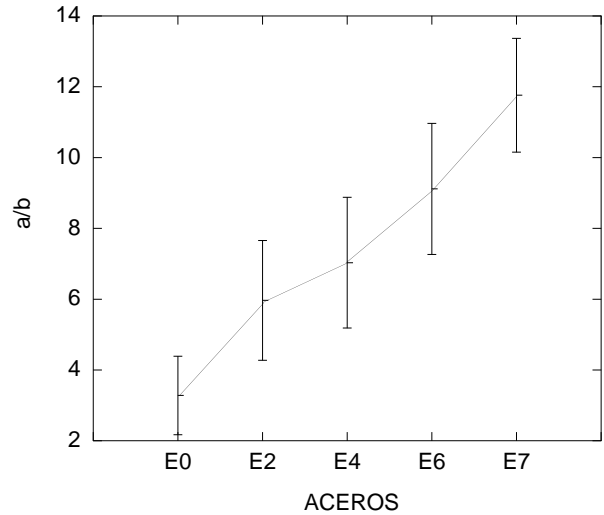


Figura 3. Evolución del factor de forma en inclusiones blandas.

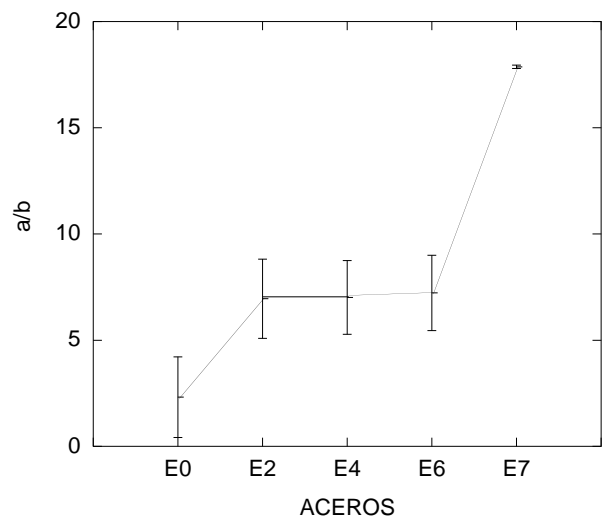


Figura 4. Evolución del factor de forma en inclusiones mezcla.

3.2. Simulación mediante el MEF.

La simulación mediante el MEF de la inclusión a lo largo del proceso de trefilado se ha realizado utilizando el programa M.S.C.Marc®. Los parámetros mecánicos de dicho proceso se detallan en estudios previos [11]. Para el estudio de la evolución de las inclusiones a lo largo del proceso, éstas fueron incorporadas en el centro del alambre, simulándose de esta forma un elipsoide de revolución. La morfología descrita coincide con la aproximada para la medición del factor de forma de los distintos tipos de inclusiones presentes en los aceros objeto de estudio.

La malla utilizada en la simulación mediante el MEF se muestra en la Figura 5. Las dimensiones de las inclusiones utilizadas en los cálculos fueron las medias obtenidas en los alambrones.

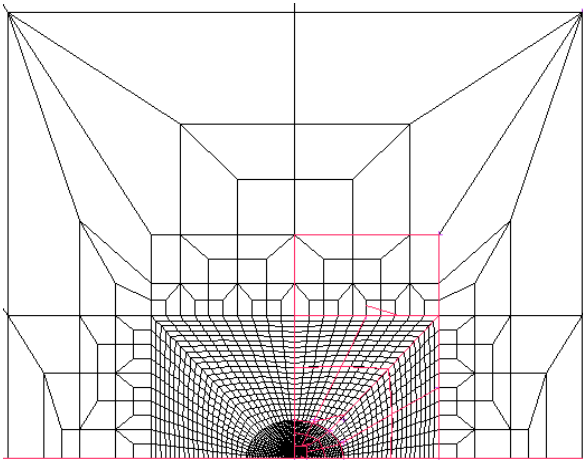


Figura 5. Representación de la malla perteneciente a la inclusión de tipo duro.

El comportamiento mecánico impuesto a las inclusiones duras se ha modelizado utilizando las características mecánicas de la alúmina (óxido de aluminio). El comportamiento mecánico de la inclusión tipo mezcla se ha aproximado teniendo en cuenta la respuesta visual observada en las micrografías a lo largo del proceso de trefilado, siendo estas inclusiones menos resistentes que la matriz perlítica. Las características geométricas y los parámetros mecánicos se detallan en la Tabla 3.

Tabla 3. Parámetros geométricos y mecánicos de las distintas inclusiones.

	Duras	Blandas	Mezcla (óxido)
a (µm)	1.6	1.6	1.6 (0.3)
b (µm)	1.25	0.496	0.496 (0.165)
E (MPa)	352	160	160 (352)
v	0.24	0.32	0.32 (0.24)

Los cálculos se han realizado con dos tipos de interfase entre la matriz perlítica y la inclusión, uno de ellos suponiendo la inclusión totalmente unida a la matriz y el otro completamente desunida.

4. DISCUSIÓN

En el análisis visual de la evolución de las inclusiones y los micro-defectos generados, realizado por medio de las micrografías pertenecientes a los distintos pasos del proceso de trefilado, se muestra la tendencia de los distintos tipos de inclusión a lo largo de dicho proceso.

En las Figuras 6, 7 y 8 se muestra la evolución de las distintas inclusiones mediante algunas de las micrografías obtenidas. Se puede observar como, a medida que se avanza en el proceso de trefilado, la matriz perlítica circundante se despega de las inclusiones de tipo duro generando micro-cavidades a ambos lados de éstas. Las micro-cavidades van a estar orientadas en la dirección del proceso de trefilado, evidenciando que son consecuencia del mismo.

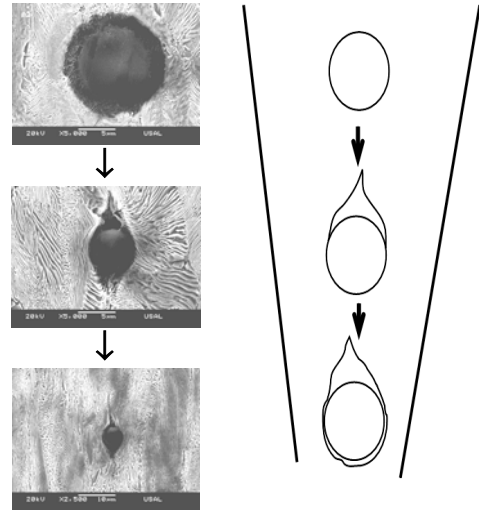


Figura 6. Evolución de las inclusiones de tipo duro durante el proceso de trefilado.

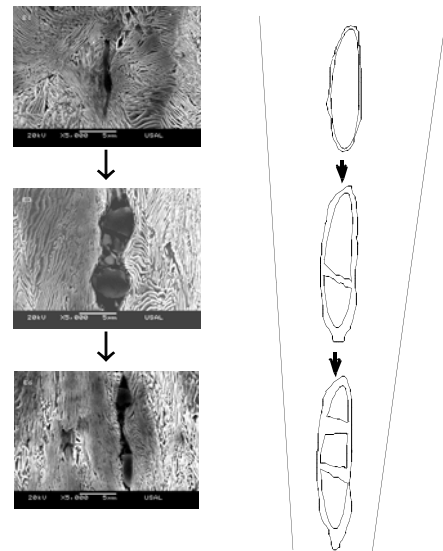


Figura 7. Evolución de las inclusiones de tipo blando durante el proceso de trefilado.

De forma similar las inclusiones blandas, que son capaces de deformarse más que la matriz perlítica, evolucionarán a lo largo del proceso de trefilado llegando a fragmentarse y generando microcavidades de menor tamaño que las anteriores. Este tipo de microcavidades también se generan a ambos lados de la inclusión y estarán orientadas en la dirección del proceso de trefilado. La inclusión puede llegar a mostrarse totalmente fragmentada, generando numerosas microcavidades alrededor de cada fragmento.

El mayor tamaño de microcavidades se ha observado en los alambres fuertemente trefilados. No obstante, en los primeros pasos del proceso de trefilado aparecen algunas microcavidades pero de menor entidad, puesto que la matriz apenas se ha despegado de la inclusión.

Las inclusiones denominadas mezcla, como se comentó anteriormente, están formadas por varias inclusiones. Las distintas inclusiones se pueden diferenciar claramente dentro de las micrografías, por la diferencia de tonalidad y forma, presentándose las inclusiones duras más oscuras y con morfologías más redondeadas.

La parte blanda de la inclusión mezcla, en los primeros pasos del trefilado, tenderá a deformarse en la dirección dicho proceso (Figura 8). A medida que avanza el trefilado la parte blanda de la inclusión se fragmentará, formando microcavidades entre los distintos fragmentos de la misma. Cabe destacar el comportamiento de la interfase inclusión blanda-dura, que no se descohesiona, quedando ambas unidas durante el proceso de trefilado.

Una vez fragmentada la parte de la inclusión blanda se produce, debido al constreñimiento de las colonias, el relleno de las microcavidades. Este relleno deja aislados los fragmentos de la inclusión, mostrándose en las micrografías como inclusiones independientes. La separación entre los fragmentos, aunque se rellena de matriz perlítica, tendrá menor resistencia que el resto del material, definiéndose como lugares débiles dentro del acero. Como resultado final del proceso, tanto las inclusiones tipo blando como las de tipo mezcla generan discontinuidades dentro de la matriz perlítica; esto se debe a que el relleno no es estrictamente completo en los bordes de los fragmentos.

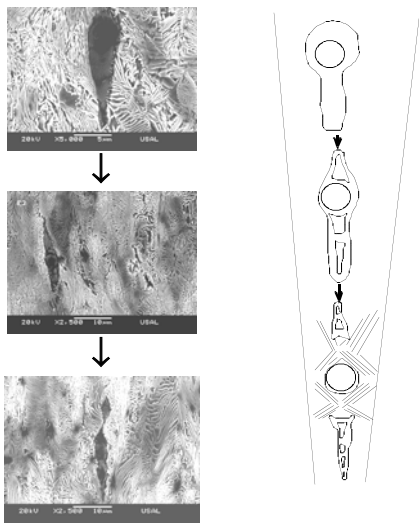


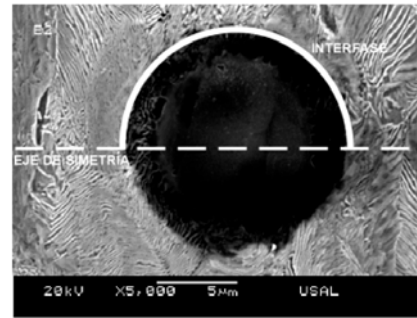
Figura 8. Evolución de las inclusiones de tipo mezcla durante el proceso de trefilado.

Una vez analizados de forma visual los cambios morfológicos generados por las inclusiones se han comparado con los cálculos obtenidos en la simulación mediante el MEF. Estos cálculos muestran los cambios geométricos del micro-defecto durante el trefilado.

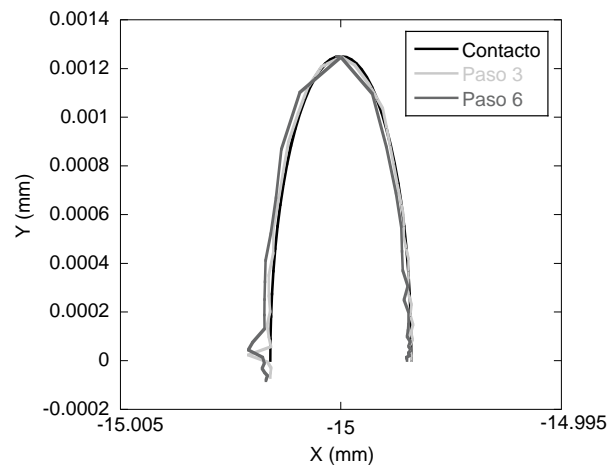
Los desplazamientos obtenidos son el resultado de imponer la interfase perlita-inclusión desunida, puesto que esta interfase unida no simula la realidad en la cual se observa la generación de microcavidades.

La interfase entre la matriz perlítica y la inclusión, Figura 9 (a), es simétrica respecto del eje de trefilado, situándose ésta en el centro del alambre en la simulación mediante MEF.

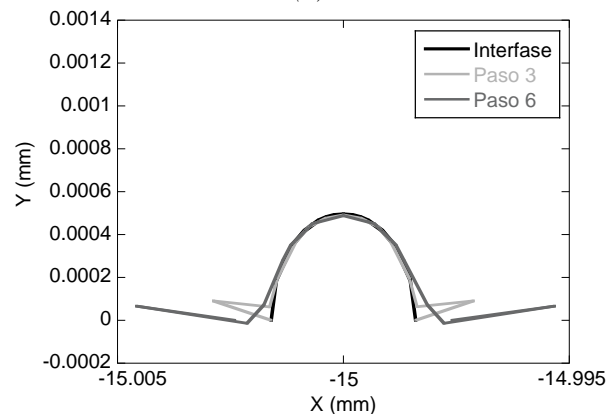
En las Figuras 9 (b) y (c) se han representado los desplazamientos de la interfase generada entre la perlita y los micro-defectos, mostrándose los datos obtenidos en tres etapas del proceso; en su estado inicial, tras haber superado el tercer paso y, finalmente, después del sexto paso del trefilado.



(a)



(b)



(c)

Figura 9. (a) Representación de la interfase simulada mediante MEF. (b) cambios morfológicos en la superficie del micro-defecto en inclusiones duras a lo largo del trefilado y (c) en inclusiones blandas.

En la figura 9 (b) se muestra la progresión de la interfase entre la matriz perlítica y la inclusión, observándose que, a medida que avanza el proceso de trefilado, dicha inclusión genera una micro-fisura orientada en dirección del trefilado (eje del alambre). A lo largo del trefilado también se observa una reducción del eje menor del micro-defecto, produciéndose como se comentó anteriormente, un apelmazamiento del material. Las microcavidades generadas se muestran en un solo lado de la inclusión siendo éste el opuesto al proceso de trefilado, mientras que en el otro se muestra un apelmazamiento del material. Las interfases analizadas han presentado un comportamiento similar en cuanto a la esbeltización a favor de la dirección del proceso. En la interfase de las inclusiones de tipo blando, Figura 9 (c), se han generado micro-cavidades a ambos lados de la inclusión y apelmazamiento de la matriz perlítica en la zona del eje menor del micro-defecto. El comportamiento de las inclusiones de tipo mezcla es análogo al mostrado por las inclusiones blandas, en cuanto a la interfase entre matriz perlítica e inclusión se refiere. Esto se debe a que la inclusión blanda, que rodea a la dura, es la que forma la interfase con el acero, con lo cual es la que influye en el comportamiento de dicha interfase perlita-inclusión.

5. CONCLUSIONES

En el presente artículo se ha realizado un análisis cualitativo y cuantitativo de los cambios morfológicos de los micro-defectos generados por las inclusiones presentes en los aceros objeto de estudio. Una vez obtenidos los resultados se han comparado con un estudio paralelo basado en la simulación mediante el método de los elementos finitos (MEF). A partir de la comparación de ambos análisis se obtienen las siguientes conclusiones:

- Todos los micro-defectos analizados, generados por las inclusiones, presentan un aumento de esbeltez como consecuencia del proceso de trefilado.
- Dicho proceso de esbeltización es más acusado con la presencia de inclusiones de tipo blando.
- Las microcavidades generadas por las inclusiones a lo largo del trefilado se presentan en el semieje mayor de la inclusión (paralelo a la dirección del proceso). Por el otro lado, en el eje menor de la misma, se genera un apelmazamiento del material.
- Las inclusiones que generan más microcavidades (concentradores de tensiones) y un mayor apelmazamiento del material son las inclusiones de tipo blando y mezcla.

AGRADECIMIENTOS

Los autores desean hacer constar su agradecimiento a las siguientes instituciones financiadoras: MCYT (Proyecto MAT2002-01831), MEC (Proyecto BIA2005-08965), MCINN (Proyecto BIA2008-06810) y JCyL (Proyectos SA067A05, SA111A07 y SA039A08). Además, agradecen el suministro de acero por parte de EMESA TREFILERÍA.

REFERENCIAS

- [1] J. Toribio and E. Ovejero. *Microstructure evolution in a pearlitic steel subjected to progressive plastic deformation* Materials Science and Engineering A234-236, pp. 579-582 (1997).
- [2] J. Toribio and E. Ovejero. *Microstructure orientation in a pearlitic steel subjected to progressive plastic deformation* Journal of Materials Science Letters 17, pp. 1037-1040 (1998).
- [3] J. Toribio, E. Ovejero and M. Toledano. *Microstructural bases of anisotropic fracture behaviour of heavily drawn steel*. International Journal of Fracture 87, pp. L83-L88 (1997).
- [4] J. Toribio, E. Ovejero, F. J. Ayaso y R. Rodríguez. *Identificación de nuevas unidades microestructurales en aceros eutectoides trefilados*. 5º Jornadas Internacionales de Metallografía y Caracterización Microestructural, INASMET, Mayo 2008.
- [5] A. D. Wilson. *The influence of thickness and rolling ratio on the inclusion behavior in plate steels*. Metallography 12, pp. 233-255 (1979).
- [6] R. Rodríguez. *Análisis del micro-daño y de la presencia de inclusiones en aceros progresivamente trefilados* (Directores: J. Toribio y F.J. Ayaso). Grado de Salamanca. Universidad de Salamanca (2008).
- [7] F.J. Ayaso, B. González y J. Toribio. *Influencia de las inclusiones sobre el comportamiento en fractura de aceros perlíticos progresivamente trefilados*. Anales de Mecánica de la Fractura 24, pp. 99-104 (2007).
- [8] C.D. Liu, M.N. Bassim and S. Lawrence. *Evaluation of fatigue-crack initiation at inclusions in fully pearlitic steels*. Materials Science and Engineering A 167, pp. 107-113 (1993).
- [9] S.R. Collins and G.M. Michal. *Inclusion engineering for improved fatigue response in forged AISI 4140 steel*. Conf. High Performance Structural Steels, Cleveland, OH, USA, pp. 269-280 (1995).
- [10] H. Yu, H. Bi, X. Liu, L. Chen and N. Dong. *Behavior of inclusions with weak adhesion to strip matrix during rolling using FEM*. Journal of Materials Processing Technology 209, pp. 4274-4280 (2009).
- [11] M. Lorenzo, D. Vergara, V. Kharin y J. Toribio. *Influencia del estado tensodeformacional residual en la fragilización por hidrogeno de alambres trefilados*. Anales de Mecánica de la Fractura 24, pp. 123-128 (2007).

EFECTO DEL SHOT PEENING EN EL COMPORTAMIENTO A FATIGA DE ACEROS INOXIDABLES DÚPLEX

P. Sanjurjo, C. Rodríguez, I. F. Pariente, F. J. Belzunce

Escuela Politécnica Superior de Ingeniería de Gijón, Universidad de Oviedo, Campus de Viesques, 33203Gijón, España
e-mail: ppsanjurjo@uniovi.es
Tfno: 985181951. Fax 985182055

RESUMEN

Para la realización de este trabajo, se seleccionó un acero inoxidable austeno-ferrítico tipo AISI 2205, utilizado para la fabricación de armaduras de refuerzo, y se sometió a distintos tratamientos de shot peening, con el fin de estudiar el efecto de dichos tratamientos sobre el comportamiento a fatiga del material. Para ello, se controlaron minuciosamente parámetros tales como la intensidad Almen, el grado de cobertura o el tipo de proyectil utilizado. A continuación, se utilizó la técnica de difracción de rayos X para caracterizar el campo de tensiones residuales de compresión generado tras cada tratamiento. Por último, se determinaron experimentalmente las curvas de Wöhler correspondientes a los distintos tratamientos realizados, y se compararon con las curvas obtenidas para el material sin tratar.

ABSTRACT

In this work an AISI 2205 duplex stainless steel, already largely used to make reinforcing bars, was the material choice. The bars were manufactured using both hot and cold rolled processes, and afterwards different shot peening treatments were used, which were fully characterised by means of the Almen intensity, the coverage ratio and the type of shot used in each case. Residual stresses were also measured by means of X-ray diffraction. The S-N fatigue curves of the bars submitted to the different shot peening treatments were determined and the improvement due to shot peening explained taking into account the shot peening effects on the surface of the bars.

PALABRAS CLAVE: acero inoxidable dúplex, shot peening, intensidad Almen, tensiones residuales

1. INTRODUCCIÓN

Con el fin de mejorar el comportamiento en servicio de las estructuras, el acero inoxidable está siendo cada vez más utilizado para el armado de grandes estructuras de hormigón sometidas a ambientes salinos. Además, es habitual que dichas estructuras se encuentren sometidas a la acción de cargas cíclicas, por lo que se debe garantizar también un buen comportamiento a fatiga [1].

Uno de los procesos más utilizados industrialmente para mejorar el comportamiento a fatiga de los componentes metálicos es el shot peening [2]. En este tratamiento, la deformación plástica producida por el impacto de gran cantidad de pequeños proyectiles esféricos sobre la superficie de un elemento metálico, genera un campo de tensiones residuales de compresión que resulta beneficioso desde el punto de vista del comportamiento a fatiga. Otra consecuencia directa del tratamiento es la modificación del acabado superficial [3], hasta el punto de que, en ocasiones, la rugosidad superficial generada puede afectar negativamente al comportamiento a fatiga.

En este trabajo se analiza cómo el efecto adverso producido por la rugosidad superficial generada tras realizar un tratamiento de shot peening, puede llegar a

contrarrestar el efecto positivo producido por el campo de tensiones residuales de compresión que se genera tras dicho tratamiento.

Para ello en primer lugar, se sometieron las barras corrugadas a un tratamiento de shot peening industrial. A continuación, se mecanizaron probetas con un buen acabado superficial, con el fin de eliminar el efecto de las corrugas y defectos iniciales. Dichas probetas se sometieron a un tratamiento de shot peening más controlado y de mayor intensidad. El campo de tensiones residuales de compresión generado tras cada tratamiento, se caracterizó mediante la técnica de difracción de rayos X. Por último, se determinaron experimentalmente las curvas S-N correspondientes a los distintos tratamientos de shot peening realizados, y se compararon con las curvas obtenidas con el material sin tratar. De este modo, se obtuvo información sobre la influencia del shot peening sobre el comportamiento a fatiga de las barras de refuerzo de acero inoxidable dúplex.

2. MATERIALES Y PROCEDIMIENTO EXPERIMENTAL

Para la realización de este trabajo, se utilizó un acero inoxidable austeno-ferrítico tipo AISI 2205. Este material nos fue suministrado en forma de barras corrugadas que habían sido fabricadas tanto por laminación en caliente como por deformación en frío. Este acero se emplea habitualmente en la fabricación de armaduras de refuerzo en casos en los que la estructura se encuentra expuesta a ambientes salinos, y se caracteriza por su microestructura dúplex que le confiere unas elevadas propiedades mecánicas junto con una alta resistencia a la corrosión [4]. Dado que el proceso de fabricación propio de cada tipo de armadura les confiere unas propiedades características, hablaremos de dos tipos de materiales distintos, que se designarán como D2205c (dúplex laminado en caliente) y D2205f (dúplex deformado en frío) [5]. En la tabla 1 se recogen los valores medios de las propiedades mecánicas a tracción de las barras.

Tabla 1. Propiedades mecánicas a tracción

Material	E [GPa]	σ_{ys} [MPa]	σ_{us} [MPa]	A [%]
D2205c	166	630	793	51
D2205f	153	965	1103	16

El proceso de shot peening industrial, llevado a cabo por la empresa *Roldán S.A.*, se realiza bombardeando las barras corrugadas con bolas de acero fundido de tamaño S-230, utilizando una máquina centrífuga de 8 turbinas. Por su parte, en la Escuela Politécnica de Ingeniería de Gijón se diseñó un segundo tratamiento de shot peening, que fue realizado en laboratorio en condiciones controladas estrictamente. Para ello se utilizó una máquina neumática de proyección por presión directa, que puede operar con presiones de trabajo entre 1.5 y 6 bar. Con el fin de poder comparar resultados, también se utilizaron proyectiles de acero fundido tipo S-230, en conformidad con las especificaciones de SAE J444 [6]. Con el fin de obtener un tratamiento de shot peening de alta calidad, dichos proyectiles fueron minuciosamente caracterizados, en cuanto a su tamaño y forma, mediante análisis de imágenes.

En ambos tratamientos, la intensidad Almen se determinó siguiendo la regla del 10%, de acuerdo con las especificaciones SAE J442 [7] y SAE J443 [8]. Se utilizaron placas Almen tipo A, grado 2, firmemente sujetas a los correspondientes bloques Almen, así como un medidor Almen digital con una precisión de 0.001 mm y soporte de sujeción magnético.

Para obtener la intensidad Almen de cada tratamiento, se ajustaron los datos experimentales mediante una ecuación de 4 parámetros:

$$h = a \cdot (1 - e^{-b \cdot t^c}) + d \cdot t \quad (1)$$

siendo h la flecha medida en la placa Almen, t el tiempo de exposición a los proyectiles y a , b , c y d los cuatro parámetros de la curva, que se obtienen por iteración mediante métodos numéricos.

Por otro lado, también se comprobó experimentalmente que el grado de cobertura se ajustaba con gran exactitud a la siguiente ecuación (2), conocida como Ecuación de Avrami:

$$C = 100 \cdot (1 - e^{-A \cdot R \cdot t}) \quad (2)$$

donde C representa la cobertura (porcentaje de superficie que ha sido impactada al menos una vez), A el área de cada huella individual, R el ratio de flujo (número de huellas creadas por unidad de tiempo y unidad de superficie) y t el tiempo de exposición.

En todos los tratamientos de shot peening se alcanzó una cobertura teórica de 98%, lo que en la práctica se identifica con la cobertura total.

Mientras que el shot peening industrial se realizó sobre las propias barras corrugadas, esquematizadas en la figura 1, el shot peening controlado se llevó a cabo sobre probetas mecanizadas como la mostrada en la figura 2. En estas probetas, se eliminó totalmente la corruga, con el fin de apreciar el efecto que ésta tiene sobre el comportamiento a fatiga del material, al eliminar el efecto de la geometría y del tosco acabado superficial que presentan las barras.

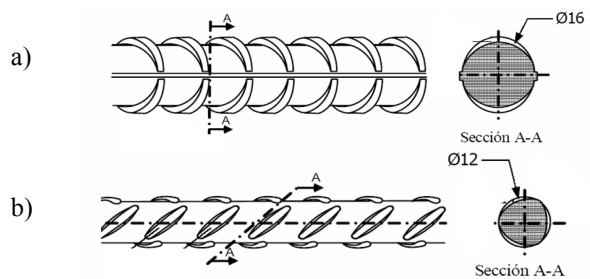


Figura 1. Esquema de las barras corrugadas: a) corrugadas en caliente, b) corrugadas en frío

A continuación, se utilizó la técnica de difracción de rayos X para caracterizar el campo de tensiones residuales de compresión generado tras cada tratamiento. Estas medidas se llevaron a cabo con el soporte técnico del Politécnico de Milán, Italia. Los ensayos se realizaron en modo ψ según la norma SAE HS-784 [9].

Por último, con el fin de estudiar el efecto del shot peening sobre el comportamiento a fatiga del material, se determinaron experimentalmente las curvas S-N correspondientes a los dos tratamientos realizados, y se compararon con las curvas obtenidas para el material sin tratar. Puesto que el fenómeno de la fatiga tiene un gran componente aleatorio, para caracterizar el campo de Wöhler se utilizó un modelo matemático que incluye

información estadística acerca de la vida a fatiga (modelo de *Castillo et al*) [10].

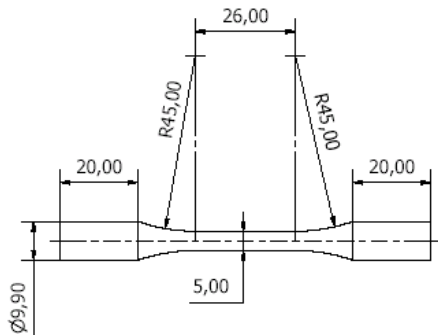


Figura 2. Esquema de las probetas mecanizadas sometidas a shot peening controlado

3. RESULTADOS Y DISCUSIÓN

3.1. Tratamientos de Shot Peening

En la figura 3 se muestra la curva de saturación obtenida para el tratamiento de shot peening industrial. Las medidas se llevaron a cabo en las instalaciones de la empresa fabricante de las barras *Roldán S. A.*, resultando una intensidad Almen de 0.13 mmA.

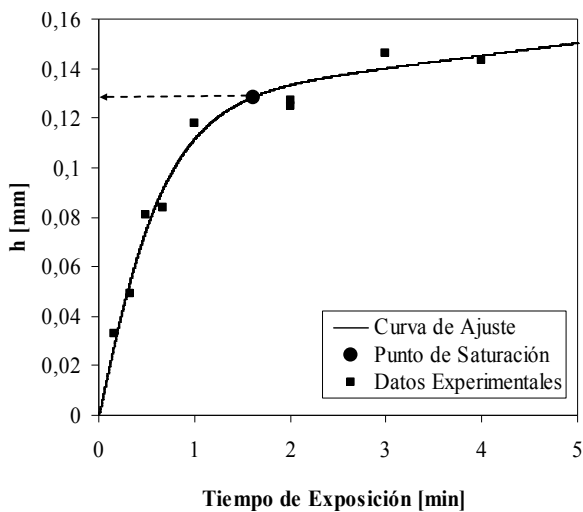


Figura 3. Curva de saturación del tratamiento de shot peening industrial (0.13 mmA)

Estudios anteriores [11] demostraron que el acero dúplex deformado en frío se ve muy poco afectado por los tratamientos de shot peening de baja intensidad, por lo que se optó por diseñar un nuevo tratamiento con una intensidad sensiblemente superior a la utilizada industrialmente. En la figura 4 se representa la curva de saturación para este nuevo tratamiento, diseñado en la Escuela Politécnica de Ingeniería de Gijón, con una intensidad de 0.33 mmA. Como se puede apreciar, en ambos casos el ajuste conseguido mediante la ecuación (1) es excelente.

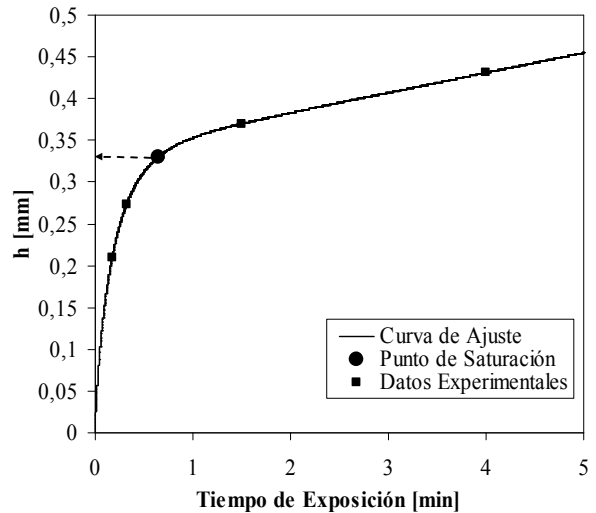


Figura 4. Curva de saturación del tratamiento de shot peening controlado (0.33 mmA)

3.2. Tensiones residuales

En la tabla 2 se recogen los resultados de las medidas de tensiones residuales realizadas sobre la superficie de las barras corrugadas antes de ser sometidas a shot peening. Aunque la mayor parte de las roturas durante el proceso de fatiga tienen lugar en la zona de acuerdo entre las corrugas y el cuerpo de la barra, las medidas de tensiones residuales tuvieron que ser realizadas en la zona de barra comprendida entre dos corrugas, ya que la complicada geometría de la zona del acuerdo entre la barra y la corruga hace prácticamente imposible la toma de resultados en esa zona. Los valores mostrados en la tabla 2, son los resultantes de aplicar la regla de las fases, pues, dado el carácter bifásico del acero inoxidable dúplex, las mediciones se llevaron a cabo tanto en la fase austenita como en la ferrita.

Tabla 2. Valores de tensión residual axial medidos sobre las barras corrugadas de acero inoxidable dúplex

	Tensión residual axial [MPa]	
	Sin tratar	Shot peening industrial
D2205c	155±14	-336±18
D2205f	-149±22	-465±14

Como se puede apreciar, mientras que las barras corrugadas en caliente (D2205c) presentan tensiones residuales de tracción de unos 155 MPa, sus homólogas corrugadas en frío muestran valores muy similares, pero de compresión (-149 MPa). De todos modos, dada la gran dificultad técnica encontrada para llevar a cabo estas mediciones, estos valores deben ser admitidos con cierta cautela.

De manera análoga, se midieron las tensiones residuales generadas sobre la superficie de las barras tras ser sometidas al tratamiento de shot peening industrial. Las medidas también se realizaron en la zona comprendida entre dos corrugas, y los resultados también se recogen

en la tabla 2. Como puede observarse, tanto en el caso de los corrugados en caliente como en frío, el proceso de shot-peening induce unas fuertes tensiones residuales de compresión. De este modo, las barras corrugadas en caliente alcanzan valores de -336 MPa, y de -465 MPa las corrugadas en frío. Comparando estos valores con los que presentaban estas mismas barras antes del tratamiento, se obtiene el incremento de tensiones residuales debido al shot peening industrial en torno a -481 MPa para el caso de las barras corrugadas en caliente y de -316 MPa para las deformadas en frío.

En definitiva, el efecto del tratamiento de shot peening industrial es más acusado en el acero corrugado en caliente, lo que parece razonable, por tratarse de un material de menor dureza y mayor ductilidad que su homólogo deformado en frío. Conviene insistir, una vez más, en que la dificultad de las mediciones hace que todos estos valores correspondan a una zona muy concreta de la superficie de las barras (zona entre corrugas), con las limitaciones que esto supone.

A la vista de los resultados obtenidos, y dada la complejidad que envuelve este tipo de medidas, se optó por eliminar el problema de la geometría y realizar, tanto el tratamiento de shot peening controlado como las medidas de las tensiones residuales, sobre superficies planas obtenidas tras cortar transversalmente las barras. De este modo, para el corrugado en caliente se midió el gradiente de tensiones residuales hasta una profundidad de 350 μm , mientras que para el corrugado en frío la profundidad alcanzada fue de 160 μm . Para verificar la isotropía del tratamiento, todas las medidas se realizaron en tres direcciones (0° , 45° y 90°) y sobre las dos fases (ferrita y austenita). En la figura 5 se muestra el perfil de tensiones residuales obtenido.

Como puede observarse, el perfil de tensiones residuales es el típico de estos tratamientos, alcanzándose, para ambos materiales, una tensión máxima de compresión a una profundidad aproximada de 0.04 mm, si bien en el caso del corrugado en caliente el valor máximo obtenido (-740 MPa) es ligeramente superior al obtenido para el corrugado en frío (-685 MPa). Conviene tener presente de nuevo, la mayor dureza y la menor capacidad de deformación de los corrugados en frío. Por otro lado, el perfil de los gradientes indican que la zona superficial de material sometida a tensiones residuales de compresión es mucho mayor (prácticamente el doble) en el corrugado en caliente.

Por otro lado, como información adicional a la medida de tensiones residuales, se obtuvieron medidas del parámetro FWHM. Este valor está relacionado con la distorsión de los granos, con la densidad de dislocación y con las microtensiones residuales. Se suele considerar que este parámetro es un índice del endurecimiento del material, de modo que cuanto mayor es el parámetro FWHM, mayor es el endurecimiento de la superficie [12].

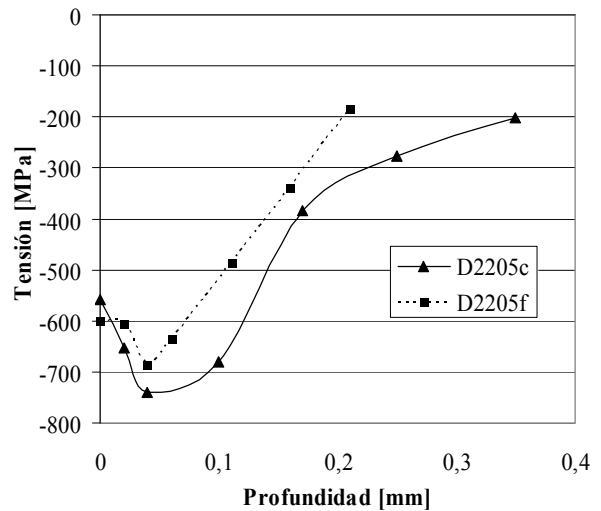


Figura 5. Perfil de tensiones residuales obtenido sobre probetas mecanizadas sometidas a un tratamiento de shot peening controlado de 0.33 mmA

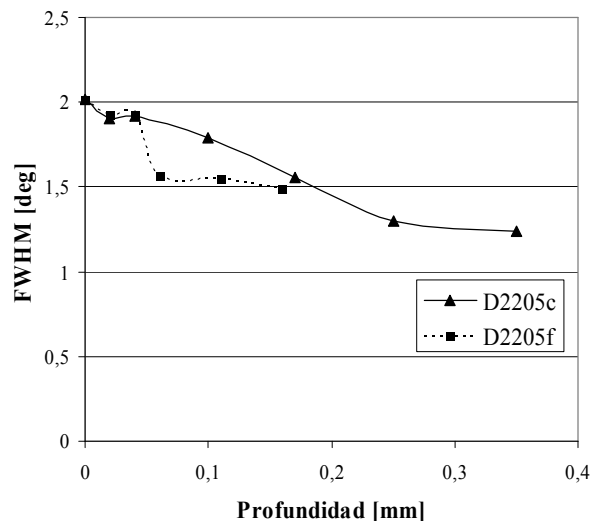


Figura 6. Evolución del parámetro FWHM sobre probetas mecanizadas sometidas a un tratamiento de shot peening controlado de 0.33 mmA

La figura 6 muestra cómo, en el dúplex laminado en caliente, el parámetro FWHM se estabiliza en torno a una profundidad de 400 μm , lo que indica que el tratamiento de shot peening ha producido una capa deformada plásticamente de un espesor de 400 μm . Sin embargo, en el dúplex deformado en frío, dicho parámetro se estabiliza en valores próximos a las 50 μm , lo que hace pensar que en este caso, el espesor de la capa endurecida por deformación plástica es de aproximadamente 50 μm .

3.3. Comportamiento a Fatiga

Tanto sobre las barras como sobre las probetas mecanizadas, se llevaron a cabo ensayos de fatiga bajo una sollicitación axial de tracción y carga senoidal de amplitud constante. Los distintos valores de la amplitud

de tensiones se obtuvieron manteniendo fija la tensión mínima y variando la tensión máxima. Para corregir el efecto de la tensión media se tuvo en cuenta la Ley de Walker:

$$\Delta\sigma_{eq} = \sigma_{\max}(1-R)^{A_3} \quad (3)$$

donde R es la relación de tensiones y A_3 es una constante que depende del tipo de material y que en nuestro caso toma los valores de 0.4 para el material laminado en caliente y 0.44 para el deformado en frío [13].

En la figura 7 se representan las curvas S-N, corregidas según la ecuación (3), para una probabilidad de fallo del 50% correspondientes a la barra corrugada en caliente antes de ser sometida a shot peening (D2205c), la barra corrugada sometida a shot peening industrial de 0.13 mmA (D2205c + SP industrial), la probeta mecanizada antes de ser sometida a shot peening (D2205 Sin Corruga) y la misma probeta tras ser sometida a shot peening controlado de intensidad 0.33 mmA. De manera análoga, la misma información se recoge en la figura 8 para el material deformado en frío.

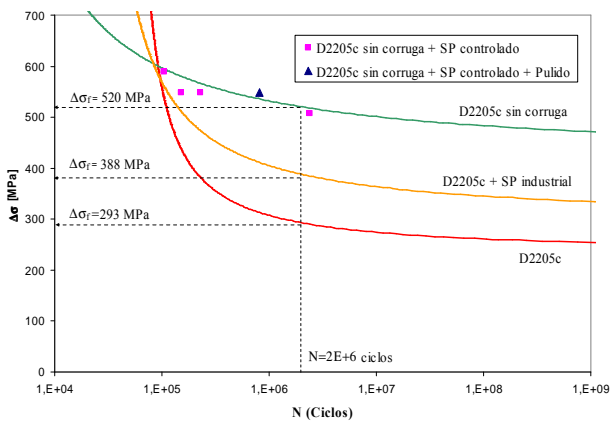


Figura 7. Curvas S-N correspondientes al acero D2205c para una probabilidad de fallo del 50%

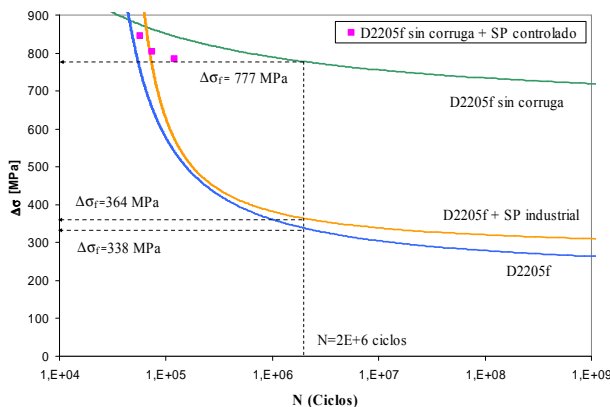


Figura 8. Curvas S-N correspondientes al acero D2205f para una probabilidad de fallo del 50%

Como se puede apreciar, el tratamiento de shot peening industrial produce una mejora en el comportamiento a fatiga de ambos tipos de corrugado, elevando la vida a

fatiga, no sólo en la zona de bajas amplitudes de tensión, sino también en la de elevadas solicitaciones. Esta mejora es debida, por un lado al campo de tensiones residuales de compresión generado, y por otro lado, al hecho de que, en este caso, el shot peening ha mejorado el acabado superficial de la barra, pues ésta, inicialmente, presentaba un acabado muy tosco e irregular.

En la figura 9 puede observarse cómo el aspecto superficial que mostraban las barras antes del tratamiento de shot peening (Fig.9.a) en la que se aprecian perfectamente las estrías en dirección de laminación, ha mejorado notablemente tras la realización de dicho tratamiento (Fig.9.b). No obstante, mientras que el incremento es notable en el caso de las barras corrugadas en caliente, las barras deformadas en frío muestran una mejora mucho más reducida. Este hecho se debe a la menor capacidad de deformación que tiene el material deformado en frío, lo que le hace ser menos sensible a los tratamientos de shot peening.

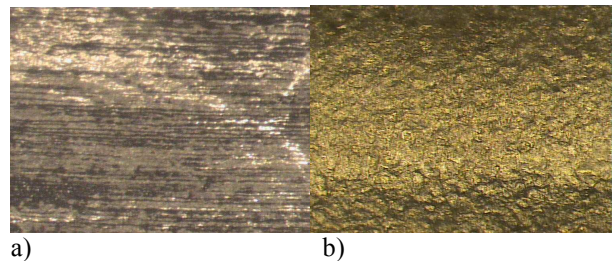


Figura 9. Aspecto superficial de las barras a) antes, b) después del tratamiento de shot peening

Por otro lado, se observa claramente cómo el efecto de las corrugas es determinante en el comportamiento a fatiga de las barras corrugadas de acero inoxidable dúplex, de modo que, mientras la barra corrugada en caliente presenta una vida a fatiga ($\Delta\sigma_f \cdot 2 \cdot 10^6$ ciclos) de 293 MPa, al eliminar las corrugas, la vida a fatiga asciende hasta los 520 MPa. En el caso del material deformado en frío, la mejora de la vida a fatiga es aún más notoria, pasando de 338 MPa a 777 MPa con el simple hecho de eliminar las corrugas.

Sin embargo, cuando se realiza un tratamiento de shot peening más severo y minuciosamente controlado sobre las probetas mecanizadas, el comportamiento a fatiga empeora ligeramente respecto al observado en las mismas probetas que no fueron sometidas a dicho proceso (puntos representados mediante cuadrados). El motivo de este empeoramiento se debe a que, en esta ocasión, al partir de una superficie inicial exenta de defectos, el shot peening empeora el acabado superficial, generando unos niveles de rugosidad que contrarrestan el efecto beneficioso de las tensiones residuales de compresión que se han obtenido, lo que parece estar de acuerdo con las observaciones de varios autores [14, 15].

La figura 10 ilustra este efecto. En la imagen, tomada mediante microscopio electrónico de barrido, se aprecia

claramente el daño generado por el tratamiento de shot peening sobre una probeta de material laminado en caliente a la que se le eliminaron las corrugas (figura 2).

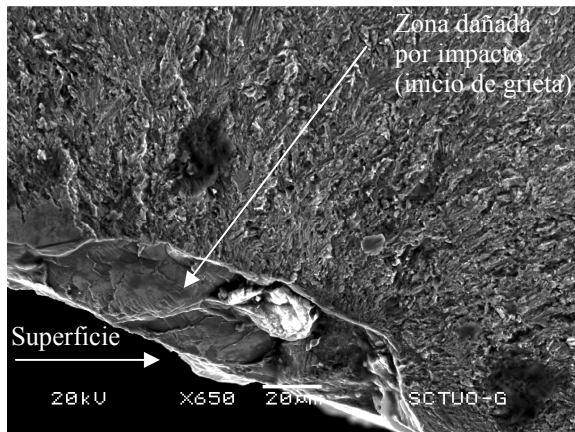


Figura 10. Daño superficial generado sobre la probeta mecanizada sometida a shot peening

Por último, a modo de comprobación, se realizó un ensayo de fatiga sobre una probeta que había sido sometida al tratamiento de shot peening controlado pero cuya superficie había sido pulida posteriormente hasta alcanzar los niveles iniciales de rugosidad (punto representado en la figura 7 por un triángulo). De este modo, se consiguió aislar el efecto de la rugosidad superficial sobre el comportamiento a fatiga. Como era de esperar, mediante este procedimiento se produce una ligera mejora en la vida a fatiga, si bien este escaso incremento hace pensar que los tratamientos de shot peening son más efectivos cuando se llevan a cabo sobre superficies que no presentan un buen acabado superficial.

4. CONCLUSIONES

Los tratamientos de shot peening generan un campo de tensiones residuales de compresión bajo la superficie del elemento tratado, a la vez que modifican su acabado superficial. Dependiendo del acabado superficial inicial, el shot peening puede mejorar o empeorar el comportamiento a fatiga del elemento. Así, en el caso de las barras corrugadas de acero inoxidable dúplex, un tratamiento de shot peening de baja intensidad es suficiente para mejorar el comportamiento a fatiga en un 45% (para los corrugados en caliente) o un 14% (para los corrugados en frío).

Sin embargo, si se eliminan las corrugas y se proporciona al material un buen acabado superficial, un tratamiento de shot peening optimizado, que genera un fuerte campo de tensiones residuales de compresión, no sólo no mejora el comportamiento a fatiga del material, sino que lo empeora ligeramente. Esto es debido a que, en este caso, el efecto adverso del incremento de rugosidad generado por el tratamiento, prevalece sobre el efecto favorable originado por las tensiones residuales de compresión.

5. REFERENCIAS

- [1] H. Castro, C. Rodríguez, F.J. Belzunce "Mechanical behaviour and corrosion resistance of stainless steel cold rolled reinforcing bars" Materials Science Forum (Trans Tech Publications LTD), 1542, 1541-1546 (2003).
- [2] Niku-Lari A., "Shot peening" Proceedings of the 1st International Conference on Shot Peening, Paris, France, 1981, pp. 1-21.
- [3] Clausen R., Stangenberg J. "Roughness of shot peened surfaces-Definition and measurement" Proceedings of the 7th International Conference on Shot Peening, Warsaw, Poland, 1999, pp. 69-77.
- [4] Belzunce F.J. "Aceros y fundiciones: estructuras, transformaciones y aplicaciones" Universidad de Oviedo, 2001.
- [5] Real E. "Influencia de la tensión media y del proceso de fabricación en el comportamiento a fatiga de barras corrugadas de acero inoxidable dúplex" Tesis Doctoral. Universidad de Oviedo. Junio 2007.
- [6] SAE J444 "Cast shot and grit size specifications for peening and cleaning", May 1993.
- [7] SAE J442 "Test strip, holder and gage for shot peening", January 1995.
- [8] SAE J443 "Procedures for using standard shot peening test strip", January 1984.
- [9] SAE HS-784-03 "Residual Stress Measurement by X-Ray Diffraction", February 2003
- [10] Castillo, E., Fernández Canteli, A. Esslinger, V.Thürlimann, B. "Statistical Model for Fatigue Analysis of Wires, Strands and Cables" Zürich, May, 1985.
- [11] Sanjurjo P., Rodríguez C., Belzunce J., Pariente I., Montero R. "Influencia del proceso de shot peening sobre el comportamiento mecánico de aceros inoxidables dúplex" CIBIM09, Las Palmas de Gran Canaria, 2009.
- [12] Fernández Pariente I., Gaugliano M. "About the role of residual stresses and surface work hardening on fatigue ΔK_{th} of a nitrided and shot peened low-alloy steel" Surface and Coatings Technology, 202, pp. 3072-3080, 2008.
- [13] Real E., Rodríguez C., Belzunce F.J., Sanjurjo P., Canteli A.F., Pariente I.F. "Fatigue behaviour of duplex stainless steel reinforcing bars subjected to shot peening" Fatigue and Fracture of engineering materials and structures, Vol. 32, 567-572
- [14] Bannantiene J.A. "Fundamentals of metal fatigue analysis" Prentice-Hall, 1990.
- [15] Forrest P. G. "Fatigue of metals" Pergamon Press Ltd., London 1962.

AGRADECIMIENTOS

Los autores desean expresar su agradecimiento al Ministerio de Fomento por la financiación recibida a través del proyecto C60/06. Asimismo, P. Sanjurjo agradece al Gobierno del Principado de Asturias la ayuda recibida a través del proyecto COF07-23, sin la cual no habría podido realizar este trabajo.

EXPERIMENTAL RESULTS IN FRETTING FATIGUE WITH SHOT AND LASER PEENED SPECIMENS

J. Vázquez, C. Navarro, J. Domínguez

Departamento de Ingeniería Mecánica y de los Materiales,
Universidad de Sevilla, Camino de los Descubrimientos s/n, 41092, Sevilla, España.
Tel. +34 954481365
E-mail: jesusvaleo@esi.us.es

RESUMEN

El objetivo de este artículo es mostrar de los tratamientos de shot y laser peening en la fatiga por fretting de un aluminio Al 7075-T651. Estos tratamientos introducen un campo de tensiones residuales de compresión en las cercanías de la superficie, zona donde aparecen altas tensiones como consecuencia del contacto. Para ello, se han realizado una serie de ensayos de fatiga por fretting sobre probetas a las cuales se les han aplicado estos tratamientos. Para completar este estudio, se han medido en cada uno de los diferentes tratamientos, el campo de tensiones residuales, la relajación de las tensiones residuales por la acción de las cargas cíclicas, el coeficiente de fricción, la rugosidad superficial y la dureza del material.

ABSTRACT

The objective of this paper is to experimentally measure the effect of laser and shot peening on fretting fatigue life in the aluminium alloy 7075-T651. These surface treatments should have a highly beneficial effect on life since they introduce a field of compressive residual stresses close to the surface of the peened specimens, where the high contact stress concentrations appear. In order to achieve this goal, some specimens previously treated with shot and laser peening were tested under fretting fatigue conditions. To complete this study, the residual stress fields, residual stress relaxation caused by cyclic loading, roughness, friction coefficient and hardness was measured in every test specimen.

KEY WORDS: Fretting fatigue tests, residual stresses, stress relaxation, shot peening, laser peening.

1. INTRODUCTION

La fatiga por fretting es un fenómeno que se produce en muchos componentes en servicio tales como uniones remachadas y atornilladas, uniones eje-cubo, cables metálicos, etc. [6]. Este tipo de fallo aparece en sistemas mecánicos donde las cargas de servicio causan movimientos cíclicos relativos de muy pequeña amplitud entre componentes que se encuentran presionados entre sí. Debido a las fuerzas de fricción, estos desplazamientos desarrollan unas tensiones cíclicas en las zonas en contacto las cuales dan lugar a la formación de grietas. Estas grietas, y por efecto de la tensión global presente en el sistema, pueden propagarse hasta que se produzca el fallo componte.

Para reducir el efecto negativo de este fenómeno, se han empleado diferentes estrategias: shot peening, laser peening, recubrimientos superficiales para reducir el coeficiente de rozamiento, tratamientos termoquímicos para mejorar las propiedades tribológicas de las superficies, uso de lubricantes, mejoras en el diseño, etc. [2]. De entre todos estos, cabe destacar los tratamientos de shot y laser peening, cuya principal característica es la de introducir un campo de tensiones residuales de compresión, que mejora en gran medida la resistencia a la fatiga por fretting de los componentes [3].

Con objeto de cuantificar el beneficio que producen los tratamientos de shot y laser peening en la fatiga por fretting, se han realizado una serie de ensayos con diferentes tratamientos y niveles de carga. Además, para entender el comportamiento frente a la fatiga por fretting observado en los ensayos realizados, se han analizado diferentes aspectos de cada uno de los tratamientos empleados, tales como: campo de tensiones residuales, rugosidad superficial, cambios en la dureza del material, coeficiente de rozamiento y relajación de las tensiones residuales.

2. MONTAJE EXPERIMENTAL

El útil de ensayos utilizado se muestra de forma esquemática en la Figura 1. Este conjunto se ha diseñado y construido para que funcione en conjunto con un equipo servohidráulico de ensayos uniaxiales. Este tipo de útil, el cual es muy similar al descrito por Wittkowsky *et al.* [4], ha sido desarrollado en el Departamento de Ingeniería Mecánica y de los Materiales de la Universidad de Sevilla [5].

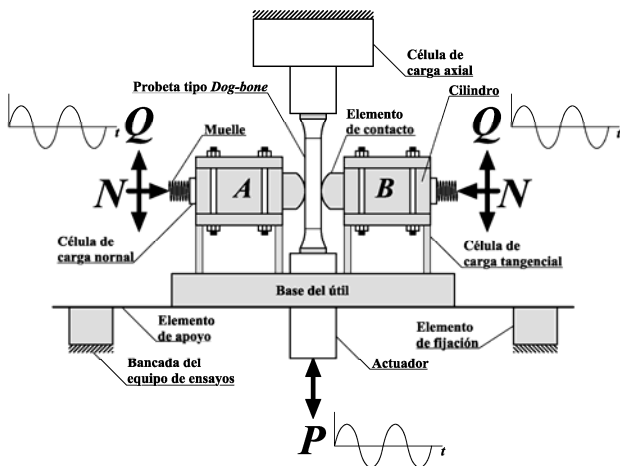


Figura 1. Esquema del útil de ensayos utilizado

Se ha utilizado un contacto esfera-plano, ya que desde el punto de vista experimental, tiene la ventaja de no presentar problemas de alineamiento y permite localizar más fácilmente el punto de iniciación de grieta. El tipo de probetas que se ha utilizado en la totalidad de los ensayos es de las llamadas *dog-bone*. En la Figura 2 y 3 se muestran los elementos de contacto y el tipo de probetas utilizadas respectivamente, donde todas las dimensiones están acotadas en milímetros.

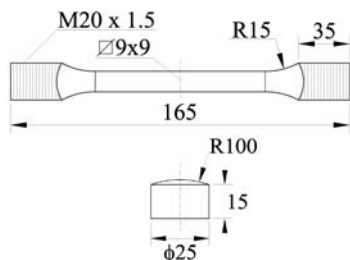


Figura 2. Probetas y elemento de contacto utilizados en los ensayos

3. MATERIAL Y TRATAMIENTOS

Tanto las probetas como los elementos de contacto han sido fabricados a partir de una barra de 25 mm de Al 7075-T651 fabricada por ALCOA. Las propiedades mecánicas de tracción del Al 7075-T651 han sido obtenida mediante una serie de ensayos, que se han realizado siguiendo el procedimiento indicado en la norma ASTM E8M-04 [6]. La velocidad de crecimiento de grieta se ha obtenido mediante la norma ASTM E647-05. En la Tabla 1 se resumen las propiedades mecánicas obtenidas según la norma anterior, excepto el coeficiente de Poisson, los parámetros de la curva ϵ -N y las constantes de Ramberg-Osgood para la curva de tensión-deformación cíclica, los cuales han sido tomados de la bibliografía [7].

Tabla 1. Propiedades mecánicas Al 7075-T651

Propiedades estáticas		
Módulo de Young	E	71 GPa
Coef. Poisson	ν	0.33
Límite elástico	σ_y	503 MPa
Límite de rotura	σ_u	572 MPa

Propiedades cíclicas		
Límite elástico cíclico	σ_y'	541 MPa
Coef. endurecimiento	K'	694 MPa
Exp. endurec.	n'	0.04
Coef. resistencia a fatiga	σ_f'	1231 MPa
Coef. ductilidad a fatiga	ϵ_f'	0.263
Exp. resistencia a fatiga	b	-0.122
Exp. ductilidad a fatiga	c	-0.806
Propiedades de crecimiento R=0		
Coeficiente	C	$4.83 \cdot 10^{-11}$
Exponente	n	3.517

En lo que se refiere a los tratamientos empleados en los ensayos, se han utilizado dos tipos de shot peening y dos tipos de laser peening.

El primer tipo de shot peening (shot peening tipo A o SP A) utilizado en los ensayos tiene la designación, según la norma AMS-S-2430, de *BA600N/F20-24A/100% Peenscan*. Este shot peening consiste en sólo bombardeo con bolas de acero, y una intensidad media, y por ello se considera un tratamiento de shot peening típico, por lo que es ampliamente utilizado en la industria aeronáutica. El segundo tipo de shot peening utilizado (shot peening tipo B o SP B) tiene la designación, según la norma anterior, *BA800N/F25-35%/100%+Glass bead peening*. En este caso el tratamiento consiste en el doble shot peening, el primero es similar al realizado con el tipo A, pero posteriormente se aplica otro con bolas de vidrio, lo que mejora la rugosidad superficial, incrementa las tensiones de compresión introducidas y limpia la superficie bombardeada de posibles restos férricos depositados en el primer shot peening aplicado.

En cuanto a los ensayos realizados con probetas tratadas con laser peening, en el primer tipo la intensidad del haz de rayos láser que incide sobre la superficie del material es de 1GW/cm^2 . Esta intensidad, se consigue incidiendo sobre un área de $4.72\text{cm} \times 4.72\text{cm}$ un pulso con una energía de 4J durante un tiempo de exposición de 8ns. Este proceso de exposición se realiza dos veces sobre todas las zonas tratadas. Para proteger la superficie en cada una de las exposiciones, se ha colocado en la superficie de aplicación un recubrimiento adhesivo metálico, que se retira una vez terminado el proceso. En el segundo tipo de laser peening utilizado, la intensidad del haz de rayos láser que incide en el material en este caso es de 2GW/cm^2 . En este caso el proceso se realiza exponiendo una zona de $5.55\text{cm} \times 5.55\text{cm}$ a un pulso de 11J durante 18ns, y al igual que en el caso anterior, también se realiza dos exposiciones sobre las zonas tratadas. De forma similar, en este tratamiento también se ha colocado un recubrimiento protector.

4. RESULTADOS EXPERIMENTALES

4.1 Tensiones residuales

Para entender el comportamiento de las probetas tratadas en condiciones de fretting, se ha medido las

tensiones residuales de cada uno de los tratamientos mediante la técnica del agujero ciego [8]. El método empleado para obtener la distribución de tensiones residuales a partir de la evolución de las deformaciones con la profundidad del taladro ha sido el método integral [9],[10]. Las distribuciones de tensiones residuales mostradas en las siguientes secciones, se han obtenido realizando la media de dos diferentes medidas. La figura 3 muestra las distribuciones de tensiones residuales, en la dirección longitudinal de las probetas, obtenidas en cada uno de los tratamientos. En esta figura se observa las principales diferencias entre los tratamientos de shot y laser peening. En primer lugar, cabe destacar cómo ambos tratamientos de laser peening producen un campo de tensiones residuales con valores significativos hasta una profundidad de 1mm aproximadamente. Mientras tanto, los dos tratamientos analizados de shot peening alcanzan valores mayores de las tensiones, respecto a las obtenidas para el laser peening, pero en este caso la zona con valores importantes se encuentra entre las 50 y las 400µm.

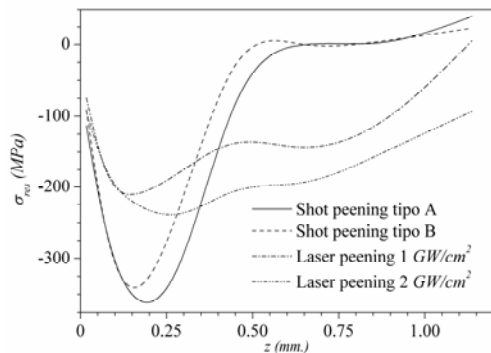


Figura 3. Tensiones residuales de los diferentes tratamientos en la dirección longitudinal

4.1 Rugosidad superficial y coeficiente de rozamiento

En el caso de la fatiga por fretting, es conocido el efecto beneficioso que se produce al incrementar la rugosidad de las superficies en contacto [11]. Este incremento de la rugosidad, es similar al alivio de tensiones a causa de una ranura, lo que puede provocar un aumento o incluso desaparición de la fase de iniciación [11]. Otro parámetro importante en la fatiga por fretting es el coeficiente de rozamiento μ entre las superficies en contacto [12]. La tabla 2 muestra los valores medios de las rugosidades superficiales y del coeficiente de rozamiento obtenidos para cada uno de los tratamientos empleados, así como de las probetas sin tratar.

Tabla 2. Coeficiente de rozamiento y rugosidad superficial

	μ	Rug. sup. (μm)		
		R_a	R_z	R_t
Sin tratar	1.20	0.5	2.9	2.9
Shot peening A	1.13	6.4	39.9	57.0
Shot peening B	1.14	5.8	35.4	48.9
Laser 1GW/cm ²	1.18	1.1	8.5	10.1
Laser 2GW/cm ²	1.19	1.4	11.7	13.5

En esta tabla se ve cómo ambos tratamientos de laser peening presentan un coeficiente de rozamiento similar y una rugosidad algo mayor que la del material sin tratar. Por el contrario, en el material tratado con shot peening, se observa un aumento considerable de la rugosidad superficial, así como un ligero descenso del coeficiente de rozamiento.

4.2 Dureza Vickers

Es sabido que los tratamiento de shot y laser peening producen cambios en las durezas de los materiales en los que se aplican [13], y como consecuencia de ello también se modifica en el comportamiento a fatiga. Por este motivo, es importante ver en qué medida ha sido modificada la dureza del material por efecto de los diferentes tratamientos. La figura 4 muestra la variación con respecto a la profundidad de la dureza Vickers HV 02 medida para cada uno de los tratamientos. También se muestra la dureza del material virgen a modo de referencia.

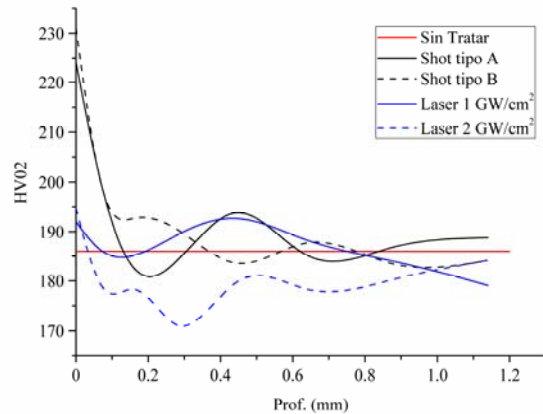


Figura 4. Variación de las durezas de los diferentes tratamientos con la profundidad

Lo primero que se observa en esta figura, es cómo todos los tratamientos producen un endurecimiento, más o menos apreciable, en las zonas cercanas a la superficie, siendo este endurecimiento bastante mayor en el caso de los tratamientos de shot peening. Comparando el endurecimiento producido por el shot tipo A con el del shot tipo B, se ve que ambos son similares, esto es, el valor máximo de la dureza se produce en la superficie y decae conforme aumenta la profundidad, hasta llegar a un determinado punto donde los valores oscilan en torno al valor de la dureza del material sin tratar. Estas medidas obtenidas con los tratamientos de shot peening, indican que las propiedades mecánicas del material, por lo menos en las cercanías de la superficie, pueden haber mejorado. En lo que respecta a los tratamientos de laser peening, el comportamiento difiere de una a otra intensidad. En el caso del laser de 1GW/cm², se produce un pequeño aumento del valor de la dureza en la superficie y posteriormente esta fluctúa alrededor del valor de material no tratado, por lo que se puede pensar que en este tipo de tratamiento no se produce un cambio significativo de la dureza, y por lo tanto, tampoco de las

propiedades mecánicas. En lo que respecta al laser de 2GW/cm², en la superficie se produce un aumento similar al del laser de 1GW/cm², pero al aumentar la profundidad se produce una apreciable disminución del valor de la dureza, de lo que se deriva que en esta zona las propiedades mecánicas del material han podido empeorar.

4.3 Ensayos realizados

Se han ensayado mediante el útil descrito anteriormente diversas probetas con los diferentes tipos de shot y laser peening. Estos ensayos se han realizado con cinco combinaciones diferentes de carga. La tabla 3 muestra los parámetros de carga utilizados junto con la vida a fatiga por fretting en ciclos N_f para cada uno de los ensayos. Los parámetros mostrados son la tensión axial σ (MPa) creada en la probeta por la carga axial P , la carga normal aplicada N (N) y las cargas tangenciales medidas con las células tangenciales colocadas en A y B, Q_a (N) y Q_b (N).

Tabla 3. Vida de los ensayos realizados

Trat.	Tipo ensayo	σ	Q_a	Q_b	N	N_f
SP A	90/1100/1200	90.7	1097	1069	1200	546671
SP A	100/1100/1200	99.3	1010	1075	1200	330796
SP A	110/900/1000	112.0	918	725	1000	1526128*
SP A	125/900/1000	123.8	868	946	1000	947249*
SP A	125/900/1000	124.6	902	830	1000	124677
SP A	125/600/650	124.1	597	530	650	1206145*
SP A	125/600/650	126.2	582	611	650	660564*
SP B	90/1100/1200	91.3	1107	1049	1200	3062815*
SP B	100/1100/1200	102.2	1106	1048	1200	1397699*
SP B	100/1100/1200	100.6	1108	1080	1200	1558286*
SP B	110/900/1000	106.2	915	894	1000	1483296*
SP B	125/900/1000	125.5	861	907	1000	840626*
SP B	125/600/650	126.3	587	596	650	1721474*
SP B	125/600/650	123.2	557	609	650	1089263*
LP 1GW	90/1100/1200	92.1	1106	1096	1200	222921
LP 1GW	100/1100/1200	97.9	1097	1057	1200	226254
LP 1GW	110/900/1000	108.0	802	867	1000	142311
LP 1GW	125/900/1000	126.3	785	860	1000	249289
LP 1GW	125/900/1000	127.5	895	910	1000	160510
LP 1GW	125/600/650	124.6	571	597	650	213187
LP 1GW	125/600/650	122.8	599	589	650	211075
LP 2GW	90/1100/1200	92.1	1099	1111	1200	231045
LP 2GW	100/1100/1200	98.3	1096	1070	1200	190805
LP 2GW	110/900/1000	111.6	849	923	1000	162137
LP 2GW	110/900/1000	108.5	870	895	1000	2437816*
LP 2GW	125/900/1000	124.4	980	1005	1000	272231
LP 2GW	125/600/650	125.3	566	599	650	284193

* Ensayos donde el fallo se ha producido fuera de la zona afectada por fretting

También se realizaron otros ensayos con las mismas cargas y tratamientos, pero en este caso modificando el acabado superficial, con el objetivo de cuantificar el efecto de la rugosidad superficial en la vida a fatiga por fretting. En estos todos estos casos, después del shot o laser peening, se pulieron las probetas, hasta obtener un acabado superficial similar al de las probetas sin tratar. Con ello se pretende tener un contacto esfera-plano más parecido al teórico de superficies planas y lisas. La tabla 4 muestra las rugosidades obtenidas en cada caso,

después del pulido. En la tabla 5 se muestran los resultados de los ensayos realizados con estas probetas.

Tabla 4. Rugosidades superficiales de los diferentes tratamientos después del pulido

	μ	Rug. sup. (μm)		
		R_a	R_z	R_t
Shot peening A	1.18	0.2	1.4	1.9
Shot peening B	1.18	0.2	1.7	2.7
Laser 1GW/cm ²	1.21	0.2	1.5	1.9
Laser 2GW/cm ²	1.19	0.2	1.5	2.3

Tabla 5. Vida de los ensayos con la rugosidad modificada

Trat.	Tipo ensayo	σ	Q_a	Q_b	N	N_f
SP A	90/1100/1200	90.6	1072	1090	1200	283522
SP A	100/1100/1200	102.1	1099	1099	1200	191755
SP A	110/900/1000	108.6	906	903	1000	238394
SP A	125/900/1000	123.7	859	900	1000	196035
SP A	125/600/650	123.9	562	602	650	588006*
SP B	90/1100/1200	89.9	1047	1086	1200	630914
SP B	100/1100/1200	101.1	1097	1103	1200	282083
SP B	110/900/1000	112.0	900	906	1000	1236088*
SP B	125/900/1000	122.8	571	602	1000	201385
SP B	125/600/650	125.3	888	895	650	1056374*
LP 1GW	90/1100/1200	92.1	1045	1088	1200	159956
LP 1GW	100/1100/1200	100.3	1095	1107	1200	142113
LP 1GW	110/900/1000	111.4	901	899	1000	133337
LP 1GW	125/900/1000	126.4	896	894	1000	90418
LP 1GW	125/600/650	126.1	580	605	650	148956
LP 2GW	90/1100/1200	88.2	1030	1097	1200	491557
LP 2GW	100/1100/1200	101.2	1101	1099	1200	201975
LP 2GW	110/900/1000	113.2	901	897	1000	170656
LP 2GW	125/900/1000	126.6	878	900	1000	169456
LP 2GW	125/600/650	124.7	570	599	650	213555

* Ensayos donde el fallo se ha producido fuera de la zona afectada por fretting

En esta nueva situación se observan una serie de diferencias con respecto a la situación anterior. La primera es que únicamente en tres de las probetas ensayadas se ha producido el fallo fuera la zona de contacto, pero conservando la similitud con la situación anterior de que este tipo de rotura sólo se da en las probetas tratadas con shot peening, y que además el shot peening tipo B sigue siendo el que presenta un mayor número de fallos de este tipo. La segunda diferencia notable es la disminución general de la vida a fretting fatiga de las probetas con shot peening, pues ensayos que antes del pulido presentaban una fractura por fatiga simple, ahora lo tienen por fretting. Sin embargo, no hay una diferencia apreciable en la vida de una serie de ensayos realizados sobre probetas tratadas con shot peening, que con este nuevo acabado superficial también presentan una rotura fuera de la zona afectada por fretting.

Por último para estudiar cómo afectan únicamente las tensiones residuales a la fatiga por fretting, se han repetido todos los diferentes tipos de ensayos, pero en esta ocasión con probetas sin tratar. Los resultados de estos ensayos se pueden ver en la tabla 6.

Tabla 6. Vida de los ensayos realizados con probetas sin tratar

Tipo ensayo	σ	Q_a	Q_b	N	N_f
90/1100/1200	89.6	1093	1097	1200	55759
100/1100/1200	100.5	1052	1092	1200	51787
110/900/1000	112.4	880	894	1000	59793
125/900/1000	123.6	857	914	1000	65614
125/600/650	125.3	603	605	650	52499
125/600/650	126.2	562	569	650	47379

A modo de resumen, en la figura 5 se muestran las vidas resultantes de todos los ensayos realizados. Lo primero que se aprecia observando los resultados mostrados en la figura 5 es que, en mayor o menor grado, todos los tratamientos con uno u otro acabado superficial producen un incremento significativo de la vida. Este incremento de la vida en general es mayor para aquellas probetas cuya rugosidad superficial no ha sido modificada, y dentro de estas las que tienen el tratamiento de shot peening tipo B son las que presentan una vida mayor.

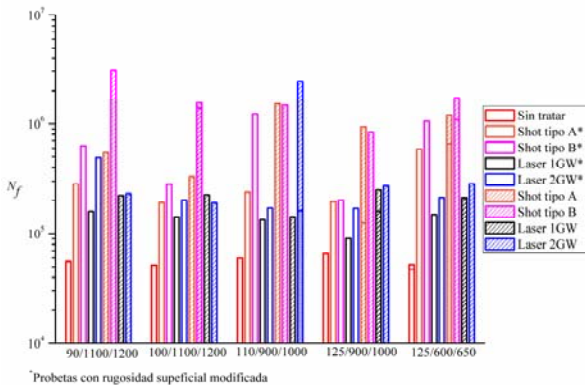


Figura 5. Comparación de la vida a fatiga por fretting de los diferentes tipos de ensayos realizados

4.4 Relajación de las tensiones residuales

Un aspecto importante de las tensiones residuales es su estabilidad. Es sabido que cargas cíclicas, incluso aquellas que producen niveles bajos de tensiones, y cargas estáticas que producen tensiones superiores al límite de fluencia, tienen como consecuencia una relajación del campo de tensiones residuales [14]. Con el objetivo de cuantificar la relajación del campo de tensiones residuales en los ensayos llevados a cabo, se han realizado una serie de medidas sobre probetas que han sido cicladas durante 20.000 ciclos, y que posteriormente han sido retiradas del útil de ensayos para medir las tensiones residuales resultantes. Las tensiones han sido medidas entre el borde de la zona de contacto y la zona de adhesión, tal y como se muestra en la figura 6.

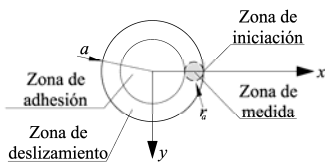


Figura 6. Zona de medida de las tensiones

Se han utilizado dos niveles de carga, correspondientes con dos de los tipos de ensayos realizados, estos son: $\sigma=125\text{MPa}$, $Q=900\text{N}$, $N=1000\text{N}$ (tipo I) y $\sigma=125\text{MPa}$, $Q=600\text{N}$, $N=650\text{N}$ (tipo II). En las figuras 7, 8, 9 y 10 se muestran las variaciones del campo de tensiones residuales que sufren cada uno de los diferentes tratamientos, para los dos tipos de cargas utilizados. Comentar de nuevo que al igual que en la sección anterior, cada una de las distribuciones de tensiones residuales mostradas a continuación se han obtenido realizando la media de dos medidas.

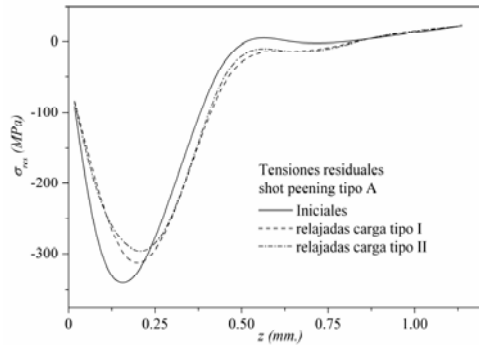


Figura 7. Tensiones residuales iniciales y relajadas para el shot peening tipo A

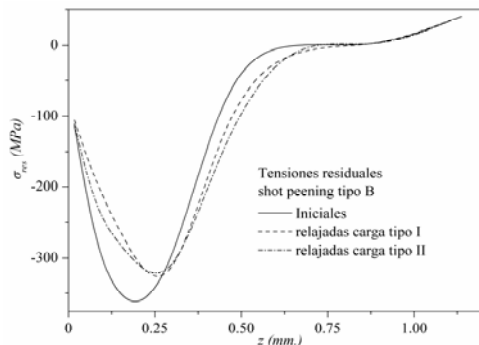


Figura 8. Tensiones residuales iniciales y relajadas para el shot peening tipo B

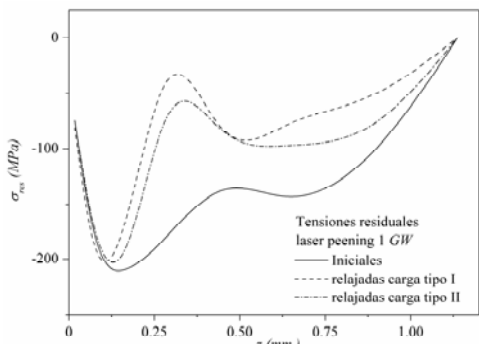


Figura 9. Tensiones residuales iniciales y relajadas para el laser peening 1GW/cm²

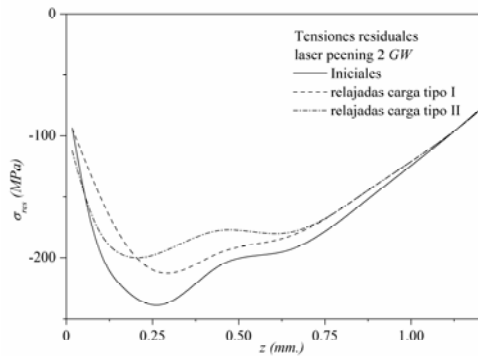


Figura 10. Tensiones residuales iniciales y relajadas para el laser peening $2\text{GW}/\text{cm}^2$

Mencionar que la relajación medida del campo de tensiones residuales corresponde en parte a una relajación debida a cargas estáticas que producen flujo plástico en los primeros ciclos de carga, y por otra parte a la acción continuada de las cargas cíclicas a las que se encuentra sometida la zona afectada por fretting.

En resumen, de los cuatro tratamientos analizados, los de shot peening en general sufren una menor relajación que los de laser peening. De todos ellos, el laser peening de $1\text{GW}/\text{cm}^2$ es el que desarrolla una mayor relajación de las tensiones residuales. También se ve como la relajación en ambos tratamiento de shot es bastante similar, aunque un poco mayor en el caso del shot peening B, al contrario de lo que ocurre con las de laser peening donde si hay diferencias notables entre las intensidades de $1\text{GW}/\text{cm}^2$ y $2\text{GW}/\text{cm}^2$. Así mismo, cabe destacar como en la totalidad de los tratamientos analizados la relajación en zonas cercanas a la superficie es despreciable.

5. CONCLUSIONES

La primera conclusión es el efecto beneficioso de los tratamientos de shot peening, frente a la fatiga por fretting. Este efecto, es bastante más notable para los ensayos que se han realizado con probetas cuya rugosidad es la original, particularmente para las probetas tratadas con shot peening tipo A y B. Los ensayos realizados muestran el importante efecto que tiene la rugosidad superficial en la vida, siendo muy notable en los tratamientos de shot peening. En estos casos, en las probetas con acabado superficial modificado, se produce una disminución de la vida, en ambos tipos de shot peening, cercano a unas 3 veces con respecto de las probetas ensayadas con la rugosidad original. Otro efecto notable en todos los tratamientos analizados, es la relajación que se produce en el campo de tensiones residuales después de 20.000 ciclos. Este efecto, es sobre todo muy importante en los tratamientos de laser peening, destacando la relajación de tensiones sufrida por el laser de $1\text{GW}/\text{cm}^2$ de intensidad. Merece la pena destacar que aunque la relajación sufrida por el laser de $1\text{GW}/\text{cm}^2$ es mayor que la del laser de $2\text{GW}/\text{cm}^2$, este fenómeno no se ve reflejado en las vidas de los ensayos realizados, ya que ambas intensidades ofrecen vidas similares. Por último, mediante las

medidas de dureza Vickers realizadas, se muestra cómo los tratamientos de shot y laser peening cambian la microestructura del material. En todos los tratamientos analizados se observa un endurecimiento del material cerca de la superficie, siendo este bastante importante para ambos tratamientos de shot peening. También se observa cómo para el laser de $2\text{GW}/\text{cm}^2$ se produce una disminución apreciable de la dureza Vickers a partir de unas $100\mu\text{m}$ de profundidad. Este fenómeno quizás explique, en cierto modo, por qué este tratamiento no supone una mejora sustancial con respecto al laser de $1\text{GW}/\text{cm}^2$, a pesar de producir el laser de $2\text{GW}/\text{cm}^2$ un campo de tensiones residuales mayor y más estable que el creado por el laser de $1\text{GW}/\text{cm}^2$.

REFERENCIAS

- [1] Waterhouse, R. B. and Lindley, T. C. ESIS Publication 18. MEP, London, 1994.
- [2] Domínguez, J. (2000) Algunas Consideraciones sobre la Fatiga por Fretting y sus Paliativos, *Anales de la Mecánica de la Fractura*, **17**, pp. 89-102.
- [3] Kevin, K.,L. ,Michael, R., H. (2009) The effects of laser peening and shot peening on fretting fatigue in Ti-6Al-4V coupons, *T. Int.*, **42**, pp. 1250-1262.
- [4] Wittkowsky, B.U., Birch, P.R, Domínguez, J. and Suresh, S. (1999) An Apparatus for Quantitative Fretting-Fatigue Testing, *Fat. Fract Eng. Mat. Struct.*, **22**, pp. 307-320.
- [5] Muñoz, S. (2007) Estimación de Vida a Fatiga por Fretting; Aplicación a Componentes Recubiertos, Tesis Doctoral, Universidad de Sevilla.
- [6] Standard Test Methods for Tension Testing of Metallic Materials (2004) ASTM Int., 24 pp.
- [7] Boller, C. and Seeger, T. (1998) Materials Data for Cyclic Loading, Elsevier Publishing Company.
- [8] Determining Residual Stresses by the Hole-Drilling Strain-Gage Method, ASTM Standard E 837.
- [9] Schajer, G.S. (1998) Measurement of Non-uniform Residual Stresses Using the Hole Drilling Method, part I, *J. Eng. Mater. Technol.*, **110**, pp. 338-343.
- [10] Schajer, G.S. (1998) Measurement of Non-uniform Residual Stresses Using the Hole Drilling Method, part II, *J. Eng. Mater. Tech.*, **110**, pp. 344-349.
- [11] Waterhouse, R. B. and Trowsdale, A. J. (1992) Residual Stress and Surface Roughness in Fretting Fatigue, *J. Phys. D*, **25**, pp. A236-A237.
- [12] Muñoz, S., Navarro, C. y Domínguez, J. (2004) Influencia del Coeficiente de Rozamiento en Fretting, *Anales de Mecánica de la Fractura*, **21**, pp. 197-202.
- [13] Peyre, P., Fabbro, R., Merrien, P. and Lieurade, H.P. (1996) Laser Shock Processing of Aluminum Alloys. Application to High Cycle Fatigue Behaviour, *Mat. Sci. Eng.*, **A210**, pp. 102-113.
- [14] Kodama, S. (1972) The Behavior of Residual Stress During Fatigue Stress Cycles, *Procs. Int. Conf. Mech. Behavior of Metals II, Soc. Mat. Sci.*, **2**, pp. 111-118.

PREDICCIÓN DE VIDA A FATIGA POR FRETTING INCLUYENDO TENSIONES RESIDUALES**J. Vázquez, C. Navarro, J. Domínguez**

Departamento de Ingeniería Mecánica y de los Materiales,
 Universidad de Sevilla, Camino de los Descubrimientos s/n, 41092, Sevilla, España.
 Tel. +34 954481365
 E-mail: cnp@us.es

RESUMEN

Este artículo analiza el comportamiento de piezas sometidas a laser y shot peening ante ensayos de fatiga por fretting. En estos ensayos el material era aluminio Al 7075-T651 y los elementos de contacto tenían forma esférica. La vida a fatiga por fretting se estima teniendo en cuenta las tensiones residuales inducidas por los tratamientos de laser y shotpeening y su relajación durante el ensayo. Estas tensiones residuales se midieron y se introdujeron en el modelo como tensiones dependientes del número de ciclos. Dos tipos de relajación fueron usadas: plástica y relajación debida a la fatiga. El modelo para estimar la vida la calcula como la combinación de la vida empleada en la fase de iniciación más la vida asociada a la fase de propagación. La longitud de transición no se fija a priori sino que depende de las condiciones particulares de carga, geometría y propiedades del material del problema analizado. Las estimaciones de vida se comparan con los resultados experimentales con el objeto de entender el efecto de la relajación de tensiones sobre la vida. También se mostrará qué tratamiento es más efectivo a la hora de incrementar la vida a fatiga por fretting y por qué.

ABSTRACT

This paper analyzes the behaviour of laser and shot-peened specimens subjected to fretting fatigue tests. The material was aluminium Al 7075-T651 and the contact pads had a spherical geometry. Fretting fatigue life is estimated taking into account the residual stress induced by the laser and shot-peening treatments and its relaxation during the test. This residual stress was measured and introduced in the model as cycle dependent stresses. Two types of relaxation were introduced: plastic and fatigue relaxation. The model to estimate life predicts the total life as a combination of the life spent during the initiation phase and the life associated with the propagation phase. The transition length is not previously fixed, but it depends on the particular load conditions, geometry and material properties of the analyzed problem. All these life estimations are compared to the experimental results in order to understand the effect of stress relaxation on life. Also, it will be shown what kind of treatment is more effective on increasing fretting life and why.

KEY WORDS: Fretting fatigue, residual stresses, stress relaxation, shot peening, laser peening, life prediction model.

1. INTRODUCCIÓN

La fatiga por fretting puede aparecer cuando dos elementos entran en contacto y hay fricción entre ellos como consecuencia de las fuerzas aplicadas. Este fenómeno puede aparecer en prácticamente cualquier máquina o estructura, aunque no es siempre la causa final de rotura [1]. El efecto es la aparición de una concentración de tensiones en la zona de contacto y la degradación de la superficie que provoca una iniciación de grietas más temprana.

Hay muchos parámetros que afectan a la fatiga por fretting [2], y controlando éstos se puede ejercer una influencia en su comportamiento. Uno de estos parámetros es la tensión residual que puede aparecer en una pieza por numerosos motivos. Dependiendo del signo de estas tensiones su efecto puede ser perjudicial o beneficioso. Algunos tratamientos, como el laser o shot peening, introducen tensiones residuales de

compresión que mejoran la vida a fatiga. Por lo tanto también se pueden aplicar a piezas sometidas a fatiga por fretting, incrementando su resistencia.

En el análisis de la vida a fatiga, y en concreto también en la fatiga por fretting, se suelen distinguir dos fases: la iniciación de grietas y su posterior crecimiento hasta la rotura. Diferentes modelos se han propuesto para estimar la vida combinando estas fases. En algunos casos la separación entre la iniciación y la propagación se hace de forma arbitraria. En este trabajo se empleará un modelo donde la longitud de grieta de transición no se fija previamente sino que depende de las condiciones particulares de carga, geometría y propiedades del material del problema analizado [3], [4]. De esta forma este modelo puede aplicarse fácilmente a distintas situaciones sin tener que ser modificado.

Este artículo desarrolla un modelo para la predicción de la vida a fatiga por fretting donde el efecto de las

tensiones residuales también está incluido. Este modelo se aplica a una serie de este tipo de ensayos donde las probetas han sido tratadas previamente con laser y shot peening [5].

2. ENSAYOS Y TENSIONES RESIDUALES

Los ensayos de fatiga por fretting se realizaron sobre una aleación de aluminio 7075-T651, cuyas propiedades se muestran en [5]. El esquema del ensayo se muestra en la figura 1 y es explicado con más detalle en [5]. La fuerza normal, N , es constante y las fuerzas axial, P , y tangencial, Q , variables. En estos ensayos los elementos de contacto eran esféricos con un radio de 100mm.

Las tensiones residuales debidas a los tratamientos de shot y laser peening fueron medidas mediante la técnica del agujero ciego e introducidas en el modelo como una tensión media dependiente del número de ciclos. La variación de las tensiones residuales en función del número de ciclos, es decir, su relajación, es debida al menos a dos factores: deformación plástica y relajación debida a la fatiga. Las tensiones son usualmente altas cerca de la superficie, por lo tanto las tensiones residuales de compresión inducen una plastificación rebajando el efecto beneficioso del laser y shot peening. Por otro lado, incluso sin plastificación sigue habiendo una relajación de tensiones residuales debido a la fatiga [6]. La distribución de tensiones residuales iniciales así como las relajadas después de 20.000 ciclos de carga se pueden ver en [5].

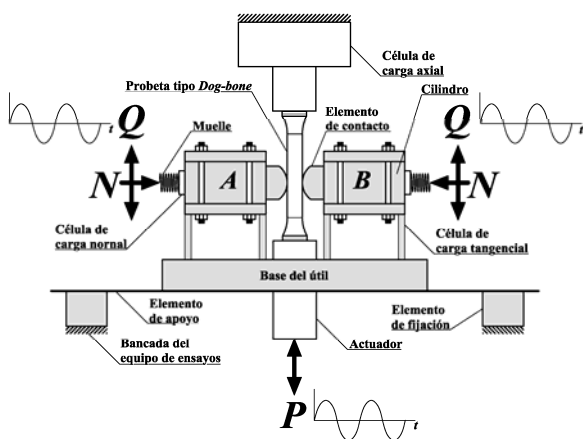


Figura 1. Esquema del útil de ensayos utilizado

3. MODELO

El modelo que se ha utilizado para predecir la vida de las probetas ensayadas era similar al desarrollado por Chen [7], pero con algunas modificaciones. Estas modificaciones se incorporan para introducir, tanto en la fase de iniciación como en la de propagación, el efecto que causa las tensiones residuales y su relajación.

3.1 Modelo de elementos finitos

En primer lugar, se va mostrar el modelo de elementos finitos que se ha utilizado, y del que se obtendrán los estados de tensión y deformación necesarios para poder calcular las fases de iniciación y propagación. Posteriormente se explicará el modo en el que se han resuelto ambas fases del crecimiento de grieta. La figura 2 muestra un esquema del MEF usado.

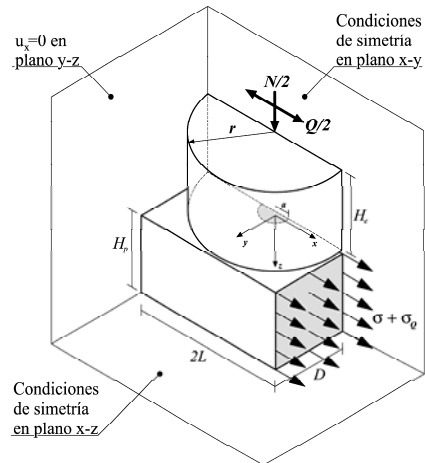


Figura 2. Geometría del modelo de elementos finitos

Para la realización del modelo de elementos finitos, se ha utilizado el código comercial ANSYS® 11.0 SP1. El tipo de elemento estructural utilizado en el modelo es el SOLID185, que consta de 8 nodos y posee tres grados de libertad en cada uno de estos. Los elementos utilizados para simular el par de contacto entre el casquete esférico y el plano son el TARGE170 y el CONTA174, ambos tomados con la opción de 4 nodos por elemento. El algoritmo de contacto usado en el modelo es el Lagrangiano aumentado, que es la opción que viene por defecto, y además con la que se ha obtenido el mejor compromiso entre tiempo de computación y precisión en la solución del modelo. La malla utilizada en las simulaciones consta de 168641 elementos. El comportamiento del material es elastoplástico con endurecimiento cinemático, y para introducir la curva tensión-deformación de este material, se ha utilizado una tabla con 30 puntos de la curva de Ramberg-Osgood dada en [5]. Las distribuciones de tensiones residuales en la parte que simula a la probeta, han sido introducidas mediante el comando ISTRRESS presente en el código ANSYS®. Para modelar la distribución de tensiones residuales en la probeta, se ha supuesto que cualquier dirección contenida en un plano paralelo a aquel donde se desarrolla la zona de contacto es principal, por lo que ambas componentes de la distribución de tensiones residuales pertenecientes a estos planos son iguales. También se ha supuesto que las componentes perpendiculares a estos planos son nulas. Para introducir de una forma correcta una distribución de tensiones en el modelo de elementos finitos, ésta ha de ser autoequilibrada, esto es, que la zona de compresión

ha de ser compensada por una zona de tracción. La distribución de tensiones residuales de tracción que se ha introducido en el modelo para que la distribución sea autoequilibrada es una similar a la descrita por Namjoshi *et al.* [8].

3.2 Cálculo de la fase de iniciación

El primer paso en esta fase consiste en calcular, mediante el modelo de elementos finitos descrito anteriormente, la variación del estado de tensiones y deformaciones durante un ciclo de carga. Para ello se toma el estado de tensiones residuales iniciales, y con éste se evalúan las tensiones y deformaciones durante un ciclo de carga a lo largo de una línea que parte perpendicular a la superficie desde el punto situado en el borde de la zona de contacto, esto es, $x=a, y=0$ y $z=0$. El segundo paso es idéntico al primero, excepto que en el modelo de elementos finitos las tensiones residuales introducidas no son las iniciales, sino las relajadas o medidas después de 20.000 ciclos. Una vez que se dispone de la distribución de tensiones y deformaciones en ambos instantes de tiempo a lo largo de la línea anterior, se puede estimar la variación de las tensiones en función del número de ciclos para cada uno de los puntos de la línea [9], que a modo de ejemplo para la componente x del tensor de tensiones viene dada por

$$\sigma_{xx}(N) = \sigma_{xx}^0 N^r, \quad (1)$$

donde N es el número de ciclos transcurridos, y σ_{xx}^0 y r son dos constantes de ajuste de modo que $s_{xx}(1) = s_{xx}^{ini}$ y $s_{xx}(20.000) = s_{xx}^{rel}$, siendo σ_{xx}^{ini} y σ_{xx}^{rel} , las tensiones obtenidas con el modelo de elementos finitos considerando las tensiones residuales iniciales, y las medidas después de 20.000 ciclos de cargas respectivamente. Del mismo modo que se ha hecho con la componente x del tensor de tensiones, se hace con el resto de componentes del tensor de tensiones e igualmente con el de deformaciones. Esto permite estimar la evolución del estado de tensiones y deformaciones con el número de ciclos de carga. Una vez que se conoce el estado de tensiones y su evolución con los ciclos de carga a la largo de la línea en estudio, el siguiente paso es calcular el número de ciclos de iniciación N_{mic} para cada uno de los puntos de la línea. Para obtener N_{mic} se ha utilizado el parámetro SWT [10], ya que ofrece un buen comportamiento cuando se utiliza con aleaciones de aluminio [11], y que se muestra en la ecuación (2). Las constantes de este parámetro se muestran en [5].

$$SWT = \sigma^{\max} \frac{\Delta \varepsilon}{2} = \sigma'_f \varepsilon'_f (2N)^{b+c} + \sigma'_f (2N)^{2b}. \quad (2)$$

Debido a que el estado de tensiones en un punto cambia con el número de ciclos, también lo ha de hacer el parámetro SWT, por lo que la obtención de N_{mic}

directamente mediante la ecuación (2) no es posible. Ya que este parámetro cambia con el número de ciclos, parece adecuado obtener los ciclos de iniciación haciendo uso de la regla de acumulación de daño de Miner [12]. Este proceso de acumulación de daño, se ha realizado de forma discreta aumentando el número de ciclos de 100 en 100. En la figura 3 se muestra el esquema de cálculo utilizado para obtener N_{mic} .

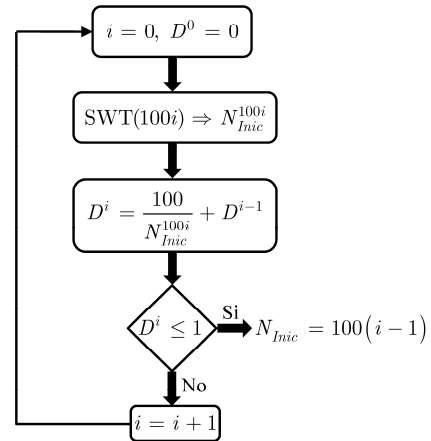


Figura 3. Esquema del proceso de cálculo para N_{mic}

Inicialmente ($i=1$), es necesario calcular mediante el parámetro SWT el número de ciclos de iniciación, que corresponde para el caso donde se han realizado 100 ciclos de carga. Con el valor de $SWT(100)$ se obtiene N_{inc}^{100} , posteriormente se calcula el daño acumulado por el material como, $D = D^0 + 100 / N_i^{100}$, donde hay que tener en cuenta que el daño inicial del material es nulo, por lo que D^0 . Si el valor de D es mayor que la unidad, el material ha fallado, por lo que en esta situación donde $i=1$, se tiene que el número de ciclos de iniciación está entre 0 y 100 ciclos, pero para ser conservativo se toma $N_{mic} = 0$. Si no es así, esto es $D < 1$, se aumenta el número de ciclos transcurridos en 100 unidades, y se vuelve a repetir el proceso anterior hasta que $D > 1$, y de esta forma se obtiene el número de ciclos de iniciación como $N_{mic} = 100(i-1)$.

3.3 Cálculo de la fase de propagación

Para calcular el factor de intensidad de tensiones (FIT) se ha considerado que la grieta crece perpendicular a la superficie, suposición que puede ser usada sin cometer un gran error en los cálculos. El FIT se ha obtenido haciendo uso de la técnica de las funciones de peso, en concreto se ha tomado la función de peso definida por Shen *et al.* [13] para grietas semielípticas que crecen desde una superficie. El FIT para una determinada longitud de grieta l se obtiene mediante la expresión dada por

$$K_I = \int_0^l w(s) \sigma_n(s) ds, \quad (3)$$

donde $\sigma_n(s)$ es la distribución de tensiones normales al plano de la grieta, que se ha calculado mediante el modelo de elementos finitos. En el trabajo de Shin *et al.* [13], esta distribución de tensiones normales es constante a lo largo de la dirección y de la grieta, y únicamente varía con la coordenada de integración s . Esta situación no modela lo que realmente ocurre teóricamente en un contacto del tipo esfera-plano, pues en este caso la distribución de tensiones normales a la superficie de la grieta varía con ambas coordenadas s e y . Para evitar este problema, la distribución de tensiones $\sigma_n(s)$ se toma igual a las distribución dada por $\sigma_{xx}(x=a, y=0, z=s)$ desarrolladas en el contacto esfera-plano. Además, cualquier estimación de vida realizada con la distribución dada por $\sigma_{xx}(x=a, y=0, z=s)$ será conservadora, ya que esta distribución es la que alcanza mayores valores en toda la superficie de la grieta.

En los casos en estudio debido a la relajación de las tensiones residuales, $\sigma_n(s)$ variará con el número de ciclos, por lo que se tendrán dos curvas diferentes que relacionan el FIT con la longitud de grieta l , una para la situación en la que las tensiones residuales son las iniciales, y otra cuando las tensiones residuales son las relajadas. En esta situación para cada longitud de grieta l se tienen dos FIT, uno correspondiente a 0 ciclos de carga (σ_{res} iniciales) y otro correspondiente a 20.000 ciclos de cargas (σ_{res} relajadas), y debido a que la variación del FIT es a causa del cambio de las tensiones residuales, parece lógico relacionar cada par de puntos correspondientes a cada longitud de grieta l de forma similar a como se hizo con la ecuación (1).

$$K_I(N) = K_I^0 N^r, \quad (4)$$

donde de nuevo N es el número de ciclos transcurridos y K_I^0 y r son dos constantes de ajuste para que $K_I(1) = K_I^{ini}$ y $K_I(20.000) = K_I^{rel}$, donde los FIT K_I^{ini} y K_I^{rel} son los obtenidos considerando las tensiones residuales iniciales y relajadas respectivamente.

Para el cálculo del número de ciclos de propagación se ha considerado que el modo principal de crecimiento de grieta es el I, y para ello se ha utilizado de la ley de Paris, donde el rango del FIT ΔK_I , se ha tomado igual a la parte positiva del rango del FIT, esto es $\Delta K_I = K_I^{max}$.

$$\frac{dl}{dN_p} = C(K_I^{max}(N_p))^n \quad (5)$$

La integración directa de la ecuación (5) no es posible, ya que tal y como se muestra en esta ecuación, K_I^{max} depende del número de ciclos de propagación N_p mediante la relación dada por la ecuación (4), por lo que se hace necesario utilizar algún método numérico. En

este caso, se ha utilizado el método de integración numérica de Runge-Kutta mediante la función *dsolve* implementada en el software de cálculo MAPLE®.

3.4 Cálculo del número de ciclos a fatiga N_f

El último paso consiste en sumar las dos curvas obtenidas, las cuales en función de la longitud de grieta l dan los ciclos de iniciación N_{iic} y propagación N_p , obteniéndose una curva N_f tal y como la que se muestra en la figura. La longitud de grieta a la cual se produce el mínimo de N_f es la longitud de iniciación l_i , y ese mínimo N^* de la suma de las vidas de iniciación y propagación, es la vida del componente.

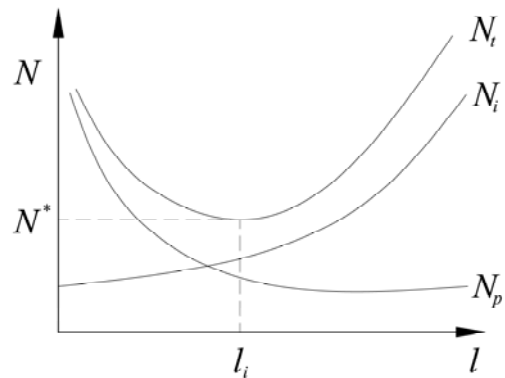


Figura 4. N_i , N_p y N_f en función de l

4. RESULTADOS

El modelo anteriormente descrito para estimar la vida a fatiga por fretting, se ha aplicado a una serie de ensayos realizados en [5]. En estos ensayos las probetas han sido tratadas con shot y laser peening, pero que su rugosidad superficial original ha sido modificada.

En la tabla 1 se muestran los resultados experimentales de estos ensayos, además de las carga axial σ , normal N y tangenciales Q_a y Q_b impuestas. También se incluyen el tipo de tratamiento aplicado en cada uno de los ensayos, donde SP A y SP B corresponden a dos diferentes tipos de shot peening, y LP 1GW y LP 2GW corresponden a tratamientos de laser peening con intensidades de 1GW/cm² y 2GW/cm² respectivamente.

Tabla 1. Vida de los ensayos realizados con la rugosidad modificada

Trat.	Tipo ensayo	σ	Q_a	Q_b	N	N_f
SP A	90/1100/1200	90.6	1072	1090	1200	283522
SP A	100/1100/1200	102.1	1099	1099	1200	191755
SP A	110/900/1000	108.6	906	903	1000	238394
SP A	125/900/1000	123.7	859	900	1000	196035
SP A	125/600/650	123.9	562	602	650	588006*
SP B	90/1100/1200	89.9	1047	1086	1200	630914
SP B	100/1100/1200	101.1	1097	1103	1200	282083
SP B	110/900/1000	112.0	900	906	1000	1236088*
SP B	125/900/1000	122.8	571	602	1000	201385

SP B	125/600/650	125.3	888	895	650	1056374*
LP 1 GW	90/1100/1200	92.1	1045	1088	1200	159956
LP 1 GW	100/1100/1200	100.3	1095	1107	1200	142113
LP 1 GW	110/900/1000	111.4	901	899	1000	133337
LP 1 GW	125/900/1000	126.4	896	894	1000	90418
LP 1 GW	125/600/650	126.1	580	605	650	148956
LP 2 GW	90/1100/1200	88.2	1030	1097	1200	491557
LP 2 GW	100/1100/1200	101.2	1101	1099	1200	201975
LP 2 GW	110/900/1000	113.2	901	897	1000	170656
LP 2 GW	125/900/1000	126.6	878	900	1000	169456
LP 2 GW	125/600/650	124.7	570	599	650	213555

* Ensayos donde el fallo se ha producido fuera de la zona afectada por fretting

El motivo por el que se ha evitado aplicar el modelo descrito a los ensayos realizados en [5] con probetas cuya rugosidad es la original, es que bajo estas condiciones, se hace necesario incluir el efecto de la rugosidad en el modelo de elementos finitos.

De las figuras 5 a 8 se muestran las predicciones que ofrece el modelo desarrollado para cada uno de los diferentes tratamientos de shot y laser peening utilizados en los ensayos. Todos los gráficos mostrados están en escala logarítmica y lo que se representa es la predicción de vida del modelo en frente a la vida experimentada en los ensayos. También se muestran dos bandas inclinadas que corresponden a unas relaciones entre la vida experimental y la predicción de $N_{pred} = 2N_{exp}$ y $N_{pred} = N_{exp} / 2$ respectivamente. Las flechas corresponden con ensayos donde el fallo se ha producido fuera de la zona afectada por fretting.

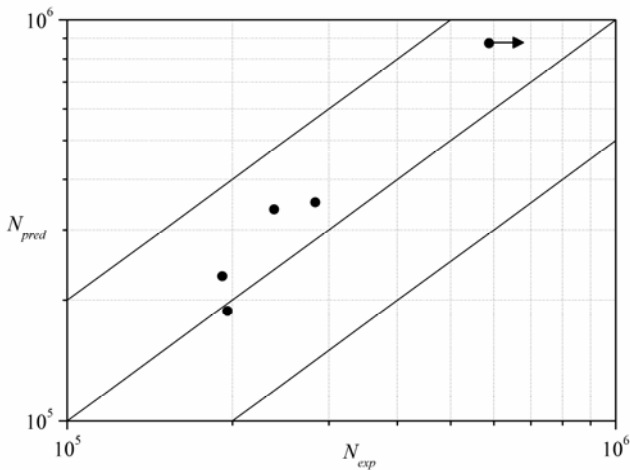


Figura 5. Predicciones para las probetas tratadas con shot peening tipo A

En la figura 5 se observa cómo las predicciones de vida N_{pred} para los ensayos de las probetas tratadas con el shot peening tipo A caen dentro de la banda comprendida entre $N_{pred} = 2N_{exp}$ y $N_{pred} = N_{exp} / 2$. De las cinco predicciones realizadas, tres de ellas son no conservadoras, prediciendo por lo tanto una vida mayor que la realmente experimentada. En lo que se refiere al ensayo tipo 125/600/650, al no haberse producido la

rotura de la probeta por la zona de contacto, se puede concluir que N_{exp} podría ser mayor, de producirse el fallo por la zona afectada por fretting, aunque no se sabe en qué cantidad, por lo que en principio no se puede concluir el carácter de la predicción es este caso. Por último comentar la buena exactitud en la predicción del modelo para el caso del ensayo tipo 125/900/1000, donde el error producido es de un 4%.

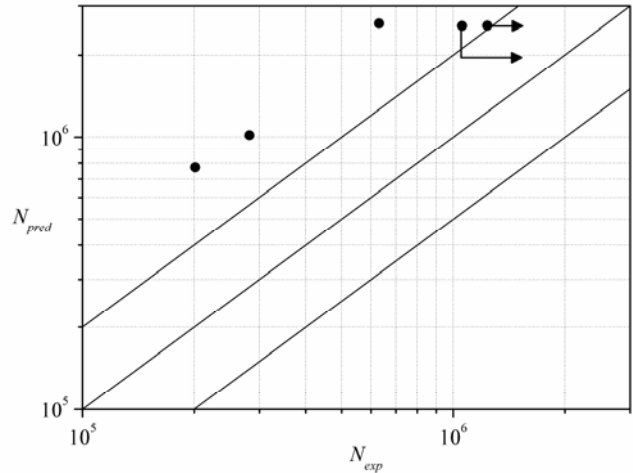


Figura 6. Predicciones para las probetas tratadas con shot peening tipo B

En la figura 6 se muestra cómo las predicciones para los tres ensayos que han tenido un fallo por la zona de contacto, se encuentran por encima de la banda definida por $N_{pred} = 2N_{exp}$ por lo que en este caso las predicciones arrojadas por el modelo no son demasiado buenas. En lo que se refiere a las probetas que han tenido un fallo fuera de la zona de contacto, se pueden obtener conclusiones similares a las expuestas anteriormente para el shot peening tipo A.

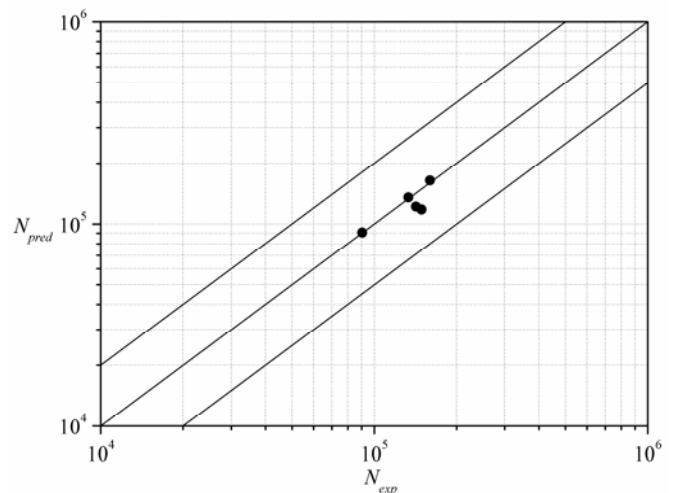


Figura 7. Predicciones para las probetas tratadas con laser peening de 1GW/cm²

Viendo los resultados arrojados por el modelo para el tratamiento $1\text{GW}/\text{cm}^2$, figura 7, se puede decir que tres de las cinco predicciones realizadas son muy buenas, cometiéndose un error máximo en la predicción para estos tres casos del 3%. Las otras dos predicciones ofrecen valores conservativos, pero también con estimaciones de vida bastantes cercanas a las experimentales, siendo en estos casos el error máximo cometido en la predicción de entorno al 26%.

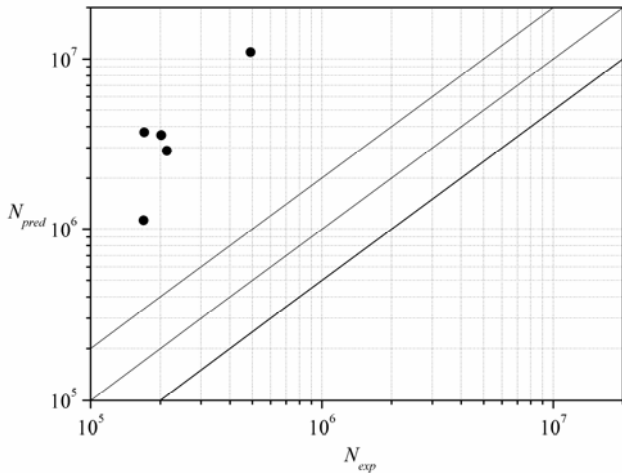


Figura 8. Predicciones para las probetas tratadas con laser peening de $2\text{GW}/\text{cm}^2$

Para este último tratamiento de laser peening con $2\text{GW}/\text{cm}^2$ de intensidad, se observa cómo todas las predicciones son de un orden de magnitud mayor que la vida experimentada por las probetas en los ensayos de fatiga por fretting, siendo por lo tanto el comportamiento del modelo en esta situación bastante no conservativo.

5. CONCLUSIONES

A la vista de los resultados ofrecidos por el modelo, se puede decir que éste ofrece buenos resultados para los tratamientos de shot peening tipo A y de laser peening de $1\text{GW}/\text{cm}^2$. Curiosamente, estos tratamientos son los dos que dentro de su clase (shot peening o laser peening), tenían el campo de tensiones residuales con valores menores [5], en lo que a tensiones de compresión de refiere. Por el contrario, el modelo tiene un mal comportamiento con los tratamientos de shot peening tipo B y de laser peening de $2\text{GW}/\text{cm}^2$. Uno de los motivos que se le puede achacar al mal comportamiento del modelo con estos dos últimos tratamientos, es que la relajación de tensiones residuales simulada, no coincide con la que realmente experimentan las probetas, debiendo de ser mayor la sufrida en los ensayos realizados. Anteriormente se asumió que la relajación de las tensiones residuales con el número de ciclos debía seguir el comportamiento definido por la ecuación (1), pero es posible que a lo

largo de los ensayos los tratamientos de shot peening tipo B y de laser peening de $2\text{GW}/\text{cm}^2$ sufran una relajación algo distinta a la definida por esta ecuación.

AGRADECIMIENTOS

Los autores agradecen al Ministerio de Educación y Ciencia de España la financiación de esta investigación a través del proyecto DPI2007-66995-C03-01.

REFERENCIAS

- [1] Waterhouse R.B and Lindley, T.C. (1994) *ESIS Publication* 18. MEP, London.
- [2] Dobromirski, J. M. (1992) Variables of Fretting Process: Are There 50 of Them?, Standardization of Fretting Fatigue Test Methods and Equipment, ASTM International.
- [3] Navarro C, García M, Domínguez J. A procedure for estimating the total life in fretting fatigue. *Fatigue Fract Engng Mater Struct* **26**, 459-468, 2003.
- [4] Navarro C, Muñoz S, Domínguez J. On the use of multiaxial fatigue criteria for fretting fatigue life assessment. *Int J Fatigue* **30**, 32-44, 2008.
- [5] Vázquez J, Navarro C, Domínguez J. Experimental results in fretting fatigue with shot and laser peened specimens. XXVII Encuentro del Grupo Español de Fractura, Oporto, 17-19 Marzo 2010.
- [6] James, M. R. (1987) Relaxation of Residual Stresses - An Overview, *Adv. in Sur. Treat., Technol., Appl., Eff.*, **4**, 349-365.
- [7] Chen, W. C. (1979) A Model for Joining the Fatigue Crack Initiation and Propagation Analysis, Doctoral Thesis, University of Illinois at Urbana-Champaign.
- [8] Namjoshi, S. A., Jain, V. K. and Mall S. (2002) Effects of Shot-Peening on Fretting-Fatigue Behavior of Ti-6Al-4V, *Journal of engineering materials and technology*, 124, pp. 222-228.
- [9] Champoux, R. L., Underwood, J. H and Kapp, J. A (1988) Analytical and Experimental Methods for Residual Stress Effects in Fatigue, ASTM STP 1004.
- [10] Smith, R. N., Watson, P. and Topper, A. (1970) A Stress Strain Function for the Fatigue of Metals, *J. of Materials JMSLA*, 5, pp. 767-778.
- [11] Zhao, T. and Jiang, Y. (2008) Fatigue of 7075-T651 Aluminum Alloy *International Journal of Fatigue*, 30, pp. 834--849.
- [12] Miner, M. A. (1945) Cumulative Damage In Fatigue, *J. Appl. Mech., Trans. ASME*, 12, pp. A159-A164.
- [13] Shen, G., Plumtree, A. and Glinka, G. (1991) Weight Function for the Surface Point of Semi-elliptical Surface crack in a Finite Thickness Plate, *Engineering Fracture Mechanics*, 40, pp. 167-176.

FRAGILIZACIÓN POR HIDRÓGENO DE ACEROS PERLÍTICOS TREFILADOS SOMETIDOS A ESTADOS TRIAXIALES DE TENSIÓN

D. Vergara¹ y J. Toribio²

¹ Departamento de Ingeniería Mecánica, Universidad de Salamanca
E.P.S., Campus Viriato, Avda. Requejo 33, 49022 Zamora
Tel: (980) 54 50 00; Fax: (980) 54 50 02, Correo-e: dvergara@usal.es

² Ingeniería de Materiales, Universidad de Salamanca
E.P.S., Campus Viriato, Avda. Requejo 33, 49022 Zamora

RESUMEN

En este estudio se han analizado las superficies de fractura de probetas entalladas de acero perlítico sometidas hasta rotura a ensayos de tracción a velocidad de extensión constante (TVEC), en un ambiente que facilita la *fractura asistida por hidrógeno* (FAH). Con el fin de obtener unos resultados generalizados, se han empleado diferentes geometrías de entalla y velocidades de sollicitación. Las superficies de fractura obtenidas se han clasificado en relación a cuatro posibles modelos teóricos. Para ello se ha realizado un análisis fractográfico de cada superficie de fractura, tanto la zona de proceso de fractura (ZPF) como el resto de zonas bien delimitadas. Los resultados obtenidos amplían el número de modelos teóricos vistos en la bibliografía científica anterior.

ABSTRACT

In this study, fracture surfaces of notched specimens of pearlitic steels subjected to constant extension rate tensile (CERT) tests are analyzed, in an environment causing *hydrogen assisted fracture* (HAF). In order to obtain general results, different notch geometries and loading rates are employed. The fracture surfaces are classified in relation to four theoretical models. To this end, fractographic analysis in each fracture surface is carried out, not only in the fracture process zone (FPZ) but also in the rest of well-delimited zones. Generated results increase the number of theoretical models found in the previous scientific bibliography.

PALABRAS CLAVE: Aceros perlíticos trefilados, entallas axisimétricas, FAH, superficie de fractura.

1. INTRODUCCIÓN

Los *aceros perlíticos o eutectoides*, después de ser sometidos a un proceso de trefilado que les confiere propiedades mecánicas con grandes prestaciones, son ampliamente empleados en ingeniería civil bajo la denominación de aceros de pretensado. Durante su vida en servicio, estos materiales se encuentran frecuentemente afectados por la presencia de hidrógeno, bien producido de manera natural bajo condiciones ambientales [1,2], o bien producido por las condiciones de protección catódica frente a la corrosión a las que suelen estar sometidos estos aceros [3,4].

Estas circunstancias causan en estos metales un fenómeno de degradación estructural conocido como *fractura asistida por hidrógeno* (FAH), que puede alterar perjudicialmente sus propiedades mecánicas y, como consecuencia, influir negativamente sobre la integridad estructural de los elementos construidos con ellos, conduciendo, en algunos casos, a roturas catastróficas [5,6]. Para estudiar este fenómeno pueden

usarse los ensayos de tracción a velocidad de extensión constante (TVEC), que generan un determinado estado tensodeformacional en el material además de someterlo a una fuente supuestamente constante de hidrógeno. Las probetas utilizadas pueden adoptar diversas formas, siendo recomendables las probetas entalladas [7,8].

En este artículo se muestran, para ensayos TVEC hasta rotura bajo condiciones de FAH, las diversas posibilidades que puede adoptar la superficie de fractura de una probeta de un acero perlítico mecanizada con una *entalla axisimétrica*. Con el fin de poder generalizar los resultados, se ha trabajado con alambres entallados con diferentes geometrías (variando los radios de curvatura de la entalla y la profundidad de ésta), con aceros que han sufrido diferentes grados de trefilado dentro de una cadena real de producción, y también, como el tiempo de exposición al hidrógeno influye en el proceso de FAH de este tipo de probetas [9,10], se han utilizado, a su vez, varias velocidades de sollicitación.

2. PROCEDIMIENTO EXPERIMENTAL

Los materiales empleados para este estudio han sido aceros eutectoides (Tabla 1) que proceden de cada una de las hileras de una cadena de trefilado. Por lo tanto se ha trabajado tanto con el alambroón perlítico, estado previo al proceso de conformación mecánica en frío, como con cada uno de los siguientes estados del material dentro de la cadena de producción, hasta llegar al producto comercial o alambre de pretensado, producto final después de sufrir 6 pasos de trefilado. Se ha establecido la nomenclatura A_i para diferenciar cada uno de los siete aceros, siendo i el número de pasos de hileras de trefilado que ha sufrido el material durante el proceso de conformación. Las principales diferencias entre unos y otros aceros son debidas a los cambios microestructurales que sufren estos materiales durante el proceso de trefilado. Los alambres presentan un mayor grado de *anisotropía microestructural* a medida que el material es procesado, ya que se ha podido comprobar que la microestructura tiende a orientarse en la dirección del eje del trefilado [11-14].

Tabla 1. Composición química del acero analizado

% C	% Mn	% Si	% P	% S	% Al	% Cr	% V
0.80	0.69	0.23	0.012	0.009	0.004	0.265	0.06

Para elaborar este trabajo se ha trabajado con alambres entallados, sometiéndolos a ensayos de tracción a velocidad de extensión constante (TVEC) hasta rotura en ambiente catódico de FAH. Los materiales empleados han sido cada uno de los aceros comentados en el apartado anterior. Se han empleado cuatro tipologías diferentes de entalla, denominadas A, B, C y D, con características distintas respecto al radio de curvatura en el fondo de entalla (R) y a la profundidad de entalla (A). Para establecer una geometría similar para todos los aceros, independientemente del grado de trefilado sufrido, se han mantenido constantes las relaciones de estos parámetros con el diámetro del alambre (\varnothing), i.e., A/\varnothing y R/\varnothing . La Figura 1 presenta un esquema de los criterios seguidos para establecer la geometría de las entallas estudiadas.

Para ejecutar los ensayos TVEC realizados con estas probetas se han empleado dos velocidades de sollicitación distintas, 0.001 mm/min y 0.01 mm/min, siendo la primera de ellas la más lenta que se puede aplicar en la máquina universal con la que se ha trabajado. Se ha denominado *velocidad tipo 1* a la correspondiente a 0.001 mm/min y *tipo 2* a la otra, 0.01 mm/min. Estas velocidades son adecuadas para que el hidrógeno pueda difundirse hacia el interior del material, de forma que el fenómeno de fractura en régimen catódico (FAH) se produzca debido a un estado de concentración crítica de hidrógeno [7,15].

El ambiente catódico se simuló con una celda electroquímica en la que se introdujo una disolución saturada

de $\text{Ca}(\text{OH})_2$ con 0.1 g/l de NaCl (pH 12.5), estando a su vez conectada a un potencióstato que mantuvo un potencial de -1200 mV ECS durante la ejecución de los ensayos. El potencial electroquímico que se ha elegido para la realización de este trabajo queda justificado en estudios previos realizados con materiales muy parecidos a los estudiados aquí [16,17]. En éstos se manifiesta que el valor de -1200 mV con respecto al electrodo de calomelanos saturado (ECS) junto al pH de 12.5 aporta unas condiciones electroquímicas que favorecen el fenómeno de fragilización por hidrógeno en los aceros eutectoides o perlíticos.

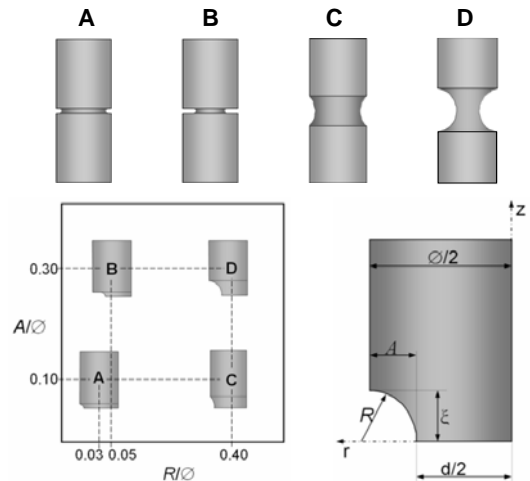


Figura 1. Esquema y geometría de las entallas estudiadas.

La nomenclatura que se ha utilizado consta de un número que indica el grado de trefilado (desde 0 hasta 6) seguido de una letra que indica el tipo de entalla (A, B, C o D) y a su derecha, después de un guión, se ha añadido un número que indica el tipo de velocidad de sollicitación empleada (1 ó 2). La Figura 2 explica esta clasificación de manera esquemática para un ejemplo concreto, 4C-2.

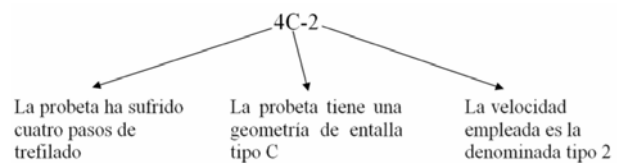


Figura 2. Ejemplo de la nomenclatura empleada para definir las probetas estudiadas.

3. ANÁLISIS FRACTOGRÁFICO

El análisis fractográfico que se ha realizado a las superficies de fractura de las probetas sometidas a los ensayos TVEC ha revelado, mediante microscopía electrónica de barrido (MEB), diversas topografías: *coalescencia de micro-huecos* (CMH), correspondiendo a un comportamiento dúctil del material; *clivaje* (C), asociado a un comportamiento de tipo frágil; *tearing topography surface* (TTS), asociado a una fractura

afectada por la presencia de hidrógeno [18]; CMH* o cuasi-CMH, reconocido como un estadio previo a la formación de la topografía TTS [19]. Aunque existen zonas de la superficie de fractura que presentan únicamente uno de los tipos anteriores, también se han encontrado otras partes que denotan una mezcla de CMH y C, en diferentes proporciones, e incluso existen otras en las que coexisten TTS y CMH*.

La zona de proceso de fractura (ZPF) es la región del material en la que se inicia el daño en el material y, posteriormente, se desarrolla hasta alcanzar un estado de separación total de las superficies. Si durante el proceso de fractura el ambiente ha favorecido la presencia de hidrógeno, la ZPF suele estar asociada a la topografía de desgarro TTS [20]. Después de haber realizado todos los ensayos planteados en el apartado anterior para cada uno de los siete aceros, con probetas mecanizadas con distinta tipología de entalla y ensayadas con diferente velocidad de sollicitación, se ha llegado a generalizar el comportamiento en fractura de estos materiales a partir de cuatro posibles modelos. Para ello se ha analizado, para todos los casos, tanto la situación de la ZPF como la dirección de propagación y la fractografía de cada zona dentro de la superficie de fractura, viendo que el comportamiento seguido se puede establecer con cuatro modelos tipo, que se han clasificado con números romanos.

En la Figura 3 se ha esquematizado el proceso de fractura concerniente al modelo I. Éste representa una ZPF formada por TTS que está situada en la superficie de la probeta y que abarca una zona no excesivamente grande (zona gris de la figura). El proceso de fractura se inicia y crece subcríticamente allí y, posteriormente, al alcanzar un estado crítico, se propaga críticamente hacia el interior del material alcanzando la superficie de la probeta prácticamente en su totalidad, i.e., la típica corona exterior de CMH se ve reducida a pequeñas áreas, formando una pseudocorona. Se han encontrado evidencias de este modelo en las probetas con entallas tipo A (0, 1 y 2 pasos de trefilado), tipo C (0 pasos de trefilado) y tipo D (0 pasos de trefilado).

El proceso de fractura según el modelo tipo II (Figura 4) se caracteriza por una ZPF formada por TTS situada también en la superficie de la probeta pero que, a diferencia del modelo anterior, abarca una zona relativamente amplia. El proceso de fractura se inicia y crece subcríticamente allí y, posteriormente, al alcanzar un estado crítico, se propaga críticamente hacia el interior de la probeta pero, en este caso, sin llegar a alcanzar la superficie de ésta ya que la pseudocorona exterior de CMH tiende a abarcar toda la superficie que no presente la topografía TTS. Se han encontrado evidencias de este modelo en las probetas con entallas tipo A (3, 4, 5 y 6 pasos de trefilado), tipo B (0, 1, 2, 3 y 4 pasos de trefilado), tipo C (1, 2, 3, 4, 5 y 6 pasos de trefilado), tipo D con velocidad 1 (1 paso de trefilado) y tipo D con velocidad 2 (1 y 2 pasos de trefilado).

El modelo III, representado en la Figura 5, se caracteriza por una ZPF formada por TTS que circunda toda la periferia de la superficie de la probeta, i.e., existe una *corona exterior de TTS* (o de TTS y CMH*). El proceso de fractura se inicia y crece subcríticamente allí y, posteriormente, al alcanzar un estado crítico, se propaga críticamente hacia el interior de la probeta. Se suele presentar en casos que ya manifiestan una clara influencia de la anisotropía microestructural: probetas con entallas tipo B (5 y 6 pasos de trefilado) y tipo D con velocidad 2 (3, 4, 5 y 6 pasos de trefilado). Aunque el esquema de la Figura 5 indica que no existe una dirección de propagación predominante, en algunos de los casos encontrados, justo donde la corona TTS tiende a acusar una mayor diferencia de dimensión de unas zonas a otras, se ha apreciado que la propagación se produce de la zona que presenta mayor grosor hacia la zona que presenta menos.

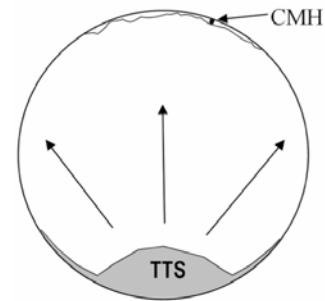


Figura 3. Esquema de la iniciación y propagación de la fractura según el modelo tipo I.

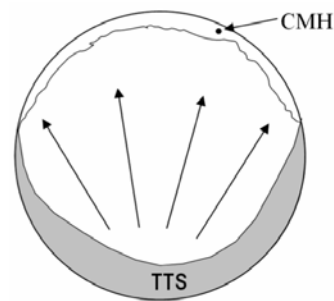


Figura 4. Esquema de la iniciación y propagación de la fractura según el modelo tipo II.

El último esquema del proceso de fractura seguido en los ensayos analizados está representado con el modelo IV (Figura 6). Éste se caracteriza por una ZPF formada por una topografía mixta en la que coexisten TTS y CMH*. Al contrario que los casos anteriores esta zona está situada en el interior de la probeta y cercana al centro de ésta. Por lo tanto, el proceso de fractura se inicia y crece subcríticamente en esta zona, y cuando alcanza un estado crítico se propaga desde el centro hacia el exterior, formando en la última etapa la típica corona exterior de CMH. Únicamente se han encontrado evidencias de este modelo en las probetas con entalla tipo D y velocidad de sollicitación tipo 1 (2, 3, 4, 5 y 6 pasos de trefilado).

En la **Figura 7** se presentan ejemplos de fotografías de superficies de fractura que identifican los modelos expuestos, pudiéndose confirmar el análisis presentado. Aunque en los aceros con pocos pasos de trefilado la superficie de fractura es isotrópica, propagándose en modo I en un plano transversal al eje del alambre, en los últimos pasos del proceso de fabricación la anisotropía microestructural del material fomenta una superficie de fractura desviada del plano perpendicular al eje de la probeta [12,17]. Hay que destacar que los modelos aquí presentados se han realizado viendo las superficies de fractura desde un punto situado en el eje de la probeta y por ello no es posible apreciar el efecto de la anisotropía microestructural.

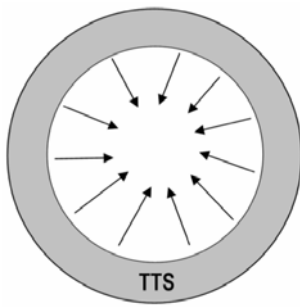


Figura 5. Esquema de la iniciación y propagación de la fractura según el modelo tipo III.

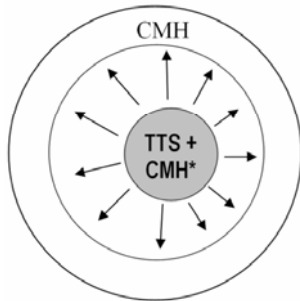


Figura 6. Esquema de la iniciación y propagación de la fractura según el modelo tipo IV.

4. DISCUSIÓN

En la ZPF de todos los modelos presentados aparece bien la fractografía TTS por sí sola o bien la mezcla de ésta con la CMH*, que no deja de ser un estadio previo de formación de la TTS. En la última fase del proceso de fractura aparece también para todos los casos una zona bien delimitada de CMH, a excepción del modelo III en el que esta fractografía ni presenta una situación predefinida ni está perfectamente delimitada, sino que la zona o zonas de CMH que aparecen en el último estadio del proceso de fractura quedan entremezcladas con otras zonas de clivaje.

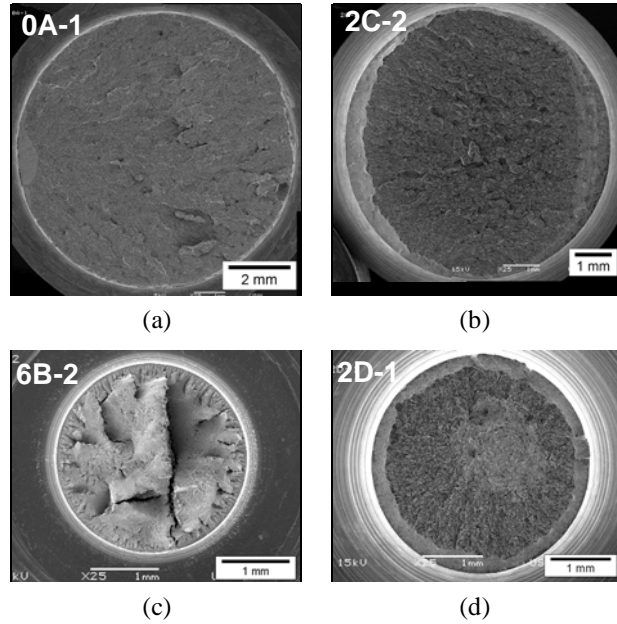


Figura 7. Superficies de fractura acordes a los modelos de fractura presentados: a) modelo I, b) modelo II, c) modelo III, d) modelo IV.

A modo de resumen, y para poder visualizar de una manera cómoda y rápida los diferentes comportamientos seguidos por las superficies de fractura de las probetas entalladas de aceros perlíticos trefilados que se han estudiado en este trabajo bajo condiciones de FAH, se ha indicado en la **Tabla 2** el modelo de fractura tipo para cada entalla y grado de trefilado.

Tabla 2. Modelo tipo seguido en cada ensayo analizado

Grado de Trefilado	Entalla A		Entalla B		Entalla C		Entalla D	
	Velocidad 1	Velocidad 2	Velocidad 1	Velocidad 2	Velocidad 1	Velocidad 2	Velocidad 1	Velocidad 2
0	I	I	I	II	I	I	I	I
1	I	I	II	II	II	II	II	II
2	I	I	II	II	II	II	IV	II
3	II	II	II	II	II	II	IV	III
4	II	II	II	II	II	II	IV	III
5	II	II	III	III	II	II	IV	III
6	II	II	III	III	II	II	IV	III

La entalla A sigue el esquema representado a la **Figura 3** (Tipo I) para los pasos de trefilado iniciales, tendiendo a la tipología II en los pasos de trefilado posteriores. La entalla B presenta superficies de fractura tipo II, aunque también se ha encontrado alguna del tipo III con una corona completa de TTS. La entalla C presenta también la tipología II pero con un tamaño de ZPF superior a la entalla A ó B. Por último la entalla D presenta una mezcla de varias tipologías; el acero sin ningún paso de trefilado sigue el esquema del modelo tipo I; en cambio en los aceros con mayores grados de trefilado se han encontrado las otras tres tipologías, si bien la tipo IV sólo en el caso de velocidades de sollicitación lentas (0.001 mm/min).

Existen estudios previos que analizan también modelos del proceso de fractura de alambres perlíticos [21], pero limitando el trabajo a un acero sin trefilar (alambroón). En ese caso se encontraron evidencias de los modelos I y III, pero no de los otros que aquí se presentan. Además, en el presente estudio existe una diferencia respecto a la bibliografía científica anterior, relacionada con el modelo de fractura seguido por los alambrones mecanizados con entallas de gran profundidad (B y D). Según los resultados encontrados en investigaciones anteriores obtenidas con probetas similares a las 0B y 0D [21], estos alambrones deberían haber seguido el modelo de proceso de fractura tipo III mientras que, en vista de los resultados aquí presentados, se han relacionado con los modelos II y I, respectivamente. Aún así, en el presente estudio también el modelo III aparece exclusivamente para las entallas B y D pero, en este caso, para aceros fuertemente trefilados (Tabla 2).

Por otro lado el grado de trefilado influye notablemente en el proceso de fractura. De acuerdo con la Tabla 2 y sin considerar las peculiaridades de cada tipo de entalla, se puede generalizar que, para velocidades de sollicitación rápidas (tipo 2), en los primeros pasos de trefilado se favorece el modelo I, posteriormente el modelo II y por último el modelo III. Además, tal como están diseñados los modelos esto indicaría que a mayor grado de trefilado se favorece una entrada de hidrógeno distribuida a lo largo de toda la superficie de la probeta (modelo III), mientras que para los pasos anteriores el hidrógeno forma una ZPF localizada en un área concreto de la superficie (modelo I). En esta explicación el modelo II supone un estado intermedio entre el modelo I y el modelo III (Figura 8). Por lo tanto, parece ser que para velocidades de sollicitación rápidas, la anisotropía microestructural inducida por el trefilado tiende a favorecer una distribución axisimétrica de la ZPF. Por otro lado, respecto a las variables que definen la geometría de la entalla, parece que es la profundidad de ésta (A) la que favorece en primera instancia que se alcance a menor grado de trefilado la distribución isotropa de la ZPF del modelo III (entallas B y D). En cambio, el radio de curvatura en el fondo de entalla (R), aunque también influye en este proceso, lo hace en menor medida. Se puede comprobar que, si A es constante, a mayor R (entallas C y D), antes se alcanza la distribución axisimétrica



Figura 8. Esquema seguido por las superficies de fractura según el grado de trefilado, para velocidades de sollicitación rápidas.

Aunque para las entallas A, B y C el proceso de fractura sigue los mismos modelos para la velocidad de sollicitación lenta (tipo 1) que rápida (tipo 2), y la conclusión anterior también sería válida, en el caso de la entalla D existen grandes diferencias en el comportamiento en fractura según sea esta velocidad. La difusión de hidrógeno asistida por un estado de tensiones transitorias (ensayos TVEC) hacia el interior de la probeta se puede deber a dos parámetros: el gradiente de concentración ∇C y el gradiente de tensión hidrostática $\nabla \sigma$ [22,23]. Entre estos dos, es precisamente el último el que juega el papel principal a la hora de establecer los cuatro modelos aquí presentados, ya que la distribución de *tensión hidrostática* σ varía notablemente de un tipo de entallas a otras, favoreciendo la máxima σ en las cercanías de la superficie de la probeta en algunos casos y en el interior de la probeta en otros [21]. Aún así es necesario que el proceso de difusión disponga del *tiempo* suficiente para que el hidrógeno alcance los puntos de máxima σ y se forme la ZPF en esa posición, por lo tanto la *velocidad de sollicitación* también juega un papel fundamental en este análisis. Debido a esto último se puede comprobar que para la entalla D, con la máxima σ en el centro de la probeta [21], sólo se forma la ZPF en el interior del material (modelo IV) para tiempos de exposición al hidrógeno altos, i.e., para velocidades de sollicitación lentas, tipo 1 (Tabla 2).

5. CONCLUSIONES

- Las superficies de fractura de alambres entallados de aceros perlíticos sometidos a ensayos de tracción a velocidad de extensión constante en un ambiente que favorece la FAH, se pueden clasificar en relación con cuatro modelos teóricos tipo.
- En todos ellos la *zona de proceso de fractura* (ZPF) está asociada bien con la fractografía TTS o bien con la mezcla de ésta con cuasi-CMH, que representa un estadio previo de la formación de la TTS.
- Para velocidades de sollicitación rápidas, el grado de *anisotropía microestructural* presente en los alambres perlíticos sometidos a un proceso de trefilado tiende a favorecer una *distribución axisimétrica de la ZPF*.
- Aunque tanto un aumento de la profundidad de la entalla como del radio de curvatura en el fondo de ésta favorecen la *distribución axisimétrica* de la ZPF, parece que es el primero de ellos el factor que más influye en los resultados.
- Aunque la posición de las diferentes fractografías dentro de la superficie de fractura se debe principalmente a la distribución de tensión hidrostática, el *tiempo de exposición al hidrógeno*, regulado por la velocidad de sollicitación, juega también un papel fundamental en la fragilización.

AGRADECIMIENTOS

Los autores desean hacer constar su agradecimiento a las siguientes instituciones financiadoras: MCYT (Proyecto MAT2002-01831), MEC (Proyecto BIA2005-08965), MCINN (Proyecto BIA2008-06810) y JCyL (Proyectos SA067A05, SA111A07 y SA039A08).

REFERENCIAS

- [1] Bergsma, F., Boon, J.W., Etienne, C.F., Détermination de la sensibilité des aciers précontrains à la fragilisation par l'hydrogène. *Revue de Métallurgie*, 1978, **75**, 153-164.
- [2] Valiente, A., Elices, M., Premature failure of prestressed steel bars. *Engineering Failure Analysis*, 1998, **5**, 219-227.
- [3] Enos, D.G., Williams, A.J., Scully, J.R., Long-term effects of cathodic protection of prestressed concrete structures: hydrogen embrittlement of prestressing steel. *Corrosion*, 1997, **53**, 891-908.
- [4] Enos, D.G., Scully, J.R., A critical-strain criterion for hydrogen embrittlement of cold-drawn, ultrafine pearlitic steel. *Metallurgical and Materials Transactions*, 2002, **A33**, 1151-1166.
- [5] Vehovar, L., Kuhar, V., Vehovar, A., Hydrogen-assisted stress-corrosion of prestressing wires in a motorway viaduct. *Engineering Failure Analysis*, 1998, **5**, 21-27.
- [6] Woodtli, J., Kieselbach, R., Damage due to hydrogen embrittlement and stress corrosion cracking. *Engineering Failure Analysis*, 2000, **7**, 427-450.
- [7] Enos, D.G., Scully, J.R., A critical-strain criterion for hydrogen embrittlement of cold-drawn, ultrafine pearlitic steel. *Metallurgical and Materials Transactions*, 2002, **A33**, 1151-1166.
- [8] Toribio, J., Ayaso, F.J., Optimization of the round-notched specimen for hydrogen embrittlement testing of materials. *Journal of Materials Science Letters*, 2004, **39**, 4675-4678.
- [9] Wang, M., Akiyama, E., Tsuzaki, K., Crosshead speed dependence of the notch tensile strength of a high strength steel in the presence of hydrogen. *Scripta Materialia*, 2005, **53**, 713-718.
- [10] Vergara, D., Lorenzo, M., Kharin, V., Toribio, J., Influencia de la velocidad de deformación en la fragilización por hidrógeno de alambres entallados de acero eutectoide, *Anales de Mecánica de la Fractura*, 2006, **23**, 213-218.
- [11] Nam, W.J., Bae, Ch.M., Void initiation and microstructural changes during wire drawing of pearlitic steels. *Materials Science and Engineering*, 1995, **203**, 278-285.
- [12] Ovejero, E., Fractura en ambiente agresivo de aceros perlíticos con distinto grado de trefilado. Tesis Doctoral, Universidad de A Coruña, 1998.
- [13] Zelin, M., Microstructure evolution in pearlitic steels during wire drawing. *Acta Materialia*, 2002, **50**, 4431-4447.
- [14] Sauvage, X., Guelton, N., Blavette, D., Microstructure evolutions during drawing of a pearlitic steel containing 0.7 at. % cooper. *Scripta Materialia*, 2002, **46**, 456-464.
- [15] Toribio, J., Kharin, V., A hydrogen diffusion model for applications in fusion nuclear technology. *Fusion Engineering and Design*, 2000, **51-52**, 213-218.
- [16] Parkins, R. N., Elices, M., Sánchez Gálvez, V., Caballero, L., Environment sensitive cracking of pre-stressing steels. *Corrosion Science*, 1982, **22**, 379-405.
- [17] Lancha, A. M., Influencia del trefilado en la corrosión bajo tensión de aceros eutectoides. Tesis Doctoral, Universidad Complutense de Madrid. 1987.
- [18] Toribio, J., Lancha, A.M., Elices, M., Characteristics of the new tearing topography surface. *Scripta Metallurgica et Materialia*, 1991, **25**, 2239-2244.
- [19] Toribio, J., Vasseur, E., Hydrogen-assisted micro-damage evolution in pearlitic steel. *Journal of Materials Science Letters*, 1997, **16**, 1345-1348.
- [20] Toribio, J., Lancha, A.M., Stress corrosion behaviour of high-strength steel: design on the basis of the crack growth kinetics curve. *Materials & Design*, 1996, **16**, 283-288.
- [21] Toribio, J., Lancha, A.M., Elices, M., Macroscopic variables governing the microscopic fracture of pearlitic steels. *Materials Science and Engineering*, 1991, **A145**, 167-177.
- [22] Toribio, J., Elices, M., Influence of residual stresses on hydrogen embrittlement susceptibility of prestressing steels. *International Journal of Solids and Structures*, 1991, **28**, 791-803.
- [23] Krom, A.H.M., Koers, R.W.J., Bakker, A., Hydrogen transport near a blunting crack tip. *Journal of the Mechanics and Physics of Solids*, 1999, **47**, 971-992.

Welding

FATIGUE CRACK GROWTH BEHAVIOR IN 6061-T6 ALUMINUM ALLOY WELDS OBTAINED BY MIEA

R.R. Ambriz^{1,2,3,4}, G. Mesmacque^{1,2,3}, A. Benhamena^{1,2,3}, A. Ruiz⁴, A. Amrouche^{1,2,3}, V. H. López⁴

¹ Université Lille Nord de France, F-59000 Lille, France. ² USTL, LML, F-59650 Villeneuve d'Ascq, France. ³ CNRS, UMR 8107, F-59650 Villeneuve d'Ascq.

E-mail: ricraf74@gmail.com

⁴ Instituto de Investigaciones Metalúrgicas, Universidad Michoacana de San Nicolás de Hidalgo, A.P. 888, C.P. 58000, Morelia Michoacán, México.

E-mail: alruiz@umich.mx

ABSTRACT

This work reports the results of the fatigue crack growth on 6061-T6 aluminium alloy welds obtained by modified indirect electric arc (MIEA). Fatigue crack growth behavior in base metal, weld metal and heat affected zone (HAZ) of the welded joint was performed by means of compact-type (CT) specimens. Experimental results indicate that the fatigue crack length depends of the mechanical properties of the material. In this context it has been observed that the HAZ tends to delay the crack growth with respect to base metal and weld metal, this aspect is attributed to the larger plastic zone formed around the crack tip which is promoted by the microstructural transformation from β'' to β' precipitates. Also, has been found that the crack growth and stress intensity factor (ΔK) adjust with good confidence according to Paris law; however when ΔK reaches a critical value $\sim 15 \text{ MPa m}^{1/2}$, the fatigue crack growth presents an important change which is related to the microstructural condition of the materials. Finally, the surfaces fractures analysis revealed interesting characteristics in terms of crack propagation.

KEYWORDS: Fatigue; crack growth; welding, 6061-T6.

1. INTRODUCTION.

The 6061-T6 aluminium alloy have a wide use in different fields like the automotive, railroad, chemical and oil industries. The main applications of this alloy are related to the high strength to weight ratio which makes them suitable for: structural parts for trucks, railroad cars, pressure vessels, pipelines, marine applications and mechanical components for machines. The most important characteristic of these alloy is that it can be solution treated and artificially aged to improve their mechanical properties ($\sigma_u \cong 310 \text{ MPa}$) [1, 2]. The metallurgical characteristics and mechanical properties of the HAZ of 6061-T6 welded joints where studied by Malin [3] who found a correlation between thermal cycles microhardness profiles, failure location and tensile properties. Microhardness profiles along the width of the welds revealed that the failure of the tensile specimens consistently occurred in the softest area of the HAZ, where the temperatures experienced in the parent metal induced detrimental changes in the microstructure of the alloy. Thus, it is well known that fusion welding of 6061-T6 aluminium alloy leads to a significant loss of mechanical strength. In recent years, a novel joint design named Modified Indirect Electric Arc (MIEA) was envisaged and used to weld 6061-T6 [4] and 2014-T6 [5] aluminium plates with the gas

metal arc welding process (GMAW). This joint is an interesting alternative to improve the mechanical properties and microstructural characteristics of these alloys, since only a single welding pass is required to weld plates of 12.7 mm in thickness, reducing thus the heat input during welding which in turn reduces the microstructural transformations in the HAZ and enhances the mechanical properties of the welded joints. In terms of fatigue behaviour, the effect of the welding profile in MIEA 6061-T6 aluminium alloy welds has been reported [6]. In this study the calculations are based on the effect of the stress concentration factor produced by the characteristic geometry of the welding profile formed after welding process. It was found that the fatigue life of welded samples using this welding technique was larger in comparison with data reported in the literature. Also, it was observed that there is a good correlation ($R^2=0.90$) between experimental and theoretical prediction according to Basquin's equation.

This study presents the experimental results of the fatigue crack growth in the base metal (BM), weld metal and heat affected zone (HAZ) of the 6061-T6 welded joints obtained by MIEA. Results are discussed in terms of growth and propagation of the cracks.

2. EXPERIMENTAL PROCEDURE.

Plates of 6061-T6 aluminum alloy with dimensions of 150 × 70 × 9.5 mm were joined by means of the MIEA welding technique [7]. GMA welding of the plates was performed using a constant-voltage power source of 300 A with a voltage range of 0 to 50 V. An ER4043 filler wire of 1.2 mm in diameter was fed at 145 mm s⁻¹ with direct current-electrode positive (DCEP) along with Ar shielding gas flowing at 23.6 L min⁻¹. The torch was displaced at 3.6 mm s⁻¹ and voltage (24 V) and current (230 A) were adjusted to produce a spray transfer mode with a visible stick out of 9 mm. Figure 1, shows the schematic representation of the MIEA welds.

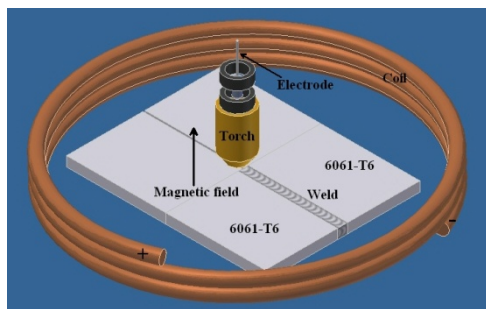


Figure 1. Schematic representation of MIEA welds.

First of all, tensile properties for the as-received 6061-T6 plates (longitudinal direction), weld metal and HAZ were evaluated. Tensile specimens were machined with the dimensions and geometry as specified by the ASTM B557-06 designation. The quasi-static tension test was performed with a head speed displacement of 0.0166 mm s⁻¹. Deformation of the tensile specimens was measured with an Instron[®] extensometer model 2620-601.

Fatigue crack growth test in standard compact-type (CT) specimens was carried out in the base metal, weld metal and HAZ of the MIEA welded joints (Figure 2). Figure 3, shows the specimen dimensions according to ASTM E647-08 designation. For the crack growth test a constant amplitude cyclic loading with a sinusoidal wave form at a frequency of 20 Hz, load ratio $R=0.1$ and load range $\Delta P=2.5$ kN were applied in atmospheric air at room temperature. The propagation of the crack was follow by means of a digital camera attached to a monitor. The crack growth a , as a function of number of cycles N , was represented by means of $a-N$ graph and the crack growth rate da/dN , was presented graphically as a function of the stress intensity factor range ΔK (equation 1).

Finally, examination of the fractured surfaces of CT specimens was performed in the scanning electron microscope (SEM) in order to characterize the type of fracture and obtain insight into the failure mechanisms.

$$\Delta K = \frac{\Delta P(2 + \alpha)}{B\sqrt{W}(1 - \alpha)^{3/2}}$$

$$(0.886 + 4.64\alpha - 13.32\alpha^2 + 14.72\alpha^3 - 5.6\alpha^4)$$

$$\alpha = \frac{a}{W} \tag{1}$$

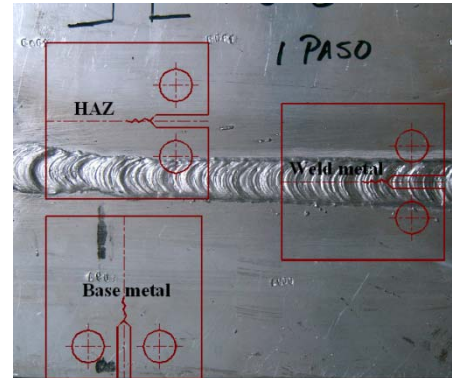


Figure 2. Welded joint and compact-type specimen.

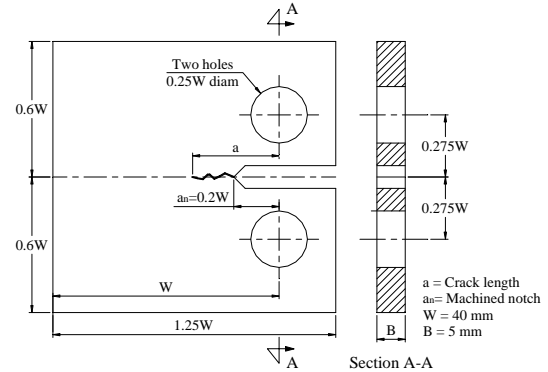


Figure 3. Standard compact-type specimen, CT.

3. RESULTS AND DISCUSSION

3.1. Tensile Behavior.

The individual mechanical behavior of the base metal, weld metal and HAZ, is shown in Figure 4 as a stress function of strain graph.

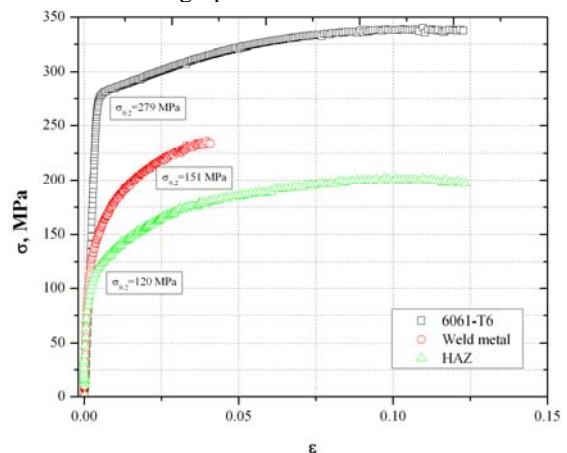


Figure 4. True stress-strain curves for as-received 6061-T6 plates, weld metal and HAZ condition.

It can be observed that the experimental results for the base metal are in agreement with nominal values found in the literature for 6061-T6 alloy [8]. Also, the base metal exhibits the best mechanical properties and the well-defined proportional limit. The tensile properties of the sample obtained from the HAZ presents a 41 % and a 19 % reduction of the ultimate strength with respect to the base metal and weld metal respectively. The loss of mechanical strength, commonly referred to as over-aging, when welding a 6061-T6 alloy is a fairly well-understood phenomenon and it is explained in terms of the precipitation sequence undergone by this alloy with temperature [9]. In a 6061 alloy, the T6 heat-treatment yields an aluminum matrix, α , in which very fine precipitates with needle shape, β'' , are homogeneously dispersed. However, during the welding process, the base metal adjacent to the fusion line is subjected to a gradient of temperature imposed by the welding thermal cycle. It causes the coarsening of β'' and its transformation into β' type precipitates the mechanism responsible of the decrease in hardening of the α matrix due to the incoherence of the β' phase caused by the thermodynamic instability of β'' in a welding process [10]. Although the weld metal shows higher tensile properties than the HAZ, during the tension test, the weld metal and the HAZ show the same behavior, i.e. both present a gradual transition from the elastic region to the plastic region. The weld metal exhibits, however, lower ductility caused by the high content of Si of the filler metal which, when mixing with the melted base metal, leads to a microstructure crowded of eutectic silicon which is a brittle phase that adversely affects the mechanical properties of the weld. The three samples have the same Young's modulus. A best fitting in the elastic region was performed and a value of $E = 68$ GPa was obtained.

3.2. Fatigue Crack Growth.

Figure 5 shows the general characteristics of the crack growth for the base metal, weld metal and HAZ. It is possible to observe that the propagation of the crack is nearly perpendicular to the applied load. Also, we can observe that the maximum displacement in function of the crack propagation is presented in the HAZ specimen, which is attributed to the mechanical properties and microstructural condition of the material.

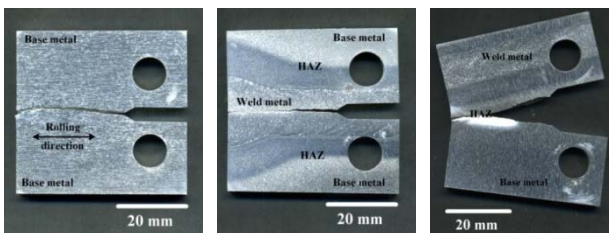


Figure 5. Macrographs of fractured CT specimens.

Fatigue crack growth as a function of number of cycles is shown in Figure 6. In this graph we can note that the fatigue crack length depends fundamentally of the tensile strength of material. In this sense we can observed that the HAZ tends to delay the crack growth in relation to base metal and weld metal. This behavior can be explained in function of the plastic zone formation (ductility) formed around the crack tip which tends to be larger than the base metal and weld metal (Figure 5). This plastic zone is promoted by the loss of hardening in the welded joint due to the microstructural transformation of very fine precipitates with needle shape β'' , to coarse precipitates with bar shape β' , formed after a fusion welding process. Thus, when the crack reaches a critical value, it tends to propagate very quickly in a similar manner to the base metal.

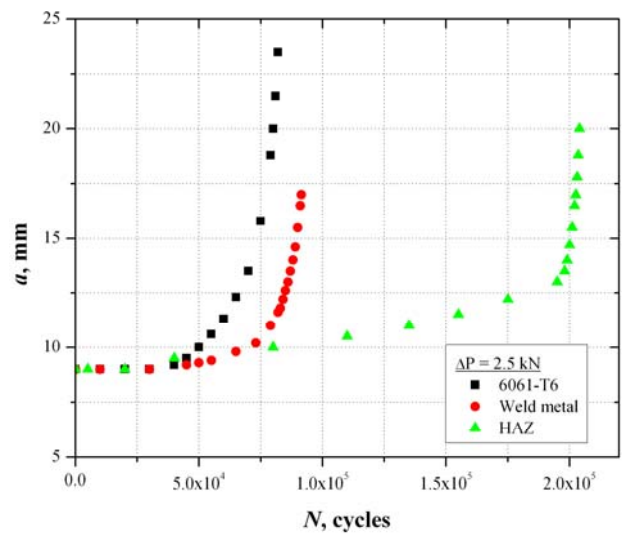


Figure 6. Crack length vs. cycles data for base metal (6061-T6), weld metal and HAZ.

The experimental data of da/dN versus ΔK are show in Figure 7. These results were fitted according to the Paris law:

$$\frac{da}{dN} = C(\Delta K)^n \quad (2)$$

where C and n are experimental values obtained from fitting curve. Table 1, summaries these values and the correlation factor R^2 . The resulting experimental curve and the prediction model are also shown in Figure 7.

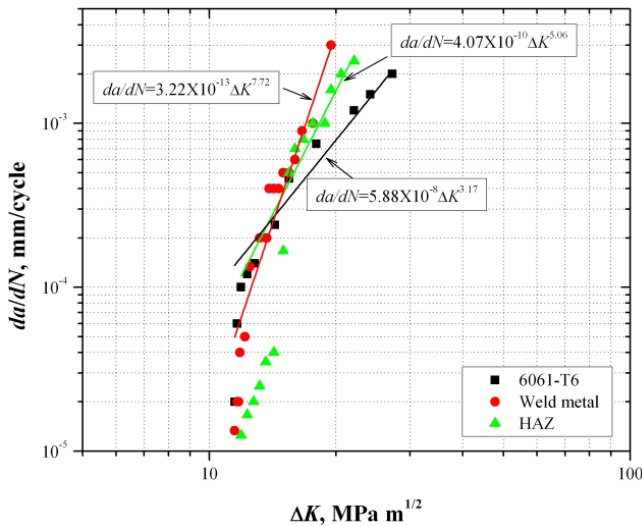


Figure 7. Fatigue crack growth rate for base metal (6061-T6), weld metal and HAZ.

Table 1. Experimental values from fitting curve.

Material	C	n	R ²
6061-T6	5.88×10^{-8}	3.17	0.97
Weld	3.22×10^{-13}	7.72	0.97
ZAT	4.07×10^{-10}	5.06	0.95

From Figure 7, we can see that there is a good correlation between experimental and theoretical predictions, independently of the mechanical properties and microstructure of the welded joint. However, it should be noted an important difference between da/dN versus ΔK behavior. It means that the crack growth behavior is divided by a critical stress intensity factor, $\Delta K_{crit} \sim 15 \text{ MPa m}^{1/2}$. Nevertheless, when $\Delta K_{crit} < 15 \text{ MPa m}^{1/2}$ the faster crack growth correspond to the base metal, followed by the weld metal and the HAZ. In contrast, when $\Delta K_{crit} > 15 \text{ MPa m}^{1/2}$ the crack growth in the base metal is the slowest. Also, is possible to observe that the crack propagation in the weld metal has the maximum crack growth rate, which is attributed to the brittle microstructure produced after welding process (see Figure 4).

3.3. Fracture Modes.

Figure 8, shows the general features of surfaces fractures for base metal, weld metal and HAZ. In these micrographs is possible to identify a pre-crack zone with a width of roughly 1 mm, as well as the different stages of fatigue failure mechanism, especially the path propagation of the fracture characterized by river patterns and the transition of propagation and failure zones. In this context we can note the flat fracture surface presented by the weld metal and HAZ, in contrast to the surface fracture of the base metal.

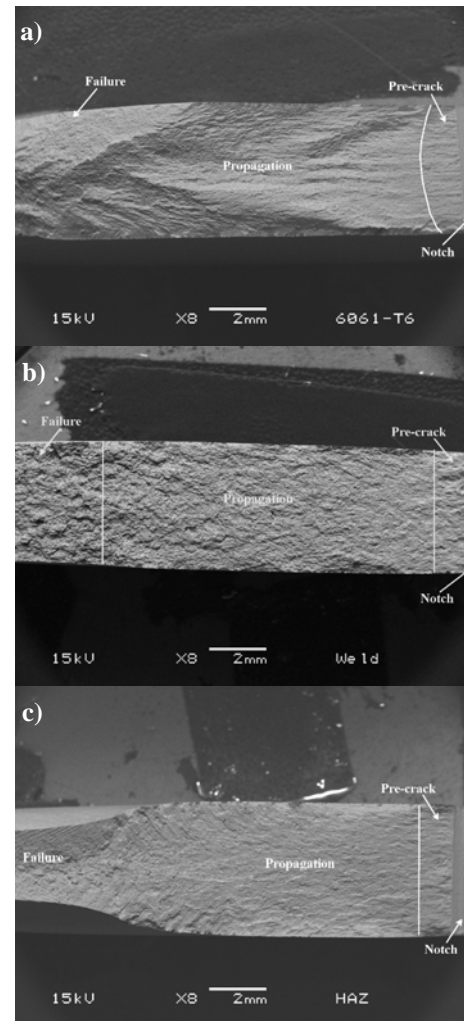


Figure 8. General view of surface fractures, a) base metal, b) weld metal and c) HAZ.

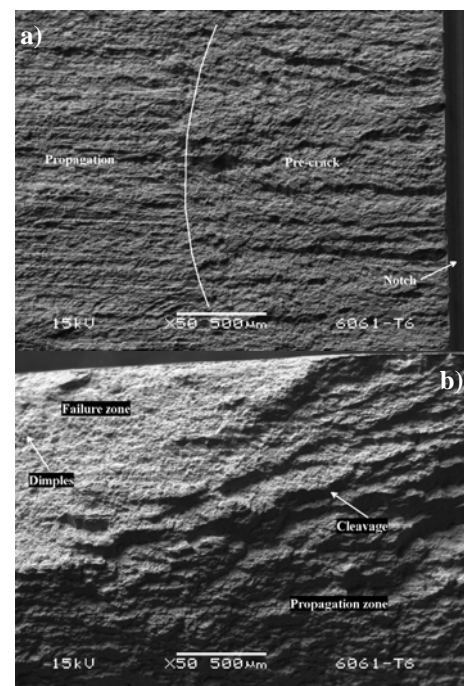


Figure 9. Details of base metal fracture, a) pre-crack and propagation and b) propagation and failure.

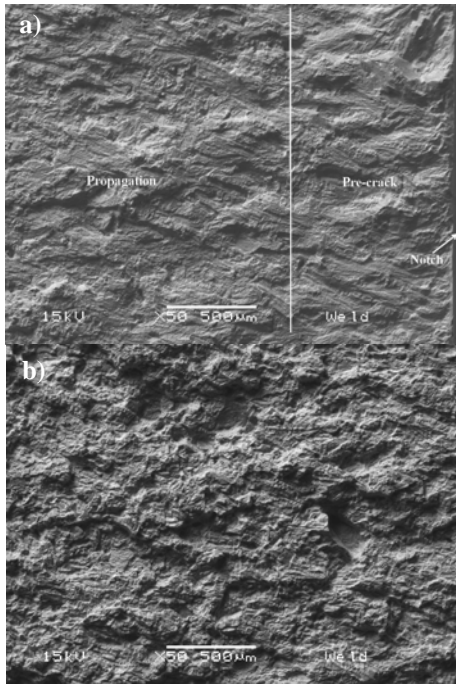


Figure 10. Details of weld metal surface fracture, a) pre-crack and propagation and b) failure.

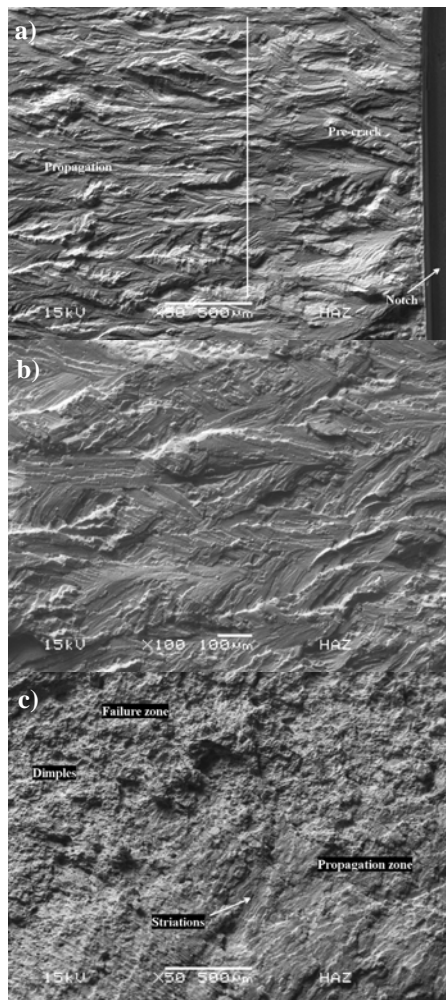


Figure 11. Details of HAZ surface fracture, a) pre-crack and propagation, b) striations in propagation zone and c) propagation and failure zone.

Details of surface fractures of the base metal, weld metal and HAZ can be seen in Figures 9-11. Figure 9a, shows the crack propagation along the grain boundaries of the base metal (rolling direction) without visible striations formation. The transition between propagation crack and failure zone of base metal is presented in Figure 9b, which is characterized by a combination of ductility (dimples) and cleavage. In contrast, some similarities can find in the surface fracture propagation of the weld metal and HAZ, as striations formation which present local variations on its distribution. Finally, we can observe that there is not similitude between failure zone of the weld metal and HAZ. In the first case the final rupture is caused by the overload with very little deformation. However, in the second case the failure zone has been delimited by a transition between cleavage (fatigue crack) and dimples (overload crack).

4. CONCLUSION

The experimental results reported in this work provide the means to observe and quantify the effect of fatigue crack growth on 6061-T6 aluminum alloy welds obtained by MIEA. In this context, it has been observed that mechanical properties and microstructural conditions have a very important effect on crack growth. These conditions present a critical point in terms of the stress intensity factor $\sim 15 \text{ MPa m}^{1/2}$. It means that under this value the crack growth of the base metal are faster than weld metal and HAZ. However above this value the weld metal has the worst conditions (crack growth), followed by HAZ and base metal (6061-T6).

5. REFERENCES

- [1] Gladman T. *Precipitation Hardening in Metals, Materials Science and Technology*, vol. 15, pag. 30-36, 1999.
- [2] Gupta A.K, Lloyd D.J and Court SA. *Precipitation hardening in Al-Mg-Si alloys with and without excess Si*. *Materials science and engineering A*, 316, pag. 11-17 2001.
- [3] Malin V. *Study of metallurgical phenomena in the HAZ of 6061-T6 aluminium welded joints*. *Welding Journal* 1995; vol. 74: 305s-18s.
- [4] Ambriz R.R, Barrera G, Garcia R and Lopez V.H. *A Comparative Study of the Mechanical Properties of 6061-T6 GMA Welds Obtained by the Indirect Electric Arc (IEA) and the Modified Indirect Electric Arc (MIEA)*. *Materials and Design*, vol. 30, pag. 2446-2453, 2009.

[5] Ambriz R.R, Gerardo Barrera, Rafael García and López V.H. Microstructure and Heat Treatment Response of 2014-T6 GMAW Welds Obtained with a Novel Modified Indirect Electric Arc Joint. *Soldagem and Inspecao* 2008; vol. 13: 255-63.

[6] R.R. Ambriz, Mesmacque G, Ruiz A, Amrouche A and López V.H. *Effect of the welding profile generated by the modified indirect electric arc technique on the fatigue behavior of 6061-T6 aluminum alloy*. *Materials science and engineering A*, in press, 2009.

[7] Ambriz R.R, Barrera G and García R. *Aluminum 6061-T6 Welding by Means of the Modified Indirect Electric Arc Process*. *Soldagem and Inspecao*, vol. 11, pag. 10-17, 2006.

[8] ASM. *Properties and Selection: Nonferrous Alloys and Special-Purpose Materials*, 1992.

[9] Myhr O.R, Grong O, Fjaer H.G and Marioara C.D, *Modelling of the Microstructure and Strenght Evolution in Al-Mg-Si Alloys During Multistage Thermal Processing*. *Acta Materialia*, vol 54, pag. 4997-5008, 2004.

[10] Dutta I and Allen S.M. *Calorimetric Study of Precipitation in Comercial Al Alloys*. *Journal of Materials Science Letters*, vol 10, pag. 323-326, 1991.

Experimental and Numerical Analysis of Fatigue Life Improvement Techniques in Welded Joints of Stainless Steels

BAPTISTA, R.* , INFANTE, V.** , BRANCO, C.M.**

*Department of Mechanical Engineering, Escola Superior de Tecnologia de Setúbal (IPS)
Campus do IPS, Estefanilha, 2910-761 Setúbal, Portugal

*Corresponding author email: r.baptista@est.ips.pt

**ICEMS/IST, Lisbon University of Technology, Av. Rovisco Pais, 1049-001
Lisbon, Portugal

Abstract

This paper presents fatigue life improvements results obtained in two types of stainless steels: Duplex S31803 and Austenitic 304L. The objectives were to compare the fatigue behavior in terms of environment (air and 3% NaCl) and weld toe treatment (as welded, toe grinding, PPAW Dressing and Hammer Peening).

The tests were carried out in tension on cruciform specimens with a constant amplitude fatigue cycle of $R=0.1$. When available these results were also compared with results obtained in the literature. Using an elasto-plastic material model and the finite element analysis, all the experimental tests were simulated, including all the weld toe treatment conditions, and the fatigue life of these specimens was predicted.

Measurements of the radius of curvature (weld toe radii) and weld toe angle were obtained in the as welded, toe grinding, PPAW dressed and hammer peened specimens, in order to more accurately predict their fatigue life. The variations in fatigue life are basically due to changes in residual stress and weld toe geometry at the weld toe zone.

Experimental and numerical results were compared, in terms of the S-N curve parameters, fatigue strength gain for a 10^5 and 10^7 cycles life and fatigue life improvement for several nominal load setups.

Key-words: Fatigue Life; Improvement; Experimental tests; Finite Element Analysis; Weld Toe Grinding; PPAW Dressing; Hammer Peening

1 Introduction: Background

Fatigue life improvement techniques are very important today, because it is imperative to increase the fatigue life of welded structures, while decreasing the global cost of producing maintaining them.

Most of the fatigue life improvement techniques were established in the 1960's and early 1970's. A number of investigations have confirmed the benefit to be gained from improvement techniques, and large increases in the fatigue strength are usually obtained. In spite of this, some reluctance has been observed towards the introduction of improvement techniques into design recommendations and only recently one method, weld toe grinding, has been allowed for in the design of offshore structures [1] and pressure vessels [2]. TIG and plasma dressing can be even more effective than grinding [3] and [4], but there is limited work to support this trend and, therefore, additional work is needed.

Fatigue life improvement techniques rely on extending the initiation phase, by reducing the severity of the weld toe details or introducing a compressive residual stress field [5]. Improvement techniques also reduce the crack propagation speed; which increases the total fatigue life of the structure. In a review recently presented by Maddox [6], conclusions and recommendations were defined for hammer peening which is now part of an official IIW document of Commission XIII [7]. The authors also have actively worked on techniques like

hammer peening and burr grinding, presenting their results on [8], [9] and [10].

The present paper reports the fatigue results obtained in [11], where the influence of fatigue life improvement techniques like the weld toe burr grinding, PPAW dressing or hammer peening, is covered over two different types of stainless Steels (Austenitic 304L and Duplex S31803 type, welded by TIG and MAG processes), and two different environments (air and aerated 3% NaCl solution).

The weld toe burr grinding, [12], is based on removing surface material from the weld toe, increasing the weld toe radii and consequently reducing the severity of this detail. The technique also reduces the residual stress field resulting from the welding process. While the PPAW dressing, [13], is based on refusing the weld toe, using the Powder Plasma Arc Welding technique to remove possible defects and increasing the weld toe radii. Finally the hammer peening technique, [14], [15] and [16] not only increases the weld toe radii as it is also based on the introduction of a compressive residual stress field, on the weld toe.

2 Experimental Details

2.1 Material and Specimens

There are two materials in study within this work, both Stainless Steels, the first one is referred as Duplex Type S31803 (DIN 1.4462) and the second one is referred as

Austenitic Type 304L (SAE 30304L, DIN 1.4306). In Table 1 and Table 2 the chemical composition of the materials can be found. Table 3 give us the normal tensile properties of both steels, becoming clear that while the duplex is more stress resistant, with 789 MPa of ultimate normal stress, the 304L steel has a much higher strain limit, showing a 52% elongation at break point.

Both Steels were received in as welded condition, with a plate thickness of 10 mm and the specimen geometry can be found in Figure 1.

Table 1 Chemical Composition of Duplex S31803 Stainless Steel

C	Si	Mn	P	S	Cr
0.024	0.220	1.550	0.023	0.002	22.400
Mo	Ni	N	Al	Cb	Cu
2.980	5.700	0.157	-	0.130	0.090

Table 2 Chemical Composition of Austenitic 304L Stainless Steel

C	Si	Mn	P	S	Cr
0.027	0.320	1.230	0.024	0.003	18.100
Mo	Ni	N	Al	Cb	Cu
0.480	8.200	-	-	0.11	0.31

Table 3 Tensile Properties

Steel	$\sigma_{0.2\%}$ [MPa]	$\sigma_{1\%}$ [MPa]	σ_R [MPa]	ϵ_R [%]
304L	256	280	698	52
S31803	478	-	789	34

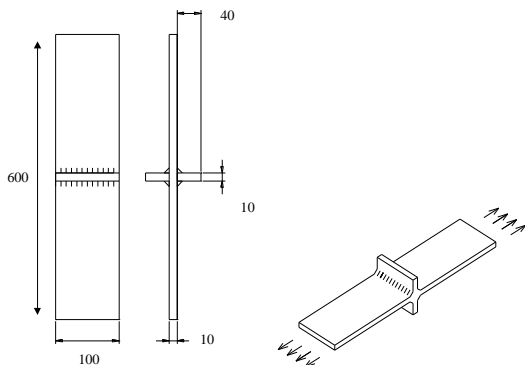


Figure 1 Transverse fillet weld joint

Measurements of the radii of curvature and weld toe angle were obtained for both Steels, in an as welded condition and after weld toe grinding, PPAW dressing and hammer peening (Figure 2 a) and b)). These measurements were made using an X-Y coordinate table, fitted with a video camera and monitor. The system has an accuracy of one micron, and is fitted with a special built-in facility to measure radii and angles.

On Table 4 it is possible to see the mean value obtained for the radii and the weld toe angle for the duplex Stainless Steel, welded by MAG, where the radii mean value measured starts from 1.645 mm in a as welded condition, increases to 5.605 mm after weld toe burr grinding, 6.412 mm after PPAW dressing and only to 2.420 mm after the weld toe is hammer peened. It is also possible to check that the PPAW dressing produces

a smaller weld toe angle on this material. Finally on Table 5 the analysis to the 304L Steel shows a more relevant increase in the weld toe radii after the hammer peening process, while the angle it is not affected by any fatigue life improvement technique.

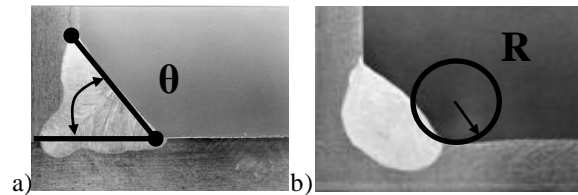


Figure 2 a) Weld toe tangent angl; b) Weld toe radii

Table 4 Weld Toe Radii and Angle values for the Duplex Steel (MAG)

	As Welded		Burr Grinded	
	Radii [mm]	Angle [°]	Radii [mm]	Angle [°]
Mean	1.645	38.238	5.605	
St. Dev.	0.630	5.310	0.869	
#	488	280	88	
	PPAW Dressed		Hammer Peened	
	Radii [mm]	Angle [°]	Radii [mm]	Angle [°]
Mean	6.412	33.395	2.420	
St. Dev.	1.612	3.333	0.683	
#	48	44	64	

Table 5 Weld Toe Radii and Angle values for the 304L Steel (MAG)

	As Welded		Burr Grinded	
	Radii [mm]	Angle [°]	Radii [mm]	Angle [°]
Mean	2.240	42.556	3.876	
St. Dev.	0.906	3.470	0.568	
#	400	256	64	
	PPAW Dressed		Hammer Peened	
	Radii [mm]	Angle [°]	Radii [mm]	Angle [°]
Mean	5.192	42.494	4.253	
St. Dev.	2.146	3.593	1.628	
#	112	112	40	

A total of 2448 measures show that the previous study can correctly characterise the weld toe geometry of the fatigue tested specimens and will be used not only to analyse those results, as recommended by Branco on [17] and [18], but most importantly to correctly model a finite element analysis of every fatigue life improvement technique.

2.2 Residual Stress Values

The influence of the weld toe grinding, PPAW Dressing and the Hammer Peening techniques was also characterized measuring the residual stresses at the weld toe. This was done using the X-Ray diffraction technique. The weld toe grinding technique decrease the residual stress level in the weld toe, introducing compressive residual stresses (Table 6). This is a beneficial effect leading to a higher fatigue life as the increase in the weld toe radii. Residual Stresses move from 76 MPa in the longitudinal direction on the Duplex Steel to - 200 MPa, and from - 71 MPa to - 196 MPa on the 304L Steel, on the weld toe. When the same results are analyzed for the weld toe PPAW Dressing technique, on can see that the residual stresses are not always decreased, in fact the increase from - 71 MPa to 10 MPa on the weld toe of the 304L Steel in the longitudinal direction and from 7 MPa to 05 MPa on the transverse direction. This is a result of a new thermal cycle that is applied to the material when the weld toe is dressed and the corresponding procedure should be revised. As expected the hammer peening technique is the one that allows obtaining the highest compression residual stresses. On the weld toe of the Duplex steel, on the longitudinal direction, the residual stress moves from 76 MPa to - 485 MPa, and from - 78 MPa to -524 MPa in the transverse direction. As a less resistance steel, the residual stresses on the 304L only manage to decrease to - 276 MPa and - 98 MPa, in the longitudinal and the transverse directions of the weld toe respectively.

Table 6 Residual Stresses obtained by X-Ray Diffraction (cont.)

Specimen	Value [MPa]			
	1.0 mm Longitudinal	1.0 mm Transverse	0.0 mm Longitudinal	0.0 mm Transverse
Duplex (MAG) As Welded			76 ± 13	-78 ± 21
Duplex (MAG) Burr Grinded	42 ± 6	-203 ± 17	-200 ± 30	-118 ± 31
Duplex (MAG) PPAW Dressed			-16 ± 29	-88 ± 52
Duplex (MAG) Hammer Peened	-269 ± 9	-162 ± 18	-485 ± 31	-524 ± 26
304L (MAG) As Welded			-71 ± 9	7 ± 5
304L (MAG) Burr Grinded			-196 ± 55	-163 ± 20
304L (MAG) PPAW Dressed			10 ± 10	95 ± 20
304L (MAG) Hammer Peened	-216 ± 21	-89 ± 16	-276 ± 22	-98 ± 5

2.3 Fatigue tests

The fatigue tests were carried out under constant amplitude loading in a ± 250 kN capacity servo hydraulic fatigue test machine. The frequency was 6-12 Hz and the stress ratio R=0.1, for every fatigue test (including the corrosion fatigue tests) in order to assess the influence of the test environment. Therefore the

frequency used in the corrosion fatigue tests may be considered high, but it was maintained between 6-12 Hz in order to equal to the frequency used in the normal fatigue tests. The bulk of the tests were carried out until complete failure of the specimen or up to a number of cycles close to 10⁷, time when the fatigue test was stopped.

3 Results and Discussion

3.1 Fatigue Data in the Welded Joints

Figure 3 show the obtained S-N curves for every fatigue test condition on the MAG welded duplex steel, in a non corrosive environment. Therefore it is possible to compare the effect of the three fatigue life improvement techniques used vs. the as welded test condition. An analysis to the mean S-N curves shows that the best technique is the weld to burr grinding, including at higher nominal test loads, the S-N curve for this technique stays above the other ones. The hammer peening technique is the second best one, especially for lower loads, while the PPAW dressing can provide better results at higher stress fatigue life tests. Table 7 quantifies the gain (1) in fatigue life obtained for the several fatigue life improvement techniques used for both a 175 MPa and 300 MPa stress test, where one can see that the burr grinding technique makes the fatigue life increase 13 time, while the hammer peening makes it only 4.19 time better for the lower stress level. When a higher stress level is applied, the gain factor of the burr grinding technique decreases to 6.8.

$$Gain = \frac{N_{rTreated}}{N_{rAs Welded}} \tag{1}$$

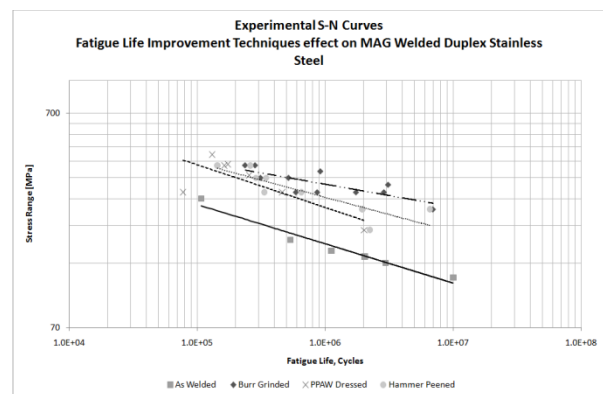


Figure 3 S-N curves experimentally obtained, for comparing the effect of several fatigue life improvement techniques on the duplex Steel

In fact one could expect to obtain better results with the hammer peening technique, especially because of the higher compression residual stresses introduced, but that fact is that the higher weld toe radii obtained with the burr grinding technique is more effective for a fatigue life increase.

Table 7 Gain factors for the fatigue life, obtained in the duplex steel

Specimen	ΔS [MPa]	Nr [Cycles]	Gain
As Welded	175	533843	
Burr Grinded	175	6954875	13.03
Hammer Peened	175	2237619	4.19
PPAW Dressed	175	2015486	3.78
As Welded	300	107287	
Burr Grinded	300	729374	6.8
Hammer Peened	300	491307	4.58
PPAW Dressed	300	461246	4.3

Table 8 compare the same results obtain with a corrosive environment, and as one would aspect the gain factor decrease considerably, to 5.54 when a 175 MPa stress level is applied to a burr grinded duplex steel specimen, and to 2.32 when the same test condition was subject of a 350 MPa stress level.

On Table 9 one can see the same analysis now applied to the 304L Steel when tested on a non corrosive environment, with a 225 MPa stress level. Again the burr grinding technique is more effective than the other two fatigue life improvement techniques, with a gain factor of 9.43, while the second best technique is now the PPAW dressing, with a 2.18 factor vs. a 1.17 factor for the hammer peening technique.

Table 8 Gain factors for the fatigue life, obtained in the duplex steel under a corrosive environment

Specimen	ΔS [MPa]	Nr [Cycles]	Gain
As Welded	175	1013402	
Burr Grinded	175	5616334	5.54
PPAW Dressed	175	2781915	2.75
As Welded	350	42929	
Burr Grinded	350	99546	2.32
PPAW Dressed	350	86715	2.02

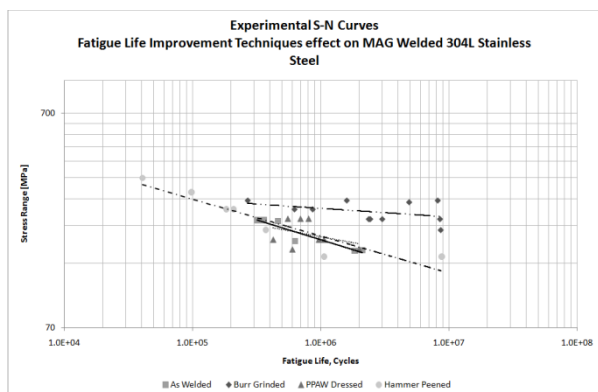


Figure 4 S-N curves experimentally obtained, for comparing the effect of several fatigue life improvement techniques on the 304L Steel

The previous results are seen on Figure 4 where the S-N curves for the four fatigue test conditions are plotted. Again the weld toe burr grinding is a clear winner vs. the as welded condition, while the other two techniques results are not so clear to check.

As a less resistant material, this stainless steel fatigue life improvement results are more limited on techniques that require plastic deformation, like the hammer peening, or thermal resistance like the PPAW dressing. Therefore the burr grinding technique that acts by removing a superficial layer of probably defective material, without deformation, is more effective on this steel.

Table 9 Gain factors for the fatigue life, obtained in the 304L steel

Specimen	ΔS [MPa]	Nr [Cycles]	Gain
As Welded	225	319382	
Burr Grinded	225	3012115	9.43
Hammer Peened	225	373408	1.17
PPAW Dressed	225	696217	2.18

3.2 Numerical Results

In order to numerically simulate the fatigue life test runs on every welded condition on study in this paper, a 1.125 mm wide slice specimen was model on the FEA program ABAQUS. The full specimen thickness was not model because the resources for numerically model the hammer peening technique are still too much to handle on a normal computer. Therefore in order to reduce the number of degree of freedom the specimen wide is reduced, fixing its lateral movement in order to simulate a plane strain state. Using the natural symmetry of the specimen only 1/8 was simulated, using model with 15'855 DOF, composed with C3D8R linear elements.

Every condition were simulated, the as welded, burr grinding and PPAW dressing techniques were modeled only by weld toe radii and angle changing, using the previously obtained values. No other effect was simulated, and therefore the stress range, medium stress and strain range, needed for the local approach method are easily obtain from the FEA simulations.

Finally the hammer peening technique was simulated using an elastic and deformable tool, also model with C3D8R linear elements that added 3'798 DOF to the original simulation. This 12 mm in diameter tool was simplified to represent only the extreme end of the full tool and the influence of its contact radius and position were also analyzed. A 800 N impact force was applied dynamically to the tool, after a experimental analysis of the hammer peening process. In this case 4 hammer peening runs, each one with 5 strokes per millimeter, where applied to the specimen.

As stated the fatigue life prediction was made using the Local Approach Method, [19], using the results obtain under the weld toe. Table 10 and Table 11 show the final results for fatigue life prediction on the MAG

welded duplex steel, using a 225 MPa and a 350 MPa Stress level. The calculated fatigue life's ranges from 434594 cycles, in a as welded condition, to 6193594 cycles when the weld toe is hammer peened, and a 225 MPa stress is applied to the specimen. This can be translated in to a 14.25 gain factor, which decreases to 3.61 when the stress level is increased to 350 MPa. But numerically the hammer peening technique is the one that gives us the best fatigue life improvement, unlike the experimental results. The second best technique is the PPAW dressing because the weld toe radii mean values experimentally obtained where larger.

Figure 5 shows the complete S-N curves for all the test conditions, and once again clearly the hammer peening technique is the one with the best results. Finally the influence of the weld toe radii is also visible on Figure 5, spanning the fatigue life from 100'000 cycles to 3'000'000 cycles, has the radii is increased using the data collected experimentally.

Table 10 Gain factors for the fatigue life ($\Delta S = 225$ MPa Stress range), obtained in the duplex steel by FEA and the Local Approach Method

Specimen	σ_m [MPa]	$\Delta\epsilon$ [μ]	Ni [Cycles]	Gain
As Welded	220.1	2020	434584	
Burr Grinded	175.9	1609	2047467	4.71
Hammer Peened	185.7	1969	6193594	14.25
PPAW Dressed	171.7	15700	2450755	5.64

Table 11 Gain factors for the fatigue life ($\Delta S = 350$ MPa Stress range), obtained in the duplex steel by FEA and the Local Approach Method

Specimen	σ_m [MPa]	$\Delta\epsilon$ [μ]	Ni [Cycles]	Gain
As Welded	200.7	3573	52442	
Burr Grinded	197.8	3188	135804	2.59
Hammer Peened	223.6	3327	189304	3.61
PPAW Dressed	196.2	3010	152273	2.90

Table 12 Gain factors for the fatigue life ($\Delta S = 225$ MPa Stress range), obtained in the 304L steel by FEA and the Local Approach Method

Specimen	σ_m [MPa]	$\Delta\epsilon$ [μ]	Ni [Cycles]	Gain
As Welded	138.9	1959	338933	
Burr Grinded	136.5	1745	494292	1.46
Hammer Peened	80.8	1745	517438	1.53
PPAW Dressed	135.1	1646	599171	1.77

For the 304L steel results are again shifted, on Figure 6, one can see that the hammer peening technique is no longer the best one. Numerically the best predicted technique is the weld toe PPAW dressing, while the hammer peening and the burr grinding lay not very far away. Table 12 and Table 13 show that the less resistant steel does not allow to obtain decreased medium stresses, and therefore the fatigue life predicted by the local approach method are smaller than one could expect. On the 304L steel is the weld toe radii the most

important factor for predicting the fatigue life, and therefore the value that should be higher.

Table 13 Gain factors for the fatigue life ($\Delta S = 350$ MPa Stress range), obtained in the 304L steel by FEA and the Local Approach Method

Specimen	σ_m [MPa]	$\Delta\epsilon$ [μ]	Ni [Cycles]	Gain
As Welded	200.7	3573	52576	
Burr Grinded	197.8	3188	73208	1.39
Hammer Peened	223.6	3327	63666	1.21
PPAW Dressed	196.2	3010	86857	1.65

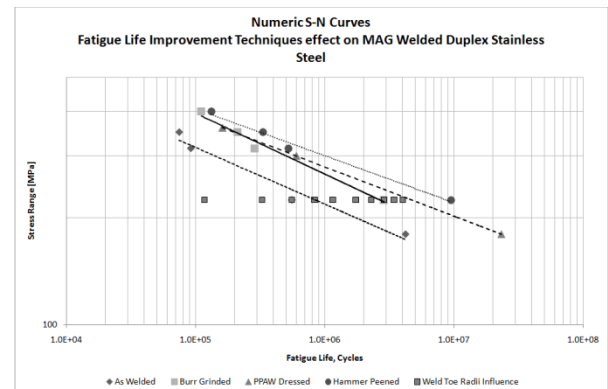


Figure 5 S-N curves numerically obtained, for comparing the effect of several fatigue life improvement techniques on the duplex Steel

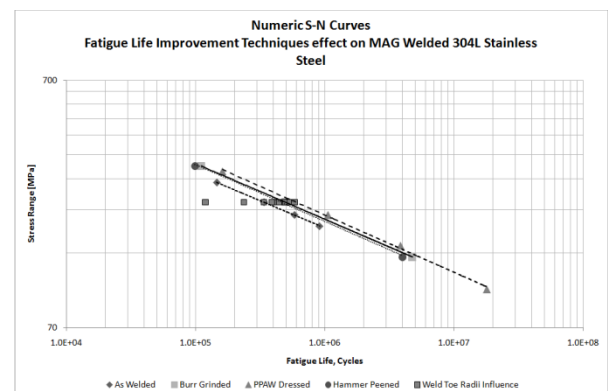


Figure 6 S-N curves numerically obtained, for comparing the effect of several fatigue life improvement techniques on the 304L Steel

4 Conclusions

- Fatigue life tests allow obtaining S-N curves for several combinations of specimen materials, welding process, and post welding fatigue life improvement techniques. Some of these combinations lead to problems, like fractures in the base material or near the grips;
- The hammer peening technique is more effective for higher loads testing conditions, while the weld toe burr grinding is more effective for lower loading conditions;

- For the 304L steel the same analysis can be made between the burr grinding and the PPAW dressing, which leads to the same conclusion;
- Under a corrosive environment, the duplex steel subjected to weld toe burr grinding has a gain factor that ranges from 1.00 to 5.54, which proves the highly efficiency of this technique;
- Under the same conditions the PPAW dressing technique is less efficient, with a 2.75 maximum gain factor;
- The most effective fatigue life improvement technique is the weld toe burr grinding, on both materials, and testing environments;
- Considering the higher resistance of the duplex steel, the fatigue life improvement results are better on this material, but all the obtained results reveal satisfactory gain factors;
- It is possible to model the fatigue life improvement techniques using a FEA program and the local approach method, especial the hammer peening technique.

ACKNOWLEDGEMENTS

The authors acknowledge: TWI for the financing of the "Improving the fatigue performance of welded steels", ECSC Contract 7210 – PR – 303.F3 project; The FCT for the PhD scholarship SFRH/BD/25984/2005 financing support.

REFERENCES

- [1] Offshore Installations; Guidance on Design, Construction and Certification, UK Department of Energy, HMSO, Fourth Edition, 1990.
- [2] "British Standard Specifications for Unfired Fusion Welded Pressure Vessels", BS5500, 1990, British Standards Institution, London, UK.
- [3] Booth, G.S. (ed.), "Improving the Fatigue Performance of Welded Joints", The Welding Institute, Cambridge, UK, 1999.
- [4] Haagensen, P.J., Slind, T., "Weld Improvement Methods and Fatigue Design Rules", Proc. Int. Conf. Fatigue and Welded Constructions, The Welding Institute, UK, 1987.
- [5] Huther, I, Lieurade, H.P., Sonissi, R., Nussbaumer, A., Chabrolin, B., Janosh, J.J., "Analysis of Results on Improved Welded Joints", *Welding in the World*, 37, 5, pp. 242-266, 1996.
- [6] Maddox, S.J., "The Application of Fatigue Life Improvement Techniques to Steel Welds", IIW Commission XIII Workshop on Improvement Methods, International Institute of Welding, Proc. 51st Annual Assembly, Hamburg, Germany, September 1998.
- [7] Haagensen, P.J., Maddox, S.J., "Specifications for Weld Toe Improvement by Burr Grinding, TIG Dressing and Hammer Peening for Transverse Welds", IIW Document, Commission XIII, Working Group 2, WG2, International Institute of Welding, 2001.
- [8] Infante, V., Branco, C.M., Baptista, R., Gomes, E.C., "Residual stresses and fracture mechanics analysis of welded joints repaired by hammer peening", Proc. 8th Portuguese Conference on Fracture, Vila Real, UTAD, Ed. SPM, Lisboa, pp. 339-354, Março 2002
- [9] Infante, V., Branco, C.M., Baptista, R. "Failure analysis of welded joints rehabilitated by hammer peening", Paper XIII 1892/01, IIW Meeting, July 2001, Ljubljana, Slovenia, Ed. International Institute of Welding
- [10] Infante, V., Branco, C.M. "A study on the fatigue behaviour of damaged welded joints repaired by hammer peening", Proc. ECF13, 13th European Conference on Fracture, San Sebastian, Spain, Ed. ESIS, 2001
- [11] TWI, "Improving the Fatigue Performance of Welded Stainless Steels", Final Report for contract No. 7210-PR-303, 2005
- [12] Haagensen, P., Maddox, S.J., "IIW recommendations for weld toe improvement techniques", Commission XIII, International Institute of Welding, July 2001
- [13] Marksmann, J. et al, "Powder plasma arc welding: a process with special applications", DVS-Berichte 194, 09/98, pp. 21.26
- [14] Infante, V., Branco, C.M., Baptista, R., "Fatigue Analysis of Welded Joints Rehabilitated by Hammer Peening", ICEMS/IST, Paper for IIW Meeting Ljubljana, Slovenia, 2001
- [15] Infante, V., Branco, C.M., "A comparative Study of the Fatigue Behaviour of Repaired Joints by Hammer Peening", Paper XIII-1836-2000
- [16] Dexter, R.J., Kelly, B.A., "Research on Repair and Improvement Methods", Proc. 50th Annual Assembly, San Francisco, EUA, WRC, 1997, pp. 74-97
- [17] Branco, C.M., Gomes, E., Infante, I., "Influência da Geometria do Pé do Cordão no Comportamento à Fadiga de Juntas Soldadas Melhoradas", Proc. 3as Jornadas Ibéricas de Fractura, Luso, Portugal, 27 a 29/03/96, Publ. Grupo Espanhol de Fractura, pp. 368-373, Madrid, 1996.
- [18] Branco, C.M., Gomes, E.C., "Fatigue Behaviour of Plasma and Pulsed TIG Joints", International Conference on Fatigue of Welded Components and Structures, SF2M, Senis, France, 12-14 June, pags. 131-138, 1996.
- [19] Dowling, N.E., "Fatigue at Notches and Local Strain and Fracture Mechanics Approaches", ASTM, STP 677, pp. 247-273, 1979

FATIGUE BEHAVIOUR OF AA6082-T6 ALUMINIUM ALLOY FRICTION STIR WELDS UNDER VARIABLE AMPLITUDE LOADING

J.D. Costa¹, J.A.M. Ferreira¹ and L.P. Borrego²

¹ CEMUC, Mechanical Engineering Department,
University of Coimbra, Rua Luís Reis Santos, Pinhal de Marrocos, 3030-788, Coimbra, Portugal.
E-mail: jose.domingos@dem.uc.pt.; martins.ferreira@dem.uc.pt.

² CEMUC, Mechanical Engineering Department,
Polytechnic Institute of Coimbra, Quinta da Nora - 3030, Coimbra, Portugal.
E-mail: borrego@isec.pt.

ABSTRACT

In addition to uncertainty such as material strength, notch geometries, defect contents and residual stresses, welded components are often subjected to variable amplitude service loads. In the case of friction stir welding of aluminium alloys, no data is available concerning fatigue behaviour under variable amplitude loading. The objective of this investigation is to determine the fatigue strength of friction stir welds in AA6082-T6 under constant and variable amplitude loading and analyse the validity of Miner's rule in this specific welding process. Fatigue tests were carried out in a servo-hydraulic testing machine using stress ratios of $R = 0$ and $R = -1$. Typified Gassner amplitude spectra were considered, using four values for the shape exponent. Microhardness tests were performed to characterize the Vickers hardness profile in the vicinity of the weld area. Friction stir welding process leads to a decrease of the static mechanical properties relatively to base material. Detailed examination revealed a hardness decrease in the thermo mechanically affected zone and the nugget zone average hardness was found to be significantly lower than the base alloy hardness. Welded specimens show significantly lower lives than base material specimens. For the welded specimens tested at a stress ratio $R=0$ a good agreement was observed between constant and variable fatigue loading, using the equivalent stress calculated by Miner's rule. For $R=-1$, Miner's rule seems to overestimate the fatigue life.

KEY WORDS: Friction Stir Welding, aluminium alloy, fatigue, variable amplitude loading.

1. INTRODUCTION

Friction stir welding (FSW) is a relatively new solid-state joining process and is very energy efficient, environment friendly, and versatile, being considered to be the most significant development in metal joining in a decade. Since its invention in 1991 at the Welding Institute (TWI) of UK [1], a large amount of research was carried out in several fields and different materials. Aluminium alloys are the materials more often studied and where this technique has shown a better performance. Comparative mechanical properties studies of base material and welded specimens, including fatigue strength tests have been performed by several authors [2-6].

In addition to uncertainty such as material strength, notch geometries, defect contents and residual stresses, welded components are often subjected to variable amplitude service loads. The lack of Miner's validity accumulation rule [7] has been demonstrated in many applications and, in consequence, its usage will introduce uncertainties which must be compensated by safety factors. In the case of friction stir welding (FSW)

no data is available concerning fatigue behaviour under variable amplitude loading

The objective of this work is to study the fatigue strength of friction stir welds under constant and variable amplitude loading and analyse the validity of Miner's rule for this specific welding process.

2. EXPERIMENTAL DETAILS

2.1 Preparation of welds

This research was conducted using the AA6082 aluminium alloy with a T6 heat treatment. The T6 heat treatment corresponds to a conversion of heat-treatable material to the age-hardened condition by solution treatment, quenching and artificial age-hardening. The alloy chemical composition and mechanical properties are shown in Tables 1 and 2, respectively.

The friction stir welds were performed in an aluminium plate with 4 mm thickness using a tool with a 5 mm diameter threaded pin and the shoulder had 16 mm diameter.

Table 1 - Chemical composition of AA6082-T6 aluminium alloy (wt%)

Si	Mg	Mn	Fe	Cr	Cu	Zn	Ti	Other
1.05	0.8	0.68	0.26	0.01	0.04	0.02	0.01	0.05

Table 2 - Mechanical properties of AA6082-T6 aluminium alloy

Tensile strength, σ_{UTS} (MPa)	300
Yield strength, σ_{YS} (MPa)	245
Elongation, ϵ_r (%)	9
Hardness, Hv,02	110

Welding parameters depend on several factors, namely, alloy type, penetration depth and joint. The following parameters were chosen in order to obtain welds with a good surface aspect and where no defects could be identified by microscopic observation: welding speed of 300 mm/min, tilt angle of 2°; rotating speed of 1500 rpm. Figure 1 is an example of the better succeeded welds concerning its surface aspect. In this weld sample, also a good penetration control of the shoulder was obtained. This is a very important aspect, because an excessive penetration will create a notch effect that could affect mainly the fatigue strength.

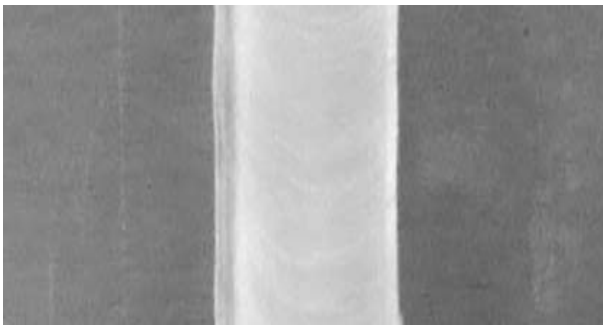


Figure 1. Surface aspect of a friction stir weld.

The penetration depth was adapted to fully penetrated butt joint. From each welded plate, the first 40 mm of the plate were not used in specimens preparation, in order to exclude possible deviation from steady state due to the typical lower temperatures during welding start. In order to analyse that no defects like root flaws, tunnel or kissing bond defects were present in the welds, cross-sectioning of the welds for metallographic analysis in planes perpendicular to the welding direction were also performed. The samples were prepared accordingly to standard metallographic practice and etched in order to enable the identification of the different weld zones. Figure 2a shows an example of a poor quality welded plate, presenting a tunnel defect size of about 0,6 mm, obtained before welding parameters optimization, while figure 2b shows the cross section of a welded plate welded with the parameters above referred, where no defects were observed by microscopy observation. The tunnel defects tend to appear in the advancing side of the nugget lower zone near the thermo-mechanically affected zone and

they are continuously formed in the weld direction. The size of these defects tends to be great at the start of the welding process due to lower temperature generally achieved.

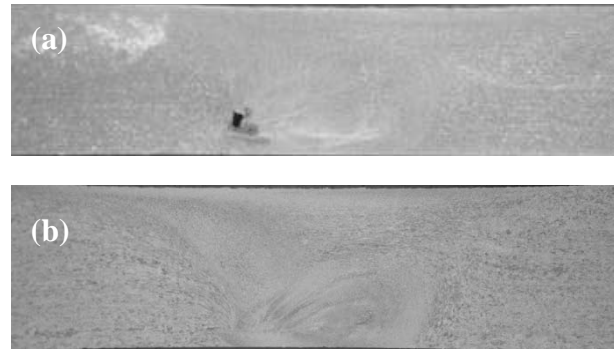


Figure 2. a) weld presenting a defect type tunnel; b) weld without defects identifiable by microscopy.

The majority of welds performed with only one passage leads to the presence of a tunnel defect formed mainly in the retracting side. Although, in some cases the tunnel defects observed had a size smaller than 30 μm , which did not influence static mechanical properties, the fatigue resistance was significantly affected. One way to avoid tunnel defects is increasing heat input by applying a higher axial force. However, an excess of axial force leads the formation of shear lips in the upper surface, creating stress concentration which also reduces fatigue life. It was realized to be very difficult to perform the correct optimization of all parameters. Therefore, to avoid the presence of the tunnel defects some welds were performed with two passages.

2.2 Fatigue details

Fatigue tests were carried out in a servo-hydraulic testing machine under constant and variable amplitude loadings. The dimensions of the fatigue specimens were 160x15x4 mm³ (length, width, thickness). The cut specimens (Fig. 3) were milled at the edges, and weld surface preparation was made only by grind removing the thickness exceeding material.



Figure 3. Photo of a fatigue specimen cut from welded plate before edges machining.

Specimens machined of plates where defects were identified, typically tunnel defects with less than 200 μm , were also tested in order to evaluate their influence on fatigue resistance. The weld was transverse to the stress axis in the S-N tests and to the material rolling direction. A sinusoidal load-time function was used, with the stress ratio R set to 0 and -1. The frequency was in the interval of 20–40 Hz depending upon the stress level. Life was defined as the number of cycles to

failure and a total of 57 specimens were tested. For the variable loading amplitude tests, typified amplitude spectra [8], according to equation 1, were considered, using four values for the shape exponent ν , namely, 1,5, 2, 4 and 5,

$$\log H_i = \left[1 - \left(\frac{S_{a,i}}{S_{a,max}} \right)^\nu \right] \log H_0 \quad (1)$$

where

- H_i cumulative frequency of load cycles for level $S_{a,i}$
- H_0 block size (number of cycles)
- ν shape exponent

Equation 2 specifies an additional number, the ‘spectrum shape factor’, SSF , that represents the distance (factor, life ratio) between an (arbitrary) Wohler S-N curve and the associated spectrum fatigue life curve (in Germany sometimes referred to as Gassner curve in honour of Ernst Gassner).

$$SSF = \log \frac{\sum n_i}{\sum n_i \left(\frac{S_{a,i}}{S_{a,max}} \right)^m} \quad (2)$$

Using the loading spectrum defined by equation 1, SSF can be more precisely calculated using the following equation

$$SSF = \log \frac{H_0}{\int_0^1 \frac{d}{dx} [-H_0^{(1-x)^\nu}] \cdot (x)^m dx} \quad (3)$$

where, $x = \frac{S_a}{S_{a,max}}$ (4)

SSF depends on the shape of the spectrum under consideration (parameters H_0 and ν) and the slope, m , of Wohler’s curve. Table 3 present SSF values for some ν values and a description of its typical applications. This factor was calculated using the Miner damage rule (without endurance limit), taking $H_0=10^6$ cycles and $m=5,5$

Table 3. Spectrum shape parameters ν and SSF for typified amplitude spectra: $H_0=10^6$; $m=5,5$.

ν	SSF	Description
∞	0	Constant amplitude loading
5	1,30	
4	1,56	$\nu > 2$ typical of bridge and crane structures
2	2,61	Stationary Gaussian process
1,5	3,14	
1	3,95	Typical for road roughness induced loads
0,8	4,39	$\nu < 1$ typical for wind gusts, wave actions, etc.

Figures 4 and 5 show the several variable loading amplitude spectra applied during fatigue tests. Figure 4 is the typical form of spectrum presentation where the normalized stress amplitude is plotted against the cumulative number of cycles, while in figure 5 a more intuitive way for spectrum interpretation is shown, depicting the number of cycles versus the normalized stress amplitude.

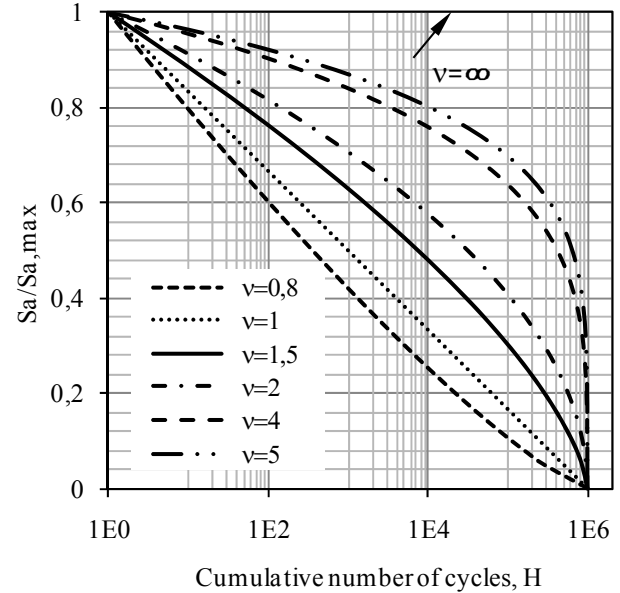


Figure 4. Typified amplitude spectra: normalized stress amplitude versus cumulative number of cycles ($H_0=10^6$ cycles).

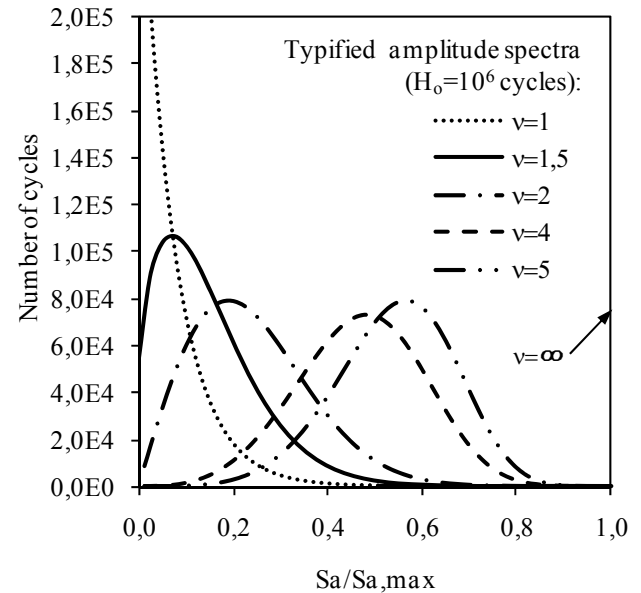


Figure 5. Typified amplitude spectra: number of cycles versus the normalized stress amplitude.

2.3 Microhardness details

Microhardness tests were performed to characterize the Vickers hardness profile in the vicinity of the weld area using a 2 N load. Measurements were performed along three lines: 0,5 mm far from both surfaces and at the

specimen middle thickness, in successive positions with 1 mm of distance.

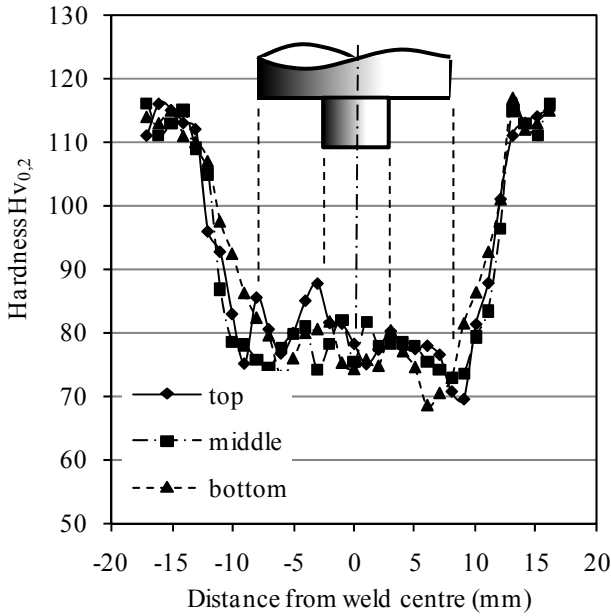


Figure 6. Hardness profiles measured along three lines.

This figure shows clearly a hardness decrease in the thermo mechanically affected zone and that the nugget zone average hardness is significantly lower than the base alloy hardness. Hardness profiles were measured in all plates. Microstructures hardness of the welds typically ranged between 70 and 80 HV_{0,2}, leading to a softening up to 60% relatively to the base material hardness (about 115 HV_{0,2}). The results show similar hardness profiles for the three measurement lines, although bottom measurements show that the lower hardness is restricted to a shorter zone.

3. RESULTS

Table 4 shows the mechanical properties of welded specimens obtained in tension tests. Compared with base material (table 2), friction stir welding process leads to a decrease of the material mechanical properties: yield and rupture stresses of friction welded specimens are significantly lower than for base material. Yield stress decreases 33% and the rupture stress decreases 20% relatively to base material values.

Table 4 - Mechanical properties of friction stir welds performed in AA6082-T6 aluminium alloy.

Tensile strength, σ_{UTS} (MPa)	241
Yield strength, σ_{YS} (MPa)	165
Elongation, ϵ_r (%)	6,8

Fatigue results obtained for the stress ratio $R=0$ under constant and variable amplitude loadings are plotted in figure 7. Fatigue data for constant amplitude loading were statistically analysed accordingly ASTM E739-91

Standard [9]. A low dispersion of fatigue data was obtained: the standard deviation was 0,04 for stress and 0,21 for fatigue life. This is a lower dispersion when compared with fatigue data obtained in tests of specimens welded by other processes. Fatigue data obtained with variable amplitude loading, using the equivalent stress range calculated accordingly to Miner's rule, are in the same scatter band of the constant amplitude loading results, indicating that Miner's rule gives real damage sum values near unity. The damage sum D ranged between 0,6 and 2 for the four spectra loadings. This conclusion is better visible in Figure 8 where the probability of occurrence is plotted against real damage sum values.

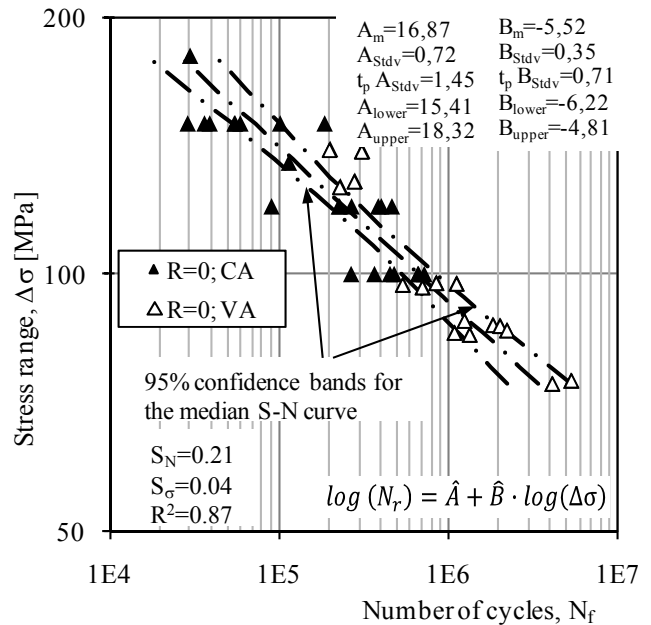


Figure 7. Wohler curves for $R=0$. Constant and variable amplitude loadings.

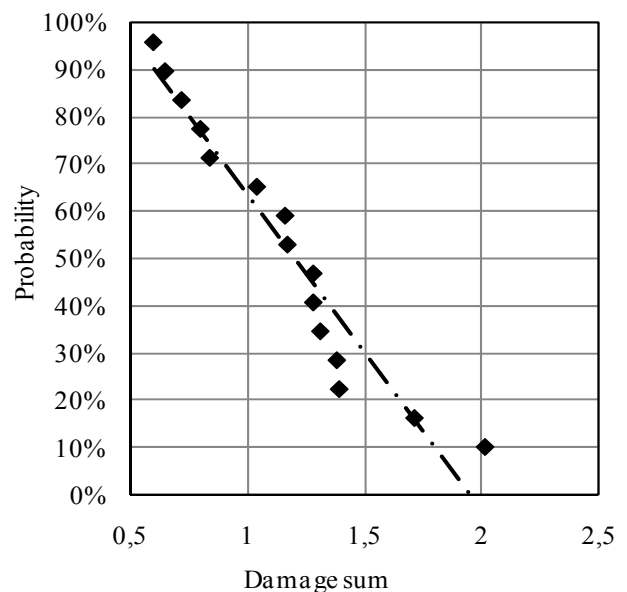


Figure 8. Real damage sum distribution.

Figure 9 compares fatigue results obtained with constant and variable amplitude loadings for the stress ratios $R=0$ and $R=-1$, plotting stress range against the number of cycles to failure. Data for variable amplitude loading and $R=-1$ were restricted to the shape exponent $\nu=2$.

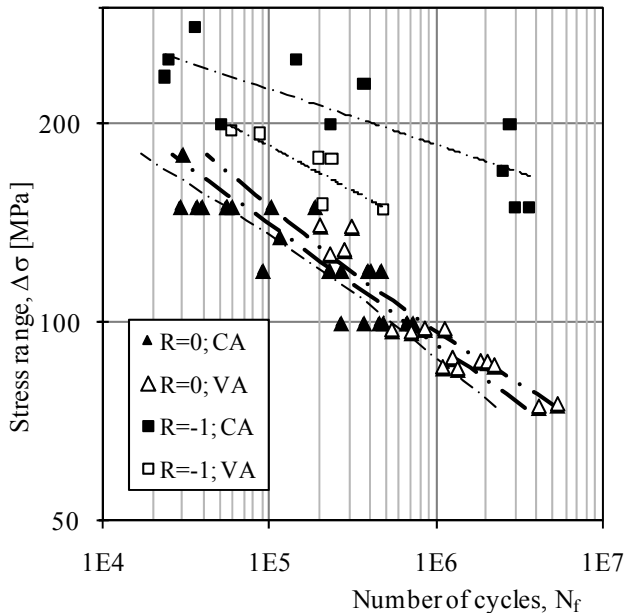


Figure 9. Wohler curves for $R=0$ and $R=-1$. Constant and variable amplitude loadings.

As expected, a significant influence of the mean stress was observed: for the same stress range, specimens tested with $R=-1$ present higher lives than specimens tested with $R=0$. For $R=-1$ fatigue data obtained under variable amplitude present lower lives than under constant amplitude loading, indicating that damage sum values are lower than unity for the majority of the tests. Therefore, Miner's rule seems to overestimate the fatigue life in the case of the stress ratio of $R=-1$. More tests are in course under variable amplitude loading for $R=-1$ and other spectrum shape exponents in order to confirm this trend.

Figure 10 shows the Wohler curve (stress range versus life) and Gassner curves (spectrum maximum stress range versus life) for $R=0$ and for several values of the spectrum shape exponent, ν . The graphical meaning of the SSF parameter is also indicated. It is clear that as ν increases the Gassner curve becomes more close to Wohler curve. As referred before $SSF=1$ when $\nu=\infty$.

Figure 11 compares fatigue results obtained in this work for $R=0$ under constant amplitude loading with results obtained by other authors [1,3] in welded specimens of the same alloy. S-N curves obtained with specimens welded by FSW, MIG and TIG processes as well as base material are superimposed in the figure for comparison. Design curve for full-penetration both-sided butt joint accordingly to Eurocode 9 (class 35-4) is also depicted in the figure.

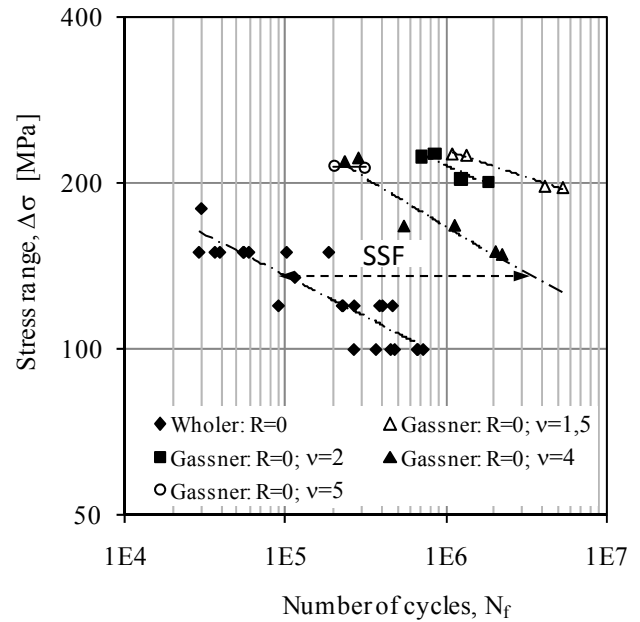


Figure 10. Wohler and Gassner curves for $R=0$.

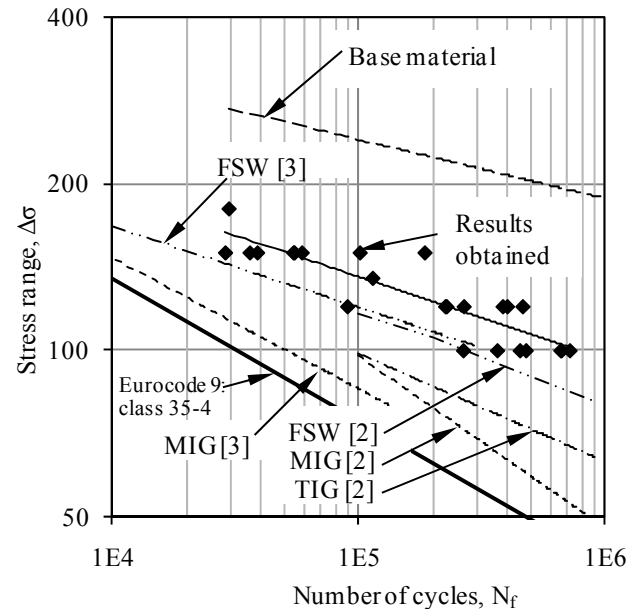


Figure 11. S-N curves for aluminium alloy AA 6082-T6 under constant amplitude loading, $R=0$.

Fatigue results obtained in this work are close with data obtained by other authors for this welding process. FSW specimens show higher fatigue resistance than specimens welded by the other two processes (MIG and TIG). However, the friction stir welded specimens presented significantly lower lives than base material. Figure 12 shows the two typical crack initiation modes identified by optical observation, from the tunnel defect (Figure 12a) or at surface near stress concentration due to shear lips (figure 12 b).

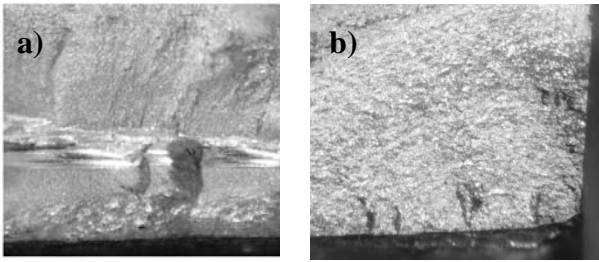


Figure 12. Fatigue crack initiation modes identified in welded specimens.

Tunnel defects revealed to be more detrimental on fatigue resistance than stress concentration due to shear lips. Therefore, to reduce the difference between FSW welds and base material fatigue strengths is crucial to avoid the presence of tunnel defects. The higher fatigue resistance was obtained when axial force during welding process was well controlled, leading to a smooth upper surface and performing two welding passages in order to eliminate completely tunnel defects. A small loss of hardness resulting from the second welding passage was observed, however fatigue resistance was not significantly affected.

Comparing with Eurocode 9 design curve, FSW welds are clearly in the safe side, indicating that a higher class than 35-4 can be attributed to butt joints welded by FSW, providing that a good control of welding parameters is performed in order to avoid severe internal defects and that stress concentration near shear lips is minimized.

4. CONCLUSIONS

Friction stir welding process leads to a decrease of the material mechanical properties: yield and rupture stress are lower than for base material. Detailed examination revealed a hardness decrease in the thermo mechanically affected zone and the nugget zone average hardness was found to be significantly lower than the base alloy hardness.

The friction stir welded AA6082-T6 specimens presented significantly lower lives than base material specimens. Tunnel defects and shear lips, formed mainly in the retracting side, lead to a significantly reduction of the fatigue lives. Tunnel defects revealed to be more detrimental on fatigue resistance than stress concentration created near shear lips. The higher fatigue resistance was obtained when the axial force was well controlled in order to obtain a smooth upper surface, and performing two welding passages to eliminate completely tunnel defects.

A good agreement was observed between constant and variable amplitude fatigue tests, plotting equivalent stress, calculated accordingly to Miner's rule, against the number of cycles to failure. The damage sum was

ranged between 0,6 and 2 for the stress ratio $R=0$ under the four spectra loadings analysed. For $R=-1$ fatigue data obtained under variable amplitude presented lower lives than under constant amplitude loading, indicating that damage sum values are lower than unity for the majority of the tests. Therefore, Miner's rule seems to overestimate fatigue life for $R=-1$.

REFERENCES

- [1] Thomas, W. M., Nicholas, E. D., Needham, J. C., Much, M. G., Templesmith, P. und Dawes, C. J., G. B. patent application No. 9125978.8 (December 1991)..
- [2] Ericsson, M., and Sandstrom, R., Influence of welding speed on the fatigue of friction stir welds, and comparison with MIG and TIG. *International Journal of Fatigue* 25 (2003)1379–1387
- [3] Moreira, P.M.G.P, Jesus, A.M.P, Ribeiro, A.S. and Castro, P.M.S.T. *Fatigue crack growth in friction stir welds of 6082-T6 and 6061-T6 aluminium alloys: A comparison*. *Theoretical and Applied Fracture Mechanics* 50-2 (2008) 1-91.
- [4] Lanciotti, A and Vitali, F. *Characterisation of friction stir welded joints in aluminium alloy 6082-t6 plates*. *Welding International* 17-8 (2003) 624-630.
- [5] Kobayashi, Y., Sakuma, M., Tanaka Y and Matsuoka K. *Fatigue Strength of Friction Stir Welding Joints of Aluminium Alloy 6082 Extruded Shape*. *Welding International* 21-1 (2007) 18–24.
- [6] Cavaliere, P., De Santis, A., Panella, F. and Squillace A. *Effect of welding parameters on mechanical and microstructural properties of dissimilar AA6082-AA2024 joints produced by friction stir welding*. *Materials and Design* 30 (2009) 609–616.
- [7] Miner MA. *Cumulative damage in fatigue*. *J Appl Mech* 1945;12: A159–A64.
- [8] Heuler P, Klatschke H. *Generation and use of standardized load spectra and load–time histories*. *Int J Fatigue* 27-8 (2005) 974–90.
- [9] ASTM E739-91, *Standard Practice for Statistical Analysis of Linear or Linearized Stress-Life (S-N) and Strain-Life (ϵ -N) Fatigue Data*. E08.04, Book of Standards, vol. 03.01, Wset Conshohocken, USA.

THERMAL INFLUENCE OF WELDING PROCESS ON STRENGTH OVERMATCHING OF THIN DISSIMILAR SHEETS JOINTS

M. Iordachescu¹, J. Ruiz-Hervias¹, D. Iordachescu², A. Valiente¹, L. Caballero¹

¹Materials Science Department, E.T.S. de Ingenieros de Caminos, Canales y Puertos, Universidad Politécnica de Madrid, C/Professor Aranguren s/n, 28040 Madrid, España
E-mail: miordachescu@mater.upm.es

²Centro Láser-UPM, Universidad Politécnica de Madrid
Campus Sur U.P.M. (Edificio “La Arboleda”), Ctra. De Valencia, km 7,3, 28031 Madrid, Spain
E-mail: danut.iordachescu@upm.es

ABSTRACT

The investigation addresses the overall performance of black and white joints (BWJ) of low carbon steel and stainless steel thin sheets achieved by laser hybrid welding. First, thermal field modelling is carried out by considering Goldak’s double ellipsoidal heat source model, together with a contribution of the authors related to the shape coefficients. In parallel, the technological development of BWJ laser hybrid welding is also addressed. Material characterisation by means of macro and microstructural examination and hardness tests is performed. The overall tensile performance of BWJ is discussed together with the weld metal strength overmatching. The tensile tests results indicate that in case of transversally loaded joints, the positive difference in yield between the weld metal and the base materials protects the weld metal from being plastically deformed; the flat transverse tensile specimens loading up to failure reveals large strains in low carbon steel, far away from the weld.

KEY WORDS: Black & White Joint, laser hybrid welding, overmatching joint, hardness, tensile test.

1. INTRODUCTION

The most common issue in dissimilar metals welding (DMW) is due to the differences in the physical properties (mainly the coefficient of thermal expansion and heat conductivity) of the base metals, as well as on certain level of metallurgical incompatibility. The weld thermal cycle produces differently featured heat affected zone (HAZ), accompanied by microstructural changes in the engineered microstructure, which may lead to an important loss of joint quality. Despite several reported weld-related failures, DMW is often used in chemical and petrochemical industry (reactors, tubes and pipelines), and in power generation, including nuclear plants (nuclear steam generator channel heads, pressurized water reactors, tube sheets and reheat piping).

Such joints may involve the combination of low carbon steel (white ferrite) and stainless steel (black austenite) known as “black and white joints” (BWJ) [1]. First, research was focused on the temperature influence on BWJ of thin sheets. This is emerging nowadays due to cost saving and satisfactory service performance. Results of this theoretical approach were used to develop Laser-GMA hybrid welding (LHW) for achieving BWJ. This process combines the advantages of both laser and GMA welding, namely fast welding

speed, low heat input, small HAZ and large weld aspect ratio (depth to width) [2]. Substantial differences in strength properties of the base metals and of the fusion zone (FZ) of the LH joints inevitably occur due to the high thermal gradients characterising this welding process. This might be explained by the carbon diffusion and formation of harmful constituents [3].

An adequate LHW technology development was based on the thermal field modelling; the temperature influence on the metals dilution and a suitable filler metal selection was addressed using Schaeffler Constitution Diagram. In addition, for an in-depth understanding of the processing temperature influence, detailed macro and microstructural examination of the BWJ and related micro-hardness analysis were performed. Finally, the overall tensile performance of BWJ was experimentally assessed, and the weld metal strength overmatching was discussed.

2. THEORETICAL APPROACH

2.1. Thermal simulation

The FE thermal simulation of the dissimilar plates butt welding was carried out using an elliptical disk moving heat source model [4, 5]. Two plates of low carbon steel and stainless steel of equal sizes (200 mm x 300 mm

and 3 mm thickness) were considered. The heat transfer in the plates was modelled as 2D heat transfer problem using SHELL element group type (*Element Group: SHELL 4, Elements: 6240*). The temperature influence through thickness was neglected; 4-noded quadrilateral elements were used for the plate's discretization together with the mesh refining in the welding area, allowing the accurate prediction of temperature distribution at specific time steps.

Considering a welding efficiency of 70%, the finite element analysis uses the heat input value of 4600 W and the welding speed of 3 m/min. The elliptical disk heat source parameters estimated values were: $a = 2.5$ mm, $c_f = 3$ mm, $c_r = 9$ mm. Consequently, the proportion coefficients for heat apportionment in the front and rear side of the welding pool values were: $f_f = 0.5$ and $f_r = 1.5$.

Table 1. Chemical composition, [%]

	C	Mn	Si	Cr	Cu	Ni	S	P
LCS	0.155	0.6	0.25	0.17	0.04	0.02	0.035	0.029
SS	0.022	1.81	0.41	18.1	0.33	9.2	0.08	0.025

Table 2. Low carbon steel, St37-2 - thermal conductivity λ , mass density ρ , and specific heat capacity c_p

St37-2 Temp. [°C]	λ [W/m·°C]	ρ [kg/m ³]	c_p [J/kg·°C]
20	48.07	7850	465
200	43.89	7770	527
400	38.04	7700	606
500	35.53	7670	685
600	31.77	7630	761
700	29.26	7610	936
800	25.50	7590	685
1000	28.01	7510	618
1300	31.35	7400	644
1600	34.28	7100	840

Table 3. Stainless steel, AISI 304L - thermal conductivity λ , mass density ρ , and specific heat capacity c_p

St37-2 Temp. [°C]	λ [W/m·°C]	ρ [kg/m ³]	c_p [J/kg·°C]
20	15.93	7920	510,7
200	17.21	7840	523,3
400	20.11	7750	540
500	21.74	7710	552,6
600	23.84	7660	569,4
700	25.58	7610	548,4
800	26.74	7560	586,1
1000	28.02	7460	598,7
1300	32.35	7310	611,2
1600	36.37	7210	619,6

The heat source model consider the heat flux losses by convection and radiation; thus, during the FE analysis, a

convection heat transfer coefficient of 15 W/m²K, the radiative emissivity of 0.7, and the Stefan-Boltzmann constant of 5.67 x10⁻⁸ W m⁻²K⁻⁴ were used.

The chemical composition of the base metals, low carbon steel (LCS) and stainless steel (SS), is presented in Table 1. Tables 2-3 contain the other materials thermo-physical data used into the finite element analysis [6, 7]. The melting temperature range is $T_{AISI\ 304L} = 1400 - 1450^\circ\text{C}$ for stainless steel and $T_{St\ 37-2} = 1430 - 1500^\circ\text{C}$ for the low carbon steel.

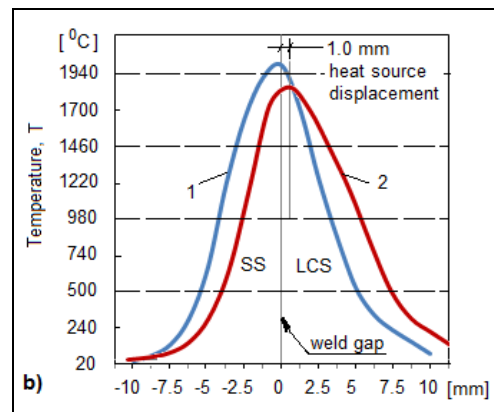
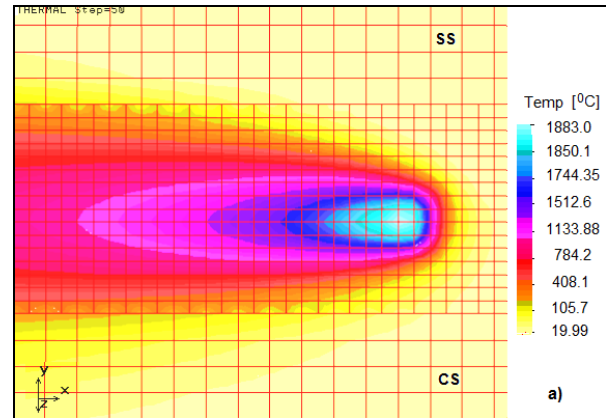


Figure 1. Temperature field on AISI 304L – St 37-2 (SS-LCS) welding: a) The heat source longitudinal axis was displaced 1 mm from the weld gap, on LCS; the welding quasi-stationary phase is corresponding to a weld time of 4s; b) Temperature transverse variation: 1 – the heat source longitudinal axis coincide with the weld gap; 2 – the heat source longitudinal axis is moved on LCS.

Figure 1a illustrates the numerical results of the thermal analysis corresponding to the welding process quasi-stationary phase, captured after a weld time of 4s. It can be noticed an emphatic asymmetry of the temperature field (related to the welding direction), as a result of different thermal properties of the base metals and of the heat source displacement of 1mm on LCS side.

Figure 1b shows the differences on temperature transverse variation in case of 1mm parallel displacement of the heat source from the weld gap; LCS participation at the weld joint formation increases and a

larger HAZ is formed on its side. Moreover, due to the base metals differences in thermal conductivity the process peak temperature decreases as well.

The thermal analysis indicate that the heat source parallel displacement at different distances from the weld gap critically influences the metals participation at the joint formation. This effect, less important in case of similar metal joining, might be very interesting, when a specific microstructure of the weld is requested.

2.2. Temperature distribution and base metals participation at joint formation

Asuming that weld obtaining, without using a filler metal, is influenced by the correspondent heat input on each base material, previous data of the temperature variation on the heat source transversal axis were used to estimate their apportionment at joint formation.

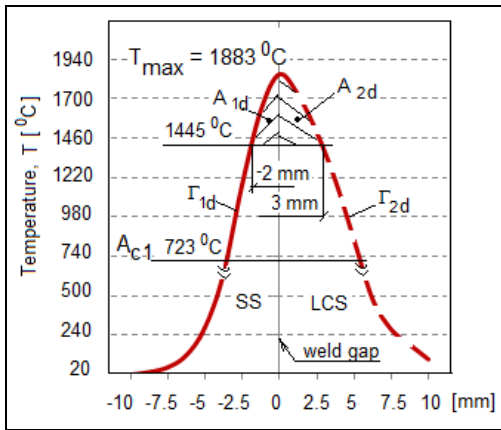


Figure 2. Estimated temperature transverse variation influence on dissimilar metals welding when the heat source longitudinal axis is moved on LCS; A_{1d} - area of heat source influence on SS; A_{2d} - area of heat source influence on LCS; Γ_{1d} - temperature distribution curves on SS; Γ_{2d} - temperature distribution curves on LCS.

As Figure 2 shows, on the temperature transverse variation chart presenting the case of 1mm parallel displacement of the heat source from the weld gap several parameters were defined: Γ_{1d}, temperature transverse variation curve in SS; A_{1d}, corresponding area of heat source influence in SS; Γ_{2d} temperature transverse variation curve in LCS; A_{2d} area of heat source influence in LCS. Previous numerical results of the thermal analysis in the temperature domain [A_{c1}, T_{max}] were considered for Γ curves estimation; the domain restriction, allowing better curves estimation, and errors reduction, respectively. Thus, two polynomial regressions of 3rd order were found:

$$\Gamma_{1d} = f_{SSd}(x) = -12.117 x^3 - 118.4 x^2 + 51.733 x + 1883 \quad (1)$$

$$\Gamma_{2d} = f_{LCSd}(x) = -1.1905x^3 - 15.303x^2 - 94.263x + 1883 \quad (2)$$

The areas of heat source influence were obtained by integrating the above Γ curves, on different x domains corresponding to each fusion zone width:

$$A_{1d} = \left| \int_{-x}^0 \Gamma_{1d}(x) dx \right| \quad x \in [-2; 0] \quad (3)$$

$$A_{2d} = \int_0^x \Gamma_{2d}(x) dx \quad x \in [0; 3] \quad (4)$$

Finally, it was assumed that the base metals dilution coefficients, K₁ and K₂ can be computed through the corresponding areas of heat source influence.

$$K_1 = \frac{A_{1d}}{A_{1d} + A_{2d}} \cdot 100 [\%] \text{ and } K_2 = \frac{A_{2d}}{A_{1d} + A_{2d}} \cdot 100 [\%] \quad (5)$$

The estimated dilution coefficients were 40% for SS and 60% for LCS.

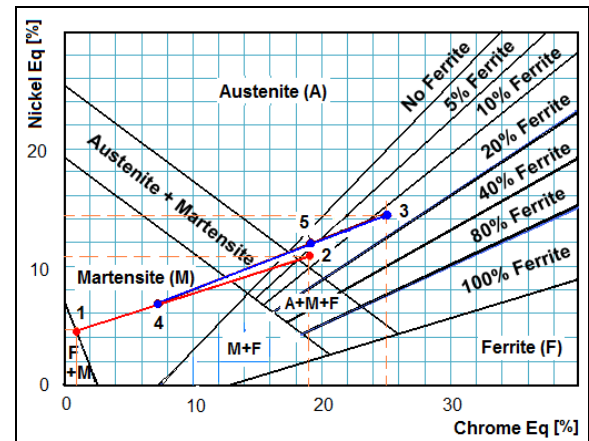


Figure 3. Estimated weld metal structure

The set of dilution coefficients together with the Schaeffler Constitution Diagram [8, 9] for stainless steel weld metal were further used for and adequate selection of the filler metal. Although nowadays WRC-1992 diagram is more accurate in predicting the ferrite content for many weld metals, Kou [8] has shown that Schaeffler Constitution Diagram is reasonable accurate for predicting the type of the weld metal constituents in case of dissimilar metal joining. In this diagram, Nickel and other elements that form austenite are plotted against Chrome and other elements that form ferrite, using the following formula:

$$Ni_{eq} = \%Ni + 30\%C + 0.5\%Mn \quad (6)$$

$$Cr_{eq} = \%Cr + Mo + 1.5\%Si + 0.5\%Nb \quad (7)$$

Thus, for St 37-2: Ni_{eq} = 4.972 and Cr_{eq} = 0.785, and for AISI 304 L: Ni_{eq} = 10.765 and Cr_{eq} = 18.715 (points 1 and 2 in Figure 3).

As shown in Figure 3, on the dilution line which couples the LCS point 1, and the SS point 2, is plotted the point 4, which estimates the weld metal constituents in case of 40% SS and 60% LCS dilution, previously found (eq. 5). The point indicates that without using a filler metal, the weld metal solidification, will be situated into the martensite region of the Schaeffler Diagram. This problem can be overcome if a higher alloyed austenitic filler metal is used.

Therefore, INTERFIL 309LSi filler wire was selected for future testing of the LHW process. The wire $Ni_{eq} = 14.24$ and $Cr_{eq} = 22.35$ couple calculus considers the chemical composition presented in Table 4.

Table 4. INTERFIL 309LSi filler metal chemical composition, [%]

C	Mn	Si	Cr	Cu	Mo	Ni	S	P	N
0.5	1.98	0.7	18.5	0.3	2.5	12.5	0.015	0.02	0.06

After plotting the wire representative point 3 and assuming the dissimilar base metals dilution of 30%, on the dilution line which couples the points 4 - 3, is plotted the point 5, which estimates the weld metal microstructure. It results that the predicted weld microstructure is a mixture of austenite with a small amount of ferrite, of about 5%. According to Berretta et al. [2] the Cr and Ni equivalent values of the point 5 are located in a region of the Schaeffler Diagram with less probability of defects formation in the weld. Lancaster [9] showed that a $\pm 4\%$ error might occur in the area of low ferrite content from the Schaeffler Diagram, which might produce the 5 point falling into the A+M+F domain.

3. EXPERIMENTAL RESULTS

3.1. Experimental procedure

The results from these theoretical approaches were applied for Laser-GMA hybrid single pass butt welding of low carbon steel, St 37, and stainless steel, AISI 304 L, plates (200 mm x 300 mm) of 3 mm thickness; INTERFIL 309LSi filler wire (1.2 mm diameter) and ARCAL*12 shielding gas were used. The Nd:YAG laser DY 033 (3300 W) focal point position relative to the upper side of the plates was -1 mm for the laser welding speed of 3 m/min. The GMAW source (Trans Puls Synergic 5000) parameters were: arc voltage, $V = 23$ V, welding current intensity, $I = 230$ A and wire feeding speed, $v_w = 8$ m/min.

The experiments involved the heating sources moving on LCS side, reproducing the thermal analysis case.

Standard procedures were used to prepare the metallographic and tensile specimens. Macro and microstructures of processed materials were analyzed by

optical microscopy after previous polishing and etching with Kalling no. 2 reagent. The bead shape measurements were made using an optical profilometer with an image analysis system. Vickers HV1 hardness measurements were made according to UNE EN ISO 6507. Tensile features of the base materials and of the welded joint were evaluated following the ASTM E-8M procedure.

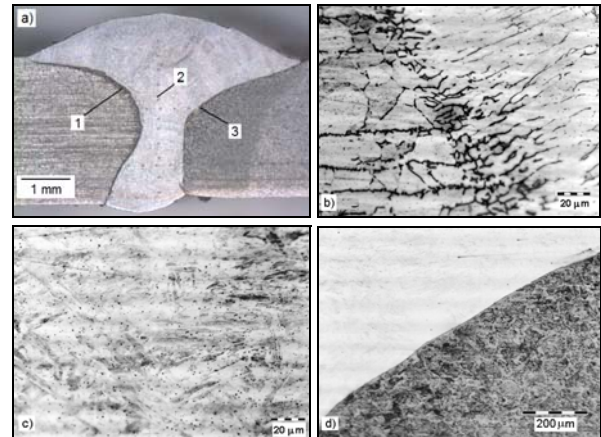


Figure 4. LHW of LCS-SS thin sheets: a) weld cross-section macrostructure; b) optical microstructure of the HAZ in SS and weld FZ; c) weld microstructure; d) optical microstructure of the FZ and HAZ in LCS.

3.2. Macro and microstructure features

The macrostructure of the LH weld cross-section is presented in Figure 4a; the geometry of the single pass LH weld being a combination of the appearance of laser and arc weld beads. The fusion zone shape, showing higher dilution of SS at the weld root is due to the metals differences in thermal conductivity (SS smaller conductivity comparing with the LCS) and heat reflexion on thin plates bottom side. LCS higher conductivity also explains the larger HAZ formation on its side, well illustrated by the weld cross-section macrostructure.

LH dissimilar joint features are presented in Figure 4b-d. Stainless steel HAZ (Figure 4b) shows the gradual transition from coarsened grains of austenite and vermicular ferrite dendrites up to the weld fusion line characterized by lacy ferrite.

Figure 4c illustrates the main weld bead microstructure as consisting essentially of martensite, as a consequence of increased carbon diffusion from LCS into the weld, dispersed δ -ferrite and small amounts of austenite. Due to increased dilution of LCS and laser processing welding speed, close to the SS fusion line (Figure 4b), the weld metal is formed by solidified fine columnar austenite between δ -ferrite epitaxial grown grains. Relatively good agreement was encountered between the weld microstructure experimentally found and the analytically predicted one; thus, compared with the

experiments, a 4% error on 7 point location in Figure 3, being obtained by evaluating the weld microstructure through the base metals dilution and Schaeffler diagram.

At the weld interface on the ferritic side, a darkly etched area with an adjacent decarburized narrow band was found (Figure 4d). St 37-2 carbon steel HAZ illustrate the transition from the grain coarsened microstructure region of Widmanstatten ferrite, bainite and acicular ferrite which follows the weld bead solidification front, up to the grain refined region.

Recent investigation of Shirzadi et al., [10], has shown that the martensite formation into the stainless steels weld bead might be capable of reducing the distortion of the weld. Therefore, the resulted weld microstructure obtained by moving the heat source longitudinal axis on LCS is beneficial for dissimilar thin sheets LH welds producing.

3.2. Joint mechanical characteristics

Several mechanical properties were used to characterize the dissimilar LH welds between LCS-SS. The goal was to ensure that the produced dissimilar LH weld is not the weakest component of a structure. In this view, pertinent mechanical tests as microhardness, and tensile tests were made.

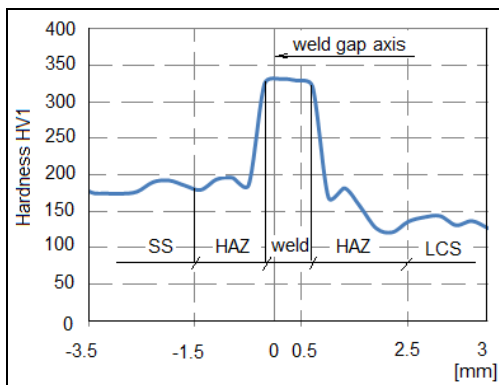


Figure 5. Microhardness profile on LHW dissimilar joint

The weld transversal hardness field features are presented in Figure 5. The microhardness of the weld bead is greater than of both AISI 304L and St 37-2 base materials; its overall average of 330 HV1 being characteristic of a combined austenitic-martensitic-ferritic structure, as the weld microscopy revealed and Missori, [11], previously reported.

The microhardness of the weld HAZs interface on both sides is less than that measured in the weld bead, but is higher than that found in the correspondent base metals. A peak value of 193 HV1 was found in the SS HAZ, on grown vermicular ferrite dendrites. Hardness measurements on the coarse grain microstructure of LCS HAZ showed maximum values of 156 HV1; this

maximum hardness value found in the LCS HAZ is comparable with the stainless steel hardness mean value of 160 HV1.

The resulted hardness profiles suggest that the weld overmatch in strength both base metals, recommending the laser-GMA hybrid welding variant, by using the heat source displacement on LCS part, for future usage in dissimilar joints producing.

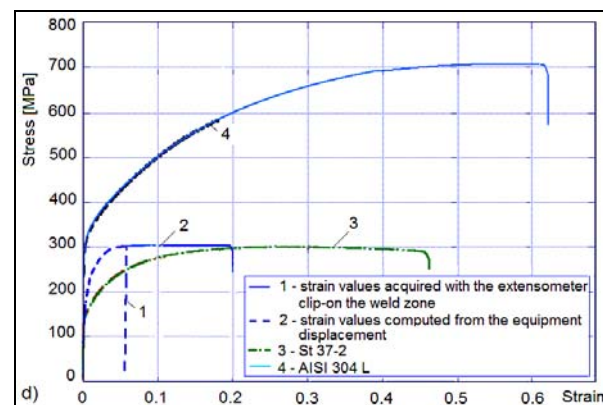
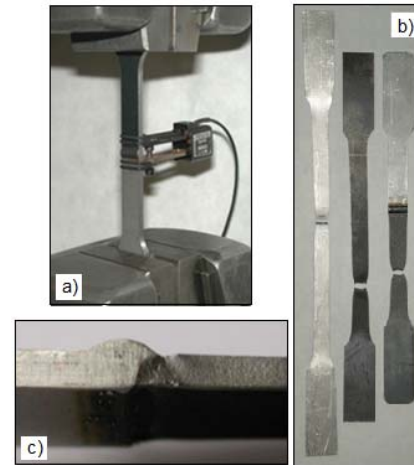


Figure 6. Tensile test results: a) extensometer clip-on position capturing the dissimilar joint; b) Flat transverse tensile specimens machined from the base metals and from the dissimilar joint; c) stiffening effect induced by the weld; d) stress-strain curves obtained by testing transverse tensile specimens of: 1- LH dissimilar (LCS-SS) welds with the extensometer clip-on position capturing weld; 2- LH dissimilar (LCS-SS) welds with strain values were computed from the machine; 3- St 37-2 (LCS) base metal; 4- AISI 304L (SS) base metal.

Transverse tensile tests (Figure 6a,c), in which the loading axis is perpendicular to the weld bead, were performed. The goal was to verify that the overload failure occurs in the lower strength base metal, rather than in the weld metal or HAZ. The test shows (Figure 6b,c) that the material starts to “flow” in the vicinity of the HAZ, in LCS, but the specimen fails far from the weld, in the base material.

Figure 6d show the stress-strain curves obtained from the flat transverse tensile specimens of the LCS-SS dissimilar joint, loaded under displacement control at 1 mm/min. Firstly, the strain values were acquired through an Instron 2620-602 extensometer capturing both sides of the joint HAZs and the fusion zone. Second, the nominal strain values were computed based on the overall displacement of the machine. Differences on specimen elongation found were due to the weld induced stiffening effect, of different magnitudes, produced by the joint heterogeneities. The joint (FZ and HAZ) nominal strain was 3.33 times smaller than the overall structural strain of 0.2.

Moreover, it was found that the stress-strain curve obtained from the flat transverse tensile specimens of the dissimilar joint lies between those of the similar joints of the constituent steels (Figure 6d). It is clear that these tests, do not give any information on the local mechanical properties of the weld regions, which were impossible to obtain, due to the small plate thickness and weld dimensions.

The investigation proved that LHW can be successfully applied for thin plates dissimilar welding of SS-LCS, even by moving the heat source longitudinal axis on LCS. In this particular case, the weld overmatching in strength both base metals was found from tensile tests, hardness profile and weld regions microstructures.

According to Davis [12], these strength-overmatched welded joints are designed to ensure the safe service of a welded structure by keeping the flaws, in an elastic weld metal, while the base metal starts to yield. Such an approach ensures that a welded structure can sustain local plastic deformation, important when temporary overloading or geometrical changes occur.

4. CONCLUSIONS

Transient thermal histories resulted from the finite element analysis were used to estimate the influence of the heat source displacement on the base metals dilution coefficients. Thus, the base metals dilution ratio was found and used for predicting the type of the weld metal constituents through the Schaeffler Constitution Diagram. A suitable filler metal chemical composition was selected for the experiments.

The results of the theoretical approaches were applied for Laser-GMA hybrid single pass welding of low carbon steel (St 37) and stainless steel (AISI 304) plates of 3 mm thickness. Macro and microstructural analysis revealed from the beginning that sound dissimilar joints were obtained. The presence of hard and brittle constituents as bainite, martensite and δ -ferrite justifies the microhardness increase in the weld region. In addition to the different thermo-physical properties of the base metals, the heat source moving to the higher

heat conductive material also explains the different dimensions of the HAZs; a narrower HAZ being found between the stainless steel and the weld.

The tensile tests results indicate that in case of transversally loaded joints, the positive difference in yield between the weld metal and the base materials (overmatching welds) protects the weld metal from being plastically deformed; Tensile tests up to failure revealed large strains in the low carbon steel side, far away from the weld. This is due to the strength overmatch, hardness profile and microstructures developed in the weld regions.

5. REFERENCES

- [1] Sun, Z., *Feasibility of producing ferritic/austenitic dissimilar metal joints by high energy density laser beam process*. Int. J. Pres. Ves. & Piping, vol. 68, 1996, pp. 153-160.
- [2] Berretta J.R., W. Rosi, M.D.M. Neves, I.A. Alameida, N.D.J. Vieira, *Pulsed Nd:YAG laser welding of AISI 304 to AISI 420 stainless steels*, Opt. Lasers Eng., vol. 45, 2007, pp. 960-966.
- [3] Scutelnicu, E., Iordachescu, M., Iordachescu, D. *Structural modifications in the heterogeneous welded joints*, Welding in the World, 2008, vol. 52 (SPEC. ISS.), pp. 185-189.
- [4] Goldak, J., Chakravarti, A., Bibby, M., *A new finite element model for welding heat source*. Metall. Trans. B 15B, 1984, pp. 299-305.
- [5] Iordachescu, D., Constantin, E., Georgescu, V., Iordachescu, M., *Antigravity arc welding processes and the weld geometry*. The Annals of "Dunarea de Jos" University of Galati, Fascicle XII, Year X-XI, 1999-2000, pp. 15-18
- [6] Rempe J.L., Knudson D.L., *High temperature thermal properties for metal used in LWR vessels*, J. Nucl. Mater., vol. 372, 2008, pp. 350-357.
- [7] Murugan S., Kumar P.V., Raj B., Bose M.S.C., *Temperature distribution during multipass welding of plates*, Int. J. Pres. Ves. Pip., vol. 75, 1998, pp. 891-905.
- [8] Kou, S., *Welding Metallurgy*, 2nd ed., New York: John Wiley & Sons, Inc., 2003.
- [9] Lancaster, J. F., *Metallurgy of Welding*, Cambridge: Abington Publishing, 1999.
- [10] Shirzadi A.A., Bhadeshia H.K.D. H., Karlson L., Withers P.J., *Stainless steel weld metal designated to mitigate residual stresses*, Sci. Technol. Weld. Join., 2009, vol. 14, no. 6, pp. 559-565.
- [11] Missori, S., *Weld metal microstructures on Dissimilar Steels Laser Beam Welded Joints*, Microsc Microanal 11(Suppl 2), 2005, pp. 1838-1839 (DOI: 10.1017/S1431927605500400)
- [12] Davis J.R., *Hardfacing, weld cladding, and dissimilar metal joining*, Metals Handbook, 1993, vol. 6, pp. 817-818.

FATIGA DE BAJO NÚMERO DE CICLOS (LCF) A ALTAS TEMPERATURAS DE TUBOS SOLDADOS DE INCONEL® 625

L. Iturrioz, M. Isasa, R. Rodríguez-Martín, I. Ocaña, M.R. Elizalde, A. Martín-Meizoso

CEIT y TECNUN (Universidad de Navarra)
Paseo de Manuel Lardizábal 15, 20018 San Sebastián
E-mail: iocana@ceit.es

RESUMEN

Las aleaciones base níquel son cada vez más utilizadas porque combinan una alta resistencia mecánica que mantienen a elevadas temperaturas y una excelente resistencia a la corrosión. Esta combinación de propiedades las convierte en candidatas como materiales de elección para diversas aplicaciones, entre las que las más extendidas son las aeronáuticas y las navales. Para asegurar su comportamiento en servicio se hace necesario el conocimiento, entre otras propiedades, de su comportamiento a fatiga a altas temperaturas.

En este trabajo se ha estudiado el comportamiento a fatiga de bajo número de ciclos (lcf) a altas temperaturas de trabajo (650 °C) de tuberías soldadas de una superaleación base níquel (Inconel® 625). Los resultados de los ensayos muestran una gran variabilidad en la vida de las diferentes muestras ensayadas, así como del comportamiento de las mismas durante los ensayos. Tras ensayarse, las muestras se sometieron a un análisis fractográfico que permitió identificar los factores geométricos y estructurales responsables de los comienzos de propagación.

PALABRAS CLAVE: Fatiga de bajo número de ciclos, soldadura, superaleaciones.

ABSTRACT

The use of Nickel based alloys is spreading because of their excellent combination of mechanical resistance at high temperature and to corrosion. This combination of properties makes these alloys the natural candidates for diverse applications (aeronautical and naval applications, among others). To assess their in-service behaviour a correct characterization of their mechanical properties is needed.

In this work the low cycle fatigue at high temperature of welded tubes made of a Nickel based superalloy (Inconel® 625) is studied. Results show a large variability in fatigue life and in behaviour during tests for the different samples. After testing, a fractographic study was carried out to determine geometric and structural factors accountable for the failure.

KEY WORDS: Low cycle fatigue, welding, superalloys.

1. INTRODUCCIÓN

El uso de las aleaciones de base níquel está cada vez más extendido por su excelente combinación de propiedades mecánicas y de resistencia a condiciones de oxidación corrosión. Como característica distintiva de las superaleaciones debe destacarse su capacidad para mantener su resistencia mecánica hasta altas temperaturas (para el caso del Inconel® 625 por encima de los 1000 °C [1,2]) lo que les convierte en materiales de elección en aplicaciones en las que la temperatura de trabajo es un factor limitante. Un claro ejemplo son las aplicaciones aeronáuticas en las que se trata de trabajar a temperaturas cada vez más altas, para aumentar los rendimientos termodinámicos.

Las excelentes propiedades del Inconel® 625 derivan de la combinación de los distintos elementos de aleación

(Tabla 1). Concretamente, el efecto endurecedor del molibdeno y del niobio en la matriz níquel-cromo originan su elevada resistencia ante entornos extremadamente corrosivos y ante fenómenos de degradación producidos por las altas temperaturas como la oxidación, la carburización y la fatiga térmica.

Adicionalmente a la alta resistencia mecánica, estas superaleaciones presentan buenas propiedades a la fluencia lenta y a la corrosión en ambientes agresivos. Esta resistencia a la corrosión hace a las superaleaciones candidatos interesantes para aplicaciones marinas, en la industria alimentaria y en la industria aeroespacial para determinados componentes de las toberas.

Evidentemente para asegurar su comportamiento en servicio se hace necesario el ensayo de los materiales y de las soldaduras a las que estos materiales dan lugar

(dado que las grandes estructuras deben ser unidas mediante soldaduras). En muchas ocasiones la fatiga de bajo número de ciclos se ha discutido como potencial fuente de fallos [3,4]. En este contexto se enmarca el presente trabajo, que pretende hacer un análisis del comportamiento a fatiga de bajo número de ciclos a altas temperaturas de tubos soldados, siguiendo la línea de un trabajo presentado con anterioridad en este mismo foro en el que se presentó un modelo numérico para el comportamiento cíclico de estos mismos materiales [5]. A la dificultad intrínseca de realizar ensayos de fatiga en control de deformación a elevadas temperaturas sobre materiales heterogéneos (la presencia de la soldadura cambia dramáticamente el comportamiento mecánico del material base) debe añadirse los provenientes de ensayar a tracción – compresión una geometría tubular.

Tabla 1. Composición química de la superaleación Inconel® 625 [1].

Elemento	% peso	Elemento	% peso
Ni	≥ 58	Cr	20-23
Fe	5	Co	1
Ti	8-10	Nb (+Ta)	3.15-4.15
Mo	0.4	Al	0.4
C	0.1	Mn	0.5
Si	0.5	—	—

2. MATERIALES Y TÉCNICAS

Se han realizado ensayos de fatiga uniaxial de bajo número de ciclos en control de deformación a 650 °C en una máquina universal servohidráulica INSTRON modelo 1342. Las muestras ensayadas son tubos de Inconel® 625 con un diámetro interno de 22.5 mm y un diámetro externo de 25 mm. La Figura 1 muestra el montaje experimental empleado y la Figura 2 un detalle del mismo en el que se muestran las patas del extensómetro de SiC en contacto con la zona caliente de la muestra. El rango de deformación alcanzado en el ensayo ha sido entre un 0.7 y un 0.8%, con R=0.

Una vez ensayadas las muestras se extrajeron probetas metalográficas de dos zonas (en la zona fría, próxima al amarre y en la zona caliente, dentro del horno) para, por comparación, evaluar a posteriori la influencia que el ciclado térmico (durante la soldadura y en el ensayo) tiene en la microestructura del material. Las secciones metalográficas (longitudinal y transversal) se engastaron para su pulido con una ruta convencional y se atacaron con una disolución de CuSO₄ y HCl en agua. Tras el ataque la metalografía cuantitativa se realizó con el programa de análisis de imagen Leica Qwin Pro 2.3.

Las superficies de fractura de las probetas se analizaron mediante microscopía óptica y electrónica de barrido para la determinación de los orígenes de fallo y el camino de propagación. Este estudio se completó con la

sección metalográfica en dirección longitudinal de la zona identificada como iniciadora de fatiga para intentar determinar los componentes estructurales asociados a la misma.



Figura 1. Ensayo de fatiga uniaxial de bajo número de ciclos realizado sobre un tubo de Inconel® 625 a 650 °C.

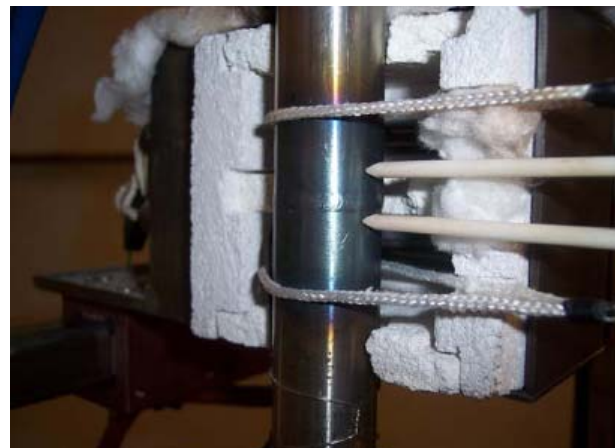


Figura 2. Detalle del montaje del extensómetro que se utilizó para controlar en deformación los ensayos de fatiga.

3. RESULTADOS

3.1 Metalografía

Las Figuras 3a y 3b muestran un aspecto de las secciones longitudinal y transversal del material base respectivamente tras ser pulido y atacado. Se observa una estructura maclada, típica de este tipo de aleaciones.

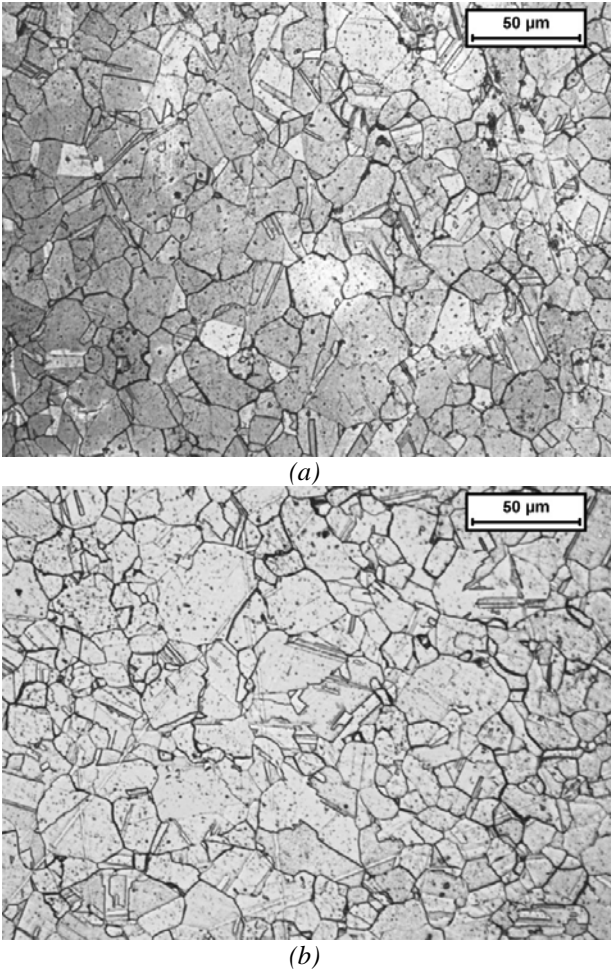


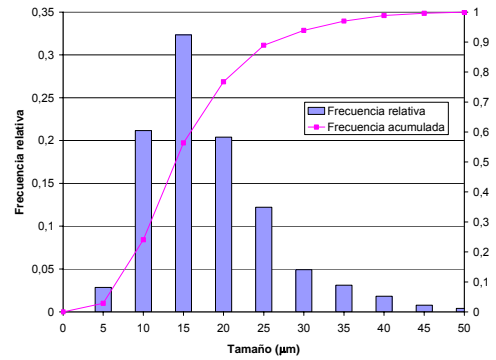
Fig. 3. Microestructura del material base. (a) Sección longitudinal y (b) Sección transversal.

En las Figuras 4 y 5 se detallan los resultados del análisis cuantitativo de metalografía realizado en la zona fría y en la zona que ha sido sometida a los ciclos térmicos durante el ensayo, respectivamente. Los resultados metalográficos se resumen en la Tabla 2.

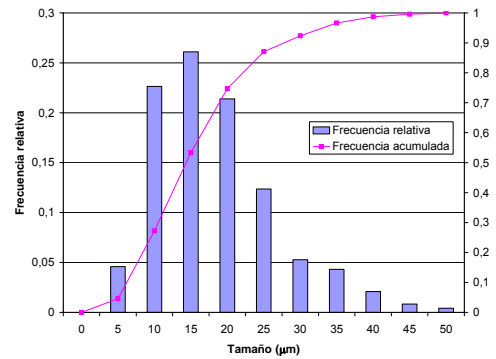
De la observación de la tabla y de las figuras parece deducirse que los granos son equiaxiales (los tamaños medios en sección longitudinal y transversal no difieren significativamente) y que en la zona próxima al cordón de soldadura, el tamaño de grano es menor (probablemente como efecto del tratamiento térmico que ha sufrido el material durante el proceso de soldadura).

Tabla 2. Resultados de tamaño medio de grano (con su i.c. al 95%) para las secciones longitudinal y transversal de las probetas metalográficas extraídas del extremo frío de las probetas y de la zona que ha sido ciclada durante los ensayos.

	Longitudinal	Transversal
Extremo frío	15.7 ± 0.6 μm	15.9 ± 0.6 μm
Zona calentada	12.5 ± 0.4 μm	13.4 ± 0.6 μm

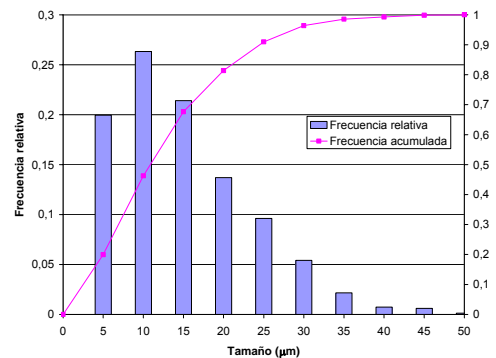


(a)

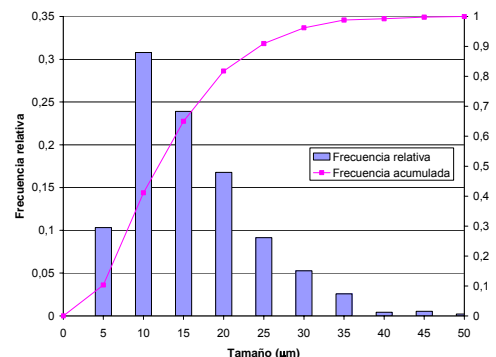


(b)

Fig 4. Distribución de tamaños y frecuencia acumulada para el tamaño de grano del material en la zona fría (a) sección longitudinal, (b) sección transversal



(a)



(b)

Fig 5. Distribución de tamaños y frecuencia acumulada para el tamaño de grano del material en la zona ciclada térmicamente (a) sección longitudinal, (b) sección transversal.

3.2 Ensayos de fatiga

La Figura 6 muestra la forma típica de la curva tensión-deformación durante los ensayos. El material endurece a medida que aumenta el número de ciclos hasta alcanzar una estabilización.

Como se indica en la Figura 7, los ensayos se condujeron hasta rotura y se considera que se produce agrietamiento cuando se detecta una caída del 10% en la tensión máxima medida durante el ensayo.

La Tabla 3 resume los datos más significativos correspondientes a los 4 ensayos que se realizaron. En el cuarto ensayo se produjo una incidencia (resbaló el extensómetro en el primer ciclo) y, por tanto, sus resultados no son comparables a los demás. La dispersión observada entre los resultados puede provenir en parte de la geometría de las muestras antes del ensayo (como efecto del proceso de soldadura, los tubos no son perfectamente rectos y, en el proceso de amarre y primer ciclo de carga se enderezan).

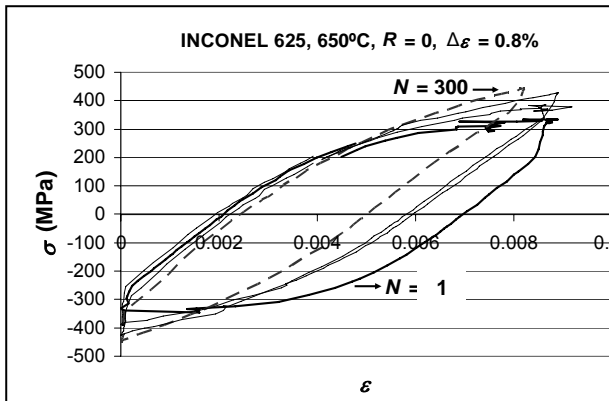


Figura 6. Respuesta cíclica del Inconel® 625.

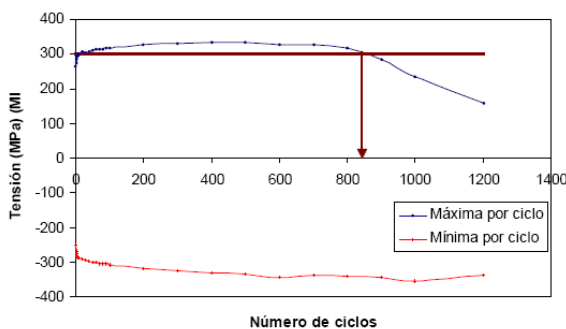


Figura 7. Evolución de la tensión máxima y mínima durante el ciclado. Se observa que, tras el endurecimiento inicial, se produce una estabilización en la tensión máxima. Cuando comienza el agrietamiento se produce una caída en la tensión máxima durante el ciclo. La flecha indica el punto en el que esta caída es del 10%.

Tabla 3. Resumen de los resultados de los ensayos. N_f es el número de ciclos necesario para producir una caída en la tensión máxima del 10%

	$\Delta\epsilon$ (%)	N_f	σ_{max} (MPa)
Tubo 1	0.70	1374	461
Tubo 2	0.72	847	334
Tubo 3	0.87	400	444
Tubo 4	0.70	1	528

3.3 Análisis de las fracturas

En todas las probetas rotas se observa que la fractura se produce bien siguiendo la zona afectada por el calor de la soldadura, bien a través del cordón de soldadura. Las figuras 8 muestran el aspecto macroscópico de las probetas una vez rotas.

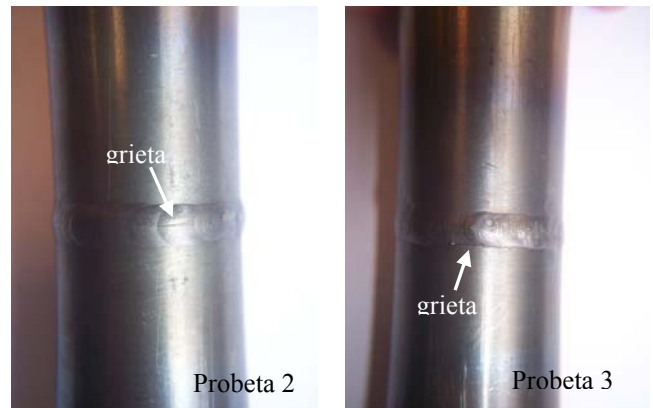


Figura 8. Aspecto de las probetas 2 y 3 tras el ensayo. Se puede observar que la grieta en la probeta 2 recorre la zona fundida del cordón de soldadura, mientras que en la probeta 3, se localiza en la zona afectada por el calor inferior adyacente a la soldadura.

Una vez ensayadas, las probetas estaban agrietadas parcialmente. Para realizar el análisis fractográfico, se acabaron de romper, consiguiendo de esta manera exponer la superficie de fractura.

En las Figuras 9 y 10 se presenta la fractografía de microscopio óptico de las probetas 2 y 3. En ambos casos, el comienzo de la fatiga se localiza en la superficie interior del tubo, probablemente en un defecto en la superficie del cordón de soldadura, ya que no se encontró evidencia de defectos de la misma (falta de fusión o unión fría, por ejemplo) o de inicio en segundas fases o en escoria.

Respecto a la propagación, para el caso de la probeta 3 (Figura 10), se muestra una superficie de propagación mucho más lisa que para la probeta número 2 (Figura 9). Esto, probablemente es debido a la forma en la que se ha realizado la soldadura (en la Figura 8a se observan claramente los distintos cordones que parecen ser los responsables de la rugosidad observada en la superficie de fractura de la probeta 2).



Figura 9. Superficie de propagación de la grieta de fatiga en la probeta 2. Se observa una rugosidad asociada a los sucesivos cordones de soldadura.

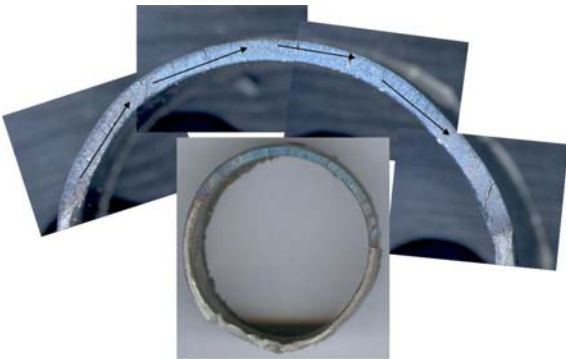
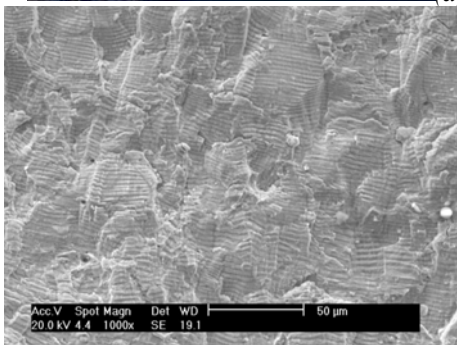


Figura 10. Superficie de propagación de la grieta de fatiga en la probeta 3. Se observa una propagación muy plana siguiendo la zona afectada por el calor adyacente a la soldadura.



(a)



(b)

Figura 11. Detalle de la superficie de fractura (a) en microscopía óptica y (b) en microscopía electrónica de barrido, en la que se aprecian las estrías típicas de la propagación de grietas por fatiga.

Las Figuras 11 muestran algunos detalles, a más aumentos, tanto de microscopía óptica como de microscopía electrónica de barrido en las que se observa la presencia de las típicas estrías asociadas a la propagación de grietas por fatiga. Estas estrías en algunos casos son muy marcadas, como se presenta en la Figura 11b.

Como ya se ha mencionado no ha sido posible la identificación de ninguna partícula (segunda fase o inclusión debida al proceso de soldadura) en la zona de origen de fatiga. Sin embargo, como se observa en la figura 12, en las muestras cuya propagación ha tenido lugar total o parcialmente por la zona afectada por el calor (3 de las 4 muestras ensayadas), se observa una clara tendencia al agrietamiento de la microestructura de grano crecido adyacente al cordón de soldadura. Esto indica la necesidad de controlar los parámetros de soldadura para evitar un crecimiento excesivo del grano en la ZAC.

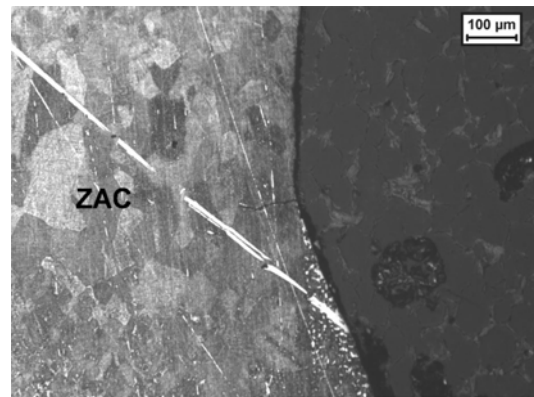
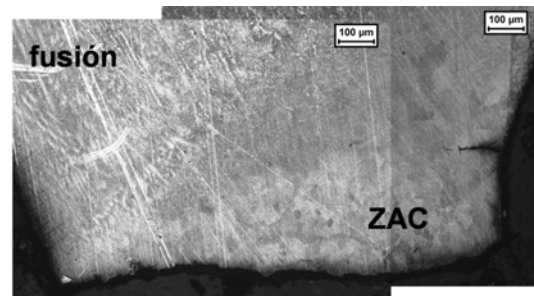


Fig. 12. Secciones metalográficas de muestras rotas en las que se aprecia la proliferación de grietas en la zona de grano crecido adyacente al cordón de soldadura.

4. CONCLUSIONES

Se han realizado ensayos de fatiga de bajo número de ciclos en control de deformación con probetas tubulares con soldadura. La dispersión en los resultados indica la necesidad de controlar el proceso de soldadura para producir probetas geoméricamente idénticas que permitan extraer conclusiones en cuanto a vida a fatiga.

La propagación de las grietas se produjo en todos los casos entorno al cordón de soldadura (bien en la zona de fusión, bien en la zona afectada por el calor).

Aparentemente la nucleación de la grieta se produjo desde un defecto superficial (probablemente relacionado con el acabado superficial de la soldadura).

La propagación de la grieta, preferentemente recorriendo la zona de grano crecido adyacente al cordón de soldadura, indica la necesidad de controlar los parámetros térmicos de soldadura para evitar el crecimiento incontrolado del grano.

5. AGRADECIMIENTOS

Los autores desean agradecer la colaboración de S. Pérez en la preparación de muestras y al Ministerio de Ciencia e Innovación la financiación recibida dentro del proyecto “Ensayos de fatiga termo-mecánica con mínimos gradientes térmicos y de fase” (MAT2008-03735/MAT). También al Gobierno Vasco la ayuda recibida dentro del proyecto PI09-09.

6. REFERENCIAS

- [1] <http://www.specialmetals.com/> [Consulta: Febrero de 2009].
- [2] Shankar, V., Rao, K.B.S. and Mannan, S.L., "Microstructure and mechanical properties of Inconel 625 superalloy", *Journal of Nuclear Materials*, vol. 288, nº 2-3, 2001, pp. 222-232.
- [3] Stekovic, S., *Tesis Doctoral*, "Isothermal low cycle fatigue of uncoated and coated nickel-base superalloys", Linköpings University, Sweden, 2004.
- [4] Wang, Z.G., Buschow, K.H.J., Robert, W.C., Merton, C.F., Bernard, I., Edward, J.K., Subhash, M. and Patrick, V., *Fatigue of Superalloys (Elevated Temperatures)*, in *Encyclopedia of Materials: Science and Technology*. 2001, Elsevier: Oxford. p. 2986.
- [5] R. Rodríguez-Martín, J. L. Pedrejón, D. González, M. R. Elizalde, I. Ocaña, A. Martín-Meizoso, J. M. Mtnez-Esnaola, “Modelización del comportamiento cíclico de la superaleación INCONEL 625” en *Anales de Mecánica de la Fractura*, vol. 26 (I) (2009), 343-347.

HYBRID FORMULATION SOLUTION FOR STRESS ANALYSIS OF CURVED PIPES WITH WELDED JOINTS UNDER BENDING

Luísa Madureira* and Francisco Q. Melo**

Department of Mechanical Engineering, Faculty of Engineering of the University of Porto, Portugal,
e-mail:luisa.madureira@fe.up.pt, fax:351 22 5081445

** Department of Mechanical Engineering, University of Aveiro, Portugal,
e-mail:francisco@ua.pt

ABSTRACT

A curved thin pipe subjected to an in-plane uniform bending moment is studied. A mixed formulation for the stress analysis of curved pipes is proposed and applied to an elbow where the stress field is evaluated, represented by a continuous analytical function obtained by unknown functions combined with trigonometric expansions. Then, these results are used as input data for the calculation of the stress intensity factor of a part-through crack existing in the plane of the flange-pipe junction. The SIF is evaluated for the defect in the flange-pipe interface of a Sandvik® 3R12 stainless steel elbow, considering different pipe thickness and crack geometries at an in-plane bending load. A comparison with results published in the literature for a welded structure with some kind of flaws due to structural defects, lack of material adhesion or porosities is presented, validating this approach.

1. INTRODUCTION

In the present work a mixed formulation solution where unknown functions, ovalization and warping, are used together with Fourier trigonometric expansions [1,2,3] is presented. These shape factors are used in the evaluation of SIF parameters for a generalized crack existing in a doubly curved surface shell. In previous works published by Viswanatha *et al* [4] stress intensity factors in elbows subjected to uniform in-plane bending where a part-through crack along the longitudinal axis at the crown pipe were obtained using a finite element method to perform the analysis. Also Oliveira *et al* [5] studied the stress intensity factors of surface elliptical cracks existing in pipe elbows using high order 8-node shell elements. The methodology presented here is a new, alternative approach, based on a coupled procedure, where in a first step, the nominal stress field of the curved pipe loaded as mentioned is evaluated; after, a database containing the parameters necessary to evaluate the stress intensity factor of part-through cracks existing in shell structures is used for the objective. In the present analysis, a previous investigation performed by Carpinteri *et al* [6] is used. These authors calculated the stress intensity factor of several geometries of elliptical profile part-through cracks existing in cylinders subjected to uniform bending. The cracked pipe structure was modelled with shell type finite elements. The analysis now presented refers to a toroidal shell that has two principal curvatures, while a cylindrical shell has in fact only one curvature. The approach taken for this purpose has the assumption that the curvature along the longitudinal direction is much larger than the one along the circumferential line. To assess the accuracy of the approach here mentioned, it was also taken a set of reference values of the stress intensity factor calculated by Gonçalves and Castro [7] referred to a part-through

crack existing in flat plate where the authors used the Line-Spring model techniques. In this work it's interesting to note that the so-obtained values of the stress intensity factor for a part-through crack in a flat plate are very similar to the same parameter for a cylindrical shell as in the work of Carpinteri *et al* [6], provided that the cylinder was not considered as a thick shell (*i.e.*, the ratio radius/thickness greater than about 20).

2. STRESS ANALYSIS IN A CURVED PIPE UNDER BENDING

In a curved pipe with end flanges, the flange-pipe interface is the main flaw location, as sketched in Fig. 1.

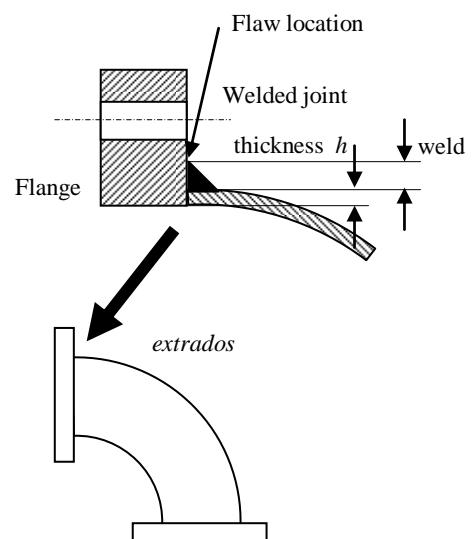


Fig 1- Part-through crack in a welded flange joint of a curved pipe

The purpose of this work is to analyze the structural integrity of a pipe where a crack similar to the one displayed in Figure 1 is detected. The stress intensity factor (SIF) associated with the crack shape is used in the analysis to quantify the remote or nominal stress field that exists in the crack zone. This work follows Carpinteri *et al* [6], where straight pipes that have a part-through crack were subjected to bending loads. Due to the presence of the defect, the pipe integrity is defined by the maximum SIF along the crack profile. The shell considered here is not cylindrical, but considering the pipe curvature radius R , much larger than the transverse section radius r , this approach is still valid.

The solution is obtained by minimizing the total elastic energy U involved in the pipe distortion process with a set of unknown functions:

$$U(\boldsymbol{\sigma}, \mathbf{u}) = \frac{1}{2} \int_{\Omega} \boldsymbol{\sigma}^T \mathbf{C}^{-1} \boldsymbol{\sigma} d\Omega + \int_{\Omega} \boldsymbol{\sigma}^T \mathbf{u} d\Omega$$

\mathbf{C} is the elastic pipe properties matrix. The first integral refers to the internal elastic deformation energy, and the second is the deformation work performed by the unknown vector $\boldsymbol{\sigma}$ of the internal stresses against the admissible displacement field \mathbf{u} .

An external entity M_0 , the bending moment, performs additional work at a bending angle $\delta\alpha$.

The system of external forces performs deformation work (called the external work) upon the displacement functions a_i and b_i . The total energy of the structure U is the sum of this external work with the corresponding elastic deformation. This value should be zero if the displacement functions are exact, but for the displacement field approximations used here (Fourier expansions), U has a residual value. This residual allows for the optimization of expressions to minimize U . The variation of the total energy U is as follows:

$$\delta U = \int_{\Omega} \delta \boldsymbol{\sigma}^T \mathbf{C}^{-1} \boldsymbol{\sigma} d\Omega + \int_{\Omega} \delta \boldsymbol{\sigma}^T \mathbf{u} d\Omega + \int_{\Omega} \boldsymbol{\sigma}^T \delta \mathbf{u} d\Omega$$

where the integral domain Ω is $[0, L] \times [0, 2\pi]$ and L represents the length of the transverse section of the center arch. The total variation in U is the result of separate contributions from variations in the stress field $\boldsymbol{\sigma}$ and in the displacement \mathbf{u} . Equilibrium is achieved by minimizing the function U separately for each of the unknowns and a system of differential equations is then obtained [4,5]. Using MAPLE[®] mathematical solver an analytical solution is achieved and the continuous stress field is evaluated [1,2] for the location in discussion.

3. EXAMPLES

A curved pipe where the shell surface close to the crack zone is approximately cylindrical is considered. The

method is applied to 3 examples of curved pipes with cracked rigid end flanges. Figure 2 shows a crack resulting from the lack of adhesion that occurs in the *extrados* curved pipe. The pipe is subjected to a bending moment that results from a prescribed in-plane flange rotation of 0.002 rad, as described in Figure 2.

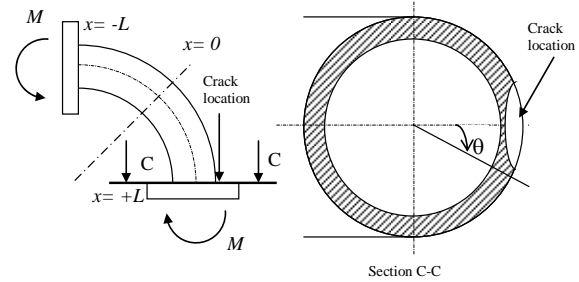


Fig 2- Part-through crack in a welded flange joint in a curved pipe

The maximum bending stress σ_M at the *extrados* (1) position in the flange weld is as shown in Figure 3. The corresponding value for the stress intensity factor in $MPa \times m^{1/2}$ is shown in Table 1. The critical SIF value for the stainless steel used here is $K_{IC} \approx 28 MPa \times m^{1/2}$ (<http://www.smt.sandvik.com/tube/>). To assess the solution method discussed here, stress analysis is carried out for several curved pipes with rigid end flanges. The material properties and dimensions are:

EXAMPLE 1

Transverse section radius $r - 50 mm$
 Wall thickness $h - 5mm$
 Mean curvature radius $R - 200 mm$
 Pipe angle $\alpha - 90^\circ$
 Transverse section center arch $L - 157.0796 mm (=R\alpha)$
 Material - stainless steel Sandvik[®] 3R12L: E=210 GPa
 $\nu = 0.3$

An in-plane uniform bending moment M_0 loads the pipe, where symmetry conditions were considered. In the calculations, a specified rotation angle of $\delta\alpha=0.002$ rad at a flanged end was prescribed.

EXAMPLE 2

With the same material dimensions are:
 Transverse section radius $r - 50 mm$
 Wall thickness $h - 2mm$
 Mean curvature radius $R - 200 mm$

EXAMPLE 3

With the same material dimensions are:
 Transverse section radius $r - 40 mm$
 Wall thickness $h - 2mm$
 Mean curvature radius $R - 200 mm$

The hoop stress at section $x=L$, as a consequence of the bending moment, is shown in Figure 3:

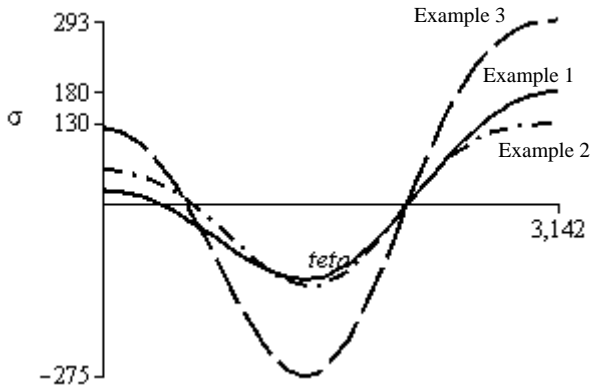


Fig. 3 – Longitudinal membrane stress σ_x at $x=L$ from uniform bending

The following parameters are necessary for evaluating the Stress Intensity Factor (SIF) associated to the crack geometry (Figure 4):

- a = maximum crack depth
- a_{el} = minor half axis of ellipse (the crack has an elliptical profile)
- $\xi = a/t$ (non-dimensional parameter; measured at the largest crack depth)
- $\alpha = a_{el}/b_{el}$ (ellipse principal axes ratio)
- $s = a_{el}/a$ (offset of ellipse major axis related to the tangent to the external pipe circumference; usually $s=1$).

An auxiliary coordinate ζ , refers to the position point in the crack profile where the stress intensity factor is measured; coordinate ζ starts at the intersection point of the crack profile with the pipe's external circumference; ζ is used as a normalized ratio ζ/h (see Figures 5)

For example 1
 D (pipe section diameter) = 100mm ($r=50mm$)
 t (equivalent thickness = pipe+weld) = 10mm

For example 2
 D (pipe section diameter) = 100mm ($r=50mm$)
 t (equivalent thickness = pipe+weld) = 5mm

For example 3
 D (pipe section diameter) = 100mm ($r=40mm$)
 t (equivalent thickness = pipe+weld) = 4mm

Semi-elliptical crack is respectively $a=2mm$ $a=3mm$ $a=1.6mm$ ($a=a_{el}$); a/t is 0.6 in example 2 and R/t is 10 or 5 and are compared to the values available in the graphical results of Carpinteri [7]

Material: austenitic stainless steel Sandvik® 3R12

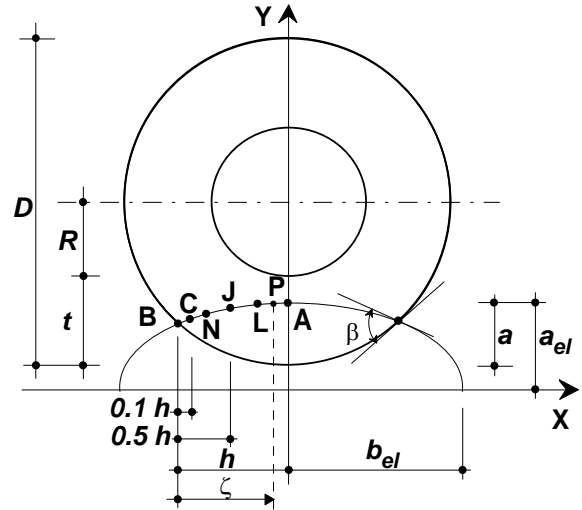


Fig. 4 – Parameterization of a semi-elliptical part-through crack existing in a pipe [7]

Given these parameters, the non-dimensional stress intensity factor, in reference to the nominal value, can be estimated:

$$K_I = \sigma_M \sqrt{\pi a}$$

The case study for example 2 has $a=3mm$; the nominal value for K_I is:

$$K_I = \sigma_M \sqrt{\pi a} = \sigma_M \sqrt{\pi \times 3E - 0.3}$$

$$= 0.097 \times \sigma_M N \times m^{1/2}$$

Figures 5 show the non-dimensional SIF for a defect in a straight pipe and with the geometric parameters described above. Again, using analysis from Carpinteri [7], the non-dimensional SIF is $K_{LM}^* \approx 1.08$. The effective value of the stress intensity factor is (Table 1):

$$K_{LM} = K_{LM}^* \times \sigma_M \sqrt{\pi a} = 1.08 \times \sqrt{\pi a} \times \sigma_M$$

$$= 1.08 \times 0.97 \times 130 = 13.6$$

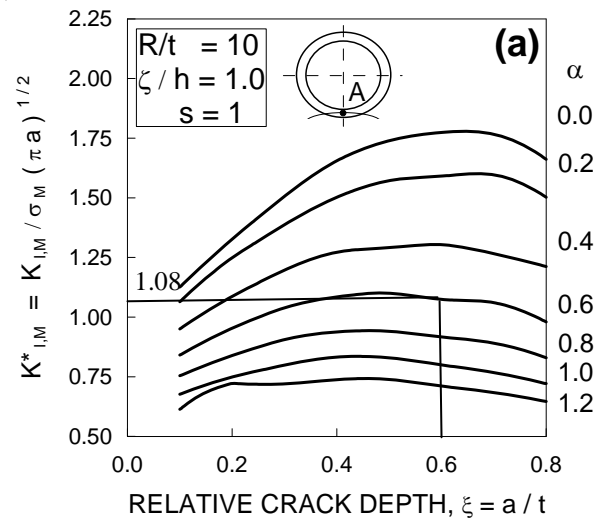


Fig. 5a – Dimensionless Stress Intensity Factor for a part-through crack with geometry parameters from [7]

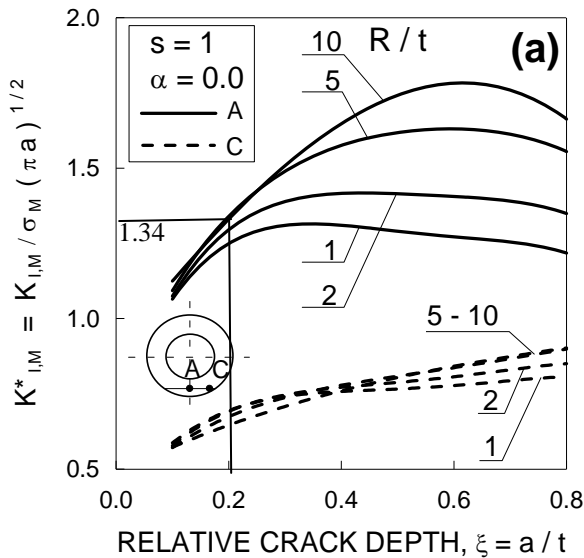


Fig. 5b – Dimensionless Stress Intensity Factor for a part-through crack with geometry parameters from [7]

In example 3 the effective value of the stress intensity factor is (Table 1):

$$K_{IM} = K_{LM}^* \times \sigma_M \sqrt{\pi a} = 1.08 \times \sigma_M \sqrt{\pi a} = 1.34 \times 0.071 \times 293 = 27.8$$

The longitudinal curvature was assumed to be much smaller than the circular transverse section, and SIF parameter results were obtained using a cylindrical shell.

This method was also validated using a toroidal shell element, assuming flat plate-like properties at the crack zone following the method of Gonçalves and Castro [7]. In these examples, SIFs of semi-elliptical part-through cracks in flat plates subjected to pure tension or bending were studied.

Table.1 – Stress intensity factors for part-through cracks in flat plates under tension

Sample (mm)	Weld (mm)	σ_{max} at $\theta=\pi$	Crack geometry	SIF
r=50 h=5	weld=5	180MPa	a=.002m	19.1
r=50 h=2	weld=3	130MPa	a=.003m	13.6
r=40 h=2	weld=2	293MPa	a=.0016m	27.8

The method used by Gonçalves [7] to calculate the SIF has the factor Q , given by the following equation:

$$Q = 1 + 1.464(a/c)^{1.65}$$

In example 2, $a/c=0.6$, giving $Q=1.63$. The SIF calculated by Gonçalves [7] applied to flat plates is

$$K_{I(plate)} / \sqrt{Q} = 1.3 / \sqrt{1.63} @ 1.018$$

The results show that the safety factor is exceeded for the third sample. In the two other examples, the defect does not give a critical threat for pipe integrity, provided that the stress σ_M remains below 280 MPa, a value close to the yield stress for the steel alloy.

This value is close to the result obtained by Carpinteri [6] using cylindrical shells. These results express that the method proposed here is suitable for thin shells with relatively large curvatures.

4. CONCLUSIONS

This result shows the method’s reliability when applied to a doubly curved shell with a part-through crack, provided that the shell has two distinct principal curvatures, where one is much smaller than the other. As can be shown by example 3 even with a smaller initial crack, because the radius is shorter, the SIF shows that under the same conditions, this is the pipe that breaks reaching the safety factor.

5. AKNOWLEDGEMENTS

The authors wish to thank Fundação para a Ciência e Tecnologia for the support under this research, and Prof Carpinteri and Prof Brighenti for permission for publishing some figures and results.

6. REFERENCES

- [1] Madureira, Luísa and Melo, Francisco (2004) “Stress Analysis of Curved Pipes with Hybrid Formulation”, *Int Jour Pressure Vessels & Piping* 81:3
- [2] Madureira, Luísa and Melo, Francisco (2000) “A hybrid formulation in the stress analysis of curved pipes”, *Engineering Computations* 17:8 pp 970-980
- [3] Millard, A., Roche, R. (1984), "Elementary Solutions for the Propagation of Ovalization along Straight Pipes and Elbows", *Int. Journ of Press. Vessels & Piping*, Vol. 16 No 1, pp 101-129.
- [4] Viswanatha, Bhate and Kushaha, (1997) “Stress-intensity factors for elbows with axial surface crack at crown”, Trans. SMiRT 14th, *International Conference in Structural Mechanics in Reactor Technology*, Lyon, France, 17-22 August, paper G06-5
- [5] Oliveira, Melo, Castro, (1991) “The elastic analysis of arbitrary thin shells having part-through cracks, using the integrated line spring and the semiloof shell elements” *Engineering Fracture Mechanics*, Vol. 39, N^o 6, pp 1027-1035
- [6] Carpinteri, Andrea; Brighenti, Roberto and Spagnoli, Andrea (1998) “Part-through cracks in pipes under cyclic bending”, *Nuclear Engineering and Design* 185 pp 1-10
- [7] Gonçalves, J P M and Castro, P M T (1999). Application of the line spring model to some complex geometries and comparison with three-dimensional results. *Int. Journ. of Pressure Vessels & Piping*. vol76:8 pp 551-560

FATIGUE CRACK GROWTH BEHAVIOUR OF FRICTION STIR WELDED ALUMINIUM-LITHIUM ALLOY 2195 T8X

P.M.G.P Moreira¹, A.M.P. de Jesus², M.A.V. de Figueiredo³, M. Windisch⁴,
G. Sinnema⁵, P.M.S.T. de Castro³

¹ INEGI, Laboratório de Óptica e Mecânica Experimental - LOME, Porto, Portugal, pmoreira@inegi.up.pt

² Universidade de Trás-os-Montes e Alto Douro, Departamento de Engenharias, Vila Real, Portugal, ajesus@utad.pt

³ Universidade do Porto, Faculdade de Engenharia, Departamento de Eng. Mecânica, Porto, Portugal, mfiguei@fe.up.pt

⁴ MT Aerospace AG, Department TEA, Augsburg, Germany, michael.windisch@mt-aerospace.de

⁵ European Space Agency ESA ESTEC, Noordwijk, the Netherlands, Gerben.Sinnema@esa.int

ABSTRACT

Al-Li alloys such as 2195 are candidate materials for reducing the structural weight of cryogenic tanks on launch vehicles due to their low density, high strength and fatigue crack growth resistance. Although there are many advantages with Al-Li alloys, important limitations remain while using conventional joining techniques. The present work was performed under the ESA TRP "Damage Tolerance of Cryogenic Pressure Vessels", a project aiming at defining potential applications for state of art Friction Stir Welding (FSW) techniques in cryogenic tanks for Expendable Launch Vehicle and Reusable Launch Vehicle.

The work presented in this paper involves the characterization of the fatigue performance of the AA2195-T8X at room temperature. SN fatigue tests and crack growth tests of base material and friction stir welded 5mm thick specimens of the AA2195-T8X were performed. For SN determination, tests were carried out at two different R ratios, 0.1 and 0.8, using for each stress ratio three different maximum loads. During crack growth tests, three different R ratios, 0.1, 0.5 and 0.8, were used per each three different material conditions - base material, heat affected zone (HAZ), and weld. Specimens containing notches at the centre of the weld, at the HAZ and at the base material, were tested. The first type of specimens has notches in the centre of the weld, which coincides with the centre of the weld nugget. In the second type of specimens the crack is located in the HAZ.

KEY WORDS: aluminium-lithium alloy, FSW, fatigue, fatigue crack growth tests.

1. INTRODUCTION

In the aeronautics and space industries one of the most effective ways to reduce weight is to reduce the density of the aluminum alloys used. For purposes of reducing the alloy density, lithium additions have been used. The rapid increase in solid solubility of lithium in aluminum over the temperature range of 0°C - 500°C results in an alloy system achieving, through precipitation hardening, good strength levels. However, the addition of Li to Al alloys presents problems, as possible decreases in ductility and fracture toughness, delamination problems and poor stress corrosion cracking resistance. Increased strength with only minimal or no decrease in toughness is therefore a major issue.

The interest in Al-Li alloys derives from the large effect that lithium additions have on the modulus of aluminum, a 6 percent increase for every weight percent added, and the density, a 3 percent decrease for every weight percent added, [1]. These changes apply for lithium additions up to 3 weight percent. There have been three early generations of Al-Li alloys, (i) those produced in the 50s to 70s, including alloys 2020 and 1420; these alloys experienced ductility and fracture

toughness problems, or were of relatively low strength; (ii) those produced in the 1980s, including alloy 2090, 2091, 8090, and 8091, with high modulus and low density, but displaying anisotropic mechanical properties, and (iii) the more recent high-strength alloys as 2195. Al-Li alloys offer attractive properties for lightweight aerospace structures, due to their low density, high strength and fatigue crack growth resistance. Although there are many advantages with Al-Li alloys, important limitations remain while using conventional joining techniques. Friction Stir Welding (FSW) is a well established solid-state joining process that is expected to reduce many of the concerns about Al-Li welding. The present work was performed under the ESA TRP "Damage Tolerance of Cryogenic Pressure Vessels". The activity aims at defining potential applications for state of art FSW techniques in cryogenic tanks for Expendable Launch Vehicle and Reusable Launch Vehicle.

2. SN FATIGUE TESTS

INEGI performed SN fatigue tests at room temperature (RT) of friction stir welded (FSW) 5mm thick

specimens of the AA2195-T8X. Also, crack growth tests were carried out at room temperature for both base and welded materials. The test results of each specimen were linked to the specimen designation of the cut-off plan [2].

Preliminary tensile tests were performed at MT Aerospace in order to obtain the strength values of the AA2195-T8X friction stir welded material. These values, presented in Table 1, were used for the definition of the load levels of the fatigue tests and to determine the maximum load to be used on the fatigue sharpening and crack propagation procedures to prevent plasticity effects.

Table 1- Strength values for test definition and performance

	Temperature	$R_{p0.2} (\sigma_{yield})$
2195 T8X	RT	510MPa
	77K (-196°C)	650MPa
2195 T8X FSW	RT	300MPa
	77K (-196°C)	380MPa

The stress life curves were evaluated according to [3, 4] using integral specimens perpendicular to the weld. The specimen geometry is presented in Figure 1 [5].

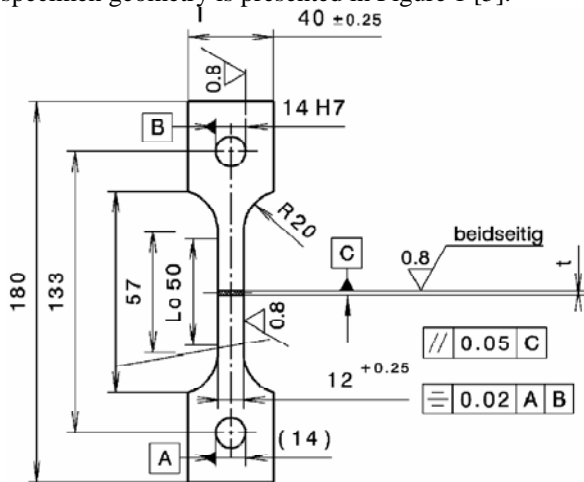


Figure 1- Geometry of the specimen to be used in the fatigue tests (SN).

For the calculation of the maximum loads to be applied in SN tests, the initial section is considered to be $5 \times 12 = 60mm^2$, and the FSW yield stress is the value presented in Table 1 (300MPa).

Tests were carried out at two different R ratios, 0.1 and 0.8, using for each stress ratio three different maximum loads. The R ratio of 0.1 represents pressure cycling (proof test, leak test etc.), and the R ratio of 0.8 represents external loads during operation. The tests were performed according to the matrix presented in Table 2.

These tests were carried out in a MTS 810 servo-hydraulic machine with a 100kN load cell.

Table 2- SN tests, definition of remote loads matrix

R ratio	Number of specimens	σ_{max}	Maximum load [kN]
0.1	2	FSW yield stress	18.00
	2	85% FSW yield stress	15.30
	2	70% FSW yield stress	12.60
0.8	1	FSW yield stress	18.00
	1	115% FSW yield stress	20.70
	1	130% FSW yield stress	23.40
	2	150% FSW yield stress	27.00

A mechanical grip fixture was developed in order to comply with the specimen geometry and maximum loads defined in the general test plan [5]. The geometry of each specimen was accurately measured before each test, especially in the section of the material affected by the welding process.

For the specimens tested at 70% of σ_{yield} some fatigue life scatter was found between the two tests; the first specimen fractured at around 800000 cycles and the second specimen remained un-fractured with a fatigue life of 10^7 cycles. Taking into account this observation a run out of 10^7 cycles was assumed. After this observation the option was to replace the third level of fatigue stress. Initially intended to be 50% of σ_{yield} , a value of 85% of σ_{yield} was chosen.

The first specimen tested with $R=0.8$, that corresponds to $\sigma_{max} = \sigma_{yield}$, did not fracture at 10^7 cycles. Taking into consideration this situation for $R=0.8$, instead of using the stress levels of 70% and 50% of yield stress previously defined, these two levels were replaced by 115% and 130% of σ_{yield} . Despite these changes in the test plan, all specimens tested at $R=0.8$ did not fracture at a fatigue life of 10^7 cycles. After this observation a higher level of remote stress, 150% of σ_{yield} , was used for the two remaining specimens. The plot of the fatigue lives for $R=0.1$ and $R=0.8$ is presented in Figure 2.

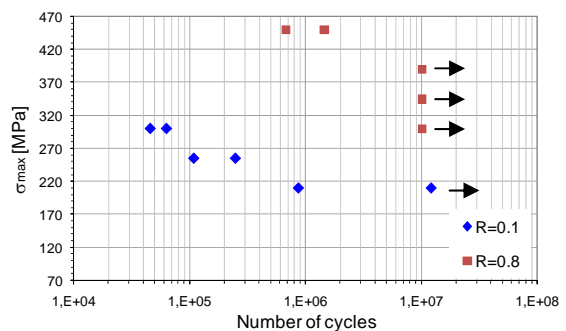


Figure 2- SN test results for $R=0.1$ and $R=0.8$.

When testing base material at $R=0.1$, max. stress corresponding to 10^5 cycles is of the order of 350 to 400 MPa, [6], whereas for the present FSW joints max. stress is of the order of 260 to 280 MPa for the same number of cycles, a reduction of just ~30%.
The location of the fracture surface in each SN specimen is presented in Table 3.

Table 3- Fracture surface identification in each SN specimen.

Spec	R	Advanc.or Retreat.	Crack initiat. surface	Weld zone
IT23	0.1	R	S	T
IT25	0.1	R	S	T
IT26	0.1	R	S	T
IT27	0.1		Did not break	
IT28	0.1	R	S	T
IT29	0.1	R	S	T
IT30	0.8		Did not break	
IT31	0.8		Did not break	
IT32	0.8		Did not break	
IT33	0.8	A	S	T
IT24	0.8	C	B	N

Table legend: A –Advancing; R- Retreading; C- Centre (weld line); S- Shoulder surface (crown surface); B- Bottom surface (root surface); T- Transition between material affected and material not affected by the shoulder (shoulder limit); N- Nugget.

Specimens IT23, IT25, IT26, IT28, IT29 and IT33 fractured in the transition from the stirred material to the base material, and the crack initiated near the surface where the shoulder contacted the plate. The IT24 specimen fractured at the centre of the weld.
The fracture initiation locations can be divided in three different groups, as presented in Table 4.

Table 4- Types of fracture location

Type	Specimens	Location
I	IT23; IT25; IT27; IT29;	Transition between material affected and material not affected by the shoulder (shoulder limit), and at the vertices of the specimen
II	IT26; IT28; IT33	Shoulder surface, at the centre of the weld line and at the middle of the specimen
III	IT24	Root surface, at the centre of the weld line and at the middle of the specimen

A macrograph of each type of fracture location found in the SN fatigue specimens is presented in Figure 3 (specs. IT23, IT26 and IT24, see a), b) and c) respectively).

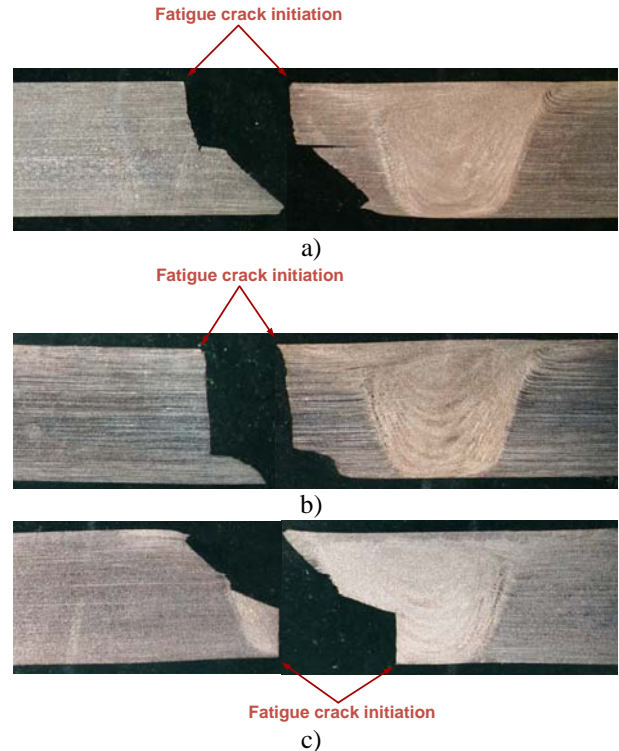


Figure 3- Fracture surface details – specimens a) IT23, b) IT26, and c) IT24.

Fracture surfaces of SN fatigue test specimens were analysed using scanning electron microscopy (SEM). As an example of typical results found, a detail of the fracture surface at 5.93mm from the initiation point (spec. IT23, Fig.3a, direction perpendicular to the figure) is presented in Figure 4.

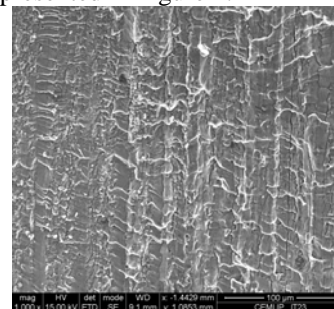
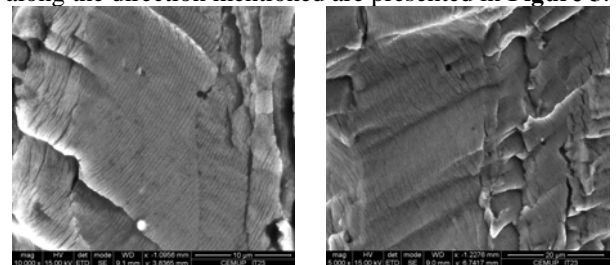


Figure 4- Detail of the fracture surface, specimen IT23.

Some details of fatigue striations in different locations along the direction mentioned are presented in Figure 5.



a) fracture surface for a crack length of 0.27mm
b) fracture surface for a crack length of 3.18mm
Figure 5- Detail of fatigue striations, specimen IT23.

3. CRACK GROWTH

Fatigue crack growth and subsequent R-curves were evaluated according to [7, 8] considering the use of CCT specimens. The specimen geometry is presented in Figure 6 [5].

For three different R ratios, R=0.1, 0.5 and 0.8, 3 specimens were tested per each three different material conditions - base material, heat affected zone (HAZ), and weld. The R ratio 0.1 represents pressure cycling (proof test, leak test etc.), and the R ratio 0.8 the external loads during operation.

The fatigue sharpening of the spark erosion was made in order to achieve a minimum of 0.2mm sharp crack extension. At the end of the fatigue crack growth test K_c values and K-R curves were evaluated with a minimum remaining ligament of 15mm; this is described in detail in ref. [9].

A crack length of 25mm was obtained before loading to fracture. This crack length should be identical at INEGI and DLR to allow the comparison of K_c values between RT and cryogenic conditions. According to [5], the crack length has been chosen such that maximum possible length for crack growth evaluation and a reasonable ligament (15mm) before fracture can be achieved.

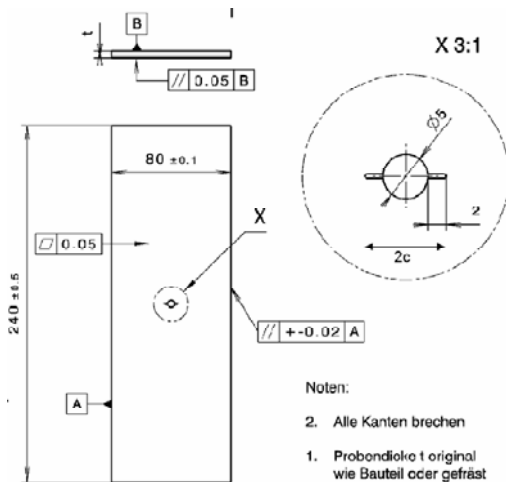


Figure 6- Definition of CCT specimen geometry.

Great experimental care was used aiming at symmetrical crack growth, which should result into a simultaneous verification of the 2a=50mm and (W-2a)/2=15mm. If unsymmetrical fatigue crack growth occurs, the criterion was to stop the fatigue crack propagation test as soon as the first ligament of 15mm was reached.

The specimens have notches introduced in the centre of the weld, in the HAZ and in the base material (BM), as presented in Figure 7 by lines 1, 2 and 3, respectively. The first type of specimens have notches in the centre of the weld (line 1), which coincides with the centre of the

weld nugget. In the second type of specimens the crack is located in the HAZ (line 2). The positioning of the notch in the HAZ was done by MT Aerospace by slightly etching the sides of each sample, which is expected to allow a positioning of the notch according to the microstructure. The location of the notch on the retreating side is based on the position of the fracture in the integral tensile specimen at room temperature.

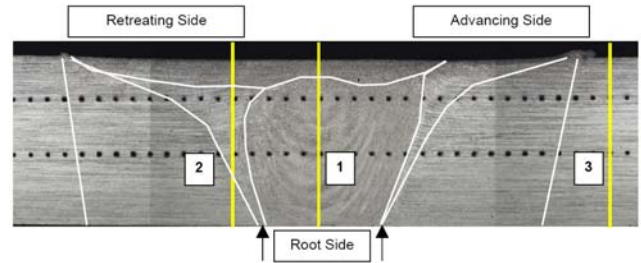


Figure 7- Through crack locations [5].

3.1 Calculation of test parameters

Table 5 presents the specimen geometry and crack size definition according to ASTM E647 [7].

Table 5- Specimen dimension according to [7].

B [mm]	5
W [mm]	80
2a, initial crack size [mm]	9.4
2a, crack size before loading to fracture [mm]	50

According to the standard [7] for the selected type of specimen the following equation should be verified,

$$(W - 2a) \geq 1.25 \cdot \frac{P_{max}}{B \cdot \sigma_{YS}} \quad (1)$$

where:

(W - 2a) is the specimens uncracked ligament, σ_{YS} considered to be the yield stress presented in Table 1.

Taking into consideration the material properties of the FSW material (σ_y=300MPa), when the initial crack size is considered, the maximum load should be

$$P_{max} \leq \frac{1}{1.25} (W - 2a) B \cdot \sigma_{YS}$$

$$P_{max} \leq \frac{1}{1.25} (80 - 9.4) \cdot 5 \cdot 300 \quad (2)$$

$$P_{max} \leq 84.72kN$$

For the crack size before loading to fracture the maximum load should be

$$P_{max} \leq \frac{1}{1.25} (80 - 50) \cdot 5 \cdot 300 \quad (3)$$

$$P_{max} \leq 36.00kN$$

For defining the loads to be applied in these tests, the selection was based on considerations proposed by the project partners [5] and previous results presented by NASA [10]. So, the ΔK aimed at in these tests should start at approximately $6 \text{ MPa}\cdot\text{m}^{0.5}$.

Taking into account this reference value and the stress intensity factor calibration proposed in the standard [7],

$$\Delta K = \frac{(P_{\max} - R \cdot P_{\max})}{B} \sqrt{\frac{\pi \cdot a}{W^2} \sec \frac{\pi \cdot a}{W}} \quad (4)$$

some calculations were performed in order to assess the load to be used for each R ratio.

Considering a value of $\Delta K=6 \text{ MPa}\cdot\text{m}^{0.5}$, Table 6 summarises the loads that should be used for each R ratio.

Table 6- Maximum load values for each R ratio

R ratio	P_{\max} [kN]
0.1	21.76
0.5	39.16
0.8	97.91

For all R ratios and considering the maximum loads presented in the previous table, the final ΔK (for the maximum crack size $2a=50\text{mm}$) is $18.41 \text{ MPa}\cdot\text{m}^{0.5}$.

Since the maximum load should be lower than 36kN , a maximum load of 35kN was considered for the specimens tested with $R=0.5$. If so, for this load ratio the tests will be performed for ΔK values between 5.36 and $16.45 \text{ MPa}\cdot\text{m}^{0.5}$. These values are within the range considered of interest for this ESA TRP programme.

For $R=0.8$, and considering a maximum load of 35kN , ΔK values would be between 2.14 and $6.58 \text{ MPa}\cdot\text{m}^{0.5}$. When $R=0.8$, according to the software ESACRACK 4 and MT Aerospace considerations, the threshold for the AA2219 T87 should be around $1.2 \text{ MPa}\cdot\text{m}^{0.5}$. Since this material is likely to have mechanical properties approximately similar to the AA2195 T8, it is expected that both alloys present approximately similar thresholds. If so, and considering that in this project vibration loads effects are necessary for the estimation of crack growth during operation, tests will be carried out at $R=0.8$ with a maximum load of 35kN .

The test output of these tests includes: da/dN curve and its respective data points as well as the basic $a-N$ data, $K-R$ curve [8] and the load-displacement curve on which it is based, description and photography of each broken specimen, fractography and some conclusions about the crack growth in the different material zones. Because of space restrictions, only da/dN vs ΔK data is presented here.

The fatigue sharpening (pre-crack) was performed under constant amplitude loading and crack length was visually determined using a travelling microscope.

For the R -curve determination a displacement clip gage was used with screw attached knife edges spanning the

crack at a certain span. This procedure to attach the clip gages to the specimen is in accordance to the standard ASTM E561 [8].

3.2 Test procedure and setup

Fatigue crack growth tests were carried out in a MTS 321.21 with a 250kN load cell. A mechanical grip fixture was developed in order to comply with the specimen geometry and maximum loads defined in the general test plan [5].

The crack extension was measured using a travelling microscope in each side of the specimen. In some comparisons between measurements obtained with a travelling microscope and crack gages, performed in the scope of another research project, we found that the use of a travelling microscope was the most effective system to have detailed an accurate crack length vs. number of cycles data.

The geometry of each specimen was accurately measured before each test, especially in the section of the material affected by the welding process.

3.3 Results

27 specimens were tested. The following paragraphs present sequentially plots of da/dN vs. ΔK for $R=0.1, 0.5$ and 0.8 .

3.3.1 Specimens tested with $R=0.1$

Analysing the crack propagation data, Figure 8, it was verified that the higher values of crack growth rates were found for the specimens containing a notch in the centre of the weld, and the lower crack growth rates for base material specimens. The specimens with a notch in the HAZ present intermediate results. Analysing the base material specimens it is verified that for the lower ΔK values, between 6 and $8 \text{ MPa}\cdot\text{m}^{0.5}$, there is a significant decrease of the crack growth rate. This zone corresponds to a crack growing in an irregular surface. In this figure it is also verified that for ΔK values between 10 and $11 \text{ MPa}\cdot\text{m}^{0.5}$ data for all specimens converge to the same crack growth rate. As a future work, it should of interest to test similar specimens at ΔK values higher than $11 \text{ MPa}\cdot\text{m}^{0.5}$.

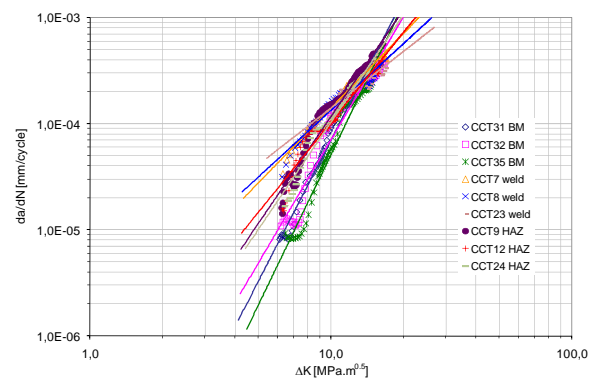


Figure 8- Crack propagation data for specimens tested with $R=0.1$.

3.3.2 Specimens tested with $R=0.5$

Analysing the crack propagation data, Figure 9, it was verified that for $R=0.5$ all type of specimens present similar crack growth results.

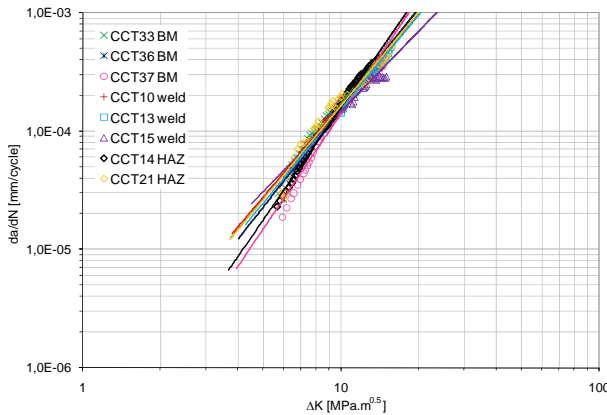


Figure 9- Crack propagation data for specimens tested with $R=0.5$.

3.3.3 Specimens tested with $R=0.8$

Analysing the crack propagation data, Figure 10, it was verified that for $R=0.8$ all type of specimens present similar crack growth results.

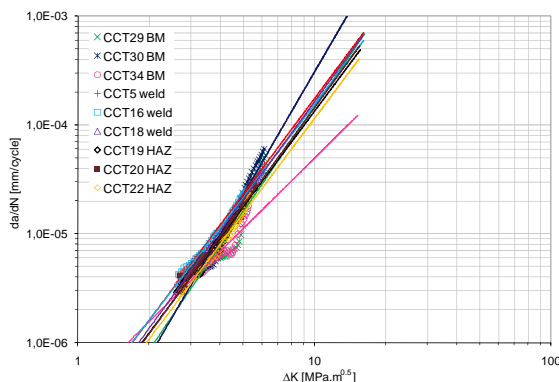


Figure 10- Crack propagation data for specimens tested with $R=0.8$.

In those cases where ΔK and R are comparable, the present da/dN results are in agreement of data of Hafley *et al* published by NASA, [10].

4. Concluding remarks

Good fatigue behaviour was found testing at room temperature FSW specimens of AA2195-T8X. When comparing base material and FSW SN data obtained with $R=0.1$ and 10^5 cycles the reduction of max. stress of FSW specimens is of the order of just 30%.

In those cases where ΔK and R are comparable, the present da/dN vs ΔK results are in agreement of existing NASA data.

Acknowledgements

The collaboration of P. Portela in the initial stages of this project, and contributions of A. Dias, D. Silva (CEMUP), F. Oliveira, J. F. R. Almeida, P. C. M. Azevedo, R. Silva, S. M. O. Tavares, V. Rêgo and J. Maeiro are acknowledged. P. Moreira acknowledges POPH - QREN-Tipologia 4.2 – Promotion of scientific employment funded by the ESF and MCTES.

References

1. Committee on New Materials for Advanced Civil Aircraft, *New materials for next-generation commercial transports*. 1996, Washington, D.C. : National Academy Press.
2. MT Aerospace, *Cut Off Plan*, in *Damage Tolerance of Cryogenic Pressure Vessels*, E.T.R. Project, Editor. 2008.
3. ASTM E466, *Constant Amplitude Axial Fatigue Tests of Metallic Materials*.
4. ASTM E468, *Standard Practice for Presentation of Constant Amplitude Fatigue Test Results for Metallic Materials*.
5. MT Aerospace, *Fracture Mechanics Test Plan*, in *Damage Tolerance of Cryogenic Pressure Vessels*, E.T.R. Project, Editor. 2008.
6. J. P. Bonnafé, D. Gabard, and E. Grosjean, *Aluminium Lithium alloys use for reusable future launcher cryogenic metallic tanks*, in *5th Conference on Aerospace, Materials, Processes, and Environmental Technology*. 2002: Huntsville, Alabama, USA.
7. ASTM E647-05, *Standard Test Method for Measurement of Fatigue Crack Growth Rates*. 2007.
8. ASTM E561, *Standard Practice for R-Curve Determination*. 2005.
9. P.M.G.P. Moreira, P.C.M. Azevedo, M.V.A. de Figueiredo, M. Windisch, G. Sinnema, and P.M.S.T. de Castro, *Fracture and fatigue crack growth behavior of friction stir welded Al-Li 2195-T8X*, in *8º Congresso Nacional de Mecânica Experimental*. 2010: Guimarães, Portugal.
10. R. A. Hafley, J. A. Wagner, and M. S. Domack, *Fatigue Crack Growth Rate Test Results for Al-Li 2195 Parent Metal, Variable Polarity Plasma Arc Welds and Friction Stir Welds*, in *NASA/TM-2000-210098*. 2000.

TENSILE-SHEARING STRENGTH IN ALUMINIUM RESISTANCE SPOT WELD AND WELDBONDED JOINTS

A.M. Pereira¹, J.A.M. Ferreira², F.V. Antunes² and P.J. Bártolo¹

¹ CDRsp, Centre for Rapid and Sustainable Product Development, Polytechnic Institute of Leiria, Morro do Lena - Alto Vieiro, 2400-901 Leiria, Portugal.
E-mail: mario.pereira@ipleiria.pt; pbartolo@ipleiria.pt

² CEMUC, Mechanical Engineering Department, University of Coimbra, Rua Luís Reis Santos, Pinhal de Marrocos, 3030-788, Coimbra, Portugal.
E-mail: martins.ferreira@dem.uc.pt; fernando.ventura@dem.uc.pt

ABSTRACT

The increasing restrictions in terms of performance, safety and energy consumptions imposed in the transport vehicles construction promotes the use of new materials and new processes searching weight reduction. Lighter materials and better joining processes, like adhesive bonding can contribute to obtain some weight gain. Present work studies the shear strength obtained by weld bonding technique and compares to the traditional resistance spot welding in aluminium based. The single lap joints were obtained with thin plates of 6082-T6 alloy and a high strength epoxy adhesive of two components (araldite 420 A/B). The strength of weldbonded joints was found to be significantly higher than equivalent spot welded joints. Numerical models were developed replicating experimental work. Nugget diameter was found to have a major influence in stiffness and stress level, while electrode indentation showed a much lower influence. The adhesive reduced significantly the stress level at nugget root.

KEYWORDS: Resistance spot welds, weldbonding, mechanical properties, finite element analysis

1. INTRODUCTION

The increasing restrictions in terms of performance, safety and energy consumptions imposed in the transport vehicles construction promotes the use of new materials and new processes searching weight reduction. Lighter materials, like aluminium alloys and better joining processes, like adhesive bonding and spot welding can contribute to obtain some weight gain [1,2]. Present work analysis the expected benefits on shear strength obtained by using weldbonding technique instead of the traditional resistance spot welding (RSW) or adhesive bonding in aluminium based thin plates.

Weld bonding is an alternative technology for joining parts based on structural adhesives and spot-welding. This hybrid process of joining is used to maximize the benefits of both joining processes [3]. The weldbonding offers advantages relatively to the other conventional joining processes, namely, acoustic isolation, vibration attenuation, reduction of corrosion problems, and more uniform stress distribution. Chang *et al.* [4], Ghosh and Vivek [5] and Santos *et al.* [6] conducted studies to characterize and compare the performance of resistance spot welding, adhesive bonding and weldbonding joining processes under static loading. Several experimental studies have been reported on the

mechanical behaviour of weldbonding joints, particularly in steel adherends. Joints with aluminium adherends are less studied. Static behaviour needs a significant research effort in order to understand the failure mechanisms and the influence of parameters like surface pre-treatment, adhesive thickness, adherends thickness or process parameters (weld current, weld time and electrode force) of spot welded joints.

Strength of weldbonded joints was predicted by Samhan *et al.* [7]. The adhesive-bonded and resistance spot-welded joints were also included in this study for comparison with weldbonding. This study demonstrated that, the major principal stress predicted in spot-welded joints is small, when compared with those associated with weldbonded and adhesive-bonded joints. In weld-bonded joints the stresses are concentrated at the overlap region as well as both ends of the welding nugget. This work also demonstrated the effective role played by the adhesive layer in strengthening weldbonded joints. Chang *et al.* [4] compared stress distributions of weld-bonded joints, spot-welded joints and adhesive-bonded joint. The numerical results showed that the stresses in the lap zone of weldbonded joints are more uniformly distributed than in spot-welded joints. The stresses of weldbonded joints in the lap zones, with the exception of the spot-weld zones,

have almost the same characteristics as those of adhesive-bonded joints. The strengths of these joints predicted from the results of the stress analysis are coincident with existing experimental results. The application of adhesives in spot welding also improves the joint fatigue performance, while the presence of weld spots in adhesive-bonding has a negative effect on the joint fatigue performance [3].

Although the effect of the process parameters in the mechanical behaviour of weldbonding on carbon and stainless steels is well documented, results for aluminium alloys still are scarce. A better understanding of the effect of process parameters on the mechanical behaviour of weldbonded joints in heat treatable aluminium alloys such as 6082-T6 is required. The objective of the current research is to investigate the effect of process parameters on shear strength and failure mode of weldbonding joints in thin sheets of 6082-T6 aluminium alloy.

2. MATERIALS PROCESSING AND TESTING

The material considered for the adherends in the current study was a 6082-T6 aluminium alloy in the form of 1.0 mm thick sheet. The single lap joints were obtained using a two components high strength epoxy adhesive (Araldite 420 A/B from Hunstman) and resistance spot welding (RSW). The nominal chemical composition and basic mechanical properties of this alloy are given in Table 1. The adherend was characterized in terms of chemical composition and mechanical properties. Table 1 shows the chemical composition of the AA 6082-T6 obtained from emission spectrometer analysis. Mechanical properties of the aluminium alloy were obtained using tension static tests and a resonant technique [8]. The mechanical properties of the adhesive were obtained from de Moura et al. [9].

Table 1. Chemical composition and mechanical properties of the 6082-T6 aluminium alloy.

Tensile strength [MPa]	Yield strength [MPa]	Alloying elements (% wt)					
		Si	Mn	Mg	Fe	Cu	Al
305.6	245.1	1.02	0.67	0.76	0.26	0.02	97.24

The weldbonding joints were obtained using a high strength epoxy adhesive of two components (araldite 420 A/B) to bond the specimen surface immediately before weld. The AA 6082-T6 sheets were cut to 100 x 25 mm² (Figure 2) and their sheet surfaces were randomly abraded with P220 grade sandpaper. At the end the surface was cleaned with dry air, to eliminate surface contamination and promote adhesion, before adhesive bonded. Surface roughness was measured after surface preparation, using a mechanical stylus contact method with a radius of 5 μm, and the average roughness is $R_z = 7.2 \pm 0.70$ [μm]. The bonding process was optimized in a previous work by Pereira et al. [10,11] and it was selected to prepare the surface pre-

treatment by abrasive polishing. For adequate bonding, the specimens were compressed with a pressure of 0.157MPa applied during all cure time (4 h at 50 °C).

The welds were done using a Sciaky RSW type PMC02 electric resistance spot welding machine, with a nominal welding power of 100 kVA. The machine employs type C18200 electrodes having an end diameter of 15.25 mm, an electrical conductivity of 0.463 m/Ωmm² and a tensile strength of 310 N/mm². The hemispherical electrode tip radius is of 101.6 mm. The welding conditions were selected based on previous tests [12]. Thirteen weld series were done, changing weld current, time and electrode force. The timing diagram used in all tests is schematically represented in Fig.1.

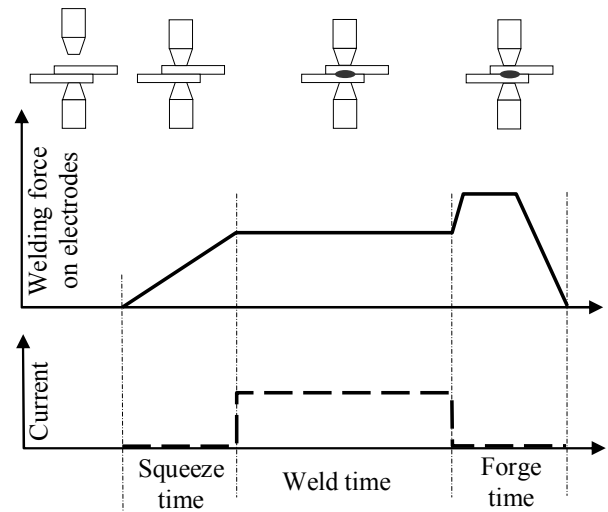


Figure 1. Typical spot-welding cycle.

The parameters were: electrode force 2354 - 4709 N, weld time 1 - 5 cycles and weld current 23.5 - 28.7 kA. The squeeze and forge times were constant in all tests. The forge force used was 6474.6 N. The welds were done in open air at room temperature. Figure 2 shows the specimen geometry and dimensions of the specimens.

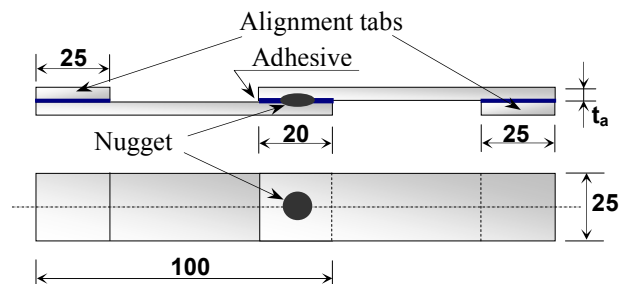


Figure 2. Dimensions of RSW and weldbonded specimens (not to scale, dimensions in mm).

Five specimens were welded in each series; four specimens to be used for static tensile shear strength testing and one for microstructure examination and hardness measurement. Specimens used for microstructure examination and hardness measurement

were cut out along the center of the nugget, at right angles to the longitudinal direction of specimens. Specimens were polished and a modified Poulton's reagent was employed to reveal the microstructure. Metallographic analysis was performed using a ZEISS HD 100 optical microscope. Hardness measurements were carried out in two directions (along the radius of the nugget and through the sheet thickness) using a Struers Duramin Vickers machine, under a load of 100 g. Finally, the shear strength testing was done in an electromechanical Instron Universal Testing machine at a constant cross-head speed of 1 mm/min, up to the final failure of the joint.

3. RESULTS AND DISCUSSION

3.1. Experimental results

Figure 3 shows typical load – extension curves obtained for RSW and weldbonding joints. It is evident that weldbonded joints have much higher failure loads and extension at failure than similar spot weld joints.

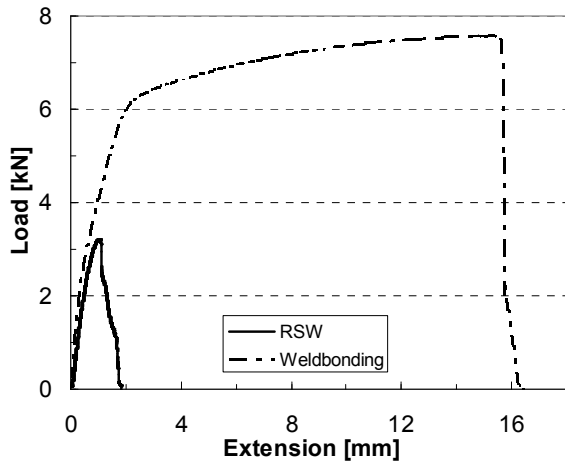


Figure 3. Load – extension curves for RSW and weldbonded joints (with 6.5 mm diameter nuggets).

Figures 4 and 5 show the failure load versus the electrode force and weld current, respectively. For comparison the results for resistance spot weld (RSW) joints and weldbonded joints were superimposed. Both figures show that weldbonded joints have much higher strength than equivalent spot welded joints. On other side, the sensibility of weldbonded joints relatively to weld current and electrode force is negligible within the parameter range studied. These two findings mean that the resistance of the joint is controlled by the bonded liaison.

In the tensile-shear testing of RSW and weldbonding joints two types of failure mode were obtained: pull out mode and interfacial mode. Figure 6 shows typical pull out failure surfaces. Similar failure surfaces were obtained for both type of joints (RSW and weldbonding).

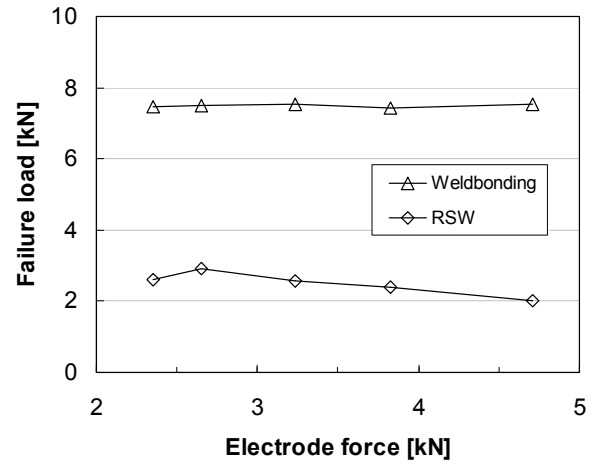


Figure 4. Load failure against the electrode force. RSW parameters: weld time, 2 cycles; weld current, 26.9 kA.

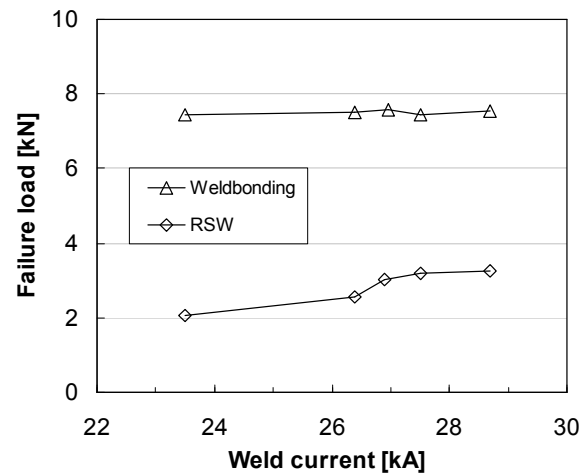


Figure 5. Load failure against the weld current. RSW parameters: weld time, 2 cycles; electrode force, 3237 N.

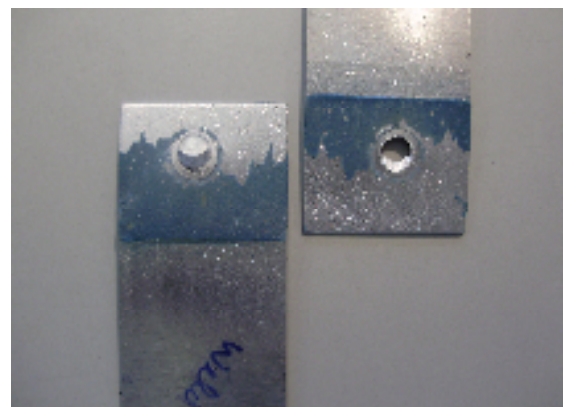


Figure 6. Typical pull out weldbonding failure.

3.2. Numerical analysis

A numerical analysis was developed to understand the deformation and failure mechanisms of resistance spot welding and weldbonded joints. Sources of complexity are electrode indentation (i.e. the plastic deformation

caused by the welding process), the small crack tip radius, the heterogeneity of the materials and the residual stresses. The material properties of spot-welded joints can vary widely between the base metal, the heat-affected zone, and the weld nugget itself. Figure 7 illustrates the model assumed. Only half specimen was studied, considering adequate symmetry conditions. The left side was fixed, replicating the upper grip of the servo-hydraulic testing machine. The rotation of the right side was inhibited, while the load was applied.

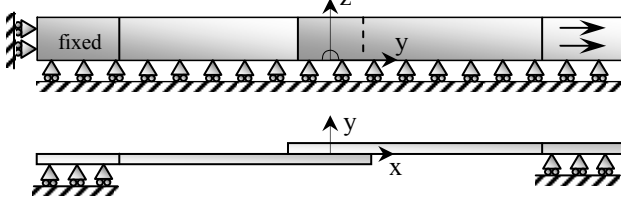


Figure 7. Physical model.

The diameter of the nugget depends of electrode force, weld time and particularly of welding current. Values in the range 5-6mm were typically obtained. The electrode indentation is also visible in figure 8. The depth depends mainly on welding time and welding current, and values up to 15% of initial sheet thickness were obtained. Figure 8 shows that at the root of the nugget, the sheets are close, which indicates that the concordance radius is quite small. A radius of 5 μm was assumed in the numerical model. At relatively large distances from the nugget, the sheets are clearly separated, and a value of 80 μm was assumed. This is also the thickness of the adhesive in the weldbonded joints. The cracks start and propagate between de nugget and heat-affected zone (HAZ). Therefore it may be expected that maximum von Mises stress occur at the edges of the nugget.

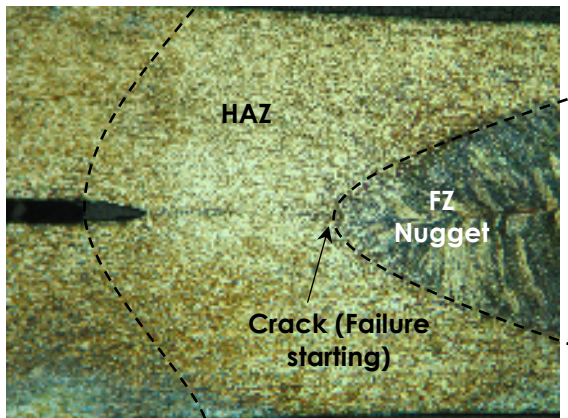


Figure 8. Geometry at the root of nugget.

Both the aluminium alloy and the adhesive were modelled as having elastic-plastic properties. The elastic properties assumed were $E=69070$ MPa, $\nu=0.35$ for the 6082-T6 aluminium alloy (obtained experimentally using the resonant technique), and $E=1850$ MPa, $\nu=0.3$ for the adhesive. The plastic behaviour was

characterised with classical tension tests. The HAZ, (figure 8) was identified with hardness measurements, as illustrated in figure 9. A gray ribbon represents the hardness of the base material. A significant decrease in hardness was observed in the nugget of all the welds shown, resulting from precipitates dissolution.

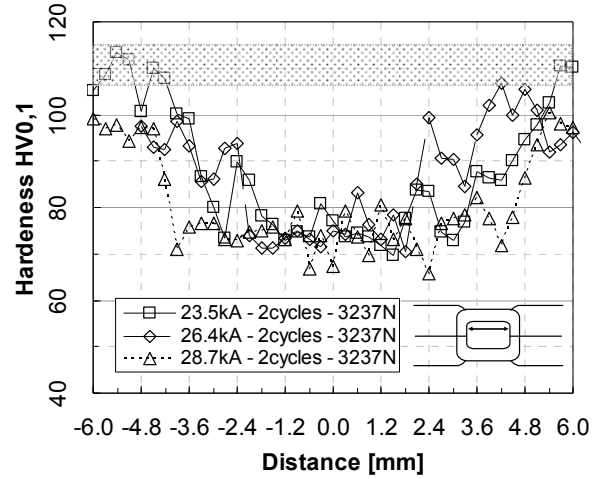


Figure 9. Hardness plot.

The evaluation of the shear strength of the nugget and HAZ of spot welds is difficult, because those regions are narrow and present microstructural gradients. Currently, the yield and tensile strength of materials are related to their hardness through empiric equations characterised by the generic equation (1), where HV and σ represent the Vickers hardness and tensile strength of the material, respectively, and K is approximately constant, assuming the elastic properties are approximately constant inside each family of materials [13,14]. In addition, according to the Tresca criterion, both the shear and tensile strength of a metal are connected by a mathematical constant (shear strength is half of the tensile strength of the material).

$$HV = K\sigma \tag{1}$$

Hardness is easier to evaluate than the tensile strength of the nugget or HAZ of the welds. While the hardness in the nugget is approximately constant, the HAZ' hardness exhibits a gradient between the nugget and the non-affected base material, as shown in Figure 9.

In previous works of Pereira et al [12] the static failure load versus nugget diameter was studied for RSW in aluminium. This diameter was found to be the geometrical controlling parameter, and a linear relation was obtained with failure load.

Figure 10 shows the finite element mesh, which is composed of 82552 linear isoparametric elements and 90204 nodes. Characteristics aspects of this model are the small radius considered at nugget root (5 μm), the thickness of the adhesive (80 μm) and the possible consideration of four distinct materials (base material, nugget, HAZ and adhesive). Notice also that there is a

region around the nugget without adhesive. This model is relatively heavy, therefore a second model was defined, proposed for parametric studies concerning geometric, load and material parameters. A sharp notch was assumed at nugget root. Figure 11 compares experimental results with numerical predictions. An acceptable agreement is evident for relatively low loads. The experimental results lie between model 1 and 2. Notice that the thickness is different in models 1 and 2, because a gap of 80 μm was considered in model 1 between the sheets. The numerical model is not predicting failure, which explains the difference for relatively high loads. Results for elastic properties of aluminium alloy are also presented. For loads above 2000N the plastic deformation is evident.

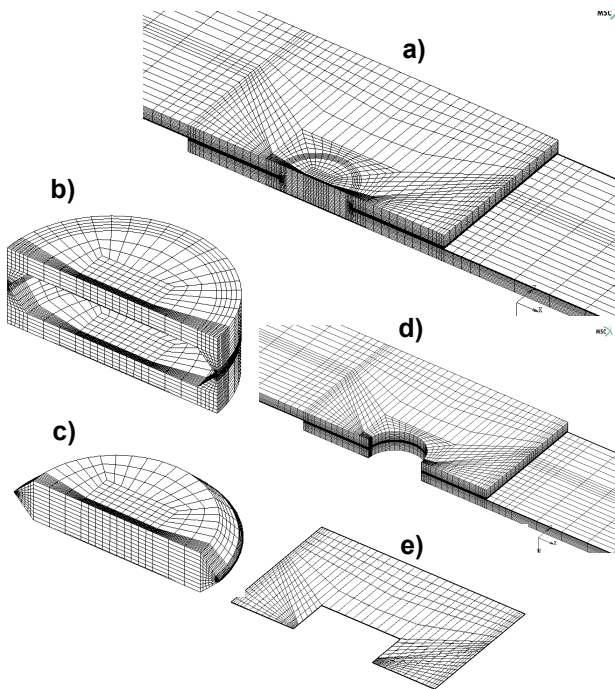


Figure 10. Finite element mesh. a) Global view. b) Heat-affected zone. c) Nugget. d) Base material. e) Adhesive.

Figure 12 shows the influence of nugget diameter (D) on global stiffness. For relatively low loads, D does not influence the deformation. When the plastic deformation initiates ($P > 2000$ N), the specimen with lower nugget diameter shows a quite reduced stiffness.

Figure 13 shows the influence of nugget diameter (D) and electrode indentation on plastic strain and longitudinal stress. d is distance from nugget root, as indicated in figure 11. The indentation has a minor influence, but diameter reduction increases significantly the stress and strain field.

Figure 14 shows the equivalent von Mises stress, starting from the root of the notch. The stress level is significantly higher for the RSW joint, which explains

its lower resistance. In other words, the adhesive has a protective effect in the spot weld.

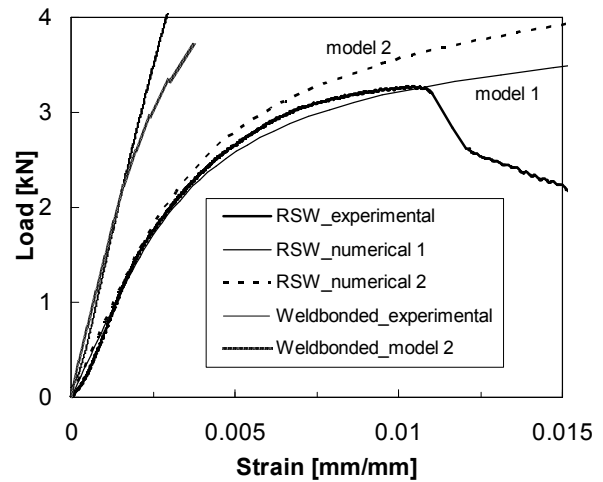


Figure 11. Numerical versus experimental results ($D = 5.7$ mm).

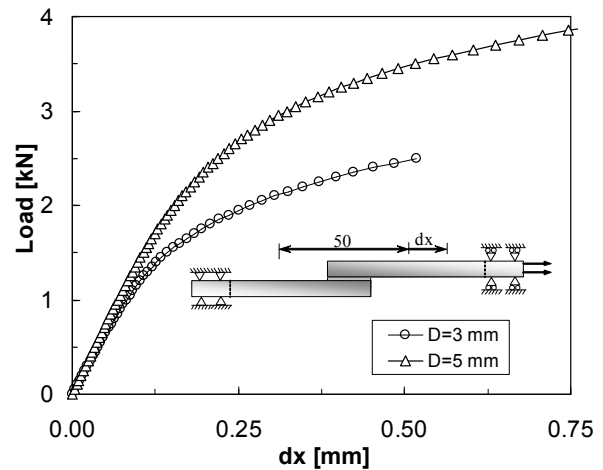


Figure 12. Influence of nugget diameter on global stiffness ($P = 2.5$ kN).

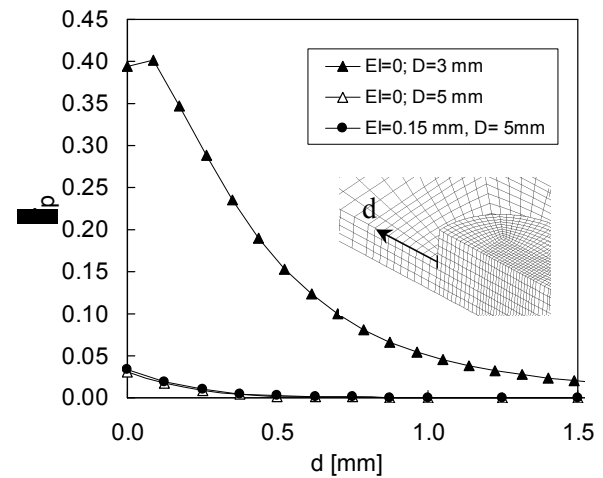


Figure 13. Influence of nugget diameter and electrode indentation (EI) on equivalent plastic strain ($P = 2.5$ kN).

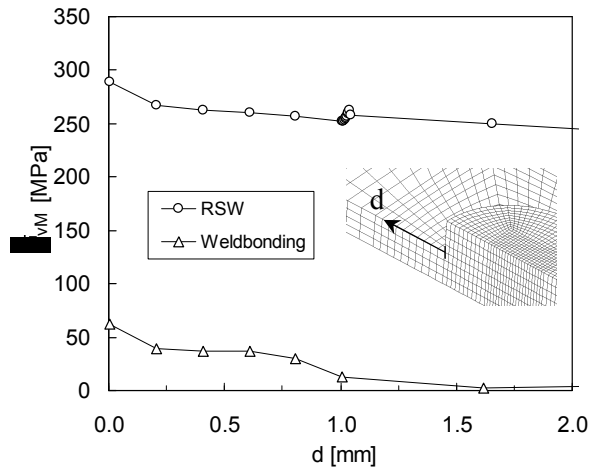


Figure 14. Influence of process joining on equivalent von Mises stress ($P=2.5\text{ kN}$).

4. CONCLUSIONS

The influence of the weld parameters on the microstructure and tensile shear strength of resistance spot welds made of aluminium alloy 6082-T6 was studied. Numerical models were developed to predict global stiffness, local stresses and failure loads. The conclusions obtained are summarised as follows:

- Weldbonded joints have much higher strength than equivalent spot welded joints;
- Sensitivity of weldbonded joints relatively to weld current and electrode force is negligible within the parameter range studied;
- Strength of the weldbonding joint is controlled by the bonded liaison;
- A good agreement was found between numerical predictions of load versus displacement curves and experimental results;
- Nugget diameter was found to have a major influence while electrode indentation has a residual effect;
- The stress level at nugget root was found to reduce significantly by adding the adhesive.

ACKNOWLEDGMENTS

The authors thank the financial support of the Portuguese Foundation for Science and Technology (grant SFRH/BD/37384/2007).

REFERENCES

[1] Barnes, T.A., Pashby, I.R., "Joining techniques for aluminium spaceframes used in automobiles Part II - adhesive bonding and mechanical fasteners", *Journal of Materials Processing Technology*, vol. 99, pp. 72-79, 2000.

[2] Pereira, A.M., Ferreira, J.M., Antunes, F.V., Bártolo, P.J., "Study on the Fatigue Strength of AA 6082 - T6 Adhesive Lap Joints", *Int. J. Adhes. Adhes.*, vol. 29, pp. 633-638, 2009.

[3] Chang, B., Shi Y., Lu, L., "Studies on the stress distribution and fatigue behavior of weld-bonded lap shear joints", *Journal of Materials Processing Technology*, vol. 108, pp. 307-313, 2001.

[4] Chang, B., Shi, Y., Dong, S., "Comparative studies on stresses in weld-bonded, spot-welded and adhesive-bonded joints", *J Mater Process Technol*, vol. 87, pp. 230-236, 1999.

[5] Ghosh, P.K., Vivek, "Weldbonding of stainless steel", *ISIJ International*, vol. 43 (1), p.85-94, 2003.

[6] Santos, I. O., Zang, W., Gonçalves, V.M., Bay, N., Martins, P.A.F., "Weld bonding of stainless steel", *Inter J Machine Tools Manufacture*, vol. 44, pp.1431-1439, 2004.

[7] Al-Samhann, A., Darwish, S.M.H., "Strength prediction of weld-bonded joints", *International Journal of Adhesion & Adhesives*, vol 23, pp. 23-28, 2003.

[8] Antunes, F.V., Ramalho, A., Ferreira, J.A.M., Capela, C., Reis, P., "Determination of Elastic Properties by Resonant Technique: a Sensitivity Analysis", *J. Testing and Evaluation*, vol. 36(1), pp. 89-99, 2008.

[9] de Moura, M.F.S.F., Daniaud, R., Magalhães, A.G., "Simulation of mechanical behaviour of composite bonded joints containing strip defects", *Int. J. Adhes. Adhes.*, vol. 26, pp. 464 - 473, 2006.

[10] Pereira, A.M., Bártolo, P.J., Ferreira, J.M., Antunes, F.V., "Laminated object manufacturing with aluminium bonded sheets". In Bártolo, P.J. et al (Eds), *Virtual and Rapid Manufacturing-Advanced Research in Virtual and Rapid Prototyping*, Taylor and Francis, London, pp. 597-601, 2008.

[11] Pereira, A.M., Ferreira, J.M., Antunes, F.V., Bártolo, P.J., "Study on the Fatigue Strength of AA 6082 - T6 Adhesive Lap Joints", *Int. J. Adhes. Adhes.*, vol. 29, pp.633-638, 2009.

[12] Pereira, A.M., Ferreira J.M., Loureiro A., Costa J.D.M., Bártolo P.J., "Effect of Process Parameters on the Strength of Resistance Spot Welds in 6082-T6 Aluminium Alloy", *Materials and Design*, doi.org/10.1016/j.matdes.2009.11.052, accepted manuscript.

[13] Salazar-Guapuriche, M.A., Zhao, Y.Y., Pitman, A., Greene, A., "Correlation of Strength with Hardness and Electrical Conductivity for Aluminium Alloy 7010", *Materials Science Forum*, vol. 519-521, pp. 853-858, 2006.

[14] Wanga, R., Shang, G., "Low-cycle fatigue life prediction of spot welds based on hardness distribution and finite element analysis", *International Journal of Fatigue*, vol. 31, pp. 508-514, 2009.

EFFECT OF FATIGUE DAMAGE ON THE DYNAMIC TENSILE BEHAVIOR OF CARBON STEEL WELDED JOINTS

C. Rubio-Gonzalez¹, E. Miranda-Paniagua² G. Mesmacque³

¹ Centro de Ingeniería y Desarrollo Industrial, Pie de la cuesta 702, Desarrollo San Pablo, 76130 Querétaro, Qro, México.

crubio@cidesi.mx

² Instituto Tecnológico de Morelia, Av. Tecnológico 1500, Morelia Michoacán, 58120, México

³ Laboratoire de Mécanique de Lille, Université de Lille 1, UMR CNRS 8107, Villeneuve d'Ascq 59650, France
gerard.mesmacque@univ-lille1.fr

ABSTRACT

In different engineering applications such as automobile and train crashes, the high speed impact of debris as well as the high speed manufacturing processes, makes it necessary to have a deep understanding of the dynamic behavior of materials and components. There are different experimental techniques to determine the constitutive material behavior. Several constitutive models have been proposed to predict the dynamic response of engineering structures. However, in all cases, initial damage-free material is assumed and the structures are without fatigue damage when tested. The dynamic response of fatigue damaged AISI 1018 steel welded joints subjected to impact loading is investigated in this work. The tensile Hopkinson bar apparatus is used in the dynamic experiments. Welded joints without post weld heat treatment are used. Samples subjected to previous high cycle fatigue are considered. An investigation of the failure modes is performed as well. Results show that previous fatigue damage affects the quasi-static and dynamic tensile behavior. The effect of the previous fatigue damage on the quasi-static and dynamic tensile behavior on the base material and the welded joint is compared. Previous fatigue damage has a detrimental effect on ductility of 1018 steel welded joints, principally under dynamic loading.

KEY WORDS: Impact loading, Welded joint, Hopkinson bar, Fatigue damage.

1. INTRODUCTION

Welding fabrication is one of the most common joining procedures of metallic structures. The vast majority of component fatigue failures take place at the welded connections [1]. Many of the welded structures and components are subjected to fatigue and impact loading.

It is well known that the mechanical behavior, such as yield stress, ductility and strength of materials, will change under different strain-rate loadings and temperatures [2]. An understanding of the deformation of metals over a wide range of temperatures and strain rates is important in metal forming, high speed machining, high velocity impact, penetration mechanics, explosive-metal interaction, and other similar dynamic conditions. Impact problems have been studied for long time. A complete material description for numerical simulation involves not only the stress-strain response, but also the damage accumulation and failure mode [3].

The dynamic behavior of different materials under the action of impact tensile loading has been investigated and reported in the open literature. The dynamic

mechanical behavior of welded joints has been studied for low alloy steels [4] and for stainless steels [5-7]. The dynamic response of welded HSLA 100 steel was investigated in [4]. High velocity impact tests were performed on 304L stainless steel joints [5] using a compressive split Hopkinson bar. Different welding procedures were applied; Gas Tungsten Arc Welding (GTAW) [5], Shielded Metal Arc Welding (SMAW) [6] and Plasma Arc Welding [7]. The results show that the impact properties and fracture characteristics of the tested weldments depend strongly on the applied strain rate.

Little work has been done to evaluate the effect of previous fatigue damage on the dynamic response of materials and structures. The effect of fatigue damage induced by cyclic plasticity on the dynamic tensile behavior of materials has been reported in [8, 9]. No works are available related to the consequences of the previous fatigue damage on the dynamic behavior of welded joints. The AISI 1018 steel is a general purpose low carbon steel. It has been successfully welded using most all the common practices including gas, resistance, oxyacetylene, and submerged melt welding. It is

desirable to investigate the response of AISI 1018 welded joints subjected to impact loading and the effect of the previous fatigue damage on the dynamic response of the welded components.

The aim of this paper is to investigate the effect of previous fatigue-damage on the dynamic tensile behavior of samples obtained from AISI 1018 welded joints by using the split Hopkinson bar apparatus. Different loading rates and previous fatigue damage levels are considered. Quasi-static stress-strain response for different damage levels are evaluated as well. Fatigue damage was introduced on the test specimens by application of cyclic loading under a stress control condition. The response of the welded joints and that of the base material are compared. Next the experimental procedure is described, followed by the results and a discussion of them. The influence of previous fatigue damage on quasi-static and dynamic mechanical properties and failure modes on both materials are analyzed. Finally, conclusions are presented.

2. EXPERIMENTAL PROCEDURE

2.1 Materials, welding process and specimen preparation

In this study, some sets of AISI-1018 steel plates with dimensions 250 × 50 × 6.3 mm were welded using an E5154-B10 (7018) filler metal. The welding process was performed using the shielding metal arc welding (SMAW) technique to butt-weld the two plates of this steel. Figure 1(a) presents a schematic diagram of the welding configuration, in which it can be seen that two plates are welded together with a 2 mm root opening gap and a V-shaped joint groove with 60° angle. After completion of the welding process, tensile specimens were obtained from the middle of the welded joint by mechanical cut. Tensile specimen dimensions are shown in Figure 1.

2.2 Tension test

Quasi-static mechanical properties of both materials were obtained on a MTS-810 testing machine applying monotonic load at a constant speed of 1 mm/min. Table 1 presents the results obtained for the mechanical properties of damage-free material at room temperature. The yield strength was calculated employing the 0.2% offset method.

2.3 Fatigue tests

Stress-controlled fatigue tests performed on an MTS810 machine allowed the determination of S-N curves applying uniaxial cyclic loading between constant stress limits with stress ratio $R = \sigma_{min} / \sigma_{max} = 0.2$. The smooth specimens used had 3.15mm in diameter at center, see Figure 1(b). Cyclic loading with sinusoidal wave form at frequency of 35Hz was applied in air at

room temperature. It was possible to induce fatigue damage on the tensile specimens at damage levels of $D=0.25, 0.50$ and 0.75 ; where $D=n/N_f$ being n and N_f the applied cycles and the applied cycles to failure, respectively.

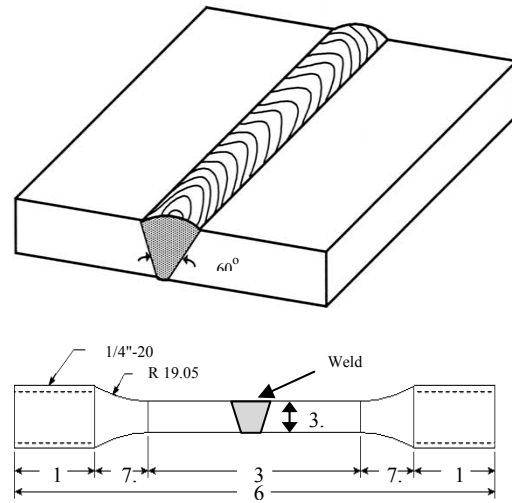


Figure 1. Schematic illustration of the welded joint and specimen used in the quasi-static and dynamic tests. Dimensions in mm.

2.4 Impact test apparatus and dynamic tests

The Hopkinson bar test has been widely accepted to produce strain rates in the order of 10^2 to 10^4 s^{-1} . The apparatus consists mainly of an air gun, a projectile, two Hopkinson pressure bars (one incident and one transmitter), a velocity measuring device and recording equipment, for a description of the Hopkinson bar test see for example [2,11,12]. Figure 2 shows an illustration of the bar used on the experiments.

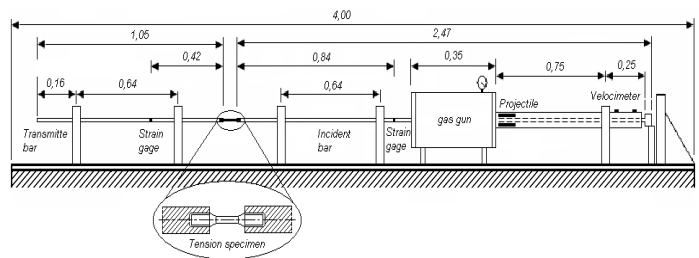


Figure 2. Schematic illustration of the tension Hopkinson bar. Dimensions in mm

3. RESULTS AND DISCUSSION

3.1 Fatigue Tests

Even though fatigue life is needed only under given stress conditions, the complete S-N curves were determined for the base material, the welded specimens with and without heat treatment. Fatigue life, N_f , may be determined from those curves for a given maximum stress σ_{max} at a stress ratio of $R = 0.2$. Fitting the experimental results, the S-N curves may be described by the following Basquin type equation

$$\sigma_{max} = AN_f^b$$

where σ_{max} in given in MPa. Results for A and b are given in [10].

3.2 Quasi-static tension tests

Quasi-static tension tests were performed on specimens with fatigue damage $D=0.25, 0.50,$ and 0.75 . To determine the influence of previous fatigue damage, quasi-static stress-strain curves were determined and shown in Figure 3 with stress-strain curves of damage-free materials included for comparison. From results of Figure 3(a), it is possible to observe no significant effect of previous fatigue damage on the stress-strain response of specimens with as weld condition and $D=0.25, 0.50$ and 0.75 . Young's modulus and yield stress are approximately the same. In other words, the stress strain curves for specimens with previous fatigue damage are almost the same, but they are different from those corresponding to the damage free specimens. The stability of quasi-static mechanical properties at different damage levels enhances the behavior of this structural welded steel. It is also worth noting that the yield stress of fatigue damaged specimens is higher than that of damage free specimens. In addition, note that after applying the stress relief heat treatment to the welded joint makes the yield stress decrease approximately 10%.

Table 1. Mechanical properties. Quasi-static condition without damage

	Base Material	Welded Joint
Young's modulus (GPa)	204.7	196.0
Yield stress (MPa)	702.0	455.0
Ultimate stress (MPa)	728.8	587.4

For a summary of the quasi-static mechanical properties see Table 2. From the quasi-static tension tests it is observed that the yield stresses increases about 35% when the damage level changes from $D=0$ to $D=0.75$ for specimens with the as weld condition. A similar behavior is exhibited by the ultimate stress, increasing approximately 12%, on the damage level interval from 0 to 0.75. The increase of the yield stress applying cyclic loading is due to the material strain hardening.

It is worth noting that the quasi-static yield stress of the welded joints is lower (around 35%) than that of the base metal.

Table 2. Quasi-static mechanical properties at different

	Welded joint			
	D=0	0.25	0.50	0.75
Young's Modulus (GPa)	196.0	210.3	214.9	227.9
Yield stress (MPa)	455.0	585.1	600.0	613.6
Ultimate stress (MPa)	587.4	613.1	610.6	655.5

damage levels

3.3 Dynamic tension tests

Dynamic stress-strain curves of the base metal and welded joint, obtained by using the Hopkinson bar apparatus are shown in Figure 4. Quasi-static stress-strain curves for damage-free materials (base metal and welded joint) are included for comparison. Comparing the dynamic stress strain curves of Figure 4 generated with projectile velocities $v=18m/s$ and $v=25m/s$ we observe no much difference between them; that is, the base metal and the welded joints are not affected significantly by the strain rate. However, it is possible to observe that values for the dynamic yield stress, σ_y , and the maximum stress, σ_u , are higher from those values obtained in quasi-static tests, for the base metal and the welded joints as well.

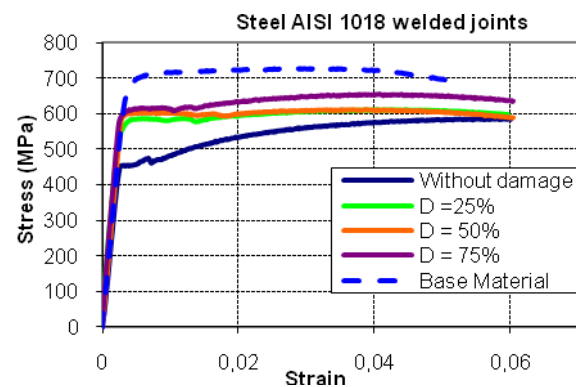


Figure 3. Quasi-static stress-strain curves of the welded joint

The effect of previous fatigue damage, on the dynamic stress strain response, is shown in Figure 5 where different damage levels were considered, the projectile velocity was 25m/s.

3.4 Effect on ductility

To assess the effect of previous fatigue damage and strain rate on ductility of the aluminum and steel samples, one ductility related parameter was evaluated: the percent reduction in area, %RA, given by [13]. This parameter compares the cross-sectional area after fracture, A_f , with the original area A_i .

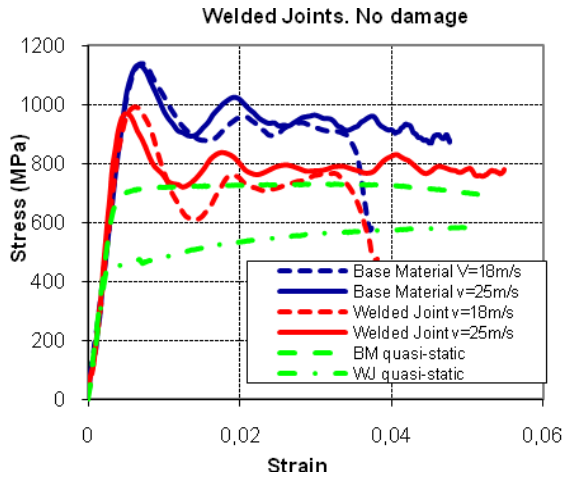


Figure 4. Quasi-static and dynamic stress strain curves of damage free welded joints and base metal at different projectile velocities.

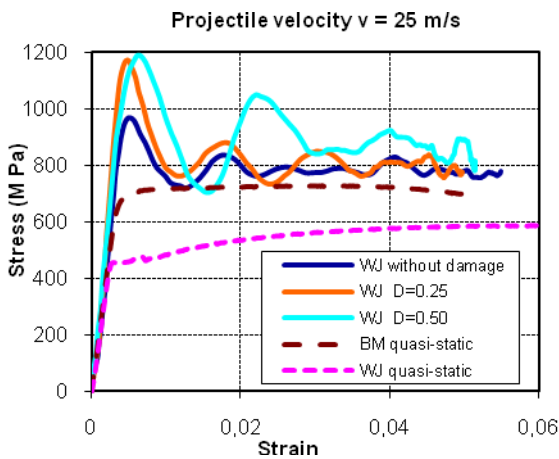


Figure 7. Quasi-static and dynamic stress strain curves of the welded joint and base metal with different damage levels. WJ and BM stand for welded joint and base metal, respectively.

Figure 8 shows the %RA for different damage levels on the welded specimens without stress relief heat treatment tested with a projectile velocity of 25m/s. The percent reduction in area changes (from approximately 48% to 38%) increasing the damage level; while the quasi-static %RA changes from 58% to 50%. Thus, fatigue damage has a detrimental effect on ductility of

welded samples in quasi-static and dynamic tension tests. Hence, previous fatigue damage has a detrimental effect on ductility of AISI 1018 steel welded joints even with stress relief heat treatment, mainly on the dynamic loading conditions. This result is due to the strain hardening because of the cyclic loading.

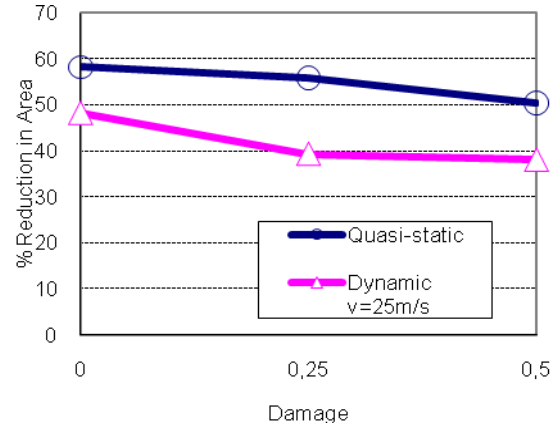


Figure 8. fatigue damage effect on ductility of AISI 1018 steel welded joints. Projectile speed for the dynamic tests $v=25\text{m/s}$, Percent reduction in area %RA

3.5 Failure modes

Figure 7 shows a photograph of a tested specimen showing the welded joint and the fracture surface. Note that the fusion line is oriented about 60° with respect to the specimen axis, and the fracture surface has approximately the same orientation.

Figure 13(a) shows the effect of fatigue damage on the failure modes of steel samples on the quasi-static experiments. We may observe that fracture surface orientation changes with the damage level D . For specimens with $D=0.25$, the fracture surface is about 60° from the specimen axis, while the angle is near 90° when $D=0.75$. In addition, note that significant necking is appreciated in all the cases. Damage occurs by void nucleation, growth and coalescence of voids at second phase particles. It is concentrated in regions adjacent to the fracture surface where plastic strains and the associated hydrostatic stresses are highest. This suggests that there is a transition on the steel behavior increasing D . A ductile response is observed at small values of D while a brittle behavior is exhibited by the material at high damage levels.

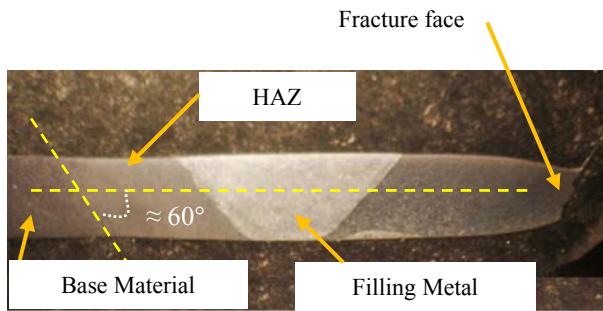


Figure 7. Photograph of a tested specimen showing the welded joint and the fracture surface.

For specimens with $D=0$, the fracture surface is about 60° from the specimen axis, while the angle is near 90° when $D=0.75$, for both specimens with and without heat treatment. In addition, a significant necking is appreciated in all the cases.

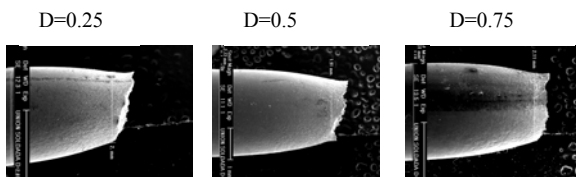


Figure 8. Fracture modes of AISI 1018 steel welded joints at different fatigue levels

4. CONCLUSIONS

The influence of previous fatigue damage on the quasi-static and the dynamic tensile behavior of AISI 1018 steel welded joints have been evaluated. Dynamic tension tests were performed on a Hopkinson bar apparatus.

From the quasi-static tension tests it is observed that the yield stresses increases when the damage level increases as well. A similar behavior is exhibited by the ultimate stress. It is worth noting that the quasi-static yield stress of the welded joints is lower (around 35%) than that of the base metal.

The dynamic experiments show that the yield stress of the welded joints is lower than that of the base metal. The projectile speed does not affect significantly the dynamic response neither of the welded joints nor that of the base metal. The dynamic response of welded specimens without stress relief heat treatment shows

that the yield stress increases when increasing the damage level.

From the failure surface analysis of the samples, it is observed that the fracture surface plane was oriented about 60° with respect to the specimen axis for damage-free specimens, while that angle was near 90° when $D=0.75$. This suggests a transition on the steel behavior when increasing D . A ductile response is observed at small values of D while a brittle behavior is exhibited by the material at high damage levels. This is in agreement with the decrease in %RA when the damage level is increased.

REFERENCES

- [1].J.M. Barsom, S.T. Rolfe, Fracture and fatigue control in structures, ASTM Publications, 1999
- [2].M. A. Meyers, Dynamic Behavior of Materials, Wiley Interscience Publication, 1994
- [3].J. A. Zucas, Impact Dynamics, Wiley. 1990.
- [4].Q. Xue, D. Benson, M.A. Meyers, V.F. Nesterenko, E.A. Olevsky, Constitutive response of welded HSLA 100 steel, Materials Science and Engineering A354 (2003) 166-179.
- [5].W. Lee, C. Lin, C Liu, F. Tzeng, Impact properties of 304L stainless steel GTAW joints evaluated by high strain rate of compression tests, Journal of Nuclear Materials 335 (2004) 335-244.
- [6].W. Lee, F. Tzeng, C. Lin, Mechanical properties of 304L stainless steel SMAW joints under dynamic impact loading, Journal of Materials Science 40 (2005) 4839-4847.
- [7].W. Lee, C. Lin, C Liu, C. Cheng, Effects of strain rate and welding current mode on microstructural properties of SUS 304L PAW welds, Journal of Materials Processing Technology 183 (2007) 183-193.
- [8].U. Sánchez-Santana, C. Rubio-González, G. Mesmacque, A. Amrouche, X. Decoopman, Effect of fatigue damage induced by cyclic plasticity on the dynamic tensile behavior of materials, International Journal of Fatigue 30(2008)1708-1719
- [9].U. Sánchez-Santana, C. Rubio-González, G. Mesmacque, A. Amrouche, X. Decoopman, Dynamic tensile behavior of materials with previous fatigue damage, Materials Science and Engineering A 497(2008)51-60
- [10]. C. Rubio-González, E. Miranda, G. Mesmacque, A. Ruiz, Dynamic tensile behavior of steel welded joints with previous fatigue damage, Submitted to International Journal of Fatigue (2009)
- [11]. H. Kolsky, Stress waves in solid media, Dover Publications, 1963.
- [12]. K. F. Graff, Wave motion in elastic solids. Dover Publications 1991.

- [13]. N.E. Dowling, Mechanical behavior of materials, Prentice Hall 2007.

MICROESTRUCTURA Y RESPUESTA MECÁNICA A ALTAS TEMPERATURAS DE UNIONES SOLDADAS DE HAYNES 230®

B. Sarasola, J. L. Pedrejón, R. Rodríguez-Martín, I. Ocaña, M.R. Elizalde

CEIT y TECNUN (Universidad de Navarra)
Paseo de Manuel Lardizábal 15, 20018 San Sebastián
E-mail: rarodriguez@ceit.es

RESUMEN

Haynes 230® es una superaleación de base níquel que presenta una excelente resistencia mecánica a temperaturas elevadas y una extraordinaria estabilidad en ambientes agresivos (procesos de oxidación y corrosión). Su uso (sector aeronáutico, industria de tratamientos térmicos, etc.) se extiende a componentes cuya temperatura en servicio asciende hasta los 1150 °C. Las notables características de esta superaleación pueden, sin embargo, deteriorarse cuando se somete a un proceso de soldadura. Dicho proceso puede alterar la respuesta mecánica del material debido a la aparición de microfisuras en la zona de fusión o a la generación de grietas durante la solidificación. En este trabajo se analiza, en primer lugar, la microestructura de uniones soldadas de la superaleación Haynes 230®. Posteriormente, se evalúan su resistencia y estabilidad mecánica mediante ensayos de tracción y creep a altas temperaturas. Finalmente, se realiza un estudio fractográfico de las muestras ensayadas para identificar los micromecanismos de fallo.

ABSTRACT

Haynes 230® is a nickel-based superalloy which possesses an outstanding mechanical response at high temperatures and an excellent stability in severe environments (oxidation and corrosion processes). Its applications (aerospace sector, heat treatment industry...) cover components that require in-service temperatures up to 1150°C. However, the remarkable characteristics of this superalloy can be deteriorated when it is subjected to a welding process. This process can change the mechanical response of the material due to the formation of microcracks in the fusion zone or the appearance of cracks during solidification. In this work the microstructure of welded Haynes 230® sheets is analysed. Then, the mechanical strength and stability are evaluated by means of tensile and creep tests at high temperatures. Finally, a fractographic study of the tested specimens is carried out to identify the micromechanisms of failure.

PALABRAS CLAVE: Superaleaciones de base níquel, soldadura, agrietamiento, creep.

1. INTRODUCCIÓN

Las superaleaciones de base níquel se han convertido en los materiales idóneos para aplicaciones que requieran elevadas temperaturas de operación: turbinas, intercambiadores de calor, cámaras de combustión, etc. Entre sus características principales se encuentran la capacidad de soportar carga a una temperatura de operación cercana a su punto de fusión, la excelente resistencia a la degradación mecánica tras un período de exposición extenso (procesos de fluencia lenta o creep) y la elevada tolerancia a ambientes severos (procesos de oxidación y corrosión). En concreto, la superaleación Haynes 230® presenta una notable resistencia y estabilidad a temperaturas elevadas y una gran resistencia a la corrosión en caliente [1, 2]. Estas cualidades son consecuencia de un endurecimiento de la matriz austenítica mediante solución sólida.

En muchas de las aplicaciones de la superaleación Haynes 230® es imprescindible la realización de

soldaduras [3, 4]. La etapa de soldadura se asocia frecuentemente con la aparición de distintos problemas: generación de tensiones térmicas como consecuencia de los gradientes térmicos inducidos durante el proceso, iniciación de grietas en la zona afectada por el calor, agrietamiento en caliente de la región soldada, etc. [5]. Todos estos problemas están relacionados con la composición química y la microestructura del material [6] e inevitablemente afectan la vida de la pieza en servicio y, por tanto, han de evitarse.

En este estudio se analiza la microestructura generada en uniones soldadas de Haynes 230® y se evalúa su influencia en la respuesta mecánica del material a altas temperaturas. Además, se comprueba la estabilidad mecánica de las uniones mediante ensayos de fluencia lenta (creep) a temperaturas elevadas.

2. PROCEDIMIENTO EXPERIMENTAL

Se ha utilizado como material base la superaleación

Haynes 230[®], cuya composición química se detalla en la Tabla 1. Sus principales constituyentes son Ni, Cr, y W.

Tabla 1. Composición química de la superaleación Haynes 230[®].

Al	B	C	Co	Cr	Cu	Fe	Mn
0.4	0.003	0.1	0.2	22.0	0.05	2.23	0.51
P	S	Si	Ti	W	La	Mo	Ni
<0.01	<0.002	0.4	<0.01	14.0	0.02	1.23	BAL

Las microestructuras presentes en el material base y en la soldadura (zona de fusión y zona afectada por el calor) se han revelado utilizando un ataque electrolítico (95 ml HCl, 5 ml H₂C₂O₄, 4 V, 4 s) y se han observado mediante microscopía óptica y electrónica. Además, se ha empleado la técnica de microanálisis de dispersión de energía de rayos X (EDS) para identificar los precipitados encontrados.

Los ensayos de tracción se han realizado a 570 y 650°C (temperaturas habituales en muchas aplicaciones de la superaleación Haynes 230[®]) en una máquina MTS 819 con horno corto y extensómetro para elevada temperatura. En la Figura 1 se especifica la geometría de la probeta ensayada. Se añade un detalle del aspecto real de la zona estrecha, donde se localiza la soldadura.

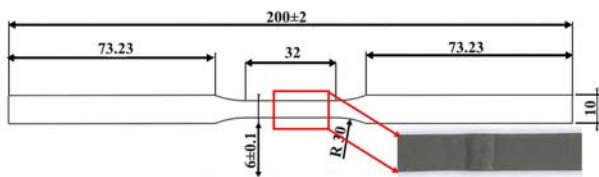


Figura 1. Geometría y dimensiones de la probeta de tracción.

Los ensayos de creep o fluencia lenta se han llevado a cabo a 650°C en un caballete de fluencia. Se ha utilizado la misma geometría de probeta, el mismo horno corto y el mismo extensómetro que en los ensayos de tracción.

Tras la realización de los ensayos mecánicos, se han analizado las superficies rotas mediante microscopía electrónica con el objetivo de establecer los mecanismos de fractura.

3. RESULTADOS Y DISCUSIÓN

3.1. Microestructura del material base

En la Figura 2 se presenta la microestructura de la superaleación Haynes 230[®]. Está constituida por una matriz austenítica con precipitados del tipo M₆C ricos en W [4, 7, 8]. Se advierte, también, la presencia de maclas.

3.2. Microestructura de la zona de fusión

La zona de fusión está formada por una microestructura dendrítica, cuya dirección de crecimiento es paralela a

la dirección de máximo gradiente de temperatura (material base → zona de fusión). Esto se comprueba en la Figura 3 a). En la región central de la zona de fusión el gradiente térmico es menos acusado y, en consecuencia, la microestructura dendrítica pierde direccionalidad. En la Figura 3 b) se muestran las dendritas de la región central, menos alargadas.

Los precipitados de la zona de fusión presentan un alto contenido de Ni y, principalmente, de Cr (Figura 4). Se trata, probablemente, de carburos M₂₃C₆ [9, 10].

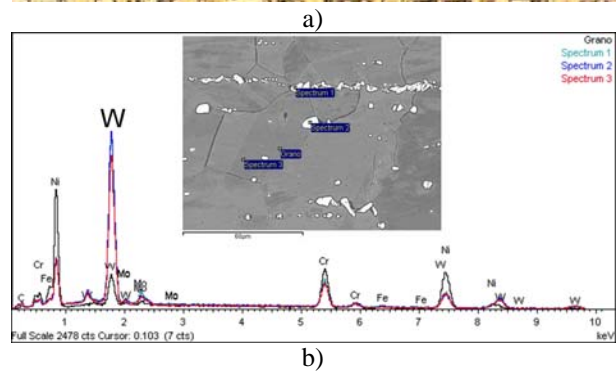
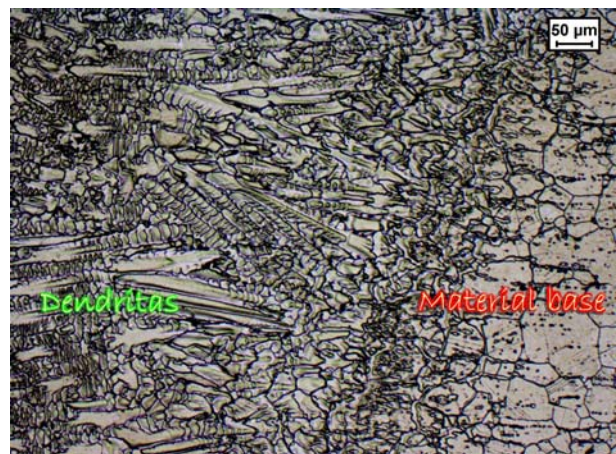


Figura 2. a) Microestructura del material base, b) análisis cuantitativo de los precipitados presentes en la superaleación Haynes 230[®].



a)



b)

Figura 3. Microestructura de la zona de fusión: a) dendritas alargadas en la zona de fusión cercana al material base, b) dendritas menos alargadas en la zona de fusión central.

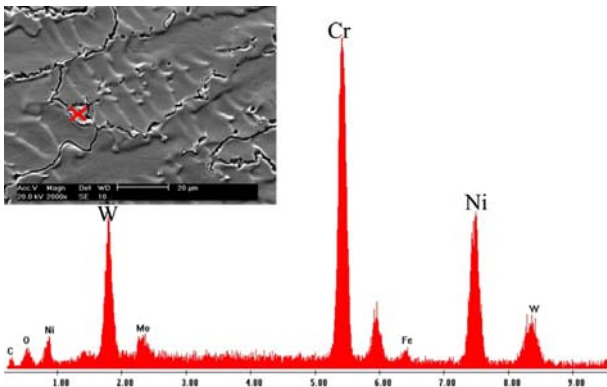
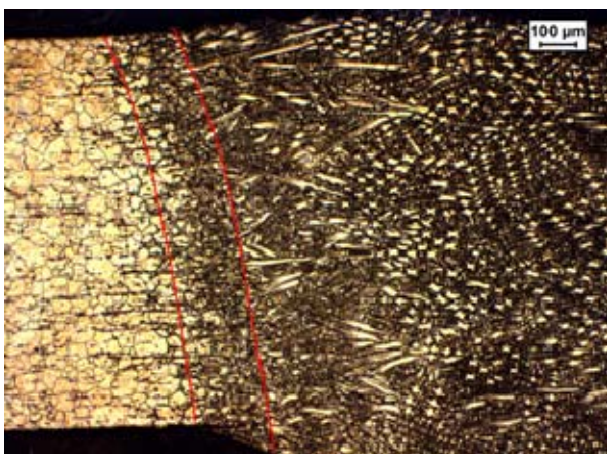


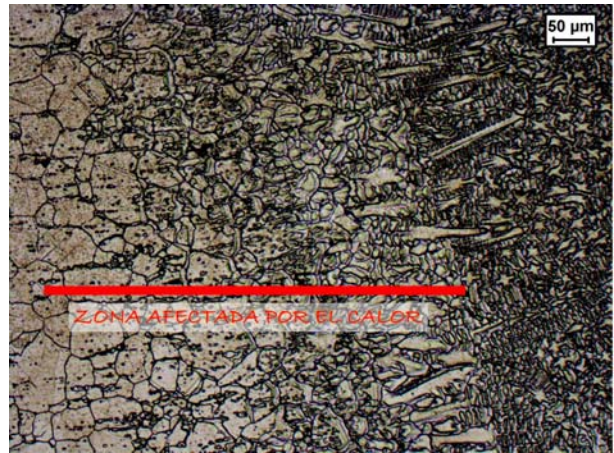
Figura 4. Precipitados de la zona de fusión.

3.3. Microestructura de la zona afectada por el calor

La zona afectada por el calor se sitúa entre el material base y la región dendrítica. Ocupa una franja de en torno a 100 μm (Figura 5). En ella se observa una distorsión y un engrosamiento de los granos equiaxiales, característicos del material base.



a)



b)

Figura 5. Microestructura de la zona afectada por el calor.

3.4. Ensayos de tracción a altas temperaturas

En la Figura 6 se resumen los resultados de los ensayos de tracción a realizados con las uniones soldadas a altas temperaturas (570 y 650°C). Se comparan los valores de resistencia a tracción (UTS), límite elástico (YS) y elongación con los obtenidos para la superaleación Haynes 230® sin soldar.

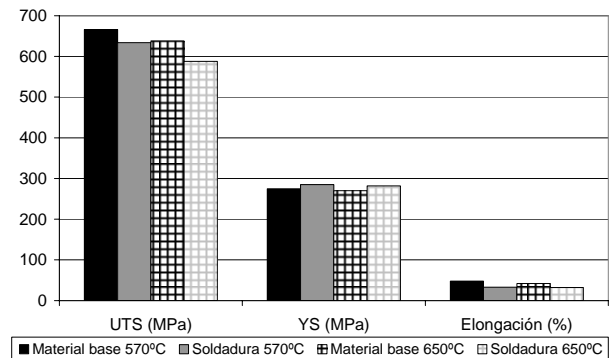


Figura 6. Propiedades de tracción del material base (Haynes 230®) y su soldadura.

Independientemente de la temperatura de ensayo, se da un incremento del límite elástico y un descenso de la elongación tras la realización de la soldadura. Esta tendencia ha sido observada por diversos autores en soldaduras de Haynes 230® y otras superaleaciones de base níquel [2, 11].

Además, todas las probetas soldadas han roto en las inmediaciones de la soldadura; esto se comprueba macroscópicamente en la Figura 7.



Figura 7. Probetas de tracción ensayadas a a) 570 °C y b) 650 °C. El origen del fallo se localiza en las cercanías de la soldadura.

Examen fractográfico

En la Figura 8 se presentan, a modo de ejemplo, dos superficies de fractura de las probetas con soldadura rotas. Todas ellas presentan microcavidades, propias de la fractura dúctil. Por tanto, las uniones soldadas de Haynes 230[®] mantienen la ductilidad.

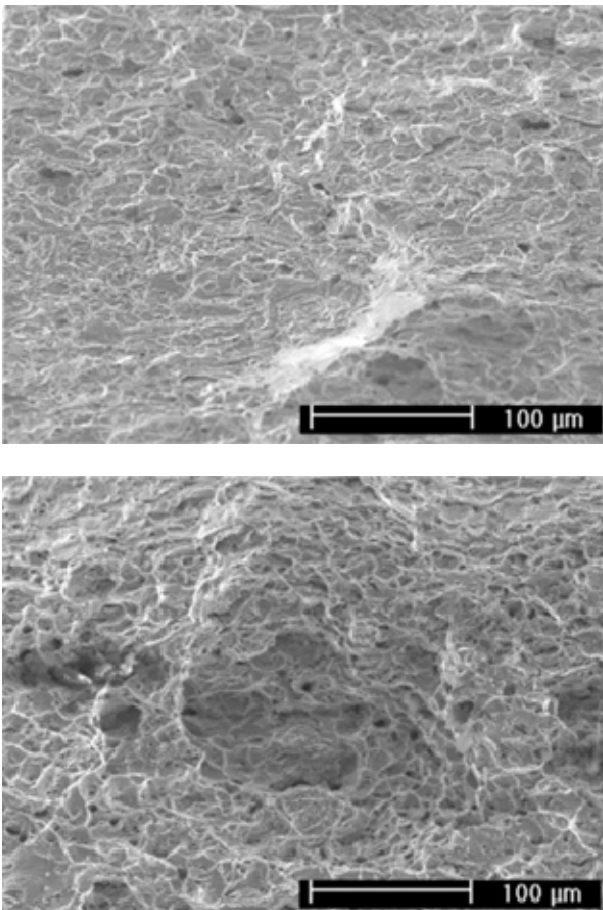


Figura 8. Superficies de fractura de las uniones soldadas ensayadas a tracción a altas temperaturas.

La caracterización microestructural de las uniones soldadas ha mostrado la existencia de diversas microestructuras. Sin embargo, según se acaba de comentar, el origen de la fractura se sitúa en una microestructura preferencial (en las inmediaciones de la soldadura). Con el propósito de identificar dicha

microestructura, se han pulido y atacado metalográficamente secciones provenientes de distintas probetas, obtenidas según se ilustra en la Figura 9.

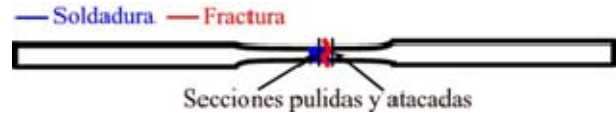


Figura 9. Obtención de secciones con el objetivo de determinar la microestructura causante del fallo.

Los resultados de este estudio han concluido que la fractura de las uniones soldadas de Haynes 230[®] está gobernada por la microestructura de la zona afectada por el calor, puesto que en todas las probetas analizadas se ha detectado la presencia de dicha microestructura en el perfil de fractura. Como ejemplo, se muestran las Figuras 10 y 11.

En todas las probetas rotas, uno de los trozos contiene la soldadura prácticamente íntegra y el opuesto está formado mayoritariamente por material base (véase la Figura 7). No obstante, independientemente del trozo analizado, se comprueba que en el perfil de fractura siempre existen los granos distorsionados propios de la zona afectada térmicamente (Figuras 10 y 11).

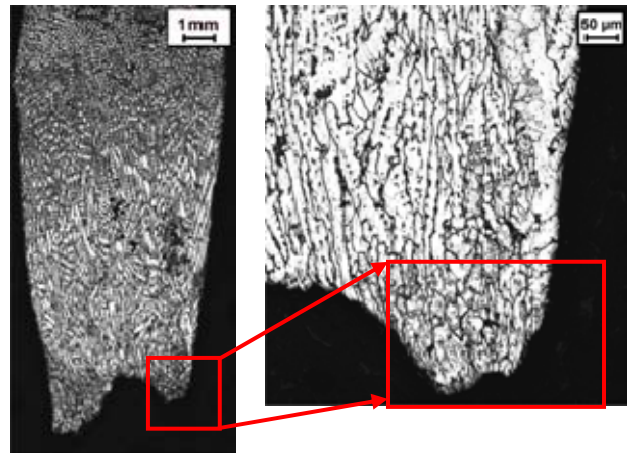


Figura 10. Perfil de fractura de una probeta ensayada a 570 °C. Se destaca en color rojo la presencia de la microestructura característica de la zona afectada por el calor.

La debilidad mecánica de la zona afectada por el calor en superaleaciones de base níquel y específicamente en Haynes 230[®] ha sido señalada por otros autores [2, 6, 12, 13].

En algún caso, se ha detectado la presencia de defectos de soldadura en las uniones soldadas. Así, en la Figura 12 a) se marca una unión fría debida posiblemente a que el material de aporte no llega a fundir y se deposita encima. Durante el ensayo de tracción, este defecto da lugar a una grieta que desencadena la fractura. Esto se verifica en la Figura 12 b).

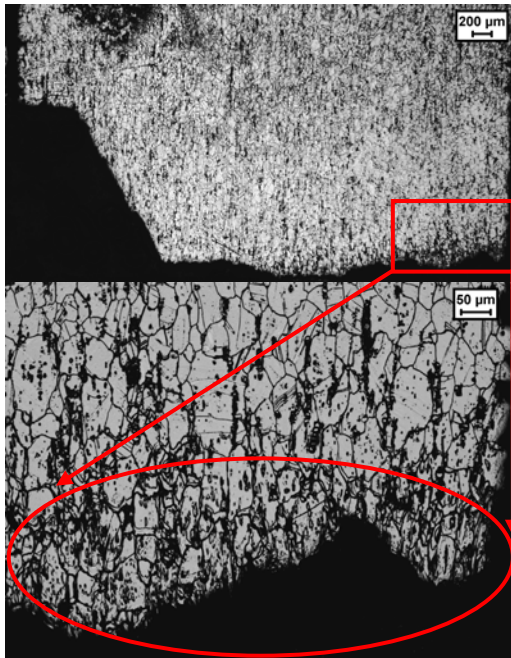


Figura 11. Perfil de fractura de una probeta ensayada a 650 °C. Se destaca en color rojo la presencia de la microestructura característica de la zona afectada por el calor.

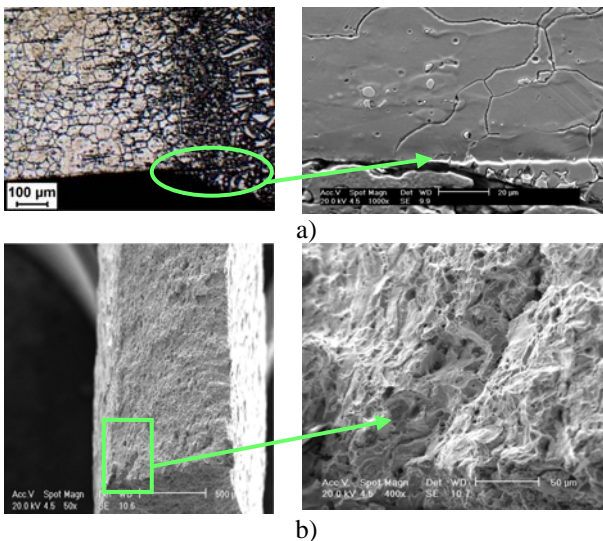


Figura 12. a) Defecto de soldadura en una de las muestras, b) formación de una grieta a partir del defecto de soldadura.

3.5. Ensayos de fluencia lenta a altas temperaturas

Los ensayos se han realizado a 650 °C y a distintos niveles de carga. En todos los casos se ha llegado a una deformación final del 5% para lo cual se han requerido distintos tiempos. Los resultados se han analizado siguiendo el método de Larson-Miller, que utiliza una relación paramétrica entre la tensión, el tiempo y la temperatura para obtener una relación maestra que permite predecir el efecto acumulado del tiempo y de la

temperatura en la tensión [14]. Los autores definen un parámetro (parámetro de Larson-Miller) como sigue:

$$LMP = T \cdot (C + \log t) \quad (1)$$

siendo T la temperatura (K), t el tiempo (h) y C una constante propia del material cuyo valor puede considerarse 20 para la mayoría de los metales según los propios autores.

El método descrito se emplea habitualmente en la evaluación del daño mediante creep y, por este motivo, y a pesar de que en este trabajo se ha mantenido la temperatura constante, se ha elegido como modo de presentar los resultados.

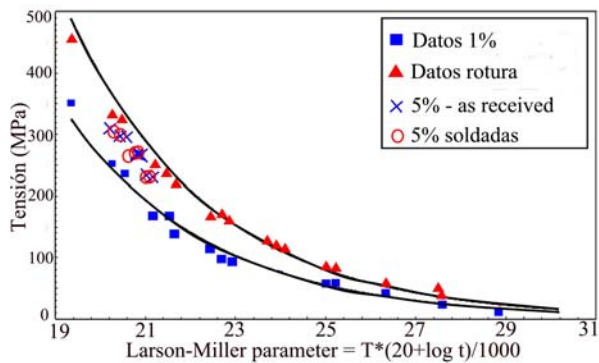


Figura 13. Diagrama de Larson-Miller [14] para distintos valores de deformación final.

En la Figura 13 se han incluido a modo de comparación resultados proporcionados por el fabricante para valores de deformación final extremos: rotura y 1%. Los ensayos realizados en este estudio, correspondientes a un 5% de deformación final, se sitúan en una región intermedia y siguen la misma tendencia en el diagrama. Si se comparan los resultados obtenidos para el material sin soldar y la soldadura, se observa muy poca diferencia. No parece, por tanto, que la presencia de la soldadura altere la respuesta del material en estos ensayos.

Examen fractográfico

Las probetas ensayadas a creep bajo las condiciones mencionadas (650 °C y deformación final del 5%) no han llegado a romper. Sin embargo, sí han comenzado a formarse grietas que se distribuyen en toda la longitud de la muestra (Figura 14). Además, se ha comprobado que en el límite de la soldadura, seguramente en la zona afectada por el calor, se generan grietas igualmente; estas grietas se van extendiendo a lo largo de toda la anchura de la muestra (Figura 15).

4. CONCLUSIONES

- Las uniones soldadas de Haynes 230® presentan una microestructura heterogénea como consecuencia del proceso de soldadura.

La zona de fusión está formada por dendritas y la zona afectada por el calor por granos distorsionados y de mayor tamaño que los granos del material base.

- La zona afectada por el calor constituye la microestructura responsable del fallo a tracción de las probetas a altas temperaturas. Si durante el proceso de soldadura se inducen defectos en las piezas, éstos también pueden desencadenar la fractura.
- Se han realizado ensayos de fluencia lenta hasta un 5% de deformación final. Bajo estas condiciones, la soldadura no afecta la durabilidad de las muestras.

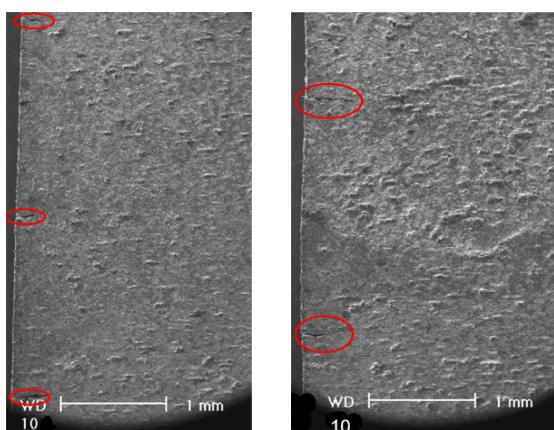


Figura 14. Grietas en una probeta ensayada a creep.

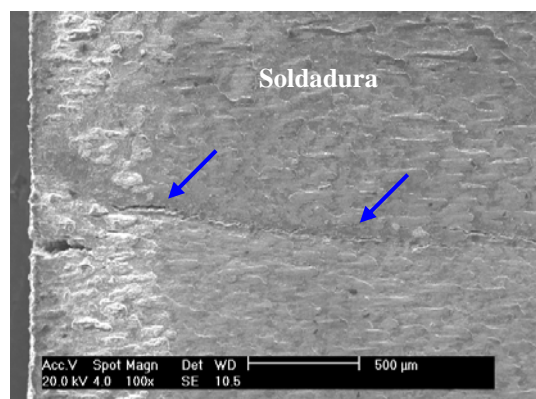


Figura 15. Grietas en la región de la soldadura.

AGRADECIMIENTOS

Los autores desean agradecer al Ministerio de Ciencia e Innovación la financiación recibida dentro del proyecto "Ensayos de fatiga termo-mecánica con mínimos gradientes térmicos y de fase" (MAT2008-03735/MAT). También al Gobierno Vasco la ayuda recibida dentro del proyecto PI09-09.

REFERENCIAS

- [1] <http://www.hightempmetals.com/>. [Consulta: Noviembre de 2009].

- [2] Cheng, C.M., Chou, C.P., Lee, I.K. and Kuo, I.C., "Susceptibility to hot cracking and weldment heat treatment of haynes 230 superalloy", *Journal of Materials Science and Technology*, vol. 22, n° 5, 2006, p. 685.
- [3] <http://www.haynesintl.com/>. [Consulta: Noviembre de 2009].
- [4] Lu, Y.L., Chen, L.J., Wang, G.Y., Benson, M.L., Liaw, P.K., Thompson, S.A., Blust, J.W., Browning, P.F., Bhattacharya, A.K., Aurrecochea, J.M. and Klarstrom, D.L., "Hold time effects on low cycle fatigue behavior of HAYNES 230 superalloy at high temperatures", *Materials Science and Engineering A*, vol. 409, n° 1-2, 2005, p. 282.
- [5] "Welding Handbook", vol. 3, AWS, Miami, FL, 1996, pp. 218-288.
- [6] Ojo, O.A., Wang, Y.L. and Chaturvedi, M.C., "Heat affected zone liquation cracking in electron beam welded third generation nickel base superalloys", *Materials Science and Engineering A*, vol. 476, n° 1-2, Langford Lane, Kidlington, Oxford, OX5 1GB, United Kingdom, 2008, p. 217.
- [7] Tawancy, H.M., Klarstrom, D.L. and Rothman, M.F., "Development of a new nickel-base superalloy", *Journal of Metals*, vol. 36, n° 9, 1984, p. 58.
- [8] Vecchio, K.S., Fitzpatrick, M.D. and Klarstrom, D., "Influence of subsolvus thermomechanical processing on the low-cycle fatigue properties of HAYNES 230 alloy", *Metallurgical and Materials Transactions A: Physical Metallurgy and Materials Science*, vol. 26 A, n° 3, Warrendale, PA, United States, 1995, p. 673.
- [9] Lu, Y.L., Chen, L.J., Liaw, P.K., Wang, G.Y., Brooks, C.R., Thompson, S.A., Blust, J.W., Browning, P.F., Bhattacharya, A.K., Aurrecochea, J.M. and Klarstrom, D.L., "Effects of temperature and hold time on creep-fatigue crack-growth behavior of HAYNES® 230® alloy", *Materials Science and Engineering: A*, vol. 429, n° 1-2, 2006, p. 1.
- [10] Meyer-Olbersleben, F., Kasik, N., Ilschner, B. and Rezaie-Aria, F., "Thermal fatigue behavior of the combustor alloys IN 617 and HAYNES 230 before and after welding", *Metallurgical and Materials Transactions A: Physical Metallurgy and Materials Science*, vol. 30, n° 4, Warrendale, PA, United States, 1999, p. 981.
- [11] Sato, Y.S., Arkom, P., Kokawa, H., Nelson, T.W. and Steel, R.J., "Effect of microstructure on properties of friction stir welded Inconel Alloy 600", *Materials Science and Engineering A*, vol. 477, n° 1-2, Langford Lane, Kidlington, Oxford, OX5 1GB, United Kingdom, 2008, p. 250.
- [12] Nakkalil, R., Richards, N.L. and Chaturvedi, M.C., "Influence of solidification mode on heat affected zone microfissuring in a nickel-iron base superalloy", *Acta metallurgica et materialia*, vol. 41, n° 12, 1993, p. 3381.
- [13] Richards, N.L., Huang, X. and Chaturvedi, M.C., "Heat affected zone cracking in cast Inconel 718", *Materials Characterization*, vol. 28, n° 3, 1992, p. 179.
- [14] Larson, F.R. and Miller, J., "A time temperature relationship for rupture and creep stresses", *Transactions of the ASME*, 1952, pp. 765-775.

APPLICATION OF TAGUCHI METHOD IN THE OPTIMIZATION OF FRICTION STIR WELDING PARAMETERS OF AN AERONAUTIC ALUMINIUM ALLOY

C. Vidal^a, V. Infante^{1, b}, P. Peças^{1, c}, P. Vilaça^{1, d}

¹ Departamento de Engenharia Mecânica,
Instituto Superior Técnico, Av. Rovisco Pais, 1096-001 Lisboa, Portugal

^a catarina.vidal@ist.utl.pt, ^b virginia@dem.ist.utl.pt, ^c ppecas@ist.utl.pt, ^d pedro.vilaca@ist.utl.pt

ABSTRACT

The Friction Stir Welding (FSW) process is still an innovative solid state mechanical processing technology enabling high quality joints in materials previously considered with low weldability such as most of the aeronautic aluminium alloys. The Taguchi method was used to find the optimal FSW parameters for improvement mechanical behaviour of AA2024-T351. The Taguchi design is an efficient and effective experimental method in which a response variable can be optimized. The parameters considered were vertical downward forging force, travel speed and pin length. An orthogonal array of L_9 (3^4) was used; ANOVA analyses were carried out to identify the significant factors affecting tensile strength (GETS), bending toughness (GEB) and hardness field. An algebraic model for predicting the best mechanical performance was developed and the optimal FSW combination was determined using this model. The results obtained were validated by conducting confirmation experiments.

KEYWORDS: Friction Stir Welding, Taguchi method, ANOVA.

1. INTRODUCTION

Significant interest has been shown in the use of advanced welding techniques for aircraft structures, particularly given the design and manufacturing benefits they afford over established mechanical joining methods. Whilst a variety of welding methods have been identified for airframe structures, friction stir welding is an important candidate technique that is distinctive in being a low energy, solid-state process [1]. Although the friction stir welding joints have a better quality compared to the fusion techniques, there are still some defects that may arise and which are very sensitive to small variations in process parameters. Typical defects that may arise in FSW joints result from: imperfect stir of the materials during the processing, inadequate surface preparation, lack of penetration of the pin and non-uniform vertical forging forces along the material thickness. Some characteristic FSW defects are lack of penetration (typically addressed as kissing-bond), root flaw (concerning weak or intermittent linking), voids on the advancing side and second phased particles and oxides alignment under the shoulder [2]. Advanced aerospace aluminium alloys have been required to allow high fracture toughness, higher fatigue performance, high formability, and superplasticity to meet the needs for lower structural weight, higher damage tolerance and durability [3].

2. TAGUCHI METHOD

The method presented in this study is an experimental

design process called the Taguchi design method. Taguchi design, developed by Dr. Genichi Taguchi, is a set of methodologies by which the inherent variability of materials and manufacturing processes has been taken into account at the design stage [4]. Although similar to design of experiment (DOE), the Taguchi design only conducts the balanced (orthogonal) experimental combinations, which makes the Taguchi design even more effective than a fractional factorial design. By using the Taguchi techniques, industries are able to greatly reduce product development cycle time for both design and production, therefore reducing costs and increasing profit [5].

Taguchi proposed that engineering optimization of a process or product should be carried out in a three-step approach: system design, parameter design, and tolerance design.

In system design, the engineer applies scientific and engineering knowledge to produce a basic functional prototype design.

The objective of the parameter design [6] is to optimize the settings of the process parameter values for improving performance characteristics and to identify the product parameter values under the optimal process parameter values. The parameter design is the key step in the Taguchi method to achieving high quality without increasing cost.

The steps included in the Taguchi parameter design are: selecting the proper orthogonal array (OA) according to the numbers of controllable factors (parameters); running experiments based on the OA; analyzing data; identifying the optimum condition; and conducting

confirmation runs with the optimal levels of all the parameters [5].

The main effects indicate the general trend of influence of each parameter. Knowledge of the contribution of individual parameters is the key to deciding the nature of the control to be established on a production process. Analysis of variance (ANOVA) is the statistical treatment most commonly applied to the results of the experiments to determine the percentage contribution of each parameter against a stated level of confidence [6]. Taguchi suggests [7] two different routes for carrying out the complete analysis. In the standard approach the results of a single run or the average of repetitive runs are processed through the main effect and ANOVA (raw data analysis). The second approach, which Taguchi strongly recommends for multiple runs, is to use the signal-to-noise (S/N) ratio for the same steps in the analysis.

In the present investigation, only the raw data analysis was performed. The effects of the selected FSW parameters on the selected performance characteristics were investigated through the plots of the main effects based on raw data. The optimum condition for each of the performance characteristics was established through the raw data analysis. An algebraic model for predicting the best mechanical performance was developed. The optimal FSW parameters were verified using a confirmation experiment.

3. EXPERIMENTAL DESIGN

3.1 Selection of FS welding parameters and their levels

The welding experiments were carried out on an ESAB Legio FSW 3UL. Plunge and dwell periods ($v_x=0$) were performed under vertical position control and weld period ($v_x>0$) was carry out under vertical downward force control.

The FSW tool that was use to perform all the welds is a patented modular concept of FSW tools. This tool is based on 3 main components: Body; Shoulder and Pin, which enable the easy replacement of any damage component and the combination between different shoulder and pin geometries. Moreover, this tool enables internal forced refrigeration and the setting of any length for the pin. The pin is 9° conical with a bottom diameter of 4mm and LH threads along its length. The shoulder is plane with 2 spiral striates scrolling an angle of 180° with outer and inner diameter of 16mm and 5mm, respectively. Mechanical properties and chemical composition of 2024-T351 aluminium alloy which was used in the experiments are shown in Tables 1 and 2.

Table 1. Mechanical properties of AA2024-T351

Young modulus (GPa)	Yield stress (MPa)	Ultimate stress (MPa)	Elongation (%)	Toughness (J/mm ³)
75.5	383.8	533.8	22.0	80.7

Table 2. Chemical composition of AA2024-T351, % weight

Al	Mg	Cu	Mn
89.87	3.38	6.20	0.55

The initial welding parameters implemented were the following: a rotation speed of 1000 rpm (CW), a travel speed of 250 mm/min, a plunge gap pin-to-anvil plate of 50 µm, a vertical downward forging force of 900 kg, a pin length of 4.17 mm and a null tilt angle. The process parameters workable range for the experiments was chosen in order to control the weld seams quality including defects in the root, the type of defect more difficult to eliminate in sound welds. Therefore, three levels of the FS welding parameters were selected as shown in Table 3.

3.2 Orthogonal array experiment

To select an appropriate orthogonal array for experiments, the total degrees of freedom need to be computed. The degrees of freedom are defined as the number of comparisons between process parameters that need to be made to determine which level is better and specifically how much better it is. For example, a three-level process parameter counts for two degrees of freedom. The degrees of freedom associated with interaction between two process parameters are given by the product of the degrees of freedom for the two process parameters [8]. In the present study, the interaction between the welding parameters is neglected. Therefore, there are six degrees of freedom owing to the three welding parameters.

Once the degrees of freedom required are known, the next step is to select an appropriate orthogonal array to fit the specific task. Basically, the degrees of freedom for the orthogonal array should be greater than or at least equal to those for the process parameters. In this study, an L₉ orthogonal array was used. This array has twenty six degrees of freedom and it can handle three-level process parameters. Each FS welding parameter is assigned to a column and twenty seven welding parameter combinations are available. A total of nine experimental runs must be conducted, using the combination of levels for each control factor (A–D) as indicated in Table 3.

Table 3. The basic Taguchi L₉ (3⁴) orthogonal array

Run	Control factors and levels			
	A	B	C	D
1	1	1	1	1
2	1	2	2	2
3	1	3	3	3
4	2	1	2	3
5	2	2	3	1
6	2	3	1	2
7	3	1	3	2
8	3	2	1	3
9	3	3	2	1

However, this study did not use all the array cells for four factors, because only three factors were considered (vertical downward forging force, travel speed and pin length). Therefore, the last column (for the fourth factor) in the L_9 orthogonal array is left empty for this specific study.

The selected parameters are listed in Table 4 along with their applicable codes and values for use in the Taguchi parameter design study.

Table 4. Friction stir welding parameters and their levels

FSW parameter	Symbol	Level 1	Level 2	Level 3
<i>Variable parameters</i>				
Vertical force (kg)	A	850	900	950
Travel speed (mm/min)	B	120	250	500
Pin length (mm)	C	4.00	4.08	4.17
<i>Constant parameters</i>				
Tilt angle		0°		
Rotation speed		1000 rpm		
Rotation direction		CW		
Plunge speed		0.1 mm/s		
Dwell time		8 s		
FSW control		Vertical force control		

3.3 Welding performance assessment

In order to conclude about the quality of the welded joint relatively to the base material properties, a coefficient called Global Efficiency to Tensile Strength, GETS (1) was developed by Vilaça [9].

$$GETS = \left(C_E \frac{E_i}{E_{BM}} + C_{\sigma_y} \frac{\sigma_{y_i}}{\sigma_{y_{BM}}} + C_{\sigma_{UTS}} \frac{\sigma_{UTS_i}}{\sigma_{UTS_{BM}}} + C_A \frac{A_i}{A_{BM}} + C_{U_T} \frac{U_{T_i}}{U_{T_{BM}}} \right) \times 100 (\%) \quad (1)$$

In analogy with the tensile tests and the GETS coefficient, a Global Efficiency to Bending, GEB (2) was also considered.

$$GEB = \left(C_F \frac{F_i}{F_{BM}} + C_d \frac{d_i}{d_{BM}} + C_{U_B} \frac{U_{B_i}}{U_{B_{BM}}} \right) \times 100 (\%) \quad (2)$$

The weights considered in (1) and (2) are shown in Table 5. These weights aim at consider the relative importance level of the mechanical properties in design of aeronautic structures.

Table 5. Weights considered for GETS and GEB

GETS		GEB	
C_{σ_y}	0.30		
$C_{\sigma_{UTS}}$	0.25	C_{U_B}	0.50
C_A	0.20	C_F	0.25
C_{U_T}	0.20	C_d	0.25
C_E	0.05		

Because the hardness results are important in assessing

the relative mechanical properties between the different zones resulting from the thermo-mechanical FSW cycle it was established the following expression (3) as a welding performance parameter:

$$HARD = \frac{\text{Minimum hardness}}{BM \text{ hardness}} \quad (3)$$

where HARD means HARDness Ration Drop, *minimum hardness* is the lowest hardness value measured at the mid-thickness of the cross section of the weld seam and *BM hardness* is the base metal hardness value.

3.4 Experimental set-up and procedure

After the orthogonal array has been selected, the second step in Taguchi parameter design is running the experiment.

The 2024-T351 aluminium alloy was used in this investigation for being one of the most popular materials in aeronautic applications. All the welds were performed in plates rolled to 4 mm thick perpendicular to the rolling direction in a butt joint arrangement with straight edge preparation.

Plates of 200 mm x 145(RD) mm were welded along their long edge. The FSW equipment used was an ESAB Legio FSW 3UL as mentioned in Section 3.1. After welding, specimens were produced and mechanical tests were carried out. Both the uniaxial tensile and bending tests were performed on an Instron 1342, with a load cell of 250kN and high resolution biaxial extensometers. Specimens were taken from each welded plate for tensile tests, with geometry according to the EN-895-2002. Bending tests of 90° were carried out. The average distance between supports (distance between the centres of support rolls) is 30 mm. Support rolls diameter is 10 mm and mandrel radius is 5 mm. Mandrel velocity used throughout the trial is 1 mm/min. From each welded condition two specimens were taken and one of them was bended with the root of the weld seam under tensile stress. All mechanical trials were performed at room temperature. The hardness field was established in the mid-thickness (middle level) of the cross section of the weld seam in according to the ISO 6507-2 with 0.5 kg and about 26 measured points.

4. ANALYSIS OF EXPERIMENTAL DATA

4.1 Computation of average performance

The procedures after the experimental runs are analyzing data and identifying the optimal levels for all the control factors. The results of GETS, GEB and HARD of each sample are shown in Table 6.

There are three categories of performance characteristics, i.e., the lower-the-better, the higher-the-better, and the nominal-the-better. To improve the mechanical behaviour of AA2024-T351, the higher-the-better performance characteristic for

GETS, GEB and HARD should be taken for obtaining optimal welding performance.

Table 6. Experimental results

Experiment number	FSW parameter level			GETS	GEB	HARD
	A	B	C			
1	850	120	4.00	0.585	0.518	0.656
2	850	250	4.08	0.627	0.362	0.773
3	850	500	4.17	0.598	0.470	0.736
4	900	120	4.08	0.585	0.629	0.742
5	900	250	4.17	0.685	0.592	0.779
6	900	500	4.00	0.530	0.277	0.871
7	950	120	4.17	0.585	0.506	0.712
8	950	250	4.00	0.555	0.329	0.755
9	950	500	4.08	0.576	0.318	0.798

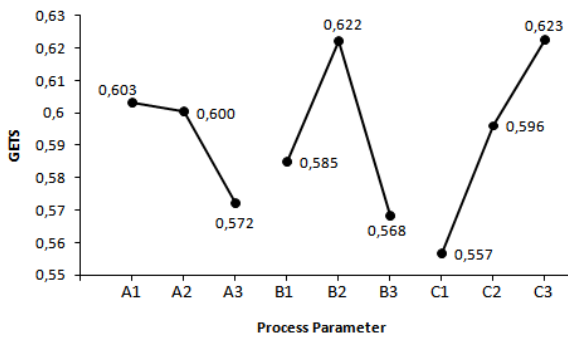


Figure 1. Effect of process parameters on GETS coefficient.

All three levels of every factor are equally represented in 9 experiments. Since the experimental design is orthogonal, it is possible to separate out the effect of each factor at each level [6]. Mean response is the average of quality characteristic for each parameter at different level. For example, the mean percentage GETS for travel speed at level 1 can be calculated by averaging GETS from the experiments 1, 4 and 7. GETS, GEB and HARD for each of the parameter at each level are calculated. These are also called as main effects. Figures 1-3 show the GETS, GEB and HARD response (main effects), respectively.

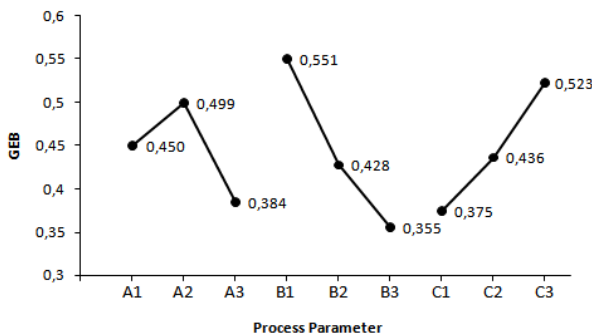


Figure 2. Effect of process parameters on GEB coefficient.

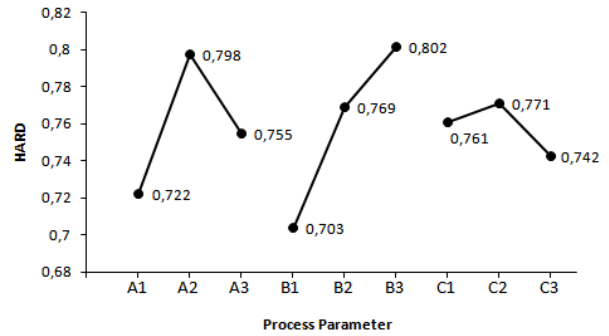


Figure 3. Effect of process parameters on hardness profile.

From Figure 1 it is observed that the GETS is highest at level 1 of vertical downward forging force (A1), level 2 of travel speed (B2) and level 3 of pin length (C3). Increase vertical downward forging force causes decrease in GETS while increase pin length causes increase in GETS. Both are related with the gage area and as such increase vertical downward forging force decrease gage area (because it reduces the thickness) and decrease pin length decrease gage area because there is no total penetration of the pin.

From Figure 2 it is observed that the GEB is highest at level 2 of vertical downward forging force (A2), level 1 of travel speed (B1) and level 3 of pin length (C3). Increase travel speed causes decrease in GEB. The higher travel speed contributes for reducing the processing on the root zone due to the insufficient visco-plastic flux. Increase pin length causes increase in GEB. Increasing pin length inhibits the formation of defects at the root and therefore improves the bending strength of FSW joints.

From Figure 3 it is observed that the HARD is highest at level 2 of vertical downward forging force (A2), level 3 of travel speed (B3) and level 2 of pin length (C2). Increase travel speed causes increase in HARD because it decreases the process' calorific energy input.

4.2 Analysis of variance (ANOVA)

ANOVA is a standard statistical technique to interpret the experimental results. The percentage contribution of various process parameters to the selected performance characteristic can be estimated by ANOVA. Thus information about how significant the effect of each controlled parameter is on the quality characteristic of interest can be obtained. ANOVAs for raw data has been performed to identify the significant parameters and to quantify their effect on the performance characteristic. The ANOVA based on the raw data identifies the factors which affect the average response rather than reducing variation. In ANOVA, total sum of squares (SS_T) is calculated by [10]:

$$SS_T = \sum_{i=1}^N (Y_i - \bar{Y})^2 \quad (4)$$

where N is the number of experiments in the orthogonal array, N=9, Y_i is the experimental result for the i^{th} experiment and \bar{Y} is given by:

$$\bar{Y} = \frac{1}{N} \sum_{i=1}^N Y_i \quad (5)$$

The total sum of the squared deviations SS_T is decomposed into two sources: the sum of the squared deviations SS_p due to each process parameter and the sum of the squared error SS_e . SS_p can be calculated as:

$$SS_p = \sum_{j=1}^t \frac{(SY_j)^2}{t} - \frac{1}{N} \left[\sum_{i=1}^N Y_i \right]^2 \quad (6)$$

where p represent one of the experiment parameters, j the level number of this parameter p , t the repetition of each level of the parameter p , SY_j the sum of the experimental results involving this parameter p and level j . The sum of squares from error parameters SS_e is:

$$SS_e = SS_T - SS_A - SS_B - SS_C \quad (7)$$

The total degrees of freedom is $D_T = N - 1$, and the degrees of freedom of each tested parameter is $D_p = t - 1$. The variance of the parameter tested is $V_p = SS_p/D_p$. Then, the F -value for each design parameter is simply the ratio of the mean of squares deviations to the mean of the squared error ($F_p = V_p/V_e$). The percentage contribution ρ can be calculated as:

$$\rho_p = \frac{SS_p}{SS_T} \quad (8)$$

Tables 7-9 show the results of ANOVA for GETS, GEB and HARD, respectively.

Table 7. Results of the analysis of variance for GETS

Source	DOF	Sum of squares	Mean square	F ratio	Contribution (%)
A	2	0.00176	0.00088	0.70138	11.35
B	2	0.00463	0.00231	1.84158	29.79
C	2	0.00663	0.00331	2.63852	42.68
Error	2	0.00251	0.00126		16.18
Total	8	0.01553			100

Table 8. Results of the analysis of variance for GEB

Source	DOF	Sum of squares	Mean square	F ratio	Contribution (%)
A	2	0.02003	0.01001	1.12742	15.43
B	2	0.05880	0.02940	3.31042	45.31
C	2	0.03318	0.01659	1.86799	25.57
Error	2	0.01776	0.00888		13.69
Total	8	0.12977			100

It can be seen from Table 7 that pin length and travel speed are the most significant parameters for GETS.

Table 9. Results of the analysis of variance for HARD

Source	DOF	Sum of squares	Mean square	F ratio	Contribution (%)
A	2	0.00864	0.00432	2.5825	30.60
B	2	0.01499	0.00749	4.4800	53.08
C	2	0.00126	0.00063	0.3775	4.47
Error	2	0.00335	0.00167		11.85
Total	8	0.02824			100

Travel speed and pin length are the most significant parameters affecting the GEB coefficient as given in Table 8. Travel speed and vertical downward forging force are the most significant parameters for HARD (Table 9).

4.3 Prediction of the optimum performance

After the optimum condition has been determined, the optimum performance Y_{opt} of the response at the optimum condition is predicted. For the “higher-the-better” quality characteristic, the study of the main effect shows that the optimum condition for GETS is $A_1B_2C_3$. Then the optimum performance (optimum value of the response characteristic) is estimated as follows [7]:

$$Y_{opt} = \frac{T}{N} + \left(\bar{A}_1 - \frac{T}{N} \right) + \left(\bar{B}_2 - \frac{T}{N} \right) + \left(\bar{C}_3 - \frac{T}{N} \right) \quad (9)$$

where T is the total of all results, N the total number of results and \bar{A}_1 , \bar{B}_2 and \bar{C}_3 are the average values of the responses at the first, second and thirteenth levels of parameters A, B and C, respectively.

In analogy with the procedure for GETS, the optimum performance for GEB and HARD coefficients can be predicted.

Table 10 shows the results of the optimum performance for GETS, GEB and HARD.

Table 10. Results of the optimum performance

	GETS	GEB	HARD
Y_{opt}	0.6645	0.6840	0.8541

4.4 Algebraic model

The algebraic model (10) presented here was developed in order to obtain a more robust parametric combination that would improve the whole properties of FSW joints and give them to greater resistance to fatigue. For this, were considered the three different combinations predicted by Taguchi method and the percentages contribution of each parameter, obtained by ANOVA. Table 11 shows the percentages contribution which were used in algebraic model:

Table 11. Percentages contribution

	Force		Travel Speed		Pin Length	
GETS	ρ_{AGETS}	11.35	ρ_{BGETS}	29.79	ρ_{CGETS}	42.68
GEB	ρ_{AGEB}	15.43	ρ_{BGEB}	45.31	ρ_{CGEB}	25.57
HARD	ρ_{AHARD}	30.60	ρ_{BHARD}	53.08	ρ_{CHARD}	4.47
TOTAL	ρ_{AT}	57.38	ρ_{BT}	128.18	ρ_{CT}	72.72

$$\begin{bmatrix} Force & x & x \\ x & Speed & x \\ x & x & Pin \end{bmatrix} = \begin{bmatrix} \rho_{AGETS} & \rho_{BGETS} & \rho_{CGETS} \\ \rho_{AGEB} & \rho_{BGEB} & \rho_{CGEB} \\ \rho_{AHARD} & \rho_{BHARD} & \rho_{CHARD} \\ \rho_{AT} & \rho_{BT} & \rho_{CT} \end{bmatrix} \begin{bmatrix} A_1 & A_2 & A_2 \\ B_2 & B_1 & B_3 \\ C_3 & C_3 & C_2 \end{bmatrix} \quad (10)$$

$$\begin{bmatrix} Force & x & x \\ x & Speed & x \\ x & x & Pin \end{bmatrix} = \begin{bmatrix} 850 & 900 & 900 \\ 250 & 120 & 500 \\ 4.17 & 4.17 & 4.08 \end{bmatrix} \begin{bmatrix} 0.1978 & 0.2324 & 0.5869 \\ 0.2690 & 0.3535 & 0.3516 \\ 0.5333 & 0.4141 & 0.0615 \end{bmatrix}$$

$$Force = 168.13 + 242.10 + 479.97 = 890 \text{ kg}$$

$$Speed = 58.1 + 42.42 + 207.05 = 308 \text{ mm/min}$$

$$Pin = 2.45 + 1.47 + 0.25 = 4.17 \text{ mm}$$

This combination will be considered the optimal FSW combination.

4.5 Confirmation test

Once the optimal level of the process parameters is selected, the final step is to verify the improvement of the performance characteristics using the optimal level of the process parameters. Therefore, confirmation experiment was carried out to validate the developed algebraic model. Table 12 shows the results of the confirmation experiment using the optimal FS welding parameters.

Table 12. Results of the confirmation experiment

	Optimal FS welding parameters		
	Prediction for GETS	Prediction for GEB	Experiment
Level	A ₁ B ₂ C ₃	A ₂ B ₁ C ₃	A _{AM} B _{AM} C _{AM}
GETS value	66.4 %		71.3 %
GEB value		68.4 %	69.2 %

Based on the result of the confirmation test, the GETS coefficient increased 4.9% and the GEB coefficient increased 0.8%. The experimental results confirm the algebraic model parameter design for the optimal FS welding parameters.

5. CONCLUSIONS

This paper has presented an application of the parameter design of the Taguchi method in the optimization of FS welding parameters. The following conclusions can be drawn based on the experimental results of this study:

- Taguchi's robust orthogonal array design method is suitable to analyze this problem as described in this paper.
- It is found that the parameter design of Taguchi method provides a simple, systematic, and efficient methodology for the optimization of the FS welding parameters.
- The improvement of GETS from initial FS welding parameters to the optimal parameters is about 2.8% and the improvement of GEB from initial FS welding parameters to the optimal parameters is about 10%.

ACKNOWLEDGEMENTS

The authors would like to acknowledge the technical support from the ESTS/Instituto Politécnico de Setúbal and the material supply by OGMA – Indústria Aeronáutica de Portugal S.A. a specialist aviation company since 1918.

REFERENCES

- [1] R. Pedwell, H. Davies and A. Jefferson, 1999, Proc. 1st Int. symposium on Friction Stir Welds, Thousand Oaks, California, 14th – 16th June.
- [2] T. Santos, P. Vilaça, L. Reis, L. Quintino, M. Freitas, *Advances in NDT Techniques for Friction Stir Welding Joints of AA2024*, TMS 2008 Annual Meeting & Exhibition, Symposium, New Orleans, USA, March 2008.
- [3] Manabu Nakai, Takehiko Eto, *New aspects of development of high strength aluminum alloys for aerospace applications*, Materials Science and Engineering, pp. 62-68, 2000.
- [4] G.S. Peace, *Taguchi Methods, A Hands-on Approach*, Addison-Wesley, MA, 1992.
- [5] Julie Z. Zhang, Joseph C. Chen, E. Daniel Kirby, *Surface roughness optimization in an end-milling operation using the Taguchi design method*, Journal of Materials Processing Technology 184, pp. 233-239, 2007.
- [6] Ross, P.J., *Taguchi Technique for Quality Engineering*, 1988 (McGraw-Hill: New York).
- [7] Roy, R.K., *A Primer on the Taguchi Method*, 1990 (Van Nostrand Reinhold: New York).
- [8] M. Nalbant, H. Gokkaya, G. Sur, *Application of Taguchi method in the optimization of cutting parameters for surface roughness in turning*, Materials and Design 28, pp. 1379-1385, 2007.
- [9] Vilaça, P., *Fundamentos do Processo de Soldadura por Fricção Linear – Análise Experimental e Modelação Analítica*, PhD Thesis, Instituto Superior Técnico, Universidade Técnica de Lisboa, Setembro 2003.
- [10] W.H. Yang, Y.S. Tarn, *Design optimization of cutting parameters for turning operations based on the Taguchi method*, Journal of Materials Processing Technology 84, pp. 122-129, 1998.

AUTHORS INDEX

Aguado, A.	283
Al-Assadi, G.	229
Albuquerque, C.M.C.	601
Aldazabal, J.	333, 491
Alegre, J.M.	297, 309, 369, 479
Allen, D.	559
Álvarez, J.A.	91, 327, 699
Ambriz, R.R.	375, 749
Amrouche, A.	375, 749
Andrade, C.	515, 521
Anglada, M	51
Antunes, F.	167, 553, 789
Arenas, M. A.	447
Arencón, D.	657
Aretxabaleta, L.	339
Ariza, M.P.	527
Atienza, J. M.	31, 303
Ayaso, F. J.	399, 467, 717
Azevedo, J.M.T.	47
Banea, M.D.	155, 625
Baptista, A.P.M.	345
Baptista, C.	147
Baptista, R.	693, 755
Bártolo, P.J.	789
Baudín, C.	179, 291
Belchior, V.	147
Belzunce, F.J.	309, 503, 667, 711, 723
Benguediab, M.	375
Benhamena, A.	375, 749
Benseddiq, N.	375
Bessa, Miguel A.	149
Betegón, C.	711
Betegón, C.	503
Biezma, M.V.	71, 685
Borja, S.M.	447
Borrego, L.P.	761
Branco, C. M.	75, 109, 693, 755
Bravo, P. M.	297, 369, 479
Bueno, R.	533
Burgos, R.L.	31
Caballero, L.	497, 767
Cabrita, A.	429
Caçada, R.A.B.	601
Calvo, J. P.	81
Camanho, P. P.	149, 215
Camara, M.	277

Camas-Peña, D.	541
Campilho, R.D.S.G.	155, 345, 625
Campos, A.	283
Canal, L. P.	161
Capel, F.	81
Capela, C.	167
Carmona, J.R.	235, 259
Carol, I.	247
Carpinteri, A.	235
Carrascal, I. A.	631
Carrascal, I.	637
Casado, J. A.	631, 637
Casati, M. J.	229
Castillo, E.	393
Catalanotti, G.	149
Catarino, P.	103
Cea, A.	661
Cendón, D.	303, 321
César de Sá, J. M. A.	583
Chaves, F. J.P.	643
Cicero, R.	85, 97, 381
Cicero, S.	85, 97, 381, 473
Claes, E.	31
Cláudio, R.A.	133
Conde, A.	447
Correia, J.A.F.O.	387, 405
Cortés, F.	339
Costa, J.	215, 221
Costa, J.D.	167, 197, 761
Cuesta, I.I.	297, 309, 369, 479
da Silva, A.L.L.	387, 405
da Silva, J.F.N.	405
da Silva, L.F.M.	155, 625, 643
Dantas, A.	147
Dávila, C. G.	149
de Andres, P.	521
de Armas Sancho, Z	51
de Castro, P.M.S.T.	139, 361, 453, 601, 613, 619, 783
de Freitas, M.	185, 429, 435
de Jesus, A.M.P.	57, 387, 405, 571, 577, 783
de Matos, P. F. P.	547
de Melo, F. Q.	357, 779
de Moura, M.F.S.F.	37, 47, 155, 643
Delgado, A.	653
Dias, M.I.R.	47
Díaz, F.A.	315
Diego, S.	631, 637
Dillard, D.	643
Domínguez, J.	423, 589, 729, 735
Dourado, N.	37, 47
Duarte, R.	133
Elices, M.	41, 303
Elizalde, M.R.	191, 559, 773, 801
Enfedaque, A.	241
Farr, R.S.	333
Fernandes, A.A.	387, 405
Fernández Canteli, A.	393, 461, 485
Fernández Fernández, P.	461
Fernández Sáez, J.	485
Fernández Zúñiga, D.	485

Fernández, J.	229
Fernández-Jiménez, A.	253
Fernández-Viña, A.	467
Ferreira, F.	553
Ferreira, J.A.M.	167, 197, 761, 789
Ferreira, L.A.A.	619
Ferreño, D.	91, 327, 699
Figueiredo, M.A.V.	387, 405, 453, 783
Fortunato, E.	147
Franco-Urquiza, E.	647
Fuenmayor, F.J.	589
Fullea, José	515, 521
Galán, J.J.	447
Gálvez, F.	321
Gálvez, Jaime C.	229
Gamez-Perez, J.	647
Garagorri, J.	191, 559
García de la Yedra, A.	351
García, A.	291
García, J.	85, 97, 327, 699
García, N.	321
García-Collado, A.	315
García-Herrera, C.M.	31
García-Manrique, J.	541
García-Montero, C.	31
Garrido, M. A.	673
Gil Sevillano, J.	333, 491
Giner, E.	485, 589
Gomez, F.J.	497
Gómez-del Río, T.	661
González, B.	399, 417
González, C.	161, 203, 209
González, D.	191
González, E.V.	215
González-Herrera, A.	541
Gorostegui-Colinas, E.	559
Gorrochategui, I.	381
Guedes Leite, R. C.	577
Guinea, G. V.	31, 41
Gutiérrez-Solana, F.	327, 473, 631, 637, 699
Hernández, J.	291
Hernández, R.	661
Herreros, M.A.	679, 685
Hoodle, A.	333
Illescas, S.	657
Infante, V.	109, 127, 553, 693, 755, 807
Iordachescu, D.	767
Iordachescu, M.	767
Irastorza, A.	491
Irausquín, I.	565
Isasa, M.	773
Iturrioz, L.	773
Jiménez-Piqué, E.	51
Kharin, V.	705
Konstantopoulou, K.	411
Lacalle, R.	85, 97, 327, 381, 699
Lamela Rey, M. J.	461
Laso, J.A.	381
Leal das Neves, L.	121
Leite, A.	173

Lezcano, R.	711
Li, B.	429, 435
Lima, A.M.V.	57
LLorca, J.	161, 203, 209
Lopes, C. S.	149
Lopes, H.	357
López Aenlle, M.	461
López, C.M.	247, 283
López, F.	679, 685
López, M.	291
López, V. H.	749
López-Crespo, P.	541, 423
López-López, E.	179
Lorenzo, M.	705, 717
Luque, A.	333, 491
Machado, P.	133
Madureira, L.	779
Maeiro, J.M.C.	387, 405
Magalhães, A.G.	345
Maimí, P.	215
Malcher, L.	583
Mantič, V.	173
Marado, B. S. D.	127
Marat-Mendes, R.M.M.	185
Marcos-Gómez, D.	191
Mariano, P.M.	509
Martín, A.	253
Martínez, A. B.	653, 657, 673
Martínez, R.	71
Martínez-Esnaola, J.M.	333, 491
Martín-Meizoso, A.	333, 351, 607, 773
Martin-Rengel, M.A.	497
Martins, O.	133
Martins, R.	147
Martins, R. F.	121, 103
Maspoch, M.Ll.	647, 667
Mateos, M.	339
Matos, C.	147
Matos, J.C.	399, 417
McNally, P.	559
Mendes, I.R.	155, 345
Méndez, D.	91
Mesmacque, G.	375, 749, 795
Mestra, A.	51
Miengo, P.	637
Miguel, S.	679
Miranda, V.	565
Miranda-Paniagua, E.	795
Molina-Aldareguía, J. M.	161, 191, 209
Monsalve, A.	447
Monteiro, J.	357
Montero, R.	503
Morais, J.J.L.	37, 47, 57
Moreira, P.M.G.P.	361, 453, 613, 783
Moreno, B.	423
Moreno, R.	179
Morgado, T.L.	75, 109
Natal Jorge, R.	577
Navarro, C.	589, 729, 735
Nieto, I.	63

Nowell, D.	547
Ocaña, I.	773, 801
Ocaña, I.	801
Oropeza, J.	667
Ortiz, M.	527
Palomo, Á.	253
Pariente, I. F.	723
París, F.	173
Pastor, J. Y.	411
Pastor, J. Y.	253
Pastrama, S.D.	361
Patterson, E.A.	315
Pavón, J.	63
Peças, P.	807
Pedrejón, J. L.	801, 351
Peixoto, D.F.C.	619
Peñuelas, I.	503
Perea, G. B.	41
Pereira, A.M.	789
Pereira, F.A.M.	47
Pereira, R. M. G.	571
Pérez-Bahillo, M.	607
Pérez-Castellanos, J.L.	565, 595
Pérez-Rigueiro, J.	41
Perpétuo, G.	435
Pinilla, P.	685
Pinto, A.M.G.	155, 345
Pires, F. M. A.	583
Planas, J.	265, 509
Plaza, G. R.	41
Polanco, J. A.	631, 637
Porrás-Soriano, R.	259
Preciado, M.	297
Queirós, E.R.M.A.	57
Radi, E.	509
Ramirez, L.	447
Reis, F.	583
Reis, L.	429, 435
Reis, P.N.B.	197
Renart, J.	221
Ribeiro, A.S.	387, 405
Ribeiro, J.	357
Ricardo, L. C. H.	115, 441
Richardson, M.O.W.	197
Richter-Trummer, V.	361, 453, 613
Ridruejo, Á.	203
Rivera, S.	711
Rodrigues, Hugo	121
Rodríguez Argüelles, D.	461
Rodríguez, C.	309, 503, 667, 711, 723
Rodríguez, J. A.	63
Rodríguez, J.	657, 661, 673
Rodríguez, M.	209, 247
Rodríguez, R.	717
Rodríguez, T.	533
Rodríguez-Martín, R.	773, 801
Rojo, F.J.	31
Rubio-Gonzalez, C.	795
Ruiz, A.	749
Ruiz, E.	91

Ruiz, G.	259
Ruiz, G.	271, 277
Ruiz-Hervias, J.	497, 767
Sabsabi, M.	589
Salazar, A.	653, 661, 673
San Cristóbal, J. R.	71
Sánchez, J.	515, 521
Sánchez, J.	533
Sánchez-Gálvez, V.	241, 321
Sanchez-Soto, M.A.	653
Sancho, J.M.	265
Sanjurjo, P.	723
Santana, O. O.	667
Santos, C.L.	57
Sanz, B.	265
Sarasola, B.	801
Sauceda, S.S.	197
Saucedo, L.	271
Segovia, A.	653, 657
Segurado, J.	161
Serrano, B.A. S.	127
Serrano, R.	527
Siegele, D.	393
Siegmann, P.	315
Silva, J.M.	553
Silva, P.	103, 121
Silva, R.F.	345
Sinnema, G.	783
Sousa e Brito, A.	75
Stickle, M.M.	509
Suárez, J.C.	679, 685
Tamayo-Ariztondo, J.	191
Tarifa, M.	277
Tavares, S.M.O.	139, 613
Teixeira-Dias, F.	565
Toledano, M.	447
Toribio, J.	399, 417, 467, 705, 717, 741
Torres, Y.	63
Tur, M.	589
Turon, A.	215
Valido, A.	133
Valiente, A.	497, 767
Varon, J.M.	473
Vaz, M.A.P.	357, 361
Vázquez, J.	729, 735
Velasco, J.I.	647
Velázquez, J.	647
Ventura, G.	235
Vergara, D.	741
Vicens, J.	221
Vidal, C.	807
Vilaça, P.	807
Windisch, M.	783
Xavier, J.M.C.	47, 149
Yu, Rena C.	259, 271, 277
Zahr Viñuela, J.	595
Zapatero, J.	423
Zhang, X.	277